

A textbook of

**Nanoscience
and
Nanotechnology**

A textbook of
**Nanoscience
and
Nanotechnology**

T. PRADEEP

With: A. Ashokreddy, B. R. Buergi, A. Chainani, J. Chakrabarti, S. K. Das,
N. DasGupta, P. A. Joy, M. A. H. Muhammed, G. U. Kulkarni,
K. Manzoor, R. Mukhopadhyay, A. S. Nair, T. Pal, S. K. Pati,
G. V. P. Kumar, V. K. Pillai, E. Prasad, R. Philip, V. R. R. Kumar,
P. R. Sajanlal, A. K. Samal, E. S. Shibu, T. S. Sreeprasad, C. Vijayan



Tata McGraw Hill Education Private Limited

NEW DELHI

McGraw-Hill Offices

New Delhi New York St Louis San Francisco Auckland Bogotá Caracas
Kuala Lumpur Lisbon London Madrid Mexico City Milan Montreal
San Juan Santiago Singapore Sydney Tokyo Toronto



Tata McGraw-Hill

Published by the Tata McGraw Hill Education Private Limited,
7 West Patel Nagar, New Delhi 110 008.

Copyright © 2012, by T. Pradeep

No part of this publication may be reproduced or distributed in any form or by any means, electronic, mechanical, photocopying, recording, or otherwise or stored in a database or retrieval system without the prior written permission of the publishers. The program listings (if any) may be entered, stored and executed in a computer system, but they may not be reproduced for publication.

This edition can be exported from India only by the publishers,
Tata McGraw Hill Education Private Limited

ISBN (13): 978-1-25-900732-3

ISBN (10): 1-25-900732-4

Vice President and Managing Director—Asia Pacific Region: *Ajay Shukla*

Publishing Manager—Professional: *Praveen Tiwari*

Editorial Researcher—Science, Technology and Computing: *Sushil Gupta*

Senior Production Executive: *Rita Sarkar*

Asst. General Manager—Sales and Business Development: *S Girish*

Deputy Marketing Manager—Science, Technology and Computing: *Rekha Dhyani*

General Manager—Production: *Rajender P Ghansela*

Manager—Production: *Reji Kumar*

Information contained in this work has been obtained by Tata McGraw-Hill, from sources believed to be reliable. However, neither Tata McGraw-Hill nor its authors guarantee the accuracy or completeness of any information published herein, and neither Tata McGraw-Hill nor its authors shall be responsible for any errors, omissions, or damages arising out of use of this information. This work is published with the understanding that Tata McGraw Hill and its authors are supplying information but are not attempting to render professional services. If such services are required, the assistance of an appropriate professional should be sought.

Typeset at Le Studio Graphique, Guru Shivir, 12, Sector 14, Gurgaon 122 001, and printed at

XXXXXXXXXXXXXXXXXXXXXXXXXXXX

Cover Design: Kapil Gupta, New Delhi

Cover Printer: XXXXXXXXXXXXXXXXXXXX

XXXXXXXXXXXXXXXXXXXX

To
Our Parents

PREFACE

Nanoscience and nanotechnology (NS&NT) manifests the convergence of various disciplines. This convergence, although has resulted in the disappearance of boundaries, has also brought forth the uniqueness of specific areas and contributed to the creation of new disciplines. For example, nanobiotechnology is the result of convergence of nanotechnology and biotechnology, the uniqueness of science at the nanometer length scales has exposed completely new directions in this area. This may be stated for other sub-areas such as nanochemistry, nanomedicine, nanomaterials, etc. These branches of science have produced newer instrumentation, methodologies and approaches. As a result, uniqueness of these areas can be observed, not only in the subject itself but also in the way in which these areas are pursued.

Nanotechnology or nanoscience is not a single discipline. It is not to be viewed as a discipline similar to electronics, semiconductor technology, biotechnology, chemical technology, or metallurgy, which also represent convergence of disciplines in some sense. However, NS&NT is in fact all and more of these. This implies that a student of this area should be in a position to appreciate the confluence of areas. How can pedagogy adapt to the rapidly evolving and smearing boundaries of disciplines? This appears to be the central issue of concern while teaching NS&NT. This is true of all emerging areas, all of which happen at the boundaries of disciplines. There is no single area in which this collapse and smearing of disciplines is manifested better than in NS&NT.

Historically, scientific disciplines have diverged from one another in the course of establishment of the subjects. The areas of overlap between disciplines have reduced making each discipline independent of the other. In nanoscience, an opposite trend is visible, as stated earlier. Convergence has been manifested in other areas such as informatics, biotechnology, genetic engineering, etc., in the recent past. However, the coalescence of disciplines seen here is unprecedented. This is dictated by the requirements of the discipline wherein each discipline finds that interdependence allows growth.

Investigation of matter at the nanometer length scale was possible because of the development of tools, which allowed seeing and measuring things. This unprecedented capability made it possible to look at problems such as motion of single molecules, chemical reactions at surfaces, consequences of chemical changes at single molecule level and processes within cells. Unprecedented capability to manipulate matter at the nanometer scale is a central aspect of development of the discipline. This

obviously makes one realize that instrumentation is central to the evolution of the area. This also makes one realize that convergence of technologies is required to make new science.

Disciplines have to be taught separately but may be converged later, while discussing advanced areas. This offers a new paradigm shift in pedagogy. It might also be possible to teach disciplines from a unified stand point, wherein basic sciences are dealt within totality rather than in isolation. Thus, practicing NS&NT can have implications to the structuring of curricula. A unified curriculum is indeed a difficult task, especially when the boundaries are rigid. In fact most of our traditional subjects do not allow modifications. Introducing anything new must happen at the expense of the allotted teaching hours and that means reducing the contents in other sections. This is contested firmly and as a result modifications do not get adopted without strong opposition.

Opportunities decide the development of a course. Nanotechnology avenues have not come up adequately in the industry right now. The opportunities currently being developed are in areas in which an understanding of traditional disciplines is more important than knowledge of nanotechnology. This refers to chemistry, physics, materials science, biotechnology, biochemistry, molecular biology, etc. Thus an overemphasis of nanotechnology practices and techniques at the expense of traditional disciplines would put the students in a disadvantageous position. This is also true when students wish to proceed for higher learning after a nanotechnology course.

The foregoing has important implications to the level at which the course is pitched. Nanoscience and Nanotechnology should be offered preferably at a level in which the core discipline is appreciated. Thus the NT course is better offered at the masters level, preferably as an MS, which would essentially add more course content to introduce NS&NT, without removing material from the core disciplines. This has to be done with practical emphasis in NS&NT as courses are better understood and appreciated while being practiced. This kind of an integrated approach is necessary to adopt the new graduates into the evolving research arena where most students will be absorbed. Even the traditional manufacturing areas in which nanotechnology graduates may have a possibility to get employed also need strong foundations in the core areas.

The present book is designed to be a complete textbook for such an advanced programme at the masters level. It assumes that the undergraduate courses, whichever one chooses, have been dealt with at sufficient rigour so that a superstructure can be built. Irrespective of the area of choice, this book allows the creation of the superstructure. It considers that the basic training on instrumentation can be acquired first followed by an appreciation of the theoretical basis and diverse variety of nanomaterials. The study could continue to specialized measurements and applications of nanomaterials. It also assumes that after the appreciation of materials, or while that process is underway, a suitable laboratory course can be designed which will emphasize the fundamental principles of technology at this length scale. An applications lab can be conducted while the theory course on applications is introduced. Depending on the constraints of the course in terms of time available, number of students and resources at disposal, some adjustments may be done in structuring the contents. However, we urge a strong laboratory programme side by side of the theory courses. In the absence of this, the intended benefits will not be passed on completely.

This book is a sequel to the book of one of the authors, *Nano: The Essentials*, which has been widely appreciated. We felt that an introduction to the experimental tools is an important aspect of understanding NS&NT. As a result, a section of the previous book on experimental methods with new additions, along with several new techniques has been added here. This book introduces a variety of new nanomaterials and also new areas of applications. It includes a discussion of societal implications. The book has an experimental course on NS&NT, with 15 experiments introducing various areas of practical applications. From these a selection of 10 to 12 experiments may be chosen to design a laboratory course.

In such a large and rapidly expanding area, it is nearly impossible to cover all. We are aware that some areas are left unexposed and in a few cases, the exposure is limited. These omissions will be removed as much as possible in the subsequent editions. Despite these limitations, we hope that the book meets most of the expectations. Please contact the authors through email (pradeep@iitm.ac.in) if there are constructive suggestions.

T. PRADEEP

ACKNOWLEDGEMENTS

This book is the result of an initiative started over five years ago. The very first ideas of this book were seeded during a meeting in February 2007 when an earlier book of the principal author, *Nano: The Essentials* had just come out. We had one meeting of all the authors in which we discussed the various aspects to be covered in a textbook. Over the next couple of years we had a series of discussions via email which resulted in several bits and pieces of this material. It had to be synthesized into a cohesive book, which took quite some time. For all that, we must first of all thank each other. As typical of any such large project, writing moved slowly. Although time was indeed difficult, all the authors were committed to the theme. That made it possible to keep the enthusiasm alive.

Several of our students offered critical suggestions and advices at various stages of the work. They looked through the chapters and made several comments and suggestions. Several figures had to be redrawn and they gladly helped in all these laborious activities. We thank Ammu Mathew, R.G. Hemalatha, Robin John and Anirban Som for going through the proofs. Vasudeva Bhat went through the appendices with extreme care. T.K. Keshav, Kulpreet Singh Viridi, B. Radha, V.V. Divya Rani, Somasundaram Vijay Harish and Shanti Nair are thanked for their support and technical contributions to various sections of the book.

We thank all our present and previous students, both in the classroom and in the lab, whose comments, questions and suggestions enriched our understanding of the subject.

All the publishers and authors readily agreed to reproduce their work, for which we are grateful. There have been a few websites from which we have used figures and we thank them for their kind permission. Several textbooks, monographs, review articles and websites have helped us in gathering information and it is our earnest hope that all the intellectual properties have been adequately acknowledged. In spite of the best intention, if any material has not been referenced adequately or appropriately we request the reader to point out such lapses, which will be corrected at the earliest available opportunity.

This work reaches you with the hard and sustained work of an excellent team at McGraw-Hill Education. We especially thank R. Chandra Sekhar, who was instrumental in taking up this assignment in the first place.

I would like to thank the Indian Institute of Technology Madras for encouragement. Financial support of the Curriculum Development Cell of the Centre for Continuing Education is acknowledged.

Finally we thank our spouses and children for their patience.

T. PRADEEP

CONTENTS

<i>Preface</i>	<i>vii</i>
<i>Acknowledgements</i>	<i>xi</i>
<i>Authors' Profiles</i>	<i>xxv</i>

PART ONE

Introduction

1. Nano: The Expanding Horizon	3
1.1 What is Nanoscience and Nanotechnology?	3
1.2 Why Nano?	6
1.3 Current Technologies and the Problems	7
1.4 Nano the Beginning	12
1.5 Nano and Energetics	16
1.6 Nano and Implications	18
<i>References</i>	19
<i>Additional Reading</i>	20
<i>Review Questions</i>	21

PART TWO

Experimental Methods of Investigation

2. Electron Microscopies	25
2.1 Introduction	25
2.2 Electron Microscopies	30
<i>References</i>	62
<i>Additional Reading</i>	62
<i>Review Questions</i>	62

3. Scanning Probe Microscopies	63
3.1 Introduction	63
3.2 Optical Microscopies for Nanoscience and Technology	74
<i>References</i>	82
<i>Additional Reading</i>	82
<i>Review Questions</i>	82
4. Photoelectron Spectroscopy for the Study of Nanomaterials	83
4.1 Introduction	84
4.2 Salient Features of PES	84
4.3 Technique of PES	85
4.4 Nomenclature	88
4.5 Applications	89
4.6 Complementary Techniques	96
4.7 Synchrotron Radiation	98
4.8 Metal Clusters and Nanoparticles	100
4.9 Semiconductor/Insulator Nanocrystals	106
4.10 Quantum Well States	108
4.11 Nanowires	110
<i>References</i>	113
<i>Additional Reading</i>	116
<i>Review Questions</i>	116
5. Structure of Materials by Diffraction Techniques	118
5.1 Merits/Demerits of X-ray vs Neutron	121
5.2 X-ray Diffraction	122
5.3 Rietveld Profile Refinement	125
5.4 The Crystallite Size	127
5.5 Broadening Due to Strain	127
5.6 Other Scattering Techniques in Vogue	128
5.7 Static Light Scattering (SLS)	128
5.8 Dynamic Light Scattering (DLS)	129
5.9 Small Angle Neutron/X-ray Scattering (SANS/SAXS)	129
5.10 Concept of Contrast Factor in SANS/SAXS Experiments	132
5.11 Reflectometry	133
<i>Review Questions</i>	134
6. Electroanalytical Techniques	137
6.1 Cyclic Voltammetry	138

6.2	Impedance Analysis	142
6.3	Differential Pulse Voltammetry	147
6.4	Scanning Electrochemical Microscopy	148
	<i>References</i>	153
	<i>Additional Reading</i>	154
	<i>Review Questions</i>	154
7.	Raman Scattering	155
7.1	Why is the Sea Blue?	155
7.2	Concept of Elastic and Inelastic Light Scattering	156
7.3	Instrumentation for Raman Scattering	159
7.4	Specific Examples of Raman Spectroscopy Application in Material Science	160
7.5	Emerging Methods in Raman Scattering	163
7.6	Conclusions	171
	<i>References</i>	172
	<i>Additional Reading</i>	174
	<i>Review Questions</i>	174
8.	Miscellaneous Techniques	176
8.1	Mass Spectrometry	176
8.2	Contact Angle (CA) Measurements	182
8.3	Conductivity Measurements	185
8.4	Zeta Potential	187
8.5	Common Analytical Tools Adapted for the Investigation of Nanomaterials	188
	<i>References</i>	198
	<i>Additional Reading</i>	198
	<i>Review Questions</i>	199

PART THREE

Synthesis

9.	Synthesis of Nanomaterials	203
9.1	Introduction	203
9.2	General Issues of Concern	205
9.3	Synthetic Methods: Common Issues of Concern	209
9.4	Variety in Nanomaterials	211
9.5	Microemulsion-based Methods for Nanomaterials	222
9.6	Solvothermal Synthesis	224

9.7	Synthesis Using Supports	225
9.8	Using Biology	227
9.9	Magnetic Nanomaterials	227
9.10	Inert Gas Condensation	228
9.11	Anisotropic Nanoparticles	228
9.12	Other Nanomaterials	230
9.13	Conclusions	234
	<i>References</i>	235
	<i>Additional Reading</i>	247
	<i>Review Questions</i>	247

PART FOUR

Understanding Nanosystems

10.	Theoretical Understanding of Nanosystems	251
10.1	Introduction	252
10.2	Optical Properties of Bulk Semiconductors	252
10.3	Quantum Mechanics of Low-Dimensional Structures	253
10.4	Exciton Confinement in Quantum Dots	256
10.5	Quantum Mechanics of Confined Nanoclusters	257
10.6	Band Gap Engineering and Optical Response	259
10.7	Computational Methods to Understand Nanoscale Phenomena	260
10.8	Conclusions	278
	<i>References</i>	278
	<i>Additional Reading</i>	279
	<i>Review Questions and Suggested Project Work</i>	280

PART FIVE

Advanced Nanomaterials

11.	Quantum Clusters of Gold	283
11.1	Introduction	283
11.2	Synthetic Approaches	285
11.3	Characterisation Techniques	290
11.4	Electronic Structure and Optical Properties	294
11.5	Photoluminescence	295

11.6	Magnetism	303
11.7	Chemical Reactivity	304
11.8	Quantum Clusters as Catalysts	307
11.9	Conclusions	308
	<i>References</i>	308
	<i>Additional Reading</i>	310
	<i>Review Questions</i>	310
12.	Nanoparticle Crystals	311
12.1	Introduction	311
12.2	3-D Superlattices (SLs) of Metals	313
12.3	Semiconductors	325
12.4	Other Important SLs	325
12.5	3D Superlattices (SLs) of Binary Nanoparticles (BNSLs)	329
12.6	Magnetic Nanoparticle SLs	332
12.7	Applications of SLs	333
12.8	Interesting Properties in SLs	338
12.9	Conclusions	340
	<i>References</i>	340
	<i>Additional Reading</i>	342
	<i>Review Questions</i>	342
13.	Anisotropic Nanomaterials	343
13.1	Introduction	343
13.2	One-, Two-, and Three-dimensional Nanoparticles	345
13.3	General Strategies for the Synthesis of One-, Two- and Three-dimensional Nanostructures	346
13.4	Properties of Anisotropic Nanoparticles	367
13.5	Applications of Anisotropic Nanomaterials	368
13.6	Conclusions	373
13.7	Prospects for the Future	373
	<i>References</i>	374
	<i>Additional Reading</i>	378
	<i>Review Questions</i>	379
14.	One-Dimensional Nanostructures: Nanorods and Nanowires	380
14.1	Introduction	381
14.2	Gold Nanorods	381
14.3	General Strategies of Synthesis	381

14.4	Properties	388
14.5	Characterization Techniques	390
14.6	Applications	391
14.7	1-D Nanostructures of Tellurium	395
14.8	Tellurium Nanowires	403
14.9	Properties	408
14.10	Conclusions	409
	<i>References</i>	409
	<i>Additional Reading</i>	411
	<i>Review Questions</i>	412
15.	Assembly of Anisotropic Nanostructures	413
15.1	Introduction	413
15.2	Gold Nanorod Assembly	415
15.3	Assembly of Anisotropic Structures of Other Metals	447
15.4	Assembly of Anisotropic Structures of CdS/CdSe	452
15.5	Some Examples of Assembly of Anisotropic Structures of Other Materials	456
15.6	Some Applications	460
15.7	Conclusions	466
	<i>References</i>	466
	<i>Additional Reading</i>	473
	<i>Review Questions</i>	473
16.	Dendritic Nanostructures	475
16.1	Introduction to Macromolecules and Dendrimers	475
16.2	Conclusions	487
	<i>References</i>	487
	<i>Additional Reading</i>	488
	<i>Review Questions</i>	489
17.	Nanohybrid Systems	490
17.1	Introduction	491
17.2	Classification of Organic-Inorganic Hybrids	491
17.3	Preparation of Organic-Inorganic Hybrids	492
17.4	Mesoporous Organo-Inorganic Hybrids	493
17.5	Evaporation-Induced Self-Assembly (EISA)	495
17.6	Nano-building Blocks-Based Hybrids	502
17.7	Methods to Graft Polymer Chains to the Nano-building Block Surface	508
17.8	Biohybrids	513

17.9	Mechanical Properties	519
17.10	Applications of Organic-Inorganic Hybrid Materials	524
	<i>References</i>	531
	<i>Additional Reading</i>	533
	<i>Review Questions</i>	534

PART SIX

Nanotechnology: Some Examples

18.	Silicon MOS Transistor from Micro to Nano	537
	18.1 Introduction	537
	18.2 Downscaling and Moore's Law	538
	18.3 Challenges for Nano-MOSFETs	538
	18.4 Emergence of NEW Materials	541
	18.5 Novel Device Structures	547
	18.6 Innovations in Process Technology	550
	18.7 Conclusions	552
	<i>References</i>	552
	<i>Additional Reading</i>	555
	<i>Review Questions</i>	555
19.	Molecular Electronics	556
	19.1 Top-down vs Bottom-up	556
	19.2 Why Molecules?	557
	19.3 Experimental Advances	558
	19.4 Transport—How to Understand	560
	19.5 Mechanisms of Molecular Transport	562
	19.6 Advanced Applications	563
	19.7 Conclusions	566
	19.8 Single Level Programme	567
	<i>References</i>	569
	<i>Additional Reading</i>	570
	<i>Review Questions</i>	570
20.	Nanolithography	572
	20.1 Nanolithography	572
	20.2 Lithography: Concepts and Definition	573
	20.3 Conventional Lithography	574

20.4	Lithography Techniques	581
20.5	Nanomanipulation	590
20.6	Conclusions	592
	<i>References</i>	592
	<i>Additional Reading</i>	594
	<i>Review Questions</i>	594
21.	Nanomagnetism	595
21.1	Magnetism and Magnetic Materials	595
21.2	Basics of Magnetism	596
21.3	Magnetic Domains and Anisotropy	600
21.4	Magnetic Nanostructures	601
21.5	Magnetism of Nanosized Materials	603
21.6	Synthesis of Magnetic Nanoparticles	607
21.7	Applications of Nanomagnetic Materials	609
	<i>References</i>	614
	<i>Additional Reading</i>	616
	<i>Review Questions</i>	616
22.	Nanobiology	617
22.1	Introduction	617
22.2	Interaction Between Biomolecules and Nanoparticle Surfaces	618
22.3	Influence of Electrostatic Interactions in Binding of Proteins to Nanoparticles	620
22.4	The Electronic Effects of Biomolecule-Nanoparticle Interaction	622
22.5	Applications of Nanomaterials in Biology	624
22.6	Theragnostics	650
22.7	Challenges in the Translation of Nanomedicine	651
22.8	Conclusions and Future Perspectives	653
	<i>References</i>	654
	<i>Additional Reading</i>	660
	<i>Review Questions</i>	661
23.	Optical Nonlinearity in Nanoscale Materials	662
23.1	Introduction	663
23.2	Optical Non-linearities in Metal Nanostructures	670
23.3	Optical Non-linearities in Semiconductor Nanocrystallites	674
23.4	Experimental Techniques	677
23.5	Technology Perspectives	685

<i>References</i>	685
<i>Additional Reading</i>	687
<i>Review Questions</i>	688
24. Nanomaterials for Environmental Remediation	689
24.1 Nanoparticles: Environmental Remediation by Chemical Degradation/Removal of Contaminants	690
24.2 Nanomaterials as Sorbents	698
24.3 Nanofiltration—A New Technique for Clean Water	699
24.4 Dendrimers—the Nanoreactors for Remediation	702
24.5 Carbon Nanomaterials—Versatile New Adsorbents for Remediation	702
24.6 Nanoscale Biopolymers—Benign Materials for Remediation	706
24.7 Conclusions and Future Prospects	707
<i>References</i>	707
<i>Additional Reading</i>	710
<i>Review Questions</i>	711
25. Catalysis Using Transition Metal Nanoclusters	712
25.1 Introduction	712
25.2 Growing and Full Grown Particles as Redox Catalysts	715
25.3 Reactions Catalysed by Mono and Bimetallic Nanoparticles	719
25.4 Size-Dependent Catalysis	725
25.5 Shape-Dependent Catalysis	727
25.6 Conclusions	728
<i>References</i>	728
<i>Additional Reading</i>	730
<i>Review Questions</i>	731
26. Nanofluids for Cooling Technology	732
26.1 Challenges in Cooling Technology	733
26.2 Evolution of Nanofluids from Micro-suspensions	734
26.3 Features and Characteristics of Nanofluids	735
26.4 Advantages of Nanofluids	736
26.5 Application of Nanofluids	738
26.6 Preparation of Nanofluids	739
26.7 Thermal Conductivity Enhancement in Nanofluids	741
26.8 Theories on Thermal Conductivity of Nanofluids	746
26.9 Convective Heat Transfer Studies in a Laminar Thermally Developing Flow	751

26.10	Convective Heat Transfer Studies in a Turbulent Flow Regime	758
26.11	Scaling Analysis	759
	<i>References</i>	761
	<i>Additional Reading</i>	765
	<i>Review Questions</i>	765

PART SEVEN

Nano and Society: A Dialogue

27A.	Nano and World Societies	769
	<i>Societal Aspects of Nanoscale Science, Engineering and Technology</i>	
27.1	Initial Reflections on a Science with a Mission to Promote Socioeconomic and Human Development	770
27.2	Studying the Nano-realm	772
27.3	Cross-perspectives I-III	773
	<i>References</i>	775
	<i>Additional Reading</i>	775
	<i>Review Questions</i>	776
27B.	Nano-Generated Wealth and World Societies	777
	<i>Nano-Economics: A New Socioeconomic Divide?</i>	
27.1	Disenchanted <i>Now You Can I</i> : the “Nano-hype”	778
27.2	Disenchanted <i>Now You Can II</i> : the “Nano-divide”	782
27.3	Disenchanted <i>Now You Can III</i> : the “Nano-business”	783
27.4	An Ethics Perspective on the Global Trade with Nanomaterial-based Technologies	787
	<i>References</i>	789
	<i>Additional Reading</i>	791
	<i>Review Questions</i>	791
27C.	Nanomaterials: World Societies and the Natural Environment	792
	<i>The Rise of Nanotoxicology</i>	
27.1	Public Debates on the Downsides of Nanotech	793
27.2	Handling Issues Revolving around Nanomaterials with Responsibility and Care	796
27.3	Epistemological, Methodological, and Practical Challenges in the Exploration of Technoscientific Newlands	799

27.4	Afterthoughts on “Grounded” Nanotoxicology	803
	<i>References</i>	804
	<i>Additional Reading</i>	806
	<i>Review Questions</i>	806
27D.	Nano-Politics: Governance and Regulation of Nanotechnoscience	807
	<i>Policy Debates and Public Engagement</i>	
27.1	Actual and Perceived Needs of Governing and Regulating Nanotechnoscience	808
27.2	Public Engagement along Fault Lines: Searching for “Cross-perspectives”	813
27.3	Closing Remarks on “Cross-perspectives”	816
	<i>References</i>	816
	<i>Additional Reading</i>	819
	<i>Review Questions</i>	820

PART EIGHT

Appendices: *A Practical Course on Nanoscience and Nanotechnology*

Part I



1.	Verification of the Beer-Lambert Law using Gold Nanoparticles	823
2.	Adsorption of Biomolecules on Gold Nanoparticles	827
3.	Determination of the Band Gap of Semiconductor Nanoparticles	836
4.	Nanochemistry of Silver Nanoparticles in Converting <i>p</i> -Nitrophenol to <i>p</i> -Aminophenol	841
5.	Surface Enhanced Raman Scattering Activity of Silver Nanoparticles	845
6.	Conversion of Gold Nanorods into Gold Nanoparticles	850
7.	Removal of Mercury by Supported Nanoparticles	854
8.	Demonstration of Liquid Magnets	860
9.	Bimetallic Nanoparticles	865
10.	Gold Nanoparticles for Enhanced Visual Detection of Pesticides	877
11.	Reactivity of Gold Clusters Towards Metal Ions	882
12.	Study of Silver Nanoparticles	887
13.	Synthesis of ZnO Nanoparticles	894
14.	Preparation of Tellurium Nanowires	899
15.	Synthesis of Luminescent Gold Nanoparticles by Core Etching	903



Part II




1. Diverse Nanoparticles Prepared by Various Routes	909
---	-----



<i>Index</i>	939
--------------	-----




AUTHORS' PROFILES




	Affiliation	Short Biography
	<p>Director, UTN Education & Research Pvt. Ltd. C/o. C-TIDES, 303A, Department of Management Studies, Indian Institute of Technology Madras, Chennai 600 036 INDIA</p>	<p>A. Ashokreddy graduated from IIT Madras with B.Tech in Civil Engineering in 2007. He worked as an Engineer at BPCL and in various research projects at IIT Madras in the field of Nanotechnology. Currently he is serving as Director at UTN Education & Research Pvt. Ltd.</p>
<p>A. Ashokreddy</p>		
	<p>Research Scholar, ARI, NUS Graduate Fellow, Tembusu College, NUS, Department of Sociology, Faculty of Arts and Social Sciences, National University of Singapore, Singapore 117 570 SINGAPORE</p>	<p>Birgit R. Buergi received her MPhil in Social Anthropology from the University of Cambridge, UK, and she holds a <i>Laurea</i> in Sociology from the University of Urbino, Italy. Emergent social life forms and practices in bioscientific knowledge generation in Southeast Asia has been the analytic focus of her work in the Social Studies of Science and Technology (STS). In her latest publication, Birgit cross-examines the institutional relationship between global health financing practices and collaborative malaria drug research and development (R&D). Her doctoral project investigates academic migration in relation to citizenship pluralism in Singapore and Thailand.</p>
<p>Birgit Ruth Buergi</p>		




	Affiliation	Short Biography
	RIKEN Harima Institute, SPring-8 Coherent X-ray Optics Laboratory, Excitation Order Research Team, 1-1-1, Kouto, Sayo-cho, Hyogo 679 5148 JAPAN	A. Chainani obtained his Ph.D from the Indian Institute of Science in 1993 and did post-doctoral studies at Tohoku University, Sendai, Japan. He then joined Institute for Plasma Research, Gandhinagar, India to work on plasma-based synthesis of materials for applied research. For the past 10 years he is working at RIKEN Harima Institute at Spring-8, a leading synchrotron centre in Japan. He works on the electronic structure of emergent materials, superconductors, Kondo and Mott-Hubbard systems. He has authored more than 150 papers in scientific journals.
Ashish Chainani		
	Associate Professor, Department of Chemical, Biological and Macromolecular Sciences, S.N. Bose National Centre for Basic Sciences, Salt Lake, Kolkata 700 098 INDIA	Jaydeb Chakrabarti earned his Ph.D from the Indian Institute of Science in 1995 and had post doctoral training at the AMOLF, The Netherlands. His research interest includes Statistical Mechanical description of static and dynamic phenomena in complex and soft condensed matter systems, including those of biological interests, both in the bulk and under confinement.
Jaydeb Chakrabarti		
	Professor, Department of Mechanical Engineering, Indian Institute of Technology Madras, Chennai 600 036 INDIA	Sarit K. Das earned his Ph.D from Sambalpur University in 1994 and had post doctoral research at University of BW Hamburg. He has authored more than 200 papers in journals and conferences and four books including a book on Nanofluids. He is the editor in chief of International Journal of Micro Nano Scale Transport. He is a fellow of the Indian National Academy of Engineering and National Academy of Sciences, India. He was the Peabody Professor at the Massachusetts Institute of Technology.
Sarit K. Das		

	Affiliation	Short Biography
	Professor, Department of Electrical Engineering, Indian Institute of Technology, Madras, Chennai 600036 INDIA	Nandita DasGupta received her Ph.D degree from IIT Madras in 1988. She was awarded Alexander von Humboldt Fellowship in 1991 and spent one year in Technische Hochschule Darmstadt, Germany. Her research interest is in the area of Semiconductor Devices and Micro-Electro-Mechanical Systems (MEMS). She has more than 100 research publications in International Journals and Proceedings of International Conferences and has co-authored a book “Semiconductor Devices—Modeling & Technology”. She has also developed a 40 hour video course on “VLSI Technology” for the web-based NPTEL program.
Nandita DasGupta		
	Scientist, Materials Chemistry Division, National Chemical Laboratory, Pune 411008 INDIA	P.A. Joy earned his Ph.D from the Indian Institute of Science in 1990 and had post doctoral training at IISc and IIT Madras. He has authored 175 scientific papers in journals. He is involved in the research work on magnetic and ceramic materials.
P.A. Joy		
	Post-doctoral Research Fellow, Department of Chemistry and Biochemistry, Florida State University, Tallahassee 32310 USA	M.A. Habib Muhammed earned his Ph.D from Indian Institute of Technology Madras in 2010 under the guidance of Prof. T. Pradeep. He is currently pursuing post doctoral research with Prof. Hedi mattoussi at Florida State University. He has authored 10 scientific papers in journals and is a co-author of a chapter in “Advanced fluorescence reporters in chemistry and biology II” published by Springer. He is involved in the synthesis and applications of noble metal quantum clusters.
M.A. Habib Muhammed		


	Affiliation	Short Biography
	<p>Professor and Dean, Academic, Chemistry & Physics of Materials Unit and DST Unit on Nanoscience, Associate Faculty member, ICMS Jawaharlal Nehru Centre for Advanced Scientific Research, Jakkur P.O., Bangalore 560 064, INDIA; Adjunct Research Professor, Birck Nanotechnology Centre, Purdue University, USA</p>	<p>G.U. Kulkarni obtained his Ph.D from the Indian Institute of Science in 1992 and carried out postdoctoral research at IISc and Cardiff University during 1993–95. He is at JNCASR since 1995 carrying out research in various areas of Nanoscience and Nanotechnology. Specific interests include innovating methods for direct write nanolithography leading to devices, molecular crystals and metal nanocrystal assemblies. He has published over 190 research articles and coauthored a book on Nanocrystals. He is recipient of many awards including Sir C.V. Raman Young Scientist Award.</p>
	<p>Professor, Amrita Centre for Nanoscience & Molecular Medicine, Amrita Institute of Medical, Science, Cochin, Kerala 682 041 INDIA</p>	<p>K. Manzoor earned his Ph.D in Physics from Defence Research Organization (DRDO) in 2004 and worked as a staff-scientist at DRDO during 1998–2006. His contributions to the area of nanotechnology for defence applications lead to prestigious awards such as Best DRDO laboratory Scientist–2003, National DRDO Young scientist–2004 and DRDO Technology award 2006. During 2007 he moved to Amrita and started research work in the area of Cancer – Nanomedicine with support from Marie-Curie Foundation, EU and Dept. of Biotechnology, Govt. of India. He has 45 international publications and 10 filed patents.</p>
	<p>Scientist, Solid State Physics Division, Bhabha Atomic Research Centre, Mumbai 400 085 INDIA</p>	<p>R. Mukhopadhyay earned his Ph.D from the University of Mumbai. He worked as visiting scientist at ISIS Facility, Rutherford Appleton Laboratory, UK during 1990–1991 and visiting professor at Universidad del Pais Vasco, Spain during 1996–1997. He has authored over 100 scientific papers in journals. He is a professor of Homi Bhabha National Institute. His research interest includes phase transition in condensed matter, molecular diffusion, transport, etc. He has expertise in neutron scattering technique and instrumentation.</p>

	Affiliation	Short Biography
	Associate Professor, Amrita Centre for Nanoscience, Kochi, Kerala, INDIA	A. Sreekumar Nair graduated with a Ph.D in Chemistry from Indian Institute of Technology (IIT) Madras (2006) and subsequently became a JSPS postdoctoral fellow (2006–2008) in Japan. He also had postdoctoral training (2008–2012) at the Healthcare and Energy Materials Laboratory of National University of Singapore. His research interests include fabrication of materials for energy conversion and storage, solar hydrogen, nanotechnology-based environmental remediation and probing charge transport mechanism in monolayer-protected clusters and 3-D superlattices.
A. Sreekumar Nair		
	Professor, Department of Chemistry, Indian Institute of Technology Kharagpur, Kharagpur 721302 INDIA	Tarasankar Pal obtained Ph.D (1979) and D.Sc.(2006) degree and visited Oak Ridge National Laboratory, GITech., USA; University of Kent, Manchester, UK; University of Paris Sud, France; Tokyo University of Science and IMS, Japan; University of Alberta, Canada and institutions in Italy, Germany and Taiwan on Visiting Professorships. He has 270 published papers and initiated research involving metal hydrosol (metal nanoparticles) in India which dates back to 1986 and now studies SERS and fluorescence with transition metal nanoparticles. One of his discoveries has become an 'arsenic' detection kit.
Tarasankar Pal		
	Professor, Theoretical Sciences Unit and New Chemistry Unit, Jawaharlal Nehru Centre for Advanced Scientific Research, Bangalore 560064 INDIA	Swapan K. Pati obtained his Ph.D from the Indian Institute of Science in 1998 and had post doctoral trainings at the University of California, Davis and Northwestern University, Evanston. He has authored a large number of research papers in eminent scientific journals and has edited a book entitled "Graphene and its fascinating attributes", World Scientific Publishing, Singapore. He is involved in developing many models and new techniques which can be used to investigate the classical and quantum phenomena in a large class of systems, ranging from small molecules to extended materials.
Swapan K. Pati		

	Affiliation	Short Biography
	Faculty of Physics and Chemistry, Indian Institute of Science Education and Research (IISER), Pune, INDIA	G.V. Pavan Kumar obtained his Ph.D from Jawaharlal Nehru Center for Advanced Scientific Research (JNCASR), Bangalore working on Raman microscopy and its applications in plasmonics. Subsequently, he was an ICFO post-doctoral fellow at ICFO—The Institute of Photonics Sciences, Barcelona and post-doctoral researcher at Purdue University. In 2010, he joined the faculty of Physics and Chemistry at Indian Institute of Science Education and Research (IISER) Pune, India with Ramanujan Fellowship (DST, India). His research interests are: optical physics, multi-scale photonics, plasmonics and Raman scattering.
G.V. Pavan Kumar		
	Director, CSIR-Central Electrochemical Research Institute (CECRI), Karaikudi 630 006, Tamil Nadu, INDIA	Vijayamohan K. Pillai received his Ph.D from the Indian Institute of Science, Bangalore. He has authored over 200 publications and 20 patents in electrochemistry and materials chemistry. His research interests include advanced materials, fuel cells, supercapacitors and rechargeable batteries. He is a member of the editorial board of Bulletin of Materials Science and is a Fellow of the Indian Academy of Sciences.
Vijayamohan K. Pillai		
	Assistant Professor, Department of Chemistry, Indian Institute of Technology, Madras, Chennai 600 036 INDIA	E. Prasad graduated from Kerala University working at NIIST (CSIR), Thiruvananthapuram. He worked as a post-doctoral fellow at Universities of Bonn, Texas Tech and Lehigh prior to joining the Chemistry Department, IIT Madras. He has been an AvH fellow at University of Bonn, Germany during 2002–2003. Prasad has authored 29 scientific papers in science journals. He has been trained in pedagogical teaching for higher education in science.
E. Prasad		

	Affiliation	Short Biography
	<p>Associate Professor, Light and Matter Physics Group, Raman Research Institute, C.V. Raman Avenue, Bangalore 560 080 INDIA</p>	<p>Reji Philip received his Ph.D from the Cochin University of Science and Technology in 1994 and had post doctoral trainings at the Tata Institute of Fundamental Research, Mumbai, and at the University of Regensburg, Germany. He has been a visiting scientist at the University of Massachusetts, Boston, and at the University of Central Florida, Orlando. He is an author of more than 100 peer-reviewed journal articles. His current research interests include Nonlinear Optics of nanostructured materials and ultrafast laser-induced plasmas.</p>
<p>Reji Philip</p>		
	<p>Researcher, Department of Chemistry, Enoki/Kiguchi Laboratory, Graduate School of Science and Engineering, Tokyo Institute of Technology, Ookayama, Meguro, Tokyo 1450061 JAPAN</p>	<p>V.R. Rajeevkumar obtained his Ph.D from IIT Madras (India). He did a post- doctoral training at NUS (Singapore). Currently, he is a JSPS Fellow at Tokyo Institute of Technology, Japan. His research interests are unconventional electronic and magnetic properties of carbon nano-materials, single molecular junctions and Raman Spectroscopy of carbon nanostructures.</p>
<p>V.R. Rajeevkumar</p>		
	<p>Post-doctoral Fellow, School of Chemistry and Biochemistry, Georgia Institute of Technology, 901 Atlantic Drive, Atlanta, GA 30332-0400, USA</p>	<p>P.R. Sajanlal obtained his Ph.D degree in 2011 for his work on shape-controlled synthesis, characterization, and applications of anisotropic meso/nano materials from the Indian Institute of Technology Madras under the guidance of Prof. T. Pradeep. Currently he is working as a postdoctoral fellow in the School of Chemistry and Biochemistry at the Georgia Institute of Technology with Prof. Mostafa A. El-Sayed.</p>
<p>P.R. Sajanlal</p>		

	Affiliation	Short Biography
	Post-doctoral Research Associate, Departamento de Química Física, Universidade de Vigo, 36310, Vigo, SPAIN	Akshaya K. Samal received his M.Sc. degree in chemistry from the Sambalpur University, India and Ph.D degree in chemistry under the supervision of Prof. T. Pradeep from IIT Madras, India. Currently, he is continuing his post doctoral research with Prof. Luis M. Liz-Marzan at University of Vigo, Spain. His current research focuses on synthesis of anisotropic nanostructures and nanoparticle based biosensors using quantum dots.
	JSPS Fellow, Nano-Bioanalysis Group, Health Research Institute, National Institute of Advanced Industrial Science and Technology (AIST) 2217-14 Hayashi-Cho Takamatsu, Kagawa 761-0395 JAPAN	E.S. Shibu received his MSc degree in Chemistry from the University of Calicut, India, in 2004 and Ph.D degree in chemistry under the supervision of Prof. T. Pradeep from the Indian Institute of Technology Madras, India. Currently he is working as a JSPS fellow in National Institute of Advanced Industrial Science and Technology (AIST-Shikoku), Japan. His current work focuses on the synthesis and exploitation of multimodal nanomaterials for bioimaging and supramolecular nanomaterials for solar cells.
	Post-doc Researcher, Department of Chemical Engineering, 1005 Durland Hall, Kansas State University, Manhattan, Kansas, USA-66506	T.S. Sreeprasad earned his Ph.D from the Indian Institute of technology Madras in 2011 and is currently doing his post doctoral training at the Kansas state university. He joined Prof. T. Pradeep's research group in IIT Madras for his Ph.D. His area of interest concerns with the reactivity of anisotropic nanosystems. Currently he is working on the band gap engineering of graphene by simple chemical and physical processes. He has authored more than 20 scientific papers and is a co-inventor of more than 5 patent applications.

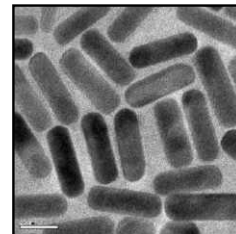
	Affiliation	Short Biography
	Professor, Department of Physics, Indian Institute of Technology Madras, Chennai 600 036 INDIA	C. Vijayan has done his M.Sc. and Ph.D from the Indian Institute of Technology, Madras, Chennai. His areas of interest are photonics and nonlinear optical properties of novel materials. He has authored 60 scientific papers in journals. He has guided 10 students for their Ph.D so far and has research collaborations with several international research groups.
C. Vijayan		

**PART
ONE**

Introduction

- **Nano: The Expanding Horizon**

NANO: THE EXPANDING HORIZON



“...the fluid preparations are... simply cases of pure gold in a divided state...”

M. Faraday, Experimental relations of gold (and other metals) to light, Philos. Trans. R. Soc. London, 1857, 147, 145

Nanoscience and nanotechnology refer to the science and technology of matter, manipulated at the atomic level. It is an area in which traditional disciplines converge. Chemists have been manipulating materials atom by atom or bond by bond throughout history. One could say that every synthetic event occurs at the nanoscale. Controlled synthesis made it possible to have life, which is a collection of the most efficient nanoscale processes. The best eco-friendly and efficient processes are all natural. Evolution therefore is the one which assembled the best nanoscale events. The science of artificial nanoscale objects learns from nature.

Learning Objectives

- Why nanotechnology?
 - Why nanometer is interesting and not nanosecond or nanoampere?
 - What are the connections between nanotechnology and biology?
 - What are wet and dry nanotechnologies?
 - What are the historical landmarks in this area?
-
-

1.1 WHAT IS NANOSCIENCE AND NANOTECHNOLOGY?

Nanoscience* is a compound word having two parts, nano and science. Although *nano* is a prefix as in nanometer, nanoampere, nanosecond, etc. referring to 10^{-9} , in nanoscience, it refers specifically to nanometer. Therefore, nanoscience is the science of objects in the size regime of nanometers. In this

* Nanochemistry, nanomaterials, nanobiology, nanobiotechnology, nanoelectronics, etc. are compound words, just as nanoscience. We will use this style throughout this book. However, there are instances where nano may be used as a distinct word.

size regime, matter exhibits unusual properties, which makes this science unique. The variation of properties as a function of size occurs in different materials differently. In some materials, it begins to be manifested early, whereas in others, it occurs at still lower dimensions. Thus the 'nano' regime of matter, where property manifestations are evident, vary. However, in general, it is now taken as the science of matter where constituent units are below 100 nanometer (nm) in dimension. Nanotechnology is the technology using objects or structures or phenomena at the nanometer scale. Macroscopic matter consisting of elementary units below this dimension is called a nanomaterial.

While properties of materials at the nanoscale are distinctly different from the bulk, the act of measurement of length at the nanometer does not offer any new phenomenon. Thus *nanometer per se* does not suggest anything unique. Similarly, measuring a quantity such as current and time at nanoampere and nanosecond precision, respectively, does not offer anything unusual. Thus it is the *nanometer* scale and not the *nanoscale* that is significant.

Several aspects have to be clarified in order to proceed further. The dimension refers to the *characteristic dimensions* and not to the length scale of the piece of matter under investigation along all axes. A nanosheet may not have nanometer dimensions along all axes. While the thickness of the sheet is in nanometers, the length and breadth may be in larger units. A nanowire has diameter in nanometers, but the length may be in micrometers. These materials are nanomaterials as the *characteristic dimension*, the width or the diameter in the cases mentioned, is in nanometers. These are characteristic dimensions as they *decide* the properties of the system. When the size of the object in length or breadth is varied, properties do not change and therefore, they are not the characteristic dimensions. A nanosphere has *radius* or *diameter* as its characteristic dimension. A nanosheet has *thickness* as the characteristic dimension, as it is this parameter which decides the properties and not the extent of the sheet area as that does not modify the properties. The concept of characteristic dimension is illustrated below (Fig. 1.1). It is important to recall that the characteristic dimension is much smaller than other dimensions one encounters in a given material. It is important to remember that in a given nanoscale object, for example in a nanowire, the length is much larger than the diameter so that it is referred to as a wire. When the length is in the scale of the diameter, the object is called a rod, or a nanorod.

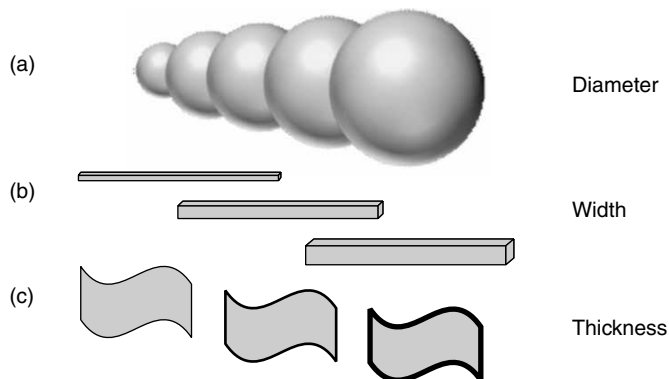


Fig. 1.1 Characteristic dimension in different nanoscale objects: (a) Nanospheres, (b) nanowires and (c) nanosheets.

All molecular processes occur at the nanoscale. For example, catalysis occurs on the surface or at an active centre, at which a few atoms are involved in the event investigated. Enzymes make biological conversions possible in which active centres are nanometers wide. However, these processes are not traditionally considered nanoscience as these do not correspond to manipulation of matter at the nanoscale. These have been well-established areas even before the advent of nanoscience. On the contrary, catalysis of materials with constituent units in the nanometer scale would be nanoscience. In that context, many catalytic processes such as those done with clays or zeolites are nanoscience. Crystallisation occurs by assembling molecules or ions one at a time and this can be considered as nanoscience, but it is not, as matter is not constructed at the nanometer length scale. A bottle of water may be considered to be composed of billions of nanodroplets, but a bottle of water is not a nanomaterial, as the constituent nano units are not discrete or observable. A dispersion of gold nanoparticles, however, is a nanofluid as nanoparticles are dispersed in a continuous phase.

The variation of properties in nanomaterials is unique. There is no example in the history of science, where properties of materials change with size without change in chemical composition, except in this size range—that is the central aspect of all properties of nanoscale materials. We see properties such as melting point, which was considered to be characteristic of a given material, change with dimension at this length scale. Although in 1871, Lord Kelvin asked whether the melting point of gold would vary with size, it took a long time to observe it experimentally. This was possible only after 105 years, in 1976¹ with the aid of experimental tools. The most prominent in this specific investigation is transmission electron microscopy. However, with a number of other tools in the broad umbrella of scanning probe microscopies, many other investigations are now possible, which unravel the uniqueness of properties at this size regime.

One important aspect of modern scientific advancements is that core subjects are becoming increasingly prominent. Chemistry is at the core of many discoveries, so are physics, mathematics and biology. It is a fact that in order to understand nanoscience and nanotechnology, and to contribute to its growing frontiers, a sound foundation in all the branches of basic science is required. Nanoscience itself is advancing at the boundaries of several of these disciplines. These advances result in the emergence of areas, such as nanochemistry, nanobiology, nanomaterials, etc. Advances of core disciplines themselves occur with the inputs of other disciplines. For example, nanomaterials encompass disciplines such as chemistry, physics, biology, mathematics and several branches of engineering. This makes the fusion of disciplines, at least along certain directions. Nowadays, nanoscience and technology have become the most prominent examples of the collapse of boundaries of disciplines. This may be said about other disciplines too, but in nano, the manifestations of this collapse are more evident. Another aspect of this science is that it allows the inputs of disciplines, completely separated from one another. There is scope for every possible idea, coming from any discipline, in this length scale.

Historically, scientific disciplines have diverged from one another in the course of establishment of subjects. The areas of overlap between disciplines have reduced, making each discipline independent of the other. In nanoscience, an opposite trend is visible, as stated earlier. Convergence has been manifested in other areas such as informatics, biotechnology, generic engineering, etc. in the recent

past. However, the coalescence of disciplines seen here is unprecedented. This is dictated by the requirements of the discipline wherein each discipline finds that interdependence allows growth.

1.2 WHY NANO?

Man has learnt a lot from nature. Yet his manufacturing practices are primitive. Everyone knows that there is a lot more to do to get closer to nature. Let us look at a few examples of natural processes. No machine has reached the efficiency of photosynthesis in storing energy. No one does energy transfer (also electron transfer) as efficiently as biomolecules. No factory does water purification and storage as efficiently as coconut trees or water melons. Brain of one person in principle can store and process more information than the common computer. It is unlikely that any movie camera can capture more vividly than the human eye. Olfactory receptors of the dog are highly sensitive than the sensors we have developed, although single molecule detectors have been demonstrated. Most early warning systems are primitive when compared to the sixth sense of animals. Chinese scientists have learnt that snakes can sense earthquakes a few days in advance.² There can be numerous other examples from life around us. Well, all of these function without any fanfare; it has been happening from time immemorial and they happen every time.

Conventional wisdom says that what happens in a factory is high-tech. Technology converts primitive and unusable materials to modern and useful materials. But this technology makes much greater impact to nature as the complexity of the technology increases. The impact of the wheel is not as immense as that of the automobile. When spaced in time, impact of technologies increases along with the progress of civilisation. Chisel was the highest technology of the Neolithic era. The man, who could make his chisels better, would have had a greater share of food. The best or most high-tech today may be the integrated circuits (ICs) in the fastest computers, which in its course of production from sand to wafers and then to integrated circuits has caused severe damage to the environment while contributing to information explosion. The impact of modern technology is evident on natural resources—water, air and everything around us. Of course, what we have developed is not high-tech in totality, from the perspective of larger common good.³ Sustainability has to be central to every technology, especially in the technology we are discussing for the future.

In our conventional high-tech, what is the best efficiency reached in energy conversion? Our best photovoltaic devices make about 16% of light conversion efficiency today, although efficiency as high as 33% may be achieved.⁴ Our best internal combustion engines work around 52% efficiency. We cook at home using 38% (at best) of the thermal energy produced by the cooking gas. But, our body utilises almost all the chemical energy it produces. The plant outside does it so well, so also the bacterium. If we were to be as inefficient as an electric motor that we are producing, we should consume several times more food than we are eating today and there will be no food for all the people! Thus it is clear that ultimate efficiency or value for money is achieved if we go along the Nature's way.

Nature, as a whole, fixes about 110–120 billion (bn) tonnes of carbon a year by photosynthesis. We as humans emit only 0.65 bn tonnes of carbon dioxide due to respiration. But carbon emissions

due to human activities is about 8 bn tonnes, 77.5% of this is due to burning of fossil fuels alone. In this process, we produce a lot of other things, such as smoke, complex organics, nitrogen oxides, etc. Obviously, the important aspect is that our methodologies are more inefficient, and therefore, low in technology. Not only that, the benefits due to our living are not too good in comparison to what we consume in the process. It is interesting to contrast the impact of our living to that of an animal, to the planet.

Eric Drexler⁵ says that there is an alternate way of producing things, by assembling things from the bottom-up, which would be called molecular nanotechnology. This is the way of the plants; it is humble. The plants take carbon dioxide and water from the environment and cook them in presence of sunlight. That makes carbohydrates on which a vast majority in this planet lives, excepting a few organisms, which can abstract other forms of chemical energy. Coming to think of it, the one CO₂ molecule is assembled by a series of chemistry to yield complex structures. This is called *the bottom-up method* of synthesis. This one-by-one assembly has made it possible to have functions with single molecules. Examples include molecular motors, muscle fibres, enzymes, etc. Each of them designed to do a specific activity. Complexity of this molecular architecture is that one molecule can communicate precisely with another molecule so that the structure as a whole achieves unusually complex functions, necessary for life. This complexity has taken a long time for the Nature to master. Maybe that is the way to go, if one has to look toward to future.

Production done by biology is extremely complex, but very cheap in real terms. A water melon is orders of times complex than the most complex integrated circuit, yet it costs far too less. On the other hand, the power to manipulate atoms and arrange them the way we please will make it possible to create complex inorganic structures at the cost of vegetables. That power would make it possible to create everything. That is nanotechnology. In many ways, this is the wet side of nanotechnology,⁶ referring to processes in biological environment, which necessarily needs water, and therefore, wet. There is a corresponding dry side where the ability to organise things atom-by-atom would make it possible to have structures and devices with functions in the solid state. That would make computers smaller, surgical procedures feasible without blood loss, harness solar energy efficiently so that we can avoid global warming.

1.3 CURRENT TECHNOLOGIES AND THE PROBLEMS

Implementing Nature's ways would imply a thorough understanding of molecular machinery. This knowledge, if put into inorganic matter, results in functional materials. Through these, a superstructure may be built, which has functions similar to those encountered in biology. Think of molecules transferring matter from one end to the other. Think of molecules, which bend, stretch or curl on external stimulus, such as temperature, and come back to the original shape upon reversing the stimulus. Consider chemical reactions which could be turned off and on by light. Think of molecules converting one chemical to the other without anything else in the medium and assume that such transformation occurs with precision and within the shortest time. This kind of functions and many more have already been achieved and the scope for the future is much more.

In the course of evolution of mankind, technologies have come and gone. One large difference between today's technology and that of the past is in the time it takes to mature it. The agrarian era, driven by the associated technologies of irrigation, tools, fertilisers, etc. took a few thousand years to mature, the time period varying depending on the location. The Industrial age, which came just after, starting around 1800s, took about 150 years to mature. Then came the information age starting from the 1950s and in many projections it is said to be mature. The impact of it may not have been felt in many societies, as technologies are absorbed differently. The next age, we are in its threshold, is expected to mature within a generation. But the way in which that technology is absorbed, will be vastly different from the earlier technologies.

Box 1.1 *A partial list of technologies of the 1900s, the year of discovery along with the people who invented them*

It is important to note that many technologies took a long time to reach the market place, but most recent technologies are already in the marketplace (see those of 1990s).

Year	Technology	Inventor
1920s:		
1924	Frozen foods	Clarence Birdseye
1926	Rocket engine	Robert Goddard
1926	Television	John Logie Baird
1928	Penicillin	Alexander Fleming
1930	Synthetic rubber	Julius Nieuwland
1930s:		
1930	Jet engine	Frank Whittle and Hans Von Ohain
1932	Automatic transmission	Richard Spikes
1934	Nylon	Wallace Hume Carothers
1937	Pulse code modulation to convert voice signals into electronic pulses	Alec Reeves
1937	Xerography or Xerox machines	Chester Floyd Carlson
1940s:		
1940	Radar	Robert Watson–Watt
1946	Microwave oven	Percy Spencer
1947	Cellular phone (conceptually)	D.H. Ring
1947	Transistor	Nillian Shockley, John Bardeen, and Walter Brattain
1949	Magnetic core memory	An Wang and then Jay Forrester

(Contd...)

1950s:

1951	The pill	Gregory Pincus
1952	Thorazine	Henri Laborit
1954	Fortran, the first high-level programming language	Griffith John Backus
1955	Polio vaccine	Jonas Salk
1956	Disk drive	Reynold B. Johnson
1958	Implantable pacemaker	Wilson Greatbatch
1958	Lasers	Schnwlow, Towns Basov, and Prokhorov
1959	Integrated circuit	Robert Noyce, Jack Kilby

1960s:

1962	Modem	US Airforce, AT&T
1968	Automated teller machines (ATMs)	Don Wetzel
1968	Mouse	Douglas Engelbart
1969	Charge-coupled devices	George E. Smith, Williard S. Boyle
1969	The Internet	UCLA, Stanford, among others

1970s:

1970	Compact disc (CD)	James T. Russell
1970	Liquid crystal displays	James Fergason
1971	Microprocessor	Intel, Busicom
1972	Computed tomography imaging	Godfrey Hounsfield, Allan Cormack
1972	Ethernet	Robert Metcalfe
1972	E-entertainment and precursor to video games	Nolan Bushnell
1974	Catalytic converter	Rodney Bagley, Irwin Lachman, Ronald Lewis
1975	Recombinant DNA	Herbert Boyer and Stanely Cohen
1979	Spreadsheet	Daniel Bricklin, Bob Frankston

1980s:

1986	Automated DNA sequencing machines	Leroy Hood, Llyod Smith and Mike Hunkapiller
1987	Mevacor to reduce cholesterol	Merck
1987	Prozac to reduce depression	Ray Fuller of Eli Lilly Company
1989	World Wide Web	Tim Berners-Lee

(Contd...)

1990s:

1994	Viagra	Albert Wood, Peter Dunn, Nicholas Terrett, Andrew Bell, Peter Ellis
1996	Protease inhibitors for patients suffering from HIV	S. Oroszlan, T.D. Copeland

2000s:

2001	Artificial liver	Dr Kenneth Matsumura and Alin Foundation
2002	Solar Tower	Jorg Schlaich
2006	The Battlefield Extraction-Assist Robot (BEAR), developed for military search-and-rescue missions	Vecna Technologies

Although technologies came and went, it is worth looking at what they have given us. The industrial age of the 1900s gave us the new agriculture with chemical fertilisers, radio, TV, air conditioning, car, jet planes, modern medicines, fabrics, etc. with which those with money can live like kings of the past, also paupers can become kings with appropriate understanding of the markets. The industrial age abolished the distinction between the king and the commoner. The information age has given us mobile phones, internet, cable TV, email, ATMs, administrative reforms, vanishing distances, etc. which changed our neighbourhood completely. It removed distances (and separations) of all sorts. The next era may remove the barrier between humans and surroundings in every possible way; life may acquire a seamless link with nature. It has been shown that neurons can be grown on integrated circuits and they can be activated by chips and vice versa.⁷ Thus a seamless link between mind, matter and life outside is possible! Many path-breaking discoveries have been made in this direction in the recent past.

This change in our lives occurred due to science. Chemistry has been the driving force in the front, which made major changes possible in the 19th and 20th centuries. The large production of ammonia, sulphuric acid, cement, iron, aluminum, drugs, fibres, dyes, polymers, plastics, petroleum products, etc. changed the world. What the world of chemistry has produced, drives the society. Chemistry contributes to more than half of the global production, including computers. Chemicals drive several economies. This growth of chemistry, although continues, a major change occurred in 1947 with the discovery of the transistor. In the 1950s and beyond, the semiconductor devices brought in consumer electronics. Everything that one purchases today has got an integrated circuit in it. Gadgets from toys to cars function with them. This, along with computers, built an era of physics. Many suggest that the next era is that of biology and materials. In that era, it is very likely that the interfaces between disciplines will contribute greatly and not the disciplines themselves.

The way in which this change has occurred left behind distinct marks in the society. The typewriter, which was a priced possession till recently disappeared completely. The electronic typewriters—

sandwiching the era between typewriters and word processors—have also disappeared. The ‘typist’ has become a non-existent position in many institutions and there is no more recruitment under this category. The factories producing goods for the typewriter vanished before our eyes, in the noticeable past. This may be contrasted to the disappearance of the blacksmith from Indian villages. The blacksmith, a reminder of the agrarian era, disappeared slowly as a result of the new factory-made agricultural implements. While the former happened in a few decades, the latter has taken centuries. As a result of the changing times, several other skills became necessary as part of the modern development. The programming skills, which were expected to be specialised, became common—part of the established set of skills. Computer knowledge is not anything special, it is expected to be part of the school training.

In spite of the large economic boom, that has taken place as a result of the developments in various fields, many problems persist. Poverty is widespread and several communities in the world are still hungry. Clean drinking water is inadequate and for many there is no access to it. In India, around 15% of the population has no access to clean drinking water. Access to clean water for the global population is one of the development goals of the United Nations (UNs). The details show that the global estimate of power requirement for 2050 is 30 PWh ($P = \text{peta}, 10^{15}$). Radically, new forms of technology will be needed to harness that power. Clean environment will be the biggest problem humanity will be facing in the years to come. Global water resources are alarmingly threatened by increasing levels of chemical contamination. Alarming depletion of non-renewable resources, forest areas and wetlands, extinction of animal and plant species, the deterioration in soil and air quality are gigantic problems. These issues are of larger importance to marginalised societies, where living is interlinked with nature. These and associated problems of healthcare, education and housing become astronomical issues even with a nominal population growth rate of 1.14% (2004 estimate) making us 10 bn people by 2050. Note that it was just 1 bn in 1820, 2 bn in 1930, 3 bn in 1960, 4 bn in 1974, 5 bn in 1988, and 6 bn in 2000. In other words, we have grown 6 times in just 180 years. The way we manage ourselves has got us into large areas with problems of overpopulation, industrial disasters, pollution (air, water, acid rain, toxic substances, etc.), loss of vegetation (overgrazing, deforestation and desertification), loss of wildlife, soil degradation, depletion and erosion. Obviously, with national boundaries and each nation having its own problems viewed with its own priorities, these issues will never be solved to the satisfaction of all. There is a larger problem of distribution of wealth. The gross domestic product (GDP) of the United States (US) is \$37,800, 13 times higher than that of India on a purchasing power parity basis (2004 estimate). What it obviously means is that there is a lot to go to achieve comparable quality of life for everyone. To get, there will take a completely new kind of technological initiative. Agriculture, which currently contributes 23.6% to the GDP in India (2004) will not be in a position to contribute further. Globally, it contributes only 4% to the GDP. In the US, its contribution is only 1.4%. Obviously, people don’t live on food alone these days. Money is made largely by industries and services, but the new industry has to be kind towards nature and should be as efficient as nature. Where can one look for solutions? Nanotechnology does suggest solutions to some of these issues, although it is not a saviour for all. Signs of nanotechnology applications for air, water and environment, and cleaner production are appearing. Several of the technologies in this direction are already in the market-place. A detailed

account of the discoveries in this area which may have a contribution to the growing problems of the world can be found in the last chapter.

1.4 NANO THE BEGINNING

Many nano forms of matter exist around us. One of the earliest nano-sized objects known is gold. Faraday prepared colloidal gold in 1856 and called it divided metal. In his diary, dated 2 April, 1856, Faraday called the particles he made as “divided state of gold” (<http://personal.bgsu.edu/~nberg/faraday/diary2.htm>), the solutions he made are preserved in the Royal Institution (Fig. 1.2).



Fig. 1.2 Faraday's gold preserved in Royal Institution (Source: <http://www.rigb.org/rimain/heritage/faradaypage.jsp>). (For clarity see colour figure.)

Indeed metal colloids are the earliest of nanoparticles which aroused scientific curiosity. Although nanoparticles of noble metals have been used in imparting colour to glasses since the time of Romans, scientific study of these particles was not started till 1600s. Colloidal gold had been incorporated in glasses and vases to give them colour. Oldest of these is the 4th-century AD Lycurgus cup made by Romans (Fig. 1.3). The cup appears red in transmitted light (if a light source is kept within the cup) and appears green in reflected light (if the light source is outside). Modern chemical analysis shows that the glass in this is not much different from that of the modern day. The compositions are as follows:

Silicon dioxide in Lycurgus cup = 73%

Silicon dioxide in Modern Glass = 70%

Sodium oxide in Lycurgus cup = 14%

Sodium oxide in Modern Glass = 15%

Calcium oxide in Lycurgus cup = 7%

Calcium oxide in Modern Glass = 10%

So what makes the glass coloured? It contains very small amounts of gold (about 40 parts per million) and silver (about 300 parts per million) in the form of nanoparticles of approximately 70 nm diameter.

The interest in the time of *Alchemy* was in gold solutions due to its redness as it was thought that the active principle of blood was its colour and blood itself was considered as the essence of life. Around 1600, Paracelsus described a method to make “Aurum portable” by reducing auric chloride by alcoholic plant extracts. Synthetic gold preparations have been used in traditional Indian medicine of Ayurveda. *Saraswatharishtam* uses gold particles and *Makaradhwaja* uses finely divided gold.⁸ The use of gold metal itself in medicine and dentistry is much older. The first book on colloidal gold was published in 1618. German chemist, Johan Kunckels published another book in 1676⁹, which described a drinkable gold which has curative properties. The presence of gold in invisible form in the solution was concluded in this book. Hans Heinrich Helcher, in a detailed book published in 1718, wrote that starch enhances the stability of the gold preparation.¹⁰ These preparations were used for dyeing in 1794. The difference in the colour of various preparations of gold was attributed to the size and nature of aggregation of the particles by Jeremias Benjamin Richters in 1818 itself.¹¹ In 1857, Faraday¹² reported the synthesis of stable colloids by a two-phase reduction method, in which gold chloride (AuCl_4^-) in water was reduced by red phosphorous in CS_2 . The term *colloid* was coined by Graham in 1861 (from the French word *colle*, meaning glue). Numerous workers have investigated colloidal gold in the 20th century. Methods using formaldehyde, hydrogen peroxide, hydroxyl amine, hydrazine and gases, such as CO and H_2 , have been reported. Various well-established synthetic methods such as citrate reduction method¹³



Fig. 1.3 The Lycurgus Cup made of glass appears red in transmitted light and green in reflected light. The glass contains 70 nm particles as seen in the transmission electron micrograph. The cup itself is dated to 4th century AD, but the metallic holder is a later addition. (Source: <http://www.thebritishmuseum.ac.uk>). (For clarity see colour figure.)

and the Brust method¹⁴ increased the momentum in this field. Various sub-nanometer gold clusters were synthesized by Schmid¹⁵ and Bartlett.¹⁶ These methodologies and the modifications introduced by later workers¹⁷ made colloidal gold science one of the most intensely pursued areas of science today. Earlier work in the area of colloidal gold, from the perspective of biology, is compiled in the book of M.A. Hayat, which also lists the various methodologies used for gold particles in a very large-size range.¹⁸ Several reviews devoted to gold and metal particles in particular are available, which may be consulted for an exhaustive review of the literature.¹⁹

Nature makes nano objects of varying kinds. Magnetite (Fe_3O_4) particles of nanometer size are made by the bacteria, *Magnetospirillum magnetotacticum*. They make the particles of specific morphology. For a bacterium, the magnetism due to the particles helps in finding the direction favourable to its growth. There are several bacteria which can take up metal ions and reduce them inside the cell and make nanoparticles. The familiar *Lactobacillus* present in buttermilk can also do that as shown in Fig. 1.4. Here, we see the transmission electron microscopic picture of single bacterium after incubation with gold ions for several hours. Fungi and viruses are known to make nanoparticles.

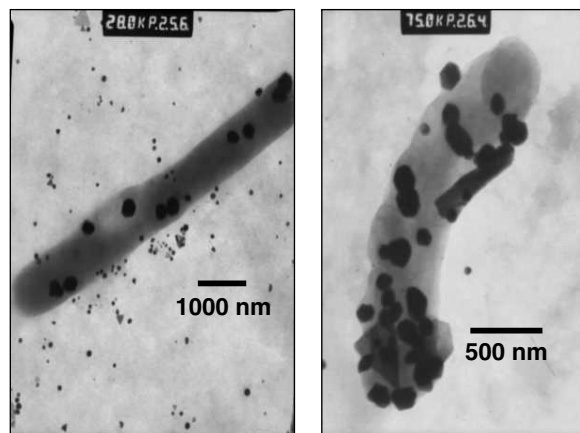


Fig. 1.4 Gold nanoparticles within the *Lactobacillus* contour. These transmission electron microscopic images show large particles of more than 200 nm in diameter. Some smaller particles are also seen (Source: Author's work).

However, the science of nanometer-scale objects was not discussed until much later. On 29th December, 1959, Nobel Prize-winning physicist, Richard Feynman, gave a talk at the annual meeting of the American Physical Society (APS) entitled, "There's plenty of room at the bottom". In this talk, he stated that, "the principles of physics, as far as I can see, do not speak against the possibility of manoeuvring things atom by atom." He, in a way, suggested the bottom-up approach, "...it is interesting that it would be, in principle, possible (I think) for a physicist to synthesize any chemical substance that the chemist writes down. Give the orders and the physicist synthesizes it. How? Put the atoms down where the chemist says, and so you make the substance. The problems of chemistry and biology can be greatly helped if our ability to see what we are doing, and to do things on an atomic level, is ultimately

developed—a development which I think cannot be avoided” (Feynman’s lecture is available at <http://www.zyvex.com/nanotech/feynman.html>). However, to put down atoms at the place one wanted, the world had to wait for a long time. In 1981, the scanning tunneling microscope was made and later a number of tools collectively called scanning probe microscopes were developed. The team (Gerber and Rohrer) got the 1986 Nobel Prize for physics and with these tools one can see and place atoms and molecules wherever needed.

Current growth of technology suggests that there has to be reductions in the dimensions of devices and active materials. This is evident in the case of computer technology. The number of transistors in an integrated circuit increased phenomenally, in the past 40 years. The observation made in 1965 by Gordon Moore, co-founder of Intel, was that the number of transistors per square inch on integrated circuits doubled every year since the integrated circuit was invented. Moore predicted that this trend would continue for the foreseeable future. In subsequent years, it was seen that the pace slowed down, but data density doubled approximately every 18 months. This is the current definition of the Moore’s Law. Most experts, including Moore himself, expect the Moore’s Law to hold for some more time. If this has to happen, device dimension must shrink, touching the nanometer regime very soon. The Pentium 4 of 2000 (see the box) used a 130 nm technology, i.e., the device structure drawn on silicon was as small as this dimension. In 2004, the technology graduated to 90 nm, well into the nanotechnology domain (under 100 nm).

Box 1.2 *The complexity of integrated circuits as seen in the evolution of Intel microprocessors*

Name	Year	Transistors	Microns	Clock Speed
8080	1974	6,000	6	2 MHz
8088	1979	29,000	3	5 MHz
80286	1982	134,000	1.5	6 MHz
80386	1985	275,000	1.5	16 MHz
80486	1989	1,200,000	1	25 MHz
Pentium	1993	3,100,000	0.8	60 MHz
Pentium II	1997	7,500,000	0.35	233 MHz
Pentium III	1999	9,500,000	0.25	450 MHz
Pentium 4	2000	42,000,000	0.18	1.5 GHz
Pentium 4 “Prescott”	2004	125,000,000	0.09	3.6 GHz
Core 2 Duo “Cedar Mill”	2006	376,000,000	0.065	3.6 GHz
Next Gen Core 2 Duo “Penryn”	2007	410,000,000	0.045	3.16 GHz

Obviously, with all these that have been achieved, it is indeed sure that there will be products in the marketplace in the immediate future. A summary of the nanotechnology products in the marketplace

at present can be found in the link, www.nanoforum.org. However, the answer to when the real need for nano products will be felt by the people varies. There are many who believe that there will be nanotech laws in the near future, as there can be economic, social, health and security implications to nanotechnology, which would be the concern of nations. The implications to society may be significant, such that nations may discuss it as part of their elections. A detailed discussion of such aspects is in the last chapter.

1.5 NANO AND ENERGETICS

Nanosystems are metastable. This means that they will transform to stable materials which have global energy minima in the free-energy landscape. If one plots free energy of the system for a fixed amount of the material (as free energy is an extensive property), nanoparticles exist at a higher energy in comparison to the bulk materials, although a given nanostructure may have a local minimum in comparison to other structures. These local minima in the limit of extremely small particles correspond to magic numbers with unusual structural/electronic stability. Such particles are referred to as clusters, which will be mentioned in a later section. In the case of isolated atoms and molecules, the total energy is much larger in comparison to the bulk. Nanoparticles constitute a regime in which the energy is in between the bulk materials and the molecules/atoms. It is possible to convert one form to the other by physical or chemical means.

In the smaller-size regime of less than 1 nm, nanoparticles possess distinct structures and may be regarded as *nanocluster molecules*. Each of these clusters may have isomeric structures and one may be more stable than the other. Various structures of a given size may have large differences in properties. In the larger-size regime, numerous structural forms can exist, but it is difficult to distinguish them. When it comes to large changes in the geometry, as in the case of a nanoparticle and a nanorod, distinction can be made on the basis of their electronic properties. Synthetic methodologies are available to make some of those structures in the case of a few metals and ceramics.

As evident from Fig. 1.5, transformation from one size regime to the other is possible. While the transformation from atoms, molecules and nanoparticles to bulk is spontaneous, stabilising the nanoparticle regime requires careful control. The formation of nanoparticles from constituent atoms is referred to as the bottom-up approach while the synthesis of nanostructures from bulk is referred to as top-down.

The fact that nanoparticles are metastable, they would go back to the bulk at infinite time. The time one considers in several cases has no practical consequence, as Faraday's colloids, made in 1856, are stable even now. Although the bulk metal is more stable, it is just as one considers the stability of graphite in comparison to diamond. Diamond, although metastable, does not become graphite at normal conditions of temperature and pressure even if kept for a millennium. The kinetics of diamond to graphite transformation is very slow, and therefore, it is insignificant under normal conditions. The situation of nanoparticles is analogous and is referred to as *kinetic stability*.

Nanoparticles, if held at close distance, will lead to inter-particle interaction and that will cause *aggregation* or *coalescence*. In aggregation, the particles retain their individuality, but part of their

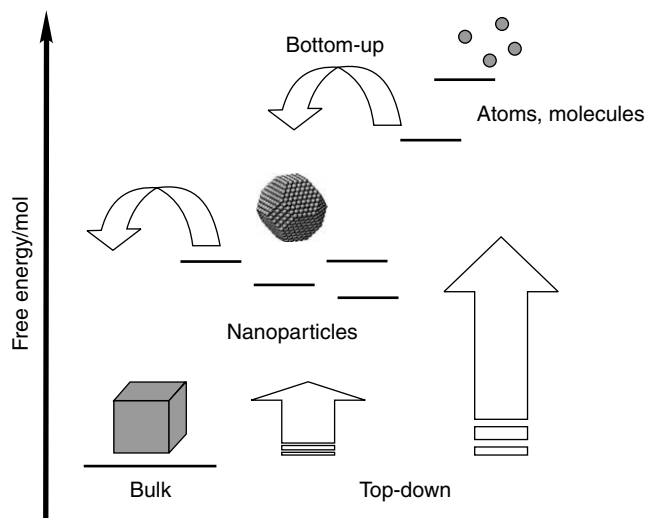


Fig. 1.5 Nanoparticles shown as a metastable system. Their energies are between that of atoms and molecules and of bulk material. There can be several different kinds of nanoparticles with distinct energies, represented by horizontal bars. Each type of nanoparticles can be converted to the bulk form. The formation, from bulk of nanoparticles, molecules and atoms is called the top-down approach. Making nanoparticles starting from atoms and molecules is called the bottom-up approach.

surface area is lost due to the interaction. Such interactions occur as the surface of the nanoparticles containing groups or molecules aid in aggregation. A familiar case is hydrogen bonding interaction or ionic interactions between the surface groups. Aggregation is also referred to as *coagulation*, especially important in cases where particles are stabilised by an electrical double layer. (Inter-particle interaction can also result in coalescence of particles. This is irreversible fusion of particles, resulting in larger particles).

The situation can be better understood in terms of two isolated particles. Nanoparticles generally contain an overlayer of stabilising groups or molecules. When they are at a finite distance, d , interactions between the particles will result in an energy minimum. The interactions can be electrostatic or only weak van der Waals (due to the type of the protecting groups) type. Most often these two kinds of interactions dominate, especially in a dielectric solvent, such as water. While the electrostatic interactions try to keep the particles away from each other, the van der Waals interactions between the particle cores bring them together. This results in a net energy minimum as shown in Fig. 1.6. These van der Waals interactions are strong at short distances and the particles coalesce in the absence of a shell which imparts repulsion. The repulsion can be additionally due to steric forces as in the case of a molecule covering the particle. Nature of the repulsive interactions change depending on the kind of the shell. For the van der Waals forces to be effective, the distance has to be short and there is a barrier, which inhibits this interaction to be dominating. The height of this barrier, if greater than the thermal energy, kT , the system is kinetically stable. As can be seen, the particles possess

greater energy to overcome this barrier at higher temperatures and the colloidal system aggregates beyond a critical value, called the *critical flocculation temperature*. It may be noted that the stability of the shell over the nanoparticle is also temperature dependent. The discussion here is analogous to that of colloids.

In the limit of a covalently bound shell on the nanoparticle surface, the shell is stable under normal conditions of temperature and pressure encountered in a nanofluid application. Thus, the system can be infinitely stable. Nevertheless, it is important to note that the nanoparticle core may undergo irreversible changes in temperature cycling. These changes correspond to structural, electrical or magnetic phase transitions. In molecular detail, the structure of the shell may also undergo transformation, such as conformational ordering. This refers to the changes in the relative orientation of the bonds in the molecule.

In most of the cases described, a discussion of stability is related to kinetic stability. Nevertheless, there are also thermodynamically stable nanoparticles. This corresponds to particles of specific shapes and structures as in the case of molecular nanoparticles. Here a given structure is thermodynamically stable under a condition of temperature, pressure and concentration of the species under question. For example, a nanocluster of Au₅₅ is a thermodynamically stable entity, with its specific number of ligands, in a medium or in the solid state. Varying conditions will lead to the collapse of the structure. This may be said about particles of specific shapes such as nanorods, which will transform to other shapes under appropriate conditions. Micelles correspond to another example, which may transform to lamellar or liquid crystalline phases upon variation in conditions. These various phases are thermodynamically stable.

1.6 NANO AND IMPLICATIONS

Nanotechnology is concerned with the manipulation of matter in-between the molecular and macroscopic length scales. As a result of the unique size, materials at this length scales have different properties, which need to be explored. Such properties span a wide range belonging to disciplines, such as chemistry, biology, physics and engineering. In fact, there is no single area of science and engineering, where such properties have no impact. As science is linked with economic development, nanotechnology has potential impact on the economy. Such development requires large-scale utilisation of nanomaterials. Just as for other materials, there are associated environmental impacts, if the use is not careful. From the preceding, it is clear that nanotechnology implications are in basic science, economy and environment.

Basic science has brought about numerous surprises. New materials and their associated properties have brought out completely new phenomena. This required newer experimental tools and application of those tools produced new properties. Discovery of fullerenes, carbon nanotubes, semiconductor nanoparticles, clusters, metal nanoparticles, anisotropic nanostructures, mesoporous structures, self-assembled structures, graphene and many others can be mentioned as examples of new materials. Unusual electronic structure, phenomena associated with surface plasmons, single molecule surface enhance Raman spectroscopy, flow through nanochannels, novel sensors, etc. can be cited as examples

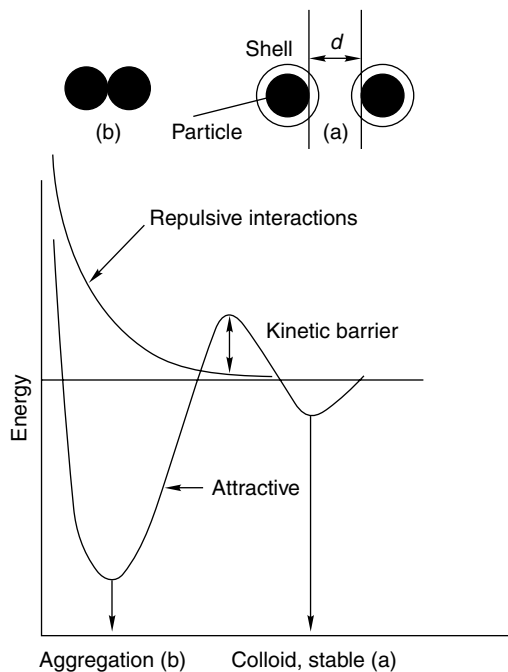


Fig. 1.6 Illustration of kinetic stability of a nanoparticle system. As the barrier for van der Waals interaction is greater than thermal energy, the isolated nanoparticles are stable. In the absence of protective shells on the nanoparticles, the kinetic barrier for aggregation would be very low compared to the thermal energy and hence the particles generally coalesce.

of new phenomena. Tough materials, property-enhancing coatings, aerogels, superhydrophobicity, new solar cells, photocatalysis, antimicrobial products, drug delivery vehicles, etc. are examples of areas, where economic activity happens currently. Environmental impacts include hazards associated with small particles inhalation, skin penetration, UV absorption and creation of radical species, unusual chemical reactivity of particles in biology, penetration into cell nuclei, gene transformations and ethical implications with unrestricted use of such technology, etc. From all these perspectives, nanotechnology has also penetrated humanities and social sciences. Even before such penetration, it came into popular literature.

REFERENCES

1. P. Buffat and J.P. Borel, 'Size effect on the melting temperature of gold particles', *Phys. Rev. A.*, 13, (1976), 2287–98.
2. Retrieved from <http://www.independent.co.uk/news/world/asia/headbanging-chinese-snakes-can-predict-earthquakes-days-in-advance-say-scientists-430093.html>.
3. A. Roy, *An Ordinary Person's Guide to Empire*, South End Press, (2004), Cambridge, MA.

4. R. Yu, Q. Lin, S.F. Leung and Z. Fan, (2011). 'Nanomaterials and nanostructures for efficient light absorption and photovoltaics', *Nano Energy*, doi:10.1016/j.nanoen.2011.10.002.
5. K.E. Drexler, *Engines of Creation*, (1986). Garden City, Anchor Press/Doubleday, New York; K.E. Drexler, C. Peterson and G. Pergamit, (1991). *Unbounding the Future: The Nanotechnology Revolution*, William Morrow and Company Inc., New York.
6. The term was first introduced by R.E. Smalley.
7. <http://ixbtlabs.com/news.html?05/98/95>.
8. S. Mahdihassan, 'Cinnabar-gold as the best alchemical drug of longevity, called makaradhwaaja in India', *Am. J. Chin. Med.*, 13, (1985), 93.
9. J. Kunckels, (1975), 'Nuetliche Observationes Oder Anmerkungen von Auro und Argento Potabili'; Schutzens: Hamburg, (1676). (b) *Savage, G. Glass and Glassware*, Octopus Book, London.
10. H.H. Helcher, *Aurum Potabile Oder Gold Tinstur*, J. Herbord Klossen, Breslau and Leipzig, (1718).
11. W. Ostwald, *Zur Geschichte des Colloiden Goldes*, *Kolloid Z.*, (1909), 4–5.
12. M. Faraday, 'Experimental relations in gold (and other metals) to light, Philos', *Trans. R. Soc.*, London 147, (1857), 145.
13. J. Turkevich, P. Stevenson and J. Hillier, 'A study of the nucleation and growth processes in the synthesis of colloidal gold', *Discuss. Faraday Soc.*, 11, (1951), 55–75.
14. M. Brust, M. Walker, D. Bethel, D.J. Schrifin and R. Whyman, 'Synthesis of thiol derivatised gold nanoparticles in a two-phase liquid/liquid system', *J. Chem. Soc. Chem. Commun.*, 7, (1994), 801–02.
15. G. Schmid, R. Boese, R. Pfeil, F. Bandermann, S. Meyer, G.H.M. Calis and van der Velden, J.W.A., $\text{Au}_{55}[\text{P}(\text{C}_6\text{H}_5)_3]_{12}\text{C}_{16}$ —ein Goldcluster ungewöhnlicher Größe ($\text{Au}_{55}[\text{P}(\text{C}_6\text{H}_5)_3]_{12}\text{C}_{16}$ —a Gold Cluster of an Exceptional size), *Chem. Ber.*, 114, (1981), 3634–42.
16. P.A. Bartlett, B. Bauer and S. Singer, 'Synthesis of water-soluble undecagold cluster compounds of potential importance in electron microscopic and other studies in biological systems', *J. Am. Chem. Soc.*, 100, (1978), 5085–89.
17. T. Yonezawa and T. Kunitake, 'Practical preparation of anionic mercapto ligand-stabilised gold nanoparticles and their immobilisation', *Colloids Surf. A Physicochem. Eng. Asp.*, 149, (1999), 193–99.
18. M.A. Hayat, *Colloidal Gold: Principles, Methods, and Applications*, Vol. 1, 2 and 3, (1989, 1989 and 1991), Academic Press, Inc. San Diego.
19. M.C. Daniel and D. Astruc, 'Gold nanoparticles: Assembly, supramolecular chemistry, quantum-size-related properties, and applications toward biology, catalysis, and nanotechnology', *Chem. Rev.*, 104, (2004), 293–346.

ADDITIONAL READING

1. S. Hawking, (1988). *A Brief History of Time*, Bantam Books, New York.
2. C.N.R. Rao, A. Müller and A.K. Cheetham, (Ed.), (2007). *Nanomaterials Chemistry: Recent Developments and New Directions*, Wiley-VCH, Weinheim.
3. D. Vollath, (2008). *Nanomaterials: An Introduction to Synthesis, Properties and Applications*, Wiley-VCH, Weinheim.

4. V.H. Grassian, (Ed.), (2008). *Nanoscience and Nanotechnology: Environmental and Health Impacts*, Wiley-VCH, Weinheim.
5. S. Hawking, (2007). *Theory of Everything: The origin and the fate of the Universe*, Phoenix Books Inc., CA.
6. A. Meyer, (2005). *Hunting the Double Helix: How DNA is solving the puzzles of the past*, Allen & Unwin, Australia.
7. S. Hawking, (1993). *Black Holes and Baby Universes*, Bantam books, New York.
8. S. Bennington, P. Harrison, A. Morrison and C. Oxlade, (1993). *Great Inventions That Shaped The World*, Southwater Publishing, London.
9. R. Matthews, (2005). *25 Big Ideas: The Science That's Changing Our World*, Oxford: Oneworld, Oxfordshire.
10. M. White and J.R. Gribbin, (2005). *Einstein—A Life In Science*, FreePress, New York.

REVIEW QUESTIONS

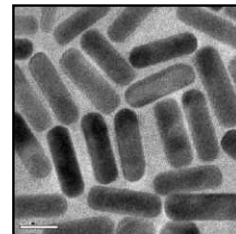
1. What is special about the *nanometer*?
2. What is nanoscience and what is nanotechnology?
3. Why nanotechnology now? Why we did not hear about it in the past?
4. Is there a systematic evolution of nanotechnology from microtechnology? Will there be picotechnology?
5. Are there nano objects around you? Are there such objects in your body? Name a few.
6. Have a look at natural objects such as sea shells, wood, bone, etc. Is there any nanotechnology in them?
7. If nature is full of nano, what limits us from making nanomaterials or nanodevices?
8. What are the likely impacts of nanotechnology?
9. What is kinetic stability?

**PART
TWO**

Experimental Methods of Investigation

- **Electron Microscopies**
- **Scanning Probe Microscopies**
- **Photoelectron Spectroscopy for the Study of Nanomaterials**
- **Structure of Materials by Diffraction Techniques**
- **Electroanalytical Techniques**
- **Raman Scattering**
- **Miscellaneous Techniques**

ELECTRON MICROSCOPIES



“With every tool, man is perfecting his own organs, whether motor or sensory, or is removing the limits to their functioning...by means of the microscope he overcomes the limits of visibility set by the structure of his retina.”

Sigmund Freud, *Civilization and its Discontents*, 1930

Central aspect of science at the nanoscale is observation. Newer tools, methods and analyses are required to understand phenomena at the nanoscale. Observation of materials on the nanoscale can be done with electrons, photons, scanning probes, ions, atoms, etc. A range of techniques are available in each of these areas and a systematic application of several of the tools lead to a complete understanding of the system. In addition, in-situ measurements of nanoscale objects become a reality with these tools. Properties of individual nano objects, such as Young’s modulus can be studied and some of the examples in this line are illustrated. It is also possible to adapt the techniques mentioned for nanomanipulation which is the basis of nanotechnology.

Learning Objectives

- What are the principal properties useful in exploring nanomaterials?
 - What are the differences between photon, electron and scanning probe techniques?
 - What are the principal electron microscopic techniques?
 - How do we study the properties of a single nano object?
 - How do we conduct experiments on single nanoscale objects?
-
-

2.1 INTRODUCTION

Observation is the key to discover new and this is especially true in the nanoscale. In fact, without seeing the objects, one cannot proceed further with the investigations, as far as nano objects are concerned. Observation is done with a probe which may be a beam of photons, electrons, neutrons, atoms, ions or even an atomically sharp pin. For nanomaterials, the probing light or particle is often of varying frequencies, from gamma rays to infrared or beyond in the case of photons or of hyperthermal

(<100 eV) to relativistic energies in the case of particles. The resulting information can be processed to yield images or spectra, which reveal topographic, geometric, structural, chemical or physical details of the material. Several techniques are available under the broad umbrella of materials characterisation, which may be used to study nanomaterials in one way or the other. A partial list is given in Table 2.1. Some of these techniques may be used in a spatially resolved fashion. In this chapter, we look at some of the more important tools in the context of nanoscience and technology.

We need to remember that nanomaterials have to be studied by a combination of techniques, as one technique is inadequate to provide information on every aspect of the material. While size is central to the constituent material, say nanoparticle, the properties of the material such as optical absorption, emission, thermal and electrical conductivities, magnetism, etc. which need other investigations. All of these together provide information in totality. Thus, it is necessary to have a range of techniques, which provide diverse measurements. It may appear that many of the techniques used for nanomaterials research are tools of materials science, organic chemistry, biochemistry, condensed matter physics, metallurgy, mechanical engineering, etc. but all of them together now provide a comprehensive understanding of matter at the nanoscale.

Table 2.1 *Common analytical tools used for the characterisation of materials*

Constituent	Lycurgus Cup
AES	Aüger Electron Spectroscopy*
AFM	Atomic Force Microscopy*
APECS	Aüger Photoelectron Coincidence Spectroscopy
APFIM	Atom Probe Field Ion Microscopy*
APS	Appearance Potential Spectroscopy
ARPES	Angle Resolved Photoelectron Spectroscopy*
ARUPS	Angle Resolved Ultraviolet Photoelectron Spectroscopy*
ATR	Attenuated Total Reflection
BEEM	Ballistic Electron Emission Microscopy*
BIS	Bremsstrahlung Isochromat Spectroscopy
CFM	Chemical Force Microscopy*
CM	Confocal Microscopy (especially with fluorescence and Raman detection)*
DRIFTS	Diffuse Reflectance Infra-Red Fourier Transform Spectroscopy
EDX	Energy Dispersive X-ray Analysis
EELS	Electron Energy Loss Spectroscopy*
	Ellipsometry, see RDS
EMS	Electron Momentum Spectroscopy
EPMA	Electron Probe Micro-Analysis*
ESCA	Electron Spectroscopy for Chemical Analysis also XPS (X-ray photoelectron spectroscopy)*

(Contd...)

Table 2.1 (Contd...)

Constituent	Lycurgus Cup
ESD	Electron Stimulated Desorption
ESDIAD	Electron Stimulated Desorption Ion Angle Distributions
EXAFS	Extended X-ray Absorption Fine Structure
FEM	Field Emission Microscopy*
FIM	Field Ion Microscopy*
FRET	Fluorescence Resonance Energy Transfer*
FTIR	Fourier Transform Infrared Spectroscopy*
FT RA-IR	Fourier Transform Reflectance-Absorbance Infrared
HAS	Helium Atom Scattering
HEIS	High Energy Ion Scattering
HREELS	High Resolution Electron Energy Loss Spectroscopy
IETS	Inelastic Electron Tunneling Spectroscopy
KRIPES	k-Resolved Inverse Photoemission Spectroscopy
ILS	Ionisation Loss Spectroscopy
INS	Ion Neutralisation Spectroscopy
IPES	Inverse Photoemission Spectroscopy
IRAS	Infra-red Absorption Spectroscopy
ISS	Ion Scattering Spectroscopy
LEED	Low Energy Electron Diffraction*
LEEM	Low Energy Electron Microscopy*
LEIS	Low Energy Ion Scattering
LFM	Lateral Force Microscopy*
MBS	Molecular Beam Scattering
MCXD	Magnetic Circular X-ray Dichroism
MEIS	Medium Energy Ion Scattering
MFM	Magnetic Force Microscopy*
MIES	Metastable Impact Electron Spectroscopy
MIR	Multiple Internal Reflection
NEXAFS	Near-Edge X-ray Absorption Fine Structure
NSOM	Near Field Scanning Optical Microscopy*
PAES	Positron Annihilation Auger Electron Spectroscopy
PEEM	Photoemission Electron Microscopy*
PED	Photoelectron Diffraction
PIXE	Proton Induced X-ray Emission

(Contd...)

Table 2.1 (Contd...)

Constituent	Lycurgus Cup
PSD	Photon Stimulated Desorption
RAIRS	Reflection Absorbtion Infra-red Spectroscopy
RAS	Reflectance Anisotropy Spectroscopy
RBS	Rutherford Backscattering
RDS	Reflectance Difference Spectroscopy
REFLEXAFS	Reflection Extended X-ray Absorption Fine Structure
RHEED	Reflection High Energy Electron Diffraction*
RIFS	Reflectometric Interference Spectroscopy
SAM	Scanning Auger Microscopy*
SCM	Scanning Confocal Microscopy also CM*
SEM	Scanning Electron Microscopy*
SEMPA	Scanning Electron Microscopy with Polarisation Analysis*
SERS	Surface Enhanced Raman Scattering*
SEXAFS	Surface Extended X-ray Absorption Fine Structure
SFS	Sum Frequency Spectroscopy
SHG	Second Harmonic Generation
SH-MOKE	Second Harmonic Magneto-optic Kerr Effect
SIM	Scanning Ion Microscope*
SIMS	Secondary Ion Mass Spectrometry*
SKS	Scanning Kinetic Spectroscopy
SMOKE	Surface Magneto-optic Kerr Effect
SNMS	Sputtered Neutral Mass Spectrometry
SNOM	Scanning Near Field Optical Microscopy*
SPIPES	Spin Polarised Inverse Photoemission Spectroscopy*
SPEELS	Spin Polarised Electron Energy Loss Spectroscopy
SPLEED	Spin Polarised Low Energy Electron Diffraction*
SPM	Scanning Probe Microscopy*
SPR	Surface Plasmon Resonance
SPUPS	Spin Polarised Ultraviolet Photoelectron Spectroscopy
SPXPS	Spin Polarised X-ray Photoelectron Spectroscopy
STM	Scanning Tunnelling Microscopy*
SXAPS	Soft X-ray Appearance Potential Spectroscopy
SXRD	Surface X-ray Diffraction
TDS	Thermal Desorption Spectroscopy

(Contd...)

Table 2.1 (Contd...)

Constituent	Lycurgus Cup
TEAS	Thermal Energy Atom Scattering
TIRF	Total Internal Reflectance Fluorescence
TPD	Temperature Programmed Desorption
TPRS	Temperature Programmed Reaction Spectroscopy
TXRF	Total Reflection X-ray Fluorescence
UPS	Ultraviolet Photoemission Spectroscopy*
XANES	X-ray Absorption Near-Edge Structure
XPD	X-ray Photoelectron Diffraction*
XPS	X-ray Photoemission Spectroscopy*
XRR	X-ray Reflectometry
XSW	X-ray Standing Wave

* Tools which are either microscopy or with which microscopy is possible.

We use microscopy in order to see objects in more detail. The best distance one can resolve with optical instruments, disregarding all aberrations is about 0.5λ (λ being the wavelength of the radiation used to probe the matter), or of the order of 250 nm with visible radiation. All forms of microscopy are aimed at improving our capacity to see. Under ideal conditions, the smallest object the eye can resolve is about 0.07 mm. This limit is related to the size of the receptors in the retina of the eye. Any microscope is designed to magnify the image falling on the retina. The advantage of the microscopes is that it effectively gets the object closer to the eye. This gets us a magnified image and more detail can be obtained.

There are several forms of microscopy one uses to study nanomaterials. They can be broadly grouped under the following categories:

1. Optical microscopes
2. Electron microscopes
3. Scanning probe microscopes
4. Others

The first three are more common, but others are also used for nano measurements. A few of the techniques which are useful also as spectroscopies, are also discussed. In the following chapters, we review all these forms of microscopic tools in some detail. The discussion, however, does not include the theoretical aspects except to a bare minimum. Detailed texts listed in the bibliography may be consulted for an in-depth discussion of each technique. Every topic, however, may not be discussed to the same extent.

Microscope is the instrument with which we form enlarged images. The word “microscope” is derived from two Greek words, *micros* meaning “small”; and *skopos* meaning “to look at”. Microscopes

of Antonie van Leeuwenhoek (1632–1723) were the state-of-the-art for about 200 years. These single lens microscopes had to be held against the eyeball, because their focal lengths were very short. With these tools, bacteria were discovered. As his research was not appreciated, van Leeuwenhoek appears to have destroyed most of his 500 and odd microscopes before his death at the age of 90. Only nine microscopes developed by Leeuwenhoek are known to exist today.

Before discussing microscopies, we need to have a few definitions.

Resolution: A measure of the capacity of the instrument to distinguish two closely spaced points as separate points, given in terms of distance.

Resolving power: Resolution achieved by a particular instrument under optimum conditions. While resolving power is a property of the instrument and is a quantity that may be estimated, resolution is equal to or poorer than the resolving power and has to be determined for the instrument.

Two kinds of microscopes exist.

1. *Transmitting*—The probe beam, passed through the specimen is differentially refracted and absorbed.
2. *Scanning*—The probe beam is scanned over the surface. The image is created point-by-point.

There are several kinds of scanning microscopes.

1. *Scanning Electron Microscope (SEM)*—In this, a monochromatic electron beam is passed over the surface of the specimen which induces various changes in the sample. The resulting particles from the sample are used to create an image of the specimen. The information derived is from the surface of the sample. The most important advantage of SEM is its large depth of field. Although the images appear to be three-dimensional (3-D), a true three-dimensional image is obtained only by using a combination of two pictures.
2. *Scanning Ion Microscope (SIM)*—Charged ions are used to image and the process etches away the top surface.
3. *Scanning Acoustical Microscope (SAM)*—Uses ultrasonic waves to form images. Best resolution achieved is of the order of 2.5 microns, limited by wavelength of sound. Advantageous in terms of its ability to look at live biological samples.
4. *Scanning Light Microscope (SLM)*—Fine beam of visible light is passed over the surface to build up the image point-by-point. It facilitates increased depth of field and colour enhancement.
5. *Scanning Confocal Microscope (SCM)*—In this, a finely focused beam of white or monochromatic light is used to scan a specimen. It allows one to optically section through a sample. This technique is more commonly referred to as confocal microscopy.

2.2 ELECTRON MICROSCOPIES

Microscopes consists of an illumination source, a condenser lens to converge the beam on to the sample, an objective lens to magnify the image and a projector lens to project the image onto an

image plane which can be photographed or stored. In electron microscopes, the wave nature of electron is used to obtain an image. There are two important forms of electron microscopy, namely scanning electron microscopy and transmission electron microscopy. Both utilise electrons as the source for illuminating the sample. An understanding of the microscope is made easier using an optical analogy. Both the tools are similar in certain aspects; both of them use similar illumination sources, but they differ in a number of other aspects. The lenses used in electron microscopes are electromagnetic lenses, which are widely different from glass lenses, though similar principles apply in both cases.

Due to its simplicity, scanning electron microscopy (SEM) will be discussed first followed by transmission electron microscopy (TEM). Although, TEM is more complex in usages, it becomes easier to get introduced to it having learned about SEM. Several other modifications to each of these techniques are possible and we will highlight out these advanced tools at appropriate places.

2.2.1 Scanning Electron Microscopy

2.2.1.1 Basics

The de Broglie wave equation relates the velocity of the electron with its wavelength, $\lambda = h/mv$ (h is Planck's constant, m is the rest mass of electron and v is its velocity). An electron of charge e (1.6×10^{-19} coulomb) and mass m (9.11×10^{-28} gm), when passing through a potential difference of V volts (expressed in joules/coulomb), acquires a kinetic energy of $1/2mv^2 = eV$. This gives us, $v = \sqrt{(2eV/m)}$ and $\lambda = \sqrt{(h^2/2meV)}$. Substituting (with conversion factors, 1 joule = 10^7 dyne.cm = 10^7 cm².gm/sec²), λ (in nm) = $1.23/\sqrt{V}$. When $V = 60,000$ volts, $\lambda = 0.005$ nm. This shows that the velocity of electron will reach the speed of light in vacuum ($c = 3.10^{10}$ cm/sec) at high extraction potentials. The electron velocities at various acceleration voltages are given in the table below.

V	λ (nm)	v ($\times 10^{10}$ cm/sec)	v/c
50,000	0.0055	1.326	0.442
100,000	0.0039	1.875	0.625
1,000,000	0.0012	5.930	1.977

However, the fact remains that the equation breaks down when the electron velocity approaches the speed of light, as mass increases. At such velocities, one needs to do relativistic correction to the mass and it becomes, $m = m_0/\sqrt{[1 - (v^2/c^2)]}$. This makes, $\lambda = 1.23/\sqrt{(V + 10^{-6}V^2)}$ nm.

After including the relativity effects, the velocity and the wavelength become as shown in the table.

V	λ (nm)	v ($\times 10^{10}$ cm/sec)	v/c
50,000	0.0055	1.326	0.414
100,000	0.0039	1.875	0.548
1,000,000	0.0012	5.930	0.941

2.2.1.2 Resolving Power

(a) *Abbe criterion*: Abbe in 1893 showed that the smallest resolvable distance between objects is about half the wavelength of light used. What does this mean for the magnification? The maximum magnification that can be used = resolving power of the eye/resolving power of the microscope. For light microscopes the resolving power is about 250 nm. What we can see is about 250 μm . So the useful magnification is, $250/0.25 = 1000\text{X}$ (X means diameter). A magnification above this has no value and it represents empty magnification, the effect of which is only a magnified blur. The resolving power of an electron microscope would be 0.0027 nm for an electron energy of 50,000 V. This means one can get a magnification of the order of 100,000,000. However, this is not achieved due to aberrations of the electron lenses and contributions due to the complex nature of electron-sample interactions. It is important to know that we have long achieved the theoretical limit of resolution as far as optical microscopes are concerned since the various aberrations have been resolved.

(b) *Rayleigh criterion*: An ideal lens projects a point of the object as a point on the image. But a real object presents a point as a disk in the image plane. The disk is called the airy disk (Fig. 2.1). The diameter of the disk depends on the angular aperture of the lens. If two points are placed close to each other, the closest distance at which they appear to be separated in the image is about 1/2 the width of the disks. That separation (shown in the arrow) can be given as, $d = 0.61 \lambda / n \sin \theta$, where n is the refractive index of the medium and θ is the semi-angular aperture of the lens. $n \sin \theta$ is the numerical aperture (N.A.) of the lens.

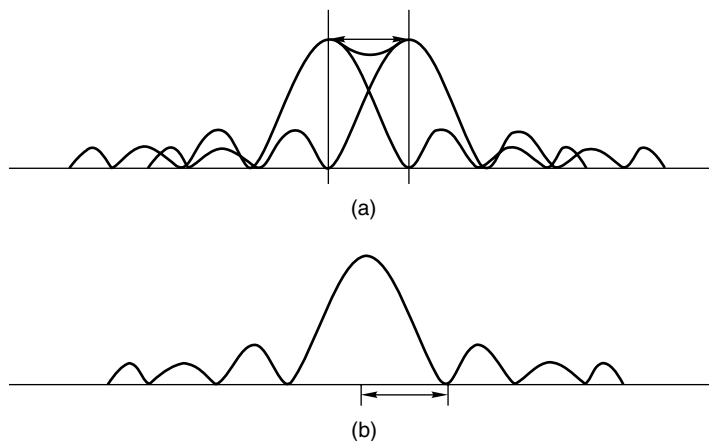


Fig. 2.1 (a) Intensity distribution at an Airy disk is the half width of the maximum. (b) Rayleigh criterion of resolution.

In order to get the maximise resolving power, λ must be decreased, n increased, or θ increased. Recall that we are concerned at the moment with an *aberration free* optical system. From this, we see that for the light microscopes, when one uses oil immersion optics ($n = 1.5$), $\sin \theta = 0.87$, $\lambda = 400$ nm (for blue end of visible), the limit is $d = 0.2 \mu\text{m}$. For the TEM, $n = 1$ (vacuum), $\sin \theta = 10^{-2}$ and λ is of the order of 0.005 nm and $d = 0.3$ nm.

2.2.1.3 Classical vs Electron Optics

Light is refracted by lenses. This is the property used in magnifying or demagnifying an object. At the lens surface, the refractive index changes abruptly and it remains constant between the surfaces. Imaging lenses are constructed using the principles of refraction. To achieve desired results, glass surfaces of the lenses are shaped. In electron optics the trajectory of the electrons is changed by applying electric or magnetic fields. The change is continuous depending on the electric and magnetic fields. Electromagnetic lenses and not electrostatic lenses are used in electron microscopy due to fewer aberrations of the former.

2.2.1.4 What Does an SEM Contain?

An SEM contains the following principal elements:

1. Electron gun

Electron gun provides a stable beam of electrons. The most common ones are thermionic emitters, where the work function of the metal is overcome by surface temperature of the filament. Typically a hairpin filament made of a tungsten wire of 100 μm , with a tip radius of 100 μm is used to generate electrons. The filament is held at a negative potential and heated to about 2000°–2700° K by resistive heating. The electrons are confined and focused by a grid cap (Wehnelt cap) held at a slightly higher negative potential than the filament. The confined beam is accelerated to the anode held at ground potential and a portion of the beam is passed through a hole. The beam current measured at the anode is used to regulate the power supply, which drives the electron gun for the desired current. The tungsten wire gradually evaporates due to the high operating temperature, its resistance decreases, and finally, it gets so thin that it breaks. Higher temperature (higher operating current) increases the evaporation rate and the filament life reduces.

The filament characteristic is given in terms of brightness, which is given as current/area \times solid angle. The brightness is of the order of 10^5 (A/cm² sr) for the tungsten filament. An order of magnitude increased brightness is possible for lanthanum hexaboride (LaB₆) based guns and still larger brightness is possible for field emission guns. This is made by reducing the emission area and thereby the extent of demagnification required in the operation is reduced significantly.

LaB₆ has greater brightness and longer lifetime compared to tungsten. The emitter is a single crystal of LaB₆ of 10 μm diameter with 500 μm length. The tip is ground to a sharp tip of 10 μm and the crystal is mounted on rhenium or graphitic carbon base. The base is resistively heated so that the tip emits electrons. The gun requires better vacuum than tungsten filament as the tip can be contaminated easily. The filament lifetime is of the order of 1000 h and increased brightness justifies an order of magnitude increase in cost.

Field emission is another way to generate electrons. This kind of sources have high brightness. In field emission, the field at the tip of the emitter reaches a magnitude of 10 V/nm, the potential barrier for electron emission gets reduced and becomes narrower so that electron can tunnel and escape the cathode. Two kinds of field emission sources are common. The cold field emitter (CFE) and the Schottky field emitter (SFE). In the CFE, a sharp single crystal of <310> tungsten tip is spot-welded on

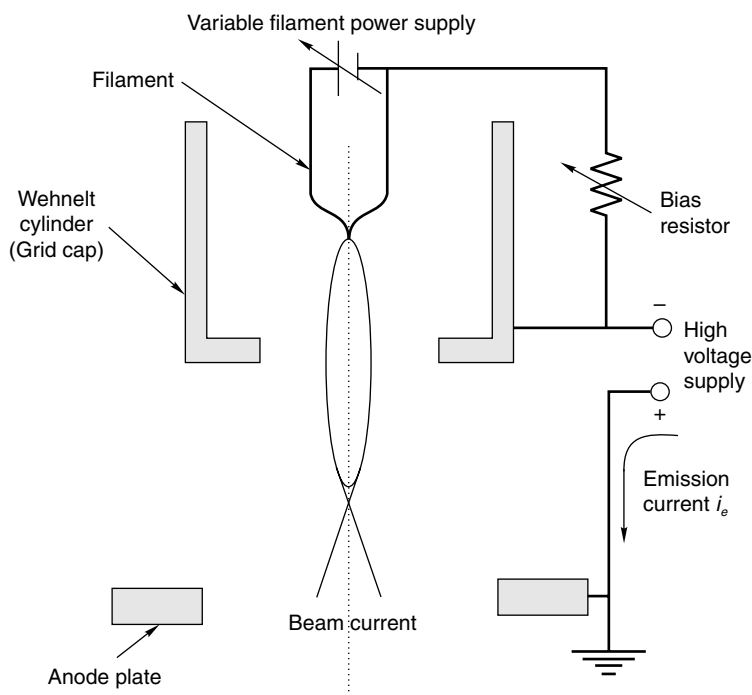


Fig. 2.2 Schematic of an electron gun. The gun is normally operated at a constant emission current, which means regulation of the current supplied to the filament (adapted from, J.I. Goldstein, C.E. Lyman, D.E. Newbury, E. Lifshin, P. Echlin, L. Sawyer, D.C. Joy and J.R. Michael, *Scanning Electron Microscopy and X-ray Microanalysis*, Kluwer Academic/Plenum Publishers, New York, 2003.¹).

a tungsten wire. The tip is made of tungsten as it has the strength required to withstand the mechanical stress produced at the tip. The tip itself is mounted in a triode configuration so that the potential difference between the tip and the first electrode is of the order of 3–5 kV to produce 10 μA emission. The potential difference between the second electrode and the tip determines the beam energy. Field emission is sensitive to adsorbed gases and by flashing the tip to a temperature of 2500 K, the surface gets cleaned. After flashing, the emission is high, but soon it reduces and stabilises as the surface is covered. The tip has to be re-flashed to get a clean surface again after several hours of operation. In each flashing, the tip gets more blunt and after several thousands of flashes, the tip is no more usable and it has to be changed. This occurs only after several years as one flashing is enough for a day.

The next class of emitters is SFEs and thermal field emitters (TFEs). They are operated at high temperatures. They are self-cleaning and the tip sharpens in the extraction field. In SFE, the field at the tip is used to reduce the work function barrier. The tip is held at a high temperature. In order to reduce the work function better, the surface is coated with ZrO_2 from a dispenser. The SFE gun is run continuously even when no current is drawn. This keeps the system clean. However, as the ZrO_2 reservoir is finite, lifetime is finite and replacement is needed every year.

2. Electron lenses

An electromagnetic lens used in electron microscopy is shown in Fig. 2.3a. This consists of a coil of wire generating a magnetic field enclosed in an iron casing. A magnetic field is generated between the polepieces by applying a current through the coils. Electron in a magnetic field undergoes rotation. As the radial component of the magnetic field reverses after the centre of the lens, the rotation in the first half of the lens is reversed. The electron leaves the lens without any net change in angular momentum, but it undergoes deflection towards the axis. Since the radial force is directed towards the axis, the magnetic lens is always convergent. Electron traveling off-axis to the beam path will spiral through the lens towards the optic axis. The point from which the beam starts bending to the point, where it crosses the lens axis, is called the focal length. The focal length can be varied by changing the current in the coils and this is a difference from the optical lenses, where the focal length is fixed. Referring to Fig. 2.3b, the focal length can be given as, $1/f = 1/p + 1/q$. From this, magnification, $M = q/p$ and demagnification, $m = p/q$, where p is the distance from the object to the centre of the lens and q is the distance from the image to the centre of the lens can be calculated.

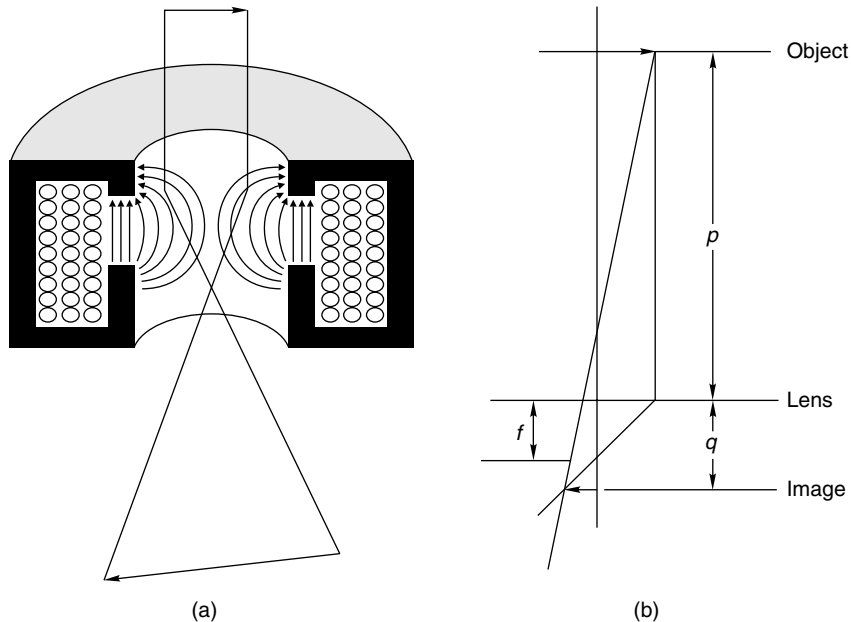


Fig. 2.3 (a) Schematic of an electromagnetic electron lens. The magnetic field lines are shown. (b) Illustration of the concept of magnification.

An electron microscope contains two kinds of lenses. Condenser lens has a large bore giving long focal length and objective lens has a strong field of short axial extent giving a short focal length, resulting in high magnification. In an electromagnetic lens, an electric current passing through a conductor gives rise to a magnetic field. If the conducting wire forms a solenoid (several turns around a cylinder) each turn contributes to the induced magnetic field at the centre. The flux density at the

centre is, $B = \mu (NI/l)$, where μ is the permeability of the surrounding material, N is the number of turns, I is the current flowing through the coil, l is the length of the solenoid. $H = NI/l$ and so by substituting, $B = \mu H$. So, μ is the flux density per unit field. For air and non-magnetic materials, $\mu = 1.0$ and $B = H$. The permeability of iron is field dependent, and it is unity at high field; and so, $B = H$. At high magnetic fields, iron reaches magnetic saturation and that is the reason for $\mu = 1$. Due to hysteresis of iron, the extent of current used to energise a magnetic lens will not give the lens characteristics, such as focal length. Hysteresis has to be kept small and soft iron is used for this reason. The current results in heating and water-cooling is needed to keep the system cool. The system is shielded from external magnetic fields. For this, a high permeability material is used (μ metal is one such material).

When the solenoid is encased in a case of soft iron, the magnetic field along the axis is increased. If the entire coil, except at a narrow annular gap, is made of soft iron a greater concentration of the magnetic field along a short axial distance occurs. The polepieces are these annular rings, which focus the magnetic field at a given location. The field strength used is below 20,000 gauss in typical instruments.

The focal length is given by, $f = K\nu/(NI)^2$, where K , a constant; ν , the relativistically corrected accelerating voltage; NI , the number of turns of the coils multiplied by the current through the coil. The focusing is achieved by varying the current through the coils. It is important to note that the focal length is not linearly related to current. Focal length of the lens is directly proportional to the accelerating voltage. So image quality is affected by varying the electron velocity.

Lens Aberrations: Electron optics suffers from aberrations. But there is no way to eliminate them unlike in light optics. All that is possible is to reduce them and this is done by proper design considerations.

Spherical Aberration: Electrons in far away trajectories from the optic axis are bent more strongly. As a result, the electron beam entering the lens near edge of the lens, is brought to focus at a different spot than those closer to the centre. This is schematically illustrated in Fig. 2.4a. The error in the image due to this becomes more pronounced as the beam is moved more away from the optical axis of the lens. The differential focusing causes the image at the perimeter to get smeared and not at the centre. As a result of this, the image appears as a disk and not as a point. The smallest disk is called the spherical aberration disk of least confusion, $d_s = \frac{1}{2} C_s \alpha^3$, where C_s is the spherical aberration coefficient and α is the angle of the outer ray through the lens. C_s is typically a few mm for lenses with short focal lengths. Spherical aberration can be minimised by removing the outer edge of the beam. This is achieved by placing a small holed aperture at the centre of the magnetic field or immediately below it. However, smaller diameter reduces beam current and also leads to aperture diffraction.

Chromatic Aberration: This aberration is due to the energy spread of the electrons. When light of different energies enter a converging lens at the same point, the extent of deflection will depend on their energy. In light optics, radiation of shorter wavelength is deflected more strongly than that of longer wavelength. In electron optics, the reverse happens, i.e., shorter wavelength is deflected less strongly. This is due to the fact that electrons are subjected to lesser deflection when the beam energy is high. As a result, the beams of two different energies form image at different points as illustrated in Fig. 2.4b. Due to this aberration, instead of a point a disk results and the diameter of the disk of least

confusion can be given as, $d_c = C_c \alpha (\Delta E/E_o)$, where C_c is the chromic aberration coefficient, and E_o is the beam energy and ΔE is the energy spread. The fractional variation in beam energy is the significant factor.

Chromatic aberration can be reduced by stabilising the energy of the electron beam. Stabilised acceleration voltage and improved gun design ensures the stability of the beam. Effect of chromatic aberration is pronounced near the perimeter of a converging lens and an aperture can be used to eliminate these electrons.

Diffraction: Wave nature of electrons makes the beam to diffract upon passing through a narrow slit. Each beam passing through the slit sets up its own waves. These will interact to give a bright spot in the middle and a set of concentric rings in the image plane called the airy disk. If the intensity distribution is plotted in one dimension, it looks like the one shown in Fig. 2.4c. The contribution to the spot size due to diffraction is given as the half diameter of the Airy disk, $d_o = 0.61 \lambda/\alpha$, where λ is the wavelength of the beam and α is the aperture half angle. In order to reduce the effects of diffraction, it is necessary to have as great an angle as possible between the optical axis and the lens perimeter. That would amount to having no aperture at all. But a smaller aperture is needed to reduce the effects of spherical aberration and chromatic aberration, which would mean that we will have diffraction problems. Thus, an optimum aperture size must be chosen.

Astigmatism: Astigmatism refers to the improper shape of the beam. A point object is focused to two-line foci at the image plane and instead of a point an ellipse appears. The two-line foci may be forced to coincide for correcting this defect. Astigmatism occurs due to defects in the focusing fields, which could be due to a composite of aspects, such as electromagnetic lenses, apertures and other column components. Imperfection in machining can cause astigmatism. Astigmatism is corrected by a set of magnets called stigmators placed around the circumference of the column. These are adjusted according to strength and position in an effort to induce an equal and opposite effect on the beam.

The effect of lens aberrations is important for the objective lens as the effects caused to the beam would be small in comparison to the diameter at other lenses. Typically spherical aberration can be corrected completely. But the correction leads to aperture diffraction, and therefore, these two should be controlled properly. Chromatic aberration is significant below an accelerating voltage of 10 kV.

3. Scan coils

The next part of the SEM consists of the scan coils. In SEM, the scanned image is formed point by point and the scan is achieved by the scan coils. There are two pairs of coils, one each for X and Y axes (Fig. 2.5). The scan coils lie within the column and move the electron beam as per the requirement across the specimen. They are electromagnetic coils and are energised by the scan generator. The scan generator is connected to other components such as the cathode ray tube (CRT) and the magnification module.

The scan is made as follows. The electron beam is swept across the sample. The pattern over the sample is synchronous with that observed in the CRT. The secondary electrons produced by the

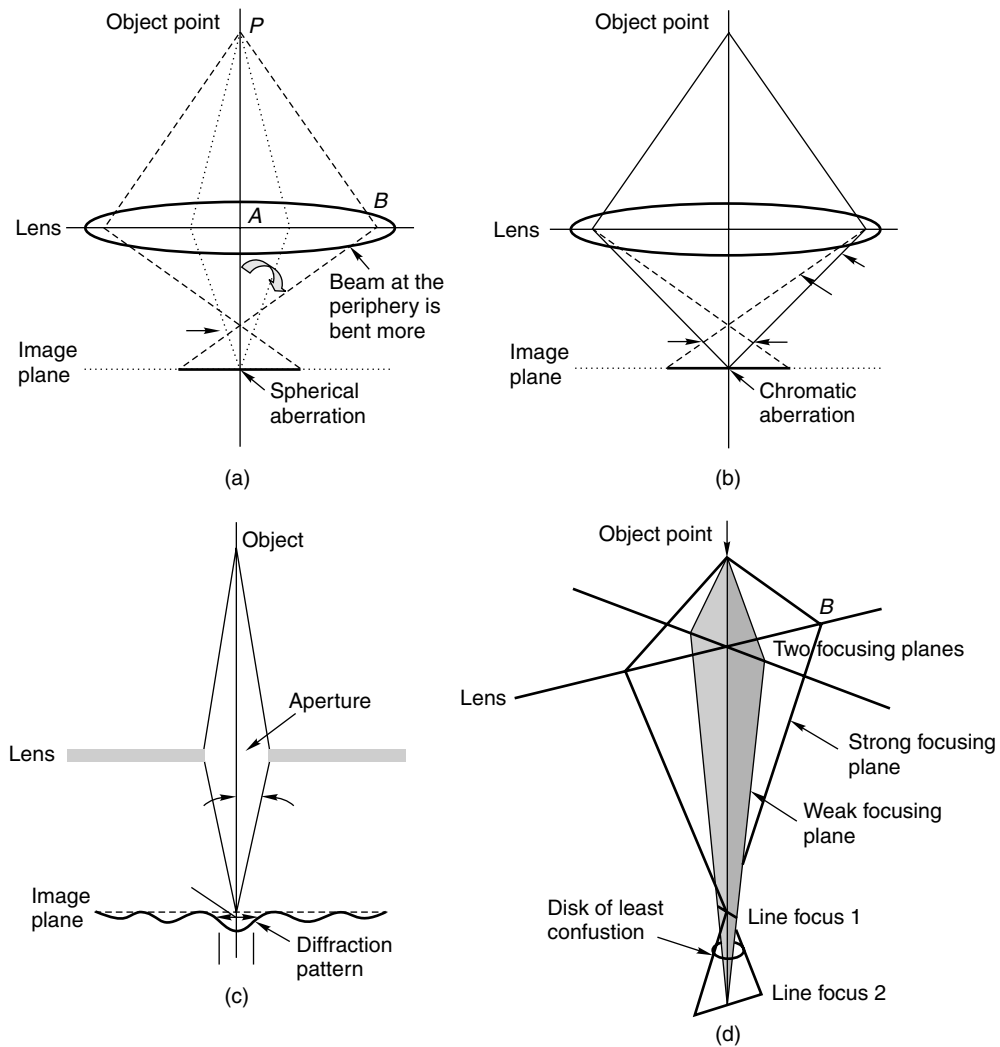


Fig. 2.4 Various aberrations of electromagnetic lenses. (a) Spherical aberration, (b) chromic aberration, (c) aperture diffraction and (d) astigmatism (adapted from, J.I. Goldstein, C.E. Lyman, D.E. Newbury, E. Lifshin, P. Echlin, L. Sawyer, D.C. Joy and J.R. Michael, *Scanning Electron Microscopy and X-ray Microanalysis*, Kluwer Academic/Plenum Publishers, New York, 2003.).

sample upon collision by the beam are detected. The intensity of the signal at the CRT is proportional to that. An intense signal can illuminate several dots on the screen, a weak signal will mean that no dots will be illuminated by the electrons. The detector, therefore, gives the intensity of the signal, the raster pattern gives the location of the signal. In this way, the image on the CRT is built up point by point to match what is happening on the surface of the sample.

This way of forming an image is the essential difference between transmission and scanning types of microscopes. A couple of things are important in this type of image formation. First, focus is dependent upon the size of the electron beam spot. The smaller the spot on the sample, the better the focus. Secondly, magnification is not produced by a magnification or enlarging lens, but rather by taking advantage of the differential between the size of the scan pattern on the sample and the size of the CRT.

The size of the CRT is fixed. The size of the scan pattern on the sample is variable and is determined by the magnification module. By narrowing the size of the area, which is scanned and conveying that to the CRT, we increase the magnification of the image. The smaller the area scanned, the lesser the distance between the raster points, the smaller the amount of current needed to shift the beam from point to point. The greater the area scanned, the lower the magnification, the greater the distance between the raster points and the greater the amount of current needed to shift the beam from point to point. In this way, when we operate the SEM at relatively low magnifications, we actually push the scan coils to their extremes.

The scan generator changes the step current to the scan coils. This current is then multiplied by a constant by the magnification module and sent to the scan coils. The higher the total magnification, the lower the multiplier constant.

4. Electron detector

There are two kinds of electrons coming out from the sample in an SEM; the back-scattered electrons, with high energies as high or less than the primary beam energy and the secondary electrons, which have energies of a few eV, or less than a few tens of eV. The most common kind of detector used in SEM is the Everhart–Thornley (E–T) detector (Fig. 2.5). In this, a scintillator material is exposed to the electrons. Energetic electrons, upon impact with the material, result in photon emission. The photons are transmitted through a light pipe. This is a glass rod or a piece of plastic. At the other end of the light pipe, a photo multiplier is placed which converts the photons to electrons by photoemission. The electrons can be made to undergo a series of collisions on surfaces producing a cascade of electrons and a gain of 10^6 can be achieved this way. The detector has a high bandwidth; that means it responds to a rapidly varying signal. This would be the case when the primary beam is scanned over the sample at high speeds.

In practical operation of the detector, a thin metal coating is applied on the surface of the scintillator. A high positive potential is applied to the metal surface so that all electrons, including the low energy secondary electrons, are accelerated to it so as to generate photons. The high voltage should not affect the primary beam and for this reason, a Faraday cage is kept over the scintillator, which is electrically insulated. By applying a desired potential in the range of -50 to $+250$ V to the Faraday cage, complete rejection or collection of secondary electrons become possible.

For collecting back scattered electrons, a separate detector can be employed. Several kinds of detectors are used and the most popular one is the solid-state diode detector. This works on the principle that in a semiconductor, electron impact can produce electron-hole pairs if the electron energy is above a threshold value, which is of the order of a few eV. Thus, when a high energy electron

falls on it several thousands of electron-hole pairs are formed. The charges can be swept in opposite directions if a bias is applied. The charge collected can be amplified and detected.

In low voltage SEM, the common electron detector is the channel plate. Here primary electrons make secondaries in a channel, and a cascade of secondary electrons is produced. Several such channels are made on a disk of a few cm in diameter and the electrons coming out at the other side are collected and amplified. As the secondary electron yield increases in the low keV range, channel plate works well for low energy operation. Low energy secondary electrons require acceleration for detection by a channel plate.

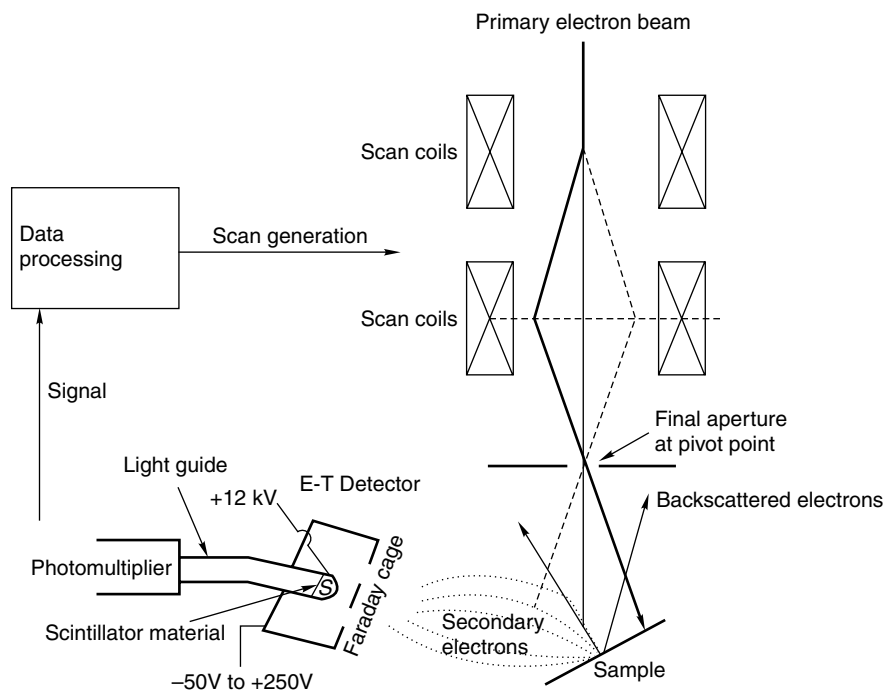


Fig. 2.5 Schematic of an SEM. The electron beam is manipulated by a set of scan coils so as to scan a surface and the secondary electrons are detected by the detector. By applying a positive potential to the Faraday cage, the secondary electrons are rejected completely (adapted from, J.I. Goldstein, C.E. Lyman, D.E. Newbury, E. Lifshin, P. Echlin, L. Sawyer, D.C. Joy and J.R. Michael, *Scanning Electron Microscopy and X-ray Microanalysis*, Kluwer Academic/Plenum Publishers, New York, 2003.).

2.2.1.5 SEM: Modern Advances

SEM is the most widely used electron microscopic technique. This is largely because of its versatility, various modes of imaging, ease of sample preparation, possibility of spectroscopy and diffraction as well as easy interpretation of the images. The method has high throughput making it an accessible facility. A very large range of magnification is available, which makes almost every detail to be visualised. Best

SEMs can get image resolutions in the range of 0.5 nm and, for this the sample, need not be especially prepared. Sample size is not a limitation in SEM and samples as large as 6" silicon wafers can be put directly in a modern machine.

Modern advanced SEMs utilise field emission sources. There have been numerous advances in various aspects of the hardware such as lenses, detectors and digital image acquisition. Coupled with advances in other areas of instrumentation, such as power supplies, high vacuum instrumentation, etc. it is now possible to acquire SEM images from almost anything, including wet biological samples.

Low-voltage SEM is another new development. The extreme surface sensitivity of this technique is a result of the reduced interaction volume. This makes it possible to measure images with nanometer scale resolution with under 1 kV acceleration. At these low energies charging is not an issue and it is possible to measure images without conductive coatings. The electron energy can be reduced further by applying a negative potential on the sample and this way beam energy can be reduced to below 100 eV and ultra low voltage SEM (ULV-SEM) becomes possible, which is extremely surface sensitive and avoids beam induced damage at surfaces.

When an electron beam interacts with matter several processes occur. These result in particle or photon emission processes, which are summarised in Fig. 2.6. The electron emission processes include elastic and inelastic scattering, emission of secondary electrons and emission of Auger electrons. Inelastic scattering occurs as the beam interacts with the sample and electronic excitations of the constituent atoms can occur. These excitations can lead to valence and core electron excitations and emission. The core hole thus created may get filled by electron de-excitation resulting in X-rays. The de-excitation can also result in electron ejection, called Auger emission. In addition, collision of the primary beam can also lead to excitations of lattice vibrations. All of these electrons can be used to gather microscopic information of the sample. In addition, they can also be used to obtain chemical or compositional information as in the case of Auger electrons or structural information as in the case of back-scattered electrons. In a normal SEM image, only secondary electrons are detected. Emissions of characteristic X-rays as well as continuous X-rays occur. The characteristic X-rays are used for qualitative and quantitative information. In addition to these, electron induced desorption, ion ejection, etc., occur.

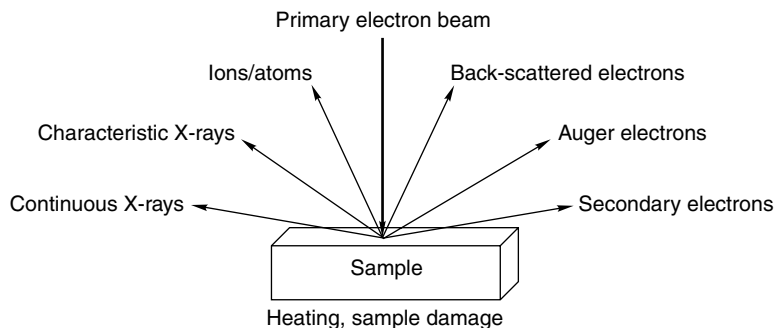


Fig. 2.6 *Electron beam-induced processes in the sample.*

High resolution SEM is now a routine analytical tool. In nanoscience and technology, this becomes an important and high throughput characterisation tool. It is important to know the dimensions of the structures fabricated and materials prepared when characterising device structures. Thus, SEM becomes an indispensable tool in nanometrology (branch involving nanoscale calibration).

2.2.1.6 Microanalysis

In both SEM and TEM, high spatial resolution microanalysis of materials is possible. The spatial resolution of the analysis is made possible by the small dimension of the excitation beam, which is of the order of a few nanometers in state-of-the-art instruments. The electron beam causes various excitations in the sample and they are characteristic of the elements present in the material. Characteristic X-rays emitted by the sample, as a result of core-hole decay, can be used for elemental identification. The intensity of the signal can be used for quantitative analysis.

Microanalysis is done in two ways. One corresponds to the energy analysis called *energy dispersive spectrometry* (EDS) and the other corresponds to wavelength analysis called *wavelength dispersive spectrometry* (WDS). While improved energy resolution is possible in WDS, it is more cumbersome and time consuming than EDS. In EDS, a signal from the detector is proportional to both the energy and intensity of the X-rays. In WDS, the wavelength of the X-ray and its intensity are determined separately.

When an electron approaches the atom, it gets decelerated due to the coulombic field. This results in a loss of energy for the electron and that energy appears as photon, referred to as bremsstrahlung or “breaking radiation”. This radiation contains photons of all energies till the energy of the original electron, as electron can lose any energy, from zero to the energy of the primary electrons. The characteristic X-rays emitted by the atoms will appear as spikes on this large smoothly varying photon intensity. There are several characteristic X-ray lines with which an atom can be identified. Intensities of these lines can be related to the concentrations of the emitting species in the sample, although there are various parameters, which determine the intensities. The important aspects related to X-ray emission intensity are, inner shell ionisation cross-section, X-ray absorption cross-section of materials and X-ray production range.

In EDS, all photons emitted by the sample are collected and measured simultaneously by a solid state X-ray detector. The common EDS detector is lithium-drifted silicon, Si(Li). Intrinsic or high purity Ge (HPGe) is also used, which is more common with TEM instruments due to their higher collection efficiency. When an X-ray photon falls on an intrinsic semiconductor (having no charge carriers), due to photoabsorption charge carriers (electrons and holes) are created. These are swept by an applied bias forming a charge pulse. This charge pulse is then converted to a voltage signal. Intrinsic condition is hard to achieve and detector crystals are made to behave like intrinsic silicon. This is made by applying Li on *p*-type Si forming a *p*-*n* junction. The junction region will behave like an intrinsic semiconductor. The width of this region can be expanded by applying an electric field at elevated temperatures. The removal of most of the *p*-type region gets a detector. However, the Li present is mobile at room temperature and cooling the detector down to 77 K is necessary to operate the detector under bias.

The intrinsic silicon active layer is covered on the front side with p-type Si and in the back with n-type Si. The front is also coated with a thin gold layer for electrical contact. The device is kept behind a Be window, which blocks visible light. Also, it mechanically seals the detector assembly from the vacuum chamber, avoiding contamination. When an energetic photon strikes the detector, charge carriers are created. The detector is reverse biased, i.e., p-type is connected to negative potential. This means that when the charge carriers are created, the holes move to the p-side and electrons move to the n-side, creating a pulse of electrons at the n-side, which can be amplified. To reduce noise and also to reduce Li mobility, to maintain the intrinsic condition, the detector is cooled. Photons of high energy above the Si K shell binding energy (1.84 keV) falls on it, photoelectron emission takes place. The photoelectron loses energy inelastically exciting electron-hole pairs. The core hole produced may be filled by photoemission or Auger emission. The photon may be reabsorbed resulting in photoemission or can undergo inelastic scattering. Thus, all the energy of the initial photon is used in generating electrons. In favourable conditions, the number of charges created in the detector per photon is = photon energy/energy required for the creation of an electron-hole pair (ϵ). For 5000 eV photon, this works out to 5000/3.86 or 1295 electrons (ϵ at 77 K is 3.86 eV for Si). However, this number is too small, generating a very small charge pulse of 2×10^{-16} C. Each charge pulse, converted to voltage, represents the energy of the photons. The resolution of the photon distinguishable by solid state detectors of this kind is 130 eV at MnK α (5890 eV). The detector resolution is a function of X-ray energy and it is about 65 eV at 282 eV. There are several advanced detectors such as the silicon drift detector, which works at 250 K, having the same resolution, but increased sampling rate. Microcalorimeter EDS works by measuring the temperature difference caused by the absorption of X-rays. With this an increased energy resolution is possible, about 4.5 eV at MnK α .

Wavelength dispersive spectrometers work on the principle of Bragg diffraction, $n\lambda = 2d\sin\theta$, where λ is the wavelength of the X-ray and θ is the angle of incidence. Therefore, at various angles of incidence, it is possible to scatter rays of different wavelength to the detector. As $\sin\theta$ cannot be larger than one, the longest wavelength diffracted is $2d$, therefore, the crystal puts a limit on the range of elements covered. There are also other limitations of the hardware. When θ is 90°, the detector has to sit at the X-ray source; when $\sin\theta$ is close to zero, the movement of the crystal near the specimen is a problem. In order to reach the low energy X-rays emitted by Be, B, C and N, it is necessary to use crystals of large d values. This is made possible by Langmuir–Blodgett films whose inter-layer spacing can be tuned by varying the chain length of the monolayer. Most of the measurements of long wavelength X-rays are done by layered synthetic microstructures. This contains evaporated alternate layers of heavy and light elements. The thickness of the layers can be easily controlled.

The detector commonly employed is a gas proportional counter. This has a gas mixture (typically 90% argon, 10% methane). The detector assembly has a thin window through which the X-ray photon falls in. It causes the ejection of a photoelectron, which is accelerated by the high voltage applied on the collector. The electron causes subsequent ionisation in the gas, and as a result, a gain factor of the order of 10^5 is achieved. There have been numerous improvements in gas filled detectors involving the use of improved windows, other gases, etc.

Spatial resolution of SEM is affected by the beam size as mentioned before. But the beam causes interaction with the sample and the region of interaction exceeds the physical dimension of the beam itself. The spatial extent increases laterally as well as depth-wise, this interaction volume depends on the material and also on the beam energy. At large energies, the beam interacts to a greater extent, the depth of interaction decreases with decrease in electron energy till about 100 eV and at very low energies of the order of a few eV, it increases again. The range of interaction is decided by the electron attenuation length. The universal electron attenuation length of materials is given in Fig. 2.7. As seen, the attenuation length increases with electron energy and has a minimum at a few ten eV. This makes it possible to design highly surface-sensitive SEMs by reducing the beam energy. This development is discussed in low-energy SEM.

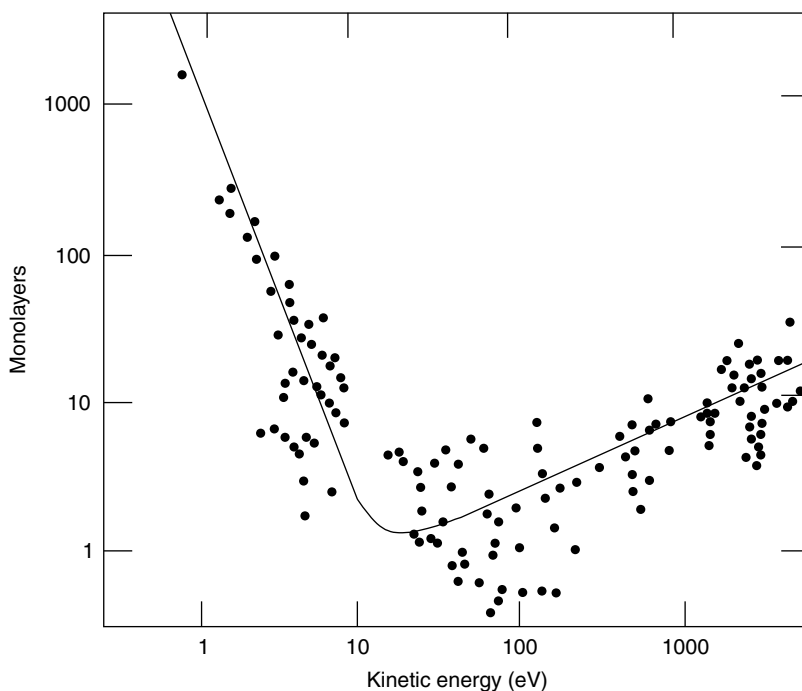


Fig. 2.7 Universal attenuation length data of materials as a function of electron kinetic energy.

At low kinetic energies, the electrons are sensitive to only a few monolayers of the material. The data points correspond to the experimental data from a number of materials and the line is an approximate fit.

2.2.2 Transmission Electron Microscopy

In TEM, the transmitted electrons are used to create an image of the sample. Scattering occurs when electron beam interacts with matter. Scattering can be elastic (no energy change) or inelastic (energy

change). Elastic scattering can be both coherent and incoherent (with and without phase relationship). Elastic scattering occurring from well-ordered arrangements of atoms as in a crystal, results in coherent scattering, giving spot patterns. This can be rings in the case of a polycrystalline material. However, inelastic scattering also occurs, which also gives regular patterns as in the case of Kikuchi patterns. Inelastic processes give characteristic absorption or emission, specific to the compound or element or chemical structure. As a result of all these diverse processes, a transmission electron microscope is a complete laboratory.

There are two main mechanisms of contrast in an image. The transmitted and scattered beams can be recombined at the image plane, preserving their amplitudes and phases. This gets a phase contrast image of the object. An amplitude contrast image can be obtained by eliminating the diffracted beams. This is achieved by placing suitable apertures below the back focal plane of the objective lens. This image is called the bright field image. One can also exclude all other beams except the particular diffracted beam of interest. The image using this is called the dark field image (Fig. 2.8).

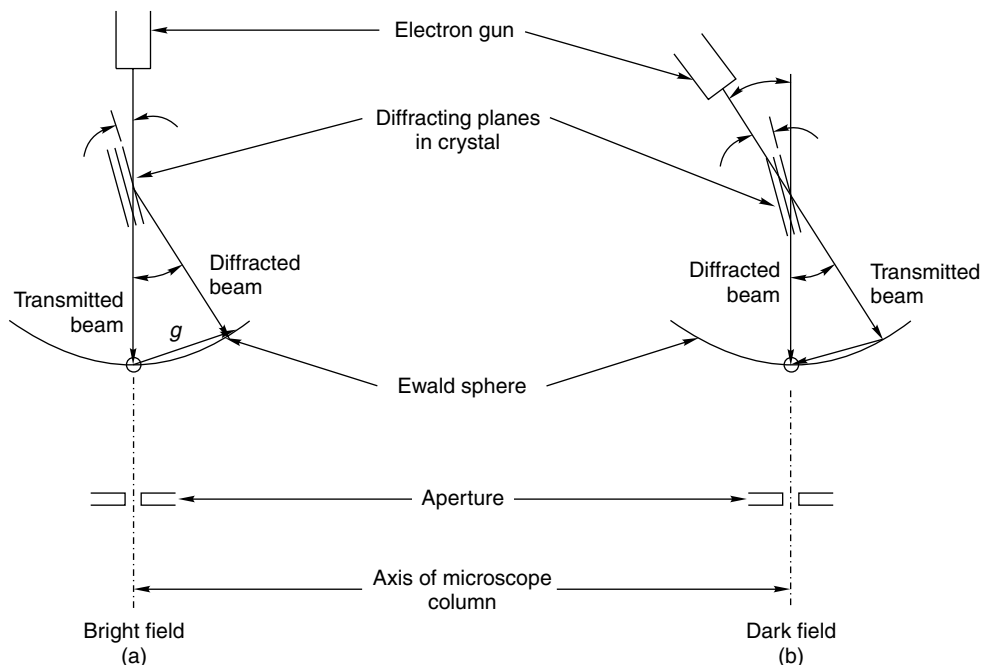


Fig. 2.8 Two kinds of image collection: (a) bright field and (b) dark field. In bright field, the transmitted beam is used for imaging. In dark field, the diffracted beam is used for imaging. The diffracted beam can be used for imaging either using a movable aperture or shifting the incident beam keeping the aperture constant (adapted from, G. Thomas and M.J. Goringe, *Transmission electron microscopy of materials*, John Wiley & Sons, New York, 1979²).

TEMs with resolving powers in the vicinity of 1Å are now common. As a result, HRTEM is one of the most essential tools of nanoscience. Interaction of the electrons with the sample produces elastic

and inelastic scattering. Most of the studies are carried out with the elastically scattered electrons, which form the bright field image. The inelastically scattered electrons are used for electron energy loss spectroscopy as well as energy filtered imaging. Electrons emerging from the sample, after a series of interactions with the atoms of the target material have to be transferred to the viewing screen to form an image. This is greatly influenced by the transfer characteristics of the objective lens. A parameter, which can be used to understand the transfer properties, is the phase contrast transfer function (CTF). This function modulates the amplitudes and phases of the electron diffraction pattern formed in the back focal plane of the objective lens. The function is given as,

$$T(k) = -\sin\left[\frac{\pi}{2}C_s\lambda^3k^4 + \pi\Delta f\lambda k^2\right]$$

where, C_s is the spherical aberration coefficient, λ is the wavelength of the beam, Δf is the defocus value and k is spatial frequency. Defocus setting (with reference to the Gaussian focus) in the electron microscope determines the shape of the CTF. This is given in Angstrom units. In the electron optical convention, overfocus means negative defocus values, underfocus (the only useful range) means positive defocus values. CTF of a 200 keV microscope will look like the one shown in Fig. 2.9.

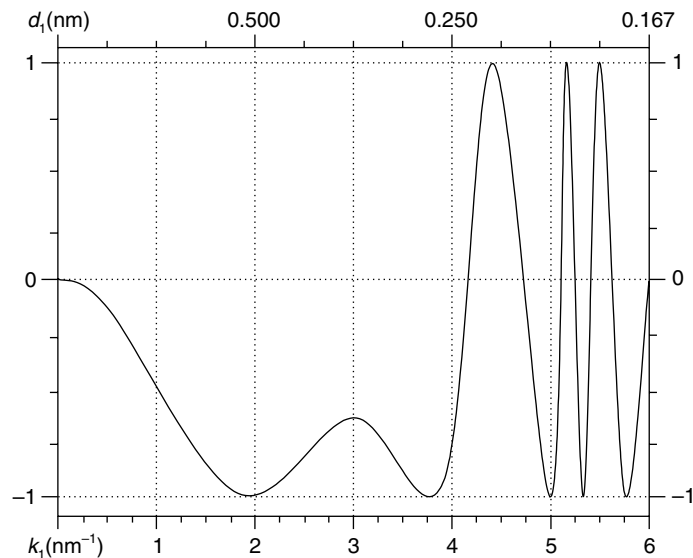


Fig. 2.9 A contrast transfer function.

The general characteristic to note is its oscillatory nature. When it is negative, we have positive phase contrast and atoms will appear dark on a bright background. When it is positive, negative phase contrast occurs, and atoms will appear bright on a dark background. When it is equal to zero, there is no contrast or information transfer. CTF can continue forever but, it is modified by functions known as *envelope functions* and eventually dies off.

In an instrument, the most important aspect is the resolution. This is the ability of the instrument to discriminate between two closely lying objects. As the wavelength of electrons is in picometer range, it is only natural that a resolution of that order is expected. This is however, not the case, because of the fact that electron lenses have aberrations and also due to the fact that a coherent electron beam is impossible. We can express the resolution as, $d \propto C_s^{1/4} \lambda^{3/4}$. C_s and λ are the spherical aberration coefficient of the objective lens and the wavelength of the electron beam, respectively.

The interpretable resolution, or the structural or point resolution is the first zero crossover of the CTF at the optimum defocus. This can be given as, $\delta \sim 0.66 (C_s \lambda^3)^{1/4}$. C_s increases with electron beam energy, but the point resolution improves with acceleration voltage as λ is reduced. C_s ranges from 0.3 mm for 100 keV to 1.5 mm for 1 MeV. The resolution changes from 0.25 to 0.12 nm. The increasing cost of the instrument at larger acceleration voltages and irradiation damages at larger acceleration voltages make it more attractive to use intermediate energy ranges. The instrumental resolution is lesser than this value, but knowing the defocus and C_s accurately, improved images can be obtained by subsequent processing. The lattice resolution refers to the finest lattice spacings observable in images. The lattice images may not yield better information about the sample in several cases as far as local atomic environment is concerned. Interpretable and instrumental resolutions are important in assessing the performance of the instrument.

2.2.3 STEM

STEM is a hybrid instrument with the features of SEM and TEM. The same probe beam in TEM can be demagnified and used as a probe beam, which can be scanned over the sample. The probe beam has to be small and bright, and therefore, field emission sources are needed to get beam dimensions smaller than a nanometer. The principal components of STEM are shown in Figure 2.10. The beam coming off the gun is demagnified by the objective lens. A set of condenser lenses are placed above the objective lens to add flexibility to the beam parameters. The scanning coils are incorporated into the objective lens itself. The beam falling on the sample produces a diffraction pattern. The pattern is a convergent beam electron diffraction and it is also called electron nano diffraction and the beam size is close to the resolution limit of the instrument. The observation screen may have an aperture and some part of the transmitted beam is used for electron energy loss spectroscopy (EELS, see below). This analysis is usually done with the central part of the beam (Fig. 2.10, bright field, a), but can be done with any of the diffracted spots (Fig. 2.10b and c). That is, the dark field images may be formed either by the deflection of the diffracted beam into a centrally placed objective aperture, or by the displacement of the aperture, which allows only a specific diffracted beam to pass through. The analysis may be either the EEL spectrum or an image using electrons with characteristic energy loss. The normal bright field image is made with no loss electrons from the central beam. Dark field images are made with electrons deflected from the beam axis with or without energy loss. Deflection coils placed after the sample are used to direct the chosen part of the diffraction pattern to the entrance aperture of the spectrometer. Common dark field STEM images are collected by imaging part of the diffraction pattern outside the central beam spot.

Detectors can be placed around the sample to detect the secondary radiations coming out from the sample. X-rays, secondary electrons and Auger electrons can be analysed, the last two are normally used for imaging purposes and the first one is used for microanalysis. In microanalysis, the important aspect is that since the sample thickness is small in STEM, the interaction volume is very small. Chemical analysis of small volumes is limited only by the quality of the signal obtained as far as X-ray is concerned. A combination of ELS and X-ray analysis may be used in most cases.

There are numerous areas where STEM can be of use in nanotechnology. With the current instrumental resolution of the order of 0.1 nm, complete characterisation of materials up to 1 nm is possible. Diffraction of objects at 1 nm is possible. All kinds of materials, such as crystalline, amorphous and biological have been investigated. With the need to know everything about nanostructure increases, applications of STEM are likely to increase.

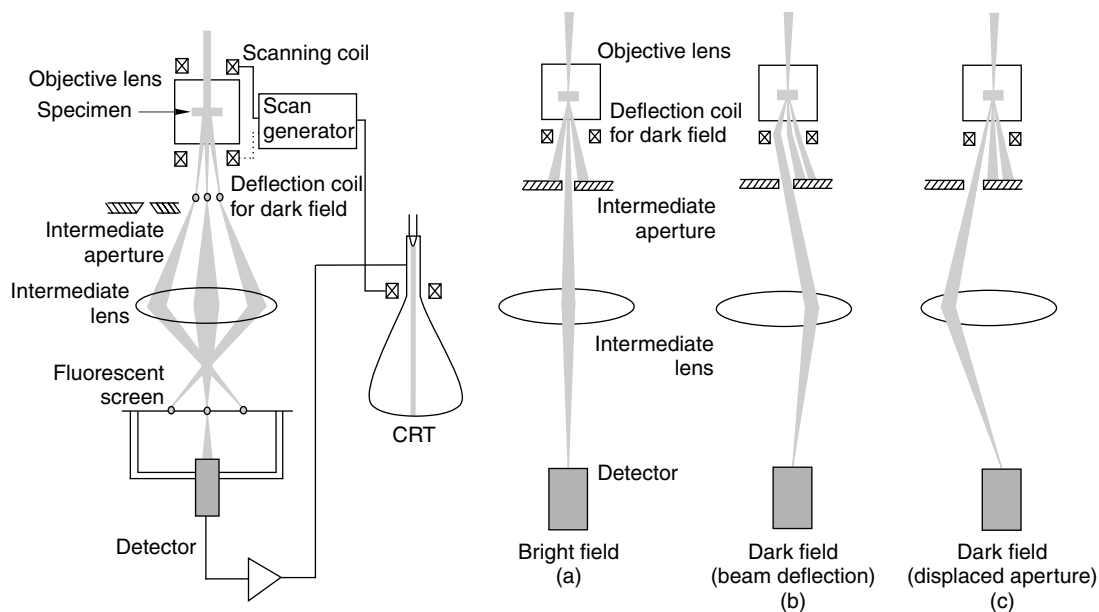


Fig. 2.10 Schematic of a STEM instrument and various ways of operation of the same (adapted from, G. Thomas and M.J. Goringe, *Transmission electron microscopy of materials*, John Wiley & Sons, New York, 1979).

2.2.4 Image Collection in Electron Microscopes

The SEM image is collected in a video monitor (CRT), which is captured by a camera or a computer. In TEM, the image is formed when transmitted electrons fall on a phosphor screen. The image formed can be photographed. Photography is a result of a series of chemical reactions. This uses the light sensitivity of silver halides. Silver bromide is used mostly; iodide and chloride are also used. When the grains of silver salt present in a gelatinous film are impinged with photons, they go to an activated state, which get reduced by a reducing agent (developer). The reduction will ultimately take place on

all the silver halide grains, including those which are not exposed to photons. As a result, one needs to stop the process of reduction. This is done by putting the film in water. The remaining silver grains can still get reduced later on. To avoid this, these grains have to be removed by a process called fixation. Thiosulfate is used for this. After the process of development and fixation, the film is dried and stored.

There are basically two types of emulsions used in photographic films. The classification is based on the light energy. Panchromatic emulsions are sensitive to all wavelengths, and therefore, are handled in total darkness till fixation. Orthochromatic emulsions are sensitive to certain wavelengths only. There is a safe light, in which it can be handled. The film has two characteristics. Light sensitivity, which decides how long one should expose and grain size, which decides how large one can enlarge the image. The extent to which the film is darkened, depends on the light intensity and duration of exposure. These parameters have to be optimised for a given film.

2.2.4.1 Digital Imaging in TEM

In digital TEM imaging, the image formed by the electron beam is captured by a charge-coupled device (CCD). CCD is an image-sensing device, in which an array of light sensitive capacitors is connected on an integrated circuit. By external control, the charge at one of the capacitors can be transferred to another. Depending on how the CCD is implemented, there are three common kinds of architectures. In the “full-frame” CCD, the charge is collected on all the available area of the CCD and the information is read out by placing a mechanical shutter over the sensor. In the “frame-transfer” CCD, half of the image area is covered with an opaque mask and the image collected is transferred immediately to the opaque area and read out slowly. As double the area (sensor and intermediate storage) is needed, this adds to the cost. But quick accumulation of image becomes possible by this way. In the “interline” architecture, every other column of the sensor is masked and the image is shifted only one pixel after collection. This adds to a fast shutter speed and smearing of the data is less, but only half the area is effectively used and so the fill-factor is only half. There are ways to improve this, however.

In the CCD detectors, used in TEM, the photons have to be generated first. For this, a scintillator plate is used. The electrons fall on this and photons are generated. The photons are transferred to the CCD by fiber-optics. At the CCD photons generate charges and they are read out, pixel by pixel. CCDs are generally cooled to reduce the noise (dark current).

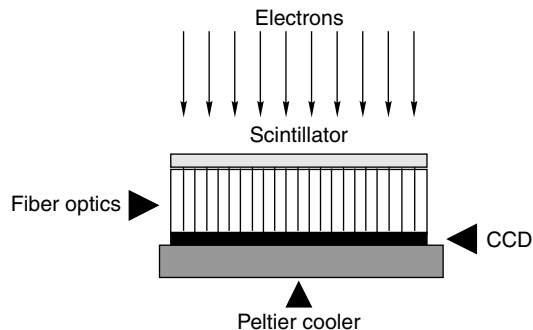


Fig. 2.11 Schematic of a CCD detector used for TEM.

2.2.5 Environmental Transmission Electron Microscopy (ETEM)

Science at the nanoscale is concerned with the variation of properties with size and shape. Structural and morphological changes occur in these materials with minor changes in temperature and other parameters, such as atmosphere. Because of these reasons, nanomaterials have to be studied at higher pressures and temperatures. Such studies have been important in areas such as catalysis. Gas-solid interactions in general have been of interest in areas such as corrosion, oxidation, etc. Biological materials need to be investigated close to their natural environment. All these requirements have necessitated the modification of conventional TEMs to work at modified conditions. These microscopes are called today as environmental transmission electron microscopes. This allows investigation of structural and chemical changes on materials upon gas-solid and liquid-solid interactions at varying temperatures.

In ETEM, the sample is confined to a high pressure region, as high as 150 torr, in such a way that the column vacuum is not significantly deteriorated. The key instrumental feature is an environmental cell, in which the pressure-temperature conditions are regulated. This can be done by using two kinds of approaches: (1) using electron transparent windows to confine the system under investigation; and (2) use of differential pumping to confine the system. The window method has an advantage that higher pressures are possible, but it is difficult to get high resolution due to the additional scattering as a result of the window material. Due to the space requirements of such a cell, this kind of cells were used only in high energy instruments because of their larger pole-piece gaps. The medium energy TEMs today have pole-piece gaps of 7–9 mm, large enough to accommodate a cell. Differentially pumped cells are used nowadays.

Such instruments are used for *in-situ* synthesis of nanoparticles, study of carbon nanotube growth, *in-situ* chemical transformations of nanoparticles, etc. Combining diffraction, microscopy and elemental analysis in ETEM makes it possible to do complete investigations as a process occurs. It is possible to make nanolithographic structures in such an instrument.

2.2.6 Electron Energy Loss Spectroscopy at the Nanometer Scale

Characterisation of materials at the nanometer scale is central to nanoscience and technology. With improvements in electron sources and optics it is possible to generate beams of sub-nanometer spatial spread and this can be an excellent probe into the chemical and structural aspects of the sample. In electron energy loss spectroscopy, one is interested in the inelastic energy losses suffered by the primary beam as a result of scattering. The energy changes may be due to collective electron oscillations or inter-band transitions of the sample or the characteristic energy losses due to core electron excitations resulting in characteristic edges superposed on a monotonically decaying background. While the former occur in the range of 5–50 eV, the other occurs within about a few thousand eV. The collective electron oscillations or inter-band transitions may not have much elemental or material significance as energies of these transitions change with size at the nanometer level. At extremely low energies, these transitions may disappear altogether as well. The core electron excitations are characteristic of the element. Thus, a qualitative analysis of the material is possible in terms of the characteristic

energy losses obtained. An energy loss at 284 eV is characteristic of carbon and that at 530 eV is due to oxygen. The intensity at this energy loss after subtracting the background suitably is related to the concentration of the atom. Thus, quantitative analysis is possible. The position and shape of the energy loss is characteristic of the chemical environment of the sample. Because of all these, electron energy loss spectroscopy at the nanometer scale is a unique probe.

Core-level excitation spectra can be calculated. In this, the approach will be to calculate the inelastic scattering cross-section. The essential aspect of these computations will be to evaluate the probability of electronic transitions between two orbitals as a result of a perturbing electric field. Atomic orbitals of the initial states and molecular orbitals of the final states can be used for such computations. By performing refined calculations, it is possible to obtain good agreement between theory and the fine structures seen experimentally.

The energy loss information can be collected as a function of space. This can be done in two different modes, either as a spectrum image where at each point defined on the sample, one collects a complete spectrum or the spectrum in an energy window ΔE is collected for a 2D space, called image-spectrum. Both the methods have their own advantages and disadvantages. The former is collected in the STEM and is superior in the sense that all spectral channels are collected parallelly as a function of space. A post column energy analyser does the energy analysis of electrons. In the image-spectrum mode, an energy filter is used. An imaging stage is put after the filter, this converts the spectrum to an image. The filter fixes the energy of the electrons to be transmitted and the slit at the exit plane of the filter decides the energy width.

EELS has been used for elemental mapping of materials at the nanometer range. Elemental mapping of doped elements in single-wall carbon nanotubes, nanobubbles in alloy matrices, segregation of atoms in ultrathin films, etc. have been performed with EELS. Mapping of individual atoms in nanostructures has been demonstrated. Apart from elemental mapping, the distribution of the bonding characteristics of an element within a material at the nanometer level can be investigated. Measuring atomic properties of nanometer sized objects is a distinct reality with EELS.

2.2.7 *In-Situ* Nano Measurements

Properties of individual nano objects have to be understood in a number of cases. This has a bearing on the properties of the bulk systems. For example, how would one measure the Young's modulus of a single carbon nanotube? There are several methods one can use for this, but it is important that the measurement is done in an instrument where the nano object is seen while the measurement is performed. There are several instances of this kind, such as the measurement of electrical conductivity, thermal conductivity, temperature stability, melting point, chemical reactivity, etc. of single nano objects. All of these are possible in the transmission electron microscope. Of course, for each of these measurements, the TEM has to be modified significantly. It is also necessary to invent new methods and appropriate theory for the nano measurements.

One of the easier kinds of *in-situ* measurements in TEM (as well as in other cases) is the temperature dependence. This measurement involves varying the sample temperature in the range of liquid

helium (or more generally liquid nitrogen) to 1200 K. Phase or morphology change of the material is investigated with specific reference to a single nano object. This kind of investigations reveal that different morphologies have different stability. For example, among a group of particles with cubic and tetrahedral particles, the cubic one is found to change to a spherical structure at a lower temperature than the tetrahedral ones. This is attributed to the lower surface energy of the [111] planes present in tetrahedral structure than the [100] present on cubes.

One of the ways to measure Young's modulus of a nanotube is to investigate the blurring contrast due to the thermal vibration of the tip of a carbon nanotube image. This is shown in Fig. 2.12 below. Some of the nanotubes, shown with arrows show blurring contrast. The blurring amplitude, u can be related to the vibration energy, which is related to the Young's modulus. By measuring the blurring contrast as a function of temperature, the Young's modulus of a multi-walled carbon nanotube is calculated to be in the range of 1 TPa.³

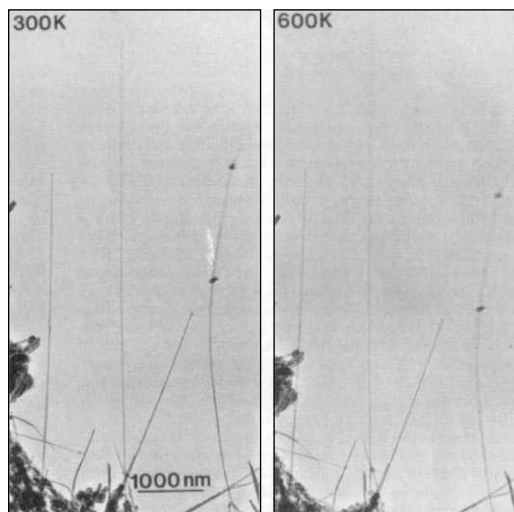


Fig. 2.12 *Low magnification TEM images of carbon nanotubes grown by arc-discharge method. The tips of the nanotubes are blurred due to thermal vibrations. The amplitude of the vibrations increases with temperature (adapted from, M.M.J. Treacy, T.W. Ebbesen and J.M. Gibson, Nature, 381 (1996) 678).*

Numerous different kinds of measurements have been demonstrated, which include *in-situ* transport measurements in a nanotube, mapping the electrostatic potential at the tips, work function measurements of individual nano objects, field emission from nanotubes and applications of single nanotubes as balances and thermometers. In several cases, it is necessary to develop new methods and appropriate theory. It is very clear that numerous kinds of nano measurements are possible in the TEM with appropriate modifications of the equipment.

2.2.8 Electron Diffraction as a Tool for Characterising Nanomaterials

2.2.8.1 Introduction to Electron Diffraction

Electron diffraction is due to an interference effect, which leads to scattering of monochromatic electron beams in specific directions. The diffraction of electrons from crystals is governed by Bragg's Law, according to which,

$$n\lambda = 2d \sin\theta;$$

where,

n is number of wavelengths in path length difference;

λ is wavelength of electron wave;

d is interplanar spacing between two identical nearest planes;

θ is angle of incidence (and reflection).

The terms are explained in Fig. 2.13.

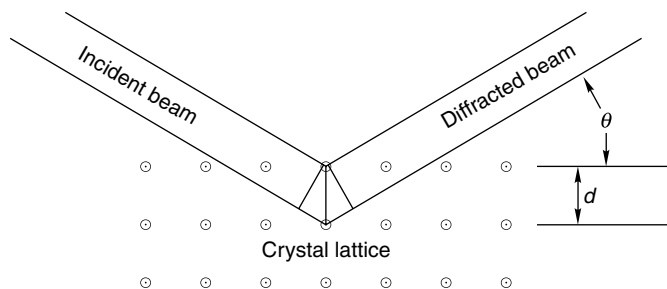


Fig. 2.13 Diffraction of electron beam from crystal lattice.

Hence, for an electron beam of given energy (i.e., constant λ), a given crystal plane shall diffract the beam in specific direction, which also depends on the orientation of the crystal lattice and the direction of propagation of the incident beam. A typical diffraction pattern for a crystalline material is shown in the following image; the very bright central spot (arising due to the transmitted beam, the beam that does not get diffracted as it passes through the lattice) is blocked. This is a common precaution taken while obtaining the diffraction pattern on a CCD (Charge Coupled Device) as very high electron intensity can damage the CCD.

2.2.8.2 Physics of Electron Diffraction

We need to know why diffraction patterns look like an array of spots. To describe this, we have to apply a mathematical approach for crystals. The starting point of all discussions is order. What distinguishes a crystalline material from an amorphous one is its periodicity in all its properties. So, a given intensive property of the system should stay the same as one transforms one's frame of reference from say origin to say a point defined by the vector \mathbf{T} .

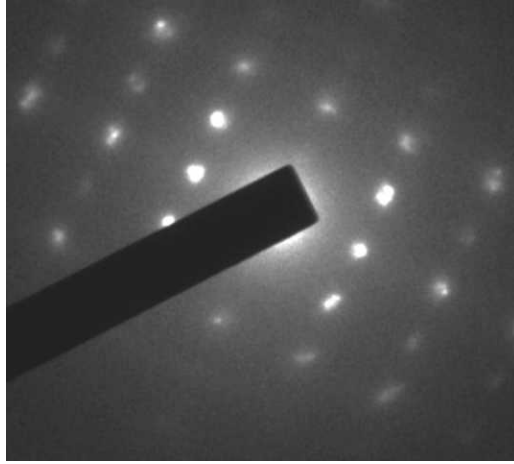


Fig. 2.14 *Diffraction pattern for a crystalline material.*

Clearly, if n is an intensive property and periodicity is to be maintained in the lattice, then

$$n(\mathbf{r} + \mathbf{T}) = n(\mathbf{r}).$$

Now, in our case, and in the case of most solid state physicists, the most important property shall be electron density, $n(\mathbf{r})$. A periodic function is better written as a Fourier transform, so we can write a one dimensional electron number density function as,

$$n(\mathbf{x}) = n_o + \sum \{C_p \cos(2\pi px/a) + S_p \sin(2\pi px/a)\};$$

where summation is over p .

Now, clearly, for a one-dimensional (1-D) electron density function described as above, the function is periodic for a displacement of axes by a distance of a .

Hence,

$$n(\mathbf{x}) = n(\mathbf{x} + \mathbf{a})$$

We describe the point $(2\pi p/a)$ as a point in the reciprocal lattice or Fourier space. The reciprocal lattice points describe the allowed terms in the Fourier expansion of the electron number density function, which satisfies the conditions of periodicity. Hence, each reciprocal lattice point which does exist, signifies a lattice plane.

One thing to remember here is that all types of planes do exist; however, not all would give rise to a diffraction spot. A classic example would be that of Au, which has FCC structure. In a diffraction pattern of Au, under any orientation, would not give rise to a spot which signifies (100) plane. It is not to say that the plane does not exist, it's just that the Fourier transform of electron number density perpendicular to that plane does not satisfy the periodicity constraints.

In three-dimensional (3-D) case, we can extend the argument to describe electron number density functions as:

$$\mathbf{n}(\mathbf{r}) = \sum \mathbf{n}_{\mathbf{G}} \exp(i \mathbf{G} \cdot \mathbf{r})$$

where the summation is over \mathbf{G} , reciprocal lattice vectors.

One thing to remember here is that the reciprocal lattice generated from a real lattice is not an arbitrary construction. Like, as in a real lattice, atoms exist only at particular location; similarly, only specific locations give rise to reciprocal lattice vectors, which are used in the equations.

The dimensions of reciprocal lattice are inverse of length, and hence the name reciprocal lattice. With respect to a given crystal lattice, a reciprocal lattice is constructed by a set of rules, such that the basis vectors of reciprocal lattice \mathbf{a}^* , \mathbf{b}^* , \mathbf{c}^* are related to the basis of crystal lattice \mathbf{a} , \mathbf{b} , \mathbf{c} as

$$\mathbf{a}^* = (\mathbf{b} \times \mathbf{c}) / (\mathbf{a} \cdot \mathbf{b} \times \mathbf{c})$$

$$\mathbf{b}^* = (\mathbf{c} \times \mathbf{a}) / (\mathbf{a} \cdot \mathbf{b} \times \mathbf{c})$$

$$\mathbf{c}^* = (\mathbf{a} \times \mathbf{b}) / (\mathbf{a} \cdot \mathbf{b} \times \mathbf{c})$$

The reciprocal lattice for common crystal systems is well known. The reciprocal lattice for an FCC material is BCC and that for a BCC material is FCC. The FCC lattice shall give diffraction spots for planes (hkl) when h, k and l are all odd or all even. The BCC lattice shall give diffraction spots corresponding to (hkl) planes when (h+k+l) is even. These rules can be understood on the basis of atomic scattering factors and structure factor of the crystals. For a detailed account of it one can refer to Section 16.3 of *Transmission Electron Microscopy*, Volume II by D.B. Williams and C.B. Carter, Plenum Press, New York.

There is, however, a rather easier physical approach to explain the phenomenon of diffraction. This approach involves the construction of Ewald Sphere. In this approach, we observe the phenomenon in reciprocal space. In reciprocal space, an incident and a diffracted electron beam shall be represented by wave vectors of length $(1/\lambda)$ \mathbf{k}_i and \mathbf{k}_d , respectively. The scattering caused is measured by subtracting vectorially, the wave vectors of diffracted and incident beams. If this difference $\Delta\mathbf{k}$ equals a reciprocal space vector, we shall observe a diffraction spot corresponding to it. The incident and diffracted beams are concentric and the incident beam wave vector terminates at the origin (the point which corresponds to the transmitted spot in the diffraction pattern).

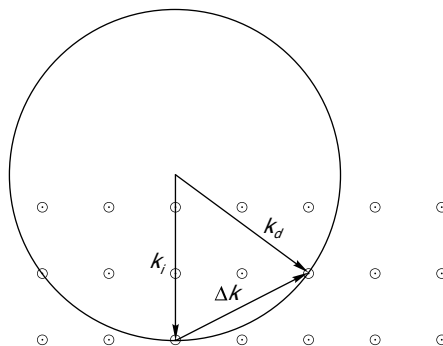


Fig. 2.15 The incident and diffracted wave vectors lead to a diffraction spot when the vector difference between the two is equal to a reciprocal lattice vector.

The interpretation can be visualised as shown in Fig. 2.15. Clearly, the condition is equivalent to constructing a sphere (in the 3-D case) of radius $1/\lambda$ and it being defined, such that the incident and the diffracted beams are radii as stated previously. Clearly, a diffraction spot shall be observed when the sphere cuts another reciprocal lattice point. This sphere is known as Ewald sphere, and whichever reciprocal lattice point it intersects shall be observed in the diffraction pattern. It should be kept in mind that the diffraction pattern changes on rotating the sample or the incident beam, as it is equivalent of rotating the Ewald sphere or the reciprocal lattice.

2.2.8.3 Understanding Diffraction Patterns

A diffraction pattern consists of an array of bright spots on the photographic film or the CCD as the case may be. Most of the information about the material lies coded in the pattern, its symmetry, and its intensities.

Electron microscopists use Miller indices in describing the crystallographic directions and planes. A diffraction pattern obtained is always characteristic of a set of planes in Bragg's condition (i.e., satisfying Bragg's law) with a particular direction, which is none other than the direction of propagation of incident beam. This direction is called as Zone Axis and is unique for patterns, where diffraction is due to a single crystal.

Every point in the diffraction pattern represents a particular crystallographic plane. The diffraction pattern changes as the sample or the electron beam is tilted.

Unless stated otherwise, electron diffraction implies Selected Area Diffraction (SAD), in which the beam striking the sample is paraxial.

The method of obtaining the crystallographic information from the diffraction pattern is referred to as indexing. To begin with the indexing, we need to know about the TEM being used. The parameters to be known are, the camera length L , and the wavelength of electron beam λ . Camera length (see Fig. 2.16) can be known by checking the settings of the TEM. Most of the modern TEM display the camera length during the course of operation in the display panel. The wavelength of electron beam is related to the acceleration voltage which is also known. The phenomenon of electron diffraction can be shown in the following schematic.

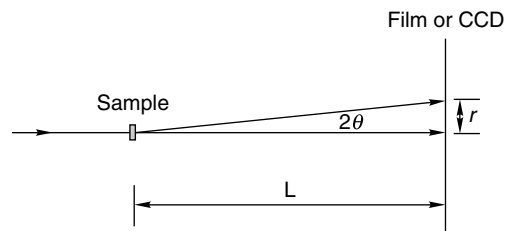


Fig. 2.16 Schematic illustrating the concept of camera length.

On the screen or on the CCD, the distance between the transmitted spot and the diffracted spot is r , and 2θ is the angle of deviation from the original path. In practice, in TEM the angle 2θ is very small, and as such

$$\tan 2\theta \approx 2\theta = r/L.$$

However, from Bragg's Law, we know that $2d \sin\theta = n\lambda$.

But, as stated earlier, angle 2θ is very small, so we shall go in for the approximation of

$$2d \sin\theta \approx 2d\theta = \lambda.$$

Hence, we get to the all important equation

$$L\lambda = rd.$$

If we know the camera length precisely, our problems are solved as we can directly find the interplanar spacings from this equation; however, that is not quite often the case. In such a scenario, a foolproof method of indexing, ignores the value of L . In this method, we find the distances of two diffraction spots corresponding to two different planes, i.e., r_1 and r_2 .

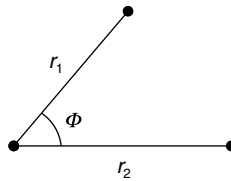


Fig. 2.17 The two diffraction spots and their distance from the transmitted spot.

We take the ratio of two distances of diffraction spots from the centre spot, i.e., find the value of (r_1/r_2) . As is known that r and d (the interplanar spacing) are inversely proportional to each other, the ratio is equal to (d_2/d_1) . These ratios can either be calculated from the crystal structure or otherwise found in material science handbooks. However, one has to keep in mind that many combinations can give almost the same ratio. As such the best option to confirm is by looking at the angle between two position vectors \mathbf{r}_1 and \mathbf{r}_2 . As more than one pair of ratios can match, but simultaneously, not more than one angle would match. In case of cubic or cubic based lattices, the angle between two planes $(h_1 k_1 l_1)$ and $(h_2 k_2 l_2)$ is given as

$$\cos \phi = (h_1 h_2 + k_1 k_2 + l_1 l_2) / (h_1^2 + k_1^2 + l_1^2)^{0.5} (h_2^2 + k_2^2 + l_2^2)^{0.5}$$

Hence, comparing the ratios and position of all the diffracted spots and comparing them with that of various crystal structures, we can ascertain the crystal structure of the material.

2.2.8.4 Indexing a Diffraction Pattern

Given that we have discussed SAD patterns in detail, it is worth indexing a real diffraction pattern just to get a feel of it. We shall choose the diffraction pattern shown in Fig. 2.14. The whole of it is not of much use, so we shall take out a section from it and solve the pattern from that.

Now, let us try to solve it. Let us take point O as our origin and points P_1 and P_2 be represented by vectors \mathbf{r}_1 and \mathbf{r}_2 , respectively. Now let us see the ratio (r_2/r_1) . It turns out to be approximately 1.16. The angle between \mathbf{r}_1 and \mathbf{r}_2 is approximately 32° . Now, we can check from tables or otherwise calculate to see that.

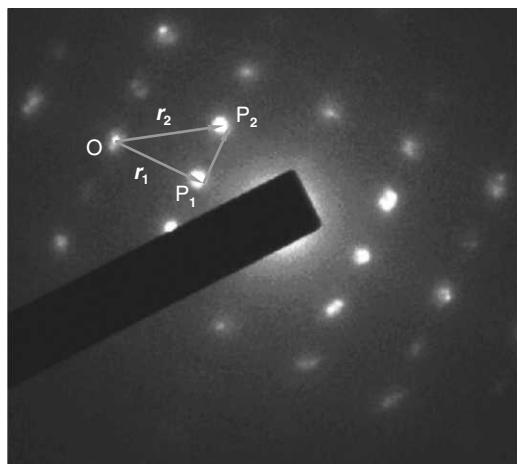


Fig. 2.18 A part of a diffraction pattern of Au.

From our data, we observe that ratio (r_2/r_1) for the plane (311) and (220) is 1.172. Now, if our assumption is correct, it should also satisfy the angular relationships. So, let us try to find the value of the included angle assuming the planes to be (311) and (220). Using the expression,

$$\cos \varphi = (h_1 h_2 + k_1 k_2 + l_1 l_2) / (h_1^2 + k_1^2 + l_1^2)^{0.5} (h_2^2 + k_2^2 + l_2^2)^{0.5}$$

we calculate the angle between (311) and (220) to be 31.48° , which is in fact almost equal to angle observed experimentally. In case angles did not match with the experimentally observed value, we would have to assume another set of values for the planes and try to check if it matches with the experimentally observed values. However, over here our assumption of planes is correct. Therefore, we can say that \mathbf{r}_1 and \mathbf{r}_2 represent the planes (220) and (311), respectively.

The zone axis can be calculated by taking cross product of any two vectors in the plane, say \mathbf{r}_1 and \mathbf{r}_2 .

2.2.8.5 Uses of Electron Diffraction

We have talked in detail about electron diffraction, but still haven't really talked about all the information that we can get out of it. The information that we can get from a diffraction pattern is given below:

- *The crystalline nature of the sample* (i.e. whether it is crystalline or amorphous): It sounds trivial, but this is the starting point of material characterisation for a crystallographer. Most of the materials around us are crystalline, be it steel used in building houses or silicon chips used in making computers, but to check the crystalline nature, one needs to take a diffraction pattern from the sample. Diffraction patterns, in which we observe diffused rings of significant thickness around a central bright spot, indicate the sample to be amorphous. This technique is widely used in characterising bulk metallic glasses made from conventional metallic materials.

- *The crystallographic characteristics of the material:* From the diffraction pattern, as we have illustrated previously, one can get information about the lattice parameter, symmetry, crystal structure, etc. of the material.
- *Estimate of size of crystals:* From the diffraction pattern, one can qualitatively get an idea about the size of the crystals in the sample. However this technique is never used to precisely calculate the crystal sizes, because more accurate methods like X-ray diffraction and HRTEM exist for this purpose.
- *Identifying various phases:* Just like X-ray diffraction process, we can identify the various phases present in the sample by calculating the interplanar spacing of all planes that are giving rise to diffraction patterns.
- *Orientation of crystals:* The electron diffraction pattern being susceptible to the orientation of crystal gives us a good idea of the orientation of a crystal by comparing the diffraction pattern with diffraction pattern of similar materials in standard orientations.
- *Check for quasi crystallinity:* There are many things about a crystal that we tend to ignore. One of the most important properties of crystal is possession of both rotational and translational symmetry. All crystal systems do follow these rules. Rotational and translational symmetry is another way of talking about order that defines the lattice. Actually, it was thought that systems are either amorphous (i.e., no order) or crystalline (i.e., possession of both rotational and translational symmetry). However there is a new class of materials which possess a five-fold symmetry, which did not comply with rules of translational symmetry.
- Now, it is not that it was all that easy to identify these quasi crystalline phases as they look more or less the same as ordinarily occurring phases. However, under diffraction, we are able to check the symmetry of the lattice. As the real and reciprocal lattices are related by unambiguous relations defined previously and as such a five-fold symmetry of real lattice is also seen in its corresponding reciprocal lattice. These quasi crystalline phases occur sometimes in nanostructures or nanocrystalline materials. These quasi crystals give the systems totally different properties, like very high strength.

2.2.8.6 Application of Electron Diffraction to Study Nanomaterials

As the size of grain decreases, it starts affecting diffraction pattern. The electron diffraction from a single crystal generates a specific diffraction pattern, which can be used to determine the nature of the crystal. However, this is the case, only when the diffraction is due to one grain, i.e., due to an ordered structure of atoms, which are arranged in a specific orientation. When the electron beam is incident on more than one grain of same or different phases, the diffraction pattern observed shall be a superimposition of the diffraction patterns of both the grains formed independently. As a result, the spots shall be observed for both the crystals.

In the case of bulk materials of nano-sized grains, one shall observe ring pattern, because the electron beam shall be diffracted by grains oriented in various directions. In case of nano particles arranged randomly and forming an aggregate, one shall also see a perfect ring pattern. Each ring shall represent a family of planes.

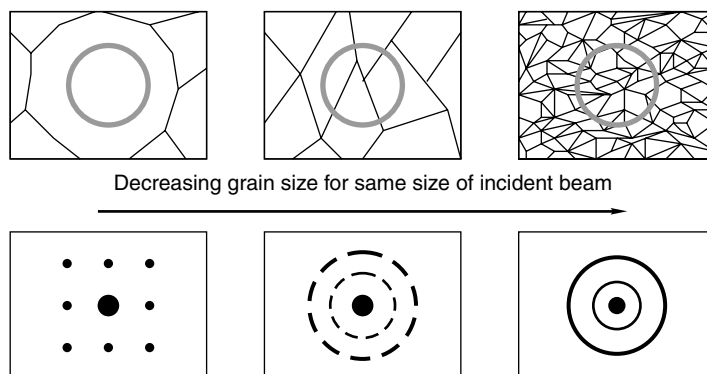


Fig. 2.19 As the electron beam gets diffracted from more crystals, the pattern changes gradually from spot pattern to ring pattern. The first row shows microstructure of bulk materials with varying crystallite sizes. The circle in the upper row represent the boundary of the area of sample irradiated by the electron beam. The second row shows the corresponding diffraction patterns.

The electron diffraction pattern does not, however, become a perfect ring in case of all nanomaterials. As stated previously, the ring pattern arises due to diffraction from many *randomly* arranged crystals. In many functional applications, we encounter nanostructures arranged in an ordered manner. In such cases, the pattern shall not be like a ring. For example, in case of epitaxially grown nano-sized thin films, it shall be a superimposition of the diffraction (spot) pattern of the two phases.

Contrary to the two extreme cases of extreme orderly arrangement and completely random arrangement of nanoparticles, one shall encounter a partially favoured orientation of nanocrystals. In such cases, the diffraction pattern shall be that of a diffused ring, but one shall see bright spots in the ring at specific points signifying the preferred orientations as seen in Fig. 2.20.

In addition to the above, the electron diffraction can help us in determining the size of the nanocrystals. This is possible by calculating the width of the rings (i.e., broadening) and relating it to the size of the grains.

2.2.8.7 Advanced Diffraction Techniques for Specific Applications

In addition to the SAD method, which has been described until now, a few other modifications of diffraction phenomenon are used in characterising materials in general and nanomaterials in particular. These techniques include:

- (a) CBED
- (b) EBSD
- (c) RHEED

CBED

CBED stands for convergent beam electron diffraction. This is an important technique used by crystallographers in characterising an unknown material in general and even more importantly to

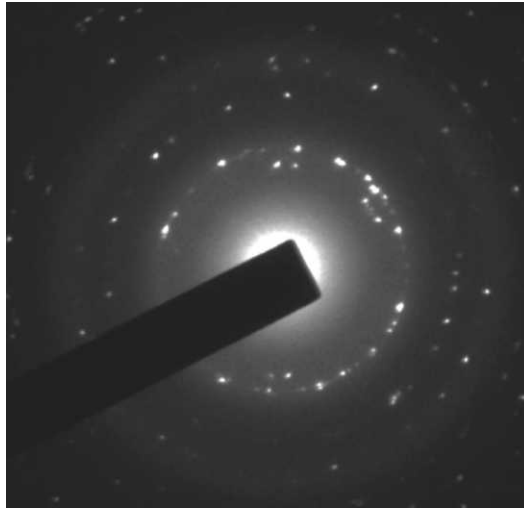


Fig. 2.20 *Electron diffraction pattern from nanoparticles of gold indicating preferred orientations of arrangement.*

study new crystal structures. What makes it different from the conventional SAD is the fact that in CBED, the beam incident upon the sample is converging and not paraxial. As a matter of fact, the Ewald sphere generated due to changed path of electron beam leads to a diffraction pattern, where spots turn to small circles.

The plus point of CBED for those dealing with nanomaterials is the fact that one can decrease the beam size small enough to analyse each phase on its own, i.e., generate diffraction pattern from a single crystal of nano-sized dimensions. In addition to it, as many a times the case is, CBED is helpful in finding a change of crystal structure occurring as one goes down to the nano dimensions. A CBED pattern also helps us as it provides us more information about the crystal structure (due to intersection of Ewald sphere with Higher Order Laue Zone).

EBSD

EBSD stands for Electron Back Scattered Diffraction. It is a technique used in SEM to find the orientation of sample. In this method, a beam of electrons is backscattered from the sample and the signal is detected by a backscattered electron detector. The beam gets inelastically scattered and forms Kossel cones (*for details refer to Section 19.2 of Transmission Electron Microscopy, Volume II by D.B. Williams and C.B. Carter, Plenum Press, New York*) which intersect with the backscattered detector screen to form a pattern of intersecting pairs of parallel lines. A computer connected to the SEM uses Hough's transformation in interpreting the areas, which cause the diffraction and finally finds the crystallographic orientations.

RHEED

RHEED stands for Reflection High Energy Electron Diffraction and is a very important tool for *in-situ* characterization of thin films while they are in the process of growth. In this process, electron beam

is incident at a sample at grazing angle of incidence and the intensity of diffraction spots is observed over the period of growth. This method is widely used in determining the extent of deposition that has occurred in a molecular beam epitaxy process. As the deposition initiates, the intensity of the diffraction, pattern starts varying. The saturation of intensity signifies the completion of deposition of one layer of the material. This method is particularly useful in accurate control over thickness is high-end technology fabrication process like molecular beam epitaxy.

REFERENCES

1. J.I. Goldstein, C.E. Lyman, D.E. Newbury, E. Lifshin, P. Echlin, L. Sawyer, D.C. Joy and J.R. Michael, *Scanning Electron Microscopy and X-ray Microanalysis*, Kluwer Academic/Plenum Publishers, New York, (2003).
2. G. Thomas and M.J. Goringe, *Transmission Electron Microscopy of Materials*, John Wiley & Sons, New York, (1979).
3. M.M.J. Treacy, T.W. Ebbesen and J.M. Gibson, *Nature*, 381, (1996), 678.
4. D.B. Williams and C.B. Carter, *Transmission Electron Microscopy: A Textbook of Material Science*, Second Edition, Springer, (2009).
5. *Introduction to Solid State Physics*, by Charles Kittel, John Wiley & Sons Inc. New York.

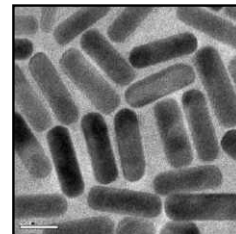
ADDITIONAL READING

1. H. Ibach and D.L. Mills, *Electron Energy Loss Spectroscopy and Surface Vibrations*, Academic Press, New York, (1982).
2. J.C. Vickerman, *Surface Analysis: The Principal Techniques*, John Wiley, Chichester, Sussex, (1997).
3. K.W. Kolasinski, *Surface Science Foundations of Catalysis and Nanoscience*, John Wiley & Sons Ltd., Chichester, (2002).

REVIEW QUESTIONS

1. Why are electrons used for imaging, why not photons?
2. What are scanning and transmission electron microscopies?
3. What is relativistic correction?
4. What is scanning transmission electron microscopy?
5. What is environmental TEM?
6. What is the application of surface sensitivity of secondary electron emission?
7. How can electron diffraction pattern be indexed?

SCANNING PROBE MICROSCOPIES



"I then most always saw, with great wonder, that... there were many very little living animalcules, very prettily a-moving. The biggest sort... had a very strong and swift motion, and shot through the water (or spittle) like a pike does through the water. The second sort... oft-times spun round like a top... and these were far more in number."
On some of the first observations of living bacteria.

Antony van Leeuwenhoek, Letter to Royal Society, dated September 17, 1683

Scanning probe microscopies (SPMs) have become the most common experimental tools for examining nanoscale materials. The capability to examine conducting, insulating, organic, inorganic, biological, composite, etc. materials has made these microscopic tools to enter into all areas. The flexibility of the ambience—whether in vacuum or in air, low temperature or high temperature—has provided additional advantage to this tool. In comparison to electron microscopies, the scanning probe techniques are an order of magnitude cheaper. Combined with the ease of use with the advancements in software and automation, SPM has even entered into the college classrooms. We will look at the whole range of SPM tools in this chapter.

Learning Objectives

- What are the principles of scanning tunneling and atomic force microscopies?
 - What are the variants of these tools?
 - How would one do atom manipulation?
 - What are the advancements in SPM?
-
-

3.1 INTRODUCTION

There are broadly two kinds of SPM techniques, scanning tunneling microscopy (STM) and atomic force microscopy (AFM). Numerous variations of these techniques exist. The objective of this section is to review some of the most prominent of these techniques so as to give a flavour of them. Those interested in additional details may consult original articles and books, a collection of which are listed in the references.

In a scanning probe technique, a probe of nanometer dimensions is used to investigate a material. The investigation is on the surface of the material. This is done by holding the tip stationary and moving the sample or vice versa. The information, that is collected by moving the sample, can be of several kinds, which differ from technique to technique. The collected data and its variation across the sample are used to create an image of the sample. The resolution of such an image depends on the sample, the control one has on the movement on the tip/sample and the inherent nature of the data.

3.1.1 Scanning Tunneling Microscopy

STM was developed¹ in 1982 and the inventors were awarded the Nobel Prize for physics in 1986. In STM, the phenomenon of electron tunneling is used to image the topography of the surface. This utilises the principle of vacuum tunneling. Here two surfaces, a tunneling probe and a surface, are brought near contact at a small bias voltage. If two conductors are held close together, their wavefunctions can overlap. The electron wavefunctions at the Fermi level have a characteristic exponential inverse decay length K , which can be given as, $K = \sqrt{(4m\phi)/\hbar}$, where m is mass of electron, ϕ is the local tunneling barrier height or the average work function of the tip and sample. When a small bias voltage V is applied between the tip and the sample, the overlapped electron wavefunction permits quantum mechanical tunneling and a current I to flow through. The tunneling current I decays exponentially with distance of separation as $I \propto Ve^{-\sqrt{(4m\phi)d/\hbar}}$ where d is the distance between the tip and the sample and ϕ is the work function of the tip. The tunneling current is a result of the overlap of electronic wave functions of the tip and the sample. By considering the actual values of electron work functions of most materials (typically about 4 eV), we find that tunneling current drops by an order of magnitude for every 1 Å of distance. The important aspect is that the tunneling current itself is very small, and in addition, it is strongly distance dependent. As a result, direct measurement of vacuum tunneling was not observed till 1970s. Tunneling, however, was observed and was limited to tunneling through a barrier.

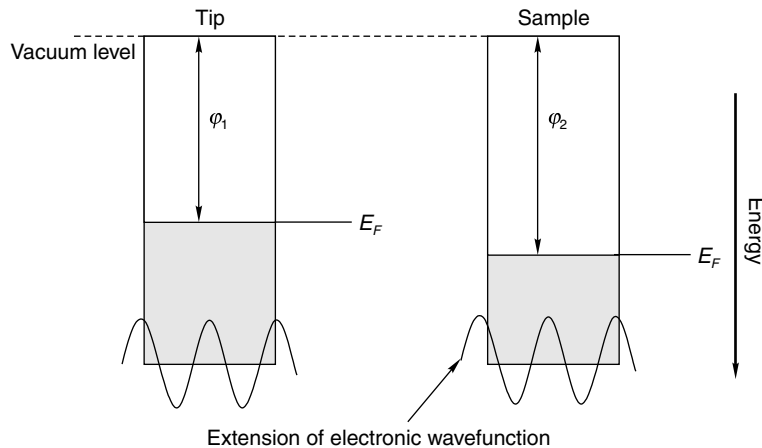


Fig. 3.1 Electron energy states of the sample and tip before the bias. When a sample and a tip are held close together, there is a possibility of their electronic wave functions to overlap.

Basic instrumental aspects in such a device are simple and is illustrated in Figs 3.1 and 3.2. In this, a tip is brought close to the sample so that electrons can tunnel through the vacuum barrier. The position of the tip is adjusted by two piezoelectric scanners, with x and y control. The z -axis position is continuously adjusted, taking feedback from the tunneling current, so that a constant tunneling current is maintained. The position of the z -axis piezo, therefore, reproduces the surface of the material. The position of the piezo is directly related to the voltage supplied to the piezoelectric drives. Scanning is possible in the constant height mode as well, but this is done only on extremely flat surfaces, so that the tip (distance modulation) does not crash by accident. The other mode of imaging is by modulating the tip at some frequency and measuring the resulting current variations. This is informative in understanding the compositional variation across the sample.

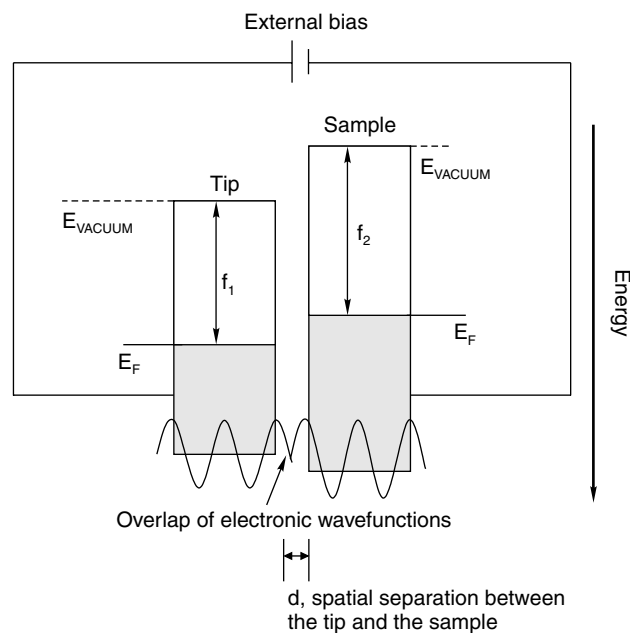


Fig. 3.2 *Electronic wavefunctions overlap at lower separations and a tunneling current is observed.*

Tunneling takes place through a few atoms and it is believed that the STM images occur as a result of tunneling to a single atom or to a few atoms. The tip manufacturing process does not make one atomically sharp tip alone. However, what appears to be happening is that electron tunneling takes place to whichever atomically sharp tip, which is closer to the surface.

STM has been used to understand numerous processes and a review of these is out of place here. Most of these studies relate to understanding various surface processes. The techniques available earlier for these studies before the arrival of STM, are low-energy electron diffraction (LEED), reflected high energy electron diffraction (RHEED), X-ray diffraction and variations of these techniques. Instead of probing the average structure of the surface as is possible with these techniques, STM allowed investigation of local structures. These studies focused on surface reconstruction, adsorption, chemical

transformations, etc. at metal, semiconductor and even on insulating surfaces (under appropriate conditions to observe tunneling current). In the brief discussion below, we shall illustrate a few of the experiments of relevance to nanoscience and technology.

STM gives information on local density of states. Density of States (DOS) represents the quantity of electrons exist at specific values of energy in a material. Keeping the distance between the sample and the tip constant, a measure of the current change with respect to the bias voltage can probe the local DOS of the sample. A plot of dI/dV as a function of V represents the LDOS. This is called scanning tunneling spectroscopy (STS). An average of the density of states mapped using STM is comparable to the results from ultraviolet photoelectron spectroscopy and inverse photoemission spectroscopy (see below). Such comparisons have been done in a few cases and the results indicate that the tip effects are unimportant. The important aspect is that such mapping of density of states is possible with spatial specificity.

Electrons can only tunnel to states, which are present in the sample or tip. When the tip is negatively biased, electrons from the tip tunnel from the occupied states of the tip to the unoccupied states of the sample. If it is the other way, electrons tunnel from the occupied states of the sample to the unoccupied states of the tip. Thus, change in polarity makes it possible to probe the occupied or unoccupied states of the sample as illustrated in Fig. 3.3.

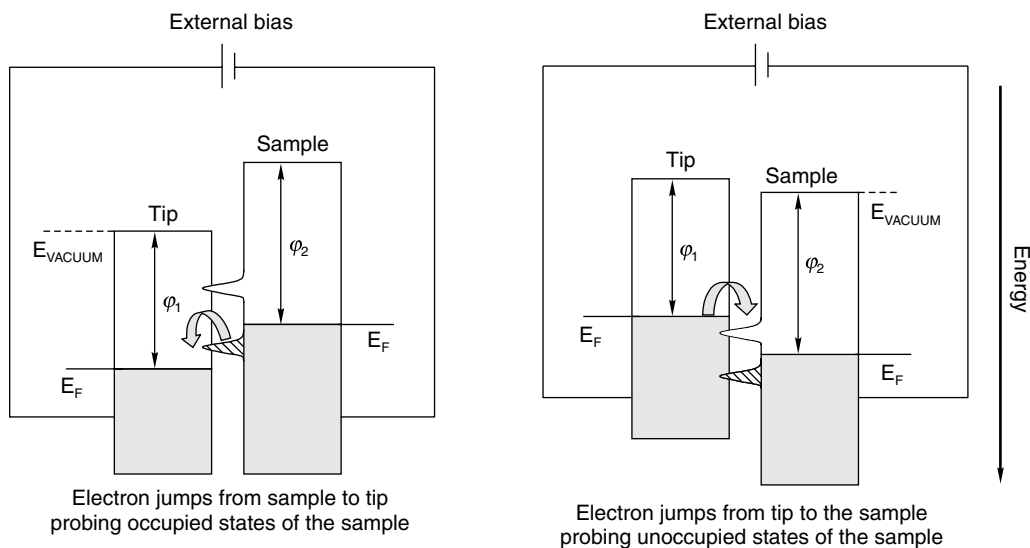


Fig. 3.3 Depending on the sample bias one can probe various kinds of states of the sample.

STM has revolutionised a number of areas of fundamental science. The capability to analyse samples with atomic resolution, to see processes as they are occurring and to do all these while the sample is in atmospheric conditions are the advantages of STM. For nanoscience and technology, the use of STM are manifold. To give the reader a feel of those, we cite an example here. STM has been used in different ways to understand the electronic structure and properties of carbon nanotubes. An

atomically resolved image² of a single-walled carbon nanotube is shown in the Fig. 3.4. The arrangement of the hexagons is seen. One has to remember that the graphitic sheet has been folded, so that the hexagons are not planar. From this, we can determine the tube axis and the chiral angle. This is 7° for this tube and the tube diameter is 1.3 nm. STS measurements determine the band gap and local electronic structure of the tubes.

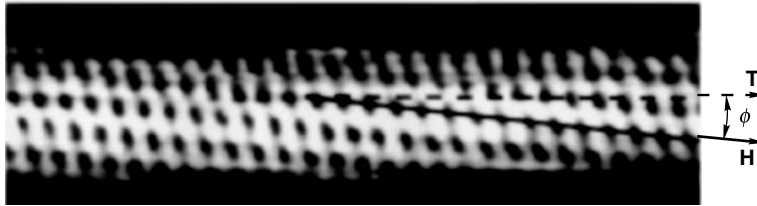


Fig. 3.4 Atomically resolved STM images of an individual single-walled carbon nanotube. The lattice on the surface of the cylinders allows a clear identification of the tube chirality. Dashed arrow represents the tube axis **T** and the solid arrow indicates the direction of nearest-neighbour hexagon rows **H**. The tube has a chiral angle $\Phi = 7^\circ$ and a diameter $d = 1.3$ nm, which corresponds to the (11, 7) type tube (Source: J.W.G. Wildoer, L.C. Venema, A.G. Rinzler, R.E. Smalley and C. Dekker, *Nature*, 391, 1998, 59).

3.1.2 STM Based Atomic Manipulations

In a normal STM imaging process, the tip-sample interaction is kept small. This makes the analysis non-destructive. However, if the interaction is made big and, as a result, the tip can move atoms on the substrate, there is a distinct possibility to write atomic structures using STM. This was done in 1990 by Eigler. When he manipulated Xe atoms on the surface of Ni(110) in a low temperature ultra high vacuum (UHV) STM instrument, a new branch of science was born.³ Process of manipulating atoms is technically simple. This is schematically illustrated in Fig. 3.5. The STM scanning process is

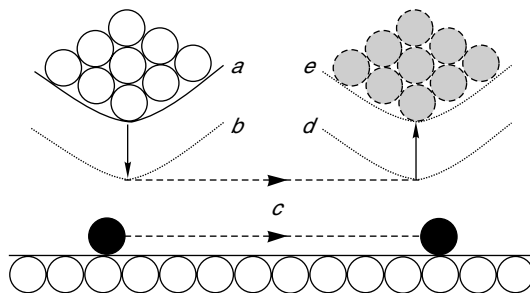


Fig. 3.5 Process of manipulating atoms on the surface. An STM tip at position *a* is brought to position *b* by vertical movement such that the tunneling current is large. Then the tip is slid over the surface to the desired location *d*, and subsequently, the tip is brought back to initial height *e*.

stopped and the tip is brought just above the sample atom. The tip is lowered to increase the interaction between the tip and the atom. This is done by increasing the tunneling current (to the tune of ~ 30 nA). Note that typical tunneling current used for imaging is of the order of 1 nA. As a result of this, the tip-atom interaction is made strong and the tip can now be moved to the desired location. The interaction potential between the tip and the atom is strong to overcome the energy barrier, so that atom can slide on the surface. It is, however, not transferred to the tip from the substrate. After moving to the desired location, the tip is withdrawn by reducing the tunneling current. This process can be repeated to get the desired structure, atom by atom. A quantum corral built by arranging 48 Fe atoms on a Cu(111) surface⁴ is shown in Fig. 3.6. The electron waves confined in the corral are seen in this picture. Confinement of the electrons comes about as a result of the nanostructure constructed. At such length scales quantum mechanical phenomena can be observed. By having an elliptical corral of Co atoms and placing another Co atom at one of its foci, the other focus manifests some of the features of the atom, where no atom exists. When the atom is moved from the focus, the effect disappears.⁵ This quantum mirage effect suggests transportation of data in the quantum mechanical size limit.

Numerous other manipulation strategies have been demonstrated. Tunneling current has been used to break chemical bonds. This has been shown in the case of oxygen and organic molecules. In the case of organic molecules, the detached fragments have been moved and further recombined in a desired fashion. Feynman's prediction of atomically constructed matter has come true.

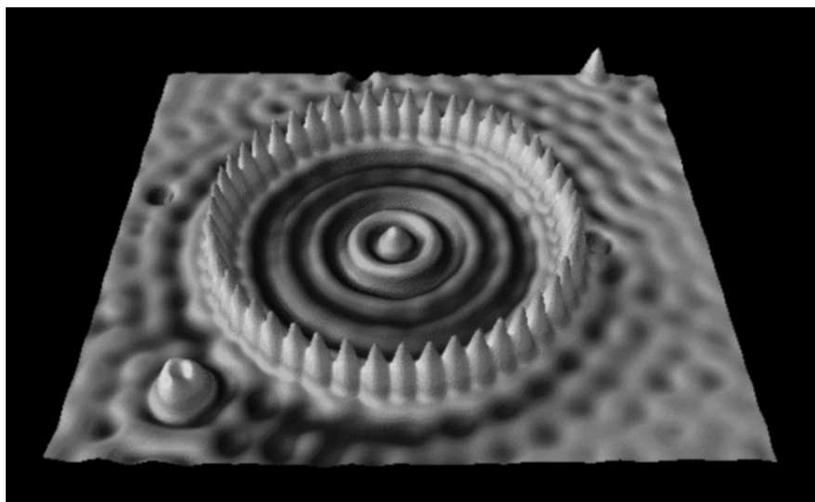


Fig. 3.6 Quantum corral made of 48 Fe atoms on a Cu(111) surface. Colour image taken from the website, <http://www.almaden.ibm.com/vis/stm/stm.html>. Original image was published in, M.F. Crommie, C.P. Lutz and E. Eigler, *Science*, 262 (1993) 218. (Copyright AAAS, Used with permission.). (For clarity see colour figure.)

Numerous modifications of STM are available. We reproduce a list of variants in Table 3.1 reproduced from Reference 9. An interested reader may consult the references and additional reading

material listed at the end of the chapter. The most current developments are in the areas of fast scanning STM, ultra low temperature STM and spin polarised STM. In the first, dynamical processes taking place at the surface, such as a chemical reaction, are monitored and the images are captured so as to construct a movie. This can be combined with a solution phase STM, so that reactions in solutions can be investigated. In spin polarised STM, a magnetic tip is used so that the tunneling current is sensitive to the spin. In ultra low temperature STM, the measurements are done at temperatures of the order of mK, so that phenomena at low temperatures can be probed.

Table 3.1 *SXM techniques and capabilities (from reference 9)*

-
1. *Scanning Tunneling Microscope* (1981), G. Binnig, H. Rohrer, 'Surface studies by scanning tunneling microscopy'. G. Binnig, H. Rohrer, Ch. Gerber and E. Weibel, *Phys. Rev. Lett.*, 49 (1982), 57–61.
 2. *Scanning Near-Field Optical Microscope* (1982), D.W. Pohl, 'Optical stethoscopy: Image recording with resolution $L/20$ '. D.W. Pohl, W. Denk and M. Lanz, *Appl. Phys. Lett.*, 44 (1984), 651. A. Harootunian, E. Betzig, A. Lewis and M. Isaacson, *Appl. Phys. Lett.*, 49 (1986), 674.
 3. *Scanning Capacitance Microscope* (1984), J.R. Matey, J. Blanc, 'Scanning capacitance microscopy'. J.R. Matey and J. Blanc, *J. Appl. Phys.*, 57 (1984), 1437–44.
 4. *Scanning Thermal Microscope* (1985), C.C. Williams, H.K. Wickramasinghe, 'Scanning thermal profiler'. C.C. Williams and H.K. Wickramasinghe, *Appl. Phys. Lett.*, 49 (1985), 1587–89.
 5. *Atomic Force Microscope* (1986), G. Binnig, C.F. Quate, Ch. Gerber, 'Atomic force microscope'. G. Binnig, C.F. Quate, and Ch. Gerber, *Phys. Rev. Lett.*, 56 (1986), 930–33.
 6. *Scanning Attractive Force Microscope* (1987), Y. Martin, C.C. Williams, H.K. Wickramasinghe, 'Atomic force microscope–force mapping and profiling on a sub 100 Å scale'. Y. Martin, C.C. Williams, H.K. Wickramasinghe, *J. Appl. Phys.*, 61 (1987), 4723–29.
 7. *Magnetic Force Microscopy* (1987), Y. Martin, H.K. Wickramasinghe, 'Magnetic imaging by "force microscopy" with 1000 Å resolution'. Y. Martin and H.K. Wickramasinghe, *Appl. Phys. Lett.*, 50 (1987), 1455–57.
 8. "Frictional" *Force Microscope* (1987), C.M. Mate, G.M. McClelland, S. Chiang, 'Atomic scale friction of a tungsten tip on a graphite surface'. C.M. Mate, G.M. McClelland, R. Erlandsson, and S. Chiang, *Phys. Rev. Lett.*, 59 (1987), 1942–45.
 9. *Electrostatic Force Microscope* (1987), Y. Martin, D.W. Abraham, H.K. Wickramasinghe, 'High resolution capacitance measurement and potentiometry by force microscopy'. Y. Martin, D.W. Abraham, and H.K. Wickramasinghe *Appl. Phys. Lett.*, 52 (1988) 1103–1105.
 10. *Inelastic Tunneling Spectroscopy STM* (1987), D.P.E. Smith, D. Kirk, C.F. Quate, 'Detection of phonons with scanning tunneling microscope'. D.P.E. Smith, G. Binnig, and C.F. Quate, *Appl. Phys. Lett.*, 49 (1987), 1641–43.

(Contd...)

Table 3.1 (Contd...)

11. *Laser Driven STM* (1987), L. Arnold, W. Krieger, H. Walther, 'Laser frequency mixing in the junction of a scanning tunneling microscope.'
L. Arnold, W. Krieger, H. Walther, *Appl. Phys. Lett.*, 51 (1987), 786–88.
 12. *Ballistic Electron Emission Microscope* (1988), W.J. Kaiser, and L.D. Bell, (1988), 'Direct investigation of subsurface interface electronic structure by ballistic-electron-emission microscopy.'
W.J. Kaiser, and L.D. Bell, *Phys. Rev. Lett.*, 60 (1988), 1406–09.
 13. *Inverse Photoemission Force Microscopy* (1988), H. Coombs, J.K. Gimzewski, b. Reihl, J.K. Sass, R.R. Schlittler, 'Local inverse photoemission with the scanning tunneling microscope',
B. Reihl, J.H. Coombs and J.K. Gimzewski, *Surface Science* 1988 (1989) 211–12, 156–64.
 14. *Near Field Acoustic Microscope* (1989), K. Takata, T. Hasegawa, S. Hosaka, S. Hosoki, T. Komoda, 'Tunneling acoustic microscope.'
K. Takata, T. Hasegawa, S. Hosaka, S. Hosoki, and T. Komoda, *Appl. Phys. Lett.*, 55 (1989), 1718–20.
 15. *Scanning Noise Microscope* (1989), R. Moller, A. Esslinger, B. Koslowski, 'Noise in vacuum tunneling: Application for novel scanning microscope.'
R. Möller, A. Esslinger, and B. Koslowski, *App. Phys. Lett.*, 55 (1989), 2360–62.
 16. *Scanning Spin-precession Microscope* (1989), Y. Manassen, R. Hamers, J. Demuth, A. Castellano, 'Direct observation of the precession of the paramagnetic spins on oxidized silicon surfaces.'
Y. Manassen, R.J. Hamers, J.E. Demuth, and A.J. Castellano Jr., *Phys. Rev. Lett.*, 62 (1989), 2531–34.
 17. *Scanning Ion-Conductance Microscope* (1989), P. Hansma, B. Drake, O. Marti, S.A.C. Gould, C. Prater, 'The scanning ion-conductance microscope.'
P.K. Hansma, B. Drake, O. Marti, S.A.C. Gould, and C.B. Prater, *Science*, 243 (1989) 641–43.
 18. *Scanning Electrochemical Microscope* (1989), O.E. Husser, D.H. Craston, A.J. Bard, 'High-resolution deposition and etching of metals with a scanning electrochemical microscope.'
O.E. Hüsser, D.H. Craston, and A.J. Bard, *J. Vac. Sci. & Tech. B*: 6 (1989), 1873–76.
 19. *Absorption Microscope/Spectroscopy* (1989), J. Weaver, H.K. Wickramasinghe, 'Optical absorption microscopy and spectroscopy with nanometre resolution.'
J.M.R. Weaver, L.M. Walpita, H.K. Wickramasinghe, *Nature*, 342 (1989), 783–85.
 20. *Scanning Chemical Potential Microscope* (1990), C.C. Williams, H.K. Wickramasinghe, 'Microscopy of chemical potential variations on an atomic scale.'
C.C. Williams and H.K. Wickramasinghe, *Nature*, 344 (1990), 317–19.
 21. R.J. Hamers, K. Markert, *Photovoltage STM* (1990), 'Atomically Resolved Carrier Recombination at Si(111)-(7 × 7) Surfaces.'
R.J. Hamers and K. Markert, *Phys. Rev. Lett.*, 64 (1990), 1051–54.
 22. *Kelvin Probe Microscopy* (1991), M. Nonnenmacher, M.P. O'Boyle, H.K. Wickramasinghe, 'Kelvin probe force microscopy.'
M. Nonnenmacher, M.P. O'Boyle and H.K. Wickramasinghe, *Appl. Phys. Lett.*, 58 (1991), 2921–23.
-

3.1.3 Atomic Force Microscopy

In this technique, interactions between a sharp probe and a sample are used for imaging. The cantilever, which probes the surface, has an atomically sharp tip and this is brought in contact with the surface. The large-scale use of AFM today is because of the use of microfabricated tips of Si or Si₃N₄. The spring constant of the tip is of the order of 1 N/m, and the shortest vertical displacement d measurable is $\langle 1/2 kd^2 \rangle \sim 1/2 k_B T$. With $k_B T$ of the order of 4×10^{-21} J at 298 K, the smallest vertical displacement observable is 0.5 Å. The interaction between the tip and the sample is of the order of a nano Newton, which is not directly measured in AFM. The extent of interaction between them is measured by the displacement of the cantilever. The displacement of the cantilever is monitored by the reflection of a laser from the back of the cantilever, detected on a segmented photodetector. A 4-segment photodiode is used for this purpose. In the very first AFM, the interaction was measured by the difference in tunneling current, the tip being fixed on the back of the cantilever. This allows the detection of normal and lateral displacements of the cantilever. Optical detection is far superior to other forms of detection, although there are problems associated with the laser, such as the heating of the cantilever and the sample. The image is generated from the interaction force. In the scan, the interaction force is kept constant by a feed-back control. The increase in the interaction force, when the tip approaches an elevated part, is related to the vertical displacement of the scanner needed to eliminate this increase in signal. This is converted to height. Thus, the basic components of the microscope are the cantilever, the detection system, scanners and the electronics. These components are schematically represented in Fig. 3.7. This also suggests that depending on the kind of interactions between the cantilever and the

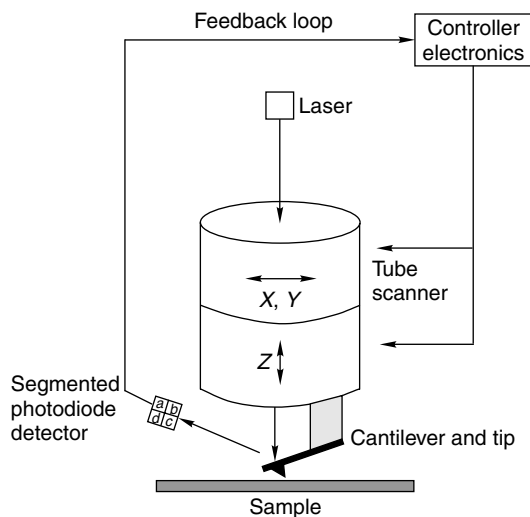


Fig. 3.7 Schematic representation of an atomic force microscope. The sample surface is scanned by the cantilever connected to a tubular scanner; the principal functional units in it are three piezoelectric scanners. The deflections of the cantilever are monitored by the segmented photodiode detector.

surface, various kinds of microscopies are possible. The probe can be made magnetic to investigate the magnetic interactions with materials. This makes magnetic force microscopy. The tip can have specific temperature probes or the tip itself can be made of a thermocouple. This makes scanning thermal microscopy (S_{Th}M). The tip may be attached with molecules, which are designed to have specific molecular interactions with the surface. This makes chemical force microscopy. There are several such variations, some of which were listed before (Table 3.1).

Resolution in scanning probe microscopy cannot be defined similar to optical methods, where the diffraction limit determines the practically achievable resolution. SPM is a 3-D imaging technique and the resolution is affected by the tip geometry. As would be seen from Fig. 3.8, improved resolution can be obtained for sharper tips. In practical description of resolution, especially in the biological context, width of DNA measured is considered as a measure of resolution. DNA, in its β form, is known to have a diameter of 2 nm. Width alone is not enough to describe the resolution as SPM is a 3-D technique and height is important.

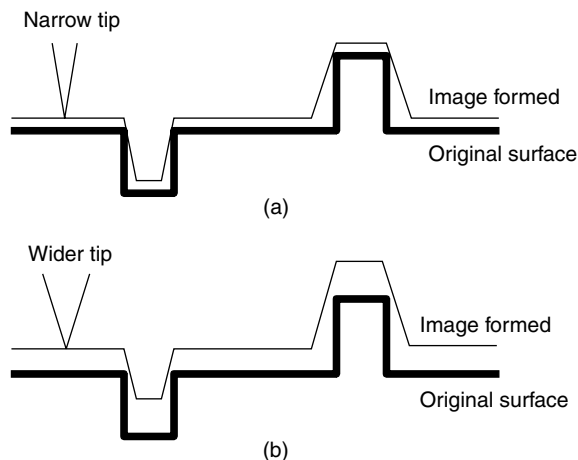


Fig. 3.8 Resolution in SPM depends on the tip details: (a) gives better resolution in comparison to (b).

AFM is commonly operated in two modes, the contact mode and the non-contact or tapping or intermittent contact mode. In the contact mode, the tip comes into contact with the surface. The force between the sample and the tip is the product of the displacement of the tip and the force constant of the cantilever ($f = -kx$). The contact with the surface allows evaluation of surface friction. When the interaction is strong, the surface damage can be significant and as a result contact mode can be difficult to use for soft materials.

In the non-contact mode of operation, the tip is oscillated at its resonant frequency by an actuator. The decrease in the amplitude of the motion when the cantilever comes close to the sample is used to measure the tip-sample interaction. The drop in the amplitude is set to a pre-determined value. The intermittent contact the tip makes is gentle and does not damage the material, although the probes are generally harder. As a result of this gentle mode of scanning, this is the most often used scanning method, especially with materials, whose surfaces are important such as a polished silicon wafer.

Typical AFM images get resolution of the order of 5 nm. Atomic features have been observed, but this is not routine. With especially fabricated tips, 1 nm can be observed. True atomic features have been demonstrated in specific cases. The best known examples of nanoscale structures are DNA strands. Images of DNA spread on mica are shown in Fig. 3.8.⁷ These images show variation in the shape and width of the curved structures depending on the type of imaging. The width of the molecule seen in AFM images need not be the actual width due to several factors. One corresponds to the relaxation of the molecule on the substrate, on which it is held for imaging. The other is to do with the tip induced deformation in the sample. The contour length of the macromolecule, on the contrary, is a measure of the molecular weight of the material.

Mechanical properties are measured using AFM. Correlation of these properties to the chemical composition and structure has to happen for a complete understanding of the material. This can be done by combining spectroscopy with imaging. Although a few such tools as confocal Raman microscopy and infrared microscopy, are available, the spatial resolution is of the order of microns or hundreds of nanometers. A combination of AFM with spectroscopy will be immensely useful. Scanning Near-field Optical Microscopy with Raman will be useful in this regard, but the current resolution of this is only of the order of 50 nm.

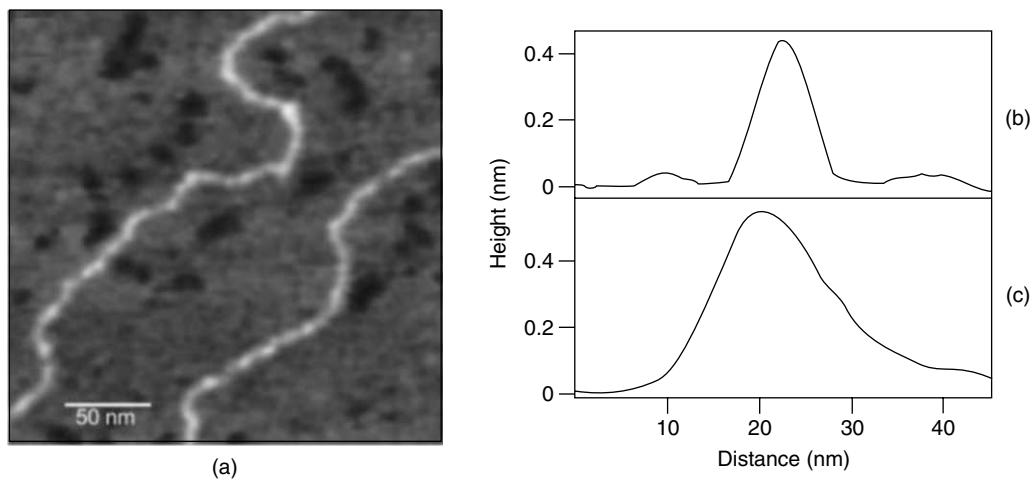


Fig. 3.9 (a) Height image obtained with an SWNT tip for double-stranded DNA adsorbed on mica. (b) Typical height cross-section from the image in (a). The FWHM is 5.6 nm. (c) Typical height cross-section from an image of the lambda-DNA obtained with a conventional Si tip. The FWHM is 14.4 nm (Source: S.S. Wong, A.T. Woolley, T.W. Odom, J-L. Huang, P. Kim, D.V. Vezenov, and C.M. Lieber, *App. Phys. Lett.*, 73, 1998, 3465–67).

3.1.4 Scanning Probe Lithography (SPL)

Manipulating objects and the tools associated are the central aspects of the development of civilisations. Depending on the tools used, we have names for various stages of civilisation, namely, Stone Age, Iron

Age, etc. In each of these ages, different kinds of tools manipulated objects, most of the time these were of large or macroscopic dimension. In the nano era, atoms are manipulated.

SPL is the use of SPM based techniques used for modifying substrates by the application of various actions, such as scratching, writing, chemistry, photoirradiation, etc. in a spatially confined manner. The structures that one can make as a result of these manipulations, are of the order of 10–100 nm. These techniques are summarised below (Table 3.2).⁸

There are basically three kinds of probes, with which SPL can be done. These are STM, AFM and SNOM, each of which is discussed separately in this book. The motivation to use these lithographic techniques is to overcome the limit of the current technology. The semiconductor industry is dependent on ultraviolet lithography, which uses ultraviolet rays to pattern surfaces, which are pre-coated with a photoresist. The chemical reactions on the resist will eventually strengthen or weaken the molecular bonding in the resist and a pattern can be made by subjecting the modified resist coated material to a solvent wash. The pattern so created can be used in an etching process. The process can be repeated and a complicated structure can be created on the surface. This process can be done on large sizes of device structures and a huge number of devices can be made on small areas, which is the basis of semiconductor technology. The lithography technique is meeting its natural limits as the size approaches the resolution limit of the optical techniques. This is given by the Rayleigh equation, $\text{resolution} = k\lambda/NA$, where k is a constant and NA is the numerical aperture of the lens system ($n\sin\theta$, where θ is the angle of incidence and n is the refractive index of the medium). It is normally taken that the resolution is approximately $\lambda/2$. The smallest structures that can be created today is of the order of ~ 90 nm, using UV light of ~ 160 nm wavelength. Though smaller structures can be patterned with waves of smaller wavelength such as X-rays and electron beams; these techniques are being surpassed by SPLs with which even smaller structures can be patterned.

Although SPL methods are important tools, they are serial techniques as the probe makes the transformation in steps. This is a distinct disadvantage in comparison to the traditional methods. However, it is important to note that the transformations carried out by lithographic methods generally involve higher temperatures of the order of 100°C and at such temperatures biological materials lose activity. SPL does not require higher temperature and the methods are generally delicate. This makes it possible to use the techniques for manipulating biological or soft materials. As the bio-nano interface is growing significantly, SPL based lithography will find newer applications.

3.2 OPTICAL MICROSCOPES FOR NANOSCIENCE AND TECHNOLOGY

One uses a microscope to see objects smaller than what the human eye can see. The microscope presents the objects with larger and larger magnification, so that the eye can see the features better. Even with larger magnification, there is a limit to which photons can magnify. This limitation is due to the diffraction limit. As mentioned previously, the minimum distance an optical microscope can resolve is $\Delta x = 0.61 \lambda/n\sin\theta$, where λ is the wavelength of the light in vacuum, θ is the collection angle and n is the index of refraction. One can improve resolution by decreasing the wavelength of illumination, increasing n or increasing θ . It can be noted that the high refractive index medium such as

Table 3.2 List of scanning probe lithography methods and their capabilities.

SPL Method	Instruments	Environment	Key Mechanism	Typical Resolution	Patterning Materials	Possible Applications
Nanoscale Pen Writing	Dip-Pen Nanolithography AFM	Ambient	Thermal Diffusion of Soft Solid	~ 10 nm	SAM, Biomolecules, Sol-Gel, Metal etc.	Biochip, Nanodevice, Mask Repair etc.
Nanoscale Scratching	Nanoscale Printing of Liquid Ink	Ambient	Liquid Flow	~ 100 nm	Etching Solution, Liquid	Mask Repair etc.
	Nanoscale Indentation	Ambient	Mechanical Force	~ 10 nm	Solid	Mask Repair etc.
	Nanografting	Liquid Cell	Mechanical Force	~ 10 nm	SAM	Biochip etc.
Nanoscale Manipulation	Nanoscale Melting	Ambient	Mechanical Force and Heat	~ 10 nm	Low Melting Point Materials	Memory etc.
	Atomic and Molecular Manipulation	Ultrahigh Vacuum (Often Low Temperature)	Van der Waals or Electrostatic Forces	~ 0.1 nm	Metals, Organic Molecules etc.	Molecular Electronics etc.
	Manipulation of Nanostructures	Ambient	Van der Waals or Electrostatic Forces	~ 10 nm	Nanostructure, Biomolecules	Mask Repair, Nanodevices etc.
Nanoscale Chemistry	Nanoscale Tweezers	Ambient	Van der Waals or Mechanical Force	~ 100 nm	Nanostructures	Electrical Measure. etc.
	Nanoscale Oxidation	Humid Air	Electrochemical Reaction in a Water Meniscus	~ 10 nm	Si, Ti etc.	Nanodevice etc.
	Nanoscale Desorption of SAM	Humid Air	Electrochemical Reaction in a Water Meniscus	~ 10 nm	SAM	Nanodevices etc.
Nanoscale Light Exposure	Nanoscale Chemical Vapor Deposition	Ultrahigh Vacuum with Precursor Gas	Nanoscale Chemical Vapor Deposition	~ 10 nm	Fe, W, etc.	Magnetic Array etc.
	Nanoscale Light Exposure	Ambient	Photoreaction	~ 100 nm	Photosensitive Materials	Nanodevices etc.

oil in immersion lenses improve the resolution significantly. All of this is done. However, irrespective of the various improvements, the fundamental limits imposed by the methodology cannot be overcome. When it comes to particle beams, such as electrons, the image resolution can be increased as electrons at high energies have very small wavelength.

Light, especially visible light, has a lot of advantages in the investigation of matter in spite of its limitations. The advantage is that light at this energy does not modify matter as the energy involved is small. Light also results in excitations in matter, which leads to phenomena such as fluorescence, which can be used for studying materials with chemical specificity. Light also leads to absorption and inelastic scattering, both of these can be used for imaging purposes. These are also molecule specific.

Improved resolution in optical microscopies can be brought about by broadly two different ways. The first belongs to far field imaging and the other belongs to near field imaging. In the first, the illumination occurs several microns away from the object to be imaged, and in the latter, it occurs within a few nanometers from the surface. While the first looks at the bulk features of the sample, the latter looks at the surface features. The diffraction limit is valid in the first, and therefore, the resolution is limited. In the latter, resolution of the order of 20 nm has been demonstrated. Obviously, one may come to the conclusion that nanoscale objects cannot be imaged by far field techniques. This is not true. The way this is done is by confocal microscopy.

3.2.1 Confocal Microscopy

Confocal means “having the same focus”. In such a microscope, a point-like light source, generally a laser, is used. This point source is derived by passing the light through a pin hole, which can be conveniently achieved by using a fiber optic connector. This is directed to the specimen through a beam splitter and an objective, which illuminates a spot. The point of illumination could be moved across the sample by a scanner and there are several ways by which this can be done. The emitted light from the sample, generally fluorescence (or less common the scattered as in the case of Raman spectroscopy), passes through the detecting pinhole and forms a point-like image on the detector. The light is scanned across the sample to get a 2-D image or the depth from which the light is collected is varied by moving either the objective or the sample giving a 3-D image of the sample. All these three points, namely, the illumination pin hole, sample spot and the detector pin hole are optically conjugated together, giving the confocal microscope (Fig. 3.10). Confocal microscope, therefore, is a confocal scanning optical microscope. The optical sectioning aspect is the most important advantage of confocal microscope. The sections can be as thin as the wavelength of light and the spatial resolution of the microscope is the best that can be achieved by optical microscopy.

Collecting the imaging involves scanning the light. The simplest approach would be to move the sample as the optical system is optimised. This process is slow as the piezoelectric scanners take time and real-time observation of processes is impossible. The other approach is to have a set of two mirrors to scan the laser in the xy plane, first doing an x scan and then making a y shift, then an x scan again and so on. The laser beam itself can be split into several smaller beams and all the beams may be used simultaneously for imaging. This way each beam needs to be moved only for a shorter distance for

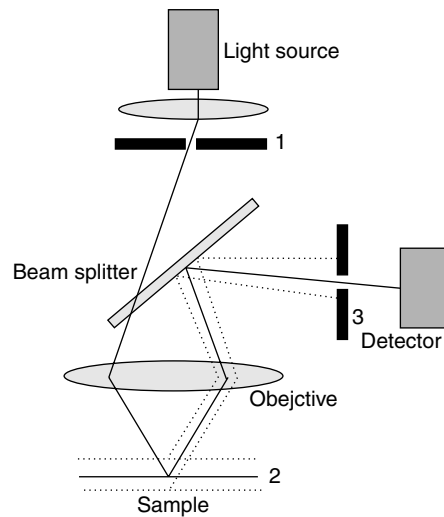


Fig. 3.10 Schematic of a confocal microscope. 1 and 3 are confocal pin holes. Light emanating from another plane of the sample, indicated in dotted line, are not detected. 1, 2 and 3 are optically conjugated in the arrangement.

imaging the whole sample. This methodology uses a Nipkow disk, in which thousands of microlenses are mounted on a disk and the light is focused into thousands of pinholes created on another disk. All the beams are focused by the objective simultaneously and the light coming out from the sample is collected through the pin holes and microlenses and detected parallelly. The holes can be arranged in a spiral fashion, so that the whole space can be scanned by rotating the disk. Increased speed of rotation will increase the speed of imaging.

As can be seen, the signal collected from the sample is confined to specific illumination volume by the use of an aperture. Thus, the aperture sits at the same focal point of the objective, rejecting all light that comes from other regions. This makes it possible to localise the illumination volume. Thus, an object, whose spatial dimension is smaller than the wavelength of light, can be studied by localising the illumination volume. In this illumination volume, one can look at the fluorescence of a molecule or a quantum dot. These can be part of a living cell or a polymeric composite. Thus, direct localisation of the illumination volume smaller than the resolution of light microscopy is possible in the confocal technique.

The principal advantage of confocal microscopy is the image contrast. This is achieved by rejecting light that comes from other focal planes of the sample. Smaller the slit, larger is the rejection, but overall signal quality decreases this way.

The most important recent development in confocal is 4pi confocal microscopy. In this technique, two objectives are used to illuminate or collect light from the sample. An interference pattern is created using the light from the objectives. This pattern has one major central peak and several side lobes. The central peak has reduced axial spread than the peak one would get from a pin hole. Depending on how

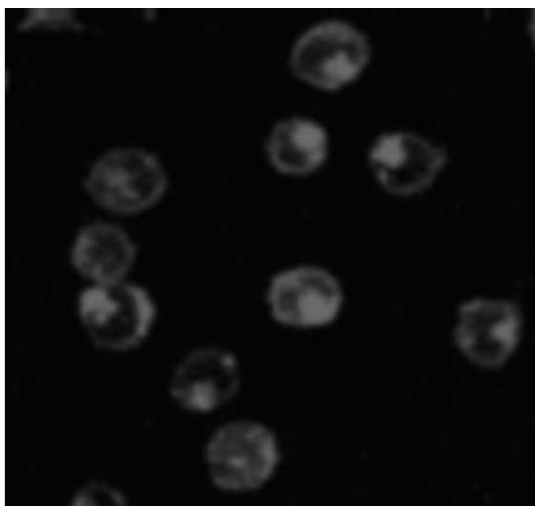


Fig. 3.11 *Confocal fluorescence image of human promyelocytic leukemia (HL 60) cells after incubation with fluorescein isothiocyanate labeled single wall carbon nanotube solution for 1 h. The image shows that nanotubes have been delivered into the cells (Source: Nadine Wong Shi Kam, Theodore C. Jessop, Paul A. Wender, and Hongjie Dai, J. Am. Chem. Soc., 2004; 126(22); 6850–51.). (For clarity see colour figure.)*

the interference pattern is created, it is possible to get even an FWHM, one-sixth of the wavelength of illumination. This makes increased resolution images by detecting only the central peak, avoiding the side lobes.

Most important application of confocal microscopy in nanoscience is in investigating the interactions of nanosystems to biology. There are numerous examples of this kind where nanoparticles, nanoshells, nanotubes and such other objects are made to interact with cells, bacteria, viruses, etc. The interaction takes place within the cell, in most cases, and confocal microscopy is used to monitor the processes. For this purpose, a fluorescent tag is often attached to the nanosystem or the nanosystem itself is fluorescent as in the case of a semiconductor quantum dot. A typical example is shown in Fig. 3.11.⁹

3.2.2 Scanning Nearfield Optical Microscopy

The finite resolution of conventional optical microscopy shows that the limit of resolution is approximately $\lambda/2$, where λ is the wavelength of light used for illumination. In three papers spanning 1928–1932, E.H. Syngé¹⁰ showed that this limit could be overcome if the illumination volume is reduced to a dimension smaller than the wavelength of light. The fundamental aspect is that the nearfield light intensity decreases rapidly when the aperture dimension is small. This was realised experimentally in 1983 and 1984 by two independent groups soon after the discovery of STM. In this method, the light source is made small by using one of the several tools discussed below. The probe is a tip, which

interacts with the sample at a close distance ($d \ll \lambda$). The sample-light interaction is detected by the photodetector placed at a distance away from the sample. The distance between the sample and the tip is held very small, by a feed-back mechanism, which is typically based on the modulation of the quartz tuning fork. The sample or the tip is scanned so as to construct an image of the sample. This process is illustrated schematically in Fig. 3.12.

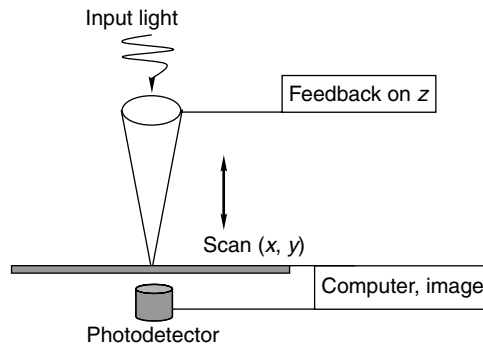


Fig. 3.12 Schematic of a scanning nearfield optical microscope.

There are numerous ways, by which probes suitable for SNOM are made. One approach is to make probes from fibres, with one end tapered. The outer surface of the fibre is coated with a metal film and the very end of the fibre is exposed. This makes the light to pass through the tip. The standard approach to make a tapered fibre is the pulling technique, in which a fibre is held in stretched position and the middle of the stretched region is melted by a CO_2 laser or a heating filament. This makes both the ends to get stretched and that creates tapered ends. The other approach is to acid etch the glass to produce a sharp tip. The fibre is then coated with a metal film, such as aluminium or gold and the coating at the tip is removed. There are several approaches to make such an opening. The more common approach is the shadowed evaporation method. Here, the metal is evaporated at a tilted direction in comparison to the probe axis. This makes it possible to evaporate the metal all over, except the tip. A uniform coating on all sides is achieved by rotation. This method makes it possible to make batch process tips, but uniformity of the tips is a problem, which depends upon the angle of evaporation, rotation, etc. The other methods used are electro-erosion and ion beam milling. Tips with physical holes are also possible. In this approach, tips are micro-machined similar to AFM tips. Holes are then made on tips by reactive ion etching or electron beam lithography. With this technique, uniform 50 nm diameter holes have been made on Si_3N_4 cantilevers.

There are several ways by which SNOM measurements are done. Illuminating the object at farfield and collecting light at nearfield, nearfield illumination and farfield collection, illumination and collection at nearfield are the common approaches. The other approach is by illuminating the object with evanescent waves and collecting the light with a nearfield probe. In this, the sample is transparent and total internal reflection of the light occurs. The evanescent waves penetrate a few hundred nanometers above the interface and they propagate into the aperture when it is brought

close to the surface. This is sometimes referred to as scanning tunneling optical microscopy (STOM) or photon scanning tunneling microscopy (PSTM). While all the above methods use tips with an aperture, apertureless tips are also employed, which utilise the interaction between the tip and the sample to enhance or scatter the nearfield signal. This depends on the tip-sample interaction. The sample is illuminated at farfield and the collection is also done at farfield.

The most important application of SNOM is in the study of single molecules. Here the signal, usually fluorescence, of a single molecule is detected. The dynamics of the molecules, the local environment of the molecule, the polarisation dependence of emission and thereby the orientation of the dipole moment of the molecule, photobleaching, etc. have been investigated.

The lateral resolution obtained by the technique is given approximately by the diameter of the aperture. There are practical limitations to the aperture diameter. Penetration of light to the metal coating of the tip, and therefore, the thickness of the coating determines the illumination volume. The amount of light that can be transmitted at farfield reduced drastically at very small aperture sizes. Increasing the light output by the sample using field enhancement of fluorescence, for example, is a way to increase the signal to noise. Nanoparticles-attached probes can be used to enhance local fluorescence intensity. Other approaches, such as fluorescence resonance energy transfer (FRET), is a promising method, in which the excitation energy of a probe is non-radiatively transferred to an acceptor at a very short distance. The energy transfer efficiency decreases rapidly with distance and it also requires an overlap of the spectra of the molecules concerned. If one of the molecules involved in FRET is attached to the probe and the other is in the sample, probing molecular distances become feasible. Currently, lateral resolution of the order of 15 nm has been reported.

Light can be used for vibrational excitations as well. Of all the techniques, Raman has been used well with SNOM. The principal problem in this is the poor Raman intensity, that one gets for normal molecules and materials. The enhancement of Raman by attaching molecules on nanoparticles of noble metals or rough surfaces, called surface enhanced Raman effect, has been used for the detection of Raman signals from single molecules.

A SNOM image of human cells (SiHa) is shown in Fig. 3.13.¹¹ This image was taken in the author's laboratory after the cells have been incubated with Au³⁺ ions for 96 h. The cells were removed and were embedded in a polymer matrix. Thin slices of 70 nm thickness of the processed material were taken with an ultramicrotome. The image shows the growth of gold nanoparticles in the cytoplasm of the cells. There are small nanoparticles in the nucleus of the cells too (as shown by TEM), but these are not revealed here as the resolution is poor.

Figure 3.13 is based on the difference in transmission of light through a probe of nanoscale dimensions. The same approach may be used for various kinds of optical methods, such as fluorescence, Raman scattering, etc. Thus, it is possible to develop spectroscopic tools for nanoscale objects. These kinds of methodologies are under development. Optical spectroscopy, namely, absorption spectroscopy, is possible at nanometer scale. With such spectra, it is possible to image the distribution of nanoparticles over micron scale samples such as human cells. This microscopic imaging is called hyperspectral imaging.

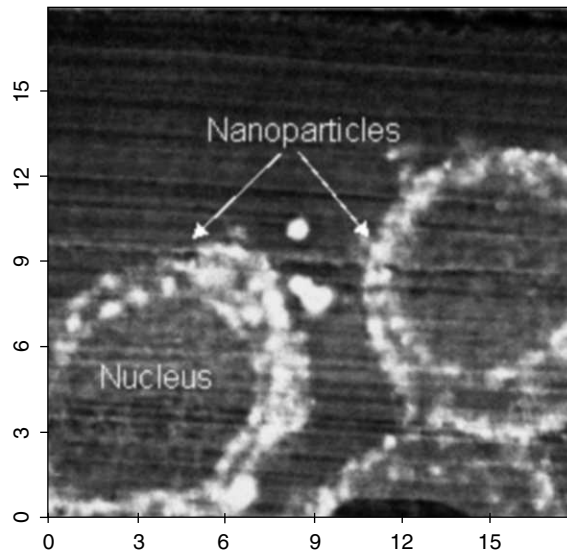


Fig. 3.13 SNOM image of SiHa cells incubated with gold ions showing the formation of nanoparticles in the cytoplasm (from the author's work). (For clarity see colour figure.)

Unlike electronic spectroscopy (UV-Visible absorption) which is an ensemble averaged measurement, the hyperspectral imaging can gather information at a single particle level though the working principle is same.¹² Either scattering (Plasmon absorption by nanoparticle) or electronic transitions as in semiconductors cause some material to absorb certain part of the electromagnetic spectrum and transmit the rest. This phenomenon is being used in hyperspectral imaging. The technique has three major stages such as (i) illumination, (ii) sample manipulation and (iii) spectrum collection.

Illumination system generally consists of a dark field condenser which illuminates the sample at a particular angle which is of the form of a cone of light. This geometry makes sure that no direct light is entered in the collection regime. The analyte (nanoparticle/biological cell) is immobilized on an optically transparent substrate such as a glass slide which will then be placed on a scanning platform enabling the X-Y movement. Only the scattered light goes to the third stage where it is being collected by an objective lens of NA less than that of the condenser lens. The light collected by the objective is energy analyzed by a grating just as in any other optical spectroscopy. Such a spectrum contributes to a pixel of the image. The X-Y scanner makes it possible to collect a number of (100 pixels /line X 100 lines) spectra and form the image.

Though the technique is limited by the optical diffraction limit, has the advantage that it carries spectral information which can be an indirect measure of the size. Even nanoparticle with sizes of the order of a few nanometer scatter light so strongly and the spectral profile depends on the size of the particle according to various scattering theories.¹³ These scattering theories are well developed that one

can calculate the size of the particle taking into account the spectral position and profile and the nature of the surrounding dielectric medium.

REFERENCES

1. G. Binning, H. Rohrer, Ch. Gerber and E. Weibel, *Phys. Rev. Lett.*, 49, (1982), 57.
2. W.G. Wildoer, L.C. Venema, A.G. Rinzler, R.E. Smalley and C. Dekker, *Nature*, 391, (1998), 59.
3. D.M. Eigler and E.K. Schweizer, *Nature*, 344, (1990), 524.
4. M.F. Crommie, C.P. Lutz and E. Eigler, *Science*, 262, (1993), 218.
5. H.C. Manoharan, C.P. Lutz and D. Eigler, *Nature*, 403, (2000), 512.
6. A. Stroscio and W.J. Keiser, *Scanning Tunneling Microscopy*, Academic Press, (1993).
7. S.S. Wong, A.T. Woolley, T.W. Odom, J-L. Huang, P. Kim, D.V. Vezenov and C.M. Lieber, *App. Phys. Lett.*, 73, (1998), 3465–67.
8. S. Hong, J. Im, M. Lee and N. Cho, in *Handbok of Microscopy for Nanotechnology*, Ed. N. Yao and Z.L. Wang, Kluwer Academic Publishers, New York, (2005).
9. Nadine Wong Shi Kam, Theodore C. Jessop, Paul A. Wender and Hongjie Dai, *J. Am. Chem. Soc.*, 126(22), (2004), 6850–51.
10. E.H. Synge, *Phil. Mag.*, 6, (1928), 356, 11, (1931), 65, 13, (1932), 297.
11. Anshup, J. Sai Venkataraman, Chandramouli Subramaniam, R. Rajeev Kumar, Suma Priya, T.R. Santhosh Kumar, R.V. Omkumar, Annie John and T. Pradeep, *Langmuir*, 21, (2005), 11562–67.
12. S. Trigari, A. Rindi, G. Margheri, S. Sottini, G. Dellepiane and E. Georgetti, *J. Mat. Chem.*, 21, (2011), 6531.
13. G. Mie, *Ann. Phys.*, 330, (1908), 377.

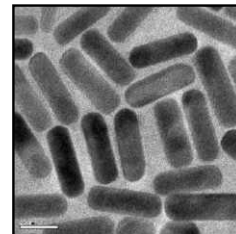
ADDITIONAL READING

1. C.J. Chen, *Introduction to Scanning Tunneling Microscopy*, Oxford University Press, (1993).

REVIEW QUESTIONS

1. What is vacuum tunneling?
2. What is the difference between profilometry and STM?
3. Why estimates of heights are different in AFM?
4. What other modifications of SPM based techniques are possible, which are not discussed in this chapter?
5. What are the potential limitations of SPM?

PHOTOELECTRON SPECTROSCOPY FOR THE STUDY OF NANOMATERIALS



*“If we can improve the energy resolution of our experiments,
new science will follow.”*

Kai Siegbahn, Nobel laureate, as told to Nils Mårtensson

Photoelectron spectroscopy is an experimental tool to study the electronic structure of materials. Photoelectron spectroscopy can be carried out using a variety of photon sources, from lasers (with energies of few eV) to soft X-rays (around 400–1500 eV) and hard X-rays (up to 10 keV), obtained from laboratory sources and synchrotron radiation. Based on the wide energy range of available photons, the technique of photoelectron spectroscopy can measure and distinguish between surface and bulk electronic structure of materials. This flexibility makes photoelectron spectroscopy a very suitable technique to study the electronic structure of nanomaterials. The applications of the method include elemental and chemical valence state identification, investigations of the changes in valence band electronic structure across magnetic and metal-insulator transitions, as well as the experimental determination of band dispersions and Fermi surfaces. A complete description of the occupied and unoccupied electronic states of a material can be achieved using photoelectron spectroscopy in combination with the complementary techniques of resonant photoelectron spectroscopy, X-ray absorption spectroscopy and inverse photoelectron spectroscopy. Electron spectroscopy can thus provide important clues to explain the chemical and physical properties of nanomaterials, as is clear from studies on clusters, nanowires, quantum well states, etc.

Learning Objectives

- What is photoelectron spectroscopy?
 - What are the applications of photoelectron spectroscopy to nanomaterials?
 - What is resonant photoelectron spectroscopy, X-ray absorption spectroscopy and inverse photoelectron spectroscopy?
 - How do you relate chemical and physical properties with electronic structure?
 - How is the electronic structure of nanomaterials different from bulk materials?
-
-

4.1 INTRODUCTION

Photoelectron Spectroscopy (PES) is one of the most important techniques to study the electronic structure of materials.¹ The electronic structure of a material is the description of the energies of electrons in a material. The energy of electrons in an isolated atom get modified when the atoms get arranged into a solid or a liquid material, or even a gaseous molecule, but they can still be described in terms of their energy levels in an atom. The type of electrons (*s, p, d, f*), the number of a particular type in an atom, and the energy they possess in a material, determines the chemical and physical properties of a material. For example, the energy distribution of electrons of a particular type existing in an insulator (such as electrons of copper atoms in cupric oxide, CuO) and in a metal (such as electrons of copper atoms in copper) are different, although they originate from the same type of atoms. This difference in energy distribution is directly related to the valency of copper in copper metal (Cu⁰) as compared to insulating cupric oxide (Cu²⁺). The electronic energy levels of a parent material also depend on very small amounts of changes in its chemical composition. This is appropriately described by the change in properties of an intrinsic semiconductor obtained upon doping very small amount of holes and electrons by chemical substitution. The best example is p-type (hole) or n-type (electron) doping in silicon achieved by site-substitution of boron or phosphorus atoms, respectively. The precise control of doping holes and electrons in various semiconductors, such as Si, Ge, GaAs, GaN, etc. is the basis of manufacturing a variety of electronic devices, from rectifier diodes and light emitting diodes (LEDs) to state-of-the-art integrated circuits (ICs), like microprocessors, memory chips, etc. Another important topic in materials science is phase transitions: a material can undergo a transformation in its geometric structure and/or properties as a function of a physical parameter, such as temperature, pressure, etc. The competition in the elastic energy of a material versus its electronic energy is often the origin of a phase transition as a function of a physical parameter. If we apply the same line of reasoning to the properties of a nanomaterial compared to its bulk form, we can see that nanomaterials can display electronic properties, which may be very different from their bulk form. This indicates that nanomaterials are a very fertile ground for generating novel scientific phenomena and properties for device applications. This, in turn, makes the elucidation of the electron energies of a material in its bulk and nano-form a major field of study in present-day research.

4.2 SALIENT FEATURES OF PES

PES is a primary tool to study the electronic structure of materials—solid, liquid or gas. It has been used to study the electronic structure of solids extensively over the last 50 years, and today, there exists a vast database of the electronic structure of materials as determined by photoelectron spectroscopy. The earliest record of experiments describing photoelectrons (that is, photon induced emission of electrons, also called photoemission) is due to the German physicist, Heinrich Hertz (1856–1894) as part of his studies on the nature of electromagnetic radiation and the experimental discovery of the photoelectric effect.² From a series of experiments, Hertz showed that the absorption of electromagnetic radiation (=photon) by a material placed near a spark gap, directly affected the current–voltage (=electric) characteristics of a spark gap: the first illustration of photoelectric effect. Since the flow

of current across a spark gap is due to electrons, it meant that the electromagnetic radiation affected the electrons in the material. Historically, these experiments were done before the discovery of the electron by J.J. Thomson in 1899 and the photoelectric effect experiments could not be reconciled with the classical or wave nature of electromagnetic radiation. It was later explained by Albert Einstein³ based on the quantum nature of electromagnetic radiation, which describes light (electromagnetic radiation) as consisting of photons and every photon has a specific frequency ν and energy $h\nu$. The Nobel Prize citation of Albert Einstein reads, “for his services to the development of Theoretical Physics, and especially for his discovery of the law of the photoelectric effect”. The photoelectric effect is described by the equation,

$$h\nu = KE + BE + \Phi; \quad (1)$$

where, $h\nu$ is the known incident photon energy, KE (E_K) is the measured kinetic energy of the emitted electron, BE(E_B) is the binding energy of the electron, and Φ is the known work function of the material under study. This equation tells us that if the incident photon energy is more than the sum of the binding energy of an electron and the work function of a material, on absorbing the photon, the electron will get emitted with a finite kinetic energy. The important features of the photoelectric effect are:

1. The rate, at which electrons are emitted, is directly proportional to the intensity of the incident light, for a given material and frequency of incident radiation.
2. For every material, there exists a certain minimum frequency of incident radiation, below which electrons cannot be emitted by the photoelectric effect, and this minimum frequency is called the threshold frequency.
3. For incident radiation above the threshold frequency, the maximum kinetic energy of the emitted electron depends on the frequency of incident radiation, but not on the intensity of the incident radiation.

These features were a direct proof of the particle nature of electromagnetic radiation and played a vital role in establishing the wave-particle duality principle in quantum mechanics. The equation (1) above is a statement of the law of conservation of energy and implicitly includes the law of conservation of momentum.

4.3 TECHNIQUE OF PES

The photoelectron “spectroscopy” experiment involves measuring the intensity of photo-emitted electrons from the core levels and valence band of a material, as a function of kinetic energy of the emitted electrons. Fig. 4.1 shows a schematic of the photoelectron process. Pioneering work on the science and technique of photoelectron spectroscopy for the study of electronic structure,⁴ or “ESCA” (an acronym for electron spectroscopy for chemical analysis), was carried out by the group of Kai Siegbahn (1918–2007) at Uppsala University in Sweden. He was awarded the Nobel Prize for “his contribution to the development of high-resolution electron spectroscopy” in 1981. The schematic of the instrumentation required for carrying out photoelectron spectroscopy is shown in Fig. 4.2.

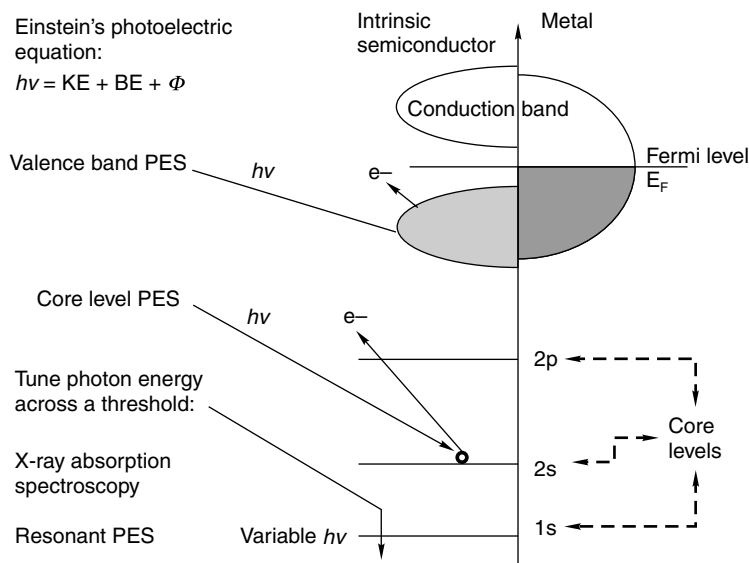


Fig. 4.1 A schematic diagram showing the energy of electrons in a material and the process of the photoelectric effect.

Since we have to measure electron kinetic energy, the experiment has to be done in ultra high vacuum, because electrons have a very short mean free path in air.^{5,6} Typically, one needs a vacuum of better than 10^{-10} mbar. Further, the electrons also have a short inelastic mean free path inside a solid.⁵⁻⁷ The inelastic mean free path (IMFP) of an electron inside a solid is defined as the average distance travelled by an electron before making an inelastic collision. Since an inelastic collision results in a change of its energy, it leads to a loss of the signal intensity that is being measured. So the technique can be extremely surface sensitive and probes typically a few angstroms to about 20\AA of the surface with conventional laboratory equipment of the type shown in Fig. 4.2. For a material with an IMFP, λ , the measured intensity I is given by,

$$I = I_0 \exp(-d/\lambda); \quad (2)$$

where, I_0 is the intensity without any inelastic losses and d is the distance from the surface from which the electrons are emitted. The IMFP λ depends strongly on the kinetic energy of the electrons and also the specific properties of the material under investigation. However, a general empirical curve, well known as the universal curve for IMFP of electrons,^{5,6} shows that the IMFP has large values (>50 – 100\AA) for very low kinetic energies (<10 eV), a broad minimum of 5 – 10\AA for kinetic energies between 30 and 100 eV and then a monotonic increase for kinetic energies above 100 eV. Typically, the IMFP is again about 50 – 150\AA at energies of 6 – 8 keV. The surface sensitivity is thus determined by the depth perpendicular to the surface from which the electrons escape, and is defined as the mean escape depth $\sigma = \lambda \cos \alpha$, where λ is the IMFP and α is the emission angle of the electrons measured with respect to the surface normal. The technique is thus most bulk sensitive at normal emission, and as the emission angle increases, it becomes more surface sensitive.

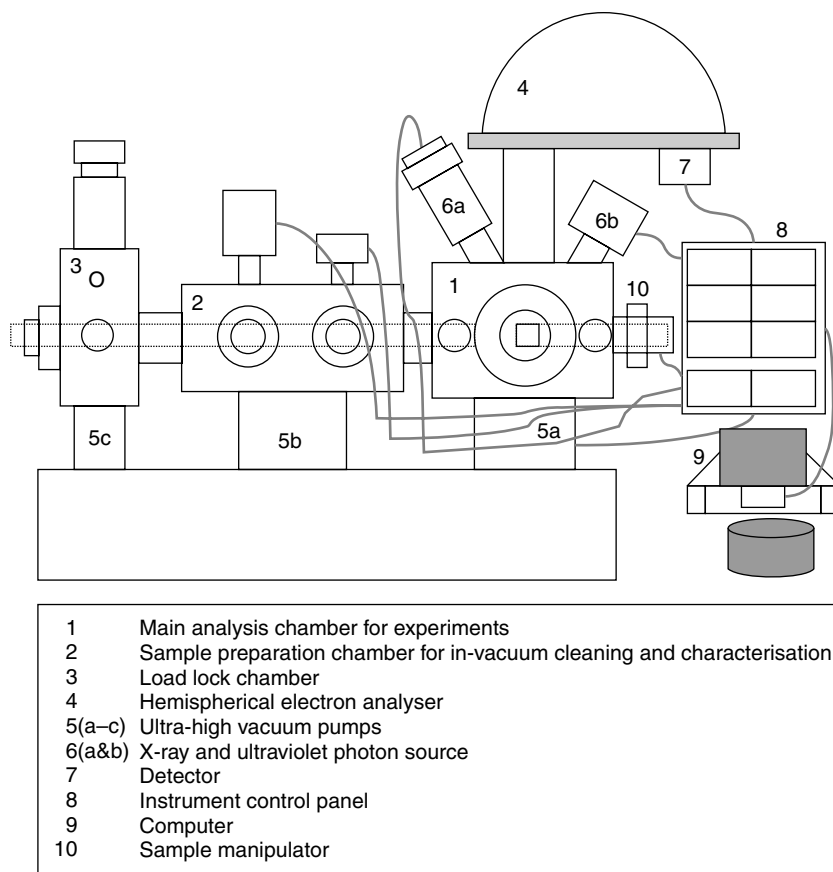


Fig. 4.2 Schematic of a photoelectron spectrometer showing various components.

The general photoelectron spectroscopy instrument consists of stainless steel chambers, which are pumped by a combination of ultra-high vacuum turbo-pumps, backed by rotary/diaphragm pumps. A typical stand alone instrument consists of three chambers: (1) the main chamber or analysis chamber has an electron energy analyser, a photon source, and sample manipulator, which facilitates sample cooling and heating, (2) a sample preparation chamber, in which the sample surface is prepared and characterised inside the ultra-high vacuum (this chamber usually has a sample cleaver or, sample annealing and ion-etching facilities, etc.) and (3) a fast entry load-lock or sample bank chamber, which alone is opened and exposed to air, for introducing the samples into the preparation and analysis chambers. This chamber is necessary for minimizing the time required to achieve ultra-high vacuum for experiments to be conducted in the preparation and analysis chambers. The spectroscopy experiments usually use a hemispherical electron energy analyser for measuring the kinetic energies of electrons, which is achieved by applying a fixed voltage to the hemispherical plates of the analyser for one particular kinetic energy. The energy analysis is computer-controlled and the spectroscopy

experiment scans over the kinetic energy of the measured electrons to obtain a spectrum: intensity as a function of kinetic energy. The spectrum can be readily presented as a function of binding energy by knowing the work function or calibrating the energy scale with a standard database of core-level energies.⁸ Photoelectron spectroscopy is often done using a fixed photon energy, but it can be done with a photon energy of a few eV (say, 6 or 7 eV) or even with few keV (say, 6 or 8 keV). It is also done as a function of tunable photon energy obtained from a synchrotron in the special case of resonant photoelectron spectroscopy.

4.4 NOMENCLATURE

The following table lists the various names and acronyms used in the literature for photoelectron spectroscopy, depending on the energy of photons used for the experiment. Also listed are names and acronyms of the complementary techniques of electron spectroscopy:

Photon energy	Name	Acronym
Ultraviolet (UV) photons He I: 21.2 eV He II: 40.8 eV	Ultraviolet Photoelectron Spectroscopy	UVPES or UPS
Laboratory X-rays Mg K α : 1253.6 eV Al K α : 1486.6 eV	X-ray Photoelectron Spectroscopy	XPS
Lasers 4th harmonic of Ti-sapphire laser: 5.95 eV frequency-tripled Nd:YVO ₄ quasi-continuous wave: 6.994 eV	Laser Photoelectron Spectroscopy	Laser-PES
UV and soft X-ray photons (30-1500 eV) obtained at a synchrotron using grating monochromators; energy tunable across a particular core level threshold	Resonant Photoelectron Spectroscopy	Resonant-PES
Hard X-rays obtained at a synchrotron using crystal monochromators (6-10 KeV)	Hard X-ray Photoelectron Spectroscopy	HX-PES
Complementary techniques		
Inverse photoelectron spectroscopy		IPES
Bremsstrahlung isochromat spectroscopy		BIS
X-ray Absorption spectroscopy		XAS
Resonant photoelectron spectroscopy		RESPES/RPES

A further classification involves the names/nomenclature used to describe specific energy levels that are measured in a material, as is known from the energy levels of the electronic states present in the atoms constituting the material. The nomenclature follows the well-known classification for hydrogenic atoms, such as *s*, *p*, *d*, *f* electrons occupying the K, L, M, N, etc. shells in an atom.⁹ The table

ahead lists a more detailed classification for electron energy levels from the K-shell to N-shell (the numbers in parentheses indicate number of electrons that can be accommodated in specific shells):

K-shell	1s(2)	K
L-shell	2s(2)	L ₁
	2p(6) : 2p _{1/2} , 2p _{3/2}	L ₂ , L ₃
M-shell	3s(2)	M ₁
	3p(6) : 3p _{1/2} , 3p _{3/2}	M ₂ , M ₃
	3d(10) : 3d _{3/2} , 3d _{5/2}	M ₄ , M ₅
N-shell	4s(2)	N ₁
	4p(6) : 4p _{1/2} , 4p _{3/2}	N ₂ , N ₃
	4d(10) : 4d _{3/2} , 4d _{5/2}	N ₄ , N ₅
	4f(14) : 4f _{5/2} , 4f _{7/2}	N ₆ , N ₇

The above classification is fully described in references 5 and 9. Photoelectron spectroscopy measures the occupied electronic states of a material and describes the core (or inner)-levels and valence (outermost) levels of a material. A related technique to photoelectron spectroscopy is Auger electron spectroscopy.^{1, 5, 6} When an electron is emitted from a core level, it results in an excited state with a core hole. This hole can get filled by a higher lying electron and the energy of this transition is given out in the form of a photon (resulting in X-ray emission), or the excess energy can be used in a non-radiative process to remove another electron. The second process, which results in the emission of an electron, is called the Auger effect, thus giving the name Auger electron spectroscopy. Later, we will discuss three related or complementary electron spectroscopies of the unoccupied and occupied electron states of a material, which go by the names of inverse photoelectron spectroscopy,¹⁰ X-ray absorption spectroscopy,¹¹ resonant photoelectron spectroscopy,¹² respectively. The method of inverse photoelectron spectroscopy (IPES) is a valuable probe of the unoccupied density of states of a material, based on the inverse process of photoelectric effect¹², i.e., absorption of an electron and emission of a photon. However, it is a very time-consuming experiment and is not very popular, because the intensities are very low due to the low transition probability for the inverse photoelectric process. The experiments of X-ray absorption spectroscopy and resonant photoelectron spectroscopy require comparatively very little time, but require a tunability of the incident photon energies.

4.5 APPLICATIONS

In the following, we describe the major applications of photoelectron spectroscopy:

1. Core-level photoelectron spectroscopy: Since atoms of each element possess a unique set of electron energy levels, the foremost application of photoelectron spectroscopy is to identify the elements present in a material, from a measurement of its core-level spectra. Using tabulated atomic sensitivity factors S_i for specific core levels (or atomic cross-sections),¹³ one can also quantify the ratio of elements present in a sample by measuring the core-level spectra of the different elements present in a sample. The atomic fraction F_β of a constituent element β in a sample is given by,

$$F_{\beta} = (I_{\beta}/S_{\beta})/\Sigma (I_i/S_i) \quad (3)$$

where, the sum is over a specific core level of each element i present in the sample and I_i are their respective intensities.

2. Identification of chemical or valence state: The chemical state of an element can be determined because the core-level binding energies of elements depends on their valency. For example, it is a routine experiment to identify and distinguish⁸ a metal and its oxide such as aluminium metal (Al^0) and aluminium (Al^{3+}) oxide or copper metal (Cu^0) and cupric (Cu^{2+}) oxide. In more complex situations, it is possible to distinguish between multiple oxidation states using core-level spectroscopy. This is best exemplified by Si 2p core-level spectra, which showed that features due to Si^0 (elemental Silicon), Si^{1+} , Si^{2+} , Si^{3+} and Si^{4+} are systematically shifted to higher binding energies, depending on the valence state.¹⁴ A spectrum obtained from a plasma oxidised surface of single crystal Silicon(100) is shown in Fig. 4.3, plotted as a function of relative binding energy. The absolute binding energy for elemental silicon 2p core level is about 99 eV, and every higher multiple oxidation state is about 1 eV higher binding energy, with the Si^{4+} occurring at about 103 eV. Thus, even suboxides can be identified and quantified using photoelectron spectroscopy and lead to a description of local bonding configurations in materials. At a general level, core-level photoelectron spectroscopy applications in surface science involve the determination of physisorption or chemisorption of molecules, as determined from the binding energies and symmetry of molecules adsorbed on surfaces.

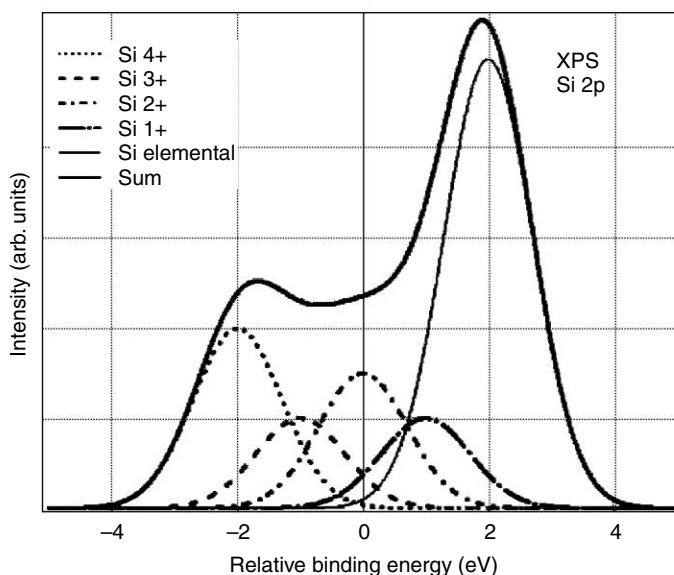


Fig. 4.3 Spectrum showing multiple oxidation states of silicon, as measured in Si 2p core-levels using X-ray photoelectron spectroscopy. The sample is a plasma oxidised surface of single crystal Silicon(100).

3. Line shape analysis: A detailed study of core-level line shapes using high energy resolution can reveal material properties—a symmetric line shape for insulators, or an asymmetric line shape

for metals. The symmetric line shape (Fig. 4.4) is described by a Voigt function: a convolution of a Gaussian function (representing the experimental energy resolution) with a Lorentzian function (representing the lifetime of the energy level). The lifetime (Δt) of a specific core level is related to the intrinsic energy width (ΔE) of the core level reflecting the Heisenberg's uncertainty principle, and is given by, $\Delta E \cdot \Delta t \geq \hbar$; $\hbar = h/2\pi$, where h is the Planck's constant.

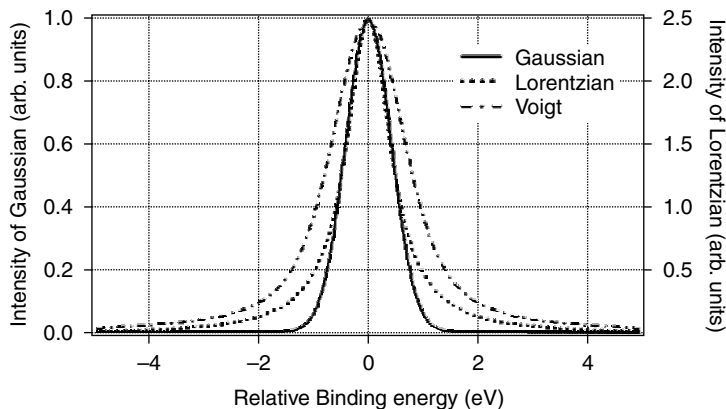


Fig. 4.4 Comparison of a Gaussian function (full line) and Lorentzian function (dotted line) of the same full width at half maximum (FWHM = 1 eV), and their convolution, a Voigt function (dash-dot line).

Metals show an asymmetric line shape that is well-described by a Doniach-Šunjić line shape,¹⁵ which is due to the excitations of electron-hole pairs at the Fermi level of a metal. Since these electron-hole excitations have infinitesimally small energies and occur when the electron is travelling within the solid, they result in a loss of kinetic energy of the emitted electron. This loss in kinetic energy causes a broadening on the low kinetic energy (high binding energy) side of an otherwise symmetric core-level, and is a characteristic of metals. Core-level line shapes also carry valence electron spin information. The splitting of the 3s core levels in a molecular gas is indicative of the exchange coupling between the s core levels and the valence electron spin⁴ e.g., the oxygen 1s core-level spectrum of molecular oxygen consists of two peaks separated by 1.1 eV and with an intensity ratio of 1:2, which is proportional to the degeneracy of the states. This behaviour is understood as follows: The photoelectron of one 1s electron results in a photohole with a spin of $s = 1/2$. Since molecular oxygen has a total valence electron spin of $S = 1$, it couples with the $s = 1/2$ spin and gives a total spin $J = 1/2$ and $3/2$. The degeneracy is given by $2J + 1$, and hence, the intensities are in the ratio of 1:2. Water, with a valence electron spin of $S = 0$ does not show this exchange splitting in the O 1s core-level spectrum. Similar behaviour is also known in the 3s, 4s and 5s core-level spectra of transition metal and rare-earth compounds.¹

4. Valence-band photoelectron spectroscopy: A direct probe of the occupied density of states (DOS, number of electronic states, which is proportional to the measured intensity of electronic states as a function of their energy) of a material is provided by valence-band photoelectron spectroscopy. Thus, one can distinguish between an intrinsic semiconductor (or insulator) compared to a metal, because

semiconductors (or insulators) have a gap in the density of states at the chemical potential, or Fermi level E_F , while a metal has no gap in the density of states (Fig. 4.1). The Fermi level of a metal (the highest occupied energy level of a metal) is identified as the highest kinetic energy level that can be measured using a specific photon energy and is called the Fermi edge. At zero temperature, it is a sharp cut-off or step-function as determined by the Fermi-Dirac distribution function, but since any experiment is done at a finite temperature, the Fermi level is broadened at the edge by the Fermi Dirac function at that temperature. The Fermi edge is often used to determine the energy resolution of a photoelectron spectrometer, defined as the Gaussian function that needs to be convoluted with the Fermi-Dirac function (Fig. 4.5), which simulates the Fermi edge spectrum accurately at the temperature of the measurement.

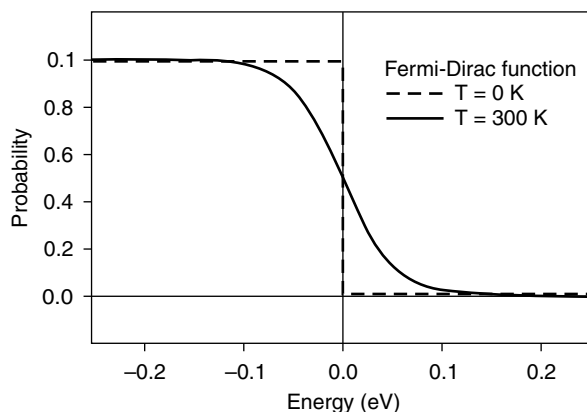


Fig. 4.5 The Fermi-Dirac function at $T = 0$ and 300 K. Note x-scale is in eV.

The present record for energy resolution in photoelectron spectroscopy of a solid is 360 micro-electron volts (μeV), obtained for the Fermi edge of gold measured at a temperature of ~ 3 K, using a laser as a photon source¹⁶ (Fig. 4.6). A high energy resolution of about 1–5 meV has been achieved by several groups in the world in the past few years. High energy resolution photoelectron spectroscopy has played a very important role in the study of phase transitions including superconductivity, metal-insulator transitions, Kondo materials, etc. and defines the frontline of research in the electronic structure of novel materials.

High-resolution photoelectron spectroscopy has been extensively used to study the nature of the superconducting gap in low- T_c ^{17–19} and high- T_c ²⁰ superconductors. A precise measurement of the gap in low- T_c superconductors has revealed the symmetry of the superconducting gap in terms of isotropic s-wave or anisotropic superconductors.¹⁹ In the weak-coupling regime, Bardeen-Cooper-Schrieffer (BCS) theory predicts that the superconducting DOS is $\omega/(\omega^2 - |\Delta_0|^2)^{1/2}$, where ω is the binding energy and Δ_0 is the isotropic superconducting gap value at $T = 0$ K. At finite temperature, the experimental spectrum needs to be compared with the Dynes function.²¹ The Dynes function is a modified BCS function for determining the superconducting energy gap value Δ at a finite temperature. It includes a thermal broadening parameter Γ , and the superconducting density of states $I(\omega, \Delta, \Gamma)$ is expressed as $I(\omega, \Delta, \Gamma) = (\omega - i\Gamma)/[(\omega - i\Gamma)^2 - \Delta^2]^{1/2}$. The real part of this equation is directly compared with

the experimental spectrum for determining Δ and Γ . This was first introduced²¹ by Dynes et al. for explaining temperature dependent tunneling spectra of Pb, and is widely used today to deduce SC gap values from tunneling and photoemission spectra of weak and strong-coupling superconductors. For anisotropic superconductors, the superconducting gap is momentum (k)-dependent, i.e., $\Delta(k)$. For HTSC, $\Delta(k) = \Delta_{\max} \cos(2\theta)$, where Δ_{\max} is the maximum value of gap and θ is the polar angle in k -space[18]. From a careful analysis of the data,^{17–20} one can extract the electron–phonon coupling parameter and also classify the type of superconductivity as BCS-like weak-coupling or strong-coupling superconductivity.

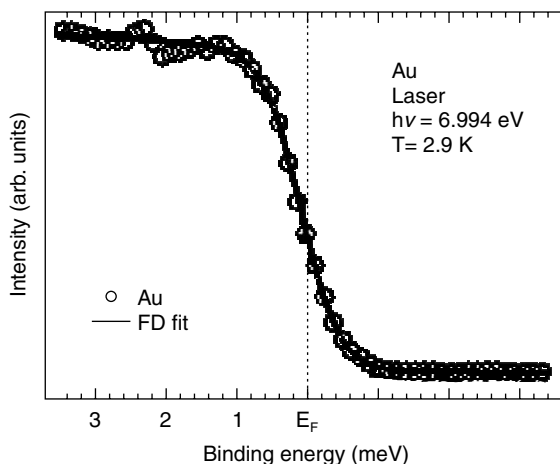


Fig. 4.6 The highest energy resolution photoelectron spectrum (circles) of gold (Au), measured for a solid using Laser PES at a sample temperature of 2.9 K, compared with a FD fit (full line), a Fermi–Dirac function convoluted with a Gaussian function having a full width at half maximum of 360 micro-eV. Note x-scale is in milli-eV (reprinted with permission from Ref. 16. Copyright (2008). American Institute of Physics).

The measurement and analysis carried out using photoemission spectroscopy for the superconducting transitions¹⁷ of the elemental metals Pb and Nb is shown in Fig. 4.7a and b. Figure 4.7a shows the ultrahigh resolution photoemission spectra above and below the superconducting transitions of Pb and Nb ($T_c = 7.12$ and 9.26 K, respectively). The intensity at and near the Fermi level (E_F) gets redistributed on lowering temperature below T_c and shows a shift of the leading edge due to superconducting gap formation. Figure 4.7b shows the Dynes function fits to the spectra, which are plotted on an expanded energy scale of up to 10 meV binding energy. The weak-coupling BCS superconductivity is isotropic s-wave type, and theory gives a reduced gap value of $2\Delta_0/k_B T_c = 3.53$, where Δ_0 is the gap at $T = 0$ K, k_B is the Boltzmann constant and T_c is the critical transition temperature. A value of $2\Delta_0/k_B T_c > 3.53$ indicates moderate or strong coupling superconductivity. The more exotic forms of superconducting gaps, such as the multiple gaps in quasi two-dimensional materials like MgB_2 ¹⁹ as well as the $d_{x^2-y^2}$ gap of the strongly correlated high- T_c cuprate superconductors,²⁰ have been established by high resolution angle-resolved photoelectron spectroscopy.

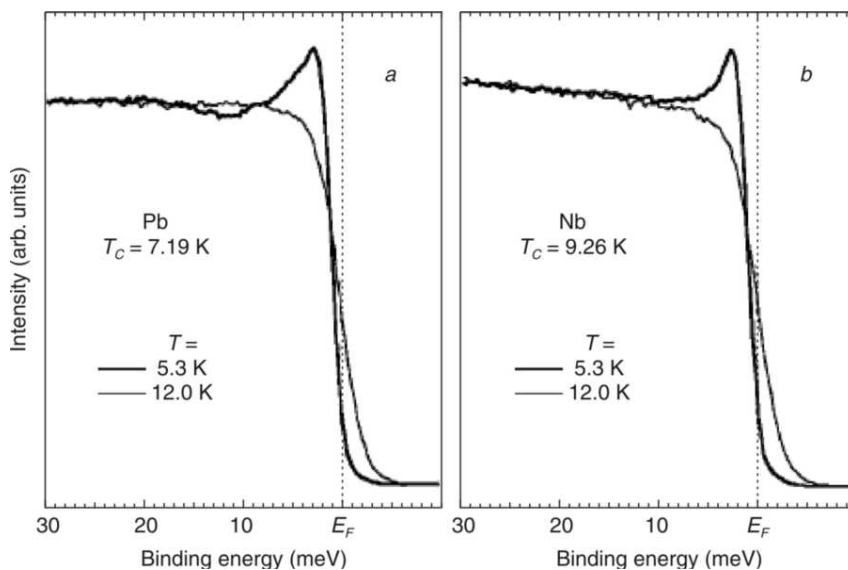


Fig. 4.7a Ultrahigh-resolution photoemission spectra of (a) Pb and (b) Nb, measured at 5.3 K (superconducting state) and 12.0 K (normal state). Redistribution of spectral weight and the opening of superconducting gaps are observed for Pb and Nb (reprinted figure with permission from Ref. 17. Copyright (2000) by the American Physical Society).

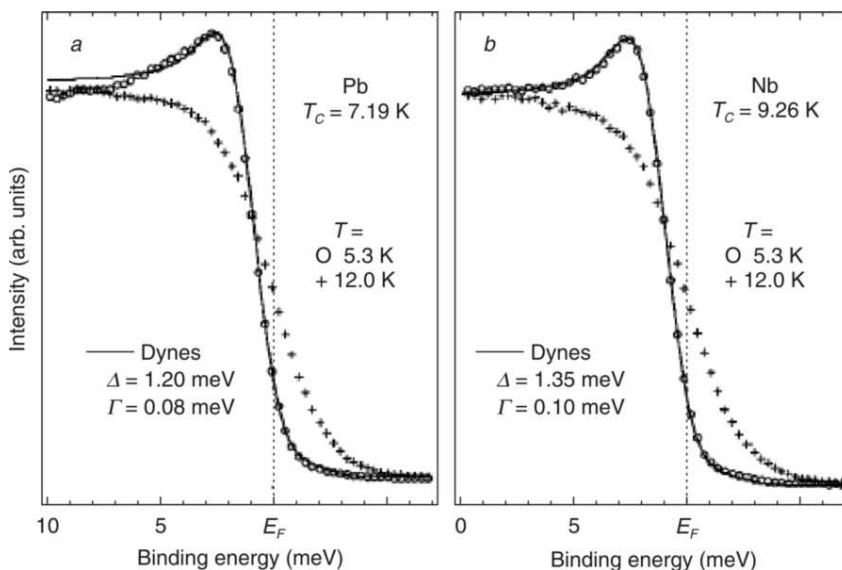


Fig. 4.7b Dynes function fits (full lines) to the superconducting DOS for (a) Pb and (b) Nb, used for estimating the superconducting-gap values (reprinted figure with permission from Ref. 17. Copyright (2000) by the American Physical Society). (For clarity see colour figure.)

5. Angle-resolved photoelectron spectroscopy: In angle-resolved photoelectron spectroscopy (ARPES) experiments, in addition to measuring the kinetic energies of the emitted electrons, one measures the spectra as a function of emission angle with respect to the surface normal, in terms of the polar and azimuth angles. Before we describe the ARPES technique, it is useful to consider the photoelectron process as involving the initial state with energy, $E_i = -BE$ (negative of the binding energy of the electron) and the final state of the electron after emission as a state with an energy $E_f = KE + \Phi$. This implies $E_f = E_i + h\nu$, from the photoelectric equation. Applying the law of conservation of momentum to the electrons in a crystalline solid with initial state energy and momentum as (E_i, k_i) and the final state to be described by (E_f, k_f) , the electron emitted from the solid has the measured momentum $K_f = k_f + G$, where G is a reciprocal lattice vector. Under the assumption of a free electron final state, with k_f resolved into the in-plane momentum $k_{||}$ and out of plane momentum k_{\perp} , the KE of emitted electron is

$$E_K = (\hbar^2/2m)(k_{||}^2 + k_{\perp}^2), \quad (4)$$

$$\text{then, } k_{||} = [(2m/\hbar^2 \times E_K)]^{1/2} \sin\theta; \quad (5)$$

where, θ is the emission angle measured with respect to the surface normal,

$$\text{and } k_{\perp} = [(2m/\hbar^2 \times E_K \cos^2\theta + V_0)]^{1/2}; \quad (6)$$

where, V_0 is the inner potential, and we refer the interested reader to a review, which discusses the details of the ARPES technique extensively.²² Equation (5) is enough to discuss quasi-one and -two dimensional systems, while Equation (6) is required in addition to (5), for the study of three-dimensional materials with ARPES. The message of the above discussion is that one can measure momentum resolved electronic structure of solids using ARPES, as will be discussed in the following for specific examples, including the observation of quantum well states. The principal use of ARPES is for determining the valence-band dispersion of electrons in solids, and is in fact, the only experimental method providing the experimental-band dispersion of solids. This capability, combined with high resolution, makes it a very important tool for the study of quantum well states and momentum dependent changes across phase transitions (such as superconducting and charge-density-wave (CDW) transitions), in low dimensional quasi-one and -two dimensional systems. A recent ARPES study²³ reports on the interplay of superconductivity and CDW transitions in quasi-two-dimensional 2H-NbSe₂. The study shows that CDW ($T_{\text{CDW}} = 33$ K) co-exists with maximal superconductivity ($T_c = 7$ K) at the same point in momentum space in 2H-NbSe₂. This was determined by measuring the superconducting gap at different momentum(k)-points, as well as the CDW induced changes as function of temperature. This is shown schematically in Fig. 4.8. The red circles and blue circles shown in Fig. 4.8 are connected by the primary CDW vectors (q_1, q_2, q_3) and secondary CDW vectors ($q_i \pm q_j$) with $i, j = 1, 2, 3$, respectively. They lie on the Fermi surfaces of 2H-NbSe₂ (green curves). The superconducting gaps measured on various points (labeled A–I) in Fig. 4.8 show different values, with the important property that the largest gap occurs at points which are connected by the CDW vectors, namely, the red and blue circles, while the other points show smaller gaps. The experimental photoemission spectra and the calculated spectra at a few specific points (A, D, and H) are shown in Figs 4.9a and b. From such a comparison, highly accurate values (± 0.1 meV) of the anisotropic

superconducting gap could be determined for 2H-NbSe_2 . The results thus showed that the strong electron phonon coupling constant leads to an enhanced, momentum-dependent superconducting gap in this anisotropic s-wave superconductor.

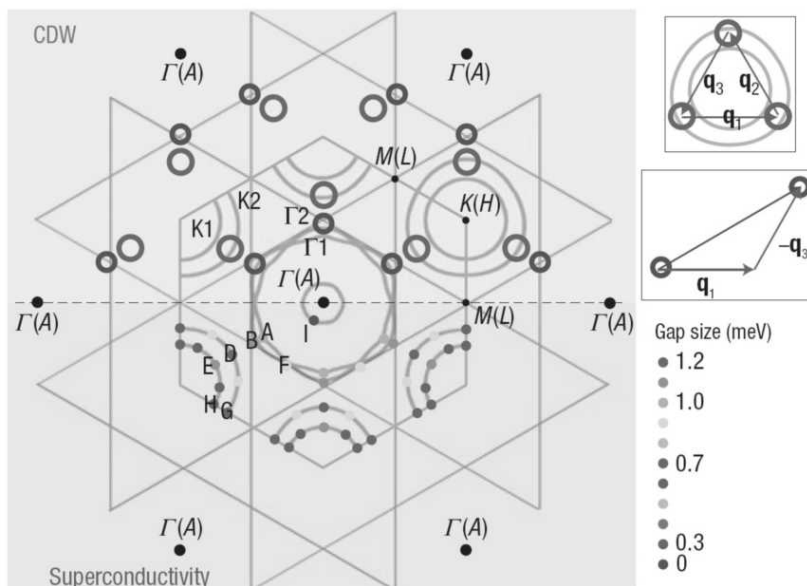


Fig. 4.8 Mapping of special k -points corresponding to CDW (upper half) and k -dependent superconducting gap (lower half). The experimentally determined Fermi Surfaces (green curves) show primary CDW vectors (q_1, q_2, q_3) connect red circles, while blue circles are connected by secondary CDW vectors ($q_i \pm q_j$) with $i, j = 1, 2, 3$. Superconducting gap values are mapped with a colour scale in the lower half of the figure (from Ref. 23).

Since the ARPES technique is very time consuming with a laboratory photon source, such as a gas discharge Helium (He) lamp, the technique has benefited tremendously from the use of synchrotron radiation sources which typically provide significantly higher incident photon flux by two or more orders of magnitude, compared to a laboratory gas discharge lamp. This advantage and the flexibility of tuning the photon energy over a wide range, also makes synchrotron radiation-based electron spectroscopy a very useful and efficient technique for a variety of experiments, such as resonant photoelectron spectroscopy and X-ray absorption spectroscopy. In the following, after the small sections discussing complementary techniques and synchrotron radiation, we discuss applications of electron spectroscopy to several examples of nanomaterials.

4.6 COMPLEMENTARY TECHNIQUES

(a) Inverse photoelectron spectroscopy: In inverse photoelectron spectroscopy,¹⁰ one carries out the inverse experiment of photoelectron spectroscopy to study the unoccupied states of a material. A

mono-energetic beam of electrons is incident on a material. It occupies an available electronic state as its final state, which is not occupied in the initial state and emits a photon. By scanning the incident electron energy and measuring detected photons at a fixed photon energy, it is possible to map out the unoccupied density of states of a material. In this mode, it is called bremsstrahlung isochromat spectroscopy (BIS).

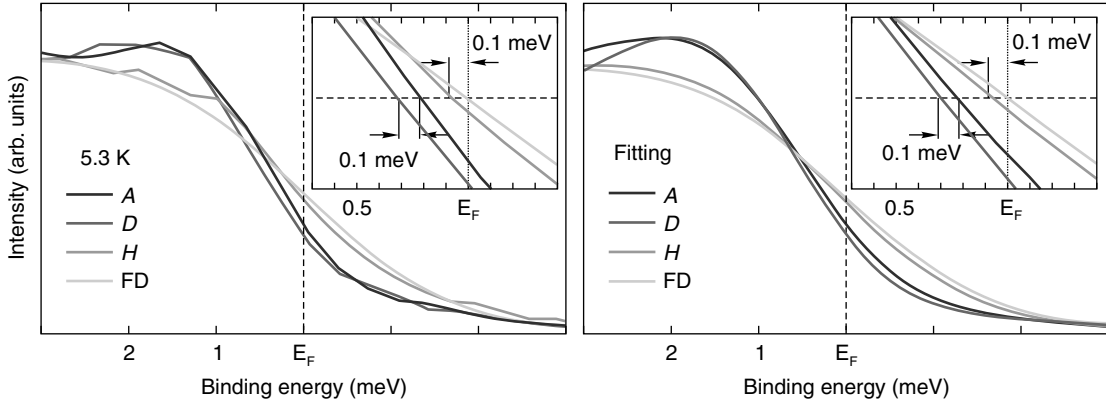


Fig. 4.9 (a) The experimental ARPES spectra measured at 5.3 K for the k -points labeled A, D and H (see Fig. 4.8). (b) shows the corresponding fits compared with the Fermi-Dirac function (FD) convoluted with the resolution function (2.0 meV). From such fits to the data, the superconducting gap values of 0.3 ± 0.1 meV for spectrum H (the smallest gap that can be discerned from experiment), 1.0 ± 0.1 meV for spectrum A and 1.2 ± 0.1 meV for spectrum D, could be determined for $2H-NbSe_2$ (from Ref. 23).

(b) X-ray absorption spectroscopy: X-ray absorption spectroscopy (XAS) is a measurement of the X-rays absorbed by a material as a function of the incident X-ray photon energy. In particular, the intensity of X-rays absorbed by a solid undergoes a sharp increase, when the incident X-ray photon energy is tuned across a core-level threshold energy.¹¹ In the simplest case, the intensity is directly proportional to

$$I_{XAS} \propto | \langle \Theta_f | \hat{\mathbf{e}} \cdot \mathbf{r} | \Theta_i \rangle |^2 \delta(E_f - E_i - h\nu) \quad (7)$$

where Θ_i , Θ_f are the initial and final states of the system, and $\hat{\mathbf{e}} \cdot \mathbf{r}$ is the dipole operator coupling the initial state with energy E_i to the final state with energy E_f on absorption of an X-ray photon of energy, $h\nu$. The material absorbs a photon and results in exciting an electron to a continuum or an unoccupied state, when the energy $h\nu$ equals $E_f - E_i$. The dipole matrix element approximation indicates that only transitions with $\Delta L = \pm 1$, and which conserve spin $\Delta S = 0$ are allowed transitions. Thus, XAS probes the site selective, element specific, angular momentum projected density of unoccupied states of a material. For soft X-rays (30–2000 eV), the quadrupole transition is very weak (usually 100 or more times weaker than the dipole transition) and is often neglected in discussions of soft XAS.

(c) Resonant photoelectron spectroscopy (RESPES) measures the occupied partial density of states¹² and is thus a complementary technique to XAS. In RESPES, the photon energy is also tuned across

a core-level threshold and one measures the valence-band photoelectron spectra as a function of the incident photon energy. In this way, one can probe the angular momentum projected density of states in the occupied valence-band, e.g., when the incident photon energy is tuned across the 2p (3d) core-level of a 3d transition metal (4f rare-earth) element or compound, the 3d (4f) partial density of states in the valence-band can be identified. The process resulting in resonant photoelectron emission involves the absorption of a photon and creation of a core hole (like XAS), and this state undergoes a de-excitation, with the core hole getting filled up and the emission of an electron from the valence-band. The remarkable increase in intensity often leading to so-called giant resonances are described by the Fano effect.²⁴ The experiments of XAS and RESPES are done across particular core-level thresholds and thus necessarily require synchrotron radiation.

4.7 SYNCHROTRON RADIATION

Synchrotron radiation²⁵ is electromagnetic radiation generated by the acceleration of relativistic (near the speed of light) charged particles, e.g., electrons, through magnetic fields. The acceleration is first done in a synchrotron, a cyclic particle accelerator, in which the electric field used for accelerating the particles and the magnetic field used for turning the particles for circulation, are synchronised to the particle beam. The high-speed electron beam can achieve a final energy that is in the GeV (giga-electron-volt) range, and it is stored in an ultrahigh vacuum ring in a closed loop. Since the electrons are forced to travel in a closed loop by strong applied magnetic fields, they undergo acceleration and thus emit electromagnetic radiation, which includes frequencies of radio waves, infra-red, visible, ultraviolet and X-rays. The synchrotron radiation sources are the brightest known sources of X-rays, which can be linearly or circularly polarised. The electromagnetic radiation can be further intensified by using insertion devices, called wigglers or undulators (composed of an array of north and south pole magnets). The storage ring has openings through which the radiation exits the storage ring and which are subsequently monochromatised using gratings or crystal monochromators to obtain a specific energy X-ray beam. Figure 4.10 shows a schematic layout of an operational beamline BL 29 XU of Spring-8, based on a crystal monochromator with X-ray optics, used for Hard X-ray (6–8 keV) Photoelectron Spectroscopy (HX-PES).²⁶ Several recent HX-PES studies have now established that photoelectron spectroscopy can indeed probe the bulk-sensitive electronic structure of solids in a reliable way.²⁶ The beamline X-ray optics is necessary for obtaining a controlled sub-micron size beam, which is focussed, collimated and delivers a high photon flux.

Typical applications of synchrotron radiation are:

- Diffraction, single crystalline and powder, of inorganic and organic materials, biomaterials (including proteins), etc.
- X-ray scattering: small angle, magnetic, inelastic, etc.
- Tomography and imaging
- Photolithography
- X-ray absorption and X-ray photoelectron spectroscopy

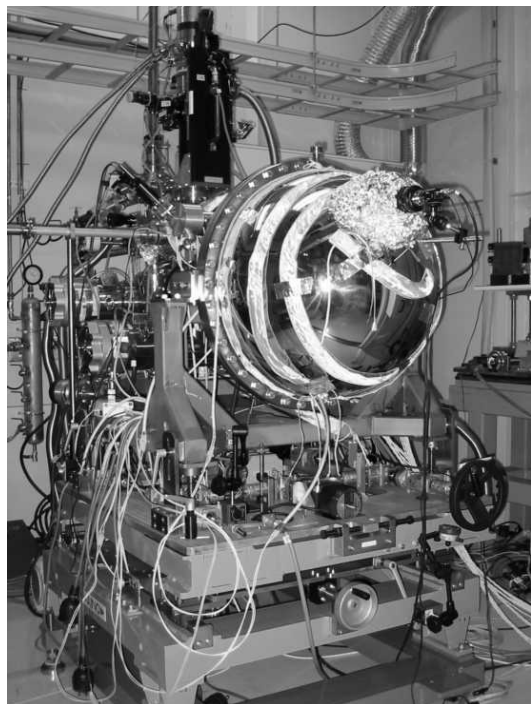
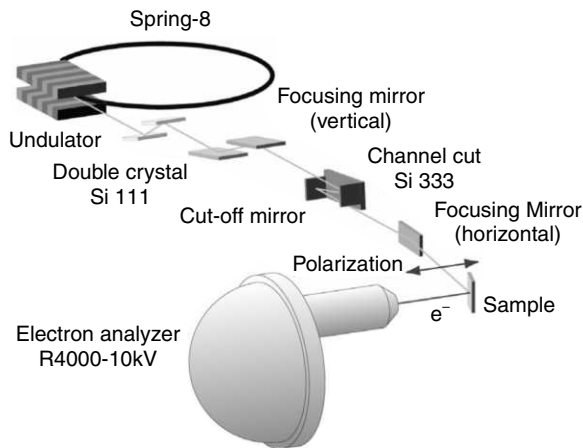


Fig. 4.10 *Synchrotron beamline schematic (above) and a photograph of the hard X-ray photoelectron spectrometer installed at the Beamline 29 XU (X-ray undulator) of SPring-8, the synchrotron centre in Hyogo, Japan.*

The ability of synchrotron radiation sources to provide highly focused, high photon fluxes over a wide energy range, which can be monochromatised to obtain a tunable photon source, plays a major role in present-day spectroscopy. During the last 10 years, since the advent of the third-generation synchrotron sources, typically, a 100- to 1000-times increase in photon flux, with an energy and spatial resolution better than laboratory sources has revolutionised spectroscopy, and also scattering, diffraction and imaging techniques. This is one of the reasons that it has become feasible to study nanomaterials. Since the decrease in size of the samples also means smaller number of atoms are available to obtain the same information, an increase in photon flux and smaller beam spot size of the probe become a necessary requirement of the experiments. Several synchrotron centres in the world have initiated developments of so-called “Nanoprobe stations”, fully devoted to the study of nanomaterials. The student is referred to a wide range of experiments^{27–35} that are already possible with available instrumentation at these synchrotrons, and these synchrotron centres invite proposals for experiments from a worldwide user community of scientists.

In the following, we discuss a few examples of synchrotron and laboratory-based spectroscopy of clusters, nanomaterials, quantum well structures, nanowires, etc.

4.8 METAL CLUSTERS AND NANOPARTICLES

The structure and properties of metal clusters and nanoparticles is a field of enduring study^{36–50} because of its importance in various device applications as well as fundamental scientific interest. The fundamental science stems from the fact that metal clusters have been proved to represent very good examples of quantum confined systems. The significant change in physical and chemical properties on reducing cluster size, as compared to bulk metal, is of direct interest in the field of catalysis, surface science, sensor technology, etc.^{38–50} The expectation of a critical cluster size, below which a metal becomes an insulator, has been borne out by a number of metals, such as Ag, Au, Pd, etc. Some of the metal clusters show coupled changes in its electrical and magnetic properties. The change in electronic properties on reducing cluster size of a metal, compared to the bulk, can be investigated by various techniques of electron spectroscopy, such as core-level PES, valence-band PES, XAS, etc. The foremost examples of changes in the electronic structure on reducing the size to the nanometer scale was the case of noble metal clusters. For clusters of Ag and Pd deposited on substrates such as amorphous graphite, it was observed that the binding energy of the core levels (Ag $3d_{5/2}$; Fig. 4.11a; Pd $3d_{5/2}$; Fig. 4.12a) increases on reducing cluster size for noble metals.^{38–42} The cluster size can be determined in terms of the nucleation site density and the coverage of metals deposited on the surface. From a combination of studies using UVPES and XPS as a function of size, it became known that Ag particles undergo a metal insulator transition^{38–39} at a critical cluster size diameter of 22\AA (2.2 nm, containing approximately 150 atoms and assuming a hemispherical shape). The bulk Ag metal valence band spectrum has a Fermi edge typical of a metal, which is also observed for large-size metal clusters. On reducing the

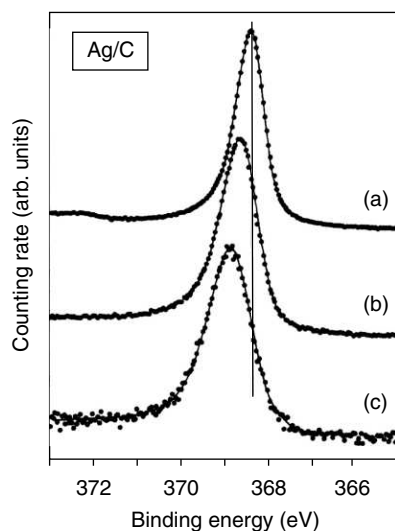


Fig. 4.11a X-ray photoelectron spectra of the Ag $3d_{5/2}$ core-level of (a) bulk Ag, and (b) and (c) clusters on sputtered carbon substrates. The coverages for (b) and (c) are 1.0×10^{15} and 2.5×10^{14} atoms/cm², respectively (reprinted figure with permission from Ref. 39. Copyright (1986) by the American Physical Society).

cluster size, the intensity at the Fermi edge gets suppressed (Fig. 4.11b), signalling a metal–insulator transition. Simultaneously, the core-level binding energy shifts to higher binding energy and the peak width becomes broader, compared to the spectrum of bulk Ag. The inverse PES (BIS) spectra⁴⁰ also confirmed that the data cannot be fully explained by final state effects alone. The results indicated coupled changes in the core levels, valence band and conduction band density of states on reducing the cluster size. For the case of Ag clusters, core-level PES studies also showed that the reactivity⁴¹ towards O₂ is strongly dependent on cluster size, with clear evidence of atomic O for cluster diameters in the range of 10–18 Å. Increasing the cluster size, results in a reduction of the reactivity, which becomes bulk-like and supports only molecular oxygen on its surface. This was correlated with the critical size for metal–insulator transition occurring at about 22 Å diameter size clusters.

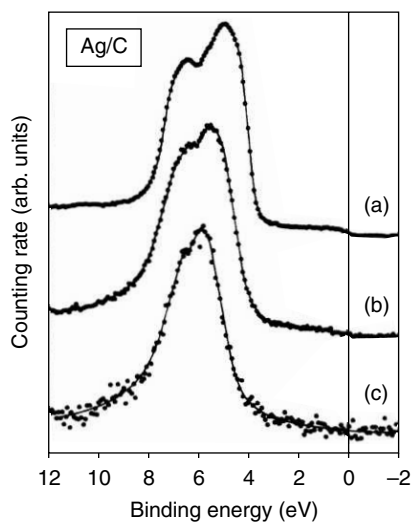


Fig. 4.11b X-ray photoelectron spectra of the valence-band of (a) bulk Ag, and (b) and (c) clusters on sputtered carbon substrates. The coverages for (b) and (c) are 1.0×10^{15} and 2.5×10^{14} atoms/cm², respectively (reprinted figure with permission from Ref. 39. Copyright (1986) by the American Physical Society).

Similar results for Pd clusters as a function of cluster size identified a metal-insulator transition using core-level (Fig. 4.12a), valence-band UVPES (Fig. 4.12b) and BIS experiments.^{39–40} In particular, the BIS spectra (Fig. 4.13a) showed that the Pd 4d character feature at and above the Fermi edge develops systematically on increasing cluster size.⁴⁰ From a difference spectra plot (Fig. 4.13b), the Pd 4d character states could be separated out from the substrate graphite character states. The difference spectra (Fig. 4.14) showed a clear shift of the Fermi edge in the unoccupied density of states. Several other studies on Pd clusters have also identified a transition to a ferromagnetic phase.^{42, 43} Palladium clusters are of significant technological importance as catalytic converters for combustion engines. They are also promising as materials for hydrogen storage, an issue of increasing interest linked to development of fuel-cell technologies.

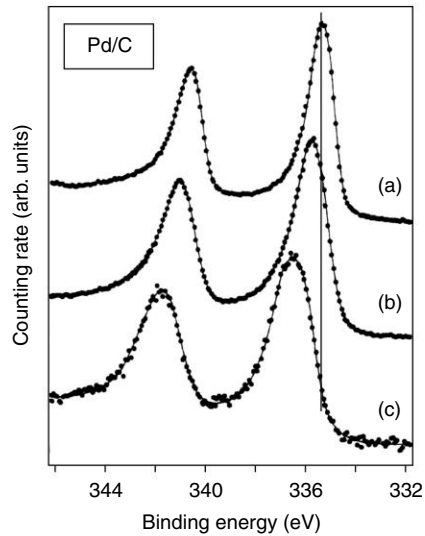


Fig. 4.12a X-ray photoelectron spectra of the Pd 3d core-levels of (a) bulk Pd, and (b) and (c) clusters on sputtered carbon substrates. The coverages for (b) and (c) are 2.0×10^{15} and 3.0×10^{14} atoms/cm², respectively (reprinted figure with permission from Ref. 39. Copyright (1986) by the American Physical Society).

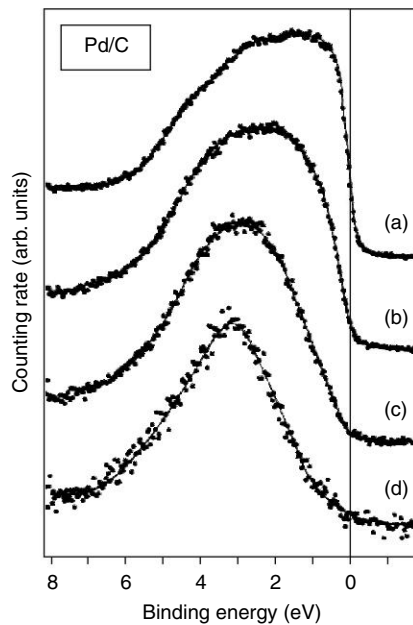


Fig. 4.12b X-ray photoelectron spectra of the valence-band of (a) bulk Pd and (b)–(d) of Pd clusters on sputtered carbon substrates. The coverages for (b), (c) and (d) are, respectively, 4.0×10^{15} , 1.0×10^{15} and 3.0×10^{14} atoms/cm² (reprinted figure with permission from Ref. 39. Copyright (1986) by the American Physical Society).

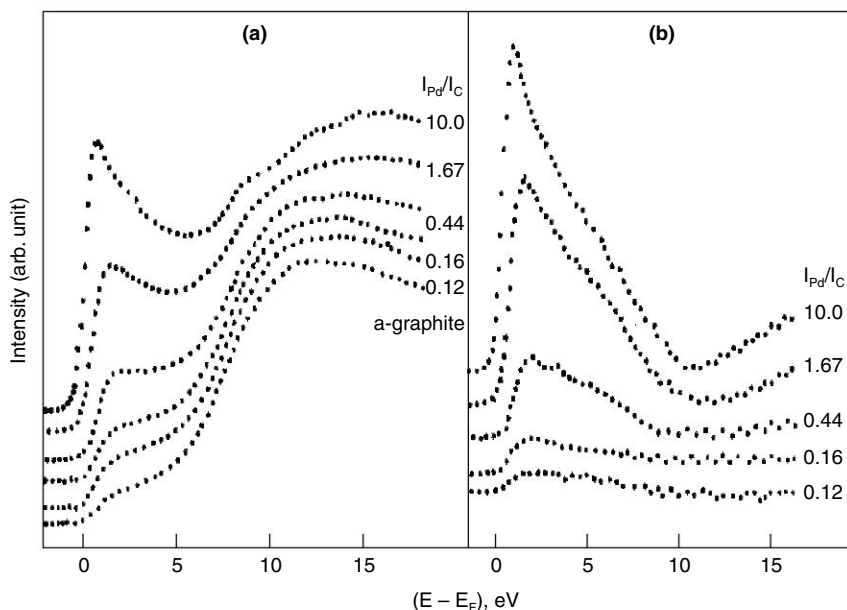


Fig. 4.13 (a) BI spectra of Pd clusters deposited on amorphous graphite at various coverages. (b) Difference BI spectra after subtraction of the substrate background (reprinted with permission from Ref. 40. Copyright (1992) American Chemical Society).

The most extensive studies have been carried out on gold clusters, for which the cluster sizes can be controlled with very high accuracy. Gold clusters can be synthesized by a variety of methods.^{36, 37, 44–50} Gold clusters consisting of a well-defined number of atoms have been synthesized, indicating the role of magic numbers of atoms for the high stability of clusters with a specific number of atoms, e.g., studies have reported clusters of 8 atoms, 55 atoms and 102 atoms, with exotic structural and electronic properties.^{44, 45} In particular, alkane-thiol monolayer protected gold and silver clusters have developed into a major field of research^{36, 37, 46–50} providing a very large number of applications such as quantum dots, self-assembled monolayers, three-dimensional quantum dot superlattice arrays, etc. Core-level (Fig. 4.15a, b) and valence-band (Fig. 4.15c) photoelectron spectroscopy studies on thiocapped gold nanoparticles have indicated the role of quantum size effects and surface effects as crucial to understand their electronic properties. The Au 4f core-level spectra showed a systematic shift to higher binding energy (Fig. 4.15a) and also a broadening (Fig. 4.15b), on reducing cluster size. A correlation of the electronic properties with structure was identified: the nanoparticles showed a lattice contraction relative to bulk gold⁴⁸ on reducing their size from 4.0 to 1.6 nm, together with changes in the core-level and valence-band spectra. The spectroscopy results were debated as due to purely final state effects as compared to a modification of initial-(or ground-) state properties which indicate changes in the density of states.⁴⁸ The similarity of results with Pd metal clusters,^{39, 40} such as a narrowing of the d-band in the occupied valence band and unoccupied conduction band density of states, together with an increase in binding energy of core levels, as well as ferromagnetic polarisation,^{42, 43, 49} favours a combination of initial and final state effects. The observations are suggestive of a metal-insulator transition in gold clusters.

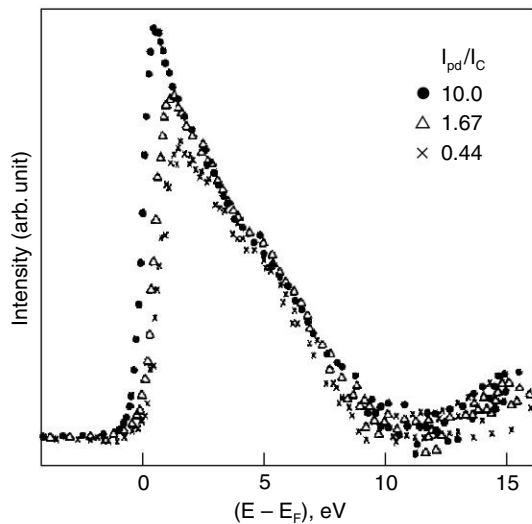


Fig. 4.14 Comparison of the difference BI spectra of Pd clusters on amorphous substrates for various coverages, showing a clear shift of the leading edge (reprinted (adapted) with permission from Ref. 40. Copyright (1992) American Chemical Society).

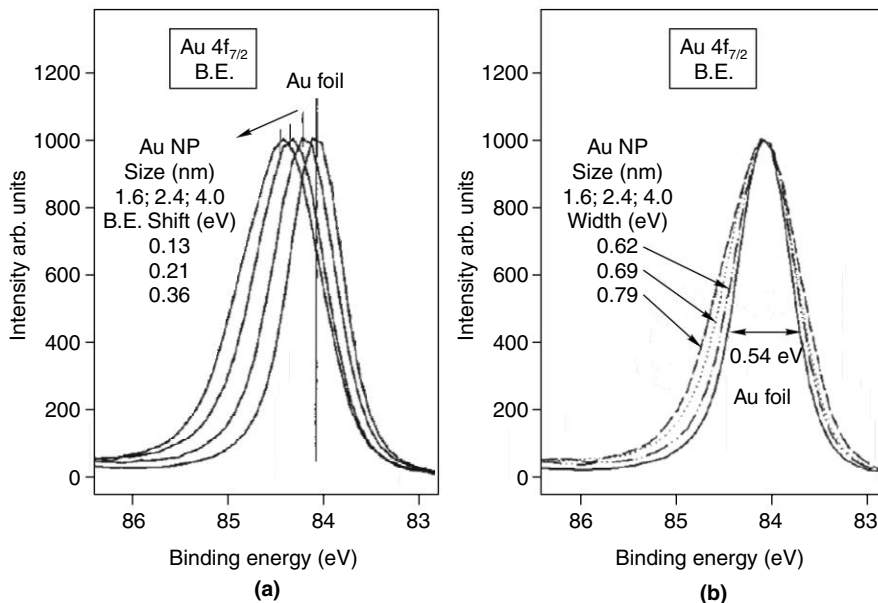


Fig. 4.15(a) and (b) Au $4f_{7/2}$ core-level photoelectron spectra showing (a) the increase in binding energy and (b) the broadening of the level, on reducing cluster size (reprinted figure with permission from Ref. 48. Copyright (2003) by the American Physical Society).

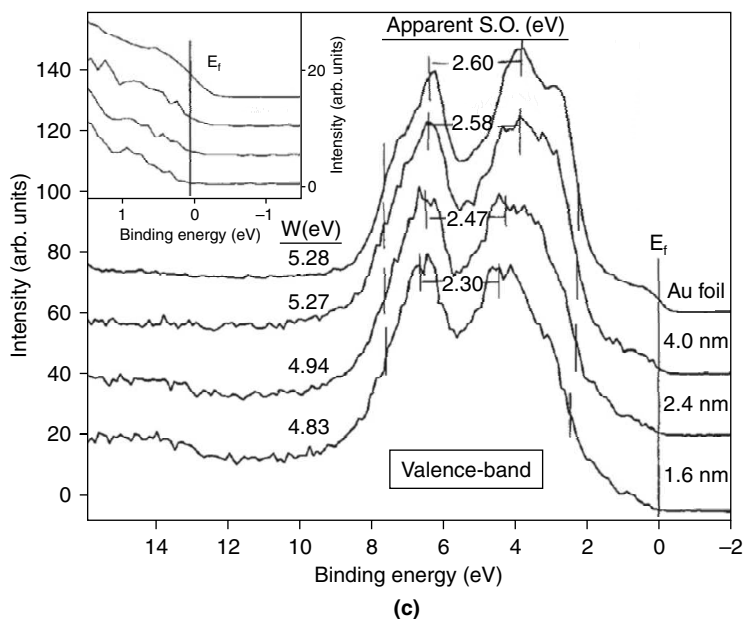


Fig. 4.15(c) Valence-band photoelectron spectra showing an apparent change in the spin-orbit split features in the Au 5d states. Inset shows an enlarged view of the Fermi level changes (reprinted figure with permission from Ref. 48. Copyright (2003) by the American Physical Society).

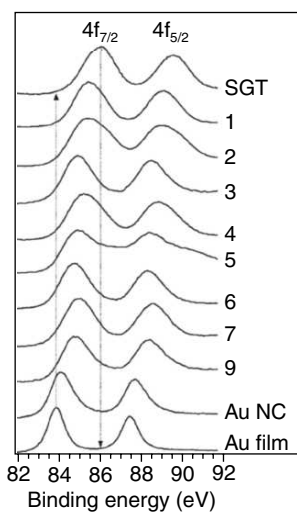


Fig. 4.16 Au 4f X-ray photoelectron spectra for $Au_m(SG)_n$ gold-glutathione samples (reprinted (adapted) with permission from, Ref. 50. Copyright (1992) American Chemical Society).

In a novel experiment⁵⁰ to bridge between gold nanocrystals with sizes of a few nanometers and gold clusters consisting of a few atoms, small gold clusters (~ 1 nm) protected by molecules of a tripeptide, glutathione (GSH) were synthesized by a low temperature process. Chemical compositions were characterised to be of the type $\text{Au}_m(\text{SG})_n$, where $m = 10, 15, 18, 22, 22, 25, 29, 33,$ and 39 and $n = 10, 13, 14, 16, 17, 18, 20, 22,$ and 24 , respectively, for the nine smallest clusters (labelled 1–9 in Fig. 4.16). The Au 4f core-level X-ray photoelectron spectra of these clusters showed a systematic increase in binding energy on reducing the number of gold atoms in the clusters, indicating substantial electron donation from the gold cores to the GSH ligands. These results identified a distinct class of gold clusters between Au-thiolate complexes and thiolate protected gold nanocrystals.⁵⁰

4.9 SEMICONDUCTOR/INSULATOR NANOCRYSTALS

Semiconducting or insulating nanocrystals play a major role in a wide variety of applications such as catalysis, luminescent materials, dilute magnetic semiconductors, photovoltaics and photoelectrochemical cells, etc. Recent studies have shown fascinating examples:

(a) CeO_x and TiO_x nanoparticles: It was shown that the chemical activity of CeO_x and TiO_x nanoparticles grown on gold substrates Au(111) can play an important role in the water-gas shift (WGS) reaction,⁵¹ which is given by $\text{CO} + \text{H}_2\text{O} \rightarrow \text{CO}_2 + \text{H}_2$. The WGS reaction is considered to be a critical reaction to obtain clean hydrogen for fuel cells and industrial applications. While clean gold substrates are not catalytically active for the WGS reaction, if the gold surfaces are covered by titania or ceria nanoparticles, they can achieve chemical activities comparable to good WGS catalysts such as Cu(111) or Cu(100) surfaces. Specifically, it was shown that water dissociates on oxygen vacancies of the oxide nanoparticles while CO adsorbs on nearby Au sites, and this dual condition facilitates the WGS reaction at the metal-oxide interface. The oxygen vacancies are observed as Ce^{3+} in CeO_x (or Ti^{3+} in TiO_x) on Au(111) substrate, and this could be measured by comparing Ce 3d core-level spectra of the sample with formally trivalent Ce_2O_3 spectra, using X-ray photoelectron spectroscopy.

In an earlier experiment with effectively reversed geometry compared to the above-discussed experiment, using Au_8 clusters on MgO substrates,⁵² it was shown that oxygen vacancy F-centres were crucial for the low-temperature oxidation of CO to CO_2 . In contrast, if the Au_8 clusters are deposited on close to perfect magnesia (MgO), i.e., in the absence of the oxygen vacancy F-centres, the Au_8 clusters remain chemically inert and the oxidation reaction of CO to CO_2 gets suppressed.

(b) Photovoltaics and photoelectrochemical cells: While early photovoltaics (devices for converting sunlight into electricity) were solid-state devices, recent studies have led to the development of a new generation of photovoltaics based on nanomaterials and polymers.⁵³ The so-called dye-sensitised nano- TiO_2 is a prime example.

These devices can have high efficiencies and are also cheap and flexible, and are thus considered important for future device applications. An important issue in this device is that the time required

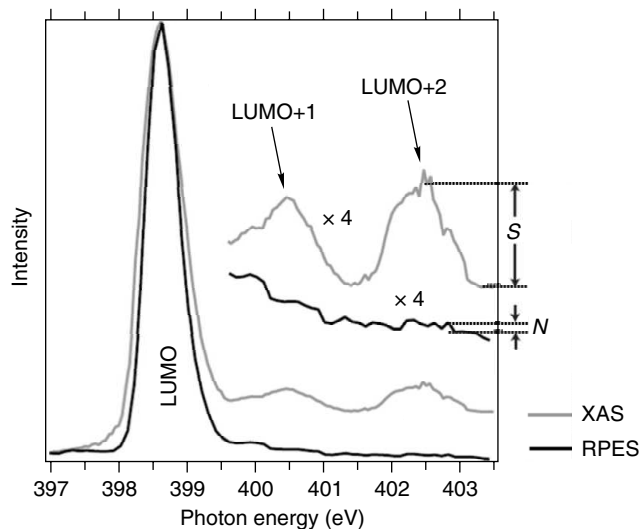


Fig. 4.17 Comparison of RPES and XAS for a bi-isonicotinic acid monolayer. Excitation to the LUMO leads to a large intensity in the RPES owing to strong resonant photoemission, indicating localisation of the excited electron on the molecule. For excitation to LUMO+1 and LUMO+2 no RPES-intensity is observed, which implies rapid excited electron delocalisation. For the LUMO+1 and LUMO+2, we estimated the maximum possible RPES signal consistent with the noise level N , and compared it to the XAS signal S , determining the upper limits in the text. The XAS has a 12:1 signal-to-noise ratio at the LUMO+2 (adapted from, Macmillan Publishers Ltd: Nature (Ref. 54), copyright (2002)).

to inject an electron from the dye into the semiconductor should be very small. Using a combination of resonant photoemission and X-ray absorption spectroscopy (Fig. 4.17) to measure the occupied and unoccupied density of states, it was shown that the time required to transfer an electron from an aromatic adsorbate (bi-isonicotinic acid) to the TiO_2 can occur in less than 3 femtoseconds.⁵⁴ This time scale is faster than other loss processes in the system, thus explaining the origin of the high efficiencies of the dye-sensitised nano- TiO_2 based photovoltaics.

(c) Nano sulphides and selenides: Nanocrystalline sulphides and selenides are providing a growing list of applications in terms of their optical properties. In a synchrotron-based core-level photoelectron spectroscopy study of PbSe nanocrystals, it was shown that the photon-energy dependence of surface sensitivity can be exploited for revealing the internal chemical structure of nanocrystals.⁵⁵ It was possible to make a careful determination of the diameters of the crystalline stoichiometric PbSe core, the non-stoichiometric Pb_{1-x}Se shell surrounding the core, and also the outermost capping layer. The study suggested that the reduction in fluorescence quantum efficiency is related to the thickness of the non-stoichiometric Pb_{1-x}Se layer. A more recent study showed the emission of white light from Mn^{2+} -doped CdS nanocrystals of average size 1.8 and 2.1 nm, grown by a size selective precipitation

method.⁵⁶ Optical non-linearity with a giant increase in the two-photon absorption coefficient was reported for capped nanocrystalline ZnS.⁵⁷

4.10 QUANTUM WELL STATES

The direct observation of quantum size effects in the electronic structure of metal overlayers was first reported in Ag films grown on Si(111) using ARPES.⁵⁸ The ARPES spectra of the Ag films (0–17 monolayers) showed quasiperiodic peaks with a separation between the peaks, which was inversely proportional to the film thickness. A similar behaviour was also observed for Na and Ba films on the Cu(111) surface which could be analysed as originating from electrons trapped in a potential well between the vacuum barrier and the Cu(111) surface.⁵⁹ In spite of copper being a metal, the Cu(111) surface has high reflectivity for electrons, with energies within an effective band gap in the measured band dispersions. A very interesting observation (Fig. 4.18) describing the important role of the substrate band dispersion in forming quantum well states was found for Ag on Au(111) system, which shows quantum well states, but the complementary system, Au on Ag(111), does not show quantum well states.⁶⁰ A recent study of Ag/Ni(111) has shown that the quantum well states can be used to probe the ground-state electronic structure of the substrate nickel, a strongly correlated metal.⁶¹ An early study (Fig. 4.19) on Ag deposited on GaAs(110) surface by low-temperature deposition (100 K) and annealing to room temperature showed quantum size effects: wave vector quantisation due to electron confinement.⁶² The ARPES spectra measured using synchrotron radiation could be

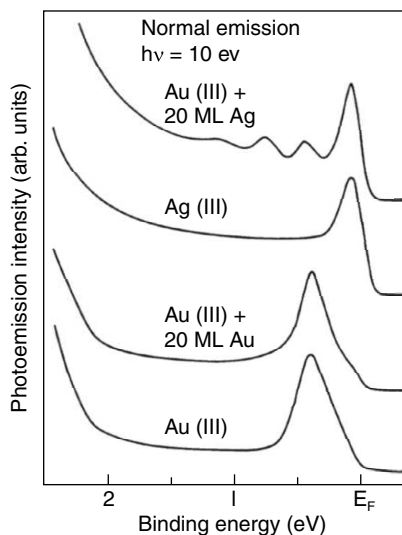


Fig. 4.18 Normal emission ARPES spectra taken with a photon energy $h\nu = 10$ eV for, from bottom to top, Au(111), Ag(111) covered by 20 ML of Au, Ag(111), and Au(111) covered by 20 ML of Ag. The binding energy scale is referred to the Fermi level (reprinted figure with permission from Ref. 60. Copyright(1988) by the American Physical Society).

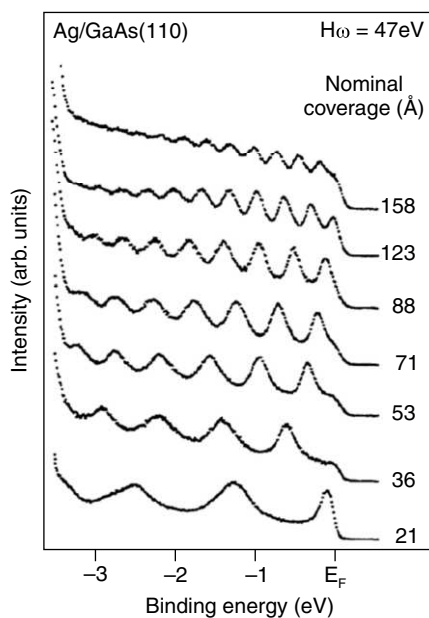


Fig. 4.19 Valence photoelectron spectra of seven Ag layers of different thicknesses as indicated, prepared by deposition at 100 K and subsequent annealing to room temperature. Spectra were recorded at 25° polar angle with respect to the surface normal along the [011] azimuth of the GaAs(110) surface (reprinted figure with permission from Ref. 62. Copyright (1993) by the American Physical Society).

well-described based on a quantum well analysis corresponding to a one-dimensional quantum well structure with hard walls and a well-width w . The energy of the n th quantised state depends on the width w as follows:

$$E_n = (\hbar^2/2m) (n\pi/w)^2 \quad (8)$$

with $\hbar = h/2\pi$, where h is the Planck's constant and m is mass of the electron. The study showed a successful analysis of quantum size effects in Ag metal deposited on GaAs. Another very interesting study showed that quantum well states can act as mediators of magnetic coupling in superlattices.⁶³ It was shown (Fig. 4.20) that Cu layers on Co(111) exhibit quantum well states for every 5.9 \pm 0.5 layers in good agreement with 5.5–6.0 layer oscillation period of the magnetic coupling in Cu/Co(111) superlattices. For Ag/Fe(100), the quantum well states connect the minority spin interface states, thus providing a magnetic coupling channel through the noble metal.⁶³ The observation of quantum well states is also observed for Pb and Pb-In films on Si(111) surfaces,⁶⁴ in the thickness range of 0–30 monolayers. A recent study⁶⁵ showed that the quantum well states in Pb modulate the superconductivity of Pb. The study reported an oscillation of the superconducting transition temperature in Pb via a modulation of the electron density of states at the Fermi level and the electron phonon coupling. This result suggests the possibility of modifying superconductivity and other properties of thin films by quantum-size effects.

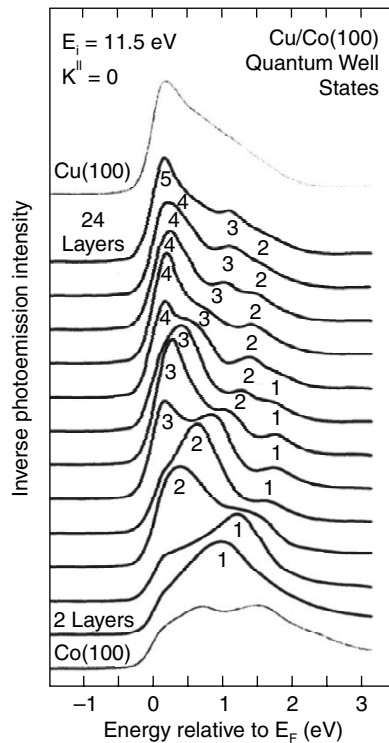


Fig. 4.20 Inverse photoelectron spectra for Cu on Co(100) at normal incidence. The *s*, *p* band continuum of bulk Cu(100)(top) is discretised into quantum well states for thin Cu films (reprinted figure with permission from Ref. 63. Copyright(1992) by the American Physical Society).

4.11 NANOWIRES

Crystalline semiconductor nanowires are one-dimensional structures of nanometer-scale diameter and are expected to play a major role as interconnects in nanoelectronic devices and as nanoscopic probe tips. The formation of silicon and germanium nanowires covered by an amorphous oxide coating, can be achieved by a laser ablation method,⁶⁶ with diameters of 6–20 and 3–9 nm, respectively, and lengths ranging from 1 to 30 micrometers. A recent photoelectron and XAS study shows that the silicon nanowire has an essentially crystalline silicon electronic structure.⁶⁷ Indeed, the recent report of coaxial silicon nanowires as solar cells, in the form of a co-axial p-type/intrinsic/n-type (p-i-n) structure has opened a new field of nanoelectronic power sources. This state-of-the-art experiment⁶⁸ further showed that individual and interconnected silicon nanowire photovoltaic cells can provide power for functional nanoelectronic sensors and logic gates.

A variety of one-dimensional chain structures have been fabricated on single crystal metal and semiconductor surfaces providing a growing list of new phenomena.

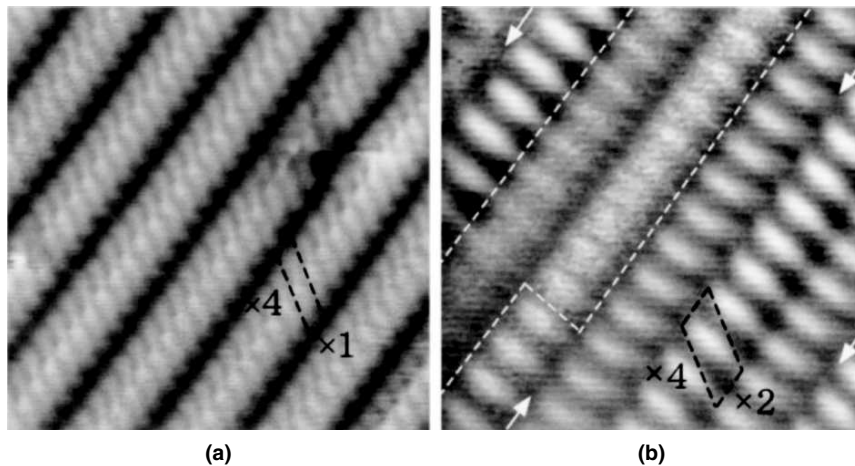


Fig. 4.21 Scanning tunneling microscopy images of (a) the room-temperature 4×1 phase and (b) the low-temperature (~ 65 K) 4×2 phase were taken at the same sample bias voltage of -1 V (filled state) in the constant-height mode. The 4×1 and 4×2 unit cells are indicated by black dashed lines. The area of the characteristic fluctuating-charge density region (white dashed lines) and the phase mismatching between the neighbouring chains (arrows) are observed (reprinted figure with permission from Ref. 69. Copyright(1999) by the American Physical Society).

Self-assembled indium chains observed by scanning tunneling microscopy on Si(111) surface (Fig. 4.21) exhibit a room temperature metal phase, which transforms into a charge density wave semiconductor at low temperature.⁶⁹ ARPES studies showed (Fig. 4.22), that the dispersive bands crossing the Fermi level undergo a gap formation at momentum values matching the periodicity of the CDW vector.⁶⁹ For the case of gold chains grown on vicinal Si(111) surfaces, the uncertainty regarding a doublet of dispersive bands could be resolved recently.⁷⁰ The doublet bands originate in spin splitting induced by spin-orbit coupling and lead to a characteristic pattern of avoided band crossings at a superlattice-zone boundary in momentum space, as was identified by ARPES experiments. In a novel experiment on Co chains, it was shown that Co chains grown on a Pt(111) surface exhibit ferromagnetic behaviour,⁷¹ which is considered to be theoretically forbidden for an infinite one-dimensional linear chain with short-range magnetic interactions. Co chains were studied using X-ray magnetic circular dichroism (MCD), measured at the Co $L_{2,3}$ edges, i.e., at the 2p-3d transition (Figure 4.23). X-ray MCD is proportional to the difference in XAS intensity obtained using right and left circularly polarised X-rays. The largest MCD signal was obtained for the Co chains and the MCD signal reduced for a monolayer film of Co, while the bulk Co showed the weakest MCD signal. These results motivated further studies on Co atoms and Co nanoclusters.⁷² Single Co atoms and Co nanoclusters deposited on Pt(111) surface were also studied using X-ray MCD at the Co $L_{2,3}$ edges. It was shown that the isotropic magnetic moment of a free atom can develop a giant magnetic anisotropy due to symmetry reduction at an atomically ordered surface. The X-ray MCD showed that the largest MCD signal occurs

for Co atoms and it gets reduced systematically on increasing the average cluster size, finally becoming close to that of bulk Co metal for a cluster containing about 40 Co atoms.⁷²

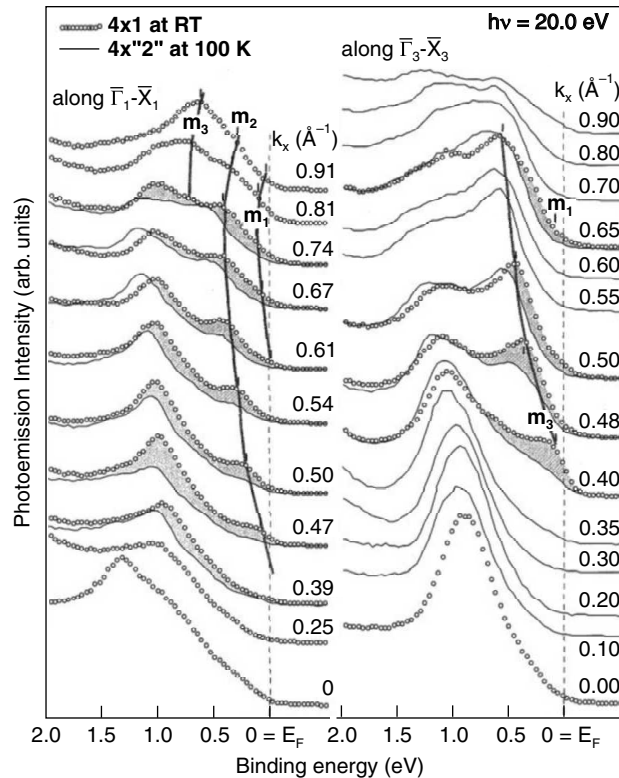


Fig. 4.22 Angle-resolved photoemission spectra for the room temperature 4×1 phase (open circles) and the low-temperature (~ 100 K) 4×2 phase (solid lines). The spectra are taken along the linear chain direction, that is along $\Gamma - X$ in the first (left) and the third (right) surface Brillouin zone (Γ at $k_x = 0 \text{ \AA}^{-1}$ and X at $k_x = 0.82 \text{ \AA}^{-1}$). At ~ 100 K, the reduction of spectral weights of the metallic states near Fermi level is evident as indicated by the hatching (reprinted figure with permission from Ref. 69. Copyright(1999) by the American Physical Society).

Such phenomena are systematically confirming the modifications of bulk phenomena when confined to low dimensions. These are some of the surprises and one expects many more intriguing results in nanomaterials. Understanding of such observations is a necessary step for definitive control of nanoscale properties and will provide the basis for the next generation of nano devices.

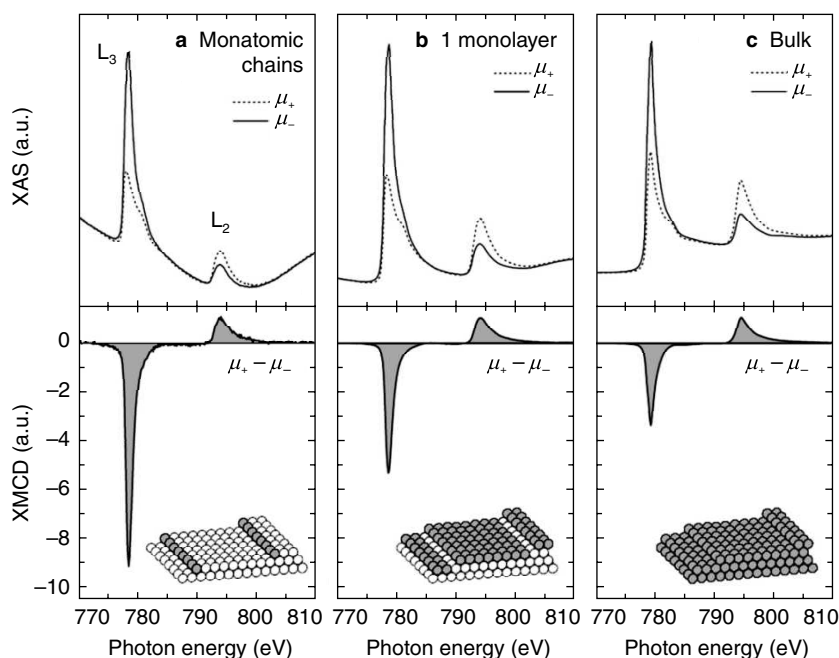


Fig. 4.23 Co X-ray absorption spectra for parallel (μ_+) and antiparallel (μ_-) direction of light polarisation and field-induced magnetisation. The dichroism signals ($\mu_+ - \mu_-$) is obtained by subtraction of the absorption spectra in each panel and normalization to the L_2 peak. a, Monatomic chains; b, one monolayer; c, thick Co film on Pt(997). Changes in the L_3 XMCD intensity indicate that the orbital moment is substantially increased in going from bulk Co to a 2D Co monolayer and, finally, to the 1D chains (reprinted figure with permission from Macmillan Publishers Ltd : Nature (Ref. 71), copyright (2002)).

REFERENCES

1. S. Hüfner, *Photoelectron Spectroscopy: Principles and Applications*, 3rd edn, Springer-Verlag, Berlin, Heidelberg, (2003).
2. H. Hertz, *Ann. Physik* 31, 983 (1887).
3. A. Einstein, *Ann. Physik* 17, 132 (1905).
4. K. Siegbahn, C. Nordling, R. Fahlman, R. Nordberg, K. Hamrin, J. Hedman, G. Johansson, T. Bergmark, S.-E. Karlsson, I. Lindgren, B. Lindberg: 'ESCA-Atomic, Molecular and Solid State Structure Studied by Means of Electron Spectroscopy', *Nova Acta Regiae Soc. Sci., Upsaliensis, Ser. IV, Vol. 20* (1967).
5. D. Briggs and M.P. Seah, *Practical Surface Analysis by Auger and X-ray Photoelectron Spectroscopy*, John Wiley & Sons, New Jersey (1983).
6. H. Ibach, *Electron Spectroscopy for Surface Analysis, Topics in Current Physics, Vol. 4*, Springer, Berlin, Heidelberg (1977).

7. S. Tanuma, C.J. Powell and D.R. Penn, *J. Vac. Sci. Techn.* A 8, 2213 (1990).
8. National Institute of Standards and Technology (NIST) Photoelectron Spectroscopy Database, <http://srdata.nist.gov/xps/>.
9. A. Beiser, *Concepts of Modern Physics*, 6th edn, McGraw-Hill Science, New York (2002).
10. V. Dose, *Appl. Phys.* 14, 117 (1977); M. Donath, *Surf. Sci. Rep.* 20, 251 (1994).
11. F. De Groot, *Chem. Rev.* 101, 1779–1808, (2001).
12. J.W. Allen, in *Synchrotron Radiation Research: Advances in Surface and Interface Science*, edited by R.Z. Bachrach, Plenum, New York, (1992), 253–323.
13. J.J. Yeh and I. Lindau, *At. Data Nucl. Data Tables* 32, 1, (1985).
14. G. Hollinger and F.J. Himpsel, *Appl. Phys. Lett.* 44, 93, (1984); M. Shioji, T. Shiraishi, K. Takahashi, H. Nohira, K. Azuma, Y. Nakata, Y. Takata, S. Shin, K. Kobayashi, and T. Hattori, *Appl. Phys. Lett.* 84, 3756, (2004).
15. S. Doniach and M. Šunjić, *J. Phys. C*, 3, 285, (1970).
16. T. Kiss, T. Shimojima, K. Ishizaka, A. Chainani, T. Togashi, T. Kanai, X.-Y. Wang, C.-T. Chen, S. Watanabe and S. Shin, *Rev. Sci. Instruments.* 79, 023106, (2008).
17. A. Chainani, T. Yokoya, T. Kiss and S. Shin, *Phys. Rev. Lett.* 85, 1966, (2000).
18. F. Reinert, G. Nicolay, B. Eltner, D. Ehm, S. Schmidt, S. Hüfner, U. Probst, and E. Bucher, *Phys. Rev. Lett.* 85, 3930, (2000); F. Reinert, B. Eltner, G. Nicolay, D. Ehm, S. Schmidt, and S. Hüfner, *Phys. Rev. Lett.* 91, 186406, (2003).
19. T. Yokoya, A. Chainani and S. Shin, in *Very High Resolution Photoelectron Spectroscopy* (Ed. S. Hüfner), 187, Springer, Berlin, Heidelberg (2006).
20. A. Damascelli, Z.-X. Shen, and Z. Hussain, *Rev. Mod. Phys.* 75, 473, (2003).
21. R.C. Dynes, V. Narayanamurti, and J.P. Garno, *Phys. Rev. Lett.* 41, 1509, (1965).
22. E.W. Plummer and W. Eberhardt, *Adv. Chem. Phys.* 49, 533, (1982).
23. T. Kiss, T. Yokoya, A. Chainani, S. Shin, T. Hanaguri, M. Nohara and S. Shin, *Nature Physics* 3, 720, (2007).
24. U. Fano, *Phys. Rev.* 124, 1866, (1961).
25. *Handbook on Synchrotron Radiation*, Vol. 1a, Ed. Ernst-Eckhard Koch, North Holland, 1983.
26. Y. Takata, in *Very High Resolution Photoelectron Spectroscopy*, Ed. S. Hüfner, 373, Springer, Berlin, Heidelberg (2006); and references therein.
27. N. Takezoe, H. Yanagida, T. Tanaka, K. Kurosawa, Y. Nonogaki, H. Noda, H. Mekaruru and T. Urisu, *Nucl. Inst. Meth. Phys. Res A* 467–68, 1279–81, (2001).
28. H. Stoll, A. Puzic, B. van Waeyenberge, P. Fischer, J. Raabe, M. Buess, T. Haug, R. Hollinger, C. Back, D. Weiss and G. Denbeaux, *Appl. Phys. Lett.* 84, 3328, (2004).
29. E. Di Fabrizio, R. Fillipo, S. Cabrini, R. Kumar, F. Perennes, M. Altissimo, L. Businaro, D. Cojac, L. Vaccari, M. Prasciolu and P. Candeloro, *J. Phys.: Condens. Matter* 16, S3517–35, (2004).
30. F. Adams, L. Van Vaeck and R. Barrett, *Spectrochimica Acta Part B: Atomic Spectroscopy* 60, 13–26, (2005).

31. S. Schmidt, N. Weber, H.-J. Elmers, F. Forster, F. Reinert, S. Hüfner, M. Escher, M. Merkel, B. Krömker, and D. Funnemann, *Phys. Rev. B* 72, 064429, (2005).
32. J.A. Ablett, *Nucl. Inst. Meth. Phys. Res B* 241, 238–241, (2005).
33. C. Balasubramanian, S. Bellucci, G. Cinque, A. Marcelli, M. Cestelli Guidi, M. Piccinini, A. Popov, A. Soldatov and P. Onorato, *J. Phys.: Condens. Matter*, (2006), S2095–S2104.
34. A. Saito, K. Takahashi, Y. Takagi, K. Nakamatsu, K. Hanai, Y. Tanaka, D. Miwa, M. Akai-Kasaya, S. Shin, S. Matsui, T. Ishikawa, Y. Kuwahara and M. Aono, *Surface Science* 601, (2007), 5294–99.
35. H.H. Solak, *J. Phys. D-Applied Phys.* 39, (2006), R171–R188.
36. *Nanomaterials Handbook* (ed) Y. Gogotsi, CRC Press, Boca Raton Florida (2006).
37. M.-C. Daniel and D. Astruc, *Chem. Rev.*, 104, (2004), 293.
38. G. Apai, S.T. Lee and M.G. Mason, *Solid State Commun.* 37, (1981), 213–17.
39. G.K. Wertheim, S.B. DiCenzo, and D.N.E. Buchanan, *Phys. Rev. B* 33, (1986), 5384–90.
40. V. Vijaykrishnan, A. Chainani, D.D. Sarma and C.N.R. Rao, *J. Phys. Chem.* 96, (1992), 8679–82.
41. C.N.R. Rao, V. Vijaykrishnan, A.K. Santra and M.W.J. Prins, *Angewandte Chemie Int. Ed. Engl.* 31, (1992), 1062.
42. T. Shinohara, T. Sato, and T. Taniyama, *Phys. Rev. Lett.* 91, 197201 (2003); Y. Oba, T. Sato and T. Shinohara, e-Jl., *Surf. Sci. Nanotech.* 4, (2006), 439–42.
43. B. Sampedro and A. Hernando, *Phys. Stat. Sol.* 1, (2004), 3670–72.
44. H.-G. Boyen, G. Kästle, F. Weigl, P. Ziemann, G. Schmid, M.G. Garnier and P. Oelhafen, *Phys. Rev. Lett.* 87, (2001), 276401.
45. Pablo D. Jadzinsky, Guillermo Calero, Christopher J. Ackerson, David A. Bushnell, Roger D. Kornberg, *Science* 318, (2007), 430.
46. N. Sandhyarani, M.P. Antony, G.P. Selvam and T. Pradeep, *J. Chem. Phys.* 113, (2000), 9794.
47. T. Pradeep, S. Mitra, A.S. Nair and R. Mukhopadhyay, *J. Phys. Chem. B* 108, (2004), 7012–20.
48. P. Zhang and T.K. Sham, *Phys. Rev. Lett.* 90, (2003), 245502; 92, (2004), 109602; P. Moriarity, *Phys. Rev. Lett.* 92, (2004), 109601.
49. Y. Yamamoto, T. Miura, M. Suzuki, N. Kawamura, H. Miyagawa, T. Nakamura, K. Kobayashi, T. Teranishi, and H. Hori, *Phys. Rev. Lett.* 93, (2004), 116801.
50. Y. Negishi, K. Nobusada and T. Tsukuda, Jr., *Am. Chem. Soc.* 127, (2005), 5261.
51. J.A. Rodriguez, S. Ma, O. Liu, J. Hrbek, J. Evans and M. Perez, *Science* 318, (2007), 1757.
52. B. Yoon, H. Hakkinen, U. Landman, A.S. Worz, J.-M. Antonietti, S. Abbet and U. Heiz, *Science* 307, (2005), 403.
53. M. Grätzel, *Nature* 414, (2001), 338.
54. J. Schnadt, P.A. Bruhwiler, L. Patthey, J.N. O’Shea, S. Sodergren, M. Odelius, R. Ahuja, O. Karis, M. Bassler, P. Persson, H. Siegbahn and N. Mårtensson, *Nature*, 418, (2002), 620.
55. S. Sapra, J. Nanda, J.M. Pietryga, J.A. Hollingsworth and D.D. Sarma, *J. Phys. Chem B* 110, (2006), 15244.
56. A. Nag and D.D. Sarma, *J. Phys. Chem. C (Lett.)* 111, (2007), 13641.

57. V.V. Nikesh, A. Dharmadhikari, H. Ono, S. Nozaki, G. Ravindra Kumar and S. Mahamuni, *Appl. Phys. Lett.* 84, (2004), 4602.
58. A.L. Wachs, A.P. Shapiro, T.C. Hsieh and T.C. Chiang, *Phys. Rev. B* 33, (1986), 1460.
59. S.Å. Lindgren and L. Walldén, *Phys. Rev. Lett.* 59, (1987), 3003.
60. T. Miller, A. Samsavar, G.E. Franklin and T.C. Chiang, *Phys. Rev. Lett.* 61, (1988), 1404.
61. A. Varykhalov, A.M. Shikin, W. Gudat, P. Moras, C. Grazioli, C. Carbone, and O. Rader, *Phys. Rev. Lett.* 95, (2005), 247601.
62. D.A. Evans, M. Alonso, R. Cimino, and K. Horn, *Phys. Rev. Lett.* 70, (1993), 3483.
63. J.E. Ortega and F.J. Himpsel, *Phys. Rev. Lett.* 69, (1992), 844.
64. M. Jalochowski, H. Knoppe, G. Lilienkamp and E. Bauer, *Phys. Rev. B* 46, (1992), 4693.
65. Y. Guo, Y.-F. Zhang, X.-Y. Bao, T.-Z. Han, Z. Tang, L.-X. Zhang, W.-G. Zhu, E.G. Wang, Q. Niu, Z.Q. Qiu, J.-F. Jia, Z.-X. Zhao and Q.-K. Xue, *Science* 306, (2004), 1915.
66. A.M. Morales and C.M. Lieber, *Science* 279, (1998), 208–11.
67. Y.F. Zhang, L.S. Liao, W.H. Chan, S.T. Lee, R. Sammynaiken and T.K. Sham, *Phys. Rev. B* 61, (2000), 8298.
68. B. Tian, X. Zheng, T.J. Kempa, Y. Fang, N. Yu, G. Yu, J. Huang and C.M. Lieber, *Nature* 449, (2007), 885.
69. H.W. Yeom, S. Takeda, E. Rotenberg, I. Matsuda, K. Horikoshi, J. Schaefer, C.M. Lee, S.D. Kevan, T. Ohta, T. Nagao, and S. Hasegawa, *Phys. Rev. Lett.* 82, (1999), 4898.
70. I. Barke, Fan Zheng, T.K. Rügheimer, and F.J. Himpsel, *Phys. Rev. Lett.* 97, (2006), 226405.
71. P. Gambardella, A. Dallmeyer, K. Maiti, M.C. Malagoli, W. Eberhardt, K. Kern, C. Carbone, *Nature* 416, (2002), 301–04.
72. P. Gambardella, S. Rusponi, M. Veronese, S.S. Dhesi, C. Grazioli, A. Dallmeyer, I. Cabria, R. Zeller, P.H. Dederichs, K. Kern, C. Carbone, H. Brune, *Science* 300, (2003), 1130.

ADDITIONAL READING

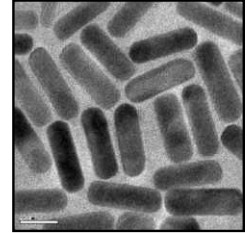
1. ‘Metal-Insulator Transitions’, M. Imada, A. Fujimori and Y. Tokura, *Rev. Mod. Phys.* 70, (1998), 1039.
2. ‘One-dimensional Electronic States at Surfaces’, F.J. Himpsel, K.N. Altman, R. Bennewitz, J.N. Crain, A. Kirakosian, J.-L. Lin and J.L. McChesney, *J. Phys.: Cond. Matter* 13, (2001), 11097.
3. Proceedings of the Workshop on Hard X-ray Photoelectron Spectroscopy, Eds. J. Zegenhagen and C. Kunz, *Nucl. Instrum. Methods. A* 547, (2005).
4. *Very High Resolution Photoelectron Spectroscopy*, Ed. S. Hüfner, Springer, Berlin, Heidelberg (2006).

REVIEW QUESTIONS

1. Cesium has a work function of 2.1 eV. If the incident photon energy is violet colour (wavelength $\nu = 445 \text{ nm}$), can it be used to emit a photoelectron from the valence band of Cesium? If yes, what is the highest kinetic energy of photoelectrons emitted from cesium using violet light? If the incident photon energy is red light (wavelength $\nu = 650 \text{ nm}$), can it be used to emit a photoelectron from the valence-band of cesium? (the velocity of light $c = \nu\lambda = 2.997925 \times 10^8 \text{ m/sec}$)

2. The work function of tungsten is 4.5 eV. For an incident photon energy of Mg $K\alpha = 1253.6$ eV, what is the highest kinetic energy of a photoelectron emitted from tungsten? Calculate its velocity. If the incident photon energy is changed to He I energy (21.2 eV), what is the highest velocity of the photoelectron emitted from tungsten?
(electron mass $m = 9.1095 \times 10^{-31}$ kg)
3. The Fermi-Dirac function at $T = 0$ is a step function. At a finite temperature, it is broadened by temperature and at a given temperature T , it is given by $FD(\epsilon) = 1/[\exp(\mu - \epsilon/k_B T) + 1]$, where $\mu = E_F$ is the chemical potential or Fermi level for a metal. Plot the Fermi-Dirac function at 10, 50, 100, 273, 300 and 400 K, on a computer, for $\epsilon = (\mu - 0.25 \text{ to } +0.25 \text{ eV})$. Determine the width in meV, as 13–87% of the Fermi-Dirac function at each temperature.
4. The inelastic mean free path of electrons in a solid determines the surface sensitivity of the photoelectron spectra, and depends on the kinetic energy of the electrons. For an electron with an inelastic mean free path λ of 30 \AA , calculate the fraction of photoelectrons which get inelastically scattered if they are emitted at a depth of 50 \AA from the surface. What is the fraction scattered inelastically, if the depth is 250 \AA ?
5. At normal emission, if the IMFP of electrons is 20 \AA , calculate the mean escape depth probed at an emission angle of (a) 30° and (b) 60° .
6. For an equiatomic alloy TiNi, if the sensitivity factors S_i for Ti 2p and Ni 2p core levels are in the ratio 1 : 5, what will be the measured relative intensities for the Ti 2p and Ni 2p core levels of TiNi?
7. For a BCS superconductor with a superconducting transition $T_c = 30$ K, what will be the value of the superconducting gap Δ_0 at $T = 0$ K, in meV?
8. Consider a strong coupling superconductor with a transition temperature of $T_c = 7.2$ K and a reduced gap value $2\Delta_0/k_B T_c = 4.5$. What is its superconducting gap value in eV?
9. Given a one-dimensional quantum well structure with hard walls and a well-width w of 100 \AA , calculate the lowest 5 quantised energy levels.
10. For a one-dimensional quantum well structure with hard walls and a well-width of 20 \AA , calculate the lowest 3 quantised energy levels. Compare your answers with the answers to question 9.

STRUCTURE OF MATERIALS BY DIFFRACTION TECHNIQUES



“The important thing in science is not so much to obtain new facts as to discover new ways of thinking about them.”

Sir Lawrence Bragg, in the inaugural Nobel Guest Lecture in 1965

The crystal structures of materials are generally obtained by the diffraction experiment. In general, there are three different diffraction methods, namely, X-ray, neutron and electron diffraction, used for the determination of crystal structure. Each method has certain advantages and disadvantages. Thus, they are used as complementary techniques.

Learning Objectives

- What is the relation between diffraction and structure?
 - What are the common diffraction techniques?
 - How many different forms of X-ray, neutron techniques exist?
 - How can X-rays and neutrons be applied to nanomaterials?
-
-

Diffraction is the phenomenon of bending of radiation towards the geometrical shadow of an object. The diffracted beams interfere to give bright or dark fringes in the shadow region, depending on the phase difference between scattered waves. This effect could be successfully explained using the Huygen’s wave theory of radiation. The diffraction gratings show such effects in the visible region of the electromagnetic spectrum. This effect was first demonstrated with X-rays by Max von Laue in 1912, after seventeen years of its discovery (1895). Since the crystal lattice consists of parallel rows of atoms equivalent to the parallel lines of the diffraction grating, the inter-planar spacing could be successfully determined, from the separations of bright fringes of the diffraction pattern. The classical Bragg’s law of diffraction relates the possibility of constructive interference to the inter-planar separations. [W.L. Bragg, “The Diffraction of Short Electromagnetic Waves by a Crystal”; *Proceedings of the Cambridge Philosophical Society*, 17(1913), 43–57.]

$$n\lambda = 2d \sin\theta \quad (1)$$

where λ = wavelength of X-rays or neutrons (\AA), θ = Bragg angle, d = inter-planar separations (\AA), n = order of diffraction.

Schematic representation of a scattering experiment is shown in Fig. 5.1. A basic quantity in a scattering experiment is the scattering vector $\mathbf{Q} = \mathbf{K}_s - \mathbf{K}_i$, which represents the difference between the wave vectors of the scattered and incident radiations. In the scattering experiment, one measures predominantly the elastic and quasielastic scattering for which $|\mathbf{K}_s| = |\mathbf{K}_i| = 2\pi n/\lambda$. Consequently, the modulus of \mathbf{Q} is related to the scattering angle 2θ , refractive index n and the wavelength of the incident radiation. For X-rays and neutrons n is close to unity.

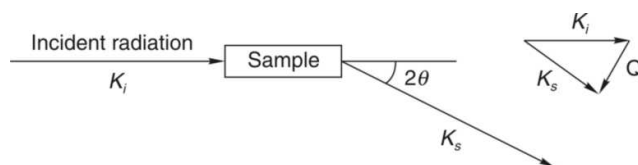


Fig. 5.1 Schematic representation of a scattering experiment.

A fundamental theorem in the theory of the scattering wave by an extended object relates the r-space density distribution of the scattering object to the Q-space scattered intensity distribution in terms of a Fourier transform. It follows from this theorem that the characteristic size in the r-space, R is reciprocally related to the characteristic width of the intensity distribution in Q-space. Therefore, to characterise the size R , one needs to do a scattering experiment, in which Q spans in a range around the value of $Q = 2\pi/R$.

Later on, successful efforts on the development of theory and experimental procedure made X-ray diffraction a unique tool for the study of solids. The scattering factor of an atom is, in general, expressed in the unit of scattering power of an electron. The scattering factor of an atom is given as

$$f = f_0 e^{-\frac{B \sin^2 \theta}{\lambda^2}} \quad (2)$$

where, f_0 = Scattering factor of an atom when it is rest, λ = Wavelength of X-ray, θ = Angle of diffraction, B = isotropic temperature factor, which is related to the amplitude of vibration of the atom and is given as, $B = 8\pi^2 u^2$, where u^2 = mean square displacement of the atom from the mean position. The exponential term is called Debye–Waller factor.

A crystal lattice consists of atoms, which form rows, and their repetition in turn gives planes in two dimensions and stacking of planes in three dimensions gives a lattice. Thus, the X-rays scattered by each atom interfere giving scattering amplitude, which is a complex quantity. The scattering power of a particular plane hkl in the lattice is called structure factor of that plane. The structure factor of a plane hkl is given as

$$F_{hkl} = \sum_{j=1}^N f_j e^{2\pi i(hx_j + ky_j + lz_j)} \quad (3)$$

F_{hkl} = Amplitude of scattered radiation from the plane hkl , f_j = Atomic form factor of the atom j at the diffraction angle θ , (x_j, y_j, z_j) = Fractional coordinates of the atom j in the unit cell, N = Number of atoms in the unit cell.

Thus, the sum can be given as

$$F_{hkl} = |F_{hkl}| \times e^{2\pi i(hx+ky+lz)} \quad (4)$$

where the $|F_{hkl}|$ is the amplitude of the resultant wave and the exponential factor is called the phase of the corresponding wave.

The sum is carried over all the atoms from 1 to N in the unit cell. The net magnitude is a complex number. The intensity of the diffracted beam is square of this structure factor. However, there are several other contributions, namely, absorption, Lorentz and polarisation factors and multiplicity of the plane. Thus, intensity of diffracted beam of a crystal at diffraction angle θ is given as:

$$I \propto F.F^*.L_p.Abs \quad (5)$$

L_p = Lorentz-polarisation factor, Abs = Absorption correction

The structure factor is related to the electron density distribution in the unit cell, which in turn represents the atom distribution in the crystal.

$$\rho(xyz) = \frac{1}{V_c} \sum_h \sum_k \sum_l f_{hkl} e^{2\pi i(hx+ky+lz)} \quad (6)$$

where V_c is volume of the unit cell.

Any experimental measurement gives intensity of the reflections hkl and the corresponding scattering angle (2θ). The scattering angle is related to the lattice dimensions, while the intensity is related to the distribution of the atoms in the unit cell. If the crystal structure is known, the intensity of the diffracted beam along with their phase can be calculated from the Equation 5. However, the reverse calculation is not easy. There are several methods, namely, direct method, Patterson heavy atom method, etc. known to estimate the relative phase of the diffracted waves and thus, the crystal structure. However, if model structures are available, then the calculated structures (from models) can be compared with the observed structure factors. Such optimisations are usually done by least square methods. The detailed theory and methods has been explained in several monographs [Martin, J. Buerger, *Crystal Structure Analysis*, John Wiley & Sons, New York (1960); Leonid V. Azaroff, *Elements of X-ray Crystallography*, McGraw-Hill Book Company, New York (1968); H. Lipson and W. Cochran, *Determination of Crystal Structure*, G. Bell and Sons Ltd, London (1966)].

It is well known that the d-spacing are related to the lattice dimensions. Each reflection can be assigned with some hkl values, which relate the inter-planar spacing with the unit cell parameters. The typical assignments of hkl values to the reflections are called indexing. There are several graphical, mathematical methods used for indexing the powder pattern. The detailed methods are explained in *The Powder Method in X-ray Crystallography* by L.V. Azaroff and M.J. Buerger, McGraw-Hill Book Company, New York (1958). The principles involved in the mathematical method are trial and error methods.

It needs to be mentioned here that the solutions obtained are usually not unique and cannot be free from mistakes. It is always the user's decision for the judging the accurate unit cell parameters. The systematic absences in the indices is used to identify the lattice type of the unit cell.

Structure analyses by diffraction of X-ray/neutrons (having wavelength $\sim \text{\AA}$) is the most convenient method of studying arrangement of atoms in crystals. Neutron are better suited for investigating materials involving lighter atoms (e.g., hydrogen), neighbouring elements and magnetic materials. High penetrability of neutron, in addition, is an advantage. Structure analysis is possible with both single crystal and powder samples.

Single crystals yield three-dimensional diffraction pattern with large number of Bragg reflections enabling *ab-initio* structure determination and analyses. It is possible to study structures of very large molecules, e.g., proteins. One can describe atomic or electronic distributions, like bonding electron, thermal motion, etc. in great detail. However, many a time, it is not possible to grow single crystals of required size, particularly for neutron as the size in the range of $\sim \text{mm}^3$. Many interesting/important materials are available only as polycrystalline samples, hence one has to seek information using powders. Diffraction of X-rays or neutrons by polycrystalline samples (commonly known as powder sample) is one of the most powerful, important and widely used techniques available to materials scientists. For most crystalline substances of technological importance, the bulk properties of a powder or a polycrystalline solid, averaged throughout the sample are required. If even a single crystal is obtained, it is not much of interest except for crystal structure determination or to study some other fundamental physical property.

Powder diffraction yields a one-dimensional spectrum with all reflections having same d-values (viz. for cubic structure (100), (010), (001) have the same d-spacing, known as multiplicity) bunched together at the same Bragg angle. Hence, it is difficult to study structures with more than 3/4 atoms per asymmetric unit using conventional method.

5.1 MERITS/DEMERITS OF X-RAY VS NEUTRON

	X-ray	neutron
1. Locating light element:	not favourable	favourable
2. Sample size:	penetration (10–100 μm)	cms (compensate for flux)
3. Scattering at high angles: (required for non-crystalline system)	poor (form factor effect)	very good
4. Resolution ($\Delta d/d$):	good	good with high flux source

Neutron scatters from the nucleus, and being point scatterer, there is no form factor effect, whereas X-ray interacts with matter through electron cloud (extend over few angstrom) via electromagnetic interaction, there is a strong form factor effect, scattering intensity falls off sharply with the angle of scattering. Therefore, information from large angle scattering is affected due to this form factor effect for X-ray, which is not the case for neutron. Particularly for disordered system, where periodicity is

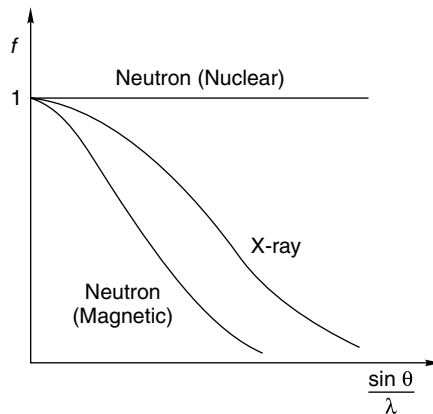


Fig. 5.2 Form factor variation in X-ray and neutron diffraction.

not long range enough it is essential to adopt neutron as the probe for structural study as to extract information on the short range ordering one has to have data in the high wave vector transfer (Q). Another point to be emphasised is the cross-section of scattering, which is proportional to the atomic number in case of X-ray, whereas for neutron, it is randomly varied with atomic number, in fact the neutron scattering cross-section for the neighbouring element can have very different values as shown in Fig. 5.3. Hydrogen, the lowest mass number element in the periodic table has only one electron and therefore it is very difficult to locate hydrogen atom in the lattice by X-ray scattering. Neutron scattering being nuclear in origin even two isotopes of an element can have very different scattering cross-section, which makes neutron a very useful probe to study structure of matter.

5.2 X-RAY DIFFRACTION

When particles, such as electrons, fall on matter with high energy, electrons can be ejected from various energy levels. Electron ejection from core orbital is also accompanied by the emission of characteristic X-rays. In the case of electron from the 1s orbital, an outer electron from the 2p or 3p orbital can fall down to occupy the vacant 1s orbital. This $2p \rightarrow 1s$ transition leads to the emission of K_{α} radiation. Similar transition is possible from the 3p level resulting in K_{β} . The K_{α} is a doublet with $K_{\alpha 1}$ and $K_{\alpha 2}$ corresponding to electronic transition from the two possible spin states of the 2p electron ($2p_{3/2}$ and $2p_{1/2}$, respectively). In most of the diffraction experiments, $K_{\alpha 1}$ and $K_{\alpha 2}$ are not separated and statistically weighted average of the two wavelengths are taken. The wavelength of a given X-ray line depends on the atomic number.

The emission spectrum of a metal is shown below (Fig. 5.4). Characteristic radiations are overlapped with the Bremsstrahlung. Various kinds of filter materials are used to avoid unwanted radiations. Monochromatisation by diffraction can also be done to improve the optical purity of the radiation. In a typical X-ray tube used to generate X-rays, high energy electrons are accelerated to a target in an evacuated tube. Only a fraction of the incident electron energy is converted to X-rays. Most

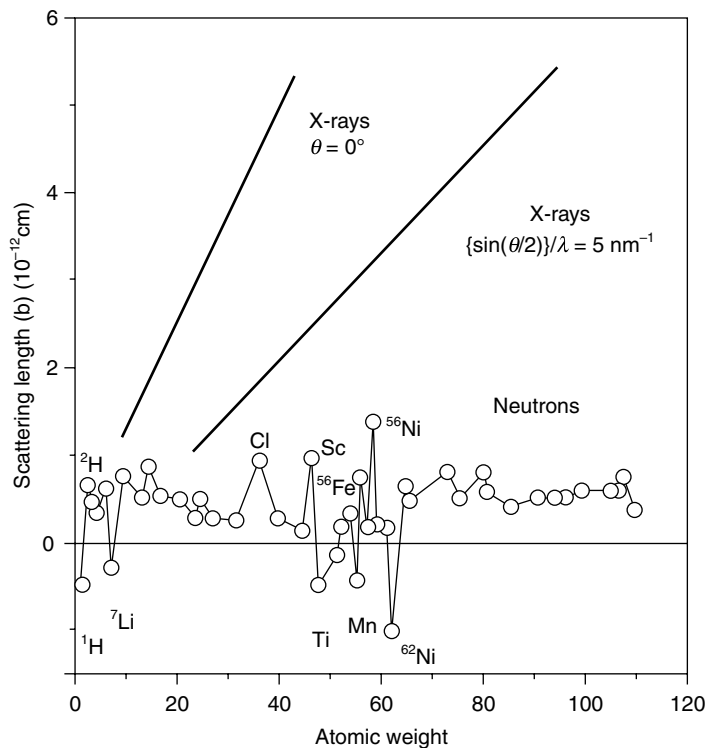


Fig. 5.3 Comparison of scattering lengths for X-ray and neutron.

of it is converted to heat and efficient cooling of the anode, is necessary to avoid it from melting. X-rays come out of the tube through a window made of small atomic number materials such as beryllium.

Diffraction of light by crystals can be understood with the help of an optical grating consisting of several parallel lines drawn on a glass plate. As light is incident on the grating, each group will act as a line source and light will be radiated in all directions. Interference occurs between the waves and in certain direction constructive interference occurs. In the Fig. 5.5, constructive interference is shown to occur in two directions marked by lines. In the bottom direction, the waves are in phase although each wave is shifted by one wavelength from the other. Between these two directions, all the other directions interference occurs reducing the intensity. In the case of several line sources, as would be present in the case of a grating, interference occurs over several waves and no intensity will be seen between the directions shown. In the case of a grating, conditions of constructive interference is that path length between the beams is an integral multiple of the wavelength. This can be written as, $n\lambda = d \sin \theta$, where d is the distance between the grooves and is θ the angle of observation. For first order diffraction, $\lambda = d \sin \theta$, as the maximum value of $\sin \theta = 1$ and $\theta = 90^\circ$ the first order diffraction will be observed at this angle. In general, the angle will be lower than 90° and d larger than λ ; for d less than λ only zero order direct beams will be observed. If d is much larger than λ individual diffracted beams of different orders will be closed to each other and we get a diffraction continuum. In the case

of visible light (4,000–7,000Å wavelength), a grating spacing of 10,000–20,000Å is used to observe diffraction.

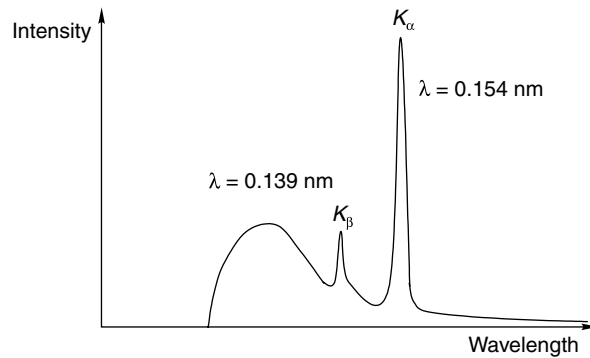


Fig. 5.4 X-ray emission spectrum from copper. Copper $K\alpha$ corresponds to 1.54nm.

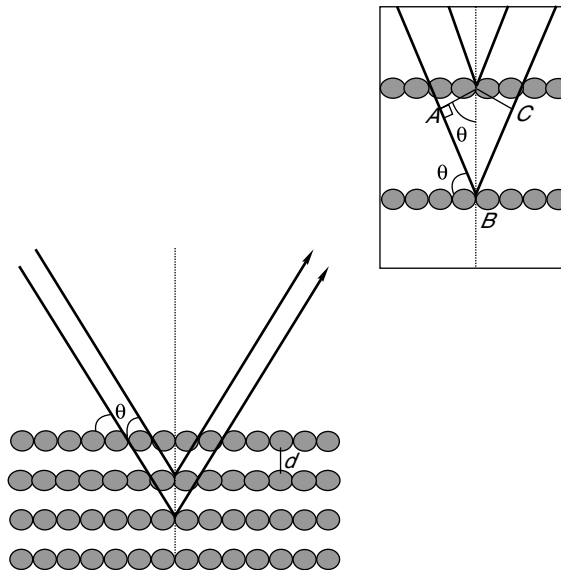


Fig. 5.5 The conventional derivation of Bragg's Law. Between the directions shown the path difference is a multiple of the wavelength and as a result, intensity will be the maximum at the outward direction.

The X-ray diffraction experiment requires the following. A radiation, a sample and a detector for the reflected radiation. For each of these cases, there can be several variations, for example, the radiation can be of many kinds, a single monochromatic source or of variable frequency. The sample can be powder, single crystal, solid piece or a thin film. The detector can be of several kinds, from a simple photographic plate, it can be a sophisticated counter or an area detector. In a powder diffraction

experiment, a finely powdered sample, there are crystals arranged in all possible orientations. The various lattice planes are also arranged in all possible orientations as well. For each crystal plane, there will be a number of orientations. The reflected X-rays may be collected on a photographic plate or using a counter and suitably connected to a recorder.

In the Debye-Scherrer method of diffraction, we use a monochromatic X-ray and a powder sample with every possible set of lattice planes exposed to the radiation (Fig. 5.6). The diffracted radiation gives rise to a cone. The condition of diffraction is that the radiation is at angle θ to the incident beam. The cone arises because there are several angular positions of the crystals. The cone is a result of several closely-separated spots (inset). In the case of a finely ground sample, the spots will be replaced by a continuous line. Each (hkl) results in one core. The detector is moved in a circle to collect all the reflections corresponding to various (hkl).

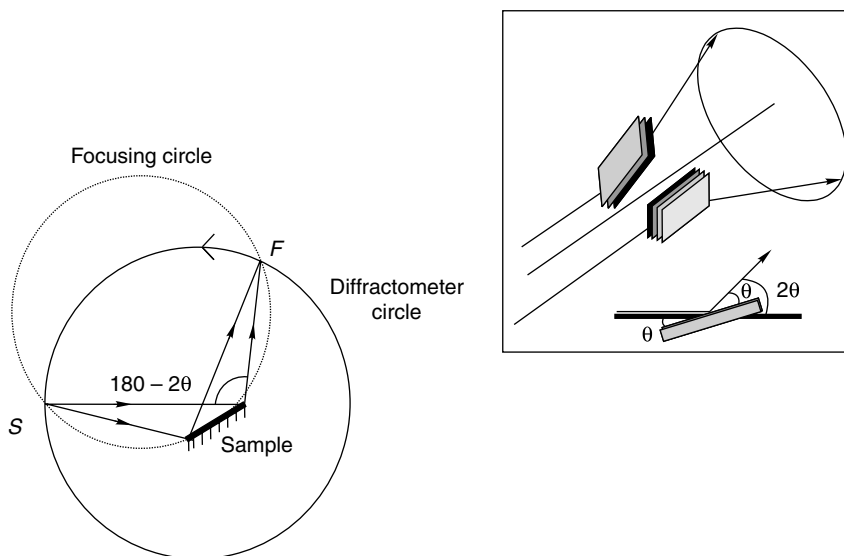


Fig. 5.6 Debye-Scherrer method of powder diffraction. Two microcrystallites of different orientation with respect to the incident beam give diffracted rays that lie in a cone. The diffraction pattern is due to all the (hkl).

In the modern diffraction method called diffractometry, a convergent beam strikes the sample and the intensity as a function of diffraction angle is measured. The position of the diffraction peak and the intensity at this point are the two factors used in the determination. Both these can be measured accurately and compared with standards in the literature. In fact, this is what one normally does in the phase identification work.

5.3 RIETVELD PROFILE REFINEMENT

Although the structure solution from the powder diffraction pattern is usually difficult, the structure can be optimised for an unknown compound if any iso-structural compound is available. The

development of Rietveld method [H.M. Rietveld, *Acta. Cryst.* **22** (1967) 151; H.M. Rietveld, *J. Appl. Cryst.* **2** (1969) 65] made the structure refinement from powder diffraction possible. In this method, the entire diffraction pattern is refined to optimise the structure.

The basic Principle of Rietveld Refinement is based on the calculation of intensity of an unknown compound assuming a model, with all the structure and profile parameters. The structure model has to be provided with the space group, position coordinates of all the atoms and the fairly correct unit cell parameters. The profile is defined by a specific function, like Gaussian, Lorentzian or their combination, e.g., pseudo Voigt function. A smoothly varying polynomial function is used for background.

$$Y_{ci} = y_{bi} + s \sum_{hkl} L \times P \times n \times |F_{hkl}|^2 \phi(2\mathcal{G}_i - 2\mathcal{G}_{hkl}) \times P_{hkl} \times A \quad (7)$$

where, Y_{ci} = Calculated intensity at the i_{th} step, y_{bi} = Background intensity at i_{th} step, L = Lorentz factor, P = Polarisation factor, $|F_{hkl}|^2$ = Structure factor for hkl reflections, $\phi(2\theta_i - 2\theta_{hkl})$ = Profile function, P_{hkl} = Preferred orientation function, A = Absorption correction and S = scale factor.

The full width at half maximum (FWHM) represented by H_{hkl} , is taken to be the Cagliotti Ricci function defined as a function of theta as:

$$H_{hkl}^2 = U \tan^2 \mathcal{G} + V \tan \mathcal{G} + W \quad (8)$$

There are several profile functions defined for fitting the Bragg peaks. It is well known that the X-ray profile shape can be Lorentzian or mixed Gaussian and Lorentzian type. The mixing can be optimised in the course of refinements.

$$D = \sum_{i=1}^n w_i (Y_{io} - Y_{ic})^2, \quad (9)$$

where w_i = weighting factor and is equal to $1/Y_{oi}$

The quantity D (residual) is minimised in the least square refinements.

There are several computer packages, like DBWS, Fullprof, GSAS, Rietan, etc., available for Rietveld Refinement. A good start is usually made with a reasonably good scale, background parameters and approximate position coordinates of various atoms. They are adjusted by the refinements in successive cycles. The unit cell parameters, half width and mixing parameters are next refined. Subsequently, the refinement of the preferred orientation parameters and asymmetry parameters are carried out. The position parameters, thermal parameters should be refined next. The progress of the refinement is usually monitored by the difference plot of the observed and calculated diffraction profiles. Usually *Dmplot* or *Winplotr* are used for this purpose. The progress of the refinement and goodness of refinement are judged by the residuals indicators. There are several residuals routinely calculated by the Rietveld refinement cycles and displayed in each step. The usual refinement indicators are called R-values and they are defined as:

$$\text{R. profile} \quad R_p = \frac{\sum (Y_{io} - Y_{ic})}{\sum Y_{ic}}$$

$$\begin{aligned}
 \text{R. weighted Profile} \quad R_{wp} &= \left[\frac{\sum w_i (Y_{io} - Y_{ic})^2}{\sum w_i Y_{io}^2} \right]^{1/2} \\
 \text{R. expected} \quad R_{exp} &= \left[\frac{N - P + C}{\sum w_i Y_{io}^2} \right]^{1/2} \\
 \text{R. structure factor} \quad R_F &= \frac{\sum |I_{hkl(o)}^{1/2} - I_{hkl(c)}^{1/2}|}{\sum I_{hkl(o)}^{1/2}} \\
 \text{R. Bragg} \quad R_B &= \frac{\sum |I_{hkl(o)} - I_{hkl(c)}|}{\sum I_{hkl(o)}} \\
 \text{Goodness of fit} \quad S &= \frac{W_{wp}}{W_{exp}} = \chi
 \end{aligned}$$

N = Number of points in the pattern, P = number of refined parameters, C = number of constraints. The peak width of the diffraction lines depend both on the particle size and also if the material is stressed.

5.4 THE CRYSTALLITE SIZE

Peaks of the pattern will broaden if the crystallites of the powder are very small. From the broadening, it is possible to determine an average crystallite size, in Å, by Debye-Scherrer formula [A. Patterson, The Scherrer Formula for X-Ray Particle Size Determination, *Phys. Rev.* 56 (1939) 978–82]

$$D_{hkl} = k\lambda / \beta \cos\theta;$$

where k (shape factor) = 0.8–1.39 (usually close to unity e.g., 0.9), λ = wavelength of the radiation, β = FWHM (full width at half maximum) in radians, β = half-width (degree) $\pi/180$, θ = the position of the maximum of diffraction. The Scherrer equation is limited to nano-size particles, it is not applicable to grains larger than about 0.1 μm .

Debye Scherrer formula provides a lower bound on the particle size, as a variety of factors can contribute to the width of a diffraction peak. Apart from crystallite size, inhomogeneous strain and instrumental effects also contributes significantly. If all other contributions to the peak width were zero, then the peak width would be determined solely by the crystallite size and the Scherrer formula would apply. If the other contributions to the width are non-zero, then the crystallite size can be larger than that predicted by the above formula.

5.5 BROADENING DUE TO STRAIN

It is known that residual stresses in materials are caused by manufacturing processes like forging, welding, machining and wear and tear effects, such as plastic deformation, creep, fretting, etc. X-ray or

neutron diffraction can be used to measure residual stresses non-destructively. While X-rays are unable to penetrate more than 100 micron in most materials, neutron can easily pass through several cms. Strains in materials are evaluated very simply by changes in lattice spacings. The shift of Bragg peak due to strains can be obtained using simple Bragg relation,

$$n\lambda = 2d \sin \theta$$

$$\Delta\theta = -(\Delta d/d) \tan\theta$$

$$\Delta\theta = -\eta \tan\theta$$

$$B_{\text{strain}} = \eta \tan\theta, \text{ where } \eta \text{ is the strain in the material.}$$

The width of the diffraction peak

$$B_{\text{result}} = B_{\text{crystallite}} + B_{\text{strain}} = \frac{k\lambda}{D \cos\theta} + \eta \tan\theta,$$

multiplying this by $\cos\theta$ we get:

$$B_{\text{result}} \cos\theta = \frac{k\lambda}{D} + \eta \sin\theta$$

Thus, when we plot $B_{\text{result}} \cos\theta$ vs $\sin\theta$, we get a straight line with slope η and intercept $k\lambda/D$.

5.6 OTHER SCATTERING TECHNIQUES IN VOGUE

The scattering techniques that are popular to the studies of condensed matter are light scattering [includes both static light scattering (SLS) and dynamic light scattering (DLS)], small-angle neutron scattering (SANS) and small-angle X-ray scattering (SAXS). In each of these techniques, the radiation (light, neutron or X-ray) is elastically scattered by a sample and the resulting scattering pattern is analysed to provide information about the structure (shape and size), interaction and the order of the components of the samples.

Figure 5.7 shows the comparison of the length scales of scattering methods which they probe. In the following, the scattering techniques are discussed to some details.

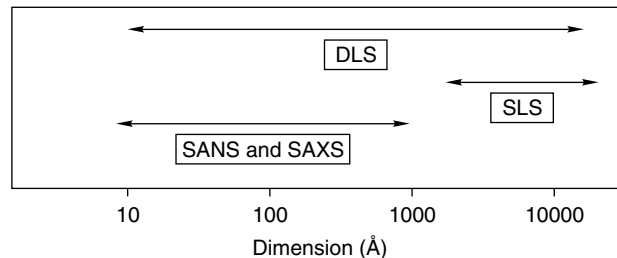


Fig. 5.7 Overview of the size range of different scattering methods.

5.7 STATIC LIGHT SCATTERING (SLS)

In SLS one measures the time averaged scattered intensity as a function of the scattering angle. The scattered intensity bears information on the static properties of the scattering medium, such as size and shape of the scatterers. It is important to mention that one can use other probing radiation than

X-rays or neutrons to study the structures in much greater details. SLS has the advantage for the easy accessibility to perform the routine applications [B. Chu, *Laser Light Scattering: Basic Principles and Practice* (Academic Press, 1991)].

5.8 DYNAMIC LIGHT SCATTERING (DLS)

DLS is based on the scattering of light by diffusing particles. At any instance, the suspended particles will have a particular set of positions within the scattering volume. The particles scatter the light to the detector, but the relative phase of scattered wavelets differ due to differing incident phases, which they experienced and due to different particle-detector distances. The intensity at the detector is the superposition of all the scattered wavelets and will have a value $I(t)$ at time t . At the time $t+\tau$, which is very small time later than t , the diffusing particles will have new positions and the intensity at the detector will have a value $I(t+\tau)$.

As time progress, the intensity at the detector will fluctuate as the Brownian processes in the sample volume continue. Small rapidly diffusing particles will yield fast fluctuations, whereas larger particles and aggregates generate relatively slow fluctuations. The rate of fluctuations can be determined through the technique of auto-correlation analysis. The general form of the auto-correlation function for monodisperse particles is given as [B.J. Berne and R. Pecora, *Dynamic Light Scattering* (John Wiley & Sons, 1978)]

$$G(Q,\tau)=1+\exp[-2DQ^2\tau]. \quad (1)$$

The particle hydrodynamic radius R_h is given by the Stokes-Einstein relation

$$R_h = kT/6\pi\eta D \quad (2)$$

where k is Boltzmann's constant, T is the temperature, D is the diffusion constant and η is the solvent viscosity.

5.9 SMALL ANGLE NEUTRON/X-RAY SCATTERING (SANS/SAXS)

The SANS and SAXS are the techniques for obtaining structural information of a material on length scale of 1–100 nm, and hence, these techniques are routinely used for studying sizes and shapes of nanoparticles [Feigin L A & Svergun D J, *Small Angle X-ray and Neutron Scattering* (Plenum Press, New York, 1987); Linder P & Zemb T (ed) *Neutrons, X-rays and Light Scattering* (North Holland, Amsterdam, 1991)]. The experiment involves scattering of a monochromatic beam of neutrons (or X-rays) from the sample and measuring the elastically scattered neutron (or photon) intensity as a function of the scattering angle. The magnitude of wave vector transfer $Q (= 4\pi\sin\theta/\lambda$, where 2θ is the scattering angle and λ is the wavelength of neutrons or X-rays) in SANS/SAXS experiments is typically in range $0.01 - 1 \text{ nm}^{-1}$. To obtain such low Q values, SANS/SAXS experiments involve small scattering angles. In short, SANS or SAXS are diffraction experiments corresponding to small scattering angles. Unlike conventional diffraction experiments, where the structure of a material is examined at atomic resolution ($\sim 0.2 \text{ nm}$), SANS/SAXS is used for studying the structure of a material with a spatial

resolution of ~ 10 nm. SANS and SAXS are similar techniques and their data analysis procedures are also similar. The two techniques mainly differ in the radiation used in the experiment. In view of this, in the following we shall discuss about SANS; this discussion is valid for SAXS also.

The small-angle intensity $I(Q)$ as a function of scattering vector for a dispersion of nanoparticles can be expressed as [Butter K, Armin H, Weidenmann A, Petukhov A V & Vroege G, *J. Appl. Cryst* 37 (2004) 847]

$$I(Q) = \frac{d\Sigma}{d\Omega(Q)} = nP(Q)S(Q); \quad (1)$$

where n is the number density of the particles. $P(Q)$ is the intraparticle structure factor and depends on the shape and size of the particle. $S(Q)$ is the inter-particle structure factor and is decided by the spatial distribution of the particles. $P(Q)$ is given by the integral,

$$P(Q) = \left| \int (\rho(r) - \rho_s) \exp(iQ \cdot r) dr \right|^2 \quad (2)$$

In the simplest case of a monodispersed system of spherical particles with a radius R , $P(Q)$ is given by

$$P(Q) = (\rho(r) - \rho_s)^2 V^2 \left[\frac{3j_1(QR)}{QR} \right]^2; \quad (3)$$

where, $V = (4/3)\pi R^3$, ρ_s = the scattering length density of the solvent, ρ = the mean scattering length density of the particle and $j_1(QR)$ = spherical Bessel function of first order. Similar expressions for $P(Q)$ for different geometrical shapes e.g., (cylinder, disk, ellipsoid, etc.) and for a system of polydisperse spheres are available in the literature [Butter K, Armin H, Weidenmann A, Petukhov A V & Vroege G, *J. Appl. Cryst.* 37 (2004) 847]. Typical curves for $P(Q)$, $S(Q)$ and $d\Sigma/d\Omega(Q)$ are shown in Fig. 5.9.

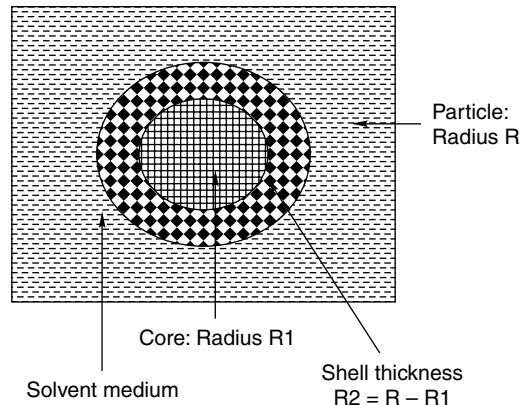


Fig. 5.8 Conventional nanoparticle.

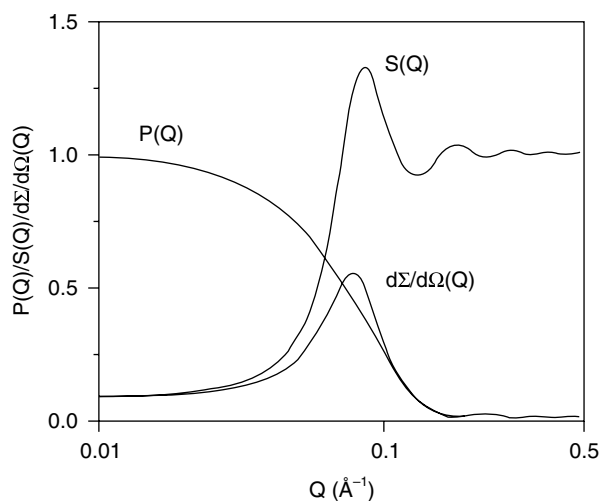


Fig. 5.9 Typical curves of $P(Q)$, $S(Q)$ and $d\Sigma/d\Omega(Q)$.

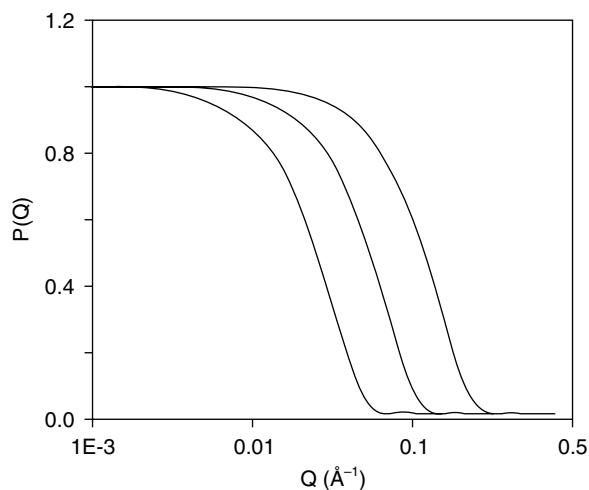


Fig. 5.10 $P(Q)$ depends on the shape and size of the particle. The width of the $P(Q)$ decreases with increase in the size of the particle. Data are shown for spherical particles with radii 25, 50 and 100 Å, respectively.

The intraparticle structure factor $P(Q)$ for a spherical particle having core-shell structure (Fig. 5.8) is given by

$$P(Q) = \left[(\rho_1 - \rho_2)V_1 \frac{3j_1(QR)}{QR} + (\rho_2 - \rho_s)V \frac{3j_1(QR)}{QR} \right]^2; \quad (4)$$

where R is the radius and V is the volume of the particle. The thickness of spherical shell around the core is given by $R_2 = R - R_1$. The ρ_1 , ρ_2 and ρ_s in Eq. (4) stand for mean scattering length densities for the core, shell and solvent, respectively. $P(Q)$ for samples with different sizes of spherical particles is shown in Fig. 5.10.

The expression for $S(Q)$ depends on the relative positions of the particles. In case of homogenous and isotropic system, $S(Q)$ can be written as

$$S(Q) = 1 + 4\pi n \int (g(r) - 1) \frac{\sin QR}{QR} r^2 dr; \quad (5)$$

where $g(r)$ is the radial distribution function. $g(r)$ is the probability of finding another particle at a distance r from a reference particle centered at the origin. The details of $g(r)$ depend on the interaction potential $U(r)$ between the particles. Figure 5.11 shows the variation in $S(Q)$ for samples with different ionic strength indicating the effect of interaction between the particles. Usually, $S(Q)$ exhibits a few peaks in the small Q range corresponding to pair-wise correlation between scattering particles; therefore, these peaks are, specifically the first one is, known as the correlation peak. In very dilute systems, $S(Q)$ tends to unity, because the extremely small Q range is not accessible in experiments. In such cases, the scattering intensity mostly represents $P(Q)$.

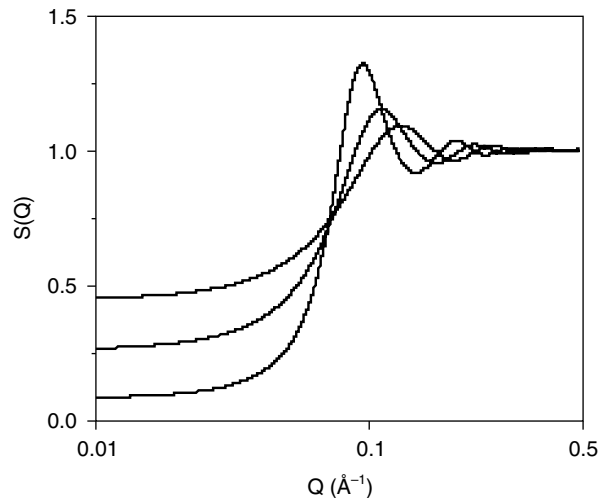


Fig. 5.11 $S(Q)$ relates to the interaction between particles. Data show the compressibility of a system [$S(Q = 0)$] increases with increase in the ionic strength.

5.10 CONCEPT OF CONTRAST FACTOR IN SANS/SAXS EXPERIMENTS

Scattered neutron (or X-ray) intensity in SANS or SAXS experiment depends on $(\rho - \rho_s)^2$ —the square of the difference between the average scattering length of the particle and the average scattering length density of the solvent. $(\rho - \rho_s)^2$ is referred to as the Contrast Factor. The values of ρ and ρ_s depend on

the chemical composition of the particle and the solvent and is different for neutrons and X-rays. The differences in ρ values for neutrons and X-rays arise from the fact that while neutrons are scattered by the nucleus of an atom, the X-rays are scattered by the electron clouds around the nucleus. It is seen that as one goes across the periodic table, the neutron scattering lengths vary in a random way and the X-ray scattering lengths increase linearly with the atomic number of the atom. The value of ρ or ρ_s for X-ray will be small for hydrogenous materials (organic compounds) as compared to that for heavier elements such as Au, Br, etc. This is not the case with neutrons. Further, the fact that scattering length of hydrogen is negative ($= -0.3742 \times 10^{-12}$ cm) and that for deuterium is positive ($= 0.6674 \times 10^{-12}$ cm), the value of ρ for neutrons changes significantly on deuteration of a hydrogenous sample. It is, in fact, possible to mix the hydrogenous and the deuterated species, and thus, vary the contrast in a continuous way in a neutron experiment.

It is because of the properties of X-rays and neutrons that one is able to determine the core and shell structure of nanoparticles. For example SAXS experiments on gold nanoparticles will give information about the size of the core. X-rays will not see the hydrogenous capping material. However, neutrons are largely scattered from hydrogenous material of the capping which constitutes the outer shell of the Au nanoparticles. For neutrons, the above particles will appear as hollow spherical shells. Micelles, which are nanoparticles of the hydrogenous materials, behave differently. In this case, neutrons see the core of the micelle and X-rays furnish information about the shell of counterions around the micelle.

5.11 REFLECTOMETRY

Thin films and/or layered materials are also considered as nanophase at least in one of the dimensions, although in the other two dimensions, it is bulk like. Neutron and X-ray reflectometry are important techniques for studying the composition and structure of thin films and layered media on a nanoscale. Neutrons are particularly useful as probes of organic and magnetic materials since the information that can be obtained is often unique. The intensity of a neutron beam reflected at a glancing angle from a flat material surface depends upon the composition and structure of the underlying matter. More specifically, if the reflected intensity is measured at an angle of reflection equal to that of the incidence, known as specular condition, the reflectivity or ratio of reflected to incident intensity, as a function of glancing angle, can be analysed to reconstruct an averaged compositional depth profile along the normal to the surface. The refractive index n of a material for neutrons can be calculated from the optical theory of refraction [J. Lekner, *Physica B*. 173 (1991) 99] by

$$n = 1 - \frac{\lambda^2 \rho}{2\pi} \quad (1)$$

where, $\rho = \sum_i N_i b_i$, λ = the wavelength of neutron, N_i = the number density of atom of species i and b_i = the coherent scattering length of the species i . The Fresnel reflectivity at an angle of incidence θ , with respect to sample, for an ideally flat medium of infinite thickness with refractive index n is given by the expression:

$$R_F = \frac{\left| \sin \theta - \sqrt{n^2 - \cos^2 \theta} \right|^2}{\left| \sin \theta + \sqrt{n^2 - \cos^2 \theta} \right|^2} \quad (2)$$

The Fresnel reflectivity gets modified for a rough surface, $R(Q)$, by a 'Debye-Waller like' factor:

$$R(Q) = R_F(Q) e^{-q^2 \sigma^2 / 2} \quad (3)$$

where Q is the momentum transfer (related to angle of reflection, θ by, $Q = 4\pi \sin \theta / \lambda$) and σ is the root mean square roughness parameter of the surface.

Polarised neutron reflectometry has been used to investigate the magnetisation profile near the surface of single crystals, and of thin films and multilayers. Surface (or interface) sensitivity derives from working in grazing incidence geometry near the angle for total external reflection. Polarised neutron reflectometry is highly sensitive, having measured the absolute magnetisation of a monolayer of iron ($\sim 10^{-4}$ emu) with 10 per cent precision [Y.Y. Huang, C. Liu, G.P. Felcher, *Phys. Rev. B* 47 (1993) 183], and has excellent depth resolution, on the order of a tenth of a nanometer even for films as thick as several hundred nanometers.

The in-plane variations of the scattering density, including possible correlations, are manifested directly in off-specular scattering, where the angles of incidence and reflection are chosen not to be equal. Neutron reflectometry combining with specular and off-specular mode can be used as non-destructive technique to study the structural, magnetic properties and surface morphology of nanoparticles confined in solid/solid, liquid/solid thin films and multilayers. Neutron reflection is now being used for studies of surface chemistry (surfactants, polymers, lipids, proteins and mixtures adsorbed at liquid/fluid and solid/fluid interfaces), surface magnetism (ultrathin Fe films, magnetic multilayers, superconductors) and solid films (Langmuir–Blodgett films, thin solid films, multilayers, polymer films). Recently, the specular and off-specular neutron reflectivity study, to understand the magnetic field dependent ordering in nanocomposite ferrofluids at SiO_2 interfaces, by A. Vorobiev, et al., [A. Vorobiev, et al., *Phys. Rev. Lett.* **93**, (2004) 267203], has demonstrated the strength of the technique to study the nanoparticles.

REVIEW QUESTIONS

- Suppose that a monatomic cubic crystal is known to be composed of close shell (and hence symmetric) ions, so that $f(Q)$ depends only on the magnitude of Q . The position of Bragg peaks reveals that the Bravais lattice is simple cubic. Discuss how one might determine whether the crystal structure was likely to be of the sodium chloride type or zinblend type.
- (a) What experiment one should perform to find out (i) location, (ii) dynamics of the hydrogen atoms in the hydrogenous material?
(b) How one can detect the thermal neutrons?
- Calculate the coherent and incoherent scattering cross-section of Vanadium ($Z = 23$, spin = $7/2$) for thermal neutrons from the following given data

$$b^+ = 0.511 \times 10^{-12} \text{ cm}$$

$$b^- = -0.752 \times 10^{-12} \text{ cm}$$

4. Calculate the energies of neutron (in meV) of wavelengths 2.0 and 1.8Å.
5. Discuss the structure function $S(Q)$ and pair distribution function for the liquids and glasses.
6. A polychromatic beam of neutrons is passed through a polycrystalline material. The maximum lattice spacing (d) for the polycrystalline material is 1.5Å. What will be the minimum wavelength of the transmitted neutrons?
7. Discuss the experiment one would perform to probe the large objects ($\sim 1 \text{ nm}$ to $\sim 1 \mu\text{m}$)?
8. A polychromatic beam of neutrons is reflected by (331) plane of Si monochromator (Bragg reflection). If the error in the determination of lattice spacing (d) for (331) plane is 0.1Å, find the range of the neutron wavelength ($\Delta\lambda$) scattered by the monochromator? Take the monochromator take off angle ($2\theta_M$) 90° and lattice constant for Si is 3.57Å.
9. The Potassium Chloride has fcc structure. There are four Potassium and four Chlorine atoms per unit cell, located as follows

K	000	$\frac{1}{2} \frac{1}{2} 0$	$\frac{1}{2} 0 \frac{1}{2}$	$0 \frac{1}{2} \frac{1}{2}$
Cl	$\frac{1}{2} \frac{1}{2} \frac{1}{2}$	$00 \frac{1}{2}$	$0 \frac{1}{2} 0$	$\frac{1}{2} 0 0$

If the atomic form factors for two ions are f_+ and f_- then show that structure factor vanishes for mixed indices. And for unmixed indices show that

- (i) $F = 4(f_+ + f_-)$ if $(h + k + l)$ is even
- (ii) $F = 4(f_+ - f_-)$ if $(h + k + l)$ is odd.

In the diffraction pattern of Potassium Chloride it has been found that all the peaks, where condition (ii) satisfies are absent, explain why?

Evaluate the incoherent scattering cross-section of $^1_1\text{H}^1$ (spin $\frac{1}{2}$) and $^2_1\text{H}^2$ (Deuterium, spin 1) for thermal neutrons from the following data given:

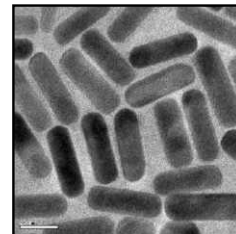
$$b_{\text{H}^+} = 1.04 \times 10^{-12} \text{ cm}, \sigma_{\text{coh}} = 1.76 \text{ barn}$$

$$b_{\text{D}^+} = 0.95 \times 10^{-12} \text{ cm}, b_{\text{D}^0} = 0.10 \times 10^{-12} \text{ cm}$$

10. Calculate the energies of neutron (in meV) of wavelengths 1.8Å and 1.2Å.
11. What is the effect of temperature on X-ray and neutron diffraction pattern?
12. What is the physical significance of $G(r, t)$?
13. What will be the form of the potential for a neutron nucleus interaction? What will be form factor for neutron nucleus interaction, compare it with the form factor for X-ray scattering and describe how X-ray and neutron scattering experiment differ in intensity at high Q value?
14. To study the structure of glass or amorphous system, which probe (X-ray or neutron) should be used and why?
15. The Bragg angle corresponding to the first order reflection from (111) planes of a crystal is 30 degrees, when X-rays of wavelength 1.75Å are used. What is the interplanar spacing?
16. Copper has an FCC structure. The lattice constant of its cubic unit cell is 3.6Å. What is the distance between the nearest neighbor copper atoms in the structure?
17. Copper has an atomic weight of 63.546 amu ($\text{amu} = 1.66 \times 10^{-27} \text{ kg}$) and an FCC structure with cubic lattice constant $a = 3.6\text{Å}$. What is the density of Copper?

18. Copper has an FCC structure with cubic lattice constant $a=3.6\text{\AA}$. What is the molar volume of Copper?
19. In a perfect crystal, which is the correct answer?
- (a) The atoms are static at all temperatures and their instantaneous positions define the crystal symmetry
 - (b) The atoms are oscillating at all temperatures, and their average positions define the crystal symmetry
 - (c) The atoms oscillate at low temperatures but are static at high temperatures
 - (d) None of the above
20. FCC copper has a cubic lattice constant value $a=3.6\text{\AA}$. What is the d -spacing of the (200) Bragg reflection?
21. What is the atomic packing fraction (ratio of the atomic volume per unit cell to the volume of the unit cell) for FCC copper?
22. What will be the number of atoms per unit cell of a metal with atomic weight=55.85 amu ($1\text{ amu}=1.66 \times 10^{-27}\text{ kg}$) having a cubic lattice parameter of 2.9\AA and density 7.602 g/cm^3 ?
23. Which one is the correct answer?
X rays are NOT:
- (A) diffracted by crystals
 - (B) radiation of wavelength approximating 1 Angstrom
 - (C) visible to the naked eye
 - (D) used to determine the structure of materials
24. Which one is the correct answer?
In a cubic solid,
- (a) $a=b \neq c, \alpha=\beta=\gamma=90$
 - (b) $a=b=c, \alpha=\beta=\gamma \neq 90$
 - (c) $a=b=c, \alpha=\beta=\gamma=90$
 - (d) $a \neq b \neq c, \alpha=\beta=\gamma=90$

ELECTROANALYTICAL TECHNIQUES



“The theoretical side of physical chemistry is and will probably remain the dominant one; it is by this peculiarity that it has exerted such a great influence upon the neighbouring sciences, pure and applied, and on this ground physical chemistry may be regarded as an excellent school of exact reasoning.”

Svante Arrhenius

In *Theories of Solutions* (1912) quoted by

R.S. Tour, *Industrial and Engineering Chemistry*, 15 (1923) 5

Changes in the electronic energy levels of materials with size and shape can be directly investigated using electroanalytical techniques. An overview of the various techniques and the application of several of these tools on nanoscale systems are presented here. Electrochemical changes of the system can be used for imaging purposes. All of these are briefly discussed here.

Learning Objectives

- What are the electroanalytical techniques used for nanomaterials research?
 - How electrochemical properties change with size?
 - What are the applications of such properties?
-
-

To understand the properties of nanomaterials and to correlate them with the inherent structure, one needs to analyse several aspects of nanomaterials by a combination of various characterisation techniques, since many of them provide complimentary data. The use of electroanalytical techniques, such as voltammetry, impedance and chronoamperometry, is especially significant to study the intrinsic size and shape dependant redox properties of nanomaterials and their assemblies. The underlying requirement in these techniques is the presence of an electroactive species in the material. Even if the nanomaterials themselves are electrochemically silent, redox-active ligands capping some of these nanoparticles can be used for investigations.

Some of the most widely used electro-analytical techniques for nanomaterials are cyclic and differential pulse voltammetry (CV and DPV, respectively), where the current response is monitored either by applying a potential ramp (CV) or a differential of a tiny potential pulse (DPV) on the sample. Another important technique involves the use of electrochemical impedance, based on the measurement of the response of an electrochemical cell after applying a small amplitude alternating current (AC). It can also give valuable information about surface coverage, dielectric constant, diffusion-coefficient and electron transfer behaviour of MPCs assemblies, both in solution and in the solid state. The response is often analysed using the complex impedance representation and the results are interpreted in terms of suitable equivalent circuits. However, this method has some inherent limitations. In the sections below, we discuss each one of the techniques in some detail with specific emphasis on nano-materials.

6.1 CYCLIC VOLTAMMETRY

Cyclic voltammetry is one of the most versatile and dynamic electroanalytical techniques for the study of electroactive species and their redox events.¹ This technique has the capability of rapidly observing redox behaviour over a wide potential range in diverse solvent-supporting electrolyte combinations. It can be used to study the electrochemical behaviour of species diffusing to the electrode surface, interfacial phenomenon at an electrode surface and bulk properties of materials in or on electrodes.

Accordingly, cyclic voltammetry is a popular member of a family of dynamic electrochemical methods in which the potential applied to an electrochemical cell is scanned. The out put of cell current vs. potential and the flexibility to vary the time scale of the experiment (for example, few mV to thousands of volts per second) to suit the phenomena under investigation is common to all dynamical electroanalytical techniques. A typical three-electrode cell suitable for studies of materials includes a reference electrode, whose potential is known at a given environment, a counter-electrode and working electrode as shown in Fig. 6.1. This figure also shows the basic instrumentation for the modern cyclic voltammetry based on a scanning potentiostat, which controls the potential of a working electrode vs the reference in a pre-designed manner, concomitantly measuring the resulting current as displayed in Fig. 6.2.

The controlling potential applied across these two electrodes could be considered as an excitation signal, which for CV, is a linear potential scan with a triangular or cyclic waveform. A cyclic voltammogram is obtained by measuring the current at the working electrode during the potential scan. The output of cyclic voltammetry is a display of current flowing through the electrochemical cell during the cyclic potential scan. The voltage-current curves are measured in a potentiostatic circuit. In a three-electrode arrangement, the potentiostat controls the potential difference between the working electrode (WE) and the reference electrode (RE), which serves as the basis for keeping the working electrode potential to a predetermined value.

Consider a solution containing electroactive species O with an inert metal as the working electrode. This solution also contains a large concentration, i.e., 0.01M to 1M of supporting electrolyte

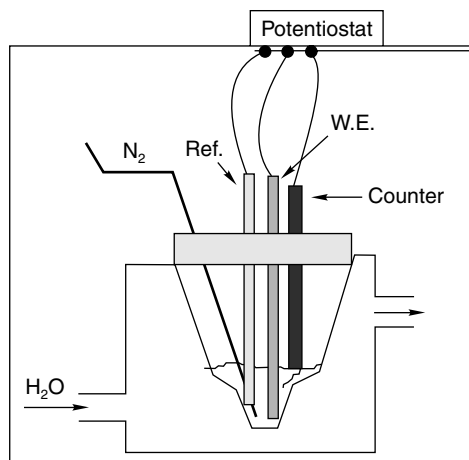
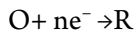


Fig. 6.1 A three-electrode electrochemical system applicable to material characterisation.

to lower the cell resistance and to minimise ionic migration. Suppose that O is reversibly and rapidly reduced.



This reaction is called diffusion-controlled because the cell current is governed by the rate of diffusion of O to the electrode surface. On the other hand, kinetic control may be active if the rate of the electrode reaction is slow with respect to the rate of potential scan. The voltammogram is characteristic with rather unsymmetrical shapes, but equal heights of anodic and cathodic peaks shown in Fig. 6.2. The separation between the peaks at 25°C should be 59/n mV (since 2.303 RT/nF at 25°C is this) as a criterion, measurable by cyclic voltammetry, can be used to decide if an electrode reaction is reversible.

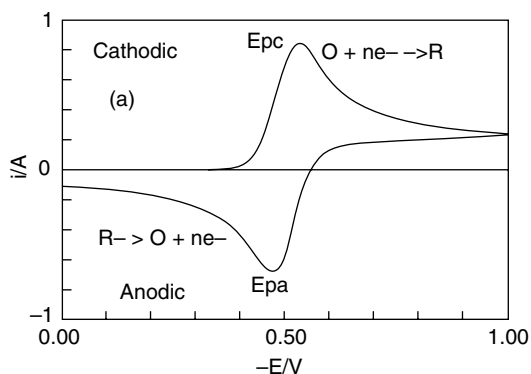


Fig. 6.2 Ideal shape of a cyclic voltammogram for reversible diffusion-controlled electrochemical reactions.

For a reversible system (Nernstian system) the peak current (i_p) is given by the Randles-Sevcik equation

$$i_p = (2.69 \times 10^5) n^{3/2} ACD^{1/2} \nu^{1/2};$$

where 'n' is the number of electrons, 'A' is the electrode area in cm^2 , 'C' is the concentration in mol/cm^3 , D is the diffusion coefficient in cm^2/s and ' ν ' is the potential scan rate in V/s . As we shall see, the screening of some materials by cyclic voltammetry requires preparation of a thin film of materials of interest on a working electrode. Suppose such a thin film contains O. At very low scan rates achievement of so-called thin layer conditions at this coated working electrode is characterised by a symmetric cyclic voltammogram peak shape shown in Fig. 6.3. This model applies to adsorbed monolayer on electrodes. Here the peak current (i_p) (in this case) is directly proportional to the concentration of the species on the electrode (ν ; surface concentration) and increases with the square root of scan rate. The peak current ratio (i_{pa}/i_{pc}) is unity for a simple reversible system, regardless of the scan rate we are giving and deviation of this ratio from unity indicates homogeneous kinetics or complication in the electrode kinetics.

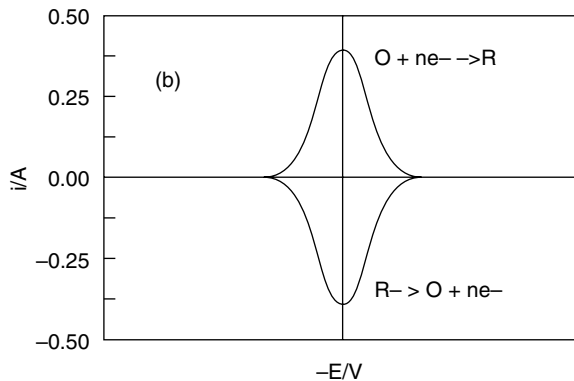


Fig. 6.3 Ideal shape of a cyclic voltammogram for thin layer reversible reactions in a thin film electrochemical reaction.

The potential for a reversible couple is between E_{pa} and E_{pc} .

$$E_0 = E_{pa} + E_{pc}$$

The separation between peak potentials for a reversible couple is given by

$$E_p = E_{pa} - E_{pc} = 59/n \text{ mV}$$

Hence, the peak separation can be used to determine the number of electrons transferred and for a fast one electron process, ΔE_p is about 59 mV. The anodic and cathodic peak potentials are independent of the scan rate, for a single electron transfer, the cyclic voltammogram consists of an anodic and a cathodic peak, but for a multielectron transfer process, it will consist of several distinct peaks, if the E° values for each electron transfer step are successively higher and well separated.

For irreversible systems, the peaks are widely separated and are reduced in size also. For such systems, we can observe the shift in peak potential with scan rate.

$$E_p = E^\circ - \frac{RT}{\alpha n_\alpha F} \left[0.78 - \ln \frac{k^\circ}{D^{1/2}} + \ln (\alpha n_\alpha F v / RT)^{1/2} \right];$$

where ' α ' is the transfer coefficient and ' n_α ' is the number of electrons involved in the charge transfer step.

The peak current is given by the equation

$$i_p = (2.99 \times 10^5) n (\alpha n_\alpha)^{1/2} A C D^{1/2} v^{1/2}.$$

Various electrochemical features of nanoparticles, such as the redox potential (E_0), double layer charging, potential of zero charge (E_{pzc}) can be investigated using cyclic voltammetric measurements, for example, since every metal interface is capable of storing charges and this efficiency of charge storage is expressed in terms of double layer capacitance. Since capacitance is a function of potential whenever a ramp is applied during voltammetry double layer gets either charged or discharged depending on the sign of dE/dt and this is known as double-layer charging or nonfaradiac current. Similarly, the potential, at which interface does not show any excess charge, is known as point of zero charge, which corresponds to the minima in the plot of capacitance against potential. Accordingly, electrochemical properties of Ag, Cu and Au particles have been investigated recently by cyclic voltammetry².

For example, electrochemical behaviour of Au MPCs shows good redox properties in aqueous electrolytes. Cyclic voltammogram of Au MPCs taken at 200mV/s is shown in Fig. 6.4, which shows an

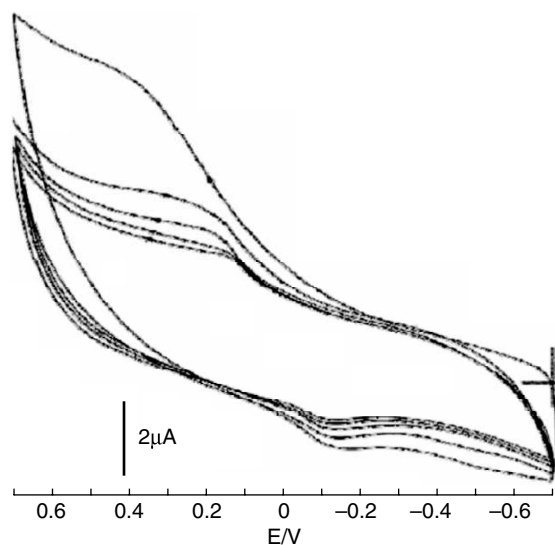
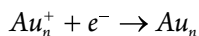
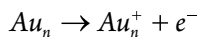


Fig. 6.4 Cyclic voltammogram taken at 200 mV/s in 0.1 M KCl using Au MPCs. Different curves correspond to different cycles and high value of capacitance along with the redox event could be clearly seen.

anodic peak at 0.5 V and a cathodic peak at 0.15 V. The value of $E_{1/2}$ calculated from this voltammogram is 0.325 V. The peak width (FWHM), ΔE of ≈ 60 mV suggests a one-electron process. So, oxidation and reduction peaks occur due to the following reactions.



Similarly, size dependent electrochemical behaviour of silver nanoparticles was also studied using cyclic voltammetry,³ which shows a change in redox potential to negative direction as the size becomes smaller and smaller, especially in the sub 10 nm range.

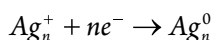
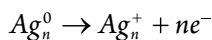


Table 6.1 Size dependent E_{pa} and E_{pc} variation of Ag-DDT nanoclusters

Cluster Type	Size	E_{pa} (V)	E_{pc} (V)	E_p (V)	$E_{1/2}$ (V)
(a)	2	0.096	-0.08	0.176	0.008
(b)	2.6	0.144	-0.08	0.224	0.032
(c)	3.3	0.094	-0.164	0.258	0.350
(d)	4.7	0.150	-0.120	0.270	0.015
(e)	7.2	0.105	-0.087	0.192	0.009

Figure 6.5 shows the size dependent cyclic voltammetric response of dodecanethiol protected silver clusters and the table below shows electrochemical parameters, such as E_{pa} , E_{pc} , E_p and $E_{1/2}$ for 2–7 nm sized DDT capped Ag nanoclusters. From the values of electrochemical parameters described in Table 1, it is clear that as the size of the particle changes anodic as well as cathodic peak potential also changes. Here, the two peaks are formed due to the oxidation and reduction of silver and the anodic peak is more distinct, which suggests that, as prepared particles are more prone to oxidation compared to reduction. Here the anodic and cathodic peaks are due to the following reactions respectively.

$$E^0 [Ag^+/Ag_1] = -1.8V, E^0 [Ag_5^+/Ag_5] = -0.4V, E^0 [Ag_{11}^+/Ag_{11}] = +0.17V$$

6.2 IMPEDANCE ANALYSIS

Electrochemical impedance is another important electroanalytical technique based on the measurement of the response of an electrochemical cell in terms of the resultant ac voltage of a circuit element to the application of an ac current¹. As a voltage signal of any frequency may be applied, the impedance is a function of the frequency, and an impedance spectrum is a representation of the impedance of a circuit element as a function of frequency. Initially, this technique was applied to the determination of the double-layer capacitance and in ac polarography, they are now applied to the characterisation of electrode processes and complex interfaces.

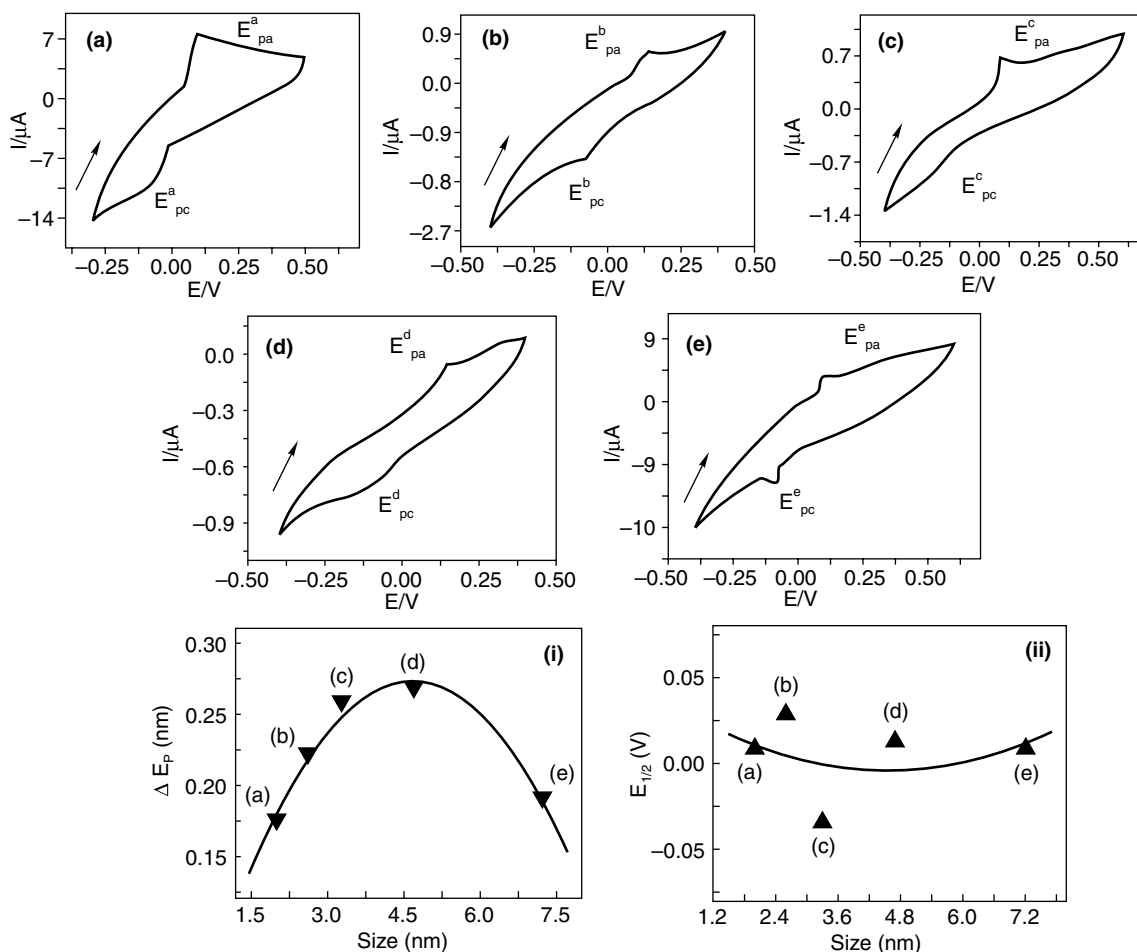


Fig. 6.5 Representative cyclic voltammograms of different sized (2 nm–7.2 nm) DDT protected Ag nanoparticles at 100 mV/s scan rate in 0.1 M aqueous KCl using a modified Pt as working electrode.

The basic concept of impedance is based on Ohm's Law, which defines resistance in terms of the ratio between voltage (E) and current (I).

$$R = \frac{E}{I}$$

Using this relation, we can calculate the resistance, but its use is limited to only one circuit element—the ideal resistor. In real cases, circuit elements exhibit much more complex behaviour, and hence, we cannot use the simple concept of resistance for systems. In its place, we use impedance, which is also a measure of the ability of a circuit to resist the flow of alternating electrical current. Electrochemical impedance is normally measured using a small excitation signal. This is done so that

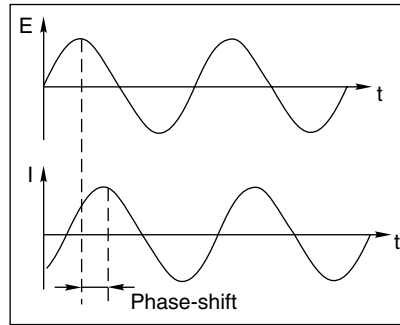


Fig. 6.6 Sinusoidal current responses in a linear system.

the cell's response is pseudo-linear. In a linear (or pseudo-linear) system, the current response to a sinusoidal potential will be a sinusoid of the same frequency but shifted in phase as seen in Fig. 6.6.

The excitation signal, expressed as a function of time, has the form

$$E(t) = E_o \sin \omega t,$$

$E(t)$ is the potential at time t , E_o is the amplitude of the signal, and w is the angular frequency.

$$\omega = 2\pi f$$

In a linear system, the response signal, I , is shifted in phase (Φ) and has different amplitude, I_o :

$$I(t) = I_o \sin(\omega t - \Phi)$$

An expression analogous to Ohm's Law allows us to calculate the impedance of the system as:

$$Z = \frac{E(t)}{I(t)} = \frac{E_o \sin \omega t}{I_o \sin(\omega t - \Phi)} = Z_o \frac{\sin \omega t}{\sin(\omega t - \Phi)}.$$

The impedance is, therefore, expressed in terms of a magnitude, Z_o , and a phase shift, f .

If we are substituting a capacitance for the resistor, then we know that

$$q = CE$$

$$i = C \frac{dE}{dt}$$

$$i = \omega CE_o \cos \omega t$$

$$i = \frac{E}{X_c} \sin\left(\omega t + \frac{\pi}{2}\right);$$

where, X_c is the capacitive reactance and $\pi/2$ is the phase angle. For convenience, the phasors are represented in terms of complex notation. Components along x-axis are real, whereas those along y-axis are imaginary and are multiplied by $j = \sqrt{-1}$.

Then $-jX_c i$

If resistance and capacitance are in series

$$E = i(R - jX_c)$$

$$E = iZ$$

where $Z = R - jX_c$ is known as impedance.

Generally, impedance can be represented as $Z = Z_{\text{Re}} - jZ_{\text{Im}}$, where Z_{Re} and Z_{Im} are the real and imaginary parts of impedance. So when impedance varies with frequency, then real and imaginary parts come into the picture. Usually impedance data can be presented in two-dimensional plots, such as Bode or Nyquist or Cole-Cole plots. In some cases, it can be represented in the form of three-dimensional plots also. Results over a wide frequency range are often conveniently summarised in terms of an equivalent circuit as shown in the inset of Fig. 6.7a, which is an electrical circuit that has identical impedance to the real physical system over the measured frequency range.

If the real part is plotted on the z-axis and the imaginary part on the y-axis of a chart, “Nyquist plot” is obtained. On the Nyquist plot, the impedance can be represented as a vector of length $|Z|$ and the angle between this vector and the x-axis is ϕ . Figure 6.7a shows typical Nyquist plot of Au MPCs. This plot can yield extensive information about the electrified surface and electron transfer reaction. The plot consists of a semicircle region lying on the axis followed by a straight line. The semicircle portion is normally observed at higher frequencies and straight line at lower frequencies. The semicircle portion corresponds to the electron-transfer-limited process (charge transfer) and the straight line is characteristic of mass transfer (diffusion limited) process. So, impedance spectra can be used to study the electron transfer kinetics and diffusion-limited processes. If the electron transfer process is very fast, the impedance spectra will be only the linear part and if it is slow, the spectra will be consisting of semicircular region. The diameter of the semicircle part directly gives the electron transfer resistance, R_{ct} , from which we can calculate the exchange current i_0 and hence rate constant k_0 using the relations

$$R_{ct} = \frac{RT}{Fi_0}$$

$$k_0 = \frac{RT}{n^2 F^2 R_{CT} C}$$

where R_{CT} is the charge transfer resistance, i_0 is the current density, C is the concentration, F is Faraday's constant, n is the number of electrons involved in the reaction. Also double-layer capacitance (C_{dl}) can be calculated using the frequency maxima (ν_{max}) of this semicircle, as

$$[C_{dl} = 1/R_{CT} \nu_{\text{max}}].$$

Also, since the low frequency region of impedance spectra is solely due to diffusion, it can be used to process information about the mass transport features. We can calculate σ from the slope of such plot and using that we can calculate diffusion coefficient D_0 . In particular, the low-frequency component (Warburg impedance),

$$W = \sigma\omega^{-1/2} - j\sigma\omega^{-1/2}$$

$$\sigma = \sqrt{2RT / An^2F^2Dc^{1/2}Cn}$$

If the rate of charge transfer is faster than the rate of mass transfer, the spectra will be consisting of linear part only, but to get R_{ct} from impedance spectra, it will be in the form of a semicircle. For that, we have to design our system in such a way that the rate of charge transfer is slow, so that we can get the spectra in the form of semicircle. Major shortcoming of the Nyquist plots is that it is not possible to identify the frequency, at which the corresponding data was recorded.

Another popular presentation method is the “Bode plot”. The impedance is plotted with log frequency on the x-axis and both the absolute value of the impedance ($|Z| = Z_0$) and phase-shift on the y-axis as shown in Fig. 6.7b.

Many researchers have used impedance as an efficient tool for the characterisation of nanomaterials. For example, Vijayamohan and Coworkers have used this technique for the characterisation of AuMPCs and they have calculated k_o and C_{dl} as 7.97×10^{-6} cm/s and $2.4 \mu\text{F}/\text{cm}^2$, respectively.

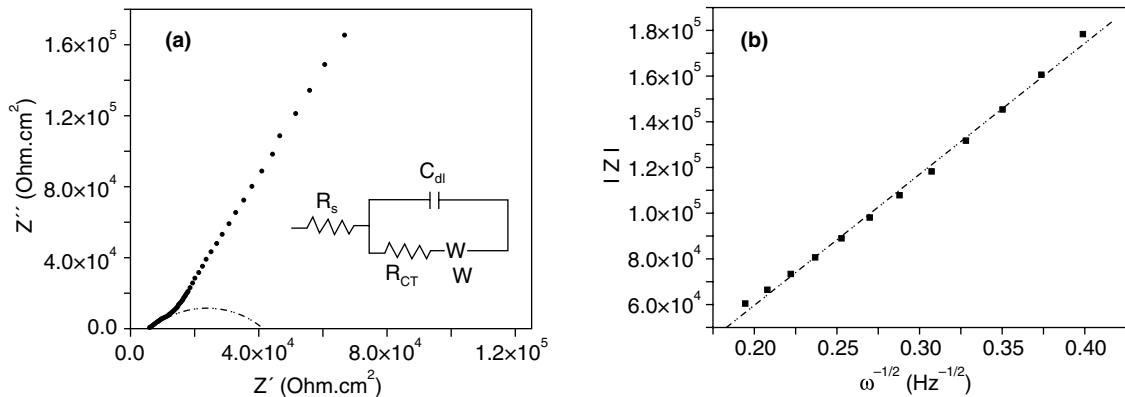


Fig. 6.7 (a) Complex plane impedance plot of Au MPCs, and inset of the simplest linear equivalent circuit for a metal-solution interface consists of double-layer capacitance (C_{dl}), charge transfer resistance (R_{CT}), solution resistance (R_s) and Warburg impedance (W). (b) Diffusion coefficient is estimated from the slope (σ) of the linearly fitted modulus of the real and imaginary parts of impedance.

Impedance measurements can give valuable information about surface coverage, dielectric constant, conductivity, concentration of carrier, and not: diffusion coefficients and electron transfer behaviour of nanomaterials both in solution and in the solid state. Eventhough it is a very sensitive technique, interpretation of impedance is difficult. Also unique equivalent circuit cannot be used and change in the impedance model with frequency makes this technique more complicated. Also EIS cannot give all the answers. It is a complementary technique and other methods must also be used to elucidate the interfacial processes.

6.3 DIFFERENTIAL PULSE VOLTAMMETRY

Differential pulse voltammetry (DPV) can provide quantitative information about electrochemical mechanisms as well as providing a basis for electroanalytical measurements^{5,6}. The technique involves application of the potential waveform (Fig. 6.8) and current is measured just before and just after the application of each pulse, as shown, and the difference between the current is plotted against the potential prior to the pulse. This gives rise to peak-shaped voltammograms and the height of the peak is directly proportional to the concentration of the corresponding species.

Height of the peak is given by the equation

$$(\delta i)_{\max} = \frac{nFA D \sigma^{1/2} C_0}{\pi^{1/2} (\tau - \tau')^{1/2}} \left(\frac{1 - \sigma}{1 + \sigma} \right)$$

n = no. of electrons

A = area

D = diffusion coefficient

C = concentration

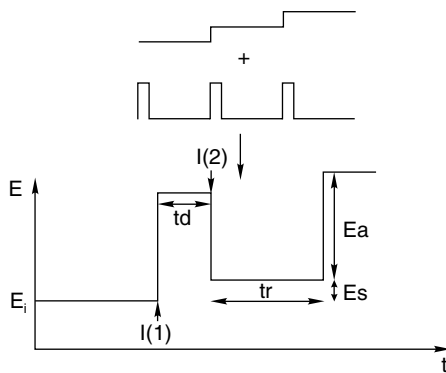


Fig. 6.8 Schematic diagram defining the potential wave form in a differential pulse voltammetry experiment. E_a is the amplitude of the applied pulse; E_s is the size of the step, t_d the duration of the pulse, t_r the time between pulses, E_i the initial potential. $I(1)$ and $I(2)$ indicate the times, at which the current is sampled, the difference being plotted against the potential prior to the application of the pulse.

Cyclic voltammetric technique can also give valuable information about electrochemical reactions, but since DPV allows discrimination between the faradaic and charging currents, it is more advantageous for measuring faradaic current as compared to that of cyclic voltammetry. The monolayer-protected metallic and semiconducting Q-dots show a multivalent redox property due to their sub-attofarad charge storage capability. This is prevalently known as single-electron transfer or quantised double-layer charging (QDL).⁷ These Q-dots show consecutive single-electron

charging in the voltammetric experiments as current peaks at an equal potential interval ($DV=e/C_{CLU}$; charging energy, $E_c > k_B T$).

The capacitance, C_{CLU} is associated with the ionic space charge formed around each Q-dot dissolved in the electrolyte solution, where the electrostatic (i.e., double layer) principles govern the electronic charging of the core. For example, the QDL charging has been reported for both metal (i.e., Au, Ag, Cu, and Pd) and semiconductor (i.e., CdS, PbS, Si, etc.) Q-dots and such behaviour has been studied using DPV. Majority of the studies have been concerned with smaller-sized Au Q-dots due to their enhanced stability.

If we assume that electron transfers is fast, the SET charging reactions of MPCs follow the Nernst relation and that each SET can be assigned a 'formal potential'. The formal potentials of these charging events are described by

$$E_{z/(z-1)}^{\circ} = E_{PZC} + \frac{(Z-1/2)e}{C_{CLU}}$$

where $E_{z/(z-1)}^{\circ}$ is the formal potential of the $z/(z-1)$ charge state couple and corresponds experimentally to DPV peak potential. z is signed such that $z > 0$ and $z < 0$ correspond to core 'oxidation' and 'reduction', respectively, and C_{CLU} is the capacitance of the MPC. The formal potentials of the charging peaks are referenced to the potential of zero charge (E_{PZC}) of the MPC. The above equation predicts a linear plot of $E_{z/(z-1)}^{\circ}$ versus charge state (popularly known as "Z plot"), which can be used to determine C_{CLU} from the slope. The QDL behaviour of larger-sized Au Q-dots (ca. $D=3.72 \pm 0.4$ nm) protected with dodecanethiol (DDT) have been investigated by Chaki *et al.*⁸ Figure 6.9 shows the representative DPV response of larger-sized Au Q-dots revealing 14 consecutive discrete single-electron charging events in both the (Fig. 6.9a) anodic and (Fig. 6.9b) cathodic scans. Figure 6.6b represents the Z plot for Au Q-dots in both the anodic and cathodic directions, respectively, where linear behaviour is due to ideal QDL behaviour. The capacitance (C_{CLU}) values calculated from the slopes of the Z plot (Fig. 6.9c) are 1.57 and 1.68 aF for the anodic and the cathodic scans, respectively. Recently Vijayamohan and co-workers have reported the single-electron charging features of RhMPCs stabilised with TDA and they have calculated C_{CLU} (1.93 aF) using DPV. Also, the core diameter of the nanoparticles can be calculated by using DPV, utilising the fact that the highest occupied molecular orbital (HOMO)–lowest unoccupied molecular orbital (LUMO) energy difference, corresponding to the differences in DPV peaks is related to the size and composition of the nanoparticle, assuming that the particle has a spherical geometry⁹.

6.4 SCANNING ELECTROCHEMICAL MICROSCOPY

Scanning electrochemical microscope is a "chemical microscope" that has a response based on mass transfer and chemical ratio at the scanning tip and the sample. Although the resolution of this technique, currently of the order of 100 nm, does not approach that of STM and AFM, it is useful in obtaining topographic and chemical information about a wide range of sample surfaces, including electrodes, polymers, and biological materials.

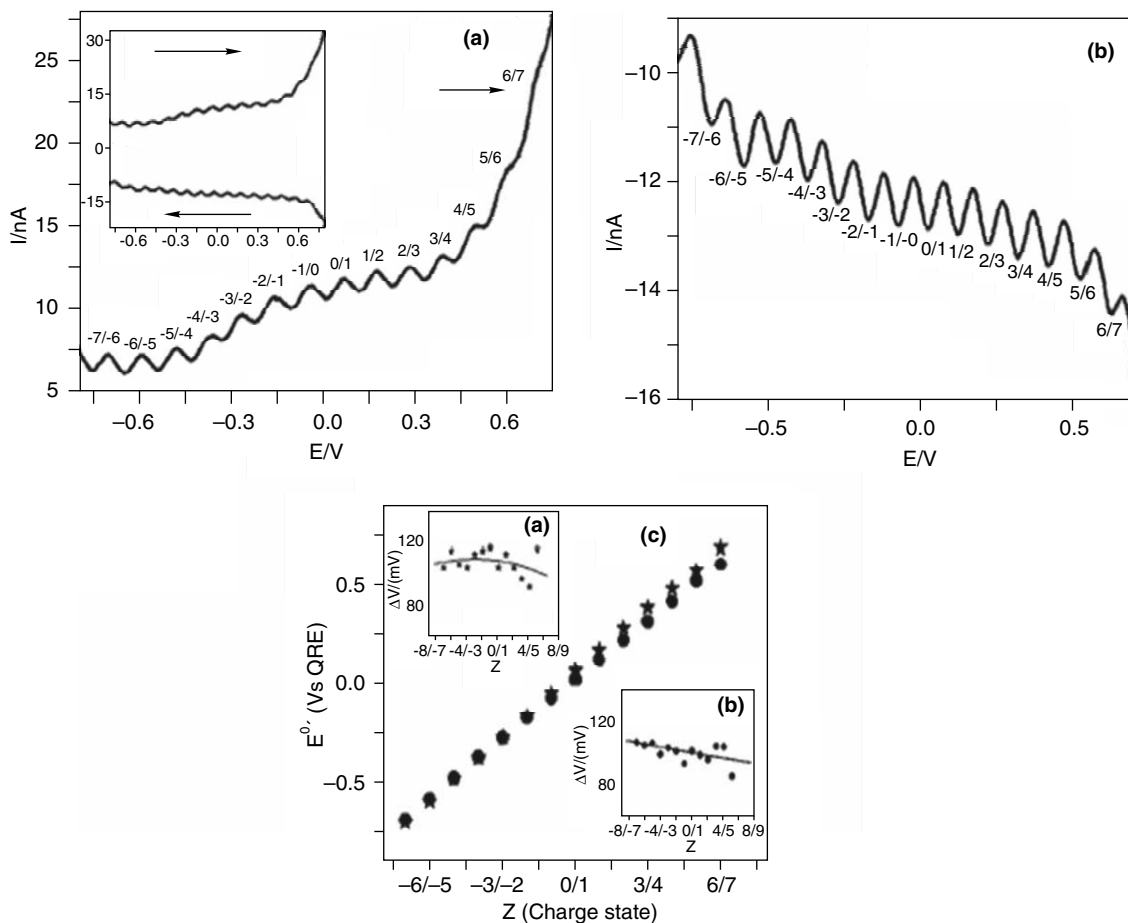


Fig. 6.9 Representative DPV response of $(3.72 \pm 0.4 \text{ nm})$ Au Q-dots, (a) anodic and (b) cathodic scan directions, respectively, (c) superimposed Z plots of E_0 vs redox couple-charge state ($Z/Z \pm 1$) in either scan directions [anodic and cathodic], revealing the expected linearity; insets (a) and (b) show the plot of ΔV vs charge state in both the anodic and cathodic scan directions, respectively, revealing more regular voltage spacing at a negative potential.

6.4.1 Basic Principles

The tip and sample are immersed in a solution that contains an electro-active species represented by Ox. The tip is one electrode in an electrochemical cell, that includes a reference electrode and an auxiliary electrode, the experimental setup is shown in Fig. 6.10. The sample, if it is a conductor or semiconductor, can also be connected as an electrode in the cell, although frequently it is not. Insulators, including minerals and biological samples, are not part of the electrochemical cell circuit and are simply positioned beneath the tip.

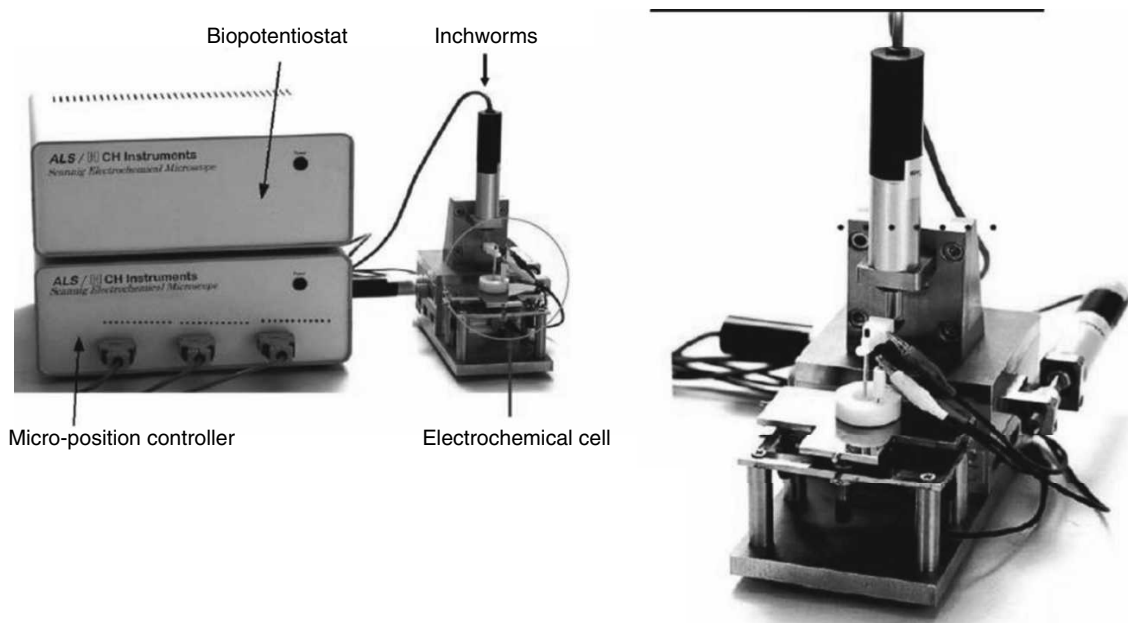


Fig. 6.10 Experimental set-up for carrying out scanning electromechanical microscopy (reprinted with permission from ALS/HCH Instruments, BAS Co Ltd).

To understand how the SECM operates, it is useful to review briefly the principles of the electrochemical cells and the behaviour of very small electrodes [so-called ultra microelectrodes (UMEs)]. An UME is a conductive disc, frequently Pt, with a diameter of 0.1 to 25 μm that is embedded in an insulating sheath. When the potential of the UME (also called “the tip”) is adjusted by the external circuit (the bipotentiostat) with respect to the reference electrode to a sufficiently negative value, the species Ox is reduced at the disc surface as per the electrode reaction, $\text{Ox} + n\text{e} \rightarrow \text{Red}$. The circuit diagram along with the schematic of working electrode reaction and i - t transient are shown in Fig. 6.11.

This results in current flow, i_T the current is characterised by a transient, the duration of which depends on the UME disk diameter that decays to a steady state value, $i_{T,\alpha}$. The steady state current is governed by the mass transfer (flux) of Ox in solution to the UME, and is given by

$$i_{T,\alpha} = 4nFCDa$$

where, F is faraday’s constant, C is the concentration of Ox in solution, D is its diffusion coefficient, and a is the diameter of the UME disk.

The above equation holds when the UMS is positioned “far” (that is several disk diameters) away from the surface. When it is closer to a sample surface, the measured current is different from $i_{T,\alpha}$. Near an insulator, the diffusion of Ox to the tip will be partially blocked, so that $i_T > i_{T,\alpha}$, approaching zero at very small separations. This decrease in current is called “negative feedback”. On the other hand, when the tip is close to a conductive surface, the species produced at the tip surface, red, can diffuse

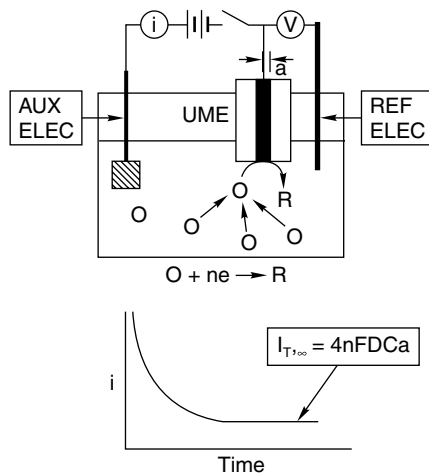


Fig. 6.11 Schematic of circuit diagram along with i - t transient of a ultramicroelectrode having diameter in the order of 0.1 to 25 μm .

to the surface and be oxidised back to Ox. When this occurs, the flux of Ox to the tip is increased, and $i_T < i_{T,\alpha}$, which is called “positive feedback”. Thus the ratio $i_T / i_{T,\alpha}$ is a measure of distance, d , between tip and substrate and an indicator of the nature (insulating or conducting) of the sample.

The UME tip is moved, with nanometer resolution, in the x - y plane by attached piezoelectronic elements (Fig. 6.1), just as in STM. These elements as well as the bipotentiostat are controlled by a personal computer, which records i_T as a function of tip position.

6.4.2 SECM Imaging

The plot of i_T as a function of tip position in the x - y plane is the SECM image. This image can be converted to a plot of d versus x - y position or plotted as a gray-scale image, for example, where high values of i_T are shown as light colours and small values as dark colours. Images of many different types of samples, including electronically conducting polymers, metal electrodes, ionomeric polymers and semiconductors have been obtained with SECM. The resolution attainable with the SECM is largely governed by the diameter of the scanning tip and the distance between tip and sample d , with a very small diameter tip moved in close proximity to the surface (that is $d/a=0.1$). For a < 100 nm, scanning at 10 nm above the surface and measuring the current becomes difficult, because stray vibrations and irregularities in the surface can cause a “tip crash”. Thus, for high resolution, the SECM must be operated in the constant current mode, as is often used with the STM, where d is adjusted by a feedback loop to the z -piezo to maintain i_T constant.

6.4.3 Imaging Surface Reactivity

The designation given above for samples as conductive and insulating types actually represent limiting conditions and implies that the rate of electron transfer at the sample surface is either very fast (diffusion

controlled) or essentially zero, respectively. However, intermediate rates for the electron transfer (ET) is also possible. Accordingly, the schematic representation of the SECM experiment for three different conditions including (a) steady-state diffusion to the tip far from substrate; (b) tip is near a conductive substrate (positive feedback); and (c) tip is near an insulating substrate (negative feedback) are shown in Fig. 6.12. Under these conditions, the feedback current has a value between two extremes and this predicts the rate constant of the reaction, k , at the substrate surface using standard kinetic models. One area of interest is the examination of electrode surfaces, where the rate of an electron transfer reaction is often a function of the nature of the electrode material. For example, the standard heterogeneous rate constant for the oxidation of Fe^{2+} to Fe^{3+} is fairly rapid on Pt or Au, but is quite slow on carbon. SECM imaging could be done either in the feedback mode or in the tip-generation substrate collection (TG/SC) mode. The former method exploits the sensitivity of the SECM feedback current to the substrate-mediator turnover rate, while the latter is for analysing systems involving irreversible reactions.

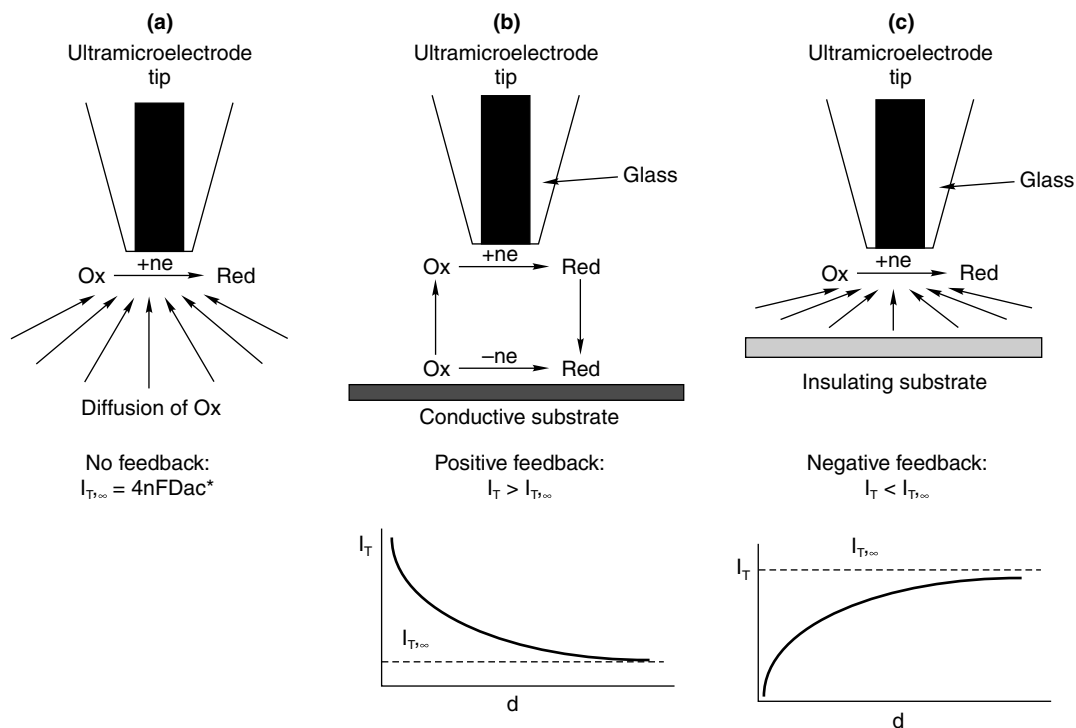


Fig. 6.12 Schematic representation of the SECM experiment. (a) Steady-state diffusion to the tip far from substrate. (b) Tip is near a conductive substrate, called positive feedback. (c) Tip is near an insulating substrate, called negative feedback.

In the feedback imaging process, with appropriate choice of a mediator or substrate potential or both, it is possible to image variations in turnover activity, this technique is known as reaction-rate imaging. At a conducting substrate, variations in the ET rate may arise because of the presence of

catalytic particles or defect site; alternatively, the electrode may be passivated by adsorbate or blocking layers. Recently, the $H^+ / \frac{1}{2}H_2$ couple has been used as a mediator in SECM to study the H_2 oxidation activity of PEFC anode catalysts^{10, 11}. This couple is especially convenient for SECM, because the addition of no other redox species is required. On the other hand, the TG/SC imaging method has been demonstrated to be useful to study O_2 reduction kinetics.

The steady-state current at microelectrodes for hydrogen evolution from strong and weak acids has been studied recently by Mirkin *et al.*¹² They found that the chemical step for proton discharge is usually kinetically controlled in weak acids, whereas a steady-state current controlled by proton diffusion is found for strong acids.

REFERENCES

1. A.J. Bard and L.R. Faulkner, *Electrochemical Methods, Fundamentals and Applications*, (Ed.) John Wiley & Sons, New York, (2001).
2. M. Aslam, N.K. Chaki, Jadab Sharma and K. Vijayamohan, *Curr. Appl. Sci.*, 3, (2003), 115.
3. N.K. Chaki, J. Sharma, A.B. Mandle, I.S. Mulla, R. Pasricha and K.Vijayamohan, *Phys. Chem. Chem. Phys.*, 6, (2004), 1304.
4. N.K. Chaki, Poonam Singh, C.V. Dharmadhikari and K. Vijayamohan, *Langmuir*, 20, (2004), 10208.
5. H.E. Keller and R.A. Osteryoung, *Anal. Chem.*, 43, (1971), 342.
6. J. Tong, X.J. Dang, H.L. Li and M. Yang, *Anal. Lett.*, 30, (1997), 585.
7. (a) R.S. Ingram, M.J. Hostetler, R.W. Murray, T.G. Schaaff, J.T. Houry, R.L. Whetten, R.L. Bigioni, D.K. Guthrie and P.N. First, *J. Am. Chem. Soc.*, 119, (1997), 9279. (b) J.J. Pietron, J.F. Hicks and R.W. Murray, *J. Am. Chem. Soc.*, 121, (1999), 5565
8. N.K. Chaki, B.A. Kakade, J. Sharma, S. Mahima and K. Vijayamohan, *J. Appl. Phys.*, (2004), 5032.
9. Bhalchandra A. Kakade, Shashidhar Shintri, Bhaskar Sathe, S.B. Halligudi and Vijayamohan K. Pillai. *Adv. Mater*, 19, (2007), 272.
10. J. Zhou, Y. Zu and A.J. Bard, *J. Electroanal. Chem.*, 491, (2000), 22.
11. K. Jambunathana, B.C. Shah, J.L. Hudson and A.C. Hillier, *J. Electroanal. Chem.*, 500, (2001), 279.
12. M.V. Mirkin, T.C. Richards and A.J. Bard, *J. Phys. Chem.*, 97, (1993), 7672.
13. (a) A.W. Adamson and I. Ling, *Adv. Chem. Ser.*, 43, (1964), 57. (b) T. Young, *Miscellaneous Works*; Peacock, G.; Ed.; Murray: London, 1, (1855), 418.
14. D.H. Jung, I.J. Park, Y.K. Choi, S.B. Lee, H.S. Park and J. Ru "he, *Langmuir*, 18, (2002), 6144.
15. (a) K.K.S. Lau, J. Bico, K.B.K. Teo, M.Chhowalla, G.A.J. Amaratunga, W.I. Milne, G.H. McKinley and K.K. Gleason, *Nano Lett.*, 3, (2003), 1701. (b) L. Feng, S. Li, Y. Li, H. Li, L. Zhang, J. Zhai, Y. Song, B. Liu, L. Jiang and D. Zhu, *Adv. Mater*, 14, (2002), 1857.
16. (a) Sze, S.M. VLSI Technology, AT&T Bell Laboratories, Murray Hill, New Jersey. (b) Wieder, H.H. "Four Terminal Nondestructive Electrical and Galvanomagnetic Measurements," in *Non-destructive Evaluation of Semiconductor Materials and Devices* (J.N. Zemel, ed.), Plenum Press, New York, (1979), 67-104.

17. (a) G. Blaser, T. Ruhl, C. Diehl, M. Ulrich and D. Kohl, *Phys. A.*, 266, (1999), 218. (b) J.H. He, C.S. Lao, L.J. Chen, D. Davidovic, Z.L. Wang, *J. Am. Chem. Soc.*, 127, (2005), 16376.

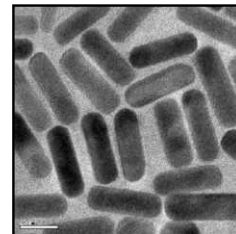
ADDITIONAL READING

1. Christophe Demaille, Mathias Brust, Michael Tsionsky, and Allen J. Bard "Fabrication and Characterisation of Self-Assembled Spherical Gold Ultramicroelectrodes", *Anal. Chem.*, 69, (1997), 2323–28.
2. Jiirgen Heinze, "Ultramicroelectrodes in Electrochemistry", *Angew Chem. Int. Ed. Engl.*, 32, (1993), 1268–88.
3. A.J. Bard, G. Denuault, C. Lee, D. Mandler and D.O. Wipf, *Acc. Chem. Res.*, 23, (1990), 357–63.

REVIEW QUESTIONS

1. What is the primary requirement for characterising a nanomaterial by electrochemistry?
2. What is the role of potentiostat in cyclic voltammetric experiment?
3. Why does SECM need the use of a bipotentiostat?
4. How can EIS measurements provide information about surface coverage and electron transfer behaviour in case of MPCs?
5. What are the diagnostic criteria for identifying a reversible chemical change voltammetrically?
6. How will you justify the fact that nanoparticles behave differently from their bulk form by means of electrochemistry?
7. Why only a small AC perturbation is applied in case of EIS techniques?
8. Why contribution of non-faradic current is less in case of differential pulse voltammetry (DPV)?
9. Discuss the role of UMEs in nanoelectrochemical studies?
10. What are the the limitations of Electrochemical methods in characterising nanomaterials?

RAMAN SCATTERING



“The only difference between a problem and a solution is that people understand the solution.” Charles F. Kettering

Charles F. Kettering: A Biography, Thomas Alvin Boyd (1957)

Interaction of light with matter is one of the most important aspects to understand the world around us. Light, in general, and laser light, in particular, acts as a powerful tool to unveil new information from materials, especially at the level of nanoscale. Laser Raman scattering is one such interaction between light and matter, which can reveal interesting properties of entities, such as molecules and materials with a good degree of accuracy. Over the years, this technique has evolved as one of the most pivotal methods to characterise nanomaterials and has become a vital tool for today’s nano-science and -technology. This chapter introduces the basic aspects of Raman scattering and unveils a window for further exploration.

Learning Objectives

- What is elastic and inelastic light scattering?
 - What is Raman scattering?
 - What is the difference between linear and non-linear Raman scattering?
 - What are the applications of Raman scattering?
-
-

7.1 WHY IS THE SEA BLUE?

It is well known in the history of science that the study of some natural phenomenon has been the starting-point in the development of a new branch of knowledge. One such example is the following. In 1919, Sir C.V. Raman was studying the phenomenon of diffraction and molecular light scattering, especially in the context of liquids. His interest in this topic was aroused by an interesting experiment¹: a beam of white light was passed through a tank containing a solution. Certain chemicals were then added to this solution so that it gradually changed from a clear liquid into a turbid one. This was due to the production of particles, which then remained suspended in the liquid. Naturally, the intensity

of the transmitted light decreased as the turbidity increased, and at one stage, the light was almost cut off. Interestingly, it was found that with the further passage of time, not only the intensity of the transmitted light increased, but also its colour went through a series of changes—indigo, blue, blue-green, greenish-yellow, and finally white. Why did such a thing happen? An explanation was necessary. Lord Rayleigh was able to explain the initial decrease in intensity of the transmitted light, but had no answer for the strange appearance of colours later. Raman was able to explain this. First, he considered the way the light wave is diffracted by the individual particles, and then how these different diffracted waves combined together, either constructively or destructively, to produce an overall effect. There was one more intriguing question: What if the diffraction is not by a suspended particle but by a molecule? In 1921, Raman was returning to India via sea after his first ever visit abroad. He was fascinated by the deep blue colour of the Mediterranean and began to wonder why the sea is blue.² Earlier, Lord Rayleigh, who had successfully explained the blue colour of the sky had declared³, “The much-admired dark blue of the deep sea has nothing to do with the colour of water, but is simply the blue of the sky seen in reflection.” In short, the sea is blue, because it is merely reflecting the blue sky—this was Lord Rayleigh’s explanation. Raman was not satisfied with this explanation and further investigated this matter in detail.⁴ His observations revealed the following: (i) light can be scattered by the molecules of water just as it can be by the molecules of air, and (ii) that the blue colour of the sea is due to such molecular scattering just as the blue of the sky is. In his seminal paper on the molecular scattering of light⁴, Raman concluded the following: “In this phenomenon, as in the parallel case of the colour of the sky, molecular diffraction determines the observed luminosity and in great measure also its colour.” Raman thus proved that the sea is blue because the molecules of water scatter light just the same way molecules of air do. This was an important result, which not only disproved Lord Rayleigh’s explanation, but also had further implications in understanding the interaction of light with molecules, especially in the context of Raman effect.

7.2 CONCEPT OF ELASTIC AND INELASTIC LIGHT SCATTERING

When light of certain frequency ν , scatters off a molecule or a material, the outgoing radiation will have three components: ν , $\nu + \Delta\nu$ and $\nu - \Delta\nu$, where $\Delta\nu$ is the change in the frequency of radiation as a result of energy gained or lost by the radiation due to its interaction with matter. Here, ν is the elastic component, and, $\nu + \Delta\nu$ and $\nu - \Delta\nu$ are the inelastic components of the scattered light. The elastic component, which remains unperturbed in terms of energy, is called as Rayleigh scattering. In the context of molecules and materials, there are different physical phenomena which results in inelastic light scattering, and one such phenomenon is the Raman scattering, in which, the $\nu - \Delta\nu$ component of radiation is called the Stokes shift and $\nu + \Delta\nu$ component is called the anti-Stokes shift.

7.2.1 Raman Scattering

With the historical perspective, the Raman scattering was already predicted on theoretical grounds⁵ in 1923. The first observations of the phenomenon were made in liquids⁶, and then in crystals⁷. First, we shall give you the classical explanation of Raman scattering. When a molecule is placed in a static electric field \mathbf{E} , the positively charged nuclei and the negatively charged electrons are spatially distorted.

The molecule is now polarised and the separation of charges creates an induced dipole moment, \mathbf{P} . The induced dipole moment of a molecule depends upon the applied electric field and is given by the relation

$$\mathbf{P} = \alpha \mathbf{E}; \quad (1)$$

where, α is the polarisability of the molecule. In its general form, both \mathbf{P} and \mathbf{E} are three-dimensional vectors and α is a tensor, whose components can be represented as elements of a matrix. Now, consider molecules subjected to electromagnetic radiation of frequency ν with an oscillatory electric field of magnitude given by

$$E = E_0 \sin 2 \pi \nu t; \quad (2)$$

This results in an oscillatory induced dipole moment whose magnitude is

$$P = \alpha E = \alpha E_0 \sin 2 \pi \nu t \quad (3)$$

This oscillation in dipole moment leads to secondary radiation, which is termed as Rayleigh scattering and represents the elastic scattering component. Since the molecules have internal degrees of freedom, like vibration or rotation, which modulate the polarisability periodically, the oscillating dipole will be a superposition of varying electric field and polarisability. In such a case, the magnitude of polarisability vector is given by

$$\alpha = \alpha_0 + \beta \sin 2 \pi \nu_{\text{vib}} t; \quad (4)$$

where, α_0 is the equilibrium polarisability, β is the rate of change of polarisability and ν_{vib} is the vibrational frequency of the molecule. In such a situation, the induced dipole moment is given by

$$P = \alpha E_0 \sin 2 \pi \nu t + \frac{1}{2} \beta E_0 \{ \cos 2 \pi (\nu - \nu_{\text{vib}}) - \cos 2 \pi (\nu + \nu_{\text{vib}}) \}. \quad (5)$$

The above equation indicates that the oscillating dipole has three frequency components, ν , $\nu - \nu_{\text{vib}}$ and $\nu + \nu_{\text{vib}}$. The component $\nu - \nu_{\text{vib}}$ and $\nu + \nu_{\text{vib}}$ are called as Stokes and anti-Stokes lines, respectively. They represent the inelastic components of the scattered radiation. It should be noted that if the vibration does not alter the polarisability of a molecule, then $\beta = 0$, and the dipole moment oscillates only with frequency of incident radiation. Therefore, for a vibrational mode to be Raman active, change in the component of molecular polarisability is a prerequisite.

Although classical theory of Raman scattering explains the origin of Stokes and anti-Stokes lines, it does not account for their differences in intensity. According to the basic principles of quantum mechanics, the energy states associated with electronic, vibrational and rotational degrees of freedom of a molecule can assume only a discrete set of values. The energy states are characterised by a specific set of quantum numbers describing the level of excitation of each quantised degree of freedom, and by a corresponding wave function. Figure 7.1 shows a schematic of the energy levels involved in the process of light interacting with a molecule. Raman scattering, fluorescence and resonant Raman scattering mechanisms are represented. Here, the virtual state refers to a transition state, which does not correspond to an eigen state of the molecule; so it is only an imaginary state, a practical convenience to represent the energy exchange between the radiation field and the molecule.

Resonant Raman scattering occurs only when the virtual state overlaps with one the eigen states of a molecule (here an electronic eigen state), whereas in infrared absorption or emission, there is a direct transition between vibrational energy levels, most often between the vibrational ground state

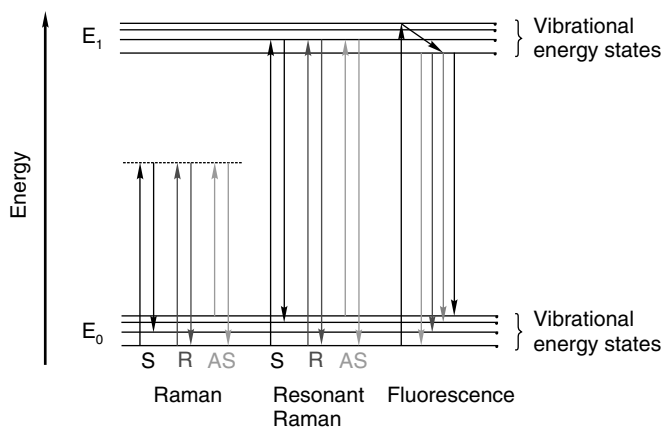


Fig. 7.1 Energy level diagram comparing Raman, resonant Raman scattering and Fluorescence. The symbols: S, R and AS represent the Stokes, Rayleigh and anti-Stokes lines, respectively. It is to be noted that the intensity of Rayleigh light > intensity of fluorescence > intensity of Raman scattering.

and the first excited state. In contrast to this, both Rayleigh and Raman scattering involve two, almost simultaneous transitions proceeding via virtual states, in which one photon of the incident radiation is absorbed and another photon, either of the same energy (Rayleigh scattering) or of lower energy (Stokes Raman) or high energy (anti-Stokes Raman) is emitted. A typical Raman spectrum of a molecule with Rayleigh, Stokes and anti-Stokes component is displayed in Fig. 7.2. It is to be noted that although the band structures of Stokes and anti-Stokes lines are identical, their intensities are different (Stokes > anti-Stokes). This is because, under equilibrium, the population of molecules in the

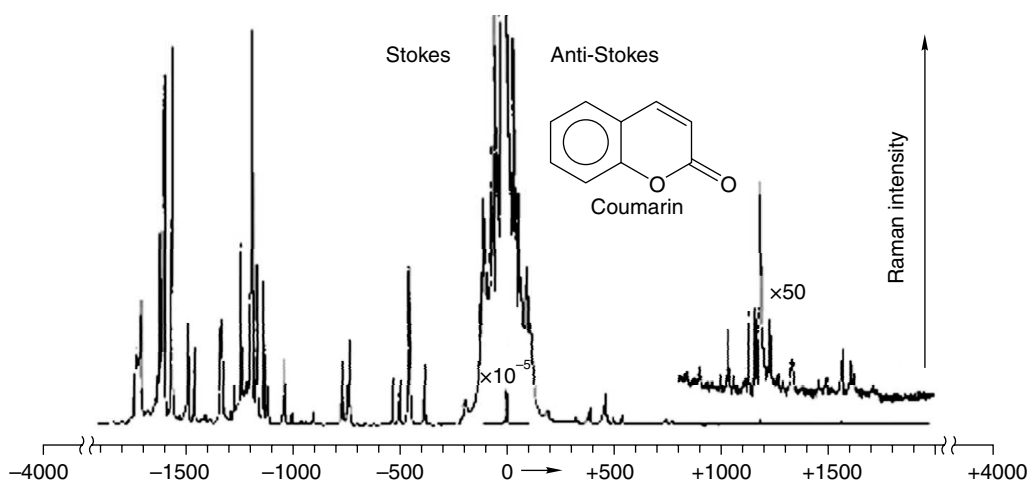


Fig. 7.2 Raman spectrum of a molecule (coumarin) showing Rayleigh (center), Stokes and anti-Stokes components.

excited state will always be lesser than the population of ground states, which further influences the intensities of Stokes and Anti-Stokes lines. Also, note that in Fig. 7.2 the intensity of the Rayleigh line at the centre of the spectrum is far greater than the other two components.

Conventionally, Raman spectrum of a molecule or a material is represented by its Stokes component (greater intensity), and along the abscissa of the spectrum, the positive values of the Raman shift are marked.

7.2.2 Intensity Ratio of Stokes to Anti-Stokes line

Under equilibrium, the population of molecules in ground state (N_{ground}) will always be greater than the excited state (N_{excited}) and are related to each other by Boltzmann equation:

$$N_{\text{excited}} \propto N_{\text{ground}} \exp(-\Delta E/k_B T); \quad (6)$$

where ΔE , k_B and T are the energy difference between the states, Boltzmann's constant, and temperature, respectively. As the intensity of Stokes and anti-Stokes lines are directly dependent on the population of molecules in ground and excited state, respectively, they are related to each other as follows:

$$I_{\text{anti-Stokes}} \propto I_{\text{Stokes}} \exp(-\Delta E/k_B T). \quad (7)$$

It can be observed that for a known mode of vibration (ΔE), one can measure the ratio of intensities of Stokes and anti-Stokes lines to obtain the local temperature of a sample. This is one of the logical consequences, which can be harnessed as local temperature probes of nanomaterials, especially in the context of confined heating as observed in plasmonic nanoparticles.⁸

7.3 INSTRUMENTATION FOR RAMAN SCATTERING

In recent years, as a result of advances in optical instrumentation technology, significant progress has been achieved in Raman spectroscopy instrumentation. Molecules and materials can be effectively characterised using modern-day Raman microscopes (these are instruments in which the Raman spectrum is used to image a material in two or three dimensions). A few vital aspects of a typical Raman microscopy system will be discussed here. Figure 7.3 shows a schematic of a conventional, upright, Raman microscopy system.

A Raman excitation light from a solid-state laser (such as frequency-doubled Nd-YAG laser), or a gas laser (such as He-Ne laser) traverses through a band pass filter and enter the input port of an upright microscope. In order to divert the laser beam towards the sample, a dichroic mirror (DM) is used. The incident light is tightly focused on to a sample using a high numerical aperture objective lens (O). The role of an objective lens is two-fold: incidence of laser light and collection of the backscattered light. Depending upon the sample type, different kinds of objective lenses are used. For solid, dry samples, such as single crystals, powders, substrates, etc., a high numerical aperture, dry objective lens serves the purpose, whereas for aqueous samples, such as nanoparticle solutions, biological cells, etc., a water-immersion objective lens can be used. It is to be noted that the collection efficiency of Raman scattering significantly depends on the kind of objective lens used. Next, the backscattered light collected by the objective lens passes through an edge filter (EF) placed at the output port of the microscope. The role of an edge filter is to reject the intense Rayleigh scattered light from the

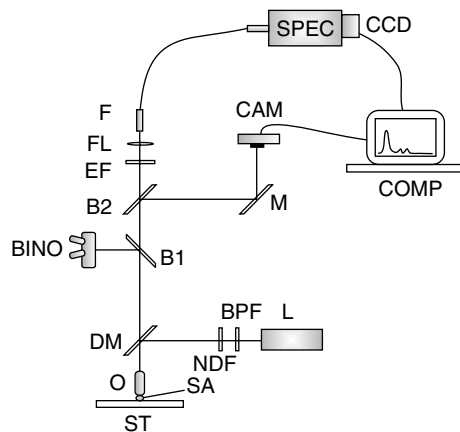


Fig. 7.3 Schematic of a micro-Raman system built using a simple viewing microscope with an epi-fluorescent attachment. ST–stage; SA–sample; O–Objective lens; L–laser; BPF–Band pass filter; NDF–neutral density filter; SM–special mirror; B1 and B2–beam splitters; M–mirror; BINO–binocular; EF–edge filter; FL–focusing lens; F–optical fiber; SPEC–spectrometer; CCD–Charged Coupled Device; COMP–computer; CAM–camera.

collected signal. Edge filters allow only the Stokes component of the Raman spectra, whereas a notch filter allows both Stokes and anti-Stokes component of the scattered light. The filtered light is now focused on to an optical fiber (F). The other end of the optical fiber is f-number matched to a Raman spectrograph. The spectrograph has a computer-controlled adjustable slit and a turret, which holds three gratings for a range of measurements. Different gratings and slit widths are chosen depending upon the needs of spectral resolution. Most of the Raman spectrographs have 3 kinds of gratings with $600 \text{ grooves mm}^{-1}$ or $1200 \text{ grooves mm}^{-1}$ or $1800 \text{ grooves mm}^{-1}$. Higher the number of grooves, greater will be the spectral resolution and lesser will be the throughput. Finally, the captured light reaches the CCD camera, which converts the light signals into electronic signals for further processing. A digital camera atop the microscope allows for registration of the focused laser spot and simultaneously captures the optical image and video. In order to perform Raman mapping, samples are placed on a computer-controlled X-Y-Z translational stage and signal is collected along X, Y and Z axis of the sample. Further, the translational stage co-ordinates with the CCD camera to reconstruct a spatially resolved Raman map.

7.4 SPECIFIC EXAMPLES OF RAMAN SPECTROSCOPY APPLICATION IN MATERIAL SCIENCE

7.4.1 Carbon Nanotubes

Carbon nanotube is a model system to study Raman spectra in one-dimensional nanomaterials, and at the same time, Raman spectroscopy has provided an exceedingly powerful tool for the characterisation of carbon nanotubes.⁹

The unique optical and spectroscopic properties observed in single-walled carbon nanotubes (SWNTs) are largely due to the one-dimensional (1-D) confinement of electronic and phonon states, resulting in the so-called van Hove singularities (vHSs) in the nanotube density of states (DOS).¹⁰ These singularities in the DOS, and correspondingly in the electronic joint density of states (JDOS), are of great relevance for a variety of optical phenomena. Whenever the energy of incident photons matches a vHS in the JDOS of the valence and conduction bands (subject to selection rules for optical transitions), one expects to find resonant enhancement of the corresponding photophysical process. In combination with the unique 1D electronic structure, the resonantly enhanced Raman scattering intensity allows one to obtain detailed information about the vibrational properties of nanotubes, even at the individual SWNT level. Figure 7.4 shows the typical Raman spectra of SWNT bundles. There are many bands in the spectrum that arise due to specific modes of vibration, and this can be utilised as signatures of electronic and phononic properties of SWNT. Table 7.1 reveals the important modes of vibration in SWNT.

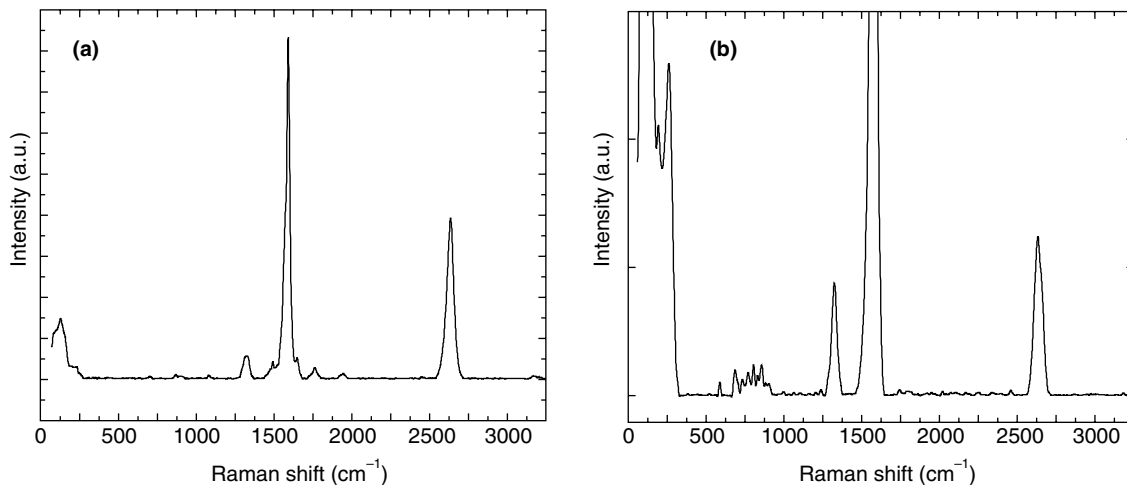


Fig. 7.4 (a) Non-resonant Raman spectrum and (b) resonant Raman spectrum of SWNT bundles. Note that in (b), the radial breathing mode is more intense compared to that in (a) owing to the resonance condition.

Many important properties of carbon nanotubes can be derived out of these modes of vibration¹¹, and this has led to better understanding of these materials.

7.4.2 Graphene

In the context of material science, graphene has emerged as one of the most promising platforms for next-generation functional devices.¹² Graphene, a one-atom thick zero gap semiconductor, has been attracting interest because of its remarkable physical properties, such as high thermal conductivity ($\sim 5000 \text{ W m}^{-1} \text{ K}^{-1}$) and ballistic charge transport at room temperature.¹³ The latter makes graphene a promising material for solar cells, hydrogen storage, biosensors, etc., and the recently demonstrated

Table 7.1 *Important Raman bands in graphite and SWNTs*

Name	ω (cm ⁻¹)	Remarks
iTA	288	In-plane transverse optic (iTA) mode
LA	453	Longitudinal acoustic (LA) mode
RBM	248/(tube diameter in nm)	Nanotube only, vibration of radius
IFM ⁻	750	Combination mode oTO – LA
oTO	860	IR-active mode in graphite
IFM ⁺	960	Combination mode oTO + LA
D	1350	LO or iTTO mode
LO	1450	LO mode
BWF	1550	Plasmon mode, only metallic carbons
G	1582	Raman active mode of graphite
M ⁻	1732	Overtone of oTO mode
M ⁺	1755	Overtone of oTO mode
iTOLA	1950	Combination mode of iTTO and LA
G'	2700	Overtone of D mode
2LO	2900	Overtone of LO mode
2G	3180	Overtone of G mode

i–in plane, o–out of plane

possibility of chemical doping without significant change in charge carrier mobility has further improved the prospects of graphene.¹⁴ Raman spectroscopy plays a pivotal role in characterising graphene, because its electronic structure is captured in the Raman spectra, which clearly evolves with the number of layers.^{11,15} Ever since Raman spectroscopy has been established as a vital characterisation tool to probe graphene,¹⁵ many interesting properties of the material has been discovered. Raman spectroscopy has been used to probe properties such as charge doping,¹⁶ effect of edges,¹⁷ effect of strain¹⁸, and many more. In all the studies of graphene, characterisation of G and G' band position, intensity ratio, line width, line profile and other band properties have been harnessed to unveil its relevant properties.¹¹

7.4.3 Raman Spectroscopy of Inorganic and Organic Nanomaterials

In solid nanomaterials, quantised lattice vibrations called phonons play a pivotal role in understanding the electronic and structural properties. Many of the phonon modes of vibration in solids are optically active and exhibit rich band structure close the Rayleigh line, and are effectively probed via infra-red and Raman spectroscopy. In contrast to infra-red spectroscopy, standard lasers are utilised as the Raman excitation source, and therefore, Raman spectroscopy is generally favoured as the optical characterisation tool to probe inorganic and organic solids. Over the years, solid-state physics and

chemistry have been immensely benefited by Raman spectroscopy to understand many important properties of condensed matter.¹⁹ Raman spectroscopy finds application in probing a variety of inorganic semiconductors such as Si, Ge, GaAs, GaP, InP, etc.,^{20–25} superconductors, magnetic materials, plasmonic materials, thermoelectric materials, and many more.^{19,26,27} It has also been effectively employed to probe heterocyclic organic compounds such as polyacetylene, polyaniline, polythiophene,^{28–30} etc.

The optical and vibrational properties of II–VI compound semiconductor nanoparticles (NPs) have been extensively studied in view of a wide variety of applications, such as biolabels, phosphors and light-emitting diodes. The synthesis of non-expensive NPs is additionally stimulated by a growing demand for bio-applications. Along with the application goal, studies of the vibrational properties of nanostructured materials are aimed at a better understanding of the fundamental physical properties of strongly confined electrons and phonons. Numerous Raman studies of semiconducting NPs^{31–36} revealed a redshift of the fundamental vibrational (LO) mode with the reduction of the NP diameter d induced by phonon confinement. The effect of the matrix has also been found in a blue shift of the LO peak due to the difference in thermal expansion coefficients of glass and NP material, with the value of the shift being dependent on the NP size and the sort of glass.³¹ Noticeable stress was also discovered in NPs capped by a thin shell of lattice-mismatched semiconductors or organic molecules, and even in free-standing NPs due to the NP surface tension. Raman spectroscopy is very efficient for the investigation of electron–phonon coupling (EPC), which is important for a better understanding of the optical and electrical properties of semiconductor nanostructures with strong confinement of electrons and phonons. Despite a number of theoretical and experimental studies of II–VI and other semiconductor nanostructures, discrepancies still exist concerning the EPC strength dependence on the NP size.³⁶ A possible reason behind these discrepancies can be a varying ‘preparation history’ of the samples, as well as the NP environment during the Raman measurements.

7.5 EMERGING METHODS IN RAMAN SCATTERING

Raman spectroscopy as a characterisation tool has advanced considerably in the last several years due to rapid developments in instrumentation and the availability of theoretical methods for accurate calculation of Raman spectrum, thus enormously facilitating the interpretation of Raman data. Recent surveys^{37,38} in Raman spectroscopy has revealed its extensive usage in the following topics: (i) art and archeology, (ii) biosciences, (iii) vibrational studies and analytical chemistry, (iv) solid state physics (minerals, crystals, glasses, ceramics, etc.), (v) liquids and liquid interactions, (vi) nano-materials (nano-tubes, nano-particles, etc.), (vii) phase transitions of various kinds, including liquid crystals (viii) resonant Raman scattering, (ix) pharmaceutical studies, (x) high-pressure physics and chemistry, (xi) forensic science, etc. Various linear and non-linear methods in Raman scattering have been developed to effectively harness this technique. Some of them are: surface-enhanced Raman scattering (SERS), tip-enhanced Raman scattering (TERS), coherent anti-Stokes Raman scattering (CARS), stimulated Raman scattering, hyper-Raman scattering, inverse Raman scattering, photo-acoustic Raman scattering, high-pressure Raman scattering, etc. Here, we will discuss the basic concepts and applications of these techniques.

7.5.1 Surface Enhanced Raman Scattering (SERS)

The intensity of Raman scattered light from a molecule is at least 10^6 times lesser than the fluorescence intensity. This is a hindrance for Raman scattering to be used as a tool for ultra-trace molecular analysis. In the last 30 years, SERS has emerged as an effective technique to circumvent the above-mentioned hindrance. In SERS, the intensity of Raman scattering is enhanced by adsorbing molecules on metallic, nanoscale surfaces exhibiting roughness.³⁹ It was first discovered while studying pyridine at a silver electrode and strong Raman scattering was observed when the surface was electrochemically roughened.⁴⁰ Later, it was reported that the Raman scattering from pyridine adsorbed on metal colloids was enhanced by a factor of 10^6 compared to the equivalent scattering for the same concentration of pyridine in solution.⁴¹ This enhancement phenomenon was called SERS and it depended upon the surface roughness and effective adsorption of the analyte to that surface. Surface enhancement has been mainly observed from silver, gold and copper surfaces, although aluminum, lithium and sodium also give enhancement to a lesser extent.

There are two fundamental enhancement mechanisms underlying SERS.^{42, 43} First is the electromagnetic enhancement mechanism, where the local electric field created at the vicinity of the roughened metal surface influences the molecule such that the Raman signal intensity is enhanced. The other mechanism is the chemical enhancement, in which there is a charge transfer between the molecule and the metal, which further influences the excited energy states of the molecule resulting in an enhanced Raman signature. Also, the polarisability of the molecule is influenced during this interaction, which results in certain selection rules of SERS. In their simplest form, the most intense bands are predicted as those from vibrational modes, which are perpendicular to the metal surface. This information can be applied qualitatively to obtain an approximate indication of the angle a molecule subtends to the surface.

In Fig. 7.5, a typical SERS spectrum of thiophenol is compared with its normal Raman spectrum. For the same experimental parameters, it is usually observed that the intensity SERS will be a few orders of magnitude greater than the conventional Raman spectra. SERS experiments can be performed either in colloidal solution or on solid substrates depending upon the application type.

7.5.1.1 Calculation of Enhancement Factor

Solution phase: First, Raman spectrum of a molecule of known concentration (C_R) is recorded in solution phase. Next, the Raman integral intensity of one of the strong bands (I_R) is calculated. This is followed by the recording of SERS spectrum of the same molecule at lower concentration (C_S) and calculation of the SERS integral intensity (I_S) of the same band as considered for the Raman spectra. G is calculated using the formula

$$G = (C_R/C_S) \times (I_S/I_R). \quad (8)$$

It is to be noted that the laser power, signal accumulation time, scattering geometry, optical instrumentation, etc., have to be the same for both Raman and SERS measurements. Generally, the sample quantity for these measurements should be at least $1 \mu\text{L}$, and the molecule to nanoparticle ratio can be 1:9 by volume. The non-resonant enhancement factor calculated by this method for thiophenol adsorbed to Ag and Au nanoparticles was of the order of 10^6 and 10^3 , respectively.

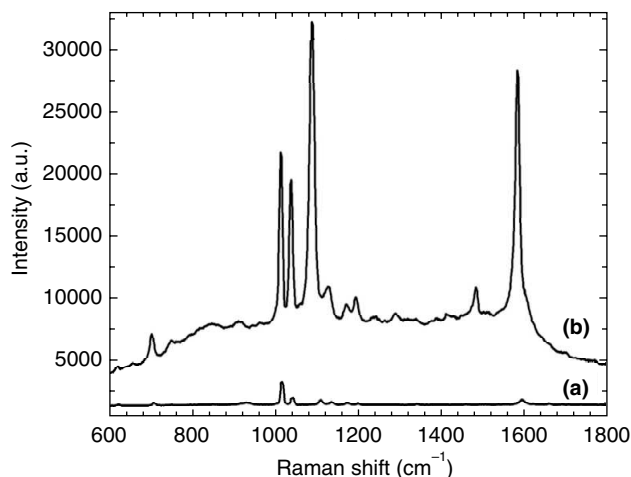


Fig. 7.5 (a) Raman and (b) SERS spectra of thiophenol. For SERS, the concentration of the molecule was $10^{-4}M$ and for Raman spectrum, neat solution of thiophenol was used.

Solid phase: Many of the SERS substrates prepared by techniques like nanosphere lithography, e-beam lithography, etc., are in solid state. In order to evaluate and compare the performance of these substrates, Raman signal enhancement is used as a benchmark. Unlike the solution phase, the concentration of the molecule cannot be directly considered to calculate the SERS enhancement factor. One has to have a priori knowledge of the number of molecules probed by the laser within a confined volume. This information can be obtained by molecular packing density. The enhancement factor, G can be calculated as follows:

$$G = (I_{\text{SERS}}/I_{\text{R}}) \times (N_{\text{R}}/N_{\text{SERS}}); \quad (9)$$

where I_{SERS} is the measured SERS intensity of the probe molecules on the nanoparticle surface, I_{R} is the measured intensity from normal Raman spectrum of the bulk sample, N_{R} is the number of the probe molecules under laser illumination in the bulk sample, and N_{SERS} is the number of the molecules probed on the nanoparticle surface. To find I_{SERS} and I_{R} , it is ideal to choose the integral intensity of the same peak in Raman and SERS spectra. The N_{SERS} is given by

$$N_{\text{SERS}} = 4 \pi r^2 C A N; \quad (10)$$

where r , C , A , and N are the average radius of nanoparticles, the surface density of the molecule under study, the area of the focused laser spot, and the surface coverage of nanoparticles (from electron microscopy or AFM measurements), respectively. The N_{R} is given by

$$N_{\text{R}} = A h \rho / m; \quad (11)$$

where A , h , ρ , and m are the area of the laser spot, the penetration depth, the density of the molecule and the molecular weight, respectively. For a more detailed discussion on enhancement factor, calculation can be found elsewhere.⁴⁴

7.5.2 Tip Enhanced Raman Scattering (TERS)

TERS is derived from surface-enhanced Raman scattering (SERS)^{45,46} and is based on the enhancement of Raman signal intensities of molecules/materials by a laser-illuminated, sharp metal-coated tip positioned in the optical near field of the sample (i.e., within a few nanometers above the sample surface).

Figure 7.6 shows a typical TERS experimental setup in which an inverted microscope equipped with piezo-driven sample stage and atomic force microscope (AFM) head is integrated with a Raman spectrometer. Since the enhancement takes place only on the sample area directly under the nanometer-sized tip, this technique allows Raman mapping with a spatial resolution of approximately 20 to 50 nm. Some of the key features of TERS are its chemical imaging capability, high spatial resolution, and single molecule sensitivity at ambient conditions.⁴⁷ Although the theoretical foundation for TERS was laid as early as 1985,⁴⁸ the concept was experimentally realised only in the year 2000.⁴⁹ Since then, a few research groups have effectively used TERS to probe different aspects of molecules and materials with a fair degree of success.^{50–52}

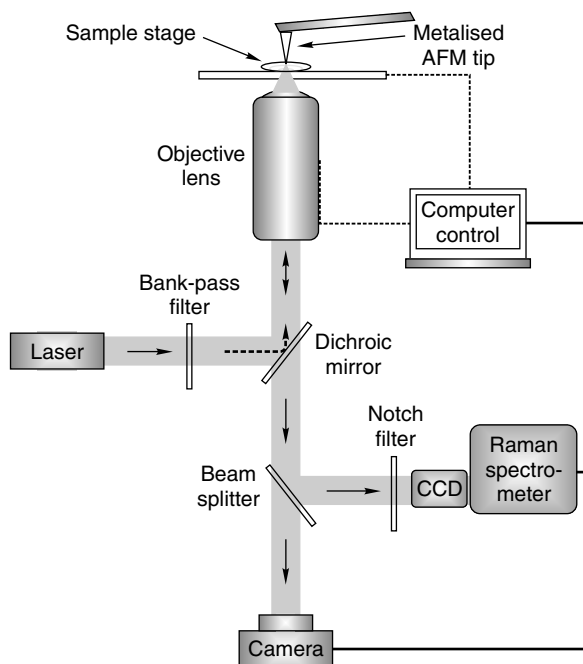


Fig. 7.6 Schematic of a tip-enhanced Raman scattering set-up.

It is to be noted that TERS is an extremely sensitive technique with high-spatial resolution. Figure 7.7 shows the result of a typical TERS experiment,⁴⁹ where enhanced Raman spectra is obtained from a flat layer of brilliant cresyl blue dispersed on a glass slide with the tip in close

proximity to the sample. Depending upon the experimental condition, the enhancement factor in TERS can be as high as 10^6 . TERS is a useful method to probe vibrational spectra of molecules and materials at the nanometer resolution, which is otherwise impossible with far-field confocal Raman spectroscopy.⁵³

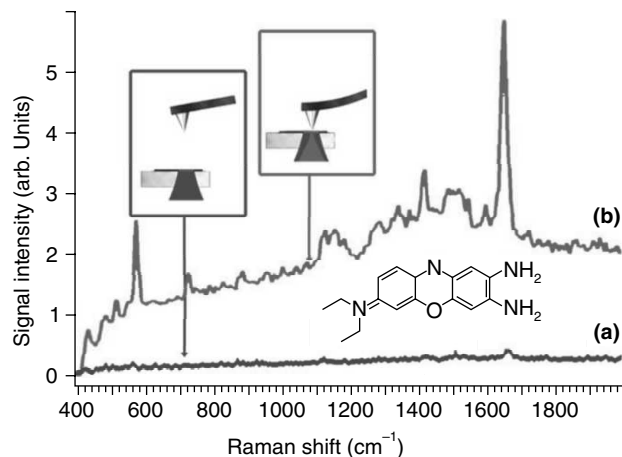


Fig. 7.7 Enhanced Raman spectrum of a flat layer of brilliant cresyl blue dispersed on a glass slide with (a) the tip retracted from the sample and (b) the tip in contact with the sample. Experimental conditions: silver coated tip (10–15 nm thickness); 488 nm excitation with a power of 1.588 mW; 60 s acquisition time. Adapted from Stöckle et al., *Chem. Phys. Lett.* 2000, 318, 131.

7.5.3 High Pressure Raman Scattering

There is a long-standing interest in understanding the behaviour of matter under extreme conditions, such as high temperatures and high pressures. Raman spectroscopy can be utilised as an effective tool to study the behaviour of molecules and materials under pressure. Valuable information about intermolecular interactions, phase transitions, structural changes, vibrational assignments, and conversions of insulators (semiconductors) to metals is obtainable, when matter is subjected to pressure. Understanding phase transitions of materials and molecules have significant implications in subjects such as geology, device physics, mechanics, etc. Pressure-induced frequency shifts are often accompanied by change in Raman scattering intensity, and can be used to identify the nature of vibrations. A diamond anvil cell (DAC) capable of reaching tens of gigapascal pressures, has been developed for high pressure Raman scattering studies. The pressure technique involves a pressure device such as DAC, in which a hard material (diamond) is used to transmit the pressure to the sample under study. Over the years, high-pressure Raman spectroscopy has been successfully used to probe phase transitions in molecular materials^{54–56} and solids nanomaterials, such as carbon nanotubes,⁵⁷ fullerenes,⁵⁸ and many other inorganic solids.^{59,60}

7.5.4 Non-linear Raman Scattering

As we have discussed before, the induced dipole moment of a molecule linearly depends upon the applied electric field of the light source. This approximation holds good only for low intensity electric fields such as conventional He-Ne lasers. For higher energy light sources, such as pulse-lasers, the induced dipole moment (\mathbf{P}) scales non-linearly with respect to the applied electric field. Then \mathbf{P} is expressed as

$$\mathbf{P} = \alpha \mathbf{E} + (1/2) \beta \mathbf{E}^2 + (1/6) \gamma \mathbf{E}^3 + \dots \quad (12)$$

For conventional light sources, the value of the terms β , γ , etc., are negligible. Their contributions become significant, however, when the sample is irradiated with extremely strong laser pulses ($\sim 10^9 \text{ Vcm}^{-2}$) created by Q-switched ruby or Nd-YAG lasers (10–100 MW peak power). These giant pulses lead to novel spectroscopic phenomena, such as the hyper-Raman effect, stimulated Raman effect, inverse-Raman effect, coherent anti-Stokes Raman scattering (CARS), and photo-acoustic Raman spectroscopy (PARS). Figure 7.8 shows transition schemes involved in each type of non-linear Raman spectroscopy.

We shall give a brief overview of these techniques

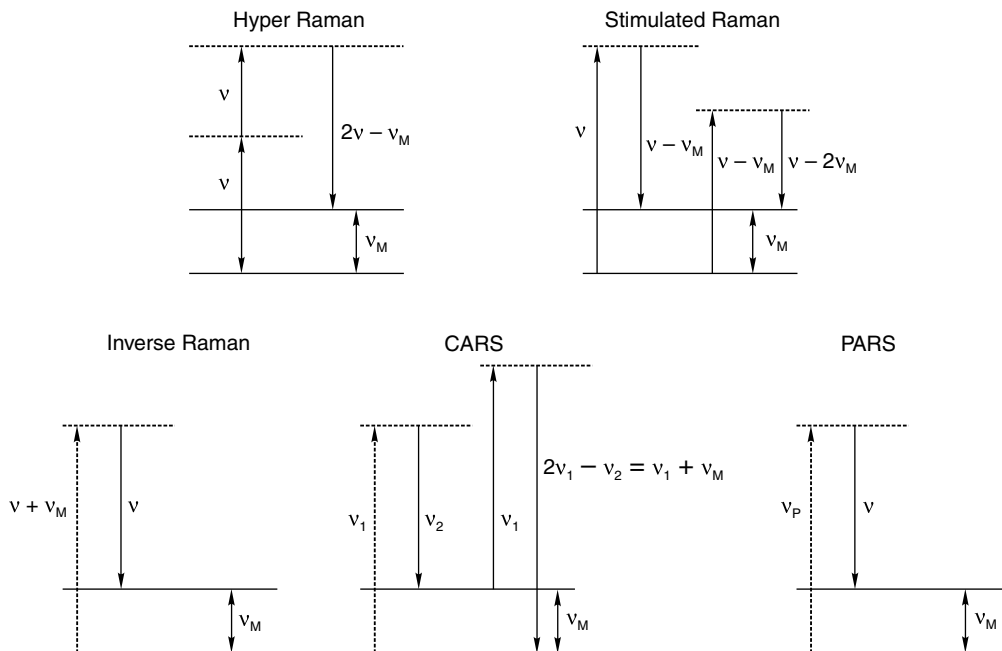


Fig. 7.8 Transition schemes involved in non-linear Raman spectroscopy.

7.5.4.1 Hyper-Raman Scattering

When the sample is illuminated by a giant pulse of frequency ν , the scattered radiation contains frequencies of 2ν (hyper-Rayleigh scattering) and $2\nu \pm \nu_M$ (Stokes and anti-Stokes hyper-Raman

scattering), where ν_M is a frequency of a normal vibration of the molecule. This is Raman scattering caused by two incident photons (2ν) of the laser (see Fig. 7.8). Hyper-Raman spectroscopy has several advantages over normal Raman spectroscopy because of a difference in selection rules.⁶¹ As already discussed, a vibration is Raman active if the derivative of the polarisability changes during the vibration. Similarly, a vibration is hyper-Raman active if one of the components of the hyperpolarisability changes during the vibration, and moreover, all the infra-red active modes of vibration are hyper-Raman active. Therefore, this technique is in a way, Raman spectroscopy equivalent of infra-red spectroscopy.

7.5.4.2 Stimulated Raman Scattering

In normal Raman scattering, laser (ν) incidence on the sample results in "spontaneous" Raman scattering ($\nu - \nu_M$), which is very weak. If the electric field of the laser exceeds $\sim 10^9$ Vcm⁻², the hyper-Raman scattering mentioned earlier is superseded by stimulated Raman scattering,⁶² which generates a strong coherent beam at Stokes frequency, ($\nu - \nu_M$) (see Fig. 7.8). Interestingly, only one normal mode (ν_M), which is the strongest in a normal Raman spectrum, is extremely strongly enhanced in the stimulated Raman effect. In benzene, it is the 992 cm⁻¹ band. In fact, ~ 50 per cent of the incident beam is converted into the first Stokes line, $\nu - \nu_M$ of this mode. Since this line is so intense, it acts as a source to excite the second Stokes line, $(\nu - \nu_M) - \nu_M = (\nu - 2\nu_M)$, and this line again acts as the source for the third Stokes line, and so forth. The high conversion efficiency of the stimulated Raman effect can be used to generate many laser lines of a variety of frequencies. Since the background fluorescence signal is significantly suppressed, stimulated Raman scattering can also be applied to label-free biomedical imaging.⁶³

7.5.4.3 Inverse-Raman Scattering

Suppose that a molecule has a Raman-active vibration at ν_M and if it is illuminated by a probe laser (ν) simultaneously with a pump continuum covering the frequency range from ν to $\nu + 3,500$ cm⁻¹, one observes an absorption at $\nu + \nu_M$ in the continuum together with emission at ν . The absorbed energy, $h(\nu + \nu_M)$, has been used for excitation ($h\nu_M$) and emission of the extra energy ($h\nu$) (see Fig. 7.8). This upward transition is called the inverse-Raman effect,⁶⁴ because the normal anti-Stokes transition occurs downward. Since the inverse-Raman spectrum can be obtained within the lifetime of the pulse, it may be used for studies of short-lived species. It should be noted, however, that the continuum pulse must also have the same lifetime as the giant pulse itself. Thus far, the inverse-Raman effect has been observed only in a few cases, as it is difficult to produce a continuum pulse at the desired frequency range.

7.5.4.4 Coherent Anti-Stokes Raman Scattering (CARS)

When the sample is irradiated by two high-energy laser beams with frequencies ν_1 and ν_2 ($\nu_1 > \nu_2$) in a collinear direction, these two beams interact coherently to produce a strong scattered light of frequency $2\nu_1 - \nu_2$. If ν_2 is tuned to a resonance condition, such that $\nu_2 = (\nu_1 - \nu_M)$, where ν_M is a frequency of a Raman-active mode of the sample, then a strong light of frequency $2\nu_1 - \nu_2 = 2\nu_1 - (\nu_1 - \nu_M) = \nu + \nu_M$ is emitted (see Fig. 7.8). This multi-photon process is called coherent anti-Stokes Raman spectroscopy

(CARS) and has several advantages such as: fluorescence rejection, fast imaging capability and with good sensitivity. This has made CARS a very attractive technique in biomedical applications.^{65, 66}

7.5.4.5 Photo-Acoustic Raman Spectroscopy (PARS)

The principle of photo-acoustic Raman spectroscopy is similar to that of CARS⁶⁷. When two laser beams, ν_p (pump beam) and ν_s (Stokes beam) are incident on a gaseous sample contained in a cell, they interact when the resonance condition, $\nu_p - \nu_s = \nu_M$, is satisfied, where ν_M is a frequency of a Raman-active mode (see Fig. 7.8). This results in the amplification of the Stokes beam and attenuation of the pump beam. Each Stokes photon thus generated transmits the molecule to excited state, and collision deactivation of these excited molecules further increases their translational energy. This change in the translational energy results in a change in the pressure of the sample in the cell that can be detected by a microphone. One of the major advantages of this technique is the absence of the strong Rayleigh band, which is a useful condition to study rotational spectra of gaseous molecules.

7.5.5 Brillouin Scattering

Apart from the above-discussed Raman scattering techniques, there is another inelastic light scattering method called Brillouin scattering, which occurs due to interaction of light with thermally excited elastic waves (phonons) in condensed matter. The first theoretical study of the light scattering by thermal phonons was done by Mandelstam as early as 1918, however, the correspondent paper was published only in 1926.⁶⁸ L. Brillouin predicted independently light scattering from thermally excited acoustic waves.⁶⁹ Later Gross gave the experimental confirmation of such a prediction in liquids and crystals.⁷⁰ In the case of a transparent solid, most of the scattered light emanates from the refracted beam in a region well away from the surface, and the kinematic conditions relating wave vector and frequency shift of the light pertain to bulk acoustic wave scattering (see Fig. 7.9). The scattering in this case is mediated by the *elasto-optic scattering mechanism*, in which dynamic fluctuations in the strain field bring about fluctuations in the dielectric constant, and these, in turn, translate into fluctuations in the refractive index. These fluctuating optical inhomogeneities result in inelastic scattering of the light as it passes through the solid.

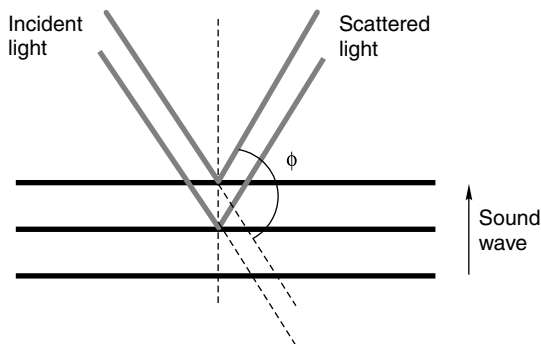


Fig. 7.9 Schematic showing interaction of light with sound waves.

The phonons present inside a solid move in thermal equilibrium with very small amplitudes creating fluctuations in the dielectric constant, which is viewed as a moving diffraction grating by an incident light wave. Therefore, Brillouin scattering can be explained by the two concepts of Bragg's reflection and Doppler shift:

Surface Brillouin scattering can be viewed as a Bragg reflection of the incident wave by the diffraction grating created by thermal phonons. According to the Bragg's Law, the grating spacing d can be expressed in terms of Bragg's angle $(\varphi/2)$ and wavelength of the laser light inside solid $\lambda = \lambda_0/n$, λ_0 , where λ_0 is the laser wavelength in vacuum and n is the index of refraction in the solid.

$$2d \sin(\varphi/2) = \lambda_0/n \quad (13)$$

The moving grating scatters the incident light with a Doppler effect, giving scattered photons with shifted frequencies Δf . Brillouin spectrum gives frequency shift (Δf) of the thermal phonon and its wavelength (d space) can be determined from the experiment geometry. Then the velocity of the phonon V_1 has a form

$$V_1 = \lambda_0 \Delta f / (2 n \sin \varphi/2) \quad (14)$$

For backscattering configuration, $\varphi = \pi$, this equation yields

$$V_1 = \lambda_0 \Delta f / (2n) \quad (15)$$

The moving corrugating surface scatters the incident light with a Doppler effect, giving scattered photons with shifted frequencies. For backscattering from surface acoustic phonons, the phase velocity (V_{SAW}) of surface acoustic wave can be written as

$$V_{SAW} = \lambda_0 \Delta f / (2 \sin \theta) \quad (16)$$

With application viewpoint, Brillouin scattering (BS) is a non-contact measurement technique that exploits light scattering to probe the properties of surface acoustic waves (SAWs), either at the surface of homogeneous solids or in thin supported layers. The near-surface elastic properties of solids often differ markedly from those of the underlying bulk material. They are a sensitive indicator of residual stress, annealing and other near-surface physical conditions. BS is widely used in the characterisation of thin (sub-micron) supported layers, whose elastic properties can differ from those of the corresponding bulk material. It can alternatively be exploited to measure other properties, like the layer thicknesses or mass density, or the presence of interfacial layers. Various systems have been studied till date including inorganic materials, such as silicon and silicides, a variety of carbonaceous materials, like diamond, CVD diamond and diamond-like films, various types of hard coatings like carbides and nitrides, Langmuir-Blodgett films, and various types of multilayers. BS can probe acoustic waves of frequencies up to 100 GHz and characterise films of thickness as thin as a few tens of nanometers.

7.6 CONCLUSIONS

As the history of science indicates, studying interaction of light with matter has led to great discoveries, such as photoelectric effect, Compton effect, Raman effect, etc., and has also led to inventions, such as lasers, radars, global positioning systems (GPS), etc. New phenomena in nature have been unveiled by understanding the intricacies of light-matter interaction. Plants and animals too make use of light

scattering principles to adapt and evolve. This adds motivation to study light scattering. With futuristic viewpoint, light scattering methods, such as Raman and Brillouin scattering, have immense potential in various branches of science and engineering. It is not only a high end optical instrumentation technique, but also a pivotal tool for analytical applications. Many challenges still remain to be probed in light scattering of condensed matter, and emergence of nanotechnology further provides a good opportunity to harness these methods. Thus, we see how an observation of a natural phenomenon, such as blue of the sky and blue of the sea has led to the discovery of the Raman effect. What started as curious observation has now turned out to be one of the most powerful aspects of analytical sciences. New questions have been asked and new applications have evolved out of this. By making an effort to understand and find solutions to interesting questions, new phenomena have also been discovered. Indeed, it is important that we never stop asking questions!

REFERENCES

1. B.A. Keen and A.W. Porter, *Philos Trans R Soc London Ser A*, 89, (1914), 370.
2. G. Venkataraman, *Raman and his Effect*, University Press (India) Ltd., Hyderabad, (1995).
3. In *The New York Times*, March 20, (1910).
4. C.V. Raman, *Proc. R. Soc. Lond. A*, 101, (1922), 64.
5. A. Smekal, *Naturwiss*, 11, (1923), 873.
6. C.V. Raman and K.S. Krishnan, *Nature*, 121, (1928), 501.
7. G. Landsberg and L. Mandelstam, *Naturwiss*, 16, (1928), 557.
8. N. Harris, M.J. Ford and M.B. Cortie, *J. Phys Chem B*, 110, (2006), 10701.
9. M.S. Dresselhaus, G. Dresselhaus, R. Saito and A. Jorio, *Physics Reports-Review Section of Physics Letters*, 409, (2005), 47.
10. M.S. Dresselhaus, G. Dresselhaus and A. Jorio, *Journal of Physical Chemistry C*, 111, (2007), 17887.
11. M.S. Dresselhaus, G. Dresselhaus and M. Hofmann, *Philosophical Transactions of the Royal Society a-Mathematical Physical and Engineering Sciences*, 366, (2008), 231.
12. A.K. Geim and K.S. Novoselov, *Nature Materials*, 6, (2007), 183.
13. A.H.C. Neto, F. Guinea, N.M.R. Peres, K.S. Novoselov and A.K. Geim, *Reviews of Modern Physics*, 81, (2009), 109.
14. T.O. Wehling, K.S. Novoselov, S.V. Morozov, E.E. Vdovin, M.I. Katsnelson, A.K. Geim and A.I. Lichtenstein, *Nano Letters*, 8, (2008), 173.
15. A.C. Ferrari, J.C. Meyer, V. Scardaci, C. Casiraghi, M. Lazzeri, F. Mauri, S. Piscanec, D. Jiang, K.S. Novoselov, S. Roth and A.K. Geim, *Phys Rev Lett.*, 97, (2006).
16. A. Das, S. Pisana, B. Chakraborty, S. Piscanec, S.K. Saha, U.V. Waghmare, K.S. Novoselov, H.R. Krishnamurthy, A.K. Geim, A.C. Ferrari and A.K. Sood, *Nature Nanotechnology*, 3, (2008), 210.
17. C. Casiraghi, A. Hartschuh, H. Qian, S. Piscanec, C. Georgi, A. Fasoli, K.S. Novoselov, D.M. Basko and A.C. Ferrari, *Nano Lett.*, 9, (2009), 1433.
18. T.M.G. Mohiuddin, A. Lombardo, R.R. Nair, A. Bonetti, G. Savini, R. Jalil, N. Bonini, D.M. Basko, C. Galiotis, N. Marzari, K.S. Novoselov, A.K. Geim and A.C. Ferrari, *Phys Rev B*, 79, (2009).

19. M. Cardona and G. Guntherodt, *Topics in Applied Physics*, 50, (1982), 1.
20. D. Bermejo and M. Cardona, *Journal of Non-Crystalline Solids*, 32, (1979), 405.
21. A.K. Sood, J. Menendez, M. Cardona and K. Ploog, *Phys Rev Lett.*, 54, (1985), 2111.
22. J.M. Calleja and M. Cardona, *Phys Rev Lett.*, 16, (1977), 3753.
23. J.B. Renucci, R.N. Tyte and M. Cardona, *Phys Rev Lett.*, 11, (1975), 3885.
24. R. Trommer and M. Cardona, *Phys Rev Lett.*, 17, (1978), 1865.
25. Weinstein.Ba and M. Cardona, *Phys Rev Lett.*, 8, (1973), 2795.
26. M. Cardona, L. Genzel, R. Liu, A. Wittlin, H. Mattausch, F. Garciaalvarado and E. Garciagonzalez, *Solid State Commun*, 64, (1987), 727.
27. A. Zawadowski and M. Cardona, *Phys Rev Lett.*, 42, (1990), 10732.
28. E. Faulques, W. Wallnofer and H. Kuzmany, *Journal of Chemical Physics*, 90, (1989), 7585.
29. F.B. Schugerl and H. Kuzmany, *Journal of Chemical Physics*, 74, (1981), 953.
30. H. Kuzmany, *Physica Status Solidi B-Basic Research*, 97, (1980), 521.
31. V.M. Dzhegagan, M.Y. Valakh, A.E. Raevskaya, A.L. Stroyuk, S.Y. Kuchmiy and D.R.T. Zahn, *Nanotechnology*, 19, (2008).
32. J.E. Spanier, R.D. Robinson, F. Zheng, S.W. Chan and I.P. Herman, *Phys Rev Lett.*, 64, (2001).
33. F.S. Manciu, Y. Sahoo, F. Carreto and P.N. Prasad, *J. Raman Spectrosc*, 39, (2008), 1135.
34. A. Li Bassi, D. Cattaneo, V. Russo, C.E. Bottani, E. Barborini, T. Mazza, P. Piseri, P. Milani, F.O. Ernst, K. Wegner and S.E. Pratsinis, *J. Appl Phys*, 98, (2005).
35. H.C. Choi, Y.M. Jung and S.B. Kim, *Vibrational Spectroscopy*, 37, (2005), 33.
36. G. Bachelier, J. Margueritat, A. Mlayah, J. Gonzalo and C.N. Afonso, *Phys Rev Lett.*, 76, (2007).
37. W. Kiefer, *J. Raman Spectroscopy*, 38, (2007), 1538.
38. W. Kiefer, *J. Raman Spectroscopy*, 39, (2008), 1710.
39. M. Moskovits, *Reviews of Modern Physics*, 57, (1985), 783.
40. M. Fleischm, P.J. Hendra and McQuilla.Aj, *Chem Phys Lett.*, 26, (1974), 163.
41. M.G. Albrecht and J.A. Creighton, *Journal of the American Chemical Society*, 99, (1977), 5215.
42. R. Aroca, *Surface-Enhanced Vibrational Spectroscopy*, John Wiley & Sons, Chichester, U.K., (2006).
43. E.C. Le Ru and P.G. Etchegoin, *Principles of Surface-Enhanced Raman Spectroscopy and Related Plasmonic Effects*, Elsevier, Amsterdam, (2009).
44. E.C. Le Ru, E. Blackie, M. Meyer and P.G. Etchegoin, *J Phys Chem C*, 111, (2007), 13794.
45. E. Bailo and V. Deckert, *Chemical Society Reviews*, 2008, 37, 921.
46. E. Bailo and V. Deckert, *Angewandte Chemie-International Edition*, 47, (2008), 1658.
47. S. Kawata and V.M. Shalaev, Elsevier, *Amsterdam*, (2007).
48. J. Wessel, *J. Opt. Soc. Am. B*, 2, (1985), 1538.
49. R.M. Stockle, Y.D. Suh, V. Deckert and R. Zenobi, *Chemical Physics Letters*, 318, (2000), 131.
50. J. Steidtner and B. Pettinger, *Physical Review Letters*, 100, (2008), 2361011.
51. X. Wang, Z. Liu, M.D. Zhuang, H.M. Zhang, Z.X. Xie, D.Y. Wu, B. Ren and Z.Q. Tian, *Applied Physics Letters*, 91, (2007), 2361011.

52. A. Hartschuh, H.N. Pedrosa, J. Peterson, L. Huang, P. Anger, H. Qian, A.J. Meixner, M. Steiner, L. Novotny and T.D. Krauss, *Chemphyschem*, 6, (2005), 577.
53. L. Novotny and S.J. Stranick, *Annual Review of Physical Chemistry*, 57, (2006), 303.
54. G. Kavitha and C. Narayana, *J Phys Chem B*, 110, (2006), 8777.
55. G. Kavitha and C. Narayana, *J Phys Chem B*, 111, (2007), 7003.
56. G. Kavitha and C. Narayana, *J Phys Chem B*, 111, (2007), 14130.
57. S.M. Sharma, S. Karmakar, S.K. Sikka, P.V. Teredesai, A.K. Sood, A. Govindaraj and C.N.R. Rao, *Phys Rev B*, 63, (2001).
58. C.S. Sundar, P.C. Sahu, V.S. Sastry, G.V.N. Rao, V. Sridharan, M. Premila, A. Bharathi, Y. Hariharan, T.S. Radhakrishnan, D.V.S. Muthu and A.K. Sood, *Phys Rev B*, 53, (1996), 8180.
59. N. Chandrabhas, D. Victor, S. Muthu, A.K. Sood, H.L. Bhat and A. Jayaraman, *Journal of Physics and Chemistry of Solids*, 53, (1992), 959.
60. S. Saha, D.V.S. Muthu, D. Golberg, C. Tang, C. Zhi, Y. Bando and A.K. Sood, *Chem Phys Lett.*, 421, (2006), 86.
61. L.D. Ziegler, *J Raman Spectroscopy*, 21, (1990), 769.
62. P. Kukura, D.W. McCamant and R.A. Mathies, *Annual Review of Physical Chemistry*, 58, (2007), 461.
63. C.W. Freudiger, W. Min, B.G. Saar, S. Lu, G.R. Holtom, C.W. He, J.C. Tsai, J.X. Kang and X.S. Xie, *Science*, 322, (2008), 1857.
64. R.R. Alfano and S.L. Shapiro, *Chem Phys Lett.*, 8, (1971), 631.
65. C.L. Evans and X.S. Xie, *Annual Review of Analytical Chemistry*, 1, (2008), 883.
66. J.X. Cheng and X.S. Xie, *J Phys Chem B*, 108, (2004), 827.
67. J.J. Barrett, *Applied Spectroscopy Reviews*, 21, (1985), 419.
68. L.I. Mandelstam, *Zh. Russ. Fiz-Khim. Ova.*, 58, (1926), 381.
69. L. Brillouin, *Ann. Phys. (Paris)*, 17, (1922), 88.
70. E. Gross, *Nature*, 126, (1930), 400.

ADDITIONAL READING

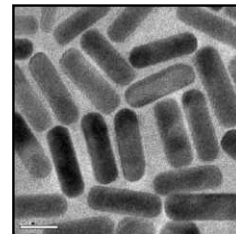
1. D.A. Long, *Raman Spectroscopy*, McGraw-Hill, (1977).
2. W. Demtroder, *Laser Spectroscopy: Basic Concepts and Instrumentation*, 3rd edition, Springer (2002).
3. J.R. Ferraro and K. Nakamoto, *Introduction to Raman Spectroscopy*, 2nd edition, Academic Press, (2002).
4. E.C. Le Ru and P.G. Etchegoin, *Principles of Surface-enhanced Raman Spectroscopy and Related Plasmonic Effects*, 1st edition, Elsevier Science, (2008).
5. R. Aroca, *Surface Enhanced Vibrational Spectroscopy*, 1st edition, Wiley, (2006).

REVIEW QUESTIONS

1. Why is the sky blue and why is the sea blue?
2. What is the difference between elastic and inelastic scattering?

3. How is Raman scattering different from infra-red spectroscopy?
4. What are Stokes and anti-Stokes line? Which is more intense and why?
5. What is surface enhanced Raman scattering?
6. What is the difference between SERS and TERS?
7. What is non-linear Raman scattering?
8. What happens to Raman spectrum when size of a nano-system is varied?

MISCELLANEOUS TECHNIQUES



“The method is surprisingly sensitive—more so than even that of spectrum analysis, requires an infinitesimal amount of material, and does not require this to be specially purified; the technique is not difficult if appliances for producing high vacua are available.”

J.J. Thomson, *Rays of Positive Electricity*, 1913

In this section, we look at the miscellaneous analytical techniques used for investigating nanoscale materials. As every tool can be used to study matter and any matter has nanoscale features, it is clear that all techniques are useful for nanoscience. Nevertheless, there are several prominent techniques as they provide information on the size, shape, electronic structure, redox properties, etc., of nanoscale materials. Here, we look at some of those techniques and present some relevant data to show their use for nanoscale systems.

Learning Objectives

- What are the advanced tools of mass spectrometry relevant to nanoscale materials?
 - How contact angle is useful in the study of nanoscale features?
 - How surface charges of nanoscale materials are measured?
 - Which optical spectroscopic tools are useful for nanomaterials?
-
-

8.1 MASS SPECTROMETRY

Mass spectrometry is one of the most sensitive analytical techniques of characterisation of molecular materials. While it has been an important technique for structural elucidation of organic compounds for long, developments progressed over the last 20 years or so have made it possible to apply it to any type of material like organic, inorganic, biological and environmental. From simple molecules to complex biomolecules and proteins, the versatility of mass spectrometry has improved in this period. All of these have become possible with the introduction of soft ionisation tools, which allow it to desorb and ionise almost any material intact. Two techniques which are helpful in this regard are matrix assisted laser desorption ionisation (MALDI) and electrospray ionisation (ESI), both of which

produce molecular ions from any kind of molecule. We will be discussing these techniques later in this chapter.

Mass spectrometry, traditionally, has involved the introduction of gaseous molecules/atoms into a vacuum system and ionisation of these by high energy electrons of the order of 100 eV. This ionisation is hard in the sense that it produces ion in an internally excited state and the internal energy of the ion is adequate to produce fragments of the molecular ion. As a result, most of the time, the intact molecular ion is not observable. This is a major problem in material characterisation. Soft ionisation techniques are extremely useful in such cases. The ions, generally positive in charge, are extracted and separated by various types of mass analysers, which are typically magnetic sectors, quadrupoles, ion traps or time of flight analysers and detected by a conversion dynode-electron multiplier detector system. This kind of mass spectrometry can be done only on those species, which can be evaporated or introduced into the vacuum chamber. This is not possible for a variety of molecules such as organometallic materials, metal complexes or large biomolecules which do not get evaporated intact. They often decompose in the process of evaporation. There are also a number of other cases, where the molecule, one wants, to analyse is in extremely small concentration, existing as a sub-monolayer on the surface.

Besides, the soft ionisation methods are useful in the case of nanoscale entities composed of fragile species such as biomolecules. A recent family of such materials is quantum clusters, which will be introduced in a later section of the book. These materials are very small in size, composed of a few atoms of metals and because of their sub-nanometer size, they cannot be seen with normal tools of electron microscopy described in this book. In order to understand the chemical composition of the cluster, the best method is mass spectrometry.

Mass spectrometry and its most popular hyphenated technique, gas chromatography mass spectrometry (GC-MS) is used extensively in studying nanomaterials-based catalysis just as in any standard catalysis.

8.1.1 Secondary Ion Mass Spectrometry

While ions are analysed in mass spectrometry, high energy ions can be used in a number of applications. Two of the common-ion-based techniques are focused-ion-beam-based lithography and secondary-ion-mass spectrometry. Ion lithography can make structures in the sub 10 nm regime today. Secondary ion mass spectrometry (SIMS), in the spatially resolved mode can get chemically specific, isotopically resolved elemental information, at a spatial resolution of 50 nm, which is impossible by any other technique. As ion ejection is extremely surface-sensitive and surface damage can be made small, nanometer thin films grown on surfaces can be analysed with isotope specificity. This analysis can be done quantitatively at trace levels. These attributes make SIMS imaging extremely important.

In SIMS, one is concerned with the mass spectrometry of ionized particles resulting from the impact of primary particles on a surface. The surface can be liquid or solid and the primary particles may be electrons, ions, neutrals or photons. The secondary particles emitted from a surface are electrons, neutral or ionic atoms or molecules, neutral or ionic clusters. In SIMS, the major concern is only about the ions, because the neutrals ejected are post-ionised and subjected to mass analysis in some cases, as

in sputtered neutral mass spectrometry (SNMS). The process of decoupling emission and ionisation allows quantitative elemental analysis. Most of the current applications are in dynamic SNMS and that was made possible using lasers.

Secondary particle emission is referred to as sputtering. Most of these will be neutrals, but a few ions also come out. Mass analysis of these ions are carried out by one of the several ways, such as time of flight, quadrupole, and magnetic sector-based methods.

The concept of SIMS can be dated back to 1910, when Sir J.J. Thompson observed the emission of positive ions from the surface of a discharge tube upon impact with primary ions. At present, the principal components of the instruments are: ion gun that gives ions or atoms of 0.5 - 50 keV, ion optics to transfer the ions to a mass spectrometer, which is followed by the detector. The mass spectrometer can be magnetic, quadrupole or time of flight. A schematic of the instrument is shown in Fig. 8.1.

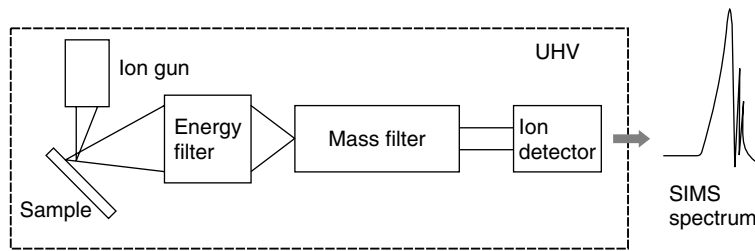


Fig. 8.1 Schematic diagram of the main components of the SIMS experiment.

In SIMS imaging the mass spectral intensities collected from a surface are used to construct images. The spatial resolution of the method depends on the dimension of the sampled area. Thus, it is necessary to have either highly focused ion beam or a highly focused collection of ions. A focused ion beam is rastered across the sample and spectrum at every point is collected. This method is called microprobe mode and lateral resolution is of the order of sub-micron levels. The other mode is the microscope mode or the direct mode. Here, the ions are collected from specific points on the sample, simultaneously by ion lenses, and are detected on a position sensitive detector. The primary ion beam is not rastered. SIMS imaging is generally done in two ways.

The ion beams commonly used are Cs^+ , O_2^+ , O^- or Ga^+ . Although highly pointed beams of Ga^+ are possible, the secondary ion emission yield is small; hence the first two are commonly used today. While Cs^+ enhances negative ions, and O_2^+ and O^- enhance positive ions.

SIMS is operated in two modes namely, the dynamic and the static modes. In the dynamic mode, where the primary ion flux is large and the rate at which the material is removed is high. This makes a fresh surface to get exposed to the primary beam continuously. But in the case of static SIMS, only a small fraction (less than 0.1%) of the surface is sampled. This makes minimal surface damage. High quality collection is necessary, and therefore, the analyser used in static SIMS is usually time of flight-based methods. Hence, static SIMS is also called TOF SIMS. In the dynamic SIMS, quadrupole and magnetic sector analysers are used.

With the current innovations in instrumentation, imaging SIMS can acquire a lateral resolution of 50 nm. The application areas include metallurgy, heterogeneous catalysis, biology and so on. Selective accumulation of ions in catalysis, incorporation of specific molecules in cell structures, separation of ions at grain boundaries, etc., are interesting problems to pursue. With sub-100 nm resolution, many of the cell organelles are accessible for high-quality chemical imaging.

In the case of an ion or atom bombardment at a surface, the energy of the primary projectile is transferred through a billiard ball type process. This is followed by a collision cascade between the target atoms and some of these collisions return to the surface resulting in the emission of atoms and clusters, some of which are ionized in the course of ejection. The major concern in SIMS quantification is that the ionization coincides sputtering. This means that calibration is a very important aspect in quantification. Particle bombardment changes the surface continuously, and to get meaningful surface analysis, the doses have to be kept low.

8.1.2 Other Mass Spectrometric Techniques of Interest to Nanoscience

Another method of carrying out SIMS is to use the fission fragments of ^{252}Cf to cause sputtering as in plasma desorption mass spectrometry (PDMS). These fragments have MeV energies and when collided on the rear of a thin foil coated with the analyte, molecular ions of high masses can get ejected. High-energy ions of $^{127}\text{T}^+$ from a tandem accelerator have also been used to achieve the same objective. High-energy neutral atoms are also used for sputtering. This form of mass spectrometry referred to as fast atom bombardment (FAB) mass spectrometry, is generally practiced for organic analytes with appropriate matrices. This results in soft ionisation of the analyte species. 'Soft' implies ionisation with lower internal energy for the ion formed, leading to lower fragmentation. Soft methods are especially important for the analyses of clusters as they are bound by lower energy and it is easy to fragment them during ejection to the gas phase. Nowadays, analysis of nanoparticles by mass spectrometry is becoming popular and soft ionisation methods are very much important for achieving this goal. Laser desorption is another soft method for desorption ionisation. This is done nowadays by a technique called matrix assisted laser desorption mass spectrometry (MALDI-MS) in which a low power ultraviolet laser (generally 337 nm N_2 laser) is used to desorb the analyte. The analyte is mixed with a matrix so that analyte concentration is small (typically 1:10 ratio). The mass analysis is generally done by the time of flight method as laser is pulsed, which can give a start time for data collection and ions need to be collected at high efficiency. Additional aspect of time of flight analysis is that there is no mass limit for the analysis in principle and the technique is well suited for large biomolecules. This methodology helps especially for the study of nano-bio conjugates. An example is shown in Fig. 8.2, where the MALDI mass spectra of myoglobin (Mb) and hemoglobin (Hb) and Mb and Hb protected Au nanoparticles are compared. It is seen that the mass spectra of the parent proteins and their nanoparticle conjugates are the same. As shown here, the MALDI-MS spectra are quite useful in the identification of proteins and such biomolecules on nanoparticle surfaces. It is also possible to extend the mass spectral investigations to understand the chemistry and biochemistry of proteins at the nanoparticle surfaces.

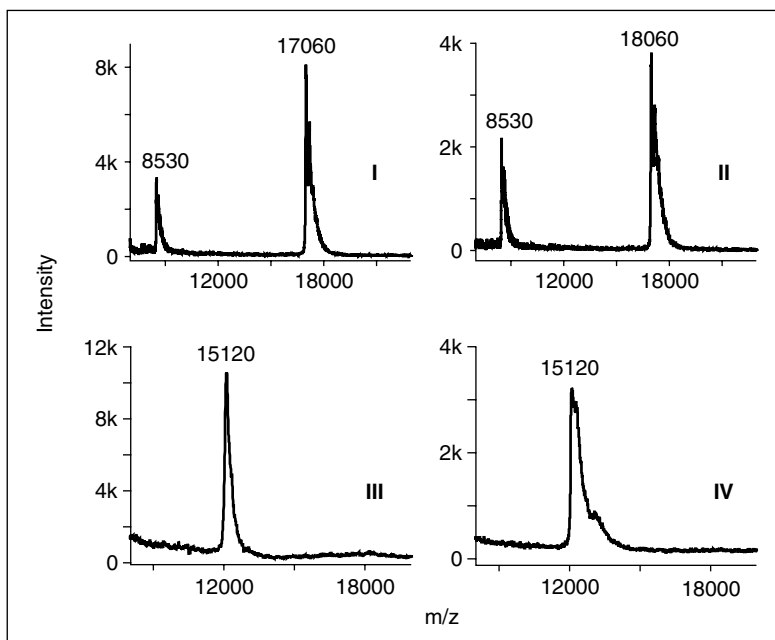


Fig. 8.2 MALDI-TOF mass spectra of the samples measured with 337 nm N_2 laser using sinapinic acid matrix. The traces (I), (II), (III) and (IV) correspond to Mb, Au@Mb, Hb and Au@Hb, respectively. The two peaks in I and II correspond to the mono- and dications. In Hb, the ion correspond to the monomer of the tetrameric protein (data are from the Authors' laboratory, originally published in, Renjis T. Tom, A.K. Samal, T.S. Sreepasad, and T. Pradeep, *Langmuir* 23 (2007) 1320–25).

The other soft ionisation technique is electrospray ionisation mass spectrometry (ESI MS), where ions are produced from a solution which is sprayed to form fine droplets in a high electric field. The solution sent through a fine needle is electrosprayed and the ions produced are generally multiply charged. This makes it possible to analyse large molecules in low mass range machines as their m/z value is small. Both these techniques are highly sensitive and femtomole analysis is possible with high resolution. ESI MS is a popular technique today in the analysis of sub-nano clusters which are difficult to be seen in TEM.

Electrospray ionised ions are collected and ionised typically in the orthogonal geometry. That is, the collection of ions happens normally at 90° with respect to the spray axis. This makes it possible to collect ions without a large dose of solvent molecules as a pump inlet can be placed just below the spray. This allows collection of solvent at much better efficiency with reduced cost of pumping. However, this geometry is not efficient in collecting species of heavy molecular mass. As a result, several gold clusters discovered recently cannot be collected efficiently by orthogonal mass spectrometers. Unfortunately, most of the mass spectrometers being made today are orthogonal instruments. Despite this, some clusters have been analysed by commercial instruments. Several examples of ESI MS and MALDI MS

of clusters will be presented in a later chapter. Compositions of intact clusters composed of tens to hundreds of atoms prepared in solutions have been determined in the author's laboratory.

Electrospray produces multiply charged species, and to get singly charged ions, the spectra have to be deconvoluted. Different algorithms are used in generating the singly charged spectra. All of these look at a series of peaks in the mass spectrum at $n, n+1, n+2, \dots$ etc., charges. Better algorithms always look at isotopic separations between peaks and the change in the peak separation with change in charge. This information is used to isolate peaks assignable to multiply charged species. Likewise, multiple series of peaks corresponding to various molecular species are identified. Assigning these peaks to specific ions require additional effort and an understanding of the possible chemical structure of the ions.

8.1.3 Focused Ion Beam (FIB)

The focused ion beam (FIB) technique utilises a liquid metal ion source and the interaction of high energy ion with the sample is used to investigate or modify the sample. Elastic and inelastic collisions occur when the ion beam strikes the sample. Elastic collisions lead to sputtering of atoms and inelastic collisions yield secondary electrons and X-rays. Ions are also ejected. The ions and electrons ejected can be used for imaging the surface. The ion beam itself can be used for milling applications. In the presence of organometallic species, the ion beam can result in the deposition of materials and can be used for material repair applications. Ion beam milling can be used for sample preparation, especially for TEM.

Ions are particles with higher momentum in comparison to the electrons for a given acceleration energy, although they travel at a lower velocity. Consequently, their collision lead to increased sputtering. The ion penetration depth is much smaller than those of electrons.

In SEM and FIB, the particles are scanned on the surface to be examined. The secondary particles (ions and electrons) are used for imaging in FIB. As the ions travel at much lower velocities, their Lorentz force is lower, [Lorentz force is the force exerted on a charged particle in an electromagnetic field. The particle will experience a force due to electric field of qE , and due to the magnetic field, $qv \times B$. Combined, they give the Lorentz force: $F = q(E + v \times B)$, where E is the electric field, B is the magnetic field, q is the charge of the particle, v is its instantaneous velocity, and \times is the cross product.].

In addition to imaging, FIB is used for ion milling. Selective sputtering can be achieved by a method known as gas assisted etching (GAE), in which one of the halogen gases is introduced to the working surface forming volatile species. Decomposition of an already deposited organometallic molecule on the surface can lead to deposition of certain atoms, for example, Pt getting deposited from a Pt precursor molecule in presence of the ion. The gas phase deposition process can be used to nucleate certain growth at the surface and the subsequent growth can be achieved by chemical vapour deposition (CVD). FIB can also be used for ion implantation.

In addition to single ion beam, an ion beam and an electron beam combination may be used to combine the capabilities of FIB and SEM. This can do lithography, imaging, and characterisation together. Such an instrument has several applications in nanotechnology.

8.2 CONTACT ANGLE (CA) MEASUREMENTS

Wettability of a solid surface is its characteristic property and is controlled by both surface chemical composition and surface topology. So wetting measurements can be used to estimate the quality of stable monolayer and multilayer films. Contact angle (CA) measurement is one such technique, which quantitatively unravels the wetting of a solid by a selected liquid like water or hexane, enabling a simple and effective method to determine the surface energies, and its relation to the structure and composition of a surface [1–2]. It is actually a comparative technique in which the wetting property can be studied by placing a small (2–4 μl) drop of the liquid onto a flat solid surface. Since wetting involves the interaction of a liquid with a solid, the spreading of a liquid over a surface along with the penetration of a liquid into a porous medium, or the displacement of one liquid by another could be monitored to understand the nature of many surfaces. It also directly provides information on the interaction energy between the surface and the liquid. For example, the water CA for a smooth solid surface exposing closely packed methyl groups ($-\text{CH}_3$) is 111° – 115° , while the hexadecane CA for the same surface is 45° – 46° highlighting the importance of hydrophobic interactions of the terminal group.

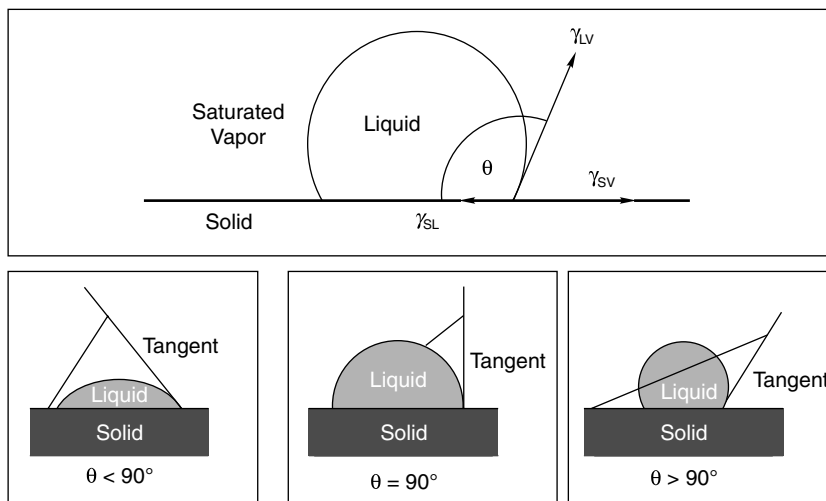


Fig. 8.3 Schematic diagram showing different possible contact angles of a liquid drops on a solid substrate.

CA is defined geometrically as the angle formed by a liquid drop at the three-phase boundary (contact line/wetting line), where a liquid, gas, and solid intersect as shown in Fig. 8.3. Low values of θ indicate that the liquid spreads or wets well, while high values indicate poor wetting. If the angle θ is less than 90° , the liquid is said to wet the solid (hydrophilicity) while values greater than 90° indicate non-wetting nature (hydrophobicity). On one side, a zero CA ideally represents complete wetting while 180° on the other side can reveal no interactions.

From a thermodynamic perspective, the shape of the liquid drop will be affected by the free energy of the surface; this forms an angle with the surface known as the CA, which in turn, is a function of the surface free energy as defined by the Young–Dupre equation as,

$$\gamma_{LV} \cos \theta = \gamma_{SL} - \gamma_{SV}$$

where, θ is the angle between the tangent to the droplet and the surface and γ_{SV} , γ_{LV} and γ_{SL} are the surface tension at solid-vapour interface, liquid-vapour interface and solid-liquid interface, respectively.³ However, this relationship is valid only for a smooth surface which is assumed to be ideal. For real, i.e., rough surfaces; Wenzel modified this expression by incorporating a roughness ($r \geq 1$) as an adjustable

parameter⁴, as $r = \frac{\cos \theta_{\text{rough surface}}}{\cos \theta_{\text{smooth surface}}}$, where, surface roughness is defined as a ratio of the observed CA

(on rough surface) to the CA on the smooth surface. According to this equation, surface roughness should increase CA for cases greater than 90° , and decrease for cases less than 90° .

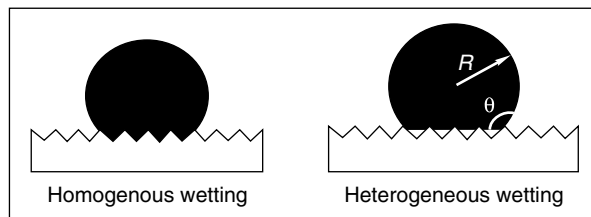


Fig. 8.4 Homogenous and heterogeneous wetting on hydrophobic rough surfaces.

Equilibrium wetting on rough surfaces is discussed in terms of a “competition” between complete liquid penetration into the rough grooves and entrapment of air bubbles inside the grooves underneath the liquid. The former is the homogeneous wetting regime usually described by the Wenzel equation, while the latter is the heterogeneous wetting regime that is described by the Cassie-Baxter equation⁵ (as shown in Fig. 8.4). In case of heterogeneous surfaces, the Cassie equation suggests for the interpretation of wettability results as,

$$\cos \theta = f_1 \cos \theta_1 + f_2 \cos \theta_2,$$

where, θ is the CA of a liquid on the heterogeneous surface composed of a fraction, f_1 is of one type of chemical group and f_2 is another chemical group with $f_1 + f_2 = 1$ and θ_1 and θ_2 represent CA of liquid on the pure homogenous surfaces of 1 and 2, respectively.

The cosine of the contact angles of homogeneous series of liquids for a given surface is a monotonic function of γ_L ,

$$\text{i.e., } \cos \theta_{SLV} = a - b\gamma_L = 1 - \beta(\gamma_L - \gamma_C)$$

This plot ($\cos \theta$ Vs γ_L) is known as Zisman plot. The line extrapolates to zero θ at a certain value of γ_L . This is known as the critical surface tension. The ability of a long chain containing monolayer like Octadecyl trichloro silane(OTS)–(SAM) to control adhesion through surface functionalisation is illustrated using the Zisman plot. Accordingly, Fig. 8.5 shows cosine of CA ($\cos \theta$) measured using various solvents with a wide range of surface tension on a full coverage of OTS monolayer (Zisman plot)

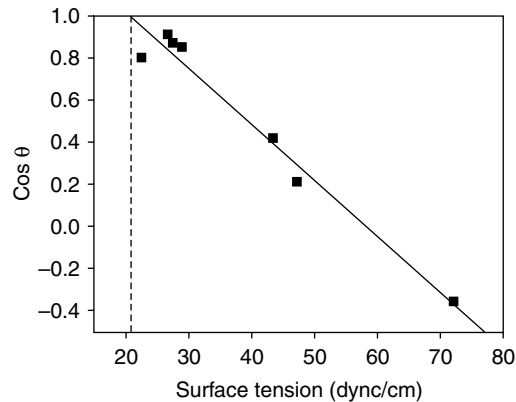


Fig. 8.5 Zisman plot for a fully covered OTS monolayer on Si (100); extrapolation to $\cos \theta = 1$ gives the critical surface tension value of 20.7 dyne/cm.

on Si substrate. As the surface tension of the solvent decreases the CA decreases, and the extrapolation of this plot ($\cos \theta = 1$) gives the critical surface tension (γ_c) for wetting.

It is well known that the water contact angle $\theta < 90^\circ$ and $\theta > 90^\circ$ can indicate surface ‘hydrophilicity’^{6,7} or ‘hydrophobicity’, respectively. A highly hydrophobic surface in which the water contact angle is larger than 150° , is commonly called a superhydrophobic surface. Since this superhydrophobic surface is having a small contact area with water, both chemical reactions and bond formation through water is limited on these surfaces. Accordingly, various phenomena such as the adherence of snow or raindrops, oxidation and friction drag are expected to be inhibited or reduced on such a surface. To reach superhydrophilicity, a combination of surface roughness and low surface energy is required. Nature exhibits this phenomenon in ‘lotus leaf’ to harness the roll-off action for self-cleaning of leaves, which has been attributed to a combined micro and nanoscale morphology of its surface. More specifically, the surface of the lotus leaf is textured with micron-sized hills and valleys that are decorated with nanometer-sized particles of a hydrophobic wax like material which prevents the penetration of water into the valleys. As a result, water cannot wet the surface but forms nearly spherical water droplets, leading to superhydrophobicity. Various strategies to develop artificial superhydrophobic surfaces (analogous to lotus leaf) have attracted significant attention in recent times due to its fundamental relevance of molecule level manipulation of surface energy and consequent implications in commercial applications ranging from self-cleaning window glasses, paints, and fabrics to low-friction surfaces. Anti-reflectivity of the superhydrophobic surface is also very important for their applications such as coatings for optical devices and photovoltaics. Artificial superhydrophobic (hierarchical surfaces) have been prepared using various strategies wherein rough surfaces are generated first and then modified with low surface energy molecules or roughening the surface of hydrophobic materials by creating well-ordered structures using micromachining and etching. Using this concept, various methods have recently been proposed to create superhydrophobic surfaces including electrochemical deposition, plasma fluorination, sol-gel, and UV irradiation and so on. It is well known that the wetting property of a solid surface is governed by both its chemical composition and geometric microstructure. In

addition, few methods have been reported to make the superhydrophobic coating on silica particles by forming polyelectrolyte multilayer films by layer-by-layer process or by forming a thin film of silica particles on substrate by Langmuir-Blodgett (LB) technique and subsequent formation of alkylsilane SAM for fabricating hydrophobic surfaces. However, these methods are tedious, complicated, time-consuming and difficult to control accurately; hence better strategies are desired to improve stability of these superhydrophobic films.

Since CA depends on liquid purity, temperature as well as the statistical errors in the actual reading of CA, reproducible studies need accurate control of temperature, relative humidity and vapour pressure of the liquid. To minimise these errors in the reading, CA measurements should be done in a vibration-less condition, preferably using a heavy table equipped with shock absorbers besides using a drop of fixed volume and an accurate syringe. This can be achieved by working in a closed, insulated compartment containing a small beaker with the liquid under study purged with water-saturated nitrogen.

8.3 CONDUCTIVITY MEASUREMENTS

There are various methods for electrical (current-voltage, I-V) characterisation, which are applicable to single crystalline as well as polycrystalline materials. However, following points need to be understood prior to the measurement: grain boundaries behave differently from individual crystallites and it is not possible to tell *a priori* whether the apparent resistivity will be greater or less than that of a single crystal of the same material. Further, it is important to note that the surface penetration can affect apparent resistivity. An inversion layer may be formed which the probes may or may not punch through. Sometimes the sample may get damaged in the process and such damage-induced defects give rise to additional charge carriers. Thus, it is expected that resistivity drops significantly for highly resistive materials. Resistivity measurements are geometry dependent and sensitive to boundary conditions and hence correction factor needs to be considered [1].

Two basic methods have been adopted for I-V characterisation, namely, 2-point probe and 4-point probe methods (Fig. 8.6), respectively as a and b. Schematic representation of 2-point probe is shown in Fig. 8.7(a). Resistivity, thus obtained also includes contact resistance, which is appreciable in case of semiconductors. Using 2-point probe, if the specimen cross-section is uniform, it can eliminate the effect of contact resistance. However, there is a need to keep current low enough to prevent heating of the sample. Besides, the voltmeter must have high input impedances (above 10^{13} ohms) and

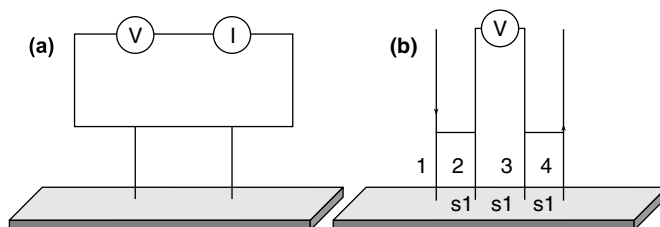


Fig. 8.6 Schematic representation of (a) 2-point probe method and (b) 4-point probe method.

measurements must be made far enough away from the contacts so that any minority carriers injected would have already recombined.

The 4-point probe is preferable over a 2-point probe because the contact and the spreading resistance associated with the 2-point probe cannot be measured. This means that the true sheet resistance cannot be accurately separated from the measured resistance. The 4-point probe consists of two current carrying probes (1 and 4), and two voltage-measuring probes (2 and 3). Since very little contact and spreading resistances are associated with the voltage probes, one can obtain a fairly accurate calculation of the sheet resistance, which is then used to calculate the resistivity. The resistivity (ρ) of a semi-infinite wafer with equal probe spacing (s) is given by:

$$\rho = 2 \times \pi \times s \times V/I, \text{ where } s = s_1 = s_2 = s_3.$$

Since wafers are not semi-infinite in extent, a combination of correction factors must be multiplied at the right-hand side of this equation[1].

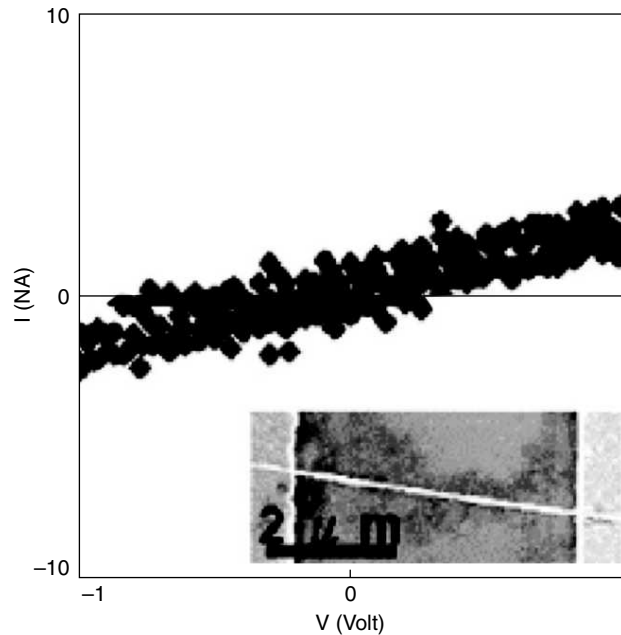


Fig. 8.7 *I-V characteristics of undoped ZnO NW with an inset showing the device to perform electrical measurements fabricated by electron beam lithography with lift-off technique.*

It is known that the 'as-synthesised' and undoped ZnO nanowires [NWs] are n-type semiconductors due to a high density of oxygen vacancies. Typical *I-V* curve of a single undoped NW as measured by Wang et al.² is given in Fig. 8.7. The current changes linearly from about -3 to 3 nA as V is varied from -1 to 1 V with a resistivity (ρ) of $390 \Omega\text{cm}$. High electrical resistivity in a single undoped NW indicates its high quality of crystalline structure with low oxygen deficiencies. However, after doping with Ni the conductivity increases by 30 times to give a final value of $\rho = 12 \Omega\text{cm}$.

8.4 ZETA POTENTIAL

Due to dipolar characteristics and ionic attributes, the colloidal particles (including nanoparticles) suspended in solvents are electrically charged. For example, the surface groups of a colloid may be ionised. This leads to a net electric charge at the surface which causes the accumulation of opposite charges (counter ions) around them, resulting in an electrical double layer. The ion (with positive or negative charge) with a set of counter ions form a fixed part of the double layer. The diffuse or mobile part of the double layer consists of ions of different polarities which extends into the liquid phase. This double layer may also be considered to have two parts, an inner region which includes ions bound relatively strongly to the surface and a diffuse region (which is sometimes called as stern layer), in which the ion distribution is determined by balance of electrostatic forces and random thermal motion. When an electric field is applied, the particles are attracted towards electrodes depending upon their polarity. The potential at which the fixed part of the double layer along with a part of the mobile layer move towards an electrode, is called Zeta potential or electrokinetic potential. It can also be defined as the potential at the shear plane of the particle when it moves in the medium.

The zeta potential depends on a number of parameters like surface charges, ions adsorbed at the interface and the nature and composition of the surrounding medium. The net charge in a specific medium depends on the particle charge and counter ions. The zeta potential is an index of interaction between the particles.

Zeta potential is calculated according to Smoluchowski's formula, $\zeta = 4\pi\eta/\varepsilon \times U \times 300 \times 300 \times 1000$, where ζ = zeta potential, ε = dielectric constant of the medium, η = viscosity of solution, U = electrophoretic mobility ($v/V/L$), v = velocity of the particles under electric field, V = applied voltage and L = distance of the electrode.

The value of zeta potential throws light on the stability of colloidal/nanoparticle solutions. If all the particles in a suspension have large negative or positive zeta values, then they will repel each other and there will not be any tendency to flocculate. However, if the particles have low zeta potential values then there is no force to prevent the particles from coagulating. The threshold of stability of colloidal/nanoparticle solution in terms of zeta potential is ± 30 mV. The greater the zeta potential, the greater will be the stability. The value of the zeta potential is largely affected by pH.

The zeta potential is measured traditionally by using the 'microelectrophoresis' method, which needs extreme dilutions and hence stringent sample handling requirements. Microelectrophoresis is a technique based on light scattering by particles. In the case of nanoparticle suspensions, however, the microelectrophoresis is not ideal due to the Doppler broadening of the scattered light from the fine particles. Modern methods used for zeta potential measurements are based on electro-acoustic methods and thereby on electrokinetic properties. In this method, the application of a high frequency electric field sets in motion the electrophoretic movements of the particles. This generates an alternating acoustic wave due to the density difference between particles and the medium. The velocity of the particles is measured by using laser Doppler electrophoresis. The velocity of these particles or mobility is converted into the zeta potential using Henry's equation:

$$U = 2\varepsilon z f(ka)/3\eta,$$

where, ϵ = dielectric constant, z = zeta potential, η = viscosity and $f(ka)$ = Henry's function. Zeta potential measurements in aqueous media and moderate electrolyte concentration generally employ $f(ka)$ value of 1.5 (Smoluchowski approximation). $f(ka)$ value is generally taken as 1 for the measurements of zeta potentials of small particles in non-aqueous media (Huckel approximation). The zeta potential measurement by micro electrophoresis is a passive technique as it does not alter the chemical properties of the systems.

8.5 COMMON ANALYTICAL TOOLS ADAPTED FOR THE INVESTIGATION OF NANOMATERIALS

8.5.1 Optical Spectroscopies

Generally, the optical absorption spectroscopy is a powerful technique for metal nanoparticles, and in particular, for gold nanoparticles. The optical properties of nanoparticles have been extensively investigated in recent years. We present a very brief discussion of the topic here. When an electromagnetic wave passes through a metal particle, the electronic and vibrational states get excited. The optical interaction induces a dipole moment that oscillates coherently at the frequency of the incident wave. The frequency of this oscillation depends on the electron density, its effective mass, the shape and size of the charge undergoing oscillation. There can be other influences such as those due to other electrons in the system. The restoring force arising from the displacement of the electron cloud relative to the nuclei results in the oscillation of the electron cloud relative to the nuclear framework. The collective oscillation of the free conduction electrons is called 'plasmon resonance' or 'dipole plasmon resonance' of the particle.¹⁵ In this resonance, the total electron cloud moves with the applied field. There can be higher modes of plasmon resonance as well. In the quadrupole mode, half the electron cloud is parallel while the other half is anti-parallel to the applied field.

The dipole plasmon frequency is related to the dielectric constant of the metal. The frequency dependent dielectric constant of a bulk metal ($\epsilon(\omega)$) is measurable. In this brief discussion, in order to simplify matters, we consider a spherical particle, whose diameter is much smaller than the wavelength of the electromagnetic radiation. Under such conditions, the electric field of light felt by the particles can be regarded as a constant. This reduces the interaction to be treated by electrostatics rather than electrodynamics. This treatment is referred to as the quasi-static approximation – 'quasi' because we consider the wavelength dependent dielectric constant. In electrostatic theory, when the incident electric field of the radiation interacts with the electrons, we get a net field due to the applied field and its induced field. This field, in reality, is a radiating one and contributes to extinction and Rayleigh scattering by the particle. The strength of extinction (note: extinction = absorption + scattering) and scattering can be given in terms of their efficiencies as,

$$\text{Extinction efficiency, } Q_{\text{ext}} = 4x \text{Im}g_d$$

$$\text{Scattering efficiency, } Q_{\text{scat}} = (8/3) x^4 |g_d|^2$$

where, $x = 2\pi R\epsilon_m/\lambda$, $g_d = (\epsilon_c - \epsilon_m)/(\epsilon_c + 2\epsilon_m)$, ϵ_c and ϵ_m are the respective dielectric constants of the metal and the medium and R is the particle radius. Dielectric functions are complex quantities and Im refers to the imaginary part.

In particles of less than 10 nm diameter, light scattering does not make a significant contribution.

$$Q_{\text{Ext}} \sim Q_{\text{Abs}} = [4(2\pi R \epsilon_0^{1/2})/\lambda] \text{Im}[(\epsilon_c - \epsilon_m)/(\epsilon_c + 2\epsilon_m)].$$

When $\epsilon_c = -2\epsilon_m$, we get the resonance condition, and Q_{Abs} goes to a maximum. Since the dielectric function is a complex quantity, this equation can be given in terms of the real and imaginary parts of the metals dielectric function, ϵ' and ϵ'' , respectively. There are two distinct size regimes of the particles; in both the plasmon resonance depends on size. For particles larger than 10 nm in diameter, the dielectric function itself is independent of size. The shape and size dependence of plasmon resonance in this regime is due to the dependence of electrodynamics on size and shape. This is called the *extrinsic size regime*. In the *intrinsic regime*, for particles less than 10 nm in diameter, the dielectric function itself changes with size. For metals, the absorption characteristics depend, to a large extent, on the conduction band electrons. The spatial confinement of the free conduction band electrons results in plasmon excitations that are restricted to a small range of frequencies, usually in the UV-visible region. Bulk metals absorb very strongly in the IR or near IR region, but colloidal metals are transparent.

The optical absorption spectrum of a nanoparticle solution of gold is shown in Fig. 8.8, made by the citrate route. The peak at 520 nm is due to the plasmon absorption, the position and shape of the absorption peak are characteristic features of the particle size. This feature is not shown by bulk gold. A smaller particle, as in the case of thiol protected gold nanoparticle in toluene, shows considerably broader plasmon absorption. The particles below 2 nm will not show any plasmon absorption as in the case of Au_{25} particles. These molecular clusters of gold (described in Chapter 11) will show distinct features due to their molecular energy levels. These spectra illustrate that plasmon resonance, if exhibited by a metal nanoparticle, is a good indicator of its size. The plasmon resonance is also sensitive to the molecular shell on the surface, its thickness is reflected in the spectrum. For a given molecular shell, the properties of the medium are reflected in the spectrum when the shell thickness is small. The

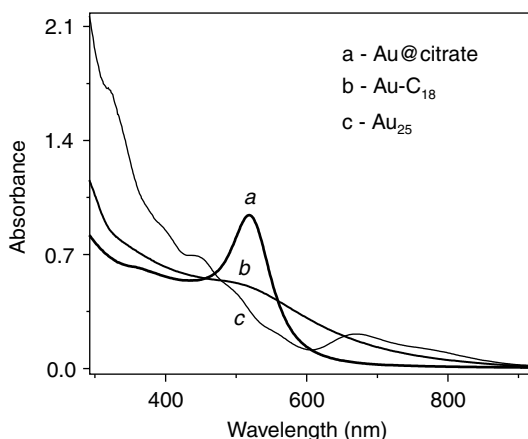


Fig. 8.8 Optical absorption (extinction) spectrum of (a) 15 nm gold particles in aqueous solution (labeled Au@citrate). The spectrum of (b) 3 nm particles in toluene is also shown. See the broadening of the plasmon feature. The spectrum of (c) Au_{25} in water. In this, there is no plasmon excitation and all the features are due to molecular absorptions of the cluster.

interactions of nanoparticles with ions or molecules in the medium and also inter-particle interaction are manifested in the absorption features. An interested reader may consult the cited references¹⁶ for a detailed discussion of plasmon resonance of gold particles and their applications.

In the case of quantum dots, one gets discrete energy levels. A complete discussion of this topic is beyond the scope of this chapter (see Chapter 10 for a more complete description), but it is important to mention that optical spectroscopy can be used to understand these energy levels, and therefore, quantum dots. The simplest of models to represent the energy states of a nanocrystal is the spherical quantum well with an infinite potential barrier. Although the model is simple, if we include the coulombic interaction between the charge carriers, electron (e) and the hole (h), analytical solutions for the Schrodinger equation are not possible. Disregarding the e - h interaction is possible in the strong confinement regime, as confinement energies scale with d^{-2} (as energy goes as n^2/d^2), while coulomb interaction scales with d^{-1} (d being the diameter of the particle). This gets states with distinct n , l , m quantum numbers referring to various symmetry, orbital angular momentum, its projection, respectively (similar to electrons in the orbitals of an atom). The wave functions are represented as products of several terms. The energies of the states can be given as

$$E_{n,l}^{e,h} = h^2 n^2 / 8\pi^2 m_{e,h} d^2,$$

where n is a quantum number. The exact nature of the wave function and the quantum number are not introduced here. The wave functions correspond to the S, P, D, ..., etc., states depending on the orbital angular momentum, l . There is one more quantum number, m , which decides the degeneracy of the states. A pictorial representation of the energy states is given in Fig. 8.9. The energies are measured from the bottom of the conduction (valence) band for electrons (holes). The energy increases as one goes higher in quantum number. Since the electron mass is much smaller than that of the hole ($m_h/m_e \sim 6$ in CdSe), the electron levels are separated more widely than the hole levels.

Electronic transitions are possible between various energy levels. As the wave functions corresponding to different n and/or l are orthogonal, it is not possible to observe all these transitions. Optical transitions between states of the same symmetry are observable. The intensity of the transition will be related to the degeneracy of the states in question.

The transitions observed are far more complex than that can be described by the spherical quantum well model. The scheme provided here is inadequate to describe the hole states. Spin – orbit and coulomb e - h interactions have to be considered to improve the energy level picture.

These transitions can be observed in optical spectroscopy as well as fluorescence spectroscopy. One of the important aspects to be considered in interpreting experimental spectra is the size range of the particles prepared in a typical synthesis. Spectroscopic size selection is possible by techniques, such as fluorescence line narrowing (FLN), spectral hole burning and photoluminescence excitation (PLE). In these techniques, a narrow energy window is used for excitation (first two) or detection (last). This makes the technique sensitive only to a specific particle size. Size selection with the red region of the spectrum is better as it selects the particles of the largest size in the ensemble. An interested reader may consult the cited references to understand the details of the application of optical spectroscopies to quantum dots.¹⁷

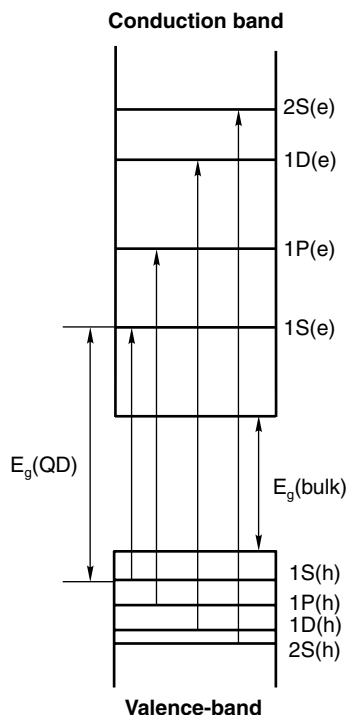


Fig. 8.9 *The electronic states of a nanocrystal. The allowed optical transitions are marked.*

8.5.2 Vibrational Spectroscopies

Vibrational spectra are characteristic of the material and are specific to the chemical bonds. Changes in the chemical characteristics of matter are reflected in the vibrational spectra. Vibrational energies are much smaller compared to the chemical-bond energies and even minute changes in the local atmosphere of a sample are reflected in the spectra. Spectroscopic information of this kind is commonly derived from infrared (IR) spectroscopy, Raman spectroscopy and electron energy loss spectroscopy (EELS). However, there are a few other less common techniques such as inelastic electron and neutron tunneling, helium scattering and sum frequency spectroscopy, which may be used to get information on vibrations. All of these techniques are resource intensive. The first three techniques are more commonly used in various ways to analyse nanomaterials.

Vibrational spectroscopy is used to derive information on the vibrational excitation of molecules. Most of the time, the excitation is limited to the fundamental vibrational frequency. As the molecule normally is at the lowest vibrational level namely $v = 0$, the harmonic oscillator approximation is a sufficient representation of the vibrational transitions. The transition frequency measured corresponds to the fundamental vibrational frequency, $\nu = 1/2\pi\sqrt{(k/\mu)}$, where k is the force constant of the bond and μ is the reduced mass of the system.

There are several fundamental vibrational modes in the system depending on the symmetry. Several of these will be observed in the infra-red and Raman spectroscopies. There are altogether $3N-6$ vibrational modes in an N atom containing non-linear molecule and $3N-5$ modes in a linear molecule. The 6 and 5 correspond to the other degrees of freedom (translational + rotational) present in the molecule. The number of modes observed in Raman and IR depend on the symmetry of the system.

IR spectroscopy is possible only if the vibration changes the dipole moment of the molecule. The probability of a transition is proportional to the square of the transition dipole moment. $M_{v'v} = \int_{-\infty}^{+\infty} \psi(v) \mu \psi(v') d\tau$, where $\psi(v')$ and $\psi(v)$ are vibrational wavefunctions of states v and v' and μ is the dipole moment of the bond undergoing vibration. The value of the integral makes a vibration active or inactive in the IR. The symmetries of the molecule and the vibration decide this. The vibrational band intensity is a function of the intensity of the electric field of the radiation and its orientation with respect to the transition dipole. A study of the variation of infra-red features as a function of the polarisation of the light can be used to study the orientation of the dipole in a condensed system.

Infra-red spectroscopy is an ideal technique to understand molecular vibrations of the nanomaterials. It is best suited for the study of the monolayers on the surface of a nanoparticle. The nature of binding, the molecular nature of the ligand, its organisation and extent of order and so on can be understood from infra-red spectroscopy. In Fig. 8.10, the infra-red spectrum of a silver nanoparticles protected with octadecanethiol (ODT, $C_{18}H_{37}-SH$) shows no peak due to the S-H frequency and it can be concluded that the thiol is absorbed in the form of thiolate (RS^-) on the surface of the metal particle. At a characteristic temperature, the C-H vibrations of methylenes ($-CH_2$) shift to a higher frequency indicating a phase transition.

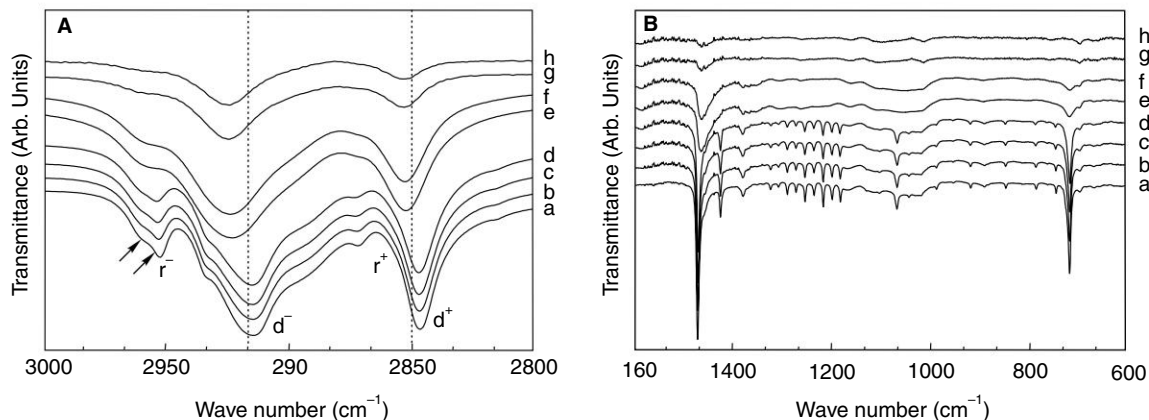


Fig. 8.10 Variable temperature FT-IR spectra of Ag nanoparticles protected with ODT. A and B corresponds to the C-H stretching and low frequency (finger print) regions, respectively. The spectra were measured in KBr matrices. The temperatures are a 298, b 323, c 348, d 373, e 398, f 423, g 448, and h 473 K. The d_- and d_+ modes are the asymmetric and symmetric modes of CH_2 stretching. See that in the spectrum at 398 K, these peaks are shifted to higher values indicating more disordered methylene units, implying phase transition.

transition. This corresponds to the 'melting' of the alkyl chain order on the monolayer assembly. Heat change corresponding to this transition is observable in differential scanning calorimetric analysis of the materials. The phase transition leads to increased freedom and the monolayers possessing orientational freedom undergo rotational dynamics above this temperature. Part of this rotational freedom is evident in the infrared spectrum. At low temperatures, the ν mode corresponding to the methyl ($-\text{CH}_3$) splits into two as the chains have no rotational freedom and the modes are non-degenerate. When the temperature increases beyond the phase transition point, the methyl groups acquire rotational freedom and the vibrations become degenerate. The chains having distinct all-trans conformation as the gauche bonds are less prominent in the spectrum. The spectrum shows characteristic features due to the progression bands suggesting the alkyl chain order. However as temperature increases, the intensities of the C-S gauche are also increase. Also, at the phase transition point, the progression bands disappear. Likewise, infrared spectrum helps in a number of ways to understand the structure of the monolayer chain. Even if the functionality is modified, it is reflected in the spectrum.

In the case of a metal nanoparticle, infrared spectroscopy does not furnish any information on the core. However, for a semiconducting or insulating nanoparticle, it provides invaluable information on the structure and phase transitions. Most of these studies are conducted with Raman spectroscopy and its variations, such as those at high pressures and high temperatures.

8.5.3 Other Vibrational Spectroscopies

Electron energy loss spectroscopy (EELS) is based on the inelastic collisions of a monochromatic beam of electrons and the study of the kinetic energy of the electrons. The energy loss of the sample corresponds to excitations in the sample. Electronic, vibrational and rotational excitations of the sample can be studied in EELS. Electronic excitations can be of the core levels or of the valence levels. While the former is referred to as inner shell EELS (ISEELS), the latter is referred to as EELS. The spectroscopy used in the study of vibrations is called high-resolution electron-energy loss spectroscopy (HREELS) and is generally used for the study of adsorbates. Due to experimental limitations, it is not possible to observe all the excitations in one kind of spectrometer. Rotational spectra are not studied with EELS as electron energy analysis is not possible at the resolution required for rotational spectroscopy in most cases. The principal aspect of the spectrometer, which limits resolution, is the electron energy analysis and analyser limits the instrumental performance. The analyser performance is given in terms of the full width at half maximum (FWHM), which is generally of the order of a few meV in HREELS. A typical vibrational frequency occurs at 100 meV (806.5 cm^{-1}).

EELS involves three kinds of excitation mechanisms. The first one is dipole excitation wherein the interaction between an electron and molecule is similar to light and matter. This leads to transitions similar to that observed in optical spectroscopy leading to specular scattering (angle of incidence is the same as scattering). The other kind of transition is impact driven, in which electron behaves like a particle. The angular distribution is complex and non-allowed transitions can be excited in this process. The third kind is resonance excitation, wherein the electron undergoes exchange with the sample, resulting in isotropic scattering. Here again, non-allowed transitions can be excited. Thus proper application of EELS can give additional information not possible from optical spectroscopy.

Infrared spectrum is measured by illuminating the sample with a polychromatic infrared light and measuring the absorption of the sample. Two kinds of methodologies are done normally; one is by a dispersive infrared spectrometer and the other by using fourier transformation of the interferogram resulting from the interference of two light beams with a difference of path-length. The latter technique, called FT-IR, is the most common analytical method these days. Raman spectrum is measured by analysing the scattered light coming from the sample. The illuminating light is generally in the visible region of the electromagnetic spectrum and hence focusing down to a few hundreds of nanometers is possible. If the light is focused on a sample using a SNOM aperture, it is possible to illuminate a single nanoobject and Raman spectral measurement of this object becomes possible. The other illumination source used for vibrational spectroscopy, namely, electrons, can be focused on the sample at smaller areas as in the case of transmission electron microscopy. As this beam is inherently of large energy and concomitantly of poor resolution vibrational spectroscopy is impossible. Despite its poor resolution, features of inner-shell excitation are useful in identifying the elemental constituents and nature of binding of materials at the nanometer regime. At lower excitation energies of the order of a few eV, the electron beam has very narrow energy width, of the order of 1 meV or less making it possible to do vibrational spectroscopy. This is normally performed on adsorbate molecules which are present on the surface at monolayer coverages. Because of this fact and also due to the fact that electrons are used, HREELS is done in ultra-high vacuum. Due to the extreme surface sensitivity of the low-energy electrons, the technique looks at the top monolayer only. In HREELS, one can observe low-energy vibrational excitations, such as those representing the adsorbate-surface interactions. These are necessarily low-energy vibrations as their force constants are small and the mass of the surface atom is large. It is not possible to see these low-energy motions in infrared as far infrared spectroscopy is rather difficult at surfaces. These may be possible to observe in Raman, but regular Raman becomes difficult due to poor scattering cross-section.

Imaging materials with vibrational spectroscopies provide complete information about the sample. This is done in IR and Raman spectroscopies and the instruments are called IR and Raman

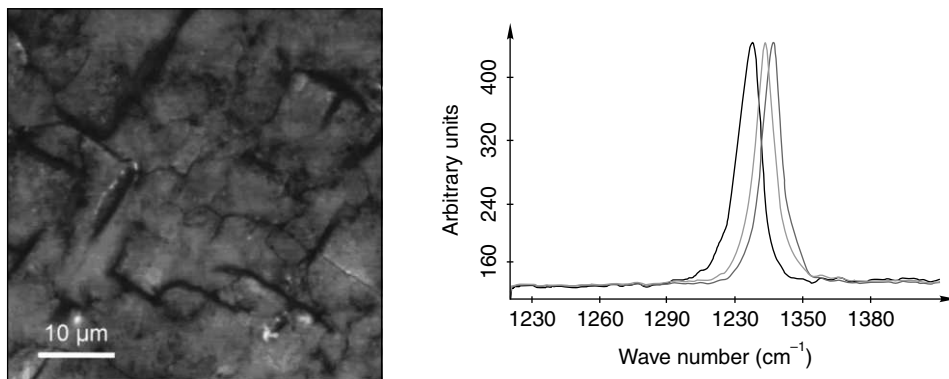


Fig. 8.11 Raman micrograph of a CVD grown diamond film. The spectra from various regions are shown on the right. Spectra of different colours are used to construct the images of the same colours (data and image are with the courtesy of, www.witec.de). (For clarity see colour figure.)

microscopes. Just as in XPS, there is microspectroscopy and spectromicroscopy. IR images of samples reveal chemical details of the sample. Peak intensities, shifts, widths, etc., can be used for imaging. Figure 8.11 shows a Raman image of a chemical-vapour-deposited diamond. The spectrum of the sample is shown on the right side. Different regions of the sample give slightly different spectrum with distinguishable shift. These shifts correspond to the strain in the sample. The shift can be used to obtain a strain distribution in the sample. This is possible with a spatial resolution of the illumination source (of the order of $\lambda/2$). Sub-micron particles have been imaged by Raman spectroscopy using the vibrational band intensity. Using confocal techniques, it is possible to confine the scattering molecule within the interaction volume and spectra from single molecules can be measured. This is possible only when the spectra can be enhanced, as in the case of surface enhanced Raman spectroscopy (SERS). Raman spectroscopy is discussed separately.

8.5.4 Elemental Analysis

In order to understand the composition of the nanomaterial, elemental analysis is often useful. This may be illustrated with the help of a gold nanoparticle protected by thiols. The elemental analysis of a fixed quantity of nanomaterial by wet chemistry or instrumental methods will get the gold content. From the sulfur content, the number of monolayer chains or the molecules can be understood. The fraction of gold to thiol is known from this and can be compared with the theoretical estimate of the starting material used. This information may also be available from the thermogravimetric analysis of the material. From the diameter obtained from TEM, the number of gold atoms present may be determined considering a spherical geometry and assuming complete coverage of the gold surface with S, an approximate estimate of the capping molecules may be arrived at. From all the information available, it is possible to find the molecular formula of the nanoparticle as, Au_nSR_m . The minimum information necessary are the core diameter and the elemental composition. This kind of an approach can be extended to any kind of nanoparticle system, although extreme monodispersity is assumed.

8.5.5 NMR Spectroscopy

NMR spectroscopy is widely used in understanding the properties of monolayers of nanoparticles. Basically, this is the extension of application of NMR to molecular structure and properties. For example, the structure of alkanethiolate monolayers in monolayer protected cluster (MPC) solids has been probed by ^{13}C NMR³ and transmission IR⁴ spectroscopies. ^{13}C NMR focuses on the dependence of chemical shifts as a function of the carbon position relative to the gold–hydrocarbon interface. Fig. 8.12 shows the ^{13}C NMR spectra of octanethiol monomer and octanethiolate-, dodecanethiolate- and hexadecanethiolate-protected Au clusters. The important findings here are that compared to the C_8 monomer (the free thiol), all the peaks in the cluster are broadened attributing to the immobilisation of the surfactant on the cluster surface. Going from the shorter to longer chain lengths, the peak width narrows, as the carbon is located further away from the thiol functionality. The other significant observations are that the resonances from carbon atoms closest to the Au core, those due to C_α , C_β and C_γ are broadened into the baseline and that there is a systematic change in both the chemical shift and the line width with the carbon position relative to the Au–hydrocarbon interface. These are attributed

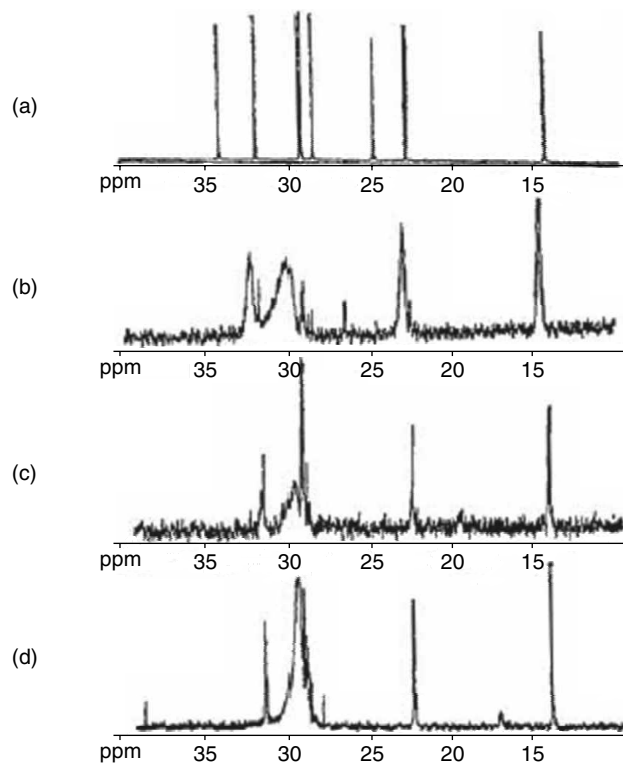


Fig. 8.12 ^{13}C NMR spectra of (a) free octanethiol and Au clusters protected with (b) octanethiol, (c) dodecanethiol and (d) hexadecanethiol. a, b, c, d to be marked. a is top. C_n represents the position of carbon from the surface (from Terrill et al.³).

to the discontinuity in the diamagnetic susceptibility at the Au–hydrocarbon interface and residual dipolar interactions in alkanethiolate monolayers. Badia et al. compared the adsorption of thiols on a cluster surface with that of Au(1) alkyl thiolates and found that the chemisorbed species on the gold nanoparticle surface is a thiolate, not a disulphide.⁵ They observed a line broadening of the C_1 and C_2 sites, which is explained as due to the chemical shift distribution resulting from the different adsorption sites and/or non-spherical particle shapes. These observations show the similarity of these 3D-SAMs to the corresponding Planar or 2D-SAMs. NMR data suggest that the long alkyl chain surfactant on gold nanoclusters is in a semicrystalline state. At room temperature, all-trans chains coexist with a smaller population of more mobile chains containing gauche conformers.³ The shorter-chain thiols are disordered even at room temperature. Broadening of the resonances as well as the disappearance of the carbons closest to the surface shows the immobilisation of the alkyl chains and the strong interaction with the metal surface, respectively. The upfield shift of C_{17} in $C_{18}\text{S}-\text{Au}$ and the Gaussian decay of the signal in the dipolar dephasing experiments suggest the presence of a motionally restricted interior of the alkyl chain and the conformationally disordered chain ends. The methyl proton line widths are lower than those of crystalline alkanes, suggesting that large-amplitude motions are taking place about

the chain axis. However, this is the case of monolayers in solution. When the MPCs are in the solid state, experiments using quasielastic neutron scattering (earlier chapter) have shown that the methyl groups on top are in a rotationally restricted state.

There are other ways, by which NMR can be useful in understanding the properties of nanoparticles. For example, the hydrodynamic radii (R_H) of Au MPCs were determined using diffusion controlled ordered ^1H NMR spectroscopy⁶. The effective average hydrodynamic radii were calculated using the Stokes–Einstein equation, $R_H = k_B T / 6\pi\eta D$. These values are in agreement with the cluster sizes measured with STM. It has been shown that the corresponding edge to edge spacings of the metal cores are considerably shorter than twice the length of the alkyl chains and are closer to the single all-trans chain length. This result suggests that the alkyl chains undergo either interdigitation to the adjacent clusters or chain folding. Wuelfing et al.⁶ used Taylor diffusion coefficients to calculate the hydrodynamic diameters under different boundary conditions for the Stokes–Einstein equation. Calculated and experimental hydrodynamic diameters of MPCs in organic solvents are in good agreement to each other, implying free draining of solvent through the outer portion of the chains.

8.5.6 Thermal Analysis

Thermal analysis refers to subjecting the material to temperature changes and measuring the properties. There are a number of methods and most common of these are thermogravimetry (TG) and differential thermal analysis (DTA). Thermogravimetry refers to the measurement of mass of the sample as a function of temperature. The mass loss/gain with temperature is plotted upon heating under a specific condition. Thermal decomposition is the most important information one derives. The differential changes in the sample with respect to a stable/unreactive standard, is often measured and the analysis is called differential thermal analysis, which provides changes in the sample such as combustion. TG is quite useful in understanding the extent of monolayer cover on a nanoparticle because the monolayer desorbs completely in most cases before the core of the nanoparticle is affected.

Calorimetric analysis of the sample is performed in several different ways. Calorimetry refers to the heat input/output in a sample upon rise in temperature. This allows the determination of specific heat and changes in specific heat allows the determination of phase transitions. The common way to conduct this analysis is differential scanning calorimetry. Isothermal calorimetry is one of the several ways of performing calorimetry, which is often used in the determination of binding events in biology such as DNA hybridisation.

8.5.6.1 Differential Scanning Calorimetry (DSC)

Phase transitions in alkanethiolate monolayers on gold clusters have been detected by DSC⁷, variable temperature NMR and variable temperature IR spectroscopies⁸. Melting points and phase transitions of the materials as well as the enthalpic changes can be measured with DSC. All the clusters with chain lengths more than 8 carbon atoms show a broad endotherm in DSC at 330 K indicating a phase transition. This transition is attributed to melting of the alkyl chains. In clusters, because of the high curvature of the surface, the chain termini of the alkyl groups are more diverged than the head group. This causes the interpenetration of the adjacent alkyl chain termini into this gap and the van der Waals

forces make this structure more ordered and stable. The observed transition is attributed to the melting of the alkyl chains in the interdigitated regions. Enthalpy associated with the transition increases with increasing chain length, because larger chain length enables more extensive van der Waals interactions and resulting enthalpic contributions. Badia et al. used variously deuterated octadecanethiolate monolayers for understanding the nature of the phase transition.⁸ The broad endotherm present in DSC suggests a thermally induced reversible phase transition.

Phase transitions of nanoparticles occur at much lower temperatures than that in the bulk. This is because of large surface energy in nanoparticles, which allows displacement of atoms to occur with reduced thermal energy. Thus investigation of nanoparticle cores is also useful by DSC.

REFERENCES

1. S.M. Sze, *VLSI Technology*, AT&T Bell Laboratories, Murray Hill, New Jersey; (b) H.H. Wieder, *Four Terminal Nanodestructive Electrical and Galvanomagnetic Measurements in Nondesstructive Evaluation of Semiconductor Materials and Devices* (J.N. Zemel, ed.), Plenum Press, New York, (1979), 67–104.
2. C. Soci, A. Zhang, B. Xiang, S.A. Dayeh, D.P.R. Aplin, J. Park, X.Y. Bao, Y.H. Lo and D. Wang, (2007). ZnO Nanowire UV Photodetectors with High Internal Gain, *Nano Lett.*, 7, (4), 1003–09.
3. R.H. Terril, T.A. Postlethwaite, C.-H. Chen, C.-D. Poon, A. Terzis, A. Chen, J.E. Hutchison, M.R. Clark, G. Wignall, J.D. Londono, R. Superfine, M. Falvo, C.S. Johnson, E.T. Samulski Jr and R.W. Murray, (1995). ‘Monolayers in Three Dimensions: NMR, SAXS, Thermal, and Electron Hopping Studies of Alkanethiol Stabilized Gold Clusters’, *J. Am. Chem. Soc.*, 117, (50), 12537–48.
4. M.J. Hostetler, J.J. Stokes and R.W. Murray, (1996). ‘Infra-red Spectroscopy of Three-Dimensional Self-Assembled Monolayers: N-Alkanethiolate Monolayers on Gold Cluster Compounds’, *Langmuir*, 12, (15), 3604–12.
5. A. Badia, L. Denners, L. Dickinson, F.G. Morin, R.B. Lennox and, L. Reven, (1997). ‘Gold–Sulfur Interactions in Alkylthiol Self-Assembled Monolayers Formed on Gold Nanoparticles Studied by Solid-State NMR’, *J. Am. Chem. Soc.*, 119, (45), 11104–05.
6. W.P. Wuelfing, A.C. Templeton, J.F. Hicks and R.W. Murray, (1999). ‘Taylor Dispersion Measurements of Monolayer Protected Clusters: A Physicochemical Determination of Nanoparticle Size’, *Anal. Chem.*, 71, (18), 4069–74.
7. A. Badia, S. Singh, L. Demers, L. Cuccia, G.R. Brown and R.B. Lennox, (1996). ‘Self-Assembled Monolayers on Gold Nanoparticles’, *Chem. Eur. J.*, 2, (3), 359–63.
8. A. Badia, L. Cuccia, L. Demers, F. Morin and R.B. Lennox, (1997). ‘Structure and Dynamics in Alkanethiolate Monolayers Self-Assembled on Gold Nanoparticles: A DSC, FT-IR, and Deuterium NMR Study’, *J. Am. Chem. Soc.*, 119, (11), 2682–92.

ADDITIONAL READING

1. C.N. Banwell, *Fundamentals of Molecular Spectroscopy*, Tata McGraw-Hill, New Delhi (1993).
2. J.H. Gross, *Mass Spectrometry*, Springer, Heidelberg (2004).
3. A.R. West, *Solid State Chemistry and its Applications*, John Wiley & Sons, Singapore (1989).

REVIEW QUESTIONS

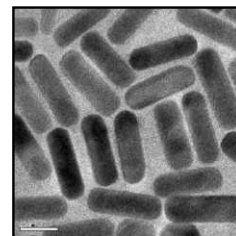
1. What is soft ionisation?
2. Why mass spectrometry is useful in nanoscience?
3. What is difference between rolling angle and sliding angle?
4. Which thermodynamic parameters can we estimate using CA measurements?
5. The CA depends on time. So how one can get rid of natural evaporation of solvent and effect of humidity?
6. In conductivity measurement, which material is used as substrate for keeping sample and why?
7. What is the effect of dilution on size of Au nanoparticles?
8. In temperature dependent IR of ODT capped Ag nanoparticles, why CH_2 vibration shift to higher energy values?
9. How molecular weights of capping agent affect particle size for Au nanoparticles?
10. What information of nanoparticles can be obtained using DSC?

PART THREE

Synthesis

- **Synthesis of Nanomaterials**

SYNTHESIS OF NANOMATERIALS



“Chemistry affords two general methods of determining the constituent principles of bodies, the method of analysis, and that of synthesis. When, for instance, by combining water with alcohol, we form the species of liquor called, in commercial language, brandy or spirit of wine, we certainly have a right to conclude, that brandy, or spirit of wine, is composed of alcohol combined with water. We can produce the same result by the analytical method; and in general it ought to be considered as a principle in chemical science, never to rest satisfied without both these species of proofs.”

Antoine-Laurent Lavoisier in *Elements of Chemistry*, (1790), trans. R. Kerr, 33

Nanomaterials are synthesised in diverse ways. There are methods starting from the bulk materials and also methods starting from the atoms. The physical methods use the bulk materials and the chemical methods start with atoms. In the former, rigorous control of size is difficult, while in the latter, atomic precision in size purity can be achieved. For shape control, chemical methods are preferred. In specific cases, only selected methods or even only one method is available. The choice of the method depends on the flexibility, one has in the synthesised material in terms of redispersability, thermal and chemical stability, monodispersity, etc.

Learning Objectives

- Why different methods are used to make nanomaterials?
 - How to control size and shape of nanoscale objects?
 - How to study distribution in particle sizes?
 - How to make unique nanomaterials?
 - Is it possible to make one material in many ways?
-
-

9.1 INTRODUCTION

In this chapter, we are concerned with the synthesis of a diverse variety of nanomaterials. The materials formed are composed of nanoparticles—both spherical and other shapes, nanotubes or

nanomolecules. They have to be synthesised by diverse routes and these methods have to be perfected such that chemical variety is possible in the materials synthesised and the physical properties can be altered with ease. The synthetic methods, at least in some cases, should have flexibility to get expanded such that commercial exploitation is possible, if suitable applications are found. In this discussion, we will focus on some of the most common methods for the common kind of materials. Mention will be made of the less popular routes such as materials formed in porous media, like zeolites, embedded particles in glasses, etc. However, this discussion will be brief.

Broadly, the methods of synthesis can be divided into two categories—physical and chemical routes. In physical, the approach is to take the bulk material or constituent materials from which nanomaterials are formed and create conditions by which nanomaterials are formed. As these methods of synthesis start from bulk materials, they are called top-down approaches. Following methods are commonly encountered:

High-energy ball milling: Materials are powdered by milling to produce nanoscale powders.

Inert gas condensation: Condensing evaporated atoms in a matrix so that particle growth happens.

Arc discharge: Evaporation of material by an AC or DC arc.

Wire explosion: Evaporation of conducting materials, such as metals by a sudden high current pulse, making an explosion.

Ion sputtering: Evaporation by the impact of high energy ions, generally of rare gases.

Laser ablation: Evaporation by a high energy laser.

In all these, the environment, in which evaporation takes place can be controlled. For example, evaporation of metals can occur in an atmosphere of oxygen, so that oxides are produced. The methods can be very effective in making large quantities of materials. However, the principal problem with the methods is that they produce a large particle size variation.

In chemical methods, which we will be describing in more detail in the subsequent sections, a range of techniques are used. In all of these, nanomaterials are made starting from atoms. Atoms are formed from ions, generally in solutions, and they are assembled to make nanomaterials. As the assembly is starting from atoms, these methods are also called bottom-up approaches. Several methods come under this category:

Chemical reduction: Reduction starting from metal ions using reducing agents.

Solvothermal synthesis: Low-temperature chemical methods in a closed system involving the use of solvents.

Photochemical synthesis: Light-induced chemical processes.

Electrochemical synthesis: Electrochemical reduction or oxidation processes.

Arrested precipitation, especially for nanocrystals of semi-conductors and oxides: Precipitating the materials from an organometallic precursor solution.

Thermolysis (pyrolysis, spray pyrolysis) routes: Thermal decomposition, reactions in flames.

Sonochemical routes: Use of ultrasound in chemical reaction system.

Micelles and microemulsions: Use of oil-in-water or water-in-oil emulsions and the use of cavities of the micelles or reverse micelles to make nanomaterials.

Interfacial synthesis: Use of organic-aqueous interfaces to make nanomaterials.

Biological methods: Use of biomolecules, living cells as synthetic reactors to make materials.

Hybrid methods: A combination of more than one of the methods above.

Solvated metal atom dispersion (SMAD): Here metal vapours are deposited in solid matrices of solvents and nanoparticles are formed when the solvent is warmed up. By adding capping agents to the solvents, it is possible to make protected clusters.

Just as any system, nanoparticles are also composed of atoms. From a general perspective, a two-phase colloidal system can be classified in terms of a dispersed phase in a dispersion medium. The dispersed phase and the dispersion medium can be any one of the three phases, namely, gas, liquid or solid; except that the first category, i.e., *gas in gas*, is unknown. From this, a solid nanoparticle dispersed in an amorphous solid may be considered as a colloidal system, and consequently, a nanofluid. Nanofluid is a term used to refer to a dispersion of nanomaterials in a fluid medium. Fluid in our description will be liquids at ordinary conditions of temperatures and pressures, and for that reason supercritical fluids and gases, as the dispersion phase, will not be considered. It may be noted that the synthesis of nanoparticles in these media, namely, solid matrices and supercritical fluids are large and advanced areas of science. From a historical perspective, it is also important to remember that some of the early applications of nanoparticles were in the form of embedded particles in glasses. Supercritical fluids are a recent area of development in nanoparticle science. Such fluids are most commonly referred to as colloids.

The nanomaterials so prepared can be in the form of a fluid or solid. In many cases, the applications of these materials will be in the form of solutions or dispersions, called nanofluids. They may also be used as powders, often referred to as nanomaterials. Particle films, pastes, emulsions and many other forms may also be used.

9.2 GENERAL ISSUES OF CONCERN

There are several factors of interest while considering a given synthetic approach. These may be grouped under:

1. Thermal stability
2. Dispersability in diverse media
3. Chemical compatibility and ease of surface manipulation

Each of these parameters is discussed in some detail below. It may be noted that several of them are intimately connected to each other.

9.2.1 Thermal Stability

Nanoparticles are metastable systems. This means that they will transform to stable materials, which have global energy minima in the free energy landscape. If one plots free energy of the system for a

fixed amount of the material (as free energy is an extensive property), nanoparticles exist at a higher energy in comparison to the bulk materials although a given nanostructure may have a local minimum in comparison to other structures. These local minima in the limit of extremely small particles correspond to magic numbers with unusual structural/electronic stabilities. Such particles are referred to as clusters, which will be mentioned in a later section. In the case of isolated atoms and molecules, the total energy is much larger in comparison to the bulk. Nanoparticles constitute a regime, in which the energy is in between that of the bulk materials and the molecules/atoms. It is possible to convert one form to the other by physical or chemical means.

In the smaller size regime of less than 1 nm, nanoparticles possess distinct structures and may be regarded as “nanocluster molecules”. Each of these clusters may have isomeric structures and one may be more stable than the other. Various structures of a given size may have large differences in properties. In the larger size regime, numerous structural forms can exist, but it is difficult to distinguish them. When it comes to large changes in the geometry, as in the case of a nanoparticle and a nanorod, a distinction can be made on the basis of their electronic properties. Synthetic methodologies are available to make some of those structures in the case of a few metals and ceramics.

As nanoparticles are metastable, they would go back to the bulk at infinite time. The time one considers in several cases has no practical consequence, as Faraday’s colloids, made in 1857, are stable even now.¹ Although the bulk metal is more stable, it is just as one considers the stability of graphite in comparison to diamond. Diamond, although metastable, does not become graphite at normal conditions of temperature and pressure even if kept for a millennium. The kinetics of diamond to graphite transformation is very slow, and therefore, it is insignificant under normal conditions. The situation of nanoparticles in appropriate media is analogous and is referred to as “kinetic stability”.

9.2.2 Dispersability in Diverse Media

A nanoparticle is composed of two entities: A “core”, often ceramic, metallic or polymeric, and a thin “shell”, which may be ionic, molecular, polymeric, ceramic or metallic. In most cases, we encounter ceramic or metallic core and a molecular shell (Fig. 9.1). The properties of the nanoparticle are principally due to the core and the shell is used to provide a protective later. Often the nature of the shell is extremely significant in a number of applications, such as luminescence of the particles. The shell and the core may have underlying structures and may be composed of more than one entity. The solubility of a nanoparticle is determined by the chemical nature of the shell. Solubility is not the appropriate terminology as the “solution” or fluid formed is in effect a dispersion, which may be separated by physical means such as centrifugation. A solution is a homogeneous mixture of substances in any phase, which cannot be separated as saltwater.

The molecular shell has characteristic chemical affinity to the nanoparticle core due to its specific atoms or groups. For example, in the case of an oxide nanoparticle, the metal at the surface can link with an alkoxide ($-OR$, where R is alkyl). In the case of a metal nanoparticle such as gold, the metal can link with a sulphur atom of the thiolate ($-SR$). Such a link present throughout the surface of the nanoparticle is called a protective monolayer, or capping layer. The nanoparticle so produced is called

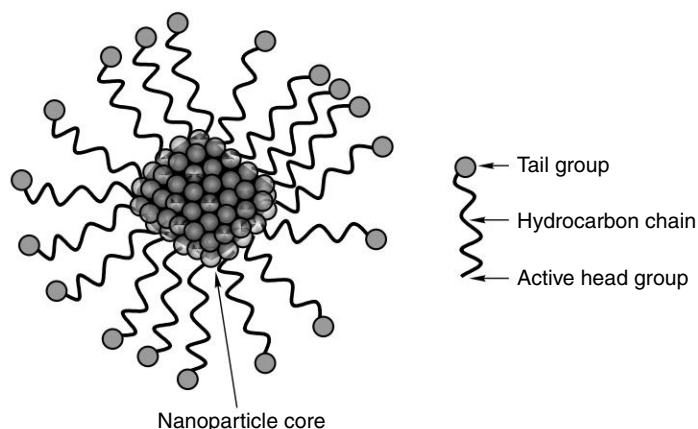


Fig. 9.1 A schematic of a nanoparticle. It is composed of a core and a shell. The core need not be a crystalline assembly, unlike the one shown here with a regular arrangement of like atoms. The core may be made of mixture of different kinds of atoms. The molecular shell has three distinct regions, one or more of these may be absent in a specific case. A hydrocarbon chain may be long as in the case of a polymer, or it may be completely absent in the case of an ion protecting the nanoparticle. The shell may also be an extended solid such as SiO_2 .

a protected or capped nanoparticle. The sulphur at the end ($-\text{SR}$) is a surface-active head group, as it links with nanoparticle surface due to its specific chemical affinity. The chemical bond so formed gives thermal stability to the nanoparticle system. The weaker it is, the easier it desorbs from the surface and the nanoparticle will be less stable. Au-S bond has a bond strength of the order of 50 kcal mol^{-1} , and the thiolate desorbs only above 270°C from the metal surface.² Thus, the metal-active head group binding is an important parameter in determining the thermal stability of the nano system. During the formation of the nanoparticle, while the monolayer binding takes place, the molecule may undergo changes. For example, the thiol (RSH) binds on gold to form RS and the H is lost. There are various ways, by which such a loss can occur, and this has been a subject of debate. The type of monolayer and its structural attributes depend on the core.

In our discussion, we are mostly concerned with large nanoparticles, the typical size of which is of the order of a few nm. However, there is a regime of materials of much smaller sizes, below 1 nm in core dimension, which is attracting significant attention in the recent past. We will be discussing this regime of materials, called clusters later in this book. In large nanoparticles, the nanoparticle core contains several thousands of atoms. For example, a 3-nm gold particle has around 1100 atoms, considering the nanoparticle to be a sphere. In reality, these particles are “faceted” or the outer surfaces terminate at specific crystallographic planes (for example, assume a cube with corners cut off). On these planes, the head groups of the protecting molecules occupy specific locations, decided by the available space, packing density and the van der Waals diameter of the molecules. If there are larger number of monolayers present on each of the crystallographic planes, the alkyl chains are arranged close-by, and their inter-chain van der Waals interaction become important (as these interactions act at

short distances). This gives additional stability to the system. In addition to breaking the nanoparticle-head group interaction, the van der Waals interaction also needs to be broken to destabilise the nanoparticle. In most of the cases, the inter-chain interaction is generally weaker in comparison with the head group-nanoparticle interaction. As the monolayer assembly gets organised, as in the case of long-molecule monolayers, the core becomes inaccessible for ions and molecules in the medium. This leads to increased chemical stability for the core. The strength of the van der Waals interaction increases with increase in the chain length. In the limiting case of a polymer or a ceramic shell, chemical bonds in the shell are comparable or stronger than those in the nanoparticle core.

The tail group is the one that interacts with the solvent or dispersion medium. As a result of favourable interaction, nanoparticles get dispersed in the medium. Thus, in order to make nanoparticles soluble in water, a hydrophilic cover is required. On the contrary, a hydrophobic cover makes the nanoparticle soluble in organic media such as toluene. By varying the polarity of the tail group, it is possible to get the system dispersed in solvents of varying dielectric constants. In the case of a hydrophilic monolayer, the shell has groups such as $-\text{COOH}$ or $-\text{NH}_2$, which may be ionised to yield $-\text{COO}^-$ or NH_3^+ , which will give a net negative or positive charge per monolayer chain to the metal surface. As the nanoparticle contains several such bound ions the particle may possess several charges. The particle may be such that there are both negative and positive charges on the same particle and the net effect of all these will be reflected in the charge of the system. At a specific pH, the net charge on the particle will be zero, say for example, in the case of an amine ($-\text{NH}_2$) terminated surface, all the monolayers will be in the form of $-\text{NH}_2$ and not $-\text{NH}_3^+$. This pH is called the “isoelectric point”. This is generally encountered in the case of proteins, where each molecule can exist as a “zwitter ion” (both negative and positive charges on the same molecule). In the case of proteins, this occurs as a result of the existence of $-\text{COO}^-$ and NH_3^+ on the same molecule. Only at the isoelectric point, the molecule is not ionised.

As mentioned earlier, the entity constituting the shell present on the nano surface need not be a molecule. In several cases the shell itself is an inherent part of the core. For example, in the case of silica nanoparticles, the surface is often a layer of hydroxyl groups and the particles can easily be suspended in water. In contrast, a hydrocarbon monolayer will make the particle disperse in organic liquids. Gold nanoparticles can be made hydrophilic or hydrophobic in a similar fashion. In the case of reactive nanoparticles such as copper, the shell can get oxidised easily, and there is always a layer of oxide on the surface, especially when the particles are exposed to air.

The tail group can change its character depending on the medium as mentioned before. This is particularly significant in cases, where the group is $-\text{COOH}$, $-\text{NH}_2$, $-\text{OH}$, etc., where the pH of the medium can greatly affect the nature of the group. For example, in acidic media, we get $-\text{COOH}$ and in alkaline media we get $-\text{COO}^-$, in the case of a $-\text{COOH}$ terminated monolayer. The pH values of a nanoparticle-dispersion (without the presence of additional base or acid) depend on the pKa of the acid in question. The change makes a large difference in the charge on the nanoparticle surface. This changes the zeta potential of the particle (see below) and may have consequent effect on the properties. Such surface charge modifications are important in applications, such as drug delivery. During changes in conditions, such as pH, it is possible that the core also gets affected.

In the early studies on thermal conductivity, the nanoparticles prepared by diverse routes were stabilised by dispersants and activators, such as laurate salts ($\text{CH}_3(\text{CH}_2)_{10}\text{COO-X}$), oleic acid ($\text{CH}_3(\text{CH}_2)_7\text{CH}=\text{CH}(\text{CH}_2)_7\text{COOH}$), etc. The purpose of this approach was to stabilise the nanoparticles in diverse media, such as transformer oil, water, ethylene glycol, etc. The general approach used is an appropriate surface functionalisation so that the nanoparticle surface is friendly to the medium.

The core-shell structure of a nanoparticle system is not limited to spherical particles. The very same general structure may be considered for nanorods, nanotubes, nanoshells, etc., where a chemically compatible shell is put around the nanosystem to make it go into the solution, biological environment, etc.

9.2.3 Chemical Compatibility and Ease of Chemical Manipulation

These parameters are significant if the same core size has to be used in diverse applications. The size, shape and properties of nanoparticles depend on the synthetic conditions. This is to be expected of a method that makes a metastable system. As we know, a given nanoparticle is kinetically trapped in a local minimum of free energy and the synthetic parameters are crucial in deciding the final result. Thus, in order to preserve the core size, it is important to follow the same methodology. Often this causes limitations in the adaptability of the system to various chemicals and conditions. For example, if a system is sensitive to a given chemical due to its core or the shell, the shell can be suitably modified so that the chemical has no access to it and the shell has no reactivity for it. This means that the shell has to be manipulated after the nanoparticle synthesis. This indeed is possible if a suitable shell were to be chosen which has distinct chemical features allowing it to be functionalised.

Solvent compatibility has been brought about by changing the whole monolayer in a post synthetic operation. This is referred to as ligand exchange, in which the ligand constituting the monolayer is exchanged with another one in the medium. This exchange process leads to an equilibrium between the molecules in the adsorbed and free states, and by repeating this process a few times, complete exchange can be achieved in several cases.

Chemical manipulation of the monolayer is similar to solution chemistry with simple molecules. The chemistry of the monolayer is utilized, as in the case of free molecules, to make suitable post synthetic changes. For example, a given monolayer may be polymerised or may be included into a polymeric matrix by utilising functional group chemistry. Chemical, thermal and photochemical processes may be utilised to achieve this. The manipulation of the nanosystem can be such that it is trapped in a cavity of a large molecule so that the nanosystem is encased in it and is shipped into a suitable medium. Examples include the use of dendrimers and cyclodextrins.

9.3 SYNTHETIC METHODS: COMMON ISSUES OF CONCERN

Nanoparticles in general, and metal nanoparticles in particular, are investigated from the context of diverse research perspectives. Among these, catalysis, biology, drug delivery, materials science,

photophysics and novel phenomena are most important. Each of these areas has specific emphasis, although the synthetic methodologies have some overlap. The particles may have to be presented in different forms and for this to happen, specific modifications in the synthetic approach are necessary. Numerous books written on nanoparticles are available, and they may be consulted for specific details on the adaptability of a given technique for specific application. Some synthetic methods are totally unrelated; for example synthesis of nanoparticles and carbon nanotubes will have more differences than similarities, although both are nanosystems.

Any synthetic methodology produces particles of a specific size distribution. In the simplest case of spherical particles, one linear dimension, namely diameter, is adequate to describe the size of the particles. It is best to describe the particle size in terms of statistical analysis. Here, we take a collection of N particles. The particles are first sorted in terms of classes with a class mark, a_i with narrower size distributions. The class has a midpoint and a distribution. The distribution of particles among various classes can be plotted as a histogram as shown in Fig. 9.2. As the number of classes increase, the width of the interval decreases, and finally we get a smooth curve. The distribution is characterised by an average and a standard deviation. The average, $\bar{a} = \sum_i (n_i / \sum_i n_i) a_i$, where the first term on RHS is the fraction of number of particles having the class mark, denoted as $f_{n,i}$. Note that this average is a number averaged diameter of particles. The standard deviation, $\sigma = [\sum_i (n_i / \sum_i n_i) (a_i - \bar{a})^2]^{1/2} = [(\sum_i n_i (a_i - \bar{a})^2) / \sum_i n_i]^{1/2}$. Deviation of a value from the mean is given by, $a_i - \bar{a}$. This can be positive or negative. It is clear that σ^2 is the number average of the “square of standard deviations”, $(a_i - \bar{a})^2$. The square root of this square, is therefore, the spread of the data. Because of this, σ is called the root mean square (rms) deviation. For computational easiness, σ is given as $(\overline{a^2} - \bar{a}^2)^{1/2}$.

The synthetic methodology becomes important if it can produce particles of a given size distribution in a simple process. Often the interest is to get as narrow a size distribution as possible. In case the methodology fails to generate the particles of narrower size distribution, post synthetic

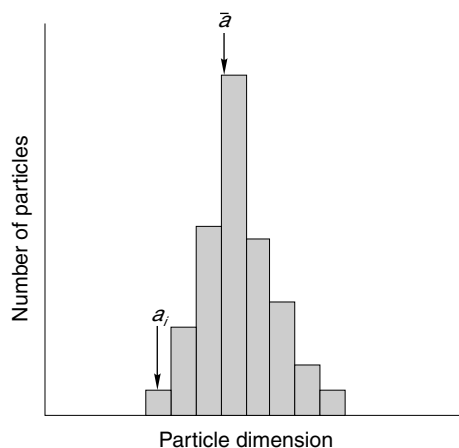


Fig. 9.2 The distribution of particles among various classes in a given synthetic approach. The number averaged particle size is shown. Class width for one class is also indicated. As the width decreases the distribution becomes a smooth line.

processes are utilised to select the particles of interest or convert one to the other. These post-synthetic processes are often laborious and lead to poor yields. Thus, one pot methodology is desirable.

In a generalised approach to nanoparticle synthesis in solution, the precursor species (metal ions, organometallics, complexes, etc.) are chemically reduced or decomposed or hydrolysed, as the case may be, in the presence of an appropriate stabiliser. The conditions of the medium are adjusted such that the nucleation of the particles is fast and the surfaces of the particles thus formed are protected with the stabiliser. Depending on the kind of reaction, the synthetic conditions vary; temperature, pH and medium are the most common variables used. In the case of thermal decomposition of precursors or more complex reactions, conditions are more complex and the procedure may be conducted in inert atmospheres. The particles synthesized in liquid medium could be precipitated out of the medium by varying the solvent polarity or by solvent evaporation at reduced pressures. The material could be purified by repeated solvent washing or dialysis or re-precipitation, depending on the case.

9.3.1 Size Control

A synthetic methodology may not be capable of giving size exclusivity. That means, a variety of sizes may exist in the as synthesised particles. Selection of a given size requires post synthetic approaches. There are several such processes, the first being size exclusion chromatography. In this, the mixture of nanoparticles is passed through a size selective stationary phase, such as a gel which has definite pore sizes. The eluent (solvent medium) used elutes the material as a function of size. Agarose[®] and Sephadex[®] are the two common media used. The other method involves solvent selective precipitation. In this, the polarity of the medium is progressively changed (from low to high) such that larger particles precipitate from the mixture. By repeating this process, proper size control is possible, although stability of the material in different media may vary. The other approach used is digestive ripening, in which the nanoparticle is digested with the protecting agent used in the synthesis, at elevated temperatures in a selected series of temperature steps. The process consumes particles of smaller sizes. The approach of Ostwald ripening or particle coarsening is a similar process, in which the “as prepared particles” are allowed to age for a finite period, during which large particles grow at the expense of smaller particles, narrowing the particle size distribution. This may be achieved along with temperature cycling.

9.4 VARIETY IN NANOMATERIALS

The following discussion includes various methods of synthesis for each category of nanoparticles. The discussion will be mostly pertaining to conventional spherical nanoparticles, other nanoparticles of different shapes will be discussed only briefly. We have separate chapters devoted to these materials later in the book. In his early review, Gleiter reviewed various methods available for nanoparticle synthesis.⁹ In the following, we will be discussing only those methods that can be useful in making redispersible nanoparticles.

9.4.1 Metals

9.4.1.1 Solution Phase Routes by Chemical Reduction

Reduction of metal ions leads to the formation of metal atoms, which upon aggregation form nanoparticle. The growth of the aggregate is arrested at some stage of its growth by adsorption of stabilising or protecting agents. The reduction reaction may be represented as



The electron is not supplied as electron *per se*, but through a reducing agent, which in turn gets oxidised in the process as given below:



where the reducing species (reductant) of finite charge gets oxidised losing certain charge. Note that both the metal and the reductant may not contain any distinct charge and those mentioned are only nominal. The feasibility of the net reaction,



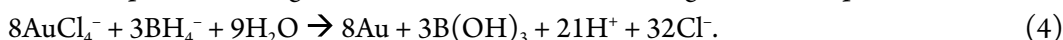
depends on the thermodynamics of the process, which, in turn, depends on the electrochemical potentials of the corresponding half-cell reactions. If the sum of reduction potentials corresponding to the reactions 1 and 2 is positive the process is thermodynamically feasible. This corresponds to a net negative free energy change as, $\Delta G = -nFE$, where ΔG is the free energy change of the reaction 3, n is the number of moles of electrons transferred per mole of the reaction 3, F is Faraday constant and E is the electrochemical potential of reaction 3. Note that we have written E and not E° of the reaction, as the potential at the appropriate conditions has to be taken. A process is thermodynamically feasible if ΔG for that process is negative.

Let us illustrate this with some examples. The standard reduction potentials of some common metal ions and reducing agents are presented in Table 9.1.

Table 9.1 Standard reduction potentials of metal ions and reducing agents²¹

Reaction	Potential (V)
For metals:	
$AuCl_4^{-} + 3e^{-} \rightarrow Au + 4Cl^{-}$	+1.002
$Ni^{2+} + 2e^{-} \rightarrow Ni$	-0.257
$Co^{2+} + 2e^{-} \rightarrow Co$	-0.28
$Fe^{2+} + 2e^{-} \rightarrow Fe$	-0.447
For reducing agents:	
ABH ₄ (A = alkali metal)	
Chemical reaction, $B(OH)_3 + 7H^{+} + 8e^{-} \rightarrow BH_4^{-} + 3H_2O$	-0.481
Hydrazine (N ₂ H ₄ forms N ₂ H ₅ ⁺ in water as it is basic)	
Chemical reaction, $N_2 + 5H^{+} + 4e^{-} \rightarrow N_2H_5^{+}$	-0.23

If the potential is positive, it implies that the process can occur spontaneously. Note that in the case of reducing agents, the reaction of importance is the reverse one, in which it gets oxidised, liberating electrons. These are the electrons, which get consumed by the metal ions in getting themselves reduced. While considering these examples, it is clear that all the metal ions mentioned above can be reduced by borohydride, i.e., if one conducts the reduction of Ni^{2+} by borohydride, in standard conditions (i.e. at 25°C , 1 atm and 1 M concentration of the ions), the electrochemical potential of the process is, -0.257 to $-0.481 = +0.224$. Therefore, the reaction is feasible. However, the reduction of Ni^{2+} by hydrazine is not possible as the potential is negative. The total ionic reduction of gold can be represented as



Above discussion suggests that the the only point of concern is the reduction potential. It is important to emphasise that, in several cases, the ions present in the solution are in complex form and the reduction or oxidation is conducted on that ion. This changes the potentials substantially. As a result, although simple Au^{3+} in the form of AuCl_4^- can be reduced by mild reducing agents, such as carboxylates or alcohols, this is not possible when the metal ion is in the presence of excess thiols. Here they form metal thiolates and reduction of these complexes is possible only by strong reducing agents, such as borohydride. However, when a reduction reaction takes place on the surface of a gold particle, even an apparently mild reducing agent would be capable of acting as an effective reducing agent. On the other hand, some of the reductions, which are not possible normally by consideration of electrochemical potentials, can happen by varying the reaction conditions. For example, the reduction of Ni^{2+} by hydrazine hydrate is possible in ethylene glycol at 60°C in the presence of sufficient hydroxyl ions as per the equation



This particular method gives 9 nm particles.²² It is important to emphasise that electrochemical potentials must be used only as guidelines in understanding the chemistry.

In certain cases, a metal ion can be reduced by a molecule or ion, which itself can act as the stabilising agent. This happens in the case of citrate, amines, alcohols, thiols, etc., for a number of metals. Reduction of HAuCl_4^- by trisodium citrate is a classic example. Numerous such examples are known in the literature in the recent past, in which a variety of amines, alcohols, thiols, complex ions, etc., are used. Alcohols by themselves are not good protecting agents, and therefore, polyols containing larger number of hydroxyl groups per molecule are used, which effectively chelate (multiple coordination) the metal ions. A summary of specific reduction processes employed are summarised in Table 9.2.

Table 9.2 Summary of various solution phase reduction processes employed to make metal nanoparticles

Method	Summary	Example	Reference
1. NaBH_4 route	Metal ion/ BH_4^-	Au, Ag	27, 28
2. Citrate route	Metalion/ Cit^{3-}	Au, Ag	18, 29, 30
3. Polyol route	metal ion/ethylene glycol	Ag, Pd	31
4. Polyvinylpyrrolidone route	metal ion/PVP	Pd	32
5. Amine route	metal ion/APS, AES	Ag	33

9.4.1.2 Strong Reducing Agents

In case, a metal to be reduced has a large negative reduction potential carrying out the reduction process is difficult and the reaction conditions require careful control. When the reducing agent is very strong, it can reduce the solvent and other reagents present in the medium. For example, water may have to be eliminated, if the reagent is too strong so that the reaction,



is avoided. The standard reduction potential of this reaction is -0.828 V . The most powerful reducing agents are solvated electrons. In the laboratory, these are prepared by dissolving alkali metals in aprotic solvents, such as diethylether or tetrahydrofuran in the presence of excess complexing agent, such as a crown ether. The reaction can be written as



If the concentration of the complexation agent is less, we can get alkalide, i.e., the alkali metal anion



Both of these reagents have low thermal stability and, as a result, it is important to conduct the reactions at low temperatures. Such synthesis has indeed been done and several nanocrystalline metals and alloys have been prepared this way.³⁰

Other strong reducing agents are trialkylborohydrides (ABEt_3H , $\text{A} = \text{Li}, \text{Na}, \text{K}$). There have been other reducing agents such as trialkyl aluminium. A variety of transition metal nanoparticles have been synthesised by these routes.^{30,31}

9.4.1.3 Most Popular Methods

In the following, we discuss two of the most common methods used for the synthesis of gold nanoparticles, namely, the citrate route and the Brust method.

The citrate route: This is the most convenient method for the synthesis of colloidal gold nanoparticles of $\sim 15\text{ nm}$ mean diameter. The method is known as the Turkevich method.¹⁵ The synthesis involves the following steps. Make $\sim 5.0 \times 10^{-3}\text{ M}$ HAuCl_4 in water. This is a stock solution. Take 1 mL and make it up to 19 mL using water. Heat the solution to boil and add 1 mL of 0.5 per cent sodium citrate solution when the boiling commences. Continue heating till the color changes to pale purple. Remove the solution from the heating mantle and allow it to cool slowly. The colloidal solution prepared will have a net gold concentration of $2.5 \times 10^{-4}\text{ M}$. TEM images of the particles obtained are shown in Fig. 9.3.

The characteristic feature of this nanoparticle solution is its colour, which is due to the plasmon resonance of the particles of this size range. The plasmon resonance, described above, is due to the collective electron oscillation of the nanoparticle. As the valence electrons in the metal particle are free, they contribute to the oscillation, which are excited when photons of characteristic energy pass through the particles. In the case of gold particles of $\sim 15\text{ nm}$ mean diameter, the oscillation occurs at 520 nm and the absorption is very strong, which results in a deep colour for the nanoparticle solution, even if the concentration is weak. Thus, the particles behave like dyes. These particles cannot be taken

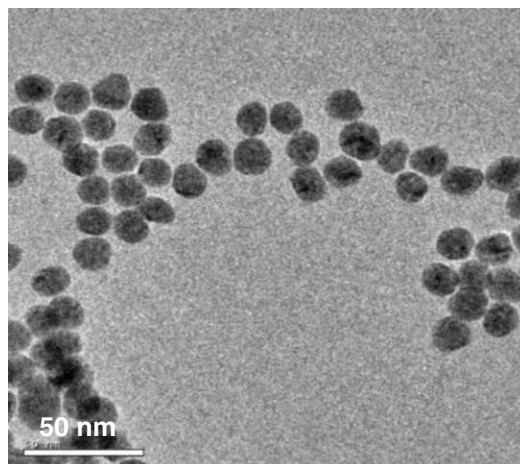


Fig. 9.3 TEM image of Au@citrate prepared by the above route with an average particle diameter of 15 nm. The samples were drop-casted from an aqueous solution onto the TEM grid. (from author's laboratory).

out of the solution and if concentrated, the particles settle irreversibly. The citrate protected particles can be subsequently covered with various molecules or ceramics, such as silica and taken out of the solution and redispersed. These particles can be good starting points for a variety of investigations in biology and materials science, and therefore, this methodology is widely practiced.³²

Brust reduction: The Brust method¹⁶ involves phase transfer of AuCl_4^- from the aqueous phase to the organic phase by a phase-transfer reagent, tetraoctyl ammonium bromide and subsequent reduction of it at the interface by NaBH_4 , in the presence of a thiol. The method produces a thiolate (RS^-)-protected gold nanoparticle with a core diameter in the range of 1–5 nm. The core dimension can be changed by varying the Au : thiol ratio used in the synthesis. Higher the thiol concentration, smaller is the particle formed. The nanoparticles can be taken out of the medium and dried. The powder can be stored for long time and can be redispersed.

In a typical procedure, an aqueous solution of HAuCl_4 (30 mL, 30 mM) was mixed with a solution of tetraoctylammonium bromide in toluene (80 mL, 50 mM). The mixture was vigorously stirred until all the tetrachloraurate was completely transferred into the organic layer (the aqueous phase becomes colourless). There is a visible change of colour when gold gets phase transferred. Then the desired thiol (depending on the Au : S ratio desired) was added to the organic phase. A freshly prepared aqueous solution of sodium borohydride (25 mL, 0.4 M) was slowly added with vigorous stirring. The solution is kept for stirring for several hours. The organic phase was separated, evaporated to 10 mL in a rotary evaporator. Solvents, such as ethanol, can be added to precipitate the particles. Washing with ethanol can be repeated to remove the free thiols. All the gold can be recovered. Depending on the dimension of the nanoparticle, the thiol content will vary, which decides the yield. Typical particle size distribution obtained in a 1 : 2 Au : S ratio synthesis is shown in the images below (Fig. 9.4).

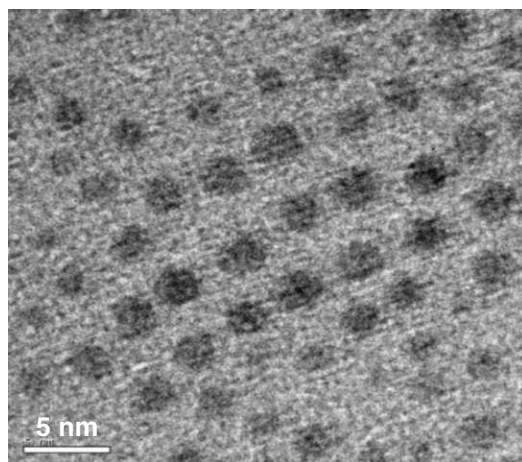


Fig. 9.4 Typical TEM image of Au@ODT nanoparticles, prepared by the Brust method. Particles are of 3 nm diameter. They organise in the free state as well as over suitable templates. The organization seen here is due to the presence of a molecular template, which is not observable in TEM (from the author's laboratory).

The method gives a lot of advantages. It is possible to functionalise the particles by using functionalised thiols in the synthesis. Another way of functionalisation is the place exchange reaction, in which one kind of thiol or another ligand is exchanged with that on the nanoparticle surface. These nanoparticles are also called monolayer protected clusters (MPCs), which has been extensively reviewed.^{8,33}

There are a variety of ways to conduct the synthesis. Phase transfer has been achieved by acid³⁴ and this method avoids the phase transfer catalyst impurity. The method produces monodisperse particles which undergo self-ordering to form two-dimensional lattices on a TEM grid. For the normal Brust method, the particle size distribution can be narrowed by digestive ripening, a process, in which the prepared particles are heated in a temperature cycle in presence of the thiol. Such particles with narrow size distribution arrange to give 2D and 3D superstructures. Superstructures can also be formed with silver². The synthesis can be achieved without phase transfer and a variety of reducing agents can be used instead of NaBH₄.

The monolayers on the nanoparticle surface are well ordered and the structure of the assembly has been a subject of detailed examination as it provides protection to the nano system. The monolayer assembly can be investigated by a variety of techniques, such as NMR, IR, Raman, fluorescence, etc., spectroscopies and the phase behaviour of the assembly can be probed by differential scanning calorimetry. A range of techniques have been used to study such systems. From all these studies, it is clear that the monolayer is well organised with a distinct phase transition temperature, which is a function of the monolayer chain length. The alkyl chain assembly is rotationally disordered in shorter chains, but no orientational freedom exists at room temperature in longer chain monolayers. The interaction between monolayers on adjacent clusters lead to superlattices and they melt to form a liquid in a first order transition.

The studies mentioned above have been performed principally on water-insoluble nanoparticles. From these studies, it is clear that when the monolayer chain is of the order of eight or more carbon atoms long, the core of the nanoparticle is not experiencing the solvent. The monolayer assembly is rigid even in the solution phase. The first few outermost carbon atoms are flexible and solvent penetration does occur to that extent. However, in the case of shorter-ligand monolayers, the entire monolayer itself can be exchanged with a new one made up of other suitable ligand molecules and such ligand-exchange chemistry can be used effectively to change the surface properties of the nanoparticles.

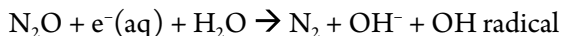
A number of water-soluble nanoparticles have been synthesised using water-soluble thiols. Among these, glutathione³⁶ and mercapto succinic acid (MSA)³⁷ need to be mentioned as both of them produce clusters with high water-solubility. The method involves reducing a methanolic solution of Au-thiolate complex by aqueous NaBH₄. The nanoparticles formed precipitate from the solution as they are insoluble in methanol. The material can be repeatedly washed in methanol and dissolved in water. The MSA clusters form well-organized superlattices³⁹. Recently Ag₉ clusters protected by MSA was synthesized in macroscopic quantities using a solid state route.³⁸ The glutathione clusters have a variety of molecular clusters in them ranging from Au₈ to Au₃₉, and various fractions of these have been synthesised by polyacrylamide gel electrophoresis (PAGE).⁴⁰ Quantum clusters of gold^{41,42} and silver⁴³ and their application in diverse areas have been well studied.

9.4.1.4 Electrochemical Reduction

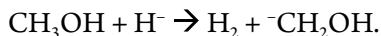
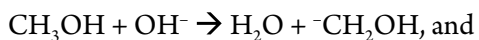
Although chemical reduction is the most extensively investigated method for making nanomaterials, various other methods have also been investigated in specific cases. One of the methods is electrochemical reduction, where the metal is dissolved at the anode and the metal ion formed is reduced at the cathode. The process is done in the presence of a stabiliser so that the particles do not deposit at the cathode and lead to electroplating. Palladium nanoparticles have been made this way by passing 0.1 mA.cm² current at 1 V in a 0.1 M tetraoctyl ammonium bromide (TOAB) solution in 4 : 1 acetonitrile : THF mixture.⁴⁴ The particles of 4.8 nm diameter were precipitated in the process and could be redispersed in THF or toluene. The methodology can be used for other metals, such as silver⁴⁵ and also for the formation of gold nanorods.⁴⁶ In a variation of the method, an aqueous solution of Sr²⁺ and Fe²⁺ produced strontium ferrites.⁴⁷

9.4.1.5 Radiation

Radiation-assisted reduction is another method for synthesising a variety of nanoparticles. Visible, UV, X-rays and γ rays have been used to achieve this task. Typically, this method involves the use of a stabilising agent, while irradiating the metal salt solution. In the extreme case of photoreduction involving gamma rays, the type of species produced in the medium depends on the photon energy absorbed. Typically, in an aqueous solution, radiolysis of water produces species such as H₂, H, H₂O₂, OH and e⁻. The electron is scavenged by nitrous oxide, used in the medium, generating OH⁻ and OH radical in the process.⁴⁸



The radicals produced are consumed by the alcohols used as per the reactions,



The reducing agent in a reaction is the $\cdot\text{CH}_2\text{OH}$ radical as per the reaction,



The products formed are the metal and formaldehyde.

The reducing power would be greater if the solvated electron itself could be used. Au,⁴⁹ Ag,⁵⁰ Cu⁵¹ and Co⁵² particles have been made this way. The radiolytic method is very useful for making complex structures, such as the core-shell particles, in which a shell of another metal is coated on an already prepared nanoparticle. Au@Ag,⁵³ Au@Pt,⁵⁴ Pt@Au,⁵⁴ Au@Pb,⁵⁵ etc., shells have been prepared. During synthesis, a metal nanoparticle is mixed with an aqueous metal ion and radiolysed using a ⁵²Co source. The radicals produced transfer the electrons to the metal nanoparticle, thereby charging it. The particle subsequently reduces the metal ion present. The metal atom gets deposited at the nanoparticle making a core-shell geometry. The approach can be used for the controlled increase of nanoparticle size. This has been demonstrated in the case of Au nanoparticles by repeated radiolysis.⁵⁶

9.4.1.6 Thermal Decomposition of Organometallics

One of the methods to make metal nanoparticles is to decompose carbonyls by heating in an inert solvent in the presence of a suitable stabilising agent. Co nanoparticles have been made in this way by heating Co₂(CO)₈ in decalin at 130–170°C.⁵⁷ The stabilisers used, often nitrogen-containing polymers, were found to form metal cluster macromolecules, in which the stabiliser acted as a complexation agent. By controlling the functionality of the polymer, particle size can be varied. Using different polymers, Fe,⁵⁸ Ni, Cr, Mo and W nanoparticles^{59,60} and alloy nanoparticles have been prepared. One of the important aspects is that the method allows the use of ligands that are stable at high temperatures as capping agents. In one such approach, a new metastable Co phase (ϵ -Co) has been formed⁶¹ stabilised by trioctyl phosphine oxide (TOPO). Without TOPO, this phase was not formed. Details of the formation of various kinetically stabilised shapes have been investigated.^{62,63} Various kinds of organometallic reagents and mixtures of those with carbonyls have resulted in FePt⁶⁴ and CoPt⁶⁵ alloy and core-shell nanoparticles. Thermal decomposition of metalloalkenes is another route for nanoparticle formation.^{66,67} The ligands 1,5-cyclooctadiene (COD), 1,3,5-cyclooctatriene (COT), dibenzylidene and cyclooctenyl (C₈H₁₃⁻) have been used for this purpose. Co, Ni, Ru, Pd, Pt nanoparticles, Co and Ni nanorods and CoPt, CoRu, CoRh and RuPt nano alloys have been prepared.

9.4.1.7 Microwave-Assisted Synthesis

This is a well-established methodology for the synthesis of a variety of organic and inorganic materials. It has both the synthesis and processing aspects.⁶⁸ A variety of materials have been synthesised and processed in this way. One of the important aspects of the synthesis is the fast time scale involved as the heating is achieved from within. Typical methodology uses the domestic microwave oven working at a frequency of 2450 MHz, and the mixture to be irradiated is placed inside the oven with an appropriate stirring mechanism. In the simplest case of metals, the metal ions and the reducing

agents in a suitable medium are placed in the oven. In the case of simple metals, such as Au and Ag nanoparticles, the methodology is known to produce narrower size distribution, in comparison to thermal reduction, using the same reducing agent.⁶⁹ Polyalcohols can effectively reduce metal ions by microwave irradiation. This approach is referred to as the microwave polyol process.⁷⁰ Irradiation of an aqueous solution of H_2PtCl_6 , PVP, ethylene glycol and NaOH produced 2–4 nm Pt particles.⁷¹ Six nm Ni particles were produced similarly.⁷² Synthesis can also be adapted to continuous flow reactors so that production can be automated.⁷³ Microwave-based methods have been reviewed recently.⁷⁴

9.4.1.8 Sonolysis

In this method, the reaction mixture is irradiated with ultrasound, typically, of 20 kHz. The process of nanoparticle formation is called cavitation. This is a process of implosion of cavities of very small dimensions in nanosecond time scale leading to local hot spots of very high temperatures (of 5000 K). Precursor species, such as organometallics, trapped in this atmosphere get decomposed due to high temperature and the products instantaneously get quenched as a result of the contact with solvent medium around. This produces amorphous nanoparticles. Several transition metal nanoparticles have been made in this way.^{75–77} For example, sonolysis of $\text{Fe}(\text{CO})_5$ in decane produces 8 nm Fe particles protected with oleic acid.⁷³ A number of alloy nanoparticles have also been prepared. Sonolysis route for the synthesis of nanomaterials has been reviewed recently.⁷⁸

A summary of all nanometals synthesised till date (September 2006) is summarised in Appendix 2.

9.4.2 Oxides

Aqueous route: If the variety in metals is large, it is even more diverse in metal oxides. As a result, many more nanoparticle systems have been investigated in this category. Metal oxides investigated are binary, ternary and quaternary and the complexity increases in this direction, not only in the structure, but also in the synthetic methodologies and properties. In general, the methodology employed involves the precipitation of the oxide or its precursor species, such as hydroxide, carbonate or oxalate, and subsequent heat treatment of the product. In both these cases, it is necessary to use protecting agents to prevent aggregation. The precursor species formed is often complex and difficult to characterise completely as it is likely to be amorphous as a result of low temperature processing. The complexity increases if there are multiple metals involved. The particles produced in the case of oxides are much more polydisperse than metal nanoparticles, although there are several recent examples of monodisperse particles. The other issue is that as the temperature increases, the extent of aggregation increases, increasing the particle size. However, most precursors decompose at lower temperatures minimising excessive growth of particles. Another aspect of importance is that, just as in the case of metal particles, high-energy metastable phases are stabilised in certain cases at low temperatures.

Certain simple oxides are prepared in aqueous solutions at low temperatures without sintering. For example, 4 nm rutile TiO_2 particles can be made by precipitating aqueous TiCl_4 by NH_4OH .⁷⁹ Poly(methyl methacrylate) is used as the stabiliser. In the case of an oxide ion-conducting electrolyte,

$\text{Ce}_{0.8}\text{Y}_{0.2}\text{O}_{1.9}$, aqueous $\text{Ce}(\text{NO}_3)_3$ and $\text{Y}(\text{NO}_3)_3$ were precipitated by oxalic acid and the product was sintered to produce nanoparticles of the above composition.⁸⁰ By varying the sintering temperature, particles of different mean diameters were produced.

Ternary oxides have also been produced. When the structures are stable, such as spinels, the hydroxides can be converted to oxides by carrying out the precipitation near boiling temperature. This has been achieved in the case of Fe_3O_4 ,⁸¹ MnFe_2O_4 ,⁸² CoFe_2O_4 ⁸³ and $\text{Pr}_x\text{Ce}_{1-x}\text{CeO}_2$.⁸⁴ In the method used by Li *et al.* the ferromagnetic CoFe_2O_4 was stabilised by dilute HNO_3 .⁸⁵ The product is a ferrofluid of considerable interest. Stable ferrofluids of Fe_3O_4 were made also by steric stabilisation by poly(vinyl alcohol), starch, etc.^{86,87}

Non-aqueous route: Several metal oxides have been prepared by the non-aqueous path. The methodology involved is useful for metals, where precipitation is difficult in aqueous media. It is also helpful if precursors of more than one metal need to be simultaneously precipitated, which require widely different pH conditions if done in water. In the case of LiCoO_2 synthesis, LiOH and $\text{Co}(\text{OH})_2$ were simultaneously precipitated by dripping an ethanolic solution of LiNO_3 and $\text{Co}(\text{NO}_3)_2$ into 3 M ethanolic KOH .⁸⁸ On heating the mixture of hydroxides, nanoparticles of LiCoO_2 were obtained. Oxides, such as $\gamma\text{-Fe}_2\text{O}_3$,⁸⁹ BaTiO_3 ,⁹⁰ and MFe_2O_4 ($\text{M} = \text{Mn, Fe, Co, Ni, Zn}$) were prepared by using various precursors in different solvent systems.⁹¹

A summary of the synthetic routes used for oxide nanoparticles is presented in Appendices Part II.

9.4.3 Chalcogenides

One of the most extensively studied nanomaterials is chalcogenides (sulphides, selenides and tellurides). These are semiconducting quantum dots, in which the dramatic effects of size quantisation are manifested. The range of properties these systems exhibit is also large, and as a result, there have been extensive investigations on establishing proper synthetic routes for particles of narrow-size distribution. This is important, as the properties vary with size just as in the case of any other nanomaterial. The chemical purity and surface functionalisation are very important for some of the properties investigated, especially fluorescence. The surface states can destroy the photophysical properties completely. From several of the properties investigated, it is now very clear that synthesis plays a key role in understanding and application of the properties of these systems. Various synthetic methods available for chalcogenide particles are reviewed.^{92,93,94}

The simplest approach for making chalcogenides is to mix a chalcogenide ionic salt with a metal salt in aqueous solution. This leads to immediate precipitation of the metal chalcogenide in most cases, but the process is extremely rapid and control becomes difficult. The alternate approach is to use covalent chalcogenides and organometallics so that reaction at a higher temperature in an organic solvent can produce nanoparticles. Suitable passivating agents may be used and the reaction is controlled kinetically (by control of reaction conditions). Optimisation of the parameters have got several semiconductors of the II-VI and II-V category.⁹⁵⁻¹⁰¹ In the typical approach, the Cd precursor used is $\text{Cd}(\text{CH}_3)_2$ and the chalcogenide precursors are, $[(\text{CH}_3)_3\text{Si}]_2\text{S}$, $[(\text{CH}_3)_3\text{Si}]_2\text{Se}$, R_3PSe and R_3PTe ($\text{R} = \text{C}_4\text{-C}_8$ *n*-alkyl). Typically, a suitable solvent that is stable at high temperature, such as trioctylphosphine (TOP) or

trioctylphosphineoxide (TOPO), is held at 340–360°C, and a room-temperature solution containing the precursors is added. This results in the nucleation of particles. Growth is controlled by controlling the temperature and duration of heating. Further addition of the reagents increases the size of the particle. The crystallinity can be controlled by annealing the mixture for extended periods. Size control in the range of 1.2–12 nm has been achieved.^{102–105} The methodology has been used for the synthesis of indium chalcogenides.^{106–108} The surface of the particles is protected by TOP or TOPO. Additional surface passivating agents have also been used. In addition to the hexagonal and cubic phases, the wurtzite phase has also been stabilised by controlling synthetic parameters.^{109–111} The methodology when used at higher precursor concentrations gets nanorods of CdSe.¹¹¹ An aspect ratio of 30 has been achieved. Other morphologies have also been observed as well.¹¹⁰ TEM image of a typical CdSe nanoparticle is shown in Fig. 9.5.

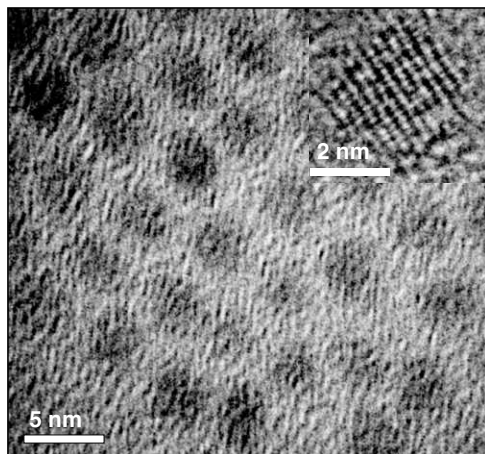


Fig. 9.5 TEM image of a collection of CdSe nanoparticles synthesised by chemical route. An expanded image of one of the particles, showing the lattice, is shown as inset. Individual lattice points are observable (data from the author's laboratory).

Dimethylcadmium is pyrophoric and conducting experiments at elevated temperatures poses high risk. Therefore, various other precursors have been employed. CdO has been used for this purpose and the methodology is similar to that described. Alkyl (C_6 or C_{14}) phosphonic acid is used as another reagent in the chemistry along with TOPO a precursor.^{112, 113} Other precursors, such as carboxylates have also been used.¹¹³

Microwave-assisted synthesis has been performed for preparing quantum dots of CdSe, PbSe etc.^{114, 115} Several other nanoparticles of oxides and chalcogenides have been prepared by the microwave route.^{116–119} Sonochemical methods have also been used for the synthesis. By using an anionic surfactant template of sodium dodecyl sulfate (SDS), hollow nanoshells of CdSe have been synthesised using the sonolysis route.¹²⁰

Applications of such materials in biological or other environments, where toxicity is a problem, requires additional precaution. The surface can be protected with various inert oxides, such as SiO_2 .

The synthetic approach is similar: make the nanoparticle, ligand-exchange with suitable molecule and then use it to grow an oxide layer.¹²¹

9.5 MICROEMULSION-BASED METHODS FOR NANOMATERIALS

Microemulsions are micellar solutions. Micelles are self-organised spherical structures of amphiphilic molecules in a suitable medium. The micellar solutions contain an amphiphilic molecule or a surfactant, an organic medium and water. There may also be a cosurfactant. In a typical micellar arrangement, water is outside the spherical structure. When the medium is organic (which is in large excess), we get reverse micelles, in which the self-assembled structure encloses water as shown in Fig. 9.6. Micelles change shape and there are several kinds of structures, such as vesicles, lamellar and cylindrical phases, which exist depending on the thermodynamic conditions. These reverse micelles, as they contain water within, can be loaded with metal ions or reducing agents. The micellar dynamics is such that two micelles in contact can fuse and exchange their contents. Brownian motion is the reason why such collisions leading to coalescence and decoalescence happen. This makes it possible to conduct reactions in confined spaces, and as a result, nanomaterials can be formed. Such materials can be purified, processed and redispersed. The important aspect is that since the concentration of the micelles is low, the synthesis does not lead to large quantities of materials unlike the chemical method. This method may also be categorised as template mediated synthesis.¹²²

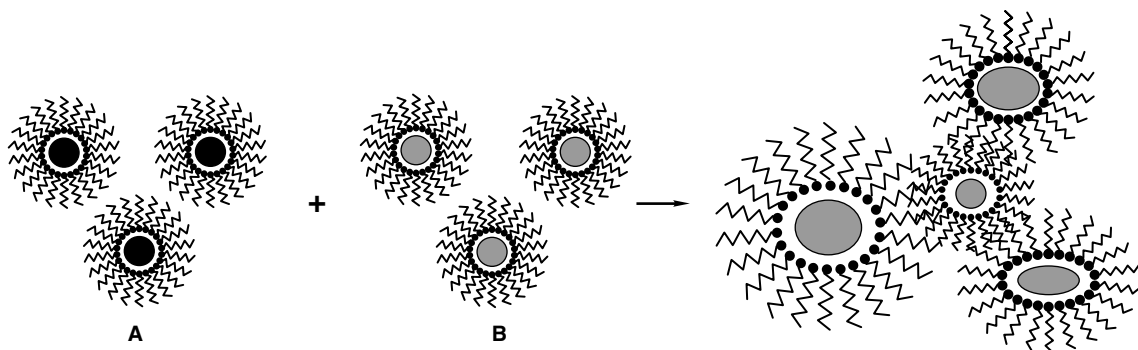


Fig. 9.6 *Microemulsion-based synthetic approach. The reverse micelles shown here are water in oil structures (with majority oil phase). The two micellar solutions—one with metal (solution A in the picture) and the other with a reducing agent (solution B), for example, can be mixed to make the nanoparticles. The micelles coalesce and a dynamic equilibrium is reached by which contents of all get mixed.*

Metals: Here, water-soluble metal ions and reducing agents are used. NaBH_4 and $\text{N}_2\text{H}_4 \cdot \text{H}_2\text{O}$ are the two commonly employed reducing agents. Reduction by gases such as H_2 is slow, but this method is also used. Two kinds of surfactants used: anionic and cationic. In the cationic kind, the most common and the oldest is the cetyltrimethyl ammonium bromide, $(\text{C}_{16}\text{H}_{33})(\text{CH}_3)_3\text{NBr}$ (CTAB). This is a quaternary ammonium salt. In the anionic kind, the more common one is sodium bis(2-ethylhexyl)

sulphosuccinate, generally referred to by its trade name, Aerosol OT or AOT. Nonionic surfactants such as polyethylene ethers (e.g. pentaethylene glycol dodecyl ether (PEGDE), $\text{CH}_3(\text{CH}_2)_{11}-\text{O}-(\text{CH}_2-\text{CH}_2-\text{O})_5-\text{H}$, or Triton-X) are also other surfactants. Structures of these are shown in Fig. 9.7. The synthetic methodology employed is simple and easily adaptable in a number of cases. As the surfactants contain ions, it is important to use suitable metal ions, which will not precipitate in presence of these ions. Ag^+ in presence of CTAB is an example. The chemistry is the same as discussed earlier, but the process occurs now in reverse micelles. In addition to metals, several alloys have also been made. Two separate microemulsions (of the two metals) may be mixed with another microemulsion of the reducing agent to achieve this. Else, a microemulsion of the two metal ions may be mixed with that of the reducing agent. A brief survey of the metal particles made by microemulsions is given in Appendices Part II. Various conditions, such as pH, temperature, etc., can be tuned to control the particle size and shape.

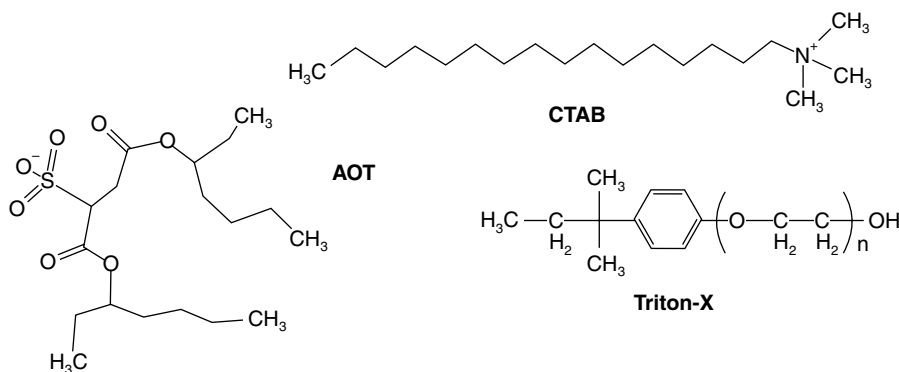


Fig. 9.7 Various surfactants used in microemulsion-based synthesis.

Synthesis of metal oxides can also proceed in the same fashion. Here metal oxides or hydroxides are precipitated by the addition of reagents, such as NH_4OH or NH_4OH taken in a reverse micelle. The precipitate is collected by centrifugation. It is subsequently calcined at the required temperature to yield the oxide. In the case of ions that are not soluble or stable in aqueous solutions, suitable precursors are taken. Like wise, metal chalcogenides are also prepared where, typically, Na_2S or Na_2Se or similar salts are used to precipitate the metal ions such as Pb^{2+} . Several of these examples of microemulsion-based synthesis are presented in Appendices Part II.

9.5.1 Core-Shell Structures

Several complex structures can be prepared by the microemulsion route. One form of complexity is to produce core-shell structures. The shell itself can have several layers, increasing the complexity further with dissimilar materials. In the simplest case of metal-on-metal kind of core-shell, the approach is to add the metal ion in reverse micelle into a solution, in which particle have already been synthesised. The solution contains excess reducing agent from the particle synthesis and the addition of the metal ion in reverse micelle produces reduction and thereby a shell is coated on the metal particles. It is likely that

the metal ion added may get reduced before encountering the metal nanoparticle already synthesised. As a result of this, there can be the presence of free-metal nanoparticles of the second kind as well as uncoated nanoparticles of the first kind, although the objective was to prepare core-shell particles. Such particles are commonly referred to as core@shell. A typical example is Fe@Au^{123, 124} systems, in which the synthesis also gives pure Fe particles.¹²⁵ The approach can be extended to get Au@Fe@Au kind of systems.^{126, 127} The difference between this and the simultaneous reduction approaches is that it is very difficult to get conditions by which a less noble metal becomes the core, as in Ag@Au during simultaneous reduction, but such possibilities exist in the microemulsion route.

The core-shell can be made of oxides. Fe₃O₄@MnO has been synthesised. The core has 10 nm diameter and the shell has 2.5 nm thickness.¹²⁸ SiO₂@Fe₃O₄ has been prepared.¹²⁹ The complexity and variety of the core-shell system can be numerous. One could coat the surface of the nanoparticle with a polymer that is prepared *in-situ* in the reaction mixture. The polymerisation can occur over the nanoparticle surface, which is already coated with an appropriate group on which polymerisation can occur. This kind of approach can be used for growing inorganic shells as well. This is the approach used by Liz-Marzan to prepare SiO₂ shells over gold nanoparticle.¹³⁰ Here, the approach is to coat the surface of gold with a monolayer of aminopropyltrimethoxysilane. The amino group binds on to the surface of gold and the trimethoxy group can be hydrolysed in the presence of tetraethoxyorthosilane (TEOS) resulting in the growth of a thin silica shell. The shell thickness can be increased further by using a method of Stöber.¹³¹ This synthetic approach can be used for other nanoparticles as well.

The synthesis of core-shell materials can also be achieved by a single step, in which all materials and reagents are added into one pot. This approach has produced Au@TiO₂ and Ag@TiO₂ particles.^{132, 133} Here, the readuction is achieved by dimethylformamide (DMF) and the precursor species are HAuCl₄, AgNO₃ and titaniumisopropoxide. A similar method can be used for Au@ZrO₂ and Ag@ZrO₂ where the Zr precursor is zirconium isopropoxide.¹³³ Corresponding alloys can also be prepared. All these core-shell materials, namely Au@SiO₂, Au@TiO₂ and Au@ZrO₂, and their Ag analogues are freely dispersible in organic media. In order to increase the dispersibility, the oxide surfaces can be coated with long chain carboxylates. In this case, the material obtained can be taken out of the solution in a powder form and stored for extended periods and redispersed.¹³⁴

Colloidal core-shell particles can be used to control the optical absorption of nanoparticles. The assemblies of these structures in various forms are also important ways of controlling optical absorption. Various aspects of such control are discussed in the article by Liz-Marzan.¹³⁵

9.6 SOLVOTHERMAL SYNTHESIS

Solvothermal method refers to conducting the reaction in a closed vessel, in which the solvent has a possibility to achieve its supercritical state. The temperatures and pressures are high (e.g., above 374°C and 218 atm for water). Although many reactions are not conducted at the supercritical state, the reactions are done in pressure bombs typically with Teflon lining. In the supercritical state, the liquid-vapour boundary disappears. The fluid achieves properties of both the liquid and the gas. Increased solubility and increased reaction rate favour many reactions, and therefore, processes are

better done at the supercritical state. However, for many reactions, increased reactivity at higher temperatures in a controlled condition is the sole aspect of interest. If the reaction is done in water, it is called hydrothermal, and in the case of other solvents it is referred to as solvothermal. Several reviews are available on this topic and an interested reader may consult them for details, such as the pressure conditions, experimental apparatus, various materials synthesised, etc.^{136–143}

One of the aspects of particular interest in this method is the significant reduction in the reaction temperatures, even for many ceramic materials. Materials thus synthesised are highly crystalline and often post synthetic annealing operations are not necessary. They are monodisperse and often, are suspendable in a suitable medium. Besides, the methodology can be adapted to suit several synthetic conditions and also can be used for large-scale synthesis. The heating process itself can be conducted in a microwave oven making it also energy efficient in addition to the distinct advantages the technique offers.¹⁴⁴ The process can also be adopted to continuous flow conditions.¹⁴⁵ All of these make it an interesting methodology for synthesis. Besides, the synthetic procedures have the advantages of being relatively inexpensive in terms of the solvents used, arguably green (when water is the solvent).¹³⁸

In a typical method, the precursor species are mixed with suitable reagents for reduction, precipitation, etc., in a suitable medium. Often stabilisation and complexation agents are added so that the process takes place happens at controlled conditions. The synthesis of anatase TiO_2 is achieved by controlled hydrolysis of $\text{Ti}(\text{OEt})_4$ in ethanol.¹⁴⁶ Monodisperse particles were prepared by this route.¹⁴⁷ The starting material can be TiCl_4 ^{148, 149} and one can also use stabilisers, such as citric acid.¹⁵⁰ Microemulsion-based synthesis often includes a solvothermal step and TiO_2 was prepared that way also.¹⁵¹ Large-scale synthesis of TiO_2 is significant in view of its application in photocatalysis, solar cells, etc., CeO_2 synthesis has been achieved with¹⁵² and without¹⁵³ stabilisers. Complex oxides, such as $\gamma\text{-Fe}_2\text{O}_3$, CoFe_2O_4 ¹⁵⁴ and ZnFe_2O_4 ¹⁵⁹ were prepared by the hydrothermal route. The microwave-hydrothermal route is very useful for many complex oxides, such as the ferrites (MFe_2O_4 , $\text{M}=\text{Mn, Co, Ni, Zn}$),¹⁵⁵ BaTiO_3 ,¹⁴⁴ $\alpha\text{-Fe}_2\text{O}_3$.¹⁵⁶ The methodology is also useful in making several other materials, especially mesoporous solids. The applications of these materials are numerous in catalysis and are extensively covered in other places.

Hydrothermal processes are used to make metal chalcogenides.¹⁵⁷ CdSe particles were made from elemental Cd and Se at 180°C in a hydrothermal route.¹⁵⁸ The products were aggregated in the absence of suitable stabilisers. In presence of TOPO, the synthesis of CdSe produces ~ 3 nm particles.¹⁵⁹ Many other chalcogenides- SnS_2 , NiS_2 , CoS_2 , FeS_2 and NiSe_2 -have been synthesised.^{160, 161}

9.7 SYNTHESIS USING SUPPORTS

Various synthetic approaches are available to use supports for the preparation of nanoparticles. These vary from the use of nanoparticles themselves to materials with nano cavities. Particles prepared by one route can be used for subsequent growth. This results in the controlled growth of particles at the nanoparticle surfaces. If the growth of smaller particles is avoided, one can get programmed increase in size. This is possible by the use of suitable reactants. For example, hydroxylamine will reduce Au^{3+} , but will do so better on Au particles. As a result, larger particles can be grown by adding Au^{3+} to a

nanoparticle solution containing this reducing agent. The approach can be termed as 'electroless plating'.¹⁶² It is useful in making various kinds of structures, such as core-shell particles. Interested readers may consult a review in this subject.^{163, 164} The templates and covers need not be metals alone. In the case of Au or Ag coated with ZrO_2 , by selectively removing the metal, one can get oxide shells.¹⁶⁵ The core-shells prepared can be redispersed even in organic solvents by suitably functionalising the oxide surface. The approach is similar to that discussed earlier in the case of metal particles.¹³⁴

The support, on which growth takes place can be a polymer. In this case, a metal-coated polymer can be obtained and subsequently, the polymer can be removed to get hollow nanoshells. An approach of this kind was developed using polystyrene coated with a positively charged polymer, such as poly(allylamine hydrochloride). This was coated with 4-(dimethylamino) pyridine-protected gold nanoparticles and the shell cover can be increased by the hydroxylamine method. The polymer can be removed by heating or by washing with organics.¹⁶⁶

Dendrimers as templates have been used for nanoparticle synthesis. This topic has been extensively reviewed recently.^{167, 168} Dendrimers are branched polymeric molecules with inner and peripheral functional groups. They are known in terms of their generation. The polyamidoamine (PAMAM) dendrimers have been studied well. The interest in this approach is that the dendrimer is of nanometer dimensions. For example, a 4th generation PAMAM is of 4.5 nm diameter, and it can encapsulate nanoparticles. These nanoparticles encapsulated in single dendrimers are different from those protected with multiple dendrimers. Depending on the functionality of the dendrimer, the nanoparticle formed can be redispersed in a variety of solvents.

In a typical approach, a solution of metal ions is mixed with the dendrimer and stirred so that the metal ions complex with the ligand locations. Then the reducing agent is added making dendrimer encapsulated nanoparticle. The particles, in general, are in water and, if necessary, they can be phase transferred to the organic phase by stirring with a thiol or suitable ligand taken in an organic phase. The dendrimer comes out and will stay in the aqueous phase. The dendrimer-encapsulated particles show high monodispersity and high catalytic activity. Other dendrimers have also been used to prepare nanoparticles.¹⁶⁹

Mesoporous solids are excellent templates. MCM-41 is one such material. The pores of these systems are of nanometer size and by incorporating metal ions in them and by subsequent reduction, several nanostructures can be obtained. The approach can be used for chalcogenides by diffusing H_2S , for example, after metal ion incorporation. Various materials have been prepared this way.¹⁷⁰⁻¹⁷² Similar approach can be made in the case of membranes—both organic and inorganic. NAFION membrane has been used to grow semiconductor nanoparticles.¹⁷³ The same approach has been used for synthesis using a sulphonic acid membrane, Dowex.¹⁷⁴ Alumina membranes have been used to grow particles this way.¹⁷⁵ Packing of nanoparticles leading to nanowires is possible in such membranes. Nanowires can be created in pores by reducing ions in the pores. The sheath can be dissolved later getting isolated nanowires.¹⁷⁶ A similar approach has been used with MCM-41 for making Pt nanowires and such material (i.e. Pt wire) have been used for catalysis.¹⁷²

Templates of carbon, especially nanotubes, are very interesting due to their one-dimensionality. Metals, alloys, semiconductors and oxides have been filled in carbon nanotube templates. The

nanotubes can then be burnt to get anisotropic nanoparticles.^{177, 178} Similar method can be used with inorganic nanotubes.¹⁷⁹

9.8 USING BIOLOGY

Nanoparticles have been found in several organisms. Silver and Fe_3O_4 nanoparticles have been found in bacteria. Therefore, it is natural to believe that the ions taken inside organisms could be subjected to reduction. The reduction of Au^{3+} by fungi has been achieved this way.¹⁸⁰ Common lactobacillus reduces gold.¹⁸¹ These reductions also occur in human cells.¹⁸² Important aspect here is that all the metal nanoparticles can be extracted and resuspended. This approach makes it possible to make large quantities of nanoparticles with less cost. It is also possible to achieve reduction extracellularly, so that the organism is alive to continue the process and thereby uses it for manufacture. This approach has been used for metal oxides, sulphides and magnetic nanoparticles.^{183, 184}

Biological templates, such as DNAs, can be used to organise nanoparticles.¹⁸⁵ Patterning of nanoparticles to form 2-D arrays on such templates has been a subject of intense investigation. The subject matter is available in reviews.¹⁸⁶⁻¹⁸⁸

9.9 MAGNETIC NANOMATERIALS

Magnetic particles are important in ferrofluidics, magnetic refrigeration, information storage, magnetic drug delivery, contrast enhancement agents in imaging besides being useful due to their intrinsic properties. These particles in the nanometer regime are superparamagnetic, i.e., they behave like paramagnetic atoms with large magnetic moment in an isolated state. Most of the magnetic particles are prepared in water in oil micelles or oil in water reverse micelles. These approaches can be adapted very well for ferrite spinels, MFe_2O_4 ($M=\text{Mg, Co, Mn, Ni, Zn, etc.}$). The particles can be redispersed in media with suitable protection.¹⁸⁹ The other approach is to inject a precursor species, such as carbonyls to a hot surfactant solution. It is also possible to mix the precursors at a low temperature followed by slow heating. Quick nucleation and slow particle growth in appropriate conditions is the key to efficient synthesis. Nanoparticles of Fe, Co, Ni, their alloys and ferrites have been prepared this way. Details may be had from.¹⁹⁰ Organometallic precursors may also be used.¹⁹¹

Magnetic Fe@Au core-shell particles have been synthesised by laser ablation. In this approach, both Fe and Au particles, protected by oleic acid and CTAB, respectively, were irradiated in hexane using 532 nm laser. The 18 nm core-3 nm shell particles so formed were superparamagnetic and had a shelf-life of 4 months.¹⁹² This method is significant as normally one would have got Fe over Au as Au is noble. FePt nanoparticles are diverse systems for a variety of applications. Various kinds of such particles with shells of Fe_3O_4 , CdS, etc., for permanent magnet and biological applications, are discussed in the review by S. Sun.¹⁹³ The approach for synthesis adopted is thermal decomposition of $\text{Fe}(\text{CO})_5$ and reduction of platinum acetylacetonate, $\text{Pt}(\text{acac})_2$, in the presence of 1,2-alkanediol with suitable stabilising agents. $\text{Fe}(\text{CO})_5$ is thermally unstable and makes Fe atoms. $\text{Pt}(\text{acac})_2$ is readily reduced by the diol and the atoms formed result in nuclei, over which Fe and Pt condense to make the nanoparticles. Oleic acid

and oleylamine (or other long-chain carboxylic acids or primary amines) may be used to stabilise the surfaces. Normal approach is to conduct the reactions in inert atmospheres in the absence of moisture. The product composition is controlled by varying the composition of starting mixture. Replacing $\text{Fe}(\text{CO})_5$ with $\text{Fe}(\text{acac})_2$ or $\text{Fe}(\text{acac})_3$ and simultaneous reduction of the salts is possible. Details of these methodologies and original references may be found in the review cited above.

9.10 INERT GAS CONDENSATION

In this method, the nanoparticle is made in the gas phase by creating a condition of supersaturation. The condition in the preparation chamber is made, such that the solid phase is more stable than the gas phase. At this point, the cluster nucleates and deposits from the gas phase. The deposition will lead to aggregation, and it can be controlled suitably by surfactants or suitable protecting agents. This makes it possible for the materials to be redispersed without much effort. The evaporation conditions can be varied such that the gas phase species undergo reactions, such as oxidation to produce oxides (forming to CuO , Al_2O_3 , etc.). The nanoparticles formed are transported and deposited by thermophoretic diffusion on a cold finger. The gas pressure in the chamber can be controlled to modify the sample morphology.¹⁹⁴ Evaporation can be achieved thermally or by the use of a laser, spark or a discharge. It is also possible to use organic precursors, which undergo decomposition in the gas phase to make appropriate species. The methods employed are: spray pyrolysis, chemical vapour deposition, flame pyrolysis, etc. A short summary of the synthetic tools¹⁹⁵ may be found in ref. 195.

A similar method is the direct condensation of gas phase species on a flowing low vapour pressure liquid.¹⁹⁶ This method is also called vacuum evaporation onto a running oil substrate (VEROS). Materials prepared by a similar route were used for early thermal conductivity measurements. An important advantage of this method is that it avoids agglomeration.

9.11 ANISOTROPIC NANOPARTICLES

Although nanoparticles often refer to spherical shapes, there are also various anisotropic shapes. These refer to all shapes other than spherical. These shapes require more than one parameter to describe their shapes. The more common ones are nanorods and nanotriangles. Several other shapes, such as tripods, tetrapods, stars, flowers, sheets, etc., are known, and in several cases synthetic flexibility does not exist. Several of these shapes are used as starting points for the synthesis of more complex shapes. Various anisotropic nanoparticles synthesized and their applications has been reviewed recently.¹⁹⁷ However, most of these are not possible to get in solution phase. We will discuss some of these materials later in this book. A short discussion of rods and triangles follows.

9.11.1 Gold and Silver Nanorods

The nanorods of gold and silver are stable colloidal solutions. They are typically of 10–30 nm diameter and 50–1000 nm long. They show two plasmon absorptions, one due to the long axis, called the longitudinal plasmon, and the other, due to the short axis, called the transverse plasmon. Nanorods

can be synthesised principally in three different ways: the electrochemical route, the photochemical route and the seed-mediated route. In electrochemical route, electrochemical reduction is employed, whereas in photochemical, light-induced reduction is used.¹⁹⁸ The seed-mediated method uses chemical reduction.^{199–201} All methods use a structure directing template for the growth of the rods. The nanorod synthesis has been reviewed adequately.²⁰²

The chemical method is done as follows: 4 nm seed particles of gold are prepared by the borohydride reduction route (0°C). The seed is allowed to grow in a growth solution, which is prepared with Au³⁺, CTAB and ascorbic acid. Ascorbic acid reduces Au³⁺ to Au¹⁺, it is not capable of reducing Au³⁺ to Au(0). However, on the surface of Au particles, Au(0) can be formed by ascorbic acid. CTAB is a structure directing agent and directs the growth of the rod on certain specific places of the gold surface. The presence of about 5 per cent silver is necessary to increase the yield of nanorods to nearly 100 per cent. However, with silver, the highest aspect ratio is achieved 6, whereas in the absence of it, the maximum aspect ratio is about 25, but the yield is less. This is the maximum length observed for gold. For silver rods, micron lengths are observed.

The CTAB used is of high concentration (0.2 M), far above the critical micelle concentration (CMC). It is also known that other counter ions, such as Cl⁻, do not help in the nanorod growth. In fact, only particles are formed this way. Iodide makes assorted particles. Br⁻ is believed to be important in making thin layers of AgBr (as it is not found as a precipitate) on certain surfaces of the nanoparticles, arresting growth along directions perpendicular to these planes.

The absorption spectrum of a typical gold nanorod solution is shown in Fig. 9.8. The rods shown are of 18 nm diameter and 60 nm long. The transverse plasmon appears at 500 nm and the longitudinal one appears at 745 nm. The position of the longitudinal plasmon is a good measure of the length of the rod. Greater the length, more red-shifted is the absorption and ultimately, the absorption is shifted to the infra-red region. This is advantageous for biological applications as the skin penetration depth of infrared is higher than that of visible. The figure also shows TEM image of a purified nanorod.

The rods are stable in solution state and with a thin layer of CTAB, it is infinitely stable at ambient conditions. The solution can be heated to boiling without apparent change in the rod morphology. Short rods are far more reactive than the larger ones and undergo radical- and ion-mediated corrosion. In presence of excess Au³⁺, rods become particles.

9.11.2 Triangles

Nanoparticles of silver become nanotriangles or nanoprisms upon irradiation. Silver nanoparticles were prepared by borohydride reduction and were protected with trisodium citrate. The irradiation using a fluorescent lamp was done in the presence of bis(*p*-sulphonatophenyl) phenylphosphine dehydrate dipotassium salt solution for extended periods (of about 70 hours). The nanotriangles thus formed as stable in the solution and undergo self-organization on drying.²⁰³ In a recent method, it was shown that irradiation of silver nanoparticles (with citrate protection) by a sodium vapour lamp produces triangles. There was no need of additional surfactant.¹⁹⁹ Gold nanoplates were prepared by the reduction of hydrogen tetrachloroaurate by smaller amounts of sodium citrate in the presence of

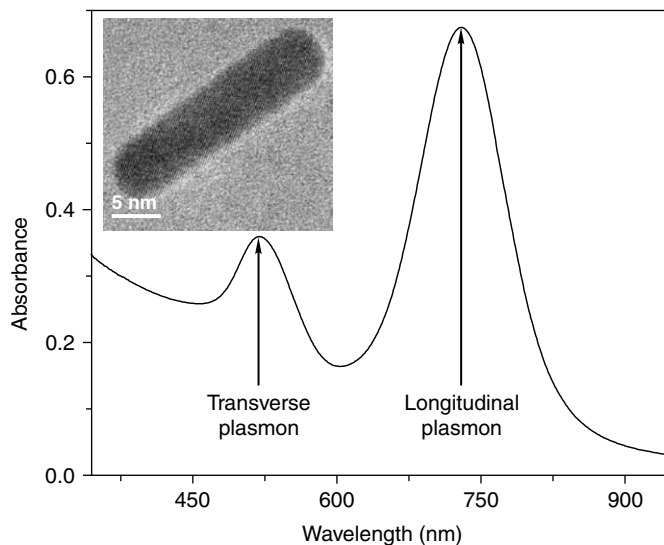


Fig. 9.8 UV/Vis absorption spectrum and TEM image of gold nanorods (from the author's laboratory).

poly(vinyl pyrrolidone) (PVP). These nanoplates are different in their optical characteristics, exhibiting strong infrared absorption, which could be tuned by varying the dimension. The IR absorption is attributed to quadrupolar plasmon resonances. Gold triangles have also been prepared by using an extract from lemon grass.²⁰⁴

A summary of the synthetic routes used for anisotropic nanoparticles is presented in Appendices Part II.

9.12 OTHER NANOMATERIALS

Instead of using inorganic materials, organic nanoparticles or nanomolecules may also be used to make nanomaterials. There are several classes of nanomolecules belonging to this category. Although there are numerous types of systems, the most important once are:

1. Fullerenes
2. Nanotubes
3. Dendrimers
4. Polymers

In this section, we outline the synthetic aspects of first two kinds of nanomaterials.

9.12.1 Fullerenes

These are all carbon spheroidal molecules of the general formula, C_{20+2n_6} (where n_6 is the number of hexagonal faces.). A closed cage requires that $12 = 3n_3 + 2n_4 + 1n_5 + 0n_6 - 1n_7 - 2n_8 - \dots$, where

n_k is the number of k -sided faces. For carbon, only values of k are 5 and 6, although 7 is also possible, which has been detected in carbon nanotubes. This means that in carbon, one has to make closed-cage structures with pentagonal and hexagonal faces. So, there should be 12 pentagonal faces in a given structure and the number of hexagonal faces is arbitrary. In C_{60} , there are 12 pentagonal faces and 20 hexagonal faces.

The most intensely explored molecules in this category are C_{60} and C_{70} . There are lesser known molecules such as C_{76} , C_{82} , etc., which are more difficult to synthesise in larger quantities. Fullerenes were discovered in the laser evaporation of carbon in 1985²⁰⁵ and were prepared in the condensed phase in 1990 by thermal evaporation of graphite in an inert atmosphere.²⁰⁶

To synthesise fullerenes, all that one needs is a welding transformer, a chamber connected to a vacuum pump (even a single stage oil sealed rotary pump is adequate) and some graphite rods. The graphite electrodes are brought in close contact with each other and an arc is struck in an atmosphere of 100–200 Torr of helium or argon. To sustain the arc, a voltage of 20 V (AC or DC) may be necessary. For a graphite rod of 6 mm in diameter, about 50–200 A current would be consumed. Generally, spectroscopic pure graphite of high porosity is used so that evaporation rate is high. The soot generated is collected on water-cooled surfaces, which could even be the inner walls of the vacuum chamber. After maintaining the arc for several minutes, the vacuum is released, soot is collected and soxhlet extracted for about 5–6 hours in toluene or benzene resulting in a dark reddish-brown solution, which is a mixture of fullerenes. 20–30 per cent of the soot so collected is soluble. The soluble material is subjected to chromatographic separation.²⁰⁷ Over the years, several simple methods have been discovered including the technique of filtration through an activated charcoal-silica gel column. About 80 per cent of the soluble material is C_{60} , which can be collected in a single pass using toluene as the mobile phase. C_{70} can be separated using toluene/*o*-dichlorobenzene mixture as eluant. Repeated chromatographic separation may be necessary to get pure C_{70} . A solution of C_{60} is violet in colour, while that of C_{70} is reddish-brown. Higher fullerenes, C_{76} , C_{78} , C_{82} , etc., require HPLC for purification. Spectroscopic properties of several of these less common fullerenes are now known. In the lab-scale, preparation of a one-gram quantity of C_{60} requires about 5 hours of work starting from graphite. But, many of the higher fullerenes require 250 hours to make about 1 mg. C_{60} and C_{70} are now commercially available from several sources. Fullerenes crystallized from saturated solutions retain solvent molecules and removing them may require long hours of vacuum drying. Crystal growth by vapour transport is an excellent method to grow millimeter-size crystals devoid of solvent for sensitive measurements. For solid-state spectroscopic measurements, it is better to use evaporated fullerene films in high or ultra-high vacuum to avoid contamination by solvent molecules. Evaporation-condensation is also used as a method of purification as there are substantial differences in the onset of evaporation between C_{60} and C_{70} .

Arc evaporation is not the unique way of making C_{60} . Fullerenes have been found in flames, upon chemical vapour deposition used to produce diamond, in a 1.85 bn-year-old bolide impact crater as well from spacecrafts. It has also been made from diamond. No one has made it by chemical reactions, but such a possibility had excited many organic chemists. It has been synthesised from camphor. Mass spectrometry has shown that higher clusters of carbons could be formed by laser evaporation

of polymers. Highly unsaturated carbonaceous ring systems, upon laser evaporation, produce C_{60} . There are several other exotic means of producing C_{60} . However, the total synthesis would indeed be a landmark in chemistry.

Solid C_{60} dissolves in a number of organic solvents such as hexane, CH_2Cl_2 , toluene, etc., yielding magenta solutions. These solutions may be stored for extended periods without degradation. However, C_{60} gets deposited on the walls of the vessel. The solubility of C_{60} is about 7.2 mg/ml at room temperature. The solutions are stable over a range of temperatures.

9.12.2 Nanotubes

Carbon nanotubes are one-dimensional cylinders of carbon with single or multiple layers (described later in the text). The diameters of the tubes are in the range of a few nanometers and the length is of the order of microns. This makes carbon nanotubes one of the materials with highest aspect ratio. As the tubes exhibit many properties as a result of the confinement of electrons to one dimension, they are new kinds of model systems, in which a number of quantum phenomena can be investigated. As a result, they are also one of the most extensively investigated nanosystems.

9.12.2.1 Synthesis and Purification

Carbon nanotubes were first noticed in the graphitic soot deposited on the negatively charged electrode used in the arc-discharge synthesis of fullerenes. In the Kratschmer-Huffman procedure,²⁰⁶ the graphite rods are evaporated in a dynamic atmosphere of helium (helium is leaked in while the vacuum system is pumped). Typically a pressure of 130 torr of helium is used and the arc is run at 30 V DC and current is maintained at ~180 A. Increasing the helium pressure to 500 torr increases the multi-walled nanotubes (MWNT) yield. The carbon deposited on the cathode has a soft inner core and a hard outer cover. The core containing MWNTs is extracted and suspended in suitable solvents. The tubes were observed as empty cylinders lying perpendicular to the electron beam along with amorphous carbon material. Multi-walled tubes were observed and the interlayer gap is 0.34 nm, close to the spacing found in graphite. The very first images taken by Iijima showed two continuous lines in the TEM. The tube's inner diameter, interlayer spacing, length as well as chiral angle θ can be determined from the TEM images. While the calculation of first three from TEM images is straight forward, that of chiral angle requires measurement of the interference pattern of the parallel planes and is often not done in routine TEM examination of nanotubes.

Nanotubes are found with closed ends on either side, although open tubes are also seen. Thus, these are three-dimensional closed-cage objects, and may be considered as elongated fullerenes. In order to make a closed-cage structure, there must be at least 12 pentagons according to the Euler's theorem, considering only pentagons and hexagons. The hexagons make the elongated body of the tube and the ends contain both hexagons and pentagons, presence of 6 pentagons on each face is a minimum. However, the tube body and the ends can have defects. While pentagons result in positive curvature, heptagonal defects make negative curvature. Presence of both of these have been observed. The former makes a larger tube smaller and the latter can remove this curvature. Various kinds of end tube morphologies have been found.

Various modifications to the arc-discharge process are reported in the literature for the synthesis of nanotubes. In the process, a smaller diameter (typically 3 mm) anode evaporates on the face of a larger diameter (6 mm) cathode in a direct current arc-discharge apparatus. The bowl that grows on the cathode contains multi-walled tubes. This can be broken, ground and the nanotubes may be suspended in a suitable solvent and deposited on TEM grids for examination.

Today, the most extensive investigations are being carried out on single-walled nanotubes (SWNTs). There are principally three different methods used for the synthesis:

1. Incorporation of transition metals in catalytic amounts during the arc-discharge process results in the formation of SWNTs. The metal catalyst is added into the anode. The most common metals used are iron and nickel, but a mixture of transition metals is better. Several bimetallic systems, such as Co-Ni, Co-Pt and Ni-Y, have been tried for this purpose. Web-like deposits are found around the cathode or the cooler regions of the reaction vessel. These materials contain significant quantities of single-walled nanotubes; they are seen in the form of ropes containing 5–100 individual SWNTs along with amorphous carbon and nanoparticles of the metal/metal-carbon compounds. Optimized synthesis utilizes Ni-Y catalyst in 4 : 1 atomic ratio and several grams of SWNT-containing material can be prepared.^{209, 210}
2. Laser evaporation is another way to produce SWNTs in good yield.²¹¹ By heating a mixture of graphite with Fe and Ni catalysts at a temperature of 1200°C and irradiating the material with a laser, it is possible to synthesize SWNTs. The yield of the nanotubes is about 50–70 per cent of the product. Nanotubes thus synthesised are found to form ropes, in which individual tubes organise into a hexagonal assembly. This very clearly shows the homogeneity of the tubes synthesised.
3. Chemical vapour deposition is another useful way for the synthesis of SWNTs and MWNTs.²¹² Here, an organometallic precursor is mixed with a carbon-containing feed gas is pyrolysed in a quartz tube and the nanotubes are collected from the cooler end of the reaction vessel. The feed gas may contain several species and is often mixed with an inert gas. Nanotubes are also grown on solid catalytic substrates, such as SiO₂, quartz, etc., which contain transition metal precursors. Such approaches are important to make supported MWNT assemblies for specific applications. By feeding suitable precursor species, it is possible to incorporate other atoms, such as nitrogen, into the nanotube structure, by substitution. It is also possible to change the morphology of the tubes by changing the precursors. CVD on surfaces with patterning done by suitable catalysts, nanotube arrays can be produced.²¹³ One of the important aspects of CVD growth is the possibility of making nanotubes in batch processes. It is also possible that by using proper precursors, suitable properties, such as elemental or ¹³C doping can be achieved.

Generally, MWNTs and SWNTs are formed along with significant quantities of carbonaceous material. One way to separate the tubes from the carbon mass is to heat-treat the product. Though, all different forms of carbon react with oxygen, they do so at different rates. All of the amorphous carbon materials can be burned off by heating the as-prepared mixture at 750 °C for half an hour.

By this process, only less than 1 per cent of the original material is left, but the product is found to be essentially nanotubes. The presence of large number of defects on amorphous carbon makes it react at a higher rate in comparison to nanotubes. There are acid-based cleaning procedures as well.

In order to make larger quantities of nanotubes, the HiPCO (high pressure CO disproportionation) method is used.^{214,215} This involves the high pressure disproportionation reaction of CO in presence of catalysts. The feed gas contains organometallic precursors, such as $\text{Fe}(\text{CO})_5$, which is passed into an oven held at 1100°C . The carbonyl decomposes and produces metal atoms which form clusters. CO undergoes disproportionation, $2 \text{CO} \rightarrow \text{C} (\text{SWNT}) + \text{CO}_2$. About 97 per cent of the material formed is nanotubes. Various methods are available to remove metal impurities from the SWNTs formed. This involves washing with HCl, liquid bromine, etc.²¹⁶

In a number of applications, it is important to have aligned nanotubes oriented perpendicular to the surface. An approach which has received significant attention in the recent times is the synthesis of aligned nanotube bundles on substrates.²¹⁷ Here, a two-furnace approach is used along with metallocenes and organic precursors. Compact aligned nanotube bundles could be obtained by introducing acetylene during the sublimation of ferrocene. Such assemblies grown on substrates, especially in a patterned fashion, can be important for applications, such as field emission displays (see below).

Using anionic, nonionic and cationic surfactants, SWNTs can be suspended in solvents to different extent. A common anionic surfactant is sodium dodecyl sulphate (SDS), which suspends nanotubes in water. An example of a cationic surfactant is cetyltrimethyl ammonium bromide (CTAB), which suspends SWNTs in organics. Typically a 0.2 per cent solution of CTAB can be used for suspending nanotubes.²¹⁸ There are several polymeric surfactants, for example, poly(vinylpyrrolidone) (PVP). Depending on the nature of the surfactant, they can suspend nanoparticles in organic or inorganic media. Notably, an aqueous suspension is important for applications in biology. In a standard protocol, the nanotubes are suspended in dimethylformamide (DMF) by repeated sonication. The dispersion is centrifuged at high speeds, typically in an ultracentrifuge at $60,000\text{--}100,000 \text{ g}$. The free-standing nanotubes are then used for investigations. Centrifugation can be done along with the surfactants. The solution is stable for extended periods.

9.13 CONCLUSIONS

In this chapter, we discussed methods of synthesis of nanomaterials. A variety of nanosystems were discussed, including metal and semiconductor spherical nanoparticles, anisotropic nanostructures, fullerenes and nanotubes. Chemical, physical, mechanical and biological routes of synthesis were outlined. In the case of nanoparticles, principally solution chemistry approaches were discussed. The discussion focused on the methods to make stable and redispersible nanoparticles. A concise summary of the various methods used for the synthesis of diverse nanoparticle systems is presented. The methods for their characterisation were outlined with specific examples in the entire range of particle sizes, from nanoparticles to clusters. The synthetic issues involved were discussed briefly. It is clear from the data presented that almost the entire periodic table could be converted in the nano form.

REFERENCES

1. <http://www.rigb.org/rimain/heritage/faradaypage.jsp>.
2. N. Sandhyarani, M.R. Resmi, R. Unnikrishnan, et al., 'Monolayer-protected cluster superlattices: Structural, spectroscopic, calorimetric, and conductivity studies', *Chem. Mater.*, 12, (2000), 104–13.
3. Y. Xuan and Q. Li, Heat transfer enhancement of nanofluids, *International Journal of Heat and Fluid Flow*, 21, (2000), 58–64.
4. T. Pradeep, 2007, *Nano: The Essentials (Tata McGraw-Hill). Handbook of Microscopy for Nanotechnology*, 2005, Ed: N. Yao and Z.L. Wang (Kluwer Academic Publishers).
5. K.L. Kelly, E. Coronado, L.L. Zhao and G.C. Schatz, 'The optical properties of metal nanoparticles: The influence of size, shape, and dielectric environment', *J. Phys. Chem. B*, 107, (2003), 668–77.
6. S. Link and M.A. El-Sayed, 'Spectral properties and relaxation dynamics of surface plasmon electronic oscillations in gold and silver nanodots and nanorods', *J. Phys. Chem. B*, 103, (1999), 8410–26.
7. D. Gammon, S.W. Brown, E.S. Snow, et al., 'Nuclear spectroscopy in single quantum dots: Nanoscopic Raman scattering and nuclear magnetic resonance', *Science*, 277, (1997), 85–88.
8. N. Sandhyarani and T. Pradeep, 'Current understanding of the structure, phase transitions and dynamics of self-assembled monolayers on two- and three-dimensional surfaces', *Int. Rev. Phys. Chem*, 22, (2003), 221–62.
9. H. Geliter, 'Nanocrystalline materials', *Progress in Materials Science*, 33, (1989), 223–315.
10. S. Mahdihassan, 'Cinnabar-gold as the best alchemical drug of longevity, called makaradhwaaja in India', *Am. J. Chin. Med.*, 13, (1985), 93.
11. J. Kunckels, Nuetliche, 'Observations oder Anmerkungen von Auro und Argento Potabili'; Schutzens: Hamburg, 1676. (b) Savage, G., 'Glass and Glassware'; *Octopus Book*: London (1975).
12. H.H. Helcher, *Aurum Potabile oder Gold Tinstur*; J. Herbord Klossen: Breslau and Leipzig, (1718).
13. W. Ostwald, 'Zur Geschichte des Colloiden Goldes', *Kolloid Z.*, (1909), 4, 5.
14. M. Faraday, 'Experimental relations in gold (and other metals) to light', *Philos. Trans. R. Soc.*, London, 147, (1857), 145.
15. J. Turkevich, P. Stevenson and J. Hillier, 'A study of the nucleation and growth processes in the synthesis of colloidal gold', *Discussions Faraday Soc.*, 11, (1951), 55–75.
16. M. Brust., M. Walker, D. Bethel, D.J. Schrifin and R. Whyman, 'Synthesis of thiol derivatised gold nanoparticles in a two-phase liquid/liquid system', *J. Chem. Soc., Chem. Commun.*, 7, (1994), 801–02.
17. G. Schmid, R. Boese, R. Pfeil, F. Bandermann, S. Meyer, G.H.M. Calis and J.W.A. van der Velden, $\text{Au}_{55}[\text{P}(\text{C}_6\text{H}_5)_3]_{12}\text{C}_{16}$ —ein Goldcluster ungewöhnlicher Größe ($\text{Au}_{55}[\text{P}(\text{C}_6\text{H}_5)_3]_{12}\text{C}_{16}$ (Gold Cluster of an Exceptional size), *Chem. Ber.*, 114, (1981), 3634–42.
18. P.A. Bartlett, B. Bauer and S. Singer, 'Synthesis of water-soluble undecagold cluster compounds of potential importance in electron microscopic and other studies in biological systems', *J. Am. Chem. Soc.*, 100, (1978), 5085–89.
19. T. Yonezawa and T. Kunitake, 'Practical Preparation of Anionic Mercapto Ligand-Stabilised Gold Nanoparticles and Their Immobilisation', *Colloids Surf. A: Physicochem. Eng. Asp.*, 149, (1999), 193–199.

20. M.C. Daniel and D. Astruc, 'Gold Nanoparticles: Assembly, Supramolecular Chemistry, Quantum-Size-Related Properties, and Applications toward Biology, Catalysis, and Nanotechnology', *Chemistry Review*, 104, (2004), 293–346.
21. 'Vogel's Textbook of Quantitative Chemical Analysis', (1989), Revised by G.H. Jeffery, J. Bassett, J. Mendham and R.C. Denny, fifth edn, (ELBS).
22. S.H. Wu and D.H. Chen, 'Synthesis and characterisation of nickel nanoparticles by hydrazine reduction in ethylene glycol', *Journal of Colloid and Interface Science*, 259, (2003), 282–86.
23. B.A. Korgel, S. Fullam, S. Connolly, and D. Fitzmaurice., 'Assembly and self-organisation of silver nanocrystal superlattices: Ordered soft spheres', *J. Phys. Chem. B*, 102, (1998), 8379–88.
24. G.B. Birrell, K.K. Hedberg and O.H. Griffith, 'Pitfalls of immunogold labeling: Analysis by light microscopy, transmission electron microscopy and photoelectron microscopy', *J. Histochem. Cytochem.*, 35, (1987), 843–53.
25. P.V. Kamat, M. Flumiani and G.V. Hartland, 'Picosecond dynamics of silver nanoclusters. photoejection of electrons and fragmentation', *J. Phys. Chem. B*, 102, (1998), 3123–28.
26. G. Frens, 'Controlled nucleation for the regulation of the particle size in monodisperse gold suspensions', *Nature*, 241, (1973), 20–22.
27. F. Bonet, S. Grugeon, R.H. Urbina, E.K. Tekaiia, and J.M. Tarascon, 'In-situ deposition of silver and palladium nanoparticles prepared by the polyol process, and their performance as catalytic converters of automobile exhaust gases', *Solid State Sciences*, 4, (2002), 665–70.
28. T. Teranishi and M. Miyake, 'Size control of palladium nanoparticles and their crystal structures', *Chem. Mater.*, 10, (1998), 594–600.
29. A. Frattini, N. Pellegrini, D. Nicastro and O. de Sanctis, 'Effect of amine groups in the synthesis of Ag nanoparticles using aminosilanes', *Mater. Chem. Phys*, 94, (2005), 148–52.
30. J.L. Dye and K.L. Tsai, 'Small alloy particles formed by coreduction of soluble precursors with alkali metal or electrides in aprotic solvents', *Faraday Discuss*, 92, (1991), 45–55.
31. H. Bonnemann, R.A. Brand, W. Brijoux, H.W. Hofstadt, M. Frerichs, V. Kempter, W. Maus-Friedrichs, N. Matoussevitch, K.S. Nagabhushana, F. Voigts and V. Caps, 'Air stable Fe and Fe-Co magnetic fluids—synthesis and characterisation', *Appl. Organomet. Chem.*, 19, (2005), 790–96.
32. B.V. Enustun and J. Turkevich, 'Coagulation of colloidal gold', *J. Am. Chem. Soc.*, 85, (1963), 3317–28.
33. A.C. Templeton, W.P. Wuelfing and R.W. Murray, 'Monolayer-protected cluster molecules', *Acc. Chem. Res.*, 33, (2000), 27–36.
34. K.V. Sarathy, G.U. Kulkarni and C.N.R. Rao, 'A novel method of preparing thiol-derivatised nanoparticles of gold, platinum and silver forming superstructures', *Chem. Commun.*, 6, (1997), 537–38.
35. B.L.V. Prasad, S.I. Stoeva, C.M. Sorensen and K.J. Klabunde, 'Digestive-Ripening Agents for Gold Nanoparticles: Alternatives to Thiols', *Chem. Mater.*, 15, (2003), 935–42.
36. T.G. Schaaff, G. Knight, M.N. Shafiqullin, R.F. Borkman and R.L. Whetten, 'Isolation and selected properties of a 10.4 kDa Gold: Glutathione cluster compound', *J. Phys. Chem. B*, 102, (1998), 10643–46.
37. S.H. Chen and K. Kimura, 'Synthesis and characterisation of carboxylate-modified gold nanoparticle powders dispersible in water', *Langmuir*, 15, (1999), 1075–82.
38. T.U.B. Rao, B. Nataraju and T. Pradeep, Ag₉ Quantum Cluster through a Solid-State Route, *J. Am. Chem. Soc.*, 132 (46), (2010), 16304–07.

39. K. Kimura, S. Sato and H. Yao, 'Particle crystals of surface modified gold nanoparticles grown from water', *Chem. Lett.*, 4, (2001), 372–73.
40. Y. Negishi, K. Nobusada and T. Tsukuda, 'Glutathione-Protected Gold Clusters Revisited: Bridging the Gap between Gold(I)-Thiolate Complexes and Thiolate-Protected Gold Nanocrystals', *J. Am. Chem. Soc.*, 127, (2005), 5261–70.
41. M.A.H. Muhammed, T. Pradeep, 'Luminescent Quantum Clusters of Gold as Bio-Labels, in Advanced Fluorescence Reporters in Chemistry and Biology, II' ed. A.P. Demchenko, Springer-Verlag Berlin, Heidelberg, vol. 9, part 4, (2010), 333–53.
42. R. Jin, 'Quantum sized, thiolate-protected gold nanoclusters', *Nanoscale* 2 (3), (2010), 343–62.
43. I. Diez and R.H.A. Ras, 'Fluorescent silver nanoclusters', *Nanoscale*, 3 (5), (2011), 1963–70.
44. M.T. Reetz and W. Helbig, 'Size-Selective Synthesis of Nanostructured Transition Metal Clusters', *J. Am. Chem. Soc.*, 116, (1994), 7401–02.
45. L.R. Sánchez, M.C. Blanco and M.A.L. Quintela, 'Electrochemical Synthesis of Silver Nanoparticles', *J. Phys. Chem. B.*, 104, (2000), 9683–88.
46. M.B. Mohamed, Z.L. Wang and M.A. El-Sayed, 'Temperature-Dependent Size-Controlled Nucleation and Growth of Gold Nanoclusters', *J. Phys. Chem. A.*, 103, (1999), 10255–59.
47. J. Asenjo, R. Amigo, E. Krotenko, F. Torres, J. Tejada, E. Brillas and G. Sardin, 'Electrochemical Synthesis of Nanoparticles of Magnetic Mixed Oxides of Sr-Fe and Sr-Co-Fe', *Journal of Nanoscience and Nanotechnology*, 1, (2001), 441–49.
48. I.G. Draganic and Z.D. Draganic, *The Radiolysis of Water*; Academic Press: New York, 1971.
49. A. Henglein, 'Radiolytic Preparation of Ultrafine Colloidal Gold Particles in Aqueous Solution: Optical Spectrum, Controlled Growth, and Some Chemical Reactions', *Langmuir*, 15, (1999), 6738–44.
50. S. Wang and H. Zin, 'Fractal and Dendritic Growth of Metallic Ag Aggregated from Different Kinds of Irradiated Solutions', *J. Phys. Chem. B.*, 104, (2000), 5681–85.
51. A. Henglein, 'Formation and Absorption Spectrum of Copper Nanoparticles from the Radiolytic Reduction of $\text{Cu}(\text{CN})_2$ ', *J. Phys. Chem. B.*, 104, (2000), 1206–11.
52. B.G. Ershov, N.L. Sukhov and E. Janata, 'Formation, Absorption Spectrum, and Chemical Reactions of Nanosized Colloidal Cobalt in Aqueous Solution', *J. Phys. Chem. B.*, 104, (2000), 6138.
53. J.H. Hodak, A. Henglein and G.V. Hartland, 'Photophysics of nanometer sized metal particles: Electron-phonon Coupling and Coherent Excitation of Breathing Vibrational Modes', *J. Phys. Chem. B.*, 104, (2000), 9954–65.
54. A. Henglein, 'Preparation and Optical Absorption Spectra of Au core Pt shell and Pt core Au shell Colloidal Nanoparticles in Aqueous Solution', *J. Phys. Chem. B.*, 104, (2000), 2201–03.
55. P. Mulvaney, M. Giersig and A. Henglein, 'Surface chemistry of colloidal gold: deposition of lead and accompanying optical effects', *J. Phys. Chem.*, 96, (1992), 10419–24.
56. A. Henglein and D. Meisel, 'Radiolytic Control of the Size of Colloidal Gold Nanoparticles', *Langmuir*, 14, (1998), 7392–96.
57. Y. Kato, S. Sugimoto, K. Shinohara, N. Tezuka, T. Kagotani and K. Inomata, 'Magnetic Properties and Microwave Absorption Properties of Polymer-Protected Cobalt Nanoparticles', *Mater. Trans., JIM.*, 43, (2002), 406–09.

58. T.W. Smith and D. Wychick, 'Colloidal iron dispersions prepared via the polymer-catalysed decomposition of iron pentacarbonyl', *J. Phys. Chem. B.*, 84, (1980), 1621–29.
59. S.W. Charles, S.Wells and J. Villadsen, 'Formation and chemical stability of metallic glass particles prepared by thermolysis of $\text{Fe}(\text{CO})_5$ ', *Hyperfine Interact.*, 27, (1986), 333–36.
60. J. van Wonterghem, S. Mørup, S.W. Charles, S. Wells and J. Villadsen, 'Formation of a metallic glass by thermal decomposition of $\text{Fe}(\text{CO})_5$ ', *Phys. Rev. Lett.*, 55, (1985), 410–13.
61. D. Dinega and M.G. Bawendi, 'A Solution-Phase Chemical Approach to a New Crystal Structure of Cobalt', *Angew. Chem., Int. Ed.*, 38, (1999), 1788–99.
62. V.F. Puentes, K.M. Krishnan and A.P. Alivisatos, 'Colloidal Nanocrystal Shape and Size Control: The Case of Cobalt', *Science*, 291, (2001), 2115–17.
63. V.F. Puentes, D. Zanchet, C.K. Erdonmez and A.P. Alivisatos, 'Synthesis of hcp-Co Nanodisks', *J. Am. Chem. Soc.*, 124, (2002), 12874–80.
64. S. Sun, C.B. Murray, D. Weller, L. Folks and A. Moser, 'Monodisperse FePt Nanoparticles and Ferromagnetic FePt Nanocrystal Superlattices', *Science*, 287, (2000), 1989–92.
65. J.I. Park and J. Cheon, 'Synthesis of "Solid Solution" and "Core-Shell" Type Cobalt-Platinum Magnetic Nanoparticles via Transmetalation Reactions', *J. Am. Chem. Soc.*, 123, (2001), 5743–46.
66. C. Amiens, D. de Caro, B. Chaudret, J.S. Bradley, R. Mazel and C. Roucau, 'Selective synthesis, characterisation, and spectroscopic studies on a novel class of reduced platinum and palladium particles stabilised by carbonyl and phosphine ligands', *J. Am. Chem. Soc.*, 115, (1993), 11638–39.
67. F. Dumestre, B. Chaudret, C. Amiens, M.C. Fromen, M.J. Casanove, P. Renaud and P. Zurcher, 'Shape Control of Thermodynamically Stable Cobalt Nanorods through Organometallic Chemistry', *Angew. Chem., Int. Ed.*, 41, (2002), 4286–89.
68. K.J. Rao, B. Vaidhyanathan, M. Ganguli and P.A. Ramakrishnan, 'Synthesis of Inorganic Solids Using Microwaves', *Chem. Mater*, 11, (1999), 882–95.
69. I.S. Pastoriza and L.M. Liz-Marzán, 'Formation of PVP-Protected Metal Nanoparticles in DMF', *Langmuir*, 18, (2002), 2888–94.
70. F. Fievet, J.P. Lagier and M. Figlarz, 'Preparing Monodisperse Metal Powders in Micrometer and Submicrometer Sizes by the Polyol Process', *MRS Bull.*, 24, (1989), 29.
71. W. Yu, W. Tu and H. Liu, 'Synthesis of Nanoscale Platinum Colloids by Microwave Dielectric Heating', *Langmuir*, 15, (1999), 6–9.
72. M. Tsuji, M. Hashimoto and T. Tsuji, 'Fast Preparation of Nano-sized Nickel Particles under Microwave Irradiation without Using Catalyst for Nucleation', *Chem. Lett.*, 31, (2002), 1232–34.
73. W. Tu and H. Liu, 'Continuous Synthesis of Colloidal Metal Nanoclusters by Microwave Irradiation', *Chem. Mater.*, 12, (2000), 564–67.
74. B.L. Cushing, V.L. Kolesnichenko and C.J. O'Connor, 'Recent Advances in the Liquid-Phase Syntheses of Inorganic Nanoparticles', *Chem. Rev.*, 104, (2004), 3893–3946.
75. K.S. Suslick, S.-B. Choe, A.A. Cichowlas and M.W. Grinstaff, 'Sonochemical synthesis of amorphous iron', *Nature*, 353, (1991), 414–17.
76. K.S. Suslick, M. Fang and T. Hyeon, 'Sonochemical Synthesis of Iron Colloids', *J. Am. Chem. Soc.*, 118, (1996), 11960–61.

77. M.W. Grinstaff, M.B. Salmon and K.S. Suslick, 'Magnetic properties of amorphous iron', *Phys. Rev. B*, 48, (1993), 269–73.
78. A. Gedanken, 'Using sonochemistry for the fabrication of nanomaterials ultrason', *Sonochem.*, 11, (2004), 47–55.
79. P.H. Borse, L.S. Kankate, F. Dassenoy, W. Vogel, J. Urban and S.K. Kulkarni, 'Synthesis and investigations of rutile phase nanoparticles of TiO₂', *J. Mater. Sci. -Mater. Electron.*, 13, (2002), 553–59.
80. Y. Gu, G.Z. Li, G. Meng and D. Peng, 'Sintering and electrical properties of coprecipitation prepared Ce_{0.8}Y_{0.2}O_{1.9} ceramics', *Mater. Res. Bull.*, 35, (2000), 297–304.
81. P.C. Kuo and T.S. Tsai, 'New approaches to the synthesis of acicular alpha-FeOOH and cobalt modified iron-oxide nanoparticles', *J. Appl. Phys.*, 65, (1989), 4349–56.
82. Z.X. Tang, C.M. Sorensen, K.J. Klabunde and G.C. Hadjipanayis, 'Preparation of manganese ferrite fine particles from aqueous solution', *Journal of Colloid Interface Science*, 146, (1991), 38–54.
83. C.N. Chinnasamy, B. Jeyadevan, O. Perales-Perez, K. Shinoda, K. Tohji and A. Kasuya, 'Growth Dominant Co-Precipitation Process to Achieve High Coercivity at Room Temperature in CoFe₂O₄ Nanoparticles', *IEEE Trans. Magn.*, 38, (2002), 2640–42.
84. T.C. Rojas and M. Ocana, 'Uniform nanoparticles of Pr(III)/Ceria solid solutions prepared by homogeneous precipitation', *Scr. Mater.*, 46, (2002), 655–60.
85. J. Li, D. Dai, B. Zhao, Y. Lin and C. Liu, 'Properties of ferrofluid nanoparticles prepared by coprecipitation and acid treatment', *J. Nanopart. Res.*, 4, (2002), 261–64.
86. K.T. Wu, P.C. Kuo, and Y.D. Yao and E.H. Tsai, 'Magnetic and optical properties of Fe₃O₄ nanoparticle ferrofluids prepared by coprecipitation technique', *IEEE Trans. Magn.*, 37, (2001), 2651–53.
87. W. Voit, D.K. Kim, W. Zapka, M. Muhammed and K.V. Rao, *Mat. Res. Soc. Symp. Proc.*, 676, (2001), Y7.8.1–Y7.8.6.
88. H. Chen, X. Qiu, W. Zhu and P. Hagenmuller, 'Synthesis and high rate properties of nanoparticled lithium cobalt oxides as the cathode material for lithium-ion battery', *Electrochem. Commun.*, 4, (2002), 488–91.
89. P. Deb, T. Biswas, D. Sen, A. Basumallick and S. Mazumder, 'Characteristics of Fe₂O₃ Nanoparticles Prepared by Heat Treatment of a Nonaqueous Powder Precipitate', *Journal of Nanoparticles Research*, 4, (2002), 91–97.
90. S. O'Brien, L. Brus and C.B. Murray, 'Synthesis of Monodisperse Nanoparticles of Barium Titanate: Toward a Generalised Strategy of Oxide Nanoparticle Synthesis', *J. Am. Chem. Soc.*, 123, (2001), 12085–86.
91. D. Caruntu, Y. Remond, N.H. Chou, M.-J. Jun, G. Caruntu, J. He, G. Goloverda, C. O'Connor and V. Kolesnichenko, 'Reactivity of 3D Transition Metal Cations in Diethylene Glycol Solutions. Synthesis of Transition Metal Ferrites with the Structure of Discrete Nanoparticles Complexed with Long-Chain Carboxylate Anions', *Inorg. Chem.*, 41, (2002), 6137–46.
92. T. Trindade, P. O'Brien and N.L. Pickett, 'Nanocrystalline semiconductors: Synthesis, properties, and perspectives', *Chem. Mater.*, 13, (2001), 3843–58.
93. C.D. Dushkin, S. Saita, K. Yoshie and Y. Yamaguchi, 'The kinetics of growth of semiconductor nanocrystals in a hot amphiphile matrix', *Adv. Colloid Interface Sci.*, 88, (2000), 37–78.

94. C. Burda, X.B. Chen, R. Narayanan and M.A El-Sayed, 'Chemistry and properties of nanocrystals of different shapes', *Chem. Rev.*, 105, (2005), 1025–1102.
95. M.L. Steigerwald and C.R. Sprinkle, 'Application of phosphine tellurides to the preparation of Group II–VI (2–16) semiconductor materials', *Organometallics*, 7, (1988), 245–46.
96. S.M. Stuczynski, J.G. Brennan and M.L. Steigerwald, 'Formation of metal-chalcogen bonds by the reaction of metal-alkyls with silyl chalcogenides', *Inorg. Chem.*, 28, (1989), 4431–32.
97. M.L. Steigerwald, *Mater. Res. Soc. Symp. Proc.*, 131, (1989), 37.
98. J.G. Brennan, T. Siegrist, P.J. Carroll, S.M. Stuczynski, L.E. Brus and M.L. Steigerwald, 'The preparation of large semiconductor clusters via the pyrolysis of a molecular precursor', *J. Am. Chem. Soc.*, 111, (1989), 4141–43.
99. J.G. Brennan, T. Siegrist, P.J. Carroll, S.M. Stuczynski, P. Reynders, L.E. Brus and M.L. Steigerwald, 'Bulk and nanostructure Group II–VI compounds from molecular organometallic precursors', *Chem. Mater.*, 2, (1990), 403–09.
100. S.M. Stuczynski, R.L. Opila, P. Marsh, J.G. Brennan and M.L. Steigerwald, 'Formation of indium phosphide from trimethylindium ($\text{In}(\text{CH}_3)_3$) and tris(trimethylsilyl)phosphine ($\text{P}(\text{Si}(\text{CH}_3)_3)_3$)', *Chem. Mater.*, 3, (1991), 379–81.
101. M.A. Marcus, L.E. Brus, C. Murray, M.G. Bawendi, A. Prasad and A.P. Alivisatos, 'EXAFS studies of cadmium chalcogenide nanocrystals', *Nanostruct. Mater.*, 1, (1992), 323–35.
102. C.B. Murray, D.J. Norris and M.G. Bawendi, 'Synthesis and characterisation of nearly monodisperse CdE (E = sulphur, selenium, tellurium) semiconductor nanocrystallites', *J. Am. Chem. Soc.*, 115, (1993), 8706–15.
103. L.R. Becerra, C.B. Murray, R.G. Griffin and M.G. Bawendi, 'Investigation of the surface-morphology of capped CdSe nanocrystallites by P 31 nuclear-magnetic resonance', *J. Chem. Phys.*, 100, (1994), 3297–3399.
104. C.B. Murray, C.R. Kagan and M.G. Bawendi, 'Self-organisation of CdSe nanocrystallites into 3-dimensional quantum-dot superlattices', *Science*, 270, (1995), 1335–38.
105. M. Danek, K.F. Jensen, C.B. Murray and M.G. Bawendi, 'Synthesis of Luminescent Thin-Film CdSe/ZnSe Quantum Dot Composites Using CdSe Quantum Dots Passivated with an Overlayer of ZnSe', *Chem. Mater.*, 8, (1996), 173–80.
106. A.A. Guzelian, U. Banin, A.V. Kadavanich, X. Peng and A.P. Alivisatos, 'Colloidal chemical synthesis and characterisation of InAs nanocrystal quantum dots', *Appl. Phys. Lett.*, 69, (1996), 1432–34.
107. A.A. Guzelian, J.E.B. Katari, A.V. Kadavanich, U. Banin, K. Hamad, E. Juban, A.P. Alivisatos, R.H. Wolters, C.C. Arnold and J.R. Heath, 'Synthesis of Size-Selected, Surface-Passivated InP Nanocrystals', *J. Phys. Chem.*, 100, (1996), 7212–19.
108. X. Peng, J. Wickham and A.P. Alivisatos, Kinetics of II–VI and III–V, 'Colloidal Semiconductor Nanocrystal Growth: "Focusing" of Size Distributions', *J. Am. Chem. Soc.*, 120, (1998), 5343–44.
109. X. Peng, L. Manna, W. Yang, J. Wickham, E. Scher and A. Kadavanich, 'Shape control of CdSe nanocrystals', *Nature*, 404, (2000), 59–61.
110. L. Manna, E.C. Scher and A.P. Alivisatos, 'Synthesis of Soluble and Processable Rod-, Arrow-, Teardrop-, and Tetrapod-Shaped CdSe Nanocrystals', *J. Am. Chem. Soc.*, 122, (2000), 12700–06.

111. Z.A. Peng and X. Peng, 'Mechanisms of the Shape Evolution of CdSe Nanocrystals', *J. Am. Chem. Soc.*, 123, (2001), 1389–95.
112. Z.A. Peng and X. Peng, 'Formation of High-Quality CdTe, CdSe, and CdS Nanocrystals Using CdO as Precursor', *J. Am. Chem. Soc.*, 123, (2001), 183–84.
113. L. Qu, Z.A. Peng and X. Peng, 'Alternative Routes toward High Quality CdSe Nanocrystals', *Nano Lett.*, 1, (2001), 333–37.
114. O. Palchik, S. Avivi, D. Pinkert and A. Gedanken, 'Preparation and characterisation of Ni/NiO composite using microwave irradiation and sonication', *Nanostruct. Mater.*, 11, (1999), 415–20.
115. J. Zhu, O. Palchik, S. Chen and A. Gedanken, 'Microwave Assisted Preparation of CdSe, PbSe, and Cu_{2-x}Se Nanoparticles', *J. Phys. Chem. B.*, 104, (2000), 7344–47.
116. O. Palchik, J. Zhu and A. Gedanken, 'Microwave assisted preparation of binary oxide nanoparticles', *J. Mater. Chem.*, 10, (2000), 1251–54.
117. O. Palchik, R. Kerner, A. Gedanken, A.M. Weiss, M.A. Slifkin and V. Palchik, 'Microwave-assisted polyol method for the preparation of CdSe "nanoballs"', *J. Mater. Chem.*, 11, (2001), 874–78.
118. H. Grisar, O. Palchik, A. Gedanken, V. Palchik, M.A. Slifkin and A.M. Weiss, 'Preparation of the $\text{Cd}_{1-x}\text{Zn}_x$ Se alloys in the nanophase form using microwave irradiation', *J. Mater. Chem.*, 12, (2002), 339–44.
119. R. Kerner, O. Palchik and A. Gedanken, 'Sonochemical and Microwave-Assisted Preparations of PbTe and PbSe. A Comparative Study', *Chem. Mater.*, 13, (2001), 1413–19.
120. X. Zheng, Y. Xie, L. Zhu, X. Jiang and A. Yan, 'Formation of vesicle-templated CdSe hollow spheres in an ultrasound-induced anionic surfactant solution', *Ultrason. Sonochem.*, 9, (2002), 311–16.
121. R.E. Bailey, A.M. Smith and S. Nie, 'Quantum dots in biology and medicine', *Physica E.*, 25, (2004), 1–12.
122. K. Holmberg, 'Surfactant-templated nanomaterials synthesis', *J. Coll. Interface Sci.*, 274, (2004), 355–64.
123. C.J. O'Connor, J.A. Sims, A. Kumbhar, V.L. Kolesnichenko, W.L. Zhou and J.A. Wiemann, 'Magnetic properties of FePt_x/Au and CoPt_x/Au core-shell nanoparticles', *J. Magn. Magn. Mater.*, 226–230, (2001), 1915–17.
124. J. Lin, W. Zhou, A. Kumbhar, J. Wiemann, J. Fang, E.E. Carpenter and C.J. O'Connor, 'Gold-coated iron (Fe@Au) nanoparticles: Synthesis, characterisation, and magnetic field-induced self-assembly', *J. Solid State Chem.*, 159, (2001), 26–31.
125. B. Ravel, E.E. Carpenter and V.G. Harris, 'Oxidation of iron in iron/gold core/shell nanoparticles', *J. Appl. Phys.*, 91, (2002), 8195–97.
126. E.E. Carpenter, A. Kumbhar, J.A. Wiemann, H. Srikanth, J. Wiggins, W. Zhou and C.J. O'Connor, 'Synthesis and magnetic properties of gold-iron-gold nanocomposites', *Mater. Sci. Eng.*, A, 286, (2000), 81–86.
127. W.L. Zhou, E.E. Carpenter, J. Sims, A. Kumbhar and C.J. O'Connor, *Mater. Res. Soc. Symp. Proc.*, 581, (2000), 107.
128. C.J. O'Connor, C.T. Seip, E.E. Carpenter, S. Li and V.T. John, 'Synthesis and reactivity of nanophase ferrites in reverse micellar solutions', *Nanostruct. Mater.*, 12, (1999), 65–70.
129. S. Santra, R. Taped, N. Theodoropoulou, J. Dobson, A. Hebard and W. Tan, 'Synthesis and Characterisation of Silica-Coated Iron Oxide Nanoparticles in Microemulsion: The Effect of Nonionic Surfactants', *Langmuir*, 17, (2001), 2900–06.

130. L.M. Liz-Marzan, M. Giersig and P. Mulvaney, 'Synthesis of Nanosized Gold-Silica Core-Shell Particles', *Langmuir*, 12, (1996), 4329–35.
131. W. Stöber, A. Fink and E. Bohn, 'Controlled Growth of Monodisperse Silica Spheres in the Micron Size Range', *J. Colloid Interface Sci.*, 26, (1968), 62–69.
132. S.I. Pastoriza, D.S. Koktysh, A.A. Mamedov, M. Giersig, N.A. Kotov and L.M. Liz-Marzan, 'One-pot synthesis of Ag@TiO₂ core-shell nanoparticles and their layer-by-layer assembly', *Langmuir*, 16, (2000), 2731–32.
133. R.T. Tom, A.S. Nair, N. Singh, M. Aslam, C.L. Nagendra, R. Philip, K. Vijayamohan and T. Pradeep, 'Freely dispersible Au@TiO₂, Au@ZrO₂, Ag@TiO₂, and Ag@ZrO₂ core-shell nanoparticles: One-step synthesis, characterisation, spectroscopy, and optical limiting properties', *Langmuir*, 19, (2003), 3439–45.
134. A.S. Nair, T. Pradeep and I. MacLaren, 'An investigation of the structure of stearate monolayers on Au@ZrO₂ and Ag@ZrO₂ core-shell nanoparticles', *J. Mater. Chem.*, 14, (2004), 857–62.
135. L.M. Liz-Marzan, 'Tailoring surface plasmons through the morphology and assembly of metal nanoparticles', *Langmuir*, 22, (2006), 32–41.
136. S.-H. Yu, 'Hydrothermal/Solvothermal Processing of Advanced Ceramic Materials', *J. Ceram. Soc. Jpn.*, 109, (2001), S65.
137. F. Cansell, B. Chevalier, A. Demourgues, J. Etourneau, C. Even, Y. Garrabos, V. Pessey, S. Petit, A. Tressaud and F. Weill, 'Supercritical fluid processing: a new route for materials synthesis', *J. Mater. Chem.*, 9, (1999), 67–75.
138. M. Rajamathi and R. Seshadri, 'Oxide and chalcogenide nanoparticles from hydrothermal/solvothermal reactions', *Curr. Opin. Solid State Mater. Sci.*, 6, (2002), 337–45.
139. U.K. Gautam, M. Ghosh, M. Rajamathi and R. Seshadri, 'Solvothermal routes to capped oxide and chalcogenide nanoparticles', *Pure Appl. Chem.*, 74, (2002), 1643–49.
140. G. Demazeau, 'Solvothermal processes: a route to the stabilisation of new materials', *J. Mater. Chem.*, 9, (1999), 15–18.
141. J. Li, Z. Chen, R.-J. Wang and D.M. Proserpio, 'Low temperature route towards new materials: solvothermal synthesis of metal chalcogenides in ethylenediamine', *Coord. Chem. Rev.*, 190–192, (1999), 707–35.
142. M. Niederberger, G. Garnweitner, N. Pinna and G. Neri, 'Non-aqueous routes to crystalline metal oxide nanoparticles: Formation mechanisms and applications', *Prog. Solid State Chem.*, 33, (2005), 59–70.
143. C.N.R. Rao, V.V. Agrawal, K. Biswas, U.K. Gautam, M. Ghosh, A. Govindaraj, G.U. Kulkarni, K.R. Kalyanikutty, K. Sardar and S.R.C. Vivekchandi, 'Soft chemical approaches to inorganic nanostructures', *Pure Appl. Chem.*, 78, (2006), 1619–50.
144. B.L. Newalkar, S. Komarneni and H. Katsuki, 'Microwave-hydrothermal synthesis and characterisation of barium titanate powders', *Mater. Res. Bull.*, 36, (2001), 2347–55.
145. T. Adschiri, Y. Hakuta and K. Arai, 'Hydrothermal Synthesis of Metal Oxide Fine Particles at Supercritical Conditions', *Ind. Eng. Chem. Res.*, 39, (2000), 4901–07.
146. Y. Oguri, R.E. Riman and H.K. Bowen, 'Processing of anatase prepared from hydrothermally treated alkoxy-derived hydrous titania', *J. Mater. Sci.*, 23, (1988), 2897–2904.

147. M. Kondo, K. Shinozaki, R. Ooki and N Mizutani, 'Crystallisation behaviour and microstructure of hydrothermally treated monodispersed titanium-dioxide particles', *J. Ceram. Soc. Jpn.*, 102, (1994), 742–46.
148. H. Cheng, J. Ma, Z. Zhao and L. Qi, 'Hydrothermal Preparation of Uniform Nanosize Rutile and Anatase Particles', *Chem. Mater.*, 7, (1995), 663–71.
149. Z. Yanqing, S. Erwei, C. Zhizhan, L. Wenjun and H. Xingfang, 'Influence of solution concentration on the hydrothermal preparation of titania crystallites', *J. Mater. Chem.*, 11, (2001), 1547–51.
150. H. Yin, Y. Wada, T. Kitamura, T. Sumida, Y. Hasegawa and S. Yanagida, 'Novel synthesis of phase-pure nano-particulate anatase and rutile TiO₂ using TiCl₄ aqueous solutions', *J. Mater. Chem.*, 12, (2002), 378–83.
151. M. Wu, J. Long, A. Huang, Y. Luo, S. Feng and R. Xu, 'Microemulsion-Mediated Hydrothermal Synthesis and Characterisation of Nanosize Rutile and Anatase Particles', *Langmuir*, 15, (1999), 8822–25.
152. T. Masui, H. Hirai, R. Hamada, N. Imanaka, G. Adachi, T. Sakata and H. Mori, 'Synthesis and characterisation of cerium oxide nanoparticles coated with turbostratic boron nitride', *J. Mater. Chem.*, 13, (2003), 622–27.
153. M. Inoue, M. Kimura and T. Inui, 'Transparent colloidal solution of 2 nm ceria particles', *Chem. Commun.*, (1999), 957–58.
154. S. Thimmaiah, M. Rajamathi, N. Singh, P. Bera, F. Meldrum, N. Chandrasekhar and R. Seshadri, 'A solvothermal route to capped nanoparticles of α -Fe₂O₃ and CoFe₂O₄', *J. Mater. Chem.*, 11, (2001), 3215–21.
155. S. Komarneni, M.C. D'Arrigo, C. Leionelli, G.C. Pellacani and H. Katsuki, 'Microwave-Hydrothermal Synthesis of Nanophase Ferrites', *J. Am. Ceram. Soc.*, 81, (1998), 3041–43.
156. H. Katsuki and S. Komarneni, 'Microwave-Hydrothermal Synthesis of Monodispersed Nanophase α -Fe₂O₃', *J. Am. Ceram. Soc.*, 84, (2001), 2313–17.
157. W.S. Sheldrick and M. Wachold, 'Solventothermal synthesis of solid-state chalcogenidometalates', *Angew. Chem., Int. Ed.*, 36 (1997), 207–24.
158. Q. Peng, Y. Dong, Z. Deng, X. Sun and Y. Li, 'Low-Temperature Elemental-Direct-Reaction Route to II-VI Semiconductor Nanocrystalline ZnSe and CdSe', *Inorg. Chem.*, 40, (2001), 3840–41.
159. U.K. Gautam, M. Rajamathi, F. Meldrum, P. Morgan and R. Seshadri, 'A solvothermal route to capped CdSe nanoparticles', *Chem. Commun.*, (2001), 629–30.
160. X.F. Qian, X.M. Zhang, C. Wang, W.Z. Wang, Y. Xie and Y.T. Qian, 'Solvent-thermal preparation of nanocrystalline tin chalcogenide', *J. Phys. Chem. Solids*, 60, (1999), 415–17.
161. X.H. Chen and R. Fan, 'Low-temperature hydrothermal synthesis of transition metal dichalcogenides', *Chem. Mater.*, 13, (2001), 802–05.
162. G.O. Mallory and J.B. Hajdu, 'Electroless Plating: Fundamentals and Applications; American Electroplaters and Surface Finishers Society', Orlando: FL, (1990).
163. M.P. Pileni, 'Fabrication and properties of nanosized material made by using colloidal assemblies as templates', *Cryst. Res. Technol.*, 33, (1998), 1155–86.
164. N. Pradhan, N.R. Jana, K. Mallick and T.J. Pal, *Surf. Sci. Technol.*, (2000), 188.

165. A.S. Nair, T.T. Renjis, V. Suryanarayanan and T. Pradeep, 'ZrO₂ bubbles from core-shell nanoparticles', *J. Mater. Chem.*, 13, (2003), 297–300.
166. Z. Liang, A. Sussha and F. Caruso, 'Gold Nanoparticle-Based Core-Shell and Hollow Spheres and Ordered Assemblies Thereof', *Chem. Mater.*, 15, (2003), 3176–83.
167. R.W.J. Scott, O.M. Wilson and R.M. Crooks, 'Synthesis, Characterisation, and Applications of Dendrimer-Encapsulated Nanoparticles', *J. Phys. Chem. B.*, 109, (2005), 692–704.
168. L.M. Bronstein and Z.B. Shifrina, Dendrimers as Encapsulating, Stabilizing, or Directing Agents for Inorganic Nanoparticles, *Chem. Rev.*, (2011), DOI 10.1021/cr2000724.
169. K.R. Gopidas, J.K. Whitesell and M.A. Fox., 'Nanoparticle-Cored Dendrimers: Synthesis and Characterisation', *J. Am. Chem. Soc.*, 125, (2003), 6491–6502.
170. J.C. Hulteen and C.R. Martin, in *Nanoparticles and Nanostructured Films: Preparation, Characterization and Applications*; J.H. Fendler, Ed.; Wiley: New York, (1998).
171. C.A. Foss, Jr., in *Metal Nanoparticles: Synthesis, Characterization, and Applications*; D.L. Feldheim, C.A. Foss, Jr., Eds.; Dekker: New York, (2001).
172. M. Ichikawa, *Metal Clusters in Chemistry*, (1999), 1273.
173. J.P. Kuczynski, B.H. Milosavljevic and J.K. Thomas, 'Photophysical properties of cadmium sulfide in Nafion film', *J. Phys. Chem.*, 88, (1984), 980–84.
174. J.C. Hoh and I.I. Yaacob, 'Polymer matrix templated synthesis: Cobalt ferrite nanoparticles preparation', *J. Mater. Res.*, 17, (2002), 3105–09.
175. G.L. Hornyak, C.J. Patrissi and C.R. Martin, 'Fabrication, characterisation, and optical properties of gold nanoparticle/porous alumina composites: The nonscattering Maxwell-Garnett limit', *J. Phys. Chem. B.*, 101, (1997), 1548–55.
176. C. Schonenberger, B.M.I vander Zande, L.G.J. Fokkink, M. Henny, C. Schmid, M. Kruger, A. Bachtold, R. Huber, H. Birk and U. Staufer, 'Template synthesis of nanowires in porous polycarbonate membranes: Electrochemistry and morphology', *Phys. Chem. B.*, 101, (1997), 5497–5505.
177. P.M. Ajayan, O. Stephan, P. Redlich and C. Colliex, 'Carbon nanotubes as removable templates for metal-oxide nanocomposites and nanostructures', *Nature*, 375, (1995), 564–67.
178. B.C. Satishkumar, A. Govindaraj, E.M. Vogl, L. Basumallick and C.N.R Rao, 'Oxide nanotubes prepared using carbon nanotubes as templates', *J. Mater. Res.*, 12, (1997), 604–06.
179. C.N.R Rao, F.L. Deepak, G. Gundiah and A. Govindaraj, 'Inorganic nanowires', *Prog. Solid State Chem.*, 31, (2003), 5–147.
180. P. Mukherjee A. Ahmad, D. Mandal, S. Senapati, S.R. Sainkar, M.I. Khan, R. Ramani, R. Parischa, P.V. Ajaykumar, M. Alam, M Sastry and R. Kumar, 'Bioreduction of AuCl₄⁻ ions by the fungus, *Verticillium* sp. and surface trapping of the gold nanoparticles formed', *Angew. Chem., Int. Ed.*, 40, (2001), 3585.
181. B. Nair and T. Pradeep, 'Coalescence of nanoclusters and the formation of sub-micron crystallites assisted by *Lactobacillus* strains', *Cryst. Growth Des.*, 2, (2002), 293–98.
182. Anshup, J.S. Venkataraman, C. Subramaniam, R.R. Kumar, S. Priya, T.R.S Kumar, R.V. Omkumar, A. John, and T. Pradeep, 'Growth of gold nanoparticles in human cells', *Langmuir*, 21, (2005), 11562–67.
183. D. Pum and U.B. Sleytr, 'The application of bacterial S-layers in molecular nanotechnology', *Trends Biotechnol.*, 17, (1999), 8–12.

184. U.B. Sleytr, P. Messner, D. Pum and M. Sara, 'Crystalline bacterial cell surface layers (S layers): From supramolecular cell structure to biomimetics and nanotechnology', *Angew. Chem. Int. Ed.*, 38, (1999), 1034–54.
185. C.A. Mirkin, R.L. Letsinger, R.C. Mucic and J.J. Storhoff, 'A DNA-based method for rationally assembling nanoparticles into macroscopic materials', *Nature*, 382, (1996), 607–08.
186. R. Bashir, 'DNA-mediated artificial nanobiostructures: state of the art and future directions', *Superlattices Microstruct.*, 29, (2001), 1–16.
187. J.J. Storhoff and C.A. Mirkin, 'Programmed materials synthesis with DNA', *Chem. Rev.*, 99, (1999), 1849–62.
188. T. Douglas, in *Biomimetic Materials Chemistry*; Mann, S., Ed.; Wiley: New York, (1996).
189. M. Han, C.R. Vestal and Z.J. Zhang, 'Quantum couplings and magnetic properties of $\text{CoCr}_x\text{Fe}_{2-x}\text{O}_4$ ($0 < x < 1$) spinel ferrite nanoparticles synthesized with reverse micelle method', *J. Phys. Chem. B.*, 108, (2004), 583–87.
190. T. Hyeon, 'Chemical synthesis of magnetic nanoparticles', *Chem. Commun.*, (2003), 927–34.
191. M. Green, 'Organometallic based strategies for metal nanocrystal synthesis', *Chem. Commun.*, (2005), 3002–11.
192. J. Zhang, M. Post, T. Veres, Z.J. Jakubek, J. Guan, D. Wang, F. Normandin, Y. Deslandes and B. Simard, 'Laser-Assisted Synthesis of Superparamagnetic Fe@Au Core-Shell Nanoparticles', *J. Phys. Chem. B.*, 110, (2006), 7122–28.
193. S.H. Sun, 'Recent advances in chemical synthesis, self-assembly, and applications of FePt nanoparticles', *Adv. Mat.*, 18, (2006), 393–403.
194. Mehmet Turker, 'Effect of production parameters on the structure and morphology of Ag nanopowders produced by inert gas condensation', *Materials Science and Engineering A.*, 367, (2004), 74–81.
195. Mehmet Turker, 'Effect of production parameters on the structure and morphology of Ag nanopowders produced by inert gas condensation', *Materials Science and Engineering A.*, 367, (2004), 74–81.
196. H. Akoh, Y. Tsukasaki, S. Yatsuya and A. Tasaki, 'Ferromagnetic ultrafine particles prepared by vacuum evaporation on running oil substrate', *J. Cryst. Growth*, 45, (1978), 495.
197. R. Prasher, P. Bhattacharya and P.E. Phelan, 'Thermal conductivity of nanoscale colloidal solutions (nanofluids)', *Phys. Rev. Lett.*, 94, (2005), Art. No. 025901.
198. P.R. Sajanlal, T.S. Sreepasad, A.K. Samal and T. Pradeep, 'Anisotropic nanomaterials: structure, growth, assembly, and functions', *Nano Reviews*, 2, (2011), 5883.
199. F. Kim, J.H. Song and P. Yang, 'Photochemical Synthesis of Gold Nanorods', *J. Am. Chem. Soc.*, 124, (2002), 14316–17.
200. C.J. Murphy, T.K. Sau, A.M. Gole, C.J. Orendorff, J. Gao, L. Gou, S.E. Hunyadi and T. Li, 'Anisotropic Metal Nanoparticles: Synthesis, Assembly, and Optical Applications', *J. Phys. Chem. B.*, 109, (2005), 13857–70.
201. K. Aslan, Z. Leonenko, J.R. Lakowicz and C.D. Geddes, 'Fast and Slow Deposition of Silver Nanorods on Planar Surfaces: Application to Metal-Enhanced Fluorescence', *J. Phys. Chem. B.*, 109, (2005) 3157–62.

202. H. Jia, W. Xu, J. An, D. Li and B. Zhao, 'A simple method to synthesize triangular silver nanoparticles by light irradiation', *Spectrochimica Acta, Part A*, 64, (2006), 956–60.
203. J.P. Juste, I.P. Santos, L.M. Liz-Marzan and P. Mulvaney, 'Gold nanorods: Synthesis, characterisation and applications', *Coordination Chemistry Reviews*, 249, (2005), 1870–1901.
204. R. Jin, Y.W. Cao, C.A. Mirkin, K.L. Kelly, G.C. Schatz and J.G. Zheng, 'Photoinduced Conversion of Silver Nanospheres to Nanoprisms', *Science*, 294, (2001), 1901–03.
205. S.S. Sankar, A. Rai, B. Ankamwar, A. Singh, A. Ahmad and M. Sastry, 'Biological synthesis of triangular gold nanoprisms', *Nature Material*, 3, (2004), 482–88.
206. H.W. Kroto, J.R. Heath, S.C. O'Brien, R.F. Curl and R.E. Smalley, 'C₆₀: Buckminsterfullerene', *Nature*, 318, (1985), 162–63.
207. W. Kratschmer, L.D. Lmb, K. Fostiropoulos and D.R. Huffman, 'Solid C₆₀: a new form of carbon', *Nature*, 347, (1990), 354–58.
208. C.J. Welch and W.H. Pirckle, 'Progress in the design of selectors for buckminsterfullerene', *J. Chromatogr.*, 609, (1992), 89–101.
209. T.W. Ebbesen and P.M. Ajayan, 'Large-scale synthesis of carbon nanotubes', *Nature*, 358, (1992), 220–22.
210. M. Takizawa, S. Bandow, M. Yudasaka, Y. Ando, H. Shimoyama and S. Iijima, 'Change of tube diameter distribution of single-wall carbon nanotubes induced by changing the bimetallic ratio of Ni and Y catalysts', *Chem. Phys. Lett.*, 326, (2000), 351–57.
211. M. Yudasaka, 'Formation of single-wall carbon nanotubes catalysed by Ni separating from Y in laser ablation or in arc discharge using a C target containing a NiY catalyst', *Chem. Phys. Lett.*, 312, (1999), 155–60.
212. A.G. Rinzler, J.H. Hafner, P. Nikolaev, L. Lou, S.G. Kim, D. Tomanek, P. Nordlander, D.T. Colbert and R.E. Smalley, 'Unraveling nanotubes-field emission from an atomic wire', *Science*, 269, (1995), 1550–53.
213. J. Kong, A.M. Cassel and H. Dai, 'Chemical vapour deposition of methane for single-walled carbon nanotubes', *Chem. Phys. Lett.*, 292, (1998), 567–74.
214. H. Dai, 'Carbon Nanotubes: Synthesis, Integration, and Properties', *Acc. Chem. Res.*, 35, (2002), 1035–44.
215. P. Nikolaev, M.J. Bronikowski, R.K. Bradley, F. Rohmund, D.T. Colbert, K.A. Smith and R.E. Smalley, 'Gas-phase catalytic growth of single-walled carbon nanotubes from carbon monoxide', *Chem. Phys. Lett.*, 313, (1999), 91–97.
216. M.J. Bronikowski, P.A. Willis, D.T. Colbert, K.A. Smith and R.E. Smalley, 'Gas-phase production of carbon single-walled nanotubes from carbon monoxide via the HiPco process: A parametric study', *J. Vac. Sci. Technol., A*, 19(4), (2001), 1800–05.
217. I.W. Chiang, B.E. Brinson, A.Y. Huang, P.A. Willis, M.J. Bronikowski, J.L. Margrave, R.E. Smalley and R.H. Hauge, 'Purification and Characterisation of Single-Wall Carbon Nanotubes (SWNTs) Obtained from the Gas-Phase Decomposition of CO (HiPco Process)', *J. Phys. Chem. B.*, 105, (2001), 8297–8301.
218. C.N.R. Rao, R. Sen, B.C. Satishkumar and A. Govindaraj, 'Large aligned-nanotube bundles from ferrocene pyrolysis', *Chem. Commun.*, (1998), 1525–26.
219. V.C. Moore, M.S. Strano, E.H. Haroz, R.H. Hauge and R.E. Smalley, 'Individually Suspended Single-Walled Carbon Nanotubes in Various Surfactants', *Nano Lett.*, 3, (2003) 1379–82.

ADDITIONAL READING

1. *Nanomaterials Chemistry: Recent Developments and New Directions* by C.N.R. Rao (Ed.), Achim Müller (Ed.), Anthony K. Cheetham (Ed.)
2. *Nanomaterials: An Introduction to Synthesis, Properties and Applications* by Dieter Vollath
3. *Nanoscience and Nanotechnology: Environmental and Health Impacts* by Vicki H. Grassian (Ed.)

REVIEW QUESTIONS

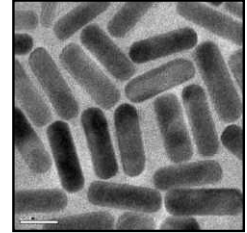
1. What are the top-down and bottom-up approaches?
2. Why chemical methods? Why physical methods?
3. How to make nanoparticles of metals with size and shape control?
4. How to make anisotropic nanostructures? Why are they needed?
5. What parameters one should consider in choosing a given method?
6. How can one study particle size distribution?
7. Why should we study biological methods?

**PART
FOUR**

Understanding Nanosystems

- **Theoretical Understanding of Nanosystems**

THEORETICAL UNDERSTANDING OF NANOSYSTEMS



“Things on a very small scale behave like nothing that you have any direct experience about.

...

Even the experts do not understand it the way they would like to, and it is perfectly reasonable that they should not, because all of direct, human experience and human intuition applies to larger objects.”

Richard Feynman, Feynman Lectures, Vol. 3, Chapter 1

Confinement of electrons in small dimensions results in interesting effects. A theoretical description of these properties is presented here. The spectroscopic manifestation of confinement is also presented. This provides a foundation to the properties described in other parts of this book. The thermodynamic properties of the nanosystems are governed by large-surface effects, which are used for numerous technological applications. Further, due to the small-length scales associated with different phenomena, the detailed chemical composition of the system becomes highly relevant. Both of these make the theoretical understanding of nanosystems difficult. In this chapter, we stress the difficulties arising out of the large-surface effects. We then illustrate how computer simulations can shed light on some of these issues. We discuss, to this end, the basic algorithms for molecular dynamics, Monte-Carlo and stochastic dynamics simulations. We also review a few recent published works to show how the basic algorithms are actually used in research and focus on the current research on the basic algorithms to understand more complicated phenomena.

Learning Objectives

- Appreciation of how the optical and electronic properties of semiconductors get altered in their low dimensional forms.
 - Overview of the interesting physical processes in quantum wells, wires and dots.
 - Detailed and quantitative understanding of the Physics of quantum confinement in semiconductor quantum dots.
 - Exposure to the methods of computation of the energy states of quantum dots and experimental investigation of their optical properties.
-
-

10.1 INTRODUCTION

The very term *quantum dots* is often described as both intriguing and imaginative. It implies the manifestation of quantum effects and the extremely small size. This term generally refers to nanostructures of semiconductor materials, in which electrons are confined to artificially designed, low-dimensional structures with suitably designed potential barriers. However, electrons can be confined to different extents in low-dimensional structures of different dimensions. To understand the interesting physical properties of these materials, it is essential to have brief look at the properties of bulk semiconductors.

10.2 OPTICAL PROPERTIES OF BULK SEMICONDUCTORS

Solids are collections of virtually infinite number of atoms put together and hence the energy levels of the individual atoms tend to merge together to form energy bands, which are regions of allowed values of electron energy. The electrons cannot take up energies between these two regions of allowed values, grouped as the valence-band and the conduction-band in crystals of insulating or semiconducting materials. The energy range in between these bands is called the forbidden energy gap or the band gap, a characteristic property of the material. The typical magnitudes of this energy gap are a few electron volts for semiconductors and several electron volts in the case of insulators.

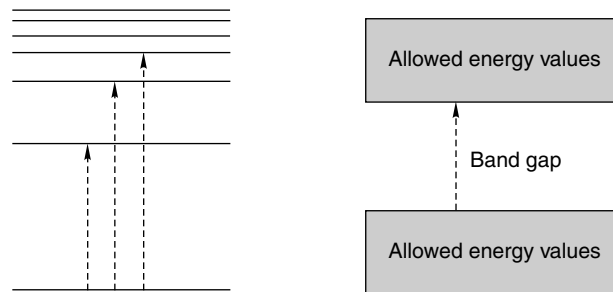


Fig. 10.1 Electronic energy levels in a typical atom (left) and a crystalline solid (right).

Semiconductors are characterised by their energy band gap, an important parameter which governs the optical and electrical properties of the material. The concept of energy bands and band gaps arises from the quantum mechanical description of the behaviour of electrons in crystalline solids. Crystals have long-range periodicity in all the three dimensions and an electron or a hole in this system experiences a potential that is very different from the Coulomb potential electrons experience in isolated atoms. The potential $V(x)$, in this case is periodic as it arises from the translational periodicity of the arrangement of positive ions within the crystal. $V(x) = V(x + a)$, where a is the lattice constant of the crystal. The wave function of the electrons is also periodic with the same periodicity, $\psi(x) = \psi(x + a)$. A quantum mechanical treatment of electrons in crystalline solids involving the solution of the Schrödinger wave equation leads to the concept of energy bands and is available in standard text books on solid state physics.

Insulating crystals are transparent as the energy gap has values greater than the quantum energy corresponding to wavelengths of visible light. Crystals can absorb incident photons with quantum energy equal to or greater than the band gap energy. Such absorption leads to the excitation of an electron from the valence band to the conduction band, across the band gap. Thus the crystals are transparent to electromagnetic waves with quantum energy less than the band gap energy and opaque to those with quantum energy greater than the band gap energy. Crystals of materials such as ZnO (band gap: 3.37 eV), are transparent to most of the visible and infra-red regions of the electromagnetic spectrum, whereas PbS (band gap: 0.41 eV) and silicon (band gap: 1.11 eV) appear black and opaque to light in the visible region. Materials such as CdS (band gap: 2.4 eV) and CdSe (band gap: 1.73 eV) appear coloured and transmit light of different colours selectively. The band gap energy at a given temperature and pressure is characteristic of the semiconductor material and is normally difficult to change. The optical properties are characterised by recording an optical absorption spectrum (Fig. 10.2) of the sample, where the optical absorption coefficient α is plotted as a function of the wavelength λ of the light incident on the crystal. The optical absorption spectra of semiconductor crystals exhibit a demarcation between the wavelength regions, in which the crystal is opaque or transparent. An analysis of this spectrum provides an estimate of the band gap.¹

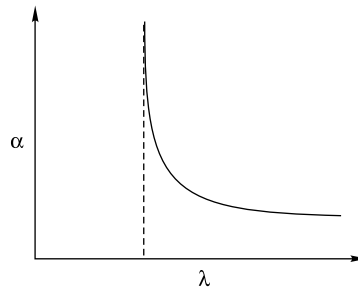


Fig. 10.2 *Optical absorption spectrum of a typical semiconductor.*

10.3 QUANTUM MECHANICS OF LOW-DIMENSIONAL STRUCTURES

Most of the physics of bulk semiconductors is well understood and has been described in standard textbooks. However, design of low-dimensional structures permits quantum mechanical confinement of electrons and holes in different geometries. Electrons, holes and excitons are free to move in along any of the three dimensions in a crystal of a bulk semiconductor. This freedom gets reduced as they get confined to lower dimensions, which affects their quantum states and modifies their density of states and consequently alters their physical properties.

Quantum wells: For example, a very thin layer of a low-band gap semiconducting material can be sandwiched between two layers of another semiconductor with a larger energy gap. The electrons in middle layer are, thus, confined to two dimensions as they find a potential barrier when they move in a direction perpendicular to the plane of the layers. Here the thickness of the middle layer is usually

much less than the length or breadth of the layer and hence this layer can be considered to be quasi-two-dimensional. Such structures are known as *quantum wells*. Figure 10.3 depicts such a structure schematically. The potential experienced by an electron in the structure shown at the top is plotted as a function of the distance along the length of the structure. Continuing in this fashion, alternating thin layers of two appropriate semiconductors with different band gaps, such as AlGaAs and GaAs can be stacked together to form a *multiple* quantum well.

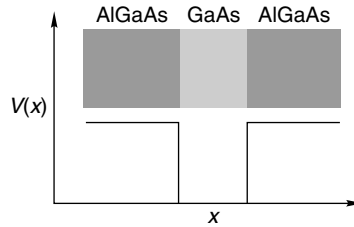


Fig. 10.3 Structure of a typical quantum well.

Study of quantum mechanical confinement in two-dimensional semiconductors resulted in the development of quantum well structures for device applications². Electrons in a quantum well are constrained to move only along two dimensions and face a potential barrier, when they try to move along the third dimension. Such a system is modeled by a one-dimensional potential well problem, where the electrons confined in a deep potential well and face steep potential walls, constraining their motion along one of the dimensions, say, along the z -axis.

The one-dimensional Schrödinger equation in this case can be written as

$$\left[-\frac{\hbar^2}{2m_e} \frac{\partial^2}{\partial z^2} + V(z) \right] \psi(z) = E_z \psi(z), \text{ where } \hbar = \frac{h}{2\pi}, h \text{ being the Planck's constant and}$$

$V(z)$ is the confining potential given by

$$V(z) = 0 \text{ for } L_z/2 < z < L_z \text{ and } \infty \text{ for } |z| > L_z/2.$$

Here L_z denotes the physical width of the confining well and m_e is the mass of the electron. Since there is no confinement for the electrons on the x - y plane, the energy eigenvalues for the electrons are

given by $E_n = \frac{\hbar^2}{2m_e} \left\{ \frac{n^2 \pi^2}{L_z^2} + k_{\perp}^2 \right\}$, where k_{\perp} is the transverse electron wave vector. This implies that

the conduction band of the quantum well structure contains a succession of energy sub-bands in the form of energy parabola

$$\frac{\hbar^2 k_{\perp}^2}{2m_e} \text{ separated by } \frac{\hbar^2 \pi^2}{2m_e L_z^2}.$$

The confinement of the electrons in quantum well structures lead to several properties of interest to optoelectronic devices as efficient lasers used in compact disc players.

Quantum wires: Further confinement of electrons to quasi-one-dimensional structures called *quantum wires* can be achieved by designing an extremely thin wire of a metallic or semiconducting material to be embedded in a dielectric medium. Quantum wires can also be fabricated from quantum wells by electron beam lithography. Confinement of the electrons to one dimension (say, along the z -axis) can be treated quantum mechanically to obtain the energy eigen values as

$$E_n = \frac{\hbar^2}{2m_e} \left\{ \frac{n_x^2 \pi^2}{L_x^2} + \frac{n_y^2 \pi^2}{L_y^2} + k_z^2 \right\}$$

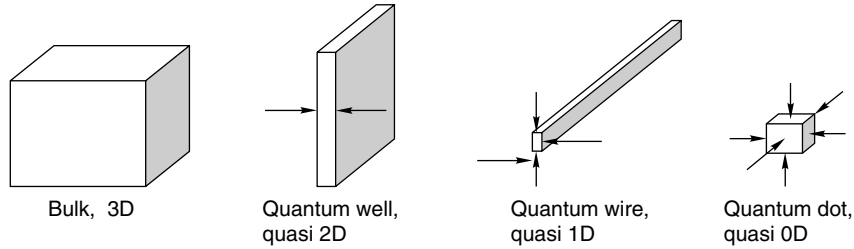


Fig. 10.4 Stages of spatial confinement.

where n_x and n_y are quantum numbers, integers which can take values 1, 2, 3 ...

Quantum dots: Quantum confinement can be extended still further by designing ‘quantum dots’, which are quasi-zero-dimensional nanostructures in the form of tiny islands of the semiconducting material surrounded by an insulating neighbourhood. Such systems, known as quantum dots, have been studied in much more detail than in the case of quantum wells and quantum wires.³⁻⁸

Electrons in these materials are confined by potential barriers along all the three dimensions. In the case of a quantum dot with dimensions L_x , L_y and L_z along the respective coordinate axes, the electron (hole) wave function can be written as

$$\Psi^{e,h} = \psi_x^{e,h}(x)\psi_y^{e,h}(y)\psi_z^{e,h}(z),$$

where $\Psi_x^{e,h} = \frac{1}{L_x} \sin(n\pi x/L_x)$ is the confined envelope along the x direction. The other component wave functions can be written in a similar fashion with the appropriate indices. The corresponding

$$\text{energy eigen values are given by } E_n = \frac{\pi^2 \hbar^2}{2m_e} \left\{ \frac{n_x^2}{L_x^2} + \frac{n_y^2}{L_y^2} + \frac{n_z^2}{L_z^2} \right\}.$$

The functional dependence of the density of states $N(E)$ on energy also changes considerably with different stages of confinement (Fig. 10.5). For bulk materials, $N(E)$ varies as $E^{(1/2)}$, whereas it has a step-like dependence for two-dimensional materials. This is further modified in the case of lower dimensions as shown in the figure.

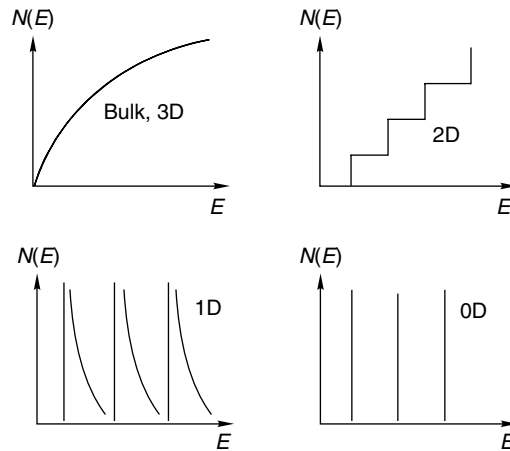


Fig. 10.5 Schematic representation of the functional form of the density of states.

The density of states of a quantum dot is a set of delta function given by

$$N(E) = 2 \sum_{n_x, n_y, n_z} \delta(E - E_{n_x, n_y, n_z}^{e,h}).$$

Thus, the energy bands in a bulk material exhibit some amount of discreteness resulting in the appearance of energy levels in the case of a quantum dot. Further, the oscillator strength, distributed over the continuum states in the energy bands for bulk material becomes concentrated on these discrete exciton levels.

10.4 EXCITON CONFINEMENT IN QUANTUM DOTS

One way of understanding quantum confinement is by examining the behaviour of the exciton in the semiconductor nanocrystal. The exciton is a bound pair of an electron and a hole, existing in the lattice, correlated quantum mechanically with each other. The electron and the hole forming a given exciton could be physically close to each other in the crystal (as in the case of Frenkel excitons) or separated by a few lattice spacings (as in the case of Mott-Wannier excitons). The Mott-Wannier exciton in semiconductors is a well-known and well-studied entity⁹ in the case of bulk semiconductors. It is a weakly bound electron-hole pair created during the interaction of the semiconductor with photons. This is a quantum mechanical system similar to hydrogen atom in the sense it consists of a positive and a negative charge held together by the coulomb interaction.

The exciton being a quantum mechanical system consisting of an electron and a hole, its energy levels can be expected to be similar to a scaled version of the energy levels of the hydrogen atom embedded in a dielectric medium with corresponding Bohr-like orbits. The scaling factor is provided by the lattice constant as the exciton resides in the semiconductor lattice. Such calculations have been

made and the exciton Bohr radius a_B of the bulk exciton has been estimated for many semiconductors and is given by

$$a_B = \frac{\hbar^2 \varepsilon}{e^2} \left[\frac{1}{m_e} + \frac{1}{m_h} \right]$$

where ε is the bulk optical dielectric constant, e is the electronic charge, and m_e and m_h represent effective mass of the electron and hole, respectively. The exciton is said to be in the regime of strong quantum confinement when the size of the nanocrystal is below the exciton Bohr diameter of the semiconductor. This size happens to be 6 nm in the case of CdS and 9 nm in the case of PbS, for example.

The effects of spatial confinement are well pronounced in the regime of strong quantum confinement. The principle of uncertainty demands that the average speed of the electron in the nanocluster is considerably larger than that in the bulk. Thus the electron can be considered to complete several revolutions in its orbit in the exciton in a short time before thermal motion causes its destruction by electron-hole recombination. Hence the exciton is long-lived in nanocrystals compared to the bulk and hence exciton features can be detected in optical absorption spectra of semiconductor nanocrystals at room temperature, unlike the case of the bulk. Similarly, exciton luminescence also can be detected at room temperatures.

10.5 QUANTUM MECHANICS OF CONFINED NANOCCLUSERS

Spatial confinement of a semiconducting nanocluster embedded in some dielectric media renders it much like a particle in a three-dimensional box in terms of quantum mechanical behaviour. Ekimov and Onushchenko¹⁰ and Efros and Efros¹¹ were the first to discuss the quantum mechanics of zero-dimensional structures. To the first approximation, we may consider the individual particle to be spherical (with a radius R) and neglect the coulomb interaction between the electron and the hole. The exciton Hamiltonian H involves the kinetic energies of the electron and the hole, the coulomb interaction energy V_C between the electron and the hole and the potentials $V_i(r_i)$ experienced by the electron and the hole due to the barrier. This can be written as

$$H = -\frac{\hbar^2}{8\pi^2 m_e^*} \nabla_e^2 - \frac{\hbar^2}{8\pi^2 m_h^*} \nabla_h^2 + V_C + V_e(r_e) + V_h(r_h),$$

where m_e^* and m_h^* are the effective masses of the electron and the hole in the lattice respectively. Also, we may take $V_i(r_i) = 0$ for $r_i < R$ and ∞ for $r_i > R$; $i = e$ or h , for electron or hole, respectively. In a simplified picture, the coulomb interaction is neglected and $V_C = 0$. The exciton wave function $\psi(\vec{r}_e, \vec{r}_h)$ is written as a product of the wave functions of the electron and the hole, $\phi_e(\vec{r}_e)$ and $\phi_h(\vec{r}_h)$ respectively, as $\psi(\vec{r}_e, \vec{r}_h) = \phi_e(\vec{r}_e) \phi_h(\vec{r}_h)$. The solution of the Schrödinger equation provides the eigen functions

$$\phi_{nlm}^i = \sqrt{\frac{2}{R^3}} \frac{J_l\left(\xi_{nl} \frac{r}{R}\right)}{J_{l+1}(\xi_{nl})} Y_{lm},$$

where the quantum numbers are restricted to $-l \leq m \leq l$; $l = 0, 1, 2, \dots$; $n = 1, 2, 3, \dots$. Here J_l are the Bessel functions of the first kind and of order l and Y_{lm} are spherical harmonics. Also, ξ_{nl} are the zeroes of the spherical Bessel function of order unity.

The spherical Bessel functions $j_l(x)$ are given by

$$j_l(x) = \sqrt{\frac{\pi}{2x}} J_{l+(1/2)}(x).$$

In the case of the infinite potential approximation, the probability of finding the electron outside the nanoclusters is zero, ϕ_i must vanish at $r = R$, the surface of the nanoclusters. This provides the boundary condition for the solution of the wave equation.

The energy eigen values are obtained as $E_{n,l}^{e,h} = \frac{\hbar^2}{8\pi^2 m_{e,h}^*} \left(\frac{\xi_{n,l}^2}{R^2}\right)$. This simple model, though it brings out the experimental observation of a $1/R^2$ dependence (known as *blue shift*), the assumptions made, particularly, the neglecting of coulomb interaction, limits the applicability of the model to certain extent.

Brus³ calculated the energy levels of the first excited state based on the models developed by Efros and Efros¹¹ and concluded that coulombic interaction could not be ignored. This treatment provided a qualitative explanation of the observed blue shift in of the optical absorption spectra.

$$E^* = E_g + \frac{\hbar^2 \pi^2}{2R^2} \left[\frac{1}{m_e} + \frac{1}{m_h} \right] - \frac{1.786e^2}{\epsilon R},$$

where E^* is the nanocrystal band gap energy (eV), E_g is the bulk band gap energy (eV), R is the radius of the quantum dot and m_e and m_h are the effective mass of the electron and hole, respectively.

The second term of the above equation represents the kinetic energy of the electron and hole and the third term represents the Coulomb interaction. The only difficulty with this model was that it overestimated the kinetic energy of the electron and hole and hence the quantitative agreement with the experimental data was not very satisfactory. One of the modifications was by Weller *et al.* (1986), who introduced a finite well depth to confine the exciton.¹² For semiconductors with rather low dielectric constants, the spatial correlation between the charge carriers can be significant and hence, Kayanuma¹³ extended the EMA model to include electron-hole interaction by introducing a size independent fourth term known as effective Rydberg energy, E_{Ry} .

$$E^* = E_g + \frac{\hbar^2 \pi^2}{2R^2} \left[\frac{1}{m_e} + \frac{1}{m_h} \right] - \frac{1.786e^2}{\epsilon R} - 0.248E_{Ry}^*$$

and E_{Ry} is given by

$$E_{Ry} = \frac{e^4}{2\epsilon^2\hbar^2} \left[\frac{1}{m_e^*} + \frac{1}{m_j^*} \right]^{-1}.$$

Thus the band gap of the semiconductor quantum dot is size-dependent due to the quantum localisation term with a $1/R^2$ dependence and the electron-hole coulomb attraction with a $1/R$ dependence. The band gap increases in energy as the particle size decreases. Another major approach to understand quantum confinement includes a semiempirical tight binding approximation by Lippens and Lannoo.¹⁴ A pseudopotential model proposed by Ramakrishna and Friesner¹⁵ described the effect of the size, shape, crystal structure and lattice constant on the exciton energies. For very small quantum dots, the EMA model fails and electronic structure should be calculated by taking into account of the finite number of atoms. The model by Kayanuma¹³ agrees reasonably well with the experimental observations in the case of most of the nanocrystal systems. Pesika *et al.* determined the effect of nanoparticle size distribution and its influence on the absorption onset by comparing with transmission electron microscope studies¹⁶ and concluded that optical absorption spectra can provide information about not only the size but size distribution as well.

Three different regimes of quantum confinement were proposed based on the ratio of the nanocrystallite radius R to the bulk exciton Bohr radius a_B . The Coulomb electron-hole interaction is negligibly small in comparison with confinement energies in the strong confinement regime ($R/a_B \ll 1$), and hence, an electron and hole can be treated as independent particles. On the other hand, the electron and hole motions are strongly correlated via the coulomb interaction in the regime of weak confinement ($R/a_B \gg 1$). When $R/a_B \sim 1$, the physical processes are determined by an interplay between quantum confinement and the electron-hole interaction.¹⁷

10.6 BAND GAP ENGINEERING AND OPTICAL RESPONSE

The remarkable alterations in the optical properties of quantum dots render them interesting candidates for applications in Photonics. The optical properties can be probed by the techniques of optical absorption and fluorescence. The optical absorption spectrum of an ideal crystalline semiconductor (shown in Fig. 10.2) exhibits a sharp cut-off at a certain wavelength corresponding to the band gap energy, particularly, in the case of direct band gap semiconductors, such as CdS. In the case of indirect band gap semiconductors, such as silicon, phonon contributions tend to make the cut-offs less sharp.

The material is essentially opaque for light with wavelength shorter than this cut-off wavelength and transparent to light with longer wavelength. This is because the value of this cut-off is a measure of the band gap energy. Optical absorption and emission properties of semiconductors are affected by the presence of excitons. Features characteristic of absorption due to excitons show up close to the optical cut-off in the optical absorption spectrum. The absorption due to the exciton can be described in terms of closely-lying energy levels close to the bottom of the conduction band and the top of the

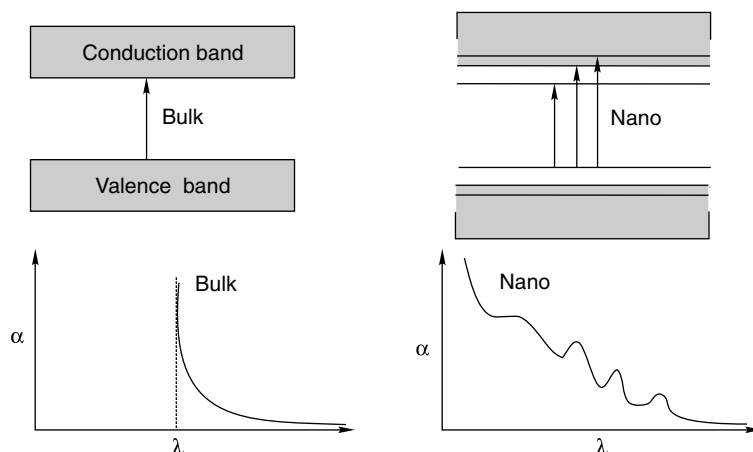


Fig. 10.6 Schematic diagram showing the band structures and the optical absorption spectra of the bulk and the nanocrystal.

valence-band. Exciton confinement, thus, causes the concept of the band itself to be modified in the case of semiconductor quantum dots. It is as if the bottom of the conduction band splits into discrete levels. Correspondingly, the sharp cut-off in the optical absorption spectrum of the bulk semiconductor gets modified with *shoulders* appearing close to it. Thus, we can talk only about an effective band gap in this case.

The recombination of the electron and hole of the exciton leads to its decay and the emission of the resulting energy as light. This shows up as a sharp peak, close to the band edge in the fluorescence spectrum. However, such features are normally observed only at lower room temperature. This is because the electron and hole cannot complete even one orbit before the thermal excitations of the lattice causes their recombination. The main feature of the fluorescence spectrum of semiconductor quantum dots is the sharp exciton peak, close to the absorption edge. Other peaks due to defect states also are observed. This is due to the relatively large ratio of the surface area to the volume of the dot. The exciton peak is found to show a size-dependence much similar to that of the absorption edge. This leads to interesting possibilities, such as designing a solid state white-light emitter by a suitable combination of quantum dots of appropriate materials with different diameters.

10.7 COMPUTATIONAL METHODS TO UNDERSTAND NANOSCALE PHENOMENA

When we talk about materials, in general, what we have in mind are the bulk systems having billions of atoms or molecules. With the advent of controlled chemical synthesis techniques, we come across materials, whose building blocks are not just atoms or molecules, but rather a large number of atoms, groups or molecules held together by strong covalent bonds. The dispersion of colloidal particles is a good example of such synthetic systems. The colloidal particles are typically micron-sized. Nowadays,

systems have been devised, such that the building blocks are only a few atoms, having sizes in the range of just a few nanometers. The down-gradation of the size is as follows: granular systems (\sim few millimeters) \rightarrow colloidal dispersions (\sim few micrometer) \rightarrow nanosystems (\sim few nanometers).

The size of the building blocks matters a lot in deciding how the material would respond to physical and chemical perturbations. Let us consider a colloidal dispersion, whose properties have been well studied in the past¹⁸. Due to large sizes, they can scatter ordinary light and can be viewed using laser light. In fact, zig-zag motion of colloidal particles is named “Brownian motion” after the British botanist Robert Brown, who could see such motion in a suspension of pollens under a light microscope. The properties of a colloidal dispersion follow similar to those of the normal atomic systems, but at substantially different scales. However, this leads to quite important feature that makes them important, both pedagogically and technologically. Due to large size, the number of colloidal particles in a given volume is much lower than atomic systems. The typical thermal energy is about one $k_B T$ [k_B being the Boltzmann constant and T the absolute temperature] per particle. Hence, the energy scale in a colloidal system is much lower than the atomic systems. The lowering is by a factor of $(d/a)^3 \sim 10^9$, d being the colloidal size and a , the typical atomic length scale. Thus the colloids can be easily perturbed by external agents that have been utilised a great deal in technological applications, as well as in the laboratories to mimic the properties of atomic systems.

What should happen if the size of the constituent basic units has been reduced to that in the nanometer range? Clearly, such nanometer sized units can have a few atoms covalently bound to each other. Let us now hit upon the key issue. The atoms/molecules on the surface are different from those in the bulk. The bulk atoms/molecules satisfy the bonds they can form due to the availability of adequate number of atoms/molecules in the neighbourhood. However, those on the surface cannot do so due to the geometrical discontinuity. Hence, the effects of the surface atoms are typically different compared to those in the bulk in determining the properties of a system. The relative importance of the effects of the surface atoms/molecules is governed by a simple geometrical ratio. Consider a spherical body

of radius R . Its volume, V , is given by $\frac{4}{3}\pi R^3$, while the surface area, S , is $4\pi R^2$, so that the ratio $S/V \sim 1/R$. This means that the smaller the R , the more important is the contribution due to the surface atoms. Even in comparison to the colloids, the nanoparticles have about thousand times enhancement in the surface contribution.

The effect of large surface contribution in case of nanoparticles can be seen in a wide variety of cases. A beautiful illustration comes from biological world. A central dogma in molecular biology is the recognition¹⁹ between large biomolecules. For instance, a large class of functional proteins can recognise particular sequences of the long De-oxyribo Nucleic Acid (DNA) molecule, the storehouse of genetic information. The size of the target region of the DNA molecule is around 3 nm, the protein being of similar size. The recognition is governed by the ability of the functional groups on the protein surface to form hydrogen bonds with the bases of the target DNA sequence. Here, the surface morphology of the protein molecule is vitally important to mediate the adequate number of hydrogen bonds to form a stable complex. Let us consider another very different phenomenon, where the

surface properties of the nanoparticles play important role. A conducting surface, having an assembly of gold or silver nanoparticles, can accumulate charges when a dipolar fluid flows over the assembly.²⁰ This is manifested in developing potential difference between conducting surfaces, which can act as a flow sensor. This phenomenon can be explained by realising that there are weakly-bound electrons on the metal nanoparticle particle surface leading to its surface plasmon excitation. The charges get knocked out due to coulomb collision by the flowing dipoles. The knocked-out charges eventually reach the electrode surface. Let us quote another still very different instance, where the large surface area compared to the volume of nanoparticles can be utilised to advantage. This is in catalysis,²¹ where the nanoparticles due to their large surface area offered to the reagents, can lead to enhanced catalytic effects. It is important to recall that almost all industrial chemical processes, which contribute the lions share to world economy are driven by catalysis, in which only the surface atoms play the most crucial role. The processes include petroleum refining leading to hydrodesulphurisation and ammonia synthesis.

In this section, we shall try to understand why fundamentally the studies on the nanosystems are different from the conventional bulk systems. With the advent of computers and very precise knowledge of the effective interactions in different systems, computer simulations have been playing a key role in understanding the nanosystems. We shall illustrate how the key features of the studies on the nanosystems to highlight the differences with the conventional systems in the bulk, taking the thermodynamics of the stability in a small cluster as an example. We shall describe computer simulation methods with some applications to nanosystems. Finally, we conclude with some perspectives of research.

10.7.1 Key Features: Why are the Nanosystems Different?

Instead of adding on examples, let us try to understand some features of nanosystems arising due to enhanced surface effects, that would not occur in a normal bulk system. This is just an attempt to provide some glimpse of how the nanosystems are different from the bulk ones without being exhaustive. Let us consider the thermodynamic properties to this end. For our purpose, we shall treat a nanoparticle as a cluster of small number of the constituent atoms/molecules. We shall refer the constituent atoms/molecules simply as particles quite often. These clusters are big enough, so that the quantum effects are unimportant, even though one should keep in mind that the bonds between the atoms in the cluster are governed by quantum mechanics.

One basic question of interest N.P: Are the nanoparticles stable? The stability of a condensed matter system is a thermodynamic concept. The question of stability is also intimately connected to the idea of a homogeneous phase of a condensed matter system. A classic example is liquid water at normal pressure and temperature. The system of H_2O is in a stable liquid phase. However, the liquid phase becomes unstable on heating at a given pressure, when liquid water changes into vapour, and similarly, the liquid changes into ice upon cooling. The thermodynamic quantity that governs a phase and its stability is the free energy. The introduction of the free energy can be motivated as follows. The minimum of the potential energy U governs the mechanical stability of a system. Note that mechanics does not have

any concept of temperature. However, at finite temperature, the effect of temperature T must be taken into account to consider the stability of the system. This is done via introducing free energy defined via $F=U-TS$, S being the entropy. The stability of a phase demands that F must have a minimum, i.e., F is a convex function in its variables. A phase becomes unstable so that it transforms to another phase if the convexity of the free energy cannot be maintained for some parameters of the system, on which F depends. Let us consider Fig. 10.7, where these ideas are represented schematically. Figure 10.7(a) shows a typical free energy for a stable phase. The minimum of F , F_{min} describes a situation, where the phase is stable. However, in a situation of Fig. 10.7(b) the convexity of F , is violated at the hump of F where the system cannot be stable. The system will eventually roll down to the global minimum.

Figure 10.7(a) shows another interesting feature. The minimum of the free energy has a finite width. This means that the system has a finite probability to have a free energy $F \neq F_{min}$, the probability being, $\exp^{[-(F-F_{min})/k_B T]}$. We know that the energy of a system increases with system size, so that it is meaningful to talk about the energy per unit volume or equivalently the energy per particle. In a similar way, the free energy depends on the system size. We formally assert that the free energy of a system is extensive. If we define the free energy per particle as f , then an interesting consequence follows: The probability, that the system will deviate from the minimum of the free energy, decreases with N , the number of particles in the system. This means that the system will fluctuate too much to higher free energy states, if the number of particles in the system is small. Thus, the phase of a cluster of a few particles is highly susceptible to fluctuations.

So far, we have not given any physical picture of the fluctuations. This can be understood easily in case of a crystal. We know that a crystal phase is characterised by the location of the atomic units at precise lattice points²². If one looks at scattering of the x-rays by a crystal, one observes strong Bragg's peaks that reflect the crystalline symmetry. However, at a normal temperature, the crystal atoms are not really fixed, but vibrate about the lattice positions. These vibrations are known as phonon modes of the crystal. The immediate consequence of the existence of the phonon modes is that the atoms in the crystal phase deviate from the ideal crystal structure. This is reflected in the broadening of the Bragg's peaks. The crystal atoms vibrate more vigorously with increasing temperature. If the vibrations are too

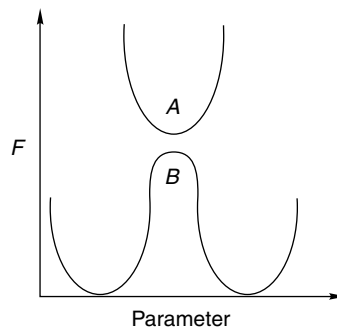


Fig. 10.7 The free energy profile F in some arbitrary parameter space: (A) a single stable phase; and (B) two stable phases separated by a barrier.

large, the system melts into a liquid state, where the crystalline structure completely disappears. The phonons are the fluctuating modes in a crystal. One can think of the whole process thermodynamically as follows. The liquid phase is entropically favourable, while the crystal phase is energetically favourable. The two phases are separated by a free energy barrier, which corresponds to the free energy cost of creating a liquid droplet in the crystal or a crystal droplet in a liquid parent phase. The free energy of such a droplet creation comes primarily from the surface tension between the two phases. If one starts from the low-temperature crystal phase, the phonon modes help to nucleate the liquid droplet in a crystal parent phase via large vibrations. The fluctuation modes are the one that helps to go from one stable phase to another by overcoming the free energy barrier. It is meaningful to talk about the stable phases of the system, only if the fluctuations are small. The difficulties associated with strong fluctuations in the finite clusters can be appreciated from Fig. 10.7(b). Unless the barrier in free energy, shown in Fig. 10.7(b), separating two stable states is not too high, the system can easily go back and forth between two phases due to strong fluctuations. This essentially means that the definition of a stable phase itself may be a difficult job. The wavelength of the fluctuating modes also depends on the system size. If the system has a volume V , the disturbances due to the fluctuations will have typical wavelength given by $2\pi/L$, where $L \sim V^{1/3}$. For a bulk infinite system, $L \rightarrow \infty$ limit the wavelength tends to zero, namely, the disturbance is relatively gentle. The long wavelength acoustic phonon mode in a crystalline solid is one such example. However, if L is finite, the wavelength is finite, implying an enhanced inhomogeneity in the system.

Due to large fluctuations in a finite cluster, the thermodynamic description of the phases in the system requires specification of the entire free-energy landscape. The difficulty really creeps in here. Let us now recall basic statistical mechanics. The statistical mechanical expression of the free energy is given by $-k_B T \ln Z$, where Z is the canonical partition function, $Z = \text{Tr} \exp(-\beta H)$, H being the Hamiltonian of the system and the trace is over the states of the system of a given N number of particles in a volume V at temperature T and $\beta = k_B T$. More explicitly, the canonical partition function is given by $Z(\beta) = N \exp(-\beta H) = \langle \psi | \exp(-\beta H) | \psi \rangle / \langle \psi | \psi \rangle$, where N stands for the trace over the N -particle states $\langle \psi |$ of the system Hamiltonian H . The explicit evaluation of Z means an exact quantum mechanical solution of the cluster Hamiltonian H , that includes interaction between the constituent particles and finally tracing over all the states. This is, by any standard, a formidable task. In a bulk system, one ignores the fluctuations at the zero level approximation, that yields the upper bound of the system free energy which is also known as the mean field free energy.²³ The effects of the fluctuations can then be included systematically with increasing order of accuracy. However, no such simplistic approach can give fruitful idea about the phases of a finite cluster due to strong fluctuations.

There is one more interesting feature of the nanosystems, which is noteworthy. Since the phenomena, that are addressed in such systems, are at nanometer-length scales, the chemical properties of the constituent atoms are vital in understanding the properties of the nanosystems. The coarse-grained²³ descriptions, where averaging has been done over certain length and time windows, usually adopted for bulk systems, fails in such systems. A classic example is the “odd-even” effect, namely, the stability of clusters for many elements depends on the number of atoms in the cluster.²⁴

In such cases, no coarse-grained description is possible. Strictly speaking, one should solve the entire quantum mechanical problem prior to the exact evaluation of the partition function to understand the thermodynamics of the cluster, both of which are formidable tasks.

Computer simulations are the techniques, which provides powerful tool of extracting the “exact” results, taking care of the atomistic details via quantum mechanical calculations. In computer simulations, the particle trajectories are obtained by the numerical solutions of the Newtonian equations of motion of the interacting particles in the system. The thermodynamic properties are calculated as time averages over the particle trajectories, invoking the ergodicity of the system, namely, the time averages and the ensemble averages are the same. The interaction forces are calculated via the quantum mechanical calculations. Here, we shall assume that the interaction potentials are known from the quantum mechanical calculations. Given such interaction potentials, the computer simulations can be performed via stochastic algorithms, where the ensemble averages are being directly calculated.

10.7.2 Computer Simulations

Computer simulations of an N -particle interacting system start with a model of the pair-interaction between the particles in a given volume. The particle positions are updated either by Molecular Dynamics (MD) or by Monte Carlo (MC)²⁵. In MD simulations, the Newton’s equation of motion for each particle, derived from the pair-interaction potential, is solved numerically over a small time step. Thus, one generates the classical trajectory of each of the particles in the interacting system. The thermodynamic properties of the system, defined in terms of the phase space variables, are calculated from the trajectories. In MC simulations, on the other hand, the ensemble averages are directly computed. Such simulations are particularly useful, if equilibrium structural quantities of an interacting system are sought for.

10.7.2.1 MD Simulations

Let us consider a simple MD algorithm. Let the pair interaction between i th and j th particle be $V(\vec{r}_{ij})$ where $\vec{r}_{ij} = \vec{r}_i - \vec{r}_j$. The force acting on the i th particle due to interaction with all other particles in the system is given by $\vec{F}_i = -\sum_j' \nabla_i V(\vec{r}_{ij})$. Here the summation excludes $i = j$ and the ∇ operator is on the i th particle coordinates. Let the velocity and the co-ordinate of the i th particle be $\vec{v}_i(t)$ and $\vec{r}_i(t)$ at time t . The co-ordinate at a later time $t + dt$ is given by a Taylor expansion of $\vec{r}_i(t + dt)$ about $\vec{r}_i(t)$:

$$\vec{r}_i(t + \delta t) = \vec{r}_i(t) + \delta t \vec{v}_i(t) + \frac{1}{2} \delta t^2 \vec{r}_i'' + \frac{1}{3!} \delta t^3 \vec{r}_i''' + \dots \quad (1)$$

m being the mass of the particle and the primes denote the differentiations with respect to time. Note that $\vec{F}_i = m\vec{r}_i''$ as per Newton’s Law. The velocity can be approximated by $\vec{v}(t + \delta t) = [\vec{r}(t + \delta t) - \vec{r}(t)] / \delta t$.

However, there is a very important issue to keep in mind in this context. The energy and the momentum of the system must be conserved. The kinetic energy and the momentum depend on the velocity, while the potential energy depends on the particle coordinates. The conservations will hold good automatically if the trajectories are exact. However, the trajectories calculated from Equation 1 are approximate ones. In such a case, the conservation laws hold good only approximately. Better are the approximations to the exact trajectories, the better ensured are the conservation laws. Hence, one puts considerable efforts in improving the algorithms.

Let us discuss one such simple algorithm having a better accuracy. This is known as the central difference algorithm. Note that

$$\vec{r}_i(t \pm \delta t) = \vec{r}_i \pm \delta t \vec{r}'(t) + \frac{\delta t^2}{2} \vec{r}_i''(t) \pm \frac{\delta t^3}{3!} \vec{r}_i'''(t). \quad (2)$$

One can straight away get from Equation 2:

$$\vec{r}_i(t + \delta t) = -\vec{r}_i(t - \delta t) + 2\vec{r}_i(t) + \delta t^2 \vec{F}_i(t)/m. \quad (3)$$

A few things are to be noted in Equation 3. The accuracy in the calculation of $\vec{r}_i(t + \delta t)$ has gone upto $O[\delta t^4]$. The price to be paid for this is to know $\vec{r}_i(t - \delta t)$, that can be calculated from the initial positions, velocities and the forces in the initial configuration. The second-time derivative of $\vec{r}_i(t)$ has been replaced by using the Newton's Law. The force needs to be calculated with the coordinates at time t . In this algorithm, however, the velocity given by $\vec{v}_i(t) = [\vec{r}_i(t + \delta t) - \vec{r}_i(t - \delta t)]/2\delta t$, has accuracy to $O[\delta t^2]$. Many variants of MD algorithms are available, where the accuracy of the integration scheme has been the major thrust.

10.7.2.2 MC Simulations

Typically, in MC simulations, a randomly selected particle i of the system is given a random movement:

$$\vec{r}_i' = \vec{r}_i + \vec{R}_i, \quad (4)$$

where \vec{R}_i is vector having components random numbers generated over an interval $(-\chi, \chi)$. Once the movement is done, we calculate the energy cost δE of the movement, where E_f and E_m are defined as follows:

$$E_m = \sum_{j \neq i} V(\vec{r}_{ij}) \quad (5a)$$

$$E_f = \sum_{j \neq i} V(\vec{r}_{ij}' - \vec{r}_j). \quad (5b)$$

Here \vec{r}_i and \vec{r}_i' are given in Equation 4. The movement is accepted via the Metropolis algorithm: Let the energy cost, δE as defined in Equation. 5 of the movement be negative. That is, if the energy is lowered by the movement, the new particle position is accepted. If the energy increases, the new position is accepted by the Boltzmann probability, $\exp(-\delta E/k_B T)$. The equilibrium properties,

depending on the position coordinates of the particles, can be calculated as average over different configurations generated by the MC moves.

10.7.2.3 Important Points

There are a few important points one should keep in mind in developing the basic algorithm given in the above section.

(a) Boundary conditions

One normally performs bulk simulations in a central box, assumed to be repeated in all the directions, known as the periodic boundary conditions (PBC). The image boxes are the identical replica of the central box. The particles move identically in all the boxes. Clearly, if a particle moves out of the central box, it is the same as another particle from the image box adjacent to the opposite side of the central box moves into the central box. Thus, the particles at the central box do not experience the effect of the boundaries of the central box. However, in case of the nanosystems, it is the boundary that is important. Hence, the boundary walls are explicitly retained. The specification of the wall-particle interactions thus becomes an additional requirement for such a system. Sometimes, the cluster is taken to lie inside a matrix far away from the boundaries, where the normal PBCs are employed. Often one simulates an aggregate of clusters, in which case the PBCs are generally used.

(b) Interaction potential

One should note that the system specification indeed goes in the simulation codes via the interaction potential. In the MD code, the forces come via the interaction potential. Similarly, the energy in the MC comes from the interaction potential. Usually, the interaction potentials are parameterised. For instance, the covalent bonding interactions are modeled via the Morse potential. Often such interactions are also treated in the harmonic approximation, where only the spring constant needs to be specified. The spring constant can be measured from experiments. For instance, infra-red experiments yield the spring constants for different homo- and hetero-nuclear bonds. The non-bonding interactions are specified by means of van der Waals interactions. The charge-charge interactions are coulombic and are generally long ranged. The long-ranged interactions require specific ways to handle in simulations²⁵. The parametrisation is usually done by the “ab-initio” calculations using quantum chemical methods²⁶. In this kind of simulations, the nuclear coordinates are held fixed due to their slow motions compared to those of the electrons. The ground-state electronic energy is calculated for the fixed nuclear coordinates. The potential energy profile is generated by repeating calculations for several inter-nuclear distances. The interaction parameters are estimated from these profiles. The nuclear coordinates are updated by the classical MC or MD algorithm using the electronic contribution of the force along with the classical inter-nuclear forces, like the coulomb forces. Thus, the coupled electronic and the nuclear coordinates are updated.

It must be recalled that the major computation time goes in computing the force in MD and energy twice in MC. The computation considers all possible pairs, and hence, the time scales up as N^2 . This is a major concern in particular for clusters having large number of constituent atoms ($N > 500$). In such cases, the computation is usually done assuming a cut-off of the interaction potential, if the

potential is short ranged. The cut-off must be less than half of the shortest box dimension. Quite often a neighbour list, named Verlet neighbour list, is maintained. The list enrolls all the atoms lying within a certain distance slightly larger than the cut-off distance about a given atom. The interaction with all the atoms within this list is calculated. The list is updated only at certain time interval depending on the movement of the particles. This saves the computation of the separation between different pairs for a large number of intermediate steps. The potential energy and the force can be tabulated at the beginning of the simulations. During the simulations one just looks up the table and uses the standard interpolations. This is particularly time saving if the interaction is long ranged as in the coulomb cases.

(c) Dimensionless quantities

Computer simulations are performed, in general, in terms of dimensionless variables. The reason can be appreciated as follows. The typical length in a system is around a few angstroms. If one computes the force, which is around $1/(\text{length})^6$, one encounters such a small number that a computer cannot handle. In fact, similar trouble arises with large numbers as well. So, one tries to scale the quantities in such a way that the numbers used for actual computation is around 1.0. If one scales all the distances by a typical length, for instance, the size of an atom, which is around a few angstroms, the reduced length will be around unity, which the machine can handle. The reduced quantities are all just numbers. The actual quantity can be calculated by multiplying the number by the corresponding unit. The choice of such reduction unit is, no way, unique and depends on the system. Let us give an example. The choice of reduced units for MC of Lennard-Jones system could be σ (= a few angstroms) as the length unit and $k_B T$ (= 40 meV at room temperature) as the energy unit. Then, every other quantity used in the simulation must be reduced as per these units. The pressure in actual unit (N/m^2) can be calculated by fixing its physical dimension, namely, multiplying the number from the simulation by $k_B T/\sigma$. Three independent units can be chosen corresponding to three fundamental quantities length, mass and time. However, one can choose other quantities as well, for instance, length, mass and energy. Then the time unit gets automatically fixed. The other quantities must be reduced to these units. For example, the time step in MD should be reduced to the time unit as per the time unit set by the above choice of the reduced quantities.

(d) Simulation step-sizes

The proper choice of the step-size is a key to perform successful simulation. The step-size means the choice of δt in MD and χ in MC. The choice of δt in MD is dictated by the realisation of the conservation laws in course of the dynamics. The δt must as well be smaller than the typical smallest time scale of the system, so that the entire system dynamics is reflected. Let us take an example. In a solution, one has large solute particles and small solvent particles. The MD simulation should take care of both kinds of particles. The solvent particles are inherently faster than the solute particles. The δt in this case must be smaller than the time scale of motion of the solvent particles. In case of MC, the choice of χ is somewhat arbitrary, for there is no time involved in the exploration of phase space by the stochastic rules. Usually, the ratio of the accepted move to the total attempted move is calculated in a given MC cycle. The ratio should be around 0.4 for a faster equilibration. This ratio can be tuned

by changing the χ . Typically, χ is fraction of the mean inter-particle separation in the system given by $\rho^{-1/3}$. However, in case of very dilute system as in a gas, the new particle position can be tried in completely random way in the box.

(e) Monitoring equilibration

One important aspect of performing simulations is to make sure that the system reaches equilibrium. The monitoring is done via the calculation of the potential energy of the system. The potential energy is given by

$$U = \sum_{i \neq j} V(\vec{r}_i - \vec{r}_j). \quad (7)$$

One calculates the potential energy for every few MC or MD steps and stores in an output file. The plot of the potential energy versus the step number should show saturation within fluctuations defined as $\text{var}(U)/\langle U \rangle^2$. Here $\langle U \rangle$ is the mean of the potential energy over the simulation steps, and $\text{var}(U)$ is the corresponding variance. The fluctuations should be of the order of $O(1/N^2)$ to ensure the equilibration. The pressure is calculated by using the mechanical virial of the interaction force,

$$w = \sum_{i \neq j} \vec{F}_i \cdot \vec{r}_i. \quad (8)$$

The fluctuation of pressure should also show a $1/N^2$ dependence.

10.7.2.4 Basic Programming for a Simulation Code

After going through the basic algorithms of an MD or an MC simulation as explained above, you can start writing your own simple simulation code. All that you need to know is some programming language, like, FORTRAN77 or 90, C, C++, PASCAL, or whatever you are comfortable with. You should keep in mind that the algorithm is independent of the programming language. The basic structures of the programs are as follows.

(a) MD Code:

1. Choose initial configuration by distributing N particles in a box. The box size is usually chosen, such that it corresponds to a certain density of the system. Typical simulations are performed with 100–100,000 particles. The initial configuration is usually chosen not too far from the target equilibrium structure. For instance, if the target equilibrium structure is liquid or a FCC lattice, then one usually chooses the particles at fcc lattice points with small random perturbations. Each particle is given an initial velocity chosen from Maxwellian distribution for the given temperature.
2. The force is computed using the interaction potential.
3. The position and the velocities for each particle are calculated using certain integration scheme, like the central difference algorithm.

4. The energy and the momentum of the system are monitored to check if the algorithm is stable, namely, the conservation holds good.
5. The average kinetic energy is monitored. Due to inaccuracy of the velocity updating algorithm, the temperature defined by the average kinetic energy may differ from the initially fixed temperature. In such cases, one usually rescales the velocity by the target temperature.
6. The average potential energy (Eq. 7) and its fluctuation are calculated. The fluctuation should go like $O(1/N^2)$ if the system reaches equilibrium. This is one way to check the equilibration of the system.
7. The fluctuation of pressure (Eq. 8) should also show a $1/N^2$ dependence.
8. After equilibration, the quantities of interest are calculated. Such quantities are both static and dynamic in nature as we explain later.

(b) MC code:

The basic steps are as follows:

1. Choose the initial configuration as in MD. You need not worry at all about the velocity, for an MC simulation does not need the velocity.
2. The *i*th particle chosen randomly.
3. Its interaction energy calculated.
4. Random movement given.
5. The energy with the new position recalculated.
6. The coordinates updated via the Metropolis algorithm: The move accepted if $\delta E < 0$. Otherwise, generate a random number z in the interval $(0, 1)$. Accept if $\exp^{-\delta E/k_B T} > z$, else reject.
7. Equilibration judged based on the potential energy (Eq. 7) and the pressure (Eq. 8) as in MD.
8. Only the equilibrium properties depending on the particle co-ordinates calculated.

10.7.2.5 Calculation of the Quantities of Interest

One major thrust of performing simulations is to calculate different quantities of interest. The equilibrium quantities can be calculated using both the MC and MD. The MD simulations in addition give the dynamic quantities as well. All such calculations must be performed after the equilibration is ensured. We discuss the two sets of quantities separately.

(a) Equilibrium properties

At the outset one must make sure of the ensemble that is generated in the given algorithm. Both the MC and MD algorithms we have given here generate the canonical ensemble traditionally denoted by (N, V, T) . One can generate other ensembles as well which we shall briefly touch upon later. Note that for a finite cluster system, the thermodynamic equivalence between different ensembles does not hold good. Hence, one should be extremely careful to use a given ensemble, in particular when comparison is made with the experimental systems.

One important quantity of profound thermodynamic interest is the histogram of the potential energy over the equilibrium configuration. The histogram reveals if the system has been in a given stable state. If the system remains in a given stable state the histogram will show a single peak with broadening proportional to $1/N^2$. Note that the broadening also gives the specific heat of the system. However, if the system does not exist in a unique equilibrium state, the histogram shows up peaks corresponding to the states.

One can generate important structural quantities from the configurations. For instance, the pair correlation function, $g(\vec{r} - \vec{r}')$ can be calculated quite easily. The pair correlation function generates the distribution of other particles around a given particle in the system. This is defined via

$$g(\vec{r} - \vec{r}') = \langle \delta(\vec{r} - \vec{r}_i) \delta(\vec{r}' - \vec{r}_j) \rangle / Z \quad (9)$$

where \vec{r}_i is the position of the i^{th} particle and Z the normalisation factor. The pair correlation function depends on $|\vec{r} - \vec{r}'|$ for a homogeneous and isotropic phase. Computationally, it is done as follows: Choose a certain binning interval, which is typically a fraction of the inter-particle separation. For a given configuration, take a pair of particles, calculate the separation, determine the bin that the pair contributes to and update the corresponding bin by 2. The procedure is to be repeated to every possible pair, and finally averaged over a large number of equilibrium configurations. The Fourier transform of $g(r)$ yield the static structure factor $S(q)$, which is measured from scattering experiments. Both $g(r)$ and $S(q)$ yield the structural information in a cluster reflecting its order, namely, a liquid order or a crystalline order. Such information is important, for instance, to interpret the high resolution microscopy data.

(b) Non-equilibrium properties

The situation, that we consider, can be depicted as follows. Let the system be in an initial equilibrium state. The system is then subjected to some time dependent perturbation, such that the initial equilibrium is disturbed. The system will tend to relax the perturbation so that a final equilibrium state is restored. The evolution of the system is assumed to be through near equilibrium states. The non-equilibrium properties are given in terms of the time correlation functions.²³ The time correlation function between two dynamical quantities $A(\vec{r}, t)$ and $B(\vec{r}, t)$ is given by:

$$C_{AB}(\vec{r}\vec{r}', t') = \langle A(\vec{r}, t) B(\vec{r}', t') \rangle. \quad (10)$$

The non-equilibrium change of $A(\vec{r}, t)$ due to a time-dependent external field $h_B(\vec{r}, t)$, in terms of the response function $\chi_{AB}(\vec{r} - \vec{r}', t - t')$, is given by:

$$\delta A(\vec{r}, t) = \int d\vec{r}' dt' \chi_{AB}(\vec{r} - \vec{r}', t - t') h_B(\vec{r}' t') \quad (11)$$

where $\delta A(\vec{r}, t) = A(\vec{r}, t) - A(\vec{r})$, $A(\vec{r})$ being the equilibrium value. The response function and the correlation function given in Equations 10 and 11 are related to each other via the fluctuation and dissipation theorem²³, namely,

$$\chi''_{AB}(\vec{q}, \omega) = \frac{1}{2k_B T} S_{AB}(\vec{q}, \omega) \quad (12)$$

for a given wave-vector \vec{q} and frequency ω . Here the double prime indicates the imaginary part of the response function. Here, $S_{AB}(\vec{q}, \omega)$ is obtained from $C_{AB}(\vec{q}, \omega)$ by subtracting out the static contribution. The real part of the response function can be extracted by using the celebrated Kramers-Kronig formula.

When A and B are the same, we call the corresponding correlation function as an autocorrelation function. Among a large number of possibilities, we shall discuss only two classes of autocorrelation functions, which provide useful dynamical information, that can be compared to the experiments. The first is the velocity autocorrelation function. The significance of the velocity autocorrelation function can be best appreciated by considering a tagged particle. The diffusion coefficient of the tagged particle is given in terms of the integral of the velocity autocorrelation function, $\int \langle \vec{v}(t) \cdot \vec{v}(0) \rangle dt$.

The diffusion is one important transport coefficient in a system. The other quantity of interest is the density autocorrelation function, also known as the Van Hove correlation function, defined as

$$\rho(\vec{r} - \vec{r}', t - t') = \left\langle \sum_{ij} \delta(\vec{r}, t) \delta(\vec{r}', t') \right\rangle. \quad \text{The Van Hove correlation function yields information on}$$

the non-equilibrium density response in a system. Its Fourier transform $S(\vec{q}, \omega)$, also known as the dynamical structure factor, can be measured from inelastic scattering experiments. The calculation of the Van Hove correlation function proceeds via generating the contribution of the particle number in a grid $\sum_i \delta(\vec{r} - \vec{r}_i(t))$ from successive configurations at a given time interval. Then, these data are correlated in the time domain. The averaging is done over all contributions those correspond to a given time difference. Given a suitable time origin, $t = 0$, the configuration pair at δt and $2\delta t$, and $3\delta t$ contribute to correlation at the time difference δt . However, those at δt and $3\delta t$ and $2\delta t$ and $4\delta t$ contribute to correlations for time difference of $2\delta t$. Clearly, the averaging gets poorer at larger time differences. Hence, one needs to perform very long simulations to extract the large time behaviour of the correlation functions.

You might wonder that we started saying that the computer simulations are theoretical aids to estimate the free-energy profile. Nevertheless, we do not touch upon the free energy at all in listing the properties of interest. This is due to the fact that the actual computation of the free energy or the partition function is a formidable task. This can be understood by noting that the computation of the partition function requires to evaluate the integral $\int d\Gamma \exp(-\beta H)$, where Γ is the phase space variable and H the Hamiltonian. In MC, for instance, one samples preferentially the region, where H is a minimum, not the entire phase space that makes the estimation of the integral rather poor. We enlist the properties, which are essentially certain derivatives of the free energy, which often suffices to understand the thermodynamics. However, if one is interested in the issues, like the phase

transformations or chemical reactions in the cluster, one needs to employ improved techniques, where indeed the free energy can be estimated. We shall refer to such computations in the further reading.

10.7.2.6 Stochastic Dynamics

Often one may be interested in the dynamics of an assembly of nano-particle clusters in a solvent. If one performs the traditional MD simulations, the time difference in the integration scheme should be smaller than the time scale of motion of the solvent. Let us now try to follow what determines the time scale of the motion. The dominant motion in a fluid is given by diffusion. The diffusion time scale is σ^2/D , where σ is the size of the particle and D the Stoke's diffusion coefficient, given by $k_B T/6\pi\eta\sigma$, η being the viscosity of the medium. Note that the time scale goes as σ^3 . The cluster of typically 10 nm in a solvent comprising of particles of a few angstroms, the difference in the time scales could be as much as a million. The time scale for the MD integration should be at least a millionth time less than the time scale of the cluster motion. Moreover, the solvent particles are numerous. Clearly, if the main interest is on the clusters alone, majority of the simulation time is spent only on the solvent. For, instance, if one is interested in the question if the clusters can self-assemble in a solvent, one faces a formidable computation task.

In such conditions, one implements the effective dynamics of the cluster, treating that as a single entity. The effects of the solvent particles are taken via friction force and a random noise acting on the cluster degrees of freedom. The resulting equation of motion is known as the Langevin equation of motion:

$$m\vec{v} = -\gamma\vec{v} + \vec{F} + \vec{F}^N. \quad (13)$$

Here Γ is the friction force. \vec{F} is the net force on the cluster due to all other clusters and any external force. \vec{F}^N , the noise force, usually is taken to be a Gaussian white noise. The numerical solution of the discretised stochastic differential equation (SDE) for different realisations of the noise is obtained. Here, the solvent particles are not considered explicitly. Hence, one can use much larger integration time, comparable to the time scale of the cluster diffusion. The quantities of interest are calculated over the trajectories as in MD and then averaging over the noise as done in MC. Thus the simulation scheme is intermediate between the deterministic scheme of the MD and completely probabilistic scheme of MC.

Further simplification can be done in the large time limit. Note that in the single particle limit, the average velocity is damped as $\exp(-\gamma t)$ with time constant $1/\gamma$. This time is much less than the cluster diffusion time for large γ . So, for time comparable to the cluster diffusion time, one can ignore the time evolution of velocity. One gets a first order SDE in coordinate space. The discretised version of the SDE yields:

$$\vec{r}(t + \delta t) = \vec{r}(t) + \frac{\vec{F}\delta t}{\gamma} + \vec{R}. \quad (14)$$

Here, \vec{R} is a Gaussian white noise. This equation can be solved numerically to yield the Brownian trajectory of a cluster. One can calculate the equilibrium properties and the transport coefficients,

which depend on the coordinates. For instance, the self-diffusion coefficient can be expressed as the time derivative in the long-time limit of the mean squared displacement from an initial position. The self-diffusion coefficient can be estimated from this scheme. Since the velocity drops out from the scheme, one cannot determine the quantities that depend on the velocity.

10.7.2.7 *Generating Different Ensembles*

As we noted, for a finite cluster simulations, the results will depend on the ensemble employed in performing the simulations. Sometimes, however, one ensemble will be preferable to the others due to the inherent nature of the problem. For example, the study of the phase transition is experimentally done in an N,P,T ensemble, P being the pressure. The MD in the N,P,T ensemble can be done by introducing additional fictitious degree of freedom that corresponds to a piston that holds the pressure constant.

This is where the MC technique has its own distinct advantage. Note that the MC movements do not correspond to any actual trajectory of the particles. This can be used to advantage in devising artificial moves in order to generate a different ensemble. For instance, the N,P,T ensemble can be generated by changing the volume of the box randomly. The Boltzmann factor here would have an additional energy term, like $P\delta V$ to account for the change in volume. The particle coordinates are rescaled in the new box, if the volume change is accepted. In a similar way, the other ensembles like the Grand Canonical, Micro-canonical ensembles can be generated.

10.7.3 *Application to Nanosystems*

In this section, we discuss a few published works in order to illustrate the methods described in this chapter. The discussion is no way exhaustive. We just quote a few examples from recent literature. The first two works are strictly illustrating the material covered in this chapter, while the following two are examples in new directions. The reader should look for more such published work in case the reader is decided to work on a related field.

The structural stability and energetics of small copper clusters (Cu_n , $n = 3, 4, \dots, 55$) have been found in Reference 27. The simulations have been done using the standard Metropolis algorithm at $T = 300\text{K}$. The pair interactions are taken in parametrised form. The simulations have been done starting from different initial conditions: starting from random distribution of particles, and adding particles onto already optimised structure with lower number of particles. They find that the structures are quite sensitive to n as shown in Fig. 10.8. Clusters with five-fold symmetry are stable for $n \leq 7$ and with icosahedral symmetry for $n \geq 13$. The stable cluster energy has been shown in Fig. 10.9.

In a recent work,²⁸ the question of solid-liquid phase coexistence has been addressed in finite size atomic clusters. The question of phase coexistence is important due to strong fluctuations induced by the finite-size effects as we have already explained. The author describes here studies based on MD simulations. The stable phase coexistence is found only for clusters having more than 931 atoms. The snapshot of the coexistence as time progresses from this study has been shown in Fig. 10.10 for typical

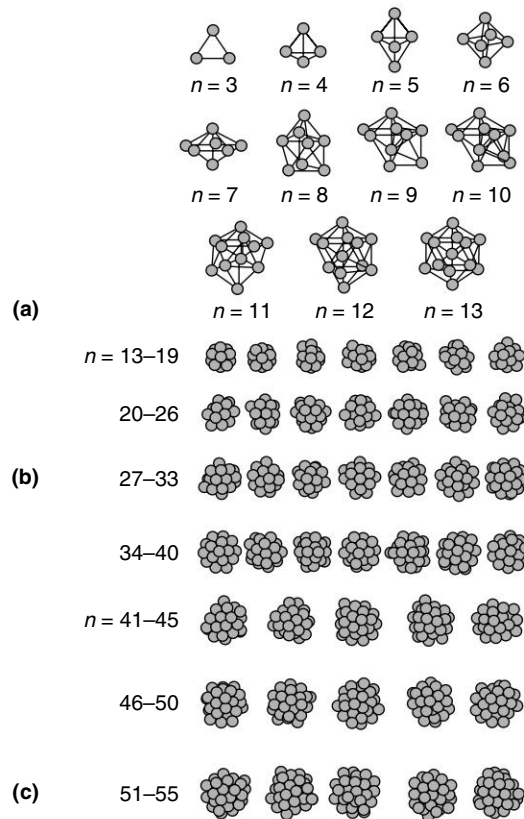


Fig. 10.8 Clusters of different symmetries for different sizes (n) (reprinted with permission from S. Erkoc and R. Shultaf (Ref. 27). Copyright (1999) by the American Physical Society).

values of the system parameters. The author also accounts for the observations from the simulations by a simple thermodynamic theory based on the stability of a critical droplet.

In the reduced description of an assembly of clusters, we often replace the effects of the solvent degrees of freedom by damping and noise terms to write down the SDE. In this case, it is natural to replace the effects of solvent on the interactions in the system. This is systematically done in the low-solute density by considering the partition function of the total system comprising of two clusters and the solvent. The degrees of freedom of the solvent are integrated out to find the effective interaction between two clusters. This effective interaction can be used to perform MC and MD simulations. Reference 29 carries out such systematic integration of the polymeric solvent in a polymer-nanoparticle systems.

We have discussed the use of long time form of SDE to describe a system of large number of clusters. This approach works nicely in low density of the clusters. However, at larger densities, an additional effect, named hydrodynamic interaction, creeps in.

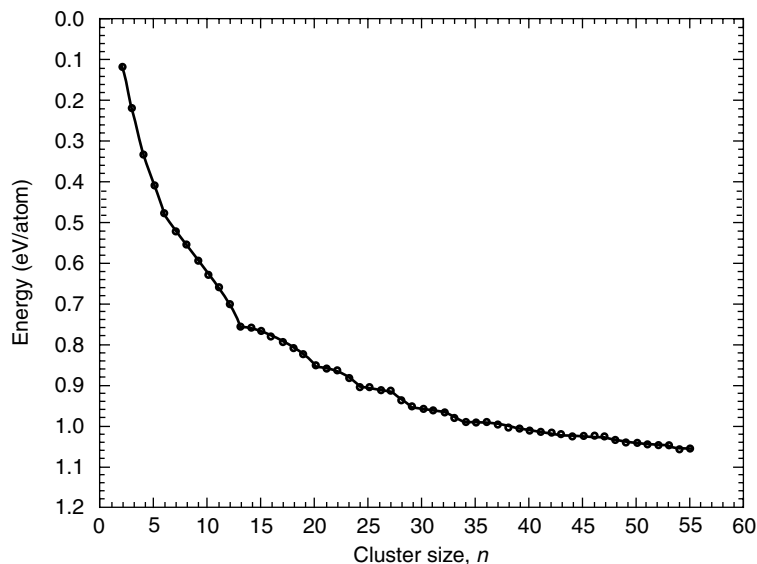


Fig. 10.9 Stable cluster energy for different value of n (reprinted with permission from S. Erkoc and R. Shultaf (Ref. 27). Copyright (1999) by the American Physical Society).

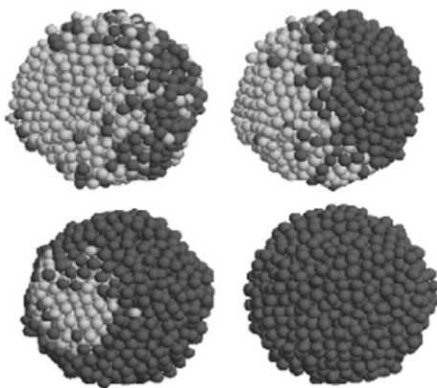


Fig. 10.10 Snapshot of liquid solid coexistence for clusters of finite size (reprinted with permission from S.C. Hendy (Ref. 28). Copyright (2005) by the American Physical Society).

This can be understood as follows. If a sphere moves in a stationary fluid, it disturbs the surrounding fluid. If a second sphere lies nearby, it experiences the disturbed fluid, while it moves. This will be important, particularly when the particles are very close to each other at high density. This effect is known as the hydrodynamic interaction, which is long ranged. Reference 30 extends the existing

simulation technique to account for the hydrodynamic effects. The fluid degrees of freedom are described by the discretised Navier-Stokes equations²³, while normal Newtonian equations of motion have been used for the clusters. Since the time scales of the motions of the fluid and the clusters are very different, the fluid degrees of freedom are updated much more frequently than the cluster degrees of freedom. The patterns of the velocity of the fluid in various cases obtained by these authors have been shown in Fig. 10.11 and 10.12. The time evolution of the aggregate of the clusters has been shown in Fig. 10.13.

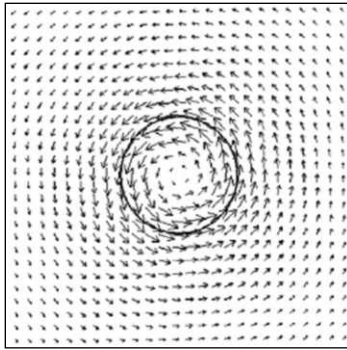


Fig. 10.11 Velocity pattern around an object, obtained from coarse grained simulation (reprinted with permission from M. Fujita and Y. Yamaguchi (Ref. 30). Copyright (2007) by the American Physical Society).

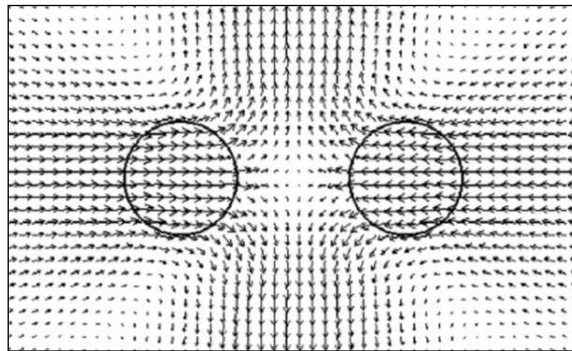


Fig. 10.12 Velocity pattern in the presence of a pair of obstacles (reprinted with permission from M. Fujita and Y. Yamaguchi (Ref. 30). Copyright (2007) by the American Physical Society).

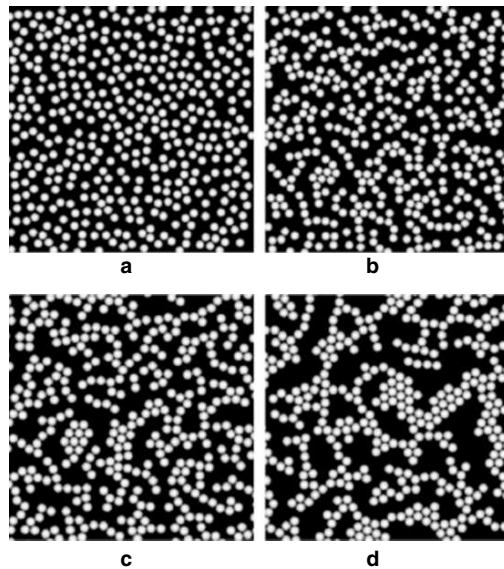


Fig. 10.13 Time evolution of the aggregates of the clusters (reprinted with permission from M. Fujita and Y. Yamaguchi (Ref. 30). Copyright (2007) by the American Physical Society).

10.8 CONCLUSIONS

In conclusion, we have emphasised throughout this chapter that the computer simulations are indispensable tool to understand different aspects of the physics of nanosystems. The algorithms described here are the basic ones, understanding which will help the reader to proceed further. We end this chapter with a perspective of future theoretical research on nanosystems, in particular the statistical mechanics. In the bulk systems, the effects of the surfaces cancel out due to small surface-to-volume ratio. The nanosystems have huge surface effects, and hence, are non-extensive in the thermodynamic sense. Recently proposed Tsallis statistics³¹ provides satisfactory thermodynamic description in a large class of non-extensive systems, despite the fact the basis of such statistics is yet not well understood. The proper thermodynamic description of clusters with large surface effects remains a major challenge today.

REFERENCES

1. Simon M. Sze and Kwok K. Ng, *Physics of Semiconductors (third edition)*, Wiley-Interscience; 2006.
2. L. Esaki and R. Tsu, *IBM J. Res. Div.*, 14, (1970), 61.
3. L.E. Brus, *J. Chem. Phys.*, 79, (1983), 5566–71.
4. A.P. Alivisatos, *J. Phys. Chem.*, 100, (1996), 13226.
5. G. Flytzanis, F. Hache, M.C. Klein, D. Richard and P.H. Roussignol, 'Nonlinear Optics in Composite Materials in Wolf', E (Ed.) *Progress in Optics, XXIX Elsevier Science*, (1991).

6. A.D. Yoffe, *Adv. Phys.*, 42, (1993), 173–266.
7. U. Woggon, U. *Optical Properties of Semiconductor Quantum Dots*, Springer, Berlin, (1997).
8. G.P. Banfi, V. Degiorgio and D. Richard, *Adv. Phys.*, 47, (1998), 447–50.
9. M.L. Cohen and J. Chelikowsky, *Electronic Structure and Optical Properties of Semiconductors*, Springer-Verlag, (1988).
10. A.I. Ekimov and A.A. Onushchenko, *Sov. Phys. Semicond.* 16, (1982), 775–78.
11. Al. L. Efros and A.L. Efros, *Phys. Semicond.* 16, (1982), 772–75.
12. H. Weller *et al.*, *Chem. Phys. Lett.*, 124, (1986), 557–60.
13. Y. Kayanuma, *Phys. Rev. B* 38, (1988), 9797–9805.
14. P.E. Lippens and M. Iannoo, *Phys. Rev. B* 38, (1989), 10935–42.
15. M.V. Rama Krishna and R.A. Friesner, *Phys. Rev. Lett.* 67, (1991), 629–32.
16. N.S. Pesika *et al.*, *Adv. Materials*, 15, (2003), 1289–91.
17. L. Banyai *et al.*, *Phys. Rev. B* 38, (1988), 8142–53.
18. A.K. Arora and B.V.R. Tata (eds), *Ordering and Phase Transition in Charged Colloids*, VCH, New York, (1996).
19. S. Neidle, *Nucleic Acid Structure and Recognition*, Oxford University Press, (2002).
20. C. Subramaniam, T. Pradeep and J. Chakrabarti, *Journal of Physical Chemistry, C*, 111, (2007), 19103.
21. B.F.G. Johnson, *Topics in Catalysis*, Springer, (2003).
22. C. Kittel, *Introduction to Solid State Physics*, (3rd Ed), Wiley Eastern Pvt. Ltd., New Delhi, (1971).
23. P.M. Chaikin and T.C. Lubensky, *Principles of Condensed Matter Physics*, Cambridge University Press, (1998).
24. V.Z. Kresin and Y.N. Ovchinnikov, *PRB*, 74, (2006), 024514.
25. M.P. Allen and D.J. Tildesley, *Computer Simulation of Liquids*, Oxford University Press, New York, (1987).
26. Donald A. Mcquarrie, *Quantum Chemistry*, University Science Books, USA, Indian Edition, (2005).
27. S. Erkoc and R. Shultaf, ‘Monte Carlo computer simulation of Copper cluster’, *Phys. Rev. A*, 60, (1999), 3053.
28. S.C. Hendy, ‘Stability of phase coexistence in atomic clusters’, *Phys. Rev. B*, 71, (2005), 115404.
29. M. Surve, V. Pryamitsyn and V. Ganesan, ‘Universality in structure and elasticity of polymer-nanoparticle gels’, *Physics Review Letters*, 96, (2006), 177805.
30. M. Fujita and Y. Yamaguchi, ‘Multiscale Simulation methods for self-organization of nanoparticles in dense medium’, *J. Comp. Phys.*, 223, (2007), 108.
31. E.G.D. Cohen, ‘Statistics and Dynamics’, *Physics A*, 305, (2002), 19.

ADDITIONAL READING

1. C. Kittel, *Introduction to Solid State Physics (seventh edition)*, Wiley Eastern Limited, 1995.
2. Peter Y. Yu and Manuel Cardona, *Fundamentals of Semiconductors: Physics and Materials*, Springer 2001.
3. Chihiro Hamaguchi, *Basic Semiconductor Physics*, Springer, 2006.
4. L. Banyai and S.W. Koch, *Quantum Dots*, World Scientific, 1993.

5. G. Schmid, *Nanoparticles : from theory to application*, Wiley-VCH, 2004.
6. Z.M. Wang, *Self-Assembled Quantum Dots*, Springer, 2007.
7. A. Rogach (Ed.), *Semiconductor Nanocrystal Quantum Dots: Synthesis, Assembly, Spectroscopy and Applications*, Springer, 2008
8. For learning computer program language, V. Rajaraman, Fortran 77.
9. For elaboration on computer simulation methods, Understanding Molecular Simulations, D. Frenkel and B. Smit (Academic Press).
10. For an advanced exposition to statistical mechanics, Statistical Mechanics, Plischke and Bergerson.

REVIEW QUESTIONS AND SUGGESTED PROJECT WORK

1. What are the most significant changes that occur in the band picture when the semiconductor is in the form of a nanocrystallite?
2. Estimate the number of molecules in a CdS quantum dot of 2 nm diameter.
3. Sketch plots of the first few wavefunctions of a particle in a spherical well. How will the spacing of the energy levels look like?
4. Find the ratio of the area to the volume of spherical particles of radii 1 nm, 1 μm , 1mm, 1cm, 10cm, 1m etc. and plot the variation of the ratio with diameter. What do you conclude?
5. What are the most significant changes that occur to the band picture when the semiconductor is in the form of a nanocrystallite?
6. How can we overcome the issue of toxicity while using quantum dots made of material such as CdS? Also suggest a few semiconductor materials that would be environment friendly.
7. Explain the physical origins of the various terms in the equation relating the band shift to the radius of the nanoparticles.

The only way to learn simulation technique is to learn by doing it. Even though a huge store of simulation programmes are available, the beginners must write codes on their own to master the techniques and develop a knack for them. With this in mind the following projects have been listed.

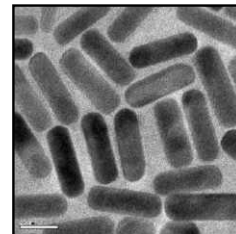
1. Numerical computation: Derive the equation of motion for a damped harmonic oscillator. Solve them numerically by discretisation for different choices of the damping parameters and compare them to the analytical solution.
2. Statistical mechanics of Ising chain: Consider a 2-d Ising Model (consult suggested reading 3). Write a monte-carlo code to calculate the magnetization in the system without any magnetic field at different temperatures and compare to the known exact results.
3. MD code: Consider a system interacting via Lennard-Jones potential. Develop an MD code (NVT ensemble) to compute the isotherms and compare with the known isotherms.
4. Effect of the boundary conditions: Develop an MC/MD code for particles in a box with both periodic and reflecting boundary conditions. Compare the thermodynamic quantities like energy, pressure and specific heat. Change the box size of system with the reflecting boundaries at a given density to check how the sensitivity of different thermodynamic properties appears with the system size.

PART FIVE

Advanced Nanomaterials

- **Quantum Clusters of Gold**
- **Nanoparticle Crystals**
- **Anisotropic Nanomaterials**
- **One-Dimensional Nanostructures:**
Nanorods and Nanowires
- **Assembly of Anisotropic Nanostructures**
- **Dendritic Nanostructures**
- **Nanohybrid Systems**

QUANTUM CLUSTERS OF GOLD



“Every experiment destroys some of the knowledge of the system which was obtained by previous experiments.”

W. Heisenberg, *Critique of the Physical Concepts of the Corpuscular Theory* in *The Physical Principles of the Quantum Theory* as translated by Carl Eckhart and Frank C. Hoyt, The University of Chicago Press, Chicago, (1930) page 20

Quantum clusters or sub-nanoclusters refer to a new group of nanomaterials with core dimension with 1 nm. They behave totally differently from the metallic nanoparticles and act as a missing link between nanoparticles and molecules. They exhibit characteristic optical features and show luminescence with high quantum yield from ultra violet to the near infrared region. Several methods have been developed to synthesise quantum clusters in large quantities. In this chapter, we present this group of materials with details on their synthesis, optical properties and applications, including biolabelling.

Learning Objectives

- What are quantum clusters?
 - How they can be synthesised?
 - What are the characterisation techniques used to study them?
 - How their optical properties differ from metallic nanoparticles?
 - How they react chemically?
 - What are their applications?
-
-

11.1 INTRODUCTION

Synthesis of novel materials with desired and tunable physical and chemical properties always interests researchers. Several methods have been followed for the synthesis of nanomaterials with a variety of shapes and sizes and they offer numerous possibilities to study size and shape-dependent variations of

electronic, optical and chemical properties. Size matters in nanoscience; in fact size is the most important property that matters here. Nanoparticles can be classified broadly into three categories; according to their sizes.¹ First class of nanoparticles can be called as large nanoparticles and they have core diameters comparable to the wavelength of visible light (about 500 nm). Second group of nanoparticles can be termed as small nanoparticles and they have core diameters equal to the electron mean free path (about 50 nm for gold and silver). Last group of nanoparticles are called sub-nanoparticles or quantum clusters and their size is equal to the Fermi wavelength of electrons (about 0.5 nm for gold and silver). Quantum clusters are totally different from the first two groups of nanoparticles. They can be treated as the “missing link” between nanoparticle and molecular behaviours.¹ They consist of only a few atoms with a core size in the sub-nanometer regime. Because of the very small size, the electronic structure of the particles is greatly different and hence they show different physico-chemical properties. Unlike metallic nanoparticles, which are represented by their core diameter, quantum clusters are generally represented in terms of their chemical composition, i.e., number of core atoms and protecting ligands. For example, Au₂₅SG₁₈, a well-known water-soluble quantum cluster of gold, consists of a core of 25 gold atoms protected with 18 glutathione ligands.² Having sub-nanometer size, these clusters cannot possess surface plasmon resonance as the density of states is insufficient to create metallicity. They show discrete energy levels and exhibit distinct, but different, optical absorption and emission features. In other words, quantum clusters show “molecule-like” optical transitions in absorption and emission and are termed also as molecular clusters. They show characteristic absorption features and can be distinguished from each other from their absorption profiles. Quantum clusters typically exhibit strong photoluminescence and their wavelength of emission can be tuned from the near infrared (NIR) to ultraviolet (UV).³

Structure of molecular and atomic aggregates, called clusters or Van der Waals molecules, has been a topic of research in the area of molecular cluster science. Many of these cluster systems have contributed to the understanding of the shell structure explained using the Mackay icosahedra (see the chapter on gas phase clusters in the book *Nano: The Essentials*) exhibiting magic numbers containing atoms, $N(k) = 1 + \sum_{k=1}^n (10k^2 + 2)$, where k is the number of atoms in the cluster and n are integers 1, 2... Evolution of electronic structure of such cluster systems has been understood using the jellium model. Very recent addition to this family of clusters is noble metal quantum clusters. This area itself is linked closely with Mackay icosahedra, the lower members being Au₁₃ and Au₅₅, synthesised in 1983 and 1981, respectively. These clusters can be called as noble metal molecules.

A range of names have been used to describe larger nanoparticles of noble metals. These include monolayer protected clusters (MPCs), 3-D self-assembled monolayers (SAMs), protected or capped nanoparticles, etc. Such nanosystems are often metallic, with a core diameter of 2 nm or larger. On the other hand, quantum clusters are semiconducting in nature and show well-defined absorption and emission features. They are molecule-like with well-defined cores consisting of a metal-metal bond. These properties are similar to molecules. However, a classification as gold molecules may not be suitable to describe them. This is because the systems being discussed also show properties of the protecting groups/ligands, while gold molecules imply that the properties are of gold alone. These clusters, now known to form with proteins and diversity of monolayer chemistry, can bring additional

properties. Therefore, the properties have both core and monolayer components along with distinct characteristics of the system as a whole. Other possible name, that has been used in the literature and is probably worthwhile from many contexts, is super atom as the cluster behaves as distinct entities with well-defined properties. However, the diversity of chemistry allows several new clusters composed of multiple atoms with numerous isomeric analogues to be developed in the coming years. This would imply super atoms of multiple elements leading to terminologies, such as AuAg super atoms besides Au and Ag super atoms. The other possible name is quantum clusters (QCs). The quantised nature of electronic energy levels due to size confinement alone is amplified in this term. The chemical composition of the core and the monolayer as well as the structural diversity of such systems is not implied in this term. Therefore, we follow this terminology in this book.

Research on these new materials started with the synthesis of water-soluble undecagold (Au_{11}) in 1978.⁴ Use of these gold QCs as high-resolution electron-density labels for electron microscopy as well as in biological studies was predicted by the discoverers. This was followed by the synthesis of triphenyl phosphine capped Au_{55} QCs.⁵ Whetten *et al.*⁶ prepared a water-soluble glutathione capped 10.4 kDa QC, $\text{Au}_{28}\text{SG}_{16}$ (later reassigned as $\text{Au}_{25}\text{SG}_{18}$ by Tsukuda *et al.*²). Dickson *et al.* synthesised a series of QCs, such as Au_5 , Au_8 , Au_{13} , Au_{23} and Au_{31} , that are encapsulated in the poly(amidoamine) (PAMAM) cavity.^{1,3} These QCs have very high quantum yields, as high as 70 per cent, which is comparable to strongly emitting organic dyes. A series of glutathione thiolate (SG-thiolate) protected gold QCs with well-defined compositions were synthesised and separated utilising polyacrylamide gel electrophoresis (PAGE) by Tsukuda *et al.*² Following these important studies, several groups have exploited the research area of QCs in detail. New QCs have been synthesised, crystal structures of a few well-known QCs have been determined and applications of them in different areas have been reported.

In this chapter, we present this new family of nanomaterials. After discussing the various synthetic methods and characterisation techniques, photophysical properties of the QCs are described in detail. These QCs are extremely useful in the area of opto-electronics and biolabelling. A significant amount of research is going on in these areas. Hopefully, this chapter initiates the reader to a new family of materials in the context of luminescence imaging and other applications.

11.2 SYNTHETIC APPROACHES

Quantum clusters of gold can be synthesised in different ways. But, before going into the details of the synthetic methods, let us have a look on the molecules, which cap or stabilise the QC core. These molecules are known as ligands. Ligands play a crucial role in determining the electronic properties of the QCs since most of the atoms of the QC are located at the surface and are subjected to chemical interactions with the ligands. Ligands influence geometry of the QC and stabilisation of the QC at a certain size and also blocks agglomeration. Water and organic soluble thiols, phosphines, amines and carboxylic acids are widely used as ligands. Dendrimers and biomolecules, such as DNA and proteins, are also used as scaffolds or templates for the *in-situ* synthesis of QCs. In the following section, we discuss the synthetic methods briefly.

All the synthetic methods reported so far can be broadly classified into four categories:

1. **Bottom-up approach:** Here the QCs are synthesised from Au^{3+} ions. In this method, Au^{3+} ions are reduced in presence of a suitable ligand to form the QCs. This method is used to synthesise both water and organic soluble QCs.
2. **Top-down approach:** In this method, the QCs are synthesised from bigger nanoparticles by core etching in presence of selected molecules.
3. **Synthesis from another QC:** In this method, an already synthesised QC is converted into another QC.
4. **Size focusing:** Here, a mixture of QCs is converted into thermodynamically most stable QC by the preferential population or size focusing method.

1. **Bottom-up approach:** The following methods of QC synthesis come under this classification.

a. **Two-phase reduction (B Brust synthesis):** This method is usually employed to make organic soluble nanoparticles with a few nanometer core sizes. It is adapted to make QC also.⁷⁻⁹ In this strategy, there are two steps. First step is the transfer of AuCl_4^- from aqueous to the organic layer by phase transfer reagent, such as tetraoctyl ammonium bromide (TOAB). Next step is the subsequent reduction at 0°C of Au^{3+} in presence of suitably selected ligands, such as thiols, phosphines, etc. Several organic soluble QCs such as Au_{20} , Au_{25} and Au_{38} were synthesised by this method as shown in Fig. 11.1.

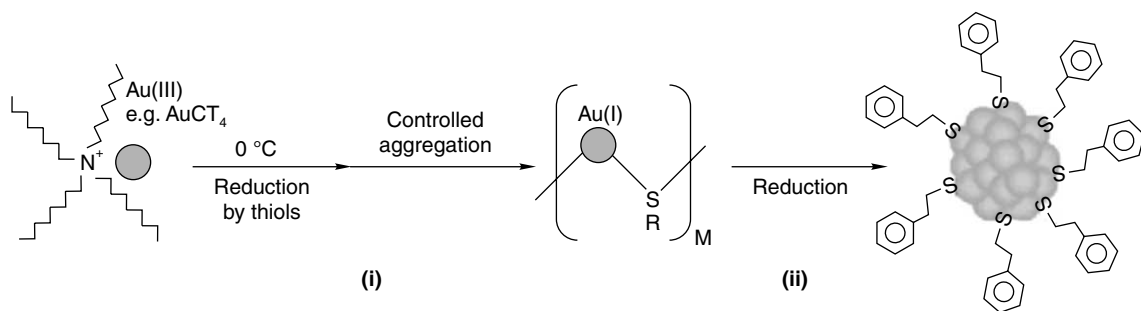
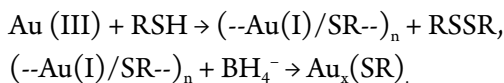


Fig. 11.1 Schematic of the formation of organic soluble QCs by the two-step Brust method (reprinted with permission from *J. Am. Chem. Soc.*, 130 (2008) 1138). Copyright (2008) American Chemical Society).

It is possible to increase the yield of QCs by controlling the kinetics of the formation of Au(I) thiolate intermediates.⁸ It is worth to note that the aggregation state of the Au(I)thiolate intermediate species is critical for subsequent growth of monodisperse gold QCs.

b. **Single phase reduction:** This method is generally used for the synthesis of water soluble QCs. Here Au^{3+} ions are reduced to Au(I) by the addition of thiols followed by the complete reduction to Au(0) by adding reducing agents, such as sodium borohydride (NaBH_4).² The reaction can be represented as,



A group of water-soluble glutathione-protected QCs with defined chemical compositions have been synthesised by reducing Au^{3+} ions in presence of glutathione.² This produces a mixture of QCs that are the kinetically trapped intermediates of the growing Au cores. These QCs can be separated from each other by PAGE.

c. Formation of QCs inside the cavities of biologically relevant molecules as well as biomolecules: As said earlier, biologically important molecules also act as templates or scaffolds for QC synthesis. This method produces water soluble QCs. A group of QCs of cores ranging from Au_5 to Au_{33} , was synthesised using G2-OH and G4-OH PAMAM dendrimers (second and fourth generation dendrimers with –OH functionality) by changing the Au^{3+} /dendrimer ratio.^{1,3} Gold ions are sequestered into the cavities of dendrimers by mixing a solution of dendrimers and gold ions. The QCs are formed by the subsequent and controlled addition of reducing agent, such as NaBH_4 . Recently, it was found that proteins can also make QCs. A simple, one-pot, green synthetic route was developed for the synthesis of gold QCs based on the reduction capability of the protein, bovine serum albumin (BSA).¹⁰ The QC produced in this method is said to have a core of Au_{25} . This process is similar to the bio-mineralisation behaviour of organisms in nature. Upon addition of Au(III) ions to the aqueous BSA solution, the protein molecules sequestered gold ions and entrapped them. The reduction ability of BSA molecules was then activated by adjusting the reaction pH to 12 and the entrapped ions underwent progressive reduction to form gold QCs *in-situ*. The ratio of gold to protein is found to be very crucial in the QC synthesis. For 5 mM Au precursor, a high BSA concentration (10–25 mg/mL) (with a concentration of amino acid residues of <20–50 mM) was required for the synthesis gold QCs. Large nanoparticles were produced if the BSA concentration was decreased while keeping Au precursor concentration constant (5 mM). Since the amount of BSA used is very high, it is difficult to use these QCs for biological studies, such as imaging as it will cause unspecific staining. So, this method is slightly modified to produce more intense QCs with relatively low amount (about half of the amount) of BSA. Here, the formation of QCs was triggered by the addition of ascorbic acid.³³

2. Top-down approach: Core etching or core size reduction of metallic nanoparticles by selected molecules, such as thiols, dendrimers and gold ions, can lead to the formation of QCs. Metallic nanoparticles are synthesised first. They are then treated with large amounts of above mentioned molecules, resulting in the formation of QCs.

The mechanism of formation of the QCs by this method is not well understood. We present below our tentative suggestions for the formation of QCs.¹¹ There are two possible routes for etching. In the first route, gold atoms are removed from the surface of the nanoparticles by excess ligands as a gold(I)-ligand complex. The gold(I) complex may undergo strong aurophilic interactions as there is a tendency for gold(I) compounds to form dimers, oligomers, chains or layers via gold(I)-gold(I) interactions due to the hybridisation of the empty 6s/6p and filled 5d orbitals to form QCs. In the second possible route, ligands may etch the surface gold atoms of the nanoparticles leading to a reduction in size of the nanoparticles in steps, resulting in the formation of a thermodynamically stable QC. The gold

atoms removed from the nanoparticle surface by the ligands deposit as gold(I) ligand complex. Some examples of the formation of QCs are given below.

*a. Etching with polyethylenimine (PEI):*¹² Polyethylenimine (PEI) is a first generation dendrimer. Dodecyl amine capped organic soluble metal nanoparticles of 8 nm diameter is synthesised by following Brust-Schiffrin method. The nanoparticles were treated with PEI, which was used as a multivalent polymer for ligand exchange reactions with dodecylamine. This reaction resulted in the size reduction of nanoparticles. Ultracentrifugation of the mixture after reaction produced a yellow supernatant and a red residue. The red residue was identified as PEI-coated gold nanoparticles of 7 nm diameter. On the other hand, the supernatant solution emits intense green light under UV light irradiation (365 nm), suggesting the presence of luminescent gold QCs. The formation of Au QCs is responsible for the size reduction of the nanoparticle. The QC produced here is identified as having a core of Au₈ from ESI-MS.

*b. Etching with thiols:*¹³ Phosphine capped polydispersed gold nanoparticles were synthesised. Monodisperse Au₂₅ nanorods and nanospheres are synthesised from these polydisperse Au nanoparticles by following one-phase and two-phase thiol etching procedures, respectively, as shown in Fig. 11.2. The nanoparticles were dissolved in dichloromethane. Phenylethane thiol was added to the solution. The solution was vigorously stirred at room temperature for <12 h. This reaction resulted in the conversion of gold nanoparticles into Au₂₅ nanorods. Au nanoparticles can also be converted into spherical Au₂₅ QCs following a two-phase thiol etching process. An aqueous solution of glutathione was added to a CH₂Cl₂ solution containing Au nanoparticles. The mixture was stirred at <55°C in order to enhance the phase transfer efficiency. This method produced monodisperse glutathione protected Au₂₅ QCs.

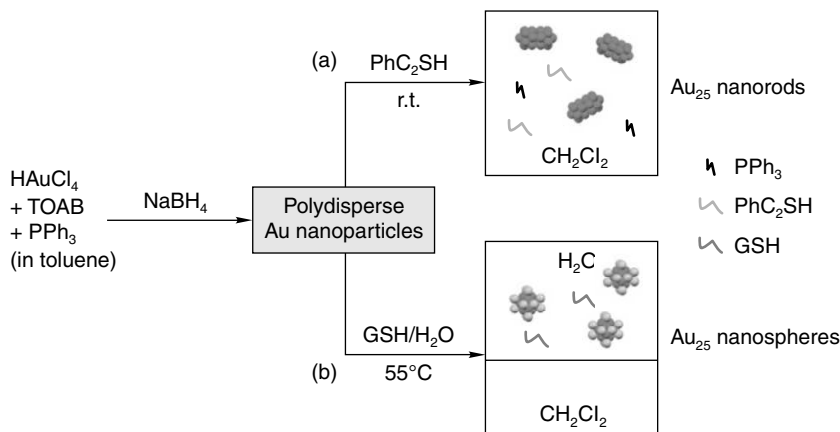


Fig. 11.2 Schematic representation of the formation of Au₂₅ rods and QCs from gold nanoparticles (reprinted with permission from *J. Phys. Chem. C.*, 113 (2009), 17599. Copyright (2009) American Chemical Society).

*c. Etching with Au³⁺ ions*¹⁴: In addition to thiols and dendrimers, Au³⁺ ions can also be used as etching agents. An organic soluble didodecyldimethylammonium bromide (DDAB) stabilised nanoparticle of diameter 5–6 nm was synthesised. A toluene solution of the nanoparticle was treated with Au precursors (HAuCl₄ or AuCl₃). This resulted in the formation of a transparent solution. A subsequent ligand exchange was carried out by adding an aqueous solution of dihydrolipoic acid (DHLLA) to the transparent solution. This resulted in the formation of brightly red emitting water soluble gold QCs.

3. Synthesis of QC from another QC: An already synthesised QC can be converted to another QC by the addition of selected reagents. Some examples are presented below.

*a. Synthesis of Au₂₅ from Au₁₁*¹⁵ As synthesised phosphine-stabilised Au₁₁ QC was treated with an aqueous solution of glutathione and stirred at 55 °C. Au₁₁ QCs underwent aggregation and dissociation to form Au₂₅(SG)₁₈ QCs selectively. This method produced Au₂₅ QCs in large scale. Cluster size increases during the ligand exchange reaction of Au₁₁ and the selective formation of Au₂₅ QCs arises due the extraordinary thermodynamic stability of the latter.

*b. Synthesis of Au₂₃ from Au₂₅*¹⁶ A novel interfacial route has been developed for the synthesis of a bright-red-emitting new QC, Au₂₃, by the core etching of Au₂₅SG₁₈. An aqueous solution of Au₂₅ QCs was mixed with toluene solution of octanethiol (OT). An interface was created and the biphasic mixture was stirred at 25 and at 55 °C, separately. A highly luminescent, water-soluble Au₂₃ QC was obtained by etching at 25 °C. In contrast, at 55 °C, an organic soluble Au₃₃ QC was formed.

*c. Synthesis of Au₇₅ from Au₅₅*¹⁷ Au₇₅ QCs were synthesised from Au₅₅(PPh₃)₁₂Cl₆ when the latter was reacted with hexanethiol and other organic soluble thiols. Laser desorption/ionisation mass spectrometry (LDI-MS) confirms the presence of a QC of mass in the 14–15 kDa range, which was proposed to be Au₇₅.

4. Preferential population of a QC by size focusing: In this method, a particular QC is preferentially populated from a mixture of different QCs by the addition of thiols.

*a. Preferential population of Au₂₅*¹⁸ A mixture of water soluble glutathione protected gold QCs was synthesised by reducing Au³⁺ ions in presence of glutathione at 0 °C. The mixture containing various QCs Au_n(SG)_m with (n, m) = (10, 10), (15, 13), (18, 14), (22, 16), (25, 18), (29, 20), (33, 22) and (39, 24). GSH was added to this mixture followed by stirring at 55 °C. This reaction resulted in the formation Au₂₅ selectively. In order to understand the mechanism, each QC separated from the mixture by PAGE was treated with free GSH under aerobic conditions. It was found that two different reaction modes are operative depending on the core size (see Fig. 11.3). The smaller QCs, Au_n(SG)_m (n < 25) are completely oxidized to Au(I)SG complexes, while the bigger QCs, Au_n(SG)_m (n ≥ 25) are etched into Au₂₅ by free GSH molecules.

*b. Preferential population of Au₃₈*¹⁹ Glutathionate protected polydisperse Au_n QCs (n ranging from 38 to 102) are synthesised by reducing Au(I)SG in acetone. Next, the size-mixed Au_n QCs were reacted with excess phenylethylthiol (PhC₂H₄SH) for 40 h at 80 °C. This led to the formation of Au₃₈(SC₂H₄Ph)₂₄ QCs selectively.

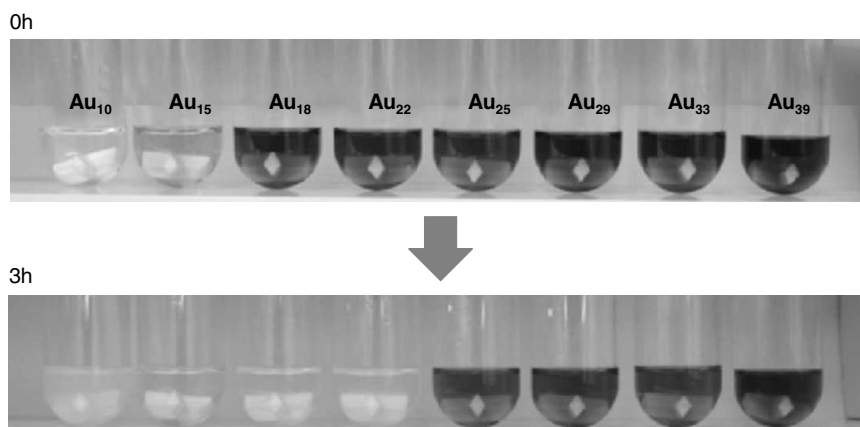


Fig. 11.3 Colour changes of aqueous solutions of $Au_n(SG)_m$ QCs with $(n, m) = (10,10), (15,13), (18,14), (22,16), (25,18), (29,20), (33,22)$ and $(39,24)$ before (0 h) and after (3 h) reaction with GSH (reprinted with permission from Small, 3 (2007) 835. Copyright (2009) John Wiley & Sons). (For clarity see colour figure.)

11.3 CHARACTERISATION TECHNIQUES

The main techniques employed for the characterisation of QCs include UV/vis optical absorption, luminescence, mass spectrometry, X-ray Photoelectron spectroscopy (XPS), transmission electron microscopy (TEM) and Fourier transform infrared (FT-IR).

1. **UV/vis optical absorption spectroscopy:** Since most of the QCs possess characteristic absorption features, the first and important characterisation technique used is UV/vis optical absorption spectroscopy. The synthesis of QCs can be monitored by the appearance of the optical absorption features. Most of the QCs can be distinguished from one another by their characteristic absorption features. For example, in Fig. 11.4, given are the optical absorption spectra of glutathione protected gold QCs from a core of Au_{10} (1) to Au_{39} (9).² It can be seen that each QC has its own absorption features. The explanation for the optical absorption features is given in the section 11.4.

2. **Luminescence spectroscopy:** Because of the quantum confinement due to sub-nanometer core size, QCs exhibit luminescence. Their emission wavelength ranges from UV to NIR as a function of QC core size.^{1,3} Quantum yield of the QCs ranges from 1×10^{-3} to 7×10^{-1} . Smaller QCs emit at lower wavelengths with higher quantum yield. On the other hand, larger QCs emit at higher wavelength with relatively lower quantum yield. So, it is important to characterise the QCs by luminescence spectroscopy.

3. **Mass spectrometry:** Metallic nanoparticles are always described by their core diameter in case of spherical nanoparticles or by aspect ratio in case of anisotropic nanostructures like nanorod or nanowire. On the other hand, QCs are generally represented in terms of their chemical composition,

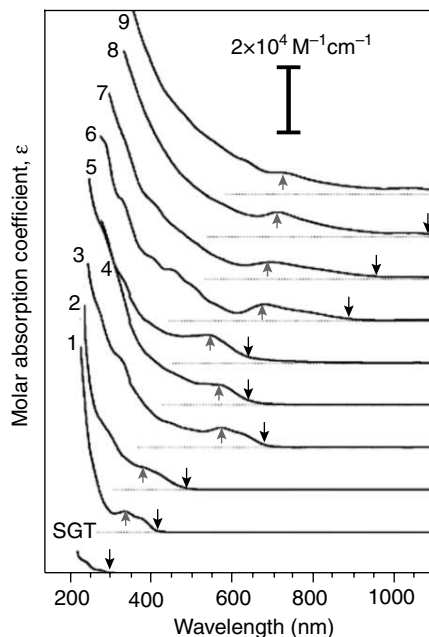


Fig. 11.4 Optical absorption spectra of a group of glutathione protected gold QCs (reprinted with permission from *J. Am. Chem. Soc.*, 127 (2005), 5261. Copyright (2005) American Chemical Society).

i.e., number of core atoms and the ligands. Two types of ionisation techniques are used widely to determine the chemical composition. They are Matrix Assisted Laser Desorption Ionisation (MALDI) and Electro Spray Ionization (ESI). Both are soft ionisation tools, known to produce intact molecular ions in the case of fragile species. As an example, ESI mass spectra of the nine fractionated (by PAGE) glutathione protected gold QCs are given in the Fig. 11.5.² Since most of the carboxyl groups of the glutathione ligands tend to be dissociated, QCs are negatively charged in solution. The charges are, therefore, due to the ligands or more precisely due to their functional groups. It is, however, important to remember that the core of the QC or the QC as a whole can be charged. The negative-ion ESI mass spectra of the QCs are comprised of a series of peaks associated with multiply charged anions. Each peak can be assigned as $[\text{Au}_n(\text{SG})_{m-x}\text{H}]^{x-}$, where n , m and x represent the numbers of gold atoms, GS ligands and dissociated protons, respectively (left panels of Fig. 11.5). The right panels represent the $\text{Au}_n(\text{SG})_m$ spectra, deconvoluted from the measured mass spectra. Theoretical spectra for $\text{Au}_n(\text{SG})_m$ are also shown by the coloured peaks with the corresponding n - m values. The chemical compositions assigned for these nine QCs from the mass spectral data are, (1) $\text{Au}_{10}\text{SG}_{10}$, (2) $\text{Au}_{15}\text{SG}_{13}$, (3) $\text{Au}_{18}\text{SG}_{14}$, (4) $\text{Au}_{22}\text{SG}_{16}$, (5) $\text{Au}_{22}\text{SG}_{17}$, (6) $\text{Au}_{25}\text{SG}_{18}$, (7) $\text{Au}_{29}\text{SG}_{20}$, (8) $\text{Au}_{33}\text{SG}_{22}$ and (9) $\text{Au}_{39}\text{SG}_{24}$. We usually observe multiply charged species in the ESI MS. This is particularly useful in instruments, in which the mass range is small. In the time of flight (TOF) instrument, in

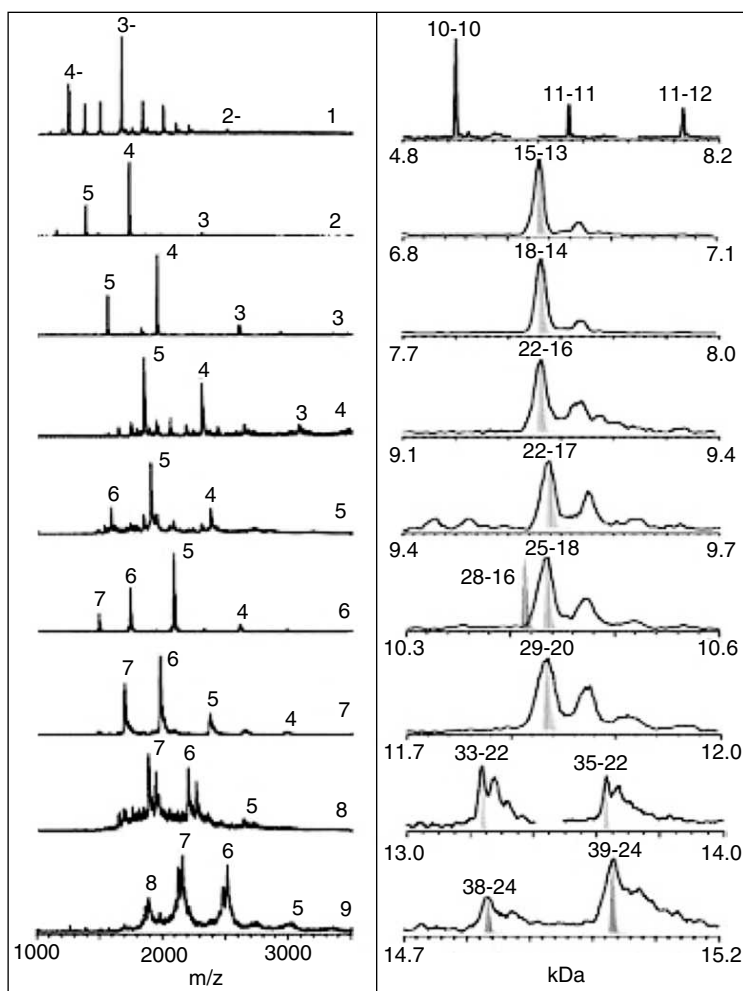


Fig. 11.5 Low-resolution ESI mass spectra of the nine fractionated gold QCs (left). The deconvoluted mass spectra (right). The calculated spectra for $Au_n(SG)_m$ are shown by the gray peaks with the corresponding $n-m$ values (reprinted with permission from *J. Am. Chem. Soc.*, 127 (2005), 5261. Copyright (2005) American Chemical Society).

which the mass spectra presented in Fig. 11.5 were measured, this is not a problem, however. On the other hand, it is possible to observe singly charged species in MALDI MS. For example, MALDI-TOF MS of $Au_{25}(SCH_2CH_2Ph)_{18}$ gave a peak at 7391 Da as 1^- and 1^+ ions in negative and positive mode, respectively.²¹ Trans-2-[3-(4-tert-butylphenyl)-2-methyl-2-propenylidene] malononitrile (DCTB) was used as matrix. This helps for the precise determination of the distribution of mixed monolayer compositions on nanoparticles prepared by ligand exchange reactions and by synthesis using thiol mixtures. MALDI MS typically uses the 337 nm N_2 laser, which causes C-S bond cleavage in thiol

protected QCs. In view of that, intact ions are not observed in standard MALDI MS instruments that use this laser source. Mass spectrometry without the matrix, called the laser desorption mass spectrometry, in which the sample in the solid state is desorbed by a laser gives several gas phase aggregation and reaction products.

4. **X-ray photoelectron spectroscopy:** The Au(4f) peak positions of the QCs are located between those of the Au(I) thiolate complexes and Au(0) film.² The Au(4f) peak widths of the Au QCs are appreciably broader than those of Au nanoparticles and Au(0) film.

5. **Transmission electron microscopy:** The sub-nano size of the QCs can be imaged using TEM, which will give faint spots due to the presence of QCs.²

6. **Fourier transform infrared spectroscopy:** This analysis provides information about the nature of ligation on the QC surface. For example, the FT-IR spectra of Au₂₅SG₁₈ shows an absence of the peak at 2526 cm⁻¹, which is due to -SH stretching vibration of glutathione, against free glutathione.²² This absence suggests a covalent linking of Au core with glutathione by Au-S bond formation.

7. **Structure determination by single crystal X-ray Diffraction:** Single crystal XRD has been used to determine the structures of several QCs, such as Au₁₃,¹³ Au₅₅,²⁴ Au₂₅,²⁵ and Au₁₀₂.²⁶ Since Au₂₅ QCs are synthesised and studied widely compared with other QCs, we describe below the crystal structure of phenylethanethiol capped Au₂₅.²⁵ The QC has an icosahedral Au₁₃ core as shown in Fig. 11.6A. It is capped by an exterior shell composed of the remaining twelve Au atoms (Fig. 11.6B), and the whole QC is covered by eighteen phenylethane thiolate ligands (Fig. 11.6C). The twelve exterior Au atoms form an incomplete shell, because out of the 20 triangular faces of the icosahedron, eight are uncapped. Each exterior gold atom has three contacts. There is one shorter Au-Au bond of length 3.02–3.12 Å to the Au₁₃ icosahedron and two longer bonds of length of 3.14–3.27 Å to the other two Au atoms on the face it is capping. The 18 ligands cap the gold core as follows (for clarity only sulphur atom of the ligand is shown in the figure): six ligands bridge the exterior Au-Au pairs (six in total) and the remaining 12 ligands bridge the exterior Au atoms and the icosahedral core.

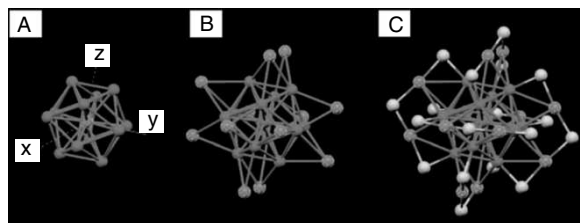


Fig. 11.6 Crystal structure of a Au₂₅(SR)₁₈ (R is phenylethyl group): (A) the icosahedral Au₁₃ core; (B) the Au₁₃ core covered by additional 12 Au atoms; (C) the whole Au₂₅ is protected by 18 thiolate ligands (for clarity, only S atoms are shown, magenta, Au; yellow, S) (reprinted with permission from *J. Am. Chem. Soc.*, 130 (2008), 5883. Copyright (2008) American Chemical Society). (For clarity see colour figure.)

11.4 ELECTRONIC STRUCTURE AND OPTICAL PROPERTIES

The electronic structure and hence optical properties of nanomaterials depend on the core size. For example, gold nanoparticles of core size ≥ 3 nm show surface plasmon resonance, which is due to the excitation of surface plasmons of nanoparticles by light.²⁵ On the other hand, nanoparticles with diameters less than 3 nm (<1000 atoms) the surface plasmon resonance (SPR) feature gradually disappear with decrease in size. When the nanoparticle size still reduces to, say around 1 nm, discrete absorption peaks emerge in the UV-vis-NIR spectra. At this size regime, the nanoparticle or the QC contains only very less number of gold atoms (less than 50 atoms). Due to this, small nanoparticles or QCs no longer support the plasmon excitation unlike the bigger, metallic nanoparticles. In order to determine whether there is a gradual transition from metallic behaviour to the appearance of molecular-like features or if there is a sudden change with a band gap opening near the Fermi level for a particular size, a study was carried out on monolayer protected QCs of various sizes.²⁷ The QCs were $\text{Au}_{25}(\text{SR})_{18}$, $\text{Au}_{144}(\text{SR})_{60}$, $\text{Au}_{309}(\text{SR})_{92}$, $\text{Au}_{976}(\text{SR})_{187}$, $\text{Au}_{2406}(\text{SR})_{326}$ with an average diameter of 1.1, 1.7, 2.2, 3 and 4 nm, respectively. A sudden change in the optical properties, such as luminescence, transient absorption, two-photon absorption is observed when the diameter of the QC is smaller than 2.2 nm. Displacively excited vibrations, which are associated with the presence of the band gap, have been detected only for particles smaller than 2.2 nm.

In order to explain the electronic structure and the corresponding absorption features of QCs, we take the example of $\text{Au}_{25}(\text{SH})_{18}^-$.²⁵ The optical absorption spectrum of Au_{25} is molecule-like, in sharp contrast to that of metallic gold nanoparticles. It has several absorption features in the 400–1000 nm range. On the other hand, spherical nanoparticles show one absorption peak (520 nm for a gold nanoparticle of ~ 15 nm core diameter). The optical absorption spectrum of Au_{25} is given in Fig. 11.7A. Three optical features, marked as ‘a’, ‘b’ and ‘c’ are present prominently in the absorption spectrum of Au_{25} . In order to explain the reason for the appearance of these three features, we take the help of Kohn-Sham orbital energy level diagram of (Fig. 11.7B) $\text{Au}_{25}(\text{SH})_{18}^-$. In the electronic structure of $\text{Au}_{25}(\text{SH})_{18}^-$, the highest occupied molecular orbital (HOMO) and the lowest three lowest unoccupied molecular orbital (LUMO) constitute the *sp* band, because they are mainly composed of 6*sp* atomic orbitals of gold. On the other hand, the HOMO-1 through HOMO-5 are mainly constructed from the 5*d*¹⁰ atomic orbitals of gold and hence constitute the *d* band. The first absorption feature is at 1.52 eV (670 nm), which is denoted by peak ‘a’ in the figure corresponding to a HOMO-LUMO transition, which is otherwise called as an intraband (*sp* to *sp*) transition (Fig. 11.7C). The second peak at 2.63 eV (marked as ‘b’ in figure) arises from mixed intraband (*sp* to *sp*) and interband (*d* to *sp*) transitions. The third peak at 2.91 eV (marked as ‘c’ in figure) arises principally from an interband transition (*d* to *sp*). The absorption peak due to intraband transition shows a blue shift with decrease in core size. For example, glutathione protected Au_{39} QCs show absorption at 1.4 eV or 730 nm due to the intraband transition while Au_{18} shows the same feature at 570 nm.

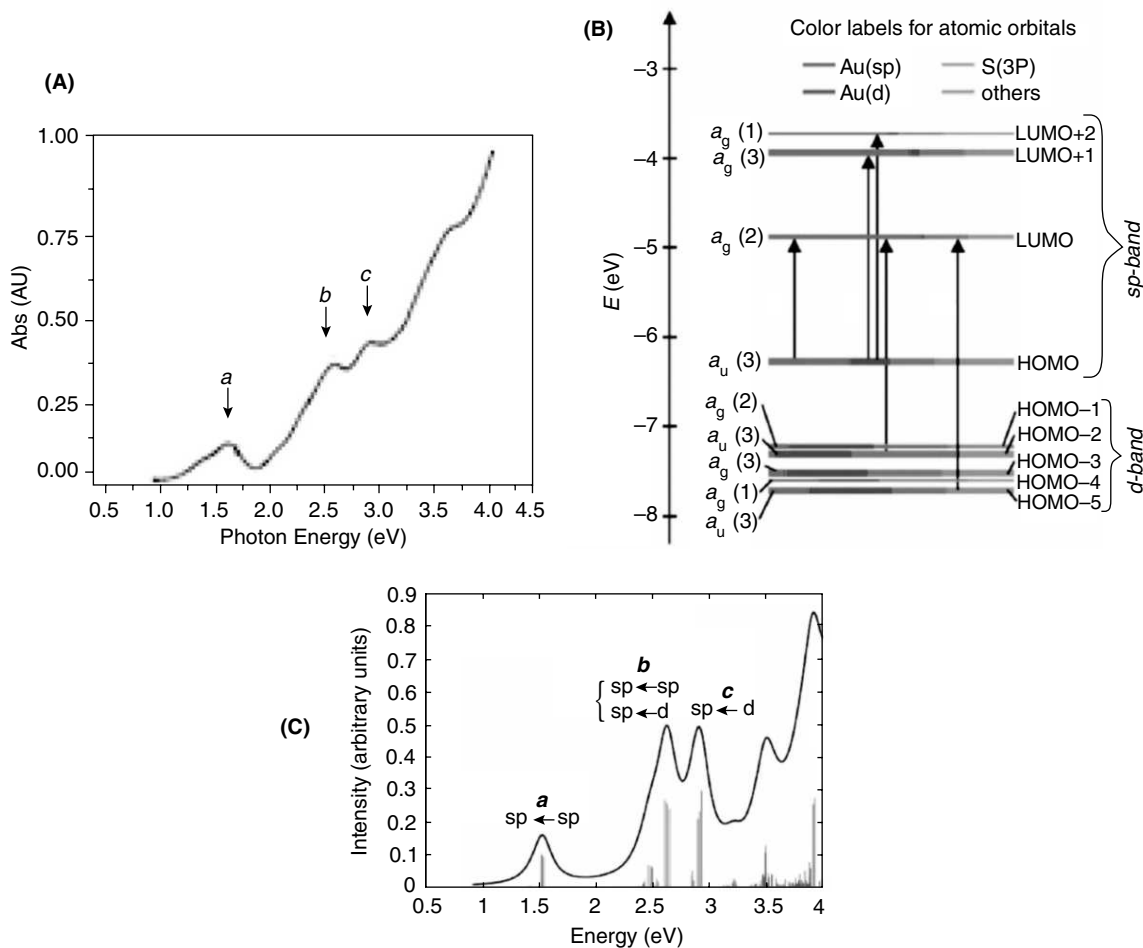


Fig. 11.7 (A) The absorption spectrum of $Au_{25}(SH)_{18}^-$. (B) Kohn-Sham orbital energy level diagram for $Au_{25}(SH)_{18}^-$. (C) The theoretical absorption spectrum of $Au_{25}(SH)_{18}^-$. Peak assignments: peak a corresponds to 1.8 eV (observed), peak b corresponds to 2.75 eV (observed), and peak c corresponds to 3.1 eV (observed) (adapted from Ref. 25. Reprinted with permission from *J. Am. Chem. Soc.*, 130 (2008), 5883. Copyright (2008) American Chemical Society.) (For clarity see colour figure.)

11.5 PHOTOLUMINESCENCE

Quantum clusters are known to exhibit luminescence with quantum yields in the range of 10^{-1} – 10^{-3} . Quantum clusters exhibiting luminescence from blue to the red region of the visible spectrum have been synthesized. QCs of gold synthesised inside the cavities of dendrimers exhibit very bright photoluminescence with quantum yields in the range of 10–70 per cent.^{1,3} The wavelength of emission

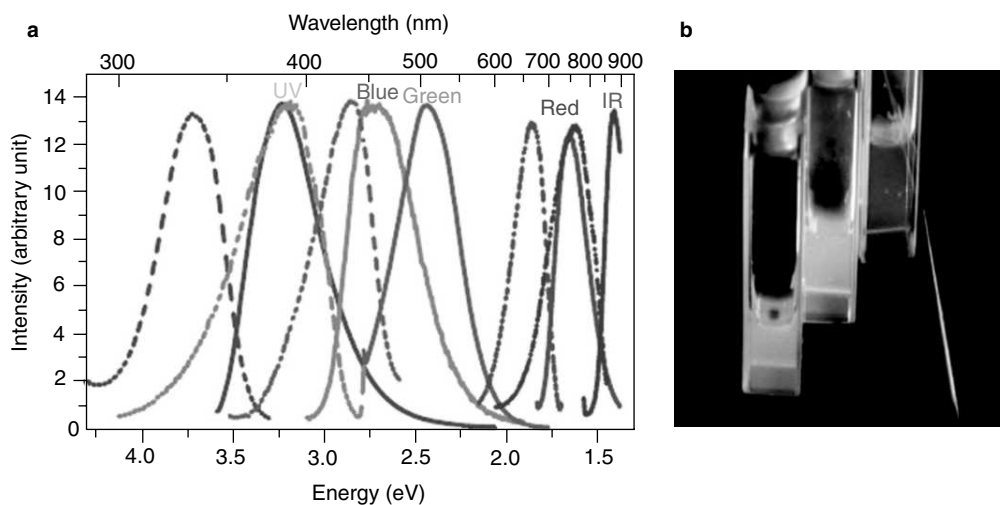


Fig. 11.8 (a) Excitation (dashed) and emission (solid) spectra of different Au QCs. Excitation and emission maxima shift to longer wavelength with increasing QC size. (b) Appearance of the three shortest wavelength-emitting Au QC solutions (from left to right) under UV irradiation (366 nm) (reprinted with permission from *Phys. Rev. Lett.*, 93 (2004), 077402. Copyright (2004) American Physical Society). (For clarity see colour figure.)

of the QCs can be tuned by changing the core size. Smaller QCs emit at lower wavelength with higher quantum yield and larger QCs emit at higher wavelength with comparatively low quantum yield. For example, Au₅, Au₈, Au₁₃, Au₂₃ and Au₃₁, grown inside dendrimers, show emissions at 3.22, 2.72, 2.43, 1.65 and 1.41 eV with quantum yields of 70, 42, 25, 15 and 10 per cent, respectively as shown in Fig. 11.8. The excitation and emission spectra of these QCs are shown in Fig. 11.8a. These QCs are generally termed as free falling QCs, since they are grown inside the cavities of dendrimers. There is another class of QCs called thiolated QCs, which are protected by various thiols. They are emitted in the NIR region with relatively low quantum yield. For example, Au₂₅SG₁₈ shows a quantum yield of 1×10^{-3} (0.1%) only.² On the other hand, Au₂₅ encapsulated by BSA show a quantum yield of 6 per cent.¹⁰ These contrasted photoluminescence properties show that thiolate passivation has a significant effect on the electronic structure and hence photophysical properties of gold QCs.² The high luminescence and biocompatibility due to the lower metallic content make QCs excellent candidates for various biological applications, such as imaging, detection, and so on, in conjunction with therapeutics. They are found to be photostable¹⁴ unlike organic dyes, a quality that widens the scope of their potential applications. They also exhibit electroluminescence at room temperature and hence provide facile routes to produce strong single-photon emitters. The photoluminescence of QCs arises due to their molecular-like electronic structure. The emission originates from radiative intraband transitions within the *sp* bands, across the HOMO–LUMO gap. As the size of the QC decreases, the spacing between the discrete states increases. That leads to a blue shift in the emission of smaller QCs, when compared with the larger analogues.

11.5.1 Photostability

Quantum clusters are highly photostable compared with organic fluorophores. In order to check the photostability of QCs in comparison with organic fluorophores and semiconductor quantum dots, a study was conducted selecting dihydrolipoic acid capped gold QC (AuQC@DHLA), polymer coated CdSe/ZnS semiconductor quantum dots and two different organic fluorophores, namely, fluorescein and Rhodamine 6G.¹⁴ For the photostability study, luminescent AuQC@DHLA dissolved in sodium borate buffer of pH 9 was loaded into a quartz cuvette and was exposed to blue-light (480 nm) excitation from the Xenon lamp of the fluorometer. Luminescence intensity at 680 nm was recorded at regular intervals of time. Quantum dots, Rhodamine 6G and fluorescein were also exposed to the same condition for the same period. Organic fluorophores show fast photobleaching as expected. On the other hand, luminescent Au QCs exhibited a much slower photobleaching rate than the organic fluorophores, though not as good as the semiconductor quantum dots. The half life of AuQC@DHLA in comparison to the organic dye is around 13 times more. This study supports the usage of QCs in various bio-labelling experiments over organic fluorophores.

11.5.2 Two-photon Emission

Two-photon emission is a process, in which electronic transition between quantum levels occurs through the simultaneous emission of two photons. Two-photon emission of Au₂₅ is observed at 830 nm by exciting at 1290 nm, as shown in Fig. 11.9.²⁸ Two-photon absorption (TPA) cross-section of Au₂₅ at 1290 nm in hexane was determined to be 2700 GM, which is superior to the TPA cross-sections of many organic chromophores with emission in the near-infrared region. In addition to the near-infrared luminescence for Au₂₅, additional luminescence in the visible region with a maximum around 510 nm was observed, which is also two-photon allowed (excited at 800 nm). Present measurements

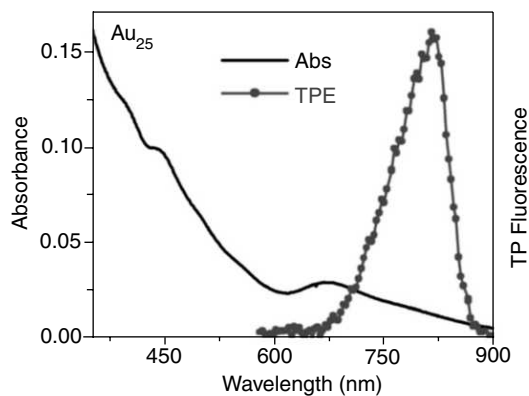


Fig. 11.9 Optical absorption of Au₂₅ and two-photon emission spectrum after excitation at 1290 nm for Au₂₅ (reprinted with permission from *J. Am. Chem. Soc.*, 130 (2010), 5032. Copyright (2010) American Chemical Society).

on Au₂₅ gold QCs suggest that they can be used as multi-photon imaging agents with near infra-red luminescence.

11.5.3 Photon Antibunching

Photon antibunching is a quantum phenomenon that occurs during luminescence, in which the emission of one photon reduces the probability that another photon will be emitted immediately afterward. Unlike single atoms, metal nanoparticles exhibit collective oscillations of free electrons and produce bunched photons. Antibunched photons cannot be observed from metallic nanoparticles since they possess continuous-band structure. On the other hand, it is possible to observe antibunched photons from QCs due to quantum confinement. Antibunched luminescence from a dendrimer encapsulated single Au₂₃ was observed when excited at 632.8 nm.¹ Photon correlations from single Au₂₃ was measured by equally splitting emission from a single Au₂₃ onto two single-photon-sensitive detectors. A dip in the photon-pair distribution was observed at zero time delay between the two detectors, indicating reduced probability of two photons being simultaneously emitted. The rise time of the antibunched signal matches the Au₂₃ lifetime.

11.5.4 Electroluminescence

Electroluminescence is a phenomenon, in which a material emits light as a response to a strong electric field. It is the result of radiative recombination of electrons and holes in a material. Electroluminescence is observed in gold QCs also. Strongly electroluminescent Au QCs were produced within 25 nm thick Au films sputtered onto clean glass cover slips.²⁹ Application of 3 V, 150 mA for 10 s produces an electromigration-induced break junction near the centre of the Au film, creating highly emissive Au QCs. The as synthesised gold QCs also strongly fluoresce in addition to electroluminescence when excited at 532 nm.

11.5.5 Luminescence Enhancement during Aqueous to Organic Phase Transfer

Luminescence of a material depends on its surrounding environment. Luminescence enhancement is observed for gold QC during aqueous to organic phase transfer. Glutathione capped Au₂₃ was phase transferred from water to toluene by TOAB.¹⁶ The quantum yield of the QC was increased from 1.3 per cent to 5 per cent after phase transfer. The luminescence enhancement can be observed visibly as well (Fig. 11.10). Both the radiative (k_r) and non-radiative (k_{nr}) rates of the QC are altered on phase transfer. This indicates a change in the kinetics of electron-hole recombination. k_{nr} rate showed a significant decrease after phase transfer, which can be explained as follows. Thiols are known to act as hole traps. Some of the studies showed that organically-soluble quantum dots when transferred to aqueous medium in presence of thiols showed significant quenching in luminescence. In this case, the QC after phase transfer is protected with a layer of TOA⁺ and this passivation of the QC by TOA⁺ makes the glutathione (thiols) less active, and hence the decrease in nonradiative decay can be attributed to the reduced ability of thiols to act as hole traps for the QC.

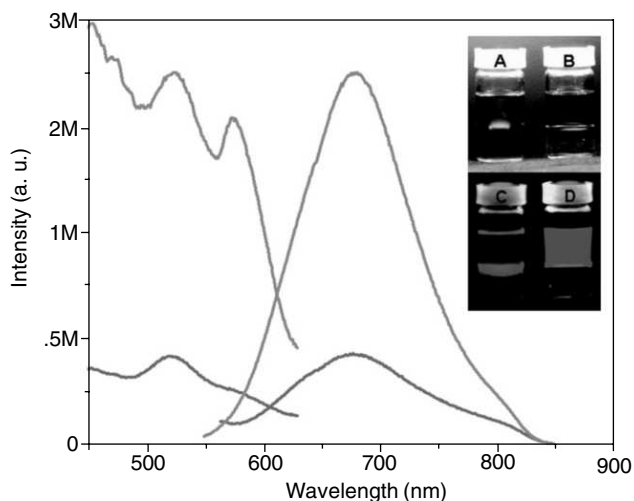


Fig. 11.10 Photoluminescence profile of Au_{23} before (pink trace) and after (orange trace) phase transfer. Emission of the QC enhances considerably after phase transfer. Photographs of the aqueous-toluene mixture containing the QC before and after phase transfer under white light (A and B, respectively) and UV light (C and D, respectively). In C, only the interface is illuminated as the UV radiation is attenuated as the sample was irradiated from the top (reprinted with permission from *Chem. Eur. J.*, 15 (2009), 10110. Copyright (2009) John Wiley & Sons). (For clarity see colour figure.)

11.5.6 Fluorescence Resonance Energy Transfer (FRET)

FRET is the transfer of energy between two chromophores. Here, when a chromophore (donor) is in an electronically-excited state, may transfer energy to another chromophore (acceptor) through nonradiative dipole–dipole coupling, when they are separated by a distance typically less than 10 nm. FRET is an ideal tool to measure the separation between an excited donor (D) and an acceptor (A) as the extent of such dipole interactions is a sensitive measure of the D–A distance. Since QCs are luminescent, they can be used in FRET. FRET, between the metal core and the ligand in $\text{Au}_{25}\text{SG}_{18}$ is demonstrated using dansyl chromophores attached to the QC core through glutathione linkers.³⁰ Dansyl chromophore was attached to the Au_{25} core by two different routes. In the first route, dansyl chloride was reacted at the amino group of the glutamate residue of some of the glutathione ligands (-SG) anchored on Au_{25} . In the second route, some of the glutathione ligands of the QC underwent exchange by the classical ligand exchange method with dansyl glutathione (-SG-D), when the aqueous solution of $\text{Au}_{25}\text{SG}_{18}$ was stirred with dansyl glutathione. Both the methods led to the formation of Au_{25} protected with a mixture of glutathione and N-dansyl glutathione. Efficient energy transfer from the dansyl donor to the Au_{25} core is observed. This can be manifested by way of the reduced lifetime of the excited state of the former and drastic quenching of its luminescence. The donor–acceptor separation observed in the two synthetic routes reflects the asymmetry in the ligand binding on the QC core, which is in agreement with the recent theoretical and experimental results on the structure of Au_{25} .

11.5.7 Photoreactivity at Single-cluster Level

Reactivity of metal QCs can be studied using spectroscopic techniques, such as single-molecule luminescence spectroscopy (SMS). By means of this technique, we can observe even individual QCs due to their luminescence. Photoreactivity of gold QCs synthesised using a photochemical method in a polymer matrix was studied at the single-cluster level by employing SMS.³¹ The formation of individual QCs can be viewed in real-time by a SMS image. The QC was synthesised by spin coating a solution of the polymer containing a radical precursor (2-hydroxy-4'-(2-hydroxyethoxy)-2-methylpropiophenone) and HAuCl_4 . Upon photoexcitation radicals, which are produced from the radical precursor, reduce the Au ions to generate gold QCs. Initially, no luminescence was observed because of the absence of QCs. But, with successive laser excitation, an increase in individually blinking luminescent species with a long off-time was observed. When these naked QCs were exposed to oxygen, a reversible and irreversible quenching of luminescence was observed. Number of luminescent species decreased significantly when the samples were exposed to O_2 . The observed decrease was recovered by 50 per cent by removing O_2 . The luminescence quenching of photoluminescence of gold QCs happened due to electron transfer. The luminescence spectra and the histogram of the luminescence maxima did not change significantly after the recovery. So, it can be concluded that there were two different quenching processes, i.e., a reversible process and an irreversible process. When the QCs are protected with octadecanethiol, luminescence quenching by O_2 was prohibited. This suggests that access of O_2 to the surface of gold QCs played a key role in quenching.

11.5.8 Quantum Clusters as Metal Ion Sensors

Luminescence of the QCs can be used as a highly sensitive and selective luminescence “turn-off” sensor for metal ions. BSA capped gold QCs ($\text{Au}_{\text{QC}}@\text{BSA}$) were used to detect Cu^{2+} ions at nM level.³⁸ No further modification of the QC was required for this application. For this study, effect of luminescence of the QC in presence of various metal ions was studied. Ions selected were Au^{3+} , Ag^+ , Cu^{2+} , Ni^{2+} , Ca^{2+} , Mg^{2+} , Na^+ , Pb^{2+} , Hg^{2+} , Zn^{2+} , Sm^{2+} , Fe^{3+} , Co^{2+} and Cd^{2+} as their nitrates or chlorides. To the aqueous solutions of the QC (1 mg/ml), metal ions were added such that the final concentration was 1 μM and the emission of the QC was measured immediately after the addition of ions. Even though there was a slight quenching of luminescence in presence of Co^{2+} , emission was quenched almost completely only in presence of Cu^{2+} and remained unaltered in presence of other metal ions. Figure 11.11A is the plot of QC emission intensity against the metal ions added. Photographs of the aqueous solutions of QCs under UV light irradiation after the addition of various metal ions are also given (Fig. 11.11B). The specific reactivity towards Cu^{2+} can be used as a detection tool to find its presence. The emission of QC quenched as a function of Cu^{2+} concentration (Fig. 11.11C). The minimum concentration of Cu^{2+} that can be detected was 15 nM, and the emission intensity decreased systematically with the increase in Cu^{2+} ion concentration. The luminescence quenching in presence of Cu^{2+} can be attributed to the QC aggregation induced by the complexation between BSA and Cu^{2+} ion. The quenching of luminescence happens due to the interaction between BSA shell of the QC and Cu^{2+} ions. There is no direct reaction between the QC and Cu^{2+} ions. When Cu^{2+} ions are added to the aqueous solution of

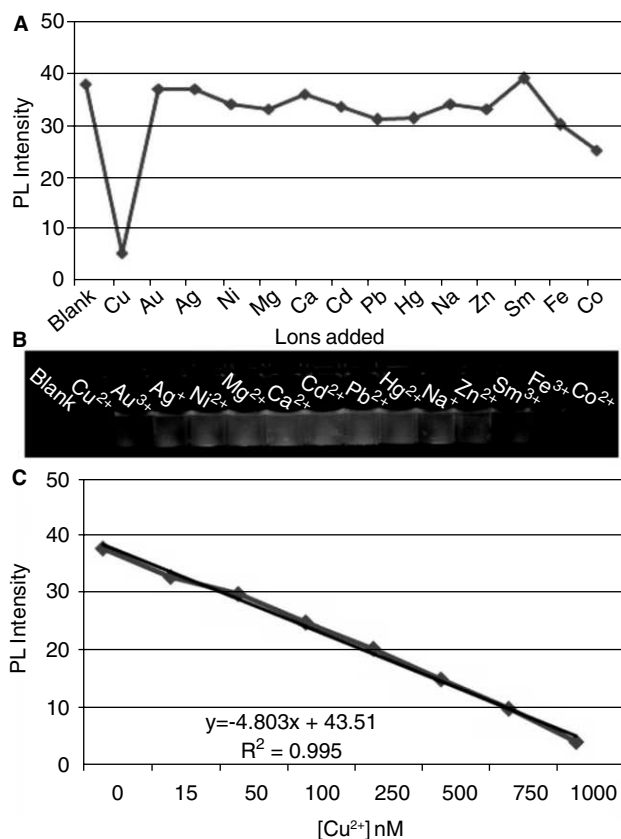


Fig. 11.11 (A) Plot of photoluminescence (PL) intensity of $Au_{QC}@BSA$ in the presence of various metal ions. (B) Photographs of aqueous solutions of the QC in the presence of the corresponding ions under irradiation by UV light. (C) Plot of PL intensity of the QC as a function of $[Cu^{2+}]$ ($y = -4.803x + 43.51$ and $R^2 = 0.995$) (reprinted with permission from *Chem. Eur. J.* 16 (2010), 10103. Copyright (2010) John Wiley & Sons). (For clarity see colour figure.)

QC, they mediate protein–protein interaction and lead to spherical aggregation of $Au_{QC}@BSA$. When the QCs are aggregated in presence of copper ions, the luminescence of the QC quenches. This effect is called aggregation induced luminescence quenching. Cu^{2+} ion has more affinity towards BSA than any other ions.

11.5.9 Fabrication of Luminescent Patterns

Since the QCs are highly luminescent, they are used to make luminescent patterns by soft lithography. Luminescent water soluble Au_{22} QCs are used to make luminescent patterns.³² Poly(dimethylsiloxane) (PDMS) is used as a stamp and a compact disk (CD) is used to make patterns on the stamp. A network

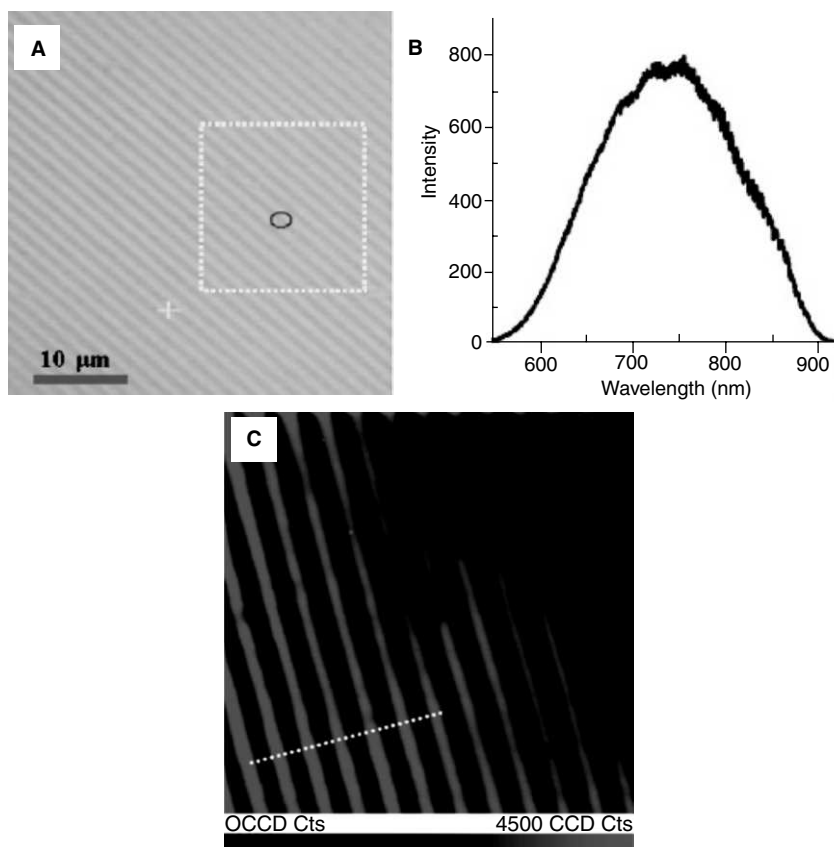


Fig. 11.12 (A) Optical image (under white-light illumination) of the Au₂₂ patterns. (B) Luminescence spectrum collected using a 532 nm laser showing an emission maximum is around 740 nm. (C) Luminescence image of the regular and periodic patterns collected from the area selected by a rectangular box in part A (20 μm × 18 μm) (reprinted with permission from *ACS Appl. Mater. Interfaces*, 1 (2009) 2199. Copyright (2009) American Chemical Society).

of straight and continuous channels is formed by this method. Approximately, 100 μl of Au₂₂ solution was dropped at one edge of the stamp to fill the channels spontaneously by capillary action. The whole setup was left undisturbed for solvent evaporation. Afterward, the stamp was removed, leaving behind the luminescent patterns on the substrate. The Luminescence image and corresponding spectrum of Au₂₂ patterns were collected using confocal Raman spectroscopy (see Fig. 11.12). The luminescence collected using a 532 nm laser showed an emission maximum of 700 nm. The luminescence image of the patterns was collected using the same excitation laser. Here the regions in red indicate the presence of the QC, and those in black indicate the blank region (initially occupied by the PDMS stamp). These luminescent patterns can be used for optical diffraction-based diagnosis.

11.5.10 Quantum Clusters for *in-vitro* Imaging

The use of QCs in biology-related experiments, such as imaging, is highly promising. There are several methods to synthesise highly luminescent water soluble gold QCs in large quantity. Moreover, these QCs possess additional benefits over organic fluorophores and fluorescent semiconductor quantum dots. It is known that organic fluorophores are prone to photo bleaching. However, QCs are found to be highly photostable.¹⁴ Fluorescent semiconductor quantum dots are generally composed of elements such as Cd and Pb, and they have to be coated with other inorganic or biological molecules to reduce their toxicity. On the other hand, QCs are composed of gold atoms and are likely to be biocompatible. Moreover, the cytotoxicity of the QCs is very low due to the low metallic content.

A process called receptor mediated endocytosis is used for the uptake of QCs by the cells.³³ For that, highly luminescent gold QCs (Au-BSA) were synthesised by controlled reduction of Au³⁺ ions, stabilised in BSA, using ascorbic acid (vitamin-C). These QCs are subsequently conjugated with folic acid (FA) through amide linkage with the BSA shell of the QCs for targeted imaging of cancer cells. The bioconjugated QCs (Au-BSA-FA) are found to be stable over a wide range of pH from 4 to 14 and quantum yield of ~5.7 per cent at pH 7.4 in phosphate buffered saline (PBS). Since the QCs show bright luminescence with a peak maximum at ~674 nm, it is possible to image QCs at NIR emission window, where the tissue-absorption of light is minimum. These gold QCs are non-toxic up to concentrations of 500 µg/ml, as evident from the cell viability and reactive oxygen toxicity studies. For the uptake study, FR+ve oral squamous cell carcinoma (KB) is selected. FA-conjugated gold QCs were found internalised by these cell lines in significantly higher concentration compared with the negative control cell lines, FR-ve lung carcinoma A549 (Fig. 11.13). This study demonstrates the potential of using non-toxic luminescent Au QCs for the targeted imaging of cancer.

11.6 MAGNETISM

Reversible switching of paramagnetism was observed in phenyl ethane thiol capped Au₂₅ QCs. Density functional theory (DFT) shows that spin in the Au₂₅ QC resides in the Kohn-Sham HOMO.³⁴ An unpaired electron is present in the HOMO of Au₂₅ QCs, when they are in the neutral charge state. The magnetic properties were measured with electron paramagnetic resonance (EPR) spectroscopy using microcrystal powders of the QCs. Microcrystalline and frozen-solution samples show an $S = 1/2$ signal with $g = (2.56, 2.36, 1.82)$. EPR studies indicate that [Au₂₅]⁰ has one unpaired spin per particle. EPR signal disappeared when [Au₂₅]⁰ QCs were reduced with aqueous NaBH₄. The reduced QCs are in anionic form, [Au₂₅]⁻. There will be no unpaired electrons in the HOMO, when the QC is in the anionic form and hence no paramagnetism is observed. It is possible to recover the paramagnetism, when the [Au₂₅]⁻ QCs were treated again with H₂O₂. Therefore, the paramagnetism can be switched on or off simply by controlling the charge state of the nanoparticle. Relevant data are given in Fig. 11.14.

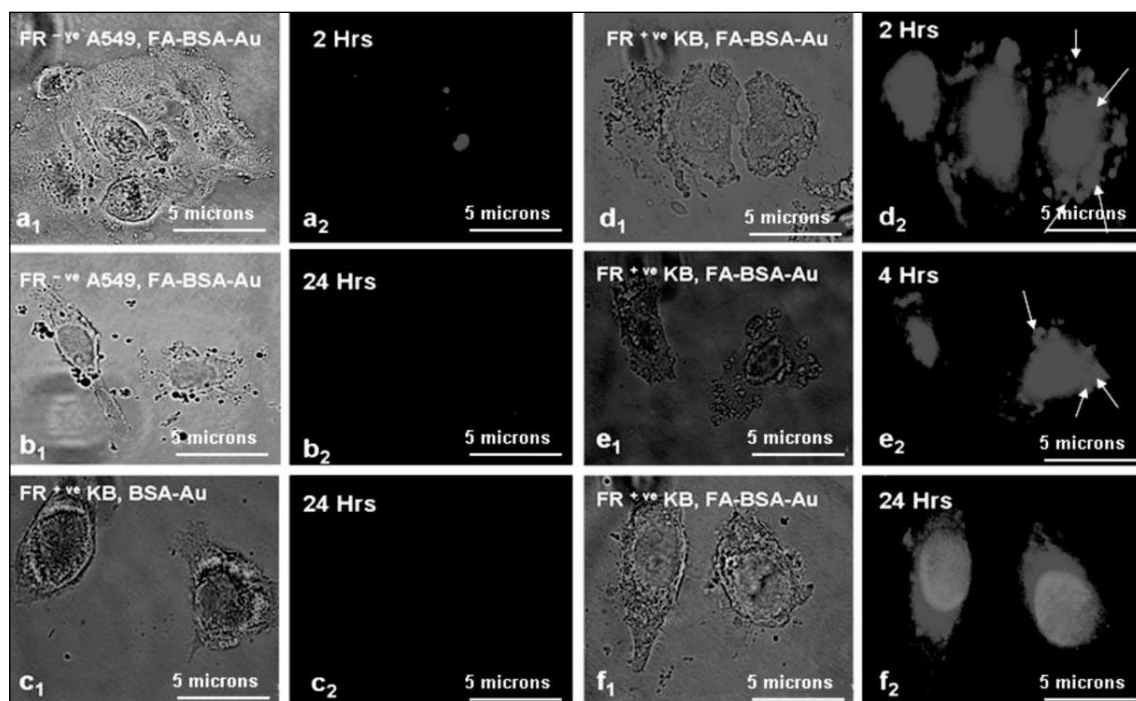


Fig. 11.13 Luminescent microscopic images showing interaction of Au-BSA-FA QCs with different types of cell lines: (a1 and a2) FR-ve lung carcinoma A549 after 2 h of incubation; (b1 and b2); FR-ve lung carcinoma A549 after 24 hours of incubation; (c1 and c2) FR+ve KB cells with unconjugated Au QCs, (d1 and d2) FR+ve KB cells with FA conjugated Au QCs at 2 h; (e1 and e2) 4 h and (f1 and f 2) 24 h of incubation (reproduced with permission from Archana, R., S. Sonali, M. Deepthy, R. Prasanth, Habeeb Muhammed, T. Pradeep, S. Nair, and K. Manzoor, *Nanotechnology*, 21 (2010), 055103. Copyright (2010) IOP publishing Ltd). (For clarity see colour figure.)

11.7 CHEMICAL REACTIVITY

11.7.1 Conversion of Anionic $[\text{Au}_{25}(\text{SCH}_2\text{CH}_2\text{Ph})_{18}]^-$ Cluster to Charge Neutral Cluster via Air Oxidation

It is possible to convert an anionic QC $[\text{Au}_{25}(\text{SCH}_2\text{CH}_2\text{Ph})_{18}]^-$ into a neutrally charged QC $[\text{Au}_{25}(\text{SCH}_2\text{CH}_2\text{Ph})_{18}]^0$ via air oxidation in solution phase. Since most of the gold nanoparticles are reported to be chemically inert, the conversion of anionic Au_{25} into neutral Au_{25} is worth exploring.³⁵ Other than the charge, there is a dramatic difference in their crystal structures. While Au_{25}^- exhibits apparent structural distortions in the $\text{Au}_{25}\text{S}_{18}$ framework, such distortions are not observed in the neutral QC. There is also a change in the optical absorption features of these QCs. Apart from the three

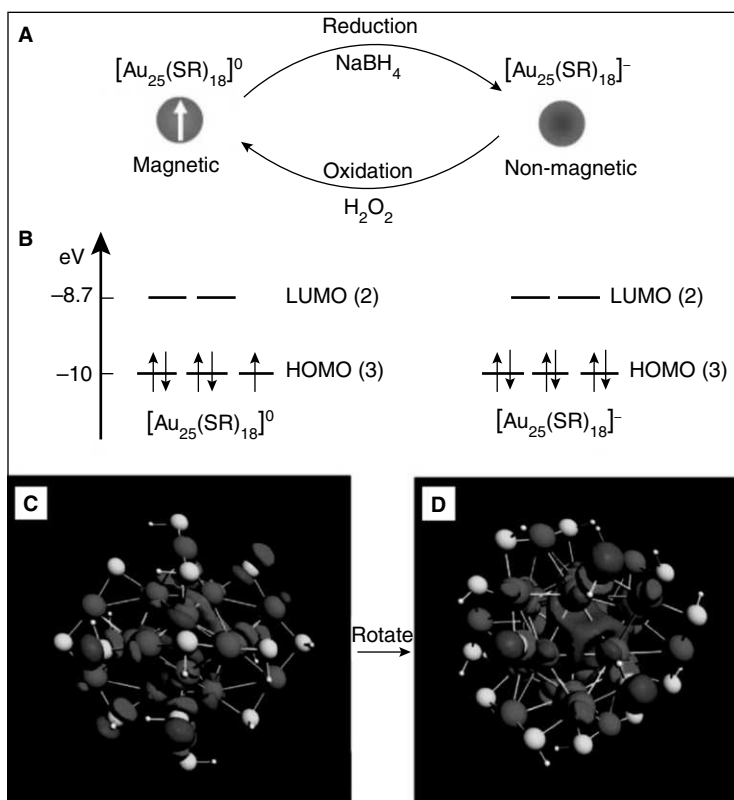


Fig. 11.14 (A) Reversible conversion between the neutral and anionic Au_{25} . (B) DFT-calculated Kohn-Sham orbital energy level diagrams for the neutral and anionic Au_{25} , respectively. (C and D) Views of the Kohn-Sham HOMO for $[Au_{25}]^0$. The HOMO possesses two lobes and exhibits distinct P-like character. (D) is rotated relative to (C) to show one of the lobes (contributed by three Au atoms in the icosahedral shell). Colour code: purple, Au; yellow, S; white, H (reprinted with permission from *J. Am. Chem. Soc.*, 131 (2009), 2490. Copyright (2009) American Chemical Society). (For clarity see colour figure.)

main absorption bands at 400, 450 and 670 nm, there are additional fine spectral features, including a broad shoulder at <800 nm, and another small shoulder at <550 nm for Au_{25}^- QC. The 400 nm peak becomes more prominent, while the 450 nm peak becomes less so. Concurrently, the 800 nm shoulder that is characteristic of the Au_{25}^- QC disappears and a new, small shoulder at 630 nm emerges. These results indicate that the 400 and 450 nm states are likely associated with one another, and the intensity is transferred from the 450 nm state to the 400 nm state upon oxidation; similarly, the 800 and 630 nm bands form another correlated pair.

11.7.2 Size Tuning of Au Nanoparticles Formed by Electron Beam Irradiation of Au₂₅ QCs

Because of the very small size and non-metallicity, QCs are found to be very reactive towards the electron beam during TEM measurements. They are found to fuse together to form bigger nanoparticles upon prolonged electron beam irradiation.³⁶ To check the size evolution of these QCs on electron irradiation, glutathione protected Au₂₅ QCs have been uniformly coated inside and outside of β -Ala-L-Ile dipeptide nanotubes (DPNT). Upon exposure to an electron beam, in a transmission electron microscope, the QCs started to transform to gold metallic nanoparticles as a function of irradiation time as given in Fig. 11.15. The nanoparticles grow to a size of 4.5 nm, and thereafter, the particle size remains unaffected by electron beam exposure. Electron beam exposure gives rise to the formation of nearly monodisperse nanoparticles. The nanotubes are intact and this template is shown to control the uniformity of the size of the nanoparticles grown. However, in the absence of nanotube template, the nanoparticles grown on electron beam irradiation are found to be highly polydisperse. The formation of monodisperse nanoparticles in presence of nanotube can be explained as follows. Glutathione capped Au₂₅ QCs are further stabilised by the functional groups (NH₂ and COOH) present in the nanotube. A uniform layer of Au₂₅ QCs is formed on the nanotubes since the functional groups are distributed uniformly throughout the tube. Upon exposure to the electron beam, the inherent instability of the QCs, when exposed to the electron beam, favours coalescence, nucleation and growth of Au nanoparticles of uniform sizes with an

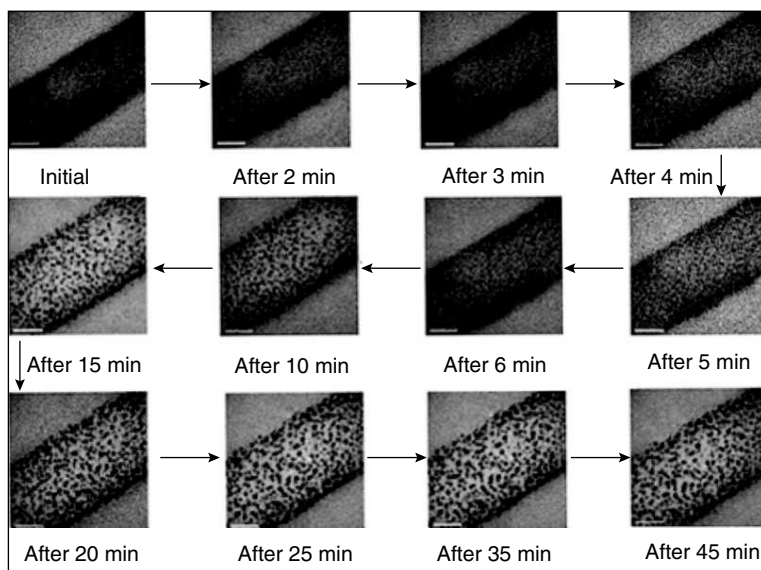


Fig. 11.15 Formation of gold nanoparticles due to the exposure of the gold QCs anchored on a dipeptide tube to the electron beam. [*J. Mater. Chem.*, 19 (2009), 8456] (reproduced by permission of The Royal Society of Chemistry).

interparticle separation of 4.5 nm. Hence, the chemistry of the surface of the DPNT, available surface area and surface curvature plays a crucial role in providing stability for the formation of a uniform layer of GSH capped Au QCs upon it, while the inherent instability of the QCs to the electron beam favours the formation of nanoparticles. This implies that the nanoparticle size can be tuned using the electron beam.

11.8 QUANTUM CLUSTERS AS CATALYSTS

Gold nanoparticles of various shapes and structures have been used as catalysts for a variety of reactions, such as selective oxidation and hydrogenation. However, the main drawback of using nanoparticles as catalysts is their monodispersity. So the catalytic activity cannot be precisely correlated to any specific size. So, 100 per cent monodisperse nanoparticles have to be synthesised to understand the origin of their catalytic properties. In recent years, there have been reports on the synthesis of highly monodisperse QCs. Since they show completely different chemical and physical properties, they can be used in catalysis.

Highly monodispersed $\text{Au}_{25}(\text{SR})_{18}$ QCs are used as catalysts for the selective hydrogenation of α , β -unsaturated ketones and aldehydes (Ref. 37). The crystal structure of these QCs is known, and therefore, it is possible to correlate the particle structure with catalytic properties. It is also possible to identify the catalytically-active sites on the particle. There are reports showing the use of conventional supported gold nanoparticle catalysts for the selective hydrogenation of α , β -unsaturated ketones to α , β -unsaturated alcohols form. However, during catalysis side products, such as saturated ketones from C=C hydrogenation and saturated alcohols from further hydrogenation, have been reported. However with QCs, only the desired products are formed. Moreover, $\text{Au}_{25}(\text{SR})_{18}$ can catalyse hydrogenation reactions even at low temperatures (0°C), which is not possible with conventional Au nanoparticles. The catalytic reaction was carried out in the solution phase at 0°C (or room temperature). The reaction was initiated by introducing H_2 . Both free (unsupported) and inorganic oxide-supported $\text{Au}_{25}(\text{SR})_{18}$ catalysts for real applications were used. It was found that the metal oxides (e.g. Fe_2O_3 , TiO_2) supported QCs show higher yields, but with same complete selectivity for the unsaturated alcohol as for unsupported QCs. The catalysts were recyclable and retained their activity even after six cycles of catalysis. The QCs retained their structures and hence their characteristic properties, even after catalysis, which was evident from UV/Vis spectroscopy and mass spectrometry. A mechanism is proposed for the catalysis. Au_{25} QC possesses a core-shell structure (details are given in the Section 11.3). Out of the 20 triangular faces on the Au_{13} icosahedral core only 12 facets are face-capped by the exterior 12 Au atoms leaving the eight facets open. These vacant faces may act as active sites for C=O activation (details are given in Fig. 11.16). According to a recent theoretical study, the C=O group can coordinate to the surface atoms of Au_{13} QCs, and subsequent charge-transfer results in a negatively charged Au_{13} core. This kind of charge-transfer effect in this system leads to C=O activation.

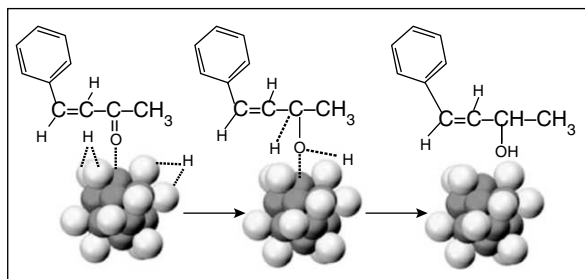


Fig. 11.16 The proposed mechanism of the chemoselective hydrogenation of α , β -unsaturated ketone to unsaturated alcohol catalysed by $Au_{25}(SR)_{18}$ QCs. For clarity, the thiolate ligands are not shown. Dark grey: Au atoms of the core; light gray: Au atoms of the shell (reprinted with permission from *Angew. Chem. Int. Ed.*, 49 (2010), 1295. Copyright (2010) John Wiley & Sons).

11.9 CONCLUSIONS

A new family of materials, called QCs, is presented. These materials show drastic difference in their chemical and physical properties compared to metallic nanoparticles due to their quantised electronic structure. They are often treated as a missing link between molecular and nanoparticle behaviours. There are numerous methods developed to synthesise both water and organic soluble QCs in large quantities. They show characteristic optical and absorption features. Some of the QCs show high quantum yield with good photostability, and hence, can be used in bio experiments, such as imaging. Even though extensive studies are not done to understand their chemical and physical properties in details, these materials are worth exploring due to their unique electronic structure. Possibility to produce these QCs in proteins and the use of them in bio-conjugation studies extend the scope of these materials.

REFERENCES

1. J. Zheng, P.R. Nicovich and R.M. Dickson, *Ann. Rev. Phys. Chem.*, 58, (2007), 409.
2. Y. Negishi, K. Nobusada and T. Tsukuda, *J. Am. Chem. Soc.*, 127, (2005), 5261.
3. J. Zheng, C.W. Zhang and R.M. Dickson, *Phys. Rev. Lett.*, 93, (2004), 077402.
4. P.A. Bartlett, B. Bauer and S. Singer, *J. Am. Chem. Soc.*, 100, (1978), 5085.
5. G. Schmid, R. Pfeil, R. Boese, F. Bandermann, S. Meyer, G.H.M. Calis and W.A. Vandervelden, *Chem. Ber.*, 114, (1981), 3634.
6. T.G. Schaaff, G. Knight, M.N. Shafiqullin, R.F. Borkman and R.L. Whetten, *J. Phys. Chem. B*, 102, (1998), 10643.
7. M. Zhu, H. Qian and R. Jin, *J. Am. Chem. Soc.*, 131, (2009), 7220.
8. M. Zhu, E. Lanni, N. Garg, M.E. Bier and R. Jin, *J. Am. Chem. Soc.*, 130, (2008), 1138.
9. H. Qian, M. Zhu, U.N. Andersen and R. Jin, *J. Phys. Chem. A.*, 113, (2009), 4281.

10. J. Xie, Y. Zheng and J.Y. Ying, *J. Am. Chem. Soc.*, 131, (2009), 888.
11. M.A. Habeeb Muhammed, S. Ramesh, S.S. Sinha, S.K. Pal and T. Pradeep, *Nano Research*, 1, (2008), 333.
12. H. Duan and S. Nie, *J. Am. Chem. Soc.*, 129, (2007), 2412.
13. H. Qian, M. Zhu, E. Lanni, Y. Zhu, M.E. Bier and R. Jin, *J. Phys. Chem. C.*, 113, (2009), 17599.
14. C-A.J. Lin, T-Y. Yang, C-H. Lee, S.H. Huang, R.A. Sperling, M. Zanella, J.K. Li, J-L. Shen, H-H. Wang, H-I. Yeh, W.J. Parak and W.H. Chang, *ACS Nano*, 3, (2009), 395.
15. Y. Shichibu, Y. Negishi and T. Tsukuda, *J. Am. Chem. Soc.*, 127, (2005), 13464.
16. M.A. Habeeb Muhammed, P.K. Verma, S.K. Pal, R.C. Arun Kumar, S. Paul, R.V. Omkumar and T. Pradeep, *Chem. Eur. J.*, 15, (2009), 10110.
17. R. Balasubramanian, R. Guo and A.J. Mills, *J. Am. Chem. Soc.*, 127, (2005), 8126.
18. Y. Shichibu, Y. Negishi, H. Tsunoyama, M. Kanehara, T. Teranishi and T. Tsukuda, *Small*, 3, (2007), 835.
19. H. Qian, Y. Zhu and R. Jin, *ACS Nano*, 3, (2009), 3795.
20. M.A. Habeeb Muhammed and T. Pradeep, *J. Clust. Sci.*, 20, (2009), 365.
21. A. Dass, A. Stevenson, G.R. Dubay, J.B. Tracy and R.W. Murray, *J. Am. Chem. Soc.*, 130, (2008), 5940.
22. M.A. Habeeb Muhammed and T. Pradeep, *Chem. Phys. Lett.*, 449, (2007), 186.
23. C.E. Briant, R.C. Brian, J.W. Theobald, L.K. White, D. Bell, M.P. Mingos and A.J. Welch, *J. Chem Comm.*, 5, (1981), 201.
24. G. Schmis, R. Boese, B. Pfeil, F. Andermann, S. Meyer, G.H.M. Calis and J.W.A. Van der Velden, *Chem. Ber.*, 114, (1981), 3634.
25. M. Zhu, C.M. Aikens and F.J. Hollander, *J. Am. Chem. Soc.*, 130, (2008), 5883.
26. P.D. Jadzinsky, G. Calero, C.J. Ackerson, D.A. Bushnell and R.D. Kornberg, *Science*, 318, (2007), 430.
27. O. Varnavski, G. Ramakrishna, J. Kim, D. Lee and T. Goodson, *J. Am. Chem. Soc.*, 132, (2010), 16.
28. G. Ramakrishna, O. Varnavski, J. Kim, D. Lee and T. Goodson, *J. Am. Chem. Soc.*, 130, (2010), 5032.
29. J.I. Gonzalez, T-H. Lee, M.D. Barnes, Y. Antoku and R.M. Dickson, *Phys. Rev. Lett.*, 93, (2004), 147402.
30. M.A. Habeeb Muhammed, A.K. Shaw, S.K. Pal and T. Pradeep, *J. Phys. Chem. C.*, 112, (2008), 14324.
31. M. Sakamoto, T. Tachikawa, M. Fujitsuka, and T. Majima, *J. Am. Chem. Soc.*, 131, (2009), 6.
32. E.S. Shibu, B. Radha, P.K. Verma, P. Bhyrappa, G.U. Kulkarni, S.K. Pal, and T. Pradeep, *ACS Appl. Mater. Interfaces*, 1, (2009), 2199.
33. R. Archana, S. Sonali, M. Deepthy, R. Prasanth, Habeeb Muhammed, T. Pradeep, S. Nair and K. Manzoor, *Nanotechnology*, 21, (2010), 055103.
34. M. Zhu, C.M. Aikens, M.P. Hendrich, R. Gupta, H. Qian, G.C. Schatz and R. Jin, *J. Am. Chem. Soc.*, 131, (2009), 2490.
35. M. Zhu, W.T. Eckenhoff, T. Pintauer and R. Jin, *J. Phys. Chem. C.*, 112, (2008), 14221.
36. P. Ramasamy, S. Guha, E.S. Shibu, T.S. Sreepasad, S. Bag, A. Banerjee and T. Pradeep, *J. Mater. Chem.*, 19, (2009), 8456.
37. Y. Zhu, H. Qian, B.A. Drake and R. Jin, *Angew. Chem. Int. Ed.*, 49, (2010), 1295.
38. M.A. Habeeb Muhammed, P.K. Verma, S.K. Pal, Archana, R., K. Manzoor, S. Nair and T. Pradeep, *Chem. Eur. J.*, 16, (2010), 10103.

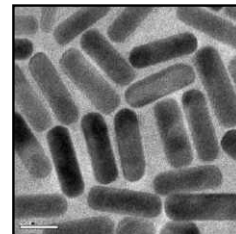
ADDITIONAL READING

1. R. Jin, *Nanoscale* 2 (2010), 343.
2. M.A. Habeeb Muhammed and T. Pradeep, 'Luminescent quantum clusters of gold as bio-labels, in Demchenko (Ed.), *Advanced Fluorescence Reporters in Chemistry and Biology*, Vol. II. Springer, Heidelberg, (2010), 333.

REVIEW QUESTIONS

1. What are quantum clusters?
2. How can such materials be made?
3. Why are they considered important?
4. What are their applications?
5. What are the unusual properties of these materials?

NANOPARTICLE CRYSTALS



“I am among those who think that science has great beauty. A scientist in his laboratory is not only a technician: he is also a child placed before natural phenomena which impress him like a fairy tale.”

Marie Curie, *Madame Curie: A Biography* by Eve Curie Labouisse, as translated by Vincent Sheean, The Literary Guild of America INC, New York (1937) page 341

Nanoparticle crystals or superlattices (SLs) are three-dimensional arrangements of nanoparticles in the micrometer regime. In SLs, the particles are periodically arranged with long-range order, and hence they show collective properties, such as inter-plasmon coupling (in the case of metal particles), metal to insulator transition, etc. Various spectroscopic, scattering and imaging techniques have been used to understand the structure of self-assembled 3-D SLs. This chapter includes various methodologies for fabrication of 3D SLs, their characterization, properties and applications. Most of the discussion will be on metal particle SLs, but other systems will also be discussed.

Learning Objectives

- Why self-assembly of noble metal particles?
 - Why collective and enhanced properties are shown by self-assembled crystals?
 - What are the important techniques for self-assembly?
 - What are particle crystals and what are their properties?
-
-

12.1 INTRODUCTION

Just as periodic arrangement of atoms produce the crystalline state of matter, periodicity of particles produces particle crystals. As crystals are viewed as bulk solids, particle crystals may be viewed as “artificial solids”.¹ Nanomaterials, in general, are man-made, and therefore, artificial solids describe synthetic materials of a new kind. The collective properties of SL crystals emerging from individual nanoparticle building blocks help us to understand the electronic effects, such as metal–insulator

transitions and changes in optical properties, such as inter-plasmon coupling. Hence, one could control the growth of these SLs, which will open up new kinds of materials for advanced applications. Diversity in nanoparticles is reflected in particle crystals as well. Both isotropic and anisotropic nanoparticles can produce artificial solids. Metallic, semiconducting and insulating nanoparticles make particle crystals. These may also be made from mixed particles of different kinds. In view of all these diverse properties, particle crystals present numerous avenues for exploration. Their structural, spectroscopic and physical properties and theoretical understanding have produced a wealth of data in the past several years. In this review, we present a bird's eye view of the results in this area.

Hierarchical self-assembly of nanoparticles into 2-D or 3-D SL helps us to manipulate the structures with enhanced and tunable quantum confinement effects. Self-assembled 3-D structures are new classes of nanomaterials, which open up diverse and potential applications in different areas, such as light emitting diodes,² solar cells,³ molecular electronic architectures,⁴ high-density data storage,⁵ catalysis,⁶ biochemical sensors,^{7,8} biocompatible materials,⁹ and so on. Remarkable interest in particle SLs is due to the collective properties of the building blocks, which help us to understand electronic effects, such as metal-insulator transition and changes in magnetic and optical properties.^{10,11} One could possibly control the assembly of such organised solids, which opens up new opportunities for fundamental studies as well as engineering advanced materials. Moreover, crystal structure of nanoparticle SLs is strongly affected by the geometrical shape of the adjacent nanoparticles.

One can see a wide verity of self-assembled systems in nature, such as DNA, proteins, cell membranes, etc. Even though individual atoms or molecules are fundamentally interesting and important, when they are self-assembled into 3-D superstructures, such organisations impart various specific functions. Like atomic or molecular self-assembly, nanoparticles themselves can act as building blocks for 3-D arrays. Among the nanoparticles, noble metal nanoparticles and their self-assembly have been investigated by in detail. The reason behind this could be the easiness of synthesis, biocompatibility and tunable optical properties.

One of the straightforward approaches for the construction of 2-D or 3-D SLs being exploited is the bottom-up assembly technique, which includes electrostatic self-assembly of oppositely charged nanoparticles of narrow size distribution,¹² evaporation of the solvent on a substrate,^{1,13-24} self-organisation of nanoparticles at interfaces,²⁵⁻²⁸ crystallisation of nanoparticles from nanoparticle solutions by precipitation or sedimentation,^{10,29} wet deposition by supramolecular interactions between the nanoparticles and surfaces,³⁰⁻³² and self-assembly of nanoparticles into micro-dimensions through hydrogen bonding.³³⁻⁴⁰

The term 'SL' is reminiscent of semiconductor thin films, which present characteristic diffraction patterns in XRD. Here, two or more materials are stacked periodically, which show two different periodicities. In typical structures, the layer thicknesses are of the order of nanometers. Unusual mechanical strength and novel electronic properties can be obtained in such structures. In the present context, this refers to the arrangement of nanoparticles so that two distinct periodicities occur. The SL has the periodicity of the particles and the particles themselves have periodicity of the atoms or the constituent species. These SLs have distinct diffraction patterns and the periodicity can also be observed in electron microscopic imaging.

This chapter provides an overview of the various methods used to synthesise 3-D SLs of metals, semiconductors, binary nanoparticle SLs of metal–metal, metal–semiconductor and semiconductor–semiconductor systems. We will also discuss the use of several techniques for the characterisation of 3-D SL arrays.

1. High resolution transmission electron microscopy (HRTEM)
2. Small angle X-ray scattering (SAXS)
3. Scanning electron microscopy (SEM)
4. UV/VIS/NIR absorption spectroscopy
5. Raman spectroscopy
6. Atomic force microscopy (AFM)
7. Confocal fluorescence microscopy
8. FT-IR absorption spectroscopy

12.2 3-D SUPERLATTICES (SLs) OF METALS

3-D self-assembly of metal nanoparticles is achieved using different methods, such as

1. Digestive ripening and solvated metal atom dispersion method (SMAD)
2. Hydrothermal method
3. Solvothermal method
4. Electrostatic self-assembly of oppositely charged nanoparticles
5. Hydrogen bonding method

12.2.1 Digestive Ripening and Solvated Metal Atom Dispersion Method (SMAD)

The key to the synthesis of SLs is monodispersity of the particles. In a typical synthesis approach, performed in solution, there is a large polydispersity. This had to be brought down to 5 per cent by a suitable method. One approach is to make the particles first and subject them to a process by which monodispersity is achieved. A successful method for this is digestive ripening. Selecting specific sizes by appropriate separation, such as centrifugation and varying solvent polarity leading to size selective precipitation are other approaches, SMAD is another approach, wherein particles are prepared in monodispersed form.

Both of the methods were used to make thiol protected gold and silver nanoparticles with high monodispersity. In the first case, the HAuCl_4 were transferred to toluene by a reaction which phase transfers Au^{3+} to the organic phase. The addition of dodecane thiol to this solution will lead to the formation of Au(I) thiolate complex. Finally, this complex is reduced by NaBH_4 using a two-phase reduction method. The nanoparticle suspension in toluene was heated at 95 °C for 1h. This will result in the formation of highly monodisperse particles. This method of heating nanoparticles at the

reflux temperature of solvent to make highly monodisperse nanoparticles is known as the digestive ripening. In the second method, the vapours of bulk metals were allowed to put down on the surface of frozen dodecane thiol-toluene mixture inside a reaction chamber. This will lead to the nucleation of nanoparticles. The nanoparticles formed by these two methods are highly monodisperse and hence they have a large tendency to self assemble into 3-D superstructures.^{21,24}

In the digestive ripening method, the nanoparticle suspension in toluene is heated up to the boiling point of the solvent in presence of surface active ligands, such as octyl-, decyl-, dodecyl- and hexadecyl thiols. The colloids remain in suspension above 80°C. However, once it is cooled to room temperature, nanoparticles tend to precipitate and will result in 2-D or 3-D SLs. The extent of arrangement is mainly determined by the length of the alkyl thiols. Klabunde and Prasad have developed these kinds of SLs and these have been reviewed recently.⁴¹ Their studies reveal that dodecanethiol capped nanoparticles form uniformly arranged 3-D SLs. Most of the crystals formed here are triangular, truncated triangular and hexagonal in shape (Fig. 12.1A-D). The sharp edges and distinct shapes suggest the formation of crystals. The edges of these crystals are sufficiently thin, so that electron transmission is adequate to collect images of ordered particles. The long-range order of nanoparticles is shown in Fig. 12.1E with *fcc* packing. The transmission is not significant when multiple layers of particles are present. Solvent evaporation method was used to make 3-D SLs of nanoparticles made by SMAD method. Here, the nanoparticles were dispersed in toluene and dropcasted on the surface of the TEM grid. The solvent was allowed to evaporate under ambient conditions. Here, particles show long-range periodic order with *hcp* packing (Fig. 12.1F) due to the irregular number of ligands per nanoparticles. Generally, the crystal or the film exposes the dense (111) plane.

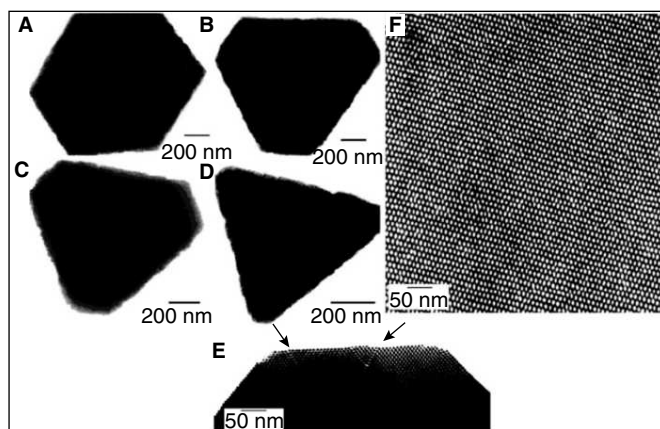


Fig. 12.1 (A–D) TEM images of different morphological crystals formed by the digestive ripening method. (E) High-resolution TEM image of SL crystals taken from the edge of one crystal showing long range order with *fcc* packing. (F) High-resolution TEM image of SL crystals developed by the evaporation of solvent (using SMAD nanoparticles). Two arrows show the dislocations in SL crystal (adapted from Refs. 21 and 24).

12.2.2 Hydrothermal Method

This is one of the fastest and *in-situ* methods for the fabrication of 3-D SLs. This uses a hydrothermal bomb. Photograph of such a bomb is shown in Fig. 12.2-I. Here, silver nanoparticle SLs were synthesised by heating silver nitrate solution in presence of binary ligands, such as sodium oleate and different

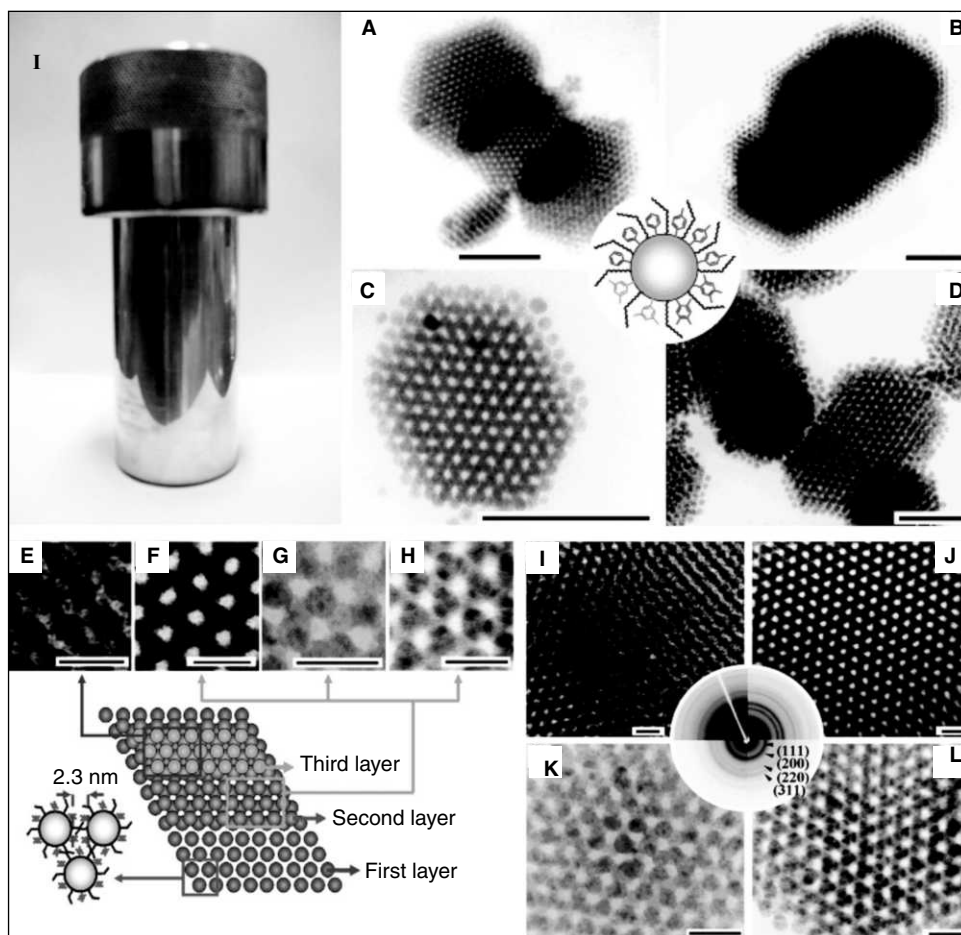


Fig. 12.2 (I) Photograph of a hydrothermal bomb. (A–D) TEM images and schematic drawing of Ag nanoparticles capped with a mixture of two capping molecules, sodium oleate and aromatic carboxylic acid; (A) benzoic acid (blue), (B) 1,4-benzenedicarboxylic acid (red), (C) 1,3,5-benzenetricarboxylic acid (grey), and (D) 1,2,4,5-benzenetetracarboxylic acid (violet). All scale bars represent 97 nm. (E–L) High-resolution TEM images and corresponding electron diffraction patterns of all the above four SLs, respectively. Schematic representation of Ag nanoparticles with two different capping molecules, view of the topology of one, two and three layers of Ag nanoparticles with mixture of capping molecules are also shown (adapted from Ref. 42). (For clarity see colour figure.)

aromatic carboxylic acids, such as benzoic acid (blue), 1,4-benzenedicarboxylic acid (red), 1,3,5-benzenetricarboxylic acid (grey) and 1,2,4,5-benzenetetracarboxylic acid (violet) at 110°C for 12 h. The SLs were characterised by HRTEM, formed with all aromatic carboxylic acids (Fig. 12.2 A-D). High-resolution TEM images and corresponding electron diffraction patterns (ED) of all these four SLs are given in Fig. 12.2 (E-L). Schematic representation of Ag nanoparticles with two different capping molecules, view of the topology of one, two and three layers of Ag nanoparticles with mixture of capping molecules are also shown. By using this method, Kang and *et al.* developed a new strategy for the fabrication of Ag nanoparticle SLs in the aqueous phase with narrow particle size distribution. In the mixture of two capping molecules, a SL of Ag nanoparticles is easily obtained without any post-procedure because of the double capping layer. This new one-step hydrothermal synthetic method for preparing SL reduces time-consuming and multi-step synthetic procedures.⁴²

The same method has been adopted for the fabrication of gold SLs using the method mentioned above.⁴³ Here, the binary ligands were replaced by trisodium citrate and cetyltrimethylammonium bromide (CTAB) surfactant, respectively. The experimental protocol was slightly altered from the initial method, which resulted in differently-sized octahedral gold crystals. For this, 9.7 mL of ultrahigh purity water, 0.055 g of CTAB, 250 μL of 0.01 M HAuCl_4 and 50 μL of 0.1 M trisodium citrate were added to a glass vial with a teflon-lined polypropylene cap and a volume capacity of 22.5 mL. CTAB concentration in the final solution was 1.51×10^{-2} M. The oven temperature was set at 110°C. Sample vials were loaded into the oven after it had reached this temperature. The samples were heated in five different temperatures such as 6, 12, 24, 48 and 72 h. After that, the vials were removed from the oven and cooled naturally to room temperature. By changing this temperature window, authors were able to harvest five differently-sized gold octahedral crystals with particle size of 31, 57, 89, 119 and 150 nm, respectively. As particle size of the octahedral gold nanocrystals increases, the surface plasmon resonance (SPR) band red-shifts from 543 to 635 nm. Presence of oxygen in this closed system may act as an oxidizing agent ($\text{O}_2 + 4\text{H}^+ + 4\text{e}^- = 2\text{H}_2\text{O}$), which slowly dissolves gold atoms into the solution ($\text{Au} + 4\text{Cl}^- = \text{AuCl}_4^- + 3\text{e}^-$). This side reaction makes gold nanocrystal growth extremely slow. Because of the slow reaction rate under the present hydrothermal synthesis conditions and in the absence of other structure modifying ions, octahedra and thick triangular nanoplates with entirely $\{111\}$ faces are considered to be the thermodynamically favourable product structures. In addition to this, presence of trisodium citrate also enhances the formation of the (111) planes. Another important factor governing the preferential growth of octahedral nanocrystals is the molar ratio of $[\text{CTAB}]/[\text{HAuCl}_4]$. By changing this molar ratio, it is possible to control the size and shape of the nanocrystals.

The SL crystals of gold octahedra discussed above are developed by the self-evaporation on a substrate. The particles of five different sizes assemble in three different ways. For the type I self-assembled structure, octahedra contact each other by their faces to form a close-packed monolayer, and the second layer has the same packing arrangement as the first layer. Because of the lack of strong forces or interactions between the layers, formation of just 2–3 layers is typically observed. This type of self-assembled structure is observed for octahedra of 90–150 nm. Type II self-assembled structure is distinctly different from that of type I structure. In order to establish type II self-assembled structure,

the octahedra should spend more time in the droplet before evaporation to build such a long-range structure. Hence, only smaller and lighter octahedral gold nanocrystals with sizes in the range of 30–60 nm were observed to form type II structure. Type III self-assembled structure is closely related to type II structure, but with their corners contacting the substrate surface. The 3-D packing arrangement is the same as that observed for the type II structure, but as the array is formed in the solution, the octahedra have their corners pointing towards the substrate. The type III structure is seemingly unstable and can only exist as large arrays for stability reason, and only octahedra with sizes of <60 nm (sample B) exhibit type III superstructure. SEM images of these three types of arrangements and their schematic illustrations are shown in Fig. 12.3.

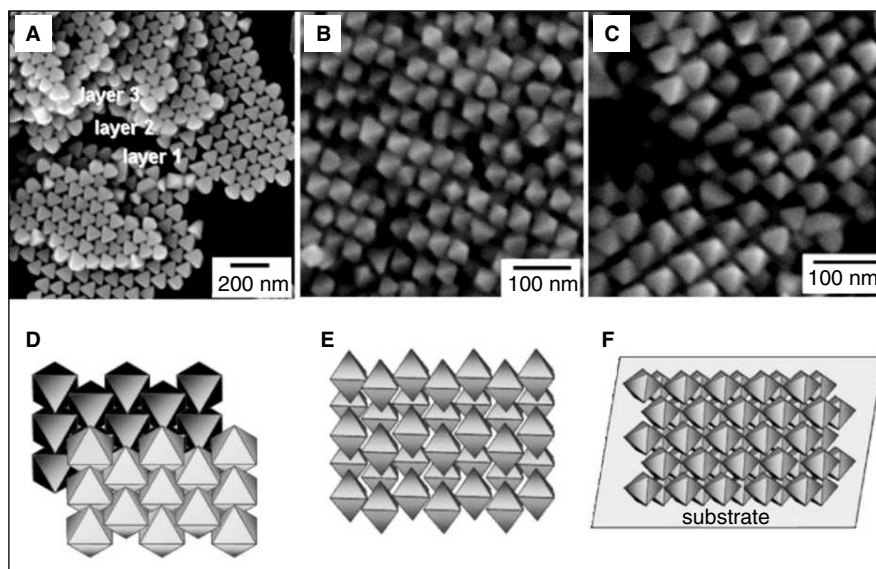


Fig. 12.3 (A, B and C) SEM images of the three types of self-assembled structures of the octahedral gold nanocrystals with particle sizes of (A) 120 and (B, C) 60 nm. (D, E and F) Cartoon representations of the three types of nanocrystal packing (adapted from Ref. 43).

12.2.3 Microwave-Assisted Solvothermal Method

This method was developed by S. Komarneni in 2005.⁴⁴ Solvothermal is a one-step interfacial method for the fabrication of 3-D SLs using a microwave irradiation approach. In this process, dodecylthiol was used as a structure-directing agent, and simple compounds, such as AgNO_3 and ethylene glycol, as reactants were used directly. Toluene was added to form an interface pre-synthesis of initial silver nanoparticles or precursor and the technique of size-selective precipitation are not required. This method shows its applicability in the direct synthesis and assembly of Ag_2S nanoparticles by simply changing ethylene glycol to an aqueous solution of thiourea (Fig. 12.4A-D). Here, dodecylthiol is the assisting agent for the assembly of silver nanoparticles. Ethylene glycol and toluene are immiscible and

form two layers with an interface when they are mixed. Dodecylthiol could be dissolved in toluene with the polar group projecting toward the polar solvent, in this case, ethylene glycol. The thiol group of dodecylthiol reacted with silver ions at the interface to form an inorgano-organic complex, which was reduced to elemental silver by ethylene glycol under microwave solvothermal conditions.

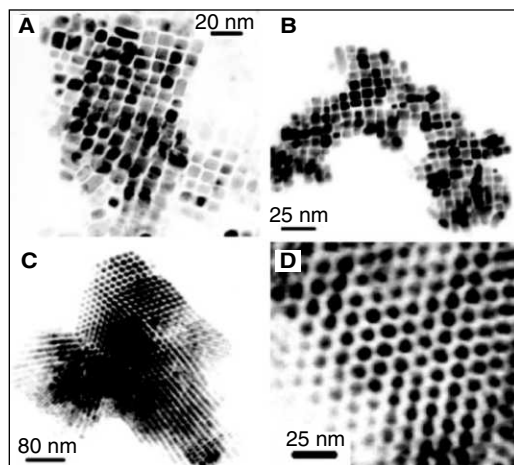


Fig. 12.4 (A and B) TEM images of the sample prepared at low ratio of ethylene glycol to dodecylthiol. (C and D) TEM images of the silver sulphide sample prepared with thiourea as the sulphur source (adapted from Ref. 44).

12.2.4 Electrostatic Self-assembly of Oppositely Charged Nanoparticles

This method was reported by Grzybowski in 2006,¹² in which self-assembly of charged, equally-sized metal nanoparticles of two types (gold and silver) leads to the formation of large, sphalerite (diamond-like) crystals, in which each nanoparticle has four oppositely charged neighbours. Formation of these non-close-packed structures is a consequence of electrostatic effects specific to the nanoscale, where the thickness of the screening layer is commensurate with the dimensions of the assembling objects. Because of electrostatic stabilisation of larger crystallising particles by smaller ones, better-quality crystals can be obtained from more polydisperse nanoparticle solutions. Here, silver and gold nanoparticles were synthesised with ω -functionalised alkane thiols $\{\text{HS}(\text{CH}_2)_{10}\text{COOH}(\text{MUA})\}$ and $\{\text{HS}(\text{CH}_2)_{11}\text{NMe}_3^+\text{Cl}^-(\text{TMA})\}$, with an average hard sphere diameter of 4.8 and 5.1 nm, respectively, so that overall diameter of both of the particles comes around 8.5 nm (Fig. 12.5A-C). Both types of NPs were stable and unaggregated when kept in separate aqueous solutions. At the concentration used (2 mM), the pH of Au@MUA solution was 9.7; so, the NPs presented deprotonated carboxylate groups, and the ratio of NP charges was $Q(\text{Ag@TMA})/Q(\text{Au@MUA}) = -0.90$. When the solutions were mixed, the positively charged Ag@TMAs interacted with the negatively charged Au@MUAs. This charge neutralisation led to the formation of soluble small aggregates, which will precipitate

rapidly when the molar ratio of nanoparticles is nearly unity and overall charge of nanoparticles is neutralised.

One problem that could occur here is the presence of excess of ammonium salt along with the crystals obtained from the nanoparticle precipitate, which may hinder the crystallisation process. This can be avoided by washing the crystals using ultra high pure water. Subsequently, the precipitate was dissolved in a 1:4 v/v mixture of water and dimethyl sulphoxide (DMSO), and crystals were grown by slow (12 h) evaporation of water at 70°C. This procedure yielded large numbers of regularly faceted crystals, each composed of several million NPs and with dimensions up to 3 mm in each direction (Fig. 12.5D).

Structure of these crystals was solved by small angle XRD (SAXS), which shows three distinct peaks located at $2\theta = 0.801^\circ$, 1.308° and 1.539° (Fig. 12.5F). This diffraction pattern characterises the sphalerite [or diamond] structure with a lattice constant, $a = 19.08 \pm 0.53$ nm and the peak positions correspond to Bragg reflections from (111), (220) and (311) planes, respectively. The lattice constant agrees with the value of $a \sim 18.5$ nm, obtained from scanning electron microscopy (SEM) measurements (Figures 12.5G and H). Scheme of an AB unit cell and the projections of $\{100\}_{SL}$, $\{110\}_{SL}$, $\{111\}_{SL}$ planes are shown in Fig. 12.5(I).

12.2.5 SL Crystal Formation at Air–Water Interface by Hydrogen Bonding Method

This method was reported by K. Kimura,^{33, 34} using mercaptosuccinic acid (MSA) capped gold nanoparticles. The gold nanoparticles passivated with dicarboxylic acid (MSA) provide OH functionality, which induces hydrogen bonding. Carboxylic acids tend to form dimers through hydrogen bonding, hence the hydrogen bonding among the OH group is assumed to be the force that connects the nanoparticles in the SL crystals. However, for thus prepared nanoparticles, the pH will be around 9–10 due the reason that all carboxylic acid groups will be in the carboxylate form. Under this circumstance, there is no possibility of hydrogen bonding among the adjacent nanoparticles. The problem was solved by adding 6 M HCl to the nanoparticle suspension. It has been optimised by trial and error method that the pH range, at which the crystals are growing, is around 1. In a typical protocol, the clean nanoparticles are dissolved in water (30 mg/mL) and the pH of the nanoparticles was adjusted to 1 by using 6 M HCl. The acidic nanoparticle solution was left undisturbed for a week, in the dark at a temperature below 25 °C in a styrofoam container. After storage for 7 days, crystallisation was noticed at the air/water interface. A formation of film with a brown mirror-like appearance indicates the formation of gold nanoparticle SLs. The quality of the SL crystals will be poor in the beginning stage of film formation and a minimum of 2–3 weeks are required for the formation of quality crystals, which gave a metallic appearance. This may be because nanoparticles take time to diffuse at the growing interface to form an ordered assembly. Fig. 12.6A-B show the structure of the ligand and a cartoon representation of Au@MSA nanoparticles showing hydrogen bonding, respectively. During the crystal formation, particles tend to make different morphologies, such as triangle, hexagons, etc. (Fig. 12.6C). In both of these morphologies, the minimum energy (111) plane is predominant. The

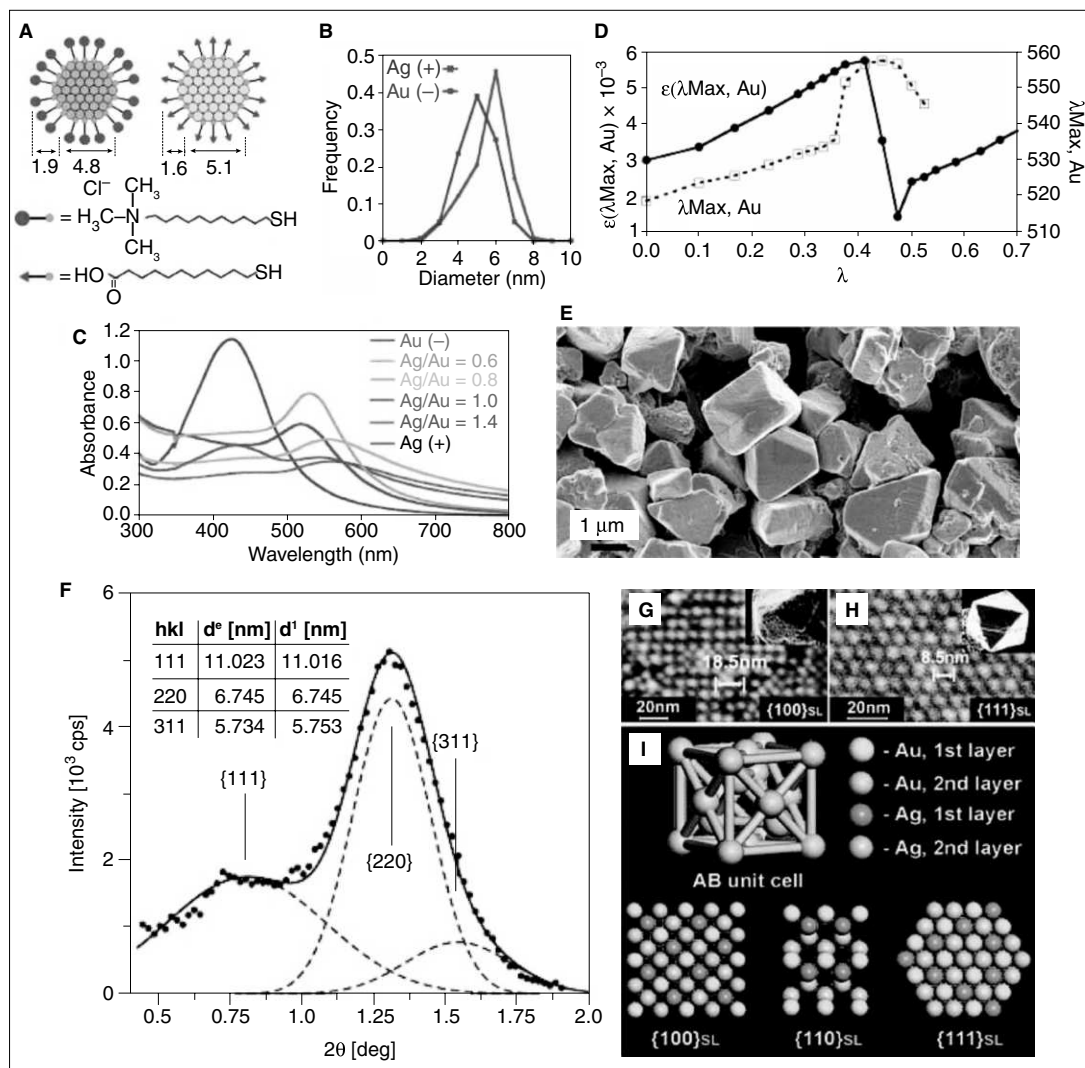


Fig. 12.5 (A) Scheme and average dimensions (in nm) of Au@MUA and Ag@TMA nanoparticles used as the model system. (B) Experimental, normalised size distributions of metallic cores of Ag and Au NPs (C) Typical UV-Vis spectra for the titration of Au@MUA solution with small aliquots of Ag@TMA solution. (D) (Solid curve) Progress of the titration represented by absorption coefficient $\epsilon(\lambda_{\text{max}}, \text{Au})$. (E) Large-area SEM image of binary crystals obtained from Au@MUA/Ag@TMA precipitates. (F) Small-angle powder XRD spectrum of the crystals. Bragg's reflections specified by Miller indices shown are characteristic of a diamond-like structure. (Inset) Comparison between experimental (d^e) and theoretical (d^t) spacing between crystal planes with Miller indices $\{hkl\}$. (G) An SEM image of a {100}_{SL} square face taken from a twinned octahedron crystal (inset). (H) An SEM image of a {111}_{SL} plane of a triangular face of an octahedron (inset) with estimated interparticle distance of 8.5 nm. (I) Scheme of an AB unit cell and the projections of {100}_{SL}, {110}_{SL}, {111}_{SL} planes (adapted from Ref. 12). (For clarity see colour figure.)

first step of SL formation is the creation of an island by the ordered arrangement of nanoparticles. The reason for the formation of epitaxial thin films at the interface can be attributed to the high tendency of heterogeneous nucleation at the interface. During the crystal formation by the hydrogen bonding method, there is a possibility of inclusion of water molecules within the crystals. This can be proved by FT-IR, since OH vibrational stretching modes have relatively high frequencies, which are largely isolated from IR bands of other chemical bonds.

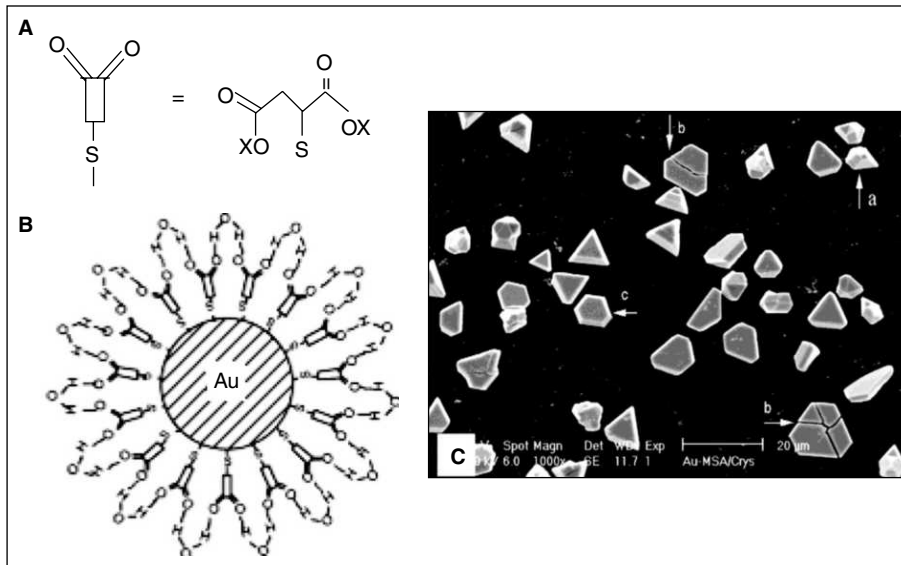


Fig. 12.6 (A) The molecular structure of MSA. (B) Cartoon representation hydrogen bonding in Au@MSA nanoparticles. (C) Large area SEM image of gold particle crystals (adapted from Refs. 33 and 34).

The same group developed five-fold symmetric crystals of Au@SGAN (N-acetyl glutathione protected nanoparticle) by the same protocol at the air–water interface.³⁴ Morphological studies revealed that the SLs formed five-fold symmetric structure, such as pentagonal rod, decahedron and icosahedron, which were probably developed by multiple twinning. Moreover, high-resolution surface images of the SLs with five-fold symmetry showed excellent ordered arrangements of nanoparticles with both close-packed and non-close-packed structures. Fig. 12.7(A–D) show different five-fold symmetric crystals formed during the synthesis. Stacking of the nanoparticles in SLs can be studied using SAXS measurements. Fig. 12.7E shows the SAXS data, which indicate that the nanoparticles in SLs are stacked in *fcc* rather than *bcc*. From the SAXS, we will get more information about the lattice constants. This helps to compare with TEM and SEM data. Thickness of the SLs made by hydrogen bonding method is around 100 nm. This will restrict the TEM analysis of these kinds of systems. However, one could carefully analyse the HRTEM of these systems by choosing the right areas such as edges.

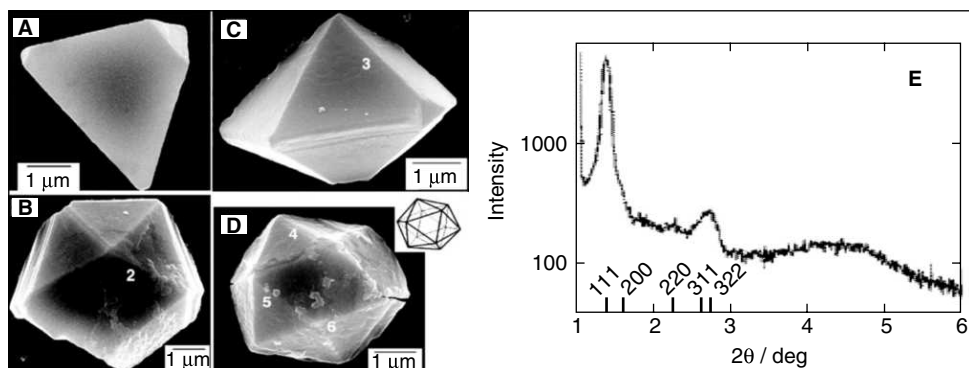


Fig. 12.7 SLs of (A) tetrahedral, (B) pentagonal rod-like, (C) decahedral and (D) icosahedral shapes. The inset in (D) shows the geometrical model of an icosahedron in the same orientation. (E) Small-angle XRD profile of the SL sample shows a long-range periodicity caused by the formation of ordered arrays of gold nanoparticles (adapted from Ref. 37).

However, one of the drawbacks of the air–water interfacial method is the time required for crystal formation; it is of the order of 2 months for the formation of high-quality crystals at the air–water interface. However to bring these 3-D nanostructures into application levels, materials should be available in gram scale and the method should be cheap. In this context, we developed a new method for the large-scale synthesis of 3-D SL of gold nanoparticles in a short time period at a liquid–liquid interface under flowing nitrogen gas.⁴⁰ Here the crystals were synthesised using a simple set-up, which is shown in scheme 3. It consists of an airtight plastic box with an inlet and an outlet. A nitrogen cylinder was connected to the inlet through a silicon tube. The gas exit was fitted with a paraffin oil trap. Using this method, authors developed Au@MSA and Au@SGAN SLs in gram scale in a shorter time. The protocol is almost similar to an earlier method reported by Kimura.^{33–39} Here, both of these nanoparticles are dissolved in water separately and pH of the solution is adjusted as in the earlier report. To this acidic nanoparticle dispersion, 5 mL of toluene was added and solution was kept inside the set-up described above under nitrogen atmosphere (stage 1). The paraffin oil-filled bubbler indicated a flow of two bubbles per second. The samples were left undisturbed for 2 days, in dark at a temperature below 25°C. The crystal formation started within a few hours at the toluene–water interface. Within 24 h, all the toluene evaporated and the SL films began to form on top of the aqueous layer (stage 2). A thick film with mirror like appearance was seen within 48 h, indicating the formation of gold nanoparticle SLs with micrometer dimensions (stage 3). Different stages of the crystal formation have been photographed and are given along with the setup in Fig. 12.8A. The top views of the grown SL film were also photographed and one picture is given in Fig. 12.8A (stage 3). Here, the constituent gold nanoparticles are stacked in a *fcc* pattern rather than *hcp* in the 3-D array, in both cases. In the case of Au@MSA, (111), (220) and (222) reflections appear as expected, and the (200) and (311) reflections are weak. Fig. 12.8B shows the shows intensity vs 2θ data obtained after background and baseline corrections (Au@SGAN and Au@MSA SLs). Fig. 12.8C and D show the HRTEM images of Au@SGAN and Au@MSA SLs fabricated by the rapid method. In both cases, the particles show a

truncated octahedral (TO) shape with $\{100\}$ and $\{111\}$ facets, which are shown in the insets of the figures. In the images, a $[110]_{\text{SL}}$ projection of the unit cell of the SL is represented by a rectangular box, where the subscript SL refers to the SL.

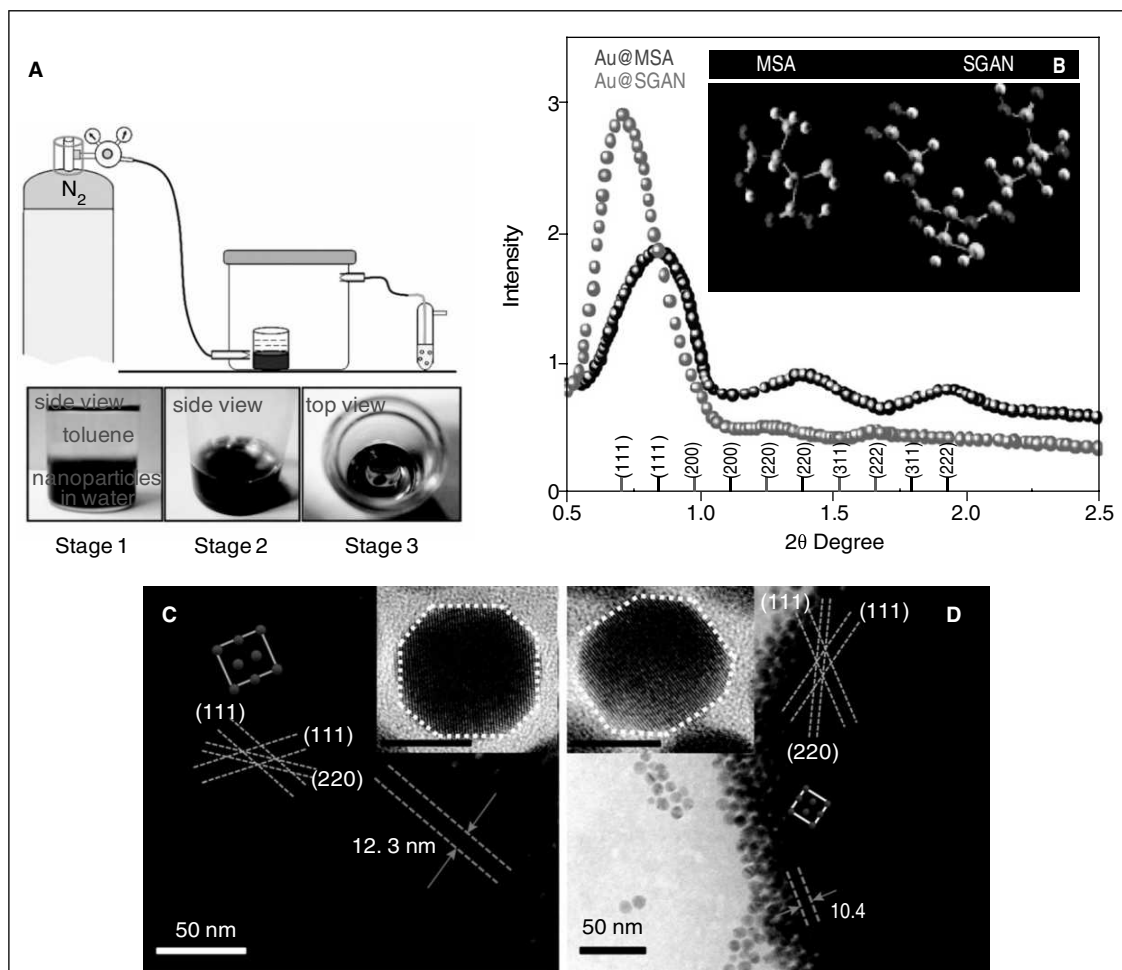


Fig. 12.8 (A) Cartoon representation of the setup used for the SL Formation. The photographs show different stages of crystal formation (stage 1 and 2). The top view of the SL crystals (stage 3) clearly shows a continuous film at the interface. (B) Background and baseline corrected intensity vs 2θ data of Au@SGAN and Au@MSA SLs, respectively. The indexing is done for a fcc unit cell in both cases. The inset shows the energy minimum structure of MSA and SGAN. (C and D) HRTEM images of Au@SGAN and Au@MSA SLs, respectively. The inset of each figure shows the truncated octahedral shape of the nanoparticles with $\{100\}$ and $\{111\}$ facets (adapted from Ref. 40). (For clarity see colour figure.)

It is possible to extend the hydrogen bonding method for the fabrication of MSA and SGAN capped silver nanoparticles also. Of these two systems, Ag@SGAN is less stable compared with Ag@MSA. Moreover, addition of HCl to Ag nanoparticles will lead the decomposition of nanoparticles. Overcoming these problems, the same group proposed a method for the fabrication of Ag nanoparticle SLs. They modified the old method to a vapour diffusion technique.³⁶ In this method, the aqueous suspension of Ag@MSA nanoparticles were synthesised by the NaBH₄ reduction method to yield particles of 5.8 nm average diameter. The HRTEM image of such nanoparticles is given in Fig. 12.9A. The schematic representation of Ag@MSA nanoparticles are given in Fig. 12.9B. The nanoparticles were kept in one vial (vial A) and HCl was kept in other vial (vial B) and both of the vials were kept in a styrofoam container (Fig. 12.9C). As the time progresses, the HCl vapours diffuse into the surface of the nanoparticle suspension, which will result in the self-assembly of nanoparticles into 3-D microstructures. An experiment reveals that, diffusion of 6M HCl results high quality crystals. Fig. 12.9D-F shows the 3-D rhombic SL crystals with 6 M Hcl at different time periods.

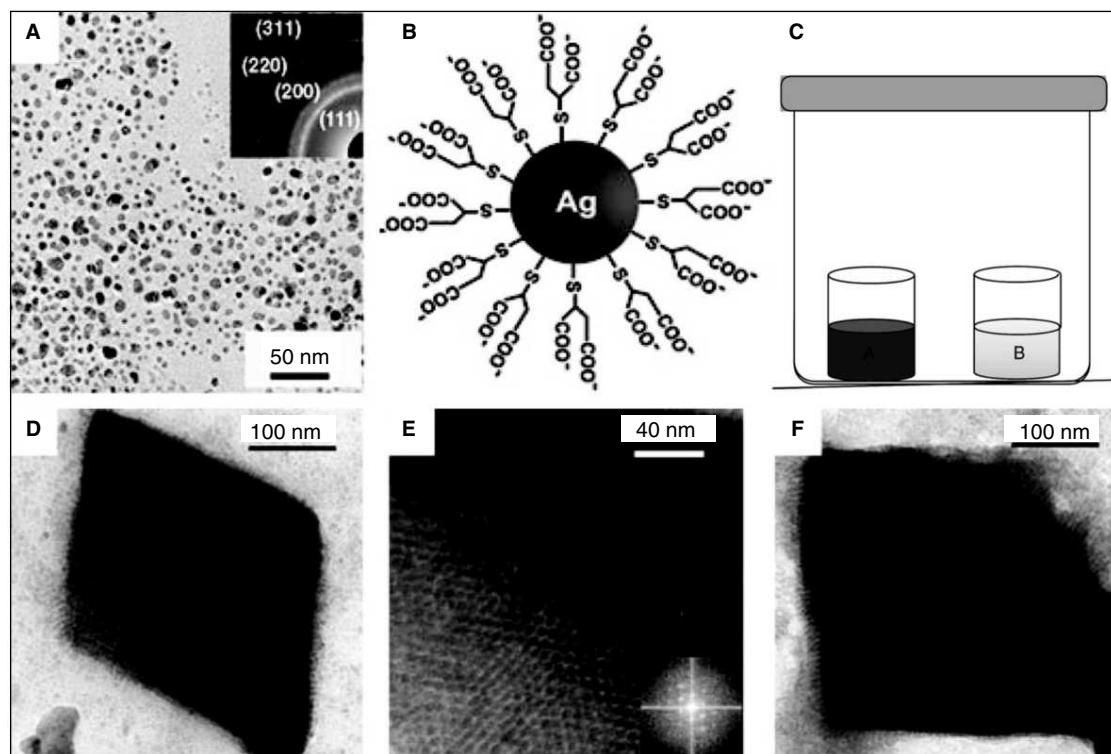


Fig. 12.9 (A) TEM image of as-prepared MSA-capped Ag nanoparticles. The inset shows the corresponding SAED pattern. (B) Model of an MSA-capped Ag nanoparticle. (C) Cartoon representation of the set-up used for the vapour diffusion method. (A) and (B) correspond to the nanoparticle dispersion and acid, respectively. (D–F) HRTEM images of 3-D rhombic SLs imaged at different time periods (adapted from Ref. 36).

12.3 SEMICONDUCTORS

In this section, we discuss the 3-D self-assembly of semiconductor nanoparticles using different methods such as

1. Precipitation or sedimentation
2. Evaporation of solvents

12.3.1 Precipitation or Sedimentation

This method was first reported by H. Weller in 2001.²⁹ Here, two types of CdSe nanocrystals were prepared by the method of controlled oversaturation in solutions. The growth technique was based on slow diffusion of a non-solvent (methanol) into the bulk of a concentrated solution of monodisperse CdSe nanocrystals in toluene. However, the direct contact of non-solvent and toluene resulted in the fast diffusion of nanoparticles that produced irregular morphology. The fast diffusion of non-solvent was controlled by the addition of a buffer layer of propan-2-ol, which results in perfectly faceted hexagonal platelets with sizes of about 100 nm, depending on the conditions of crystal growth. The schematic of the technique (Fig. 12.10A) and optical images of the crystals formed in two different methods are given (Fig. 12.10B and C). In quantum dot solids formed this way, individual CdSe nanocrystals playing the role of building blocks (artificial atoms in the next level of hierarchy) are aligned in a regular *fcc*-like 3-D SL, as confirmed by TEM (Fig. 12.10D and E).

12.3.2 Evaporation of Solvents

Here, the faceted SLs are obtained from saturated solutions of CdSe nanocrystals (3.5 and 5.3 nm, separately) in presence of nonanoic acid.⁴⁵ To prepare saturated solutions for the growth of SLs, dry powder of NCs was added to nonanoic acid (NA) in excess such that the solid did not dissolve completely after intensive stirring. Saturated solutions were separated from the solid by centrifuging and were deposited as drops on optical microscope glass slides and on gold TEM grids. The liquid was allowed to evaporate slowly. The slow evaporation of NA is also accelerated by short-term exposure of the slides to vacuum. Here, reproducible crystal growth is promoted by low solubility, slow solvent evaporation and a size-selective effect. Different morphological crystals formed in this method are analysed by optical imaging technique (Fig. 12.11A). Fluorescent crystals, which are emitted at different wavelengths (red and green) formed by differently-sized nanoparticles, are also analysed by fluorescence imaging technique (Fig. 12.11B and C). The HRTEM and wide-angle as well as small-angle electron diffraction showed that each individual SL is composed of nanocrystals of uniform size assembled into an *fcc* lattice (Fig. 12.11D-K).

12.4 OTHER IMPORTANT SLS

12.4.1 Cu₂S SLs

Cu₂S is also known as chalcocite, which is a p-type semiconductor with a bulk band gap of 1.2 eV. Cu₂S has an anisotropic hexagonal crystal structure, and the arrangement of atoms along the c-axis

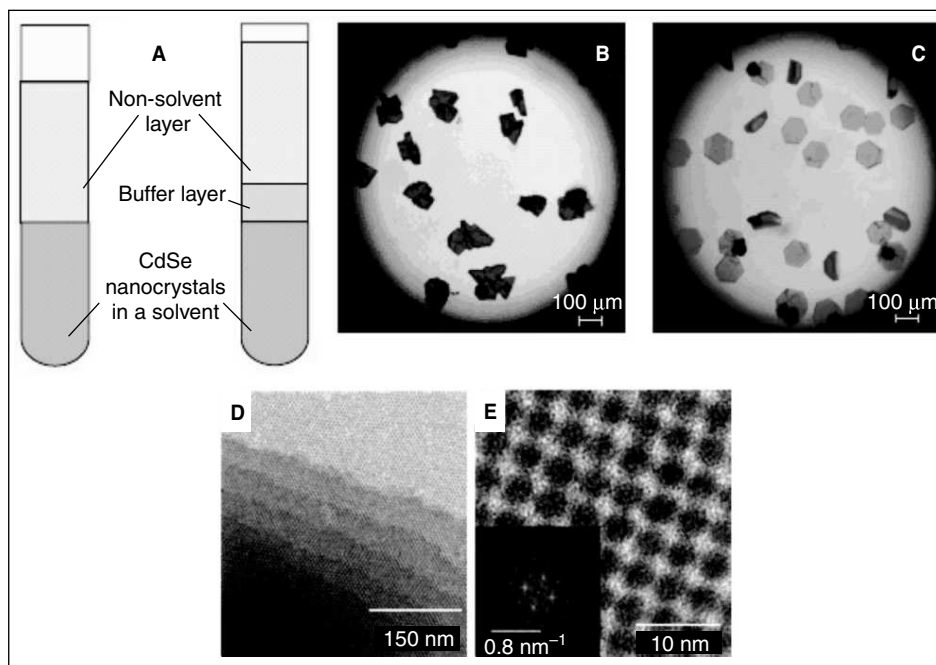


Fig. 12.10 (A) Cartoon representation of the concept of the nucleation procedure. Left tube: The non-solvent (methanol) diffuses directly into a dispersion of CdSe nanocrystals in toluene. Right tube: A buffer layer of propan-2-ol slows down the diffusion of methanol. (B and C) Optical micrographs of colloidal crystals of CdSe nanocrystals taken by a digital camera through the objective of an optical microscope. (B) Faster nucleation, irregular shaped crystals and (C) slower nucleation and perfectly faceted hexagonal platelets. Transmission electron microscopy images of a 3-D arrangement of the 3.5 nm CdSe nanocrystals. (E) Overview of a fcc-like superlattice (adapted from Ref. 29). (For clarity see colour figure.)

is reasonably different from the other axes. Hence, it is possible to adjust the growth rate along $[001]$ and $[100]$ directions to obtain plate-like nanocrystals with different diameter/thickness ratios. The anisotropic structure also has a dipole moment along the $[001]$ direction, which may be useful for the stacking of nanocrystals in the construction of SLs of these structures. Lie and co-workers reported a novel water–oil interface method to synthesise monodisperse Cu_2S nanocrystals and their multilayer SL assemblies.⁴⁶ In this two-phase reaction system, dodecanethiol (or its toluene solution) is the oil phase at the top, which plays the roles of sulfur source, ligand and reducer. The aqueous phase at the bottom contains copper ion and other added anions, such as Ac^- or Cl^- , which help in the growth of Cu_2S . The synthesis was performed in an autoclave at 200 °C. The Cu_2S nanocrystals formed at the interface of water and dodecanethiol were capped by dodecanethiol molecules. Fig. 12.12A shows the TEM image of as prepared Cu_2S in presence of Ac^- . Particles are spherical in shape with narrow-size distribution (Fig. 12.12B) with an average diameter of 8.2 ± 0.7 nm. The HRTEM image (Fig. 12.12C)

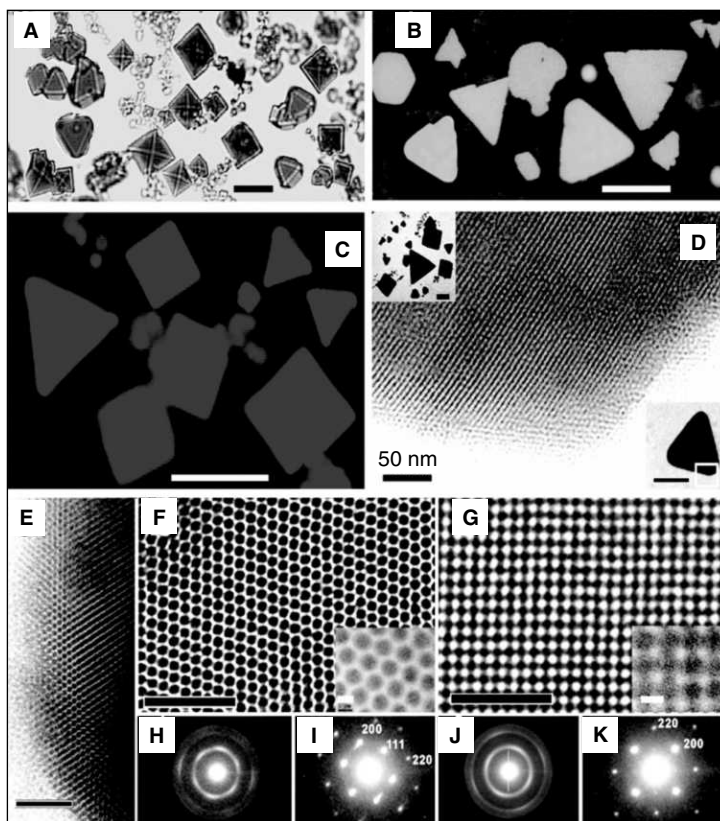


Fig. 12.11 (A) optical transmission micrograph of three-dimensional, faceted SLs formed from 5.3 nm NC solution; (B) and (C) fluorescence microscope images of crystals obtained, respectively, from 3.5 and 5.3 nm NCs; (D) TEM image taken from the edge of a colloidal crystal formed from 5.3 nm CdSe NCs. (E) typical image of a crystal edge; (F and G) $\langle 110 \rangle$ and $\langle 100 \rangle$ projections obtained in the thin areas close to the edges (H and I) show partial alignment of NCs within an fcc superlattice identified by small-angle electron diffraction (J and K) (adapted from Ref. 45). (For clarity see colour figure.)

shows the lattice fringes, which can be indexed as the (110) plane. This indicates that the nanocrystal is terminated by the $\{001\}$ plane. Fig. 12.12D-F shows the products obtained under lower concentration of Cu^{2+} and dodecanethiol. In this concentration regime, the nanocrystals changed their shape from spherical to an elongated shape, but remained uniform (Fig. 12.12E). The length of the elongated nanocrystal is 13.6 ± 0.8 nm with a width of 8.8 ± 0.7 nm. The HRTEM image (Fig. 12.12F) shows the lattice fringes, which can be indexed as $(1\bar{1}1)$ and (002) . Fig. 12.12G-J shows the product obtained in the presence of Cl^- , illustrating the formation of rod-like nanocrystals. Here, it was found that they are face-to-face packed hexagonal nanoplates in nature. The thickness of the nanoplate is 5.2 ± 0.9 nm with a diameter of 26 ± 4 nm. They have a wider size distribution (Fig. 12.12H), which makes them

not as good as the formers for the construction of multilayer SLs. The HRTEM image (Fig. 12.12J) shows that the nanoplate lies on the $\{001\}$ plane. The circular and elongated nanocrystals have strong tendency to assemble into multilayer SLs because of their high uniformity. The nanocrystal SLs are formed spontaneously during the preparation stage. Figure 12.12 shows the TEM images of the nanocrystal assemblies. The circular nanocrystals can close pack into a layer, and the second-layer of nanocrystals fit into the voids between the first-layer of nanocrystals. Two types of packing symmetry can be adopted by the third-layer nanocrystals to build *fcc* (Fig. 12.12K) or *hcp* (Fig. 12.12L) SLs. The inset FFT patterns show the high stacking order with a sixth-fold axis. The upper layer nanocrystals can also fit into the voids between the lower layers, thus forming a multilayer structure (Fig. 12.12M and N). The anisotropic cell structure of Cu_2S has a dipole moment along the $[001]$ direction of the nanocrystals, and this will also be useful for the stacking of building blocks in superstructures. The inner nanocrystals in the SLs have different orientation, and hence the dipole moment orientations are different in the two types of nanocrystal SLs. It is vertical to the layers in the case of circular

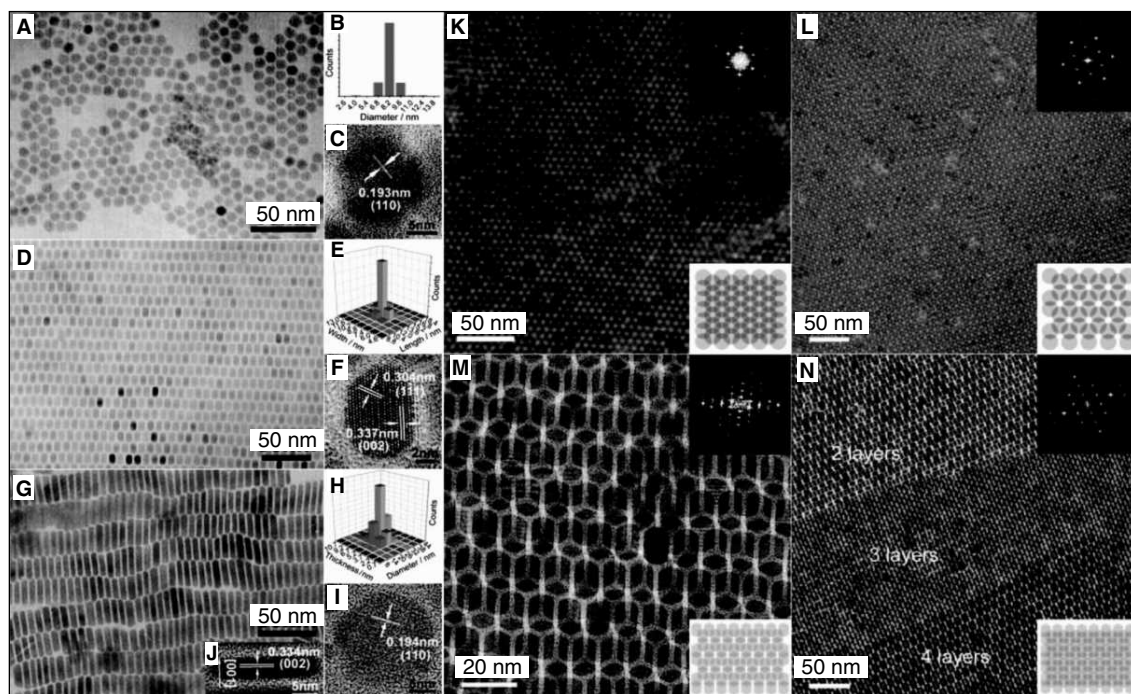


Fig. 12.12 TEM image (A, D and G), size distribution (B, E and H) and HRTEM image (C, F, I and J) of circular Cu_2S nanocrystals, elongated Cu_2S nanocrystals; and Cu_2S hexagonal nanoplates. TEM images of Cu_2S nanocrystal superlattices: (K) 'fcc' packed circular nanocrystals; (L) 'hcp' packed circular nanocrystals; (M) two layers of closepacked elongated nanocrystals; (N) multilayers of elongated nanocrystals. The top insets are the corresponding FFT patterns, and the bottom insets are the schemes of the stacking of nanocrystals (adapted from Ref. 46).

nanocrystal assemblies, which may lead to a strong tendency to form a multilayer structure. However, in the elongated nanocrystal assemblies, the dipole moment is along the side face of the nanocrystals. The van der Waals interactions depend on the distance of the two species strongly, and the elongated nanocrystal may have larger “closest regions” and result in larger interactions.

12.5 3D SUPERLATTICES (SLs) OF BINARY NANOPARTICLES (BNSLs)

12.5.1 Au–CdSe SLs

Semiconductor and metal nanocrystals and their hybrid assemblies have attained significant attention in the area of nanoscience and technology. Hybrid assemblies built by metals and semiconductor brings not only the combined properties of both, but also generate new materials and collective phenomena based on the inter-plasmon coupling at the nanoscale. Binary SLs (BNSLs) of gold and CdSe nanoparticles were first developed by Paul Alivisatos, *et al.* in 2008.⁴⁷ Here, monodisperse 8.7 nm CdSe NCs and 5.5 nm Au NCs were synthesised using the procedure reported elsewhere. BNSLs of CdSe and Au were self-assembled from the toluene solutions on ultrathin carbon films supported by a copper grid with different ratio of gold and CdSe nanoparticles. By changing the ratio of Au to CdSe nanoparticle ratio, one can possibly make different kinds of SLs. Here, a BNSL isostructural with the AuCu intermetallic compound has been formed using a particle number ratio of CdSe:Au of 1:0.7 (Fig. 12.13A and E). A BNSL isostructural with AlB₂ was obtained using a particle ratio of CdSe:Au of 1:5 (Fig. 12.13B and F). The same particle ratio led to the formation of CaCu₅-type (Fig. 12.13C and G) and cub-AB₁₃-type (Fig. 12.13D and H) SLs, when small amounts of dodecanethiol and trioctylphosphine oxide were added to the colloidal solutions of NCs, respectively. Photoluminescence studies of these BNSLs show that the fluorescence of CdSe NCs in the BNSL is only 5–15 per cent of the fluorescence intensity of a CdSe NCs-only sample of an approximately comparable particle density, measured under the same excitation conditions (Fig. 12.13I). Moreover, fluorescence lifetime also has been drastically decreased (Fig. 12.13J). This clearly indicates that energy is transferred to the surrounding Au NCs and that the Au NCs most probably also influence the radiative rate of the CdSe NCs.

12.5.2 CdSe/CdSe BNSLs

Same group developed binary SLs of same semiconductor quantum dots CdSe/CdSe,⁴⁸ with different particle size (3.5 nm/5.5 nm). BNSLs were formed with thiol concentrations similar to those optimised for the CdSe/Au system. In this case, two structures, AB and AB₅ were obtained with a dodecanethiol-in-toluene concentration of 1.8 per cent (Fig. 12.14A and B). It is possible to use the optimised concentration of thiol for a variety of binary systems.

12.5.3 CdSe/CdTe SLs

This has been developed by the same group.⁴⁹ Here, two different kinds of semiconductor quantum dots of CdTe (core diameter 8.1 nm) and CdSe (core diameter 4.4 nm) nanoparticles were used for making

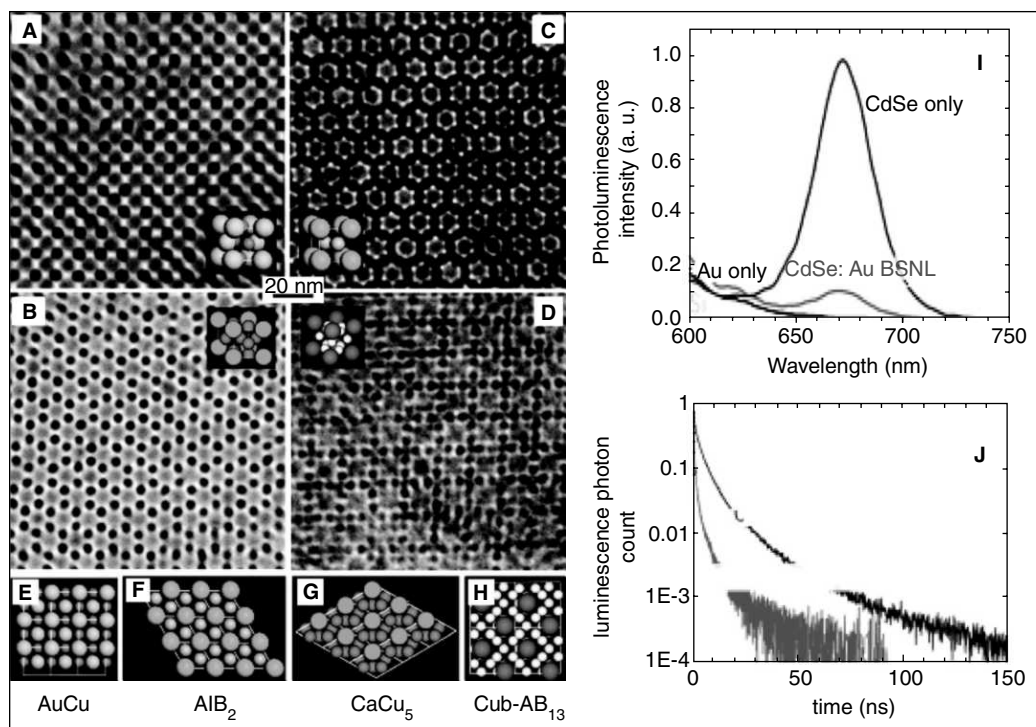


Fig. 12.13 TEM images of (001) projections of BNSLs self-assembled from 8.7 nm CdSe and 5.5 nm Au NCs and isostructural with (A) AuCu, (B) AlB₂, (C) CaCu₅ intermetallic compounds and (D) cub-AB₁₃. Insets in (A–D) depict the unit cells of subsequent structures. (E–H) Modeled (001) projections of AuCu, AlB₂, CaCu₅, and cub-AB₁₃ lattices, respectively. (I) Time-integrated fluorescence spectra and (J) time-resolved fluorescence transients of a close-packed CdSe NCs-only superlattice (blue curves) and of a BSNL of CdSe and Au NCs (red curves). Integrated fluorescence spectra of the Si substrate and of a superlattice of Au NCs are also shown in (I) (adapted from Ref. 47). (For clarity see colour figure.)

BNSLs, such a system is a means to include two discretised, quantum-confined, and complimentary semiconductor units in close proximity, for purposes of band gap matching and/or energy transfer. Here, two types of SL structures, called cuboctahedral-AB₁₃ (cub-AB₁₃) and AB₅ isostructural with

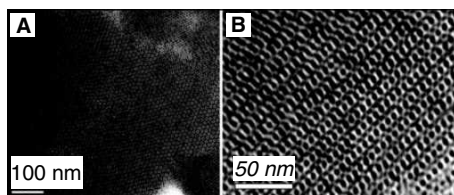


Fig. 12.14 TEM images of (A) AB₅ and (B) AB structures from 3.5 nm CdSe and 5.5 nm CdSe nanoparticles (adapted from Ref. 48).

intermetallic alloy CaCu_5 , were observed on the TEM grid during analysis, after slow drying the binary nanocrystal solution with a proper $\text{CdTe}:\text{CdSe}$ concentration. Schematic of cub-AB_{13} and AB_5 are given in Fig. 12.15 (A and B). The cub-AB_{13} structure can be described as a simple cubic lattice with the A particles located at the corners of the cube and with the B particles occupying two inequivalent positions: a B_I particle at the body centre of the cube is surrounded by twelve B_{II} particles forming a regular cuboctahedron. The AB_5 structure can be described as a simple hexagonal lattice of A particles. These A particles are surrounded by a regular arrangement of six B_I particles occupying the trigonal prismatic interstices of the basal planes. TEM image of the AB_5 SL in the $[001]_{\text{SL}}$ zone axis, obtained after slow drying the binary solution with the $\text{CdTe}:\text{CdSe}$ concentration ratio $\sim 1:8$ and $1:6$ are shown in Fig. 12.15C (structural model of $[001]$ zone axis given in Fig. 12.15D). A large view of the nanoparticle arrangement is given in Fig. 12.15E. TEM images of the AB_{13} SL along the $[001]_{\text{SL}}$ and $[110]_{\text{SL}}$ zone axis obtained after slow drying the binary solution with the $\text{CdTe}:\text{CdSe}$ concentration ratio $\sim 1:13$ and $1:16$ are shown in Fig. 12.15 ($[001]_{\text{SL}}$ zone axis are shown in F, G, H and $[110]_{\text{SL}}$ zone axis are given in

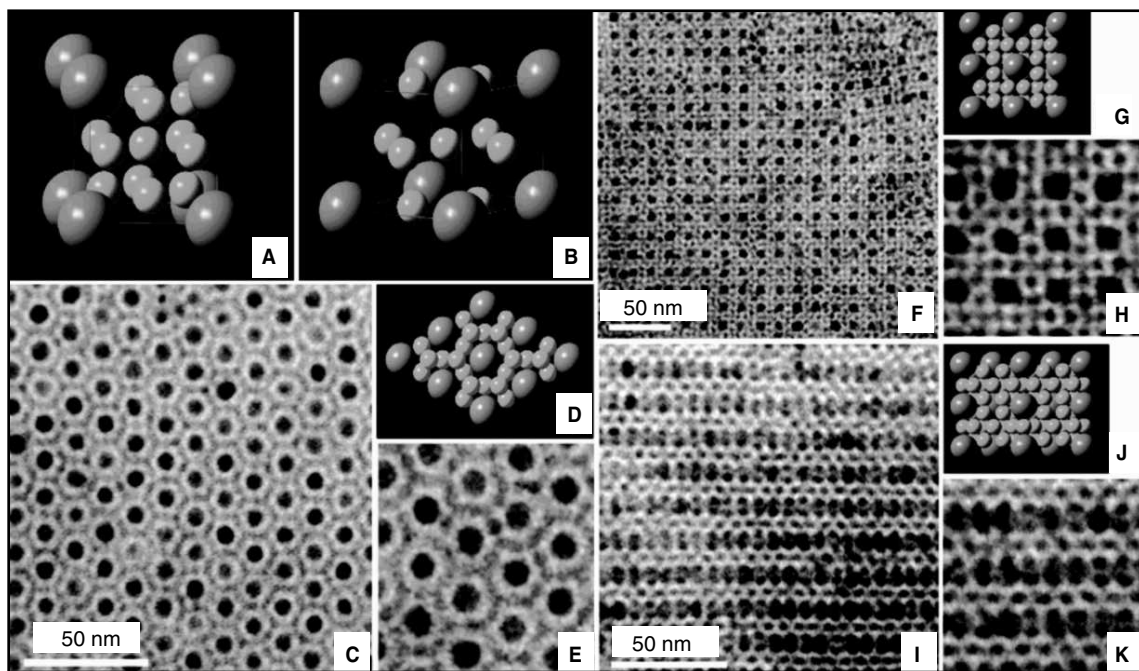


Fig. 12.15 Structure models of (A) cub-AB_{13} and (B) CaCu_5 structures. TEM images of the AB_5 superlattices isostructural with CaCu_5 in the $[001]_{\text{SL}}$ zone axis. (C) Large view TEM image. (D) Structural model in the $[001]$ zone axis. (E) Details of nanoparticle arrangement in SL. TEM images of the cub-AB_{13} superlattices in the (F, G, H) $[001]_{\text{SL}}$ and (I, J, K) $[110]_{\text{SL}}$ zone axis. (F) and (I) Large view TEM images. (G) and (J) Structural model in the respective zone axis. (H) and (K) Details of the nanoparticle arrangements (adapted from Ref. 49).

I, J and K). Detailed views (Fig. 12.15G and J) of the experimental images obtained in these two-zone axes show an excellent agreement with the model of the crystal displayed in the same figure.

12.6 MAGNETIC NANOPARTICLE SLs

12.6.1 CoPt₃ SLs (Magnetic Metal Alloy SLs)

CoPt₃ SLs were developed by H. Weller *et al.* in 2002.⁵⁰ Here, high quality CoPt₃ with narrow size distribution can be prepared in a reproducible manner via simultaneous reduction of platinum acetylacetonate and thermal decomposition of cobalt carbonyl in presence of 1-adamantanecarboxylic acid and hexadecylamine as stabilising agents. Here, the slower nucleation results in the formation of larger nanocrystals with narrower size distribution (st. div. ~7%), while fast nucleation yields smaller nanocrystals with broader (st. div. ~14%) size distributions. The CoPt₃ nanocrystal size increases with increasing the concentration of the stabiliser (1-adamantanecarboxylic acid). This effect was attributed to the slower rate of nucleation at high concentration of the stabiliser. Due to the narrow particle size

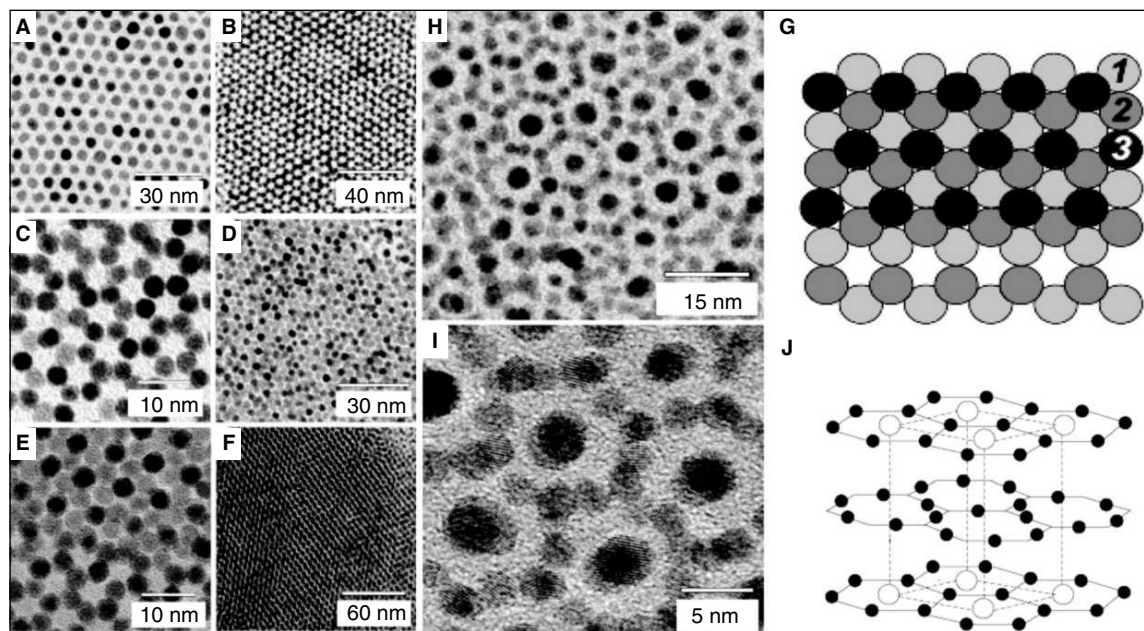


Fig. 12.16 TEM images (A) of monolayer of 4.8 nm CoPt₃ nanoparticles, (B, C) of two layers of 3.6 and 4.0 nm CoPt₃ nanoparticles, (D) of three layers of 3.6 nm CoPt₃ nanoparticles, (E) of three layers of 4.0 nm CoPt₃ nanoparticles (HRTEM), (F) of more than five layers of 4.5 nm CoPt₃ nanoparticles and a graphical illustration (G) of three-layer arrangement of CoPt₃ nanocrystals. (H) TEM and (I) HRTEM images illustrating 3-D superlattices of CoPt₃ nanoparticles formed in a mixture of two different sizes (4.5 and 2.6 nm); (J) illustrative drawing of the AB₅ structure (Adapted from Ref. 50).

distributions and uniform spherical shape, CoPt_3 nanocrystals had a strong tendency to self-organise into 2-D and 3-D SLs. Spontaneous self-assembly was observed when colloidal solutions of CoPt_3 nanocrystals were spread onto a substrate with subsequent slow evaporation of the carrier solvent. It is possible to make different kinds of self-organised superstructures, depending on the particle size and conditions of solvent evaporation. Figure 12.16A shows a TEM overview image of a close-packed monolayer of 4.8 nm CoPt_3 nanocrystals. If the surface coverage with nanocrystals was higher than one monolayer, nanocrystals of the second layer occupied positions between the nanocrystals in the first layer, which can be seen in Fig. 12.16B and C. Fig. 12.16D and E show the *ccp* arrangement of nanoparticles. Figure 12.16F presents a TEM image of multilayer 3-D SL where the 4.5 nm CoPt_3 nanocrystals are arranged in a nearly defect-free 3-D structure exhibiting long-range order. Graphical representation of the three-layer arrangement of CoPt_3 nanocrystals is depicted in Fig. 12.16G.

12.6.2 Fe_3O_4 -Co BNSLs

Fe_3O_4 -Co BNSLs was first reported by J. Cheon (Ref. 51). Here, the 3-D SLs are formed by the co-assembly of Fe_3O_4 and Co nanoparticles. By controlling the size of both of these particles, they could make two different kinds of assemblies, such as AB and AB_2 . Two crucial parameters determine the binary assembly pattern of the spheres: (i) the size ratio ($\gamma = R_{\text{small}}/R_{\text{large}}$) and (ii) the stoichiometric ratio between the two spheres. Mixing of Fe_3O_4 (18 nm) and Co (7.5 nm) particles results in the formation of SLs. Figure 12.17A shows the unit-cell structure and 2-D projections of AB structures. The unit cell is cubic, and the structure consists of two interpenetrating face-centered arrays of Co and Fe_3O_4 nanoparticles (NaCl type). Here, each Co nanoparticle is surrounded by six equidistant Fe_3O_4 nanoparticles situated at the corners of an octahedron. Similarly, each Fe_3O_4 nanoparticle is surrounded by six Co nanoparticles. As shown in Fig. 12.17D, a TEM image of the binary SL corresponds to the $[001]_{\text{SL}}$ projection of AB structures (Fig. 12.17C). Alternative views of the binary structure shown in Fig. 12.17F and H are consistent with the $[111]_{\text{SL}}$ and $[110]_{\text{SL}}$ projections of the AB structure (Fig. 12.17E and G), respectively. However, when Fe_3O_4 nanoparticles and two molar excess of Co nanoparticles were mixed and co-crystallised, the resulting SLs shows AB_2 structure rather than AB. In this SLs, bilayers (Fig. 12.17M) composed of hexagonal close packed Fe_3O_4 and second layer of Co (Fig. 12.17I–K) were observed with an inter-planar distances of 9.6 nm for $[220]_{\text{SL}}$ and 16.7 nm for $[110]_{\text{SL}}$. A small-angle diffraction pattern of our bilayer structure (Fig. 12.17L) shows discrete reflection spots from the hexagonally ordered structures. The inner hexagonal spots marked p and q positioned 30° apart from each other are contributions from the $[200]_{\text{SL}}$ and $[110]_{\text{SL}}$ reflections, respectively.

12.7 APPLICATIONS OF SLs

1. Fluorescent SLs (functionalised SLs)
2. Detection of biomolecules (e.g., BSA)
3. Surface enhanced Raman scattering (SERS)

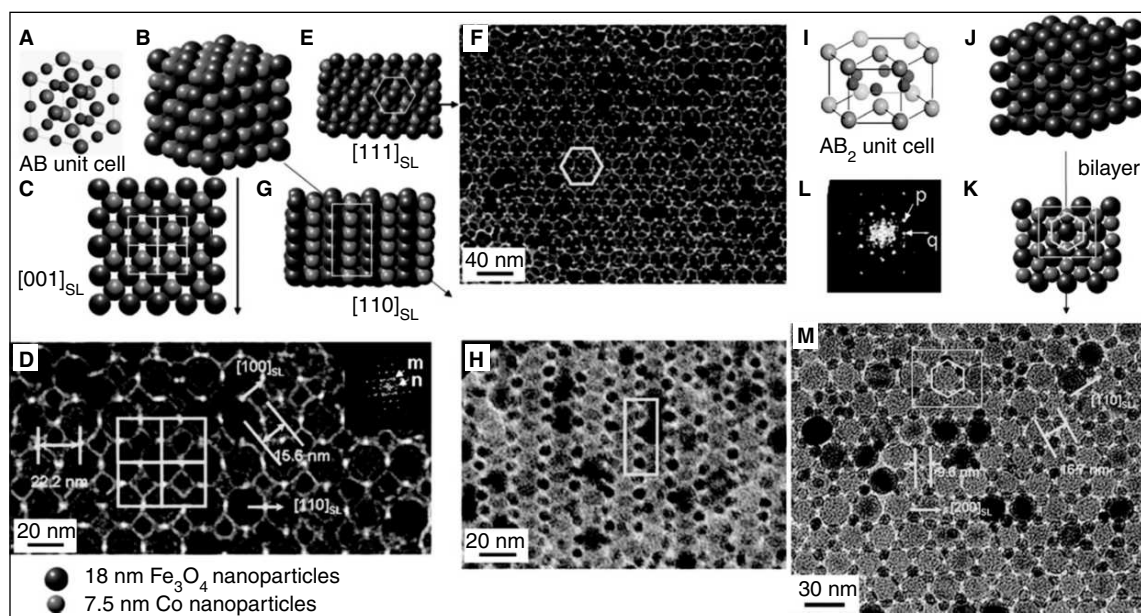


Fig. 12.17 (A and B): The unit cell (A) and the extended cell (B) of the NaCl type AB binary structure. (C–H): TEM images of our binary SLs (D, F and H) and the corresponding AB structure (C, E and G). (I–K): Figures of the unit cell (I), the extended cell (J) and bilayers along c axis (K) of the hexagonal AB_2 binary structure. (L) Small-angle electron diffraction (SAED) pattern of AB_2 bilayers. (M) TEM image of our AB_2 SLs (adapted from Ref. 51). (For clarity see colour figure.)

12.7.1 Fluorescent Molecule-tagged Nanoparticle SLs

It is possible to make different functionalities on SLs by selecting different functional groups on the ligands. Glutathione protected nanoparticles have an $-NH_2$ and $-COOH$ group each. These help to make covalent functionalisation on the ligands. One can make different functionalities depending on the requirements. For example, if we are in need of a fluorophore on the ligands, we can synthesise a fluorescent marker on the ligand by simple organic synthesis. One can tag the fluorophore on the nanoparticle by different methods, like exchange reaction of nanoparticles with fluorescent ligands or synthesise the nanoparticles using the fluorescent molecule-tagged ligands by coupling such species on well-studied ligands, like MSA or GSH. Assembly of these fluorescent tagged nanoparticles will lead to the formation of fluorescent SLs. On this basis, the present authors developed fluorescent SLs. A fluorescein-based dye conjugated mercaptosuccinic acid (SAMSA) was used to make nanoparticles along with free MSA ligands. The number of ligands per nanoparticle was calculated using the ϵ value of the ligands. SLs crystals were developed by the hydrogen bonding method. Fig. 12.18A shows the fluorescence image of Au@MSA/SAMSA SL crystal. Fig. 12.18B shows the white light image of the corresponding triangle. Fig. 12.18C shows the emission collected from the surface of the triangle using 514.5 nm excitation.³⁸

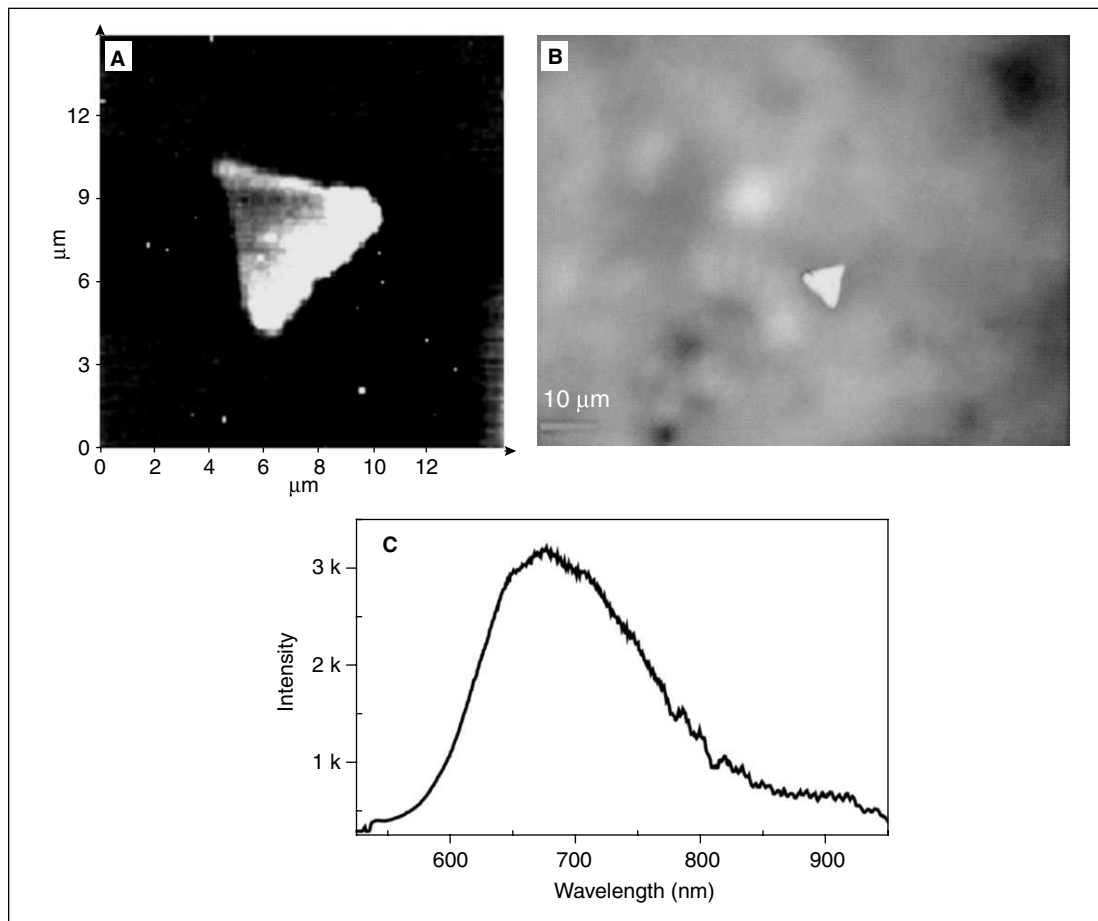


Fig. 12.18 (A) Fluorescence image of Au@MSA/SAMSA SL triangle. (B) White light image of corresponding SL triangle. (C) Emission spectrum collected from the surface of the crystal using 514.5 nm excitation (adapted from Ref. 38).

12.7.2 Detection of Bimolecules (BSA)

To study the fluorescent SLs in great detail, authors developed a cheap and easily available fluorophore, dansylglutathione (DGS) based SLs in gram scale. Dansyl glutathione is a green emitting molecule and can be easily synthesised from dansyl chloride and oxidised form of glutathione. These classes of molecules are known as 'environment sensitive fluorophores'. In this method, total content of fluorophore based ligand is excessively high, this results in more enhanced fluorescence from the system.

The crystals of Au@SGAN/SGD nanoparticles result in two different kinds of triangular morphologies, first one resembles a prism and second one is pyramidal with upper and lower surfaces having different thicknesses. Moreover, it has a depression at the centre. Authors studied the unusual

triangular morphology of SL crystals by SEM and inverted fluorescence microscope imaging. Both the results resemble each other. Fig. 12.19(A–D) shows SEM and fluorescence images collected from two different triangular crystals of Au@SGD/SGAN SL. Fig. 12.19 (E–T) shows the confocal fluorescence images and corresponding overlay structure collected from Au@SGD/SGAN SL triangle at different depth.

Detection of biomolecules using gold nanoparticles has been attracting considerable interest over the past few years.⁵² The fluorescence of the dansyl moiety in Au@SGAN/SGD SLs was utilised for the specific detection of bovine serum albumin (BSA). Serum albumin is the major protein constituent of blood plasma. Specific delivery of ligands by BSA is considered to be due to the presence of two selective binding sites, namely site I and site II.⁵³ Dansyl amides are known to bind with site I through hydrophobic interactions.⁵³ The SL sample coated on quartz plate was excited at 330 nm and emission was collected at 587 nm, where there is no emission from BSA. After this, 10 μ l BSA solutions (1 nmol/l) in phosphate buffer were dropped on the film and emission was collected using the same excitation wavelength. As expected, authors observed emission spectra with greater intensity compared with the blank SL film. A further enhancement with a bathochromic shift from 587 to 592 nm was observed with higher concentrations (μ mol/l and mmol/l) of BSA (a, d). This rapid fluorescence enhancement of the dansyl fluorophore is attributed to the specific binding of the naphthalene ring of the dansyl moiety with site I of BSA. Fig. 12.19U shows the corresponding fluorescence spectra during the fluorimetric titration experiment. A schematic representation of the specific binding of the naphthalene ring with BSA is shown in Fig. 12.19V.

12.7.3 Surface Enhanced Raman Scattering (SERS)

SERS promises extraordinary potential for the detection of a range of molecules, such as pesticides⁵⁴ and explosives⁵⁵ as well as biological objects, such as DNA^{56,57} and anthrax spores.⁵⁸ It is widely used in areas, such as enzyme immunoassay,⁵⁹ detection of protease activity,⁶⁰ etc. One of the promising approaches for the design of SERS substrates is the fabrication of nearly adjacent metallic nanostructures with a nanoscale gap. A possible system to build such structures is 2-D or 3-D self-assembled monolayers of gold and silver nanoparticles. These crystals are new materials for SERS studies. This is because, in such an SL, nanometer scale voids exist in a periodic fashion due to the periodic arrangement of nanoparticles. In these locations, the electric field due to the surface plasmon resonance of the nanoparticles is expected to be large. It presents a new possibility for creating SERS active substrates through self-assembly.

There are a few reports on SERS from organised assemblies of gold and silver nanoparticles.⁶¹ Authors recently reported SERS from Au@SGAN and Au@MSA SL crystals using crystal violet (CV) molecules as the analyte with a detection limit of 10^{-8} M.⁴⁰ The SERS spectrum was used to map the Raman images of the SL crystals. SERS from the edges of the crystal showed more enhancement than from the flat surfaces, which is in good agreement with theoretical reports of such anisotropic structures. The sides of the crystals are not sharp, and they show corrugations at the nanometer scale. This helps to produce more “hot spots” at the edges, which result in larger electric field enhancement from these locations. The enhancement factors (EF) for Au@MSA and Au@SGAN SLs were calculated to be around 1.47×10^6 and 3.60×10^5 , respectively. More enhancements from Au@MSA SL compared

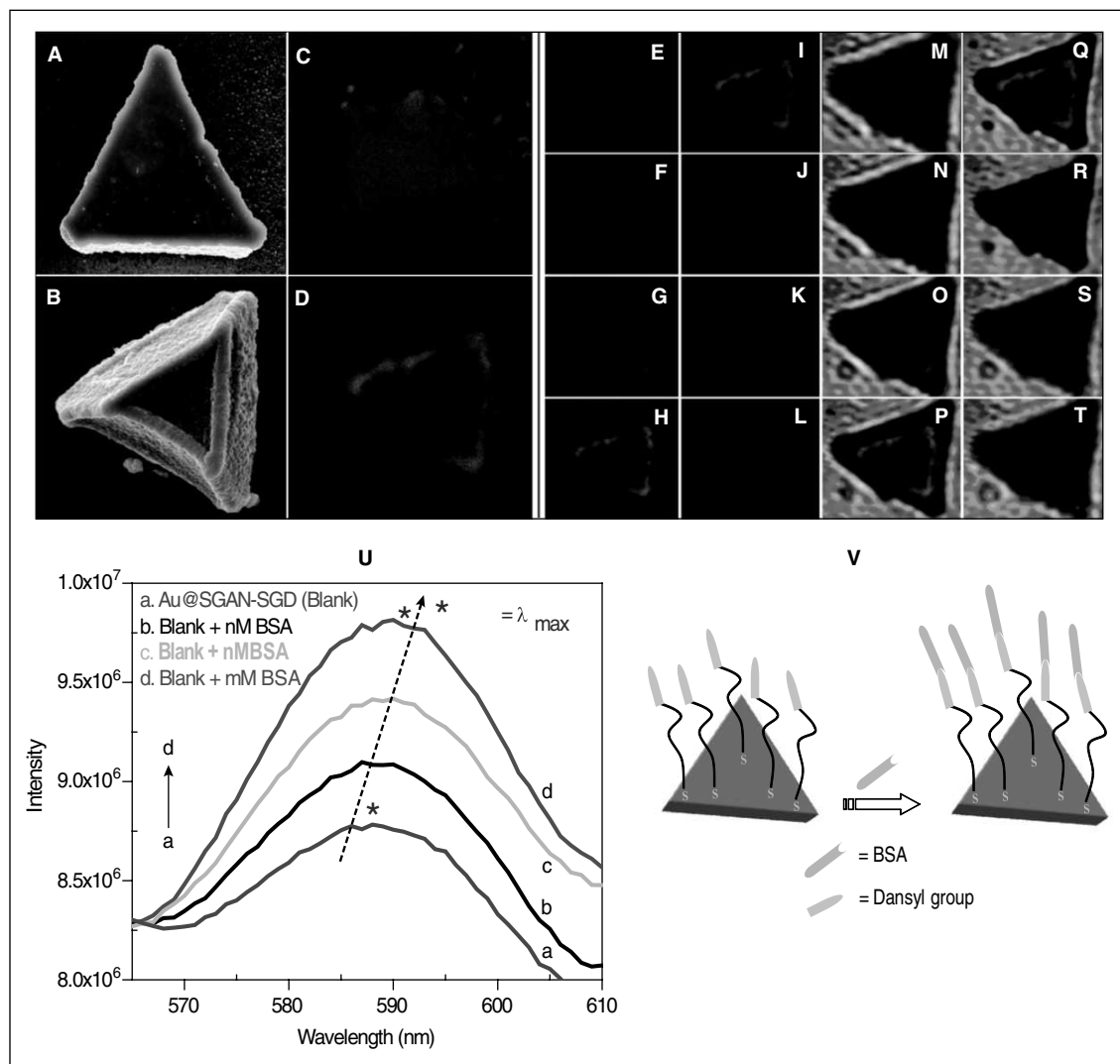


Fig. 12.19 (A–D): The two different morphological crystals of Au@SGAN/AGD and their corresponding fluorescence images. (E–T): The inverted confocal fluorescence images and corresponding overlay structure of triangle 2. (U) Fluorescence spectra of Au@SGAN/SGD superlattice film during the course of fluorimetric titration with different concentrations of BSA; a, blank; b, nM; c, μ M and d, mM. The excitation wavelength was 330 nm. The spectra show a bathochromic shift from 587 to 592 nm. (V) Schematic representation of the specific binding of the naphthalene ring with BSA (adapted from Ref. 39). (For clarity see colour figure.)

with that of Au@SGAN could be attributed to the smaller chain length of the MSA molecule, which allows closer analyte approach to the nanoparticle surface. Figure 12.20A shows the optical image of

Au@MSA SL triangle, which was used for Raman mapping (Fig. 12.20B and C). The SERS spectra collected from the surface and edges of the crystal are shown in Fig. 12.20D.

12.8 INTERESTING PROPERTIES IN SLS

SL crystals are formed as a result of the periodic self-assembly of nanoparticles with nanoscale gap. These particle crystals show additional properties than the individual nanoparticles. Inter-plasmon

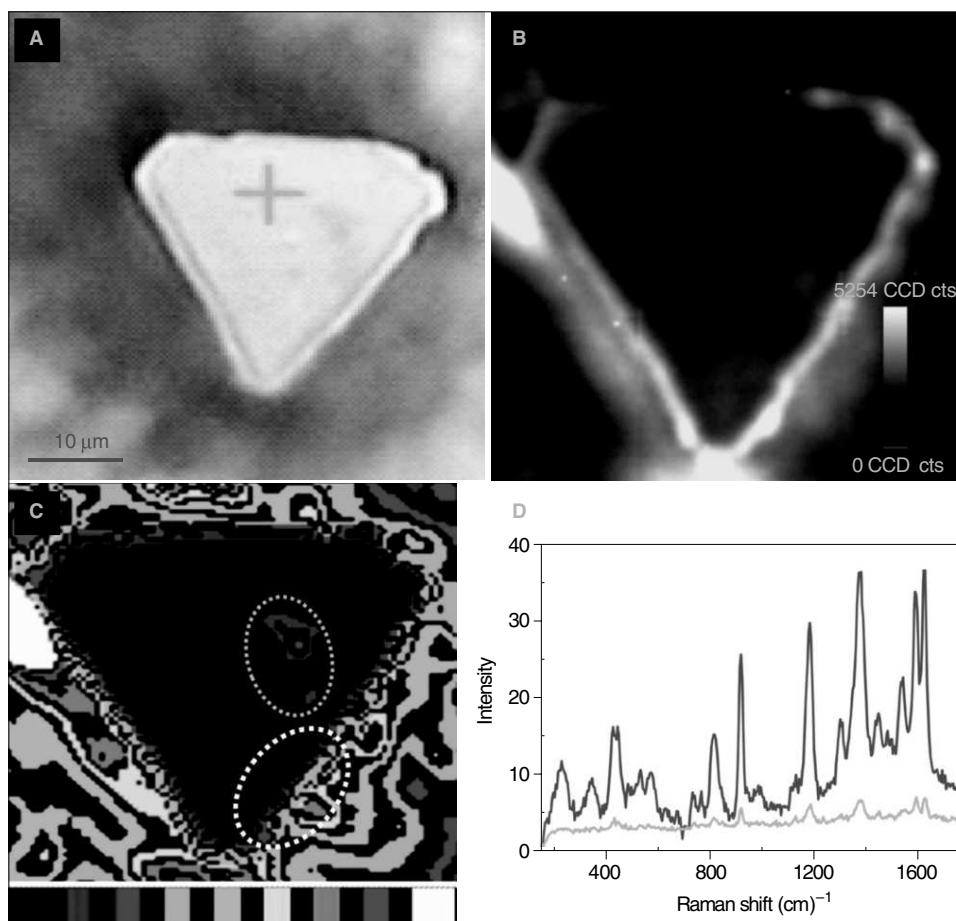


Fig. 12.20 (A) Optical image (under white light illumination) of the Au@MSA SL triangle. (B) Raman image of the same crystal (at 514.5 nm excitation) collected from an area of $12 \mu\text{m} \times 12 \mu\text{m}$ using the intensities of CV features in the $200\text{--}2000 \text{ cm}^{-1}$ window. The concentration of CV exposed was 10^{-5} M . (C) Colour coded Raman image of Au@MSA SL triangle shown in part A. The intensity is in the order: green>blue>pink>black. (D) Raman spectra collected from the edge (blue) and surface (green) of the crystal shown in part B (adapted from Ref. 40). (For clarity see colour figure.)

coupling and metal to insulator transition are such phenomena that were first observed by Heath *et al.*¹ while compressing a film of silver nanocrystals using a Langmuir trough. When the inter-particle distance in particle crystal is large enough, the coulomb band is large. However, when the nanoparticles in particle crystals are compressed, the inter-particle distance (D) reduces and at large pressures, D is comparable to the diameter ($2R$) of the particles. In this regime, the coulomb gap will reduce. Heath *et al.* explained this effect using a cartoon representation shown in Fig. 12.21A. At a $D/2R$ of 1.3–1.5, metal to insulator transition is expected. At low $D/2R$ value, the inter-plasmon coupling occurs. Here, we have discussed two different examples showing the presence of inter-plasmon coupling and metal to insulator transition. Fig. 12.21B is the UV/Vis spectra collected from differently-sized gold octahedra.⁴³

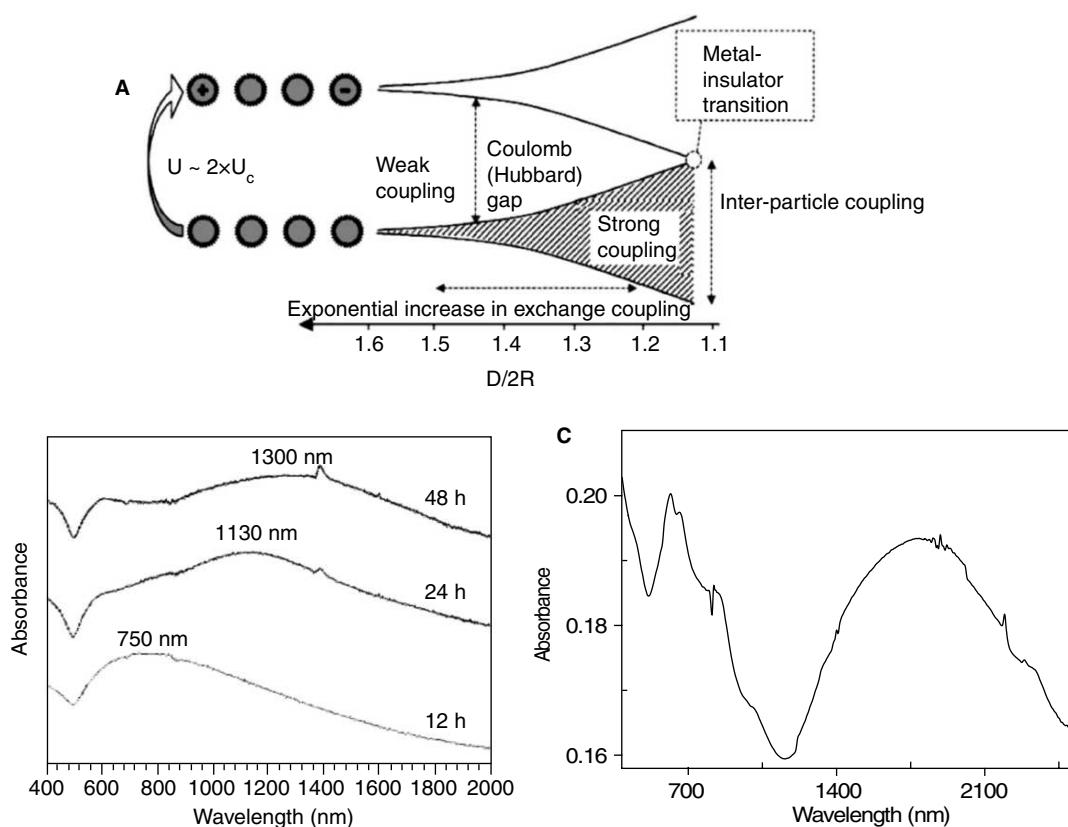


Fig. 12.21 (A) Cartoon of inter-particle interactions. At large inter-particle distance (D), NCs are electrically isolated and the superlattice is an insulator with a coulomb gap. As the interparticle distance decreases, exchange interactions become significant and the localised electronic wave functions of the individual NCs spread out over multiple NCs in the superlattice. (B) UV/Vis spectra collected from gold octahedra SLs showing inter-plasmon coupling. (C) UV/Vis spectrum collected from Au@SGAN/SGD SL film shows the presence of both inter plasmon coupling and metal to insulator transition (adapted from Refs. 1, 39 and 43).

Here, the surface plasmon of gold octahedra shifted to higher wavelength. This clearly indicates the inter-plasmon coupling in SLs crystals. Fig. 12.21C shows the UV/Vis spectrum collected from Au@SGAN/SGD SL film.³⁹ Here, in addition to 650–700 nm absorption (inter-plasmon), there is a broad absorption in the IR region (1000–2500 nm). This could be due to the metal to insulator transition. Even though one is starting with metal nanoparticles, they can form insulating materials depending on the D/2R values. Hence, one can possibly tune properties of SLs by adjusting D/2R values.

12.9 CONCLUSIONS

In this chapter, we had an introduction to the various SL structures of nanoparticles. SLs are self-assembled crystals of nanoparticles exhibiting periodicity in the as in the case of a regular crystal, but the lattice points are nanoparticles and not atoms. Noble metal nanoparticles, semiconductor nanoparticles, anisotropic nanoparticles and mixed nanoparticles were used to form SLs. The ways, by which these structures are formed, their packing and properties were examined. These materials are useful for applications, such as SERS and gas sensing. These materials are also useful to obtain new properties, such as metal-insulator transition.

REFERENCES

1. C.P. Collier, T. Vossmeier and J.R. Heath, *Ann. Rev. Phys. Chem.*, 49, (1998), 371.
2. M. Achermann, M.A. Petruska, S. Kos, D.L. Smith, D.D. Koleske and V.I. Klimov, *Nature*, 429, (2004), 642.
3. I. Gur, N.A. Fromer, M.L. Geier and A.P. Alivisatos, *Science*, 310, (2005), 462.
4. S.A. Maier, P.G. Kik, H.A. Atwater, S. Meltzer, E. Harel, B.E. Koel and A.A. Reguicha, *Nat. Mater.*, 2, (2003), 229.
5. J. Hoinville, A. Bewick, D. Gleeson, R. Jones, O. Kasyutich, E. Mayes, A. Nartowski, B. Warne, J. Wiggins and K. Wong, *J. Appl. Phys.*, 93, (2003), 187.
6. J. Grunes, J. Zhu, E.A. Anderson and G.A. Somorjai, *J. Phys. Chem. B*, 106, (2002), 11463.
7. M. Zayats, A.B. Kharitonov, S.P. Pogorelova, O. Lioubashevski, E. Katz and I. Willner, *J. Am. Chem. Soc.*, 125, (2003), 16006.
8. K. Motesharei and D.C. Myles, *J. Am. Chem. Soc.*, 120, (1998), 7328.
9. J. Spinke, M. Liley, H.-J. Guder, L. Angermaier and W. Knoll, *Langmuir*, 9, (1993), 1821.
10. A.P. Alivisatos, K.P. Johnson, X. Peng, T.E. Wilson, C.J. Loweth, M.P. Bruchez and P.G. Schultz, *Nature*, 382, (1996), 609.
11. C.B. Murray, C.R. Kagan and M.G. Bawendi, *Science*, 270, (1995), 1335.
12. M. Alexander, Kalsin, M. Fialkowski, M. Paszewski, S.K. Smoukov, K.J.M. Bishop and B.A. Grzybowski, *Science*, 312, (2006), 420.
13. S.A. Harfenist, Z.L. Wang, R.L. Whetten, I. Vezmar and M.M. Alvarez, *Adv. Mater.*, 9, (1997), 817.
14. C.B. Murray, C.R. Kagan and M.G. Bawendi, *Ann. Rev. Mater. Sci.*, 30, (2000), 545.
15. P.C. Ohara, J.R. Heath and W.M. Gelbart, *Angew. Chem. Int. Ed. Engl.*, 36, (1997), 1078.

16. E.V. Shevchenko, D.V. Talapin, N.A. Kotov, S. O'Brien and C.B. Murray, *Nature*, 439, (2006), 55.
17. A. Taleb, C. Petit and M.P. Pileni, *Chem. Mater.*, 9, (1997), 950.
18. M.-C. Daniel and D. Astruc, *Chem. Rev.*, 104, (2004), 293.
19. A.L. Rogach, D.V. Talapin, E.V. Shevchenko, A. Kornowski and M. Haase, *Adv. Funct. Mater.*, 12, (2002), 653.
20. F.X. Redl, K.S. Cho, C.B. Murray and S. O'Brien, *Nature*, 423, (2003), 968.
21. S.I. Stoeva, B.L.V. Prasad, S. Uma, P.K. Stoimenov, V. Zaikovski, C.M. Sorensen and K.J. Klabunde, *J. Phys. Chem. B.*, 107, (2003), 7441.
22. B.O. Dabbousi, C.B. Murray, M.F. Rubner and M.G. Bawendi, *Chem. Mater.*, 6, (1994), 216.
23. M.P. Pileni, *J. Phys. Chem. B.*, 105, (2001), 3358.
24. S. Stoeva, K.J. Klabunde, C.M. Sorensen and I. Dragieva, *J. Am. Chem. Soc.*, 124, (2002), 2305.
25. W.H. Binder, *Angew. Chem. Int. Ed.*, 44, (2005), 5172.
26. M.K. Sanyal, V.V. Agrawal, M.K. Bera, K.P. Kalyanikutty, J. Daillant, C. Blot, S. Kubowicz, O. Kononov and C.N.R. Rao, *J. Phys. Chem. C.*, 112, (2008), 1739.
27. K.V. Sarathy, G.U. Kulkarni and C.N.R. Rao, *Chem. Commun.*, 6, (1997), 537.
28. Y. Lin, H. Skaff, T. Emrick, A.D. Dinsmore and T.P. Russell, *Science*, 299, (2003), 226.
29. D.V. Talapin, E.V. Shevchenko, A. Kornowski, N. Gaponik, M. Haase, A.L. Rogach and H. Weller, *Adv. Mater.*, 13, (2001), 1868.
30. A.K. Boal, F. Ilhan, J.E. DeRouchey, T. Thurn-Albrecht, T.P. Russel and V.M. Rotello, *Nature*, 404, (2000), 746.
31. L.M. Demer, D.S. Ginger, S.-J. Park, Z. Li, S.-W. Chung and C.A. Mirkin, *Science*, 296, (2002), 1836.
32. A. Sanyal, T.B. Norsten, O. Uzun and V.M. Rotello, *Langmuir*, 20, (2004), 5958.
33. K. Kimura, S. Sato and H. Yao, *Chem. Lett.*, 30, (2001), 372.
34. S.H. Wang, S. Sato and K. Kimura, *Chem. Mater.*, 15, (2003), 2445.
35. S.H. Wang, H. Yao, S. Sato and K. Kimura, *J. Am. Chem. Soc.*, 126, (2004), 7438.
36. Y. Yang, S. Liu and K. Kimura, *Angew. Chem. Int. Ed.*, 45, (2006), 5662.
37. H. Yao, T. Minami, A. Hori, M. Koma and K. Kimura, *J. Phys. Chem B.*, 110, (2006), 14040.
38. N. Nishida, E.S. Shibu, H. Yao, T. Oonishi, K. Kimura and T. Pradeep, *Adv. Mater.*, 20, (2008), 4719.
39. E.S. Shibu, M.A.H. Muhammed, K. Kimura and T. Pradeep, *Nano Res.*, 2, (2009), 220.
40. E.S. Shibu, K. Kimura and T. Pradeep, *Chem. Mater.*, 21, (2009), 3773.
41. B.L.V. Prasad, C.M. Sorensen and K.J. Klabunde, *Chem. Soc. Rev.*, 37, (2008), 1871.
42. Y.H. Kim, D.K. Lee, H.G. Cha, C.W. Kim and Y.S. Kang, *Chem. Mater.*, 19, (2007), 5049.
43. C.C. Chang, H.L. Wu, C.H. Kuo and M.H. Huang, *Chem. Mater.*, 20, (2008), 7570.
44. F. Gao, Q. Lu and S. Komarneni, *Chem. Mater.*, 17, (2005), 856.
45. N. Zaitseva, Z.R. Dai, F.R. Leon and D. Krol, *J. Am. Chem. Soc.*, 127, (2005), 10221.
46. Z. Zhuang, Q. Peng, B. Zhang and Y. Li, *J. Am. Chem. Soc.*, 130, (2008), 10482.
47. E.V. Shevchenko, M. Ringle, A. Schwemer, D.V. Talapin, T.A. Klar, A.L. Rogach, J. Feldmann and A.P. Alivisatos, *J. Am. Chem. Soc.*, 130, (2008), 3274.

48. C. Lu, Z. Chen and S. O'Brien, *Chem. Mater.*, 20, (2008), 3594.
49. Z. Chen, J. Moore, G. Radtke, H. Siringhaus and S. O'Brien, *J. Am. Chem. Soc.*, 129, (2007), 15702.
50. E.V. Shevchenko, D.V. Talapin, A.L. Rogach, A. Kornowski, M. Haase and H. Weller, *J. Am. Chem. Soc.*, 124, (2002), 11480.
51. J. Cheon, J. Park, J.S. Choi, Y.W. Jun, S. Kim, M.G. Kim, Y.M. Kim and Y.J. Kim, *PNAS*, 103, (2006), 3023.
52. D.J. Maxwell, J.R. Taylor and S. Nie, *J. Am. Chem. Soc.*, 124, (2002), 9606.
53. R.K. Pandey, S. Constantine, T. Tsuchida, G. Zheng, C.J. Medforth, M. Aoudia, A.N. Kozyrev, M.A.J. Rodgers, H. Kato, K.M. Smith and T.J. Dougherty, *J. Med. Chem.*, 40, (1997), 2770.
54. N. Weibenbacher, B. Lendl, J. Frank, H.D. Wanzenböck, B. Mizaikoff and R. Kellner, *J. Mol. Struct.*, 539, (1997), 410.
55. F.T. Docherty, P.B. Monaghan, C.J. McHugh, D. Gramam, W.E. Smith and J.M. Cooper, *IEEE Sens. J.*, 5, (2005), 632.
56. K. Kneipp, H. Kneipp, V.B. Kartha, R. Manoharan, G. Deinum, I. Itzkan, R.R. Dasari and M.S. Feld, *Phys. Rev. E*, 57, (1998), 6281.
57. K. Faulds, W.E. Smith and D. Graham, *Anal. Chem.*, 76, (2004), 412.
58. X. Zhang, *et al.*, *J. Am. Chem. Soc.*, 127, (2005), 4484.
59. X. Dou, T. Takama, Y. Yamaguchi and H.Y. Ozaki, *Anal. Chem.*, 69, (1997), 1492.
60. A. Ingram, L. Byers, K. Faulds, B.D. Moore and D. Graham, *J. Am. Chem. Soc.*, 130, (2008), 11846.
61. W. Luo, W. Van der Veer, P. Chu, D.L. Mills, R.M. Penner and J.C. Hemminger, *J. Phys. Chem. C.*, 112, (2008), 11609.

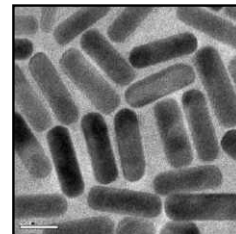
ADDITIONAL READING

1. K.J.M. Bishop, C.E. Wilmer, S. Soh and B.A. Grzybowski, *Small*, 5, (2009), 1600.
2. C.N.R. Rao and K.P. Kalyanikutty, *Acc. Chem. Res.*, 41, (2008), 489.

REVIEW QUESTIONS

1. What are SL crystals?
2. Why the SL crystals are important?
3. Why self-assembly of noble metal particles?
4. What are the important techniques for self assembly?
5. What are properties of the SL crystals?

ANISOTROPIC NANOMATERIALS



“If you want to understand function, study structure.”

Francis Crick, (1988). *What Mad Pursuit, a Personal View of Scientific Discovery*, Basic Books, New York

Anisotropic nanomaterials are a class of materials, in which their properties are direction-dependent and more than one structural parameter is needed to describe them. Most of the traditional nanomaterials are spheres, in which properties are isotropic in all directions. Anisotropic particles exist in the form of rods, wires, tubes, plates, stars, tetrapods, etc. They can also be classified as one-dimensional (1-D), two-dimensional (2-D), and three-dimensional (3-D) materials, depending on the dimensional units required to describe them. 1-D materials are those, wherein there is one majority axis and the other structural parameters are much smaller than this, making the materials one-dimensional. In 2-D materials, there are two major structural parameters, others are smaller making the materials appear similar to sheets. In 3-D, there are three or more structural parameters. 1-D, 2-D and 3-D structures are also materials, in which their properties depend upon the confinement of electrons in one, two and three dimensions. A brief outline of the synthesis of a variety of such structures, their properties and applications are presented here.

Learning Objectives

- What make anisotropic nanomaterials novel?
 - How to tune the shape of nanomaterials?
 - How property varies depends on size and shape?
 - Significance of anisotropic nanomaterials in view of applications.
-
-

13.1 INTRODUCTION

The interesting aspect in nanoscience and technology is the unique and unusual properties that can occur when the size of a material reduces to the nanoscale regime. Apart from the size, the shape also plays an important role in determining the properties of such materials. Due to this reason, enormous

attention has been paid to synthesising nanomaterials of desired geometry, so as to make materials with desired properties.

Quantum size effects and surface area are the two important factors responsible for the unusual optical and electronic properties of nanomaterials. Compared with macro structures, larger proportion of atoms or molecules of a nanostructure lie at the surface. Nanoparticles, normally, will have large surface to volume ratio compared with the corresponding bulk entity. These factors can lead to changes in their physical and chemical properties. There is also shape dependence of the fraction of surface atoms. For example, consider two nanoparticles of the same volume, one is spherical in shape and the other one is star-shaped (Fig. 13.1). The surface to volume ratio will be substantially high in the latter compared with the former nanoparticle, which can influence the reactivity, magnetic property, hardness, catalytic and opto-electronic properties.

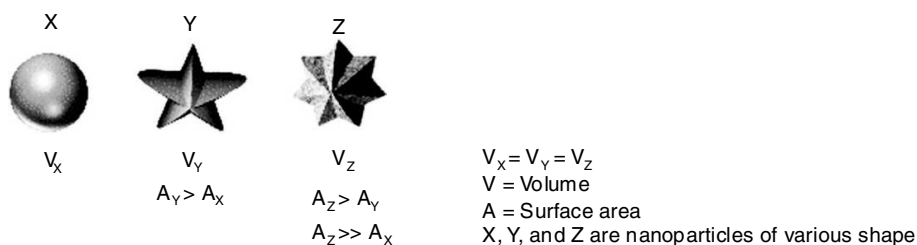


Fig. 13.1 Schematics showing the variation in surface area in accordance with shape anisotropy.

Nanoparticles can be classified, in general, on the basis of their dimensionality. Based on that, nanoparticles are categorised into zero-, one-, two- and three-dimensional particles. It may be of shapes, such as spheres, fibers or rods, films or plates and three-dimensional polycrystalline materials, examples of which are shown in Fig. 13.2.

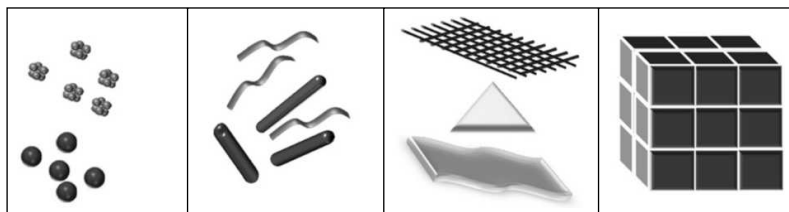


Fig. 13.2 Various kinds of nanocrystalline materials: (A) 0-D (zero-dimensional) spheres, clusters; (B) 1-D (one-dimensional) nanofibers, wires, tubes and rods; (C) 2-D (two-dimensional) films, plates, network and layers; (D) 3-D (three-dimensional) polycrystals.

Apart from dimensionality, depending on geometry, nanomaterials can be classified into isotropic and anisotropic nanomaterials. Isotropic nanoparticles are those with no specific direction of growth, which possess same properties in all directions. Zero-dimensional nanoparticles are included in this category. They constitute the simplest building blocks for nanomaterial design. Nanoclusters, quantum dots, spherical nanoparticles, etc., come under this category. Detailed discussion on

zero-dimensional nanoparticles has been given in the previous section (see Section 5.12). A reference to nanoparticles often implies spherical nanoparticles. Anisotropic nanoparticles are the particles which exhibit direction and dimension dependent physical and chemical properties. One-, two-, and three-dimensional nanostructures come under this category. Anisotropic nanostructures have drawn significant attention and have been studied extensively due to their shape anisotropy, which offers exceptional advantages over isotropic nanoparticles and enables functional manipulation of various properties. Multiple surface plasmon resonance (SPR) in gold nanorods is an example of one such property exhibited by anisotropic nanoparticles. Introducing anisotropy into the nanoparticles can make a substantial change in their magnetic properties. The coercive field of ferromagnetic particles can be increased considerably by introducing shape anisotropy.¹

In order to achieve multiple properties at the nanoscale, an enormous amount of attention has been paid to make nanoparticles of various shapes with increasing degree of anisotropy.² This explosion of anisotropic nanomaterials research is reflected in the graph displayed in Fig. 13.3, which summarises a literature search on the number of papers including selected keywords (nanotubes, nanowires, nanorods, nanoplates and nanoflowers) in their titles, over the past 10 years. Even though anisotropic nanomaterials are interesting, limited information exists on their growth mechanisms.

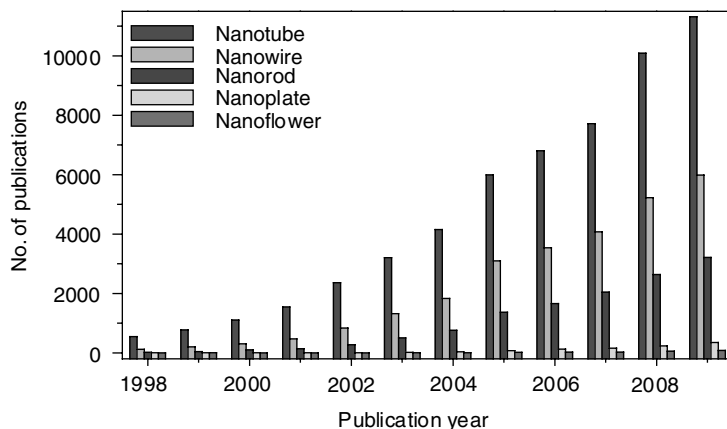


Fig. 13.3 Time evolution of the number of papers published during the last decade (1998–2009), including certain keywords (as indicated) in their title (source: ISI Web of Science). (For clarity see colour figure.)

13.2 ONE-, TWO-, AND THREE-DIMENSIONAL NANOPARTICLES

1-D materials are those, wherein there is one majority axis and the other structural parameters are much smaller than this, making the materials one-dimensional. In 2-D materials, there are two major structural parameters, others are smaller making the materials appear similar to sheets. In 3-D, there are three or more structural parameters. Anisotropic nanomaterials are coming under the category of one-, two- and three-dimensional nanoparticles. A wide range of nanoparticles, such as rods, wires, tubes,

belts, etc. (1-D), triangles, plates, hexagons, sheets, etc. (2-D), and beams, right pyramids, octahedrons, stars, flowers, etc. (3-D), are included in this category. There are various synthetic protocols used for making anisotropic nanoparticles. Detailed descriptions of various synthetic protocols for making anisotropic nanoparticles are given in the following sections.

13.3 GENERAL STRATEGIES FOR THE SYNTHESIS OF ONE-, TWO- AND THREE-DIMENSIONAL NANOSTRUCTURES

Nanoparticles with anisotropic shapes are very interesting in view of exploring the origin of the anisotropy. Many techniques, including both top-down and bottom-up approaches, have been developed and applied for the synthesis of anisotropic nanoparticles. Top-down approach includes milling and lithography and bottom-up approach includes various chemical methods. As nanoparticles produced by top-down approach have a relatively broad-size distribution, varied particle shape or geometry and use expensive synthetic pathways, which are industrially non-scalable, bottom-up approaches are far more popular in the synthesis of nanoparticles. Wet chemical synthesis is a potential bottom-up method to produce anisotropic nanoparticles, such as rods, wires, urchins, disks, triangular prisms, plates, cubes and branched particles in high yield and structural purity with varying size, shape, structure, composition and surface chemistry. However, a general mechanism for the formation of these morphologies has not been fully understood yet. Preferential adsorption of capping molecules to specific facets can block/enhance the crystal growth in some directions. In certain cases, formation of surfactant micelles or structural defects would physically direct the anisotropic growth. Other aspects, such as oxidative etching and control of the nucleation, can also induce the anisotropic growth of the nanoparticles. The energetic aspects can also play an important role in determining the anisotropic growth of nanoparticles. The formation of anisotropic structures is the direct consequence of the energetics being dominated by surface energy nanometer regime. Anisotropic nanoparticles have higher surface to volume ratios than spheres, and consequently, higher energy per atom, even though they can expose facets with lower-surface energies (111 in *fcc* metals, for example). Moreover, the surface-to-volume ratio scales inversely with the size of the particles. Hence, whenever anisotropic nanoparticles (more energetic) are formed together with spherical ones (less energetic) and their shape is not allowed to change, the reduction in the total surface to volume ratio of the system is higher, and consequently, in the total energy per atom, when the anisotropic particles increase in size. In this section, we discuss various bottom-up synthetic protocols for making anisotropic metal nanostructures.

13.3.1 Seed-mediated Synthesis

Even though large numbers of methods have been used for making anisotropic nanostructures, seed-mediated growth process is a widely used method, which can yield various nanostructures, such as rods, wires, triangles, stars, flowers, etc. This method involves two steps. The first step in this process is the synthesis of 'seed nanoparticles' by simple reduction process, in which the metal salt is reduced by reducing agents in presence of stabilising agents. Sodium borohydride is the commonly used reducing agent. The seed need not always be a metal nanoparticle. Growth of the seed nanoparticles

into the desired shape is the second step of this process. The growth solution contains surfactant or shaping agent and a mild reducing agent. In this process, metal salts will get reduced on the surface of seed nanoparticles. The surfactant molecules will form suitable templates, which facilitate the growth process to yield nanoparticles of desired morphology. Nanorods and wires of gold and silver can be easily made by this method (see Section 5.9). The size of the nanoparticles can be tuned by changing the amount of seed nanoparticles added. In the case of gold nanorods, the size can be reduced by increasing the amount of seed particles. External agents, such as various molecules or ions, can alter the growth direction of the nanoparticles and can result in the formation of variously shaped nanoparticles. With the addition of a small amount of iodide ion in a growth solution of gold nanorod synthesis, the shape of the resultant nanoparticles can be changed into triangular nanoprisms³ (Fig. 13.4). For the growth of nanoprisms, the growth solution was prepared by adding 10 ml of a mixture of a solution identical with that used to synthesise gold nanorods in addition to small concentrations of KI. To this solution, 0.2 ml of 0.1 M ascorbic acid was added, which resulted in a colourless solution. Then, 0.025 ml of Au@citrate seed was mixed with the solution. Here, the iodide ion adsorption appeared to suppress the crystal growth along the Au(111) direction, resulting in Au(111)-faced triangular nanoprisms (Fig. 13.4A). When the counter anions of the surfactant cetyltrimethylammonium bromide (CTAB) were replaced with chloride ions (CTAC), a drastic change in the morphology from rod to rice-shape was observed (Fig. 13.4B), which demonstrates the effectiveness of the adsorption of halide ions.

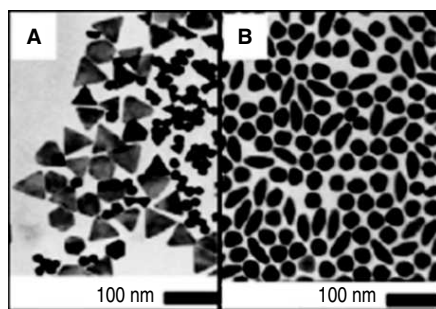


Fig. 13.4 TEM images of diverse gold nanostructures formed (A) in the presence of iodide ions; (B) under the CTAC template (adapted from Ref. 3. Copyright (2007) American Chemical Society.).

There are various factors, which influence the size and shape of the nanostructures. The concentration of surfactant molecules is one parameter, which plays an important role in the shape determination, since the shape of the micelles formed by the surfactant during the growth varies with the concentration. Synthetic method of gold nanoprism developed by Mirkin *et al.*⁴ is an example for the dependence of surfactant concentration on the morphology determination. In this approach, small gold seed nanoparticles of ~5 nm is subjected to a three-step growth process in an aqueous solution containing the capping agent CTAB, gold ions, reducing agent (ascorbic acid) and NaOH, resulting in the formation of gold nanoprisms in very good yield. Nanoprisms were formed only when saturated CTAB solution was used, which is a clear indication of the concentration dependence on

the morphology of the nanoparticles. TEM image of the nanoprisms synthesised by this method is shown in Fig. 13.5A. The UV/vis absorption spectrum of nanoprisms (Fig. 13.5B) shows three different absorptions. The peak in the near-infrared (NIR) region is attributed to in-plane SPR of nanoprisms and that at 540 nm is due to their out of plane SPR. A broad band in the UV/vis/NIR spectrum at 800 nm is assigned to the in-plane quadrupole mode of the nanoprisms (Fig. 13.5B). This assignment is based upon the characterisation of these prisms by electron microscopy and on discrete dipole approximation (DDA) calculations, which predict plasmon bands that match the experiment. The observed absorption spectrum of the nanoprisms was in good agreement with the theoretical spectrum. The edge length of these Au nanoprisms can be controlled while preserving their original shape, crystal properties and thickness. Importantly, edge length control is a way of tailoring the optical properties of these structures. For that, the prisms have to be used as seeds, and reinitiate the particle growth by exposing them to Au ions in the presence of a reducing agent in a step-by-step manner.⁵ By this method, the edge length of the nanoprism could be varied from 100–300 nm without changing their crystallinity and thickness.

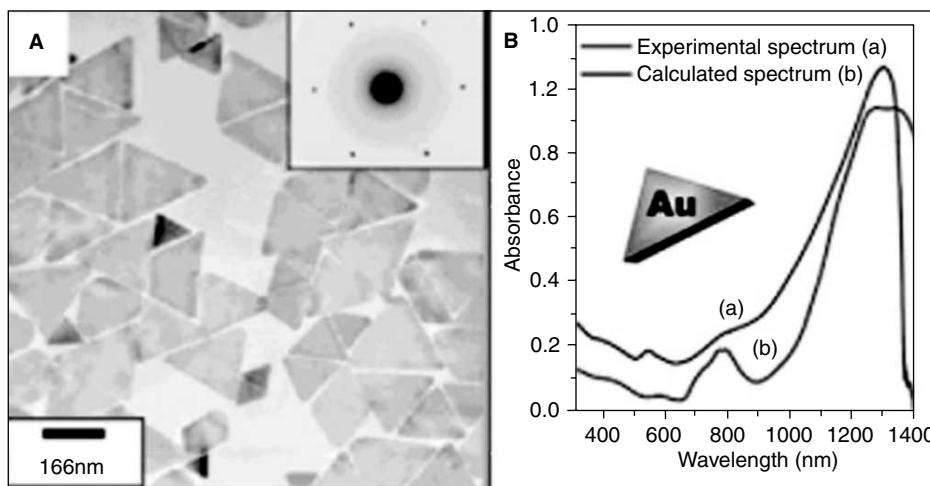


Fig. 13.5 (A) TEM image of Au triangular nanoparticles. The inset is the SAED pattern taken from individual nanoprism. (B) UV/vis/NIR spectra of purified Au nanoprisms (a) and DDA calculation (b) (adapted from Ref. 4. Copyright (2005) American Chemical Society).

It is also possible to make an aligned array of the nanotriangles on ITO surface⁶ by using the seed-mediated approach at low temperature. Here, 4-nm gold seed nanoparticles attached to the conducting glass surface were grown into gold nanotriangles by applying an electric potential. In this case, low temperature and electric field were found to be the critical factors that favour the nanotriangle growth. Silver nanoplates with sizes of 40–300 nm have been synthesised via a simple room-temperature solution-phase chemical reduction method in the presence of diluted CTAB and ~15 nm Ag@citrate seed particles.⁷ The interesting finding in this case is that the size of nanoplates can be easily controlled by using a CTAB solution of 10–15 times dilution of that normally use in the seed-mediated synthesis

(100 mM). Structure and surface analysis data revealed that the selective adsorption of CTAB on the (111) plane of silver seeds and the formation of silver bromide in contact with the seeds play critical roles in nanoplate formation.

Another variety of nanomaterial, core-shell nanocube, made of Au and Pd (Au@Pd nanocubes) can be synthesised by using a modified two-step seed-mediated growth method.⁸ Au nanoparticles of about 3 nm in diameter were first synthesised as the seeds for growing about 30 nm Au nanooctahedra, which acts as the core. Then the uniform Au@Pd nanocubes were overgrown on the octahedral Au cores in high yield by reducing H_2PdCl_4 with ascorbic acid under the assistance of a surfactant CTAB (Fig. 13.6A-C). Two other kinds of binary metal core-shell nanoparticles, Au@Ag nanocubes and Au@Pt nanospheres, were also synthesised in the similar reaction conditions as shown in Fig. 13.6. It was found that Au@Ag nanoparticles exhibit uniform cubic shape and are well monodispersed. In case of Au@Pt, uniform nanospheres with a rough surface were observed. This dramatically different morphology suggests a 3-D heterogeneous nucleation and growth, rather than the layer-by-layer epitaxial growth for Pt shell on Au seeds. The growth of heterogeneous metal shells on the gold core presents two different forms, the conformal epitaxial growth for Au@Pd and Au@Ag nanocubes (Fig. 13.6D), and the heterogeneous nucleation and island growth for Au@Pt nanospheres (Fig. 13.6E). In order for the epitaxial layered growth of heterogeneous core-shell nanocrystals to

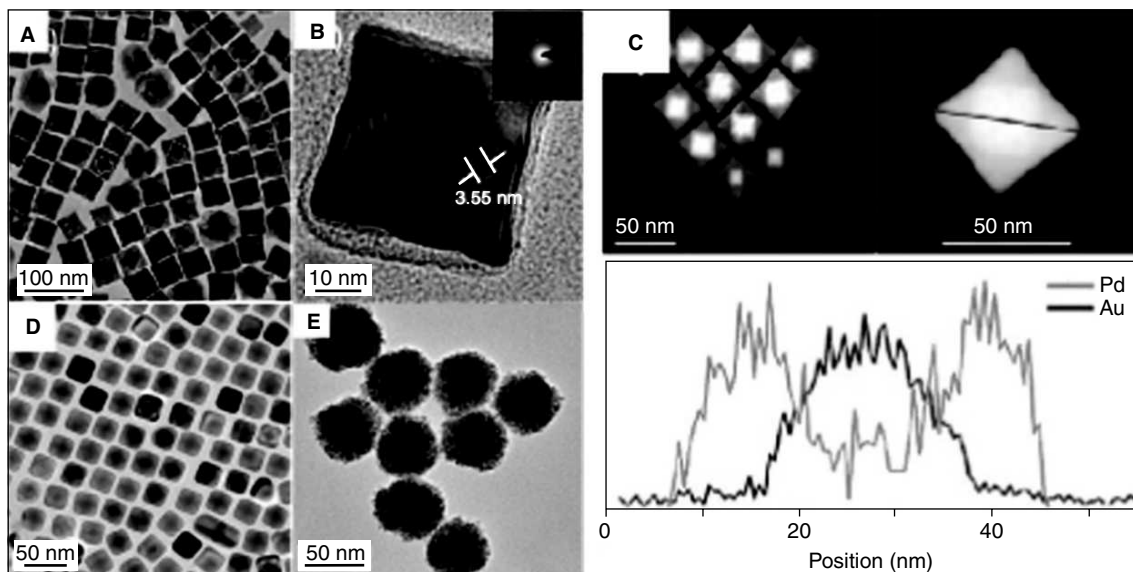


Fig. 13.6 (A) TEM image of Au@Pd nanocubes. (B) TEM image of a single Au@Pd nanocube at high magnification. The inset is the SAED pattern taken from individual nanocube. (C) STEM images of the octahedral Au seed within a cubic Pd shell and cross-sectional compositional line profiles of an Au@Pd nanocube along the diagonal (indicated by a line). (D) and (E) are TEM images of Au@Ag nanocubes and Au@Pt nanoparticles, respectively (adapted from Ref. 8. Copyright (2008) American Chemical Society).

Table 13.1 Shapes of gold particles and corresponding reaction conditions

[CTAB]/M	[Au] _{max} /M	[Au ³⁺]/M	[AA]/M	Shape/Profile	Dimension [§]	% Yield
1.6×10^{-2}	1.25×10^{-8}	2.0×10^{-4}	6.0×10^{-3}	Cube	66 nm	~ 85
1.6×10^{-2}	1.25×10^{-8}	2.0×10^{-4}	3.0×10^{-3}	Hexagon	70 nm	~ 80
1.6×10^{-2}	1.25×10^{-7}	2.0×10^{-4}	6.0×10^{-3}	Triangle	35 nm	~ 80
1.6×10^{-2}	1.25×10^{-8}	4.0×10^{-4}	6.4×10^{-4}	Cube	90 nm	~ 70
9.5×10^{-2}	1.25×10^{-7}	4.0×10^{-4}	6.0×10^{-3}	Tetrapod	30 nm	~ 70
1.6×10^{-2}	1.25×10^{-8}	4.0×10^{-4}	1.2×10^{-2}	Star	66 nm	~ 50
5.0×10^{-2}	6.25×10^{-7b}	5.0×10^{-4}	3.0×10^{-3}	Tetrapod	293 nm	~ 75
9.5×10^{-2}	2.5×10^{-7}	4.0×10^{-4}	6.4×10^{-4}	Branched	174 nm	~ 95

happen, the following rules have to be taken care of: (i) the lattice constants of two metals should be comparable with the lattice mismatch smaller than about 5 per cent. The shell metal with smaller atom radius is easier to epitaxially grow on the core as they could uniformly release the lattice strain resulting from the lattice mismatch. (ii) The electronegativity of the shell metal is lower than the core metal in order to avoid the displacement reaction and to easily wet the surface of the core. Otherwise, the shell metal intensively tends toward galvanic displacement of the core metal instead of the epitaxial growth. Apart from this, a fine control of the nanoparticle shape can be achieved by the systematic variation of the experimental parameters.⁹ Table 13.1 shows the various experimental conditions, at which gold particles of different shapes can be formed. Corresponding, TEM images of these structures are presented in Fig. 13.7A–D. This solution-based chemical route produces a number of structural architectures, from rod-, rectangle-, hexagon-, cube-, triangle- and star-like Au particles

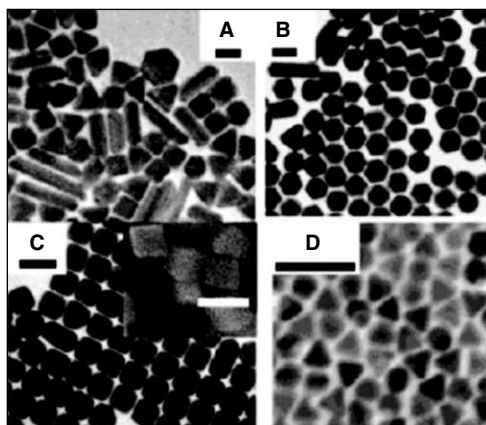


Fig. 13.7 A-D are the TEM images of various anisotropic Au nanoparticles synthesised under different conditions. Inset of C shows the corresponding SEM image. Scale bars are (100 nm) (adapted from Ref. 9. Copyright (2004) American Chemical Society).

in high yield at room temperature in the presence of a single surfactant in aqueous solution. With an altered order of reactant mixing and by the addition of NaOH, seed nanoparticles can grow into gold nanostars of size less than 100 nm (Fig. 13.8A and B).¹⁰ Even though the exact mechanism of formation of gold nanostars is unclear, it is believed that the addition of NaOH may lead to more rapid growth due to forced reduction of gold ions. Single particle spectroscopy revealed that these nanoparticles have multiple plasmon resonances resulting in polarisation-dependent scattering with multiple spectral peaks, which correspond to the different tips on the nanostar (Fig. 13.8C). The gold nanostars described here provide a multispectral signal from a single nanoparticle that could be used to detect 3-D orientations of molecules by exploiting their multidirectional polarised scattering. Gold nanostars with single crystalline tips can be synthesised in extremely high yield through the reduction of HAuCl_4 in a concentrated solution of poly(vinylpyrrolidone) (PVP) in *N,N*-dimethylformamide (DMF), in presence of preformed Au nanoparticle seeds.¹¹

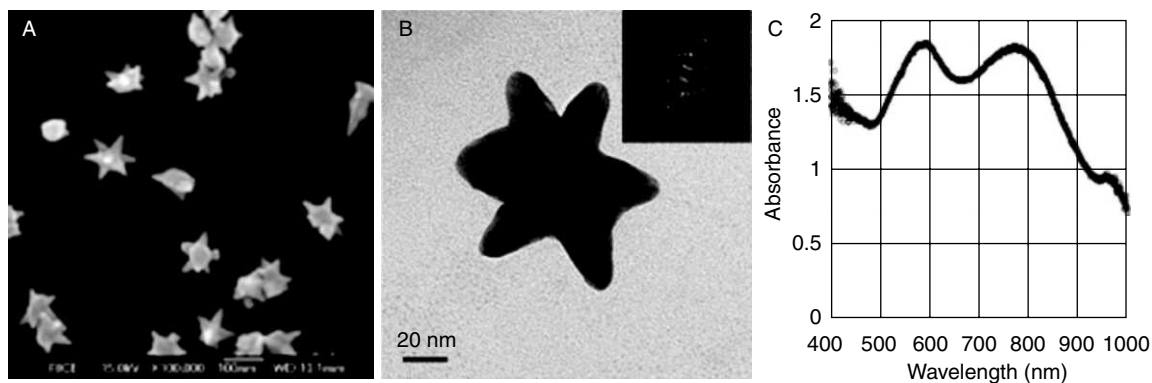


Fig. 13.8 (A) and (B) are SEM and TEM images, respectively, of star-shaped gold nanocrystals. Inset of (B) shows the SAED pattern taken from a single nanostar. An extinction spectrum of the nanostar solution exhibits broad peak in the visible and NIR regions (C) (adapted from Ref. 10. Copyright (2006) American Chemical Society).

The morphology of the seed particle is one important parameter that decides the anisotropic growth. Beautiful gold mesoflowers (Fig. 13.9A and B) can be synthesised in large quantity by the seed-mediated method from an oligoaniline-capped Au nanoparticle seeds at 80 °C.¹² These mesoflower are made up of large number of spiky stems projecting outward from a core in all directions (Fig. 13.9B). The stems are bearing high resemblance to a hierarchical array of scales or plate-like subunits, which themselves have the shape of stars, forming a pyramid of stars (Fig. 13.9C). Each stem has ridges along its corners, which provide a unique morphology. The presence of five edges is giving a star-shaped appearance to the stem as it is viewed from the top and ridges along the corners of the stems give a stacked appearance (Fig. 13.9D). In this case, presence of multiple twinning in the seed particle leads to anisotropic growth at high temperature. By stopping the reaction at predetermined time or by controlling the amount of seed nanoparticle, it is possible to tune the size of the mesoflowers from 100–3000 nm.

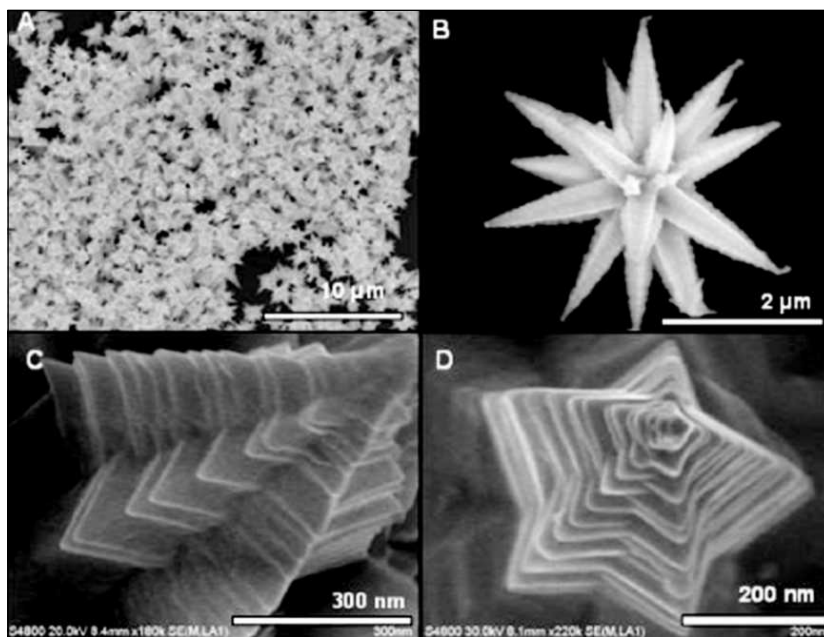


Fig. 13.9 Large area (A) and corresponding single particle (B) FESEM images of gold mesoflowers. (C) An enlarged FESEM image of a single stem of the mesoflower showing ridges along the edges. (D) Top view of a single stem of the mesoflower showing the pentagonal structure (reprinted from Ref. 12. Copyright (2009) Springer).

In certain cases, it is possible to synthesise anisotropic 3-D nanoparticle even in the absence of surfactant, using this approach. Here, Au^{3+} and NH_2OH were added to a chosen amount of AgNO_3 solution. Under vigorous stirring, colloidal gold seeds were added rapidly resulted in the formation of 3-D nanothorns. The formation and structural changes of these 3-D thorny gold nanoparticles can be explained by the site specific deposition of AgCl precipitates on the surface of gold nanoparticle seeds.¹³

13.3.2 Polyol Synthesis

Polyol synthesis is a simple and versatile route developed in 1989 by Fiévet *et al.*,¹⁴ to make colloidal particles of various shapes and sizes, made of metals and their alloys. The present form of the polyol synthesis is developed by Xia *et al.* They have made a number of modifications to the conventional protocol. The polyol synthesis involves the reduction of an inorganic salt precursor by polyol at an elevated temperature. Polyol refers to alcohols containing multiple hydroxyl groups. Ethylene glycol, propylene glycol, pentane diols, glycerols, etc., are commonly used polyols. Many precursor salts can easily dissolve in polyol. Apart from this, temperature-dependent reducing power and relatively high boiling points make polyol suitable solvent for making anisotropic nanoparticles. PVP is commonly used stabiliser to prevent agglomeration of the colloidal particles in polyol synthesis. This method

is good for making nanostructures of Ag as polyol have relatively high dielectric constant and can serve as a good solvent for both AgNO_3 and PVP. At elevated temperatures, ethylene glycol can reduce Ag^+ ions into Ag atoms and thereby induce the nucleation and growth of silver nanostructures in the solution phase. Due to the presence of oxygen and nitrogen atoms in the pyrrolidone unit, PVP can adsorb onto the surface of silver and can stabilise the resulting structure. Moreover, the extents of interaction strengths of PVP with different crystallographic facets of a silver lattice are different and could, therefore, induce anisotropic growth of silver.

In a typical polyol synthesis, anhydrous ethylene glycol was heated at $160\text{ }^\circ\text{C}$ for 1 hr. Then, separate solutions of AgNO_3 and PVP in ethylene glycol were simultaneously injected into the reaction flask by using a two-channel syringe pump. The first step of the growth is the reduction of AgNO_3 by ethylene glycol at elevated temperature and the formation of elemental silver. In the subsequent steps, these silver atoms nucleate and will form clusters (fluctuating structures) and then roughly spherical particles (Fig. 13.10A). In the next step, silver atoms generated from the reduction of AgNO_3 get diffused to the surface of the nuclei and will deposit at active surface sites, forming metallic bonds with their neighbours. By adjusting the molar ratio between PVP and AgNO_3 , the thickness of PVP coating and the location of PVP chains on suitable crystal planes can be modified. This modification alters the resistance of each facet to growth (addition of silver atoms) and led to the formation of silver nanostructures with distinct shapes.

Most silver nuclei incorporate twin boundary defects, because such defects enable a lower surface energy. As the growth proceeds, changes in the defect structure of the nuclei become too costly relative to the available thermal energy, and they become trapped in a given morphology. As illustrated by Fig. 13.10A, this process results in various kinds of seeds, such as multiply twinned, singly twinned and single-crystal seeds, with the five-fold symmetry. Multiply twinned decahedra are the naturally abundant seed morphology and are also the most reactive. Silver atoms preferentially add to the twin defects of decahedra leading to the formation of nanowires (Fig. 13.10B). Nanowire formation also requires the presence of NaCl and iron salt. In the absence of chloride ions, the seeds rapidly aggregated to form irregular particles. The Cl^- ions adsorb on seeds and electrostatically stabilize them against aggregation.¹⁶

In order to retard the growth of nanowires, one must prevent the formation of decahedral seeds. Monodispersed nanocubes¹⁷ of silver have been synthesised in large quantities by introducing a small amount of hydrochloric acid to the conventional polyol synthesis (Fig. 13.10C). Hydrochloric acid plays an important role in selectively etching and dissolving twinned decahedral seeds.¹⁸ The presence of protons slows down the reduction reaction and thereby facilitates the formation of single-crystal seeds and nanocube formation. Even though the role of chloride ion is not completely understood, it is likely that the corrosive effect of Cl^- can etch twinned seeds as in the case of corrosion of steel.

If NaCl was substituted with $60\text{ }\mu\text{M}$ NaBr and the temperature was lowered to $155\text{ }^\circ\text{C}$, the reaction produced silver nanobars in 1 h (Fig. 13.10D). Storage of nanobars in a 5 wt per cent aqueous solution of PVP for 1 week resulted in their transformation into single-crystal nanorice with rounded corners and edges (Fig. 13.10E). Seeds with single twin planes are necessary to produce Ag right bipyramids (Fig. 13.10F). To produce such seeds, the extent of etching must be moderated. So that, the most

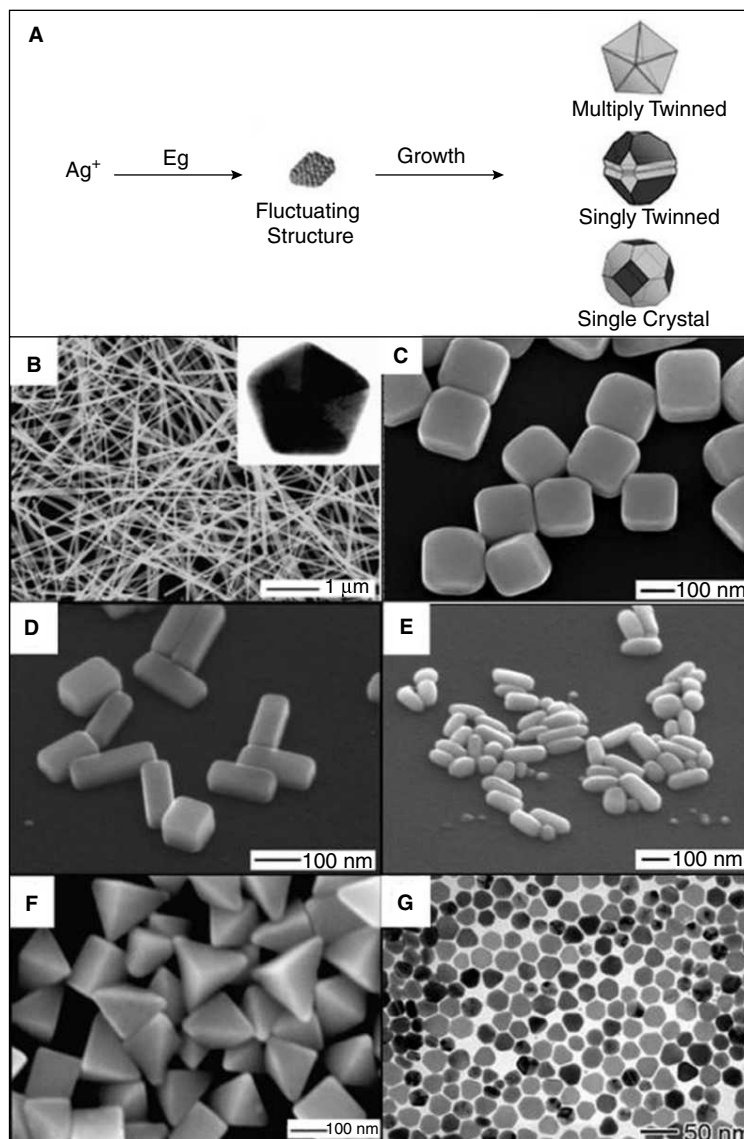


Fig. 13.10 (A) Schematic showing the reduction of Ag^+ ions by EG, leading to the formation of various kinds of nuclei. (B) Large area SEM image of Ag nanowires. Inset shows a cross-sectional TEM image of a microtomed nanowire, revealing its 5-fold twinned crystal structure and pentagonal profile (adapted from Ref. 16. Copyright (2007) American Chemical Society). (C) SEM image of Ag nanocubes (adapted from Ref. 17. Copyright (2002) Science). (D) SEM image of the Ag nanobars produced when NaCl was substituted with NaBr. (E) SEM of nanorice at a 45° tilt. (F) SEM images of bipyramids approximately 75 and 150 nm in edge length (adapted from Ref. 19. Copyright (2007) American Chemical Society). (G) SEM images of silver nanoplates prepared in the presence of PAM at 135°C for 3 h (adapted from Ref. 19. Copyright (2007) Royal Society of Chemistry).

reactive multiply twinned seeds can be etched away. This is achieved by reducing the amount of bromide by half relative to the nanobar reaction. Bromides enable sufficient etching to remove the multiple twinned seeds, but not so much as to eliminate singly twinned seeds.

Singly twinned seeds could also be grown slowly over 24 h to form silver nanobeams. Silver nanobeams are so named, because they have a cross-sectional aspect ratio similar to that of a beam of wood. In comparison to the synthesis of right bipyramids, here, the concentration of AgNO_3 and PVP was doubled and the temperature was lowered by 12°C , while the concentration of NaBr was kept the same. Although the concentration of the silver precursor was doubled, the lower reaction temperature resulted in a slower reduction rate.

In certain cases, polymers can alter the growth rate of the nanoparticles during polyol synthesis. Ag nanoplates (Fig. 13.10G) can be obtained in high yield by introducing polyacrylamide (PAM) into a polyol synthesis.¹⁹ Here, PAM serves as a dual-functional agent in the synthesis. It can act as both a steric stabiliser to prevent the agglomeration of nanoparticles and can form complexes with Ag^+ ions. This coordination effect can slow down the reduction rate to enable kinetic control.

The rapid reduction of gold precursors in refluxing 1,5-pentanediol results in a series of gold nanocrystals in the shape of octahedra, truncated octahedra, cuboctahedra, cubes, and higher polygons by incremental changes of silver nitrate concentration, which may be attributed to the selective deposition of silver species on the seed surface during the reaction.²⁰ In this case, silver species generated from AgNO_3 during the growth process determine the morphology of final nanocrystal by the selective growth of $\{111\}$ and/or the restriction of $\{100\}$. Single crystalline Au octahedral nanoparticles can also be synthesised in an ethylene glycol solution by a straightforward poly-(diallyldimethylammonium) chloride (PDDA)-mediated polyol route.²¹ Formation of Au nanooctahedra was attributed to the preferential adsorption of PDDA molecules on the $\{111\}$ planes of Au nuclei that inhibit the growth rate

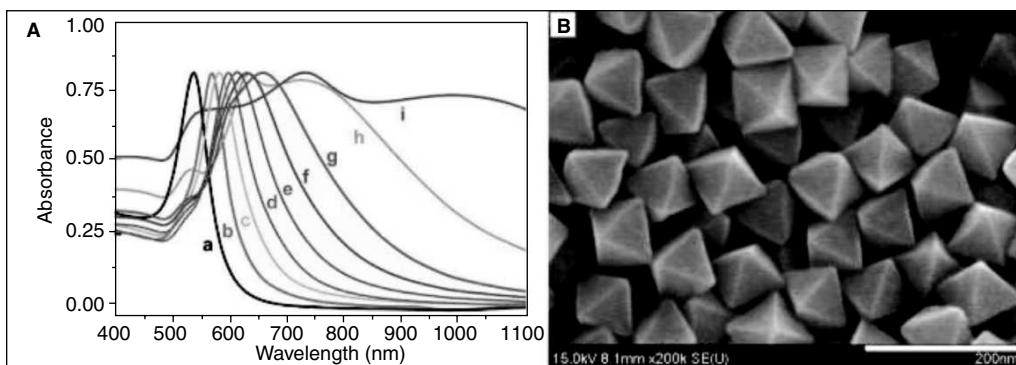


Fig. 13.11 UV/Vis absorption spectra for Au octahedra with different edge lengths dispersed in water. The edge lengths of Au octahedra for curve 'a' to curve 'i' were 20, 50, 63, 80, 95, 110, 125, 160, and 230 nm, respectively. (B) SEM images of Au octahedra with average edge lengths of 63 nm synthesised at 195°C by introducing 1 M HCl solution to the initial gold precursor. Scale bars: 200 nm (adapted from Ref. 21. Copyright (2008) American Chemical Society).

along the (111) direction. By adjusting the pH of the solution, Au octahedra with different dimensions can be synthesized (Fig. 13.11). A systematic increase in the UV/Vis absorption maxima was observed as the edge length of the octahedra increases (Fig. 13.11A). The synthetic strategy has the advantage of one-pot and requires no seeds, no foreign metal ions, and no pretreatment of the precursor, so that this is a practical method for controllable synthesis of Au octahedra.

13.3.3 Biological Synthesis

Biological systems are capable of making functional superstructures of inorganic nanomaterials, such as amorphous silica, magnetite (magnetotactic bacteria) and calcite.^{22a} In biological systems, shape controlled synthesis of nanomaterials has been achieved either by growth in constrained environments such as membrane vesicles, or through functional molecules, such as polypeptides that bind specifically to crystallographic planes of inorganic surfaces. Single crystalline equilateral triangular (Fig. 13.12A–C) and hexagonal silver nanoparticles have been synthesised biologically using *Pseudomonas stutzeri* AG259,^{22b} a bacterial strain that was isolated from a silver mine. Flat, triangular gold nanocrystals have been made using specific polypeptide repeat sequences in proteins secreted by the bacterium *Escherichia coli*.²³

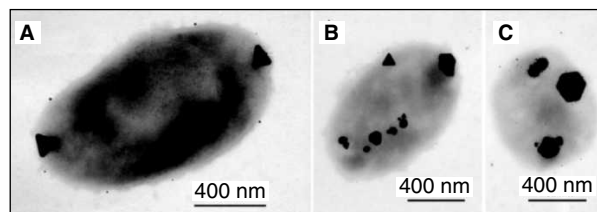


Fig. 13.12 (A) TEM image of large, triangular, Ag-containing particles at both poles produced by *P. stutzeri* AG259. An accumulation of smaller Ag-containing particles can be found all over the cell. (B and C) Triangular, hexagonal, and spheroidal Ag-containing nanoparticles accumulated at different cellular binding sites (adapted from Ref. 22b. Copyright (1999) *Proceedings of National Academy of Science*).

Triangular gold nanoprisms (Fig. 13.13A) can be synthesised biologically²⁴ in high yield at room temperature by the reduction of aqueous chloroaurate ions (AuCl_4^-) by the extract of the plant lemongrass (*Cymbopogon flexuosus*). During the reaction, a visible colour change from pale yellow to a ruby red, indicating formation of gold nanoparticles. The reducing sugars (aldoses) present inside the lemongrass extract were found to reduce the Au^{3+} into nanoprisms. By simple variation in the concentration of the lemongrass extract in the reaction medium, it is possible to vary the size of the nanoprisms²⁵ thereby the longitudinal SPR band in NIR region can be easily tuned (Fig. 13.13B). It is reported that tamarind leaf extract can also be used as the reducing agent for making gold nanotriangles.²⁶ On treating aqueous Au^{3+} solution with tamarind leaf extract, rapid formation of flat and thin single crystalline gold nanotriangles was observed. The effect of different organic solvent vapours like methanol, benzene and acetone on the conductivity of these gold nanotriangles was investigated by measuring the I-V characteristics. The results suggest that these nanotriangles can be used as vapour sensors.

Cinnamomum zeylanicum leaf broth is another reducing agent, which can reduce Au^{3+} into gold nanoprisms.²⁷ Nanoparticles of diverse shape such as hexagon, truncated triangle, and triangle can also be synthesised by reducing aqueous chloroauric acid solution with the seaweed extract *Sargassum sp.* at room temperature²⁸ (Fig. 13.13C).

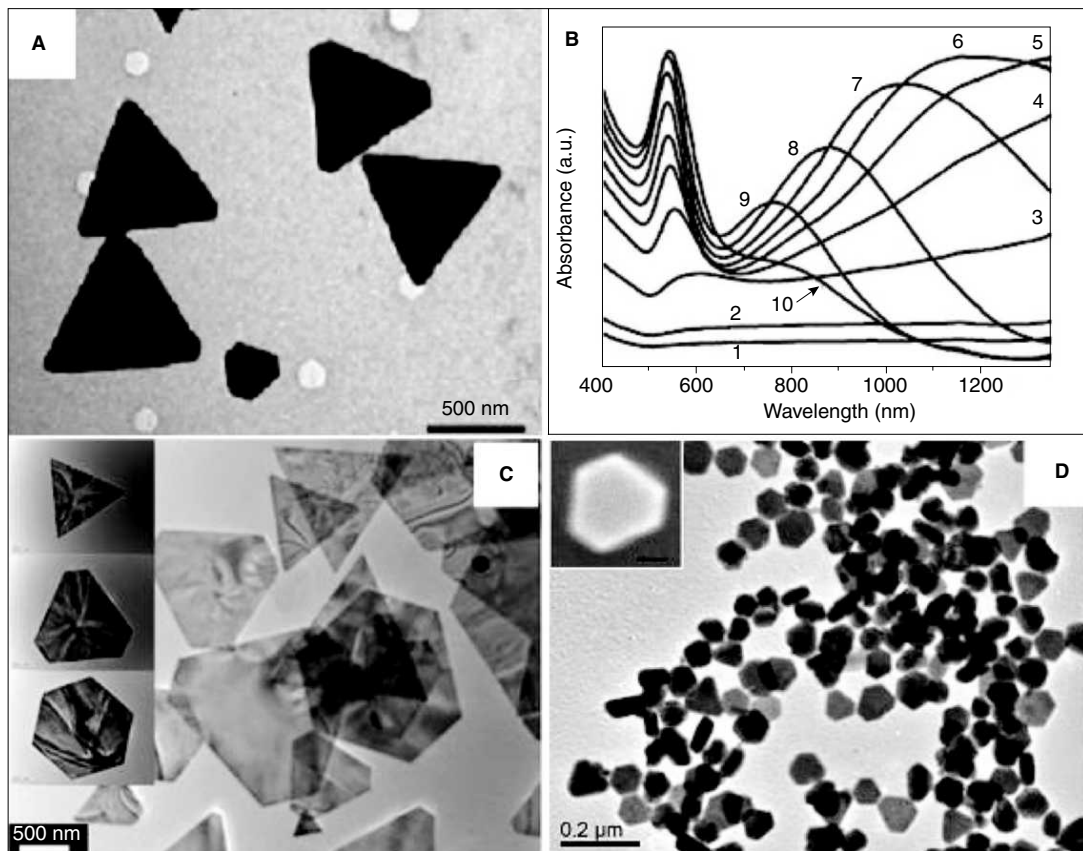


Fig. 13.13 (A) TEM image of gold nanotriangle synthesised by the reduction of aqueous HAuCl_4 solution with lemon grass extract (adapted from Ref. 25. Copyright (2005) American Chemical Society). (B) UV/Vis/NIR spectra of gold nanoparticles synthesised by adding different amount of lemon grass leaf extract to 5 mL of 10^{-3} M HAuCl_4 solution. Curves 1–10 correspond to solutions with 0.2, 0.3, 0.4, 0.5, 0.6, 0.7, 0.8, 1.0, 1.2, and 1.6 mL of extracts in 5 mL of 10^{-3} M HAuCl_4 solution, respectively. (C) TEM images of gold nanoplates synthesised by the reduction of aqueous AuCl_4^- by seaweed extract (adapted from Ref. 28. Copyright (2005) American Chemical Society). Single-crystalline Ag nanoplates synthesised in aqueous medium at room temperature using an extract of the unicellular green algae *Chlorella vulgaris* (Fig. 13.13D) (adapted from Ref. 29. Copyright (2007) American Chemical Society).

Here, the seaweed acts both as the reducing agent and the capping agents necessary for the gold nanoplate formation. During the nanoparticle growth, the capping agents may assist to limit the size and control the shape. It would bind non-specifically on all exposed surfaces of gold and lead to anisotropic growth. An extract of the unicellular green alga *Chlorella vulgaris* is also found to reduce Ag^+ into single-crystalline gold nanoplates in aqueous medium at room temperature (Fig. 13.13D).²⁹ Proteins in the extract reduce the Ag^+ ion into various nanoparticles. Hydroxyl groups in Tyr residues and carboxyl groups in Asp and/or Glu residues were identified as the most active functional groups for the reduction of Ag^+ ion and the anisotropic growth of Ag nanoplates, respectively. *Chlorella vulgaris* green alga can also reduce Au^{3+} ions into single-crystalline gold nanoplates at room temperature.³⁰ A cell-free extract (CFE) of *Rhodospirillum rubrum* has been used to synthesise gold nanowires with a network structure.³¹ Nanoparticles formed in bacteria are typically observed in aggregated state and in several cases, polyhedral shapes are seen. Synthesis of such structures of gold and silver was reported by Nair and Pradeep.³²

13.3.4 Hydrothermal Synthesis

In this method, nanoparticles have been synthesised in hot water/solvent under high pressure in an autoclave under high pressure. Here, H_2O serves both as a catalyst and occasionally as a component of solid phases. The synthetic method is also categorised as solvothermal,³³ since various solvents can also be used in accordance with the general process principle. It is also possible that additives are employed to modify the initial properties of pure hydrothermal water. In order to widen the range of applicability of this synthesis method, polar solvents (e.g., aqueous solutions containing HF, or other acids or bases to trim pH) or non-polar solvents (e.g., pure, supercritical) can be used for the dissolution–recrystallisation process. Up to date hydrothermal synthesis of a number of different materials has been demonstrated.

Ultralong ZnO nanowire/nanobelt arrays with honeycomb-like micropatterns on zinc substrates were made under hydrothermal conditions in large scale.³⁴ Novel Pd-Cd nanostructures with a high capacity for hydrogen storage were synthesised by this method. In this method, a series of Pd-Cd nanostructures with varying concentrations of Cd were directly grown onto Ti substrates using a facile hydrothermal reduction method.³⁵ Uniform Cryptomelane-type manganese oxide (OMS-2) 3D dendritic and spherical nanostructures were synthesised under mild and organic template-free hydrothermal conditions. In this case, by suitably adjusting the temperature, the shape evolution of OMS-2 was achieved.³⁶ In presence of electric field, hydrothermal synthesis can yield hierarchical Co-doped ZnO hexagonal ring-like superstructures (Fig. 13.14A–C) composed of nanorods. Here, the electric dipole interaction of nanorods plays an important role in the alignment of nanorods.³⁷ Other interesting structures, such as nanorings and microloops (Fig. 13.14D–F), of $\text{Ag}_2\text{V}_4\text{O}_{11}$, can also be synthesised by this method. In a particular synthesis, AgNO_3 and V_2O_5 powders were treated with distilled water at 170 °C for 12 h in a hydrothermal bomb.³⁸ Self-coiling of $\text{Ag}_2\text{V}_4\text{O}_{11}$ nanobelts will take place during this hydrothermal process without the use of any template or organic surfactant, results in the formation of nanorings and loops.

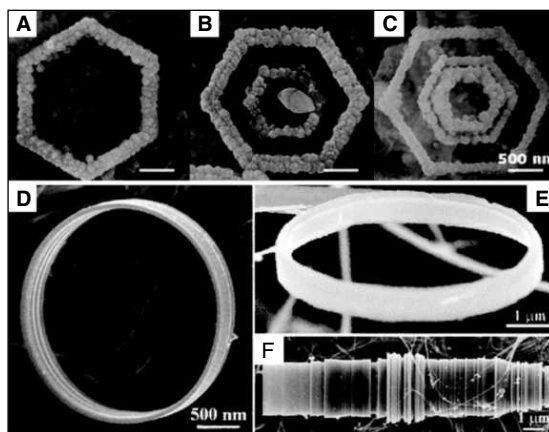


Fig. 13.14 SEM images showing (A) single-, (B) double-, and (C) triple-turn hexagonal ring-like superstructures of hexagonal single-crystal Co-doped ZnO nanorods (adapted from Ref. 37. Copyright (2008) American Chemical Society). (D) and (E) are SEM images of the $\text{Ag}_2\text{V}_4\text{O}_{11}$ nanorings (F) SEM image of the $\text{Ag}_2\text{V}_4\text{O}_{11}$ microloops formed by rolling of several nanobelts (adapted from Ref. 38. Copyright (2006) American Chemical Society).

Nanomaterials made of Bi_2S_3 of various morphologies, including nanorods, dandelion-like nanostructures, nanoleaves, nanoflowers, and nanocabbages were successfully synthesised from the single-source precursor $\text{Bi}(\text{SCOPh})_3$ or multiple-source precursors by using a colloidal solution method or hydrothermal method.³⁹

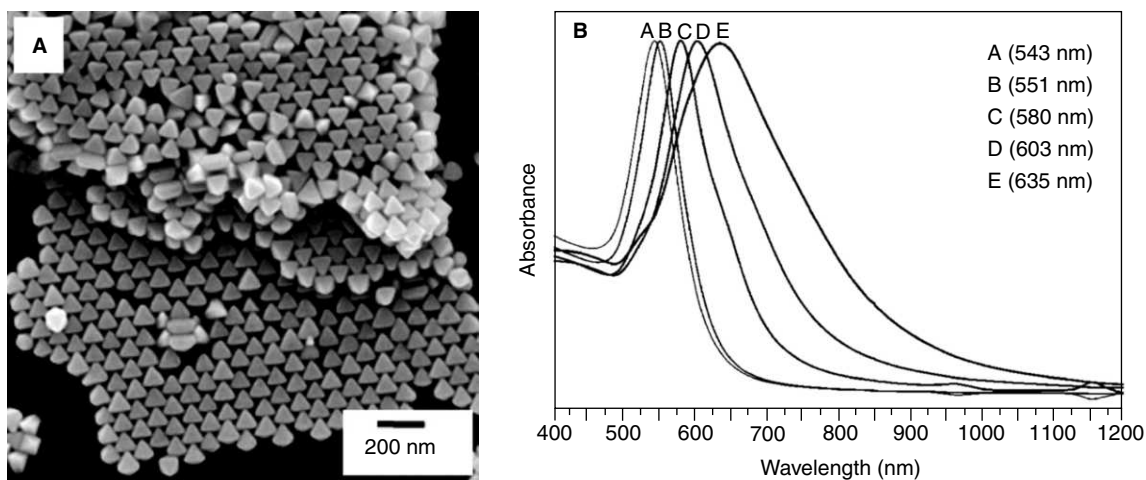


Fig. 13.15 (A) SEM image of the octahedral gold nanocrystals. The imaged regions show extensive self-assembled structures. (B) UV/vis absorption spectra of octahedral nanoparticles of different sizes. Maximum absorbance of the spectra has been normalised (adapted from Ref. 40. Copyright (2008) American Chemical Society).

Octahedral gold nanocrystals (Fig. 13.15A) were synthesised via a hydrothermal method from an aqueous solution of HAuCl_4 , trisodium citrate, and CTAB surfactant.⁴⁰ These mixtures were heated at 110 °C for 6, 12, 24, 48, and 72 h to obtain gold octahedra with approximate average sizes of 30, 60, 90, 120, and 150 nm, respectively. From the structural characterisation, it was confirmed that the octahedra are bounded by $\{111\}$ faces. The SPR bands were red-shifted from 543 to 635 nm (Fig. 13.15B), as the size of the nanoparticle increases.

The hydrothermal method is an interesting synthetic protocol in various aspects, since it is a low cost, environmentally-friendly technique, which can be used on large area, as well as fabrication of many nanostructures. The low substrate temperature enables this method to create various nanostructures on temperature sensitive substrates.

13.3.5 Galvanic Replacement Reactions

“Electroless” plating is a method introduced by Brenner and Riddell⁴¹ to describe the spontaneous reduction of metal ions to metallic particles and films in the absence of an external electric field. This method is attractive due to its simplicity of operation, cost-effectiveness, and it requires only simple equipment. This method is applicable to make a wide range of metal/substrate combinations, including metal-on-metal, metal-on-semiconductor, and metal-on-insulator. This is particularly important in the area of electronics with regard to metal deposition on a circuit board, for example. The process “electroless deposition” includes three fundamentally different mechanisms, such as autocatalytic, substrate catalysed, and galvanic displacement (immersion) processes. In which galvanic displacement reaction proceeds in an entirely different manner, in that deposition is carried out in the absence of an external reducing agent. Galvanic replacement reactions are single-step reactions that work based on the differences in the standard electrode potentials of various elements, leading to deposition of the more noble element and dissolution of the less noble component. The reducing electrons are derived from the valence-band electrons of the substrate (Fig. 13.16A). The process will continue as long as oxidised substrate ions are able to pervade through the metal film into solution, or until a dielectric layer of oxidised substrate forms, thereby arresting electron transfer. Although the detailed mechanism of galvanic displacement is not fully understood, mixed potential theory provides a useful tool to predict reactivities of metal/substrate systems.

A replacement reaction is a basic and simple method to synthesise nanostructured materials in a number of different systems. This method has advantages over other synthetic methods. For example, even though surfactant-based approaches have been used for making preparing anisotropic nanostructures with smooth surfaces, the attachment of surfactant molecules present on the surface are not desirable for many applications. These can increase electrical resistance, when the nanoparticles are used as conductive components in electronics. The surfactant molecules adversely influence in labeling of specific molecules. On the other hand, electroless deposition can avoid the use of surfactant molecules to produce metal nanostructures with various nonspherical shapes.

A simple method to synthesise nanoplates of pristine Ag on semiconducting GaAs wafers has been reported⁴² through the galvanic reaction between an aqueous solution of AgNO_3 and GaAs (Eqn. 1). In

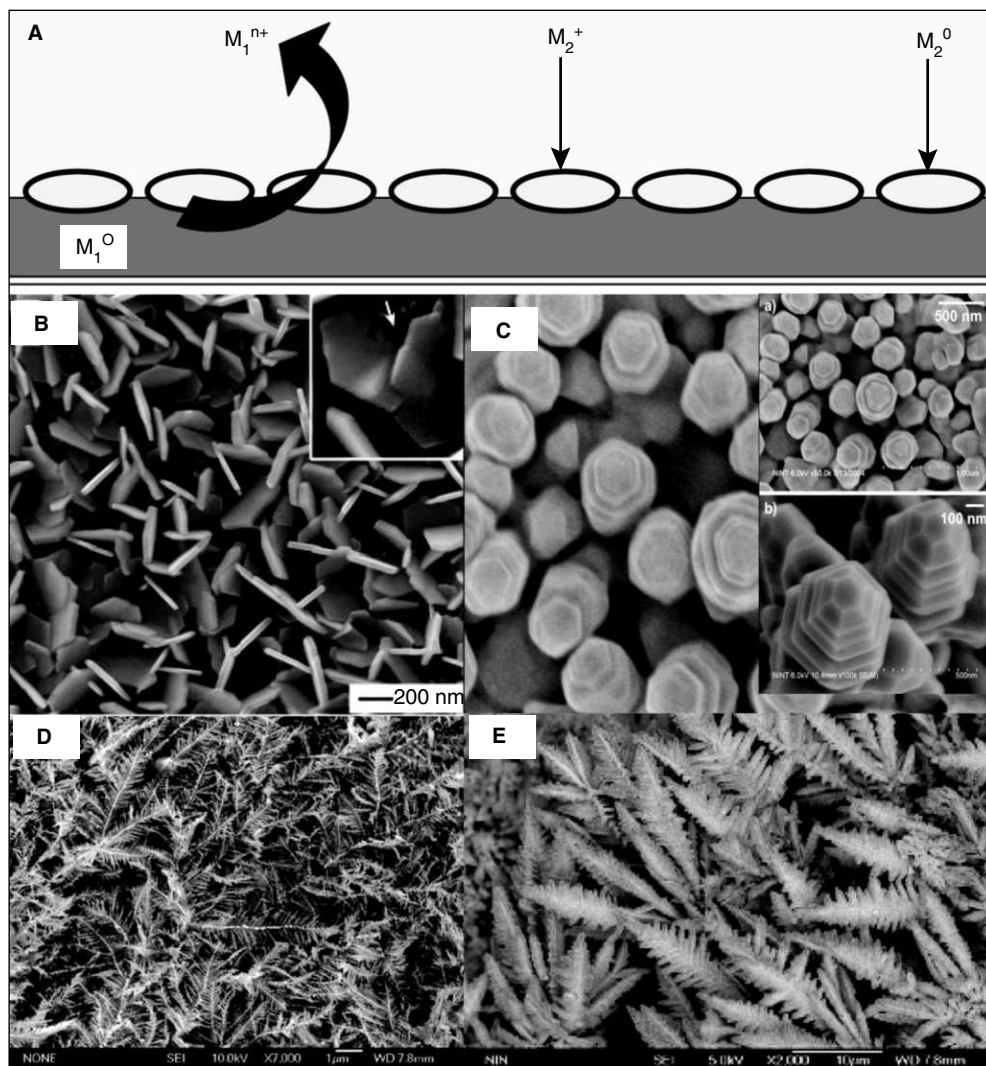
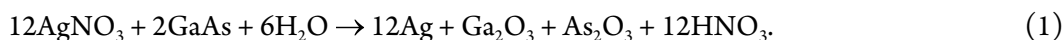


Fig. 13.16 (A) Schematic of galvanic displacement reaction. (B) SEM image of Ag nanoplates formed on the surface of n-type (110) GaAs wafer (adapted from Ref. 42. Copyright (2007) American Chemical Society). (C) Silver nano inukshuks prepared by immersing n-type Ge(100) in aqueous AgNO_3 solution. Insets show the close-up views of facets on the tips of silver metallic nano inukshuks (adapted from Ref. 43. Copyright (2005) American Chemical Society). SEM images of silver (D) (adapted from Ref. 44. Copyright (2007) American Chemical Society) and gold (E) (adapted from Ref. 45. Copyright (2006) Institute of Physics) dendrites formed on zinc plates).

a typical synthesis, onto the GaAs wafer, which is treated with aqueous hydrofluoric acid (HF) solution, a droplet of aqueous solution of AgNO_3 was placed to initiate the growth of silver nanostructures (and microstructures) via the galvanic reaction.



The morphologies and lateral parameters of Ag nanoplates can be successfully tuned by suitably adjusting the concentration of AgNO_3 . At a high concentration of AgNO_3 , an increase in the thickness of the as-grown Ag nanoplates was observed. In this case, germanium-germanium bonds in the crystal lattice provides the electron for the reduction of the Ag^+ ions in solution, leading to $\text{Ag}(s)$ and subsequent oxidation of $\text{Ge}(s)$ into Ge^{4+} in a spontaneous redox reaction. The resulting Ge^{4+} product, germanium oxide, can be removed easily, as it is soluble in water.

Silver nanoinukshuks (Fig. 13.16C), an unusual variety of Ag nanostructures can be synthesised by immersing n-type $\text{Ge}(100)$ in aqueous AgNO_3 solution.⁴³ Silver nanoinukshuks are formed at concentrations around 10^{-3} M of aqueous AgNO_3 solution at room temperature on flat or rough, native oxide-capped germanium surfaces. The nanoinukshuks had 300-nm diameter stacked hexagons with facets and can grow perpendicular to the (111) planes of the silver hexagons. Different Ag salts, such as AgClO_4 and $\text{Ag}(\text{CH}_3\text{CO}_2)$, can also yield nanoinukshuks. AgSO_4 consistently produces more flat dendritic structures. Inset shows the close-up view of facets on the tips of silver metallic nanoinukshuks. Through a simple electroless metal deposition route, gold dendritic nanostructures can be synthesised using HAuCl_4 , H_2O , and zinc. The zinc plate was immersed in the container with HAuCl_4 solution, at room temperature and ambient pressure, resulted in dendritic nanostructures.⁴⁴ The same approach can be extended to make Ag dendritic nanostructures.⁴⁵

Galvanic replacement reaction can be used as a versatile route to make metal nanostructures with controllable hollow interiors and porous walls. The replacement reaction between metal nanoparticle and a salt precursor containing a relatively less active metal plays an important role in this type reaction. This method has been widely used to produce gold-based hollow nanostructures with different morphologies, including cubic nanoboxes, cubic nanocages, nanorings, nanoboxes, single-walled nanotubes, and multiple-walled nanoshells or nanotubes. In addition to gold, hollow platinum and palladium nanostructures have also been synthesised by using appropriate salt precursors for the replacement reaction. These hollow and porous metal nanostructures show fascinating physical and chemical properties, which can be used for biological applications.

Ag nanocubes with truncated corners undergo replacement reaction to form pores at the corners by the addition of Au^{3+} ions. A wet etchant, such as $\text{Fe}(\text{NO}_3)_3$ or NH_4OH , has been used for the selective removal of Ag from the Au/Ag alloy nanostructures after thin layers of Au have been deposited onto the Ag nanocube surface.

Au-based nanoboxes and nanocages can be synthesised by a template-engaged hollowing-out mechanism by the titration of an aqueous suspension of Ag nanocubes with an aqueous solution of Au^{3+} . Here, the Ag nanocubes act as sacrificial template. During this process, AuCl_4^- oxidises the Ag template to AgCl . This is highly soluble in water at the elevated reaction temperature. The electrons generated in the oxidation process migrate to the Ag nanocube surface, which reduces Au^{3+} to Au atoms. The Au atoms can grow epitaxially over the Ag nanocubes since Au and Ag are having same face-centered cubic structure with closely matched lattice constants. In the initial stage of the reaction, small pits are generated on the surface of each nanocube. This allows the ionic species to diffuse

continuously in and out of the oxidation sites. As the reaction proceeds, this pit evolves into a deep hole, with its opening at the surface eventually being closed, results in a seamless nanobox composed of Au/Ag alloy. Upon adding more amount of Au^{3+} , dealloying of the nanobox takes place, which leads to the formation of Au-based nanocages with porous walls⁴⁶ (Fig. 13.17A).

Au nanoframes⁴⁷ (Fig. 13.17B) were obtained in high yield through a facile galvanic replacement reaction between Ag nanocubes and AuCl_2^- . Cubic nanoframes of Pd and Fe have also been reported. Here, Pd nanocubes were synthesised by reducing Na_2PdCl_4 in ethylene glycol, water, and PVP. The resultant solution then aged in an oxidising environment that corroded the structures to form nanoframes.⁴⁸ In the case of iron, nanoframes were synthesised from the thermal decomposition of a Fe(II)-stearate complex in the presence of sodium oleate and oleic acid.⁴⁹

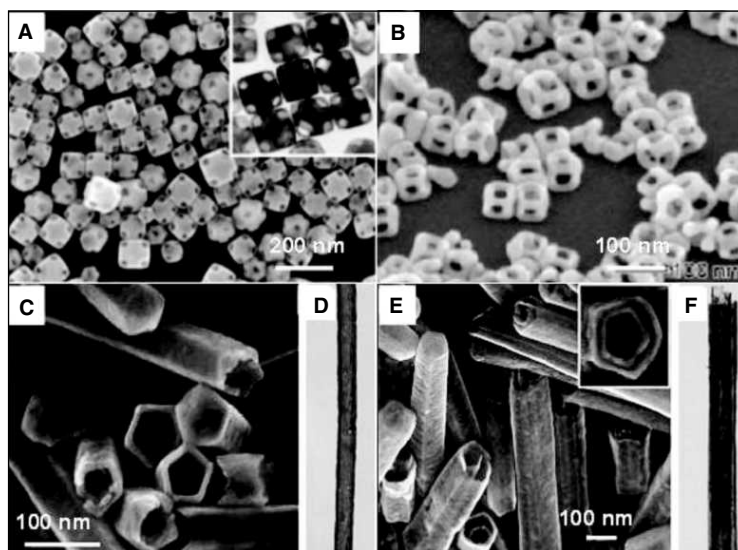


Fig. 13.17 (A) SEM and TEM (inset) images of Au nanocages (adapted from Ref. 46. Copyright (2004) American Chemical Society). (B) SEM image of the Au nanoframes (adapted from Ref. 47. Copyright (2008) Springer). C, E are SEM images, and D, F are TEM images of single-walled nanotubes of Au/Ag alloy and double-walled nanotubes of Au/Ag alloy, respectively (adapted from Ref. 50. Copyright (2008) Wiley).

The unique combination of the galvanic replacement reaction and the electroless deposition of Ag can also be extended to prepare metal nanotubes with single and multiple walls (Fig. 13.17C and E). Here, Ag nanowires act as the sacrificial template.⁵⁰ When Ag nanowires are treated with aqueous solution of Au^{3+} , the galvanic replacement reaction generates a tubular sheath of Au, whose morphology is complementary to that of the Ag nanowire. Following the same procedure for multiwalled nanoshells, coaxial nanotubes with more than two walls can be synthesised.

13.3.6 Photochemical Synthesis

It has been found that the reduction of metal salt precursors can also be done by the radiolytic and photochemical methods. The main advantages of such technique include the reduction of metal ions without using excess reducing agents. In this case, radiation is absorbed regardless of light-absorbing solutes and products. Also, the rate of reduction reaction is known, since the number of reducing equivalents generated by radiation is well defined. Apart from this, photochemical synthesis does not require a specific and costly instrument.

A photo-induced method has been reported for synthesising large quantities of silver nanoprisms in high yield in the form of a colloidal suspension.⁵¹ This photo-mediated route has led to a colloid with distinctive optical properties that directly relate to the shape. The initial step of the reaction includes the synthesis of spherical silver particles by the injection of NaBH₄ solution to an aqueous solution of AgNO₃ in the presence of trisodium citrate. Subsequently, as a stabilising agent, bis(*p*-sulfonatophenyl) phenylphosphine dihydrate dipotassium salt solution (BSPP) was added drop-wise. The system is then irradiated with a conventional fluorescent light. It is possible to tune the edge lengths of these nanoprisms to 30–120 nm range.⁵² The growth process can be controlled using dual-beam illumination of the nanoparticles, and appears to be driven by surface plasmon excitations. Depending on the illumination wavelengths, the plasmon excitations lead the fusion of nanoprisms. The observed bimodal growth process occurs through an edge-selective particle fusion mechanism with four type-1 nanoprisms coming together in step-wise manner to form a type-2 nanoprism (Fig. 13.18). Gold nanorods with controlled aspect ratios have also been synthesised via a simple photochemical process in the presence of silver ions. In the photochemical approach, it has been noted that the amount of Ag⁺ ions plays critical role in the formation of NRs with controllable aspect ratios instead of spherical NPs. The gold nanoparticles of various morphologies, such as triangular or hexagonal shapes, can be generated using the photo-reduction method by mixing Au³⁺ with sodium oxalate and a reducing agent in aqueous solution under illumination of a mercury lamp for more than 10 min. The size of the gold nanoparticles varies from 25 to 200 nm, which mainly depends on the duration of light illumination and the concentration of sodium oxalate.⁵³

Using a photochemical route, electrically-conductive CdS nanowires can be fabricated on DNA scaffolds. In this process, UV light was irradiated to a mixture, which contains cadmium perchlorate (Cd(ClO₄)₂) and thioacetamide (TAA). Obtained nanowires were found to be electrically conductive and stable for more than three months without any changes in their optical properties.⁵⁴ Crown-shaped platinum nanoparticles can be synthesised under the UV-light irradiation in the presence of fourth generation NH₂-terminal (G4-NH₂) PAMAM dendrimers. Aggregates of the G4-NH₂ PAMAM dendrimers formed in the aqueous solution, served as templates for the formation of such crown-shaped nanoparticles.⁵⁵

13.3.7 Electrochemical Synthesis

Electrochemical methods have been widely used for making various nanoparticles, especially of noble metals. This technique has many advantages over other approaches, since it has a lower processing

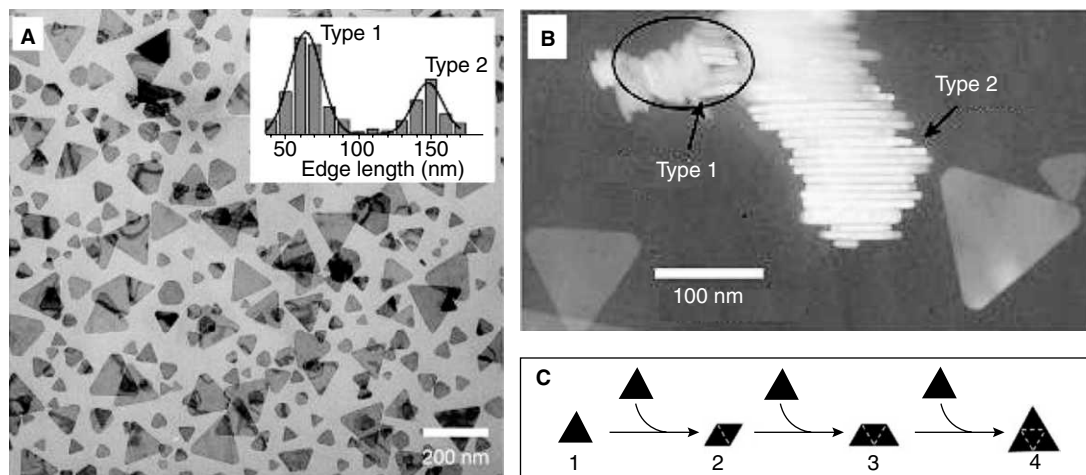
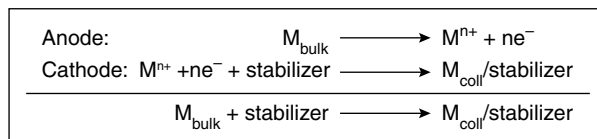


Fig. 13.18 The bimodal growth of Ag nanoprisms. (A) TEM image of a sample of Ag nanoprisms formed using single-beam excitation; inset, histograms used to characterise the size distribution as bimodal. (B) TEM images of nanoprism stacks showing that nanoprisms have nearly identical thicknesses. (C) Schematic diagram of the proposed light-induced fusion growth of Ag nanoprisms (adapted from Ref. 52. Copyright (2001) Nature).

temperature, high-quality products uses modest equipment and low cost. In 1994, Reetz *et al.* showed that the electrochemical reduction method can be used for making highly size-selective nanoparticles by adjusting the current density.⁵⁶ The experimental set-up contains a two-electrode set-up for 50–250 mL electrolyte solutions, in which the sacrificial anode consists of the bulk metal to be transformed into metal colloid. In the overall process, the bulk metal is oxidised at the anode. At the same time, the metal cations migrate to the cathode and reduction takes place with formation of metal colloid in presence of a stabilising agent (Scheme 13.1).



Scheme 13.1 Electrochemical synthesis metal colloids.

Gold nanocubes of uniform size can be synthesised by an electrochemical method, using a surfactant solution and acetone.⁵⁷ A two-electrode set-up can be used for this synthesis. The experimental set-up contains a gold plate and a platinum plate as the anode and cathode, respectively. These electrodes were placed vertically face-to-face inside the cell, which were separated by Teflon spacers. An aqueous solution of CTAB and a much more hydrophobic cationic co-surfactant tetradecyltrimethylammonium bromide (TTAB) were used as the growth solution. Apart from this, acetone was also added during the growth reaction. The electrolysis was carried out by constant ultrasonication resulted in the formation

of Au nanocubes. During the reaction, gold at the anode was oxidised to gold cations, which is then migrated to the cathode, where reduction occurs with the formation of gold adatoms (Fig. 13.19A). These adatoms were trapped by the surfactant to form nanocubes (Fig. 13.19B). The surfactant as the electrolyte and the stabiliser is generally regarded as a micelle template to control the size and shape of the nanoparticles. It was found that the shape of the gold nanoparticles can be changed by altering the rate of injection of acetone. At a lower concentration of acetone, spherical nanoparticles were formed. The UV/vis absorption (Fig. 13.19C) spectra of gold nanostructures were red-shifted as the amount of acetone injected was increased.

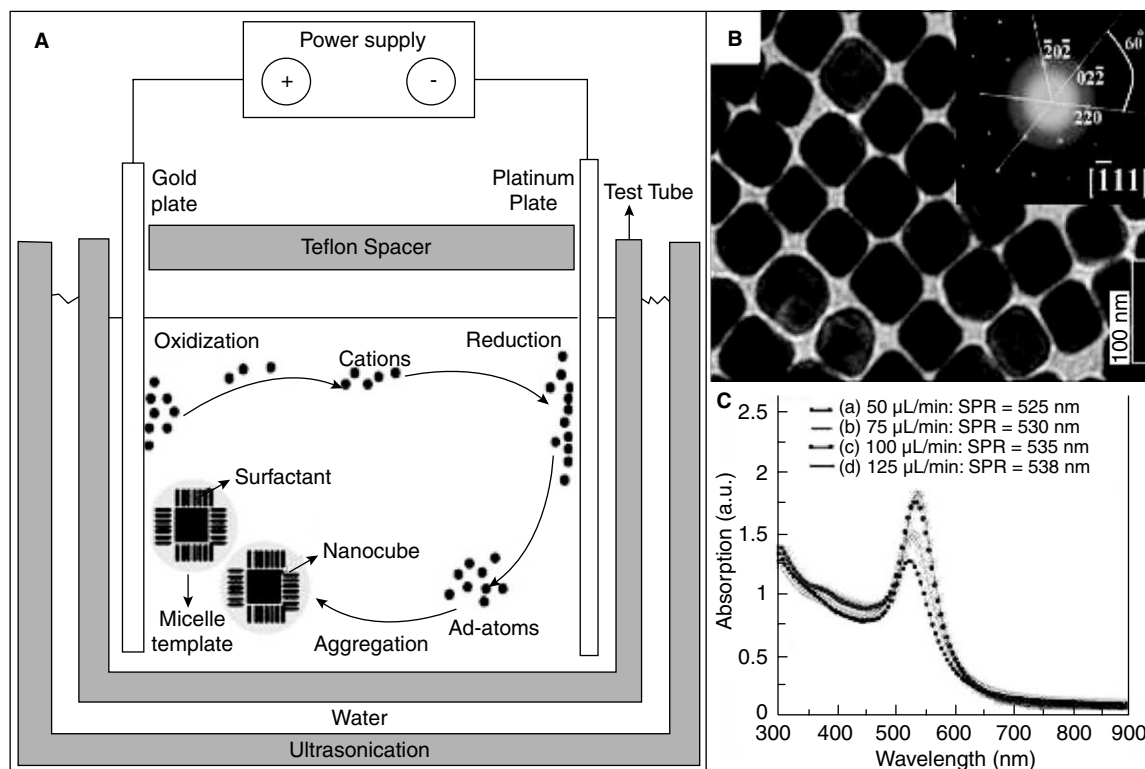


Fig. 13.19 (A) Schematics of the electrochemical set-up used for the synthesis of gold nanocubes. (B) TEM images of gold nanocubes. Inset shows a SAED pattern taken from any individual nanocube by directing the electron beam perpendicular onto one of its square faces. (C) UV/vis absorption spectra of various gold nanoparticles obtained with different injection rates of acetone (adapted from Ref. 57. Copyright (2008) American Institute of Physics).

Gold nanorods have been synthesised via an electrochemical method using a simple two-electrode cell.⁵⁸ Here, a gold metal plate is used as the anode and a platinum plate is used as the cathode. These electrodes are immersed in an electrolytic solution consisting of a cationic surfactant, hexadecyltrimethylammonium bromide and a rod-inducing co-surfactant, resulted in the formation of gold nanorods. Using a standard three-electrode cell with a potentiostat, a platinum foil counter electrode

and a saturated calomel electrode (SCE), platinum nanothorns were synthesised electrochemically at room temperature.⁵⁹ Here, platinum nanothorn (Fig. 13.20) were electrodeposited on glassy carbon substrate in 2 mM K_2PtCl_6 and 0.5 M H_2SO_4 solution by square wave potential between -0.20 V and 0.80 V at 10 Hz for 20 min.

Single-crystalline Ag dendrites can be fabricated on the Ni/Cu substrate by using a templateless, surfactantless, electrochemical method.⁶⁰ The morphology and geometry of the Ag particles were controlled by the applied potential. When the potential was decreased from -0.4 to -2.0 V, the morphology of the resulting product was changed from Ag polyhedrons to Ag dendrites. These dendrites grow preferentially along the (211) directions in a fractal mode.

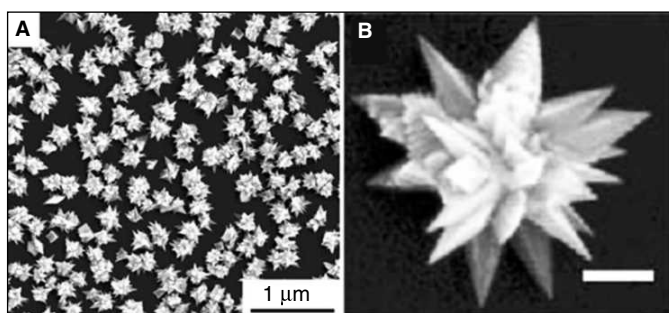


Fig. 13.20 SEM images of platinum nanothorns. (A) Large area SEM image; (B) high magnification SEM image of a platinum nano-thorn. The scale bar in (B) is 100 nm (adapted from Ref. 59. Copyright (2006) Royal Society of Chemistry).

13.4 PROPERTIES OF ANISOTROPIC NANOPARTICLES

The physical and chemical properties of nanoparticles depend on the type of motion their electrons can execute, which depends on the degree of their spatial confinement. The optical properties of colloidal nanoparticles in the UV/vis/NIR spectral range are mainly determined by the so-called localised surface plasmon resonances (LSPRs).⁶¹ The optical features, such as absorption, peak width, etc., depend on the shape, size, composition, surface charge, interparticle interactions, surface-adsorbed species, and the refractive index of the surrounding medium.⁶² Noble metal nanorods are better example to demonstrate the shape dependent LSPR properties. The optical spectrum of rod-shaped anisotropic nanoparticles does not show only one well-defined resonance peak as in the case of nanospheres. They exhibit two bands in the vis–NIR spectral range. Theoretical studies suggest that the band near 530 nm has been assigned to a transverse LSPR, which is polarised across (corresponding to electron oscillation perpendicular to) the long axis of the nanorod, and the other one, appearing at a longer wavelength, has been assigned to a longitudinal LSPR mode, which is polarised along (parallel to) the long axis (see section 5.9). For other anisotropic nanoparticles such as disks and triangular prisms, the LSPRs are typically split into distinctive dipole and quadrupole plasmon modes.⁶³

The localised electromagnetic fields surrounds to the metal nanoparticles, generated by the excitation at their LSPR, are the direct consequence of the polarisation associated with the collective oscillation of their electrons. In the case of spheroid, the field enhancement at the tip is larger than the sphere of similar dimensions.⁶⁴ Anisotropic metal nanoparticles show “lightning-rod effect”, another kind of field enhancement refers to an enhanced charge density localisation at a tip or vertex of a nanoparticle. When an electromagnetic field (e.g., laser light) excites the free electrons of a metallic tip, a highly localised, strong electric field develops at these sharp tip or vertex with large curvatures, leading to large field enhancement in those regions.⁶⁵ This is the reason for the high SERS activity of anisotropic nanoparticle.

The large particle surface area of anisotropic nanoparticles influences its chemical reactivity. It has been found that the rate of photochemical reaction of the molecules adsorbed on Ag nanoparticle can be controlled by the surface geometry of nanoparticles.⁶⁶ During galvanic replacement reaction between nanoparticles and metal ions, shape anisotropy plays important role in their chemical reactivity.⁶⁷

Increasing the anisotropic nature of the nanoparticle can enhance its catalytic activity. Large surface areas for a given quantity of materials make them good for catalysis. Studies on the platinum nanoparticles showed enhanced and selective catalytic activities for different morphologies compared to spherical nanoparticles.⁶⁸ Increasing the number of edges, crystallographic facets, corners, and faces, are of critical importance in controlling the catalytic activity and selectivity of metal nanoparticles. It has been shown that cubic Pd nanoparticles had higher turnover frequencies compared to its spherical counterpart for the hydrogenation of butyne-1,4-diol and of styrene oxide.⁶⁹

13.5 APPLICATIONS OF ANISOTROPIC NANOMATERIALS

Due to the size and shape dependent physical and chemical properties of the nanoparticles, anisotropic nanomaterials have been used for various applications. Few of the important applications of different kinds of nanostructures are mentioned below.

13.5.1 Bioconjugation and Labeling

Gold nanocage, functionalised with biological molecules, such as antibodies, nucleic acids, and small-molecule inhibitors can be used to target cancer cells for early-stage diagnostics and thermal therapy of tumors. Schematic illustration of the protocol used to conjugate antibodies to the surface of Au nanocages (Fig. 13.12A). A breast cancer cell line, SK-BR-3, which overexpresses epidermal growth factor receptor 2 (EGFR2 or HER2), has been used to test the molecular specific binding of bioconjugated gold nanocages.⁷⁰ In a typical process, primary antibodies (monoclonal anti-HER2 antibody from mouse) were immobilised on the cancer cells by incubating the SK-BR-3 cells in anti-HER2 antibodies. Gold nanocages were conjugated with a secondary antibody, such as anti-mouse immunoglobulin G or IgG, following the conventional protocol (Fig. 13.21) protocol. Finally, a buffer solution containing IgG-conjugated gold nanocages was applied to SK-BR-3 cells bound with anti-HER2 antibodies. After that, a fluorescence image was taken. The cells revealed a uniform green

colour indicating a homogeneous distribution of the primary anti-HER2 antibody on the cell surface (Fig. 13.21B).

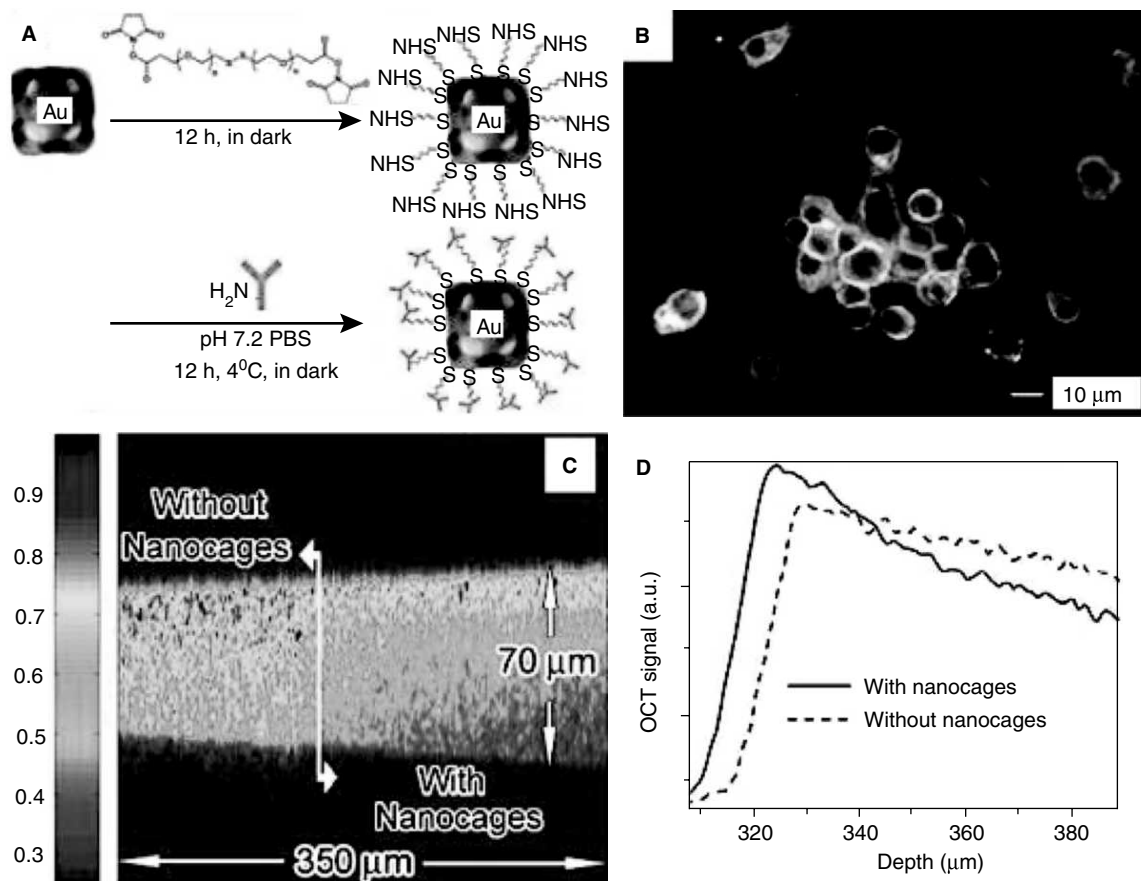


Fig. 13.21 (A) Schematic illustration of the protocol used to conjugate antibodies to the surface of Au nanocages. (B) A fluorescence image of SK-BR-3 cells whose surfaces were treated with the anti-HER2 antibodies, followed by incubation with fluorescence-labeled IgG (adapted from Ref. 71. Copyright (2007) Wiley). (C) OCT image of a gelatin phantom embedded with TiO_2 , and the concentration of TiO_2 was controlled at 1 mg/mL to mimic the background scattering of soft tissues. (D) Plots of the OCT signals on a log scale as a function of depth (adapted from Ref. 70. Copyright (2005) American Chemical Society). (For clarity see colour figure.)

13.5.2 Optical Contrast Agents

Au nanocages are attractive contrast agents because of their strong, tunable SPR peaks in the NIR region and comparatively smaller size.⁷⁰ To demonstrate the potential use of gold nanocages as optical

contrasting agent, optical coherence tomography (OCT) imaging was performed on phantom samples with and without nanocages. OCT imaging (Fig. 13.21C) was conducted using a 7-fs Ti:sapphire laser with a centre wavelength at 825 nm and a bandwidth of 155 nm. Preliminary studies show significantly improved spectroscopic image contrast for tissue phantoms containing Au nanocages. Gold nanocages showed an absorption cross-section of $2.90 \times 10^{-20} \text{ m}^2$ at 800 nm, about 5 orders of magnitude stronger than conventional dye Indocyanine Green (ICG). The results suggest that gold nanocages can be used as a good absorption contrast agents for OCT imaging. The log of the OCT signal as a function of depth is plotted in Fig. 13.21D.

13.5.3 Photothermal Therapy

The extremely large absorption cross-sections of Au nanocages can make them a good candidate for thermal therapeutic agent. Due to the large absorption cross-sections of Au nanocages, the

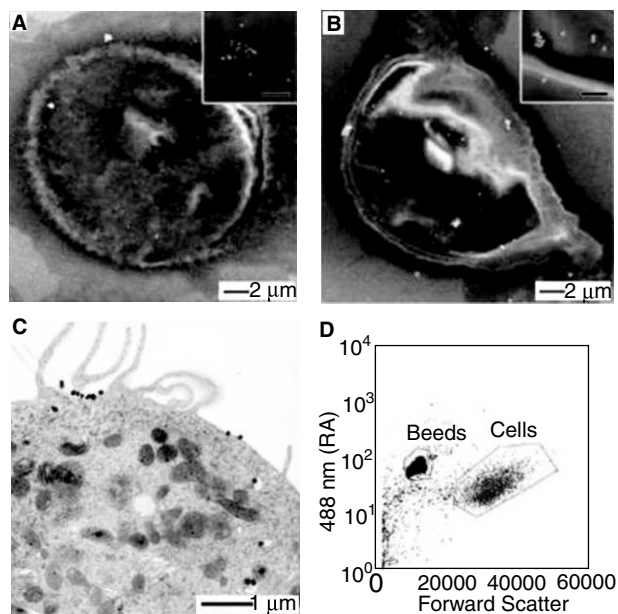


Fig. 13.22 SEM images of SK-BR-3 cells targeted with immuno Au nanospheres (A) and nanocages (B). SEM images at higher magnification (insets) reveal that the bright spots in the SEM images are indeed nanospheres and nanocages, respectively. The scale bar in the insets represents 500 nm. (C) TEM image of a microtomed SK-BR-3 cell conjugated with immuno Au nanocages. (D) Typical flow cytometry graph indicating how the forward scatter (x-axis) and right angle scatter (y-axis) can be used to differentiate the size difference between beads and cells (adapted from Ref. 72. Copyright (2008) American Chemical Society).

absorbed photons are converted into phonons and can increase the temperature. In biological systems, the Au nanocages are capable of producing a local temperature rise that can provide a therapeutic effect on cancer cells that are selectively targeted by bioconjugated Au nanocages. Such therapy is less invasive than chemotherapy or surgery and holds strong promise as a new form of cancer treatment. Most recent studies demonstrate the photothermal destruction of breast cancer cells *in vitro* by using immuno-targeted Au nanocages as an effective photo-thermal transducer.⁷¹ Gold nanocages with an average edge length of 65 ± 7 nm (absorption peak at 800 nm) were conjugated with anti-HER2, a monoclonal antibody to target breast cancer cells (SK-BR-3) through the epidermal growth-factor receptor.⁷² Then the targeted cells were irradiated with a pulsed NIR laser. By varying the power density, the duration of laser exposure, and the time of response after irradiation it is possible to optimise the treatment conditions to achieve effective destruction of the cancer cells. It was found that cells targeted with the immuno-Au nanocages responded immediately to laser irradiation and cellular damage was occur irreversibly at power densities greater than 1.6 W/cm^2 (Fig. 13.22). The percentage of dead cells increased with increasing exposure time.

Various other anisotropic nanostructures, such as gold nanostars and nanorods have also been used for the same applications.⁷³ Nanotriangle is another candidate, which can be used for cancer cell treatment. The large NIR absorption of the nanoparticle has potential applications in hyperthermic treatment of cancer cells. The flat nature of the nanotriangle would facilitate thermal contact between the nanoparticle and cancer cells, thereby we can reduce the exposure times. Nanotriangles can also be used to target specific delivery to the cancer cells, resulting in low-dosage requirement and thus reducing the metal toxicity.

13.5.4 Surface Enhanced Raman Scattering Substrates

It is known that anisotropic nanostructures are very good SERS substrate.^{6,12} Langmuir–Blodgett (LB) assemblies of various polyhedral Ag nanocrystals (Fig. 13.23A-C), made by polyol process, can perform low-level arsenate and arsenite sensing in aqueous solutions.⁷⁴ Using this SERS substrate, it is possible to achieve arsenate detection at 1 ppb (Fig. 13.23D), an order of magnitude below the standard set by the WHO. The high SERS response of octahedra LB arrays coated with various organic species, such as benzenethiol, hexadecanethiol, mercaptodecanoic acid is shown in Fig. 13.23E. The development of a reliable, portable, and simple-to-use device for detecting arsenic in groundwater is urgently needed in developing nations, where contaminated groundwater is at the root of a public health crisis. This SERS chip is reliable, reproducible, highly portable, and could be easily implemented in field detection. Au nanoflower (AuNF) is another SERS substrate nanoparticle, which exhibits strong SERS activity. The AuNF particles could be developed into Raman-active tags by packaging RhB@AuNF particles with denatured BSA molecules. The application of these Raman-active tags in living cells was demonstrated by using the RAW264.7 macrophage cell line.⁷⁵

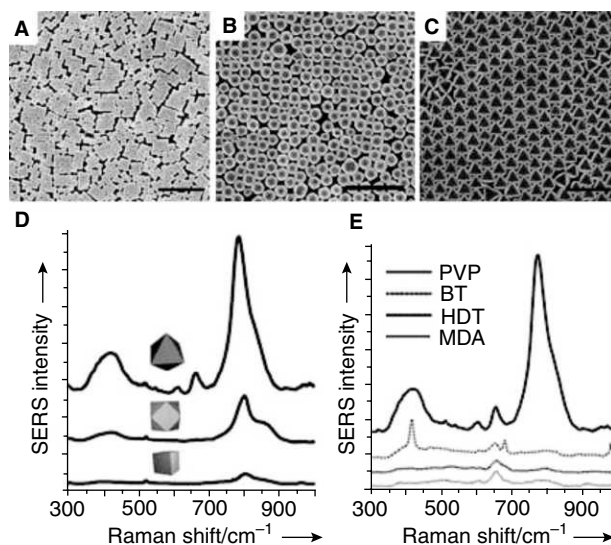


Fig. 13.23 SEM images showing close packed films of the three nanocrystal shapes: (A) cubes, (B) cuboctahedra, and (C) octahedra; scale bars are 1 μm. (D) SERS spectra collected on Langmuir–Blodgett films of each of the nanocrystal shapes 1 × 10⁻⁶ M arsenate solution. Peaks at 800 and 425 cm⁻¹ can be assigned to Na₂HAsO₄. (E) SERS response of octahedra LB arrays coated with various organic species. BT: benzenethiol, HDT: hexadecanethiol, MDA: mercaptodecanoic acid (adapted from Ref. 74. Copyright (2008) Wiley).

13.5.5 Superhydrophobic Surfaces

The wettability of a surface is an important feature governed by the chemical composition and the morphology of the surface of the materials. The surface hydrophobicity can be increased by creating a local geometry with a large geometric area relative to the projected area or by using roughness combined with hydrophobic coatings. Superhydrophobic surfaces exhibit very high water-repellent properties. Water droplets which are in contact with a superhydrophobic surfaces (contact angle >150°), form nearly spherical beads. Inorganic or organic contaminants on such self-cleaning surfaces are picked up by water droplets or adhere to the droplet and will be removed from the surface when the water droplets roll off. Anisotropic nanomaterials can be used in this regard for making superhydrophobic surfaces. A dendritic film of single-crystalline Ag having a thickness of about 10 μm with a self-assembled monolayer of *n*-dodecanethiol yields a superhydrophobic surface with a contact angle of 154.5 ± 1.0° and a tilt angle lower than 2°.⁵⁸ From the contact angle measurements, it was found that the presence of Ag crystallites on a particular substrate make substantial improvement in the hydrophobicity compared to the other substrates without Ag crystallites (Fig. 13.24).

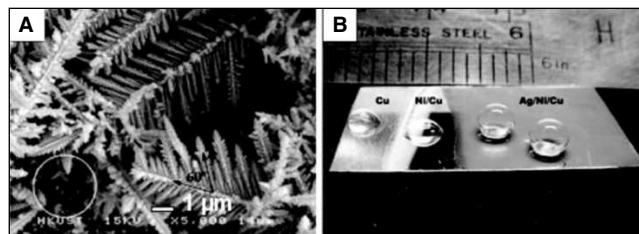


Fig. 13.24 (A) SEM image of Ag crystallites. (B) Photograph of water droplets on the Ag dendritic film surface, Ni surface, and Cu surface. All surfaces were modified with *n*-dodecanethiol (adapted from Ref. 60. Copyright (2008) American Chemical Society).

13.5.6 Infra-red Absorbing Material

It has been recognised that (NIR) absorbing films based on gold can be used as an alternative to reflective coatings for blocking IR radiation. Nanoparticle based approaches are highly efficient and can be economically viable than other methods. NIR-IR absorption exhibited by the certain nanomaterials has been used for the development of infrared filters. Using a prototypical device, it was demonstrated that gold mesoflowers can absorb a significant amount of heat thereby reducing the temperature rise in an enclosure exposed to daylight.¹² The heat absorption measurements were done with a monolayer and a bilayer of mesoflower-coated glass slides along with a blank glass substrate as the control. Compared with the blank glass substrate, the mesoflower-coated glass gave an average temperature inside the cardboard box, which was lower by 2 °C, whereas the bilayer-coated substrate showed a reduction of 4.3 °C. It is also suggested that the NIR-IR absorbing property of gold nanotriangle can be used as heat-absorbing optical coatings for windows.^{6, 12, 25}

13.6 CONCLUSIONS

In this section, we have outlined the synthesis and properties of a variety of anisotropic nanomaterials. Although a variety of materials are known, only a few have been explored for interesting properties. It is likely that such structures will have possibilities in novel chemistry and materials science. New synthetic methods have been established, which allows large-scale creation of such structures with shape purity. Currently, several applications have been demonstrated in optical absorption in the entire visible and NIR window leading to their use in infrared windows and cancer therapy.

13.7 PROSPECTS FOR THE FUTURE

In future, development of anisotropic nanoparticles of the same chemical composition, but with different morphologies, can show considerably different physical and chemical properties. Monitoring the growth of anisotropic nanoparticles at single particle level using new characterisation tools can

provide new insight in understanding the origin and evolution of anisotropy of various nanoparticles. Incorporation of multiple functionalities in nanoparticles can make them useful for constructing fast-performing nanodevices. Anisotropic nanomaterials will find applications as smart catalysts, enhancers in photovoltaics and other energy conversion devices, better therapeutic and imaging agents, probes for single-molecule sensing of drugs, toxins, explosives, and environmental pollutants, and in novel opto-electronic devices.⁷⁶ In parallel, the study of cytotoxicity of nanoparticles as a function of its size, shape, and surface coating may find much attention in future.

REFERENCES

1. R.C. O'Handley, *Modern Magnetic Materials, Principles and Applications*, Wiley-Interscience Publication (2000).
2. L.M. Liz Marzán, '(Non-carbon) anisotropic nanomaterials', *J. Mater. Chem.*, 16, (2006), 3891–92.
3. T.H. Ha, H-J. Koo and B.H. Chung, 'Shape-controlled syntheses of gold nanoprisms and nanorods influenced by specific adsorption of halide ions', *J. Phys. Chem. C*, 111, (2007), 1123–30.
4. J.E. Millstone, S. Park, K.L. Shuford, L. Qin, G.C. Schatz and C.A. Mirkin, 'Observation of a quadrupole plasmon mode for a colloidal solution of gold nanoprisms', *J. Am. Chem. Soc.*, 127, (2005), 5312–13.
5. J.E. Millstone, G.S. Métraux and C.A. Mirkin, 'Controlling the edge length of gold nanoprisms via a seed-mediated approach', *Adv. Funct. Mater.*, 16, (2006), 1209–14.
6. P.R. Sajanlal and T. Pradeep, 'Electric-field-assisted growth of highly uniform and oriented gold nanotriangles on conducting glass substrates', *Adv. Mater.*, 20, (2008), 980–83.
7. S. Chen and D.L. Carroll, 'Silver nanoplates: Size control in two dimensions and formation mechanisms', *J. Phys. Chem., B*, 108, (2004), 5500–06.
8. F-R. Fan, D-Y. Liu, Y-F. Wu, S. Duan, Z-X. Xie, Z-Y. Jiang and Z-Q. Tian, 'Epitaxial growth of heterogeneous metal nanocrystals: From gold nano-octahedra to palladium and silver nanocubes', *J. Am. Chem. Soc.*, 130, (2008), 6949–51.
9. T.K. Sau and C.J. Murphy, 'Room temperature, high-yield synthesis of multiple shapes of gold nanoparticles in aqueous solution', *J. Am. Chem. Soc.*, 126, (2004), 8648–49.
10. C.L. Nehl, H. Liao and J.H. Hafner, 'Optical properties of star-shaped gold nanoparticles', *Nano Lett.*, 6, (2006), 683–88.
11. K.P. Senthil, P.-S. Isabel, R.-G. Benito, F.J.G.d. Abajo and L.M. Liz Marzán, 'High-yield synthesis and optical response of gold nanostars', *Nanotechnology*, 19, (2008), 015606.
12. P.R. Sajanlal and T. Pradeep, 'Mesoflowers: A new class of highly efficient surface-enhanced Raman active and infrared-absorbing materials', *Nano Res.*, 2, (2009), 306–20.
13. H. Yuan, W. Ma, C. Chen, J. Zhao, J. Liu, H. Zhu and X. Gao, 'Shape and SPR evolution of thorny gold nanoparticles promoted by silver Ions', *Chem. Mater.*, 19, (2007), 1592–1600.
14. (a) F. Fivet, J.P. Lagier and M. Figlarz, 'Preparing monodisperse metal powders in micrometer and submicrometer sizes by the polyol process', *MRS Bull.*, 14, (1989), 29; (b) G. Viau, F. Fivet-Vincent and F. Fivet, 'Nucleation and growth of bimetallic CoNi and FeNi monodisperse particles prepared in polyols', *Solid State Ionics*, 84, (1996), 259–70.

15. (a) Y. Sun, Y. Yin, B.T. Mayers, T. Herricks and Y. Xia, 'Uniform silver nanowires synthesis by reducing AgNO_3 with ethylene glycol in the presence of seeds and poly(vinyl pyrrolidone)', *Chem. Mater.*, 14, (2002), 4736–45; (b) B. Wiley, Y. Sun, B. Mayers and Y. Xia, 'Shape-controlled synthesis of metal nanostructures: The case of silver', *Chem. Eur. J.*, 11, (2005), 454–63.
16. B. Wiley, Y. Sun and Y. Xia, 'Synthesis of silver nanostructures with controlled shapes and properties', *Acc. Chem. Res.*, 40, (2007), 1067–76.
17. Sun, Y. and Y. Xia, 'Shape-controlled synthesis of gold and silver nanoparticles', *Science*, 298, (2002), 2176–79.
18. S.H. Im, Y.T. Lee, B. Wiley and Y. Xia, 'Large-scale synthesis of silver nanocubes: The role of HCl in promoting cube perfection and monodispersity', *Angew. Chem. Int. Ed.*, 44, (2005), 2154–57.
19. Y. Xiong, A. Siekkinen, J. Wang, Y. Yin, M.J. Kimb and Y. Xia, 'Synthesis of silver nanoplates at high yields by slowing down the polyol reduction of silver nitrate with polyacrylamide', *J. Mater. Chem.*, 17, (2007), 2600–02.
20. D. Seo, J.C. Park and H. Song, 'Polyhedral gold nanocrystals with O_h symmetry: From octahedra to cubes', *J. Am. Chem. Soc.*, 128, (2006), 14863–70.
21. C. Li, K.L. Shuford, M. Chen, E.J. Lee and S.O. Cho, 'A facile polyol route to uniform gold octahedra with tailorable size and their optical properties', *ACS Nano*, 2, (2008), 1760–69.
22. (a) Yu S H. 'Bio-inspired crystal growth by synthetic templates', *Top Curr. Chem.*, 271, (2007), 79–118; (b) T. Klaus, R. Joerger, E. Olsson and C-G. Granqvist, 'Silver-based crystalline nanoparticles, microbially fabricated', *Proc. Natl. Acad. Sci., USA*, 96, (1999), 13611–14.
23. S. Brown, M. Sarikaya and E. Johnson, 'A genetic analysis of crystal growth', *J. Mol. Biol.*, 299, (2000), 725–35.
24. S.S. Shankar, A. Rai, B. Ankamwar, A. Singh, A. Ahmad and M. Sastry, 'Biological synthesis of triangular gold nanoprisms', *Nat. Mater.*, 3, (2004), 482–88.
25. S.S. Shankar, A. Rai, A. Ahmad and M. Sastry, 'Controlling the optical properties of lemongrass extract synthesised gold nanotriangles and potential application in infrared-absorbing optical coatings', *Chem. Mater.*, 17, (2005), 566–72.
26. B. Ankamwar, M. Chaudhary and M. Sastry, 'Gold nanotriangles biologically synthesised using tamarind leaf extract and potential application in vapor sensing', *Synth. React. Inorg. Me.*, 35, (2005), 19–26.
27. S.L. Smitha, D. Philip and K.G. Gopchandran, 'Green synthesis of gold nanoparticles using cinnamomum zeylanicum leaf broth', *Spectrochim. Acta A.*, 74, (2009), 735–739.
28. B. Liu, J. Xie, J.Y. Lee, Y. P Ting and J.P. Chen, 'Optimisation of high-yield biological synthesis of single-crystalline gold nanoplates', *J. Phys. Chem. B.*, 109, (2005), 15256–63.
29. J. Xie, J.Y. Lee, D.I.C. Wang and Y.P. Ting, 'Silver nanoplates: From biological to biomimetic synthesis', *ACS Nano*, 1, (2007), 429–39.
30. J. Xie, J.Y. Lee, D.I.C. Wang and Y.P. Ting, 'Identification of active biomolecules in the high-yield synthesis of single-crystalline gold nanoplates in algal solutions', *Small*, 3, (2007), 672–82.
31. S. He, Y. Zhang, Z. Guo and N. Gu, 'Biological synthesis of gold nanowires using extract of rhodospseudomonas capsulate', *Biotechnol. Prog.*, 24, (2008), 476–80.
32. B. Nair and T. Pradeep, 'Coalescence of nanoclusters and formation of submicron crystallites assisted by lactobacillus strains', *Cryst. Growth Des.*, 2, (2002), 293–98.

33. C. Lu, L. Qi, J. Yang, L. Tang, D. Zhang and J. Ma, 'Hydrothermal growth of large-scale micropatterned arrays of ultralong ZnO nanowires and nanobelts on zinc substrate', *Chem. Commun.*, (2006), 3551–53.
34. F. Cansell, B. Chevalier, A. Demourgues, J. Etourneau, C. Even, Y. Garrabos, V. Pessey, S. Petit, A. Tressaud and F. Weill, 'Supercritical fluid processing: A new route for materials synthesis', *J. Mater. Chem.*, 9, (1999), 67–75.
35. B.D. Adams, G. Wu, S. Nigro and A. Chen, 'Facile synthesis of Pd–Cd nanostructures with high capacity for hydrogen storage', *J. Am. Chem. Soc.*, 131, (2009), 6930–31.
36. J. Yuan, W-N. Li, S. Gomez and S.L. Suib, 'Shape-controlled synthesis of manganese oxide octahedral molecular sieve three-dimensional nanostructures', *J. Am. Chem. Soc.*, 127, (2005), 4184–85.
37. Yi-Jin Li, Chiu-Yen Wang, Min-Yen Lu, Kun-Mu Li and Lih-Juann Chen, 'Electrodeposited hexagonal ringlike superstructures composed of hexagonal Co-doped ZnO nanorods with optical tuning and high-temperature ferromagnetic properties', *Cryst. Growth Des.*, 8, (2008), 2598–2602.
38. G. Shen and D. Chen, 'Self-coiling of $\text{Ag}_2\text{V}_4\text{O}_{11}$ nanobelts into perfect nanorings and microloops', *J. Am. Chem. Soc.*, 128, (2006), 11762–63.
39. L. Tian, H.Y. Tan and J.J. Vittal, 'Morphology-controlled synthesis of Bi_2S_3 nanomaterials via single-and multiple-source approaches', *Cryst. Growth Des.*, 8, (2008), 734–38.
40. C-C. Chang, H-L. Wu, C-H. Kuo and M.H. Huang, 'Hydrothermal synthesis of monodispersed octahedral gold nanocrystals with five different size ranges and their self-assembled structures', *Chem. Mater.*, 20, (2008), 7570–74.
41. A. Brenner and E. Riddell, *J. Res. Natl. Bur. Std.*, 37, (1946), 31.
42. Y. Sun, 'Direct growth of dense, pristine metal nanoplates with well-controlled dimensions on semiconductor substrates', *Chem. Mater.*, 19, (2007), 5845–47.
43. M. Aizawa, A.M. Cooper, M. Malac and J.M. Buriak, 'Silver nano-inukshuks on Germanium', *Nano Lett.*, 5, (2005), 815–19.
44. J. Fang, H. You, P. Kong, Y. Yi, X. Song and B. Ding, 'Dendritic silver nanostructure growth and evolution in replacement reaction', *Cryst. Growth Des.*, 7, (2007), 864–67.
45. J. Fang, X. Ma, H. Cai, X. Song and B. Ding, 'Nanoparticle-aggregated 3D monocrystalline gold dendritic nanostructures', *Nanotechnology*, 17, (2006), 5841–45.
46. Y. Sun and Y. Xia, 'Mechanistic study on the replacement reaction between silver nanostructures and chloroauric acid in aqueous medium', *J. Am. Chem. Soc.*, 126, (2004), 3892–3901.
47. L. Au, Y. Chen, F. Zhou, P.H.C. Camargo, B. Lim, Z-Y. Li, D.S. Ginger and Y. Xia, 'Synthesis and optical properties of cubic gold nanoframes', *Nano Res.*, 1, (2008), 441–49.
48. Y. Xiong, B.J. Wiley, J. Chen, Z.-Y. Li, Y. Yin and Y. Xia, 'Corrosion-based synthesis of single-crystal Pd nanoboxes and nanocages and their surface plasmon properties', *Angew. Chem. Int. Ed.*, 44, (2005), 7913–17.
49. D. Kim, J. Park, K. An, N.-K. Yang, J.-G. Park and T. Hyeon, 'Synthesis of hollow iron nanoframes', *J. Am. Chem. Soc.*, 129, (2007), 5812–13.
50. Y. Sun and Y. Xia, 'Multiple walled nanotubes made of metals', *Adv. Mater.*, 16, (2004), 264–68.
51. R. Jin, Y. Cao, C.A. Mirkin, K.L. Kelly, G.C. Schatz and J.G. Zheng, 'Photoinduced conversion of silver nanospheres to nanoprisms', *Science*, 294, (2001), 1901–03.

52. R. Jin, Y.C. Cao, E. Hao, G.S. Me´traux, G.C. Schatz and C.A. Mirkin, 'Controlling anisotropic nanoparticle growth through plasmon excitation', *Nature*, 425, (2003), 487–90.
53. W-C. Huang and Y-C. Chen, 'Photochemical synthesis of polygonal gold nanoparticles', *J. Nanopart. Res.*, 10, (2008), 697–702.
54. S. Kundu and H. Liang, 'Photochemical synthesis of electrically conductive CdS nanowires on DNA scaffolds', *Adv. Mater.*, 20, (2008), 826–31.
55. X. Luo and T. Imae, 'Photochemical synthesis of crown-shaped platinum nanoparticles using aggregates of G4-NH₂ PAMAM dendrimer as templates', *J. Mater. Chem.*, 17, (2007), 567–71.
56. M.T. Reetz and W. Helbig, 'Size-selective synthesis of nanostructured transition metal clusters', *J. Am. Chem. Soc.*, 116, (1994), 7401–02.
57. C.-J. Huang, P.-H. Chiu, Y.-H. Wang, W.R. Chen and T.H. Meen, 'Synthesis of the gold nanocubes by electrochemical technique', *J. Electrochem. Soc.*, 153, (2006), D129–D133.
58. Y.-Y. Yu, S.-S. Chang, C.-L. Lee and C.R.C. Wang, 'Gold nanorods: Electrochemical synthesis and optical properties', *J. Phys. Chem. B.*, 101, (1997), 6661–64.
59. N. Tian, Z.-Y. Zhou, S.-G. Sun, L.Cui, B. Ren and Z.-Q. Tian, 'Electrochemical preparation of platinum nanothorn assemblies with high surface enhanced Raman scattering activity', *Chem. Commun.*, (2006), 4090–92.
60. C. Gu and T.-Y. Zhang, 'Electrochemical synthesis of silver polyhedrons and dendritic films with superhydrophobic surfaces', *Langmuir*, 24, (2008), 12010–16.
61. (a) V. Myroshnychenko, J. Rodriguez-Fernandez, I. Pastoriza-Santos, A.M. Funston, C. Novo, P. Mulvaney, L.M. Liz-Marzan and F.J. Garcia de Abajo, 'Modelling the optical response of gold nanoparticles', *Chem. Soc. Rev.*, 37, (2008), 1792; (b) C. Noguez, 'Surface plasmons on metal nanoparticles: The influence of shape and physical environment', *J. Phys. Chem. C.*, 111, (2007), 3806–19.
62. U. Kreibitz and M. Vollmer, 'Optical properties of metal clusters' (1995), Springer, Berlin.
63. (a) J. Nelayah, M. Kociak, O. Stephan, F.J. Garcia de Abajo, M. Tence, L. Henrard, D. Taverna, I. Pastoriza-Santos, L.M. Liz Marzan and C. Colliex, 'Mapping surface plasmons on a single metallic nanoparticle', *Nat. Phys.*, 3, (2007), 348; (b) C. Bohren and D. Huffman, 'Absorption and scattering of light by small particles', (1983), John-Wiley, New York.
64. (a) A. Wokaun, J.P. Gordon and P.F. Liao, 'Radiation damping in surface-enhanced Raman scattering', *Phys. Rev. Lett.*, 48, (1982), 957; (b) H. Xu, J. Aizpurua, M. Kall and P. Apell, 'Electromagnetic contributions to single-molecule sensitivity in surface-enhanced Raman scattering', *Phys. Rev. E.*, 62, (2000), 4318.
65. (a) P.F. Liao and A. Wokaun, 'Lightning rod effect in surface enhanced Raman scattering', *J. Chem. Phys.*, 76, (1982), 751; (b) J. Gersten and A. Nitzan, 'Electromagnetic theory of enhanced Raman scattering by molecules adsorbed on rough surfaces', *J. Chem. Phys.*, 73, (1980), 3023.
66. N.H. Jang, J.S. Suh and M. Moskovits, 'Effect of surface geometry on the photochemical reaction of 1, 10-phenanthroline adsorbed on silver colloid surfaces', *J. Phys. Chem. B.*, 101, (1997), 8279.
67. (a) X. Lu, H.-Y. Tuan, J. Chen, Z.-Y. Li, B.A. Korgel and Y. Xia, 'Mechanistic studies on the galvanic replacement reaction between multiply twinned particles of Ag and HAuCl₄ in an organic medium', *J. Am. Chem. Soc.*, 129, (2007), 1733; (b) Y. Yin, C. Erdonmez, S. Aloni and A.P. Alivisatos, 'Faceting of nanocrystals during chemical transformation: From solid silver spheres to hollow gold octahedra', *J. Am. Chem. Soc.*, 128, (2006), 12671.

68. I. Lee, R. Morales, M.A. Albiter and F. Zaera, 'Synthesis of heterogeneous catalysts with well-shaped platinum particles to control reaction selectivity', *Proc. Natl. Acad. Sci. USA*, 105, (2008), 15241; A. Fukuoka, N. Higashimoto, Y. Sakamoto, S. Inagaki, Y. Fukushima and M. Ichikawa, 'Preparation and catalysis of Pt and Rh nanowires and particles in FSM-16', *Microporous Mesoporous Mater.*, 48, (2001), 171.
69. M.M. Telkar, C.V. Rode, R.V. Chaudhari, S.S. Joshi and A.M. Nalawade, *Appl. Catal. A-Gen*, 'Shape-controlled preparation and catalytic activity of metal nanoparticles for hydrogenation of 2-butyne-1,4-diol and styrene oxide', 273, (2004), 11.
70. J. Chen, F. Saeki, B.J. Wiley, H. Cang, M.J. Cobb, Z.-Y. Li, L. Au, H. Zhang, M.B. Kimmey, X. Li and Y. Xia, 'Gold nanocages: Bioconjugation and their potential use as optical imaging contrast agents', *Nano Lett.*, 5, (2005), 473–77.
71. S.E. Skrabalak, J. Chen, Y. Sun, X. Lu, L. Au, C.M. Cobley and Y. Xia, 'Gold nanocages: Synthesis, properties, and applications', *Adv. Mater.*, 19, (2007), 3177–84.
72. L. Au, D. Zheng, F. Zhou, Z.-Y. Li, X. Li and Y. Xia, 'A quantitative study on the photothermal effect of immuno gold nanocages targeted to breast cancer cells', *ACS Nano*, 2, (2008), 1645–52.
73. H. Liao, C.L. Nehl and J.H. Hafner, 'Biomedical applications of plasmon resonant metal nanoparticles', *Nanomedicine*, 1, (2006), 201–08.
74. M. Mulvihill, A. Tao, K. Benjauthrit, J. Arnold and P. Yang, 'Surface-enhanced Raman spectroscopy for trace arsenic detection in contaminated water', *Angew. Chem. Int. Ed.*, 47, (2008), 6456–60.
75. J. Xie, Q. Zhang, J.Y. Lee and D.I.C. Wang, 'The synthesis of SERS-active gold nanoflower tags for in vivo applications', *ACS Nano*, 2, (2008), 2473–80.
76. (a) T.K. Sau, A.L. Rogach, F. Jackel, T.A. Klar and J. Feldmann, 'Properties and applications of colloidal nonspherical noble metal nanoparticles', *Adv. Mater.*, 22, (2010), 1805–1825. (b) T.K. Sau and A.L. Rogach, 'Nonspherical noble metal nanoparticles: Colloid-chemical synthesis and morphology control', *Adv. Mater.*, 22, (2010), 1781–1804.

ADDITIONAL READING

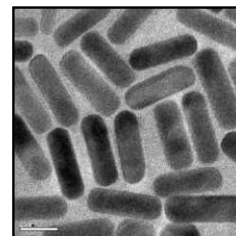
1. L.A. Lyon, S.J. Stranick and C.D. Keating, *Anisotropic Nanoparticles-Synthesis, Characterisation and Applications*, Materials Research Society, (2001), 635.
2. T.C.R. Rocha, F. Sato, S.O. Dantas, D.S. Galvao and D. Zanchet, 'New Insights on the Growth of Anisotropic Nanoparticles from Total Energy Calculations', *J. Phys. Chem. C*, 113, (2009), 11976–79.
3. N.R. Jana, 'Gram-Scale Synthesis of Soluble, Near-Monodisperse Gold Nanorods and Other Anisotropic Nanoparticles', *Small*, 1, (2005), 875–82.
4. S. Jadab and I. Toyoko, 'Recent Advances in Fabrication of Anisotropic Metallic Nanostructures', *J. Nanosci. Nanotechnol.*, 9, (2009), 19–40.
5. Challa S.S.R. Kumar, *Metallic Nanomaterials*, Wiley-VCH, (2009).
6. E. Hao, G.C. Schatz and J.T. Hupp, 'Synthesis and Optical Properties of Anisotropic Metal Nanoparticles', *J. Fluores.*, 14, (2004), 331–41.

7. C.J. Murphy, T.K. Sau, A.M. Gole, C.J. Orendorff, J. Gao, L. Gou, S.E. Hunyadi and T. Li, 'Anisotropic Metal Nanoparticles: Synthesis, Assembly, and Optical Applications', *J. Phys. Chem. B*; 109, (2005), 13857–70.
8. M.A. El-Sayed, 'Some interesting properties of metals confined in time and nanometer space of different shapes', *Acc. Chem. Res.*, 34, (2001), 257–64.
9. C.N.R. Rao, A. Müller and A.K. Cheetham, *Nanomaterials Chemistry: Recent Developments and New Directions*, Wiley-VCH, (2007).
10. C. Guozhong, *Nanostructures and Nanomaterials, Synthesis, Properties and Applications*, Imperial College Press, London, (2004).

REVIEW QUESTIONS

1. What are anisotropic nanomaterials and how are they classified?
2. What is meant by seed-mediated growth method?
3. What are the important factors which determine the epitaxial growth of heterogeneous core-shell nanocrystals?
4. What is the importance of polyol and PVP in polyol synthesis?
5. What are the different steps involved in the growth process of polyol synthesis?
6. What are the parameters which can influence the morphology of nanoparticles? Illustrate with examples.
7. What is galvanic replacement reaction? What are the advantages of this method over others?
8. Explain the electrochemical synthesis of anisotropic gold nanoparticles.
9. What are the applications of anisotropic nanoparticles?
10. How can anisotropic nanoparticles be used for photothermal therapy?

ONE-DIMENSIONAL NANOSTRUCTURES: NANORODS AND NANOWIRES



“We must not forget that when radium was discovered no one knew that it would prove useful in hospitals. The work was one of pure science. And this is a proof that scientific work must not be considered from the point of view of the direct usefulness of it. It must be done for itself, for the beauty of science, and then there is always the chance that a scientific discovery may become like the radium a benefit for humanity.”

Marie Curie, Lecture at Vassar College, May 14, 1921

One-dimensional (1-D) nanostructures are some of the most fascinating nanomaterials. Gold nanorod is a classic example of anisotropic structures and it has been studied in detail for various properties originating due to anisotropy. In this chapter, a section is devoted on the synthesis, properties, characterisation techniques, and various applications of these materials. To begin with, the reader would be taken through the various protocols utilised for the synthesis of gold nanorods and associated growth mechanisms. Seed-mediated synthesis, one of the most popular synthetic procedures, is discussed in detail; the most recent single-pot synthesis of gold nanorods is also mentioned. The origin of various novel properties in gold nanorods is illustrated with a discussion on the use of optical absorption and Raman scattering phenomena as well as various techniques used for their characterisation. The topic on nanorods is concluded with a detailed discussion of their applications. Nanowires are an important member of the family of 1-D nanostructures, especially due to their possible role in electrical transport. A number of semiconductor nanowires have been synthesised and used for applications in electronics. This chapter focuses on the various synthetic protocols used for the nanowire synthesis; a special focus is laid on wet chemical synthesis of semiconducting nanowire, tellurium and tellurium-based alloys. The chapter is concluded with various applications of nanowires.

Learning Objectives

- What are the 1-D nanostructures?
- What is special about of gold nanorods?
- What are the different methods of preparation of gold nanorods and how can one tune the aspect ratio?
- What are the properties of gold nanorods?
- What are the applications of gold nanorods?

- What are the general synthetic protocols for the nanowires?
 - What are the applications of nanowires?
-
-

14.1 INTRODUCTION

One-dimensional (1-D) nanostructures, such as nanorods, nanowires, nanowhiskers, nanobelts, carbon and non-carbon nanotubes, nanocables and nanofibers or fibrils have been subjects of intense scientific research. They exhibit a number of novel properties, which may be used for applications in electronics, optoelectronics, sensing, imaging, photothermal therapy, energy harvesting, thermoelectricity, magnetoresistance, infrared detection, etc. The differentiation between 1-D nanostructures and nanoparticles begins with the concept of anisotropy. Spherical nanoparticles are classified as isotropic (one parameter describes the structure, e.g., in a sphere, it is the radius), whereas 1-D nanostructures exhibit anisotropy (more than one parameter describes the structure, e.g. for a rod, both length and breadth are needed). The structural aspects affect the properties. For example, the optical spectrum or transmission measured along any direction of a spherical nanoparticle will be the same, whereas it depends on the direction of the measurement (longitudinal and transverse) of a nanorod. In this chapter, two specific 1-D nanostructures are discussed in detail: nanorod and nanowires. The chapter discusses the method of synthesis, characterisation techniques, properties and their applications. In order to illustrate the important concepts, the subject matter in this chapter reviews the existing knowledge on gold nanorod and tellurium-based nanowires, which are two well-characterised materials.

14.2 GOLD NANORODS

Gold nanorod is a special member of noble metal-based nanomaterial family. It is one of the most researched nanostructures in the recent times. It has found applications in a number of areas: sensing, detection of biomolecules, cell imaging, photothermal therapy, two-photon luminescence, etc. The origin of novel properties in nanorods vis-à-vis nanoparticles is attributed to anisotropy. The distinct difference in the electron cloud density at the transverse and longitudinal axes leads to the variation of its properties vis-à-vis gold nanoparticles. This variation in the electron density leads to all the major applications of gold nanorods.

14.3 GENERAL STRATEGIES OF SYNTHESIS

A number of synthetic protocols have been developed for the preparation of gold nanorods. Various methods have been followed for the syntheses to improve the quality of the materials, yield, time and effort. Template mediated, electrochemical, photochemical and seed-mediated syntheses are used for the preparation of gold nanorods. Among all the methods, seed-mediated approach is the widely used

synthetic method due to the high yield and ease of synthesis. In this chapter, one-pot synthesis of nanorods is discussed in particular.

14.3.1 Template-mediated Synthesis

Martin and co-workers^{1,2} introduced the template-assisted synthesis of gold nanorods. In this method nanoporous polycarbonate or alumina is used as a template. The protocol is based on electrochemical deposition of Au in the template structure. To begin with, a small quantity of Ag or Cu is sputtered on the template in order to make a conductive film for electrodeposition. Thereafter, Au is electrochemically deposited on the conductive alumina template. The conductive film based on Ag or Cu and the template is removed by selective dissolution in presence of a polymeric stabiliser (e.g., polyvinylpyrrolidone). Finally, nanorods are dispersed either in water or organic medium by means of sonication. Fig. 14.1 describes the template-mediated synthesis for the gold nanorods.

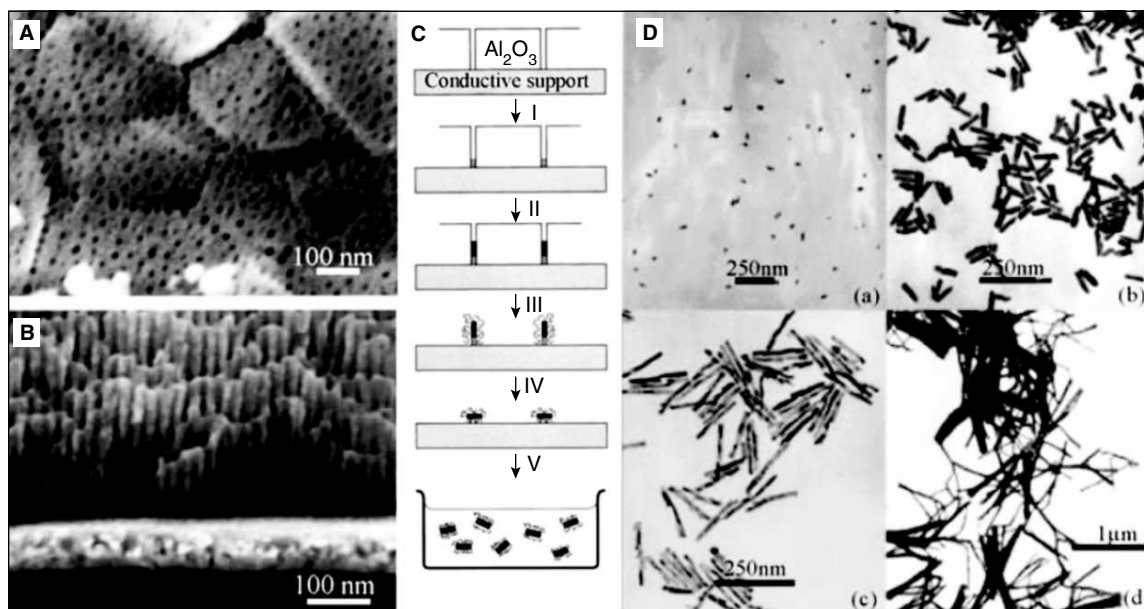


Fig. 14.1 (A and B) Field emission SEM images of an alumina membrane. (C) Schematic representation of the successive stages during formation of gold nanorods via the template method. (D) TEM micrographs of gold nanorods obtained by the template method (reprinted with permission from Van der Zande, et al. (Ref. 4) Copyright (2000) American Chemical Society).

Nanorods of different diameters can be synthesised using this method by controlling the pore size of the template.³ Likewise, the length of the nanorods is controlled by controlling the amount of gold deposited in the template.⁴ An advantage of this method is that the alumina template is optically transparent, therefore, the colour changes due to the aspect ratio of the gold nanorods can easily be observed. Poor yield was the major limitation of this method.

14.3.2 Electrochemical Synthesis

Electrochemical synthesis was reported by Wang and co-workers.^{5,6} In this method, gold nanorods are formed by the electrochemical reaction. Two plates ($3 \times 1 \times 0.05$ cm) made of gold (acts as anode) and platinum (acts as cathode) are immersed in the electrolytic solution. The solution contains shape-inducing cationic surfactant, hexadecyltrimethylammonium bromide ($C_{16}TAB$) and a hydrophobic cationic co-surfactant, tetradodecylammonium bromide ($TC_{12}AB$). A constant current of 3 mA is applied throughout the synthesis. The synthesis was carried out in an ultrasonication bath and was maintained at a temperature of 36°C . Gold ions are generated in the form of AuBr_4^- from the anode and complexes with the surfactant $C_{16}TAB$ during electrolysis. Gold ions are then reduced to gold atoms in the interfacial region of the cathodic surface within the electrolytic solution. $C_{16}TAB$ surfactant is used as a stabilising agent for preventing agglomeration. Both the surfactants play a critical role in the growth of rod-shaped structure. Appropriate amount of acetone and cyclohexane are added to the electrolytic solution for the facile synthesis of gold nanorods. Acetone is used for the loosening the micellar framework and cyclohexane is used for inducing the rod-shaped structure.

Figure 14.2 describes the electrochemical set-up used for gold nanorod synthesis and micrographs of the gold nanorod obtained through this process.

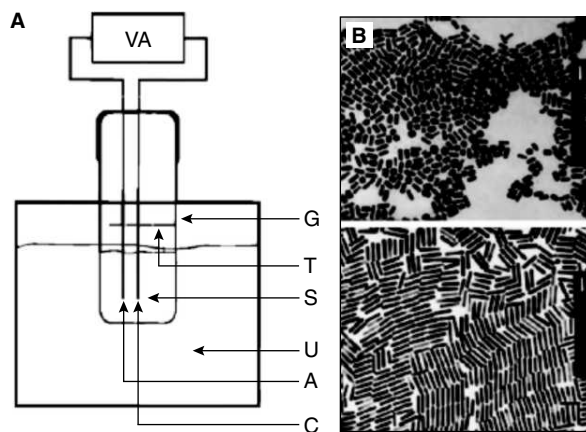


Fig. 14.2 (A) Schematic diagram of the set-up for preparation of gold nanorods via the electrochemical method containing; VA, power supply; G, glassware electrochemical cell; T, teflon spacer; S, electrode holder; U, ultrasonic cleaner; A, anode; C, cathode. (B) TEM micrographs of Au nanorods with different aspect ratios 2.7 (top) and 6.1 (bottom). Scale bars represent 50 nm (reprinted with permission from Chang, et al. (Ref. 6) Copyright (1999) American Chemical Society).

14.3.3 Photochemical Synthesis

Rod-like gold colloids were synthesised by the reduction gold salt by UV irradiation.⁷ In this method, gold salt (AuCl_4^-) binds to the rod-like micelle hexadecyltrimethylammonium chloride (HTAC).

The reduction of gold ion to Au^0 is achieved through photochemical reduction ($\lambda_{\text{max}} = 253.7 \text{ nm}$). Synthesis of uniform rods and controlling the aspect ratio is reportedly difficult in this method, because an increase in the length of nanorods also increases the concentration of spherical particles. Well-controlled aspect ratio and uniform nanorods were synthesised using a photochemical method suggested by Yang *et al.*⁸ This method is similar to the electrochemical method and used concepts from template-assisted synthesis. The solution contains a surfactant hexadecyltrimethylammonium bromide (CTAB) and tetradodecylammonium bromide and precursor hydrogen tetrachloroaurate ($\text{HAuCl}_4 \cdot 3\text{H}_2\text{O}$). The reduction of gold salt is achieved by photo-irradiation for 30 h ($\lambda_{\text{max}} = 254 \text{ nm}$, $I = 420 \mu\text{W}/\text{cm}^2$). Acetone and cyclohexane are used for loosening the micellar structure. The novelty of this method is in the use of silver nitrate for controlling the aspect ratio (ratio of length to width) of the nanorods. It is suggested that increase in the silver ion concentration leads to increase in the aspect ratio accompanied by a decrease of the width of the nanorods; in case of absence of silver ion, the number of spherical particles is predominant.

14.3.4 Seed-mediated Synthesis

It is the most widely used method for the synthesis of gold nanorods. The method was first reported by Murphy and co-workers in 2001.⁹ The method found widespread use for the synthesis of gold nanorods due to use of simple wet chemistry in the process, which leads to the production of high quality and quantity of nanorods. The novelty of this method is the use of seed particles for gold nanorod synthesis and the use of ascorbic acid as a mild reductant for gold ions. The roles of other chemicals (CTAB, silver nitrate, cyclohexane and acetone) have been emphasised in other approaches previously discussed for nanorod synthesis. In a typical approach, citrate capped spherical seed particles (3–4 nm) are prepared by the reduction of gold ions using sodium borohydride (NaBH_4) as a reductant. A growth solution is prepared separately by partial reduction of gold ion using ascorbic acid. The seed particles are then added to the growth solution, which also contains CTAB and silver nitrate. The advantage of this method is that aspect ratio of gold nanorods can easily be tuned by varying the seed-to-metal salt ratio.

The synthesis of gold nanorods with high aspect ratio (> 10) is difficult using this method. A variant of this method has been reported by Murphy and co-workers for the synthesis of long rods up to an aspect ratio of 25.^{10, 11} The synthesis involves a three-step procedure and doesn't require silver nitrate. In the first step, citrate capped seed particles are added to the growth solution containing gold salt, CTAB and ascorbic acid. In the second step, calculated quantity of the solution from the first step is used as seed for the second growth step, which is sequentially used as seed for the third growth step.^{12, 13} The aspect ratio of gold nanorods depends on the size and surface functionality of the seed particles.¹⁴ The aspect ratio of the nanorods increases as the seed size decreases. In this method, large spherical particles are also formed along with the long rods leading to difficulties in separating the rods from the spheres.

In 2003, Nikoobakht *et al.* synthesised gold nanorods through a two-pot strategy (preparation of gold seed and addition of seed to the growth solution).¹⁵ In the first step, the seed particles are

synthesised by the reduction of AuCl_4^- using NaBH_4 in presence of cationic surfactant CTAB (instead of citrate as used in the earlier reported method). Au^{3+} is reduced to metallic gold (Au^0) nanoparticles with a size of around ~ 3 to 5 nm. CTAB acts as a capping/stabilising agent for the gold nanoparticles. In the second step, a calculated amount of seed solution is added to the growth solution. The growth solution contains AuCl_4^- , CTAB, AgNO_3 and L-ascorbic acid (AA). L-AA, a mild reducing agent, reduces Au^{3+} to Au^{1+} in the presence of CTAB and Ag^+ in the growth solution. When seed solution is added to the growth solution, Au^{1+} reduces to Au^0 . The reaction mixture containing seed and growth solution is kept undisturbed for 3 h. After 3 h, the solution is centrifuged thrice in order to remove unwanted ions and re-dispersed in deionised water for further studies.

Synthesis of nanorods depends on various parameters, such as seed particles, concentration of gold salt, CTAB, AgNO_3 , and L-AA, each of those significantly affecting the quality of gold nanorods.¹⁴ The size, nature of protecting agent/surface functionalities and the concentration of the seed are most important factors for the control of the aspect ratio of nanorods.¹⁴ Concentration of CTAB and CTAB from different suppliers alters the aspect ratio and affects the yield of nanorods.¹⁶ Similarly, the concentration of gold salt, silver nitrate, and L-AA alter the aspect ratio of the gold nanorods. The absence of silver nitrate in the growth solution leads predominantly to spherical particles. The detailed mechanism for the synthesis of gold nanorods is discussed below.

14.3.4.1 Growth Mechanism

The growth mechanism of gold nanorods was proposed by different groups. Murphy *et al.* suggested the growth process is based on preferential surfactant binding to certain facets of the seed particle.^{12, 17, 18} The gold seed particles are face-centered cubic (fcc) in nature. The preferential binding of CTA^+ head group to certain crystal faces of the seed causes symmetry breaking and leads to elongated growth of the nanorods. Crystal structure of gold contains five side-faces containing (100) surfaces and ten end-faces containing (111) surfaces, as shown in Fig. 14.3A. The surface energy of (100) plane is higher than that of (111) plane. The preferential binding of side-faces, which is more comparable in size with CTA^+ head group than end-faces, stabilises the high energy side-faces. Due to the preferential binding of CTA^+ head group on side-faces, the nucleation of gold is inhibited there. Therefore, the growth of nanorods takes place along the (110) common axis on (111) faces, which do not contain the CTA^+ head groups. The surfactant CTAB has a hydrophobic as well as a hydrophilic group. The quaternary ammonium ion present on the hydrophilic surface forms a covalent bond with the gold surface thereby opening the hydrophobic group outwards. The hydrophobic group of another CTAB molecule forms a bilayer with the outward projecting hydrophobic group of attached CTAB molecule; the hydrophilic group of second CTAB molecule interacts with water leading to stabilisation of gold nanorod in aqueous medium. The free energy of bilayer stabilisation between CTAB molecules is found to be approximately 6 kJ/mol per two methylene groups; this energy is higher than the energy available at the room temperature (~ 2.5 kJ/mol). The bilayer formation on gold surface through alkyl groups can be visualized in a zipper fashion (Fig. 14.3B). Due to inhibited growth on the side-faces, the reduction of Au^{3+} followed by nucleation happens on the end-faces. Therefore, by controlling the ratio of seed to growth solution, the elongation of gold nanorod can be controlled.

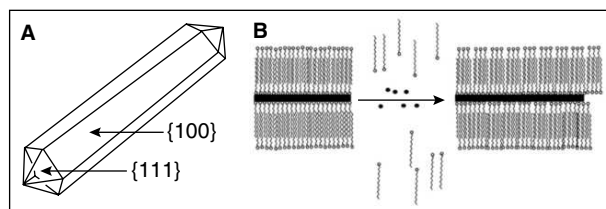


Fig. 14.3 Cartoon representation of (A) 3-D morphology showing (111) end faces and (100) side faces. The common five-fold axis of elongation is (110). (B) Illustration of “zipping” mechanism for the formation of the bilayer of CnTAB (squiggles) on the nanorod (black rectangle) surface may assist nanorod formation as more gold ion (black dots) is introduced (reprinted with permission from Murphy, *et al.* (Ref.12,13) Copyright (2005 and 2003) American Chemical Society).

In a separate study, Mulvaney *et al.* proposed the electric-field-directed growth mechanism of gold nanorods.¹⁹ In this mechanism, it is suggested that ascorbic acid reduces AuCl_4^- -CTAB complex to AuCl_2^- -CTAB through following reaction (I).



The reduction of Au^{1+} occurs through electron transfer at the surface of the electron-rich CTAB capped seed particles via reaction II. The rate of rod formation depends on the collision of AuCl_2^- -CTAB complex and CTAB capped seed particles, which is controlled by the electrical double-layer interaction between the CTAB and gold rods.

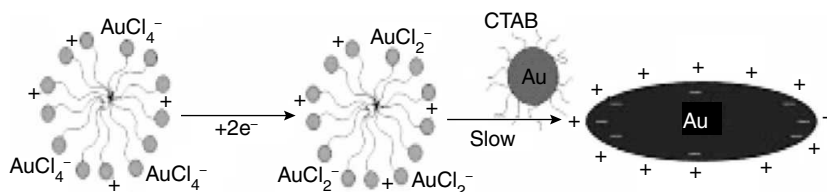


Fig. 14.4 Proposed mechanism for gold nanorod formation. The transport of the gold ions bound to the C_{16}TAB micelles to the growing seed particles is controlled by the double-layer interaction (reprinted with permission from Perez-Juste, *et al.* (Ref. 19) Copyright (2004) Wiley-VCH).

14.3.5 Seedless Synthesis

In 2009, Samal *et al.* synthesised gold nanorods through one-step process, whereby the use of seed particles was eliminated.²⁰ The study suggested that the nature of metal seed (seed made from various metals having different crystal structures) doesn't affect the formation and monodispersity of gold nanorods. Further investigations revealed that NaBH_4 present in the seed solution played a critical role

in the formation of gold nanorod, i.e., gold nanorods can be synthesised by direct addition of NaBH_4 to the growth solution. This study explained the importance of this reagent in the gold nanorod synthesis. An earlier report had also suggested the use of silver seed for gold nanorod synthesis.²¹

In this method, various metal seed particles of different crystal structures, such as Fe (bcc), Ru, and Cd (hcp), Cu, Pb, Ag, and Au (ccp), Hg (rhombohedral), In (tetragonal), and Sb (trigonal) are prepared from their respective salts by reduction with NaBH_4 and added to the growth solution. The size of the seed particles is around 3–5 nm. All the seed particles successfully formed gold nanorods. HRTEM image of the gold nanorods synthesised by various metal seeds of different crystal structures formed *fcc* gold nanorods (Fig. 14.5). There is no signature of other metals present in the nanorods, which was confirmed by the EDAX spectrum. This suggested that the seed particles may not be directly affecting the growth of gold nanorod. Further experiments were conducted for understanding the role of NaBH_4 (present in the seed solution) added to the growth solution. It was found that seeds are formed *in-situ* in this method. To make gold nanorods, calculated amount of ice-cold NaBH_4 solution is added directly to the growth solution containing Au^{3+} , CTAB, Ag^+ , and L-AA and kept undisturbed for 10 minutes.

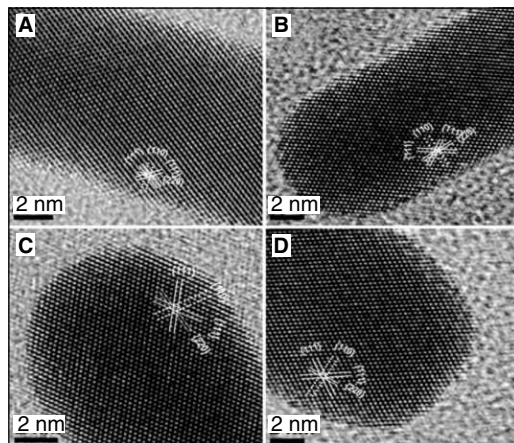


Fig. 14.5 HRTEM images of nanorods formed using different seed particles: (A) Fe (bcc), (B) Cd (hcp), (C) Sb (trigonal), and (D) In (tetragonal). Although the metals are of different crystal structures, the gold nanorods formed are *fcc* (reprinted with permission from Samal, et al. (Ref. 20) Copyright (2010) Springer-Netherlands).

The nanorods synthesised by this route (direct addition of NaBH_4 to growth solution) are chemically, structurally, and spectroscopically similar to those obtained from the seed-mediated approach and are highly uniform, so that a purification step can be avoided for a large-volume synthesis. This protocol provides a simple and easier method for the synthesis of gold nanorods. One-pot synthesis, less time consuming, high quality and yield of nanorods, may be used even in undergraduate laboratories as well as for the large-scale synthesis of gold nanorods.

14.4 PROPERTIES

14.4.1 Optical Properties

The colour of bulk gold is yellow, whereas the colloidal solution of gold nanoparticles is wine red. This property is related to the variation in optical property of the material with its size. The optical properties arise due to the interaction of electromagnetic radiation with the material. When this occurs, the vibrational and electronic states of the material get excited. In the specific case of metal nanoparticles, the surface plasmon frequency falls in the visible region of the electromagnetic spectrum. Thus, a feature appears in the absorption spectrum, which is called as surface plasmon resonance (SPR). The SPR is dependent on the particle size, shape, the dielectric properties of the metal, and the surrounding medium; as all such properties affect the electron charge density on the particle surface.

Mie (1908) proposed a theory for the visible light absorption by metal nanoparticles, based on the solutions of Maxwell's equations. This theory is widely applicable to the spherical colloidal nanoparticles. Metals nanoparticles based on gold, silver, and copper show a strong SPR band in the visible region. For example, gold colloids of size ~ 20 nm exhibit a surface plasmon at 520 nm; whereas gold colloids of size 4 nm exhibit a surface plasmon at 507 nm. In case of isotropic structures, only one absorption feature appears, because the interaction of electromagnetic radiation is the same throughout the spherical diameter. But, in the case of anisotropic nanoparticles, such as nanorods, where the length and width are different and interaction of electromagnetic radiation is different depending on the polarisation of the incident light. The interaction of electromagnetic radiation with the length and width are different. It gives two-surface plasmons in the absorption spectrum, when it interacts with the length and width of the nanorods. The interaction of electromagnetic radiation with short axis of the nanorod produces transverse surface plasmon (TSP) and interaction with long axis of nanorods produces longitudinal surface plasmon (LSP). TSP and LSP of the nanorods appear in the visible and near NIR region in the absorption spectrum, respectively. This is illustrated in Fig. 14.6.

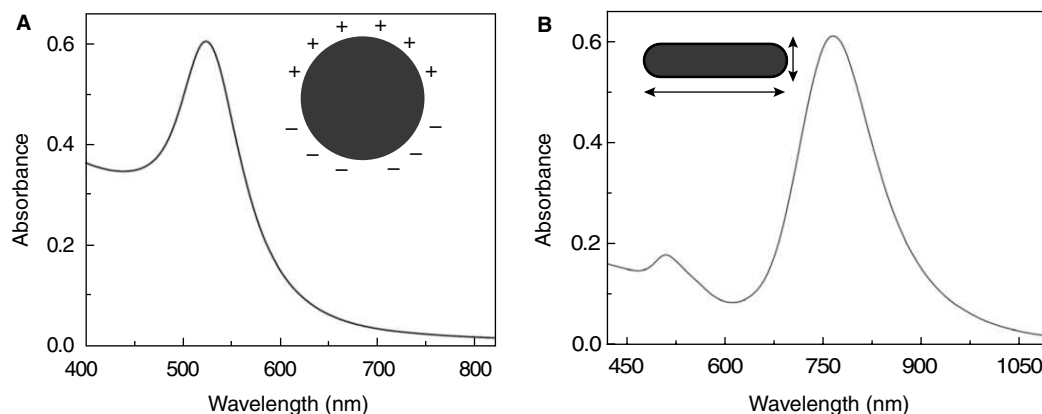


Fig. 14.6 Absorption spectra of gold nanoparticles (A) and nanorods (B). The arrows in B correspond to the electron motions.

Figure 14.6A shows the surface plasmon of spherical gold nanoparticles (diameter = ~20 nm), which appears at 520 nm. Fig. 14.6B shows the absorption of gold nanorods, in which the LSP and TSP appear at 670 and 509 nm, respectively. Wavelength of the LSP can be tuned by changing the length of the nanorod, while altering the aspect ratio of the nanorods. As the length of the nanorods increases, the LSP of the nanorods red shifts in near NIR region.

The LSP of the nanorods may be shifted from visible region to near NIR depending on the length of the nanorod, whereas TSP remains constant as the diameter of the nanorod is usually constant. While the control of length is easy, the width change is not trivial. The intensity of the absorbance depends on the concentration of the nanorods. The fact, that LSP of gold nanorods can be varied from visible to NIR region by varying the aspect ratio of gold nanorods, has been used in a number of applications.

14.4.2 Surface Enhanced Raman Scattering (SERS)

SERS was discovered in 1974 using pyridine adsorbed on roughened silver electrodes.²² These Raman signals were attributed later to the new phenomenon, called SERS.^{23, 24} SERS is a highly sensitive technique utilised for understanding the vibrational signatures of the molecules adsorbed onto the roughened metallic substrates. Due to the high specificity, sensitivity, and short acquisition time, SERS is widely employed in ultra-low concentration detection of molecules. Colloidal particles of coinage metals, such as Ag, Au, Cu have been used as substrates for SERS, where vibrational signatures of adsorbed molecules are enhanced by 10^{14} – 10^{15} times.^{25, 26} This has led to the possibilities of single molecule detection.

The concept behind Raman enhancement has been explained by two mechanisms: (i) Electromagnetic (EM) and (ii) Chemical (CHEM) enhancement mechanisms. EM enhancement occurs due to the interaction of surface plasmons of the metal with the electromagnetic radiation, which creates a high local electromagnetic field. The high local electromagnetic field helps the molecules adsorbed on the metallic surface exhibit enhanced Raman features. CHEM enhancement is due to the electronic resonance or charge transfer between the adsorbed molecule and the metallic surface. SERS is highly morphology-dependent, which is explained by the high electromagnetic enhancement at sharp tips and corners.²⁷ Nanorods and nanowires of gold and silver have enhanced electric fields at the tips compared to their spherical nanoparticles, which increases the SERS activity.⁹ The polarisation dependence of SERS for silver NWs, such as aligned NW rafts,²⁸ NW bundles,²⁹ coupled NWs,³⁰ and single NWs,³¹ has been studied extensively. Nikoobakht *et al.* observed surface enhancement factors of 10^4 – 10^5 for the adsorbed molecule, 2-aminothiophenol (2-ATP) on the gold nanorods.^{32, 33} However, there is no such enhancement on nanospheres under similar experimental condition. The enhancement of nanorods over nanosphere is not due to EM, as the plasmon band (695 nm) for nanorod is far from the excitation wavelength (1064 nm). The contribution of enhancement is attributed to CHEM mechanism for 2-ATP adsorbed on the Au(110) surface. In a separate study, various shapes of the gold nanoparticles, including nanorods, were electrostatically immobilised on self-assembled monolayers on gold substrates.³⁴ The enhancement factor for the nanorods was observed the order of 10^8 for

4-mercaptobenzoic acid (4-MBA) adsorbed on nanorod surface. Murphy *et al.* reported the aspect ratio dependent SERS of gold nanorods.³⁵ For this experiment, four different aspect ratios, such as 1, 1.7, 4.5, and 16, were used. The optimum aspect ratio was observed as 1.7, wherein the enhancement factor was higher by 10^1 – 10^2 greater than nanorods of other aspect ratios. Larger SERS enhancement for this aspect ratio nanorods is due to the EM contribution, which arises from the plasmon resonance with the excitation source and is consistent with the theoretical calculations for wavelength-dependent EM contributions.

14.5 CHARACTERIZATION TECHNIQUES

14.5.1 Surface Plasmon Resonance (UV/vis/NIR)

Discussed in subsection 14.4.1

14.5.2 Transmission Electron Microscopy

Transmission Electron Microscopy (TEM) is the most important technique utilised for the study of nanorod morphology. The purified and diluted nanorod sample is drop casted on carbon-coated copper grids and allowed to dry in ambience. The length, width, interplanar distance and distribution of nanorods can be investigated through this technique. Individual atoms can be visualised through high resolution TEM (HRTEM). Lattice parameter can be obtained and respective planes of the crystal can be indexed. Figure 14.7A represents the typical large area TEM image of the gold nanorods. The length is found to be 35–40 nm and width is around 15 nm. Figure 14.7B shows the HRTEM images of the body of a single nanorod. The interplanar spacings are shown which correspond to the lattice plane of gold. No planar defects or dislocations are observed, suggesting that nanorods are single crystalline. The presence of Au can be known from elemental analysis (EDAX). Similarly, gold nanorods can be characterised through the scanning electron microscopy (SEM) and SEM-EDAX. XRD confirms the *fcc* crystal structure of gold.

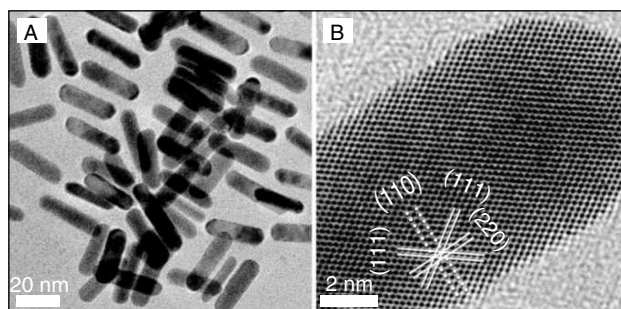


Fig. 14.7 (A) TEM image of gold nanorods synthesised by one-pot synthesis, and (B) HRTEM image of a body of a single nanorod shows the interplanar distance (reprinted with permission from Samal, *et al.* (Ref. 20) Copyright (2010) Springer-Netherlands).

14.6 APPLICATIONS

14.6.1 Cancer Cell Imaging

Gold nanorods are ideal candidates for cancer cell imaging due to strong absorption and scattering in the near infrared region (650–900 nm).³⁶ As synthesised nanorods (aspect ratio of 3.9) are centrifuged in order to remove other ions and excess cationic surfactant, CTAB. Nanorod surface is modified by negatively charged polystyrene sulfonate (PSS) and are mixed with an antibody solution in HEPES buffer. Nanorods conjugated to anti-epidermal growth factor receptor (anti-EGFR) monoclonal antibodies are incubated in the cell culture. Two malignant cells, such as HOC 313 clone 8 and HSC 3 and one non-malignant HaCat cell are used in the experiment. The anti-EGFR antibody-conjugated nanorods bind specifically to the surface of the malignant type cells, with a much higher affinity due to the over expressed EGFR on the cytoplasmic membrane of the malignant cells.

Fig. 14.8 shows the light scattering images of anti-EGFR-conjugated gold nanorods after binding to malignant and non-malignant cells. The orange colour of the gold nanorod is the most dominant, which corresponds to the surface plasmonic enhancement of the longitudinal oscillation in the near-infrared region. Anti-EGFR-conjugated gold nanorods have specific interaction to cancerous cell, HOC 313 clone 8 and HSC 3 and non-specific interaction to the noncancerous cell, HaCat. The nature of interaction is distinguished through the light-scattering imaging. Fig. 14.8 shows the quantity of nanorods bound to the cell. From the extinction spectra, it is clear that the intensity of the cancerous cells is around double of the non-cancerous cells. It is due to the nature of interaction between anti-EGFR-conjugated gold nanorods and cells: specific interaction to the malignant cells and non-specific interaction to non-malignant cells.

14.6.2 Photothermal Therapy

Photothermal therapy uses electromagnetic radiation leading to the emission of heat, which can destroy the affected cancerous cells. Thermal therapies for cancer cells have utilized a variety of heat sources such as microwaves, ultrasound and laser light. A major limitation of such therapies is that they are non-specific, i.e., they destroy both malignant and non-malignant cells. In a different approach, different shapes of gold nanoparticles (e.g., pentagon, prism), which absorb the wavelength in NIR region can be used as photothermal agents. The concept is that gold nanoparticles are transferred to the cells, preferably to malignant cells, and then those are irradiated with electromagnetic light. However, a limitation with the gold nanoparticles is that wavelength of the electromagnetic radiation can't be tuned for maximum efficiency. Gold nanorods can be suitable for the photothermal therapy as the aspect ratio of the gold nanorods can be controlled, by controlling the concentration of silver ion during the growth process.

In a typical approach, gold nanorods are conjugated to anti-EGFR antibody similar to cancer cell imaging and incubated for 30 min. The gold nanorod conjugated anti-EGFR antibody are exposed to continuous wave (CW) Ti:sapphire laser of different power values, such as 40, 80, 120, 160, and 200 mW with a focus spot of 1 mm diameter for 4 min each as reported.³² The cell stability was checked

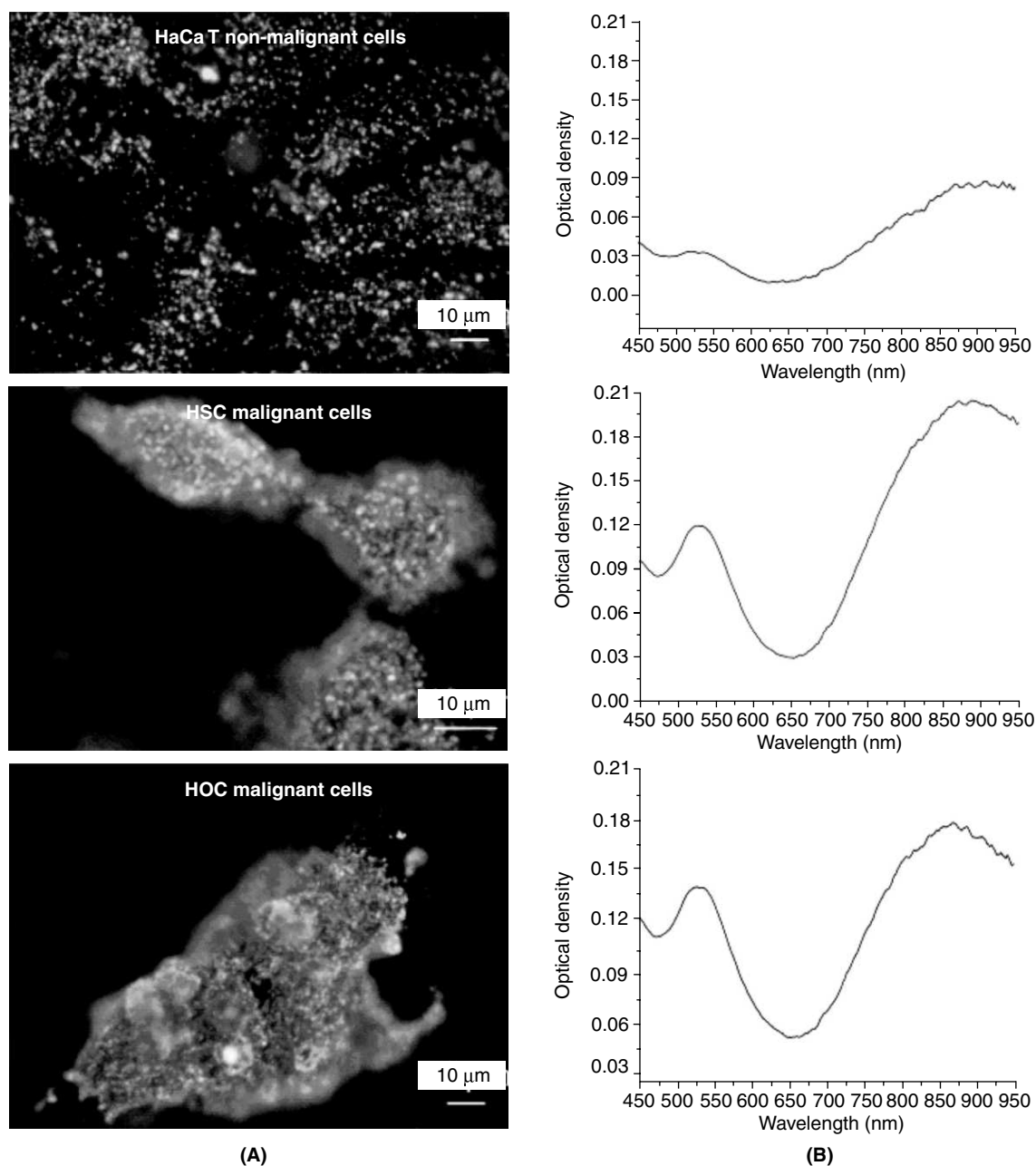


Fig. 14.8 (A) Light scattering images of anti-EGFR-conjugated Au nanorods after incubation with cells for 30 min at room temperature. (B) Average extinction spectra of anti-EGFR-conjugated Au nanorods from 20 different single cells for each kind (reprinted with permission from Huang, et al. (Ref. 36) Copyright (2006) American Chemical Society).

by staining with trypan blue. Two malignant cells, such as HOC 313 clone 8 and HSC 3, and one non-malignant HaCat cell and Ti:sapphire laser of wavelength at 800 nm were used in this experiment.

Figure 14.9 shows the exposure of laser at 800 nm of different powers to three cell cultures; left shows the HaCat normal cells, middle shows the HSC malignant cells and extreme right shows the HOC malignant cells. In case of HaCat normal cells, at and above 160 mW (20 W/cm^2), the cells are photodestructed; this can be detected by the cell viability test with trypan blue. Blue spot in a circular region, which matches the laser spot size, indicates the cell death. Due to the exposure of high energy, the cells outside the laser spot are also possibly destroyed. As the laser power reduces to 120 mW, the proportion of dead cells in the laser spot decreases. At this energy, the cell undergoes destruction only in the laser spot region; the injury to cells at the edge of the laser spot is not severe. At the laser power of 80 and 60 mW, the blue-dead-cell spots become smaller in area compared to as observed at

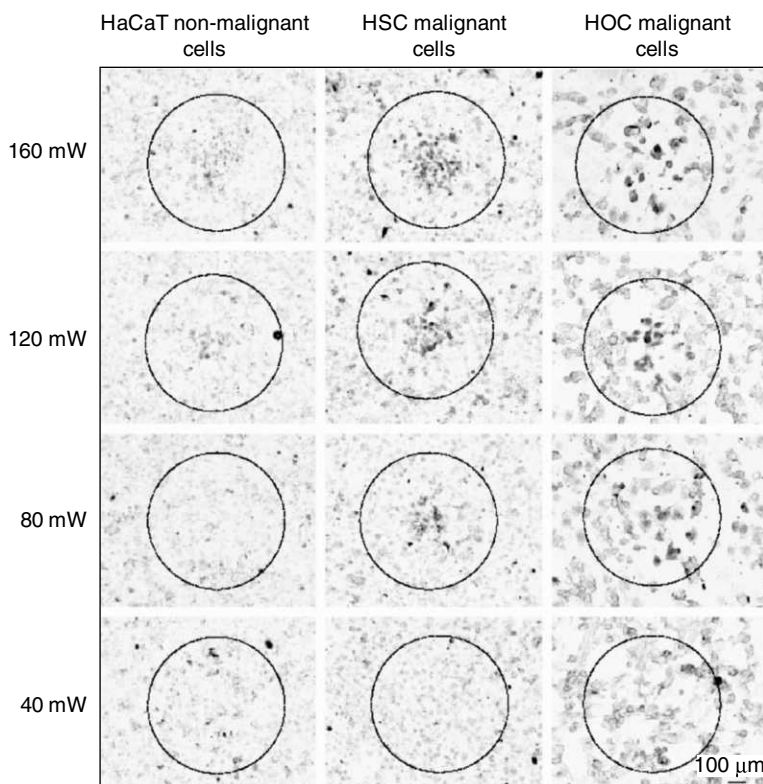
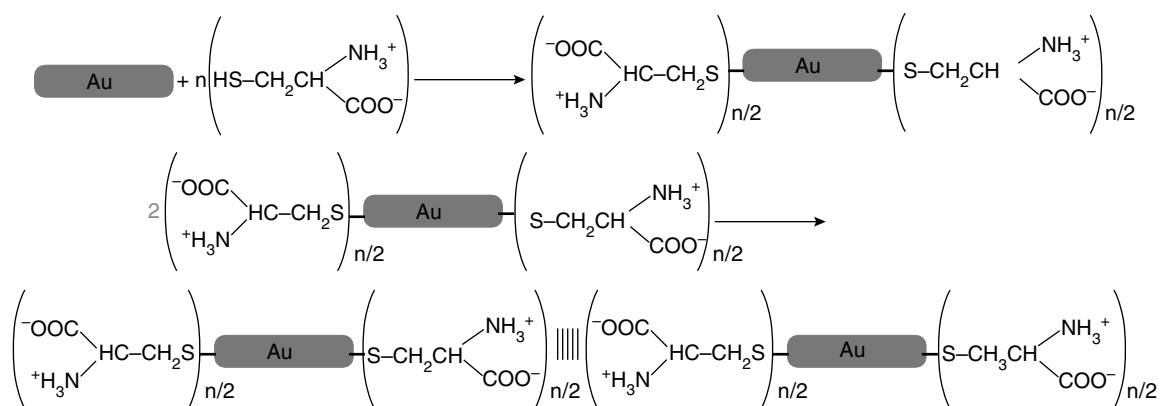


Fig. 14.9 Selective photothermal therapy of cancer cells with anti-EGFR/Au nanorods incubated. The circles show the laser spots on the samples. At 80 mW (10 W/cm^2), the HSC and HOC malignant cells are obviously injured while the HaCat normal cells are not affected. The HaCat normal cells start to be injured at 120 mW (15 W/cm^2) and are obviously injured at 160 mW (20 W/cm^2) (reprinted with permission from Huang, et al. (Ref. 36) Copyright (2006) American Chemical Society).

higher laser power. However, in case of HSC malignant cells, photothermal destruction of cells occurs even at lower power. At power of 80 mW and above, the cell death takes place within the laser spots due to photothermal destruction. The energy required for the photothermal destruction of malignant cells is about half of the energy of non-malignant cells. This is attributed to predominant transport of anti-EGFR antibody-conjugated gold nanorods in the malignant cell than non-malignant cell. The gold nanorods, which absorb the laser energy, and the emission of this heat causes the photochemical destruction of the cells.

14.6.3 Detection of Biomolecules

Selective detection of amino acids, such as cysteine and glutathione, were studied using gold nanorods.^{37,38} Thiol group present in the cysteine and glutathione selectively bind on the edges of the nanorods and the other end containing $-\text{NH}_2$ and $-\text{COOH}$ are free for further interaction. Cysteine forms zwitterions at its isoelectric point (5.02) and forms end-to-end self-assembly through a two-point electrostatic interaction resulting into intermolecular hydrogen bonding between amino and carboxylic groups as shown below.



Scheme 14.1 Schematic representation end-to-end assembly of gold nanorods by cysteine and glutathione (adapted from Ref. 37).

For the formation of well-ordered assembly, three functional groups ($-\text{SH}$, $-\text{NH}_2$ and $-\text{COOH}$) are necessarily important. $-\text{SH}$ group selectively binds to edges of the nanorods and the $-\text{NH}_2$ and $-\text{COOH}$ are forming zwitterions at a particular pH. Aminoacids without thiol or zwitterionic groups are impossible to form such well-ordered assemblies.

14.6.4 Sensor

Gold nanorods are capable for sensing purposes. These are used as sensors in numerous fields. Gold nanorods act as a mercury sensor.³⁹ It is possible to determine the presence of mercury in tap water samples at the parts-per-trillion (ppt) level. Selectivity and sensitivity of mercury is due to the

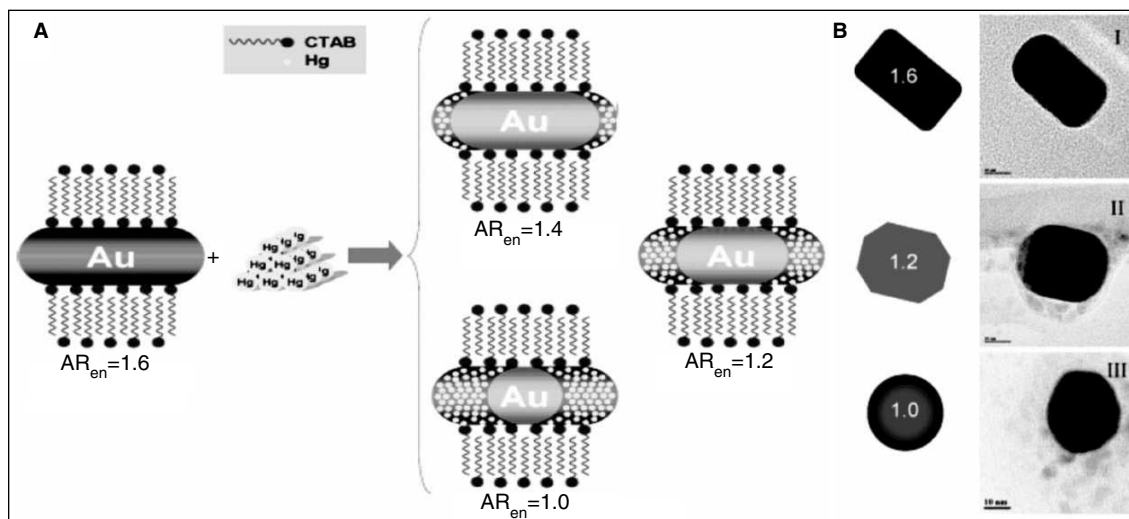


Fig. 14.10 (A) Schematic representation of the amalgamation of Hg with gold nanorods. (B) TEM images of gold nanorods in the absence and the presence of Hg. I) no Hg; II) $1.25 \times 10^{-5} M$ and III) $1.57 \times 10^{-4} M$ of Hg^{2+} (reprinted with permission from Rex, et al. (Ref. 39). Copyright (2006) American Chemical Society). (For clarity see colour figure.)

amalgamation of mercury and gold. The entire sensing process takes place less in than 10 min with no sample separation. Ultra-low levels of Hg have been detected. Fig. 14.10 shows the schematic representation and experimental evidence of the amalgamation of Hg with gold nanorods. The aspect ratio of gold nanorods decreases with increase the concentration of Hg^{2+} at constant $NaBH_4$ concentration. The direct correlation between the wavelength shift and mercury concentration makes quantitative analysis (Fig. 14.11). In tap water, the detection limit is $6.6 \times 10^{-13} g.L^{-1}$.

14.7 1-D NANOSTRUCTURES OF TELLURIUM

14.7.1 Introduction

Tellurium is a narrow-band-gap semiconductor ($E_{dir} = 0.35 eV$). The structure of elemental tellurium is considered to have a spiral chain of atoms held together by covalent bonds. The chains oriented along c-axis are held together by weak Van der Waal forces.⁴⁰ Due to the anisotropic crystal structure, it has a great tendency to form 1-D nanostructures, such as nanowhiskers, nanotubes, nanobelts, nanorods and nanowires. Tellurium exhibits many useful and interesting properties, such as photoconductivity, thermoelectric effect, catalytic activity and strong piezo-electric effect.⁴¹⁻⁴⁴ Tellurium can react readily with the other elements to produce many functional tellurides, such as, Ag_2Te , $ZnTe$, $CdTe$, Bi_2Te_3 , etc., which can enhance the physical as well as chemical properties. The controlled preparation of various 1-D nanostructures of tellurium might be useful in many applications in future nanodevices. Different methods are reported for the synthesis of various 1-D nanostructures as discussed below.

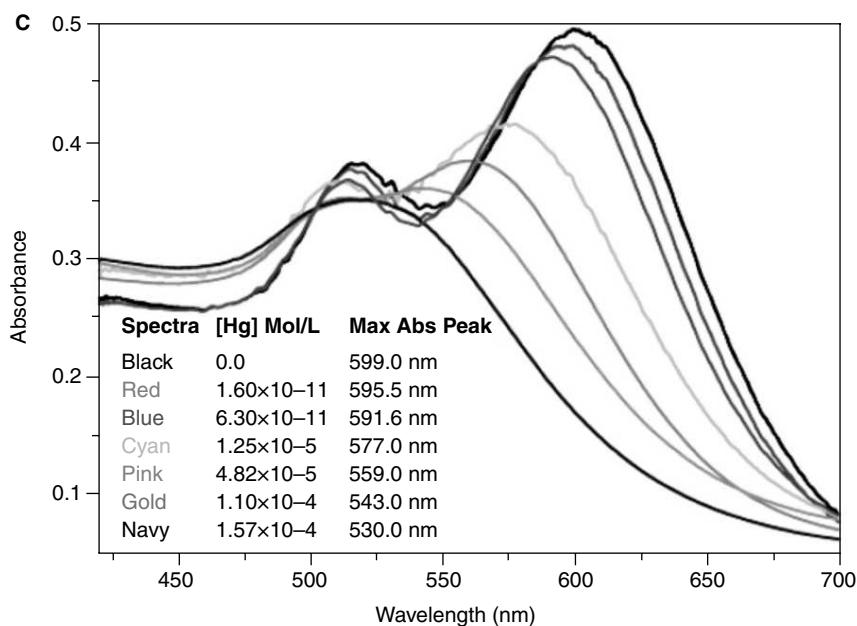


Fig. 14.11 UV/vis absorption shift in the concentration range between 1.6×10^{-11} and 6.3×10^{-11} M of Hg(II) (reprinted with permission from Rex, et al. (Ref. 39). Copyright (2006) American Chemical Society).

14.7.2 General Strategies for 1-D Growth

Different strategies have been reported for the synthesis and growth of 1-D nanostructures. Among these, some techniques have been used extensively and others have attracted far less attention. Synthesis of 1-D nanostructures need to pay attention on their control over morphologies, monodispersity (uniformity), and high yield. Various techniques have been developed with different levels of control over the growth parameters.⁴⁵ These are: (a) the use of anisotropic crystallographic structure of a solid to generate 1-D growth (Fig. 14.12A); (b) introduction of a solid-liquid interface to reduce the symmetry of a seed (Fig. 14.12B); (c) the use of various templates to direct the formation of 1-D nanostructures (Fig. 14.12C); (d) the use of supersaturation control to modify the growth of a seed; (e) the use of capping agent to kinetically control the growth rates of various facets of a seed (Fig. 14.12D); (f) self-assembly of 0-D nanostructures (Fig. 14.12E); and (g) size reduction of 1-D microstructures (Fig. 14.12F).

14.7.3 Synthesis of 1-D Nanostructures of Tellurium

14.7.3.1 Vapor Phase Synthesis

Various morphologies, including whiskers, were grown by the sublimation of metallic tellurium on the surface of platinum substrates at various temperatures.⁴⁶ Different morphologies of tellurium, such as

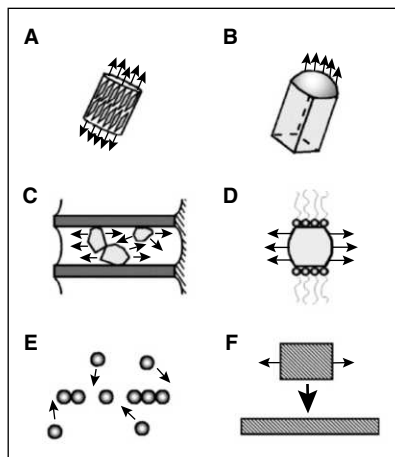


Fig. 14.12 Schematic representations of six different strategies that have been demonstrated for the 1-D growth: (A) dictation by the anisotropic crystallographic structure of a solid; (B) confinement by a liquid droplet as in the vapor-liquid-solid process; (C) direction through the use of template; (D) kinetic control provided by a capping reagent; (E) self-assembly of 0-D nanostructures; and (F) size reduction of a 1-D microstructure (reprinted with permission from Xia, et al. (Ref. 45) Copyright (2003) Wiley-VCH).

spine-(s), filament-(f) and needle-(n) shaped whiskers were grown at different temperatures.⁴⁷ The whiskers were grown parallel to the (001) direction of hexagonal lattice of tellurium (Fig. 14.13).

Various morphologies of tellurium whiskers are shown in Fig. 14.13. Spine-(s) shaped whiskers were observed with triangular cross-sections and tapered tips were seen at $T_s \sim 90\text{--}100^\circ\text{C}$ (Fig. 14.13B). Filament-(f) shaped whiskers were observed with elongated triangular cross-sections and long tapered tips at $T_s \sim 100\text{--}140^\circ\text{C}$. When temperature increased to $130\text{--}200^\circ\text{C}$, needle-(n) shaped whiskers were observed.

Trigonal and hexagonal nanotubes of tellurium were synthesised by vaporising metallic tellurium at 350°C and condensing the vapours on Si(100) substrate in an inert atmosphere.⁴⁸ A downstream of Ar was used to carry the vapors. The formation of nanotubes was strongly dependent on the structure of the substrate surface, Ar gas flow rate, and the deposition temperature. For example, when the substrate is Si(111) or sapphire (0001) or argon flow rate is increased to 500 sccm, nanowires and nanorods were predominant.

Figure 14.14A shows the FESEM image of the tellurium nanotubes on a Si(100) substrate. Figure 14.14B and C show the individual triangular and hexagonal nanotubes, respectively. The edge length of the triangular nanotube varies from 100 to 250 nm, whereas the external diameter of the hexagonal nanotubes varies from 100 to 200 nm. At the temperature range of $150\text{--}200^\circ\text{C}$, triangular and hexagonal tellurium nanotubes were deposited on a substrate. However, at temperature lower than 150°C , tellurium nanowires were exclusively formed (Fig. 14.14D). These nanowires had diameters

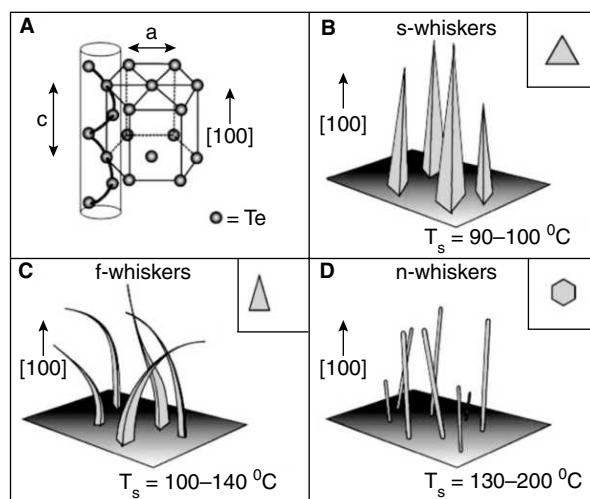


Fig. 14.13 (A) Schematic representation of hexagonal lattice of tellurium. The crystal structure of *t*-Te is highly anisotropic, with the basic unit being helical chains of covalently bound tellurium atoms. These chains are held together to form a hexagonal lattice via weaker Van der Waals forces. Depending on the substrate temperature (T_s), *t*-Te crystals exhibit a number of different morphologies: (B) triangular, spine-shaped whiskers at $T_s \sim 90$ – 100 °C; (C) filamentary, blade-shaped whiskers when T_s was raised to 100 – 140 °C; and (D) needle-like whiskers when T_s was controlled in the range of 130 – 200 °C. The inset of each plate indicates the cross-section of that particular type of whisker (reprinted with permission from Mayer and Xia (Ref. 47) Copyright (2002) Royal Society of Chemistry).

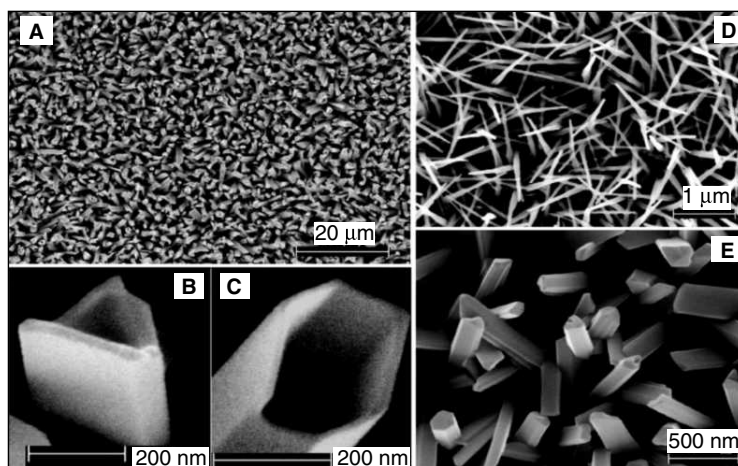


Fig. 14.14 FESEM image of (A) tellurium nanotubes synthesised on a Si (100) substrate, (B) nanotube with triangular and (C) hexagonal cross-section, (D) tellurium nanowires deposited on a Si (100) substrate, (E) Te nanorods with triangular and hexagonal cross-sections deposited on a Si(100) substrate (reprinted with permission from Mohanty, et al. (Ref. 48). Copyright (2006) American Chemical Society).

varying from 30–60 nm and lengths up to a few micrometers. Increasing the Ar flow rate from 25 to 500 sccm, nanorods having triangular and hexagonal cross-sections were deposited exclusively on the Si(100) substrate (Fig. 14.14E).

14.7.3.2 Solution Phase Synthesis

Solution phase synthesis of 1-D nanostructures of tellurium was carried out at different solvents.⁴⁷ Three different solvents, such as water, ethylene glycol (EG), and water-EG mixtures were used. These solvents were refluxed at temperatures in the range of 20–200 °C. Hydrazine was used for the reduction of orthotelluric acid. EG was used to reduce TeO₂ at 180 °C. First, the reaction mixtures were stirred and heated for ~10 min to complete the reduction. Then the mixtures were cooled, and aged in the dark at room temperature. Various morphologies of tellurium nanostructures were formed, which were highly dependent on the solvents and the refluxing temperatures.

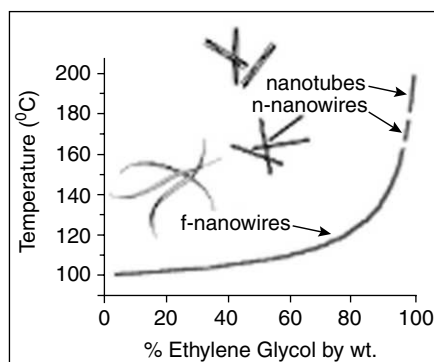


Fig. 14.15 The boiling points of EG and water mixtures having different ratios. The general morphologies of tellurium nanostructures observed at different solvent compositions (and thus refluxing temperatures) are also indicated in this figure. Needle-shaped nanowires were formed exclusively in a very narrow range of temperature (174–182 °C). Below this temperature range, filamentary nanowires were generated. Above this temperature range, tubular nanostructures with tri-tipped whiskers were observed (reprinted with permission from Mayer and Xia (Ref. 47). Copyright (2002) Royal Society of Chemistry).

When the reaction mixture was refluxed at temperatures below 100 °C in water, products were a mixture of crystalline tellurium (t-Te) and spherical colloids of amorphous tellurium (a-Te). a-Te colloids slowly dissolve and transfer to t-Te. When the reflux was carried out above 100 °C in pure EG (or mixtures with water), it leads to form crystalline tellurium (t-Te) (Fig. 14.16). The morphologies of tellurium depend on the reflux temperature (Tr). For example, spines (Tr < 100 °C), filaments (Tr = 100–160 °C), needles (Tr = 160–180 °C), and tubular structures (Tr > 180 °C) were formed, respectively.

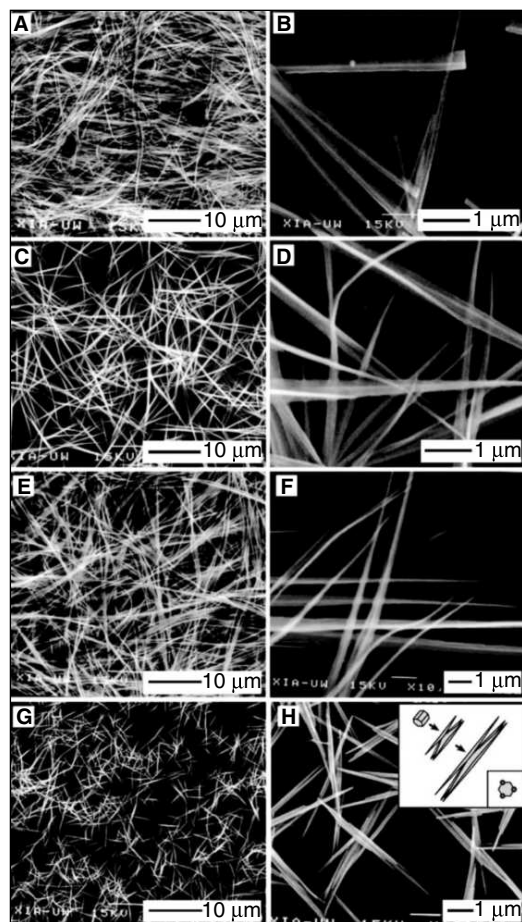


Fig. 14.16 Low and high magnification SEM images of *t*-Te nanowires synthesised by reducing orthotelluric acid with hydrazine in EG refluxed at (A, B) 100 °C, (C, D) 140 °C, and (E, F) 180 °C. All these nanostructures had a distinct shape similar to that of *f*-whiskers, and this morphology changed very little with temperature. (G, H) When the refluxing temperature was increased to 196 °C, a remarkable change in morphology occurred. Reduction of telluric acid by EG yielded uniform hexagonal nuclei of *t*-Te. Subsequent addition of hydrazine induced the growth of filamentary nanowires at the edges of each seed giving a tri-tipped, tubular structure. Inset shows a schematic of the growth process from hexagonal seed to tri-tipped nanotubes. The lower right corner of the inset shows a cross-sectional view of the nanotube (reprinted with permission from Mayer and Xia (Ref. 47). Copyright (2002) Royal Society of Chemistry).

Different morphologies were observed in the vapour phase at different temperatures and solution phase using different solvents and temperatures which are tabulated in Table 14.1.

Table 14.1 Comparison of various morphologies as a function of solvents and temperatures in vapour phase and solution phase syntheses.

Morphology	Vapour Phase Synthesis ⁴⁶	Solution Phase Synthesis ⁴⁷
Spine like	90–110 °C	20–100 °C (Water)
Filamentary	100–140 °C	100–196 °C (Ethylene glycol)
Needle like	130–200 °C	178 °C (Water/ethylene glycol)

14.7.3.3 Sonochemical Synthesis

Large-scale synthesis of bundles of t-Te nanowhiskers was carried out from metallic Te powder by sonication.⁴⁹ Sonication was used as the driving force for the growth of nanowhiskers under ambient pressure. In this synthesis, high-quality, uniform and crystalline nanowhisker bundles of t-Te were formed within 1 hr. Te powder along with KOH and water was stirred to form a dark purple solution. The unreacted Te powder was centrifuged and redispersed in water. The mixture was sonicated for 1 hr at 65–75 °C at different intervals of time.

In this method, ultrasound wave is the driving force for the formation of various nanostructured materials. During sonication, microscopic bubbles are formed in the solution by a process known as cavitation and these bubbles grow and may implode.⁵⁰ The implosion leads to the formation of large heat and pressure that speed up the reaction. During implosion, it forms extremely high temperatures as high as 5000°K, and pressures up to ~1800 atm and cooling rates can often exceed ~10¹⁰ K/s.⁵¹ This large amount of energy released can enhance the chemical reactivities and cause physical effects. In case of tellurium bundles of nanowhiskers, sonication leads to hot spots, which could cause local fluctuation in the solubility of tellurium and induce the seeding and growing of t-Te.

Zhu *et al.* synthesised tellurium nanorods and branched nanorod structures by ultrasonication process.⁵² Tellurium nitrate powder is used as the Te source for sonication. The nanorods synthesised were of 30–60 nm in diameter and of length up to 200–300 nm. Ultrasonication leads to two kinds of tellurium nuclei, such as a-Te colloids and t-Te nuclei. Growth of nanorods occurs due to a-Te deposited on the surface t-Te, in which t-Te acts as seed. The growth of branched structures is due to the result of multi-nuclei growth in monomer colloid. Every nuclei sitting on the surface of each colloid could act as a new seed and enhances the growth site for the nanorod branched structure.

14.7.3.4 Hydrothermal Synthesis

Thin single-crystal nanobelts and nanotubes of tellurium were synthesised through hydrothermal route by *in-situ* disproportion of sodium tellurite (Na₂TeO₃) in aqueous ammonia at 180 °C.⁵³ The thickness of the nanobelts obtained is ~8 nm, width of 30–500 nm and length up to several hundred micrometers. The nanotube were synthesised have outer diameter of 150–400 nm, wall thickness 5–15 nm and length up to 5–10 μm. Based upon the TEM images of nanobelts and nanotubes (Fig. 14.17), the formation can be explained through two different mechanisms. These were template-roll-growth and template-twist-join-growth for nanobelts and nanotubes, respectively. TEM images of the

nanobelts and nanotubes suggest that formation of nanotubes is seemingly related to the twisting or curling of the nanobelts.

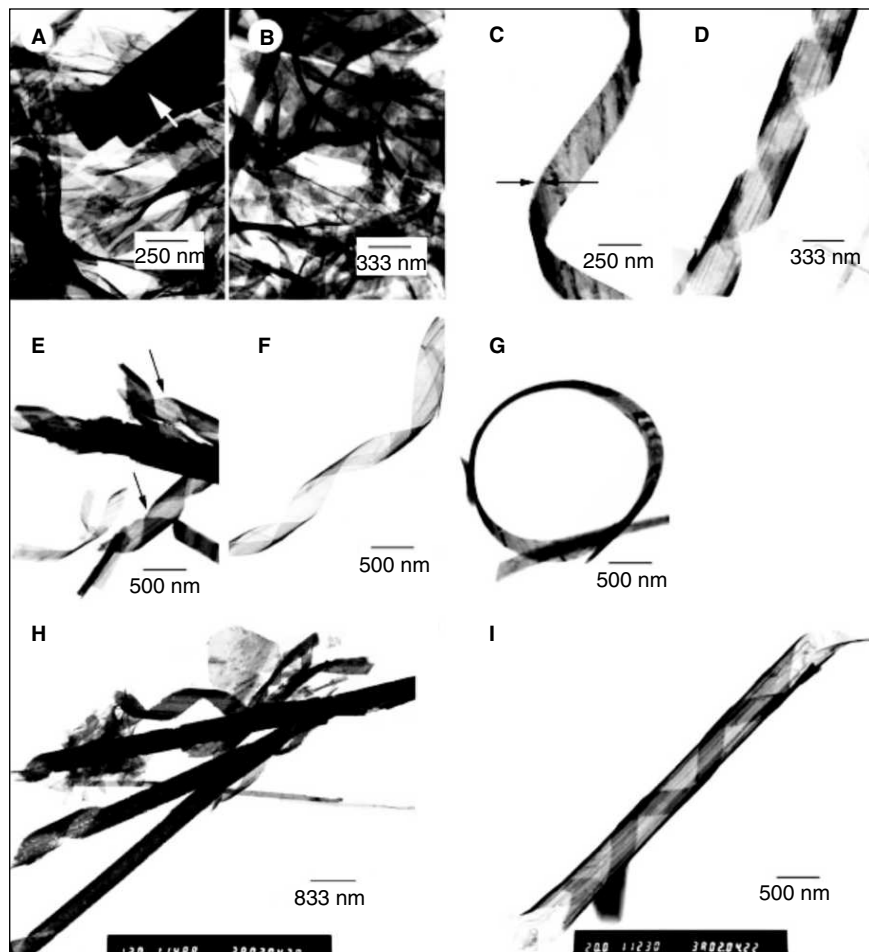


Fig. 14.17 Representative TEM images of the as-synthesised tellurium nanobelts and nanotubes showing their geometric shapes. (A-C) Some straight and twisted tellurium nanobelts, displaying the shape characteristics of the nanobelts. (D-F) Several helical nanobelts (as indicated by arrow), displaying the helical twisting property of the nanobelts. (G) A nanobelt bending in a circle, displaying the bending property of the nanobelts. (H) TEM image of several belt-twisted tellurium nanotubes. (I) A typical belt-rolled tellurium nanotube (reprinted with permission from Mo, et al. (Ref. 53). Copyright (2002) Wiley-VCH).

Liu *et al.* synthesised tellurium nanotubes by hydrothermal redox method.⁵⁴ In this process, homogeneous solution of Na_2TeO_3 and Na_2SO_3 in distilled water were autoclaved at 180 °C for 12 hr. The nanotubes obtained were with the average width of 140 nm.

Single-crystalline tellurium nanowires were synthesised by the biomolecule-assisted reduction method under hydrothermal conditions.⁵⁵ The biomolecule, alginic acid is used as both reducing agent and directional template. H_2TeO_4 powder was used as the Te source and autoclaving was done at 150°C for 15 hr. The formation of the nanowires might be due to the presence of large number of hydroxyl (-OH) groups on the surface of alginic acid, which react with TeO_4^{2-} and decomposition of the intermediate results in tellurium crystals. The nanowires were formed having average diameter 80 nm and lengths up to tens of micrometer.

Wang *et al.* synthesised hexagonal tellurium nanotubes in polyethylene glycol (PEG)-mediated hydrothermal method using tellurium powder as the tellurium source.⁵⁶ The reaction mixture was autoclaved at 160°C for 48 hr. The growth of nanotubes occurred through a dissolution-recrystallization process. PEG was used to enhance the dissolution of tellurium powder into water and control the morphology to form nanotubes. The formation mechanism of tellurium nanotubes is the combined effect of the selective adsorption of PEG on different crystal faces of tellurium and the insufficient feeding of tellurium atoms or atom clusters for the growth of tellurium crystal. It is believed that first the spherical particles are formed during the hydrothermal process. These particles serve as seeds for the growth of tellurium nanotubes. It was found that the diameters of these spherical particles are close to the tellurium nanotubes. The nanotubes obtained were mainly composed of hexagonal cross-section. SEM images (Fig. 14.18) shows the nanotube synthesised, in this method, were having diameters in the range of 200–400 nm and lengths in the range of 5–20 μm .

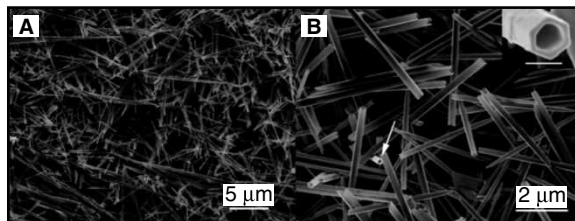


Fig. 14.18 (A, B) SEM images of the as-obtained tellurium sample with different magnification. The inset in (B) is a magnified image of the nanotube indicated by an arrow shows the hexagonal cross-section; scale bar is 200 nm (reprinted with permission from Wang, *et al.* (Ref. 56). Copyright (2008) American Chemical Society).

14.8 TELLURIUM NANOWIRES

Nanowires are cylindrical 1-D nanostructures of a few tens of nanometers diameter and several tens of micrometers in length. 1-D nanowires are ideal systems to investigate the effect of size confinement on electrical, optical, mechanical and other properties. Examples of semiconducting nanowires are Si, Ge, Te, GaAs, Gap, GaN, InAs, InP, ZnS, ZnSe, CdS, CdSe, and mixed compounds. These nanowires have potential applications in electronic and optoelectronic devices, solar cells, etc. Many unique and fascinating properties have been already studied. The properties of the nanowires are completely

different from the corresponding bulk material. It shows many more exciting, novel, and enhanced properties, which have not been observed in bulk or 3-D materials. This is because electrons are quantum confined in nanowires and the energy levels are different from bulk materials. Nanowires may be either metallic or semiconducting. The properties of metallic and semiconducting nanowires are different. For example, the optical properties of the metallic nanowires depend upon the surface plasmon, which is the collective oscillation of electrons, due to the interaction of electromagnetic radiations. For example, gold nanorods, which are metallic in nature, show two plasmons called TSP and LSP (discussed earlier). But in the case of semiconductors, the optical properties depend on the transitions between the conduction and valence-bands of the semiconductor. For example, tellurium nanowires show two peaks due to interband transitions (Fig. 14.22). Peak I is due to the transition from p-bonding valence-band (VB2) to the p-antibonding conduction band (CB1). Peak II is due to the transition from p-lone pair valence-band (VB3) to the p-antibonding conduction band (CB1). Tellurium nanowires shows very narrow band gap (0.35 eV). Due to the anisotropic nature of Te, it has a great tendency to form anisotropic structures, and growth of nanowire occurs in the (001) direction.

14.8.1 Synthesis of Tellurium Nanowires

Very recently, high quality, large yield, aspect-ratio controlled tellurium nanowires were synthesised in aqueous phase at room temperature.⁵⁷ In this green chemistry method, luminescent t-Te nanowires were synthesized by the reduction of TeO₂ using concentrated hydrazine hydrate as the reducing agent. The reaction mixture containing hydrazine and TeO₂ were allowed to react at room temperature under constant stirring. Sodium dodecyl sulfate (SDS) was added to the reaction mixture in order to control the aspect ratio of the nanowire during synthesis. The as-prepared solution was purified by centrifugation to remove excess hydrazine and SDS. The residue was redispersed in deionised water and centrifuged twice for the complete removal of unreacted species.

The reduction of TeO₂ by hydrazine was carried out in alkaline medium. TeO₂ forms metalloid oxyanion tellurite (TeO₃²⁻) in the alkaline medium, which is reduced to Te by hydrazine. The proposed reaction is given below:



When TeO₃²⁻ was reduced by hydrazine, two kinds of tellurium were formed in the solution. Amorphous Te (a-Te) and trigonal Te (t-Te). t-Te acts as seed particles, whereas a-Te was dissolved in the solution and deposited on t-Te. This is because a-Te has higher free energy than t-Te. When all the a-Te was deposited on t-Te, Te²⁻ (formed during reduction of Te, shown in the reaction) present in the solution were oxidised and form Te atoms and deposited on t-Te. Due to the highly anisotropic nature of t-Te, it has a great tendency to form a cylindrical shape. a-Te and oxidised Te²⁻ both deposited in the t-Te. It forms an elongated structure in the (001) direction. The length nanowires depend on

the quantity of a-Te and oxidised Te^{2-} present at constant quantity of hydrazine in the system. So, the aspect ratio of the nanowires can be controlled by controlling the molar ratio of $\text{TeO}_2/\text{N}_2\text{H}_4$ in the solution. Shorter and thicker nanowires can be prepared by high molar ratio of $\text{TeO}_2/\text{N}_2\text{H}_4$ due to the formation of a-Te and Te^{2-} in the beginning of the reaction. Schematic representation (Fig. 14.19) illustrates the growth of tellurium nanowires.

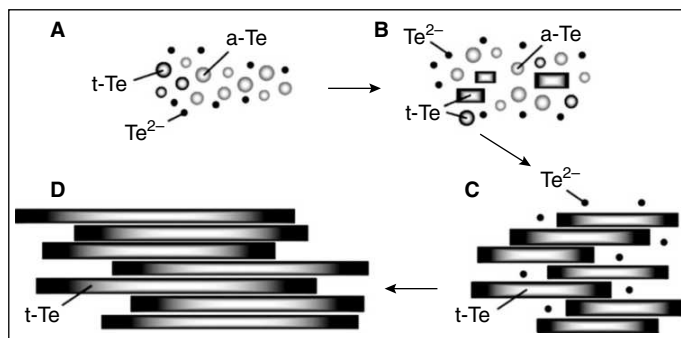


Fig. 14.19 Schematic illustration of a plausible mechanism for the formation of t-Te nanowires; (A) Reduction of TeO_3^{2-} with concentrated N_2H_4 solution at room temperature in an aqueous medium produce Te^{2-} and spherical colloids of a-Te and t-Te, (B) t-Te nanostructures were formed from a-Te colloids through Solid-Solution-Solid transformation, (C) Most a-Te colloids disappeared, and the nanostructures were t-Te nanowires in the solution and (D) t-Te nanowires still grew to extend their length through the deposition of Te atoms that were produced from the oxidation of Te^{2-} (reprinted with permission from Lin, et al. (Ref. 57). Copyright (2008) American Chemical Society).

The growth mechanism suggested in the above schematic is supported by the time-dependent TEM images of Te nanostructures shown in Fig. 14.20. TEM images were observed at different intervals of time, during growth of nanowires. The growth of tellurium nanostructures can be controlled by adding SDS. At a period of 10 min, two kinds of colloids, such as a-Te and t-Te, were formed with diameters less than 7 nm (Fig. 14.20A). Over the reaction period of 10–30 min, a-Te colloids were dissolved and deposited onto t-Te colloids. After 40 min of the reaction, t-Te nanowires were observed with an average diameter of $8.2 (\pm 1.7)$ nm and an average length of $251 (\pm 42)$ nm. TEM images suggest that the length of t-Te nanowires can be tuned by carefully controlling the reaction time. Upon increasing the reaction time, the lengths of t-Te nanowires increased. At different time intervals, such as 60, 80, 100, and 120 min, the lengths for t-Te nanowires were $456 (\pm 110)$, $595 (\pm 150)$, $785 (\pm 170)$, and $879 (\pm 170)$ nm, respectively.

14.8.2 Telluride Nanowires

Due to reactive nature of tellurium, it readily forms various functional tellurides, which can enhance the numerous physical and chemical properties than tellurium. Tellurides are very fascinating applications

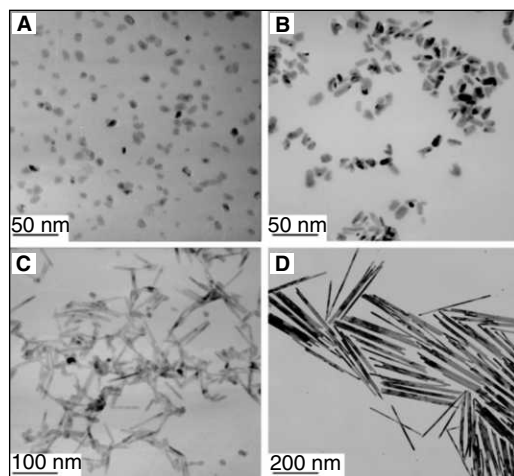


Fig. 14.20 TEM images of an aqueous solution containing 10 mM TeO_2 and 80% N_2H_4 after the reaction at room temperature for (A) 10 min, (B) 20 min, (C) 30 min, and (D) 40 min (reprinted with permission from Lin, *et al.* (Ref. 57) Copyright (2008) American Chemical Society).

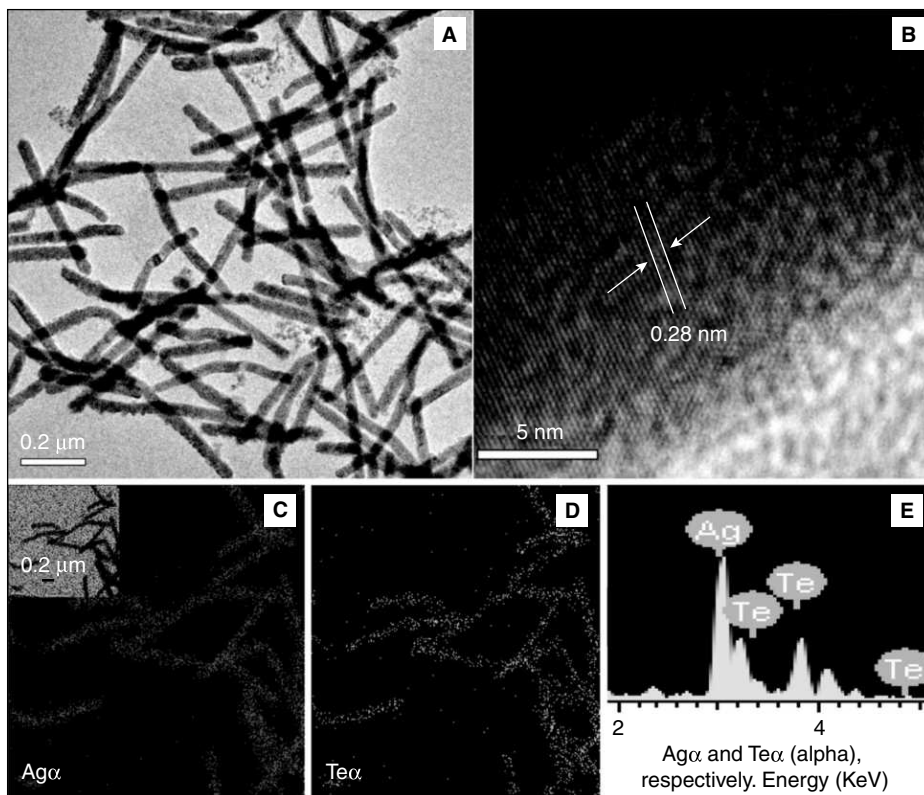
such as thermoelectric (Bi_2Te_3 , Sb_2Te_3 , $\text{Bi}_x\text{Sb}_{2-x}\text{Te}_3$, CdTe , Ag_2Te , PbTe , La_2Te_3), solar cell (CdTe , HgTe), detectors for X-rays & gamma rays ($\text{Zn}_x\text{Cd}_{1-x}\text{Te}$) and photovoltaic (CdTe).

14.8.2.1 Silver Telluride (Ag_2Te) Nanowires

Silver chalcogenides, for example silver telluride (Ag_2Te), have been receiving a tremendous attention due to the specific semiconducting properties. Ag_2Te is a narrow band-gap semiconductor (0.04–0.17 eV).⁵⁸ It is known to show a phase transition from the low-temperature monoclinic phase ($\beta\text{-Ag}_2\text{Te}$) to the high temperature face-centered cubic phase ($\alpha\text{-Ag}_2\text{Te}$) at $\sim 423^\circ\text{K}$.⁵⁹ Low-temperature $\alpha\text{-Ag}_2\text{Te}$ is a narrow band-gap semiconductor with high electron mobility and low-lattice thermal conductivity.⁶⁰ In the cubic phase, silver cations can move freely, which enhances the conductivity, leading to superionic conductivity.⁶¹ It shows a huge magnetoresistance in the case of n- and p-type Ag_2Te .^{62,63} Bulk Ag_2Te is known to show a thermoelectric effect. Its Seebeck coefficient was investigated in the temperature range of 2–450°K.⁶⁴ The values of n- and p-type Ag_2Te were investigated in the range of 55–500°K.⁶⁵ Aliev *et al.* studied this in the temperature range of 80–300°K and explained the data on the basis of carrier-scattering mechanism.⁶⁶ Maximum Seebeck coefficients for Ag_2Te nanowires were observed -170 and $-142 \mu\text{V K}^{-1}$ elsewhere.^{67,68} In addition, Ag_2Te nanowires show SERS using crystal violet (CV) as analyte and sensitive up to 10^{-7} M .⁶⁸

Bulk Ag_2Te is prepared by the solid state reaction between elemental Ag and Te at high temperature.⁶⁹ Ag_2Te nanocrystals were synthesised by the ultra sonication of AgNO_3 and Te mixture in ethylenediamine.⁷⁰ The rod-like structure of Ag_2Te was synthesised by the reaction of AgCl and Te powder in mixed solvents, such as ethylenediamine and hydrazine hydrate.⁷¹ Ag_2Te nanotubes have been

synthesised hydrothermally, when sodium tellurate (Na_2TeO_3) and AgNO_3 in hydrazine/ammonia mixture was autoclaved at 393°K .⁵⁹ Ag_2Te nanowires synthesised by cathodic electrolysis in dimethyl sulfoxide solutions containing NaNO_3 , AgNO_3 and TeCl_4 using porous anodic alumina membrane as the template.⁵⁶ The electrodeposition was carried out using a three-electrode system with an Ag/AgCl as reference electrode and a platinum plate as the counter electrode. Ag_2Te nanowires cathodically deposited on porous anodic alumina template. Li *et al.* synthesised Ag_2Te nanowires by a composite-hydroxide-mediated (CHM) method, where AgNO_3 and Te powder were heated at 225°C in a teflon vessel containing ethylenediamine and hydrazine hydrate along with mixed hydroxides (NaOH/KOH)(51.5:48.5).⁶⁷ The synthesis of Ag_2Te nanorods in a reaction of tellurium nanorods and AgNO_3 in hydrazine and Na_2EDTA at 333°K has been studied.⁷² Samal *et al.* demonstrated room-temperature-solution phase route for the synthesis of Ag_2Te nanowires by the direct reaction of Te nanowires with AgNO_3 , where Te nanowires acts as templates.⁶⁸ In this method, purified Te nanowires was allowed

**Fig. 14.21**

(A) Large area TEM image of Ag_2Te nanowires, (B) lattice resolved HRTEM of a single Ag_2Te nanowire, (C) elemental mapping using Ag and (D) Te and (E) EDAX spectrum of Ag_2Te nanowires. The TEM image corresponding to the elemental maps of C and D is shown in the inset of C (reprinted with permission from Samal, *et al.* (Ref. 68). Copyright (2008) American Chemical Society). (For clarity see colour figure.)

to react with AgNO_3 and stirred for 12 hr. The colour changed from blue to black. The product was purified by centrifuging twice and redispersed in deionised water for further characterisation. Ag_2Te nanowire powder can be prepared by freeze drying the concentrated solution.

Various microscopic and spectroscopic tools are used for the characterisation of Ag_2Te nanowires. Detailed morphologies of these nanowires are characterised by HRTEM and SEM. EDAX and XPS confirms chemical composition of the nanowires. XRD and DSC shows the crystal structure and phase transition of the nanowire. Figure 14.21A shows the TEM image of slightly bent Ag_2Te nanowires and Fig. 14.21B shows the lattice resolved HRTEM image of a single Ag_2Te nanowire synthesised by room-temperature solution phase.⁶⁸ The interplanar spacing is 0.28 nm, which corresponds to the (220) lattice plane of Ag_2Te nanowire. The atomic ratio of Ag to Te obtained from quantitative analysis of AgLa and TeLa in the EDS spectrum is 1.99:1, indicating a deficiency of silver in Ag_2Te .

14.9 PROPERTIES

14.9.1 Optical Properties

Te nanowires are semiconductors. The optical properties of the semiconductors depend on the transitions between conduction and valence bands. For example, Te nanowires show two peaks, peak I and II, in the optical absorption spectrum due to interband transitions.⁵⁷ Peak I is due to the transition from p-bonding valence band (VB2) to the p-antibonding conduction band (CB1). Peak II is due to the transition from p-lone pair valence band (VB3) to the p-antibonding conduction band (CB1). Generally, peak I ranges between 250–350 nm and peak II ranges between 600–850 nm. For example, the absorption spectra of Te nanowires prepared for different reaction times is shown in Fig. 14.22.

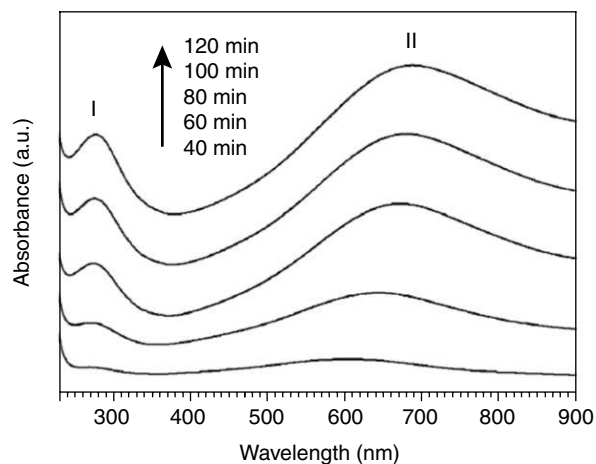


Fig. 14.22 UV/vis. absorption spectra of *t*-Te nanowires that were prepared for different reaction times (40–120 min). Peak I represents the transition from VB2 to CB1, and peak II represents the transition from VB3 to CB1 (reprinted with permission from Lin, et al. (Ref. 57). Copyright (2008) American Chemical Society).

14.10 CONCLUSIONS

1-D nanostructures are a new class of materials. Although several of the 1-D nanostructures, such as carbon nanotubes, are discussed as separate materials and have been around for a long time, several new structures made of metals and semiconductors are attracting attention these days. These materials are having unique properties due to the confinement of electrons in one dimension. The synthetic strategies involve confining growth in one direction by the choice of suitable templates or chemical agents. This kind of growth is also possible in certain anisotropic crystal structures. The properties of these materials are studied to a limited extent. Although there are many promising avenues in terms of their medical and materials science applications more work is needed to bring these into reality.

REFERENCES

1. C.A. Foss Jr, G.L. Hornyak, J.A. Stockert and C.R. Martin, *J. Phys. Chem.* 96, (1992), 7497.
2. C.R. Martin, *Science*, 266, (1994), 1961.
3. J.C. Hulteen and C.R. Martin, *J. Mater. Chem.* 7, (1997), 1075.
4. B.M.I. Van der Zande, M.R. Boehmer, L.G.J. Fokkink and C. Schoenenberger, *Langmuir*, 16, (2000), 451.
5. Y.Y. Yu, S.S. Chang, C.L. Lee and C.R.C. Wang, *J. Phys. Chem. B*, 101, (1997), 6661.
6. S.S. Chang, C.W. Shih, C.D. Chen, W.C. Lai and C.R.C. Wang, *Langmuir*, 15, (1999), 701.
7. K. Esumi, K. Matsuhisa and K. Torigoe, *Langmuir*, 11, (1995), 3285.
8. F. Kim, J.H. Song and P. Yang, *J. Am. Chem. Soc.*, 124, (2002), 14316.
9. N.R. Jana, L. Gearheart and C.J. Murphy, *Adv. Mater.*, 13, (2001), 1389.
10. N.R. Jana, L. Gearheart and C.J. Murphy, *J. Phys. Chem. B*, 105, (2001), 4065.
11. B.D. Busbee, S.O. Obare and C.J. Murphy, *Adv. Mater.*, 15, (2003), 414.
12. C.J. Murphy, T.K. Sau, A.M. Gole, C.J. Orendorff, J. Gao, L. Gou, S.E. Hunyadi and T. Li, *J. Phys. Chem. B*, 109, (2005), 13857.
13. J. Gao, C.M. Bender and C.J. Murphy, *Langmuir*, 19, (2003), 9065.
14. A. Gole and C.J. Murphy, *Chem. Mater.*, 16, (2004), 3633.
15. B. Nikoobakht and M.A. El-Sayed, *Chem. Mater.*, 15, (2003), 1957.
16. D.K. Smith and B.A. Korgel, *Langmuir*, 24, (2008), 644.
17. C.J. Murphy, L.B. Thompson, A.M. Alkilany, P.N. Sisco, S.P. Boulos, S.T. Sivapalan, J.A. Yang, D.J. Chernak and J. Huang, *J. Phys. Chem. Lett.*, 1, (2010), 2867.
18. C.J. Johnson, E. Dujardin, S.A. Davis, C.J. Murphy and S. Mann, *J. Mater. Chem.*, 12, (2002), 1765.
19. J. Pérez-Juste, L.M. Liz-Marzán, S. Carnie, D.Y.C. Chan and P. Mulvaney, *Adv. Funct. Mater.*, 14, (2004), 571.
20. A.K. Samal, T.S. Sreepasad and T. Pradeep, *J. Nanopart. Res.*, 12, (2010), 1777.
21. Z.C. Xu, C.M. Shen, C.W. Xiao, T.Z. Yang, H.R. Zhang, J.Q. Li, H.L. Li and H.J. Gao, *Nanotechnology*, 18, (2007), 115608.

22. M. Fleischmann, P.J. Hendra and A.J. McQuillan, *Chem. Phys. Lett.*, 26, (1974), 163.
23. D.L. Jeanmaire and R.P. Van Duyne, *J. Electro. Chem.* 84, (1977), 1.
24. M.G. Albrecht and J.A. Creighton, *J. Am. Chem. Soc.*, 99, (1977), 5215.
25. S. Nie and S.R. Emory, *Science*, 275, (1997), 1102.
26. K. Kneipp, Y. Wang, H. Kneipp, L.T. Perelman, I. Itzkan, R.R. Dasari and M.S. Feld, *Phys. Rev. Lett.*, 78, (1997), 1667.
27. A. Campion and P. Kambhampati, *Chem. Soc. Rev.*, 27, (1998), 241.
28. D.H. Jeong, Y.X. Zhang and M. Moskovits, *J. Phys. Chem. B.*, 108, (2004), 12724.
29. S.J. Lee, A.R. Morrill and M. Moskovits, *J. Am. Chem. Soc.*, 128, (2006), 2200.
30. A.R. Tao and P.D. Yang, *J. Phys. Chem. B.*, 109, (2005), 15687.
31. P. Mohanty, I. Yoon, T. Kang, K. Seo, K.S.K. Varadwaj, W. Choi, Q.H. Park, J.P. Ahn, Y.D. Suh, H. Ihee and B. Kim, *J. Am. Chem. Soc.*, 129, (2007), 9576.
32. B. Nikoobakht, J. Wang and M.A. El-Sayed, *Chem. Phys. Lett.*, 366, (2002), 17.
33. B. Nikoobakht and M.A. El-Sayed, *J. Phys. Chem. A*, 107, (2003), 3372.
34. C.J. Orendorff, A. Gole, T.K. Sau and C.J. Murphy, *Anal. Chem.*, 77, (2005), 3261.
35. C.J. Orendorff, L. Gearheart, N.R. Janaz and C.J. Murphy, *Phys. Chem. Chem. Phys.*, 8, (2006), 165.
36. X. Huang, I.H. El-Sayed and M.A. El-Sayed, *J. Am. Chem. Soc.*, 128, (2006), 2115.
37. P.K. Sudeep, S.T.S. Joseph and K.G. Thomas, *J. Am. Chem. Soc.*, 127, (2005), 6516.
38. X. Hu, W. Cheng, T. Wang, E. Wang and S. Dong, *Nanotechnology*, 16, (2005), 2164.
39. M. Rex, F.E. Hernandez and A.D. Campiglia, *Anal. Chem.*, 78, (2006), 445.
40. S. Sen, U.M. Bhatta, V. Kumar, K.P. Muthe, S. Bhattacharya, S.K. Gupta and J.V. Yakhmi, *Cryst. Growth Des.*, 8, (2008), 238.
41. V.B. Ufimtsev, V.B. Osvensky, V.T. Bublik, T.B. Sagalova and O.E. Jouravlev, *Adv. Perf. Mater.*, 4, (1997), 189.
42. T. Ikari, H. Berger and F. Levy, *Mater. Res. Bull.*, 21, (1986), 99.
43. S. Fujiwara, T.S. Ike, K. Okada, M. Aoki, N. Kambe and N. Sonoda, *Tetrahedron Lett.*, 33, (1992), 7021.
44. K. Ariki and T. Tanaki, *Jpn. J. Appl. Phys.*, 11, (1972), 472.
45. Y. Xia, P. Yang, Y. Sun, Y. Wu, B. Mayers, B. Gates, Y. Yin, F. Kim and H. Yan, *Adv. Mater.*, 15, (2003), 353.
46. N. Furuta, H. Itinose, N. Maruyama and Y. Ohasi, *Jpn. J. Appl. Phys.*, 11, (1972), 1113.
47. B. Mayers and Y. Xia, *J. Mater. Chem.*, 12, (2002), 1875.
48. P. Mohanty, T. Kang, J. Park and B. Kim, *J. Phys. Chem. B.*, 110, (2006), 791.
49. B. Zhou, J.R. Zhang, L. Zhao, J.M. Zhu and J.J. Zhu, *Ultrason. Sonochem.*, 13, (2006), 352.
50. T.J. Mason and J.P. Lorimer, *Sonochemistry: Theory, Applications and Uses of Ultrasound in Chemistry*, John Wiley & Sons, New York, 1988.
51. K.S. Suslick, *Science*, 247, (1990), 1439.
52. W. Zhu, W. Wang, H. Xu, L. Zhou, L. Zhang and J. Shi, *J. Crystal Growth*, 295, (2006), 69.

53. M. Mo, J. Zeng, X. Liu, W. Yu, S. Zhang and Y. Qian, *Adv. Mater.*, 14, (2002), 1658.
54. X. Liu, M. Mo, X. Chen and Y. Qian, *Inorg. Chem. Commun.*, 7, (2004), 257.
55. Q. Lu, F. Gao and S. Komarneni, *Adv. Mater.*, 16, (2004), 1629
56. Z. Wang, L. Wang and H. Wang, *Cryst. Growth Des.*, 8, (2008), 4415.
57. Z.H. Lin, Z. Yang and H.T. Chang, *Cryst. Growth Des.*, 8, (2008), 351.
58. W. Gorbachev, *Semiconductor Compounds A₂^I B^{VI}*, Metallurgy, Moscow, 1980.
59. A.M. Qin, Y.P. Fang, P.F. Tao, J.Y. Zhang and C.Y. Su, *Inorg. Chem.*, 46, (2007), 7403.
60. R. Chen, D. Xu, G. Guo and L. Gui, *J. Mater. Chem.*, 12, (2002), 2435.
61. M. Kobayashi, K. Ishikawa, F. Tachibana and H. Okazaki, *Phys. Rev. B.*, 38, (1988), 3050.
62. R. Xu, A. Husmann, T.F. Rosenbaum, M.L. Saboungi, J.E. Enderby and P.B. Littlewood, *Nature*, 390, (1997), 57.
63. I.S. Chuprakov and K.H. Dahmen, *Appl. Phys. Lett.*, 72, (1998), 2165.
64. P.F. Taylor and C. Wood, *J. Appl. Phys.*, 32, (1961), 1.
65. D.V. Damodara and D. Karunakaran, *Phys. Rev. B.*, 40, (1984), 2036.
66. C. Wood, V. Harrap and W.M. Kane, *Phys. Rev.*, 121, (1961), 978.
67. F. Li, C. Hu, Y. xiong, B. Wan, W. Yan and M. Zhang, *J. Phys. Chem. C.*, 112, (2008), 16130.
68. A.K. Samal and T. Pradeep, *J. Phys. Chem. C.*, 113, (2009), 13539.
69. R. Coustal, *J. Chem. Phys.*, 38, (1958), 277.
70. B. Li, Y. Xie, Y. Liu, J.X. Huang and Y.T. Qian, *J. Solid State Chem.*, 158, (2001), 260.
71. Y. Jiang, Y. Wu, Z.P. Yang, Y. Xie and Y.T. Qian, *J. Cryst. Growth.*, 224, (2001), 1.
72. P. Zuo, S. Zhang, B. Jin, Y. Tian and J. Yang, *J. Phys. Chem. C.*, 112, (2008), 14825.

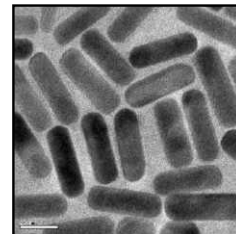
ADDITIONAL READING

1. X. Huang, S. Neretina and M. El-Sayed, *Adv. Mater.*, 21, (2009), 4880.
2. C.J. Murphy, T.K. Sau, A.M. Gole, C.J. Orendorff, J. Gao, L. Gou, S.E. Hunyadi and T. Li, *J. Phys. Chem. B.*, 109, (2005), 13857.
3. J. Pérez-Juste, I. Pastoria-Santos, L.M. Liz-Marzán and P. Mulvaney, *Coord. Chem. Rev.*, 249, (2005), 1870.
4. S.V.N.T. Kuchibhatla, A.S. Karakoti, D. Bera and S. Seal, *Prog. Mater. Sci.*, 52, (2007), 699.
5. Y. Xia, P. Yang, Y. Sun, Y. Wu, B. Mayers, B. Gates, Y. Yin, F. Kim and H. Yan, *Adv. Mater.*, 15, (2003), 353.
6. G. Cao, *Nanostructures and Nanomaterials: Synthesis, Properties and Applications*, Imperial College Press, (2004).
7. C.N.R. Rao, A. Muller and A.K. Cheetham, *The Chemistry of Nanomaterials: Synthesis, Properties and Applications*, Wiley-VCH Verlag GmbH & Co. KGaA, Weinheim, (2004).
8. T. Pradeep, *Nano: The Essentials*, Tata McGraw-Hill Publishing Company Ltd., (2007).

REVIEW QUESTIONS

1. What are the one-dimensional nanostructures?
2. How are these structures different from the sphere or other nanostructures?
3. What are the special properties of gold nanorods?
4. How can you control the aspect ratio of gold nanorods?
5. What are the different methods of preparation of gold nanorods?
6. What are applications of gold nanorods?
7. What are the differences between nanorods and nanowires?
8. What are the general synthetic protocols for the nanowires?
9. What are the applications of nanowires?

ASSEMBLY OF ANISOTROPIC NANOSTRUCTURES



“We have to remember that what we observe is not nature herself, but nature exposed to our method of questioning.”

W. Heisenberg, *Physics and Philosophy: The Revolution in Modern Science* (1958)
Lectures delivered at University of St. Andrews, Scotland, Winter 1955–56

Creating assembled structures starting with nanomaterials is the central aspect of nanotechnology. Without organised structures, many of the properties of nanomaterials cannot be used for fruitful applications. Creating assembly required monodisperse materials with shape purity. One such material of the anisotropic category is nanorods. We present an overview of the various superstructures made with gold nanorods. There are also other assembled structures made with nanorods of other materials. A brief review of the assemblies with other anisotropic structures is also presented. The chapter ends with the various applications of such assembled structures. The chapter illustrates the importance of anisotropic structures and their self-organisation. How to impact such self-assembly through chemical and physical forces is touched upon.

Learning Objectives

- The need of assembled structures.
 - Advantage of anisotropic nanoparticle assembly.
 - Enhancement in properties.
 - Advantages of programmed self-assembly vs other techniques.
 - Advantages of assembled structures for applications.
-
-

15.1 INTRODUCTION

Nanotechnology and nanoscience deal with the construction of well-designed materials and devices with atom by atom precision. By definition, for a material to be a nanomaterial, one or more of its dimensions should be between 1–100 nm. This basic concept makes it possible to classify nanomaterials into broadly two categories, namely, isotropic and anisotropic. Anisotropy in physics is

often used when a substance has the quality of exhibiting different properties, when measured along different axes and isotropy refers to homogeneity in all directions. In botany, the term ‘anisotropic’ is used when certain flowers or plants have different dimensions along different axes. Similarly in nanoscience, the term, “anisotropic nanoparticle” is used when the dimensions of the particle are different along different directions.

Assembling smaller building blocks to larger structures is an essential aspect for the creation of functional entities. Nature adopts self-assembly to create larger structures. Assemblies of all scales are present in nature itself. Starting from the basis of life, DNA to the galaxies can be considered as assemblies. Assembly is a process, in which, through specific local interactions among the disordered components, structural organisation happens, resulting in an organised structure or pattern. When the process takes place without being guided or managed by an outside source, it is called “self-assembly”. Even though the nucleotides and amino acids are interesting and carry specific functions, when they are arranged into superstructures like DNA or proteins, the properties get modified and the system becomes more useful or functional. Some interesting examples of assembled systems found commonly are lipid bilayers, phase separation in polymers, and self-assembled monolayers. In biology, the folding of polypeptide chains to form proteins and the formation of functional forms, like DNA by the folding of nucleic acids, are examples of self-assembled biological structures.

The current interest in nanoscience stems from the spectacular properties displayed by materials when the dimension goes into the nanoregime. The interesting, mechanical, electrical and optical properties associated with nanomaterials make them interesting candidates for various applications. Harvesting these properties and to apply them in useful devices require not just a few but a collection of nanoparticles, structured in some uniform way to produce regular superstructures. It is desirable to find processing routes, in which regular nanoscale arrays will form spontaneously. An alternate is to assemble them post-synthetically. The advance in synthetic methods helped researchers in making size and shape selective nanostructures with a high degree of control and monodispersity. The next challenge is to assemble them into well-ordered micro-arrays to reap the benefits of their properties for device applications. As a result, periodic assemblies of nanostructures, such as superlattices, described earlier in this book, have been explored intensely. It is also possible to create self-assembled architectures of anisotropic nanosystems, such as nanorods (NRs) and nanowires (NWs) as well.

Nanoscience uses diverse methods to create assembled structures. One of this is the lithographic technique. Nanolithography deals with the fabrication of patterns of nanometer-scale structures with at least one of the dimensions of the pattern in the nanoscale regime. Most common nanolithographic techniques employed are: (a) photolithography or optical lithography where use of very short wavelengths (~ 193 nm) is used to create patterns; (b) X-ray lithography, where a low wavelength X-ray (~ 1 nm) is used; (c) electron-beam direct-write lithography (EBDW), which uses a beam of electrons to produce patterns—generally on a polymeric resist (e.g. PMMA); (d) extreme ultraviolet lithography (EUV) is another form of optical lithography, which uses ultrashort wavelengths (~ 13.5 nm it is 13.5 nm, EUV is 5–50 nm); (e) scanning probe lithography (SPL) uses scanning tunneling microscope (STM), where individual atoms may be manipulated using the tip of a STM. The first commercially available SPL technology is called “Dip-Pen Nanolithography” (DPN) which is based on atomic force microscopy.

Assembling nanomaterials by simple means such as chemical methods or through self-assembly have much larger scope, since they are cheaper and easy compared to the physical methods. Assembling process can be driven by the structural attributes of the nanoparticles as well as the chemical functionalities present on their surfaces. The structures so derived can be transferred to substrates and can be used to derive patterns. These structural assemblies are predicted to be the building blocks for nanoscale device structures. We shall explore the diversity of this subject area in this chapter.

Assembling spherical nanoparticles into 1-D, 2-D, and 3-D superstructures or superlattices has already been discussed earlier. Because of their isotropic nature, in a spherical nanoparticle assembly, the nature of interaction between the nanoparticles is same, irrespective of whether it is 1-D, 2-D, or 3-D assembly. In this case, only the number of interactions will differ with the dimensionality of the assembly. The added advantage of anisotropic nanoparticle assembly is that the same nanomaterial can be assembled in different ways. In other words, because of the inherent anisotropy in the structure, they can be arranged in different ways where the interaction between the constituent nanoparticles is different. Since the different interactions can give rise to different properties, the resultant properties of these superstructures will differ drastically from each other. So from the same building blocks, we can create assemblies having different properties depending on the dimensionality as well as the nature of interaction between the building blocks.

Anisotropic nanoparticle are diverse and different shapes like nanorods, nanotubes, nanowires, nanobelts, nanotriangles, nanocubes, nanoplates, etc., that have been synthesised with astonishing monodispersity. Gold nanorods (GNRs) are one of the most-studied anisotropic systems. GNRs are covered by a protecting double layer of CTAB, which provides them stability in solution. The photophysical properties of GNRs are explained in an earlier chapter. Because of the interesting properties, which can be regulated precisely by controlling the size, it becomes an ideal candidate for many applications. Assembly of GNRs is a widely studied area of research. Due to the unique anisotropic rod shape, its assembly into different superstructures is possible. We will look into this in detail.

15.2 GOLD NANOROD ASSEMBLY

As discussed earlier, for spherical particles, since the interactions are the same in all directions, the collective effect and the resultant property of the assembly will be the same; only extent of effect will vary, depending upon the dimensionality of the assembly. But, in the case of anisotropic nanoparticles, the inherent anisotropy makes the assembly and the interactions between nanoparticles direction-dependent.

Before going into assembly, first the crystal structure of GNR has to be understood. The crystal structure of anisotropic gold nanostructures is drastically different for the isotropic analogues. The surface structure of spherical nanoparticles are isotropic, mostly consisting of either $\{111\}$ or $\{100\}$ planes. But the surface structure of anisotropic nanoparticles is drastically different. For example, the surface structure of gold nanorods is well studied (Fig. 15.1A, B). The formation mechanism and synthesis have been explained in an earlier chapter. In the case of gold nanorods, since CTAB, which facilitates the formation of gold nanorods and stabilises them, has a higher affinity towards the $\{110\}$

plane, it attaches more to this plane and growth takes place anisotropically and in the GNRs formed, the side faces are composed of $\{110\}$ and the tips by either $\{111\}$ or $\{100\}$. So by the attachment of CTAB on to $\{110\}$ which is conventionally less stable, it gets extra stability and so this facet becomes prominent in GNRs. Also the CTAB bilayer coverage on the side faces will be thicker. The tips of the gold nanorods are composed of mainly $\{111\}/\{100\}$ facets. Since CTAB has a lesser affinity to these faces, the amount present on the tip is lesser compared to the side faces. Figure 15.1B shows a lattice resolved image of a GNR showing the specific planes.

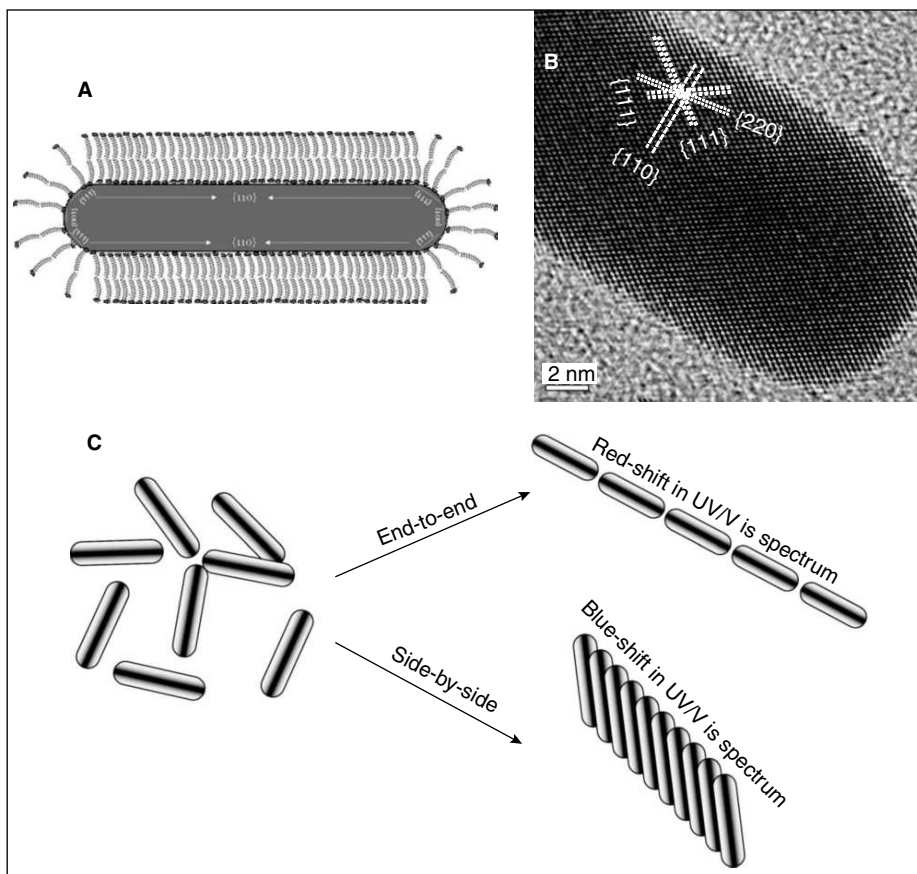


Fig. 15.1 (A) Schematic of a single gold nanorod (B) HRTEM showing the different crystal planes and lattice structure (C) Schematic showing the different ways of arranging the nanorods.

Due to the anisotropic crystal structure and the resultant difference in surface reactivity, anisotropic nanoparticles can be selectively functionalised to bring forth specific interactions between the constituent nanostructures giving different types of assembled structures. The amount of CTAB covering being less in the end faces, functionalising this facet is easy and specific functionalisation of the end faces can trigger the interaction of ends of nanorods resulting into the end-to-end assembly of

GNRs. Another kind of interaction possible is in which the sides of the nanorods are interacting with each other. The removal of CTAB from the side faces comprising of $\{110\}$ facet is considered to be very difficult. So fictionalisation of this face is done through rigorous procedures. This fictionalisation results in side-to-side assembly. The different interaction as well as different kind of resultant assembly is depicted in Fig. 15.1C.

The plasmonic coupling between nanostructures in assembled structures gives rise to characteristic changes in UV/Vis spectrum. Unlike spherical nanoparticles, depending on the type of interaction, specific peaks change to different extent depending on the type of interaction. It has been proven that a side-by-side assembly leads to a blue shift in the UV/Vis spectrum, whereas the end-to-end assembly gives rise to a red shift. The extent of shift in the spectra depends on the extent of assembly also. In a 2-D or 3-D assembly, where multiple interactions can be there, the resultant shift can be a combination of all these interactions.

When assembly takes place without any external aid, it is called self-assembly. Gold nanorods are known to self-assemble under optimum conditions, such as concentration, pH, ionic strength, etc. Self-assembly can be modified by controlling the interactions between the constituents to get the desired assembly. This is usually done by regulating the environmental conditions, such as pH and ionic strengths. This is often referred to as “programmed self-assembly”. Chemical modifications or functionalisation are usually done in order to control the assembly. Surface-functionalised GNRs, with specific molecular groups can lead to precisely controlled self-assembled structures. It is generally observed that programmed self-assembly with functionalised NRs can be an efficient means of nanofabrication owing to its simplicity, versatility, and low cost. But, this method normally provides ordered structures with a lesser area, and do not allow us to control over the design or interparticle distance in the NR architecture. The manipulation of the assembly after initiation is also very difficult normally. But with the advent of new techniques and with the developing understanding of the system these limitations are slowly getting negated. Depending upon the functionalising molecule, the assembly can be formed through a wide variety of operating forces. The operating forces can be covalent, hydrogen bonding, electrostatic, biochemical interaction, Van der Waals and dipole interactions, etc. Assembling on templates or template assisted assembly using a wide variety of templates also has been performed. In the following sections we will be briefly mentioning the different kinds of assemblies reported and categorised based on the operating forces in the assembly.

(a) Self-assembly of gold nanorods upon solvent evaporation

Gold nanorods are covered with a stabilising bilayer of CTAB and because of the electrostatic repulsion between the head groups of CTAB on different rods, the suspension gets stabilised devoid of any tendency to aggregate. But, when the excess surfactant is removed by centrifugation and the conditions, like concentration, pH, ionic strength, etc., are optimum, there can be a convenient situation, where the electrostatic repulsion is being compensated by the hydrophobic-hydrophobic interaction between the CTAB tails. This will facilitate the assembly of nanorods, where the distance between the nanorods depends on the compensation of the above-mentioned interactions. Hence, upon solvent evaporation, the nanorods tend to assemble at an optimum distance between each other, where all the forces are compensated.

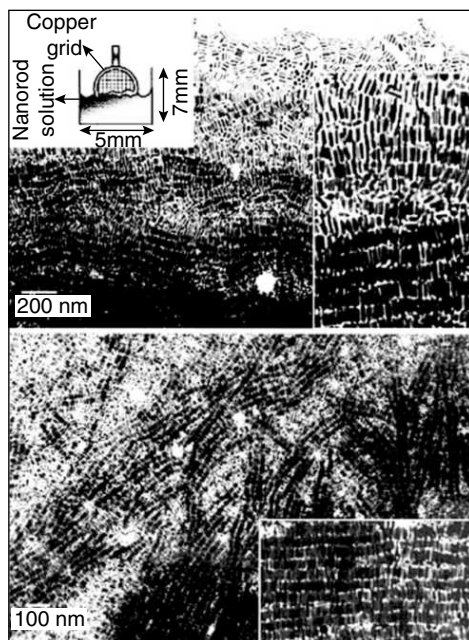


Fig. 15.2 Electron micrograph showing the border of the self-assemblies. The thickness increases from top to bottom. The inset shows a magnified part of an assembly. Scheme of the deposition method is also shown in the figure (adapted from El-Sayed, *et al.* (Ref. 1). Copyright (2000) by the American Chemical Society).

One of the first attempts to study the self-assembly of gold nanorods was by El-Sayed *et al.* in 2000.¹ Electrochemically prepared GNRs (aspect ratio~4.6) was centrifuged at 14,000 rpm and was diluted to an optical density of 1.5–1.7. A 1:1 dilution of the above solution was prepared with 0.1 M NaCl. Drop-casting of the sample on TEM grid was done in a special way depicted in inset Fig. 15.2. Upon solvent evaporation, they got long range 1-D, 2-D and 3-D assembly of gold nanorods over micrometer areas of the grid. Factors, which can affect the assembly, were studied. The effect of free surfactant concentration, ionic strength, particle concentration, particle shape, size distribution, and the position of the grid in the solution were looked at. Studies showed that higher surfactant concentration caused unwanted organic crystallites and formation of net-like structures in-between nanorods, preventing the well-ordered assembly. When the surfactant concentration was very low, the nanoparticles tend to aggregate both in solution and on the substrate. Optimised surfactant concentration for a well-defined assembly was found to be 0.001 M. To study the effect of ionic strength, electrolytes such as NaCl, NaBr, NaI, and NaOH were used. Through TEM as well as UV/Vis spectral observations, it was concluded that small concentrations of NaCl is favourable for the assembly. The optimum concentration was found to be 0.05 M. Large area assemblies were seen in the vicinity of water-air-substrate interface. When the grids are inserted completely into solution, assemblies over smaller areas only were seen. Inhomogeneity in size or shape of the constituent particle is an important criterion,

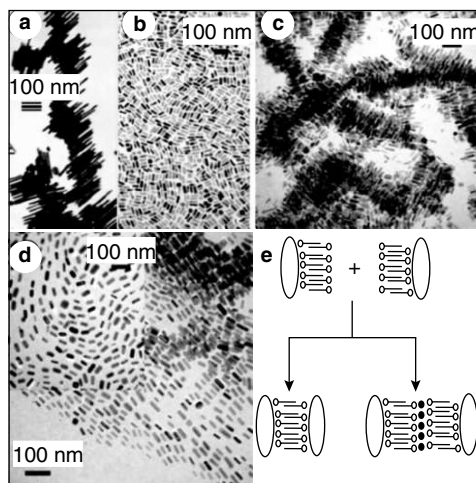


Fig. 15.3 Self-assembly patterns formed by gold nanorods (a) Ribbon structure formed from nanorods of different aspect ratios; (b) globally isotropic, but locally ordered arrangement (c) smectic arrays of short rods (d) “swirling” and smectic (e) Cartoon of CTAB-mediated self-assembly of gold nanocrystals (large ovals). As adjacent NRs approach each other, CTAB bilayers on the nanocrystals (open circles denoting the cationic headgroups, lines denoting hydrophobic tails) can either share a layer of counterions (filled circles), to give 9 nm nanocrystal-nanocrystal spacings (adapted from Murphy and Sau, (Ref. 2). Copyright (2005) by the American Chemical Society).

which determines the quality of the former assembly. The prepared nanoparticle suspensions always have some amount of spherical nanoparticles, which are mostly removed while the centrifugation and redispersion procedure. If these nanoparticles get into the assembly, it causes unequal spacing between the arrays of nanorods and will result in the distortion of the 2-D and 3-D assemblies.

The formation of assembly in the interface was explained by a theory originally explained by Dimitrov *et al.* According to this theory, the lateral immersion or capillary forces may be one of the main factors causing the self-assembly of particles confined in thin films. The operating force is believed to be depending upon the interparticle separation, particle radius, and surface tension of the liquid and the corresponding meniscus deformation around the participating particles. The self-assembly process involves the convective transfer of particles from the bulk solution to the thin film due to the evaporation of solvent from thin film and the interaction between the colloidal particles in the thin film, which leads to the formation of assembled structures. The driving force for the convective transfer is the evaporation of water from the film. During evaporation, the curvature of the menisci between the particles increases, which results in the increase of the capillary pressure or the capillary interparticle forces. Evaporation thins down the film and results in the increase of the disjoining pressure of the film. This gives rise to a situation, where the pressure of the thin film on the substrate compared to the pressure in the suspension is lesser. So a pressure gradient (ΔP) gets created and this ΔP produces a suspension incursion from the bulk of the solution towards the thin film. This incursion has water and

nanoparticles in it. The water compensates for the evaporated water and the nanoparticles flux causes particle accumulation. After carrying the nanorods to the array's edge, water then presses the rods to the array to form dense assemblies. The hydrostatic pressure makes the thickness of the vertical film to increase from substrate-air-solution contact line downwards. The monolayers and bilayers are getting formed by the successive continuous particle flux, which fills up space between and film surface. By this model, they successfully explained the formation of nanorod array on the substrate-air-solution interface and the increase in array thickness as going down from the contact line. One explanation given to the parallel assembly of nanorods is that the capillary forces along the length of the nanorods will be compared to that along the width. Lateral capillary forces are proportional to R^2 , where R is the diameter of the particle. So, there is anisotropy in interaction between the nanorods and it may be an important driving force for the parallel assembly. So as per the model, depending on the balance between the hydrodynamic pressure of the water stream and lateral capillary forces, smaller or larger ordered domains could be formed.

Later Murphy *et al.* found that the removal of excess CTAB and at appropriate nanorod concentrations, they will self-assemble by themselves without the addition of electrolyte.² They found that large aspect ratio gold nanorods will form liquid crystalline assembly, when the as-prepared rods are centrifuged to remove the associated spherical particles and redispersed in an optimum concentration of CTAB (1–100 mM). They proved the assembly using UV/Vis and SAXS measurements of the self-organised structures. With the same aspect ratio gold nanorods, different kinds of assemblies were found at different places of the grid (Fig. 15.2b–d). This was seen with the sample with relatively high concentration of nanorods. The reason behind this may be the difference in local concentrations created by inhomogeneities of the thin solvent film, before the complete evaporation of water, creating unsymmetrical sections on the grid. The interparticle distance between the nanorods was also found to be varying. This was explained to be due to the presence of CTAB and the involvement of CTAB in facilitating this kind of assembly. When the solvent is evaporated, CTAB molecules are believed to be aiding the formation of the assembly also. They draw the nanocrystals closer and can either share a common layer or can interdigitate CTAB tails from neighbouring nanocrystals. So, the distance between the nanocrystals was found to be varying. It was found that the interparticle distance varies between 3.4 to 9.0 nm upon drying the concentrated solution in different parts of the grid. The length of CTA tail was reported to be 2.2 nm. So, 3.4 is less than twice the length of CTA molecule. This distance can be formed by the inter-digitation of CTA tail in the neighbouring gold nanorod in an assembly. Interparticle distance of 9 nm points to 4 molecules of CTA, which can occur when the bilayer of CTAB protecting GNR comes to close proximity, sharing a common counter ion. This is illustrated in Fig. 15.2d. So, they concluded that at optimum concentration, CTAB can act both as the protecting agent as well as the “glue”, facilitating the assembly. Self-assembly, being a natural process, will not have perfect long-range order and controlling this assembly to get desired structure is difficult. This can be achieved in assemblies obtained by functionalising the nanorods in a desired manner.

(b) Assembly of GNR involving biological interaction and biorecognition

In biology, almost all functional entities are assembled structures. The operating forces in biology have the advantage that they are very specific. This specific interaction has been utilised to assemble gold nanorods.

One of the first efforts in this direction was done by Mann *et al.*³ They produced selective and reversible DNA-driven assembly of gold nanorods. Gold nanorods of aspect ratio 4.7 were made electrochemically, centrifuged and redispersed in distilled water to an optical density of 0.5 around 850 nm corresponding to the LSP of GNR. Nanorods were functionalised with thiolated DNAs in two different ways. In one case, two non-complementary strands of DNA were immobilised on the surface of two batches of gold nanorods. When they were mixed, no assembly was formed. But, a third strand, half complementary to each of the grafted sequences induced hybridisation. In the second case, two directly complementary strands of thiolated DNA were anchored on to GNR. When they were mixed, through bio-recognition between complementary pairs, facilitate an assembly was formed. The samples after mixing were analysed using UV/Vis spectroscopy also. A colour change from purple to blue was observed as the hybridization of DNA took place. After 24 hr, macroscopic precipitation also was observed. Figure 15.3 shows the TEM images of the assembled structures and the associated UV/Vis spectral changes during the assembly. Both in the case of three-strand system (Fig. 15.1a) as well as in the case of two-strand system, assembled structures of nanorods were seen. The distance between the nanorods was around 6 nm, which corresponds to the length of a 24-base pair helix with two propyl spacers.

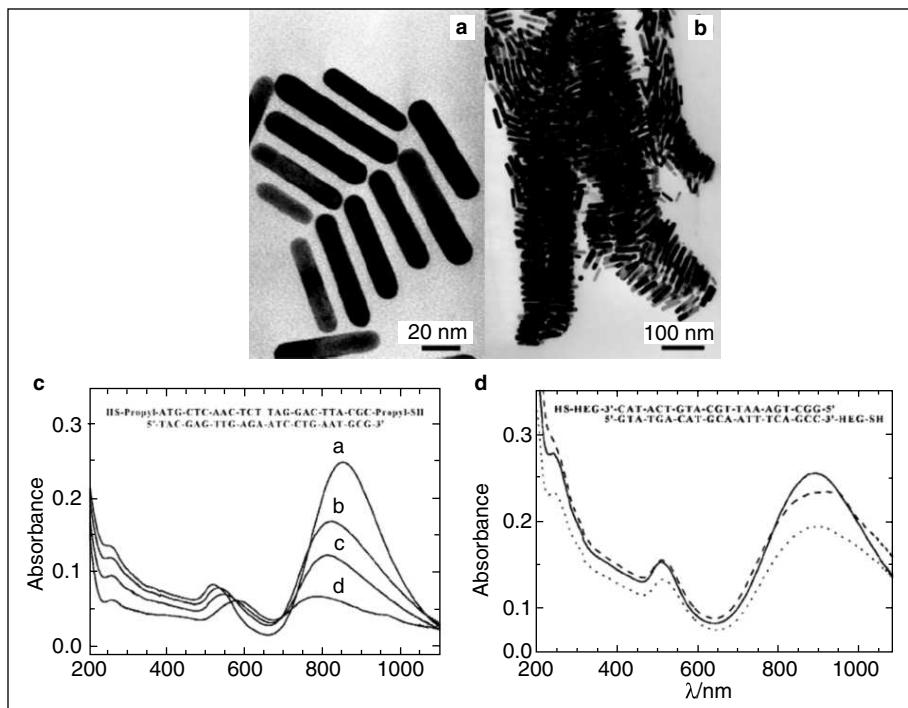


Fig. 15.4 TEM images of bundles of DNA-linked GNRs. (a) The three-strand, (b) two-strand DNA linking systems. UV-vis spectra of (c) a suspension of non-complementary DNA functionalised NRs and (d) the two-strand nanorod system before (—) and after (---) duplexation at 25°C (adapted from Wang, *et al.* (Ref. 3). Copyright (2001) by the Royal Society of Chemistry, London).

GNRs, surface-functionalised with mercaptoalkyloligonucleotide, were assembled preferentially in an end-to-end fashion by the addition of a target oligonucleotide by Cui *et al.*⁴ Here, the thiol groups in the mercaptoalkyl oligonucleotide binds to the ends of the nanorods, which further assemble in an end-to-end fashion through hybridisation with the target oligonucleotide. This oligonucleotide hybridisation-based assembly strategy was used to prepare binary (two component) materials comprising of two different shaped oligonucleotide-functionalised nanoparticles. Through this two-component nanoparticle-based strategy, they were able to assemble a binary system comprising of nanorods and nanoparticles. Since this method utilises rod–sphere assembly by oligonucleotide hybridisation, which can be examined with signals sensitive to particle aggregation or distance, this was utilised in devising a highly selective nucleic acid detection systems. With an unoptimised system, <1 pM of be oligonucleotide was able to be detected. The method should be particularly useful in assays, where expense and simplicity in instrumentation and operation are important.

Oriented assembly of gold nanorods in solution by a biomolecular recognition system, where antigens specifically bind to antibodies, was reported by Tan *et al.*⁵ Thiocetic acid (TA) was used as a binding agent in this work. TA molecules were made to self-assemble onto gold nanorods. The rigid conformation of TA containing both a disulfide and a ring structure facilitates the preferential binding of TA molecules to the ends of gold nanorods. TA monolayer containing a terminal carboxyl group at the end surface of gold nanorod opens up conjugation with various immunoglobulins, or other biomolecules. The carboxyl groups of adsorbed TA molecules were chemically activated by treating with sulfo-N-hydroxysuccinimide (sulfo-NHS) and 1-ethyl-3-(3-dimethylaminopropyl)-carbodiimide (EDC). EDC reacts with carboxylic acid and EDC-derived ester intermediate in presence of excess sulfo-NHS forms a water-stable sulfosuccinimidyl intermediate. The succinimidyl intermediate subsequently gets attached to anti-mouse IgG by nucleophilic substitution with the primary amine group on the surface of anti-mouse IgG. The mouse IgG having two binding sites when added into the above solution initiates the linking of two gold nanorods. The biomolecular recognition can drive the assembly of gold nanorods to nanorod chains, with different orientations. The control of concentrations of the nanorods and the biomolecules has led to a controlled assembly of nanomaterials. Stepwise increasing concentration of anti-mouse IgG allows a long linear assembly of gold nanorods.⁵

A similar approach to detect protein, like IgG, was demonstrated by Su *et al.*⁶ They reported an enhanced detecting limit of 60 ng mL⁻¹ compared to that reported based on spherical gold nanoparticles as probes with a detection limit of 0.1 µg mL⁻¹. They observed aggregation of GNRs oriented preferentially in a lateral (side-to-side) fashion was driven by the bio-recognition process. This was reflected in the LSPR bands. This makes them extremely sensitive reporters of molecular binding events with excellent biosensing capability. In principle, the design concept presented herein may be extended to act as the platform for using GNRs with various aspect ratios to develop multiplex assays for the detection of molecular binding events.⁶

Biotin-streptavidin interaction is one of the most common and strong non-covalent interactions known in biology. This interaction was utilised for the preferential end-to-end assemblies of GNRs. GNRs were surface-functionalised with biotin disulfide and upon the addition of streptavidin linker; they assembled preferentially in an end-to-end fashion. The preferential end-to-end assembly was

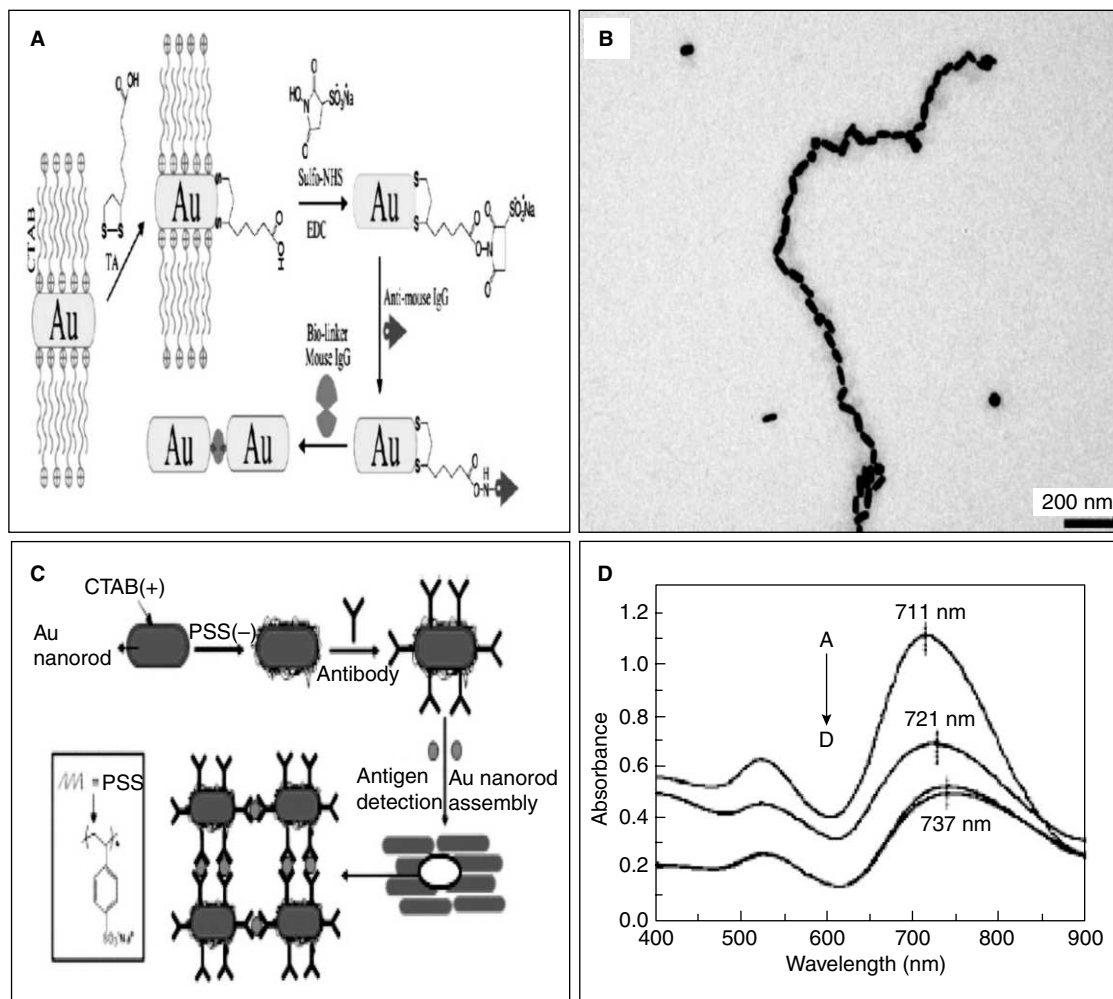


Fig. 15.5 (A) Schematic illustration of antibody–antigen directed assembly of gold nanorods. (B) TEM image of GNRs arranged into successive chains via addition of mouse IgG (adapted from Tan, et al. (Ref. 5). Copyright (2005) by the Royal Society of Chemistry, London). (C) Schematic representation of detection of h-IgG through the assembly of GNRs driven by antibody–antigen recognition. (D) UV-vis absorption spectra at different stages of the assembly (adapted from Su, et al. (Ref. 6) Copyright (2007) by the American Chemical Society).

reasoned out based on the following postulate: due to the strong binding of CTAB to the side faces of GNR, biotin disulfide was unsuccessful at displacing the CTAB bound to the length of the gold nanorods, and thus preferentially bound to the {111} ends of the rods. This results in preferential end-to-end linkages upon the addition of streptavidin. Also, even though biotin binds all over the rods,

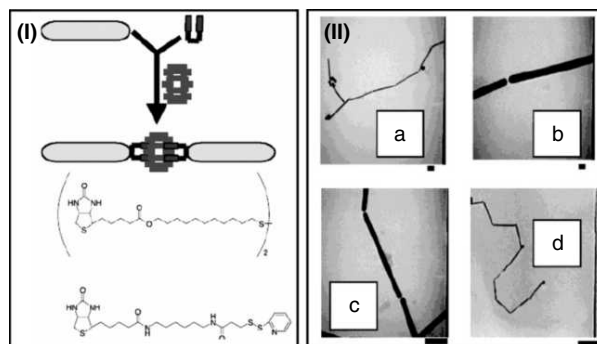


Fig. 15.6 (I) Scheme showing the assembly of gold nanorods (golden ovals) by surface functionalisation with the biotin disulfide (red), and subsequent addition of streptavidin. (II) TEM images of GNRs, surface derivatised with biotin disulfide, after addition of streptavidin. Scale bars—100 nm (a), 20 nm (b), 100 nm (c), and 500 nm (d) (adapted from Murphy, et al. (Ref. 7). Copyright (2003) by the American Chemical Society).

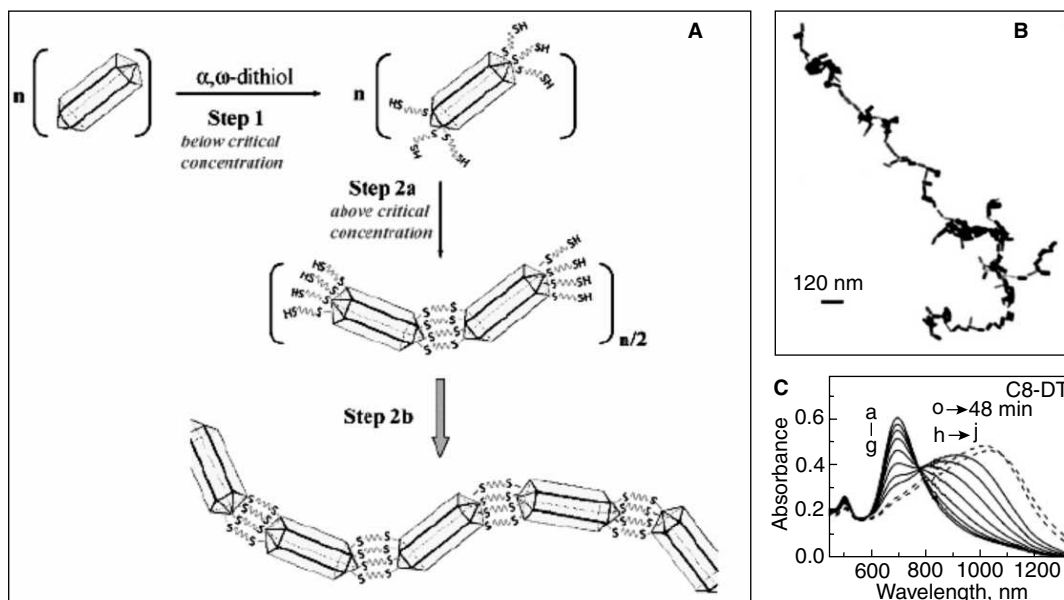


Fig. 15.7 (A) Schematic showing the stepwise formation of nanochains through covalent bonding. (B) TEM images of GNR chain through covalent bonding. (C) UV/vis spectral changes during the assembly (adapted from Thomas, et al. (Ref. 9). Copyright (2005) by the American Chemical Society).

streptavidin may be sterically constrained to bind to the ends of the rods. Hence, possibly that the preferential localisation of biotin disulfide on the pentahedral twin boundaries on the ends of the rods may be the driving force of this longitudinal assembly.⁷

Recently, Huang *et al.* reported a simple and versatile approach for the end-to-end assembly of GNRs through the specific molecular recognition between thymine rich (T-rich) oligonucleotides and mercury(II). Because of the specificity of the oligonucleotide, the process was found to be highly selective. The limitation of the use of biomolecules for the use of self-assembly is in the cumbersome of the synthesis and easy denaturation of the biomolecules depending upon the external environmental conditions, such as temperature, pH, etc. In this study, by utilising the specific recognition between thymine-rich (T-rich) DNA and mercury(II) this problem was solved to some extent. The formation of DNA–Hg(II) complexes can take place at wider range of temperature, ion strength or pH, compared to antibody–antigen or aptamer–protein systems.⁸

(c) Gold nanorod assembly involving covalent bonding

The interactions between Au nanorods and α,ω -alkanedithiols of varying chain lengths leading to the longitudinal assembly of GNRs was investigated using absorption spectroscopy and transmission electron microscopy by Thomas *et al.*⁹ Mechanism of the end-to-end assembly was also investigated. They observed a decrease in the longitudinal plasmon absorption after the addition of dithiols. Simultaneously, a new red-shifted band appeared above critical concentrations of dithiols due to the interplasmon coupling in assembled nanorods. Below this concentration, no appreciable change was observed indicating that no assembling takes place below this concentration. At the incubation step, one of the thiol groups of α,ω -alkanedithiols preferentially binds onto the edges of the nanorods, leaving the other thiol group free. Above the critical concentration, through the interlocking of nanorods, nanorods become initially to dimers and subsequently to oligomers, which results in longitudinal inter-plasmon coupling. This happens through the covalent binding of two thiol groups to form a disulphide. A clear isosbestic point was observed in the time-dependent absorption spectrum and TEM investigations proved the formation of dimers and this confirmed the involvement of the dimerisation step in the chain-up process. The study revealed that the process is not diffusion controlled, but activation controlled with large activation energy.⁹

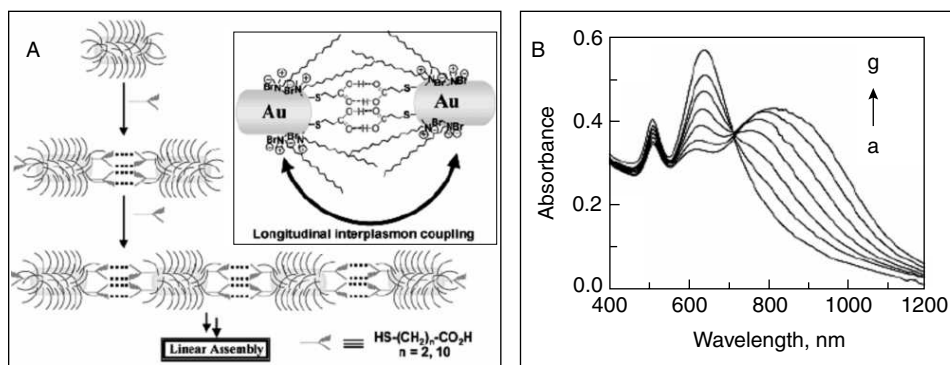


Fig. 15.8 (A) Pictorial representation of mechanism of formation of nanochains through hydrogen bonding. (B) UV-vis spectral changes during the assembly (adapted from Thomas, *et al.* (Ref. 10). Copyright (2004) by the American Chemical Society).

(d) Gold nanorod assembly through hydrogen bonding

The formation of cooperative intermolecular hydrogen bonding between two thioacids anchored on to the end faces of GNRs were utilised to precisely control the longitudinal assembly and modulate the plasmon coupling. It was found that the plasmonic positions can be modulated by the concentration of thioacids added into the mixture. As the concentration increased, the plasmon shifted to higher and higher wavelength. This approach for connecting nanomaterials into desired shapes can be useful in tuning optoelectronic properties.¹⁰

Recently, Liz-Marzán *et al.* investigated hydrogen-bonding-directed assembly of GNRs in aqueous solution. The mechanism behind the formation of end-to-end assembly of GNRs modified with bi-functional linking molecules were probed experimentally and theoretically.¹¹ For different linking molecules, studies were carried out at both higher and lower pH values with respect to their respective pK_a values, time-dependently, and found that hydrogen bonding between protonated and unprotonated linking molecules is responsible for nanorod assembly in aqueous solution. Results obtained from density functional calculations gave information about the stability of the hydrogen-bonded superstructures.¹¹

(e) Gold nanorod assembly through electrostatic forces

Electrostatic forces are one of the most common forces operating in the living world and in assemblies. The electrostatic interactions between the amino acids anchored onto the gold nanorod surfaces were utilised to assemble nanorods.¹² Two amino acids, namely, cysteine and glutathione, containing thiol moieties when added into the GNR solution, get anchored on to the GNR end faces and because of the electrostatic interaction between the aminoacids, a preferential longitudinal assembly gets formed. This results in the red shift of LSP. The change in the plasmonic characteristics was used for the specific detection of cysteine and glutathione in the micromolar concentrations in presence of other aminoacids. Yan *et al.* reported assembling of bi-pyramids and rods into different types of nanonecklaces using a similar approach.¹³

For a particular concentration of assembly-inducing agents, the time-dependent shift in LSP was constant and was not controllable in any of the reports discussed above. A more controllable fabrication of gold nanorods, in which the shift in the LSP can be stopped at desired point to get a stable suspension with desired absorption regime, was reported more recently by Nogami *et al.*¹⁴ They found that the addition of sodium citrate into gold nanorods results in the gradual red shift of LSP, which can be stopped at any point simply by the addition of CTAB into the reaction mixture. Added citrate anions get adsorbed onto the end faces of GNRs preferentially, and will neutralise the surface charge of the GNR ends, which results in the end-to-end assembly of the GNRs. GNRs with an aspect ratio of 16 was found to be assembling in an end-to-end fashion upon decreasing the CTAB concentration in the solution. On further decreasing the CTAB concentration, the assembled GNRs were welded at their connecting points.

A pH dependent self-assembly of gold nanorods of aspect ratio 3.3 ± 0.3 (20.6 ± 5.5 nm width) into ordered structures using adipic acid was reported by Murphy *et al.*¹⁵ As-prepared gold nanorods have a net positive charge in aqueous solutions because of the cationic surfactant present on the surface.

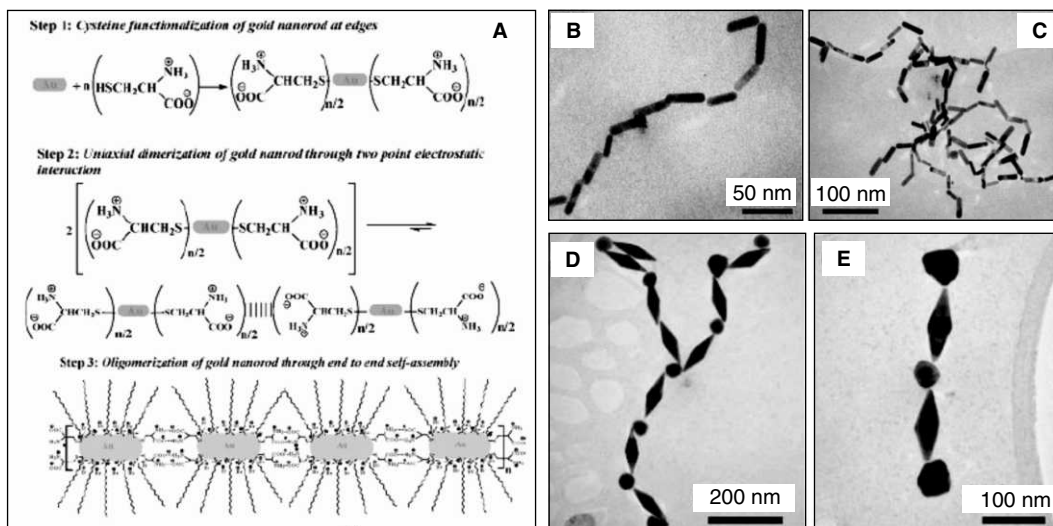


Fig. 15.9 (A) Schematic of the general mechanism of GNR nanochain formation between electrostatic interaction between cysteine and glutathione (adapted from Thomas, et al. (Ref. 12). Copyright (2005) by the American Chemical Society). (B) TEM image of Au nanorods assembled into a chain. (C) TEM image of Au nanorods end-to-end assembled into branched chains. (D and E) TEM images of Au bipyramids and nanospheres assembled into chain structures (adapted from Tan, et al. (Ref. 13). Copyright (2007) by the Royal Society of Chemistry, London).

The electrostatic interactions between the cationic surfactant bilayer around the nanorods and the negatively-charged deprotonated adipic acid results in the pH dependent self-assembly of nanorods into 2-D ordered structures. Absorption spectra and light scattering measurements of these nanorods suggest that assembly is initiated in solution in the presence of 10^{-5} M adipic acid at pH=7-8, but not at pH=3, to form small aggregates of nanorods and subsequent solvent evaporation yields 2-D side-to-side assemblies containing about 20–200 nanorods. Zeta potential measurements show that the assembly has significantly less positive charge in the presence of deprotonated adipic acid than when adipic acid is fully protonated confirming that the assembly is due to the electrostatic interaction.

A similar method was adopted by Pradeep *et al.*¹⁶ to assemble gold nanorods into 1-D, 2-D, and 3-D superstructures. They found that the addition of dimercaptosuccinic acid (DMSA) into the nanorod solution was found to induce self-assembly of the latter to 1-D “tape-like”, 2-D “sheet-like” and 3-D “superlattice-like” structures depending on the DMSA concentration. A smectic structure, where the nanorod long axes are parallel to each other was found to be followed all through the assembly. The effect of the DMSA concentration as well as the pH of the medium was also studied. The UV/Vis spectral changes were visible immediately after the addition of DMSA into the nanorod solution. The peak position was found to be stable (after the initial shift) even after 24 hr of incubation. A gradual shift was observed for LSP, while TSP remained without any change. The red shift continues to increase

as the concentration of DMSA in the solution increases. The width of LSP was also found to increase slightly. At lower concentrations, a longitudinal assembly was formed, which changed to lateral assembly upon increase of DMSA concentration. As the concentration was increased, the assembly changed from 1-D “tape-like” to 2-D “sheet-like” and finally to 3-D “superlattice-like” structures. At certain places, the nanorods were found to be arranging perpendicular to the substrate (TEM grids). Assembly was not observed at lower pH, lesser than the pKa of DMSA, where they are not ionised, and hence, cannot facilitate the assembly. On the basis of several control experiments utilising similar molecules, charge neutralisation of the nanorods by the carboxylic group of DMSA was found to be the principal reason for such an assembly, while the mercapto groups render additional stability to its structure. A mechanistic model of the assembly was also proposed.¹⁶

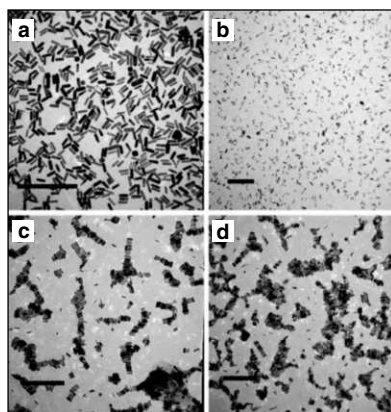


Fig. 15.10 TEM micrographs of GNRs assembled in (a) pure water, (b) 10^{-5} M adipic acid at pH= 3, (c) 10^{-5} M adipic acid at pH= 7, and (d) 10^{-5} M adipic acid at pH= 8. All scale bar corresponds to 500 nm (adapted from Murphy, et al. (Ref. 15). Copyright (2005) by the American Chemical Society).

(f) Gold nanorod assembly involving Van der Waals and dipole interaction

Gold nanorods, which are hydrophilic in nature, can be made hydrophobic by treating with mercaptopropyltrimethoxysilane (MPS) and subsequently octadecyltrimethoxysilane (ODS). Takai *et al.* found that such hydrophobic nanorods can be arranged into well-ordered 2- or 3-D structures on a substrate by solvent evaporation. The hydrophobisation was done in three steps: (i) binding MPS onto the nanorods; (ii) hydrolysis of methoxysilanes; and (iii) immobilisation of ODS by dehydration condensation, through which a hydrophobic covering was created on the nanorods surface. 2-D assemblies were dependent on the concentration of the nanorods. At a low concentration, the nanorods assembled parallel to the substrate, whereas they stood on the substrate at a high concentration. In vertical assembly of the nanorods, they arranged in a hexagonal array. The average centre-to-centre distance between the closest adjacent nanorods was 13.0 nm. When the nanorods, where in solid state, it was observed that the nanorods formed a 3-D assembly, where the gold nanorods were arranged in a hexagonal close-packed structure by their side-by-side interaction and the hexagonal arrays accumulated

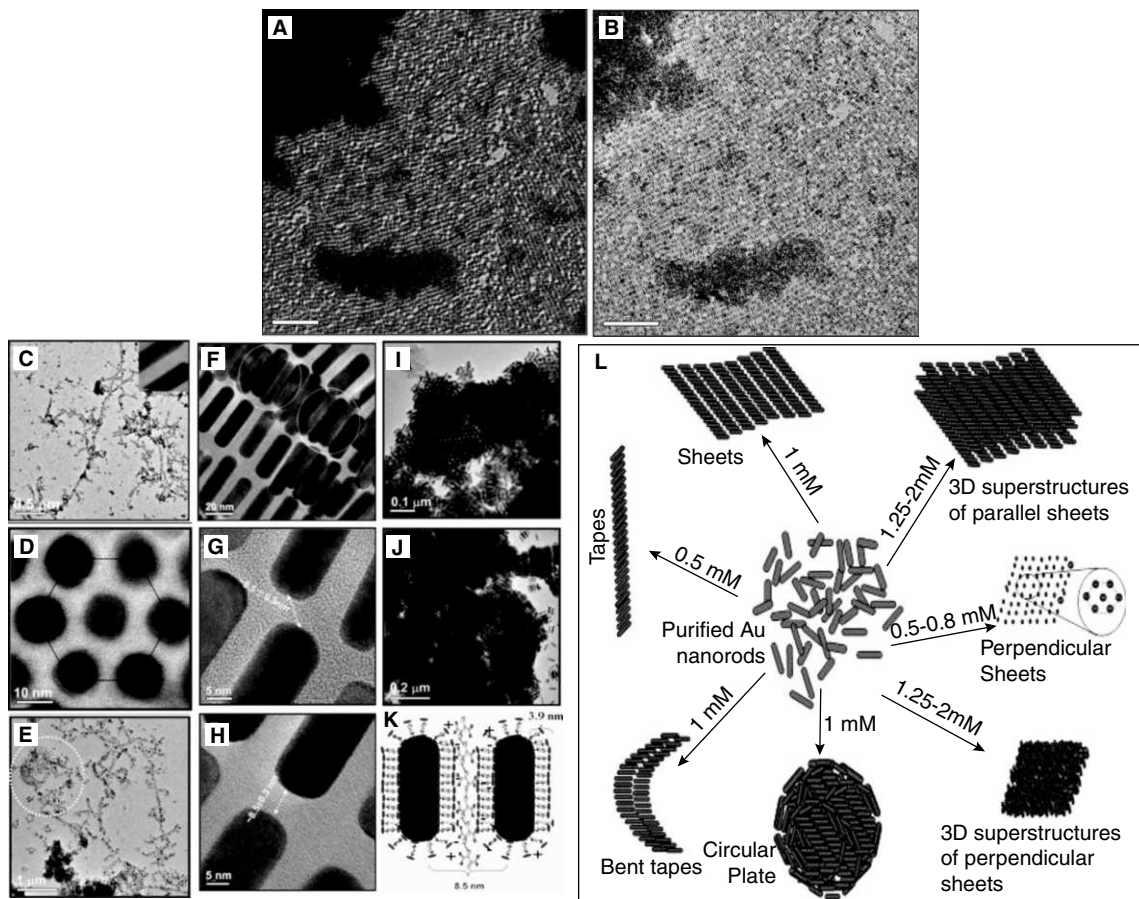


Fig. 15.11 TEM images taken in the (A) Low MAG and (B) MAG I modes of the same area, showing self-assembly of NRs, induced by DMSA. Scale bars are 500 nm. Different self-assembled structures obtained at different concentrations of DMSA. (C) a parallel assembly of nanorods leading to a tape-like structure (D) High-magnification image perpendicularly-oriented assembly showing the hexagonal nature. (E) Circular structures and bent tapes (F) magnified portion of the same assembly showing the staggered configuration of nanorods in the same plane. The nanorods in the top layer (circled) are located in the grooves of the bottom layer. (G) and (H) High magnification images showing the spacing between the nanorod in a monolayer. TEM images of 3-D superstructures formed by (I) perpendicular orientation and (J) parallel orientation with respect to substrate. (K) Schematic showing the mechanism of the self-assembly. (L) Cartoonic representation of various superstructures formed from Au nanorods in the presence of different concentrations of DMSA (adapted from Pradeep, et al. (Ref. 16). Copyright (2008) by the American Chemical Society).

in a lamellar structure over small regions. The assembly was believed to be initiated by the interaction between nanorods caused by the induced dipole moment, in addition to the steric hindrance. The induced dipole moment that gets generated by the instantaneous polarisation or fluctuation of electron

density in the nanorod induces the oppositely directed polarisation in the adjacent nanorods. This results in the generation of a dipole-dipole interaction between adjacent nanorods. Since the induced dipole moments can be more effectively compensated in the side-by-side interaction, this leads to an assembly which is preferentially side-by-side.

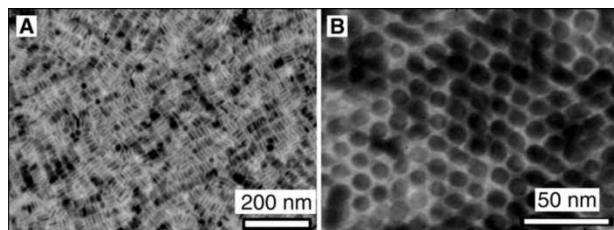


Fig. 15.12 TEM images of assemblies of hydrophobic gold nanorods arranged (A) parallel (B) perpendicular to substrate (adapted from Takai, *et al.* (Ref. 17). Copyright (2007) by the American Chemical Society).

A surface-directed lateral or perpendicular assembly of GNRs were reported by Torimitsu *et al.*¹⁸ A peptide called 1,2-dipalmitoyl-*sn*-glycero-3-phosphothioethanol (DPPTe) were synthesised, and they were anchored onto GNR surface. The self-assembled superstructures of the complex were dependent on the drying method and the hydrophilic or hydrophobic nature of the Si surface. The GNR-DPPTe complex formed characteristic 1-D and 2-D self-assemblies induced by intermolecular interactions of surface-anchored lipids via a controlled drying process. The combination of solvent evaporation from the sample drop and interfacial hydrophilicity or hydrophobicity led to a variety of self-assembled features. The organisation in the self-assembled structure was determined by the balance of Van der Waals, capillary, surface tension, and other forces. The inter-particle distance between neighbouring NRs was around 5.0 nm, which was consistent with the thickness of the lipid bilayer. UV/Vis spectra showed a slight blue shift of LSP upon addition of DPPTe, which indicates a 100 per cent side-by-side interaction and parallel assembly, where nanorod long axes are parallel to each other. Furthermore, they observed the anisotropic configurations of the NR complex, preferentially oriented in a lateral or perpendicular fashion, in a 2-D assembled structure is dependent on the interfacial hydrophilicity or hydrophobicity of the silicon surface. On the hydrophilic Si surface, the NR complex in the 2-D array is orientated lateral to the substrate. The distance between neighbouring NRs in laterally arranged 2-D structure, as well as parallel 1-D and 2-D assemblies was found to be constant (5nm).¹⁸

A pH-dependent reversible end-to-end assembly of gold nanorods (GNRs) functionalised with disulfide-modified poly(L-glutamic acid) (SSPLGA) was reported by Gupta *et al.*¹⁹ The changes were induced by changes in the secondary conformation of the peptide with changes in pH. The disulfides make the polyacids to anchor onto the end of the gold nanorods in an ethanolic solution. A layer of poly(vinyl pyrrolidone) gets adsorbed on the positively charged, surfactant-stabilised GNR and will screen the surfactant bilayer charge, which in turn provides stability for GNR in ethanol. This irreversible end-to-end assembly was compared with an assembly using a bidentate ligand, namely 1,6-hexanedithiol. Both these assemblies were characterised using dynamic light scattering (DLS),

UV/vis absorption spectroscopy and transmission electron microscopy (TEM). At a pH < 3.5, GNR–SSPLGA solution, where the PLGA is in an α -helical conformation, the modified GNR tend self-assemble into 1-D nanostructure. When the pH is increased to 8.5, the assembly got disrupted and disordered nanorods were formed due to the change in conformation of the polypeptide to a random coil, which occurs rapidly within minutes. Changing the pH between low and high pH values resulted in the formation of nanostructures of GNRs to get them dispersed in solution. It was found that this can be repeated several times without any change in the nanorods structure.¹⁹

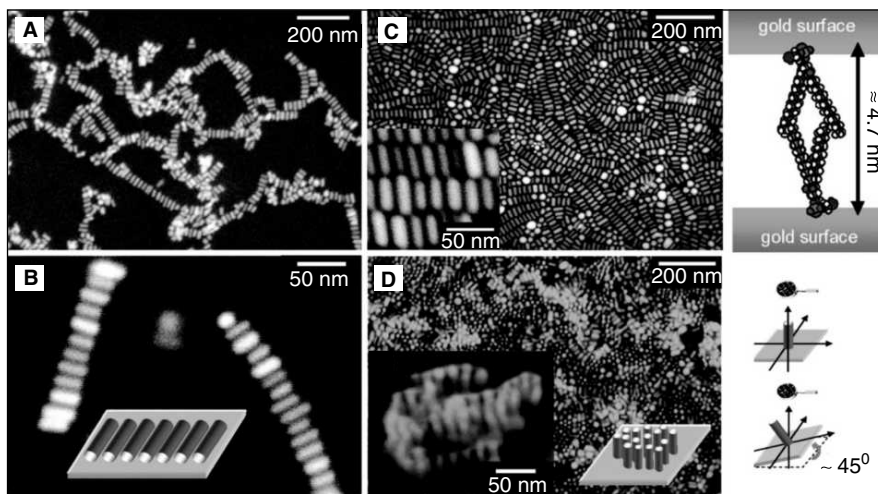


Fig. 15.13 SEM images of self-assembly of the Au NRs coupled with 1.0 mM of DPPE on Si(111) substrate (A) and (B) 1-D, (C) 2-D where nanorod long axis is parallel to the substrate and (D) 2-D perpendicular assembly. The mechanism of assembly is also depicted schematically (adapted from Torimitsu, *et al.* (Ref. 18). Copyright (2008) by the American Chemical Society).

Recently, through bis(terpyridine)–metal connectivity GNRs were assembled, disassembled and reassembled by Newkome *et al.*²⁰ Using [(disulfide-modified terpyridine)₂–MII] (M=Fe or Cd) interconnectors, end-to-end linear and branched assembly of GNRs into multicomponent structures were made. The prepared [(terpyridine)₂–MII] complexes are unstable in basic conditions, and hence, the addition of NaOH resulted in disassembly. When the metal used for assembly was Cd, which forms labile complexes with bis(terpyridine), the assembly was also found to be labile. In presence of small concentrations of Cd assemblies get formed. In presence of excess Cd(II) ion, the superstructure disassembles. When Fe(II) was added into this disassembled system, they again reassembled into end-to-end chains. This assembly can be again disassembled by mere change in pH as mentioned above.²⁰

(g) Assembly on templates

Gold nanorods have been arranged over templates also. The first work in this direction was done by Liz-Marzán *et al.*²¹ where they used multi-walled carbon nanotubes (MWNT) as templates. They first interchanged the CTAB covering on gold nanorods with poly(vinylpyrrolidone) (PVP). MWNTs were

coated with a polyelectrolyte, mainly polystyrene sulfonate (PSS), followed by poly(diallyldimethyl) ammonium chloride (PDDA). This wrapping produces adsorption sites on the CNTs, on which GNRs can get deposited electrostatically. This resulted in a preferential end-to-end assembly of GNRs forming a string-like alignment. The resulting nanocomposites showed broadened absorption features, because of the end-to-end plasmon coupling between neighbouring nanorods in the string-like alignment. They also proved that these nanorods can serve as a label to monitor the alignment of carbon nanotubes within polymer films.^{21,22}

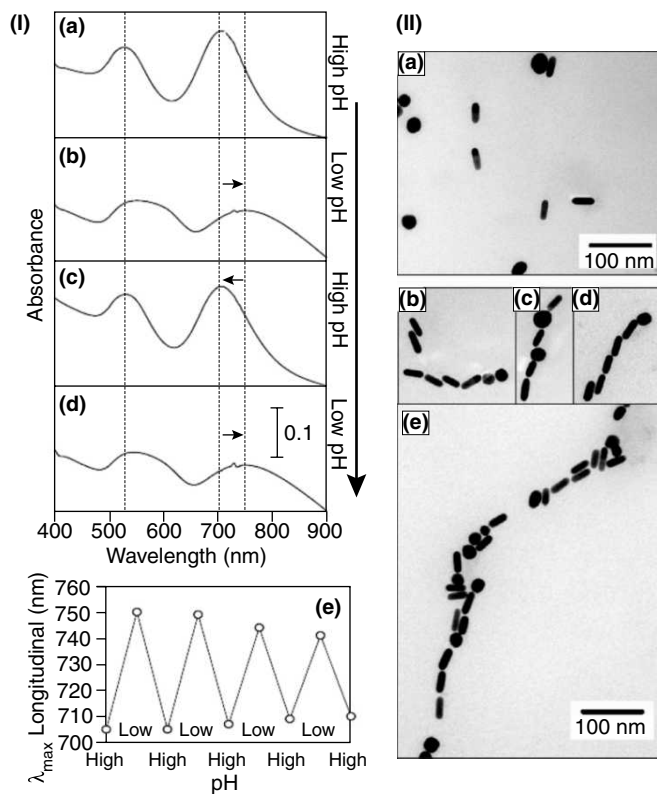


Fig. 15.14 (I) Optical absorption spectra of GNR-SSPLGA solutions subjected to pH changes from a high to a low pH. (II) TEM image of GNR-SSPLGA (a) prior and (b)–(e) after end-to-end linking (adapted from Gupta, et al. (Ref. 19). Copyright (2008) by the Institute of Physics Publishing, UK).

Rings of nanorods, where the drying droplet acts as the template, was demonstrated by Zubarev and Khanal.²³ They described a simple and quantitative method to form rings of GNRs. A spontaneous assembly of hybrid gold/polymer core-shell nanorods into ring-like arrays was seen, where the rings are templated by water droplets that condense on the surface of nonpolar solvents from humid air. For attaining this, 4-mercaptophenol in THF was added to GNR solution thereby replacing CTAB from the GNR surface. These modified GNRs were redispersed in dichloromethane and covalently coupled

with carboxybiphenyl-terminated polystyrene, which forms a thick coverage over GNR surface through covalent linkage. The presence of a dense polymer shell ensures high solubility and stability of the nanorods in organic solvents. When the organic solution ($(\text{CH}_2\text{Cl}_2$ or $\text{CHCl}_3)$) of GNR was dropcasted on the TEM grid, they found a large number of rings of gold nanorods. They proposed a mechanism for this ring formation also. The fast evaporation of the organic solvent will lead to the condensation of numerous water droplets (Fig. 15.5a) This will be surrounded by the organic solution of GNRs on carbon grids. GNRs, being highly hydrophobic, cannot enter the aqueous drop and being highly soluble in organic solvents they will remain in the organic layer until the last drop of organic solvent evaporates. After evaporation of organic solvent, the temperature of the substrate will rise to room temperature and GNRs get concentrated around the circumference of water droplets. After some time, the water droplets also will get evaporated leaving behind rings of gold nanorods on the substrate.²³

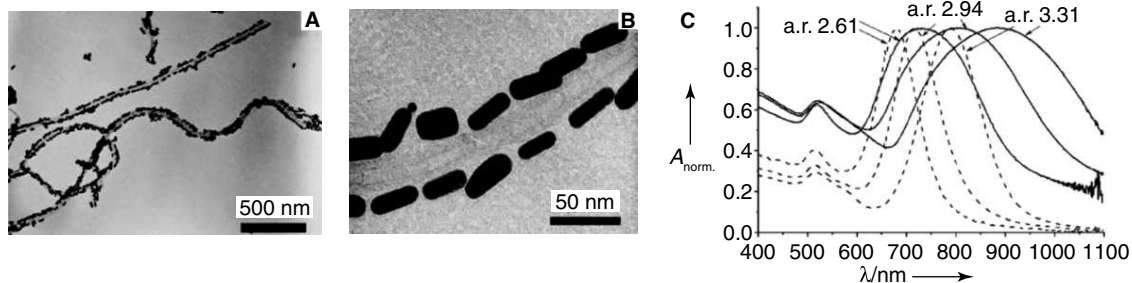


Fig. 15.15 TEM images of Au nanorods (average aspect ratio 2.94), assembled on MWNTs (average diameter 30 nm) at various magnifications (A and B). (C) UV/Vis spectral changes (adapted from Liz-Marzán, *et al.* (Ref. 21). Copyright (2005) by the John Wiley & Sons, Inc.).

A solution-phase method for assembling nanorods into a hexagonal pattern using microgels was reported by Pradeep *et al.*²⁴ Gold nanorod-coated poly(*N*-isopropyl acrylamide) microgels were synthesised. The poly(*N*-isopropyl acrylamide) (PNIPAm) microgel particles required for the self-assembly experiments were prepared using precipitation polymerisation. These microgels were loaded with cetyltrimethylammonium bromide (CTAB)-coated gold nanoparticles of 4–5 nm size, which were used as seed particles and gold nanorods were synthesised *in-situ* using the reported procedure mentioned in the earlier chapter. By this method, the required population of nanorods on the microgels was achieved. These nanorod-loaded microgels were allowed to self-assemble. This resulted in the hexagonal pattern formation. The various materials prepared were characterised by UV-vis spectroscopy and transmission electron microscopy. Similar experiments were done with nanoparticle-coated or prefabricated nanorod-coated microgels, which did not give such hexagonal patterns because of the reduced number density of the nanoparticles. The interpenetration and interlocking of the nanorod structures were thought to be the reason for the formation of these patterns.²⁴ The affinity of NRs for polyNIPAm-based microgels allows their sequestering by cationic, anionic, and close-to-neutral-state microgels as reported by Kumacheva *et al.*²⁵ They made the prepared microgels cationic, anionic or near-neutral by adjusting the pH of the solution. GNR got sequestered independent of the charge of

the microgel when added into the above solution. Their results suggest that electrostatic interactions alone are not governing the loading of microgels with NRs. The strong binding forces between gold NRs and polyacrylamide microgels can overcome electrostatic repulsion between the nanoparticles and microgels. They also proved that in order to sequester gold nanorods, the synthesis of temperature-responsive polyacrylamide microgels may not require the incorporation of anionic functional groups and thus unwanted shift of the volume–temperature transitions can be avoided and the range of compositions used for microgel synthesis can be expanded.²⁵

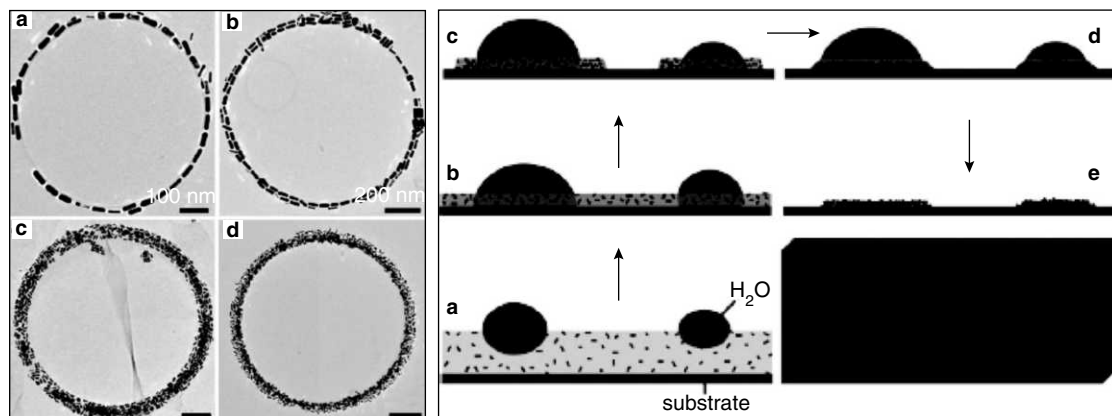


Fig. 15.16 TEM images of rings formed by AuNR(PS)_n rods from a solution in CH_2Cl_2 (1 mg mL^{-1}). Schematic of the mechanism of water droplets template formation of GNR rings (adapted from Zubarev and Khanal (Ref. 23). Copyright (2007) by the John Wiley & Sons, Inc.).

GNR-embedded silica particles with different surface coverages, by the assembly of GNRs on silica particles using electrostatic interaction and subsequent coating of silica with controllable thickness, were made by Su *et al.*²⁶ Amino-functionalised silica spheres were prepared. The CTAB coating on GNR was interchanged with PVP. The negatively-charged PVP-modified GNRs were assembled on the positively-charged surfaces of amino-functionalised silica spheres through the electrostatic interaction. By varying the ratio between the silica particles and the GNRs in solution, GNR-coated silica particles with different surface coverage were obtained.²⁶

(h) Assembly on substrates

Highly aligned GNRs grown directly on a NH_2 -functionalised Si (100) was reported by Zamborini *et al.*²⁷ A remarkable degree of parallel alignment was observed over large areas. They did not find any arrangement when similar reaction was done on amorphous glass. But since the alignment direction changes throughout the sample, showing no direct correlation with the arrangement of Si atoms, they concluded that the crystallinity of the substrate is not a big governing factor of the assembly. The mechanism of the assembly is still not well understood. The alignment was not observed on mercaptopropyltrimethoxysilane (MPTMS)- and (aminopropyl) triethoxysilane (APTES)-

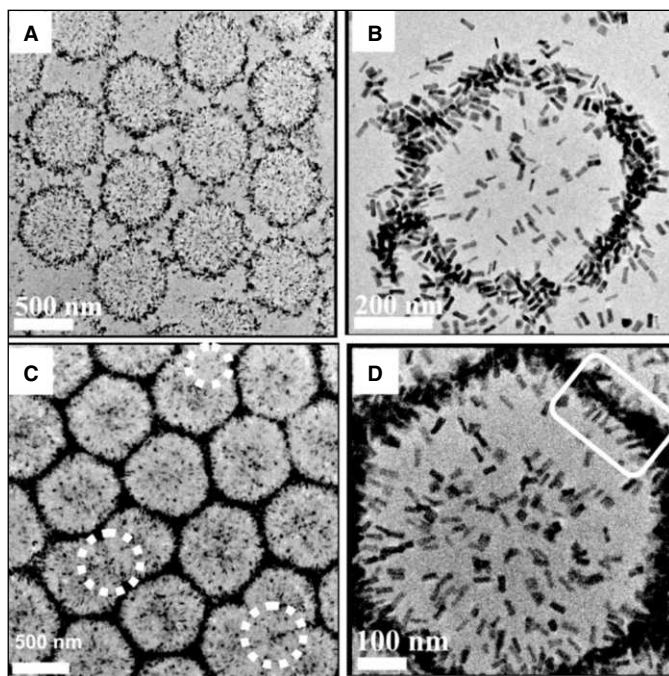


Fig. 15.17 (A) and (B) TEM images of the gold nanorod-PNIPAm composite. (C) Large-area image of the hexagonal pattern with defect sites marked with dashed circles. (D) Higher magnification image of the one cell of hexagonal pattern confirming that the anisotropic structures sitting on the microgels are gold nanorods (adapted from Pradeep, *et al.* (Ref. 24). Copyright (2008) by the American Chemical Society).

functionalised or bare Si(100). This indicates that surface chemistry plays a major role, but the role of the amidation reaction on alignment is not clear. Surface hydrophobicity does not affect the alignment, which was evident since acetic and succinic acid surfaces both showed alignment.²⁷

End-to-end alignment of phosphatidylcholine-passivated gold nanorods (GNRs) adsorbed on polyanion-modified glass substrates was reported by Yamada *et al.*²⁸ Glass substrate to deposit GNRs was modified with water soluble polymers using layer-by-layer method. The glass substrate was treated with a 1:1 aqueous solution of hydrogen peroxide and ammonia to make them hydrophilic. Then by layer-by-layer method, poly(allylamine hydrochloride) (PAH) and poly(sodium styrene sulfonate) (PSS) were anchored onto the substrate making the outer most layer of the substrate negatively charged. These substrates were immersed in aqueous colloidal solutions of phosphatidylcholine (PC)-passivated GNRs containing different concentrations of aminoethanethiol hydrochloride (AHT). The GNRs on glass substrates formed end-to-end assemblies showing red-shifted and broadened longitudinal surface plasmon (SP) bands. Addition of aminoethanethiol (AHT) induced dampening of SP bands, but increased the density of GNRs on the glass surfaces. Thiol groups of AHT were found to be effective to change the properties of GNRs assemblies on glass surfaces.²⁸

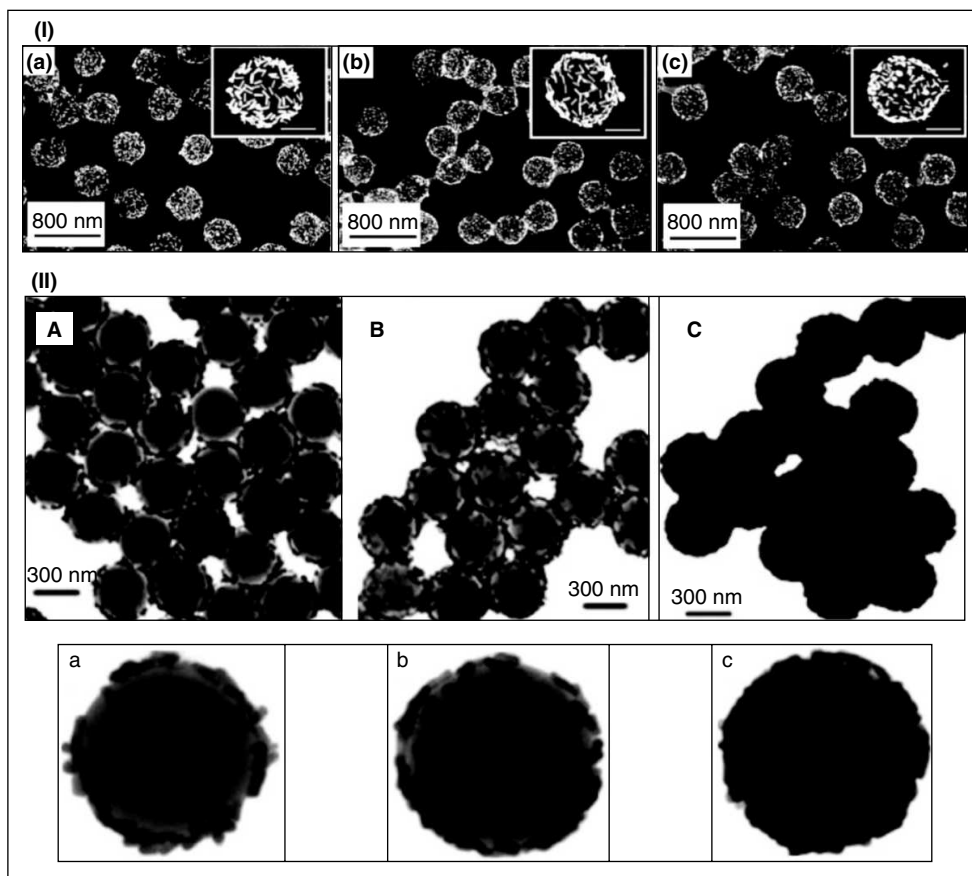


Fig. 15.18 (I) TEM images of hybrid poly (NIPAm-AA-VI) microgels loaded with gold NRs at different pH values: (a) pH=4.5, (b) pH=6.3, (c) pH=7.5 (reprinted with permission from Kumacheva, et al. (Ref. 25). Copyright (2008) by the John Wiley & Sons, Inc.). (II) TEM images of approximately 320 nm silica particles after deposition of GNRs with different surface coverage: (A) 0.8, (B) 1.2, and (C) 2.0 mL of 8 mM GNR ethanol solution were added to 1 mg of silica spheres dispersed in 1.5 mL of ethanol (adapted from Su, et al. (Ref. 25). Copyright (2008) by the John Wiley & Sons, Inc.).

A patterned silicon substrate with hydrophobic stripes was successfully applied for growing gold NR superlattices by Imae *et al.*²⁹ The formation of perpendicular superlattices was also possible in this method. The substrate surface was found to be a crucial factor for the assembly. GNRs should be either positively attracted or not repelled by hydrophobic (ODS-SAM) surfaces for forming a well-defined assembly. When the silicon substrate was hydrophilic, GNRs preferred to stay in the solvent. They prepared *n*-octadecyltrimethoxysilane (ODS) self-assembled monolayer (SAM) on a silicon substrate. ODS-SAM patterns were also prepared. GNR solution was made in CHCl_3 and the assembly of GNRs was prepared by gradual evaporation of the solvent. Under low GNR concentration, domains of closely

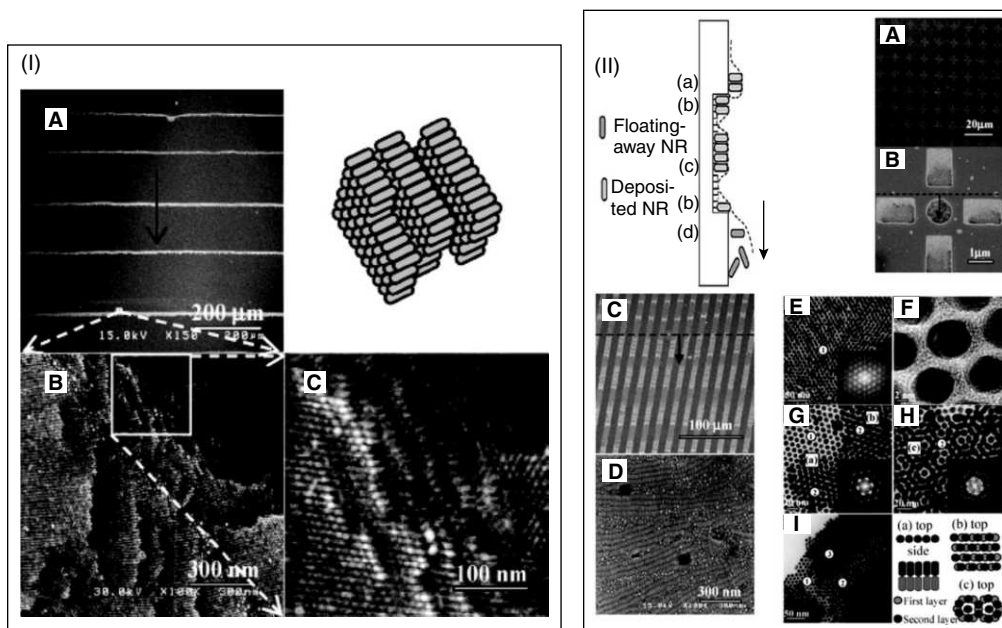


Fig. 15.19 (I) SEM images of a gold NR monolayer with a parallel (A) and perpendicular (C) orientation on an ODS-modified silicon substrate. (B) and (D) are the magnified images of the square region in (A) and (C), respectively. The experimental cell is also illustrated. (II) Schematic showing the GNR confinements at the contact line in different parts (prior to, within, and over the etched pattern, listed as a, b, c, and d) on the substrate. (A) SEM image of a pattern with different shapes and small sizes, which is vertically immersed in the NR suspension. (B) Enlarged view of one set in the pattern. The arrow denotes downtrend of the liquid interface. (C) SEM image of a spontaneous pattern of NRs. (D) Enlarged SEM of the bright region in (C). The arrow denotes downtrend of the liquid interface. TEM images of the perpendicular arrangement of gold NRs: (E) monolayer, (F) high-resolution image of the monolayer, (G, H) bilayer, and (I) trilayer. Insets show corresponding FFT diffractions. The numbers represent the number of array layers. The schemes from (a) to (c) illustrate details of the layer structure (adapted from Imae and Zhang (Ref. 29). Copyright (2009) by the American Chemical Society).

packed parallel arrangements of GNRs were seen on an ODS-SAM substrate with spherical particles perturbing and separating the ordered domains of GNRs. The uniformity of particles without shape difference is essential for the assembly. Perpendicularly arranged GNR assemblies were also seen at some places with hexagonal geometry. But, parallel structure dominated on the substrate. Under much lower concentration, no vertical orientation of GNRs was observed. When the nanorod concentration was increased, many parallel stripes or lines were deposited, extending over the whole homogeneous ODS-SAM substrate, with an interval between the stripes in the range of 100–200 μm, and the width of each stripe was about 10 μm. Particles are scarcely observed between the stripes. Aligned GNR arrays with the parallel or perpendicular direction were seen within each stripe. Similar patterns were

made on a topological pattern created via photolithographic technology. It was found that when the GNR concentration was low, the domains of GNRs appeared on both the top and bottom edges of the ODS stripe and only on the bottom edge of the silicon stripe.²⁹

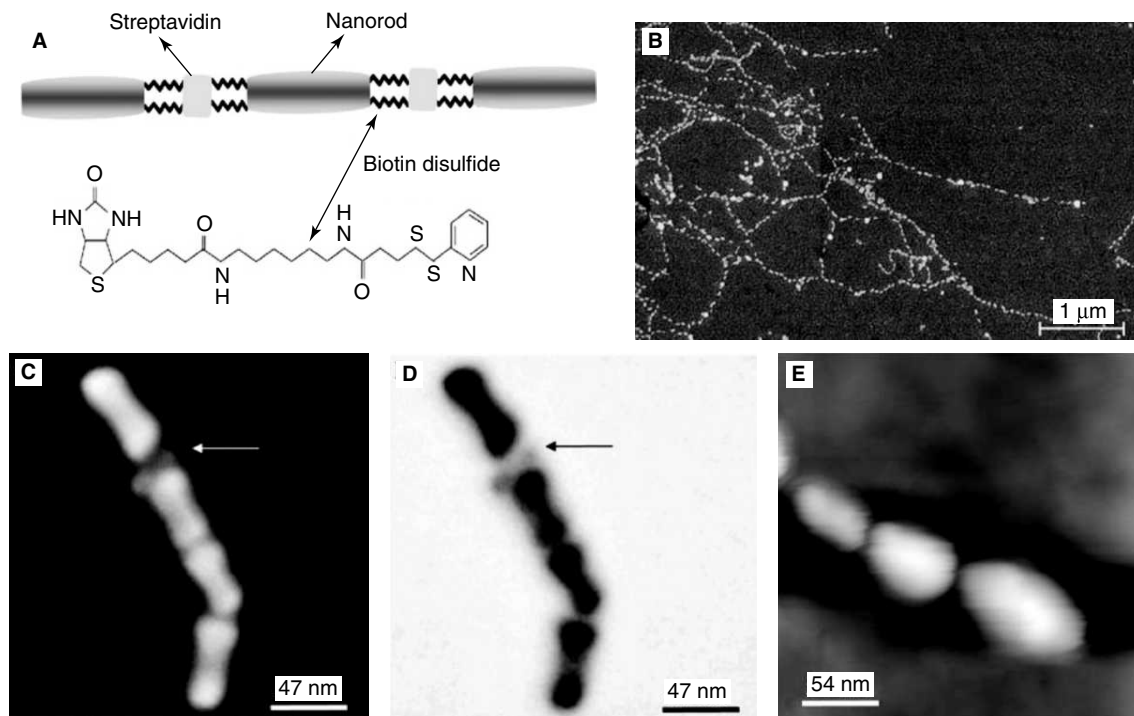


Fig. 15.20 (A) Schematic of the attachment process. (B–E) SEM images of chains of nanorods attached to a derivatised substrate. Region which may contain more than one streptavidin binder indicated by larger distance between NRs are marked by arrows (adapted from Cortie, et al. (Ref. 30). Copyright (2007) by the John Wiley & Sons, Inc.).

The mechanism of assembly preferentially on the edges of the pattern was also explained. The growth of the assembly can depend on the wetting properties and topological patterning of the substrate. At the bottom edge of the silicon stripe, GNR suspensions are driven to form droplets due to the edge effect of the pattern and convective flow tries to pull down the GNRs in the droplets toward the edge. The combined effects of convective flow and attractive capillary force will lead to the formation of GNR domains at the top and bottom edges of the ODS stripe. Since the interaction of GNRs with the relatively hydrophilic ODS-modified silicon stripe being weak, the GNR suspension cannot remain on the silicon stripe surface when the liquid interface descends over the pattern and no GNRs will deposit at this region. At a higher concentration of GNR, even the hydrophobic ODS-modified surface will get occupied by GNR with the aid of GNR/substrate interaction.²⁹

A protocol to directly grow end-to-end assembled structures on a substrate into long chains attached on top of a mixed self-assembled monolayer, that has been functionalised with streptavidin,

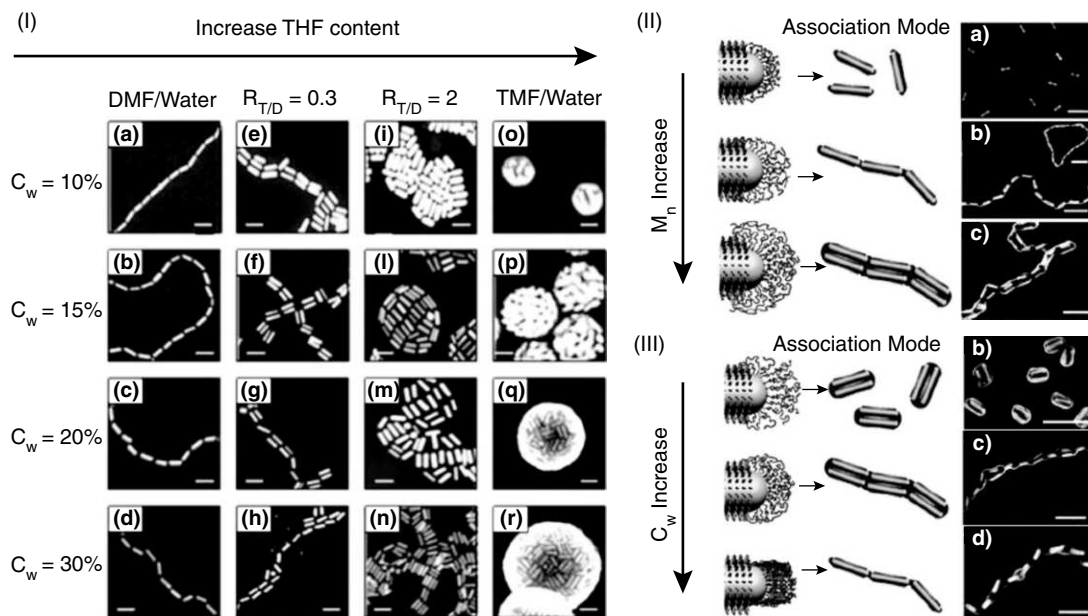


Fig. 15.21 (I) Self-assembled structures obtained at various THF/DMF ratios ($R_{T/D}$) and various water contents (C_w). The scale bar is 50nm in panels (i), (m), (o), (p), and 60 nm in all other panels (adapted from Kumacheva, et al. (Ref. 31). Copyright (2008) by the John Wiley & Sons, Inc.). (II) and (III) Left column: Schematics of the relative location of PS molecules with varying molecular weight with respect to the central gold block. Central column: Schematics of the self-assembled structures of triblocks when water is added to the solution of NRs in DMF in in (II) and Schematics of the self-assembled structures of triblocks with 50K-PS in (III). Right column in (II): SEM images of the self-assembled structures with different mol. wt. PS. Right column in (III): SEM images of corresponding assembled structures of triblocks with 50K-PS in water/DMF mixture with different water content (adapted from Kumacheva, et al. (Ref. 33). Copyright (2008) by the American Chemical Society).

was reported by Cortie *et al.*³⁰ They were able to get assemblies, which extent over a micrometer in length, with 5 nm inter rod separation. A special gold-coated silicon surface, functionalised with a SAM composed of a mixture of disulfide-modified biotin and 1,4-phenylenedimethanethiol, was prepared for the assembly. 1,4-phenylenedimethanethiol acts as a spacing molecule between the biotin molecules in the SAM, and minimises steric-hindrance effects. Now streptavidin is added such that about 50 per cent of the surface is functionalised with streptavidin. Then biotin derivatised GNRs were exposed onto this surface and due to biotin-streptavidin interaction, the nanorods were found to assemble into chains. The dynamics of the assembling process was monitored by using surface plasmon resonance (SPR) spectroscopy, and the imaging of the assembly was done by using scanning probe microscopy.³⁰

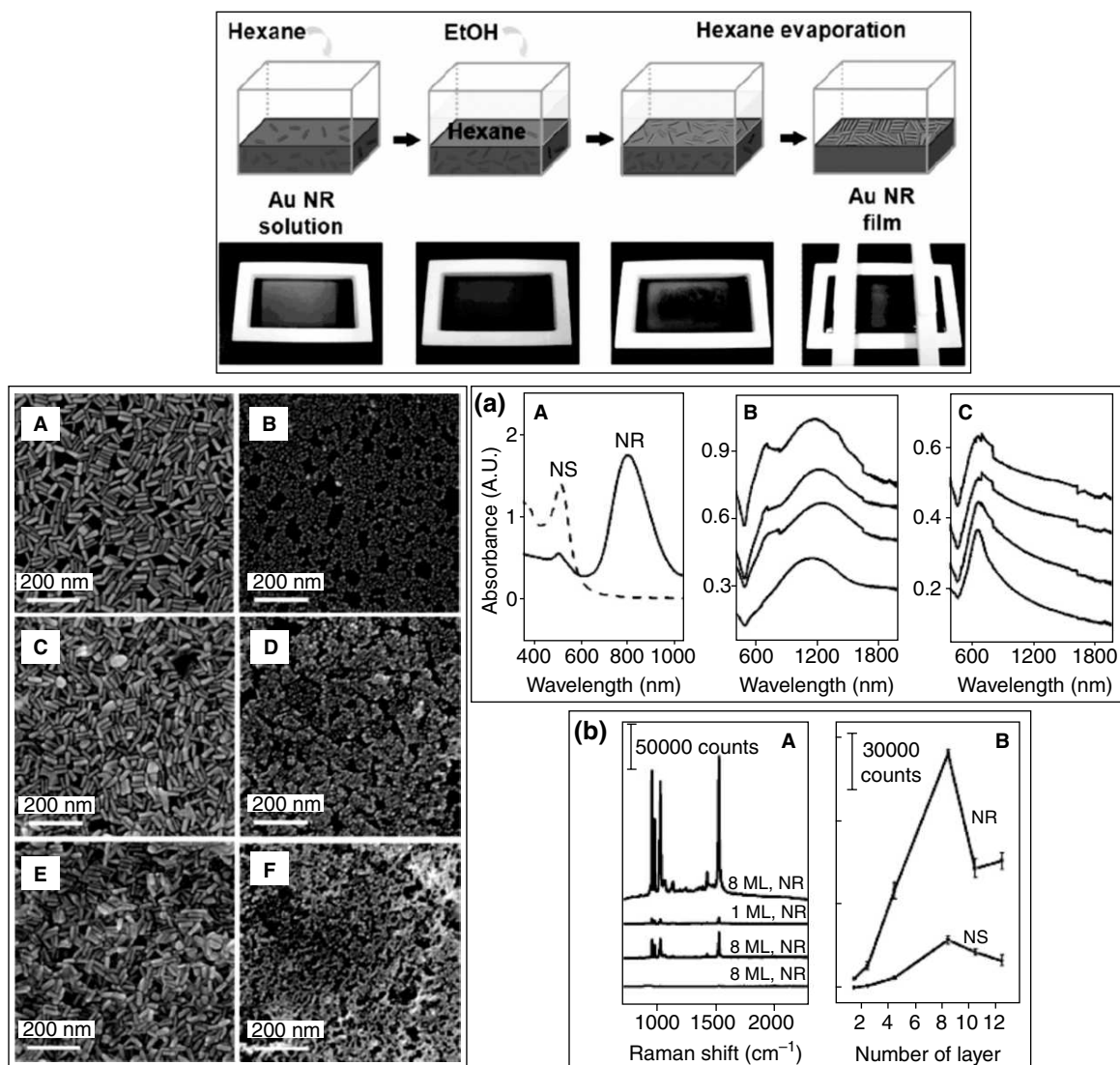


Fig. 15.22 Schematic representation and the corresponding optical images of the gold NR film formation at the water/hexane interface (above). FESEM images for gold NR and films with (A) one, (C) two, and (E) four monolayers. In (a) (A) UV-Vis absorption spectra of gold nanospheres (NSs) and nanorods (NRs) in solution phase. (B) and (C) UV-vis absorption spectra (on glass slides in air) for different numbers of gold NR monolayer and NS films (adapted from Park, et al. (Ref. 34). Copyright (2007) by the American Chemical Society).

(i) Assembling by polymer tethering

Kumacheva *et al.* reported a new way of self-organising GNRs into a predefined pattern by attaching multiple polymer arms termed as “pom-poms”.^{31,32,33} In the DMF/water mixtures, GNRs end-terminated

with PS molecules self-assembles into higher order structures. The ordering is determined by the length and distribution of PS molecules between the ends of GNRs and the longitudinal facet of GNRs. The assembly was controlled by changing the structure of the polymer pom-poms. The variation in the molecular weight of the polymer molecules and their relative location with respect to the long side of the GNRs resulted in different kinds of nanorod assemblies, namely, bundles, bundled chains, and chains involving their side-by-side and end-to-end assembly. The change from one form to another can be also controlled by changing the concentration of water in the system.

The mechanism was also studied. They found that the evolution of self-assembled structures of GNRs end terminated with polystyrene molecules takes place through competition between side-to-side and end-to-end assembly. Different solubilities of the polystyrene and the CTAB-coated metal blocks in the solvent mixture give rise to this competition. Tendency towards side-to-side aggregation was found to be dominant over most of the compositional range. At high DMF or water content, and at very low THF/DMF weight ratios, this tendency gets reduced significantly.^{31, 32, 33}

(j) Layer-by-Layer assembly of gold nanorods into gold nanorod films

A strategy for assembling gold nanorods into 2-D arrays at a water-hexane interface without the aid of any linker molecule was reported by Park *et al.*³⁴ In this method, the film thickness can be controlled systematically and they were able to get aggregates of gold nanorods with a relatively clean surface with controlled nanorod density. Hydrophilic nanoparticles have a contact angle of $<90^\circ$ at a water-hexane interface and will be suspended in the water phase. But, the particles tended to adsorb to the water-hexane interface, when their contact angle is approximately equal to 90° . A medium having high dielectric constant can separate the charged particles from each other. When a miscible solvent with a lower dielectric constant is added into this, the dielectric constant of the medium gets decreased. The surface charge of the particles also decreases progressively as a function of the amount of the miscible solvent added. Upon the addition of ethanol to water-hexane interface, the surface charge density of the nanoparticles decreases. So the nanoparticles are brought to the interface. The driving force for the entrapment of nanoparticle is the reduction in interfacial energy at the water-oil interface upon the reduction of the dielectric constant of water. The thickness-dependent SERS of the adsorbed molecules on this nanorod films were studied and found that nanorod films have an order of magnitude stronger SERS enhancement than the nanosphere films under similar experimental conditions.³⁴

(k) Gold nanorod assembly by surface anchored crown ethers

Assembly of gold nanorods end functionalised with crown ethers and initiated by the addition of specific metal ions was reported by Torimitsu *et al.*³⁵ Two thiol-modified crown ethers, 2-[(6-mercaptohexyl)oxy]methyl-15-crown-5 (15-crown-5-SH) and 2-[(6-mercaptohexyl)oxy]methyl-12-crown-4 (12-crown-4-SH) were synthesised. This was added to the purified nanorod solutions upon which the crown ethers get attached covalently onto the end faces of the nanorod through the thiol moieties. Addition of specific metal ions corresponding to the anchored crown ethers resulted in the assembly of nanorods. The structure of the GNR aggregates, assembled side-to-side and end-to-end, was found to be dependent on the concentrations of crown ethers and cations added. Corresponding changes were observed in the absorption spectrum as well. The longitudinal absorption intensity of the GNRs

gradually decreased and the peak was initially red-shifted and then blue-shifted. When K^+ was added into the solution, it formed a 2:1 sandwich complex between the 15-crown-5 moiety and coupling of the plasmon absorbance occurred. The changes in the spectral features were used for the specific detection metal ion also. This will be explained in detail later in the same chapter.³⁵

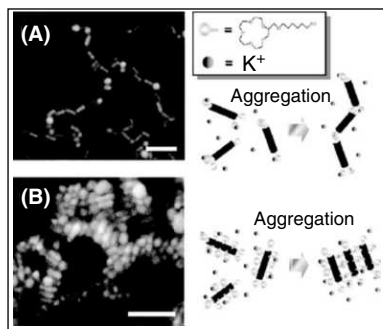


Fig. 15.23 SEM images of the aggregates of the gold nanorod complex on silicon substrate: (A) end-to-end type by addition of 5 mL of 15-crown-5-SH in KCl solution; and (B) side-to-side type by addition of 50 mL of 15-crown-5-SH in KCl solution. Scale bar: 100 nm (adapted from Torimitsu, *et al.* (Ref. 35). Copyright (2007) by the Royal Society of Chemistry, London).

(I) Gold nanorod assembly induced by magnetic field

Pt-doped Au nanorods were homogeneously coated with metallic Ni through hydrazine reduction in aqueous solution, leading to quasi-epitaxial growth of Ni shell on GNRs. Pt acts as a “nucleation agent” and because of its higher redox potential, it can be much more easily reduced than nickel, leading to formation of small nuclei on which Ni is catalytically reduced. The Ni coated GNRs (Au@Ni nanorod) were allowed dry on a TEM grid under the influence of an external magnetic field (0.2 T), and the NRs tend to align in a chain-like structure, in the direction of the applied field. The orientation of individual rods within the chains was not found to be the same and both the “side-to-side” and “end-to-end” assembly found to be co-existing pointing to the complex magnetic response of the system.³⁶

15.2.1 Assembly of High Aspect Ratio Gold Nanorods and Nanowires

Because of the presence of a dense bilayer of CTAB on the surface of GNR, the interaction between nanorods at a favourable distance and optimum concentration can give rise to assembly. These CTAB molecules can act as “glue” between nanorods, when they get assembled, as explained earlier in the chapter. High aspect ratio nanorods are more susceptible for this kind of interaction since they possess longer side faces and the probability of the interactions between nanorods is much higher compared to the low aspect ratio nanorods. So even during the post synthetic purification procedure during different syntheses, they are known to assemble even into 3-D superstructures on substrates during solvent evaporation. Surfactant coated nanorods with an aspect ratio of 13–18 was reported to spontaneously form liquid crystalline assemblies in concentrated solutions by Murphy *et al.*³⁷ They

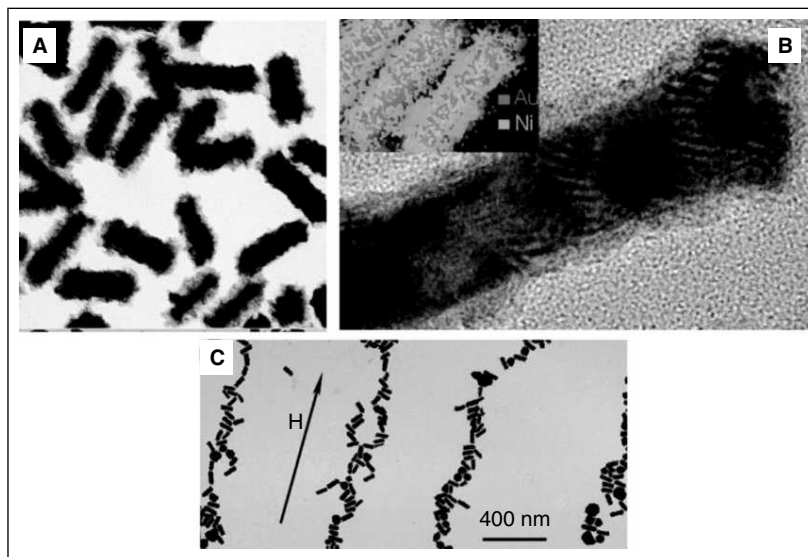


Fig. 15.24 (A) Large area TEM of nickel coated GNRS in the absence of magnetic field. (B) High magnification image of a single Au@Ni NR. Inset shows STEM–XEDS analysis of Au@Ni NRs, showing the relative distribution of the elements (Au = red; Ni = green). (C) Au@Ni NRs, dried on the TEM grid under an external magnetic field (0.2 T) (adapted from Liz-Marzán, et al. (Ref. 36). Copyright (2007) by the John Wiley & Sons, Inc.). (For clarity see colour figure.)

found that surfactant-mediated interactions between gold nanorods of uniform shape and size can result into well-ordered liquid crystalline arrays in concentrated dispersions. The thermodynamic stability of these superstructures is due to the gain in translational entropy which overcomes the loss of orientational entropy. They observed alignment only at a concentration window of 1–100 mM of CTAB in aqueous suspensions, suggesting that interactions between surfactant molecules in solution with surface-adsorbed amphiphiles were important for the assembly process. Higher concentrations of CTAB resulted in clustering of CTAB and lesser concentrations resulted in GNR aggregation.³⁷

Prior to assembly, GNRs are hydrophilic in nature with the surfactant molecules in the outer layer of the surface coating oriented with their cationic head groups exposed to the solvent. During the formation of the assembly, GNRs approach each other in solution, the outermost ‘cationic head out’ CTAB molecules gets ejected with their associated counter ions. As a result, the GNRs become hydrophobic with the remaining CTAB hydrophobic tails face the solvent which drive a spontaneous self-assembly in a side-on fashion in order to minimise the unfavourable hydrophilic–hydrophobic interactions with water, which in turn results in the inter-digitation of the surfactant tails. Gold nanorod self-assemblies were fabricated on the silicon substrate from rod and sphere mixtures, utilising the shape self-selective behaviour of GNRs.³⁸ The assembly showed significant shape dependence and GNRs were found to get arranged separately from spherical particles. This was explained on the basis of capillary force interaction between the surfaces of nanoparticles. They found that according to

theoretical predictions, the capillary forces experienced by GNRs will be different in the longitudinal and transverse direction and the transverse capillary force is always stronger than longitudinal capillary force. This drives GNRs to prefer side-by-side alignment. Also the transverse capillary force experienced by GNRs is always higher than that experienced by spherical particles. This prevents spheres from intermixing at transverse direction during the GNR assembly.³⁸

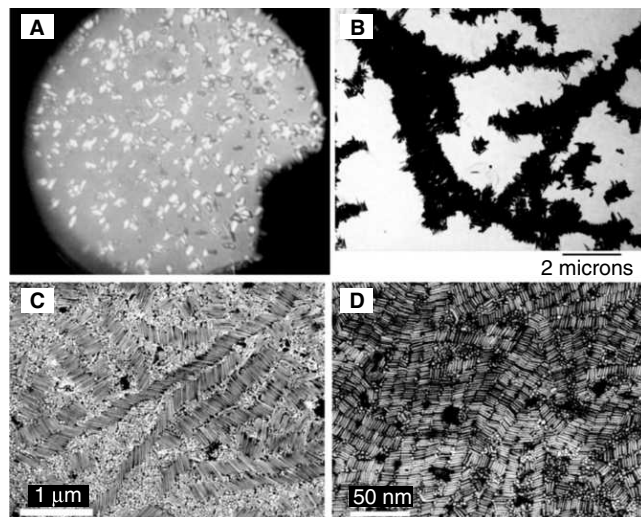


Fig. 15.25 (A) Polarising light microscope image of 5–10 wt% concentrated gold nanorods (B) TEM image of ~5–10 wt% dispersion, showing linear stacks of gold nanorods (adapted from Murphy, *et al.* (Ref. 37). Copyright (2002) by the Royal Society of Chemistry, London). (C) and (D) SEM images of gold nanorod self-assemblies with different aspect ratios through self-selective behaviour (adapted from Gao, *et al.* (Ref. 38). Copyright (2006) by Elsevier B.V.). (For clarity see colour figure.)

Surfactant interactions are known to arrange 1-D structures. Utilising the surfactant interactions, nanowires (NWs) were precisely placed and oriented onto surfaces from solution.³⁹ Gold nanowires were functionalised with self-assembled monolayers of thiol-based surfactants. After the evaporation of excess solvent, nanowires were assembled from solution onto patterned functional surfaces. Nanowire assembly onto surfaces with patterned wettability resulted in the placement of nanowires on hydrophilic regions with a specific orientation. Hydrogen bonding and carboxylate salt attachment of mercaptoundecanoic acid functionalised nanowires to reactive regions of patterned surfaces is believed to be the reason for the specific attachment. Electrostatic interactions between charged nanowires and surfaces drive the preferential assembly of nanowires onto oppositely charged surface regions.³⁹ Microtubules (MTs) were used as biotemplates for synthesising gold nanowires and nanowire arrays by Dunn *et al.* First, MT arrays were prepared and Au was deposited on it to produce the nanowire arrays.⁴⁰ Liley *et al.* fabricated nanowire arrays using patterned block polymer templates. Specific adsorption of 10 nm Au nanoparticles followed by oxygen plasma treatment, which triggers the aggregation resulted in the continuous nanostructures.⁴¹ DNA-directed assembly of Au nanowires

having 0.2 μm diameter and up to 6 μm length was reported by Riess *et al.*⁴² Oligonucleotides were adsorbed as monolayer coatings on these wires through Au-thiol linkages. Au-coated glass slides were functionalised with complementary oligonucleotides and duplexes were allowed to form between strands on the nanowires and on Au-coated glass slides, which binds the two surfaces together giving the pattern.⁴² Chien *et al.* reported a method for assembling nanowires in suspension into scaffolds using ac electric fields. They found that the nanowires get aligned and transported by electric field and its gradient, respectively. The efficiency of assembling and its morphology depends strongly on the frequency of the applied AC voltages and varies as square of the voltage. The morphology of the assembly was found to be independent of the applied voltages.⁴³

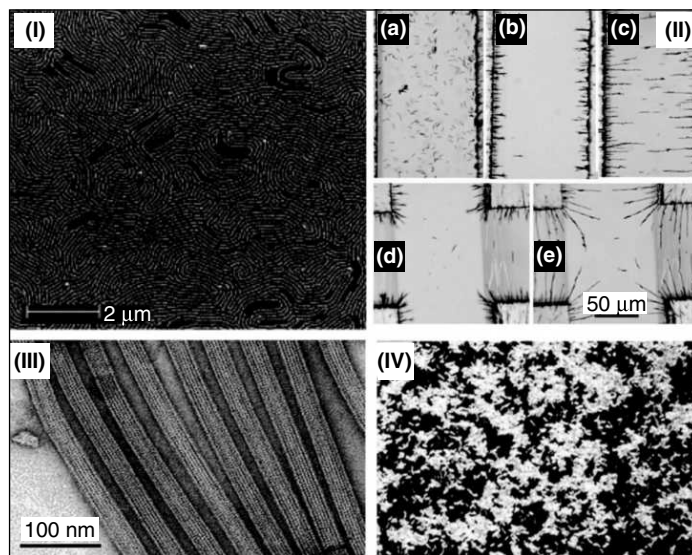


Fig. 15.26

(I) Closely packed bright nanowire assembly template on block polymer arrays (reprinted with permission from Liley, *et al.* (Ref. 41). Copyright (2005) American Chemical Society). (II) Photographs of nanowire assemblies under electric fields (a) 2 V dc; (b) and (d) 10 kHz, 7.5 V ac; (c) and (e) 0.5 MHz, 7.5 V ac (adapted from Chien, *et al.* (Ref. 43). Copyright (2006) by the American Institute of Physics). (III) TEM image of an array of MTs formed through the addition of tau proteins (reprinted with permission from Bruce, *et al.* (Ref. 40). Copyright (2008) by the John Wiley & Sons, Inc.). (IV) Optical microscope images of Au nanowires coated with ssDNA II and assembled onto an Au surface coated with complementary ssDNA (adapted from Mallouk, *et al.* (Ref. 42). Copyright (2001) by the John Wiley & Sons, Inc.).

15.2.2 Examples of Assembly of Some Other Anisotropic Structures of Gold

The variety of anisotropic nanoparticles available and the ability to synthesis them with precise monodispersity enables us to assemble them to useful components. A few examples of assembled

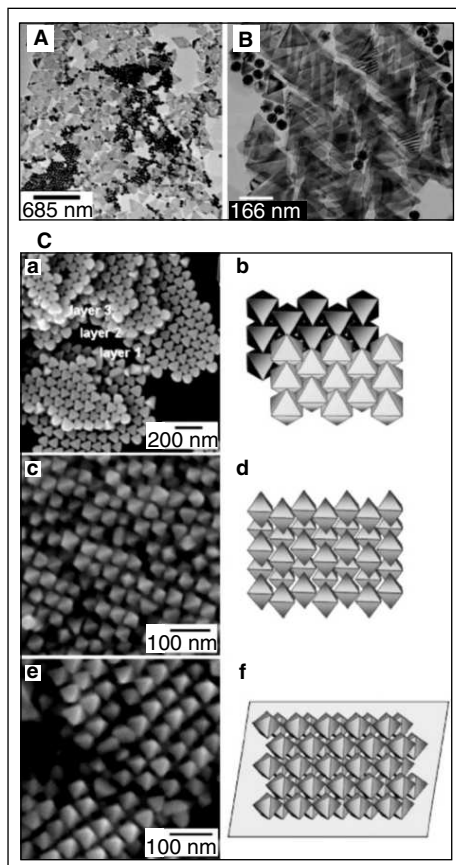


Fig. 15.27 (A) and (B) TEM images of self-assembly of Au triangles during seed mediated synthesis (adapted from Mirkin, *et al.* (Ref. 44). Copyright (2005) by the American Chemical Society). (C) SEM images of the three types of self-assembled structures of the octahedral gold nanocrystals different edge lengths. The schematic representation of the assembly also is shown (adapted from Huang, *et al.* (Ref. 45). Copyright (2008) by the American Chemical Society).

structures made up of anisotropic nanostructures having morphology other than rod like are cited in this section. Nanotriangles (NTs) are interesting due to their unusual optical properties. When they are in the arranged state, the plasmonic coupling is possible and changes will be manifested in the optical spectrum. Because of the comparative difficulty in preparing these structures, the effort to assemble them also is far and few. But during synthesis itself, due to surfactant interactions between the prisms they tend to get assembled. Mirkin *et al.* observed that during the post-synthetic cleaning and redispersion, NTs get assemble into small range assemblies.⁴⁴ Recently, Huang *et al.* reported a hydrothermal method for the synthesis and self-assembly of octahedral gold nanoparticles of different size regime. They found that all these octahedrons tend to self-assemble spontaneously into long-

range ordered superstructures upon solvent evaporation. They identified three types of self-assembled structures with faces, edges, or corners of the octahedra contacting with the substrates. They also found that the size of the constituent particle can affect the type of packing structure.⁴⁵

15.3 ASSEMBLY OF ANISOTROPIC STRUCTURES OF OTHER METALS

15.3.1 Assembly of Anisotropic Structures of Silver

Anisotropic nanostructures of silver are more diverse compared to gold. But, the synthesis of these structures in a monodisperse fashion is often a tedious job. The advancement in nanotechnology has enabled us now to prepare these particles either in a monodisperse manner or size select and separate the nanostructures post-synthesis to yield highly monodisperse samples. Since all these synthetic strategies involve surfactants to cap the formed nanostructures and to avoid them getting aggregated, the surfactant-induced assembly of these structures upon solvent evaporation is highly probable similar to GNRs, explained in detail earlier in the chapter. Following a similar strategy to that used for making GNRs, Murphy *et al.* devised a seed-mediated growth approach for the preparation of silver nanorods of varied aspect ratios. They found that after shape-separation, these rods self-assemble in a 2-D smectic liquid crystal-like manner upon slow solvent evaporation.⁴⁶

Recently, Kitaev *et al.* reported a new method to produce monodisperse size-controlled faceted pentagonal silver nanorods by thermal regrowth of decahedral silver nanoparticles (AgNPs) using citrate as the reducing agent.⁴⁷ Because of its monodispersity, these NRs showed great tendency to self-assemble into smectic mesophases, like densely-packed rafts and 3-D arrays upon drying the dispersions. Even though the NRs are having five-fold symmetry, the 3-D arrays followed a hexagonal arrangement. They found that slower solvent evaporation (>5 min) as well as a NR concentration in the range of 2–5 mM (in terms of silver) is favourable for the assembly. They also found that the order between the layers can be disturbed very easily, but within a single layer, the arrangement is always consistent. Here, the five-fold symmetry of the constituent NRs is always over-ridden by the long-range hexagonal order within the layers. This might be because five-fold symmetry is not compatible with the close packing that result from evaporation-induced self-assembly. They also studied the dependence of aspect ratio of the participating nanorod on the assembly and found that well-defined layered structures start to be observed for the pentagonal AgNRs with aspect ratio (AR) of 2. When the AR reached 4, there was not enough mobility for the NRs to self-assemble and only local ordering was found. An aspect ratio of 2.5 was found to be optimum for the best possible assembly.⁴⁷

Langmuir-Blodgett (LB) technique is one of the most used methods to assemble a large-area monolayer of nanosystems. Using this technique, nanowires that are ~50 nm diameter and 2–3 μm length were assembled into a large area of about 20 cm^2 by Yang *et al.*⁴⁸ The poly(vinyl pyrrolidone) (PVP) capping of the as prepared nanowires were changed with 1-hexadecanethiol ligands, making them hydrophobic. The hydrophobic nanowires redispersed in chloroform were then dispersed onto a water surface of the LB trough and were assembled through the LB method. The nanowires were aligned side-by-side over large areas, similar to a nematic 2-D ordering of a liquid crystal. These aligned nanowire areas exhibited alternating extinction patterns when the sample was rotated every 45°.⁴⁸

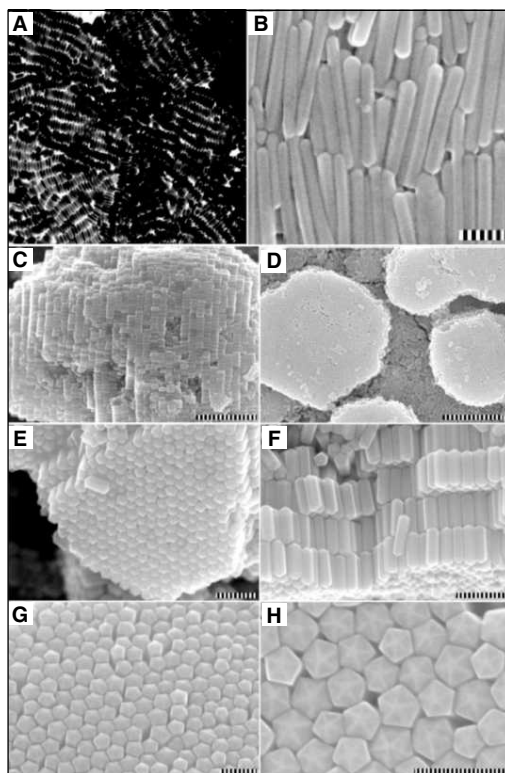


Fig. 15.28 (A) TEM image of shape-separated silver nanorods self-assembled on TEM grids (adapted from Murphy, *et al.* (Ref. 46). Copyright (2001) by the Royal Society of Chemistry, London). (B) SEM images of longer pentagonal faceted rod AgNRs aligned on a glass plate. (C)-(H) SEM images of self-assembled packing of monodisperse faceted pentagonal rod AgNRs with different aspect ratio forming 3-D superlattices (adapted from Kitaev, *et al.* (Ref. 47). Copyright (2008) by the American Chemical Society).

Following a similar methodology, the same group was able to create novel superlattice architectures composed of different polyhedral building blocks, such as truncated cubes, cuboctahedra, and octahedra of Ag nanocrystals.⁴⁹ They found that the choice of NC building blocks determines the lattice packing and dimensions of the lattice packing. Truncated cubes formed a square lattice by assembling in a face-to-face manner. The more truncated polyhedral particles, like cuboctahedra, are arranged to form a rhombohedral unit cell, which is getting formed by the shears experienced by the square lattice. Octahedral Ag nanocrystals formed a hexagonal pattern, where their triangular facets lay flat on the substrate forming an interlocked triangle involving three octahedra.⁴⁹

The assembly of Ag nanoprisms was reported by Han *et al.*⁵⁰ They were able to assemble the prisms with anisotropic orientation and studied the orientation-dependent properties of these assemblies. Two kinds of assembled structures were fabricated. One was fabricated simply by dropping Ag

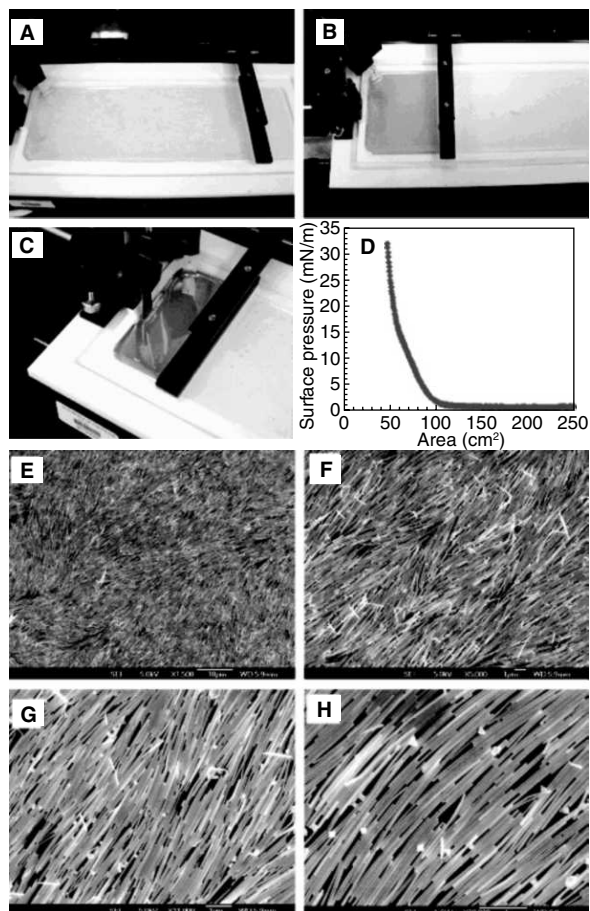


Fig. 15.29 (A-C) Photographs of Langmuir-Blodgett (LB) nanowire assembly process at different compression stages. (D) Surface pressure curve recorded during the process. (E-H) Scanning electron microscopy images (at different magnifications) of the silver nanowire monolayer deposited on a silicon wafer (adapted from Yang, et al. (Ref. 48). Copyright (2003) by the American Chemical Society).

nanoprism solution onto the clean substrates like glass, indium-tin oxide (ITO) glass, Si and TEM grid and solvent was allowed to evaporate slowly (Assembly A). They found that upon solvent evaporation, nanoprisms tend to stack face-to-face in rows with their edges perpendicular to the substrate. Nature of the substrate used did not have any effect on the alignment of the nanoprisms and they assembled with upright orientation on all the substrates. This is explained to be due to the higher attractive force between nanoprism faces than that between face and substrate. The second kind of assembly was made by using the interfacial entrapment method (Assembly B). In this, they used a crown ether derivative which can transfer Ag nanoprisms in water solution to the water-oil interface and direct the self-assembly of nanoprisms at the liquid-liquid interface in face-down fashion. The repulsion between

crown ether derivatives adsorbed on the nanoprism faces, which can overcome the tendency to stack in the face-to-face manner can be considered as the reason for this parallel alignment of nanoprisms, which are very close to each other.⁵⁰

Assembly of Ag nanocubes by the selective functionalisation of each face selectively was reported by Xia *et al.*⁵¹ Five distinct SAM-modified Ag nanocubes were prepared from the possible combinations of hydrophobic and hydrophilic faces and were assembled into four different nanostructures and one microstructure. The assembly was explained on the hydrophobic interaction and solvation free energy. Due to a hydrophobic driving force that is proportional to the solvation free energy of the water surrounding the SAM-functionalised Ag nanocubes, they are brought together with their hydrophobic faces adjacent and parallel to form assembled structures. Depending upon the number of hydrophobic and hydrophilic faces present on each cube, the enthalpy or the solvation free energy will be varied.

The self-assembly is facilitated by the drive to reduce solvation free energy by reducing their hydrophobic surface area exposed to the solvent, in this case water. The procedure adopted for the selective functionalisation of Ag cube faces is given in Fig. 15.30(c). The selective functionalisation was carried out by protecting Ag nanocube faces in contact with a clean Si substrate and functionalising other faces sequentially with solutions of alkanethiols, and PDMS inked with alkanethiols. An aqueous suspension of nanocubes is dispersed onto a plasma-cleaned Si substrate and dried. The sample was immersed in a mercaptohexadecanoic acid (MHA) solution for 1 hr, removed and washed with ethanol. This functionalises all the exposed five faces with MHA. This was immersed in octadecanethiol (ODT) and the sample was sonicated in order to detach the nanocubes from the substrate and sixth face gets functionalised with ODT giving five hydrophilic and one hydrophobic faces. Another set of substrate containing the aqueous suspension of nanocubes is printed with a PDMS stamp inked with ODT in ethanol, and then thoroughly washed with ethanol. Here, the top face of the Ag nanocube gets functionalised. This was immersed in MHA solution and the four exposed faces get functionalised with MHA. This was then immersed in octadecanethiol (ODT) solution and sonicated, upon which the nanocubes from the substrate and the sixth face get functionalised with ODT giving four hydrophilic and two hydrophobic faces. Varying the strategy give distinct SAM-modified Ag nanocubes. The assemblies formed by the nanocubes were observed under SEM. Unfunctionalised cubes did not show any kind of assembly. When only one face of the nanotube was functionalised with hydrophobic ODT, the nanocubes tend to form dimers, joined at the hydrophobic faces in order to try and move this face away from water. Nanocubes with two opposing faces functionalised with ODT-formed linear chains. Cubes having four ODT-functionalised faces are assembled in a sheet-like manner. Ag nanocubes with four hydrophobic faces and one hydrophobic face were mixed in 1:4 ratio, and star-shaped structures were obtained.

When all the six faces were functionalised, they formed 3-D superlattices. Since it is highly hydrophobic, they aggregated spontaneously upon dispersion in water forming black particles at the bottom of the container. The formation of a black suspension on the surface of the meniscus was also seen over time. The structures from this black suspension had 3-D lattices of the Ag nanocubes which increases in size up to 1.2 μm as time goes on. Well-ordered structures of Ag nanocubes were collected only on the surface of the meniscus, while the middle portion was sparsely populated and

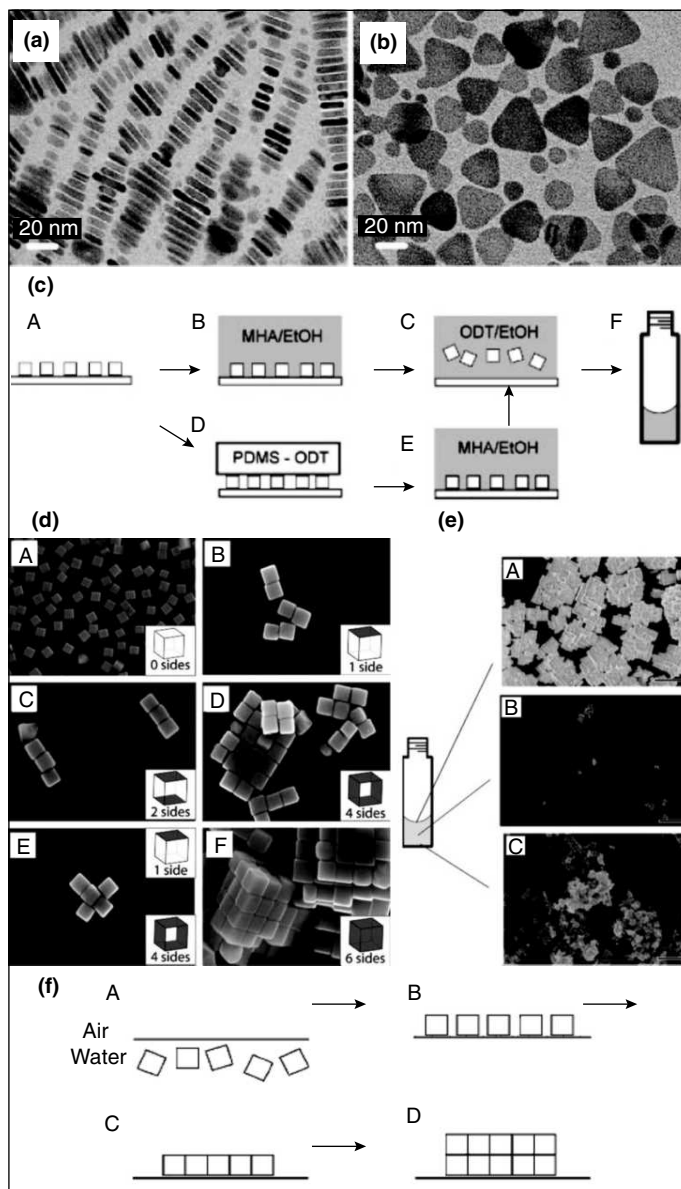


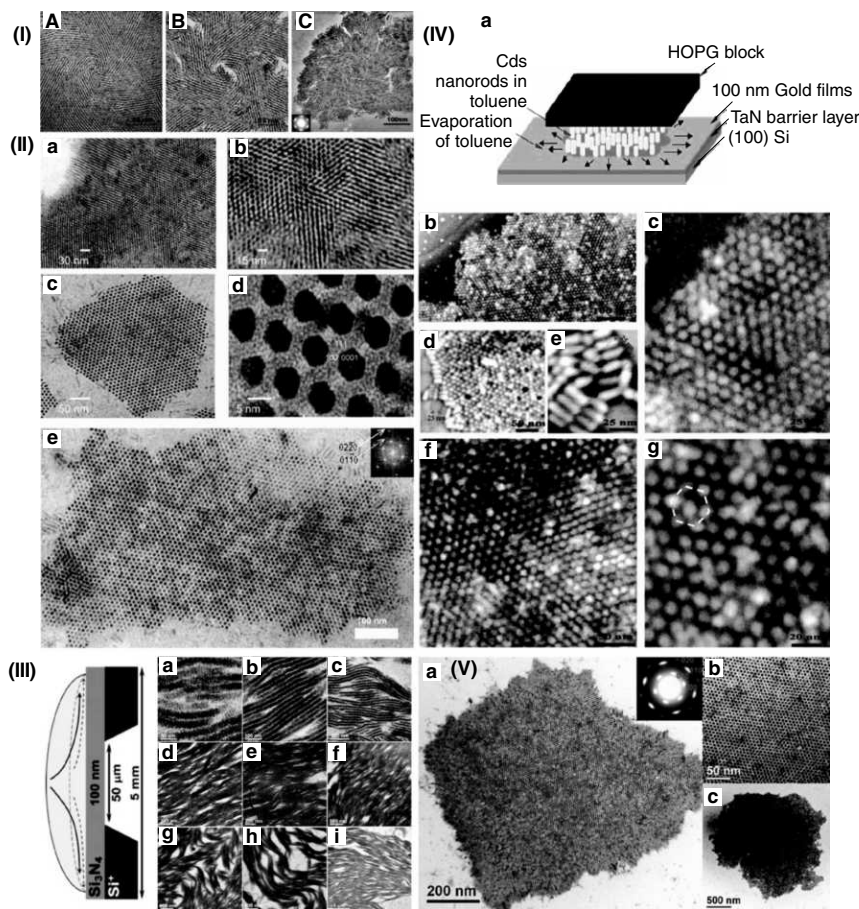
Fig. 15.30 TEM images of Assembly A (a) and B (b) (adapted from Han, et al. (Ref. 45). Copyright (2008) by the American Chemical Society). (c) A schematic representation of specific functionalisation of Ag nanocube faces. (d) SEM images of Ag nanocubes and the assemblies depending up on the functionalisation. (e) SEM images of ODT-functionalised Ag nanocubes sampled at different parts in a reaction vessel. (f) Schematic depicting the mechanism of formation of self-assembly at the air-water interface (adapted from Xia, et al. (Ref. 51). Copyright (2008) by the John Wiley & Sons, Inc.).

the structures did not show any face-to-face assembly. Aggregates formed at the bottom of the vial did not have any face-to-face assembly and only had large indiscriminate aggregates. A schematic depicting the mechanism of Ag nanocubes completely functionalised with a hydrophobic SAM self-assemble into a cubic lattice at the air-water interface is given in Fig. 15.30(f). With the aid of sonication, hydrophobic nature and the surface tension of water, Ag nanocubes are floated onto the water surface. The nanocubes then self-assemble face-to-face at the interface to form a 2-D sheet. As more and more nanocubes come up to the water surface, they get added to the existing structure from the water side, pushing the entire structure upward forming 3-D structures at the interface.⁵¹

15.4 ASSEMBLY OF ANISOTROPIC STRUCTURES OF CdS/CdSe

After gold and silver, Cd-based material is one of the most studied nanostructures owing to its properties. These materials are interesting, because it is possible to design electronic structure inside nanocrystals, like type I and type II heterostructures and make them interesting entities to be used in nanoelectronic devices. The assembly of these materials is well studied. A few interesting examples are given here. The liquid crystalline arrangement of rod-like CdSe nanorods with orientational order and positional disorder was reported by Alivisatos *et al.*⁵² Macroscopic alignment of CdSe nanorods was reported in 2003 by the same group.⁵³ They reported alignment into a nematic liquid-crystalline phase, and to some extent, superlattice structures were formed when these were deposited on a substrate. The formation of superlattice was found to be determined by the liquid-crystalline phase that gets formed prior to complete evaporation of the solvent.⁵³ Weller *et al.*, in 2004, reported the self-assembly of CdSe nanorods into nematic, smectic, and crystalline solids.⁵⁴ The versatility of the method was demonstrated by using CdSe nanorods of varying diameters and lengths as well as utilising highly luminescent CdSe/CdS nanorod heterostructures for the assembly. Layered-colloidal crystals obtained by the assembly exhibited anisotropic optical properties with characteristic birefringence, which was assigned to specific spherulite-like texture of each nanorod assembly. The crystals were grown by the slow destabilisation of a nanocrystal solution upon allowing the diffusion of a nonsolvent into the colloidal solution of nanocrystals. This can be considered as the first report to induce the organisation of nanorod building blocks into highly luminescent 3-D superlattices.⁵⁴

Perpendicular arrays of semiconductor nanorods have potential applications in photovoltaic, field emission, and data storage devices. Several attempts were made to organise CdS/CdSe nanorods in a perpendicular fashion. Russell *et al.* reported “self-corralling” nanorods under an applied electric field, where ligand-functionalised CdSe nanorods in a polymer-matrix phase separate.⁵⁵ They showed that the combined forces of an applied external field and interfacial energy can control the orientation of nanorods and can form dense packing of CdSe nanorods. Because of the permanent dipole moment of CdSe nanorods and due to the inherent dielectric properties, these nanorods in solution will drive the alignment along their long axis, parallel to the field lines of the external field. They got densely packed hexagonal arrays of nanorods aligned along the direction of the applied field. The “corralling” of the nanorod was driven in order to minimise the interfacial energy between the array of nanorods and the surrounding polymer.⁵⁵

**Fig. 15.31**

(I) (A-C) TEM images vertex structures formed when CdSe NRs are deposited on carbon films and after the solvent evaporation self-assembled into superlattices (adapted from Alivisatos, et al. (Ref. 52). Copyright (2002) by the American Chemical Society). (II) TEM images of perpendicularly aligned nanorod superlattices made under electric field (adapted from Alivisatos, et al. (Ref. 56). Copyright (2006) by the American Chemical Society). (III) Schematic of the device used for creating the assembly. (a-i) TEM images of CdSe NR tracks assembled into extended lamella-like superstructures shown at various magnifications (reprinted with permission from Drndic, et al. (Ref. 58). Copyright (2008) by the John Wiley & Sons, Inc.). (IV) (a) The 3-D schematic showing the setup used for monolayer-nanorod assembly (b-g) HRSEM images of a typical perpendicularly aligned nanorod superlattice at various magnifications. Highlighted area in (g) shows hexagonal ordering in the assembled structure (reprinted with permission from Ahmad and Ryan, et al. (Ref. 57). Copyright (2007) by the American Chemical Society). (V) (a-c) TEM image of TDPA- and TOP-capped CdS nanorods with self-assembled organisation in large scale at different magnifications. The inset in (a) shows the diffraction pattern of the bundle (reprinted with permission from Chou, et al. (Ref. 59). Copyright (2008) by the American Chemical Society).

A similar method was adopted by Alivisatos *et al.* also to align CdS nanorods into superlattices.⁵⁶ They found that the combination of a DC electric field and slow evaporation of solvent, like toluene, can be used to generate superlattices of II-VI semiconductor nanorods (CdS) with perpendicular orientation.⁵⁶ A non-electric field induced self-assembly of CdS nanorods into perpendicular monolayers was reported by Ahmed and Ryan.⁵⁷ They used highly-oriented pyrolytic graphite (HOPG) as a template to produce the perpendicular assembly. On a variety of substrates, hexagonally-oriented domains of the size range of $2 \mu\text{m}^2$ were created by this method.⁵⁷ Millimetre-long smectic assembly composed of CdSe nanorods achieved rapidly under non-equilibrium conditions utilising the capillary flow in a drying droplet of a pinned droplet was reported by Drndic *et al.*⁵⁸ This method is important, since this did not need any particular synthesis or solvent, pre-treatment of the substrate or NRs, or external fields. Many nanorod tracks are obtained in the flow due to the strong NR-NR interactions, where nanorods are assembled in a side-by-side manner and to the edge of the droplet forming a coffee ring. When the nanorod arrays reach droplet perimeter, the capillary pressure, which is directed radially outward from the droplet drive the nanorod tracks to stack side-by-side concentrically. A smectic superstructure, which continually grows inward from the droplet perimeter until no more material flows to the area is resulted. The final result is a smectic superstructure, in which nanorods arranged in a parallel manner with respect to each other forming nanorod tracks, which themselves are aligned parallel to each other and to the coffee-ring contours. Hence, the individual nanorods are getting aligned perpendicular to the coffee-ring contours.⁵⁸

Recently, Chou *et al.* reported a strategy to make micrometer long 2-D self-bundled CdS nanorods without the aid of an external directing process. CdS nanorods with tri-*n*-octylphosphine (TOP) and tetradecylphosphonic acid (TDPA) capping having the optimum ratio were prepared. The as-prepared CdS nanorods started to pack together when the concentration was higher than 2.0 wt % in toluene. As the solvent evaporates, the concentration of the solid increases. This results in the decrease of the interfacial energy of the nanorods by interlacing the alkyl chains of surfactants. The first portion of nanorods, standing normal to the substrate, serves as a nucleation site. Hence, the other incoming nanorods tend to assemble in the same direction with the assistance of the hydrocarbon chains on surfactants. Therefore, the self-assembly have leaning bundles at the outer edges and hexagonal packing perpendicular to the substrate inside.⁵⁹

Manna *et al.* recently developed a seeded-growth approach for the synthesis of CdS nanorods in which CdSe nanoparticles were used as seeds to produce asymmetric core-shell CdSe/CdS nanorods.⁶⁰ This on solvent evaporation at the toluene-water interface or under the applied electric field produced large area perpendicularly aligned nanorod arrays. Theoretical study to understand the force that operates in the assembly of nanorods and binds them together was done by Korgel *et al.*⁶¹ They calculated the dipole-dipole attractive force and Van der Waals attraction for the self-alignment of CdS nanorods and found that side-by-side alignment was more favourable than the end-to-end mode of alignment. But, the experimental studies by the same group showed that end-to-end stripes are getting formed instead of side-by-side assembly. So, they concluded that formation of stripes was kinetically controlled and mediated by solvent evaporation.⁶¹ Self-assembly of CdSe nanorods at the oil-toluene-water interface using drying droplet was reported by He *et al.*⁶² The interfacial tension, in-

plane compression and the decrease in surface due to the solvent evaporation was concluded to be the operating force of the assembly. A method to synthesise cylindrical crystalline CdSe/CdS nanorods supercrystals (SCs), which exhibit linearly polarised photoluminescence along their axial direction, were reported recently by Cao *et al.*⁶³ They found that the anisotropic interparticle interactions between nanorods as well as solvophobic interactions between an SC and the surrounding solvent play major

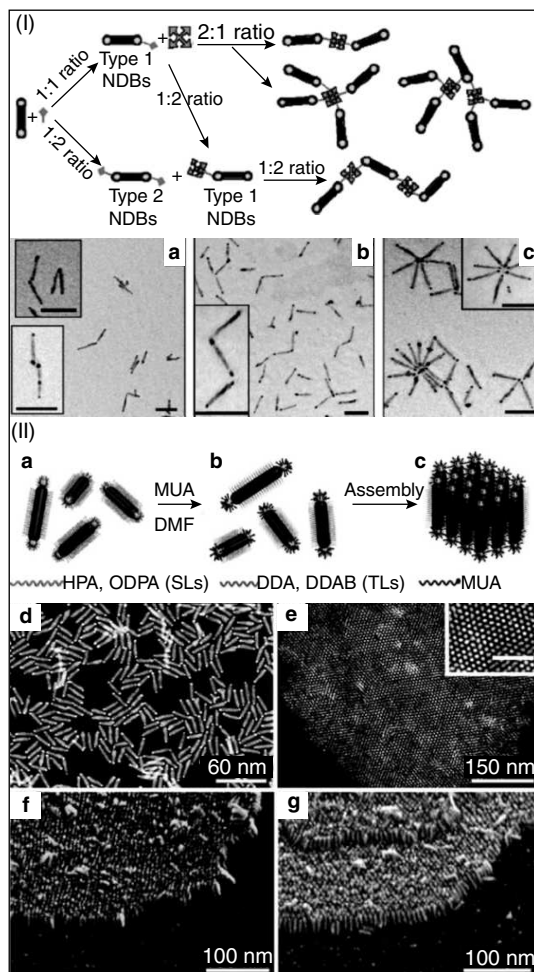


Fig. 15.32

(I) Scheme showing the process of assembling the NRs. (a-c) TEM images (a) dimers of NDBs in different conjugation angles, (b) trimers, and (c) flowers (50 nm scale bars) (adapted from Ubin, *et al.* (Ref. 64). Copyright (2006) by the American Chemical Society). (II) (a-c) Schematic depicting the steps involved in the self-assembly of Au-tipped CdSe NRs. Dark-field TEM image of Au-tipped CdSe NRs, (d) before assembly and (e) top view of the assembly. (f, g) Side view SEM images of the nanorod arrays showing the perpendicular orientation (adapted from Kumacheva, *et al.* (Ref. 65). Copyright (2009) by the American Chemical Society).

roles in controlling the shape of the SCs. SCs adopt the single- or multi-layered structures depending upon their volume.⁶³

The incorporation of different materials, such as metals and semiconductors to form composite nanostructures is an interesting area of research, because it increases functionality many folds. Synergetic properties can arise from the individual properties of constituent NRs or from the combination of the properties of these components. One such material is hybrid metal-tipped semiconductor nanorods termed nanodumbbells (NDBs). Many examples exist and Au tipped CdSe nanorods are one of them. Assembling them into well-ordered structures is interesting, because they may give several new properties. The use of gold tips as anchoring points for the self-assembly using simple dithiol molecules, which preferentially binds onto the gold tips resulting in nanorod chains, was reported by Banin *et al.*⁶⁴ The same group using a similar approach created dimers and trimer chains of NDBs. A biochemical linking strategy was followed in this study. The strong and specific avidin-biotin interaction was utilised to construct head-to-tail assemblies of NDBs. Using disulfide modified biotin, where the disulfide end conjugates to the gold tip, biotin was available for further conjugation with avidin. Avidin can conjugate up to four biotin which results in a flower-like assembly of the NDBs.

A solution-based side-by-side self-assembly of Au-tipped CdSe nanorods into large 2-D superlattices over micrometer area was reported by Kumacheva *et al.*⁶⁵ By changing the total hydrophilic or hydrophobic nature of the solvent for the ligands coating the long side of CdSe nanorods, the assembly was initiated. In the hybrid nanorod, the CdSe segment was coated with a mixture of octadecylphosphonic acid (ODPA) and hexylphosphonic acid (HPA) termed as side ligands (SLs). The Au tips were stabilised with dodecylamine (DDA) and didodecyldimethylammonium bromide (DDAB) termed as tip ligands (TLs). The presence of alkyl chains in SLs and TLs make these structures easily soluble in nonpolar solvents and insoluble in polar solvents. TLs were selectively replaced with 11-mercaptoundecanoic acid (MUA) to render difference in solubilities. MUA was added in a polar solvent and was used for ligand exchange and self-assembly was made in a mixed solvent (dimethylformamide-toluene). In order to minimise the exposure of nonpolar SLs with the polar solvents, nanorods underwent side-by-side assembly. MUAs present on the tip stabilised the formed superstructure by intermolecular hydrogen bonding through carboxylic groups of MUA attached to neighbouring nanorods.⁶⁵

15.5 SOME EXAMPLES OF ASSEMBLY OF ANISOTROPIC STRUCTURES OF OTHER MATERIALS

The scope of this chapter does not allow the complete description of the assembly of all anisotropic structures reported. A few examples pointing towards the diversity of materials and their assembly is given in this section. Pt nanocrystals are important because of their catalytic activity. The self-assembled structures are believed to be ideal catalysts for reducing pollutant gases from the exhausts of automobiles, producing hydrogen from methane, and in the direct methanol fuel cell, etc. The 2-D self-assembly or 3-D structured superlattices of these materials provide opportunity of fabricating nanodevices and templating for the assembly of other structures. The self-assembly of Pt nanoparticles of various shapes

was studied by El-Sayed *et al.* in 2001.⁶⁶ They reported that the addition of dodecanethiol to acrylic acid capped Pt nanoparticle sample containing various shapes and sizes leads to self-assembly. The assembled structures followed an hcp structure. Nanocubes are the most studied system in case of Pt. Tiley and Ren in 2006 reported a strategy to synthesise monodispersity Pt nanocubes, which, due to their high degree of monodispersity, can be readily arranged into 2-D long-range arrays.⁶⁷ The shape-controlled platinum nanocubes and their assembly into 2-D and 3-D superlattices was reported by Petit *et al.*⁶⁸ Assembly of bimetallic Pt-based cubes also has been reported. Oriented assembly of FePt cubes was reported by Sun *et al.*⁶⁹ They prepared FePt nanocrystal superlattice arrays with controlled texture and magnetic alignment. Palladium nanostructures are important, since they show high hydrogen solubility and can act as an effective catalyst for Stille, Heck, and Suzuki reactions. Xu *et al.* recently reported a versatile seed mediated method for the preparation of Pd nanocubes with a high degree of monodispersity.⁷⁰ Because of the monodispersity, they tend to self-assemble into ccp arrays on the SEM plate.⁷⁰ The monodisperesed synthesis and self-assembly of Pd nanobricks was reported by Umar and Oyama.⁷¹ Assembling icosahedral Pd nanoparticles into superlattice structures was reported by Lee *et al* recently.⁷² Formation self-assembled structures of Au@Pd nanocubes was reported by Tian *et al.*⁷³

Cu₂S, commonly known as chalcocite, is a p-type semiconductor with a bulk band gap of 1.2 eV. It has been widely used in solar cells, cold cathodes, and nanoscale switches, etc. The anisotropic hexagonal crystal structure of Cu₂S can be utilised to adjust the growth rate along [001] and [100] directions to obtain shape controlled nanocrystals. A solventless synthesis for the preparation of Cu₂S crystals of shape ranging from circular to hexagonal plates was reported first by Korgel *et al.*⁷⁴ They found that these sterically stabilised colloidal copper sulfide nanodisks spontaneously assemble with face-to-face close packing, when the solvent is evaporated from concentrated dispersions to form a columnar assembly. The long-range orientational order was confirmed by SAXS and GISAXS. Time-resolved SAXS showed phase transition from the isotropic-to-columnar phase upon solvent evaporation and GISAXS proved that the columns orient perpendicular to the substrate. They also found that hexagonal close-packed ordering of the columns is relatively extensive, but within the column, the disks are not periodic.^{74, 75} Li *et al.* reported a water-oil interface confined method to synthesise monodisperse Cu₂S nanocrystals and their multilayer superlattice assemblies.⁷⁶ The phase-selective synthesis of monodisperse CuS and Cu_{1.75}S nanodisks with controlled sizes and shapes by high-temperature chemical reaction of CuCl₂ and S in oleylamine and their self-assembly into monolayer or multilayer ribbon-like nanostructures by face-to-face stacking was reported by Yang *et al.*⁷⁷ Through simple solution-phase thermolysis of the copper dodecanethiolate polymer precursor, Cu₂S nanocrystals and superlattices were synthesised by Mai *et al.*⁷⁸ Cu₂S nanodisks, spheres and hexagon nanoplates were assembled into superstructures through this method. They believed that the assembled structures are closely related to the lamellar structure of the copper thiolate precursor.⁷⁸

Zinc oxide (ZnO), an n-type semiconductor with a wide band gap energy of 3.3 eV, high exciton binding energy of 59 meV, is an important material, which can function as a component in UV light-emitting diodes and as an electron-transporting layer in organic and dye sensitised solar cells and sensors. Takai *et al.* reported a process to fabricate films of hexagonal ZnO nanorod arrays on Si

surfaces modified with hydrofluoric acid (HF) etching and self-assembled monolayers (SAMs).⁷⁹ An aqueous solution-based wet chemical method has been reported for synthesising ZnO nanorod arrays with controllable diameter and lengths on different substrates by Chen and Gao.⁸⁰ Through thermal decomposition of zinc acetate, a thin film of ZnO nanocrystals were coated on the substrate. This was used as a seed layer for the subsequent growth of nanorods in aqueous solutions at low temperature. Highly-ordered nanorod film spread over large area was fabricated using this method.⁸⁰ Hexagonally patterned, vertically aligned ZnO nanorod arrays using nanosphere lithography technique was reported by Xie *et al.*⁸¹ A polystyrene microsphere self-assembled monolayer was first prepared and hexagonal patterns of gold particles were prepared on it through wet-etching method. This act as a catalyst for the nanorod growth. Through catalyst-initiated epitaxy, ZnO nanorods were grown on each of these catalyst sites, preserving the original hexagonal pattern.⁸¹ Lee *et al.* reported a seed-layer based solution chemistry route to make tunable arrays of ZnO needles and nanorods.⁸² They studied the effect of pH and 1,3-diaminopropane additive concentration on the morphology of ZnO nanorod and nanoneedle arrays.⁸² Tasaka *et al.* reported a room-temperature electrochemical method for the electrophoresis deposition of anionic polystyrene spheres on a conductive glass substrate followed by the electrodeposition of ZnO in aqueous solutions to fabricate arrays of nano-cauliflower shaped ZnO nanoparticles.⁸³

ZnS is one of the most important II-VI semiconductors. Efrima and Pradhan reported a method to synthesis highly uniform ZnS nanorods and nanowires of extremely small widths and assemble supercrystals of uniform nanorods and ordered assemblies of nanowires.⁸⁴ Through a synchronous end-to-end attachment process of nanorods, nanowires were made. They found that after synthesis, nanorods and wires spontaneously self-assemble into highly-ordered crystalline phases. Using capping agents of varying alkyl chain lengths, the interparticle spacing in these supercrystals can be tuned. The assembly can be obtained in various substrates through various techniques. The nanowires were assembled into large-scale parallel superstructures and crossed-wire, grid-like two-layer arrays.⁸⁴ A phase-controlled synthesis of ZnS nanocrystals and the ordered assembly nanorods and nanodots was reported by Li *et al.*⁸⁵ The mechanism and the strategies of assembling 1-D ZnS nanorods on 2-D scale were also discussed in this report. Upon deposition of a drop of dilute solution of NRs on substrate, the solvent evaporation makes the concentration to increase with time. The free volume available to each rod also decreases as the solvent gets evaporated. This makes the rods to aggregate or align side-by-side under the influence of directional capillary force and Van der Waals attraction. This results in the increase in the viscosity and finally freezes the local liquid-like structure to form lyotropic crystalline phase. The concentration of the nanorods in solution, the nature of the capping molecules, and the evaporation rate of the solvent are three main factors, which can affect the quality as well as the range of the assembly.⁸⁵

Trigonal-tellurium (t-Te), a p-type semiconductor, has a very narrow band gap and has attracted a great deal of interest because of its good photoconductivity, photoelectricity, thermoelectricity, catalysis, nonlinear optical properties, and high piezoelectricity. Self-assembly of Te nanorods to Te microrods was reported by Sanyal *et al.*⁸⁶ Te nanorods were prepared by reducing bulk Te powder using an aqueous solution of sodium dithionite and then oxidising the solution in air to get Te nanorods.

Centimeter-long rods were made by controlling the airflow, upon which these nanorods self-assemble to give the microstructure.⁸⁶ The self-organisation of Te nanorods to v-shaped assemblies was reported by Kotov *et al.*⁸⁷ They found that in a suspension of Te nanorods, short nanorods of length 50 nm tend to form v-shaped or checkmark-like assemblies while long nanorods of length 2200 nm remained as such. Using Brownian dynamics simulations, they modeled this observation and explained the experimental observations.^{87,88} Alignment of Te nanorods on a solid substrate via the magnetisation-alignment-demagnetisation (“MAD”) process was reported by Muller *et al.*⁸⁹ Te nanorods covered with a shell of poly(*tert*-butyl methacrylate) was prepared and they were made magnetic by the treatment with magnetite nanoparticles, which assembles on the surface of the rods through a hydrophobic interaction in THF to form magnetic nanocylinders. This, upon interaction with magnetic field, aligns in the direction of the magnetic field. On acid etching, the magnetic nanoparticles are etched away leaving the assembled nanostructures behind.⁸⁹

Titanium dioxide (TiO₂), is a useful material having numerous potential applications in diverse area such as photocatalysis, liquid solar cells, and electroluminescent hybrid devices. Assembly of anisotropic TiO₂-based systems has been well studied. Self-assembled end-to-end structure of oligomeric TiO₂ nanorods using the biotin-avidin interaction was reported by Rajh *et al.*⁹⁰ One of the recent studies was on the 2-D self-assembly of TiO₂ nanoleaves via supramolecular interactions. It was found that the assembly occurs in a facet-selective manner. The single-crystalline TiO₂ nanoleaves were functionalised with catechol-group-terminated Zn(II)-porphyrin (ZnP), which was coordinated with *trans*-2,2'-ethylene 4, 4'-bipyridyl (EB). EB cross-links the adjacent TiO₂ nanoleaves along the [101] face, resulting in a face-selective, self-assembled, 2-D stacking structure in a “side-by-side” fashion.⁹¹

Barium chromate (BaCrO₄) nanoparticles were assembled into different structures by Mann *et al.*⁹² They demonstrated that BaCrO₄ can be organised into complex structures through the interfacial activity of reverse micelles and microemulsions. The interdigitation of surfactant molecules attached to specific nanoparticle crystal faces are the driving force for the assembly. They produced linear chains, rectangular superlattices and long filaments of BaCrO₄ nanocrystals as a function of reactant molar ratio, which influences the fusing of reverse micelles and microemulsion droplets.⁹² 2-D nanorod monolayer assembly of BaCrO₄ using Langmuir-Blodgett technique was reported by Yang *et al.*⁹³ Pressure-induced isotropic-nematic-smectic phase transitions and transformation from monolayer to multilayer nanorod assembly were also discussed in this work.⁹³ Rare-earth nanocrystals have drawn great interest owing to their unique physical and chemical properties and potential applications in the fields of luminescence devices, biochemical probes, and medical diagnostics. Evaporation-induced self-assembly of rare-earth oxide nanopolyhedra, nanoplates, and nanodisks was reported by Yan *et al.*⁹⁴ Self-assembly of LaF₃ triangular nanoplates was also reported by the same group.⁹⁵ They also reported the self-assembly of sodium rare-earth fluoride nanocrystals of various shape.⁹⁶ All these assemblies were of short-range order. Langmuir-Blodgett mediated controllable assembly of diverse rare-earth nanocrystals was reported by the same group recently.⁹⁷ Using this technique, large-area films of various nanoparticles, like NaYF₄, Yb, Er spherical nanoparticles, LiYF₄ nanopolyhedra, triangular-shaped LaF₃, square shaped CaF₂, hexagonal EuF₃ nanoparticles, were assembled.⁹⁷ Langmuir-Blodgett (LB) assembly of vanadium dioxide (VO₂) nanowires functionalised with stearic acid (SA)

and cetyltrimethylammonium bromide (CTAB) was reported by Dai *et al.*⁹⁸ Ringer *et al.* reported the self-assembly and self-orientation of truncated octahedral magnetite nanocrystals.⁹⁹ External magnetic field induced self-assembly of octahedral magnetite nanocrystals was recently reported by Xiong *et al.*¹⁰⁰ The self-assembly of lead zirconate titanate (PZT) cubes into single crystal like microcrystals was reported by Riman *et al.*¹⁰¹ A method to prepare transparent WO₃ nanorod film through the assembled coating of WO₃ nanorod suspension onto ITO-coated glass was reported by Lee *et al.*¹⁰² The assembly was dependent on the drying rate of the film, the concentration of suspension, and the aspect ratio of nanorods, but independent of the surface properties of substrates. The assembly occurred through an aggregation-deposition process.¹⁰² β -ferric oxyhydroxide (β -FeOOH), is an interesting iron based material, which shows a tunnel-type structure in which the iron atoms are strongly bonded to the framework forming the tunnels and is reported to be a promising candidate for an active iron-based material for lithium batteries. Zocher and Heller reported the formation of “Schiller layers” in the stable sol sediments containing ordered structures and found that they exhibit brilliant interference colours from β -FeOOH.^{103, 104, 105} The assembly of this system has been very well studied. The atomic force microscopic investigation of smectic or multilayer, structures in dry sol sediments of β -FeOOH was reported by Maeda and Maeda.¹⁰⁶ They found that the smectic structure locally has an in-layer square morphology.¹⁰⁶ A longer-ranged bond-orientational order will exist even after the defects destroy the 2-D crystallinity. The coexistence of several smectic domains, each of which has a distinct orientation, and mono- and several-folded layers confined in the sols was also observed.¹⁰⁶

15.6 SOME APPLICATIONS

Some of the useful applications projected from such assemblies are given below. This, in no way, includes all the applications that are possible with such regular architectures with diverse properties. Since a review of all the applications is beyond the scope of the present chapter, some specific examples are only cited. Since most part of the review concentrated on the assembly of GNR assemblies and assembly of Au and Ag nanostructures, some examples utilising such assemblies are given. Some examples of applications based on semiconducting and oxide nanostructure assemblies are also given.

(i) Plasmonic waveguides

Nanomaterials are interesting in photonic device applications, because, through careful fabrication, it is possible to guide electromagnetic energy with a lateral mode confinement below the diffraction limit of light, which is not possible through conventional waveguides or photonic crystals. It can be achieved along chains of closely spaced metal nanoparticles, which convert the optical mode into non-radiating surface plasmons. These arrays can be prepared through electron beam lithography or self-assembly techniques. Maier *et al.* showed experimentally that through closely-spaced silver nanorods, electromagnetic energy can be transported from a localised sub-wavelength source to a localised detector over distances of about 0.5 μm .¹⁰⁶ The individual rods in the waveguide structures consist of 90 nm long Ag nanorods (30 nm \times 30 nm width/thickness) and an inter-particle spacing of 50 nm between adjacent particles. The long axes of the individual nanorods were oriented perpendicular to the waveguide chain axis, which allows an increased near-field coupling between the particles. Using

the tip of a near-field scanning optical microscope, the waveguide was excited by laser light from a dye laser at a wavelength of 570 nm, corresponding to the single-particle resonance and using fluorescent nanospheres (carboxyl-coated polystyrene nanospheres filled with fluorescent molecules), the energy transport through the waveguide was probed. The local excitation subsequently propagates along the nanoparticle structure and excites a fluorescent nanosphere placed on top of a waveguide at a distance from the excitation source. Energy transport through the waveguide results in dye emission from the fluorescent particle which proves the energy transfer. Energy attenuation lengths of several hundred nanometres propose the use of these plasmon waveguides as functional end-structures in integrated optical devices.¹⁰⁷

(ii) Detection of micromolar concentration of aminoacids

The change in absorption characteristics shown by the GNRs upon assembling was used for the selective detection of specific amino acids at concentrations as low as $\sim 2 \mu\text{M}$. The shift in LSP of GNRs upon the addition of cysteine and glutathione was used for the selective detection of these two amino acids in presence of various other amino acids. As described earlier in the chapter, the addition of cysteine or glutathione resulted in the end-to-end assembly of GNRs and the LSP shifted to higher wavelength region and decreased in intensity as the concentration of the amino acids was increased. They were able to detect as low a concentration as $1.75 \mu\text{M}$ in the case of cysteine.¹⁰⁸

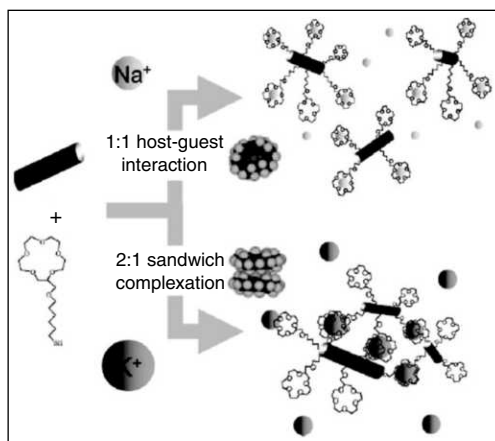


Fig. 15.33 Schematic images of selective ion recognition mechanisms in the gold nanorods with 15-crown-5-SH system via 1:1 (Na^+) or 2:1 sandwich (K^+) complexation in aqueous solution (adapted from Torimitsu, et al. (Ref. 35). Copyright (2007) by the Royal Society of Chemistry, London).

(iii) Specific detection of ions

GNR anchored with specific crown ethers was used for the selective detection of ions. Depending upon the size of the crown ether, it will specifically attach to ions of matching sizes, resulting in the assembly of nanorods and corresponding UV/Vis spectral changes. For example, gold nanorods

functionalised with 15-crown-5-SH will only get attached on to K^+ ions and will remain unaffected with other metal ions. This is because only K^+ can bind with 15-crown-5-SH via the formation of a 2:1 sandwich complex between the two while others cannot due to the difference in size. GNRs anchored with 12-crown-4-SH can only bind with Na^+ by the formation of analogous 2:1 sandwich complex, because the sizes of 12-crown-4 cavity and Na^+ ionic diameter are comparable as that between 15-crown-5 and K^+ . Hence in this way K^+ and Na^+ was detected selectively.¹⁸

(iv) Arsenic detection from drinking water

Anisotropic nanoparticles are proclaimed to be ideal substrates for SERS-based applications. The Raman signals when a molecule is adsorbed on a corrugated metal are about 6 to 12 orders of magnitude higher than the signal it would give if deposited on a flat substrate. This enhancement is generally called as SERS. A discussion of SERS may be found elsewhere in this book. In metallic nanoparticles, due to surface plasmon resonance, there is an intense local amplification of the electric field. Size, shape and proximity of nanostructure can affect the magnitude of the localised surface plasmons and its frequency, which in turn affects the extent of Raman enhancement. Anisotropic nanostructures exhibit higher enhancement near the tips. When they are assembled into superstructures, they come in very close proximity and the electromagnetic coupling between nanostructures can result in higher enhancement. These spots are often referred to as “hot spots”. In a regular assembly, there will be numerous “hot spots” making this assembled structures ideal substrate for SERS-based application.

Yang *et al.* made self-assembled structures of silver polyhedral structures like cubes, cuboctahedra, and octahedra, by LB method as explained earlier. These assembled structures were transferred onto a Si substrate and were used for sensing As from contaminated waters. In Fig. 15.34d the SERS spectra obtained from various crystals are shown. The intense peak at 800 cm^{-1} corresponds to the ν_1 (A1) symmetric As-O stretch. The broad peak at 425 cm^{-1} is a superposition of ν_2 (A1) and ν_5 (E) stretching modes of the arsenate ion. The octahedral particles gave both the highest enhancement factor and best sensitivity for 1 ppb arsenate. A linear dose response was also shown with increasing concentrations enabling the quantitative determination of arsenate concentration at levels that are an order of magnitude below the current WHO guidelines. Using this method, they found that the two most common oxidation states of arsenic, namely, arsenate (As^V) and arsenite (As^{III}) can be distinguished. For a mixture of both arsenate and arsenite, both can be detected simultaneously. The ν_1 (A1) symmetric As-O stretch for arsenite comes around 750 cm^{-1} , whereas that for arsenate appears at 800 cm^{-1} (Fig. 15.34e). They also found that low-arsenic concentrations can be detected even in the presence of high concentrations of other ions like sulphates (10 mM) and phosphates (1 mM).¹⁰⁹

(v) Molecular sensing using SERS

LB assembly of silver nanowires was used for molecular sensing applications by Yang *et al.* These assemblies showed an enhancement factor of the order of 2×10^9 for Rhodamine 6G (R6G) molecule. The observed large enhancement factors suggested that these assemblies can be used as solid substrates for carrying out molecular sensing with high sensitivity and specificity. They tested this capability for the detection of 2,4-dinitrotoluene (2,4-DNT), the most common nitroaromatic compound for

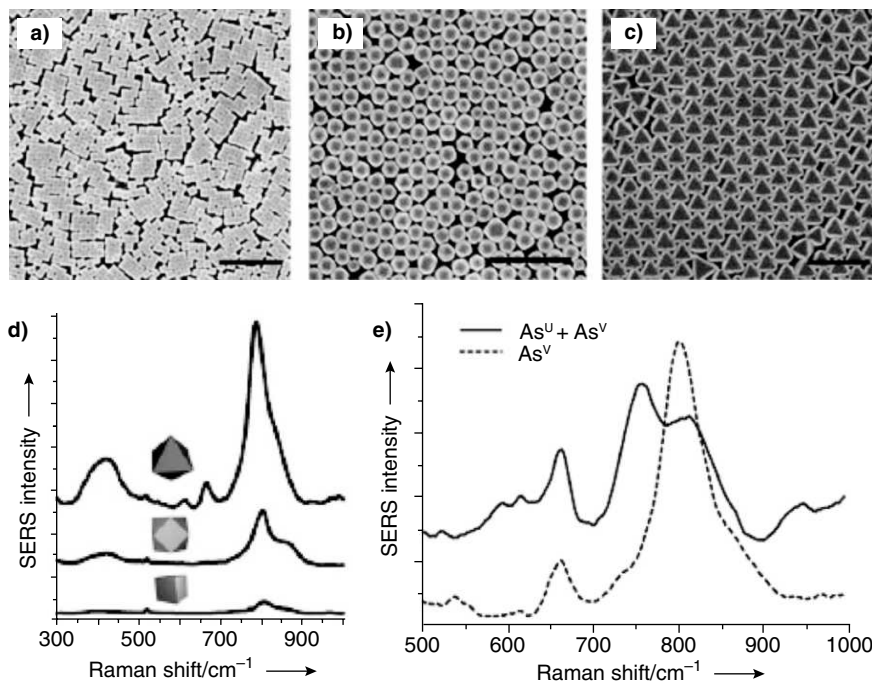


Fig. 15.34 SEM images showing close packed films of (a) cubes, (b) cuboctahedra, and (c) octahedra; scale bars are 1 μm . (d) SERS spectra collected on LB films of each of the nanocrystal shapes exposed to $1 \times 10^{-6} \text{M}$ arsenate solution. (e) Spectra showing the chemical sensitivity of the system. The spectra were obtained for 18 ppb arsenate and arsenite solutions (adapted from Yang, *et al.* (Ref. 109). Copyright (2008) by the John Wiley & Sons, Inc.).

detecting buried landmines and other explosives. Figure 15.35 shows the SERS spectrum of 2,4-DNT. The feature at 1348 cm^{-1} corresponding to the vibration of nitro group, used for the detection of 2,4-DNT can be clearly seen. A sensitivity of approximately 0.7 pg was achieved.

The advantages of using this substrate are: (i) the surface properties of these nanowire films are highly reproducible and well-defined as compared to other systems; (ii) the sharp vertices, noncircular pentagonal cross-sections and inter-wire coupling of the nanowires can result in larger field enhancement factors, offering higher sensitivity; (iii) strong inter-wire coupling within the film enables SERS experiments with a variety of excitation sources; and (iv) these substrates can be readily used for both solution phase and solid phase experiments.⁴⁸

(vi) Assembled semiconductor nanorod heterostructures as biomarkers

Ryan *et al.* recently devised a strategy to fabricate water dispersible close-packed disk-shaped assemblies of CdS, CdSe and CdTe using triblock copolymer surfactants of the form PEO_xPPO_yPEO_x (PEO: polyethylene oxide, PPO: polypropylene oxide). They used these assemblies as fluorescent biomarkers.

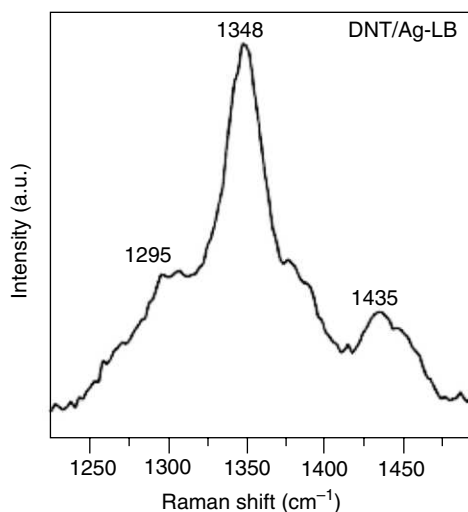


Fig. 15.35 SERS spectrum of 2,4-DNT on the thiol-capped Ag nanowire monolayers (adapted from Xia, *et al.* (Ref. 48). Copyright (2003) by the American Chemical Society).

In-vitro studies were undertaken and they showed an excellent uptake by human vascular smooth muscle (VSM) cell. High loading into the cells was possible since the uptake was done without the use of any transfection agents. The uptake was very easy, fast and irreversible internalisation starts during the first 20 min of incubation with no excretion or further aggregation even after 24 hr. The assembled structures showed strong membrane and cell-specific fluorescence at low laser intensity in a cell line. Two types of interactions were seen between the nanorods assemblies and cell lines. (i) Adsorption of the nanostructures on the cell membrane giving membranous fluorescence in the blue spectral region; and (ii) internalisation of the NRSCs inside the cell-giving intracellular fluorescence in the red region. For these superstructures, the total intensity of emission is proportional to the number of rods and their size can potentially be tuned to specifically match different biological entities, which are not possible in discrete nanorods making the superstructures more interesting.¹¹⁰

(vii) Gold nanooctahdra based glucose biosensor

Chio *et al.* recently reported a molecularly mediated assembling strategy to fabricate a layered superstructure of gold nano-octahedra.¹¹¹ They used this assembled structure as the host matrix for a glucose sensor. Single-layered Au nanooctahedra/glucose oxidase (GOx) system and spherical particles/GOx system were compared to check the performance of the sensor. Au nanooctahedra system exhibited a greater voltammetric response compared to spherical particle system under the same conditions showing the dependence of the sensor activity on the shape of the Au particles used. Au nanooctahedra-based glucose biosensor showed a high level of sensitivity in the range of $0.349 \mu\text{A mM}^{-1}$. The system gave a fast response (within several seconds), and a wide response range (from 0.125 to 12 mM) also.¹¹¹

(viii) TiO₂ nanorod assemblies and ZnO nanopillar self-assemblies for photovoltaic devices

Hashimoto *et al.* fabricated an array of TiO₂ nanorod assemblies on a flat TiO₂ surface via a low temperature sol-gel reaction in a reverse micelle system.¹¹² Conjugated with a semiconducting polymer, these arrays were used for constructing photovoltaic devices. They found that these TiO₂ nanorod assemblies can function as an efficient exciton collector in polymer photovoltaic devices. This resulted in improved power conversion efficiency (PCE) with a relatively high fill factor. Since these structures are projected from the flat TiO₂ substrate, they can provide direct pathways for electron transport making them ideal for photovoltaic applications. For a simulated solar light irradiation of 100 mW/cm², a short circuit current density (*I*_{sc}) of 0.33 mA/cm², an open circuit voltage (*V*_{oc}) of 0.87 V, and a fill factor (FF) of 0.49 were seen, resulting in a PCE of 0.14 per cent for the device with flat TiO₂ alone. But for the device containing the nano-assembled structure, an increased performance was obtained. A PCE up to 0.39 per cent and *I*_{sc} of 0.95 mA/cm², *V*_{oc} of 0.88 V, and FF of 0.47 was also obtained. External quantum efficiency (EQEs) plots showed that EQE is maximum under 510 nm radiation and under a monochromatic light of 510 nm wavelength (0.2 mW/cm²), the FF for the device reached as high as 0.64. Such a high FF of the device with the TiO₂ nanostructures was explained to be due to the effective electron transport within the TiO₂ nanorods, because of their single crystalline nature and good connection with the flat TiO₂ layer.¹¹²

Feng *et al.* through a low temperature strategy inserted oriented zinc oxide nanopillars into organic photovoltaic devices based on a blend of poly(3-hexylthiophene) and fullerene.¹¹³ The dependence of ZnO morphology on the photovoltaic performance on was also studied. The stability of the device was also studied. The photovoltaic performance of devices with a ZnO layer was enhanced compared to that without a ZnO layer. The performance improved further when an oriented ZnO porous nanopillar structure was used. This photovoltaic cell demonstrated a high efficiency, a monochromatic EQE of over 50 per cent at the peak wavelength, an *I*_{sc} of 5.79 mA cm⁻², a *V*_{oc} of 0.43 V, an FF of 49 per cent and a PCE of 1.22 per cent under an illumination intensity of 100 mW/cm². They found that the oriented ZnO nanopillar array plays an important role in collecting photogenerated electrons and acts as a conducting path to the electrode.¹¹³

(ix) Application of self-assembled vanadium pentoxide (V₂O₅) nanorods in lithium-ion batteries

A facile method to self-assemble V₂O₅ nanorods into microspheres was reported by Wan *et al.*¹¹⁴ The as-prepared vanadium hollow microspheres when calcined changes into crystalline V₂O₅ without changing their morphologies. These crystalline V₂O₅ products showed improved electrochemical properties upon using as the cathode material in lithium-ion batteries. The charge–discharge capability of the microspheres was investigated by using V₂O₅ as the cathode in a lithium-ion battery. The capacity was as high as 286.4 mAhg⁻¹ with charge–discharge efficiency up to 97.2 per cent in the potential range from 2.0 to 4.0 V implying the utility of this assembled structure as a cathode material.¹¹⁴

(x) Micropatterned ZnO/SiO₂ core/shell nanorod arrays and DNA hybridisation detection

Zhi *et al.* fabricated micropatterned ZnO/SiO₂ core-shell nanorod arrays on nanocrystalline diamond (NCD) film surfaces and used these patterns as a fluorescence signal enhancing platform

for DNA hybridisation detection.¹¹⁵ Since amine groups are useful for attaching biomolecules, amine-functionalised silica shells were coated onto ZnO nanorod surfaces by a co-condensation of TEOS and APTES. This was utilised to obtain a specific interaction between DNA and ZnO nanostructures. The hybridisation test results indicated that the materials had high sensitivity and specificity. They found that by using ZnO/SiO₂ nanorod arrays, the fluorescence signal getting collected is greatly enhanced. Nonspecific adsorption effect was also decreased giving it an advantage over single ZnO structures. This procedure has considerable benefits to various applications, such as enzyme biosensors, electrogenerated chemiluminescence (ECL) detection, nucleic acid and protein assays, DNA separation, purification, and genetic engineering.¹¹⁵

15.7 CONCLUSIONS

In this chapter, we saw that there are several ways to assemble anisotropic nanostructures, especially 1-D nanostructures. The assembly utilises weak interactions between the protecting molecules, groups or ions. Monodispersity of the starting materials is an important quality of the materials used. However, inherent properties of the nanosystems, such as magnetism or dipole moment, can also be used to create assembly. Assembled structures can be created on substrates or free-standing assemblies can be created. They can also form crystals. These materials often exhibit liquid crystalline order. The type of self-assembly and the properties of the assembly depend on the precursor material. Luminescence, magnetism, optical transport, etc. can all be seen in such systems. These assemblies may be used for diverse applications. A selection of these is presented.

REFERENCES

1. B. Nikoobakht, Z.L. Wang and M.A. El-Sayed, 'Self-assembly of gold nanorods', *J. Phys. Chem. B*, 104, (2000), 8635.
2. T.K. Sau and C.J. Murphy, 'Self-assembly patterns formed upon solvent evaporation of aqueous cetyltrimethylammonium bromide-coated gold nanoparticles of various shapes', *Langmuir*, 21, (2005), 2923.
3. E. Dujardin, S. Mann, L.-B. Hsin and C.R.C. Wang, 'DNA-driven self-assembly of gold nanorods', *Chem. Commun.*, (2001), 1264.
4. B. Pan, L. Ao, F. Gao, H. Tian, R. He and D. Cui, 'End-to-end self-assembly and colorimetric characterisation of gold nanorods and nanospheres via oligonucleotide hybridisation', *Nanotechnology*, (2005), 1776.
5. J.-Y. Chang, H. Wu, H. Chen, Y.-C. Ling and W. Tan, 'Oriented assembly of Au nanorods using biorecognition system', *Chem. Commun.*, (2005), 1092–94.
6. C. Wang, Y. Chen, T. Wang, Z. Ma and Z. Su, 'Biorecognition-driven self-assembly of gold nanorods: A rapid and sensitive approach toward antibody sensing', *Chem. Mater.*, 19, (2007), 5809.
7. K.K. Caswell, J.N. Wilson, U.H.F. Bunz and C.J. Murphy, 'Preferential end-to-end assembly of gold nanorods by biotin-streptavidin connectors', *J. Am. Chem. Soc.*, 125, (2003), 13914.

8. Y. Wang, Y.F. Li, J. Wang, Y. Sanga and C.Z. Huang, 'End-to-end assembly of gold nanorods by means of oligonucleotide–mercury(II) molecular recognition', *Chem. Commun.*, 46, (2010), 1332.
9. S.T. Shibu Joseph, B.I. Ipe, P. Pramod and K.G. Thomas, 'Gold nanorods to nanochains: Mechanistic investigations on their longitudinal assembly using α,ω -alkanedithiols and interplasmon coupling', *J. Phys. Chem. B.*, 110, (2005), 150.
10. K.G. Thomas, S. Barazzouk, B.I. Ipe, S.T.S. Joseph and P.V. Kamat, 'Uniaxial plasmon coupling through longitudinal self-assembly of gold nanorods', *J. Phys. Chem. B.*, 108, (2004), 13066.
11. W. Ni, R.A. Mosquera, J. Pérez-Juste and L.M. Liz-Marzán, 'Evidence for hydrogen-bonding-directed assembly of gold nanorods in aqueous solution', *J. Phys. Chem. Lett.*, 1, (2010), 1181.
12. P.K. Sudeep, S.T.S. Joseph and K.G. Thomas, 'Selective detection of cysteine and glutathione using gold nanorods', *J. Am. Chem. Soc.*, 127, (2005), 6516.
13. S. Zhang, X. Kou, Z. Yang, Q. Shi, G.D. Stucky, L. Sun, J. Wang and C. Yan, 'Nanonecklaces assembled from gold rods, spheres, and bipyramids', *Chem. Commun.*, (2007), 1816.
14. G. Kawamura, Y. Yang and M. Nogami, 'End-to-end assembly of ctab-stabilised gold nanorods by citrate anions', *J. Phys. Chem. C.*, 112, (2008), 10632.
15. C.J. Orendorff, P.L. Hankins and C.J. Murphy, 'pH-triggered assembly of gold nanorods', *Langmuir*, 21, (2005), 2022.
16. T.S. Sreeprasad, A.K. Samal and T. Pradeep, 'One-, two-, and three-dimensional superstructures of gold nanorods induced by dimercaptosuccinic acid', *Langmuir*, 24, (2008), 4589.
17. K. Mitamura, T. Imae, N. Saito and O. Takai, 'Fabrication and self-assembly of hydrophobic gold nanorods', *J. Phys. Chem. B.*, 111, (2007), 8891.
18. H. Nakashima, K. Furukawa, Y. Kashimura and K. Torimitsu, 'Self-assembly of gold nanorods induced by intermolecular interactions of surface-anchored lipids', *Langmuir*, 24, (2008), 5654.
19. D.A. Walker and V.K. Gupta, 'Reversible end-to-end assembly of gold nanorods using a disulfide-modified polypeptide', *Nanotechnology*, (2008), 435603 (9pp).
20. Y.-T. Chan, S. Li, C.N. Moorefield, P. Wang, C.D. Shreiner and G.R. Newkome, 'Self-assembly, disassembly, and reassembly of gold nanorods mediated by bis(terpyridine)–metal connectivity', *Chem. Eur. J.*, 16, (2010), 4164.
21. M.A. Correa-Duarte, J. Pérez-Juste, A. Sánchez-Iglesias, M. Giersig and L.M. Liz-Marzán, 'Aligning Au nanorods by using carbon nanotubes as templates', *Angew. Chem. Int. Edit.*, 44, (2005), 4375.
22. M.A. Correa-Duarte and L.M. Liz-Marzán, 'Carbon nanotubes as templates for one-dimensional nanoparticle assemblies', *J. Mater. Chem.*, 16, (2006), 22.
23. B.P. Khanal and E.R. Zubarev, 'Rings of nanorods', *Angew. Chem. Int. Edit.*, 46, (2007), 2195.
24. V.R.R. Kumar, A.K. Samal, T.S. Sreeprasad and T. Pradeep, 'Gold nanorods grown on microgels leading to hexagonal nanostructures', *Langmuir*, 23, (2007), 8667.
25. M. Das, L. Mordoukhovski and E. Kumacheva, 'Sequestering gold nanorods by polymer microgels', *Adv. Mater.*, 20, (2008), 2371.
26. C. Wang, Y. Chen, T. Wang, Z. Ma and Z. Su, 'Monodispersed gold nanorod-embedded silica particles as novel raman labels for biosensing', *Adv. Funct. Mater.*, 18, (2008), 355.

27. J. Mieszawska, G.W. Slawinski and F.P. Zamborini, 'Directing the growth of highly aligned gold nanorods through a surface chemical amidation reaction', *J. Am. Chem. Soc.*, 128, (2006), 5622.
28. K. Honda, Y. Niidome, N. Nakashima, H. Kawazumi and S. Yamada, 'End-to-end assemblies of gold nanorods adsorbed on a glass substrate modified with polyanion polymers', *Chem. Lett.*, 35, (2006), 854.
29. X. Zhang and T. Imae, 'Perpendicular superlattice growth of hydrophobic gold nanorods on patterned silicon substrates via evaporation-induced self-assembling', *J. Phys. Chem. C.*, 113, (2009), 5947.
30. M.H. Zareie, X. Xu and M.B. Cortie, 'In-situ organization of gold nanorods on mixed self-assembled-monolayer substrates', *Small*, 3, (2007), 139.
31. D. Fava, Z. Nie, M.A. Winnik and E. Kumacheva, 'Evolution of self-assembled structures of polymer-terminated gold nanorods in selective solvents', *Adv. Mater.*, 20, (2008), 4318.
32. Z. Nie, D. Fava, E. Kumacheva, S. Zou, G.C. Walker and M. Rubinstein, 'Self-assembly of metal-polymer analogues of amphiphilic triblock copolymers', *Nat. Mater.*, 6, (2007), 609.
33. Z. Nie, D. Fava, M. Rubinstein and E. Kumacheva, 'Supramolecular assembly of gold nanorods end-terminated with polymer pom-poms : Effect of pom-pom structure on the association modes', *J. Am. Chem. Soc.*, 130, (2008), 3683.
34. S. Yun, Y.-K. Park, S.K. Kim and S. Park, 'Linker-molecule-free gold nanorod layer-by-layer films for surface-enhanced Raman scattering', *Anal. Chem.*, 79, (2007), 8584.
35. H. Nakashima, K. Furukawa, Y. Kashimura and K. Torimitsu, 'Anisotropic assembly of gold nanorods assisted by selective ion recognition of surface-anchored crown ether derivatives', *Chem. Commun.*, (2007), 1080.
36. M. Grzelczak, B. Rodríguez-González, J. Pérez-Juste and L.M. Liz-Marzán, 'Quasi-epitaxial growth of Ni nanoshells on Au nanorods', *Adv. Mater.*, 19, (2007), 2262.
37. N.R. Jana, L.A. Gearheart, S.O. Obare, C.J. Johnson, K.J. Edler, S. Mann and C.J. Murphy, 'Liquid crystalline assemblies of ordered gold nanorods', *J. Mater. Chem.*, 12, (2002), 2909.
38. Z.-C. Xu, C.-M. Shen, C.-W. Xiao, T.-Z. Yang, S.-T. Chen, H.-L. Li and H.-J. Gao, 'Fabrication of gold nanorod self-assemblies from rod and sphere mixtures via shape self-selective behavior', *Chem. Phys. Lett.*, 432, (2006), 222.
39. J.J. Boote, K. Critchley and S.D. Evans, 'Surfactant mediated assembly of gold nanowires on surfaces', *J. Exp. Nanosci.*, 1, (2006), 125.
40. Z. Jing, G. Yao, A.M.-M. Alfredo, J. Xiaoye, Y. Dong, L. Joseph, H. Toshikazu, S.O. Cengiz, O. Mihrimah, H. Evelyn and D. Bruce, 'Microtubule-based gold nanowires and nanowire arrays', *Small*, 4, (2008), 1507.
41. C. Minelli, C. Hinderling, H. Heinzelmann, R. Pugin and M. Liley, 'Micrometer-long gold nanowires fabricated using block copolymer templates', *Langmuir*, 21, (2005), 7080.
42. J.K.N. Mbindyo, B.D. Reiss, B.R. Martin, C.D. Keating, M.J. Natan and T.E. Mallouk, 'DNA-directed assembly of gold nanowires on complementary surfaces', *Adv. Mater.*, 13, (2001), 249.
43. L. Fan, F.Q. Zhu, R.C. Cammarata and C.L. Chien, 'Efficiency of assembling of nanowires in suspension by ac electric fields', *Appl. Phys. Lett.*, 89, (2006), 223115.
44. J.E. Millstone, S. Park, K.L. Shuford, L. Qin, G.C. Schatz and C.A. Mirkin, 'Observation of a quadrupole plasmon mode for a colloidal solution of gold nanoprisms', *J. Am. Chem. Soc.*, 127, (2005), 5312.

45. C.-C. Chang, H.-L. Wu, C.-H. Kuo and M.H. Huang, 'Hydrothermal synthesis of monodispersed octahedral gold nanocrystals with five different size ranges and their self-assembled structures', *Chem. Mater.*, 20, (2008), 7570.
46. N.R. Jana, L. Gearheart and C.J. Murphy, 'Wet chemical synthesis of silver nanorods and nanowires of controllable aspect ratio', *Chem. Commun.*, (2001), 617.
47. B. Pietrobon, M. McEachran and V. Kitaev, 'Synthesis of size-controlled faceted pentagonal silver nanorods with tunable plasmonic properties and self-assembly of these nanorods', *ACS Nano*, 3, (2008), 21.
48. Tao, F. Kim, C. Hess, J. Goldberger, R. He, Y. Sun, Y. Xia and P. Yang, 'Langmuir-blodgett silver nanowire monolayers for molecular sensing using surface-enhanced Raman spectroscopy', *Nano Lett.*, 3, (2003), 1229.
49. Tao, P. Sinsersuksakul and P. Yang, 'Tunable plasmonic lattices of silver nanocrystals', *Nat. Nanotechnol.*, 2, (2007), 435.
50. Y. Bae, N.H. Kim, M. Kim, K.Y. Lee and S.W. Han, 'Anisotropic assembly of Ag nanoprisms', *J. Am. Chem. Soc.*, 130, (2008), 5432.
51. M. Rycenga, J.M. McLellan and Y. Xia, 'Controlling the assembly of silver nanocubes through selective functionalisation of their faces', *Adv. Mater.*, 20, (2008), 2416.
52. L.-S. Li, J. Walda, L. Manna and A.P. Alivisatos, 'Semiconductor nanorod liquid crystals', *Nano Lett.*, 2, (2002), 557.
53. L.-S. Li and A.P. Alivisatos, 'Semiconductor nanorod liquid crystals and their assembly on a substrate', *Adv. Mater.*, 15, (2003), 408.
54. D.V. Talapin, E.V. Shevchenko, C.B. Murray, A. Kornowski, S. Forster and H. Weller, 'Cdse and cdse/cds nanorod solids', *J. Am. Chem. Soc.*, 126, (2004), 12984.
55. S. Gupta, Q. Zhang, T. Emrick and T.P. Russell, 'Self-corralling nanorods under an applied electric field', *Nano Lett.*, 6, (2006), 2066.
56. K.M. Ryan, A. Mastroianni, K.A. Stancil, H. Liu and A.P. Alivisatos, 'Electric-field-assisted assembly of perpendicularly oriented nanorod superlattices', *Nano Lett.*, 6, (2006), 1479.
57. S. Ahmed and K.M. Ryan, 'Self-assembly of vertically aligned nanorod supercrystals using highly oriented pyrolytic graphite', *Nano Lett.*, 7, (2007), 2480.
58. C. Querner, M.D. Fischbein, P.A. Heiney and M. Drndic, 'Millimeter-scale assembly of cdse nanorods into smectic superstructures by solvent drying kinetics', *Adv. Mater.*, 20, (2008), 2308.
59. C.-C. Kang, C.-W. Lai, H.-C. Peng, J.-J. Shyue and P.-T. Chou, '2-D self-bundled CdS nanorods with micrometer dimension in the absence of an external directing process', *ACS Nano*, 2, (2008), 750.
60. L. Carbone, C. Nobile, M. De Giorgi, F.D. Sala, G. Morello, P. Pompa, M. Hytch, E. Snoeck, A. Fiore, I.R. Franchini, M. Nadasan, A.F. Silvestre, L. Chiodo, S. Kudera, R. Cingolani, R. Krahne and L. Manna, 'Synthesis and micrometer-scale assembly of colloidal CdSe/CdS nanorods prepared by a seeded growth approach', *Nano Lett.*, 7, (2007), 2942.
61. A. Ghezelbash, B. Koo and B.A. Korgel, 'Self-assembled stripe patterns of CdS nanorods', *Nano Lett.*, 6, (2006), 1832.

62. J. He, Q. Zhang, S. Gupta, T. Emrick, T.P. Russell and P. Thiyagarajan, 'Drying Droplets: A Window into the Behaviour of Nanorods at Interface', *Small*, 3, (2007), 1214.
63. J. Zhuang, A.D. Shaller, J. Lynch, H. Wu, O. Chen, A.D.Q. Li and Y.C. Cao, 'Cylindrical superparticles from semiconductor nanorods', *J. Am. Chem. Soc.*, 131, (2009), 6084.
64. A. Salant, E. Amitay-Sadovsky and U. Banin, 'Directed self-assembly of gold-tipped cdse nanorods', *J. Am. Chem. Soc.*, 128, (2006), 10006.
65. N. Zhao, K. Liu, J. Greener, Z. Nie and E. Kumacheva, 'Close-packed superlattices of side-by-side assembled au-cdse nanorods', *Nano Lett.*, 9, (2009), 3077.
66. J.M. Petroski, T.C. Green and M.A. El-Sayed, 'Self-assembly of platinum nanoparticles of various size and shape', *J. Phys. Chem. A.*, 105, (2001), 5542.
67. J. Ren and R.D. Tilley, 'Preparation, self-assembly, and mechanistic study of highly monodispersed nanocubes', *J. Am. Chem. Soc.*, 129, (2007), 3287.
68. A. Demortière, P. Launois, N. Goubet, P.A. Albouy and C. Petit, 'Shape-controlled platinum nanocubes and their assembly into two-dimensional and three-dimensional superlattices', *J. Phys. Chem. B.*, 112, (2008), 14583.
69. M. Chen, J. Kim, J.P. Liu, H. Fan and S. Sun, 'Synthesis of FePt nanocubes and their oriented self-assembly', *J. Am. Chem. Soc.*, 128, (2006), 7132.
70. W. Niu, Z.-Y. Li, L. Shi, X. Liu, H. Li, S. Han, J. Chen and G. Xu, 'Seed-mediated growth of nearly monodisperse palladium nanocubes with controllable sizes', *Cryst. Growth Des.*, 8, (2008), 4440.
71. A.A. Umar and M. Oyama, 'Synthesis of palladium nanobricks with atomic-step defects', *Cryst. Growth Des.*, 8, (2008), 1808.
72. Q. Zhang, J. Xie, J. Yang and J.Y. Lee, 'Monodisperse icosahedral Ag, Au, and Pd nanoparticles: Size control strategy and superlattice formation', *ACS Nano*, 3, (2008), 139.
73. F.-R. Fan, D.-Y. Liu, Y.-F. Wu, S. Duan, Z.-X. Xie, Z.-Y. Jiang and Z.-Q. Tian, 'Epitaxial growth of heterogeneous metal nanocrystals: From gold nano-octahedra to palladium and silver nanocubes', *J. Am. Chem. Soc.*, 130, (2008), 6949.
74. T.H. Larsen, M. Sigman, A. Ghezelbash, R.C. Doty and B.A. Korgel, 'Solventless synthesis of copper sulfide nanorods by thermolysis of a single source thiolate-derived precursor', *J. Am. Chem. Soc.*, 125, (2003), 5638.
75. A.E. Saunders, A. Ghezelbash, D.-M. Smilgies, M.B. Sigman and B.A. Korgel, 'Columnar self-assembly of colloidal nanodisks', *Nano Lett.*, 6, (2006), 2959.
76. Z. Zhuang, Q. Peng, B. Zhang and Y. Li, 'Controllable synthesis of Cu₂S nanocrystals and their assembly into a superlattice', *J. Am. Chem. Soc.*, 130, (2008), 10482.
77. H. Zhang, Y. Zhang, J. Yu and D. Yang, 'Phase-selective synthesis and self-assembly of monodisperse copper sulfide nanocrystals', *J. Phys. Chem. C.*, 112, (2008), 13390.
78. X.-S. Du, M. Mo, R. Zheng, S.-H. Lim, Y. Meng and Y.-W. Mai, 'Shape-controlled synthesis and assembly of copper sulfide nanoparticles', *Cryst. Growth Des.*, 8, (2008), 2032.
79. C. Liu, Y. Masuda, Y. Wu and O. Takai, 'A simple route for growing thin films of uniform ZnO nanorod arrays on functionalized Si surfaces', *Thin Solid Films*, 503, (2006), 110.

80. Z. Chen and L. Gao, 'A facile route to ZnO nanorod arrays using wet chemical method', *J. Cryst. Growth*, 293, (2006), 522.
81. D.F. Liu, Y.J. Xiang, X.C. Wu, Z.X. Zhang, L.F. Liu, L. Song, X.W. Zhao, S.D. Luo, W.J. Ma, J. Shen, W.Y. Zhou, G. Wang, C.Y. Wang and S.S. Xie, 'Periodic ZnO nanorod arrays defined by polystyrene microsphere self-assembled monolayers', *Nano Lett.*, 6, (2006), 2375.
82. Y.-J. Lee, T.L. Sounart, J. Liu, E.D. Spoecker, B.B. McKenzie, J.W.P. Hsu and J.A. Voigt, 'Tunable arrays of ZnO nanorods and nanoneedles via seed layer and solution chemistry', *Cryst. Growth Des.*, 8, (2008), 2036.
83. M. Izaki, M. Watanabe, H. Aritomo, I. Yamaguchi, S. Asahina, T. Shinagawa, M. Chigane, M. Inaba and A. Tasaka, 'Zinc oxide nano-cauliflower array with room temperature ultraviolet light emission', *Cryst. Growth Des.*, 8, (2008), 1418.
84. N. Pradhan and S. Efrima, 'Supercrystals of uniform nanorods and nanowires, and the nanorod-to-nanowire oriented transition', *J. Phys. Chem. B*, 108, (2004), 11964.
85. Y. Li, X. Li, C. Yang and Y. Li, 'Ligand-controlling synthesis and ordered assembly of ZnS nanorods and nanodots', *J. Phys. Chem. B*, 108, (2004), 16002.
86. S.K. Batabyal, C. Basu, A.R. Das and G.S. Sanyal, 'Self-assembly of tellurium nanorods', *Proceedings of 5th IEEE Conference on Nanotechnology*, 622, (2005), 627.
87. Z. Tang, Y. Wang, S. Shanbhag, M. Giersig and N.A. Kotov, 'Spontaneous transformation of CdTe nanoparticles into angled Te nanocrystals: From particles and rods to checkmarks, X-marks, and other unusual shapes', *J. Am. Chem. Soc.*, 128, (2006), 6730.
88. S. Shanbhag, Z. Tang and N.A. Kotov, 'Self-organization of Te nanorods into V-shaped assemblies: A brownian dynamics study and experimental insights', *ACS Nano*, 1, (2007), 126.
89. J. Yuan, H. Gao, F. Schacher, Y. Xu, R. Richter, W. Tremel and A.H.E. Müller, 'Alignment of tellurium Nanorods via a Magnetization–Alignment– Demagnetization ("MAD") process assisted by an external magnetic field', *ACS Nano*, 3, (2009), 1441.
90. N.M. Dimitrijevic, Z.V. Saponjic, B.M. Rabatic and T. Rajh, 'Assembly and charge transfer in hybrid TiO₂ architectures using biotin-avidin as a connector', *J. Am. Chem. Soc.*, 127, (2005), 1344.
91. C. Yang, Z. Yang, H. Gu, C.K. Chang, P. Gao and B. Xu, 'Facet-selective 2d self-assembly of TiO₂ nanoleaves via supramolecular interactions', *Chem. Mater.*, 20, (2008), 7514.
92. M. Li, H. Schnablegger and S. Mann, 'Coupled synthesis and self-assembly of nanoparticles to give structures with controlled organization', *Nature*, 402, (1999), 393.
93. F. Kim, S. Kwan, J. Akana and P. Yang, 'Langmuir-blodgett nanorod assembly', *J. Am. Chem. Soc.*, 123, (2001), 4360.
94. R. Si, Y.-W. Zhang, L.-P. You and C.-H. Yan, 'Rare-earth oxide nanopolyhedra, nanoplates, and nanodisks', *Angew. Chem. Int. Edit.*, 44, (2005), 3256.
95. Y.-W. Zhang, X. Sun, R. Si, L.-P. You and C.-H. Yan, 'Single-crystalline and monodisperse LaF₃ triangular nanoplates from a single-source precursor', *J. Am. Chem. Soc.*, 127, (2005), 3260.
96. H.-X. Mai, Y.-W. Zhang, R. Si, Z.-G. Yan, L.-d. Sun, L.-P. You and C.-H. Yan, 'High-quality sodium rare-earth fluoride nanocrystals: Controlled synthesis and optical properties', *J. Am. Chem. Soc.*, 128, (2006), 6426.

97. R. Si, Y.-W. Zhang, H.-P. Zhou, L.-D. Sun and C.-H. Yan, 'Controlled-synthesis, self-assembly behavior, and surface-dependent optical properties of high-quality rare-earth oxide nanocrystals', *Chem. Mater.*, 19, (2006), 18.
98. L. Mai, Y. Gu, C. Han, B. Hu, W. Chen, P. Zhang, L. Xu, W. Guo and Y. Dai, 'Orientated Langmuir-blodgett assembly of VO₂ nanowires', *Nano Lett.*, 9, (2009), 826.
99. R.K. Zheng, H. Gu, B. Xu, K.K. Fung, X.X. Zhang and S.P. Ringer, 'Self-assembly and self-orientation of truncated octahedral magnetite nanocrystals', *Adv. Mater.*, 18, (2006), 2418.
101. H. Qi, Q. Chen, M. Wang, M. Wen and J. Xiong, 'Study of self-assembly of octahedral magnetite under an external magnetic field', *J. Phys. Chem. C.*, 113, (2009), 17301.
101. X. Liu, E.F. McCandlish, L.E. McCandlish, K. Mikulka-Bolen, R. Ramesh, F. Cosandey, G.A. Rossetti and R.E. Riman, 'Single-crystal-like materials by the self-assembly of cube-shaped lead zirconate titanate (PZT) microcrystals', *Langmuir*, 21, (2005), 3207.
102. J. Wang, E. Khoo, P.S. Lee and J. Ma, 'Synthesis, assembly, and electrochromic properties of uniform crystalline WO₃ nanorods', *J. Phys. Chem. C.*, 112, (2008), 14306.
103. H.Z. Zocher, 'Spontaneous structure formation in sols; a new kind of anisotropic liquid media', *Anorg. Allg. Chem.*, 147, (1925), 91.
104. H. Zocher and W.Z. Heller, 'Iridescent strata produced by the slow hydrolysis of iron chloride', *Anorg. Allg. Chem.*, 186, (1930), 75.
105. J.H.L. Watson, R.R. Cardell, Jr. and W. Heller, 'The internal structure of colloidal crystals of β -FeOOH and remarks on their assemblies in schiller layers', *J. Phys. Chem.*, 66, (1962), 1757.
106. H. Maeda and Y. Maeda, 'Atomic force microscopy studies for investigating the smectic structures of colloidal crystals of β -FeOOH', *Langmuir*, 12, (1996), 1446.
107. S.A. Maier, P.G. Kik, H.A. Atwater, S. Meltzer, E. Harel, B.E. Koel and A.A.G. Requicha, 'Local detection of electromagnetic energy transport below the diffraction limit in metal nanoparticle plasmon waveguides', *Nat. Mater.*, 2, (2003), 229.
108. P.K. Sudeep, S.T.S. Joseph and K.G. Thomas, 'Selective detection of cysteine and glutathione using gold nanorods', *J. Am. Chem. Soc.*, 127, (2005), 6516.
109. M. Martin, T. Andrea, B. Kanokraj, A. John and P. Yang, 'Surface-enhanced raman spectroscopy for trace arsenic detection in contaminated water', *Angew. Chem. Int. Edit.*, 47, (2008), 6456.
110. A. Sanyal, T. Bala, S. Ahmed, A. Singh, A.V. Piterina, T.M. McGloughlin, F.R. Laffir and K.M. Ryan, 'Water dispersible semiconductor nanorod assemblies via a facile phase transfer and their application as fluorescent biomarkers', *J. Mater. Chem.*, 19, (2009), 8974.
111. X.-J. Huang, C.-C. Li, B. Gu, J.-H. Kim, S.-O. Cho and Y.-K. Choi, 'Controlled molecularly mediated assembly of gold nanooctahedra for a glucose biosensor', *J. Phys. Chem. C.*, 112, (2008), 3605.
112. Q. Wei, K. Hirota, K. Tajima and K. Hashimoto, 'Design and synthesis of TiO₂ nanorod assemblies and their application for photovoltaic devices', *Chem. Mater.*, 18, (2006), 5080.
113. X. Ju, W. Feng, K. Varutt, T. Hori, A. Fujii and M. Ozaki, 'Fabrication of oriented ZnO nanopillar self-assemblies and their application for photovoltaic devices', *Nanotechnology*, 19, (2008), 435706 (6pp).
114. A.-M. Cao, J.-S. Hu, H.-P. Liang and L.-J. Wan, 'Self-assembled vanadium pentoxide (V₂O₅) hollow microspheres from nanorods and their application in lithium-ion batteries', *Angew. Chem. Int. Edit.*, 36, (2005), 4391.

115. J. Zhao, L. Wua and J. Zhi, 'Fabrication of micropatterned ZnO/SiO₂ core/shell nanorod arrays on a nanocrystalline diamond film and their application to DNA hybridization detection', *J. Mater. Chem.*, 18, (2008), 2459.

ADDITIONAL READING

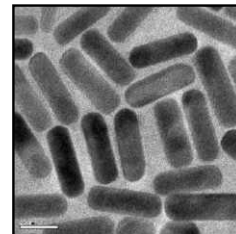
1. M.-C. Daniel and D. Astruc, 'Gold nanoparticles: Assembly, supramolecular chemistry, quantum-size-related properties, and applications toward biology, catalysis, and nanotechnology', *Chem. Rev.*, 104, (2004), 293.
2. D.V. Talapin, J.-S. Lee, M.V. Kovalenko and E.V. Shevchenko, 'Prospects of colloidal nanocrystals for electronic and optoelectronic applications', *Chem. Rev.*, 110, (2010), 389.
3. S. Liu and Z. Tang, 'Nanoparticle assemblies for biological and chemical sensing', *J. Mater. Chem.*, 20, (2010), 24.
4. Z. Nie, A. Petukhova and E. Kumacheva, 'Properties and emerging applications of self-assembled structures made from inorganic nanoparticles', *Nat. Nanotechnol.*, 5, (2010), 15.
5. X. Chen and S.S. Mao, 'Titanium dioxide nanomaterials: Synthesis, properties, modifications, and applications', *Chem. Rev.*, 107, (2007), 2891.
6. S.C. Glotzer and M.J. Solomon, 'Anisotropy of building blocks and their assembly into complex structures', *Nature Mater.*, 6, (2007), 557.
7. K.J.M. Bishop, C.E. Wilmer, S. Soh and B.A. Grzybowski, 'Nanoscale forces and their uses in self-assembly', *Small*, 5, (2009), 1600.
8. Y.J. Min, M. Akbulut, K. Kristiansen, Y. Golan and J. Israelachvili, 'The role of interparticle and external forces in nanoparticle assembly', *Nature Mater.*, 7, (2008), 527.
9. J. Zhang, Z.-L. Wang, J. Liu, S. Chen and G.-Y. Liu, *Self-assembled nanostructures* (2002), Kluwer Academic Publishers, New York, Boston, Dordrecht, London, Moscow.
10. Peidong Yang (Editor), *The Chemistry of Nanostructured Materials* (2003) by World Scientific Publishing Co. Pte. Ltd.
11. C.P. Poole, Jr. and F.J. Owens, *Introduction to Nanotechnology* (2003), John Wiley & Sons, Inc., Publication.
12. Bharat Bhushan (Ed.), *Springer Handbook of Nanotechnology* (2004), Springer-Verlag Berlin Heidelberg New York.

REVIEW QUESTIONS

1. Why assembled materials are important?
2. What are the different methods for producing assembled nanostructures?
3. What are the advantages of assembling anisotropic/non-spherical particles compared to isotropic spherical nanoparticles?
4. Whether the inherent properties of the constituent particles change during assembly? How can we modulate the change in optical properties of gold nanorods by assembling?

5. What are the common methods adopted for assembling gold nanorods?
6. What is programmed self-assembly?
7. Give examples where assembled structure shows improved performance over individual particles for specific applications.
8. Why do assembled nanostructures act as a good SERS substrate?
9. Citing specific examples describe the reason for the formation of assembled structures, even though thermodynamically, the process is hindered since the entropy is decreasing during the process.
10. What are the advantages of programmed assembly over other techniques like lithography?
11. What are the advantages of nanoparticle based waveguides compared to conventional waveguides? Which orientation of nanorods are better for waveguide application and why?
12. Give some applications of self-assembled structures.

DENDRITIC NANOSTRUCTURES



“Architecture is a consequence of special atom relationship and just as observed for small molecules, different properties should be expected for new polymeric architectures.” (referring to dendrimers)

Professor Paul Flory as quoted in, D.A. Tomalia and J.M. Fréchet, *Journal of Polymer Science: Part A: Polymer Chemistry*, 2002, 40, 2719–28

Dendrimers are nano-sized synthetic macromolecules with unique structural properties. As the word suggests (dendros = branch or tree and meros = part; in Greek), dendrimers resemble a branched tree. The branching starts from the core unit and the branching pattern replicates to the periphery of the molecule. Typically, the number of times branching occurs in dendrimers can vary in between zero and ten, resulting in different ‘generations’ of dendrimers. This distinctive structural aspect of dendrimers results in organic materials with nano and sub-nano metered internal voids, possessing interesting material properties. The potential applications of dendrimers span over a range of frontier research areas, such as light energy harvesting, controlled drug delivery, specific catalytic activity, nanoparticle stabilisation and host-guest chemistry. The following part of discussion will briefly cover the historical perspective as well as the state-of-art status of the field, with special emphasis on the use of dendritic nanostructures in guest encapsulation and bio-medical research.

Learning Objectives

- Define dendrimers.
 - List some of the important properties of dendrimers.
 - Identify the potential applications of dendrimers.
 - Correlate between dendrimers and nano-structured biomaterials.
-
-

16.1 INTRODUCTION TO MACROMOLECULES AND DENDRIMERS

Dendrimers are categorised as macromolecules. A molecule is labeled as macromolecule based on its size. In Greek, *macros* means *large*. The word, *macromolecule*, was first coined by Staudinger to refer

molecules with molecular weight higher than 10,000.¹ Macromolecules receive significant attention due to their unique chemical as well as material properties. Also, bio-macromolecules, such as carbohydrates, proteins and nucleic acids, play vital role in our lives. Nonetheless, systematic studies of structure-property relations are lacking in many important macromolecular systems. Since macromolecules are relatively larger in size compared to other organic molecules, the size range falls into the 'nano' regime, whereas the size of small organic molecules fall in 'angstrom' size range (an order of magnitude less than nano). Thus, macromolecules constitute 'nano' organic systems, having numerous applications in material chemistry. Until early 1980s, chemists were familiar with different types of polymeric systems as synthetic macromolecules, where each monomer was added to the backbone of the polymer chain to form a large structure of linear assembly. Later, another class of macromolecules was developed in laboratories, where the 'monomers' were added to one core unit with further possibility of branching out to the periphery in a globular fashion. They were structurally different from conventional polymers, and were associated with certain distinct properties. A scientist, named Donald A. Tomalia from USA, named this class of molecules as 'dendrimers' due to their resemblance with highly-branched trees ('dendros' in Greek means 'branch or tree' and 'meros' means 'part').² While the origin of dendrimers was received with much skepticism among scientists, it was later proved beyond doubt that they can be efficiently synthesised in chemical laboratories and can be characterised with routine spectroscopic techniques, such as NMR, Mass and IR.

16.1.1 Structural Features of Dendrimers

Dendrimers are hyper-branched macromolecules with a core unit, identical repeating units in three dimension and identical or different peripheral functional groups.

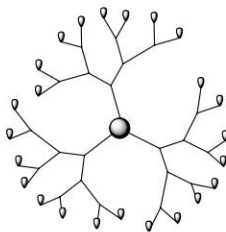


Fig. 16.1 Cartoon representation of a dendrimer. The central portion represents the core, from which the branching starts and peripheral units are attached to the end of the branches.

This type of a unique structural concept was first practiced by Fritz Vögtle, Kekule Institute of organic chemistry and biochemistry, University of Bonn, Germany in 1978.³ The synthetic procedure involves the reaction between an amine and acrylonitrile and the procedure was termed as *cascade synthesis*.

Later, Tomalia's poly (amidoamine) {PAMAM} dendrimers and Newkome's 'arborol' systems have received widespread attention.⁴ PAMAM dendrimers were the first class of dendrimers appeared in the market. The number of branching points from the centre to the periphery defines the generation of the dendrimer and the number of peripheral groups increases exponentially as the generation increases. In 1990, Fréchet introduced the aromatic poly-ether dendrimers, which were hydrophobic

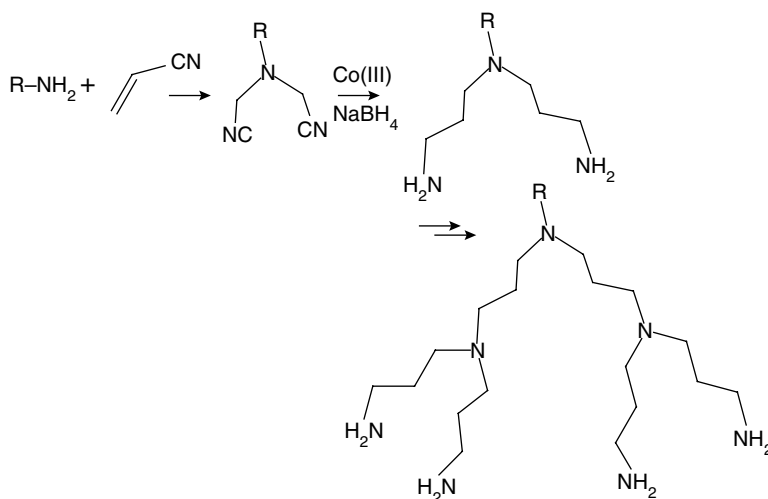


Fig. 16.2 The first report on 'cascade' synthesis by Vögtle in 1978.

due to the large number of aromatic units present in the system.⁵ Dendrimers containing amino acids and peptide chains have been reported recently. Indeed, the structural diversity in the repeating unit is impressive, which varies all the way from pure hydrocarbons to metal complexes, numerous fluorophores and bio-molecules.⁶ This resulted in well-defined and aesthetically-attractive dendrimer systems and a variety of such dendritic scaffolds have become already accessible. One of the fundamental advantages of dendrimer synthesis over conventional polymer synthesis is the achievement of perfect monodispersity compared to the case of polymer synthesis, where distribution of molecular weights is unavoidable. Dendrimers have potential uses in many areas including organic light emitting diodes, energy/light harvesting, host-guest chemistry, drug release, ion sensing, catalysis and information storage.⁷ The field of dendrimer chemistry is, thus, currently in an explosive growth phase.

Since its very beginning, the field of dendrimers has attracted considerable attention of many research groups to explore the numerous possibilities of these monodisperse macromolecules. The aesthetically appealing structural features of dendrimers distinguish them from normal polymers in two main aspects: (i) They are constructed from Ab_n monomers (n usually 2, 3, or 4) rather than the standard AB monomers, which produce linear polymers. This will result in hyper-branched structures; and (ii) They are synthesised in an iterative fashion. Due to these two main reasons, dendrimer formation will be processed by a non-linear, step-wise synthetic growth, which will eventually result in the large, spherically-shaped molecular architecture. One of the advantages of such strategy is the perfect control about the size of the dendrimer, where polymers always possess a distribution of molecular weights as mentioned above.

One of the most studied classes of dendrimers is PAMAM dendrimer. PAMAM dendrimer is commercially available up to tenth generation. The diameter of a fourth-generation PAMAM dendrimer with ethylene diamine as the core unit is 4.5 nm.⁸ Thus, these molecules can be categorised as nano-structured organic molecules, provided their globular structure is preserved in solution state.

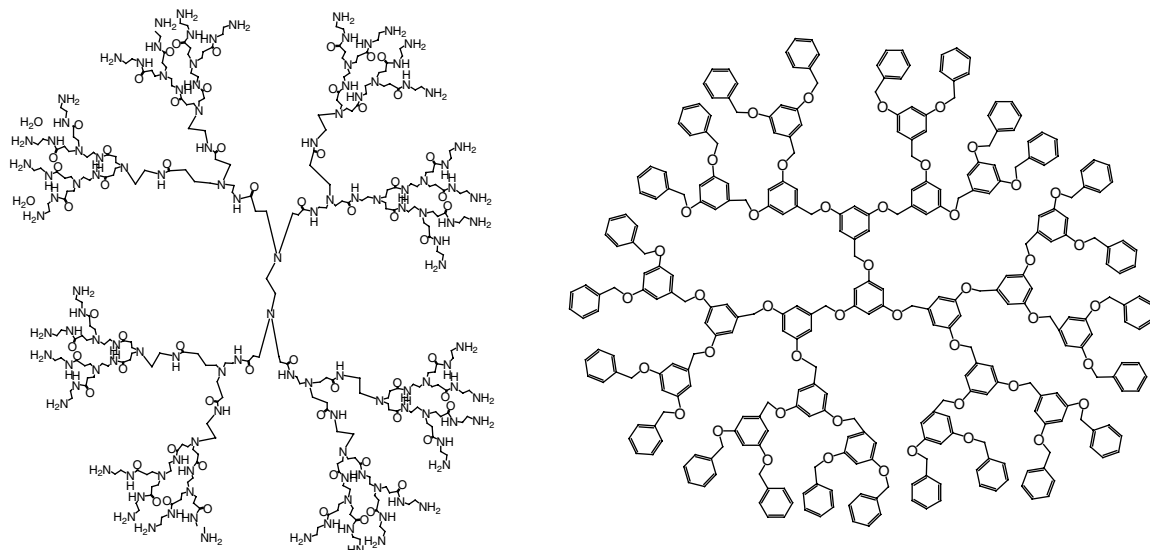


Fig. 16.3 Chemical structures of two different types of widely used dendrimers (a) Poly(amidoamine) [PAMAM] dendrimer (b) Poly aryl ether (Fréchet type) dendrimer.

The size of PAMAM dendrimer in solution is strongly dependant on several factors, such as pH, solvent milieu, and generation of dendrimer. For example, lowering the pH of the system leads to protonation of nitrogen atoms in PAMAM dendrimers, which results in an 'extended' structure, where dendritic arms are extended outward from the core due to the repulsive force between the positively charged nitrogen atoms. Conversely, higher pH values in the system results in considerable back

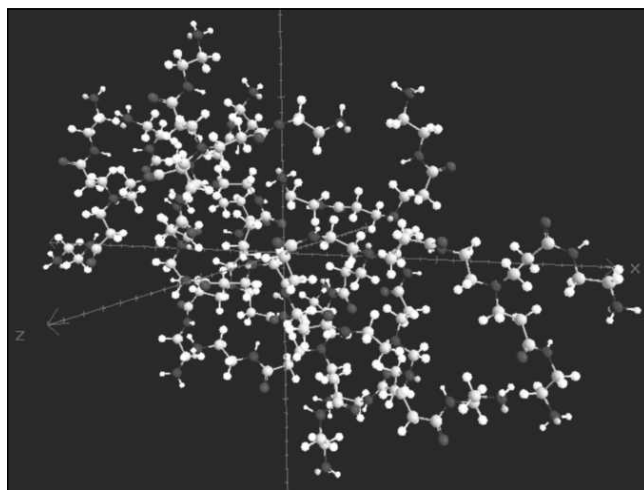


Fig. 16.4 Energy minimised 3-D structure of second generation PAMAM (using Chem 3-D Pro. MM2).

folding of the dendritic arms due to secondary interactions, such as hydrogen bonding between the peripheral amines and internal carbonyl units. As a result, the dendrimer swells to a smaller sized, compact, globular structure.⁹ Similarly, polar solvent solvates the outer functional groups leading to an extended structure, whereas non-polar solvents directs more back folding. Back folding in dendritic structures becomes significant in higher generations of dendrimers because of the exponential increase in the number of peripheral units. For example, in generation 1 (G1) PAMAM dendrimer, there are eight amino groups present at the periphery while in generation 4 (G4) PAMAM dendrimer, there are 64 amino groups present at the surface.

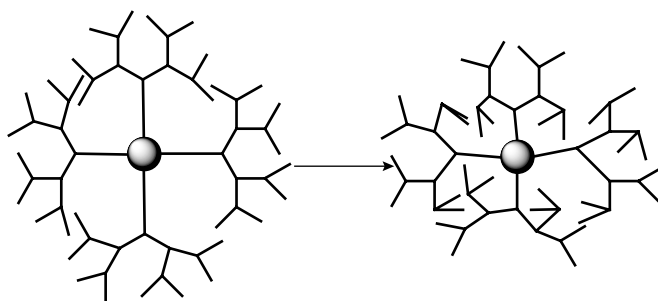


Fig. 16.5 Peripheral groups orient towards the core-back folding-in dendrimers, which increases the core density substantially.

In addition to Fréchet and PAMAM types dendrimers, other classes of dendrimers based on poly(glutamic acid), poly(propelineamine) {PPI}, poly(melamine) and polyester dendrimers are also available and mostly utilised for a variety of applications in biochemistry. The solubility of dendrimers can be highly tuned by simply incorporating hydrophilic or hydrophobic groups to the branching units. The PAMAM type dendrimers are highly water soluble due to the polar nature of the molecules. Conversely, Fréchet type dendrimers are highly insoluble in water due to the presence of large number of aromatic groups.

16.1.2 How do you Synthesis Dendrimers?

The two main synthetic strategies for synthesising dendrimers have emerged over the last two decades: the *divergent* and *convergent* methods. In the divergent methods, developed by Tomalia and Newkome, the dendrimers are built from the core to the periphery. Early examples of divergent synthesis come from the work of Denkewalter, Vögtle, Mulhaupt, Meijer, Tomalia, and Newkome. The convergent approach was started by Hawker, Fréchet, Miller, and Moore. This method builds dendrimers from the periphery to the central core. The advantage of this method over the divergent approach is that dendrimer formed will be rather free from defects. In the divergent approach, every step involves multiple interactive points which might lead to products with unreacted or partially reacted periphery resulting defects in the system.

A different approach towards synthesising dendrimers has been put forward by Malkoh in which click chemistry and classical esterification/etherification reactions are combined to eliminate

additional steps, such as activation of functional groups.¹⁰ The authors claim that this approach is more practical as it takes fewer steps to synthesis higher-generation dendrimers with better yields compared to the conventional methods.

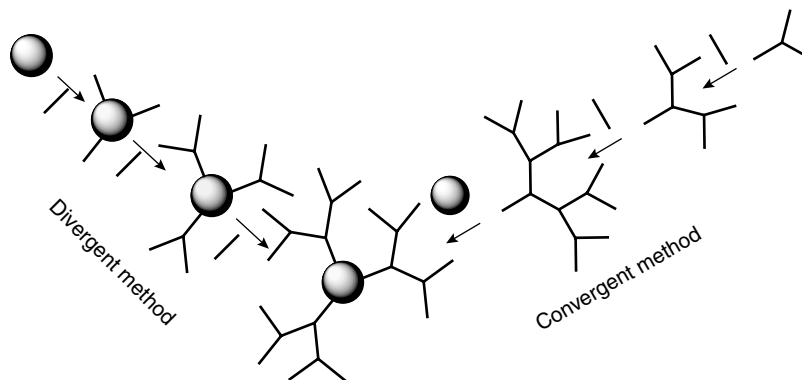


Fig. 16.6 Convergent and divergent synthetic approaches in dendrimer synthesis.

A few types of dendrimers are available commercially. For example, Sigma-Aldrich chemical company provides PAMAM dendrimers up to tenth generation with a variety of core units and peripheral functional groups. Dendritech Inc., MI, USA is another source for commercial production and supply of dendrimers. The price for these macromolecules is largely dependent on the generation, difficulty involved in the synthesis as well as potential applications of the class of dendrimer. For example, fourth generation PAMAM dendrimer with ethylene diamine core unit, which is largely used in designing drug and gene delivery agents, cost ~ \$ 900.00 per 10 g of the compound as 10 wt per cent solution in methanol.

16.1.3 Host-Guest Properties of Dendritic-Nanosystems

Since some of the dendrimers are available commercially, in different generations, a wide range of applications is possible by means of these macromolecules. The field of dendrimers has, thus, attracted ample interest among material scientists since its inception. While dendrimers can be considered as unique class of polymers, the morphological differences exhibited by dendritic structures lead to several interesting properties to these macromolecules compared to conventional polymers. It has been foreseen much earlier that the monodispersity and highly flexible structural features of dendrimers can have significant contributions in the host-guest chemistry.

Due to the large size and number of functional groups in dendrimers, encapsulation of guest molecules is possible either in the interior part or on the periphery of the dendrimer.¹¹ Since 1980, many research groups have been proposing the possibility of constructing a dendritic 'core-shell molecule' for entrapping small molecules. Theoretical calculations as well as computations studies on the Tomalia's PAMAM dendrimers showed that for higher generations, these dendrimers adopt a globular structure with large hollow cavities inside. Nonetheless, as the generation increases back

folding increases and as a result the size of the globular structure of dendrimers can be slightly altered. As a consequence, the space available inside the dendritic cavity will be reduced, which might have an adverse impact on the guest encapsulation property of dendrimers.

Newkome *et al.* have studied the micellar properties of dendrimers with a completely hydrophobic interior.¹² The advantage of these types of dendrimers is that they form concentration independent micelles in contrast to the conventional examples, which form the micelles only at a characteristic critical micellar concentration (CMC). Meijer and co-workers have reported the synthesis of an inverted unimolecular dendritic micelle by reacting the amino end group of poly(propyleneamine) dendrimers (PPI) with aliphatic acid chlorides. They observed the encapsulation of molecules, such as rose bengal in the dendritic interior in hexane solution. By the addition of toluene solution, the guest molecule is displaced from the dendrimer.¹³ In addition to these examples, several reports are available in literature dealing with the host-guest chemistry of dendrimers. Meijer *et al.* designed a dendritic system with peripherally decorated by L-phenylalanine derivatives. Various sizes of guest molecules (*p*-nitrobenzoic acid and Bengal rose) were entrapped in the interior cavities of the dendrimer prior to the peripheral modifications. Upon partial hydrolysis, only larger sized guest molecules were leached out, keeping the smaller one inside the dendritic cavity. The complete hydrolysis after the larger guests molecules move apart, leads to the release of smaller guests inside the dendrimers. The strategies are developed based on the hypothesis that external stimuli can control the host-guest chemistry of dendrimers, where the guest can be released at a desirable time.¹⁴

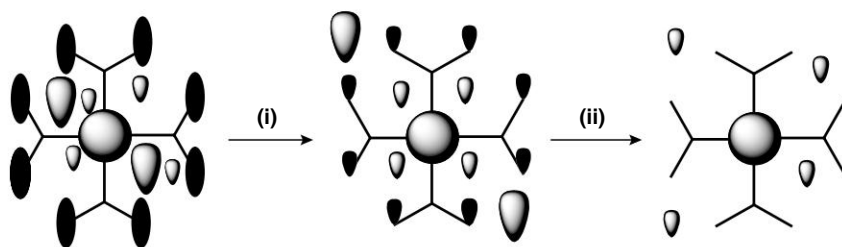


Fig. 16.7 The selective removal of peripheral groups in dendrimers leading to controlled guest release. In step i, the crowded periphery is partially opened by partial hydrolysis so that only large guest molecules are released. In step ii, the peripheral decorations are completely removed and smaller guests also diffuse apart.

Recently, Meijer *et al.* describes the step-wise non-covalent synthesis of dendrimer based host-guest assembly in water using dynamic light scattering studies, cryogenic transmission electron microscopy, atomic force microscopy and various NMR techniques.¹⁵ Another interesting host-guest chemistry between PAMAM dendrimer and micophenolic acid was described by Xu *et al.* and the NMR analysis of the binding properties between the host and guest provides necessary information for understanding the physicochemical properties of the system.¹⁶ The host-guest chemistry was investigated by ¹H NMR as well as NOESY spectroscopy. While ¹H NMR provides the necessary details of the peripheral complex formation between the dendrimer and micophenolic acid, NOESY techniques render detailed pictures of guest encapsulation in the interior portions of the dendrimer

through hydrogen bonding and hydrophobic interactions. Based on the experimental results, two schemes of dendrimer-guest interactions are proposed as shown below.

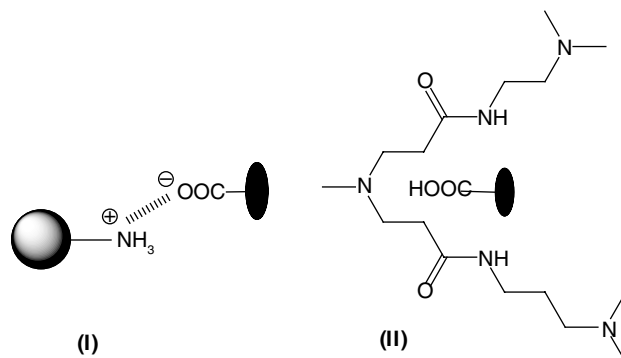


Fig. 16.8 Two different types of dendrimer-guest interactions: (I) at the periphery and (II) between the dendrons in PAMAM dendrimer and micophenolic acid.

Synthetic approaches to develop dendrimers with photoactive groups on the periphery for selective encapsulation/release of guests molecules was attempted by Vögtle and co-workers. The fourth generation poly(propylene imine) dendrimer with 32 terminal amino groups was modified with azobenzene units, which undergo photoisomerisation from *trans* to *cis* position upon irradiation with a light of 313 nm. Also, upon irradiation with 254-nm light, the *cis* form will revert to the *trans* form. This photocontrolled dendrimer host was utilised to encapsulate and release eosin guest molecules through a photochemically controlled pathway.¹⁷

16.1.4 Dendrimer Interaction with Bio-Nano Systems

It was envisaged much earlier that dendrimers, especially the higher generations, can mimic proteins. While large structural variations exist between tertiary structure of a functional protein and dendrimer, the comparison was valid based on the intermolecular interactions and molecular size. Another interesting similarity between dendrimers and proteins is that dendrimers can adopt 'native' and 'denatured' structures, similar to that of proteins as a function of pH, solvent polarity and additives.

While dendrimers are bio-compatible molecules, their toxicity has been a question of concern among scientists, especially for dendrimer with large number of amino groups, which led to a methodical investigation in this direction, yet yielding often contradictory results in the literature. However, results from various studies collectively suggest that peripherally modified PAMAM dendrimers are rather toxic free, their IC_{50} values comes in acceptable range and hence can be utilised for studies in the *in-vivo* systems.¹⁸

16.1.5 Dendrimer-DNA Interaction

It is intriguing to study the mechanism of interactions between two interesting topologies, i.e., dendrimers and DNA and more than 500 research papers have been already published in this area.

The first use of DNA to elaborate the structure of dendrimer was in 1993. It has been reported in the literature that PAMAM dendrimers can form complex with DNA through electrostatic as well as covalent interactions.¹⁹ The recent reports also suggest higher transfection efficiency and lower cytotoxicity through the interaction between a novel derivative of PAMAM dendrimer and DNA. Single- and double-stranded DNA can be covalently connected to (i) dendrons, (ii) two dendrimers on either side or (iii) periphery of the dendrimers. While numerous reports of DNA bound dendrimers in a covalent fashion are available, electrostatically bound DNA-dendrimer complexes are also known. It is now known that DNA wrap around the dendrimer in a better fashion if the generation of dendrimer is higher than five. The study in this area suggests that interaction between DNA and dendrimer will be efficient if the dendrimer is protonated to a greater extent. In some cases, the DNA-dendrimer complex was found to be precipitating, and interestingly, this precipitate aggregates to an ordered array leading to the formation of a nematic type liquid crystalline material. Some theoretical studies suggest that the complex formation is extremely depending on the sequence of the oligonucleotide. Studies carried out in this area abundantly suggest that the combination of the two topologies results in synergic effects on each other, leading to fruitful results.

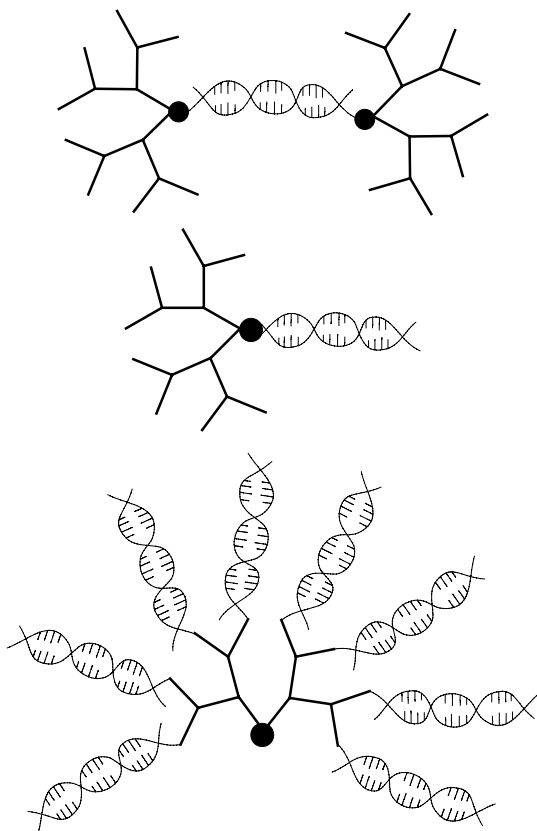


Fig. 16.9 Dendrimer-DNA assemblies: different ways of combining two interesting topologies.

16.1.6 Dendrimer-Protein Interaction

The aggregation of prion proteins in brain cells constitutes an example of protein misfolding. The adverse effects on such protein aggregation can lead to fatal diseases, such as Creutzfeldt-Jakob's disease, mad cow disease, and other neuro-generative illness (e.g., Alzheimer's). The first example of cationic dendrimer interaction with prion proteins came from Supattapone and co-workers.²⁰ The initial studies indicate that dendrimers can dissolve the prion protein aggregates, which causes the neuro-generative diseases. Higher generations of PAMAM, PPI and PEI dendrimers with amino terminal groups were also found to be effectively solubilising prion protein aggregates. It was also pointed out that the terminal amino groups play an essential role in the process as hydroxy substituted dendrimers were found to be less sufficient in de-aggregating the proteins. The important aspect was that the solubilisation of proteins occurs in presence of surprisingly low concentrations of dendrimers (7 µg/mL).

16.1.7 Dendrimers and Drugs

Since dendrimers are bio-compatible and similar in size with several bio-nanosystems, they were considered as potential candidates for drug carriers.²¹ Fundamentally, two different types of dendrimer-drug interactions are practiced: (i) covalent or non-covalent binding of drugs to the periphery of the dendrimer; and (ii) placing the drug in the interior voids of the dendrimer. Careful studies regarding the toxicity of dendrimers have been carried out and the results can be summarised as follows.

- (a) Dendrimers toxicity can be tuned.
- (b) Cationic dendrimers are less toxic than corresponding anionic dendrimers.
- (c) Interactions with DNA and other long chain alkyl groups [e.g.: poly(ethylene)glycol] considerably reduce the toxicity of dendrimers.

It has been shown that fifth-generation PPI dendrimers can encapsulate large drug molecules up to five numbers per dendrimer. One of the strategies adopted to keep the encapsulated drug molecule inside the dendrimer is to modify the dendrimer periphery by bulky groups, such as *tert*-butyl groups. In the case of encapsulation of small as well as big drug molecules, selective release of guest molecules has been demonstrated by step-wise hydrolysis of the dendrimer periphery. If the dendrimer core is hydrophobic as in the case of dendrimers with cyclophane cores, large number of water-insoluble drugs can be incorporated in the dendrimer core and made water soluble. These types of dendrimers were reported to be excellent carriers for steroids. In another classical work, Zimmerman showed the importance of specific guest binding by dendrimers in order to develop sensors for specific antibody in cells. The core of the dendrimer will be selectively chosen and then polymerised to a dendritic network through easily hydrolysable bonding, such as ester bonds. Once the dendritic structure is formed, the core unit is hydrolysed and taken away from the system to generate a hole at the core of the dendrimer, which can efficiently detect the core unit present in the cell with a binding constant as high as 10^5 M^{-1} .²²

Large number of attempts has been reported to enhance the efficiency of drug loading and delivery by PAMAM dendrimers for treating cancer cells.²³ Functionalised dendrimers were connected via DNA oligonucleotides to generate clustered molecules targeting cancer cells. Majoros *et al.* have recently reported that partial acetylation of fifth-generation PAMAM dendrimer leads to enhanced solubility during the conjugation reaction between fluorescein isothiocyanate and the dendrimer, which prevent non-specific targeting of cancer cells during drug delivery. Various attempts have been made to encapsulate anti-cancer drugs, such as methotrexate and doxorubicin inside PAMAM dendrimers and the results have shown that up to 26 drugs molecule can be incorporated per dendrimer monomer. PAMAM dendrimers have been widely used as a carrier for various drugs against the treatment of lymphoblastoid leukemia, Chinese hamster ovary cell lines, and KB cells.

16.1.8 Dendrimer Encapsulated Nanoparticles (DENS)

Due to the large size and number of peripheral functionality of dendrimers in higher generations, encapsulation of guest molecules is feasible either in the interior part or on the periphery of the dendrimer. Thus, various metal ions can be introduced to the dendritic systems, which either penetrate to the interior part or complex at the periphery of the dendrimers to form metal containing dendritic systems. Subsequent reduction of the metal ions with mild reducing agents generally leads to the formation of dendrimer encapsulated metal nanoparticles (DENS), which are stabilised by the unique structural features of the dendrimer.²⁴ The key role of dendrimers in such cases is to prevent the agglomeration of nanoparticles to form larger-sized particles. Elegant work by Esumi, Dickson and Crooks have demonstrated that stable, monodisperse silver and gold nanoparticles can be generated inside the dendritic environment by reducing the corresponding metal ions with common reducing agents such as NaBH_4 .

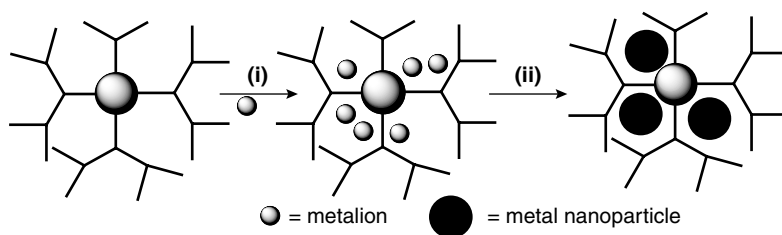


Fig. 16.10 Generating dendrimer encapsulated metal nanoparticles (DENS). (i) represents the introduction of metal ions to the dendrimer, leading to the effective encapsulation of them in the interior portions of the dendrimer due to secondary interactions, such as co-ordination bond formation. (ii) Subsequent reduction by common reducing agents leads to the formation of nanoparticles/nanoclusters, etc., which are stabilised by the dendrons.

Precise control over the size and shape of the metal nanoparticles generated inside dendritic environments is a matter of supreme importance since the properties of nanostructured materials are enormously dependant on their size and shape. It is established that the ratio of the metal ions to

the capping agents (dendrimers) play a vital role in determining the size of the metal nanoparticle. Furthermore, a recent report from Yang and Yan has suggested that precise size control of nanoparticles in presence of capping agents can be achieved by controlling the reduction methodology.²⁵ In general, metal nanoparticles generated and stabilised in the interior portions of the dendrimers (they are generally referred to as *intra* type DENs) fall in the size range of 1 to 4 nm, while that generated at the periphery of dendrimers (*inter* type DENs) are greater than 5 nm in size.²⁶

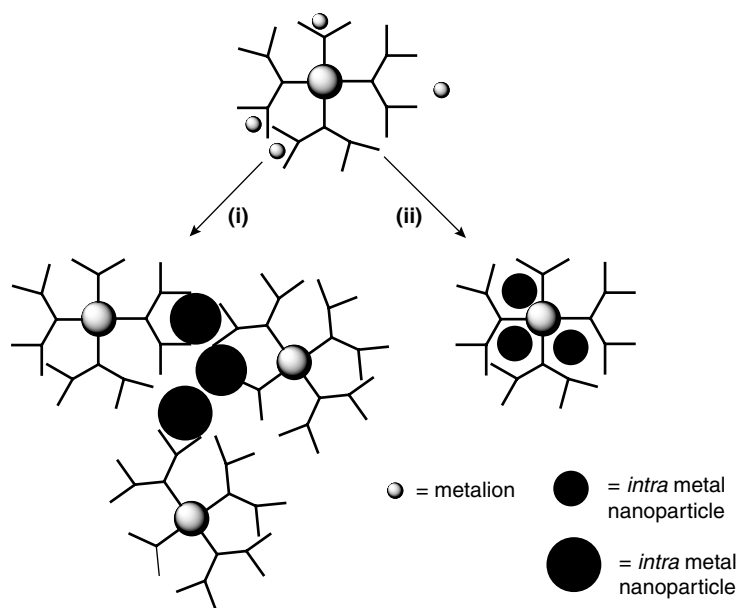


Fig. 16.11 Two different types of DENs formation. *Inter* type DENs form in between two or three dendrimers and *intra* type DENs form within single dendrimer cavity. Electron microscopic analysis can easily suggest which type has been formed in a given system.

Although the reducing agents utilised to generate gold or silver nanoparticles are mild, additional procedures are essential to remove the by-products of the reaction prior to utilise the system for any applications. An attractive alternative is to generate these metal nanoparticles by utilising reagents, which can act both as reducing and stabilising agents.

Latest studies have shown that polyethylene glycol (PEG) of suitable molecular weight can act as both the capping as well as reducing agent for silver nanoparticles so that additional reducing agents can be avoided from the system.²⁷ Chen and co-workers have reported the formation and self-assembly of monodisperse silver nanoparticles by oleylamine-liquid paraffin system.²⁸ Another interesting study from Kéki *et al.* suggests that prolonged UV irradiation of AgNO_3 solution in presence of poly(amidoamine) {PAMAM} dendrimers leads to the formation of silver nanoparticles in the absence of other reducing agents.²⁹ The UV irradiation results in a photo-induced electron transfer from the primary amines of the dendrimer to the metal ions encapsulated inside the dendritic cavities.

Results from our own research group suggest that silver nanoparticles can be generated and stabilised at ambient temperatures by PAMAM dendrimers in the absence of additional reducing agents as well as UV irradiation.³⁰ Surprisingly, experimental results also suggest a strong correlation between the size/shape of the metal nanoparticles and the aggregate propensity of the dendrimers, which can be altered by the selective choice of peripheral functional groups. Mechanistic studies indicate that tertiary amines present in the dendrimers act as mild reducing agents for the encapsulated metal ions and primary and secondary amines are passive towards the reduction process. In addition to silver, gold nanoparticles can also be prepared by adopting similar protocols with an added advantage of eliminating side reactions, such as polymerisation, which is frequently observed in aliphatic or aromatic amine-induced reduction of gold ions.

16.2 CONCLUSIONS

Dendrimers, the hyper-branched nanostructured organic molecules, provide a useful structural platform for generation, stabilisation and transportation of various nano-structured materials in condensed medium. Since dendrimers render flexible structural scaffolds with extensive possibilities of functional group choice, the opportunities with which one can design the dendrimer-nano systems are quite enormous. Recent research in dendrimer chemistry suggests that dendrimers can aggregate under appropriate conditions, resulting in larger macromolecular self-assembled systems with unique host-guest and metal ion encapsulation properties. While challenges in optimising the synthetic procedures as well as issues related to toxicity and bio-degradability of dendritic systems do exist, it is hoped that the futuristic research currently being carried out in the field, will come up with fruitful solutions so that dendrimers and dendritic systems can be better utilised in the nano-world.

REFERENCES

1. R.J. Silbey, R.A. Alberty and M.G. Bawendi, *Physical Chemistry*, Fourth edition, Wiley Dreamtech (P) Ltd. New Delhi, India, (2006), 763.
2. D.A. Tomalia and J.M.J. Fréchet, *J. Polym. Sci. Part A: Polym. Chem.*, 40, (2002), 2719.
3. E. Buhleier, W. Wehner and F. Vögtle, *Synthesis*, (1978), 155.
4. (a) D.A. Tomalia, J.R. Dewald, M.R. Hall, S.J. Martin and P.B. Smith, Reprints of the 1st SPSJ International Polymer Conference, Society of Polymer Science Japan, Kyoto, (1984), 65; (b) D.A. Tomalia, H. Baker, J. Dewald, M. Hall, G. Kallos, S. Martin, J. Roeck, J. Ryder and P. Smith, *Polym. J.*, 17, (1985), 117; (c) G.R. Newkome, Z.-Q. Yao, G.R. Baker and V.K. Gupta, *J. Org. Chem.*, 50, (1985), 2003.
5. C.J. Hawker and J.M.J. Fréchet, *J. Am. Chem. Soc.*, 112, (1990), 7638.
6. G.R. Newkome, C.N. Moorefield and F. Vogtle, *Dendrimers and Dendrons: Concepts, Synthesis, Applications*; Wiley-VCH, (2001); Weinheim.
7. (a) S.-C. Lo and P.L. Burn, *Chem. Rev.*, 107, (2007), 1097 (b) A. Nantalaksakul, D.R. Reddy, C.J. Bardeen and S. Thayumanavan, *Photosynthesis Research*, 87, (2006), 133; (c) J.M.J. Fréchet, *PNAS*, 99, (2002), 4782; (d) U. Boas and P.M.H. Heegaard, *Chem. Soc. Rev.*, 33, (2004), 43.

8. P.K. Maity and W.A. Goddard III, *J. Phys. Chem. B.*, 110, (2006), 26628.
9. W. Chen, D.A. Tomalia and J.L. Thomas, *Macromolecules*, 33, (2000), 9169.
10. P. Antoni, D. Nyström, C.J. Hawker, A. Hult and M. Malkoh, *Chem. Commun.*, (2007), 2249.
11. A.M. Naylor, W.A. Goddard III, G.E. Kiefer and D.A. Tomalia, *J. Am. Chem. Soc.*, 111, (1989), 2339.
12. G.R. Newkome, C.N. Moorefield, G.R. Baker, M.J. Saunders and S.H. Grossman, *Angew. Chem. Int. Ed. Engl.*, 21, (1991), 1287.
13. S. Stevelmans, J.C.M. Van Hest, J.F.G.A. Jansen, D.A.G.J. Van Boxtel, E.M.M. De Brabander Berg and E.W. Meijer, *J. Am. Chem. Soc.*, 118, (1996), 7398.
14. J.F.G.A. Jansen, E.W. Meijer and E.M.M. De Brabander Berg, *J. Am. Chem. Soc.*, 117, (1995), 4417.
15. T.M. Hermans, M.A.C. Broeren, N. Gomopoulos, A.F. Smeijers, B. Mezari, E.N.M. Van Leeuwen, M.R.J. Vos, P.C.M.M. Magusin, P.A.J. Hilbers, M.H.P. Van Genderen, N.A.J.M. Sommerdijk, G. Fytas and E.W. Meijer, *J. Am. Chem. Soc.*, 129, (2007), 15631.
16. J. Hu, Y. Cheng, Y. Ma, Q. Wu and T. Xu, *J. Phys. Chem. B.*, 113, (2009), 64.
17. A. Archut, G.C. Azzellini, V. Balzani, L.D. Cola and F. Vögtle, *J. Am. Chem. Soc.*, 120, (1998), 12187.
18. (a) J. Haensler and F.C. Szoka, Jr., *Bioconjugate Chem.*, 4, (1993), 372; (b) K. Rittner, A. Benavente, S. Bompard, F. Heitz, G. Divita, R. Brasseur and E. Jacobs, *Mol. Therapy*, 5, (2005), 104.
19. A.-M. Caminade, C. d.-O. Turrin and J.-P. Majoral, *Chem. Eur. J.*, 14, (2008), 7422.
20. S. Supattapone, H.-O.B. Nguyen, F.E. Cohen, S.B. Prusiner and M.R. Scott, *PNAS*, 96, (1999), 14529.
21. P. Willmann, T. Marti, A. Furer and F. Diederich, *Chem. Rev.*, 97, (1997), 1567.
22. S.C. Zimmerman, M.S. Wendland, N.A. Rakow, I. Zharov and K.S. Suslik, *Nature*, 418, (2002), 399.
23. A.D. Emanuele and D. Attwood, *Adv. Drug. Deliv. Rev.*, 57, (2005), 2147.
24. H. Ye, J.A. Crooks and R.M. Crooks, *Langmuir*, 23, (2007), 11901.
25. Y. Yang, Y. Yan, W. Wang and J. Li, *Nanotechnology*, 19, (2008), 175603-1-10.
26. R.M. Crooks, M. Zhao, S. Li, V. Chechik and L.K. Yeung, *Acc. Chem. Res.*, 34, (2001), 181.
27. M. Popa, T. Pradell, D. Crespo and J.M. Calderón-Moreno, *Colloids and Surfaces A: Physicochem. Eng. Aspects*, 303, (2007), 184.
28. M. Chen, Y.-G. Feng, X. Wang, T.-C. Li, J.-Y. Zhang and D.-J. Qian, *Langmuir*, 23, (2007), 5296.
29. S. Keki, J. Torok, G. Deak, L. Daroczi and Y. Takaguchi, *J. Colloid. Interface Sci.*, 229, (2000), 550.
30. M. Kavitha, M.R. Parida, E. Prasad, C. Vijayan and P.C. Deshmukh, *Macromol. Chem. Phys.*, 210, (2009), 1310.

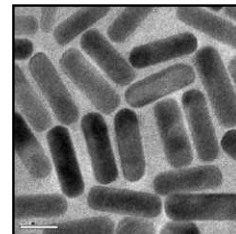
ADDITIONAL READING

1. U. Boas, J.B. Christensen and P.M.H. Heegaard, *Dendrimers In Medicine And Biotechnology: New Molecular Tools*, RSC Publishing (2006).
2. M.J. Jean Fréchet and A. Donald Tomalia, *Dendrimers and Other Dendritic Polymers* (Eds.), Wiley (2002).
3. F. Vögtle, G. Richardt and N. Werner, *Dendrimer Chemistry: Concepts, Syntheses, Properties, Applications*, Wiley-VCH, Weinheim (2009).

REVIEW QUESTIONS

1. Define a macromolecule.
2. What is 'generations' in dendrimers?
3. What is back folding in dendrimer?
4. State the difference between convergent and divergent synthetic methods. Which method is considered as a better method and why?
5. Dendrimer is said to be a unimolecular micelle. Why?
6. What are the different ways of drug loading in dendrimers?
7. Describe the general methods of preparation of dendrimer encapsulated nanoparticles.

NANOHYBRID SYSTEMS



“Design in art, is a recognition of the relation between various things, various elements in the creative flux. You can’t invent a design.

You recognize it, in the fourth dimension.

That is, with your blood and your bones, as well as with your eyes.”

David Herbert Lawrence,

“Art and Morality,” Part 4, Phoenix: The Posthumous Papers of D.H. Lawrence, Edited by E. McDonald, 1936

Organic-inorganic hybrids are receiving considerable attention nowadays. There is a belief among the scientific community that the future optical materials will use such hybrids. The research on such materials is driven by intellectual curiosity, potential financial benefits and the possibilities of the unknown. The definition, classification and the chemistry behind the process are discussed in this chapter. Hybrids are made using organic templates, nano-building blocks and bio-inspired methods. Materials formed through these routes, especially have unusual mechanical properties as in the case of biological structures. The interaction between organic and inorganic components as well as micro and nanostructures present in the hybrids determine their mechanical properties. Hybrid materials offer the possibility of making new solid state devices out of the existing library of functional organic molecules. Few applications of hybrid materials discussed here include gel-glass dispersed liquid crystalline devices, non linear optical materials and dye-sensitised solar cells. It is important to remember that such hybrids are central aspects of biology.

Learning Objectives

- Why one makes hybrid materials?
 - What are the categories of hybrid systems?
 - What are their specific properties?
 - What are their typical applications?
-
-

17.1 INTRODUCTION

For any specific application, the materials used contain multiple components. This is true of many of the parts being made in factories. These include everyday used items like paper, toothpaste, detergent, etc. A plastic item, such as the one providing cover to a laptop, contains many materials, which provide specific attributes to the finished product. Of late, the need to improve properties has increased significantly which requires that the material formed has molecular ingredients mixed in intimate fashion. This has resulted in composites, and those having structures at nanometer scale are the so-called nanocomposites. These composites have improved properties. The possibility of making such materials has given rise to new properties; for example, nanoscale coatings on several substrates have become possible only because of our competence in making composites at the molecular scale. When we look at biological objects such as bones or shells, we realise that many of these are nanoscale hybrids. As natural materials are much better in terms of their properties, their structure-function relations have made many researchers to look at biomimetic structures for improved properties. These explorations have also generated great interests and incredible results in this area of research. In this chapter, we briefly look through some of the achievements in this area.

If we try to mix two components, A and B, at the nanoscale, the properties of the mixture are expected to be better than the sum of the properties of individual components. This is expressed as, $A \cup B \geq A + B$. The properties of the mixture cannot be attained by using any one of the components. The synergy term $A \cup B$ is the reason for this. In the case of hybrids, the two components, A and B, will have the same size, whereas in nanocomposites, one component is larger than the other, $A \ll B$. Thus, the term 'organic-inorganic hybrids' refers to nanocomposites, where the organic and inorganic components are combined over length scales ranging from a few Angstroms to a few tens of nanometers. By reducing the dimension of the participating constituents into the nanometer level, the interfacial contact between the organic and inorganic constituents is greatly increased, which gives these materials their unusual properties. The sudden explosion in this field is because of the rapid progress occurred in the soft chemistry processes like sol-gel process (also called as *Chimie douce* in French). Based on the interaction that holds the organic and inorganic components, hybrids are classified into the following two classes.

17.2 CLASSIFICATION OF ORGANIC-INORGANIC HYBRIDS

17.2.1 Class-I Hybrids

A Class-I hybrid is made by mixing a polymerisable alkoxide precursor with a functional organic molecule. The commonly used alkoxide precursors include $\text{Si}(\text{OR})_4$, $\text{Zr}(\text{OR})_4$ and $\text{Ti}(\text{OR})_4$. A weak bond like van der Waals interaction or hydrogen bond holds the organic and inorganic parts together.

17.2.2 Class-II Hybrids

In Class-II hybrids, the bonding between organic and inorganic domains is strong. A molecule of the type $\text{R}'\text{M}(\text{OR})_{n-1}$ can be used for making Class-II type hybrid material. The alkoxide group (OR)

undergoes hydrolysis generating a hydroxyl group on the metal center (M). The hydroxyl group undergoes further condensation reaction progressively generating the silicon network. The R' group provide a handle for imparting various properties to the silica network. In Class-II type hybrids, the interaction that holds the organic and inorganic components can be covalent, iono-covalent or Lewis acid-base.

17.3 PREPARATION OF ORGANIC-INORGANIC HYBRIDS

The methods used for making organic-inorganic hybrids are classified into three types. They are: sol-gel methods, self-assembly route and nano-building-block approach.

17.3.1 Sol-Gel Methods

Route 1: This route involves the hydrolysis of the organically modified alkoxides. The general formula of the alkoxides can be written as $R'M(OR)_{n-1}$, wherein the R' group contains the functionality. The controlled hydrolysis followed by condensation of it leads to silica network with the organic group imparting various properties.

Route 2: This method uses bridged siloxanes with the general formula, $X_3Si-R-X_3$ (R is an organic spacer, X may be OR, Cl or Br).

Route 3: This involves hydrothermal synthesis of materials in polar solvents in the presence of organic templates. The medium is normally a polar solvent, like water or formamide. This method is used to make zeolites.

17.3.2 Nano-building Blocks

Nano-building blocks are preformed, perfectly calibrated building units. Nano-building blocks keep their identity in the final material. This path utilises clusters, pre- or post-functionalised nanoparticles or layered materials like layered silicates and layered double hydroxides, in order to disperse the organic component. The use of nano-building blocks leads to a better definition of the inorganic part in the final hybrid material.

17.3.3 Self-Assembly

The organic template usually self-assembles to give the mold, over which one can grow the inorganic template. The organic structure-directing agents normally used include surfactants and nano-building blocks.

Route 1: The classic example for a hybrid produced by this method is periodic mesoporous silica. This method can produce periodic mesoporous materials with the walls decorated with functional groups.

Route 2: In this method, the surfactant provides the template and the bridged silsesquioxane is used as the precursor for the inorganic phase.

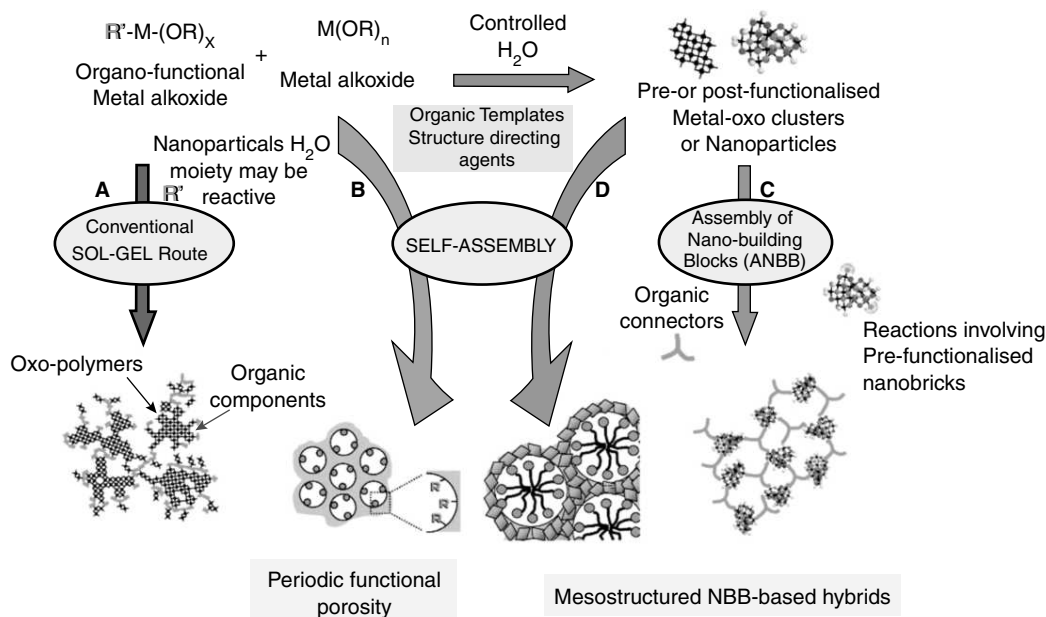


Fig. 17.1 Schematic describing the classification of the strategies to make hybrid materials (reprinted from Ref. 1. Copyright (2001) American Chemical Society).

Route 3: Templated assembling in combination with nano-building block approach is used in this route to make hybrid materials.

These approaches are summarised in Fig. 17.1.

17.4 MESOPOROUS ORGANO-INORGANIC HYBRIDS

If a surfactant is dissolved in water, the molecule organises in such a way that the hydrophilic part is in contact with water and hydrophobic part is away from it. This results in the formation of spherical or cylindrical structures. On further increasing the concentration of the surfactant, the spherical micelles form cubic close packed arrangements, whereas the rod-shaped cylindrical structures stack parallel to each other to form hexagonal mesophases. Any further increase in concentration leads to the formation of sandwich-shaped bilayers. The bilayers can change shape to vesicles on increasing the concentration further. The important phases of a surfactant in water are shown in Fig. 17.2.

Researchers at Mobil Corporation made the first successful attempt to create porous materials using such organic templates.² The interfacial energy has to be reduced in order to combine the organic and inorganic phase. This was achieved by adding soluble silica species into the surfactant solution. The silica-surfactant self-assembled to form hexagonal mesophases. The removal of the template after the silica wall formation resulted in structures with uniform pores. The schematic of the method is shown in Fig. 17.3.

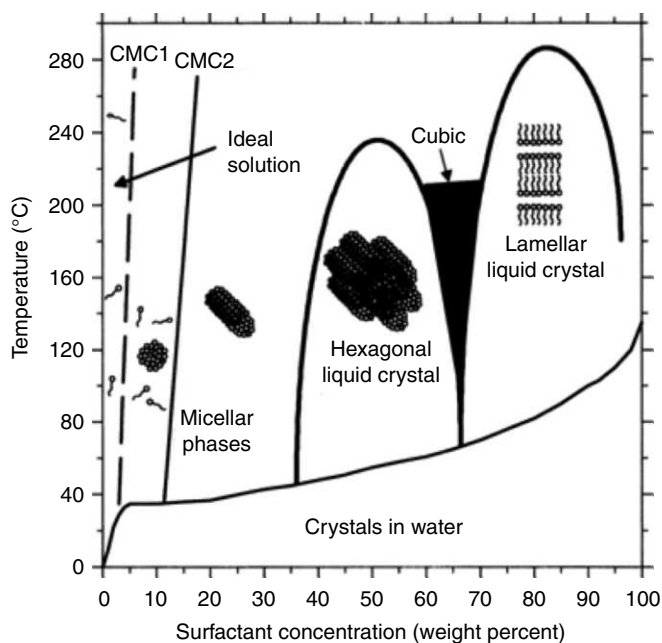


Fig. 17.2 Schematic phase diagram of CTAB in water (reprinted from Ref. 2. Copyright (1996) American Chemical Society).

There is a competition between the silicate anion and the counter ion for binding with the positively-charged surfactant head group. For example, counter ion, like ClO_4^- , prevents the silicate anion from binding with the surfactant thereby delaying the nucleation process. The order of silica-surfactant mesophase formation follows the binding constant of the counter ion ($\text{ClO}_4^- < \text{NO}_3^- < \text{Br}^- < \text{SO}_4^{2-}$, $\text{SO}_3^{2-} < \text{Cl}^- < \text{F}^-$).

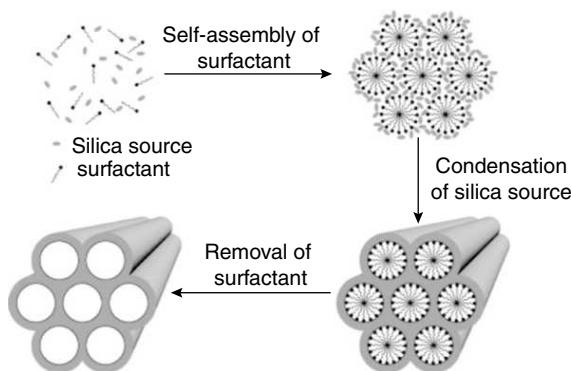


Fig. 17.3 Schematic showing the preparation of periodic mesoporous silica (reprinted from Ref. 3. Copyright (2005) American Chemical Society).

The increase in pKa value with the progress of the reaction makes silica-based materials more in comparison with the other compounds. The pKa of $\text{Si}(\text{OH})_4$ is 8. As the condensation proceeds, the pKa increases. Thus, the silica becomes more and more acidic and hence highly charged ($\text{Si}(\text{OH}_2^+)$). This increases the binding constant between the silica species and the head group of the surfactant. Thus, silica species get accumulated around the surfactant, which helps in the formation of a thick silica wall around the surfactant.

From the value of the packing parameter, it is possible to predict the change over from one silica-surfactant mesophase to another. The packing parameter is given by the equation, $g = V/Ia_0$, where V is the volume of the hydrophobic surfactant, I denotes the surfactant chain length and a_0 is the effective head group area of the surfactant. The g value increases in the order, spherical micelle ($g < 1/3$) < hexagonal ($g = 1/3-1/2$) < cubic ($g = 2/3-3/4$) < lamellar ($g = 1/2-1$). Thus, surfactants with long tail or silica with plenty of charges give structures with large g values. By selecting suitable conditions, it is possible to create a rich variety of materials.

The charge matching and organic packing are the two important factors that affect the silica-surfactant mesophase structure. The charge matching is achieved by changing the pH. Based on the pH, silica can be Si-O^- or $\text{Si}(\text{OH}_2^+)$. The organic packing can be changed by adding a cosurfactant or solvent. The morphology of the final silica nanoparticle can be changed by adding alkoxy silanes into the system. The alkoxy silanes insert their hydrophobic tail into the micellar core thereby reducing the head group charge density which results in structures with lower g values. This favours side growth resulting in spherical particles, whereas the hydrophilic alkoxy silanes favour the formation of spherical particles.⁴

17.5 EVAPORATION-INDUCED SELF-ASSEMBLY (EISA)

The surfactant-based route gave material with well-defined porosity. But, for making devices, it is necessary that the mesoporous materials be made in the form of a thin film. A major breakthrough was achieved by the evaporation-induced self-assembly method (EISA). In this method, soluble silica species, surfactant, alcohol and acid were dissolved in water. The concentration of the surfactant in the initial solution was well below the critical micelle concentration. Preferential evaporation of alcohol from the solution left the remaining solution enriched with surfactant, silica and acid. The gradual evaporation of the alcohol took the surfactant concentration above its critical micelle concentration. This initiated the formation of micellar-silica mesophases. The fast hydrolysis rate and slow condensation rate that is required for the formation of small oligomeric silica species was achieved by bringing the pH of the solution close to isoelectric point of silica ($\text{H}^+/\text{Si} \sim 0.14-0.004$). After its job as the catalyst, the excess hydrochloric acid is evaporated off from the solution.⁵

Two mechanisms have been suggested in the literature for the evaporation-induced self-assembly (EISA). They are:

1. Liquid crystal template mechanism
2. Cooperative self-assembly

According to the first mechanism, the inorganic phase condenses around the mesophase created by the self-assembly of the surfactant. In the second mechanism, the oligomeric silica species combine with the surfactant to form a new surfactant species, which has the capability to form a mesophase.

17.5.1 EISA in Non-silicate Systems

TiO₂-based mesostructured thin films were prepared by using TiCl₄/Ti(OCH₂CH₃)₄ as the inorganic precursor and pluronic F127, as amphiphilic block copolymer((OH(CH₂CH₂O)_x(CHCH₃CH₂O)_y(CH₂CH₂O)_xH), where $x = 106$ and $y = 70$) is the surfactant. *In situ* SAXS (Small-angle X-ray scattering) was used to study the intermediate phases, in which the system passes through before becoming the final mesostructured thin film. The whole process can be divided into five stages. The first sudden decrease of the film thickness in the region 1 is due to the rapid evaporation of the volatile alcohol from the system. This is followed by the small changes in film thickness due to the evaporation of water and acid from the film (region 2). Once the system reaches the drying line, there is not much difference in the film thickness (region 3). Initially, the worm-like phase appears. This is followed by the Im3m body centered cubic phase (spherical micelles). At last, the system freezes to triclinic phase. A pictorial representation of the drying process and the time-dependent evolution of various phases are depicted in Fig. 17.4.

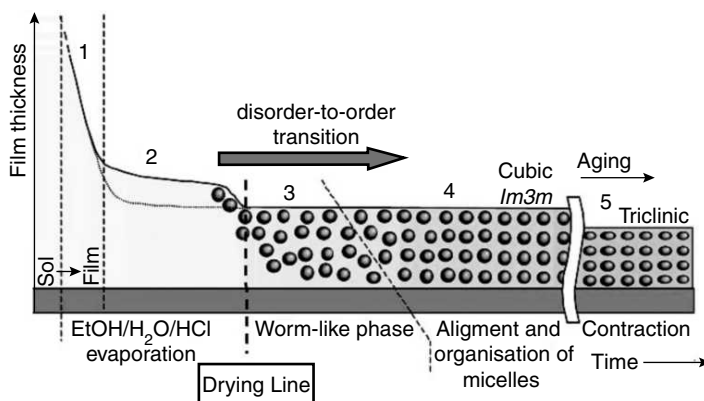


Fig. 17.4 The Schematic describing the film formation process during the EISA in TiO₂ based systems. The dashed lines perpendicular to the x axis indicate the five stages of the process (reprinted from Ref. 4. Copyright (2003) American Chemical Society).

To graft organic functional groups onto silica framework, the localization of the functional group of the surfactant is very important. The whole structure for the silica-CTAB system can be compartmentalised into three regions (see Fig. 17.5A). The silica framework (I), the organic region formed by the aggregation of alkyl chain of the surfactant (zone II) and the ionic interface formed by the surfactant head groups and charged oligomeric silica species (III). Polymeric surfactants are also used to make mesostructured thin films. An example is polyethylene oxide-polypropylene oxide-polyethylene oxide

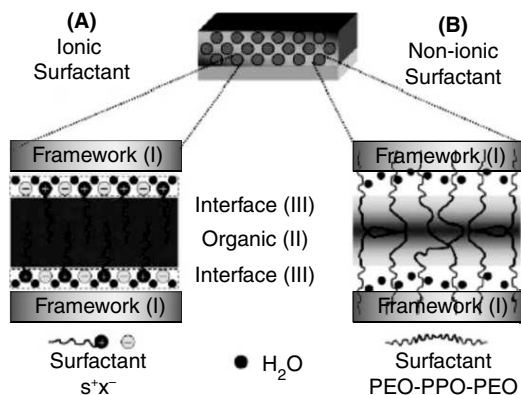


Fig. 17.5 The schematic describing the various interfaces formed during the EISA process (reprinted from Ref. 5. Copyright (2005) Royal Society of Chemistry).

(PEO-PPO-PEO). The polyethylene oxide (PEO) is hydrophilic in nature while the polypropylene oxide (PPO) is hydrophobic. The corresponding compartmentalisation is shown in Fig. 17.5B.

17.5.2 Applications

It is possible to combine EISA with dip pen lithography, microcontact printing and micropen lithography. This has resulted in applications like microfluidic devices and optical switches. Few of the applications are discussed below.

17.5.2.1 pH-Sensitive Microfluidic Device

In the following example, EISA has been used to make pH-sensitive microfluidic device. A three-step method has been used to make such a device. The steps involved are: (1) microcontact printing, (2) dip coating, and (3) derivatisation with a dye.

Microcontact printing is used to create a surface with hydrophilic and hydrophobic regions. The schematic of such a surface is shown in Fig. 17.6. The hydrophilic and the hydrophobic regions are

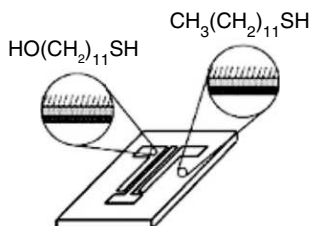


Fig. 17.6 The surface patterned with hydrophilic and hydrophobic region using microcontact printing. The structure of hydrophilic and hydrophobic regions are shown in circles (reprinted from Ref. 5. Copyright (2005) Royal Society of Chemistry).

shown in circles in Fig. 17.6. The 11-mercaptoundecanol-coated region represents the hydrophilic region and the 1-dodecane thiol coated one represents the hydrophobic region.

The ink is made up of soluble silica monomers, aminopropyl trimethoxy silane and cetyl trimethyl ammonium bromide. Dip coating was used to deposit a thin layer of ink onto the patterned surface. During dip coating, the ink wets only the hydrophilic surface (the region patterned with 11-mercaptoundecanol terminated SAMs). When the ink was spread on the surface, preferential evaporation of the ethanol from the solution left the remaining ink enriched with water. This was followed by the silica-surfactant self-assembly, leading to the formation of mesoporous material with walls decorated with amino groups. The TEM image of the amine-functionalised mesoporous film is shown in Fig. 17.7A.

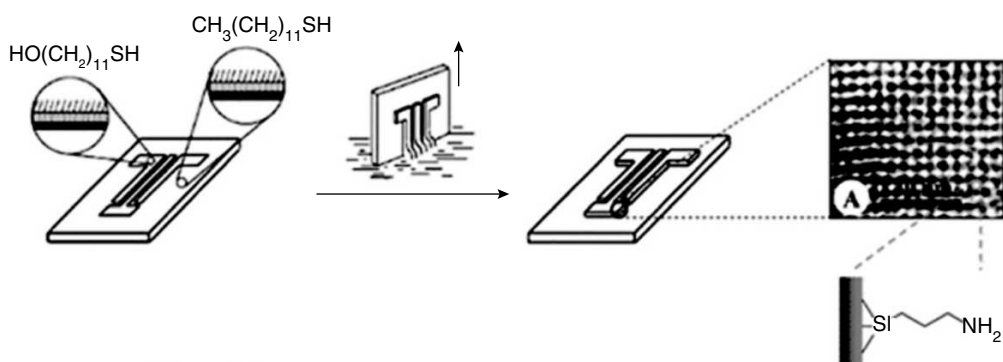


Fig. 17.7 Selective dewetting of the patterned surface through dip-coating. One of the region is coated with hydroxyl terminated thiol and the other with methyl terminated thiol. The arrow indicates the direction of withdrawal of the substrate during dip coating. The TEM image of the dip-coated material is shown in Fig. A. The final mesoporous materials has amine decorated walls (reprinted from Ref. 5. Copyright (2005) Royal Society of Chemistry).

In the third step, dye molecules were attached to the terminal amino groups. The free amino groups were treated with 5,6-carboxy fluorescein succinimidyl ester. An amide linkage is formed by the reaction between ester group of the fluorescein dye and the terminal amino group(s) present on the walls. The fluorescein dye is sensitive to pH. Hence the functionalisation with dye makes the device sensitive to pH. The derivatisation of the terminal amino groups with fluorescein dye is schematically shown in Fig. 17.8.

Now the microfluidic system was charged with solutions of varying pH and the solutions were taken to the imaging area by capillary action. The fluorescence image of the patterned mesoporous structure is shown in Fig. 17.9. The change in colour with the solution pH is also shown in Fig. 17.9. The microfluidic device after charging with solutions of pH = 4.8, 7.7 and 12 shows pH-dependent fluorescence.

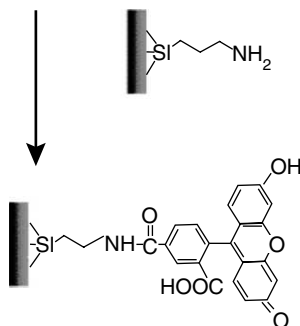


Fig. 17.8 Figure illustrating the second step of the process. During this, the terminal amine groups were changed to fluorescein derivative. The yellow region indicates the mesoporous wall. The amino groups were then derivatised by treating with 5,6-carboxy fluorescein succinimidyl ester leading to a dye conjugated mesoporous film (reprinted from Ref. 5. Copyright (2005) Royal Society of chemistry).

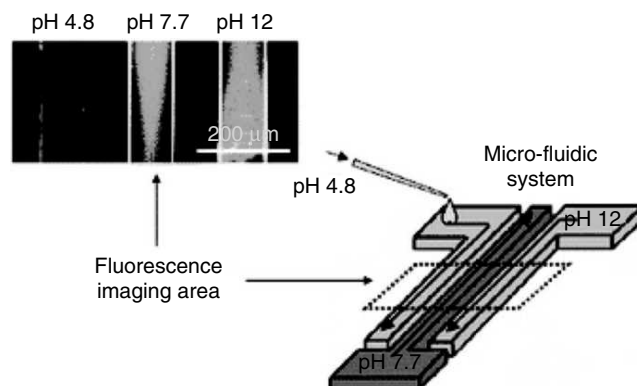


Fig. 17.9 The fluorescence image of the microfluidic device with region marked with dots shows pH dependence. The device was charged with solutions of pH 4.8, 7.7 and 12 (reprinted from Ref. 5. Copyright (2005) Royal Society of Chemistry). (For clarity see colour figure.)

17.5.2.2 Nanolaminates

Evaporation-induced self-assembly can be used to create alternating layers of organic and inorganic materials. The phase diagram illustrating the evolution of nanolaminate structure during dip coating is shown in Fig. 17.10. The vertical axis shows the distance/time above the sol reservoir surface. The horizontal axis shows the film thickness/surfactant concentration. The points marked A and B in Fig. 17.10 represent the formation of bilayer and nanolaminate. Further details about these structures are explained in Fig. 17.11 and Fig. 17.12.

The solution contains monomer, cross-linking agent and initiator apart from oligomeric silica species, alcohol, water and HCl. The preferential evaporation of the alcohol takes the monomer, cross-

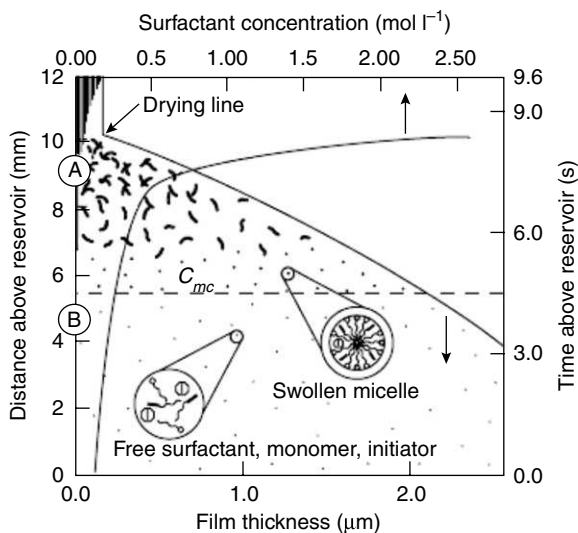


Fig. 17.10 Phase diagram describing the evolution of nanolaminate during dip coating (reprinted from Ref. 6. Copyright (1999) Wiley-VCH-Verlag GmbH & Co.).

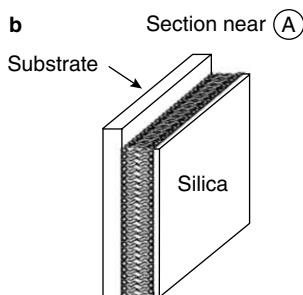


Fig. 17.11 Figure showing the first bilayer formed near the substrate. This bilayer acts as the nucleation site and additional bilayers grow over this to form the laminate structure (reprinted from Ref. 6. Copyright (1999) Wiley-VCH-Verlag GmbH & Co.).

linking agent and the initiator into the micellar core. Initially, a bilayer formation occurs below critical micelle concentration. This provides the organised surface for the growth of additional layers. This initial bilayer is shown in Fig. 17.11.

On further evaporation, at the point B, the lamellar silica-surfactant mesophase stacks over the bilayer creating a nanolaminate. The structure of the lamellar silica-surfactant mesophase near the substrate surface is shown in Fig. 17.12. The hypothetical arrangement of the monomer, cross-linking agent, initiator near to the oligomeric silica species inside the laminate is shown in Fig. 17.12.

The hypothetical arrangement of various molecules at the inorganic interface after polymerization is shown in Fig. 17.13. The polymerization can be initiated by light or heat thereby completing the

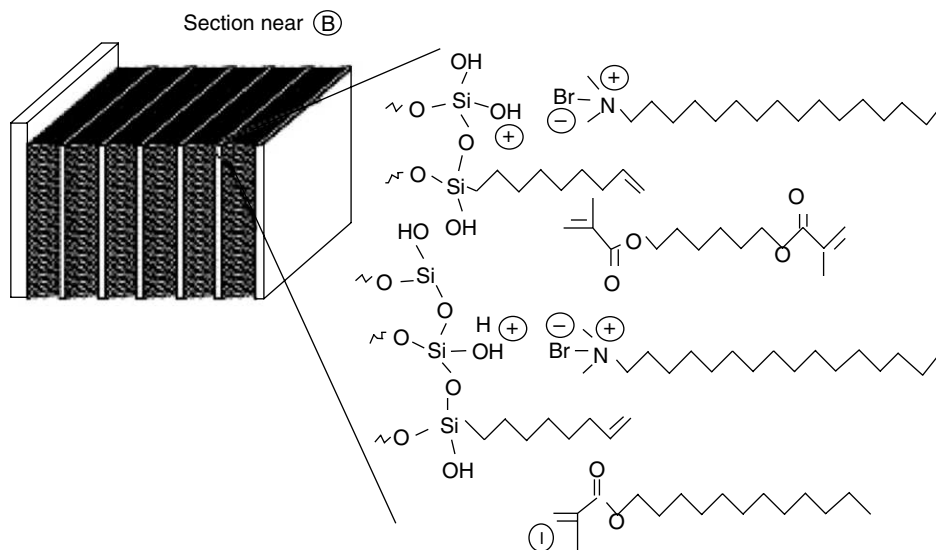


Fig. 17.12 Phase diagram describing the evolution of nanolaminate during dip coating. The structure of the lamellar silica-surfactant mesophase near the substrate surface is shown in the figure. The hypothetical arrangement of the monomer, cross-linking agent, initiator near to the oligomeric silicate surface inside the lamellar mesophase is also shown in the figure (reprinted from Ref. 6. Copyright (1999) Wiley-VCH-Verlag GmbH & Co.).

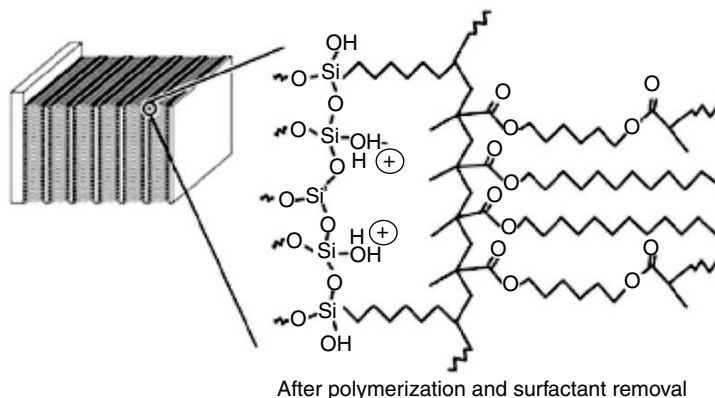


Fig. 17.13 Figure showing the hypothetical arrangement of molecules near the surface after polymerization (reprinted from Ref. 6. Copyright (1999) Wiley-VCH-Verlag GmbH & Co.).

nanolaminate structure. Thousands of alternating layers of organic and inorganic phases can be created in a single dipping step. Because of the dynamic nature of the process, they are self-healing and the films made are of optical quality in nature, which may allow their use in applications like automobile coating.

17.5.2.3 Molecular Valves or Gates

Azobenzene can exist in two forms, namely, *cis* and *trans*. The *cis* to *trans* conversion of azobenzene is UV-sensitive. The *trans* isomer, on irradiation with UV changes to *cis* form, whereas the *cis* form, on heating reverts back to the *trans* form. An amphiphilic molecule containing azobenzene unit, namely, 4-(3-triethoxysilylpropylureido)azobenzene is used to make photoresponsive mesoporous films. The photoresponsive mesoporous film is made by adding 4-(3-triethoxysilylpropylureido)azobenzene into the reaction medium containing tetraethyl orthosilicate and a nonionic surfactant brij56 ($C_{16}H_{33}(OCH_2CH_2)_nOH$, $n=10$). Due to the hydrophobicity, the propylureidoazobenzene is positioned in the hydrophobic micellar core. The hydrophilic silicic acid condenses with the orthosilicate. This results in the formation of a mesoporous film with the pore walls functionalised with azobenzene molecules which are oriented towards the pore interior. The *cis-trans* isomerisation, triggered by the light, can be used to open or close the valve. The schematic of the mesoporous photoswitchable valve is shown in Fig. 17.14. Each of the grey circle in the circle coloured with brown represents the mesoporous valve. The valve in the left side has a small hole at the centre, whereas the hole is larger at the right side valve.

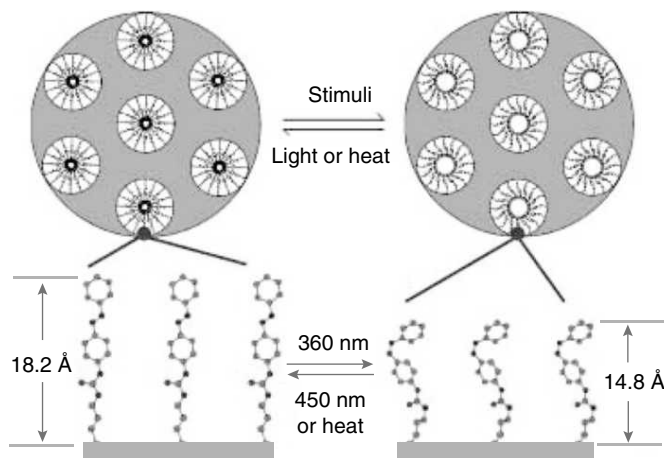


Fig. 17.14 Schematic showing the opening of the pores by the light. When the azobenzene molecule is in the *trans* state, the valve shuts down (the picture on the left side with small hole) and when it changes to the *cis* form, the valve opens up (the picture on the right with a large hole). The configuration of azobenzene is shown at the bottom of each figure. When it is in the *trans* state, the length of the molecule is 18.2 Å. The molecule on changing to the *cis* form, the length reduces to 14.8 Å (reprinted from Ref. 7. Copyright (2003) John Wiley & Sons, Inc.).

17.6 NANO-BUILDING BLOCKS-BASED HYBRIDS

Nano-building blocks are preformed, perfectly calibrated objects. The definition of inorganic part in a hybrid material is best met with such nano-building blocks. They keep their integrity in the final

material. The commonly used nano-building blocks include silsesquioxanes, organozirconia clusters, organotin clusters and polyoxometallates. Atom transfer radical polymerization (ATRP), Reversible addition fragmentation chain transfer polymerization (RAFT) and surfactant-assisted free radical emulsion polymerization reactions are used to coat the organic part around the nano-building block surface. Few of the commonly used nano-building blocks are listed below.

Metal alkoxides are in general not very stable towards nucleophiles and undergo hydrolysis. This led to the use of perfectly calibrated pre-formed objects called NBBs for making hybrid materials. Few of the NBBs are listed below:

- 17.6.1 Silsesquioxanes
- 17.6.2 Organozirconia Oxoclusters
- 17.6.3 Organotin Oxoclusters
- 17.6.4 Polyoxometallates

17.6.1 Silsesquioxanes

Rice hull ash contains amorphous silica (80–98%) and amorphous carbon (20–2%). The surface area of the silica is 20–50 m²g⁻¹. Due to its high surface area, it is highly reactive. It is a potential candidate for the production of silicon containing chemicals. It is possible to depolymerise the silica present in rice hull ash by treating with quaternary ammonium hydroxide. This results in the formation of octasilicate anions. The structure of the octasilicate anion made from rice hull ash is shown in Fig. 17.15.

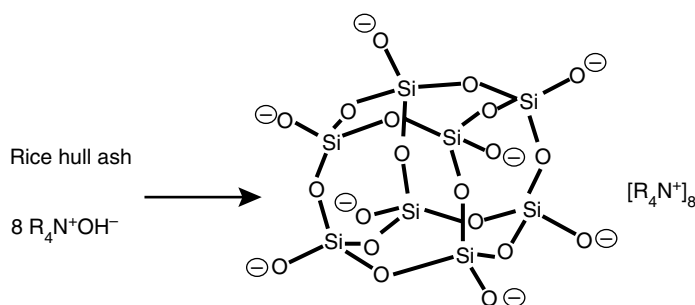


Fig. 17.15 Schematic of the depolymerization of rice hull ash silica by tetra alkyl ammonium hydroxide (reprinted from Ref. 8. Copyright (2005) Royal Society of Chemistry).

Octasilicate anion (OSA) can be functionalised at eight positions, each with functional group in a different quadrant. Even though the octasilicate anions contains highly nucleophilic, negatively charged oxygen, the high water of hydration and the presence of quaternary ammonium ions associated with the cube makes the nucleophilic substitution reaction extremely difficult. The only way to functionalise the OSAs is by silylation reaction, as shown in Fig. 17.16.

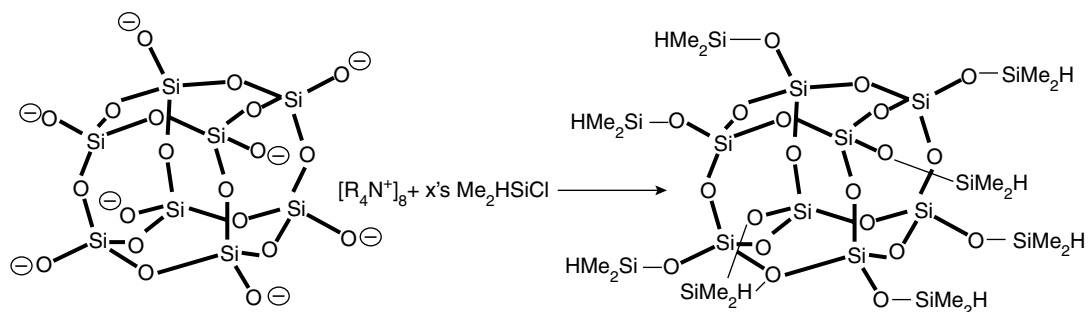


Fig. 17.16 The functionalisation of octasilicate anion by silylation reaction. This nano-building block can be functionalised at eight positions (reprinted from Ref. 8. Copyright (2005) Royal Society of Chemistry).

17.6.2 Zirconia-based Nano-building Blocks

An example, for a zirconia-based nano-building block is $Zr_6(OH)_4(OAc)_{12}$. The cluster contains a $Zr_6O_4(OH)_4$ core. The structure is built upon a Zr_6 octahedron, wherein faces are alternatively occupied by μ_3 -O and μ_3 -OH groups. The cluster contains 12 carboxyl groups with three chelate zirconium atoms at one triangular face and the nine carboxyl bridges at the other edges. The structure of the oxo cluster is shown in Fig. 17.17. The double bonds of the methacrylate group can be polymerised to give the hybrid material. The carboxyl ligands can be exchanged with other molecules giving plenty of Zr_6 building blocks. These oxoclusters are also used to crosslink polymers.

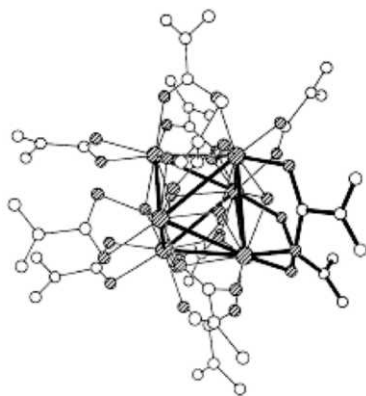


Fig. 17.17 Structure of oxozirconium methacrylate cluster $Zr_6O_4(OH)_4(OMc)_{12}$. The Zr_6 octahedron is drawn with thick line (reprinted from Ref. 9. Copyright (1999) Elsevier Science S.A.).

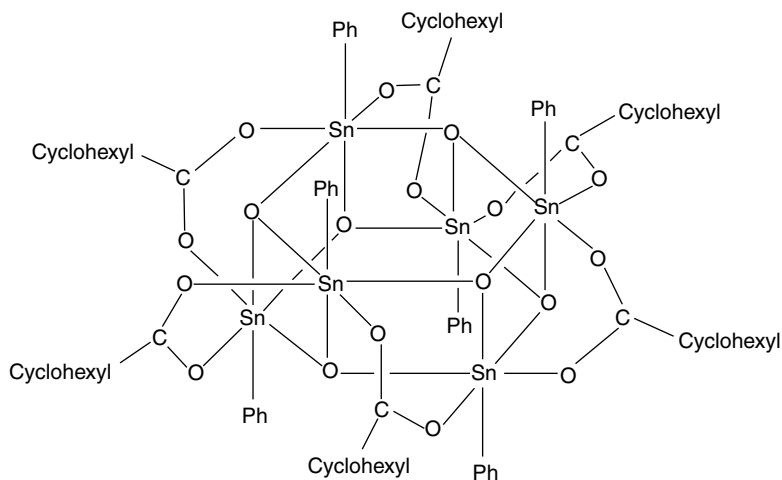


Fig. 17.18 The Tin-6 molecular structure. The drum-shaped framework is clear from the figure (reprinted from Ref. 10. Copyright (1989) American Chemical Society).

17.6.3 Tin-based Nano-building Blocks

Like carbon-silicon bond, the carbon-tin sp^3 bond is also covalent and hence stable towards the attack by nucleophiles. Few of the tin-based nano-building blocks and the corresponding hybrid materials are discussed below.

17.6.3.1 Tin-6 Octahedra

The cluster is drum shaped. The carbon atoms carrying the organic group are in the same plane and the organic group point outwards. The organic group can be functionalised with various molecules. The structure of the cluster is shown in Fig. 17.18.

17.6.3.2 Tin-12 Octahedra

Another oxo cluster used to make hybrids is $\{(R\text{Sn})_{12}(\mu_3\text{-O})_{14}(\mu_2\text{-OH})_6\}^{2+}$. The cluster is called Tin-12. The structure of the cluster is shown in Fig. 17.19. The methods used to functionalise the cluster are

1. Covalent bonding of a polymerisable function F
2. Polymerisable function linked via electrostatic interactions and hydrogen bonds
3. Telechelic di-anions linking nano-building blocks via electrostatic interactions and hydrogen bonds

The methods used to functionalise Tin-12 are summarised in Fig. 17.19.

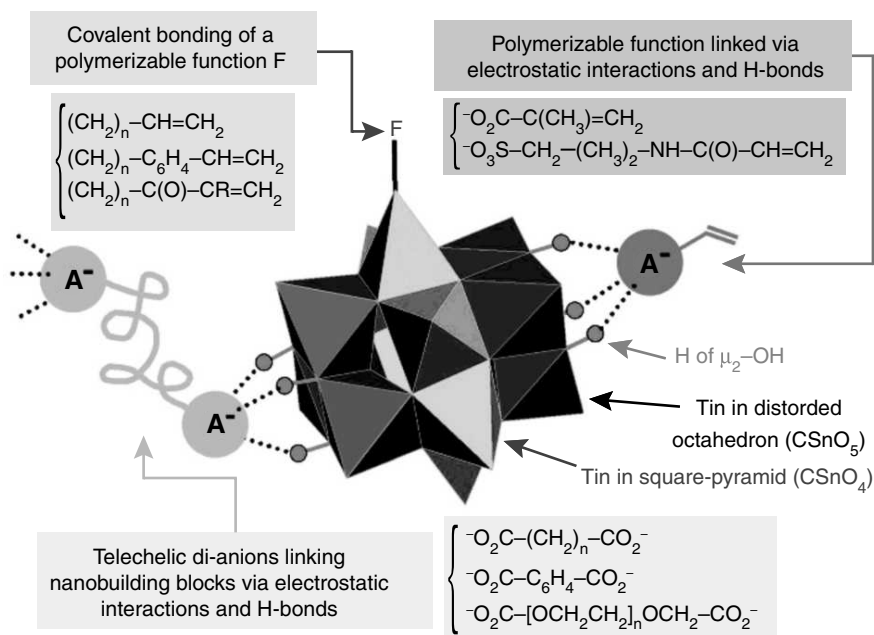
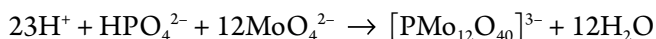
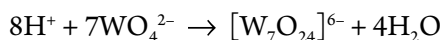


Fig. 17.19 Schematic describing the structure of tin-12 and various strategies used to functionalise the oxocluster (reprinted from Ref. 11. Copyright (2001) American Chemical Society).

17.6.4 Polyoxometalate-based Nano-building Blocks

They belong to the class of metal-oxygen cluster anions. They are of two types, namely, isopoly anions $[\text{M}_m\text{O}_y]^{p-}$ and heteropoly anions $[\text{X}_x\text{M}_m\text{O}_y]^{q-}$ ($x \leq m$), where X represents the hetero atom and M is the addenda atom. The heteroatom X is located at the centre of the polyanion. Hence, it is also called the central atom. The hetero atoms normally present are P^{5+} , As^{5+} , Si^{4+} , Ge^{4+} , B^{3+} , etc. The addenda atom is normally molybdenum or tungsten in their highest oxidation state, and is octahedrally coordinated. The polyoxometalates are formed by edge sharing and corner sharing MO_6 octahedra. Out of the six oxygen atoms around each addenda atom, five oxygens are shared and the sixth one is pointing outwards. All these MO_6 units are held together by the central atom, which is tetrahedrally coordinated. This terminal oxygen atom can be protonated. Polyoxometalate anions are prepared by the self-assembly of $(\text{MO}_4)^{2-}$ ions in acidic solutions. Some of the examples are shown below.



Lindqvist anion ($[\text{W}_6\text{O}_{19}]^{2-}$), keggin anion ($[\text{PW}_{12}\text{O}_{40}]^{3-}$) and Dawson anion ($[\text{P}_2\text{W}_{18}\text{O}_{62}]^{6-}$) are some of the well-studied polyoxometalates. The formula and structure of these anions are shown in Fig. 17.20.

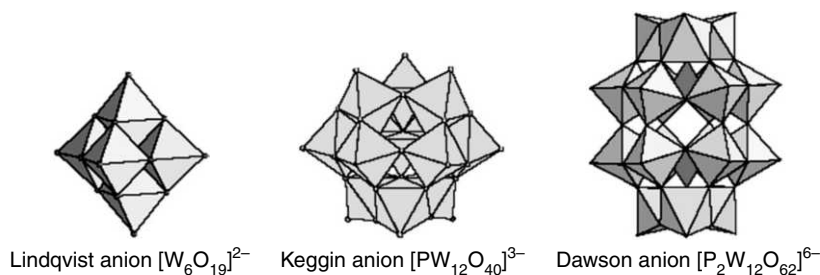
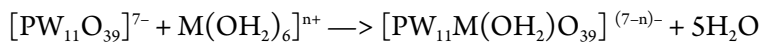


Fig. 17.20 Figure showing structures of some of the well-known polyoxometalate anions: of Lindqvist anion, Keggin anion and Dawson anion (from infochim.u-strasbg.fr/recherche/GDRE/PDF/Secheresse_ppt.pdf).

The saturated kegggin type heteropoly anions have the formula $[PW_{12}O_{40}]^{3-}$. The lacunary polyoxotungstates anions can be imagined to be formed by successive removal of WO_6 octahedron from the kegggin structure. They are named as monovacant, divacant or trivacant depending on the number of WO_6 that have been removed from the parent structure. They are prepared by the controlled hydrolysis of kegggin anion. The structure of various kegggin type anions are shown in the Fig. 17.21.

$[PW_{11}O_{39}]^{7-}$ acts as a pentadentate ligand. It can expel the five coordinations of an octahedral complex of the type $[M(OH_2)_6]^{n+}$ resulting in $[PW_{11}M(OH_2)O_{39}]^{(7-n)-}$. The structure of $[PW_{11}M(OH_2)O_{39}]^{(7-n)-}$ is shown in Fig. 17.22.



In one of the literature reports, divacant anion modified with thiol was used as the functionalising agent. Since polyoxometalate is sensitive to reducing agents, exchange reaction is used to functionalise the gold nanoparticle surface. The thiol group connected the POM to the surface of gold nanoparticles. The exchange reaction is never complete. Citrate ions coexist along with the polyoxometalate. A schematic of the synthesis is shown in Fig. 17.23a. The TEM image of the polyoxometalate-based hybrid is shown in Fig. 17.23b.

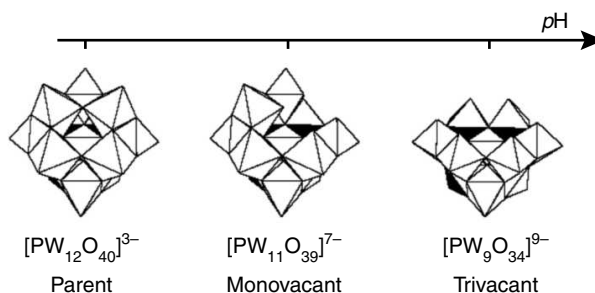


Fig. 17.21 Structure of kegggin type anions. The structure of parent, monovacant and trivacant kegggin type anions are shown (from infochim.u-strasbg.fr/recherche/GDRE/PDF/Secheresse_ppt.pdf).

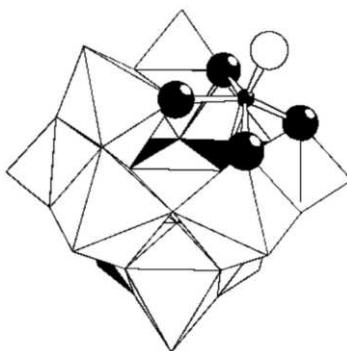


Fig. 17.22 Structure of $[PW_{11}M(OH_2)O_{39}]^{(7-n)-}$. The $[PW_{11}O_{39}]^{7-}$ acts as a pentadentate ligand when it is treated with an octahedral complex $M(OH_2)_6$. It expels the five water molecules of the octahedral complex resulting in $[PW_{11}M(OH_2)O_{39}]^{(7-n)-}$ (from, infochim.u-strasbg.fr/recherche/GDRE/PDF/Secheresse_ppt.pdf).

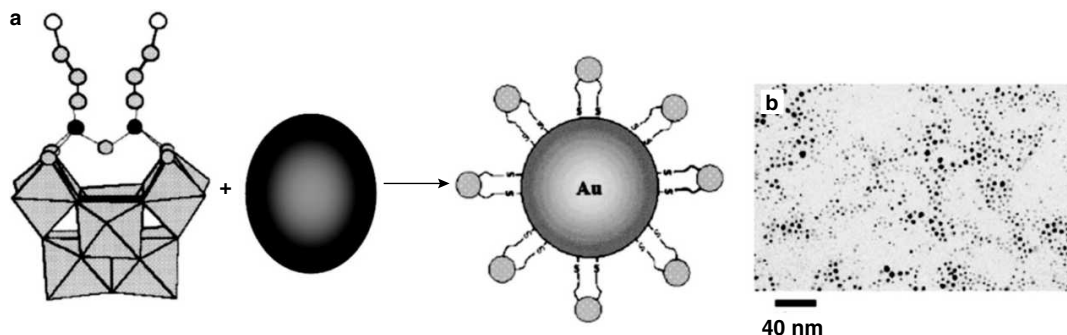


Fig. 17.23 The synthesis of polyoxometalate-based hybrid material. Thiol-derivatized polyoxometalate is treated with citrate protected gold nanoparticles. The exchange reaction leads to the formation of nanoparticles protected with polyoxometalate. The TEM image of the polyoxometalate protected gold nanoparticles is shown in b (reprinted from Ref. 11. Copyright (2002) Wiley-VCH Verlag GmbH and Co.).

17.7 METHODS TO GRAFT POLYMER CHAINS TO THE NANO-BUILDING BLOCK SURFACE

The general methods used to attach the polymer chain onto the nano-building block surface include Reversible Addition Fragmentation Chain Transfer Reaction (RAFT), Atom Transfer Radical Polymerization Reaction (ATRP) and Free Radical Polymerization Reaction. The methods are discussed below.

17.7.1 Free Radical Polymerization

The polymerization of monomer in the presence of nanoparticles may result in core-shell structures. Hydrogel-coated gold nanoparticles were made by polymerising PNIPAm in the presence of gold nanoparticles. The monomer-NIPAm, the cross-linking agent-N,N-methylene bis acryl amide, the catalyst-, N,N,N,N-tetra methyl ethylene diamine and the free radical initiator-ammonium persulfate were added to citrate-stabilised gold nanoparticle dispersion. The polymer formed during the reaction gets deposited on the surface, the resulting in the formation of core-shell of type nanoparticles. Since ammonium persulfate reacts with gold nanoparticles, the method is not of first choice when it comes to making hydrogel-coated gold nanoparticles. A schematic of the synthesis is shown in Fig. 17.24.

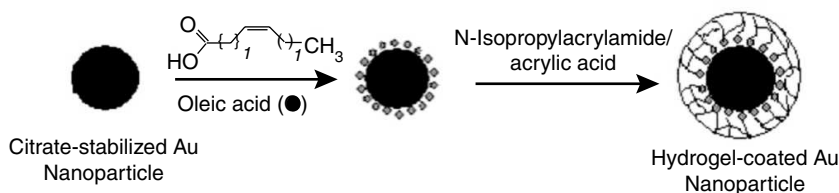


Fig. 17.24 Preparation of thermosensitive gold nanoparticles using free radical polymerization reaction. Citrate-stabilised gold nanoparticles were first treated with oleic acid. The oleic acid stabilised nanoparticles were coated with hydrogel by precipitation polymerization using N-isopropylacrylamide and Acrylic acid (reprinted from Ref. 12. Copyright (2004) American Chemical Society).

17.7.2 Reversible Addition Fragmentation Chain Transfer Method (RAFT)

Using this method, one can graft polymeric chains onto nanoparticle surfaces. The polymerization involves an initiator and a chain transfer agent. The chain transfer agent normally used includes S-benzyl dithiobenzoate, and 2,2'-azobisisobutyronitrile is the commonly used initiator. The initiator breaks down and generates the radical. The radical reacts with the monomer and the chain propagates. When the propagating polymer chain interacts with the chain transfer agent, it generates another radical capable of starting the polymerization. This method is capable of generating polymers with narrow molecular weight distribution. The mechanism of the RAFT method is shown in Fig. 17.25.

RAFT method has been used to attach thermo-sensitive polymers onto gold nanoparticle so that the polymer-protected gold nanoparticle is temperature sensitive. The polymer, PNIPAm, is used to make temperature-sensitive gold nanoparticles. This polymer is soluble in water and forms a clear solution below LCST. Above the lower critical solution temperature (LCST), the polymer forms a coacervate phase and the solution becomes opaque. The use of S-benzyl dithiobenzoate as the chain transfer agent leads to a PNIPAm polymer chain end get functionalised with dithioester. The thiol group is released from the dithioester-terminated PNIPAm polymer by reaction with sodium borohydride. Since the polymer is end-functionalised with thiol, a monolayer-protected gold nanoparticle can be

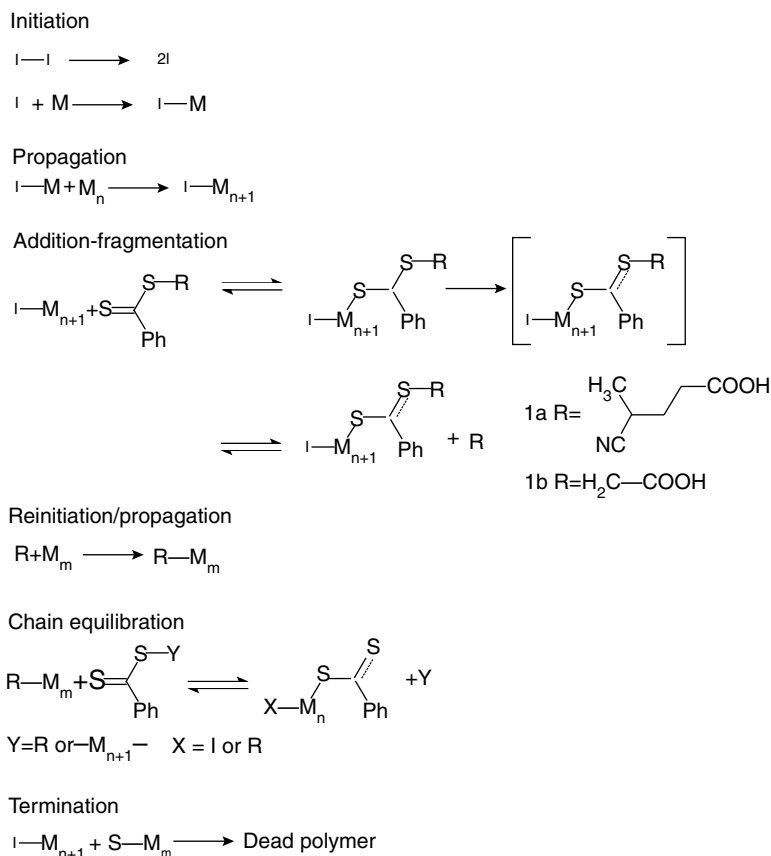


Fig. 17.25 Mechanism of reversible addition fragmentation chain transfer reaction. The initiator (I) breaks down and generates the radical, leading to the formation of the propagating polymer chain. When such a growing polymer chain encounters the chain transfer agent, the latter releases a new radical capable of reinitiating the polymerization. The reinitiation leads to the formation of a monodisperse polymer chain (reprinted from Ref. 13. Copyright (2001) American Chemical Society).

made by exchange reaction with citrate capped gold nanoparticle. The temperature-dependent, clear to opaque transition was sharp and reversible, and the coacervate phase did not show any tendency to precipitate. The schematic of the synthesis is shown in Fig. 17.26.

The citrate-stabilised particles tend to aggregate when a drop of the solution is dried on the TEM grid (Fig. 17.27A). The polymer stabilised particles were well-separated from each other when they dry on the TEM grid (Fig. 17.27B). When the polymer changes to globule, the solution turns cloudy, leading to a decrease in the transmittance at 520 nm. The transmittance of the polymer solution at 520 nm with heating-cooling cycles is shown in Fig. 17.27C.

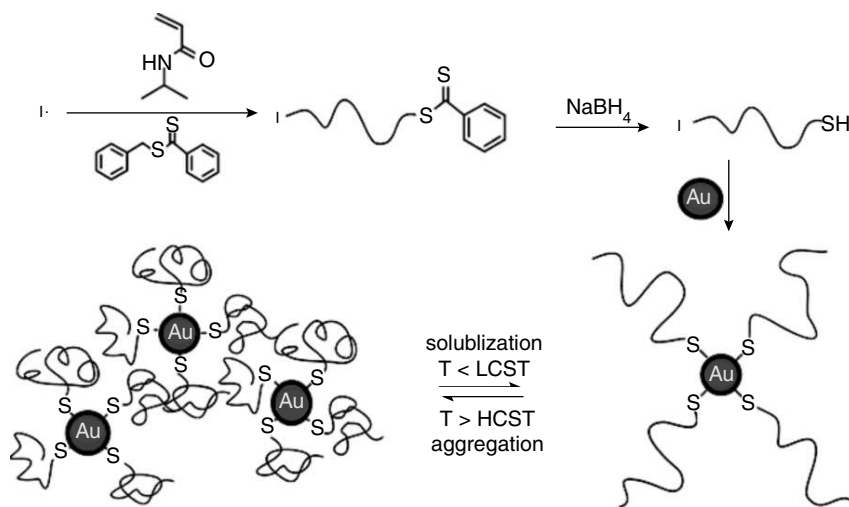


Fig. 17.26 Schematic describing the preparation of thermo-sensitive gold nanoparticles using RAFT method. Thiol-terminated polymers can be released from the thioester-terminated polymers prepared by RAFT method by treating with sodium borohydride. Citrate-protected gold nanoparticles are then treated with the thiol-terminated polymers. The thiol head group displaces some of the citrate ions resulting in thermo-sensitive nanoparticles (reprinted from Ref. 14. Copyright (2004) American Chemical Society).

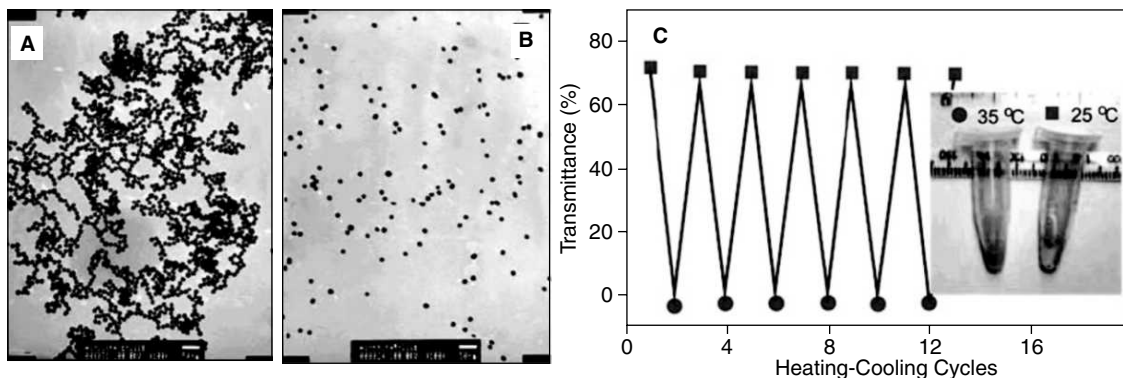


Fig. 17.27 Synthesis of thermosensitive gold nanoparticles. TEM images of (A) citrate-stabilized gold nanoparticles and (B) PNIPAm-stabilized gold nanoparticles. A monolayer of the polymer around each gold nanoparticles prevents them from aggregating when they dry on the TEM grid. The transmittance of the solution at 520 nm during temperature cycling is shown in C. The red square in C indicates the transparent state and the blue circle indicates the opaque state. The inset figure in C shows the photograph of the PNIPAm-coated gold nanoparticle solution at 35 °C and 25 °C respectively (reprinted from Ref. 14. Copyright (2004) American Chemical Society).

17.7.3 Atom Transfer Radical Polymerization Method (ATRP)

Atom transfer radical polymerization has been used to attach functional polymeric chains onto nano-building block surface. In this method, a monomer is polymerised by treating with an initiator, a transferable halogen atom and a catalyst, composed of transition metal and a ligand. ATRP involves an active form of the polymer, known by the name propagating radical, and an inactive form of the polymer, called dormant species. The first step is the formation of propagating radicals by a reversible redox process catalysed by transition metal complex. They are reversibly deactivated to form the dormant species. The reactivation of the dormant species permits the growth of the polymer chain again. This growing chain will again be deactivated later. This results in the formation of a polymer chain that grows slowly, but steadily. Thus the transition metal complex controls the equilibrium between the active form and the dormant species. Normally, the dormant form is preferred over the active form minimising the side-chain reactions. The polymers made by this route have large molecular weight and low polydispersity index. The mechanism of the polymerization reaction is schematically shown in Fig. 17.28.

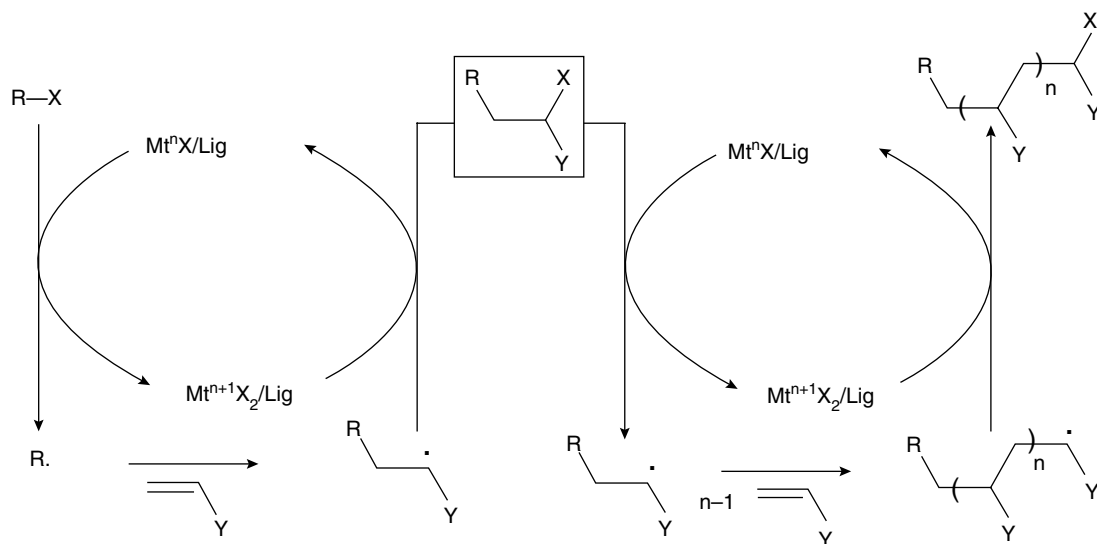


Fig. 17.28 Mechanism of Atom Transfer Radical Polymerization. The transition metal complex controls the equilibrium between the active species and the dormant species.

The synthesis of core-shell type hybrid using ATRP is shown in Fig. 17.29a. A shell of polystyrene was coated around magnetic nanoparticles using ATRP reaction wherein 2-chloropropionic acid was used as the ATRP initiator. A transition metal complex, derived from $CuCl$ and $dNbipy$, was used to catalyse the polymerization. The abstraction of halogen by the transition metal complex initiates the polymerization reaction.

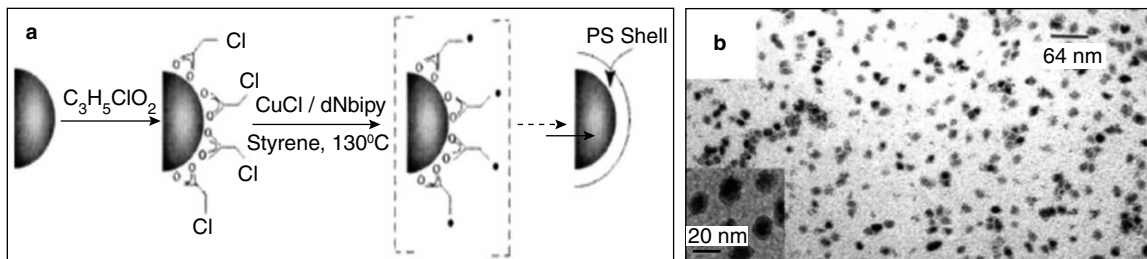


Fig. 17.29 The synthesis of core-shell type material through ATRP route. A schematic of the synthesis is shown in a. A large area TEM image of the core-shell type material is shown in b. The inset at the bottom left corner of b shows the core-shell geometry of few nanoparticles (reprinted from Ref. 15. Copyright (2002) American Chemical Society).

The synthesis of a core-shell type hybrid through a surface-driven atom transfer radical polymerization is schematically shown in Fig. 17.30. Initially, silsesquioxane was functionalised with the 2-bromoisobutyrate, initiator for the atom transfer radical polymerization. Then with the help of the initiator sitting on the surface, a polystyrene monolayer was grafted onto the silsesquioxane surface through atom transfer radical polymerization. A poly(benzylmethacrylate) chain was attached to the end of polystyrene chain by another atom transfer radical polymerization. A schematic of the method is shown in Fig. 17.30a. Figure 17.30b shows the TEM image of the core-shell type material. Atomic force microscopy studies on the core-shell material indicated the glassy and rubbery regions characteristic of each polymer.

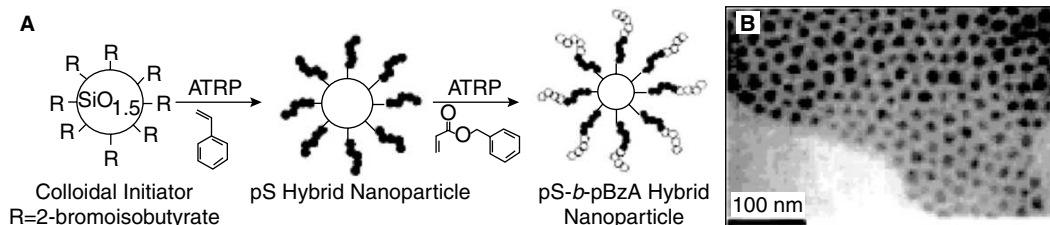


Fig. 17.30 (A) Schematic describing the synthesis of core-shell type material using silsesquioxane based nano-building block. The thick line represents the polystyrene chain. The line with white circles represents the poly(benzylmethacrylate). The TEM image of the material is shown in (B) (reprinted from Ref. 16. Copyright (2001) American Chemical Society).

17.8 BIOHYBRIDS

The unusual properties of the biological materials have always inspired material scientists. Superhydrophobicity of lotus leaf, unusual hardness of abalone shell and beautiful silica architecture of diatoms are some examples. Unravelling the mechanism, by which the nature makes such materials, will enable us to make smart, environment-friendly, materials. An example for a bionanocomposite is

nacre in the abalone shell. The organic part constitutes only a small portion of the whole material. Even then, the material has unusual mechanical properties. Analysis of the nacre has proved the secret behind the unusual hardness of such shells. A fibrous protein present in the nacre is the main reason for the toughness of the shell. The nacre tablets that are stacked one over the other are glued by the protein, lustrin A. The SEM image of the abalone shell is shown in Fig. 17.31A. The TEM picture of freshly cleaved abalone shell, clearly showing the fibrous protein, is shown in Fig. 17.31B.

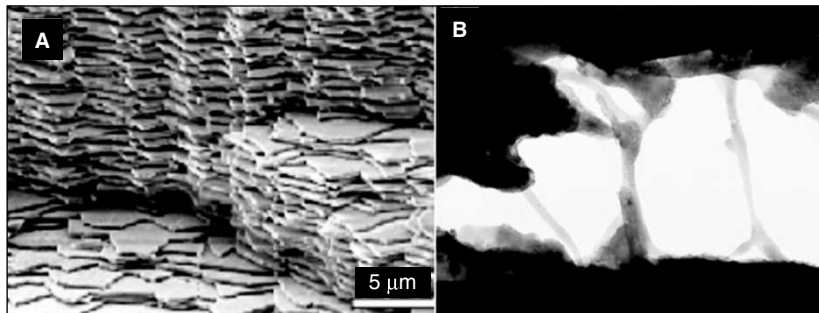


Fig. 17.31 (A) The SEM images of a nacre tablets in the abalone shell. The tablets of calcium carbonate are stacked with the help of a fibrous protein acting as glue, Royal Society of Chemistry. (B) TEM image of a freshly cleaved abalone shell clearly shows the glue, a protein, the main reason for holding the inorganic tablets together (reprinted with permission from <http://hansmalab.physics.ucsb.edu/biomatsresoverview.html#biomin>).

Let us consider three molecules: A small molecule, a long molecule and a long molecule with modules. The force-extension curve corresponding to each molecule is shown in Fig. 17.32. Consider a long molecule that contains a lot of small loops with intermediate bond energy. When such a molecule is stretched, the tension in the molecule rises, but when the tension threatens to break the backbone of the molecule, a small loop opens up, thus releasing the energy stored in the fiber as heat. Whenever the applied force tries to break the backbone, a small loop unwinds and the force reduces to a minimum again. The process continues until all the intermediate loops are opened. If the applied force is increased further, the main backbone breaks. This leads to a saw-tooth shaped force-extension curve. The module structure of a molecule can be analysed by using atomic force microscopy. The molecule to be analysed is attached between a flat surface and the cantilever of an atomic force microscope (AFM). If a molecule has a modular structure, then the rupture events will appear as a saw-tooth structure in the force-extension curve as shown in Fig. 17.32.

Analysis of a freshly cleaved abalone nacre surface showed a saw-tooth nature in the force-extension curve. This led to the conclusion that a modular mechanism may be operating in the case of the abalone shell, which results in unusual hardness. The saw-tooth shaped force-extension curve indicates that the molecule that holds the calcium carbonate tablets has modular structure.

The silica formation in laboratory requires extreme pH conditions. But, the same hydrolysis happens at a neutral pH and at temperatures close to zero in biological systems. This is because the polypeptides present in nature can hydrolyse as well as act as templates for producing silica with

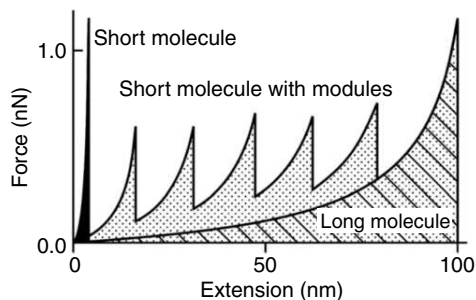


Fig. 17.32 The force-extension curve for three types of molecules. The line with area under the curve filled with dark black represents the curve for small molecules. The line with area filled with slanted lines and dots is that for a long molecule and the saw tooth curve with area filled with dots represents the curve for a long molecule with modular structure (adapted from Ref. 17).

beautiful architectures. An example for this is the diatom's silica cell wall (Fig. 17.33a). The polycationic polypeptides isolated from the cell wall were found to produce silica nanoparticles within seconds when treated with metastable silicic acid. Due to their high affinity towards silica, these peptides coprecipitate with silica. Hence, they are known by the name, silafins. Such protein-silica biocomposite is the reason for the beautiful diatoms silica architecture. The proposed structure of the polycationic peptide is shown in Fig. 17.33d.

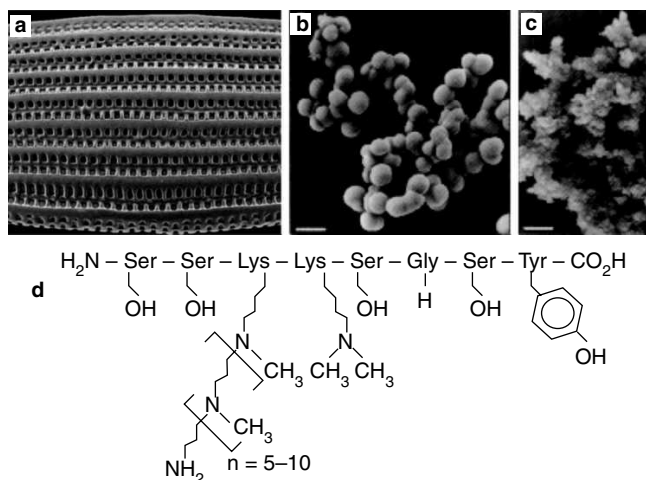


Fig. 17.33 (a) SEM image showing the silica architecture of benthic diatom *Cylindrotheca fusiformis*. (b) That of silica nanoparticle prepared by treating silicic acid with polycationic peptide. (c) That of silica-peptide composite made from the silafins. (d) Proposed structure of the polycationic peptide isolated from the cell wall is shown (adapted from Ref. 18 and 19).

The ability of cationic polypeptides to form amorphous silica extended the studies to peptide based block copolymers. The polypeptide, used to mimic the amorphous silica production, should have the structure-directing ability as well as the capacity to hydrolyse tetraethyl orthosilicate. The peptide used contain a block of lysine, which can hydrolyse tetraethyl orthosilicate. It has another block of cysteine-lysine that renders it amphiphilic; hence, the peptide can self-assemble into various structures. The optical micrograph of silica prepared by the peptide template in the absence of air is given in Fig. 17.34a. When the oxidised form of the template was used, silica with a different morphology was obtained. This is due to the oxidation of side chain thiols to form disulfide linkages. The optical micrograph of the silica formed in the presence of air is shown in Fig. 17.34b.

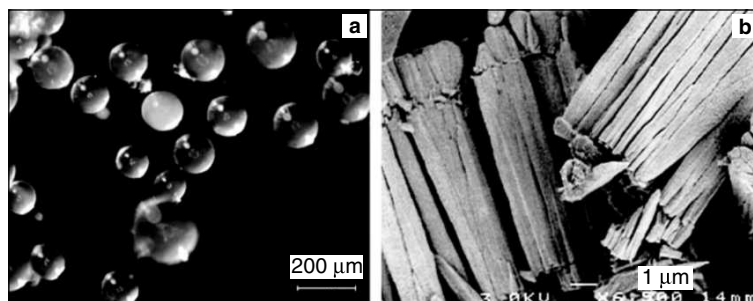


Fig. 17.34 Optical micrograph images of the silica made by the synthetic peptide based co-polymer (a) in the absence of air and (b) in the presence of air (adapted from Ref. 20. Copyright (2001) American Chemical Society).

A new way of making hybrids is to look for materials with interlayer space and keep the organic part inside the cavity in order to improve the mechanical or thermal properties. Some of the layered materials used for making this type of nanocomposites include layered silicates, molybdenum disulfide, and layered double hydroxides. This methodology leads to three types of nanocomposites, namely, phase separated, intercalated and exfoliated. In intercalated nanocomposites, polymeric chains are inserted into the interlayer gallery space. In exfoliated composites, the individual layers are far apart. These three morphologies are shown in Fig. 17.35.

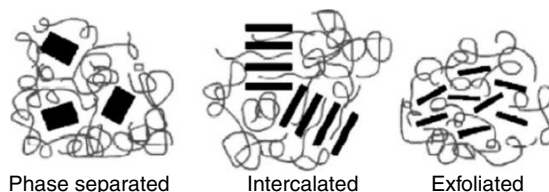


Fig. 17.35 Schematic describing various types of hybrids made from layered materials (reprinted from Ref. 21. Copyright (2005) American Chemical Society).

Layered double hydroxides (LDHs): These are compounds having the general formula $[M^{II}_x M^{III}_{1-x}(\text{OH})_2]_{\text{intra}}[A^{m-}_{x/m} \cdot n\text{H}_2\text{O}]_{\text{inter}}$. They contain positively charged layers made up of edge

sharing $M(OH)_6$ octahedra. The M^{2+} ions may be Mg^{2+} , Zn^{2+} , Cu^{2+} or Ni^{2+} and the M^{3+} ions can be Al^{3+} , Cr^{3+} or Fe^{3+} . Partial replacement of M^{2+} ions in $M(OH)_2$ that has neutral layers by M^{3+} makes the layers positively charged. This charge is balanced by the negative ions present in the interlamellar space. The interlamellar anions normally present are CO_3^{2-} , Cl^- , NO_3^- , SO_4^{2-} and PO_4^{3-} (Fig. 17.36). It is possible to exchange the interlamellar anions with various other species. The species normally intercalated include proteins, enzymes, peptides, polysaccharides, aminoacids, polymers, nucleic acids, DNA etc.

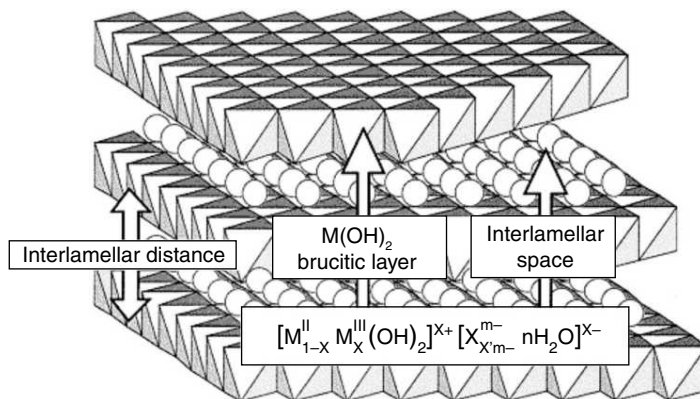


Fig. 17.36 Sheets made up of edge-sharing $M(OH)_6$ octahedra in LDHs (reprinted from Ref. 22. Copyright (2001) American Chemical Society).

Due to the high charge density present within each layer (ca. 300 mEq/100 g LDH), LDHs resist the exfoliation of their layers. Hence, commonly used methods, such as entrapping and restacking, fail when it comes to intercalating large anions into the LDH layers. Three methods are generally used to make LDH-based hybrids. They are: direct ion-exchange, coprecipitation and reconstruction. In the reconstruction route, the LDH is subjected to a moderate thermal treatment. This causes the removal of few hydroxides from the lattice and the resulting amorphous material can regain its structure on cooling in air or when soaked in aqueous solution. Such a memory effect is used to intercalate large anions like polyoxometallates into the host lattice.

The layer charge density plays an important role in determining the orientation of the guest molecule within the host structure. When mesotetrakis(para-carboxyphenyl) porphyrin (*p*-TCCP) and mesotetrakis(ortho-carboxyphenyl) porphyrin (*o*-TCCP) were intercalated into the LDH layer, the para isomer adopted a perpendicular configuration, whereas the ortho isomer adopted a parallel orientation with respect to LDH layers. These two possible arrangements of porphyrin molecule inside $[Zn-Al]$ LDH structure are shown in Fig. 17.37. In perpendicular configuration, the four anionic groups orient in such a way as to neutralise the charge on LDH layers. *p*-TCCP-intercalated LDH, when subjected to vacuum dehydration, lead to structures with same interlamellar space. Such pillaring effect is possible when the molecules stand perpendicular to the $[Zn-Al]$ LDH layer.

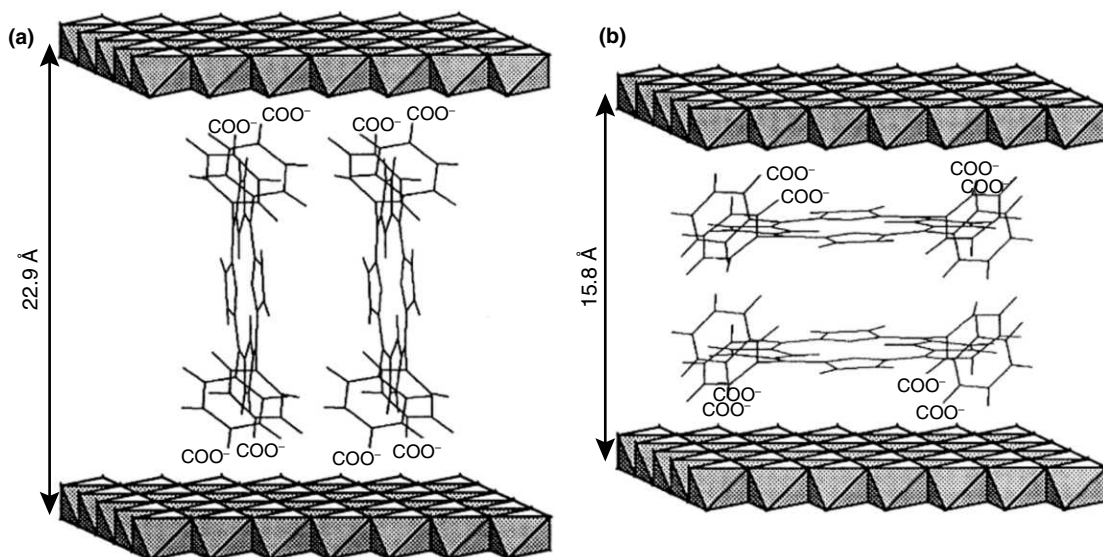


Fig. 17.37 Pictorial representation of the orientation of (a) *p*-TCCP and (b) *o*-TCCP within the [Zn-Al]LDH layer. The *p*-TCCP takes a perpendicular configuration whereas the *o*-TCCP adopts a parallel configuration with respect to the [Zn-Al]LDH layers (reprinted from Ref. 23. Copyright (1996) American Chemical Society).

One possible application of intercalated hybrids is the delivery of charged molecules into cells. An example for a molecule of relevance in biology is DNA. The DNA to be delivered is intercalated between the interlayer spaces. The negative charge of DNA molecule is screened by the [Zn-Al]LDH. This avoids the unnecessary interaction between the cell surface and DNA allowing the smooth entry of the DNA into the cells. The methodology is schematically represented in Fig. 17.38.

Hydroxyapatite (HAP)-based hybrids: Hydroxyapatite-based hybrid is one of the widely studied bionanocomposite. HAP is the main mineral constituent of bone and teeth. Two of the advantages of HAP are its biocompatibility and its biodegradability. Collagen, in combination with hydroxyapatite, is used to make artificial bones. HAP in combination with polysaccharides like chitosan or proteins like collagen, gelatin and silk fibroin is an attractive candidate for reinforcing materials for bone tissue engineering. Ivory is an example of a biomineral showing hierarchical architecture. It is composed of HAP crystals packed with the help of oriented collagen fibrils.

Layered silicates-based hybrids: Examples for layered silicates include kaolinite and montmorillonite (mmt). Layered silicates are made up of two kinds of sheets: the tetrahedral and the octahedral. The sheets are formed by the fusion of tetrahedra and octahedra. The tetrahedral sheet is made up of SiO_4 tetrahedra. The SiO_4 tetrahedron contains a central silicon atom surrounded by four oxygen ions at the four corners of a regular tetrahedron. The octahedral sheet is made up of $\text{Al}(\text{OH})_6$ octahedra. The structure of the montmorillonite clay is shown in Fig. 17.39. The octahedral

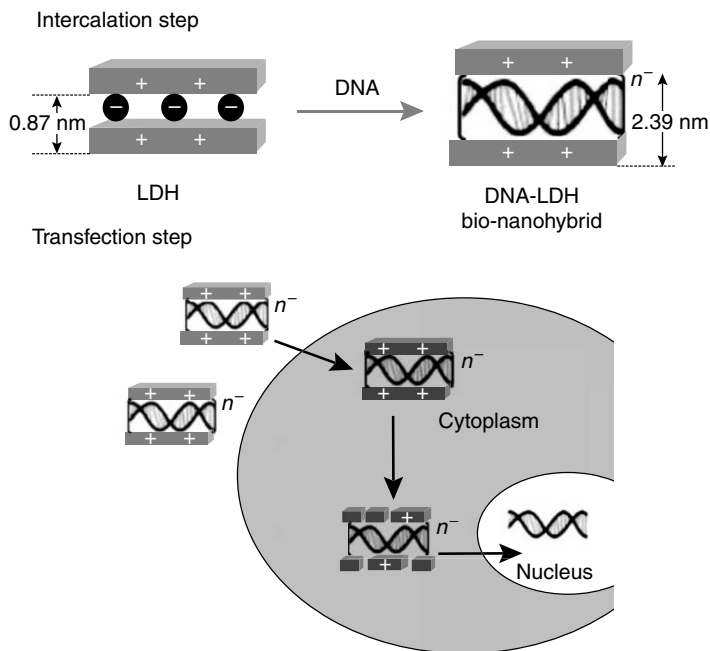


Fig. 17.38 Schematic describing the delivery of DNA into the cells using intercalated hybrids (reprinted from Ref. 24. Copyright (2005) Royal Society of Chemistry).

and tetrahedral layers are arranged in a sequence as shown in Fig. 17.39. Montmorillonite contains interstitial spaces for intercalating foreign molecules.

In order to make the hybrid, at first the clay is organically modified by replacing the gallery cations with surfactants. The surfactant is later replaced by the polymer to be intercalated. A favourable enthalpy of mixing is a must in order to overcome the loss of entropic stabilization. This is achieved either by increasing the polymer-mmt interactions or by decreasing the surfactant-mmt interactions. The polymer-mmt interactions can be increased by using functionalised polar polymers. Many molecules can also be inserted in between the clay sheets.

17.9 MECHANICAL PROPERTIES

The mechanical response of hybrid materials have to be studied for manipulating their properties to suit different applications. The mechanical response is a resultant of the interactions between the constituting components of hybrid materials. Different methods with different conditions are used to study the mechanical properties. Dynamic thermo mechanical analysis (DMA) is used to derive information about the thermomechanical properties of materials using an oscillatory force, and a sinusoidal stress is applied to the sample. This generates a sinusoidal strain in the sample. The phase lag

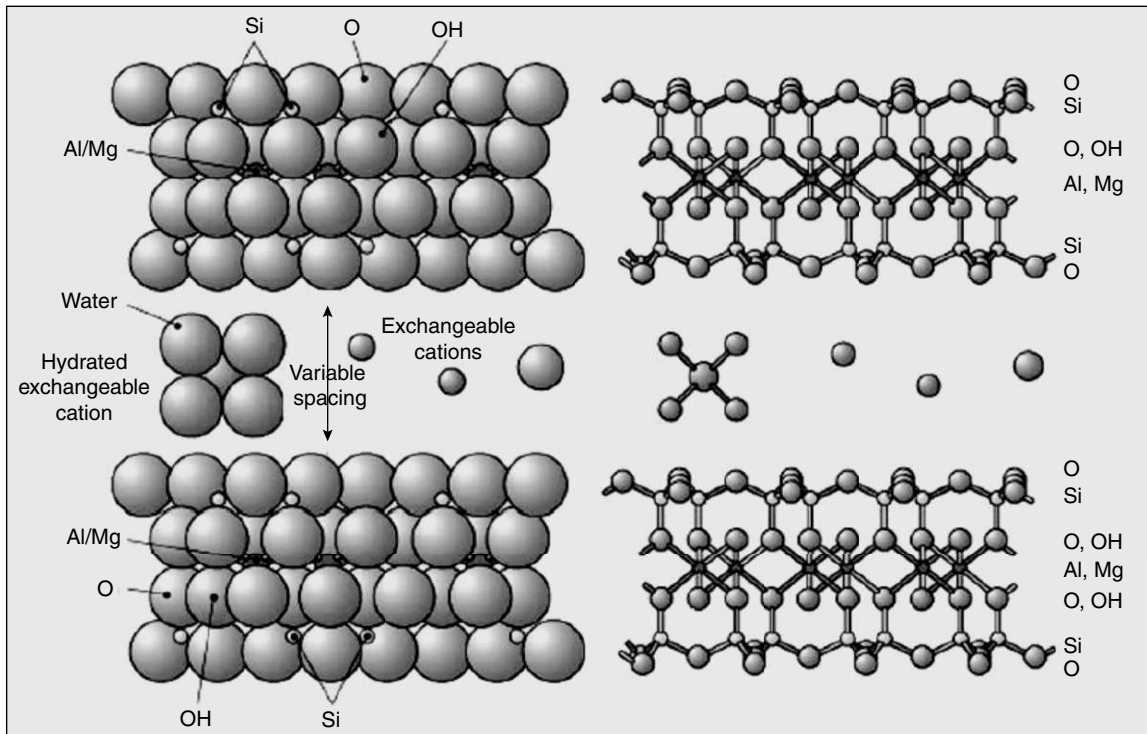


Fig. 17.39 Structure of montmorillonite. Reprinted with permission from <http://www.landfood.ubc.ca/soil200/components/mineral.htm>.

between the stress curve and strain curve, and the amplitude of deformation at the peak of the curve, provide useful information about the material properties. If the strain developed is in phase with the applied stress, the material is termed as elastic. When the phase difference is 90° , the material is termed as viscous. Generally, polymers show a behaviour in between the elastic and viscous, and are termed as viscoelastic. Depending on the polymer content of the hybrid, they can be called ceramics, on the one end, and polymers, on the other end. The Young's modulus obtained from DMA analysis is a complex quantity and is quite different from that measured from the slope of the classical stress-strain curve. It is given by the relation,

$$E^* = E' + i E''$$

Here E' denotes the energy stored elastically during the deformation (storage modulus) and E'' represents the energy converted to heat during the deformation (loss modulus). These terms can be explained with the following analogy (see Fig. 17.40). If a ball is dropped onto the floor, the ball bounces up. But, it cannot come to the height from which it has been dropped. A part of the energy is lost to the floor and the remaining is stored in the ball. The energy lost is called loss modulus and the energy stored is called storage modulus. The storage modulus is a measure of the elastic response

of the material. The ratio of the storage modulus to the loss modulus is called loss tangent ($\tan \delta$), analogous to that of a resistive inductor.

$$E'/E'' = \tan \delta$$

The elastic modulus, storage modulus and the loss tangent are temperature dependent. In the DMA analysis, these parameters are measured as a function of temperature.

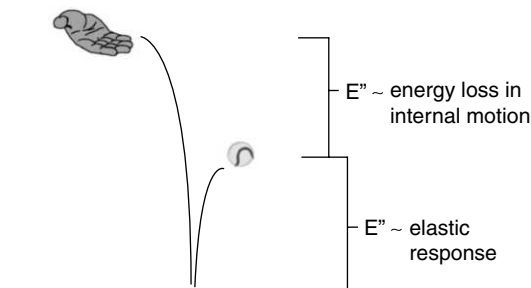


Fig. 17.40 Analogy to explain the storage modulus and elastic modulus (reprinted from Ref. 26).

When a polymer is heated, the free volume increases. Initially, the free volume available to the molecule in order to exhibit the dynamics is very small. At this value, only the vibrations will be permitted. On further increasing the temperature, a gradual increase in the free volume will permit the side chains of the polymer to move. Below the glass transition temperature, the free volume available to the material is very small. As a result, only the side chains of the polymer have the freedom to exhibit motions. Above the glass transition temperature, the larger segments of the polymer chain start executing motion. Thus, the glassy polymer shows rubbery behaviour above the glass transition temperature. At the glass transition temperature, there is a sudden drop in the storage modulus. The region after the glass transition temperature is called rubbery plateau. Often the interaction between the organic and inorganic phase leads to a better rubbery plateau for the storage modulus. A similar flat rubbery plateau is not observed in a pure polymer. The last region is called the terminal zone. At the T_m , the material has large free volume so that it starts flowing. Figure 17.41 shows the variation of storage modulus with temperature.

A weak interaction between the organic and inorganic components leads to a loss in the polymer chain mobility leading to an increase in the glass transition temperature. Any interaction between the organic and inorganic component is also shown up as a rubbery plateau in the E' vs. T curve. The rubbery plateau is absent for the pure polymer. Another proof for the interaction between the components is the broadening of the $\tan \delta$ peak. If the interaction between the inorganic and the organic phase is covalent in nature, then the inorganic part cross links the organic component leading to a much better rubbery plateau for the storage modulus.

Nanoindentation analysis: This technique has been used to measure the mechanical properties of thin films. On the application of a load, the indenter penetrates through the sample. On removing the load the material will try to regain its initial shape. But the material is prevented from going back to

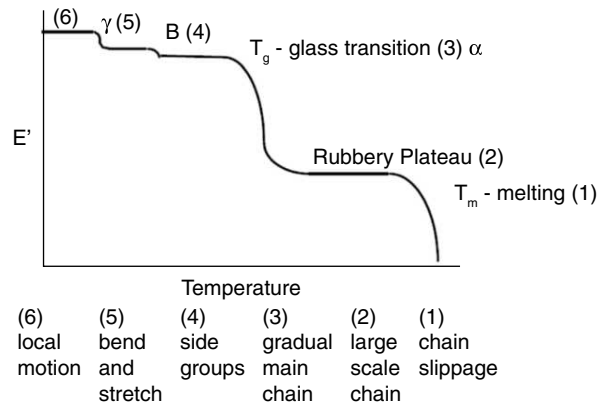


Fig. 17.41 Temperature dependence of storage modulus. The molecular motion corresponding to each stage is written below the y-axis (reprinted from Ref. 26).

the initial shape by the plastic deformation, leaving a residual impression on the surface of the film (Fig. 17.42). In an actual experiment, the load is applied by sending an electric current through a coil. This generates a magnetic field which interacts with the permanent magnet sitting on the shaft to which indenter is attached. The load as well as the displacements are measured as the tip penetrates through the sample.

The equation for the loading curve is

$$F = ah^m \tag{1}$$

Here, 'F' represents the load applied to the indenter and 'h' is the penetration depth. The value of m depends on the geometry of the indenter. 'a' is a constant.

Similarly, the best fit for the unloading curve is

$$F = k(h - h_r)^m \tag{2}$$

where 'h_r' represents the residual depth and $1 > m > 0$

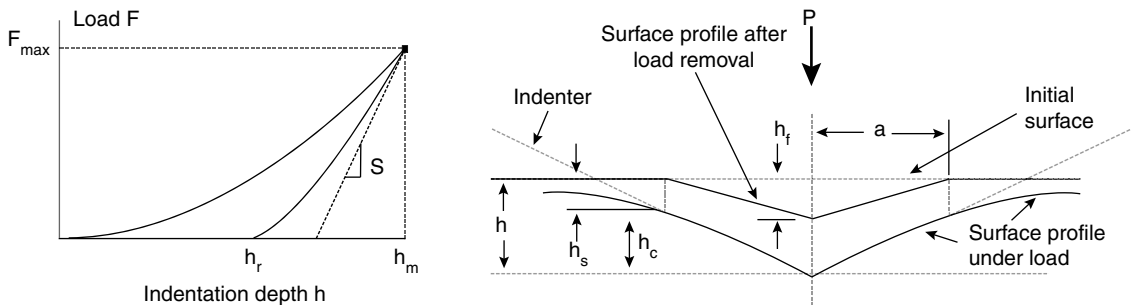


Fig. 17.42 A typical load-displacement curve. The diagram on the right hand side shows the cross-section of the surface profile under load, and after removal of load (reprinted from Ref. 27 and 28. Copyright (2002) Elsevier B.V.).

The next quantity required is the contact stiffness at the peak load (S_{\max}). This is obtained by the differential of equation (2) with respect to h at the maximum depth of penetration, $h = h_{\max}$,

$$S_{\max} = \frac{dF}{dh} = km(h_{\max} - h_r)^{m-1} \quad (3)$$

Next quantity required is the elastic displacement of the surface at the contact perimeter (h_s). It is given by the equation

$$h_s = \frac{(\pi - 2)}{\pi} (h - h_f) \quad (4)$$

$$\text{Also } (h - h_f) = 2 \frac{F}{S} \quad (5)$$

Substituting equation (5) into equation (4) gives

$$h_s = \frac{2}{\pi} (\pi - 2) \frac{F_{\max}}{S}$$

$$h_s = \varepsilon \frac{F_{\max}}{S} \quad (6)$$

$$\text{where } \varepsilon = \frac{2}{\pi} (\pi - 2)$$

At any time during the loading, we can write

$$h = h_c + h_s \quad (7)$$

At the peak load the equation (7) changes to

$$h_c = h_{\max} - h_s \quad (8)$$

Substituting equation (6) into equation (8) gives

$$h_c = h_{\max} - \varepsilon \frac{F_{\max}}{S} \quad (9)$$

The above equation expresses h_c in terms of experimentally measurable quantities. Next quantity required is the tip sample contact area A_c . From the geometry of the indenter, we can calculate A_c . Let us consider a Berkovich indenter shown in Fig. 17.43:

$$\text{From the Fig. 17.43, } \tan 60^\circ = \frac{l}{a/2}$$

$$\text{Hence } l = \frac{\sqrt{3}}{2} a$$

$$\text{Since } A_c = \frac{al}{2} = \frac{\sqrt{3}}{4} a^2$$

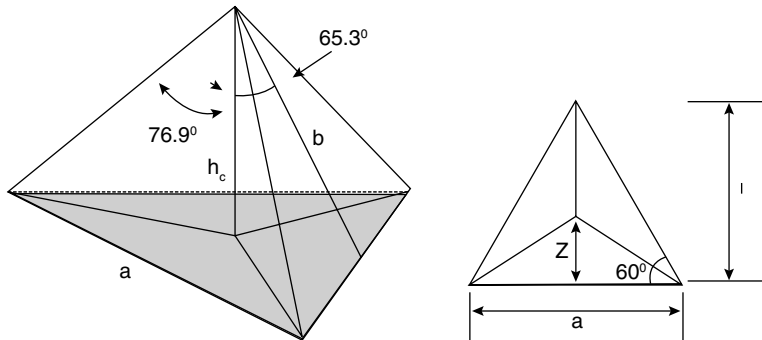


Fig. 17.43 A pictorial representation of projected area of a Berkovich indenter (reprinted from Ref. 29).

Also, From the triangle AGF, $\cos 65.3^\circ = \frac{h_c}{b}$

$$h_c = \frac{a \cos 65.3^\circ}{2\sqrt{3} \sin 65.3^\circ} = \frac{a}{2\sqrt{3} \tan 65.3^\circ}$$

$$a = 2\sqrt{3} h_c \tan 65.3^\circ$$

$$A_c = 3\sqrt{3} h_c^2 \tan^2 65.3^\circ = 24.56 h_c^2$$

Once we know the value of A_c , the reduced elastic modulus, E_r , can be calculated using the equation,

$$E_r = \frac{\sqrt{\pi}}{2} \frac{S}{\sqrt{A_c}} \text{ and the hardness can be calculated from the equation, } H = \frac{F_{max}}{A_c}.$$

17.10 APPLICATIONS OF ORGANIC-INORGANIC HYBRID MATERIALS

Some of the applications of hybrid materials are:

- (i) Electro-optical devices
- (ii) Dye-sensitised solar cells
- (iii) Non-Linear Optical (NLO) materials

17.10.1 Gel-Glass Dispersed Liquid Crystalline Devices (GDLC)

The main component of the GDLC is a porous thin film. The pores can hold droplets of the liquid crystalline molecules inside. A large area SEM image of a porous film is shown in Fig. 17.44A. A high magnification SEM image is shown in Fig. 17.44B. The pore size is of the order of 1–2 μm .

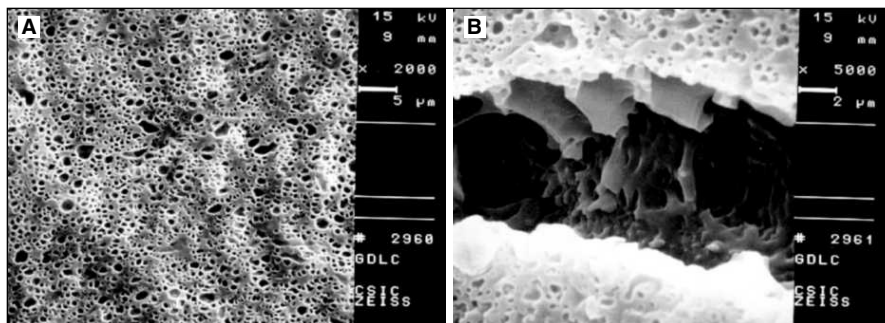


Fig. 17.44 SEM images of thin silica film showing the porous structure. These pores hold the micro droplets of the liquid crystalline molecule (reprinted from Ref. 30. Copyright (2005) Royal Society of Chemistry).

In GDLC, micro droplets of liquid crystalline molecules are dispersed inside the pores of the gel matrix. When a liquid crystalline molecule, such as azobenzene, is inside the pore, the molecule adopts a configuration determined by the anchoring groups present on the surface of the pores. The hydrophilic part of the liquid crystalline molecule will be in contact with the hydrophilic groups present on the pore surface and vice versa (see Fig. 17.45). This leads to scattering of light and the material will be opaque. This corresponds to the OFF state of the device.

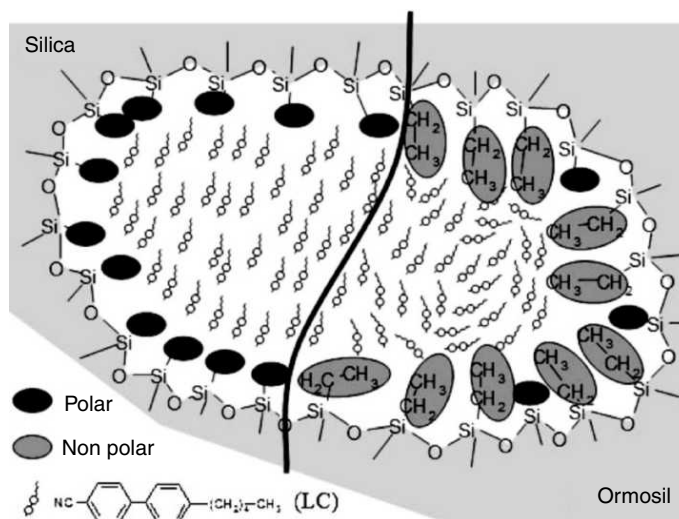


Fig. 17.45 A schematic describing the orientation of liquid crystalline molecules inside the micro droplet for two hybrids with two different polarities of pore surface. The black circles indicate polar surface groups. The gray circles represent hydrophobic (nonpolar) anchoring groups. The orientation of the liquid crystalline molecule on the inner surface depends on the polarity of the surface groups (reprinted from Ref. 30. Copyright (2005) Royal Society of Chemistry).

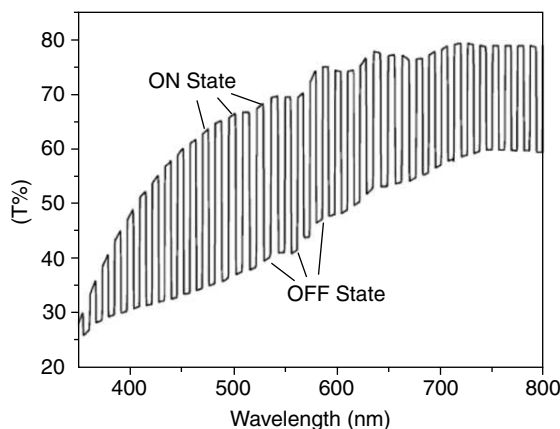


Fig. 17.46 The ON and OFF states of the GDLC film measured at various wavelengths using UV-Vis spectrophotometry. During the OFF state, the transmittance goes down and during the ON state, it goes up. The opaque and transparent states can be attained by turning the applied voltage off and on, respectively (reprinted from Ref. 30. Copyright (2005) Royal Society of Chemistry).

Now, if an electric field, which is capable of breaking such interactions, is applied on the device, the liquid crystalline molecule will orient in the direction of electric field. The new configuration will permit the passage of light through the sample, which makes the material transparent. The device is now in the ON state. Again when the electricity is turned off, the molecule reverts back to its initial configuration making the film opaque. This can be repeated many times. The switching of the film between the transparent and opaque states during the operation is shown in Fig. 17.46. The ability of the material to switch between ON and OFF states implies that such materials can be used to make smart windows.

17.10.2 Dye-sensitised Solar Cells

The high surface area along with the high optical transparency in the visible region makes hybrids as the ideal candidates for making components of solar cells. Dye-sensitised solar cells generate electricity from sunlight. The design of dye-sensitised solar cell is shown in Fig. 17.47.

On irradiation with light, the dye, coated on TiO_2 nanoparticles, ejects electrons into the conduction band of the semiconductor. These electrons are taken through the semiconductor into the external circuit. The dye is then regenerated by gaining electrons from the redox couple, I^-/I_3^- . The schematic of a part of the process taking place in a typical dye-sensitised solar cell is shown in Fig. 17.48. The excitation of the dye molecule by light triggers the ultrafast injection of electrons into the conduction band of the semiconductor (K_{inj}). The dye cation immediately receives electrons from I^-/I_3^- couple (K_r), regenerating the molecule. In order for the device to work better, the re-reduction of the couple should be faster than the back electron transfer from the semiconductor (K_{ct}). The recombination

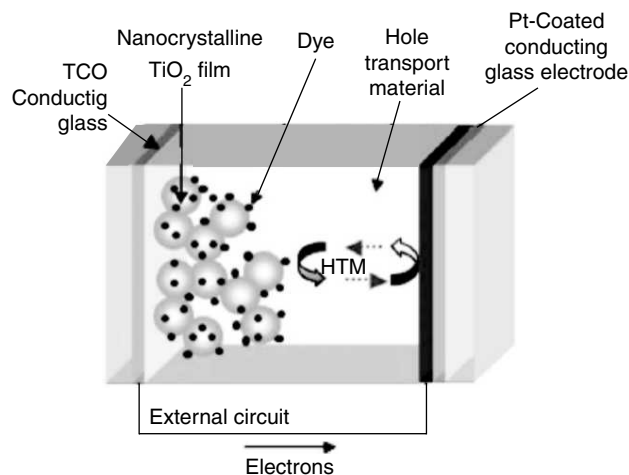


Fig. 17.47 The design of a typical dye-sensitised solar cell. The spheres represent TiO_2 nanoparticles. The black dots sticking to the spheres represent dye molecules (reprinted from Ref. 31. Copyright (2005) Royal Society of Chemistry).

reaction between the injected electrons in the conduction band and the I^-/I_3^- couple result in dark current losses within the cell ($\text{K}_{\text{cr}2}$).

Instead of passing through the external circuit, the ejected electron may disappear through two other pathways: (i) By recombining with the oxidised dye or (ii) by combining with oxidized form

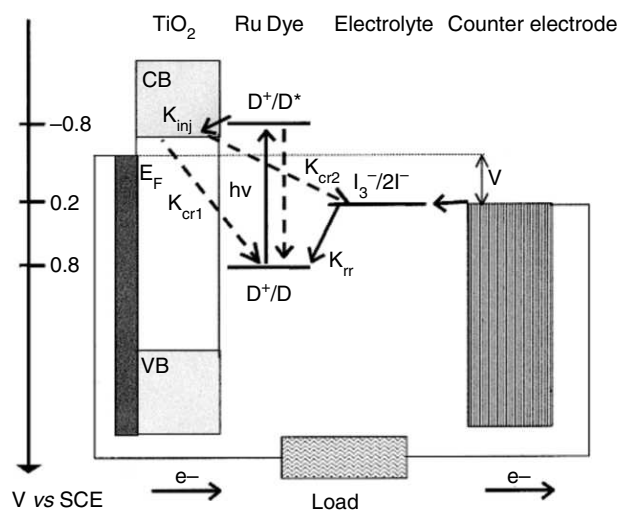


Fig. 17.48 Figure showing the electron processes in a dye-sensitized solar cell. The process of light irradiation and subsequent electron emission due to irradiation is shown. The electron passes through the external circuit and finally gets delivered back to the dye (reprinted from Ref. 32. Copyright (2001) American Chemical Society).

of the redox couple. Both of these processes decrease the efficiency of the cell. One way to avoid the recombination process is by coating the nano-crystalline semiconductor with a thin layer of another semiconductor with large band gap. For TiO_2 , alumina coating is used to increase the efficiency of the solar cell.

The problems associated with the use of liquid electrolytes can be overcome by the use of solid-state electrolytes. The I^-/I_3^- couple is solubilised in a polymer matrix. One of the advantages with these solid-state devices is their large open circuit potentials. However, the solid-state electrolyte has some serious demerits. Few of them are listed below.

1. They reduce the ionic mobility leading to voltage losses. This limits the use of such cells in high power applications.
2. The reduced mobility of I^- through the polymer slows down the re-reduction of the cationic dye, thus affecting the quantum yield of the process adversely.

17.10.3 Non-Linear Optical (NLO) Materials

When a molecule is placed in an oscillatory electric field, the applied electric field induces an oscillatory charge-displacement within the molecule and the electrons oscillate with the same frequency as that of the applied field. The polarisability of such a molecule is given by the relation as,

$$\mu = \mu_0 + \alpha E.$$

But, this holds true only when the strength of the electric field is small. At larger field strengths, the polarisability is no longer proportional to the applied field; it is related to E by the relation,

$$\mu = \mu_0 + \alpha E + \beta EE + \gamma EE + \dots$$

Here, ' μ ' is the induced dipole moment. ' μ_0 ' is the permanent dipole moment, and ' α ' is the polarisability of the molecule. A material with nonzero β could exhibit second harmonic generation.

In a composite material, these induced oscillations have important consequences and several non-linear optical effects occur. Please see the chapter on optical non-linear properties for a summary of these properties.

For a material to exhibit second harmonic generation, it should have a noncentrosymmetric orientation of NLO molecules. In order to achieve noncentrosymmetric orientation in the collection of noncentrosymmetric molecules, the material is subjected to poling, by application of an external DC electric field. During poling, the randomly oriented dipoles, are aligned in the field direction. A schematic of the poling process is shown in Fig. 17.49.

Due to their large hyperpolarisabilities, organic molecules show good NLO properties; yet they are limited by their low stability. However, the preparation of the hybrid type NLO material has overcome the limitations of the organic based NLO materials.

The Class-I type NLO materials are made by mixing NLO chromophore with network forming precursors. The general formula of the alkoxide precursor used for making the host-guest type hybrid is $\text{M}(\text{OR})_4$, where ($\text{M} = \text{Si}, \text{Ti}, \text{Zr}, \text{Al}$). The precursor undergoes hydrolysis and condensation to

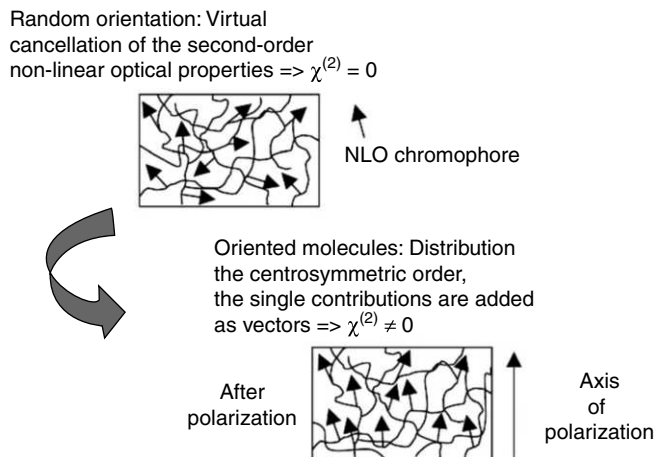


Fig. 17.49 Schematic showing the effect of poling in a hybrid NLO material (reprinted from Ref. 33. Copyright (2005) Royal Society of Chemistry).

network. The NLO molecule is trapped inside the network. The chromophore inside the pores will be in a random orientation. In order to align the chromophores in the same direction, the material is subjected to an electric field. Once aligned, the network prevents their orientational relaxation, thereby retaining the NLO activity. The amount of NLO molecules that can be doped with such an approach is limited to few percent. A picture of a Class-I type NLO material is shown in Fig. 17.50.

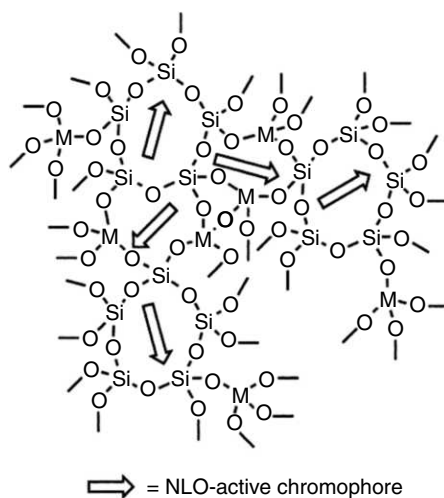


Fig. 17.50 The picture of Class-I type NLO material. Arrows represent NLO molecules, which trapped inside the pores of the silica network (reprinted from Ref. 34. Copyright (2001) American Chemical Society).

Another approach is to graft the NLO chromophore to silica network. The highly cross-linked 3-D silica network can prevent the thermally induced orientational relaxation of the NLO. The mobility may be restricted further by clamping end of the NLO chromophores at both the ends. A multiple-point attachment can further improve the performance (see Fig. 17.51).

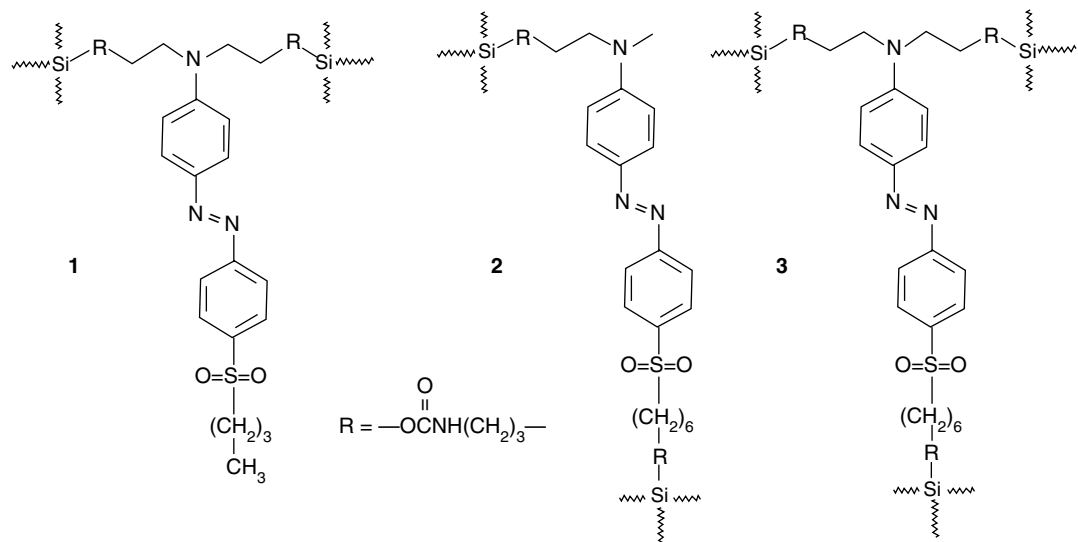


Fig. 17.51 Schematic showing an NLO material, where (1) one end, (2) both ends and (3) three ends of the NLO molecule is grafted to the silica network (reprinted from Ref. 33. Copyright (2005) Royal Society of Chemistry).

17.10.4 Optical Limiting Materials

Fullerene (C_{60}) and fullerene derivatives are potential entities for making optical limiting materials. The molecule has a strong absorption in the UV region and a weak absorption in the visible region. The first singlet excited state and the lowest energy triplet state shows larger absorption cross-section compared to the ground state. The NLO property is explained in terms of reverse saturable absorption. Generally, reverse saturable absorption takes place when the absorption from the excited state is more than that from the ground state. Fullerene has both singlet and triplet states. All the states are associated with a number of vibrational levels. The light absorption can take the molecule to the first excited state, S_1 (Fig. 17.52). From there, it can either go to the higher excited state (S_n) or cross over to the first triplet state (T_1). The light absorption from T_1 stage will take the molecule to higher triplet excited states T_n with an absorption cross-section, σ_e^T . The more the number of molecules in the excited state, the greater is the absorption. When the molecule meets the condition, $\sigma_e^S > \sigma_g^S$, it becomes a reverse saturable absorber.

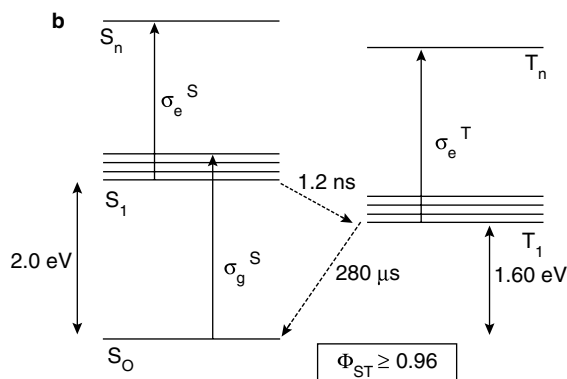


Fig. 17.52 A schematic showing the principle behind the reversible saturable absorption (RSA) in C_{60} (reprinted from Ref. 35. Copyright (2001) American Chemical Society).

REFERENCES

1. C. Sanchez, G.J. de A.A. Soler-Illia, F. Ribot, T. Lalot, C.R. Mayer and V. Cabuil, 'Designed Hybrid Organic-Inorganic Nanocomposites from Functional Nanobuilding Blocks', *Chem. Mater.*, 13(10), (2001), 3061-83.
2. N.K. Raman, M.T. Anderson and C.J. Brinker, 'Template-based Approaches to the Preparation of Amorphous, Nanoporous Silicas', *Chem. Mater.*, 8(8), (1996), 1682-1701.
3. B. Hatton, K. Landskron, W. Whitnall, D. Perovic and G.A. Ozin, 'Past, Present, and Future of Periodic Mesoporous Organosilicas—The PMOs', *Acc. Chem. Res.*, 38(4), (2005), 305-12.
4. E.L. Crepaldi, G.J. de A.A. Soler-Illia, D. Grosso, F. Cagnol, F. Ribot and C. Sanchez, 'Controlled Formation of Highly Organized Mesoporous Titania Thin Films: From Mesostructured Hybrids to Mesoporous Nanoanatase TiO_2 ', *J. Am. Chem. Soc.*, 125(32), (2003), 9770-86.
5. L. Nicole, C. Boissiere, D. Grosso, A. Quach and C. Sanchez, 'Mesostructured hybrid organic-inorganic thin films', *J. Mater. Chem.*, 15, (2005), 3598-3627.
6. A. Sellinger, P.M. Weiss, A. Nguyen, Y. Lu, R.A. Assink, W. Gong and C.J. Brinker, *Nature*, 394, (1998), 256.
7. N. Liu, Z. Chen, D.R. Dunphy, Y-B. Jiang, R.A. Assink and C.J. Brinker, 'Photoresponsive Nanocomposite Formed by Self-Assembly of an Azobenzene-Modified Silane', *Angew. Chem. Intl. ed.*, 42(15), (2003), 1731-34..
8. M.Z. Asuncion, I. Hasegawa, J.W. Kampf and R.M. Laine, 'The selective dissolution of rice hull ash to form $[OSiO_{1.5}]_8[R_4N]_8$ ($R = Me, CH_2CH_2OH$) octasilicates. Basic nanobuilding blocks and possible models of intermediates formed during biosilicification processes', *J. Mater. Chem.*, 15, (2005), 2114-21.
9. G. Kickelbick, P. Wiede and U. Schubert, 'Variations in capping the $Zr_6O_4(OH)_4$ cluster core: X-ray structure analyses of $[Zr_6(OH)_4O_4(OOC-CH=CH_2)_{10}]_2(\mu-OOC-CH=CH_2)_4$ and $Zr_6(OH)_4O_4(OOCR)_{12}(PrOH)$ ($R = Ph, CMe = CH_2$)', *Inorg. Chim. Acta.*, 284(1), (1999), 1-7.

10. R.R. Holmes, 'Organotin cluster chemistry', *Acc. Chem. Res.*, 22(5), (1989), 190–97.
11. C.R. Mayer, S. Neveu and V. Cabuil, 'A Nanoscale Hybrid System Based on Gold Nanoparticles and Heteropolyanions', *Angew. Chem. Intl. Ed.*, 41(3), (2002), 501–03.
12. J.-H. Kim and T.R. Lee, 'Thermo- and pH-Responsive Hydrogel-Coated Gold Nanoparticles', *Chem. Mater.*, 16(19), (2004), 3647–51.
13. Y. Mitsukami, M.S. Donovan, A.B. Lowe and C.L. McCormick, 'Water-Soluble Polymers. 81. Direct Synthesis of Hydrophilic Styrenic-Based Homopolymers and Block Copolymers in Aqueous Solution via RAFT', *Macromolecules*, 34(7), (2001), 2248–56.
14. M.-Q. Zhu, L.-Q. Wang, G.J. Exarhos and A.D.Q. Li, 'Thermosensitive Gold Nanoparticles', *J. Am. Chem. Soc.*, 126(9), (2004), 2656–57.
15. C.R. Vestal and Z.J. Zhang, 'Atom Transfer Radical Polymerization Synthesis and Magnetic Characterization of MnFe₂O₄/Polystyrene Core/Shell Nanoparticles', *J. Am. Chem. Soc.*, 124(48), (2002), 14312–13.
16. J. Pyun, K. Matyjaszeski, T. Kowalewski, D. Savin, G. Patterson, G. Kickelbick and N. Huesing, 'Synthesis of Well-Defined Block Copolymers Tethered to Polysilsesquioxane Nanoparticles and Their Nanoscale Morphology on Surfaces', *J. Am. Chem. Soc.*, 123(38), (2001), 9445–46.
17. B.L. Smith, T.E. Schäffer, M. Viani, J.B. Thompson, N.A. Frederick, J. Kindt, A. Belcher, G.D. Stucky, D.E. Morse and P.K. Hansma, 'Molecular mechanistic origin of the toughness of natural adhesives, fibres and composites', *Nature*, 399, (1999), 761–63.
18. N. Kroger, R. Deutzmann, and M. Sumper, 'Polycationic Peptides from Diatom Biosilica That Direct Silica Nanosphere Formation', *Science*, 286(5442), (1999), 1129–32.
19. R. Wetherbee, 'Biom mineralization: The Diatom Glasshouse', *Science*, 298(5593), (2002), 547.
20. L.A. Estroff and A.D. Hamilton, *Chem. Mater.*, 13(2001), 3227.
21. R.Y. Kannan, H.J. Salacinski, P.E. Butler and A.M. Seifalian, 'Polyhedral Oligomeric Silsesquioxane Nanocomposites: The Next Generation Material for Biomedical Applications', *Acc. Chem. Res.*, 38(11), (2005), 879–84.
22. F. Leroux and J.-P. Besse, 'Polymer Interleaved Layered Double Hydroxide: A New Emerging Class of Nanocomposites', *Chem. Mater.*, 13(10), (2001), 3507–15.
23. S. Bonnet, C. Forano, A. de Roy, J.P. Besse, P. Maillard and M. Momenteau, 'Synthesis of Hybrid Organo—Mineral Materials: Anionic Tetraphenylporphyrins in Layered Double Hydroxides', *Chem. Mater.*, 8(8), (1996), 1962–68.
24. E. Ruiz-Hitzky, M. Darder and P. Aranda, 'Functional biopolymer nanocomposites based on layered solids', *J. Mater. Chem.*, 15, (2005), 3650–62.
25. <http://www.landfood.ubc.ca/soil200/components/mineral.htm>.
26. K.P. Menard, *Thermomechanical Analysis: A Practical Introduction*, (1999), CRC Press, USA.
27. F. Mammeri, E.L. Bourhis, L. Rozes and C. Sanchez, 'Mechanical properties of hybrid organic–inorganic materials', *J. Mater. Chem.*, 15, (2005), 3787–3811.
28. J. Malzbender, J.M.J. den Toonder, A.R. Balkenende and G. de With, 'Measuring mechanical properties of coatings: a methodology applied to nano-particle-filled sol–gel coatings on glass', *Mater. Sci. Eng., R*, 36(2–3), (2002), 47–103.

29. web.kaist.ac.kr/~nano/NT512/Nano_indentation_lecture1.ppt.
30. M. Zayat and D. Levy, 'The performance of hybrid organic–active-inorganic GDLC electrooptical devices', *J. Mater. Chem.*, 15, (2005), 3769–75.
31. E. Coronado and E. Palomares, 'Hybrid molecular materials for optoelectronic devices', *J. Mater. Chem.*, 15, (2005), 3593–97.
32. A.F. Nogueira, M.-A. de Paoli, I. Montanari, R. Monkhouse, J. Nelson and J.R. Durrant, 'Electron Transfer Dynamics in Dye Sensitized Nanocrystalline Solar Cells Using a Polymer Electrolyte', *J. Phys. Chem. B*, 105(31), (2001), 7517–24.
33. P. Innocenzi and B. Lebeau, 'Organic–inorganic hybrid materials for non-linear optics', *J. Mater. Chem.*, 15, (2005), 3821–31.
34. F. Chaumel, H. Jiang and A. Kakkar, 'Sol–Gel Materials for Second-Order Nonlinear Optics', *Chem. Mater.*, 13(10), (2001), 3389–95.
35. P. Innocenzi and G. Brusatin, 'Fullerene-Based Organic–Inorganic Nanocomposites and Their Applications', *Chem. Mater.*, 13(10), (2001), 3126–39.

ADDITIONAL READING

1. C. Sanchez and P. Gomez-Romero, *Functional Hybrid Materials*, (2004), Wiley VCH. Weinheim.
2. D.A. Loy and K.J. Shea, Bridged Polysilsesquioxanes. 'Highly Porous Hybrid Organic-Inorganic Materials'. *Chem. Rev.*, 95(5), (1995), 1431–42.
3. F. Ribot and C. Sanchez, Organically Functionalized Metallic Oxo-Clusters: 'Structurally Well-Defined Nanobuilding Blocks for the Design of Hybrid Organic-Inorganic Materials'. *Comments Inorg Chem.*, 20(4–6), (1999), 327–71.
4. T.L. Simpson and B.E. Volcani, *Silicon and Siliceous Structures in Biological Systems*, (1981), Springer, New York.
5. C. Oliver and G.M. Pharr, 'An improved technique for determining hardness and elastic modulus using load and displacement sensing indentation experiments', *J. Mater. Res.*, 7, (1992), 1564–83.
6. N. Sneddon, 'The relation between load and penetration in the axisymmetric boussinesq problem for a punch of arbitrary profile', *Int. J. Engng. Sci.*, 3(1), (1965), 47–57.
7. A.C. Fischer-Cripps, *Nanoindentation*, 2nd Ed., (2004), Springer-Verlag, New York.
8. P.N. Butcher and D. Cotter, *The Elements of Nonlinear Optics*, 1st Ed., (1990), Springer-Verlag.
9. C. Sanchez, B. Julian, P. Belleville and M. Popall, 'Applications of hybrid organic-inorganic nanocomposites', *J. Mater. Chem.*, 15(35–36), (2005), 3559–92.
10. H. Roussel, V. Briois, E. Elkaim, A. de Roy and J.P. Besse, 'Cationic order and structure of [Zn-Cr-Cl] and [Cu-Cr-Cl] layered double hydroxides: A XRD and EXAFS study', *J. Phys. Chem. B*, 104(25), (2000), 5915–23.
11. F. Leroux and C. Taviot-Gueho, 'Fine tuning between organic and inorganic host structure: new trends in layered double hydroxide hybrid assemblies', *J. Mater. Chem.*, 15(35–36), (2005), 3628–42.

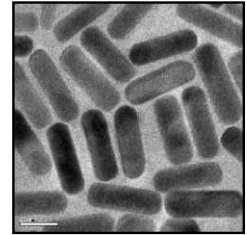
REVIEW QUESTIONS

1. What is the difference between a hybrid material and a nanocomposite?
2. Explain Class-I and Class-II type hybrids with examples.
3. Why do all hybrids exhibit unusual new properties?
4. Explain evaporation induced self-assembly (EISA).
5. Describe the phase diagram of cetyl trimethyl ammonium bromide (CTAB) in water.
6. How does a co-surfactant affect the morphology of the final silica structure?
7. What is the reason for the unusual hardness of abalone shell?
8. Illustrate the structure of layered double hydroxides. List some of the species which form intercalated hybrids with layered double hydroxides.
9. Explain the structure of montmorillonite. Discuss one application of montmorillonite-based hybrid.
10. Why does a hybrid material show a rubbery plateau?
11. Why does a material show non-linear optical properties?
12. What is the property of fullerene which makes it highly useful as a non-linear optical material?
13. Explain the principle behind the working of dye-sensitised solar cells.
14. How can one minimise the rate of recombination process in dye-sensitised solar cells?
15. Explain the working of gel-glass doped liquid crystalline device. Explain the effect of organic functional group in the functioning of the GDLC device.

Nanotechnology: Some Examples

- **Silicon MOS Transistor—From Micro to Nano**
- **Molecular Electronics**
- **Nanolithography**
- **Nanomagnetism**
- **Nanobiology**
- **Optical Nonlinearity in Nanoscale Materials**
- **Nanomaterials for Environmental Remediation**
- **Catalysis using Transition Metal Nanoclusters**
- **Nanofluids for Cooling Technology**

SILICON MOS TRANSISTOR FROM MICRO TO NANO



“We know very little, and yet it is astonishing that we know so much, and still more astonishing that so little knowledge can give us so much power.”

Bertrand Russell, *The ABC of relativity* (first published in 1925),
Fourth revised edition (Edited by Felix Pirani), chapter 15, p. 155

The downscaling of transistors has been continuing for the last 40 years pushing the transistor dimensions from micro to nano. As the microelectronics industry is poised to become nanoelectronics, various challenges loom large. Some of these challenges vis-à-vis the innovative solutions for a smooth transition from micro to nanoelectronics will be discussed.

Learning Objectives

- What are the challenges for nano-MOSFETs?
 - What are the new materials used in nano-MOSFETs?
 - What are the different novel transistor structures?
 - What are the innovations in process technology?
-
-

18.1 INTRODUCTION

According to Wikipedia, a “nanostructure” has an intermediate size between molecular and microscopic (micrometer-sized) structures. This means, at least 1-D of the structure must be between 0.1 to 100 nm, so that it can qualify as a nanostructure. Going by this simple definition, Silicon MOS transistor has entered the nanoelectronics regime in 2003, when its minimum feature size became less than 100 nm. According to the International Technology Roadmap for Semiconductors (ITRS), the shrinkage in the transistor size will continue at least till 2016, by which time, the gate length is expected to be around 9 nm.

This relentless downscaling has thrown up many problems and many possible downsizing limits have been predicted at various points of time. Fortunately, till now, every predicted limit has been

overcome. It is very difficult to predict a real limit, though the ultimate limit may be the distance between two silicon atoms in the crystal lattice, which is about 0.3 nm. However, integration issues, such as manufacturing tolerances and economics, may dictate an end to the scaling of silicon devices before this fundamental limit is reached. In the subsequent sections, we shall briefly review the history of downscaling, major challenges for the nano-MOS transistors and the possible remedies.

18.2 DOWNSCALING AND MOORE'S LAW

In 1965, when the integrated circuit industry was still in infancy, Gordon Moore published an assessment of bipolar memory component growth, which proved to be remarkably accurate. In his original paper, Moore observed an exponential increase of the number of components per integrated circuit (IC) over the years and predicted that this trend would continue¹. This analysis, known as Moore's Law, became the productivity criterion by which the IC industry grew. According to Moore's law, which predicts a decrease in feature size by a factor of 0.7 every 3 years, silicon transistors have been continuously scaled down, in order to achieve higher integration densities, higher speed, lower power consumption and lower costs. Through worldwide relentless technology advances, Moore's Law has been maintained, and continues to hold true even today. Since the 1960s, the numbers of transistors per unit area and the speed, at which they switch, have doubled every 18–24 months². This remarkable increase in performance is a result of the shrinking of the transistor to smaller and smaller sizes and has been the main driving force behind the doctrine of downscaling. The original scaling methodology was based on constant electric-field scaling principles, where all the three physical dimensions (length, width and thickness) as well as the supply voltage were scaled by the same factor, so that the electric field in the down-scaled transistor remained the same as in the bigger device. However, the downscaling of supply voltage could not be sustained at the same rate as that would require downscaling of the threshold voltage, and consequently, an increase in the leakage current. Thus, since 1984, the supply voltage has been scaled less rapidly than the dimensions^{3, 4}. This has led to an increase in power dissipation and channel electric field, which are serious concerns today. In addition, we are about to encounter a situation, where downscaling of transistor dimensions may not automatically guarantee an improvement in the total performance of the integrated circuit. This is because, rather than the transistor, the resistance and capacitance of the interconnect lines are now going to determine the speed of the circuit. Also, the actual performance improvement of the transistor with further downscaling has now become questionable as new materials and process technologies are required to sustain the downscaling. How far we can continue with silicon-based CMOS transistor will depend on finding innovative solutions to the challenges thrown up by this relentless downscaling.

18.3 CHALLENGES FOR NANO-MOSFETS

Figure 18.1 shows the basic structure of a silicon MOSFET. Despite the aggressive scaling over the last four decades, the basic structure has remained largely unaltered. The overall simplicity of the fabrication process coupled with the self-aligned technology has made silicon MOSFET the undisputed workhorse

of the IC industry. However, various challenges are faced by the nano-MOS today and it remains to be seen whether the scaling of the conventional MOSFET can continue beyond 10 nm. Some of the major challenges are discussed ahead.

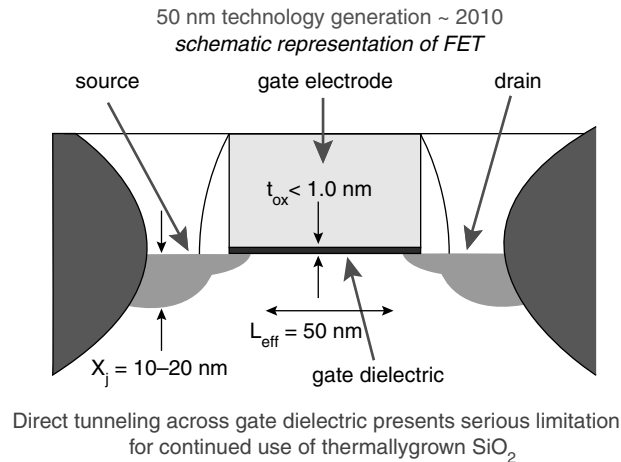


Fig. 18.1 Basic structure of a MOSFET.

Power Dissipation: Increase in the power dissipation is one of the most serious concerns in present-day integrated circuit. As shown in Fig. 18.2, the heat generated in a high-end microprocessor chip is fast approaching that on the surface of a rocket nozzle. This is because active power for a circuit operating at a fixed Frequency (f), which is on for a fraction α (activity factor) of the total time period, is given by αCV^2f . Therefore, as the speed of the circuit (and hence the frequency) increases, active power will also increase unless the supply voltage can be reduced. However, the supply voltage cannot be downscaled at the same rate as that will require downscaling of the threshold voltage. This will increase the off-state leakage current and hence increase the standby power dissipation. Thus, power dissipation in integrated circuits is increasing continuously. Alternative device structure, such as MOS transistors on Silicon-On-Insulator (SOI) substrates as well as dynamic threshold MOSFETs and advanced packaging, are expected to alleviate this problem.

Short-channel Effects: The short-channel effect (SCE) is the reduction in the threshold voltage as the device dimensions are reduced. This is caused by the proximity of the source and drain. As the separation between source and drain becomes smaller, the source-drain potential begins to exert more influence on the field pattern in the channel and the electric-field distribution in the channel becomes 2-D unlike in a long-channel MOSFET where this can be approximated as 1-D. This reduces the potential barrier, and consequently, the threshold voltage. Increase in the drain voltage further aggravates this problem and is commonly referred to as Drain-Induced Barrier Lowering (DIBL). In order to reduce SCE and DIBL, the thickness of the gate oxide has to be scaled down, so that the control of the gate over the channel remains dominant. However, the reduction in the gate oxide thickness below 2 nm has increased the gate leakage current significantly. In addition, ultra-shallow source/drain junctions and

tailored doping profile in the channel have been proposed to overcome SCE, which will complicate the device fabrication.

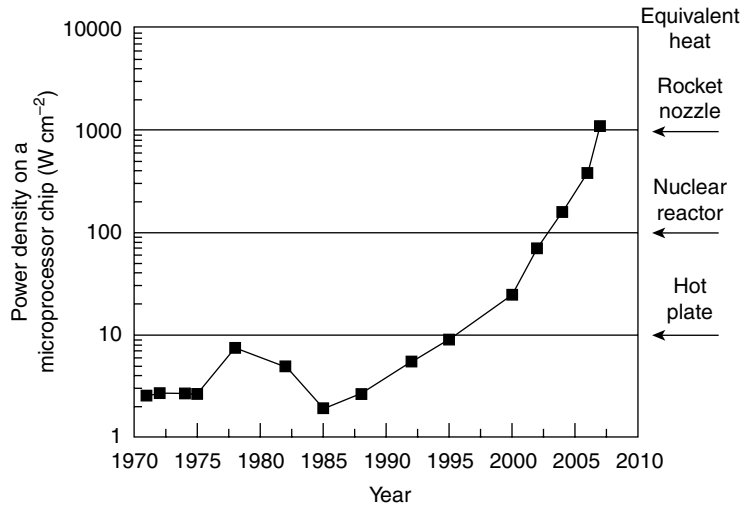


Fig. 18.2 Heat generated in a high-end microprocessor chip (adapted from data available at www.intel.com).

Leakage Current: As the channel length, junction depth and gate oxide thickness are scaled down, the off-state leakage current increases. Gate leakage is already a major concern as the gate oxide thickness has already reduced to 1.5 nm for the 130 nm technology node. High- k materials e.g. HfO_2 replacing SiO_2 as gate dielectric has offered some relief but the long-term reliability is still an issue. Also, the source to drain tunneling may eventually affect the switching capability of the device in the sub-10 nm channel length regime. According to the 2001 ITRS, the standby power dissipation due to leakage is likely to become the dominant component of the total power dissipation by 2005.

Process Limitation: As device dimensions are shrunk, processing limitations make precise control of the structural parameters more difficult. This leads to a variation in the electrical characteristics of the devices and may lead to circuit malfunction. Some typical structural variations⁵ related to process limitations are discussed below.

- Variation in film thickness: For the nano-MOS, precise control of the thickness of the gate dielectric is required. When the thickness of the gate dielectric is reduced to 1 nm, a non-uniformity of even 0.1 nm can cause significant variation in the threshold voltage.
- Variation in line-edge definition: During gate lithography, the roughness at the edge of the patterned gate may become a significant fraction of the actual gate length. A variation in the gate length will affect the current drive and the circuit speed.
- Random dopant fluctuation: As the total volume of the device is reduced, the actual number of dopants contained in the active region of the nano-MOS becomes so small, that even

the addition or removal of one dopant atom may cause an unacceptable change in the device performance. For example, in 90 nm technology node, the channel volume becomes $5 \times 50 \times 80 \text{ nm}^3$. Assuming a threshold—tailoring implant of $10^{18}/\text{cm}^3$ the total number of implanted boron atoms is about 20 per transistor. For 45 nm node, this number may become 5 and control becomes extremely difficult.

Reliability and Yield Degradation: As the transistor dimensions are shrunk and new materials as well as novel device structures are being used, reliability and yield degradation become major concerns. With the introduction of new materials, such as high- k dielectric for gate, the nature of the interface has changed. New defects are also created by new process technologies. As yield is a function of the defect density and die size, the yield at maturity is expected to be lower at successive technology nodes featuring downscaled devices. In addition, careful reliability studies are essential. Negative Bias Temperature Instability (NBTI) has already proved to be a major reliability issue with thin gate oxides.

From the above discussion, we see that many challenges are to be overcome in order to sustain the scaling of MOSFETS in the nano domain. Furthermore, the solutions to these problems are often contradictory in nature. For example, a reduction in the active power dissipation requires a reduction in the supply voltage. However, a reduction in the supply voltage means scaling down of threshold voltage. Consequently, the noise immunity of the circuit is compromised and the off-state leakage current increase. Thus there is no single full-proof solution, which will allow the continuous scaling of MOSFETs in the nano regime. Many innovations in device structure, process technology as well as new circuit and system architecture are proposed to meet these challenging requirements. Most importantly, the process technology will become more application specific, that is, a circuit for high-speed operation will have a significantly different process flow compared to a circuit designed for low-energy consumption.

18.4 EMERGENCE OF NEW MATERIALS

For a long time, integrated circuit technology used only a few materials. Silicon dioxide and silicon nitride were used as dielectric and passivation layers while polysilicon and aluminum were used for making contacts. However, today the situation has changed and many new materials now find application in IC technology. Material scientists play an important role in making this transition from micro to nano domain. In the subsequent sections, we shall discuss about the emergence of some of these new materials.

18.4.1 High- k Gate Dielectric

One of the most critical issues of MOS downscaling is the reduction of the gate oxide thickness (t_{ox}) from 100 nm in the early 1970s to about 2 nm in present technologies. This is done in order to maintain the same degree of gate control over the channel when the dimensions of the transistors are shrunk and the supply voltages are lowered. SiO_2 has so far been unparalleled in quality and used exclusively

as the gate dielectric. However, the Equivalent Oxide Thickness (EOT, defined as $\epsilon_{\text{ox}}/C_{\text{ox}}$, where ϵ_{ox} is the dielectric constant of SiO_2 and C_{ox} is the gate capacitance/area) of the MOS transistor is predicted to be below 1 nm by 2012⁶. For future technologies, a conventional SiO_2 gate transistor may not be feasible since the thickness requirement of ~ 1 nm corresponds only to about 3 monolayers of SiO_2 and the leakage current due to direct tunneling will be too large. The motivation for going to high- k materials is that the physical thickness can be increased and correspondingly the direct tunneling current is decreased.

18.4.1.1 Review of High- k Materials

The key equations governing the performance of a MOSFET using high- k dielectric in terms of its switching time (τ) consisting a load of one transistor and saturation current (I_{Dsat}) are given by

$$\tau = \frac{C_g V_{DD}}{I_{\text{Dsat}}} \quad (1)$$

$$I_{\text{Dsat}} = \left(\frac{w}{2L_{\text{phys}}} \right) \left[\frac{(k_{\text{SiO}_2} \epsilon_0 A)}{EOT_{\text{high-}k}} \right] \mu (V_{DD} - V_t)^2 \quad (2)$$

$$EOT_{\text{high-}k} = \left(\frac{k_{\text{SiO}_2}}{k_{\text{high-}k}} \right) T_{\text{physical}} \quad (3)$$

where C_g is the gate capacitance, V_{DD} is the power supply voltage, V_t is the threshold voltage and L_{physical} and w are the physical length and width, respectively of the MOSFET. The important parameters used to monitor the effectiveness of the scaling are the decrease in τ while increasing the physical thickness of the gate dielectric (T_{physical}) to minimize the direct leakage current and retaining sufficient I_{Dsat} by maintaining a low value of EOT ⁷. While oxynitrides and oxide/nitride stacks were widely used in the early 90s to provide a slightly higher value of dielectric constant (k) than SiO_2 (pure Si_3N_4 has $k \sim 7$), they were at best considered as a short-term alternative to SiO_2 . Materials like Ta_2O_5 , SrTiO_3 and Al_2O_3 with dielectric constants ranging from 10 to 80 were the first group of high- k materials to be studied as potential alternative gate dielectrics, since they have been already used for memory application and the technology was quite mature. Al_2O_3 has many favourable properties, as shown in Table 18.1, including a high band gap as well as thermodynamic stability on Si up to high temperatures. The drawback is that Al_2O_3 has comparatively low dielectric constant (~ 8 – 10). Several groups have also studied the properties of various group IIIB metal oxides, e.g. Y_2O_3 , La_2O_3 and Pr_2O_3 as high- k gate dielectrics^{8–12}. The results demonstrate that the group III metal oxides have many promising and encouraging properties for gate dielectric application.

An excellent review of the high- k dielectric materials for MOS gate applications is given by Wilk et al.¹³ A lot of research was focused onto the group IVB metal oxides, specifically TiO_2 , ZrO_2 and HfO_2 as potential candidates to replace SiO_2 ^{14–21}. The TiO_2 system was attractive because it has a high permittivity of 4–86 depending on the crystal structure and method of deposition. However, as Ti has several oxidation states, oxides of Ti have many oxygen vacancies, acting as carrier traps and high

leakage paths. It is also important to note that TiO_2 is not stable on Si during deposition by CVD as well as subsequent annealing, leading to the formation of an interfacial layer at the channel interface, which may be a mixture of TiO_2 and SiO_2 ²⁰. Also use of TiO_2 as gate dielectric, requires metal electrodes/gates to prevent reaction at the gate interface.

Group IVB metal oxides such as ZrO_2 and HfO_2 as well as pseudobinaries, such as $(\text{ZrO}_2)_x(\text{SiO}_2)_{1-x}$ and $(\text{HfO}_2)_x(\text{SiO}_2)_{1-x}$, have emerged as the most promising candidates as alternative gate dielectrics^{13,17}.

18.4.1.2 Important Issues Regarding the Choice of High- k Material

However, many issues had to be sorted out before high- k dielectric could be accepted as a serious contender for mainstream MOS gate dielectric. Material properties play key roles in determining the selection of an alternative gate dielectric for CMOS gate and have been discussed in detail in literature¹³. In this section, we will summarize some of the important issues concerning the proper choice of the high- k gate dielectric materials.

Dielectric constant and barrier height: As already mentioned, a gate dielectric with a higher dielectric constant than that of SiO_2 is clearly vital for continued scaling of MOSFETs. For higher value of permittivity, the dielectric layer can be physically thicker. Thus gate leakage will be reduced while maintaining the same gate capacitance. However, this should not come at a cost of reduced barrier height as that will again increase the leakage due to direct (band to band) tunneling. Electrons tunneling from the Si substrate to the gate see a barrier height equal to the conduction band offset (ΔE_C) given by

$$\Delta E_C = q[\chi - (\Phi_M - \Phi_B)] \quad (4)$$

where Φ_M is the metal work function, χ is the electron affinity of the semiconductor and Φ_B is the barrier height seen by the electrons traveling from the gate to the Si substrate (as shown in Fig.18.3). For direct tunneling, the leakage current (J_{DT}) is given by²²

$$J_{DT} = \frac{A}{t_{diel}^2} \exp \left\langle -2t_{diel} \sqrt{\frac{2m^*q}{h^2} \left\{ \Phi_B - \frac{V_{diel}}{2} \right\}} \right\rangle \quad (5)$$

Here, A is a constant, t_{diel} is the physical thickness of the dielectric, V_{diel} is the voltage drop across the dielectric, and m^* is the electron effective mass in the dielectric. Thus, we see that the leakage current due to direct tunneling increases exponentially with decreasing barrier height as well as dielectric thickness. Moreover, with a reduction in barrier height and/or with high density of defects present in the dielectric film, other conduction mechanisms, such as thermionic emission and defect assisted Frenkel Poole tunneling may also come into picture and increase the total leakage current. Values of ΔE_C , E_g and dielectric constant of some high- k dielectric materials are shown in Table 18.1. As a rule of thumb, if the bandgap is small, Φ_B is also small.

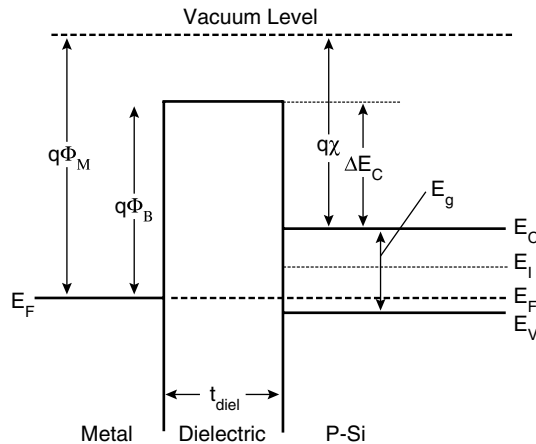


Fig. 18.3 Energy-band diagram for ideal Metal-Dielectric-Semiconductor (*p*-Si) capacitors.

Table 18.1 Comparison of relevant properties of high-*k* candidates.¹³

Material	Dielectric Constant (<i>k</i>)	Band Gap E_g (eV)	ΔE_c (eV) to Si
SiO ₂	3.9	8.9	3.2
Si ₃ N ₄	7	5.1	2
Al ₂ O ₃	9	8.7	2.8
Y ₂ O ₃	15	5.6	2.3
La ₂ O ₃	30	4.3	2.3
Ta ₂ O ₅	26	4.5	1–1.5
TiO ₂	4–86	3.5	1.2
HfO ₂	25	5.7	1.5
ZrO ₂	25	7.8	1.4

As can be seen from this table, both Ta₂O₅ and TiO₂ have comparatively small values of E_g and correspondingly small ΔE_c . These small values of ΔE_c imply high leakage currents for both these materials. Thus pure Ta₂O₅ or TiO₂ are clearly unsuitable as gate dielectrics. However, it is also observed from Table 18.1 that La₂O₃, HfO₂, and ZrO₂ offer relatively higher values for both k and E_g and are more promising candidates for MOS applications.

Thus, we can conclude that it is not only a high value of dielectric constant (with $k > 25$, as originally thought) that forces our choice of the material most likely to replace SiO₂. The more relevant consideration is whether the required drive current can be obtained under normal operating conditions with adequate on/off current ratio and acceptable reliability characteristics.¹³ It is therefore more important to find a dielectric material with a value of k in the vicinity of 20–25, but with a large tunneling barrier.

Thermodynamic stability on silicon: Unfortunately most of the promising high- k gate materials are not thermodynamically stable on silicon. They react with the channel as well as the polysilicon gate electrode under equilibrium conditions to form an undesirable interfacial layer. Thus, a very thin interfacial SiO₂ layer between the high- k dielectric and silicon channel may still be required to provide long-term stability. Also polysilicon gate may not be sustainable with high- k dielectric and a transition to metal gate technology seems imminent as discussed in more detail in the next section. Specifically, metal gates such as TiN and Pt have been used with most of the high- k gate dielectrics researched so far to prevent reaction at the gate interface.

Interface quality: The near-ideal interface between Si and SiO₂ has been the biggest cause of the phenomenal success of CMOS technology. Typical values of interface state density D_{it} for a state-of-the-art MOS process is as low as 10¹⁰ states/cm²-eV. By contrast, most of the MOS structures using high- k materials reported so far, show $D_{it} \sim 10^{11} - 10^{12}$ states/cm²-eV. Deposition techniques have to be improved considerably to achieve a better interface and reduce D_{it} . Also, oxides such as ZrO₂ and HfO₂ have been reported to have high oxygen diffusivities.²³ This will seriously compromise the quality of the interface upon thermal processing in oxygen ambient resulting in inadvertent growth of interface layers containing SiO₂.

The ideal gate dielectric stack may well turn out to be a stack of two high- k materials. While a thin moderately high- k layer can be deposited first to provide a stable interface with silicon, a different higher- k material can be used on top of the interfacial layer. According to a recent simulation study, Al₂O₃/La₂O₃ can be a potential candidate as such a high- k gate dielectric stack.²⁴

Film morphology: Though most high- k dielectric materials form polycrystalline films under the prevalent processing conditions, this morphology is not the most optimal choice. As grain boundaries serve as high-leakage paths, polysilicon gate dielectrics are usually more leaky than amorphous films. An interfacial amorphous layer is required to suppress leakage as has been observed by researchers.²¹ Interestingly, electrical results for a polycrystalline ZrO₂ layer on an amorphous SiO₂ layer also support this.²⁵ In addition, variations in grain size and orientation in a polycrystalline film can cause significant variations in k , leading to non-reproducible properties. Single crystal oxides can in principle avoid grain boundaries while providing a good interface. However precise control of film thickness may require expensive process tools like MBE. By contrast, amorphous films exhibit isotropic electrical properties, do not suffer from grain boundaries, and can easily be deposited by various inexpensive techniques.

Reliability: The long-term electrical reliability of these new gate dielectrics must also be considered critically before application in CMOS technology. It is still too early to determine whether or not the proposed high- k dielectric materials satisfy the strict reliability criteria espoused by the IC industry, though some preliminary projections for reliability, as determined by stress-induced leakage current (SILC), time-dependent dielectric breakdown, and mean time to failure measurements, appear to be encouraging for Al₂O₃ and HfO₂ films.^{19,26} One thing is however certain – high- k dielectric materials are sure to exhibit reliability characteristics different from those of SiO₂. This may necessitate new benchmarking of reliability criteria for future technology nodes.

Thus, it is evident that a lot of research has gone into developing a suitable high- k gate dielectric which can replace SiO_2 for nano-MOS. However, the technology is still not quite mature and there is ample scope for further innovation. As the properties of the high- k dielectric material strongly depend on the deposition process, new process technologies need to be developed to integrate the high- k gate dielectric material into the CMOS process flow. Various deposition techniques have been suggested in literature including Jet Vapour Deposition (JVD), Atomic layer Deposition (ALD) and pulsed laser deposition (PLD)²⁷⁻³¹ with varying degrees of success. Of these, ALD is the technique most preferred currently by IC industries for the excellent control over deposition and will be discussed in some detail in section 18.6.2.

Industries, like Intel and IBM, have been considering the adaptation of high- k dielectric material in their process flow for quite some time. In 2003, Intel announced that high- k /metal gate is a technology option for replacing the silicon dioxide/polysilicon gate in their 45 nm logic technology process for 2007 production.³² Subsequently, in 2007 Intel announced that they have used MOSFETs with Hf-based gate dielectric and metal gate for their 45 nm Penryn processor series.³³ In the next couple of years, use of high- k dielectric is expected to be widespread in CMOS technology.

18.4.2 Metal Gate

As already mentioned in the previous section, polysilicon gates are usually not compatible with the high- k gate dielectrics proposed so far. Also, metal gates are desirable for eliminating dopant depletion effects and sheet resistance constraints. For the present technology node, the width of the depletion region in polysilicon is comparable to the gate oxide thickness and this significantly increases the effective gate oxide thickness. In addition, use of metal gates in a replacement gate process can lower the required thermal budget by eliminating the annealing step needed for dopant activation in the poly-Si electrode.

For CMOS scaling in the longer term, however, current roadmap predictions indicate that poly-Si gate technology is likely to be phased out beyond the 70 nm node, after which a metal gate substitute appears to be necessary. TiN and TaN are two possible gate metal substitutes currently being considered for future CMOS technology. In fact in January 2007, Intel announced that “Intel’s transistor technology breakthrough represents biggest change to computer chips in 40 years”. They revealed that Intel Corporation is using two dramatically new materials to build the insulating walls and switching gates of its 45 nanometer (nm) transistors. “The implementation of high- k and metal materials marks the biggest change in transistor technology since the introduction of polysilicon gate MOS transistors in the late 1960s,” said Intel Co-Founder Gordon Moore.³²

18.4.3 Copper Interconnect and Low- k Interlayer Dielectric

By 45 nm technology node, the interconnect delays is expected to become the dominating factor in deciding circuit speed. In order to sustain improved circuit performance, the IC industries came up with an innovative solution in 1997 which led to significant reduction in the resistance as well as the capacitance associated with the interconnect lines and has since become a mainstream industry

practice.³⁴ This includes a two-way approach—changing the interconnect metal from aluminum to copper and changing the interlayer dielectric from SiO₂ to a low-*k* dielectric material. Copper interconnects provide lower resistivity than aluminum as well as better electromigration reliability while low-*k* dielectric separating metal lines results in lower interconnect capacitance. Copper interconnects with low-*k* dielectric have demonstrated several advantages as discussed below.

Complexity Advantage: The higher conductivity of copper simplifies inter-connect routing. This reduces the number of interconnect levels from 12 to 6, which removes more than 200 process steps and improves device yield.

Power Advantage: Chips with copper interconnect operate with approximately 30 per cent less power at a given frequency than chips with aluminum interconnect.

Cost Advantage: The reduction in critical process steps with the dual-Damascene copper process reduces the overall cost by 30 per cent per interconnect level.

Speed Advantage: At 0.13 μm, the interconnect delay for copper and low-*k* materials is approximately one-half that of aluminum and SiO₂.

However, copper interconnects are not without problems. Unfortunately, copper has a tendency to migrate into the silicon substrate and thereby poison the system. Thus a dielectric diffusion barrier is necessary to isolate the copper conductors from the metal oxide substrate. The diffusion barrier, that prevents copper migration into the silicon substructure, is the key to the successful use of copper as a conductor in ICs. Tantalum Nitride, Tantalum Silicon Nitride, Titanium Nitride, Titanium Silicon Nitride, Tungsten Nitride and Tungsten Silicon Nitride are some of the commonly used diffusion barriers for copper interconnect technology.

The low-*k* dielectric separating the metal lines should have a dielectric constant <3. Also the material is required to have good thermal stability, high thermal conductivity and low coefficient of thermal expansion. Many materials, such as Si-based polymers, C-based polymers, inorganic and organic porous materials as well as plastic resins, are being used for this purpose.

Already the IC industry is looking beyond copper. Optical interconnects as well as interconnects based on carbon nanowires/nanotubes are being actively researched for future technology nodes and may very soon become a reality.

18.5 NOVEL DEVICE STRUCTURES

As scaling of the conventional bulk CMOS to increase the device performance is reaching its fundamental limit, the basic structure of MOSFET is also undergoing significant changes. Novel device structures, which can improve performance without the need for aggressive scaling have become attractive and gained much attention. In the subsequent sections, we shall discuss two such schemes for high performance device structures—the first one is based on silicon-on-insulator (SOI) substrates and the second one utilises the superior carrier transport properties of a strained silicon channel. Both the approaches may be combined for future MOS devices.

18.5.1 SOI-based Devices

Silicon-on-insulator (SOI) has been around for a long time. Initially it was used primarily for space applications due to its superior radiation-resistance properties. However, SOI-based structures have become particularly attractive today for various reasons as below:³⁵

- Presence of the semi-insulating substrate (Back oxide) provides reduced parasitic capacitances and leakage currents and thus reduces power dissipation.
- Fully-depleted SOI MOSFETs have near-ideal device properties, such as sharper subthreshold slope, lower-body effect and smaller vertical-field mobility degradation.
- Thin films and dielectric isolation in SOI MOSFET result in simplified submicron CMOS processes
- Also, threshold voltage roll-off is minimised, radiation tolerance is higher, reliable ultra-shallow junctions are easily obtained, wells and latch-up are suppressed and complicated lateral isolation process can be avoided. Thus, SOI process yield may actually be higher than that of bulk process, since SOI devices and circuits are much more tolerant to defects.

The impact of the improved FD SOI CMOS characteristics on speed and power consumption has already received a lot of attention in digital circuitry. Circuits built on FD SOI CMOS showed twice the speed or half the power consumption of similar bulk CMOS circuits. It has been suggested that around 40 per cent of the improvement results from the capacitance reduction and the other 60 per cent from the drive current increase.

A major advantage of SOI-based MOSFETs is that novel device structures can be easily realised to obtain better control of the gate over the channel and thus reduce the short channel effects. To prevent the encroachment of electric field lines from the drain on the channel region, special gate structures can be used as shown in Fig. 18.4.³⁶ These novel SOI-based MOSFET structures include double-gate transistors, triple-gate transistor, gate-all-around and Π gate SOI MOSFETs. Such multigate structures have much better control of drain current, excellent coupling between gate voltage and channel, resulting in short channel effect reduction. Thus SOI-based technology effectively tackles two major problems faced by nano-MOS—power dissipation and short-channel effects.

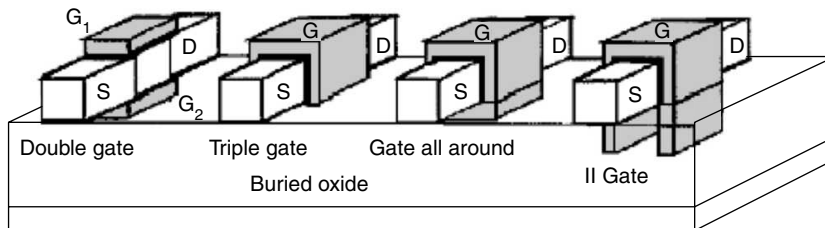


Fig. 18.4 Double-gate, triple-gate, gate all around (GAA) and Π gate SOI MOSFETs.³⁶

18.5.2 Strained Channel MOSFET

In this approach, MOSFET has ceased to be an all-silicon affair. Strained channel MOSFETs use heteroepitaxy of $\text{Si}_{1-x}\text{Ge}_x$ over Si to create a strained layer. Silicon/Silicon-Germanium heterostructure MOSFETs are being seriously considered as an effective means of extending scaling for future high-performance applications, since it offers superior transport properties. The Si/SiGe heterostructure p-channel MOSFETs reported in literature can be classified into three groups based on their structures, (a) compressively strained $\text{Si}_{1-x}\text{Ge}_x$ buried channel PMOSFETs with a Si cap layer, (b) tensile-strained-Si/relaxed $\text{Si}_{1-x}\text{Ge}_x$ surface channel MOSFETs and (c) dual-channel tensile-strained-Si/compressively-strained- $\text{Si}_{1-x}\text{Ge}_x$ /relaxed- $\text{Si}_{1-y}\text{Ge}_y$ MOSFETs.

(a) Compressively strained $\text{Si}_{1-x}\text{Ge}_x$ buried channel PMOSFETs: When a thin epitaxial film of $\text{Si}_{1-x}\text{Ge}_x$ layer is grown pseudomorphically on a silicon substrate, the lattice mismatch between SiGe and Si leads to compressive strain in the $\text{Si}_{1-x}\text{Ge}_x$ layer and provides type-I band alignment. This band alignment favours the confinement of holes in compressively strained $\text{Si}_{1-x}\text{Ge}_x$ layer and provides higher mobility for holes.^{37–38} The hole mobility enhancement in strained $\text{Si}_{1-x}\text{Ge}_x$ results from the suppressed inter-band scattering due to subband splitting and the reduced in-plane hole effective mass due to strain. The high mobility of holes in the $\text{Si}_{1-x}\text{Ge}_x$ layer results in high transconductance for the p-channel MOSFETs. In addition to this buried channel in strained $\text{Si}_{1-x}\text{Ge}_x$ layer, a parasitic (unwanted) channel is also formed at the Si/SiO₂ interface for high negative gate voltages.

(b) Tensile-strained-Si/relaxed $\text{Si}_{1-x}\text{Ge}_x$ surface channel MOSFETs: When a thin epitaxial film of Si is grown on relaxed $\text{Si}_{1-x}\text{Ge}_x$ layer, the lattice mismatch between Si and SiGe leads to biaxial tensile strain in the Si layer and provides type-II band alignment. This band alignment favours the confinement of holes in relaxed $\text{Si}_{1-x}\text{Ge}_x$ layer and electrons in tensile strained silicon layer. Since, the mobility of holes in relaxed $\text{Si}_{1-x}\text{Ge}_x$ layer is low due to the dislocations present in this layer, it is necessary to avoid confining holes in relaxed $\text{Si}_{1-x}\text{Ge}_x$ layer. To avoid hole confinement in relaxed $\text{Si}_{1-x}\text{Ge}_x$ layer, a modified structure with a grade-back layer inserted just below the strained silicon channel has been proposed.³⁹ For higher negative gate voltages, the hole concentration at the Si/SiO₂ interface increases and forms a channel with enhanced mobility. This enhancement of mobility is due to the strain in silicon cap layer. Thus, this structure provides higher mobility for both electrons and holes in tensile strained silicon cap layer, making it practical for both n-type and p-type devices.^{39–41}

(c) Dual-channel tensile-strained-Si/compressively-strained- $\text{Si}_{1-x}\text{Ge}_x$ /relaxed- $\text{Si}_{1-y}\text{Ge}_y$ structures: The mobility enhancements of electrons and holes in strained silicon layer grown on relaxed- $\text{Si}_{1-x}\text{Ge}_x$ virtual substrate with low Ge content are roughly 80 per cent and 60 per cent respectively, compared with bulk silicon.⁴² Although the hole mobility will increase for higher Ge content in relaxed- $\text{Si}_{1-x}\text{Ge}_x$ virtual substrate, it will limit the usable thickness of strained-Si layer. A solution to this problem has been proposed in the form of dual-channel tensile-strained-Si/compressively-strained- $\text{Si}_{1-x}\text{Ge}_x$ p-channel MOSFETs on relaxed- $\text{Si}_{1-y}\text{Ge}_y$ virtual substrate where $x < y$.^{42–44}

Currently, an all-germanium channel grown on silicon is also being pursued for MOS transistors. This is in order to harness the better hole mobility of Ge.

While heteroepitaxial channels have used biaxial strain to improve carrier mobility, it has been demonstrated that mobility enhancement through uniaxial tensile and compressive strain can be achieved by simply depositing a layer of high-stress Si_3N_4 over the channel and by creating SiGe source and drain respectively.⁴⁵ These strain-engineered structures have now become widely accepted in Industry.

18.6 INNOVATIONS IN PROCESS TECHNOLOGY

In the previous sections, we have seen how the use of new materials and novel device structures has helped the MOSFET to make a transition from a microstructure to a nanostructure. Implementation of these novel ideas would not have been possible without innovations and advances in process technology. In the subsequent sections, we shall discuss some of the major recent innovations in semiconductor process technology.

18.6.1 Optical Immersion Lithography

Traditionally, the light source wavelength and numerical aperture (NA) have dictated the resolution of a lithography system. For years, extensive research has been going on to develop extreme UV lithography using a wavelength of 13 nm that will significantly enhance the resolution of optical lithography and allow realisation of fine patterns on the substrate. EUV is expected to allow semiconductor manufacturers to etch circuit lines smaller than one-tenth of a micron, but the process is not yet ready for production. However, by the use of a simple but innovative recent process⁴⁶, it has been possible to improve the resolution of the conventional optical lithography significantly without any major change in the optics or the wavelength of light used. In the simplified approximation of coherent illumination, the resolution of an Optical lithography is given by

$$R = K_1 (\lambda / NA), \quad (6)$$

where K_1 is the Rayleigh constant and NA is the numerical aperture. For conventional lithography, K_1 is limited to 0.5 (the state at which only one set of diffracted order can pass through the optical system). Reducing K_1 causes image quality degradation. NA, on the other hand, is derived from $NA = n \sin q$, where n is the refractive index of the medium through which the exposure light passes, and q is the angle the exposure light forms. Normal exposure is processed in air, and in that case $n = 1$. In immersion lithography, by contrast, a liquid that has a refractive index that is greater than 1 is introduced between the projection lens and the wafer. In terms of the definition of the projection optics NA, the n increases in the equation $NA = n \sin q$. With the same angle of incidence, the minimum resolution can be reduced (improved). In an immersion lithography exposure system using an ArF laser as the light source, a liquid with an index of refraction > 1 is introduced between the projection lens and the wafer. Although this method is used conventionally in microscopes, only in recent years has serious research started for applications to immersion lithography exposure tools. With the 193-nm wavelength, the typical liquid used is ultra-pure, degassed water. Immersion techniques may help extend the use of the 193-nm wavelength to the 45-nm feature-size node and beyond.

Most agree that 193-nm immersion will make use of pure water. But the next step is to improve what researchers call the refractive index of water. Researchers are looking to develop additives in order to improve the index, which, in turn, could propel immersion technology even further down the scaling curve.

18.6.2 Atomic Layer Deposition (ALD)

Currently, atomic layer deposition (ALD) is viewed as an important process step in future semiconductor industry for high- k dielectric deposition and for the deposition of barrier materials for copper interconnects. ALD is based on sequential and self-limiting surface reactions that allows conformal atomic layer deposition with a high degree of control. It is a modified form of chemical vapour deposition (CVD), where the reaction is broken into two halves. The precursor gases are kept separate during the two halves of the reaction, making it possible to deposit layers with atomic scale precision.⁴⁷ Pulses of precursor gases are sent to the ALD system in sequence, where they either chemisorb on the surface or react with the surface species already present. Let us consider the deposition of ZrO_2 by ALD as an example. The process involves four steps. In the first step, $ZrCl_4$ vapour is introduced in the chamber and a monolayer of it is chemisorbed on the wafer surface. This is followed by a purging step, where the chamber is purged of $ZrCl_4$ vapour by an inert gas. In the third step, H_2O vapour is introduced in the chamber and it reacts with the chemisorbed monolayer of $ZrCl_4$ on the surface to produce ZrO_2 . Since there is only a monolayer of $ZrCl_4$ on the surface, only a monolayer of ZrO_2 can be formed. This is again followed by a purging step. This process sequence can be continued to grow ZrO_2 film of desired thickness. ALD can also be used to grow a multi-stacked layer (e.g., HfO_2 and Al_2O_3), which is useful for high- k dielectric gate structures as already discussed. Typically ALD is carried out at a temperature range of 200–400°C.

18.6.3 Chemo-mechanical Polishing (CMP)

Planarized surfaces have become the key to the success of advanced semiconductor devices/circuits/chips. With the advent of copper interconnects, CMP, previously perceived as a “dirty technology” has become an accepted processing step for ICs. CMP is a process in which the silicon wafer is held on a chuck and rotated rapidly while being pressed against a large rotating polishing pad.⁴⁷ A slurry containing SiO_2 or alumina (Al_2O_3) abrasive particles as well as some reactive material like ammonia is introduced on the pad. While SiO_2/Al_2O_3 provides mechanical abrasion, the chemically reactive species polish the surface chemically, justifying the term CMP. Polishing of silicon dioxide by CMP was the first step into production. Planarization of SiO_2 (used as an interlayer dielectric (ILD) between different levels of metal lines) by CMP made it possible to realize six levels of metal interconnects with high yield. Another example of CMP in ULSI is during the fabrication of tungsten plugs, where tungsten is first deposited by CVD into contact holes and vias. This is then removed from the unwanted regions by CMP, leaving only the plug holes filled with tungsten. Other CMP steps in use include polysilicon/oxide polishing during shallow trench isolation. Today, CMP is used wherever planarization is required globally on the chip. However, the success of CMP is dependent to a large

extent on optimization of various factors e.g. chemical composition of the slurry, rotating speed of the pad and wafer carrier, pressure applied by the pad, etc. The pattern on the chip is also a key factor that affects the CMP process. These challenges are bound to become more severe as we progress into the nano regime.

18.7 CONCLUSIONS

In this chapter, we have briefly reviewed the problems faced by silicon MOSFET as it continues its journey from micro to nano regime. New materials, such as high- k gate dielectric and novel device structures as well as innovative and improved process technology, are the key factors in making this transition successful. Eventually, however, nanotubes and nanowires may replace the single-crystal silicon as the ubiquitous material for integrated circuits as the device dimensions become less than 10 nm. In particular, single-wall carbon nanotubes are viewed as a most promising candidate for future nanoelectronics. However, their acceptance for future IC application will need many technological breakthroughs. To conclude, let us recall William Shockley's prediction that semiconductor devices started with germanium, progressed to silicon and will finally embrace carbon. Considering many of his predictions were truly prophetic, probably the future of nanoelectronics lies with carbon nanotubes (CNT)!!

REFERENCES

1. G.E. Moore, 'Cramming more components onto integrated circuits', *Electronics*, 38, (1965), 114–17.
2. G.E. Moore, 'No Exponential is Forever ... but We Can Delay 'Forever'', *International Solid State Circuits Conference*, February 10, (2003), 114–17.
3. G. Bacarani, M. Wordeman and R.H. Dennard, 'Generalised Scaling Theory and its Application to a 1/4 Micron MOSFET Design', *IEEE Trans. Electron Devices*, 31, (1984), 452–62.
4. R.H. Dennard, 'Evolution of the MOSFET dynamic RAM—a personal view', *IEEE Trans. Electron Devices*, 31, (1984), 1549–55.
5. *International Technology Roadmap for Semiconductors (ITRS)*, 2002 Edition (2002), Semiconductor Industry Association, San Jose, CA, December, http://www.itrs.net/1999_SIA_Roadmap/Home.htm.
6. H.C. Lin and S.M. Sze, 'Nanoelectronic Technology: In search of the Ultimate Device Structure', *Future Trends in Microelectronics* edited by S. Luryi, J. Xu and A. Zaslavsky, John Wiley & Sons, (2004).
7. H.R. Huff, A. Hou, C. Lim, Y. Kim, J. Barnett, G. Bersuker, G.A. Brown, C.D. Young, P.M. Zeitzoff, J. Gutt, P. Lysaght, M.I. Gardner and R.W. Murto, 'High- k gate stacks for planar, scaled CMOS integrated circuits', *Microelectronic Engineering*, 69, (2003), 152–67.
8. S.C. Choi, M.H. Cho, S.W. Whangbo, C.N. Whang, S.B. Kang, S.I. Lee and M.Y. Lee, 'Epitaxial Growth of Y_2O_3 Films on Si (100) Without an Interfacial Oxide Layer', *Appl. Phys. Lett.*, 71, (1997), 903.
9. J. Kwo, M. Hong, A.R. Kortan, K.T. Queeney, Y.J. Chabal, J.P. Mannaerts, T. Boone, J.J. Krajewski, A.M. Sergent and J.M. Rosamilia, 'High- k Gate Dielectrics of Gd_2O_3 and Y_2O_3 for Silicon', *Appl. Phys. Lett.*, 77, (2000), 130–32.

10. S. Guha, E. Cartier, M.A. Gribelyuk, N.A. Borjarczuk and M.A. Copel, 'Atomic Beam Deposition of Lanthanum and Yttrium Based Oxide Thin Films for Gate Dielectrics', *Appl. Phys. Lett.*, 77, (2000), 2710–12.
11. H.-J. Mussig, J. Da browski, K. Ignatovich, J.P. Liu, V. Zavodinsky and H.J. Osten, 'Initial stages of praseodymium oxide film formation on Si(0 01)', *Surface Science*, 504, (2002), 159–66.
12. U. Schwalke, K. Boye, K. Haberle, R. Heller, G. Hess, G. Müller, T. Ruland, G. Tzschöckel, J. Osten, A. Fissel and H.J. Müssig, 'Process Integration of Crystalline Pr₂O₃ High-*k* Gate Dielectrics', Proceedings of the 32nd European Solid-State Device Research Conference, *ESSDERC*, September, (2002), 407.
13. G.D. Wilk, R.M. Wallance and J.M. Anthony, 'High-*k* Gate Dielectrics: Current Status and Materials Properties Considerations', *Journal of Applied Physics*, 89, (2001), 5243–75.
14. H.S. Kim, D.C. Gilmer and D.L. Polla, 'Leakage Current and Electrical Breakdown in Metal-Organic Chemical Vapour Deposited TiO₂ Dielectrics on Silicon Substrates', *Applied Physics Letters*, 69, (1996), 3860–62.
15. S.A. Campbell, D.C. Gilmer, X.C. Wang, M.T. Hsieh, H.S. Kim, W. Gladfelter and J. Yan, 'MOSFET Transistors Fabricated with High Permittivity TiO₂ Dielectrics', *IEEE Transactions on Electron Devices*, 44, (1997), 104–09.
16. C.S. Hwang and H.J. Kim, 'Deposition and Characterisation of ZrO₂ Thin Films on Silicon Substrate by MOCVD', *J. Mater. Res.*, 8, (1993), 1361.
17. C.H. Lee, H.F. Luan, W.P. Bai, S.J. Lee, T.S. Jeon, Y. Senzaki, D. Roberts and D.L. Kwong, 'MOS characteristics of ultra-thin rapid thermal CVD ZrO₂ and Zr silicate gate dielectrics', *IEDM*, (2000), 27–30.
18. Y. Kim, G. Gebara, M. Freiler, J. Barnett, D. Riley, J. Chen, K. Torres, J. Lim, B. Foran, F. Shaapur, A. Agarwal, P. Lysaght, G.A. Brown, C. Young, S. Bothakur, H.-J. Li, B. Nguyen, P. Zeitzoff, G. Bersuker, D. Derro, R. Bergmann, R.W. Murto, A. Hou, H.R. Huff, E. Shero, C. Pomarede, M. Givens, M. Mazanec and C. Werkhoven, 'Conventional N-channel MOSFET devices using single layer HfO₂ and ZrO₂ as high-*k* gate dielectrics with polysilicon gate electrode', *IEDM*, (2001), 455–58.
19. C.H. Lee, H.F. Luan, W.P. Bai, S.J. Lee, T.S. Jeon, Y. Senzaki, D. Roberts and D.L. Kwong, 'High quality ultra-thin CVD HfO₂ gate stack with poly-Si gate electrode', *IEDM*, (2000b), 31–34.
20. H.R. Huff, A. Hou, C. Lim, Y. Kim, J. Barnett, G. Bersuker, G.A. Brown, C.D. Young, P.M. Zeitzoff, J. Gutt, P. Lysaght, M.I. Gardner and R.W. Murto, 'High-*k* gate stacks for planar, scaled CMOS integrated circuits', *Microelectronic Engineering*, 69, (2003), 152–67.
21. Ravneet Singh, Roy Paily, Amitava Das Gupta, Nandita Das Gupta, Pankaj Misra and Lalit M. Kukreja, 'Optimised Dual Temperature Pulsed Laser Deposition of TiO₂ to Realise MTOS (Metal-TiO₂-SiO₂-Si) Capacitors with Ultrathin Gate Dielectric', *Semiconductor Sc. & Technol.*, 20(1), (2005).
22. S.M. Sze, *Physics of Semiconductor Devices*, 2nd edition, Wiley Eastern Limited, New Delhi, (1981).
23. A. Kumar, D. Rajdev and D.L. Douglass, 'Effect of Oxide Defect Structure on the Electrical Properties Of ZrO₂', *Journal of American Ceramic Society*, 55(9), (1972), 439–45.
24. P.V. Nagaraju and Amitava Das Gupta, 'Study of gate leakage current in symmetric double gate MOSFETs with high- κ /stacked dielectrics', *Thin Solid Films*, 504(1–2), (2006), 317–20.

25. M. Houssa, V.V. Afanasev, A. Stesmans and M.M. Heyns, 'Variation in the Fixed Charge Density of SiO_x/ZrO₂ Gate Dielectric Stacks During Post Deposition Oxidation', *Applied Physics Letters*, 77(12), (2000), 1885–87.
26. D.A. Buchanan, E.P. Gusev, E. Cartier, H. Okorn-Schmidt, K. Rim, M.A. Gribelyuk, A. Mocuta, A. Ajmera, M. Copel and S. Guha *et al.*, '80 nm polysilicon gated n-FETs with ultra-thin Al₂O₃ gate dielectric for ULSI applications', *Technical Digest*, International Electron Devices Meeting, (2000), 223–26.
27. D. Wang, T.-P. Ma, J.W. Golz, B.L. Halpern, J.J. Schmitt, 'High-quality MNS capacitors prepared by jet vapour deposition at room temperature', *Electron Device Letters*, 13(9), (1992), 482–84.
28. S. Dueñas, H. Castan, H. Garcia, J. Barbolla, K. Kukli, J. Aarik and A. Aidla, 'The electrical-interface quality of as-grown atomic-layer-deposited disordered HfO₂ on p- and n-type silicon', *Semicond. Sci. Technol.*, 19, (2004), 1141–48.
29. K. Hirano Tai, T. Yamaguchi, S. Ando, T. Hiyama, S. Wang, J. Nagahama, Y. Kato, T. Yamanaka, M. Terauchi, S. Kanda, S. Yamamoto, R. Tateshita, Y. Tagawa, Y. Iwamoto, H. Saito, M. Nagashima, N. Kadomura, S., 'High Performance pMOSFET with ALD-TiN/HfO₂ Gate Stack on (110) Substrate by Low Temperature Process', Proc. of the 36th European Solid State Device Research Conference (ESSDERC-2006), (2006), 121–24.
30. D.B. Chrisey and G.K. Hubler (eds.), *Pulsed Laser Deposition of Thin Films*, John Wiley, (1994).
31. Roy Paily, Amitava Das Gupta, Nandita Das Gupta, Pijush Bhattacharya, Pankaj Misra, Tapas Ganguli, Lalit M. Kukreja, A.K. Balamurugan, S. Rajagopalan and A.K. Tyagi, 'Pulsed Laser Deposition of TiO₂ for MOS Gate Dielectric', *App. Surf. Sc.*, vol. 187, no. 3–4, (2002), 300–07.
32. S. Datta, G. Dewey, M. Doczy, B.S. Doyle, B. Jin, J. Kavalieros, R. Kotlyar, M. Metz, N. Zelick and R. Chau, 'High Mobility Si/SiGe Strained Channel MOS Transistors with HfO₂/TiN Gate Stack', (IEDM, 2003).
33. <http://www.intel.com/pressroom/archive/releases/20070128comp.html>.
34. C.Y. Su, S.L. Wu, S.J. Chang and L.P. Chen, 'Strained Si_{1-x}Ge_x graded PMOSFET grown by UHVCD', *Thin Solid Films*, vol. 369, no. 2, 372–74, July 2000.
35. L. Geppert, Solid State [Technology 1998 Analysis & Forecast], *IEEE Spectrum*, 35, (1998), 23–28.
36. J.P. Colinge, *Silicon-on-Insulator Technology: Materials to VLSI*, Kluwer Academic Publishers, (1991).
37. J.T. Park and J.P. Colinge, Multiple-Gate SOI MOSFETs: Device design guidelines, *IEEE Trans. Electron Devices*, 49, (2002), 2222–28.
38. G.S. Kar, S.K. Ray, T. Kim, S.K. Banerjee and N.B. Chakrabarti, 'Estimation of hole mobility in strained Si_{1-x}Ge_x buried channel heterostructure PMOSFET', *Solid-State Electronics*, vol. 45, no. 5, 669–76, May 2001.
39. C.K. Maiti, N.B. Chakrabarti and S.K. Ray, 'Strained Silicon Heterostructures: Materials and Devices', Chap. 3, *Institution of Electrical Engineers*, (2001).
40. D.K. Nayak, K. Goto, A. Yutani, J. Murota and Yasuhiro Shiraki, 'High mobility strained-Si PMOSFET's', *IEEE Trans. on Electron Devices*, vol. 43, no. 10, 1709–15, Oct. 1996.
41. K. Rim, J. Welser, J.L. Hoyt and J.F. Gibbons, 'Enhanced hole mobilities in surface-channel strained-Si p-MOSFETs', 517–20, *IEDM*, (1995).

42. J. Jung, M.L. Lee, S. Yu, E.A. Fitzgerald and D.A. Antoniadis, 'Implementation of both high-hole and electron mobility in strained Si/strained Si_{1-y}Ge_y on relaxed Si_{1-x}Ge_x ($x < y$) virtual substrate', *IEEE Electron Device Letters*, vol. 24, no. 7, 460–62, July 2003.
43. J. Jung, S. Yu, M.L. Lee, Judy L. Hoyt, E.A. Fitzgerald and D.A. Antoniadis, 'Mobility enhancement in dual-channel P-MOSFETs', *IEEE Trans. on Electron Devices*, vol. 51, no. 9, 1424–31, Sept. 2004.
44. S. Yu, J. Jung, J.L. Hoyt and D.A. Antoniadis, 'Strained-Si/strained-SiGe dual channel layer structure as CMOS substrate for single workfunction metal-gate technology', *IEEE Electron Device Letters*, vol. 25, no. 6, 402–04, June 2004.
45. T. Ghani et. al. (2003), *IEDM Tech. Dig.*, 978
46. L. Geppert, Chip Making's Wet New World, *IEEE Spectrum*, 41, (2004), 29–33.
47. http://www.icknowledge.com/misc_technology/Atomic%20Layer%20Deposition%20Briefing.pdf.
48. S. Franssila, *Introduction to Microfabrication*, John Wiley & Sons, Ltd., (2004).

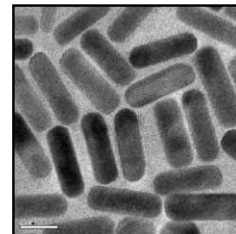
ADDITIONAL READING

1. *Future Trends in Microelectronics* by S. Luryi, J. Xu and A. Zaslavsky, John Wiley & Sons, (2004).
2. *Introduction to Nanoelectronics* by V.V. Mitin, V.A. Kochelap and M.A. Stroscio, Cambridge University Press, (2008).

REVIEW QUESTIONS

1. What are the principal challenges before nano-MOS transistor?
2. How does high- k dielectric reduce the gate leakage problem?
3. What are the advantages of a multi-gate SOI transistor?
4. How does immersion lithography offer better resolution than conventional optical lithography despite using UV light of the same wavelength?
5. How is ALD different from a conventional CVD process?

MOLECULAR ELECTRONICS



“Life ... is a relationship between molecules.”

Linus Pauling, quoted in T. Hager,
Force of Nature: The Life of Linus Pauling (1997) 542

To overcome the limitations of present solid-state electronic technology, molecular electronics, a fairly new and fascinating area of research has emerged. It involves the search for a single or a small group of molecules that can be used as the fundamental units for computing. The promise that it holds and the challenges that need to be overcome are discussed in this chapter.

Learning Objectives

- What is Molecular Electronics?
 - What are the differences between the Molecular Electronics and the Silicon Electronics?
 - What is so interesting about Molecular Electronics?
 - What are the applications of Molecular Electronics?
-
-

19.1 TOP-DOWN VS BOTTOM-UP

Richard Feynman, on 29th December in 1959, at the annual meeting of American Physical Society at the California Institute of Technology in a classic speech, entitled “There is Plenty of Room at the Bottom”, envisaged a scenario, long before the means to achieve it was even vaguely known—i.e., to write the entire pages of the *Encyclopedia Britannica* on the head of a pin, which would require to reduce the writing by 25,000 times. And 40 years later, research in the field of “nanotechnology”, which involves manipulating materials at the very atomic level, has moved so much forward, with everyday bringing in new advances owing to various developments in the experimental front with the advent of the scanning tunneling microscope (STM)¹, the atomic force microscope (AFM)², the mechanically controllable break junction (MCBJ) technique,³ etc.

Technologically speaking, there have been two approaches to reach the nanoscale devices as the semiconductor microelectronics industry has always been driven by the need for powerful computational devices with high computing speeds. The first is the one, which has been described at length, in previous chapter, the so-called “top-down” approach. This method relies on lithographic approach, which involves the miniaturisation of existing silicon-based chips for the faster and powerful circuitry. However, the “top-down” approach is expected to reach its physical limit in the next few years owing to certain factors. As has been outlined in previous chapter, this rate of downscaling is expected to hamper the performance of such devices when issues, such as quantum tunneling, interconnect delays, gate oxide reliability, and excessive power dissipation, start gaining importance. Also, at the nanometer scale, the electronic properties of semiconductor structures fabricated via conventional lithographic processes are quite difficult to control, as the band-structure itself change drastically with reduction in size. Although some of these issues can be overcome by improving the device design, the increasing cost of fabrication has motivated research in other directions. It has led to the replacement of the “top-down” lithographic approach by a “bottom-up” synthetic chemical approach of assembling nanodevices and circuits directly from their molecular constituents, leading to the next generation of electronics known now as “molecular electronics”. The term “molecular electronics” covers a broad range of topics. It can be molecular-scale electronics or molecular materials for electronics. While the second one deals with crystals or films that contain many trillions of molecules per functional device unit and thus measured on the macroscopic scale, the molecular-scale electronics, on the other hand, deal with one to a few thousand molecules per device, thus requiring measurement at the molecular scale. Henceforth, we will deal with “molecular-electronics”, which describes molecular-scale electronics.

19.2 WHY MOLECULES?

Almost all electronic processes in nature, from photosynthesis to signal transduction, occur in molecular structures. Molecules are small, of the order of nanometer, a natural scale for use as functional nanodevices with additional advantages in cost, efficiency, and power dissipation. Their abilities of selective recognition and a thermodynamically-driven self-assembly provide molecular building blocks through cheap methods of fabrication. Their dynamical stereochemistry also ensures that molecules can have many stable geometric structures or isomers, which can have very different optical and electronic properties. Their conformational flexibility can also give rise to interesting transport properties. In addition, just by choice of composition and geometry, a molecule’s binding, optical, and structural properties can be extensively varied. Moreover, in comparison with molecules, which are such natural nanostructures, solids have the significant disadvantage that it is relatively difficult and expensive to fabricate them into many millions of nearly identical structures that will be needed in each ultra-dense computer chip. However, molecules have their own disadvantages too such as instability at high temperatures. But overall, the advantages render molecules ideal entities for electronics applications.

19.3 EXPERIMENTAL ADVANCES

Hans Kuhn *et al.* performed some of the earliest electrical transport measurements through organic molecules, as early as the 1970s, by depositing organic adlayers on solid substrates.⁴ It was the time when effective self-assembly techniques, through which molecules adhere to surfaces by strong molecular bonds, were developed. The first suggestion, however, that molecules could be used as alternatives to silicon chips came from Aviram and Ratner⁵ who, in 1974, in their far-sighted paper, discussed theoretically the possibility to construct a molecular rectifier, based on a single organic molecule.

They suggested that a single molecule with a donor-spacer-acceptor structure (Fig 19.1) would behave as a p-n junction diode when placed between two electrodes. This was the first attempt to predict and characterise a molecular-scale phenomenon. At that time, however, the lack of good experimental techniques led to a road block and the hypothesis remained so until Metzger⁶ more than 20 years later, studied Langmuir-Blodgett (LB) films of γ -(n-hexadecyl) quinolinium tricyanoquinodimethide (Donor- π spacer-acceptor species) between metal electrodes and convincingly demonstrated rectifying behaviour. Over the years, with the advent of the scanning probe microscopy and other techniques, researchers have developed ways of addressing, imaging, manipulating, and performing measurements on one to hundreds of molecules connecting metal leads. Advances in synthesis of organic molecules, their assembly and measurement have also led to an increasing interest in the field of molecular electronics. Charge transport through molecules can now be probed in a controlled way and the field is reaching a stage of trustable and reproducible experiments. Several prototype devices, such as conducting wires, insulating linkages, rectifiers, switches, and transistors have already been demonstrated. A few of the modern techniques for measuring tunneling current are summarised below.

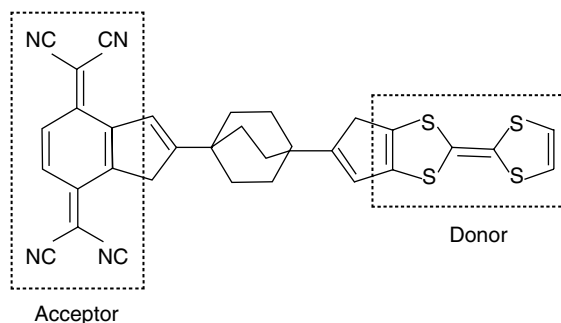


Fig. 19.1 Organic analogue of a p-n junction, composed of a donor moiety tetrathiafulvalene (TTF) connected by a methylene bridge to an acceptor moiety tetracyanoquinodimethane (TCNQ) (adapted from *Chem. Phys. Lett.* 29, 277 (1974) (Ref. 5)).

Break-Junction Technique: Break-junctions offer a new class of tunneling experiments on freshly exposed surfaces of a fractured sample without the oxide barrier required for junction stability. Numerous experiments have been carried out on the application of break-junction techniques, from superconductivity to molecular electronics. In this technique, a small metallic wire is broken, applying

a mechanical strain, resulting in two microscale electrodes. Now, molecules with preferred end groups, which can chemically bind with those electrodes, can be introduced to bridge between the break junction, resulting in an experimental setup for molecular electronics. Due to very low surface area of the electrodes, they can accommodate very few molecules, sometimes even a single one, although it is rather difficult to estimate the exact number. Thus, using this technique one can effectively measure the transport property of a single to hundreds of molecules.



Fig. 19.2 *Break-junction setup: a very narrow contact is stretched by flexing the support until single atom makes the contact (adapted from a website (ref. 7)). (For clarity see colour figure.)*

Nanopore: A nanopore is a small pore in an electrically insulating membrane that can be used as a single-molecule detector. It can be a biological protein channel in a lipid bilayer or a pore in a solid-state membrane. The detection principle is based on monitoring the ionic current of an electrolyte solution passing through the nanopore as the voltage is applied across the membrane. The molecule of interest is driven through the pore, also by the applied voltage, blocking the flow of ions as it does so. This ion flow can be measured as a current flowing in the electrical circuit, and because the pore is chosen to have a diameter sufficiently smaller than the molecule which is forced to pass through. Through this, even the molecular properties, like length and size, can be determined based on the duration of current blockage, and variations in its magnitude.

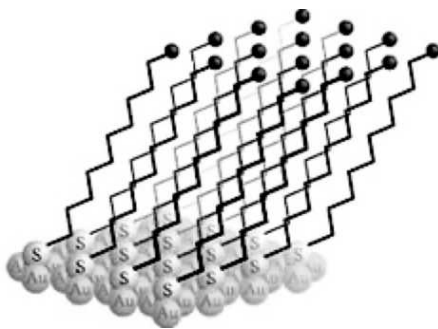


Fig. 19.3 *Self-Assembled Mono layer of alkane dithiols on Au(111) surface (adapted from Chem. Rev. 105, 1103, (2005)).*

Self-Assembly: Scanning tunneling microscope (STM) images of self-assembled monolayers of different molecules on different substrates have been a study of great interest in recent past. Such images are obtained by recording the distance of the tip from the molecular monolayers as it scans its surface at a fixed current. Generally, self-assembled monolayers are prepared by attaching the end thiol group to the gold substrate, which give strong chemical bonding as well as good orbital overlap. The other contact is typically an STM tip, which usually couples weakly to the molecules. It is commonly assumed that the applied potential is dropped entirely between the tip and the molecule, while the molecular potential remains fixed with respect to the substrate. The lateral conduction through the molecular monolayer is essentially neglected. SAM also can be sandwiched between two ferromagnetic electrodes to fabricate potential organic spintronic devices, such as organic spin-valves, spin dependent organic FETs, etc., which require injection of electron in particular spin orientation for their proper operation.

19.4 TRANSPORT—HOW TO UNDERSTAND

Technological interest aside, molecular electronics is receiving a growing interest also due to the number of fundamental issues it poses. Understanding quantum transport of electrons through a nanoscale conductor, such as a single molecule attached to large macroscopic electrodes, is very challenging. First of all, it is important to understand the changes in the various scales that happen as we go from the macro to the nanoscale regime. The most obvious one is the length scale and there are some characteristic length scales defined to determine truly when the classical regime ends and the quantum regime begins. These are the Fermi wavelength, λ_F , the momentum relaxation length, L_m , and phase relaxation length, L_ϕ .

Fermi wavelength: Since the conductor is confined in one or two directions, the quantum modes (k vectors) in the directions normal to the electron propagation direction are discretised. For a 2-D wire of width W , the number of quantum modes is determined by the ratio of the width of the wire to the de-Broglie wavelength of the conduction electrons at E_F , the Fermi energy, through the expression $N = \text{Int}(2W/\lambda_F)$, where $\text{Int}(x)$ is the integer that is just smaller than x . It was shown by Landauer⁸ that the conductance of a nanoscale system depends on the transmission probabilities of electrons through these modes, resulting in quantisation of conductance in these conductors. A changing width hence results in steps in the conductance as opposed to continuous dependence of conductance on dimensions in macroscopic conductors (Ohm's Law). de-Broglie wavelengths range from 1 nm in metals to 100 nm in semiconductors.

Momentum relaxation length: This determines the average distance an electron can travel before colliding with impurities and defects in the sample and losing memory of its initial momentum. This mean free path is usually of the order of μm or nm and gains relevance in low-dimensional conductors.

Phase relaxation length: Scattering of electrons due to fluctuating/dynamic scatterers like phonons, electrons and magnetic impurities can result in randomisation of the phase of the incoming electrons.

The phase relaxation length measures the distance traveled by the electron before such phase randomising collisions take place. When the length of the conductor is less than this length, quantum effects, such as interference, gain prominence. Other length scales, such as the spin diffusion length, plays an important part when we deal with spin-transport through nanoscale conductors.

Apart from length scales that differ markedly when one goes from a macroscopic to a nanoscale conductor, the energy scales of whole system consisting of the molecule with its discrete energy levels attached to macroscopic metallic electrodes with a continuous band structure poses much of the challenge in understanding molecular electronic transport. The main issues that one encounters in trying to understand molecular transport are the following.⁹

Role of molecule-electrode coupling: When a molecule is attached to macroscopic electrodes, based on the strength of the coupling, the energy levels of the molecule get broadened due to hybridisation of the molecular orbitals with the delocalised metal wavefunctions. This broadening (Γ) is inversely related to the lifetime of the electron in the molecular energy level, and is also a measure of the rate at which electrons can escape from the level into the contacts. Hence, a stronger coupling results in a higher current through the molecular conductor. Different kinds of experimental set-ups result in different strengths of metal-molecule coupling, and thus, influence the transport characteristics of the molecule. The contact surface physics and metal-molecule coupling thus play a key role in current characteristics.

Location of the contact Fermi energy: When a molecule is connected to leads, the Fermi energy of the metal falls somewhere in the HOMO - LUMO gap of the molecule. Also, the molecule no longer remains necessarily neutral as the broadening of the molecular levels allows for fractional transfer of charge from the contact into the molecule. The charging energy per electron determines how much the molecular energy levels shift when the fractional charge is injected in. This gives an idea about the lineup of the energy levels with respect to the Fermi energy of the metal. This has a significant effect on the shape of the current-voltage characteristics of the molecular conductor.

Device electrostatics: The application of an external electric field shifts the electrochemical potentials at the contacts. But the shifting of the molecular levels depends on the shape of the potential profile inside the molecule. This depends on the nature of the molecule-metal coupling. A strong coupling would more likely result in a ramp-kind of potential profile, whereas a weak metal-molecule coupling would give rise to a large resistance and hence voltage drops at the interface and an almost rigid shift in the middle. The profile also depends on the extent of polarisability of the molecule and how the charge distribution in the molecule would screen the potential seen by it.

Electronic structure of the molecule: The nature of the transport channels of the molecule, which are the molecular orbitals, plays a very important role in determining the nature of the current characteristics of the molecular conductor. Hence, a very accurate description of the electronic structure of the molecule is required to understand transport in these molecules. At such small scales, electron-electron correlations are very important and a description of the non-equilibrium situation involving scattering and many-body effects are very essential.

19.5 MECHANISMS OF MOLECULAR TRANSPORT

Ballistic or Coherent resonant tunneling regime: Electron transport is divided into three regimes: ballistic, diffusive and classical, based on the characteristic length scales mentioned before. When the length of the conductor is smaller than the momentum (L_m) and phase relaxation lengths (L_ϕ), the transport is said to be ballistic. It is also called the coherent resonant tunneling process as the energy of the tunneling electrons is resonant with the conduction band of the wires and does not undergo any scattering that can change its momentum or phase. The rate of electron transport obeys Landauer's formula, which describes it in terms of its transmission probability and is independent of the length of the molecular bridge. The conductance scales linearly with the transmission and the number of eigen-modes in the wire. Interestingly, the conductance of even a ballistic sample is finite as was found by Landauer, due to the resistance at the interface of the small conductor and the large contacts. Measurements on atomic point contacts and metallic-carbon nanotubes have clearly demonstrated this behaviour, where the transmission of each available channel is nearly unity. However, in general, the molecular orbitals are not fully delocalised leading to a transmission that might be less than 1.

Diffusive or coherent non-resonant tunneling regime: When the molecular orbitals of the molecular wire allow the electrons to transport from one electrode to the other without loss of energy or phase, the resultant mechanism is that of coherent electron motion. If the HOMO-LUMO gap of the molecule is large (of several eV), then the electronic states are far above in energy as compared to that of the tunneling electron, and hence, the conduction would be non-resonant. This is an intermediate regime where $L_\phi \gg L_m$ and the transport is diffusive. But, the phase of the electron wave is not completely lost, and hence, quantum interference effects are still present. The rate of electron transfer in this case is exponentially dependent on the length of the molecular bridge $G=A [\exp(-\beta N)]$, where N is the number of sites of the wire, β is the characteristic decay parameter, which depends on the electronic structure of the wire and A is related to the contact conductance and depends on the electrode-wire interactions. This mechanism holds, especially for short wires with large HOMO-LUMO gaps, such as oligoalkane-thiols. It is also known sometimes as "superexchange", where the electron transfer proceeds through "virtual" orbitals, which are energetically well separated from the Fermi levels at the electrodes.

Classical or incoherent transfer: The case when $L \gg L_\phi \gg L_m$ is the classical transport regime, wherein inelastic and incoherent scattering occurs and interference effects are too small that they can be neglected. This happens, especially, when the electronic levels in the molecular wire couple to the vibrational or rotational degrees of motion. The wire in this case would behave as regular electrical wire with its resistance directly proportional to its length. In such long wires with high scattering, the resistance no longer shows an exponential behaviour as in the diffusive regime, but begins to obey Ohm's Law.

In addition, conduction could also be mediated by quasiparticles, like solitons and polarons, in the molecule. These are, by and large, the most commonly-observed mechanisms of electron transport in molecular wires. A change in the parameters, such as the electronic structure, metal-molecule coupling, environment effects, etc., could profoundly alter the nature and mechanism of conduction through the wire.

Let us now describe the conduction mechanism of a molecular system in the simplest case, i.e., in the ballistic tunneling regime. A molecule in the isolated condition has discrete energy levels, called molecular orbital levels. When the molecule is attached between two macroscopic electrodes or between an electrode surface and STM tip, the coupling between the molecule and electrodes would result in some change in the molecular energy-level structure to bring in equilibrium situation.

Depending on the coupling, the discrete molecular energy level might get broadened to accommodate the charge balancing and thereby the Fermi energy of the electrodes. Assuming that the Fermi energy of the electrode is pinned at the middle of the highest occupied molecular orbital (HOMO) and lowest unoccupied molecular orbital (LUMO), which is usually the case for charge neutrality, at zero bias, the molecular energy levels and the electrodes continuum energy spectrum are shown in Fig. 19.4a. Now, once the bias is turned on by way of a voltage circuit, for a bias value of V volts, we would expect the left and right electrodes chemical potentials to rise and fall by $V/2$. Assuming that the molecular energy levels are hardly perturbed due to potential, the scenario shown in Fig. 19.4b reveals that there is an empty molecular level, which is within the chemical potential of left and right electrodes. In fact, conduction occurs through this molecular level and the level is called to be in “resonance”. Charge conduction is defined as the flow of charge carriers through a medium. In this case, since the charge conduction is discretised, the conduction will occur through single-electron tunneling. What it means is that the current in a molecule is equivalent to putting an electron from left electrode and taking one out through the right electrode, where the charge is collected. In this case, since there is an empty level available for conduction, the current is due to negatively charged particle, or the conduction is said to be n-type. If we keep increasing the bias voltage, this level will become off-resonant and one needs to increase the bias further to bring in another empty molecular energy level into the “resonance”, i.e., within the bias window of the left and right electrode chemical potentials. Thus one would see step-like behaviour of the current as a function of applied voltage.

On the other hand, if it so happens that instead of an empty level, a filled level is in “resonance”, such that the filled molecular level is within the left and right electrode chemical potentials, will there be any resonant current? The answer to this question does not seem to be in line with the definition that current in a system is equivalent to putting an electron from left electrode and taking one out through the right electrode. However, we can always have second thing first and the first occurrence second. That is, we can first collect the electron from the molecular level in the right electrode and then put an electron from the left electrode into the molecular level. Since it is not known which occurs first, this also results in a charge flow and thereby current. Effectively, it amounts to flow of hole or absence of electron. The transport of this type is called p-type conduction. The mechanism of this conduction is shown in Fig. 19.4c.

19.6 ADVANCED APPLICATIONS

In 1997, Reed *et al.* measured the conductance of a single molecule of benzene-1,4-dithiol in a mechanically controllable break junction.¹⁰ This method was one of the first where measurements were made by mechanically fracturing a metal wire on a flexible substrate leading to an adjustable

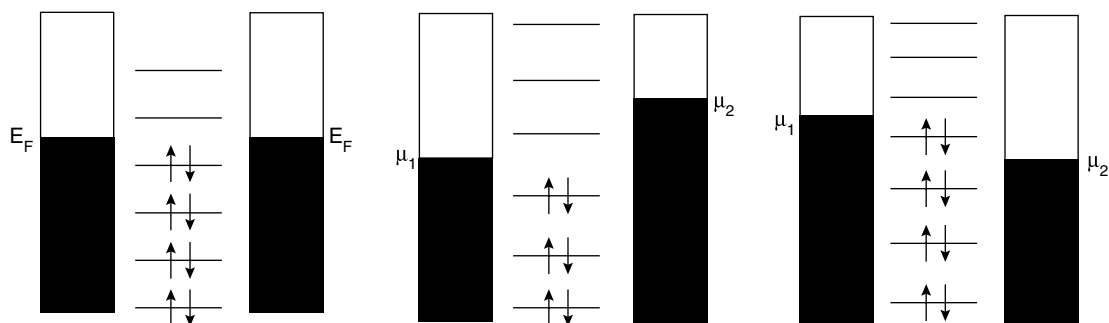


Fig. 19.4 Schematic representation of electron tunneling between two bulk electrodes through the discrete molecular energy levels. E_F represents Fermi energy and μ_1 , and μ_2 are the left and right electrode's chemical potentials.

tunnel gap, in which the organic molecule was adsorbed. This resulted in at least a single molecule contacting the two facing electrodes, leading to a single molecule junction. More complex anthracene based molecules were later studied by Reichert *et al.*, using the same method and wire and diode like properties were demonstrated in symmetric and asymmetric molecules, respectively.¹¹

A large number of experimental work has also emerged on the conducting behaviour of oligo(phenylene-ethynylene) (OPE) molecules, synthesised by Tour and co-workers. Bumm *et al.* used the tip of a scanning tip microscope (STM) to measure the conductivity of an OPE molecule embedded in a self-assembled monolayer (SAM) support composed of dodecanethiolate (DT).¹² They inferred that the OPE molecules have a greater conductivity than DT and can hence be a good molecular wire. Kushmerick and co-workers used the crossed wire method to measure transport through OPEs and observed molecular wire and diode behaviour in symmetric and asymmetric molecules made from OPEs.¹³ Reed and Tour *et al.* reported negative differential resistance (NDR) behaviour in OPEs functionalised by NH_2 and NO_2 groups, which they attributed to the effects of charging. The strong NDR peak with a peak-to-valley ratio (PVR) of 1030:1 that they observed at 60K, however, reduced with increasing temperature. They also reported electronically programmable memory behaviour in the NO_2 functionalised devices. Their experiments were performed using the nanopore setup, which was constructed by etching a small hole of 30–50-nm diameter in a silicon nitride membrane via e-beam. The bowl-shaped geometry with a hole at its bottom was then filled with gold and placed in a solution containing OPE. After the SAM formed, the bottom gold electrode was deposited. Very recent experiments performed by Tao *et al.* using a STM break junction method, where a Au tip was driven into contact with a Au surface in a solution containing the organic molecules have proven to be very effective “single” molecule junctions. The conductance was then measured as the tip was retracted. Their experiments confirmed earlier observations by indicating sharp NDR peaks in the NO_2 functionalised OPEs. Charge transport measurements through molecules on doped silicon surfaces have also been reported to show NDR behaviour due to the semiconducting nature of the electrode.¹⁴ Joachim and Gimzewski did one of the first demonstrations of how the conductance of a molecular junction could change as a function of change in its electronic structure on a C_{60} molecule

between a substrate and a STM tip.¹⁵ They showed that its conductance increased by two orders of magnitude upon distortion, thus behaving as an electromechanical amplifier.

A family of molecules, known as rotaxanes, have also shown possibilities for being used as switching and logical devices. The rotaxane consisted of a molecular “rod” and two “stations” (benzidine and benzophenol) with a “bead” structure (tetracationic cyclophane) threaded onto it. During oxidation/reduction, due to electrostatic repulsion, the “bead” moved from one “station” to the other resulting in switching behaviour. Similarly, a catenane-based molecule has been shown to exhibit bistable I-V characteristics with the application of bias. Molecules, such as bipyridyl-dinitro oligophenylene-ethynylene dithiol (BPDN-DT) [BPDN] and thiol substituted oligoaniline molecules have also been demonstrated to show bistable conductance switching. pH and photo-induced molecular switching have also been observed in some molecules.

Building a single molecule FET is considered to be a critical step towards the ultimate goal of molecular electronics. However, experimental demonstration of this FET behaviour in single molecules has been a difficult challenge, because it would require placing the gate electrode a few Angstroms away from the molecule to achieve the necessary gate field. Xu *et al.* have described a single molecule FET made of perylene tetracarboxylic diimide by adjusting the electrochemical gate voltage. The energy levels of the molecule's empty states were shifted to the Fermi level of the source and drain electrodes, resulting in a 1000-fold increase in the source-drain current, just like in a n-type FET. Another regime, where molecules exhibit interesting behaviour is where electron charging energies are very high and temperatures are very low resulting in coulomb blockade behaviour. Such a signature has been observed by Park *et al.* In a molecule incorporating a transition metal complex, designed in such a way that electron transport occurs through well-defined charge states of a single atom. They examined two related molecules containing a Co ion bonded to polypyridyl ligands, attached to insulating tethers of different lengths. Changing the length of the insulating tether altered the coupling of the ion to the electrodes, enabling the fabrication of devices that exhibit either single-electron (coulomb blockade) phenomena or even the exotic Kondo effect. Single-electron transistor behaviour has been observed in transport through semiconductor quantum dots, metallic and semiconducting nanoparticles, and even in single π -conjugated organic molecules with several distinct charged states which can control its transport properties.

Carbon nanotubes and semiconductor nanowires represent another emerging area in this field with major advances in their synthesis and purification. Carbon nanotubes, which were first discovered in 1991, have been found to have large elastic and phase scattering lengths^{16,17}. Most of their properties depend on the diameter, chirality and lengths of the tube. Their ability to display both metallic and semiconducting characteristics, just depending on their diameter and chirality is very unique, and has heightened their potential use of a wide range of applications in nanoelectronics. Carbon nanotubes connected to metallic electrodes allow to study many different regimes in electron transport, exhibiting either ballistic or diffusive behaviour,¹⁸ Luttinger liquid features,¹⁹ etc. Some experiments have even demonstrated that carbon nanotubes, weakly coupled to normal leads, can exhibit Coulomb Blockade²⁰ and Kondo effects.²¹ A related molecule, the fullerene or bucky-ball, encapsulated inside a short nanotube, has even been proposed for use as nonvolatile memory element. Dekker and co-workers have also fabricated a carbon nanotube field-effect transistor.²²

Bio molecules, apart from natural self-assembly also have self-recognition properties. Lots of transport measurements have been performed on DNA, the blueprint of life, which have reported contradictory results ranging from conducting, semi-conducting to even insulating behaviour. The first direct electrical transport measurement on a single, 16 μm long DNA molecule was published in 1998 by Braun *et al.*, where the DNA was stretched on a mica surface and connected to two-metal electrodes. Electrical transport measurements through the single molecule yielded no observable current up to 10 V. In 1999, measurements on small bundles of DNA were made by Hans-Werner Fink and Christian Schenberger.²³ They measured the conductance by touching bundles of DNA with a metal tip and obtained large conductance indicating that DNA bundles almost 1 μm in length appear to behave like an Ohmic conductor. Soon afterwards, Danny Porath and co-workers made measurements on very short DNA molecules comprising of one strand that contained only Guanine bases and a second strand that contained only cytosine bases and they obtained results that showed that DNA would behave as a semiconductor. More recent experiments by Arnold Storm and co-workers at Delft University, who measured the conductance of DNA molecules between nano-electrodes using the AFM tip, showed that DNA was an insulator with no conduction observed even for large lengths. In parallel, Kasumov *et al.* reported Ohmic behaviour of the resistance of DNA molecules deposited on a mica surface and stretched between rhenium/carbon electrodes. This behaviour was measured at temperatures ranging from room temperature down to 1°K, below which an unexpected result was observed: proximity-induced superconductivity. Biomolecular electronics has got tremendous impetus over the last few years. In fact, Mrauccio *et al.* have even demonstrated a field-effect transistor based on a DNA base, deoxyguanosine derivative.²⁴

Proteins also offer significant advantages over other biological polymers in the construction of derived electronic devices, especially because of their redox properties. In recent years, several groups have demonstrated the ability to attain high-contrast tunneling images of metalloproteins and enzymes under a variety of controllable conditions. Recently, Maruccio *et al.* have fabricated a protein field-effect transistor (Pro-FET) based on the blue copper protein azurin operating at room temperature and ambient pressure.

19.7 CONCLUSIONS

To summarise, we have reviewed current status of this new field, molecular electronics, which hold the proposal and promises of plentiful device concepts for superior electronics applications. Already many electrical device applications have been demonstrated, i.e., resistors, diodes, switches, capacitors, field-effect transistors, flash memories, single-electron transistors, amplifiers and negative differential resistance, involving a large class of molecular systems. Many of these applications have already been commercialised. However, difficulties in controlling the electrical tunneling resistance and room temperature measurement of negative differential resistance have prevented commercialisation of NDR devices as amplifiers. Electrical interconnect and dearth of reliable data and characterisation techniques are unfortunately preventing this field to challenge the silicon electronics. However, molecular electronics is a field that is rapidly advancing with almost everyday announcements of

new results, discoveries and breakthroughs. Interestingly, many new concepts and phenomena such as multistability and hysteresis, which arise out of structural changes in a molecule during current transport together with inelastic processes due to interactions at different energy and length scales in various systems are turning out to be futuristic potential molecular devices, which can perform multiple tasks in parallel. In fact, those practicing are constantly looking forward to such advancements in this field. Even by the time this book is printed, we would expect our knowledge to have greatly enhanced and our expectations as to where the field is moving towards would have undergone some shifts, compared to what we were at while writing this sentences.

19.8 SINGLE LEVEL PROGRAMME

This programme was written in Fortran 90. It can be converted to fortran 77 arc, if needed.

```
! Copyright (c)
! Jawaharlal Nehru Centre for Advanced Scientific Research,
! S.Lakshmi and Swapan K. Pati, 2008.
! The programme calculates charge density and current through a discreet energy level
! (say of a molecule) within the bias range -2 volts and +2 volts at room temperature.
! The input requirements are self energies or molecule-electrode coupling strengths
! (self1 and self2) of left and right electrodes, energy required for putting
! (removing) an electron into (from) the level (charging_energy), Fermi energy of
! the electrodes (efermi) and energy of the discreet level (ener0). Note that self-
! energy is of the eV order and efermi and ener0 should be close enough to observe
! the current.
! Tune in these parameters and see how charge-density and current behave with bias voltage change.
  program single_energy_level
    implicit none
    integer*4:: i
real(kind=8)::current,voltage,noofelecs,ener,efermi,distfunction1,distfunction2
real(kind=8)::self1,self2,eqlbm_nelecs,p1,pold,diff_p,ener0
real(kind=8)::chem_potential1,chem_potential2,charging_energy
real(kind=8),parameter::pi=3.142, kb=8.6174e-5, T=300.0
! Output Files
  open(unit=20, file="current")
  open(unit=15, file="charge_den")
  write(*,*)'self1,self2,charging_energy,efermi,ener0'
  read(*,*)self1,self2,charging_energy,efermi,ener0
  voltage=0.0
  if(T.ne.0)then
    distfunction1=1.0/(exp((ener0-efermi)/(kb*T))+1)
  endif
  if(T==0)then
    if(ener0<efermi)then
      distfunction1=1.0
    else
```

```

distfunction1=0.0
endif
endif
eqlbm_nelecs=2*distfunction1
print*,"Number of electrons at equilibrium",eqlbm_nelecs
!Bias Range
do voltage=-2.1d0,2.1d0,0.1d0
  p1=0.0
  chem_potential1=efermi-voltage/2.0
  chem_potential2=efermi+voltage/2.0
111 format (A10,F8.4)
112 format (A17,F8.4,A17,F8.4)
write(*,111)"Bias = ",voltage
write(*,112)"ChemPotLeft = ",chem_potential1, "ChemPotRight = ", chem_potential2
write(*,*)"
! SCF loop
100 ener=ener0+p1
  if (T.ne.0) then
    distfunction1=1.0/(exp((ener-chem_potential1)/(kb*T))+1.0)
    distfunction2=1.0/(exp((ener-chem_potential2)/(kb*T))+1.0)
  endif

  if (T==0) then
    if (ener+(voltage/2.0)<efermi) then
      distfunction1=1.0
    else
      distfunction1=0.0
    endif

    if (ener-(voltage/2.0)<efermi) then
      distfunction2=1.0
    else
      distfunction2=0.0
    endif
  endif

  noofelecs=2.0*((self1*distfunction1)+(self2*distfunction2))/(self1+self2)
  pold=p1
  p1=pold+0.02*(charging_energy*(noofelecs-eqlbm_nelecs)-pold)
  diff_p=abs(pold-p1)
  if (diff_p>10e-4) go to 100
  current=(self1*self2)*(distfunction2-distfunction1)/(self1+self2)
  write(15,*)voltage,noofelecs
  write(20,*)voltage,current
enddo
end program single_energy_level

```

REFERENCES

1. G. Binnig, H. Roher, C. Gerber and E. Weibel, 'Tunneling through a controllable vacuum gap', *Appl. Phys. Lett.*, 40, (1982), 178.
2. G. Binnig, H. Roher, C. Gerber and E. Weibel, 'Atomic Force Microscope', *Phys. Rev. Lett.*, 56, (1986), 930.
3. J. Moreland and J.W. Ekin, 'Electron tunneling experiments using Nb-Sn "break" junctions', *J. Appl. Phys.*, 58, (1985), 3888.
4. B. Mann and H. Kuhn, 'Tunneling through Fatty Acid Salt Monolayers', *J. Appl. Phys.*, 42, (1971), 4398.
5. A. Aviram and M.A. Ratner, 'Molecular Rectifiers', *Chem. Phys. Lett.*, 29, (1974), 277.
6. R.M. Metzger, B. Chen, U. Hopfner, D.V.M.V. Lashmikantham, T. Kawai, X.L. Wu, H. Tachibana, T.V. Hughes, H. Sakurai, J.W. Baldwin, C. Hosch, M.P. Cava, L. Brehmer and G.J. Ashwell, 'Unimolecular Electrical Rectification in Hexadecylquinolinium Tricyanoquinodimethanide', *J. Am. Chem. Soc.*, 119, (1997), 10455.
7. www.cnano-rhone-alpes.org/spip.php?article60.
8. S. Lakshmi, S. Dutta and S.K. Pati, 'Molecular Electronics: Effect of Electric Field', *J. Phys. Chem. C.*, 112, (2008), 14718.
9. R. Landauer, 'Spatial Variation of Currents and Fields Due to Localised Scatterers in Metallic Conduction', *IBM J. Res. Dev.* 1, (1957), 223.
10. M.A. Reed, C. Zhou, C.J. Muller, T.P. Burgin and J.M. Tour, 'Conductance of a Molecular Junction', *Science*, 278, (1997), 252.
11. J. Reichert, R. Ochs, D. Beckman, H.B. Weber, M. Mayor and H. Lohneysen, 'Driving Current through Single Organic Molecules', *Phys. Rev. Lett.*, 88, (2002), 176804.
12. L.A. Bumm, J.J. Arnold, M.T. Cygan, T.D. Dunbar, T.P. Burgin, L. Jones, D.L. Allara, J.M. Tour and P.S. Weiss, 'Are Single Molecular Wires Conducting?', *Science*, 271, (1996), 1705.
13. J.G. Kushmerick, D.B. Holt, J.C. Yang, J. Naciri, M.H. Moore and R. Shasidar, 'Metal-Molecule Contacts and Charge Transport across Monomolecular Layers: Measurement and Theory', *Phys. Rev. Lett.*, 89, (2002), 086802.
14. N.P. Guisinger, M.E. Greene, R. Basu, A.S. Baluch and M.C. Hersam, 'Room Temperature Negative Differential Resistance through Individual Organic Molecules on Silicon Surfaces', *Nano Lett.*, 4, (2004), 55.
15. C. Joachim, J.K. Gimzewski, R.R. Schlittler and C. Chavy, 'Electronic Transparency of a Single C₆₀ Molecule', *Phys. Rev. Lett.*, 74, (1995), 2102.
16. R. Saito, G. Dresselhaus and M. Dresselhaus, *Physical Properties of carbon Nanotubes*, Imperial College Press, London, (1998).
17. P.L. McEuen, 'Carbon-based Electronics', *Nature*, 393, (1998), 15.
18. A. Javey, J. Guo, Q. Wang, M. Lundstrom and H. Dai, 'Ballistic carbon nanotube field-effect transistors', *Nature*, 424, (2003), 654.
19. M. Bockrath, D.H. Cobden, J. Lu, A.G. Rinzler, R.E. Smalley, L. Balents and P.L. McEuen, 'Luttinger-liquid behaviour in carbon nanotubes', *Nature*, 397, (1999), 598.

20. M. Bockrath, D.H. Cobden, P.L. McEuen, N.G. Chopra, A. Zettl, A. Thess and R.E. Smalley, 'Single-Electron Transport in Ropes of Carbon Nanotubes', *Science*, 275, (1997), 1922.
21. J. Nygard, D.H. Cobden, and P.E. Lindelof, 'Kondo physics in carbon nanotubes', *Nature*, 408, (2000), 342.
22. S.J. Tans, A.R.M. Verschueren and C. Dekker, 'Room-temperature transistor based on a single carbon nanotube', *Nature*, 393, (1998), 49.
23. H.W. Fink and C. Schonberger, 'Electrical conduction through DNA molecules', *Nature*, 398, (1999), 407.
24. G. Maruccio, P. Visconti, V. Arima, S. D'Amico, A. Biasco, E. D'Amone, R. Cingolani and R. Rinaldi, 'Integrated Semiconductor Nanocrystal and Epitaxial Nanostructure Systems: Structural and Optical Behaviour', *Nano Lett.*, 3, (2003), 479.
25. C. Dekker, 'Carbon Nanotubes as Molecular Wires', *Phys. Today*, 52, (1999), 22.
26. F. Zahid, M. Paulsson and S. Datta, *Advanced Semiconductors and Organic Nano-Techniques*, H. Morkoc, Acamedic Press, New York, (2003).
27. J.R. Heath and M.A. Ratner, 'Molecular Electronics', *Physics Today*, 43, (May 2003).
28. R.A. Bisell, E. Cordova, A.E. Kaifer and J.F. Stoddart, 'A chemically and electrochemically switchable molecular shuttle', *Nature*, 369, (1994), 133.
29. J. Park, A.N. Pasupathy, J.I. Goldsmith, C. Chang, Y. Yaish, J.R. Petta, M. Rinkoski, J.P. Sethna, H.D. Abruna, P.L. McEuen and D.C. Ralph, 'Coulomb blockade and the Kondo effect in single-atom transistors', *Nature*, 417, (2002), 722.
30. S. Lakshmi, PhD Thesis, 'Theoretical Modeling of electron transport through Molecular bridges', JNCASR, Bangalore.

ADDITIONAL READING

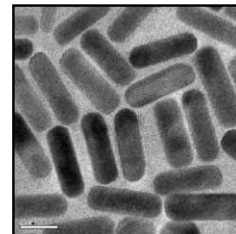
1. M.A. Ratner and D. Ratner, *Nanotechnology: A Gentle Introduction to the Next Big Idea*, Prentice Hall PTR, (2002).
2. Supriyo Datta, *Quantum Transport: Atom to Transistor*, Cambridge University Press, (2005).
3. E.L. Wolf, *Quantum Nanoelectronics: An Introduction to Electronic Nanotechnology and Quantum Computing*, Wiley-VCH, (2009).

REVIEW QUESTIONS

1. What is Molecular Electronics?
2. What is Coulomb Blockade behaviour? Does it obey Ohm's Law?
3. What are the differences between Quantum dots and Molecules?
4. What is the working principle of AFM? How is it different from STM?
5. What is ballistic transport? How is it different from diffusive transport?
6. Is there a difference between "charge transfer" and "charge tunneling"?
7. What is negative differential resistance? Why is it so important in Molecular Electronics?

8. What is Spintronics? Electrons have both charge and spin. Can we separate them?
9. Can you propose a molecule which acts as a diode? Give reasons to support your answer.
10. Can DNA conduct electricity? Does the conduction depend on base pairs sequence?

NANOLITHOGRAPHY



“I saw the angel in the marble and carved until I set him free.”

Michelangelo

Bull, George Anthony.

Michelangelo: A Biography. New York: Viking, 1995

Writing at the nanoscale is nanolithography. This branch has become one of the most important areas of research as nanometer scale structures are the cornerstone of modern devices. This chapter is an illustration of the variety of techniques used for this application. Nanoscale patterns are made with atoms, molecules and even nanomaterials. The kind of patterns derived and the modern research frontiers in this area are briefly outlined.

Learning Objectives

- What is nanolithography?
 - What are the diverse tools in this branch?
 - What are clean room facilities?
 - How do we create patterns in conventional lithography?
 - How is scanning probe microscopy used in lithography?
-
-

20.1 NANOLITHOGRAPHY

Nanolithography is the lithography at the nanoscale. Although the basic ideas of lithography are old, the fabrication of structures on the nanometer-length scale has made nanolithography an exciting new field of research during the last one decade or so. The study of quantum phenomena in confined structures demands patterning periodic arrays, gratings or address systems at the nanoscale made of desired materials. This has resulted in a new class of electronic devices with interesting functionalities. Such applications demand the availability of highly sophisticated techniques capable of fabricating reproducible structures and devices in the nanometer regime. Nanolithography, thus, has far-reaching implications in the fabrication and integration of nanodevices, which explains the importance given to it.

Nanolithography has been applied extensively to pattern new materials or to create new and complex structures using known materials and studying the various properties, either individual or collective. Repetitive structures, such as line grating or arrays of dots or nanopillars, have been patterned; while varying structural parameters such as the feature size and inter-feature distance. The properties of patterned materials, especially electronic, magnetic and optical, have been studied extensively.¹ Patterned materials have also been used as templates for the catalytic growth of other nanostructures such as carbon nanotubes and nanowires.²

Another field of nanoscience where lithography is on high demand, is the fabrication of nanocircuitry. Here, the materials are to be patterned across specified nanoelectrodes and studied for their characteristics. There are a few important issues that come into play, namely,

1. laying nanoelectrodes;
2. placing an active element like a nanotube or a quantum dot at the desired location either by nanomanipulation or by selective masking;
3. soldering to improve the nanoelement-nanoelectrode coupling and finally; and
4. feeding and deriving electrical or optical signals from the nanocircuit.

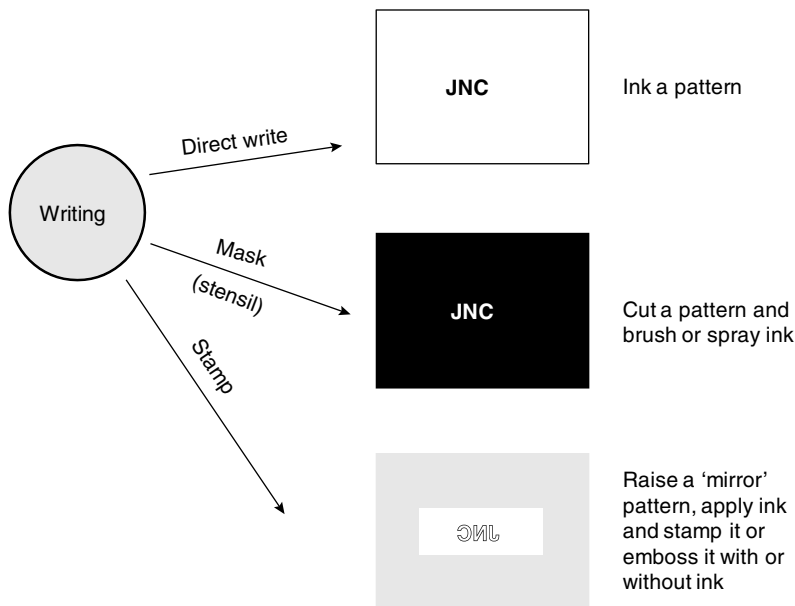
Indeed, each of these issues has developed into matured fields of research and technology.

Both repetitive and non-repetitive nanopatternings borrow several ideas from conventional microlithography. The lithography beam is essentially a photon or charged particle (electron or ion) beam. In order to achieve the desired resolution, light of smaller wavelength is used—extreme UV and even soft X-ray photons. A new set of techniques unique to nanolithography have emerged in the recent years. These techniques essentially make use of the scanning probe microscopy set-ups. Stamping methods have also been downsized to reach nanoscale dimensions.

20.2 LITHOGRAPHY: CONCEPTS AND DEFINITION

In Greek, litho means 'stone' and gráphein means to 'write'. It is virtually creating impressions on any surface. Although, caveman knew writing on the wall, it was Aloys Senefelder in 1796, who invented a repetitive process of reproducing a drawing on Bavarian limestone, then transferring onto paper. Lithography is a generic term for a process, in which something is printed on a surface that is receptive to 'ink' in some regions and repels 'ink' in other regions. In present-day usage of the term, lithography refers to creating repetitive or non-repetitive patterns of a material on a given substrate with a wide choice for both, the patterns being anywhere between submicron to nanometric in dimension. The processes involved are not very different from creating ink impressions on paper (Fig. 20.1). Writing can be done in three different ways, the easiest of all, is direct writing method, where patterns are created on the surface directly using the ink. The surface, on which the patterns are created, is known as substrate and the ink can be referred to as resist. In another method, the impression of a pattern is first cut-out on a surface, generally known as mask or stencil, which is then used to transfer the pattern onto a substrate using a brush carrying the ink or sprayed on the substrate with the mask. The advantages of using this method is firstly, the stencil or mask, which is cut-out can be used several times to create the

same pattern, and secondly, the excess of resist/ink used is removed by lift-off of stencil after the inking process. Yet another way shown in the Fig. 20.1 is to create an impression is to raise a 'mirror pattern' as a mould or stamp, which is inked and stamped to create the impression.



Lithography materials: 'ink', 'paper', 'pen', 'brush', 'mask' and 'stamp'

Fig. 20.1 Different ways of creating ink impressions on paper.

20.3 CONVENTIONAL LITHOGRAPHY

Microlithography, where the feature size is of the order of microns, is considered conventional, but much of the ingredients and terminology remain similar for nanolithography. Typically, in microlithography based on light, a substrate is coated with a light sensitive resin (resist), which, upon exposure to light, transforms in such regions to another form with different properties so that such regions can be selectively retained or washed away. The active (desired) material such as a metal, is brought in during the second stage to finally create metal patterns on the substrate.

20.3.1 Preparing the Substrate

The substrates (also called wafers) used for lithography should be free from contamination. There are several methods to clean the substrate. The most commonly used method is ultrasonication, which physically removes particulate matter from the substrate. The medium can be organic solvents like acetone or alcohols or simply distilled water. Wet methods include RCA1 and RCA2 cleaning.

The RCA1 cleaning is done to remove the organic dirt while RCA2 is performed to remove metal impurities. The composition of RCA1 and RCA2 reaction mixtures are $\text{NH}_3:\text{H}_2\text{O}_2:\text{H}_2\text{O}::1:1:5$ and $\text{HCl}:\text{H}_2\text{O}_2:\text{H}_2\text{O}::1:1:6$, respectively (Caution: this mixture reacts violently with organic matter). The cleaning in each case is done by heating the reaction mixture at 80°C for 10 min. The distilled water rinse is followed after every chemical treatment. After the cleaning, the substrate is dried under argon or nitrogen gas. Other methods employed for cleaning the substrates are heating the substrates at high temperatures in vacuum or in oxygen or to use plasma etching techniques. The commonly used substrates are Si substrates or Si substrates with thermally grown oxide as a dielectric layer (for electronic applications), quartz, glass, etc. For growing the oxide, the cleaned substrate is subjected to a high temperature ($> 850^\circ\text{C}$) in the presence of oxygen flow. Depending on the required thickness of the oxide, the temperature and duration of oxidation is controlled.³

Once the cleaning process is completed and the substrate is spin-coated with the resist to produce a thin uniform layer. This is a crucial step for effective pattern transfer. The thickness of the resist is varied depending on its application. The volume of resist taken, its viscosity and the spinning rate are crucial for uniform resist film. In some cases, a monolayer of adhesion promoter, hexamethyldisilazane vapours (HDMS) is employed to make the surface hydrophobic. Sometimes, dry film resists, a photosensitive resin in a multilayer configuration with a carrier film and cover films are used in photolithography to form precision patterns.

20.3.2 Positive and Negative Resists

The main component to perform lithography is the resist, which undergoes the chemical changes on exposure of light or electron beam. The polymers that on exposure to light undergo chemical transformations are known as photoresists. Polymers undergo chain scission or cross-linking on exposure of light resulting in an effective decrease or increase, respectively in their molecular weight (Fig. 20.2). After exposure to light, these polymers show selective dissolution in some solvents known as developers. Based on this property, photoresists can be classified into two types, positive and negative photoresists. In the case of a positive resist, the region exposed to light solubilises in the developer (due to chain scission and decrease in the molecular weight) and the unexposed regions remains insoluble. In other words, the exposed resist leaves windows of the bare underlying material; hence, “whatever shows, goes”. Negative resists behave in just the opposite manner. For a negative resist, the regions exposed to light become relatively insoluble in the developer compared to the unexposed regions (Fig. 20.2).

Originally, the resists were mostly of the negative type, but since 1970s, the positive resists have also come into play. A well-known example of a positive photoresist is polymethylmethacrylate (PMMA). It undergoes chain scission under UV illumination. Sometimes, to increase the sensitivity of the resist, a sensitizer is added. Phenolic Novolak–Diazonaphthoquinine is an example of such resist, where diazoquinone ester is the photoactive species and phenolic novolak is the resin. Examples for negative photoresists are Kodak KTFR, which is an azide-sensitised polyisoprene rubber. Similarly, for electron beam lithography, polymers, which undergo chemical change on exposure to electron

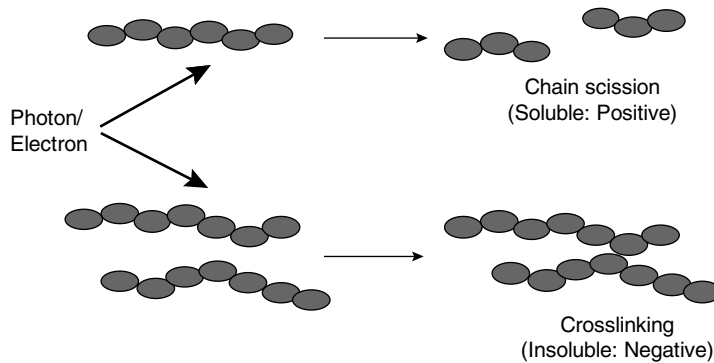


Fig. 20.2 Schematic of the chemical changes undergone by positive and negative resist on exposure to photon/electron source.

beam are used. The best example for a positive e-resist is PMMA and for negative tone, examples are polystyrene and calixarene. There are other commercially available resists for both photolithography and electron beam lithography, such as Shipley, DUV, SU and ZEP series. After spin-coating a resist, the excess of solvent is removed by prebaking or soft baking. This step is performed in order to achieve the maximum adhesion of the resist to the substrate. Over-baking should be avoided as the resist film can decompose or it can degrade the photosensitivity of the resist either by reducing the developer solubility or actually destroying a portion of the sensitizer. Under-baking will prevent the light from reaching the sensitizer.

A “mask” is defined as a tool that contains patterns, which can be transferred to a resist coated substrate or to another mask in a single exposure. A reticle is defined as a tool that contains a pattern image that needs to be stepped and repeated in order to expose the entire wafer or mask. The mask used for a positive resist contains an exact copy of the pattern, which is to remain on the substrate, whereas the mask used for negative photoresist contains the inverse (or photographic “negative”) of the pattern to be transferred. Figure 20.3 shows the difference in the patterns generated from the use of positive and negative resist using a same mask.

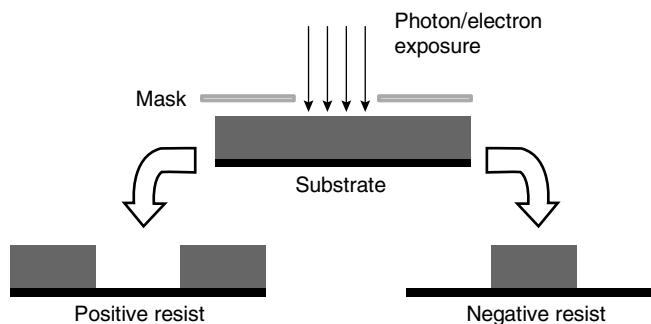


Fig. 20.3 Patterns generated on positive and negative resist using a mask.

Exposure or dosage is a process to bring about the chemical changes in the resist using the light or e-beam. The dosage is very crucial as it decides the quality of patterns on the resist material. Under-exposure may result in incomplete pattern transfer, whereas over-exposure may cause undue broadening of the pattern. In case of photolithography, dosage is defined as the energy (in mJ) dosed per unit area (in cm^2), whereas in the case of electron beam, lithography dosage is defined as charge (in μC) dosed per unit area (in cm^2). The exposure can be done in two ways: using a focused scanning beam or using a broad beam to project an entire pattern. The major advantage of the second method is a higher pattern writing speed, compared to serial writing of the focused beam, where only small areas of pattern can be written at a time. Photolithography is more popular, because it is mainly a projection based lithography, and therefore, large areas can be patterned in a very short span of time, whereas the non-optical based techniques which use charged particles like electrons, are mostly focused scanning based, making the patterning process slow.

20.3.3 Developing

After the exposure, the substrate is developed in a developing solution. Development is carried out by immersion developing, spray developing or puddle developing. For example, in the case of PMMA, a mixture of methylisobutyl ketone: isopropyl alcohol (MIBK: IPA) in the ratio 1:3 has been found to be the best developing solution. At low-exposure energies, the negative resist remains completely soluble in the developer solution. As the exposure is increased above the threshold energy, more of the resist film remains after development. At exposures two or three times the threshold energy, very little of the resist film is dissolved. For positive resists, the resist solubility in its developer is finite even at zero-exposure energy. The solubility gradually increases until, at some threshold, it becomes completely soluble. Developing time varies from a few seconds to minutes. Higher the developing time, one has a better control for high definition patterns. Regardless of the method used, it should always be followed by thorough rinsing and drying to ensure that the developing action will not continue after the developer has been removed from the wafer surface. In order to remove the excess solvent and to harden the photoresist and improve adhesion of the photoresist, post baking/hard-baking is necessary. There are also physical methods such as reactive ion etching and plasma etching to develop the pattern. In these cases, the polymer does not come in contact with the solvents. This is particularly advantageous in the case of negative photoresists as the swelling of the polymer is avoided.

20.3.4 Resolution, Sensitivity and Contrast

The resolution of a resist is defined as the smallest line-width to be consistently patterned. For positive resist, it is related to rate of chain scission and the rate of solubility with the molecular weight. Lower the molecular weight of the polymeric resist, higher the resolution. A disadvantage of negative resists is the fact that their exposed portions swell as their unexposed areas are dissolved by the developer. This swelling, which is simply volume increase due to the penetration of the developer solution into the resist material, results in distortions in the pattern features. This swelling phenomenon can limit the resolution of a negative resist. The unexposed regions of positive resists do not exhibit swelling and

distortions to the same extent as the exposed regions of negative resists. This allows positive resists to attain better image resolution. Lithography sensitivity is defined as the critical dosage required for removal (positive) or retention (negative) of half the thickness of the resist film. Resist sensitivity increases with increasing molecular weight. If the molecules are larger, then fewer cross-links are required per unit volume for insolubility. The sensitivity of a resist can be obtained from its response curve—a plot of normalised film thickness versus $\log D$ (dose). To construct such a curve, a series of varying dosages is given to a resist layer and developed. The thickness of the resist in the exposed region is measured and this value is normalised with the initial thickness and plotted against the cumulative or the total dosage. Sensitivity is then read out as the dosage at half the normalised thickness. The other important parameter is the resist contrast, γ .⁴ The polymer molecules in the unexposed resist will have a distribution of length or molecular weights and thus a distribution of sensitivities to radiation. The narrower the distribution, the higher will be the contrast, γ . Contrast is determined by the slope of the curve (Fig. 20.4). It is a sigmoid response function obtained for different dosage. Contrast is calculated for positive and negative resists as

$$\gamma_p = (\log(d_c/d_0))^{-1} \quad (1)$$

$$\gamma_n = (\log(d_0/d_c))^{-1} \quad (2)$$

where d_0 is extrapolated dose at the kink of the contrast curve, d_c is the dose to clear all of the positive resist. In the case of a negative resist, d_l is the minimum dose required for the retention of the resist. Contrast decides the resolution. Typical contrast values fall in the range of 2 to 5 for novolak based positive resists, and 5 to 10 for DUV resists.

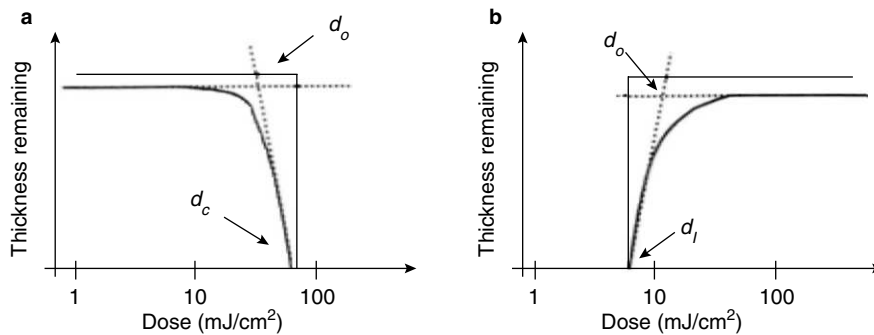


Fig. 20.4 Sensitivity plot for (a) positive and (b) negative resist. The slope of curve gives the contrast parameter of the resist (reproduced from ref. 5).

20.3.5 Clean Room

Although the concept of clean room is more than 100 years old and is rooted in control of infections in hospitals, a clean environment for industrial manufacturing is only a recent requirement. In semiconductor fabrication industry, clean room processing is rigorous practice else, the dust particles, for example, can cause electrical breakdown of IC components. Coming to Nanotechnology, where

fabrication is done using various nanolithographic techniques, it is necessary to avoid the dust and other contaminations as they can interfere with the fabrication. In such cases, a very high standard of cleanliness is required. Hence a clean room is a room that has a ‘low’ level of environmental pollutants such as dust, other contaminant particles and chemical vapours. More accurately, a clean room has a controlled level of permissible contamination that is specified by the number of particles in the ambient per cubic meter at a specified particle size. According to the definition provided by the International Organisation of Standardization (ISO) standard 14644-1,

“A room in which the concentration of air-borne particles is controlled, and which is constructed and used in a manner to minimise the introduction, generation, and retention of particles inside the room and in which other relevant parameters, e.g., temperature, humidity, and pressure, are controlled as necessary.”

Clean rooms are classified according to the number and size of particles permitted per volume of air. ISO standard cleanliness N with particle concentration C_n (particles/m³) is calculated as

$$C_n = 10^N \times (0.1 \mu\text{m}/D)^{2.08} \quad (3)$$

where D is particle size in micrometers.

Large numbers like “class 100” or “class 1000” refer to the number of particles of size 0.5 μm or larger permitted per cubic foot of air. Clean rooms are rated as “class 10,000,” where there exists no more than 10,000 particles larger than 0.5 microns in any given cubic foot of air; “class 1000,” where there exist no more than 1000 particles; and “class 100,” where there exist no more than 100 particles. The standard also allows interpolation, so it is possible to describe, e.g., “class 2000”⁶. For example, the computer hard disk drive fabrication requires a class 100 clean room. A clean room used for photolithography is shown in Fig. 20.5.



Fig. 20.5 A clean room for lithography usually hosts a self-contained infrastructure. Commonly seen facilities are spin-coater, mask aligner, photolithography stage, lamellar chemical hood, physical vapor deposition unit, microscopes, etc. (reproduced from ref. 7). (For clarity see colour figure.)

20.3.6 A typical Lithography Recipe

Consider a set of useful patterns on a plane solid substrate. There are alternative recipes depending on the type of resist, mask and the order of metal deposition, prior or after resist coating. A typical procedure to obtain the desired pattern using a positive resist is explained here in Fig. 20.6. The positive resist is spin coated on the substrate and prebaked. The light is exposed on the resist either using a mask or a fine beam is moved around to write the pattern. The resist after light exposure is developed using the developing solution, e.g., for PMMA, the developer is MIBK:IPA solution taken in 1:3 ratio. The features patterned on the resist are transferred to the substrate by lift-off. In a lift-off process, the desired metal is deposited on the patterned resist either by physical vapour deposition or by e-beam evaporation. Now, the resist is stripped off completely. The metal that is deposited directly on top of the substrate, where there is no resist, will stay, but the metal that is deposited on top of the resist will be lifted off along with the resist. The desired metal patterns are thus obtained on the substrate (see Fig. 20.6). Further, the metal pattern can be used as etching mask for the substrate, if one plans to etch away some thickness of the substrate. Another method to get the metal patterns using a positive resist is direct etching method. In this method, the metal is first deposited on the substrate and the pattern development on the resist is followed as described above. After developing the resist, the metal, which is not protected by the resist, is etched away, e.g., for Au metal etching, cyanide solution is used. Alternatively, plasma etching can be done to remove the unprotected metal. After metal etching, the rest of the resist is washed away to get the metal patterns.

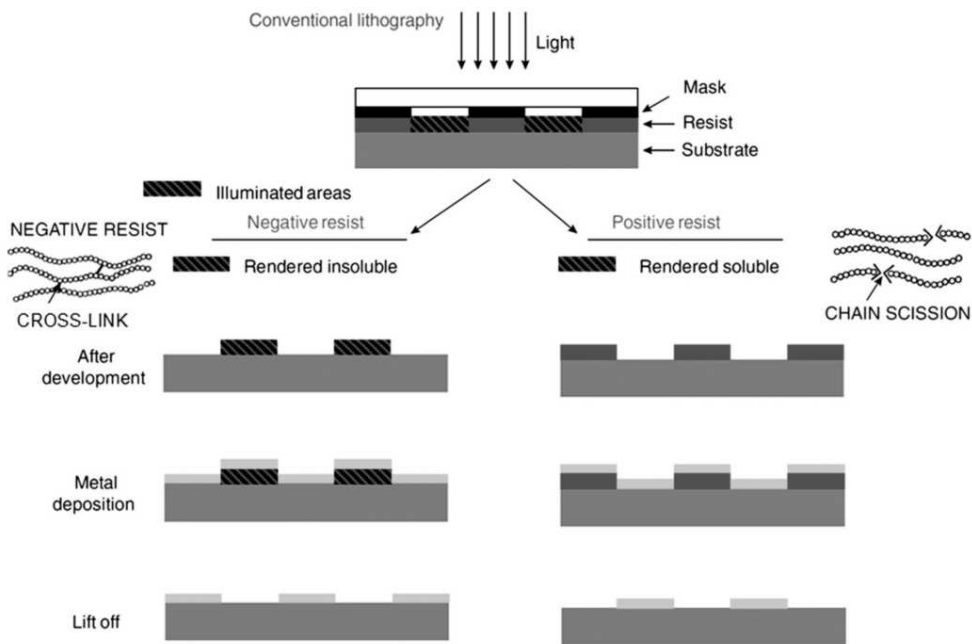


Fig. 20.6 A typical photolithographic procedure adopted to get metal patterns by lift off process. (For clarity see colour figure.)

20.4 LITHOGRAPHY TECHNIQUES

The different lithography techniques are briefly described in the following sections.

20.4.1 Photolithography

The resolution limit in conventional projection optical lithography is largely determined by the well-known Rayleigh's equation. The resolution, R and the corresponding depth of focus (DOF) are given by the following⁹,

$$R = k_1\lambda/NA, \text{ and} \quad (10)$$

$$\text{DOF} = k_2\lambda/NA^2; \quad (11)$$

where λ is the exposure wavelength, NA is the numerical aperture of the optical system, and k_1 and k_2 are constants that depend on the specific resist material, process technology, and image formation technique used. High resolution photolithography, therefore relies, photon beam wavelengths shorter than visible range, deep in UV such as from excimer lasers (248 nm and 193 nm) (Fig. 20.7). At such short wavelengths, absorption loss from the optical components and air is considerable and may call for preventive measures using suitable instrumentation involving vacuum. There are many variations of photolithography aimed at circumventing the diffraction limit.

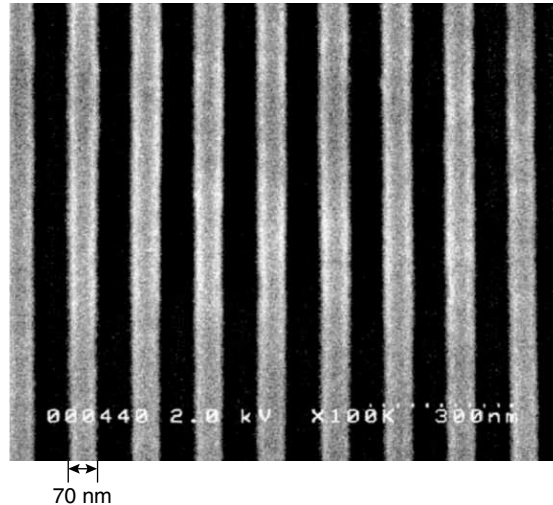


Fig. 20.7 Patterns generated on PMMA by EUV microlithography system (reproduced from ref. 10).

The simplest photolithography technique is contact lithography, wherein the mask and the resist-coated substrate are brought intimate contact and exposed. The resolution purely depends on the mask dimension and diffraction at mask edges. Proximity lithography is a modification of contact lithography, where there is a small gap of 3–50 μm between the mask and the resist-coated substrate. The photon source gets diffracted by the mask patterns and produces the final pattern. In another type

projection lithography, the optical system provides an image of the mask on the resist-coated substrate, with reduction projection, features of $1\ \mu\text{m}$ can be brought down to $0.2\ \mu\text{m}$ easily.

A method of phase shift lithography includes forming a chromeless phase reticle with a pattern of parallel, spaced phase shifters. The phase shift reticle is placed between an exposure source (e.g., UV light) and a substrate having a layer resist formed thereon. Following an initial exposure, the phase shift reticle is rotated and the substrate is exposed a second time. The resist is then developed to form features in areas of resist that have not been exposed. These areas correspond to the projected points of intersection of the phase shifters. Using a positive tone resist, solid resist features are formed. These solid features can be used as mask blocks for etching the substrate to form field emitter sites for a field emission display. Using a negative tone resist, open areas are formed in the resist and can be used to deposit a material on the substrate, such as a contacts for a semiconductor structure. The method of the invention can also be implemented using two different reticles with intersecting patterns or using a single reticle having intersecting phase shift areas.

The stencil method is based on selective deposition of material through shadow masks (micro- and nanostencils). The main added value of this technique is that it does not rely on photoresist processes. Although photolithography is still the main method used for creating micro- and nanostructures in thin films, it requires several process steps, for example, application of photoresist, exposure, development, evaporation of a thin film, and lift off. The stencil method can create a structured thin film in one process step. The deposited structures can either be used directly, transferred into a sub-layer, combined by lift-off processes, or refined by self-assembly or other growth processes. The stencil method typically uses solid-state membranes with structures in the nanometer range ($<100\ \text{nm}$) in combination with micrometer features ($>10\ \mu\text{m}$). These patterns can be transferred to a substrate in a single process step, potentially in a non-contact mode. These specifics make the stencil method applicable to surfaces that are either mechanically unstable, such as cantilevers and membranes, and/or functionalized for, e.g., bio-sensor applications.

Collimated X-rays are also used as source and this process is known as X-ray lithography (XRL). Being much shorter in wavelength ($\sim 1\ \text{nm}$), X-rays provide increased lateral resolution and in addition, a higher depth of focus. Scattering is also relatively less in case of X-rays. The most commonly known X-ray resist is PMMA, which is a positive resist and is being extensively used whereas negative resists, such as polyglycidylmethacrylate (PGMA), have also been developed. The mask used for XRL basically consists of a pattern of X-ray absorbing materials, such as Au (high atomic number material) on a substrate relatively transparent to X-rays such as Ti, Si, SiC, Si_3N_4 , BN and B (low atomic number materials).¹¹ For resist removal and etching, usually physical methods are employed (Fig. 20.8).

20.4.2 Charged Particles-based Techniques

Apart from using light sources for lithography, charged particle beams of electrons, protons or ions are extensively used for patterning the polymeric films. These are preferred over the light-based techniques because the de Broglie wavelengths of these particles are sufficiently short ($<0.1\ \text{nm}$) that they minimise the effects of diffraction that currently limit many photolithographic approaches. In addition, they allow high depth and fine focus. These techniques are generally performed in high

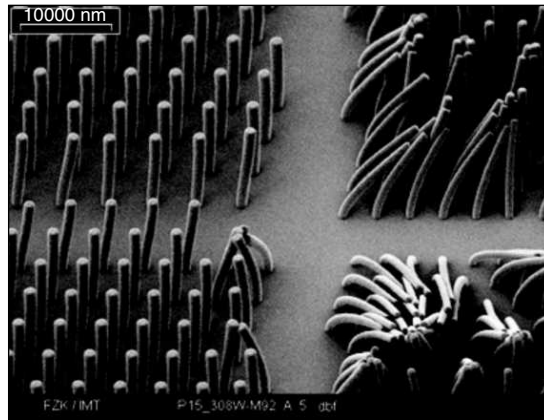


Fig. 20.8 Patterns generated by X-ray lithography on a 10 μm SU-8 film, fields of columns with different diameter and pitch. Patterns themselves indicate for the limit of stability (reproduced from ref. 11).

vacuum conditions unlike photolithography. The exposure dose has units of charge deposited by the beam per unit area ($\mu\text{C} \cdot \text{m}^{-2}$). Electron beam lithography (EBL), in which a beam of electrons is used as the exposure source, has extremely high-resolution capabilities combined with a large depth of focus. The patterning can be done in serial or parallel method depending on the type of patterns to be generated. Field emission sources are preferred over thermionic guns, because of high achievable beam currents and focus. The beam current is in the range of pico to nanoamperes. The shorter wavelength possessed by the 2–50 kV electrons are not limited by diffraction unlike photolithography. While using a finely-focused electron beam makes it possible to delineate extraordinarily fine patterns down to 10 nm, EBL does suffer from proximity effect due to secondary electrons.¹² Besides, writing of chip-scale patterns with a single e-beam is rather a slow process. According to the pattern complexity, the exposure time for writing also becomes very long, hence low throughput. Therefore, EBL remained as a high-end technique and was primarily employed to make high resolution masks and reticular structures. However, with the advent of high current sources and faster electronics for the last two decades, EBL is now being applied for raised patterns of metals, semiconductors and polymers in fine-scale devices. EBL is also used in the small-scale production of the specialised very high frequency devices (Fig. 20.9).

PMMA was one of the first resists developed for EBL in 1968 and is the highest resolution resists commonly available. PMMA is a chain-scission type resist, which allows for high resolution because of its high contrast. Another popular positive resist is ZEP. Negative resists such as hydrogen silsesquioxane (HSQ), work by cross-linking and in general the patterns they produce in EBL are not as good as those produced with positive resists. The patterns suffer due to swelling during development and bridging between features. The sensitivity of a e-resist is dependent on the beam current and the e-beam voltage. Sol gel precursors are also cast into the patterns generated by EBL (Fig. 20.10). As a rule of thumb, the sensitivity scales proportionally with the acceleration voltage. For example, ZEP

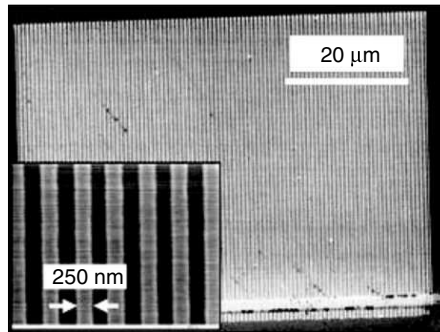


Fig. 20.9 SEM image of the stripe-electrode structure fabricated by e-beam lithography, with a detail (reproduced from ref. 13).

has its sensitivity of $200 \mu\text{C}\cdot\text{cm}^{-2}$ at an acceleration voltage of 100 kV. This dose will be reduced to around $60 \mu\text{C}\cdot\text{cm}^{-2}$ at 30 kV! PMMA can be patterned using electron dosage of $10 \mu\text{C}\cdot\text{cm}^{-2}$ at 30 kV. If the dosage is increased, it behaves like a negative resist, however, the resolution will be degraded to about 50 nm. Generally for most resists, the e-dosage varies from few $\mu\text{C}\cdot\text{cm}^{-2}$ to $\text{C}\cdot\text{cm}^{-2}$. The dosage is calculated based on the dose given per pixel.

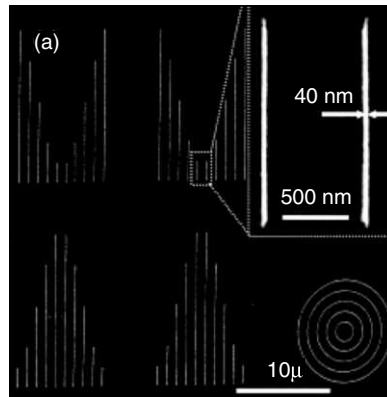


Fig. 20.10 Backscattered electron image of ZnO patterns starting with sol-gel precursor on SiO_x substrates annealed in air at 700°C for 20 min (reproduced from ref. 14).

$$\text{Area dose} = (\text{beam current} \times \text{exposure time} \times \text{number of passes}) / \text{area per pixel} \quad (12)$$

$$\text{Line dose} = (\text{beam current} \times \text{exposure time} \times \text{number of passes}) / \text{length of the pixel} \quad (13)$$

By analogy to EBL, focused-ion beam lithography (FIB)^{15,16} scans an ion beam across a surface to form a pattern. Application of a very high electric field onto a liquid metal source, such as Ga, generates ions (Ga^+), which are focused by electrostatic lenses. The development of liquid metal ion source (LMIS) is crucial for the development of FIB. The ion beam may be used for directly sputtering the

surface, or to induce chemical reactions in the resist layer. Re-deposition of the sputtered material is a common occurrence, which affects the final surface profile. In the case of resist exposure, even though the beam spot size is smaller, secondary electrons limit the achievable resolution to about 30 nm. FIB is commonly used for repair of photomasks, such as Au on Si. PMMA is the commonly used resist for patterning. Other ions used are H^+ , He^+ and Ar^+ ions. Of late, H^+ based ion beams are increasingly used in lithographic techniques, known as proton beam lithography. Neutral metastable atoms can also be used for particle-based lithography. Neutral atoms are attractive partly, because they do not electrostatically interact with one another. Their neutrality requires, however, development of new types of optics based on light forces. Initial results are encouraging: features as small as ~ 50 nm have been fabricated in a single step over large areas with stencil masks and ~ 70 nm features have been produced using directed deposition with light force lenses. 3-D nanostructuring is also done using FIB (Fig. 20.11).

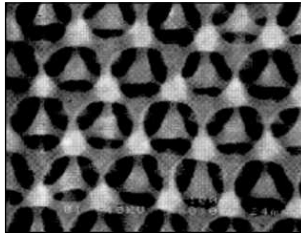


Fig. 20.11 3-D inverse cylinder structure created using FIB (reproduced from ref. 17).

20.4.3 Scanning Probe Lithography Techniques

Scanning probe lithography (SPL)¹⁸ encompasses techniques that use sharp (< 50 nm) tips scanned near the surface of a sample in the configuration of scanning tunneling microscopes (STMs) and atomic force microscopes (AFMs) or many variations. Although scanning probes were originally designed to provide high-resolution images of surfaces, their lithographic capability was demonstrated in a set of experiments with an STM, just five years after the first STM images were recorded. A large electrical bias applied between a tungsten tip and a Ge surface caused transfer of a single atom from the tip to the surface.¹⁹ Since then, STMs and AFMs are being employed in many different ways to perform sophisticated lithography. Of the two, AFM is more popular due to variations possible.

Advantages of SPL methods include resolution that approaches the atomic level, the ability to generate features with nearly arbitrary geometries, and the capability to pattern over surface topography that deviates significantly from planarity. However, these methods are serial and have writing speeds that are typically limited by the mechanical resonances of the tips and the piezoelectric elements that maintain constant separation between the tips and the sample. This problem is partially overcome in AFM by hosting parallel cantilever tips to perform repetitive patterning.

There are many variations of AFM-based lithography techniques. A biased AFM tip under the influence of water from the ambient can locally oxidise the substrate (usually Si), which is termed as

local anodic oxidation (LAO)²⁰ (Fig. 20.12). A slight variation of this technique is the electrostatic nanolithography, which refers trench formation when conducting tip ploughs patterns out of polymer films coated on substrates.²² Thus, formed trenches may be filled with molecules and nanoparticles. There are combinations of these techniques as well. Dip-pen lithography (DPN)^{23, 24}, a AFM-based technique has become a powerful tool for patterning nanostructures. In DPN, a material (ink) coated on the tip of the SPM cantilever is transferred to the substrate during slow scanning, facilitated by diffusion through a water meniscus. Hence, it is a direct-write method and the variety of materials that can be patterned is boundless. Furthermore, the simplicity of the technique and the higher resolutions achieved render it a more attractive one. Initial success with patterning of alkanethiol molecules was followed by other self-assembling molecules on substrates, such as silicon, mica, glass and gold films. The molecular patterns can act as resists for the patterning of underlying films or can be modified further to attach nanoparticles or metal ions. Since DPN is based on the spatial confinement of materials, the pattern resolution chiefly depends on the tip diameter; however, humidity, temperature, nature of the ink, scan rate, etc., also affect the ultimate dimensions of the pattern. In the literature, DPN has been used to pattern colloids, fluorescent molecules, biomolecules like oligonucleotides, proteins and collagen, conducting polymers, and precursors for solid structures. The magnetic nature and chemical

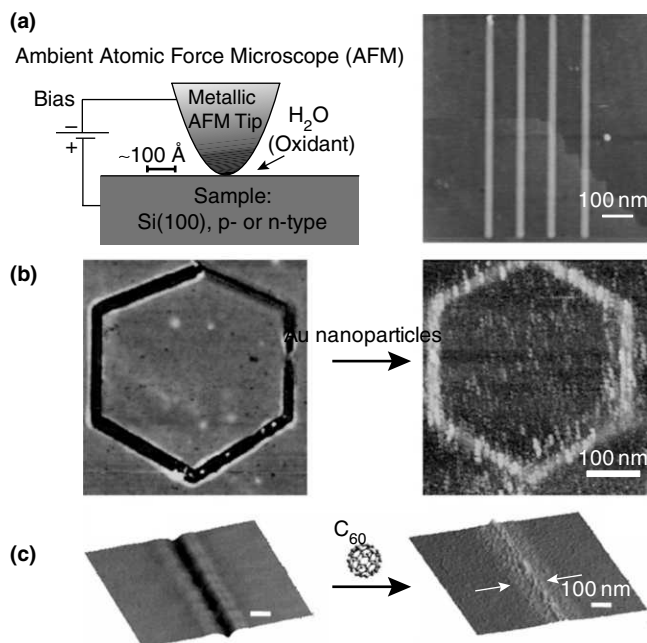


Fig. 20.12 (a) Local anodic oxidation (LAO) patterning using a conducting AFM setup. Electrostatic nanolithography to cut nanotrenches in a polymer film to selectively fill in (b) Au nanoparticles and (c) fullerene molecules. The arrows on the right image in (c) point to chemical adsorption of fullerene on extended regions of the trench (reproduced from refs. 21 and 22). (For clarity see colour figure.)

identity of nanopatterns have also been probed. Patterning of Ni catalyst for the selective growth of GaN nanotubes has also been demonstrated. Large-scale patterning is also feasible by employing parallel pen plotters and inkwells. Recently, nanofountain pen technology has been utilised to dispense liquid materials directly on to the substrate (Fig. 20.13).

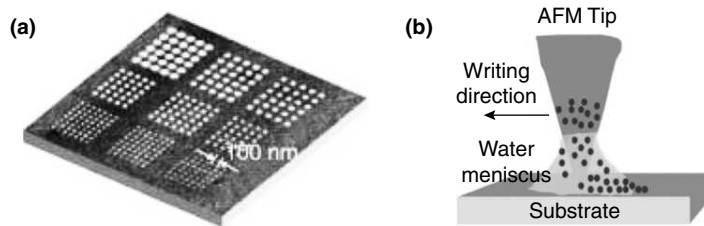


Fig. 20.13 (a) Nanoscale dot arrays written on a polycrystalline Au surface with mercaptohexadecanoic acid and (b) A schematic of the DPN technique (reproduced from ref. 25).

20.4.4 Soft Lithography

This is an extension of stamping method to micro and nanolithography. Soft lithography^{26,27} (see Fig. 20.14) is the collective name for a set of lithographic techniques: replicamolding (REM), microcontact printing (μ CP), micromolding in capillaries (MIMIC), microtransfer molding (μ TM), solvent-assisted micromolding (SAMIM), and near-field conformal photolithography using an elastomeric phase-shifting mask. These techniques use a patterned elastomer (usually PDMS) as the mold, stamp, or mask to generate or transfer the pattern with feature sizes down to 100 nm. Soft lithography offers immediate advantages over photolithography and other conventional microfabrication techniques for applications, in which patterning of nonplanar substrates, unusual materials, or large area patterning are the major concerns. It provides a convenient, effective, and low-cost method for the formation and manufacturing of micro- and nanostructures. It is especially promising for microfabrication of relatively simple, single-layer structures for uses in cell culture, as sensors, as microanalytical systems, in MEMS, and in applied optics. The initial success of soft lithography indicates that it has the potential to become an important addition to the field of micro- and nanofabrication. Nanoimprint lithography is a novel method of fabricating nanometer scale patterns. It is a simple process with low cost, high throughput and high resolution. It creates patterns by mechanical deformation of imprint resist and subsequent processes. The imprint resist is typically a monomer or polymer formulation that is cured by heat or UV light during the imprinting. Adhesion between the resist and the template is controlled to allow proper release.

20.4.5 Direct Write Techniques

Dip-pen lithography (DPN) is a good example of a direct write technique. Direct write techniques are simple and straightforward. In other words, the number of process steps are minimal, usually 'filling the ink' and 'writing'. Post processing may be as simple as drying in air! EBL or FIB based direct write

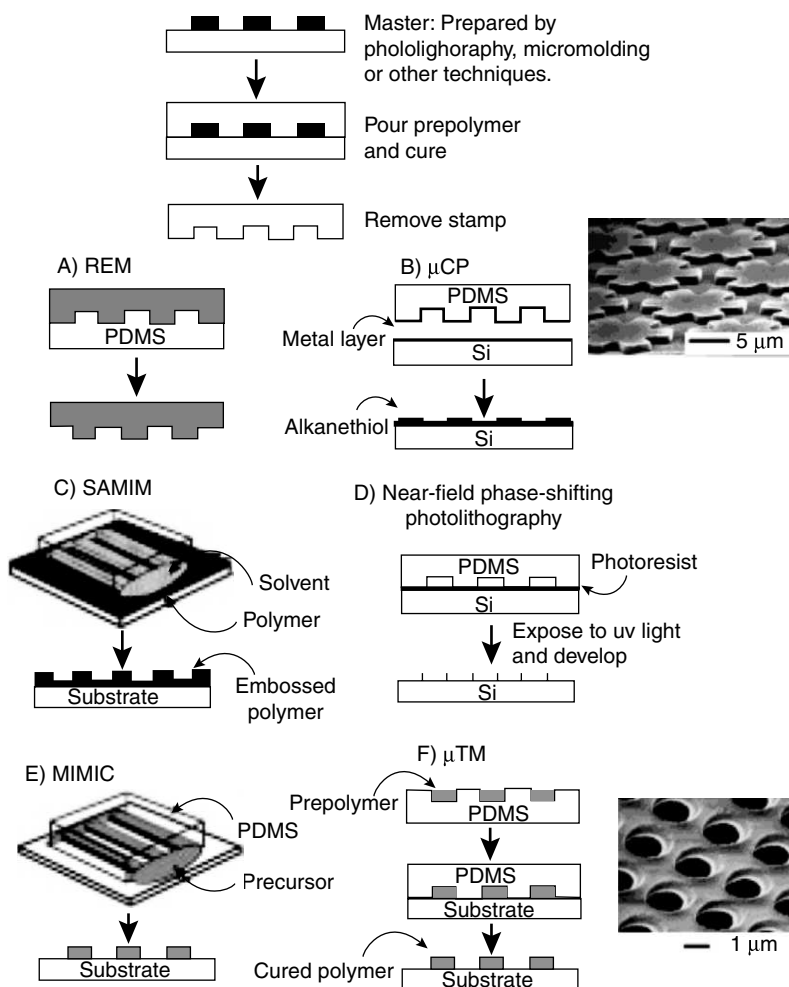


Fig. 20.14 Different soft lithographic processes with some typical examples (reproduced from ref. 26–31).

techniques^{31–33} have been around for quite some time. Electron or focused ion beam-induced deposition (EBID or FIBID) is a direct-write process, in which a pattern is defined directly by a focused electron (ion) beam, without any additional processes or treatments. In a typical setup, metal-organic precursor molecules (generally of W, Fe, Au and Pt) are directed onto a substrate by a gas nozzle in the e-beam vacuum chamber. Under the influence of a focused e-beam, the adsorbed molecules are dissociated into volatile and non-volatile fragments (Fig. 20.15). Depending on the precursor molecules, these fragments form a metal rich deposit. The volatile components are pumped away by the vacuum system. These techniques are usually employed to define interconnects soldering nanoelements in circuitry. The deposit may have poor electrical characteristics, because of carbon contamination from the organics.

Instead of cracking the vapour phase precursors by the electron beam, there is increasing interest worldwide, to innovatively come up with direct write resist precursors (Fig. 20.16), that may be coated in the solid form on substrates. These resists uniquely possess the ability to pattern (resist action) and at the same time, transform into desired nanomaterial in a single-step processing. Recently, there are innovations in stamping methods that allow direct patterning of the nanomaterial (Fig. 20.17).

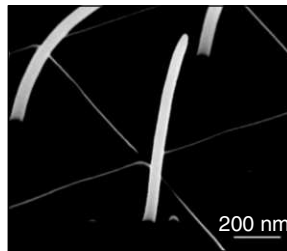


Fig. 20.15 Electron beam deposition of 50 nm thin, 1 μm tall, Pt nano-wires (reproduced from ref. 35).

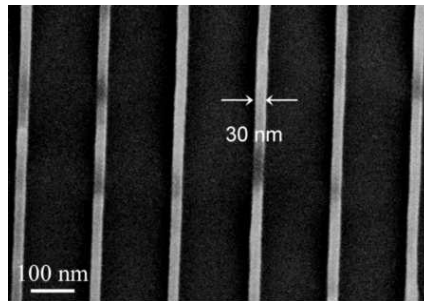


Fig. 20.16 SEM image showing thermolyzed Pd nanowires of ~ 30 nm width (reproduced from ref. 36).

20.4.6 Sub-100-nm Lithography

The terminology, sub-100-nm lithography, is applied to clearly distinguish those recipes, which enable one to perform patterning below 100 nm as against those which do not. Such a distinction is but natural as materials below 100 nm behave differently due to quantum confinement. Accordingly, the implications and their potential applications are of immense importance. The sub-100-nm recipe itself may have been derived from any known lithography technique or from a new combination of techniques. SPL techniques, such as DPN²³ are good examples for sub-100-nm lithography techniques. EBL, EBID and FIBID techniques as well, on routine basis, can reach below 100 nm. The smallest values identified so far are 1.9 nm for lines and 0.72 nm for dots! The de Broglie wavelengths of the charged particles can be sufficiently short (< 0.1 nm), keeping broadening due to diffraction effects minimal, unlike many photolithographic approaches. However, phase-contrast photolithography and such methods have intelligently brought the resolution down to below 100 nm. Scientists at IBM have

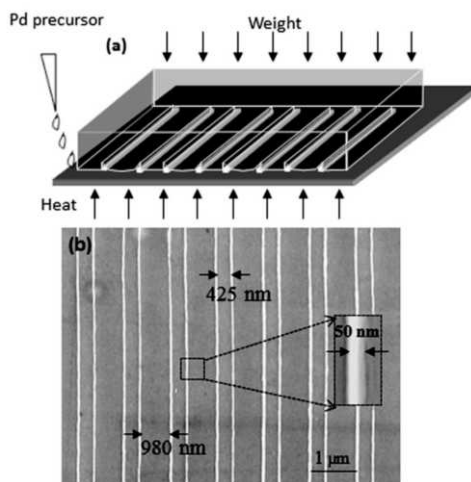


Fig. 20.17 (a) Schematic image showing the formation of nanochannels while direct molding of nanomaterial, (b) Large-area SEM micrograph of patterned Pd nanowires formed on Si substrate with a magnified view in the inset showing an individual nanowire of width 50 nm (reproduced from ref. 37).

fabricated distinct and uniformly spaced ridges only 29.9 nm wide using 193-nm lithography. This has beaten the 32-nm mark that industry had held as the limit for photolithography.³⁸ Among stamping methods, nanoimprint lithography is able to pattern below 100 nm. Examples from other inexpensive soft stamping methods are not common. Once in place, they would replace all other methods because of achievable speed.

20.5 NANOMANIPULATION

There have been major developments in techniques that enable manipulation of individual nanoobjects or a group of nanoobjects. Nanomanipulation, as a cousin of nanolithography, makes use of similar instrumentation, and therefore, has seen considerable growth side-by-side. In one sense, if nanolithography forms the body, nanomanipulation represents its limbs and hands. The finest example of manipulation came out the first, way back in 1993, when a sharp STM tip was used as a billiard stick to place individual atoms to form quantum corral (Fig. 20.18).³⁹ Since then, probe techniques are being extensively used to displace and transport atoms molecules and nanoobjects like, nanoparticles and nanotubes. The cantilever tip on AFM setup has been used as a shaving blade to rip off portions of SAMs (Fig. 20.19). By electrically activating or deactivating AFM tip, nanoobjects can be lifted and dropped⁴¹ much the same way a crane works in the macroscopic world. In this sense, AFM tip has served as a gripper. Of late, 'pick-and-place' technology is becoming popular, wherein, the desired material is picked up using a gripper and the released in the desired location (see Fig. 20.20). A more advanced gripper prototype is the triple shafts, which stabilise the structure

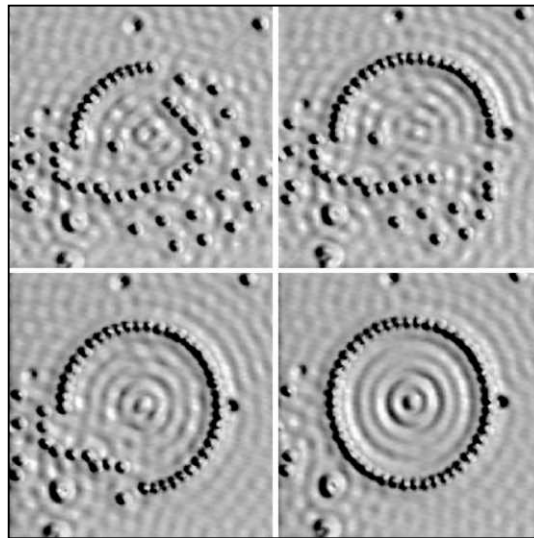


Fig. 20.18 Arrangement of 48 Fe atoms on the surface of a Cu substrate. These images show the various stages of the process. Once complete the circular arrangement of the iron atoms forced the electrons in the surface of the copper to specific quantum states as shown by the rippled appearance of the surface (reproduced from ref. 39).

and provide multiple points of control. The gripper can be opened and closed by placing electrostatic charge on a shaft, heating a shaft with a current, or a combination of the two approaches. Mechanical grippers activated by piezo- drivers allow manipulation at submicron length scales, if not truly at the nanoscale.

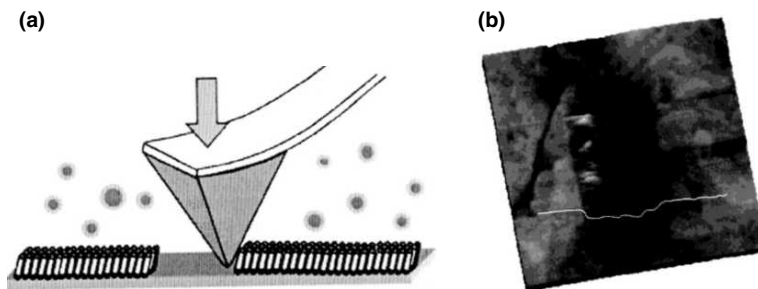


Fig. 20.19 Nanoshaving and removing regions of SAMs, a square hole within octadecanethiolate SAMs on Au (reproduced from ref. 40).

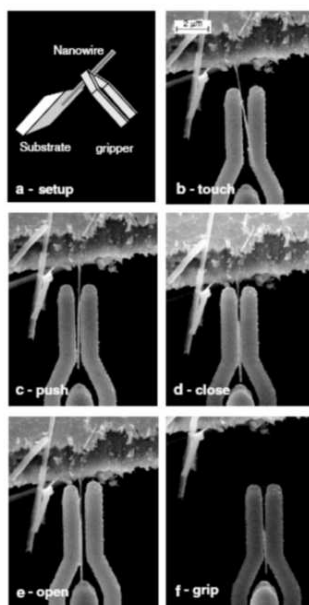


Fig. 20.20 *Picking up a silicon nanowire extending over the edge of a substrate. (a) Illustration of a part of the configuration as seen from the side—the SEM images view the gripper surface from the top. The nanowires located on the upper silicon surface of the substrate were usually adhering too strongly to be moved. Wires extending from the edge of the gold surface were generally much easier to move and some of these were possible to pick up. (b) The gripper was moved into contact with the wire. (c) Moving the wire and sliding the gripper along it could not release the wire. (d) The gripper was closed around the wire and reopened (e) without removing the wire. (f) The wire could only be peeled from the substrate when the gripper was kept closed and pulled away (reproduced from ref. 42).*

20.6 CONCLUSIONS

In this chapter, we examined various ways by which patterning is done at the nanoscale to create objects. These methodologies use photons, particles and scanning probes. In each one, there are diverse tools at various levels of spatial accuracy. We have reviewed various processes involved in pattern making. The practical requirements of nanolithography facilities were briefly touched upon.

REFERENCES

1. C.N.R. Rao, P.J. Thomas and G.U. Kulkarni, *Nanocrystals: Synthesis, Properties and Applications*, Springer-Verlag, (2007).
2. C.N.R. Rao and A. Govindaraj, *Nanotubes and Nanowires*, RSC Publishing, (2006).

3. R.C. Jaeger, *Introduction to Microelectronic Fabrication*, Upper Saddle River: Prentice Hall, (2001).
4. B. El-Kareh, *Fundamentals of Semiconductor Processing Technologies*, Kluwer Academic Publishers, Dordrecht, The Netherlands, (1995).
5. S. Franssila, *Introduction to Microfabrication*, Wiley Publishers, (2004).
6. W. Whyte, *Cleanroom Technology*, Wiley Publishers, (2001).
7. http://www.bo.imm.cnr.it/site/files/Photolyto4_lowres.jpg.
8. www.jncasr.ac.in/kulkarni.
9. M.V. Klein and T.E. Furtak, *OPTICS*; John Wiley & Sons: New York, USA, (1986).
10. T. Ito and S. Okazaki, *Nature*, 406, (2000), 1027.
11. H.I. Smith and M.L. Schattenburg, IBM, *J. Res. Develop.*, 37, (1993), 319.
12. B. Cord, J. Yang, H. Duan, D.C. Joy, J. Klingfus, and K.K. Berggren, *J. Vac. Sci. Technol. B* 27, (2009) 2616.
13. G. Le Rhun, I. Vrejoiu, L. Pintilie, D. Hesse and M. Alexe, *Nanotechnology*, 17, (2006), 3154.
14. S. Donthu, Z. Pan, B. Myers, G. Shekhawat, N. Wu and V.P. Dravid, *Nano Lett.*, 5, (2005), 1710.
15. A.A. Tseng, K. Chen, C.D. Chen and K.J. Ma, *IEEE Trans., Elect. Pack. Manufact.*, 26, (2003), 141.
16. F. Watt, A.A. Bettiol, J.A. Van Kan, E.J. Teo and M.B.H. Breese, *International Journal of Nanoscience*, 4, (2005), 269.
17. C.C. Cheng, V. Arbet-Engels, A. Scherer and E. Yablonovitch, *Physica Scripta*, 68, (1996), 17.
18. Loos, *J. Adv. Mater.*, 17, (2005), 1821.
19. R.S. Becker, J.A. Golovchenko and B.S. Swartzentruber, *Nature*, 325, (1987), 419.
20. J.A. Dagata, F. Perez-Murano, G. Abadal, K. Morimoto, T. Inoue, J. Itoh and H. Yokoyama, *Appl. Phys. Lett.*, 76, (2000), 2710.
21. T. Vijaykumar, PhD. Thesis, Jawaharlal Nehru Centre for Advanced Scientific Research, Bangalore, 2008.
22. T. Vijaykumar and G.U. Kulkarni, *Nanotechnology*, 18, (2007), 445303.
23. D.S. Ginger, H. Zhang and C.A. Mirkin, *Angew. Chem. Int. Ed.*, 43, (2004), 30.
24. R.D. Piner, J. Zhu, F. Xu, S.H. Hong and C.A. Mirkin, *Science*, 283, (1999), 661.
25. L.M. Demers and C.A. Mirkin, *Angew. Chem.*, 113, (2001), 3159.
26. Y. Xia, J.A. Rogers, K.E. Paul and G.M. Whitesides, *Chem. Rev.*, 99, (1999), 1823.
27. Y. Xia and G.M. Whitesides, *Angew. Chem. Int. Ed.*, 37, (1998), 550.
28. Y. Xia and G.M. Whitesides, *Annu. Rev. Mater. Sci.*, 28, (1998), 153.
29. J.A. Rogers, K.E. Paul, R.J. Jackman and G.M. Whitesides, *J. Vac. Sci. Technol. B.*, 16, (1998), 59.
30. X.-M. Zhao, Y. Xia and G.M. Whitesides, *Adv. Mater.*, 8, (1996), 837.
31. C. Marzolin, S.P. Smith, M. Prentiss and G.M. Whitesides, *Adv. Mater.*, 10, (1997), 571.
32. B.D. Myers and V.P. Dravid, *Nano Lett.*, 6, (2006), 963.
33. W.F. Van Dorp, B. van Someren, C.W. Hagen and P. Kruit, *Nano Lett.*, 5, (2005), 1303.
34. S. Lipp, L. Frey, C. Lehrer, E. Demm, S. Pauthner and H. Ryssel, Proceedings of the 7th European Symposium, (1996), 1779.
35. www.s3.infm.it/fib.html.

36. T. Bhuvana and G.U. Kulkarni, *ACS Nano*, 2, (2008), 457.
37. B. Radha and G.U. Kulkarni, *Small*, 5, (2009), 2271.
38. www.optics.org/cws/article/research/24274.
39. M.F. Crommie, C.P. Lutz and D.M. Eigler, *Science*, 262, (1993), 218.
40. J.C. Garno, Y. Yang, N.A. Amro, S. Cruchon-Dupeyrat, S. Chen and G.-Y. Liu, *Nano Lett.*, 3, (2003), 389.
41. A. Bachtold, P. Hadley, T. Nakanishi and C. Dekker, *Science*, 294, (2001), 1317.
42. K. Mølhave, T. Wich, A. Kortschack and P. Bøggild, *Nanotechnology*, 17, (2006), 2434.

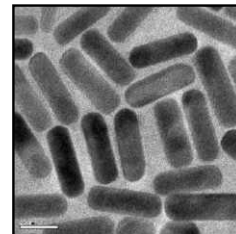
ADDITIONAL READING

1. M.J. Madou, *Fundamentals of Microfabrication: the science of miniaturization*. CRC Press, (2002).
2. D. Qin, Y. Xia and G.M. Whitesides, *Nat. Protocols*, 5, (2010), 491.
3. D.S. Ginger, H. Zhang and C.A. Mirkin, *Angew. Chem. Int. Ed.*, 43, (2004), 30.
4. A.A. Tseng, A. Notargiacomo and T.P. Chen, *J. Vac. Sci. Technol. B.*, 23, (2005), 877.

REVIEW QUESTIONS

1. Why nanolithography?
2. What are the methods of conventional lithography?
3. How are clean rooms classified?
4. How scanning probe techniques are modified to include lithography?
5. What is nanomanipulation?

NANOMAGNETISM



“The small is great, the great is small; all is in equilibrium in necessity...”

Victor Hugo, Victor Hugo and Charles E. Wilbour (trans.), *Les Misérables* (1862), 41

When bulk magnetic materials are reduced to nanometer size range, there are associated changes in several magnetic properties, such as magnetisation, coercivity, Curie temperature. The interesting, and sometimes, the unexpected properties of the magnetic nanoparticles are due to the dominating surface contributions. As the percentage of atoms on the surface of a particle becomes significant when the size of a material approaches the nanoscale, the type of bonding and the coordination geometry are affected on the surface. This leads to properties different from that of the bulk. The modified properties are useful in many applications and devices. Depending on the enhanced properties of the nanomaterials, when compared to that of the bulk, several high quality applications have been predicted. The expansion of research in the area of magnetic nanomaterials is driven by the extensive technological and medical applications.

Learning Objectives

- What is nanomagnetism?
 - What are the differences between the magnetism of nanoparticles and bulk?
 - What makes nanomagnetism interesting?
 - What are the applications of nanomagnetic materials?
-
-

21.1 MAGNETISM AND MAGNETIC MATERIALS

Magnetism is the power of attracting one material by another and it is one of the most interesting phenomena of materials. The history of magnetism dates back to many centuries before Christ. The oldest magnetic material is the so-called “magnetite”, which is an oxide of iron (Fe_3O_4). The word “magnet” is a Greek word, and is thought to come from the name of the district of Magnesia of the modern Turkey, where the mineral was initially found. In general, “the magnet” was known for its

attraction towards iron, nickel and cobalt. It was a belief that a piece of iron can become magnetic if it were touched or rubbed with “the magnet”. Later on, it was found that a freely hanging magnetic needle automatically orients towards the north-south pole direction of the Earth. This led to the discovery of the “compass”, an instrument used quite effectively for navigation purposes, and this has aided the faster development of civilisation. A major breakthrough for understanding the principles of magnetism was made through the discovery of the relation between electricity and magnetism in the 19th century. The development of quantum mechanics gave more insights to the microscopic principles of magnetism, which has been able to explain various magnetic properties quite successfully.

The numerous applications of magnetic materials, ranging from “Compass” to ‘Spintronics’, make them one of the most important and extremely interesting areas of modern materials research. Magnetic materials are used in various day-to-day applications such as in motors, generators, electromagnets, low and high frequency transformers, magnetic field screening, permanent magnets, loudspeakers, analogue and digital data storage, telecommunications, etc. Some of the widely used permanent magnetic materials are magnetite, magnetic carbon steel, alnico magnets (alloys based on Al, Co, and Ni), cobalt platinum magnets, hard ferrite magnets ($\text{SrFe}_{12}\text{O}_{19}$ and $\text{BaFe}_{12}\text{O}_{19}$), samarium cobalt, neodymium iron boron magnets, and samarium iron nitride. The oxide ferrimagnetic materials (ferrites, garnets, etc.) are discovered in the early 1940s and they still occupy a key position among the technologically important magnetic materials. In simple words, without magnetic materials, we can not think about modern technological revolutions. The present trend in magnetic materials research is on nanometer-sized materials. The main emphases, at present, are on the synthesis, characterisation, studies on the differences in the properties with respect to the corresponding bulk counterparts and on the application of magnetic nanomaterials for the benefit of man kind.

Magnetic nanoparticles have been the subject of much research interest even before the 1950s.¹ Because of the surge in the field of nanoscience and nanotechnology, studies on nanomagnetism emerged as a major area of research due to the potential applications of the nano-sized magnetic materials. Thus, investigation of magnetic nanoparticles is a subject of intensive research from the viewpoint of probing their magnetic behaviour (size and surface effects) and applications.² Some of the major applications of magnetic nanoparticles are in information storage where single nanoparticle can act as an individual bit of information providing high density data storage, in magneto-optical switches, sensors based on giant magnetoresistance (GMR), magnetically controllable single-electron transistor devices, in magnetic resonance imaging (MRI), targeted drug delivery, detection of biomolecular interactions, detection of DNA hybridisation, diluted magnetic semiconductors (DMS), etc. Modern scientific research is aiming at improving and enhancing capabilities of devices based on “spintronics” (spin + electronics).³ This is towards the development of smallest and cheapest microchips for use in computers, cell phones and other electronic components for military applications.

21.2 BASICS OF MAGNETISM

It is essential to know some of the basic aspects of magnetism before trying to understand magnetism of nanomaterials.⁴ Magnetism is a universal phenomenon associated with all materials that are

composed of charged particles. A material may respond to an applied magnetic field in two ways, (i) it may get attracted or (ii) repelled. Accordingly, magnetic materials are said to be either paramagnetic or diamagnetic, respectively. Paramagnetism is observed in materials that contain atoms/ions with unpaired electrons, whereas paired electronic systems behave as diamagnetic. Diamagnetism can be regarded as originating from the shielding currents induced by an applied magnetic field in the filled electron shells. The magnitude of the diamagnetic response is very small in most of the materials except for superconductors, which are perfect diamagnets.

In a uniform magnetic field H , if a magnetic pole of strength p is placed at an angle θ to another pole and separated by a distance l , then a couple acts on the magnet, called as magnetic moment m . The magnetic moment per unit volume is called intensity of magnetisation or simply magnetisation and is given by $M = m/V$, where V is the volume of the material. The magnetic properties of a material are characterised not only by the magnitude and sign of M , but also the way in which M varies with H . The magnetisation per unit magnetic field is called the magnetic susceptibility $\chi = M/H$. Commonly, the origin of magnetic moment in the atoms of a material is the motion of electrons. In any material, the origin of magnetism lies in the orbital and spin motions of electrons and how the electrons are distributed in the orbitals and interact with one another. The interesting fact is that, all materials are magnetic. It's just that some materials are 'more magnetic' than others. The main distinction is that in some materials the total magnetic moment arising from the individual atoms/ions is zero and in others there will be a finite value. Also, in certain materials there is no collective interaction of individual magnetic moments, whereas in others there are very strong interactions between individual moments. Depending on the values and orders of the magnetic susceptibility, substances are divided into certain categories. The most significant ones are paramagnetism, ferromagnetism, ferrimagnetism, and antiferromagnetism.

The magnetic moment due to the unpaired electrons is regarded as arising from spin and orbital motion of the electrons. The atoms or ions containing unpaired electrons have an overall magnetic moment given by, $\mu_j = [4S(S+1)+L(L+1)]^{1/2}$, where S and L are the spin and angular momentum quantum numbers, respectively, and J is the total quantum number resulting from the coupling of the spin and orbital angular momentum. In most cases, especially in the case of the transition metal ions, L is negligible and the spin only moment can be calculated as $\mu_s = g[S(S+1)]^{1/2}$, where g is the gyromagnetic ratio ≈ 2 . For a single electron, $\mu_s = 1.73$ Bohr Magnetron (BM), which is given by $1 \text{ BM} = eh/4\pi mc = 0.927 \times 10^{20} \text{ erg/Oe}$, where e and m are charge and mass of the electron, respectively, h is the Planck's constant and c is the velocity of light. Bohr magneton is also represented by the symbol μ_B and $1 \mu_B$ is equal to the magnetic moment of an electron in the first Bohr orbit.

A paramagnetic substance consists of atoms or ions, each of which has a net magnetic moment μ . The atoms with incomplete inner electronic shells (transition metal ions and rare earth ions) can have a large net moment and compounds of these elements are strongly paramagnetic. In the absence of an applied magnetic field, these atomic moments point at random and cancel each other, so that the net magnetisation of the substance is zero. When an external magnetic field is applied, there is a tendency for each atomic moment to turn towards the direction of the field depending on the strength of the applied field. If there is no opposing force, complete alignment of the atomic moments would

be produced, and as a whole, the specimen would gain a very large magnetic moment in the direction of the field. But, thermal agitation opposes this tendency and tends to keep the moments pointed at random directions. Therefore, only a partial alignment of the moments will be possible in the field direction, and as a result, a small positive susceptibility could be seen. The effect of an increase in the temperature is to increase the randomising effect of thermal agitation, and therefore, to decrease the susceptibility.

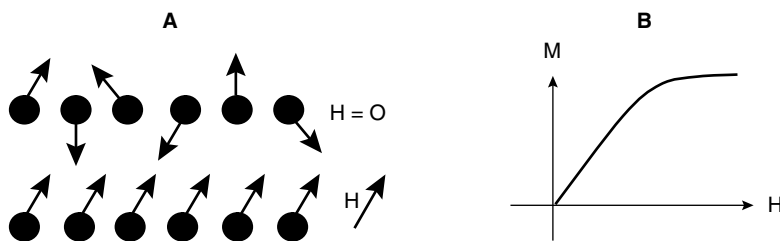


Fig. 21.1 (A) Orientation of magnetic moments in the individual atoms or ions in a paramagnetic substance in the absence of a field ($H = 0$) and in a strong applied magnetic field H . (B) Magnetisation as a function of applied field for a paramagnetic substance. The magnetisation is saturated only at very high applied fields.

According to the first systematic measurements of the susceptibility of a large number of substances over a wide range of temperature, made by the French physicist Pierre Curie, χ was found to be independent of temperature for diamagnetic substances, but it varied inversely with the absolute temperature for paramagnetic substances. The magnetic susceptibility of the paramagnetic substances, as a function of temperature, can be expressed as, $\chi = N\mu_{\text{eff}}^2/3kT$, where N is the Avogadro number, k is the Boltzmann constant and μ_{eff} is the effective magnetic moment and is given by $\mu_{\text{eff}} = g [J(J+1)]^{1/2}$. $N\mu_{\text{eff}}^2/3k$ is a constant, and therefore, the magnetic susceptibility equation can be written as $\chi = C/T$. This relation is called the Curie's Law and C is the Curie constant. The effective magnetic moment, μ_{eff} , can be calculated from the slope of the plot of $1/\chi$ vs T , which will be linear for a paramagnetic substance.

The essence of paramagnetism lies in the criterion that there is hardly any *interaction* between the individual magnetic moments. In order to achieve the saturation magnetisation of a paramagnet, where all the moments are aligned parallel to the direction of the applied field, very high magnetic fields are required, simultaneously with very low temperatures. But, there are systems, which are paramagnetic only above a critical temperature. Such materials undergo spontaneous ordering of magnetic moments below the critical temperature, because of the interaction between the moments. Based on the types of ordering, such magnetic systems may be classified as ferromagnetic, antiferromagnetic, and ferrimagnetic.

Ferromagnetism is a property exhibited by certain metals like Fe, Co, Ni, some alloys containing these elements, and compounds of the transition metal ions (iron group), rare-earth, and actinide elements. In ferromagnetic materials, the atomic magnetic moments tend to line up in a common

direction even in the absence of a magnetic field below a certain temperature. This critical temperature is called the Curie temperature (T_C). In ferromagnetic materials, below Curie temperature, magnetic moments align parallel to each other. These materials will attain saturation of magnetization, M_s , under relatively small applied magnetic fields. Within a region of a ferromagnetic substance, all the atomic moments are essentially aligned giving a net magnetic moment even after the removal of the external magnetic field. Ferromagnetic materials are like paramagnets above the T_C .

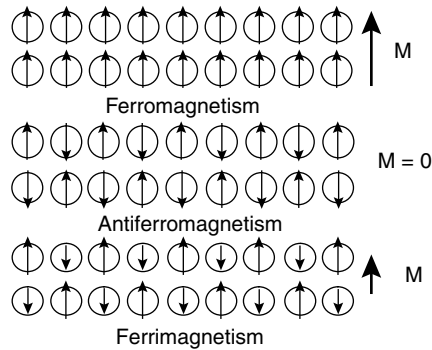


Fig. 21.2

In the case of antiferromagnetic substances, the individual magnetic moments align in a regular pattern with neighboring moments pointing in the opposite directions. A simple antiferromagnet can be considered as consisting of two magnetic sub-lattices, each of which being ferromagnetically ordered, but coupled antiferromagnetically (moments in opposite direction) in the unit cell of a solid. In the case of antiferromagnetism, moments cancel out each other due to antiparallel alignment, below a critical temperature called the Neel temperature, T_N . Below T_N , the two sublattices of an antiferromagnet spontaneously magnetise in the same way as in a ferromagnet, but the net magnetisation is zero due to the opposing orientation of the sublattice's magnetisation. If an external field, H , is applied, a small net magnetisation can be detected. The resultant magnetisation depends upon the orientation of the field with respect to the magnetisation axis. Antiferromagnetic materials are like paramagnets above the T_N .

Ferrimagnetism is a phenomenon where there can be incomplete cancellation of antiferromagnetically arranged moments giving a small net magnetic moment. Ferrimagnetism is also a situation of antiparallel alignment of moments, but the moments are of unequal magnitudes, so that there is a net magnetization. In other words, ferrimagnetism is called uncompensated antiferromagnetism. Like ferromagnets, ferrimagnetic materials also can hold a spontaneous magnetisation below an ordering temperature T_N and they are like paramagnets above the T_N . Ferrimagnetism is exhibited by ferrites (oxides containing more than one metal and Fe is one of the constituents) and magnetic garnets. The oldest-known magnetic substance, the magnetite, is a ferrimagnetic material.

21.3 MAGNETIC DOMAINS AND ANISOTROPY

Magnetism in solids arises from the magnetic ions or atoms distributed throughout a regular crystalline lattice on equivalent sites. The cooperative magnetism in solids, arising from the interaction (coupling) between the atomic moments, is more complex than that of the isolated atoms. Because of the alignment of the magnetic moments across many unit cells in a solid, ferromagnetic, ferrimagnetic and antiferromagnetic materials are said to exhibit “long-range ordering” of the moments in the lattice. For ferro- and ferrimagnetic substances, the field dependence of magnetisation is non-linear and at large values of H , the magnetisation M becomes constant at its saturation value M_s , as shown in the Fig. 21.3. But once saturated, a decrease in H to zero does not reduce M to zero. Hence, it possesses some magnetisation, called remnant magnetization (M_r). In order to demagnetise the substance after saturation, a reverse field is required. The magnitude of this field is called coercivity (H_c). The M - H curve in the case of ferro- and ferrimagnets is called the magnetic hysteresis loop.

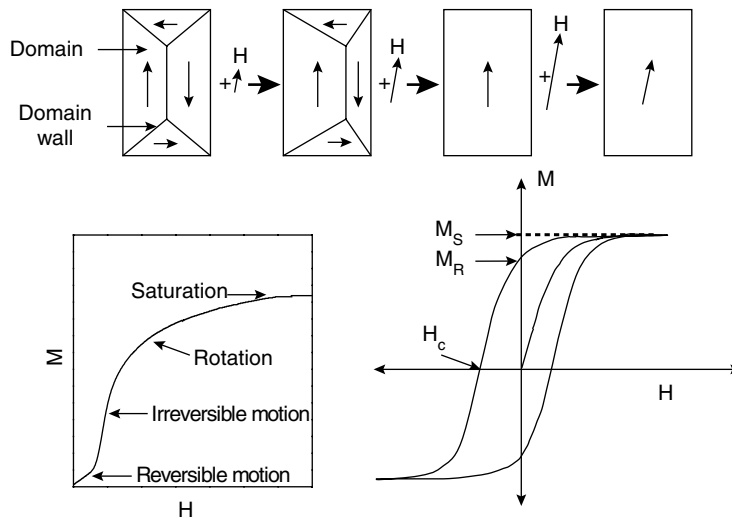


Fig. 21.3 The behaviour of a multidomain material in an increasing magnetic field (top), the associated changes in the magnetisation (bottom left) and a typical magnetic hysteresis loop (bottom right).

In a crystalline material, the magnetic properties depend up on the direction of magnetisation. This is known as magnetocrystalline anisotropy. Magnetocrystalline anisotropy originates from the spin-orbit interactions of the electrons. The magnetic moments are directed towards certain directions in the crystal lattice, called the easy directions and it is easy to attain saturation magnetisation when the magnetic field is applied along these directions of a crystal. Along the hard directions, very large fields are required for saturation. Very large magnetic fields are required to rotate the moments away from the easy axis, and therefore, higher negative fields are required to demagnetise the material. Therefore, high magnetocrystalline anisotropies give rise to larger coercivities. Apart from the magnetocrystalline

anisotropy, there are also other contributions to magnetic anisotropy, such as magnetostatic anisotropy coming from the shape of the substance, magnetostrictive anisotropy from the elastic shape changes in the presence of an applied field, induced anisotropy and exchange anisotropy.

When a ferromagnet is cooled below its T_C in the absence of an applied field, there develops a magnetisation by the exchange coupling and this is called spontaneous magnetisation. Nevertheless, the material as a whole will remain unmagnetised because of the presence of several small regions of ferromagnetism within the material. These small regions are called “domains”.⁵ In a domain, all groups of spins point in the same direction and act cooperatively. In larger particles, it is the energetic considerations which favour the formation of the magnetic domains. Such particles are called multi-domain particles. Individual domains are separated by regions called domain walls with a characteristic width. The directions of magnetisation of the various domains are such that the specimen as a whole has no net magnetisation.

In the case of the multi-domain ferromagnetic particles, magnetisation occurs through the nucleation and motion of these walls. The role of an applied magnetic field is to convert a multi-domain specimen to a single-domain state, magnetised in the direction of the applied field. The nature of this field dependence is mainly controlled by magnetic anisotropy, which encourages the magnetisation only in particular directions in the crystal, and also by exchange energies. In a typical M-H curve of a ferro- or ferrimagnet, magnetisation at low fields increases due to the motion (movement) of the domain wall. As a result, domains which are favourably oriented to the direction of the applied field, grow at the expense of others. At still higher fields, changes in the magnetisation occur by domain rotation, leading to saturation of magnetisation. When the temperature increases, the saturation magnetisation of a ferromagnetic substance decreases and at T_C the domain structure is collapsed, so that the material will act as a paramagnetic substance above T_C .

21.4 MAGNETIC NANOSTRUCTURES

Solids may be classified into two main categories: crystalline materials with complete long-range order and amorphous materials with short-range order. However, in nanometer-sized crystalline materials, little long-range order and little-short range order coexist. These materials are polycrystalline, in which the size of the individual crystallite or particle is in the order of 1–100 nm. These nanostructured materials consist of two components. A crystalline component, formed by all atoms located inside the crystallites or particles and an interfacial component comprising all the atoms, which are situated in the boundaries between the crystallites or in the interface (surface). The interfacial component is proposed to represent solid-state structures without long- or short-range order. Nanostructured magnetic materials⁶ exhibit interesting and unexpected properties due to their very high surface area to volume ratio, where the percentage of atoms at the surface of the material becomes significant. Interestingly, the morphology and the shape of the nanoparticles can be varied with different specialised synthetic routes. Similar to other nanomaterials, the magnetic particles can also be made in to different shapes, such as nanospheres, nanorods, nanocubes, nanotubes, nanowires, nanoribbons or nanoplates.

Magnetic nanostructures can be divided into different groups based on their properties and morphologies as shown in the Fig. 21.4. These range from isolated magnetic nanoparticles to magnetic nanocomposites and nanosized magnetic clusters in a long-range ordered crystalline matrix. Apart from the magnetic properties of the individual particles or clusters, there can be magnetic interactions between the particles depending on the packing of these nanostructures in the medium, their surface characteristics and various other factors. There are several reasons to study these nanosized magnetic materials. First, the materials may possess quite different properties when compared to the bulk due to the changes in their intrinsic properties. Second, any new properties can be explored for many potential applications. Third, new theories may have to be proposed in order to explain the experimental observations.

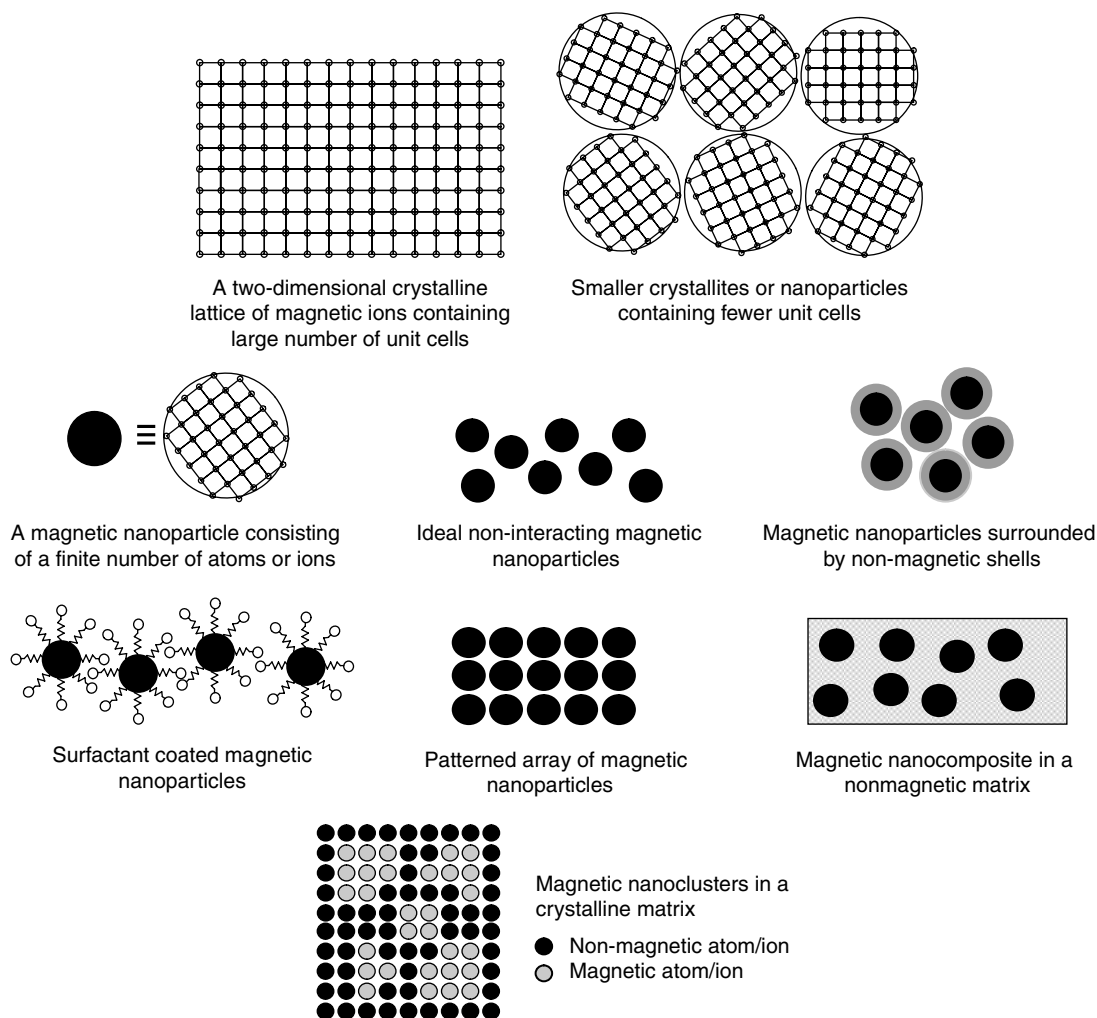


Fig. 21.4

21.5 MAGNETISM OF NANOSIZED MATERIALS

Fine particle magnetism has been traditionally dealt with the size effect, which is based on the magnetic domain structure of the magnetic materials.⁷ It assumes that the state of lowest free energy of ferromagnetic particles has uniform magnetisation for the particles less than a certain critical size (single domain particles) and non-uniform magnetisation for the particles larger than the critical size (multi-domain particles). As the particle size decreases toward some critical value, the formation of domain walls becomes energetically unfavourable and the particles are called single domain. Changes in the magnetisation can no longer occur through domain wall motion and instead require the coherent rotation of spins, resulting in large coercivities. Nanosized magnetic particles exhibit behaviour similar to paramagnetism at temperatures below the Curie or the Neel temperature. It is half-way between ferromagnetism and paramagnetism. In this case, below the Curie or Neel temperature, the thermal energy is not sufficient to overcome the coupling forces between neighbouring atoms, whereas the energy is sufficient to change the direction of the magnetisation of the entire particle. The resulting fluctuations in the direction of magnetisation cause the magnetic moments average to zero. Thus, the material behaves in a manner similar to paramagnetism, except that instead of each individual atom being independently influenced by an external magnetic field, the magnetic moment of the entire particle tends to align with the magnetic field. Thus, these particles are called “superparamagnetic” particles. “Superparamagnetism” occurs when the material is composed of very small particles.⁸

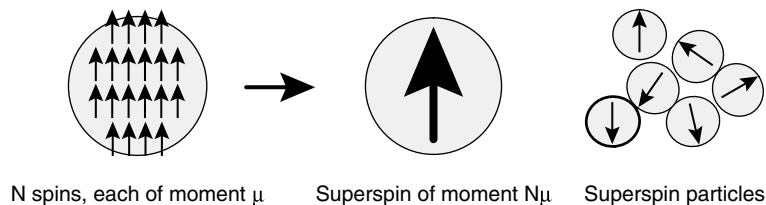


Fig. 21.5

A number of interesting magnetic phenomena arise when one or more of the dimensions of a magnetic particle are reduced to the atomic size, that are of the order of single domain. Some changes in the magnetic properties like saturation magnetisation, Curie temperature, coercive force and magnetic anisotropy could be recognised as the effects of reduced dimensions.^{9, 10} Apart from the magnetocrystalline and magnetostatic anisotropies present in the bulk materials, which are also operative in nanoparticles, other kinds of anisotropy contributions also come into picture in magnetic nanoparticles.¹¹ These are the surface anisotropy due to the changes in the coordination, broken bonds and magnetic exchanges at the surface of a particle. Since the surface area to volume ratio of a fine particle is larger than that of the bulk, the surface anisotropy contributions to the total anisotropy is considerable. Again, due to the smaller size of the particles, there will be considerable strain on the surface and this also contributes in the form of strain anisotropy. Finally, if the magnetic nanoparticles are closer together, there will be magnetic dipolar interactions between the particles and different types of magnetic exchange interactions at the interface between the particles. These two interactions

also contribute to magnetic anisotropy. Hence, for magnetic nanoparticles, the additional magnetic anisotropy contributions determine the over all magnetic properties.

For a magnetic material, the coercivity is small when the particles are very large. Initially, the coercivity increases as the particle size is decreased due to the decreasing size of the domains and their number. After reaching a maximum value of the coercivity, at a critical particle size, the coercivity decreases further as the particle size is decreased due to the randomisation effect of thermal energy. The coercivity becomes zero below certain dimensions. Typical variation of the coercivity as a function of particle size is shown in the Fig. 21.6.

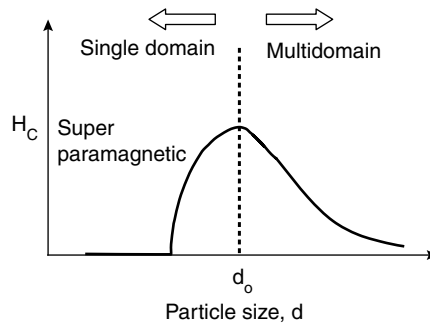


Fig. 21.6 Particle size dependence of coercivity.

Superparamagnetic particles are ferro/ferri magnetic single domain particles, so small that thermal energy at that temperature of the experiment is of the same order or smaller than the energy barrier, preventing spontaneous reversal of magnetisation. Thus, in a period comparable to the time of the experiment, the thermal energy equilibrates the magnetisation of an assembly of such particles and the average magnetisation is zero. For magnetic nanoparticles with spherical shapes, the magnetocrystalline anisotropy energy E_A can be approximated as the total magnetic anisotropy of single domain particles and can be expressed as $E_A = KV \sin^2\theta$, where K is the magnetic anisotropy constant, V is volume of a particle and θ is the angle between the direction of magnetisation and the easy axis of magnetisation. When E_A becomes comparable to thermal activation energy kT , where k is the Boltzmann constant, the magnetisation direction starts flipping randomly and goes through rapid superparamagnetic relaxation. The temperature, above which the thermal activation energy overcomes the magnetic anisotropy energy barrier and the nanoparticles become superparamagnetically relaxed, is known as the superparamagnetic blocking temperature, T_B . For isolated magnetic nanoparticles, the relaxation time is given by

$$\tau^{-1} = f_0 \exp(-KV/kT),$$

where $f_0 \approx 10^9$ Hz. $\tau \approx 100$ s for typical superparamagnets and $KV \approx 25kT_B$. KV is an important parameter for designing high anisotropy magnetic nanoparticles for data storage. The magnetic properties of the superparamagnetic particles can be finetuned for many potential applications. As the equation predicts, T_B depends on the volume of the particle and thus on the particle size. Generally, the blocking temperature decreases with decreasing particle size.

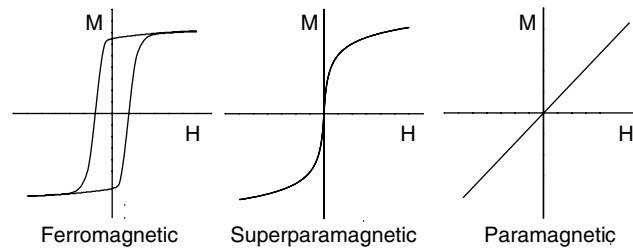


Fig. 21.7 Magnetic field dependence of the magnetisation of ferromagnetic, superparamagnetic and paramagnetic particles.

The conditions for superparamagnetism are that the coercivity is zero and the magnetisation measured as a function of field, at different temperatures, superimposes when plotted as a function of H/T . Apart from this, superparamagnetic particles are characterised by a maximum in the temperature variation of ac susceptibility and zero-field-cooled susceptibility measured in a small dc magnetic field. In the zero field cooled (ZFC) magnetic measurements, the sample is cooled to the lowest possible temperature in the absence of a magnetic field and measurements are made while heating the sample in the presence of a small dc magnetic field. The temperature, at which a maximum is observed, is at the superparamagnetic blocking temperature T_B . The shapes of the zero-field-cooled or ac susceptibility curves are determined by the particle size, shape and size distribution. Thus, it is possible to have the same T_B for a fine particle system with wider or narrower size distributions, but the shape of the curves will be different in the two cases; broader in one case and narrower in the other.

Another measurement is called a field cooled (FC) magnetisation measurement. In an FC measurement, a sample is cooled to the lowest possible temperature in the presence of a small magnetic field and measurements are made while cooling or heating in the same field after cooling. When the same sample is cooled under a magnetic field, the magnetisation remains almost constant below the blocking temperature. Thus FC and ZFC magnetisations deviate below T_B and overlap when the temperature rises above T_B . Such temperature dependence of the ZFC magnetisation and the divergence of ZFC and FC magnetisations below T_B are the characteristic features of superparamagnetism. Opening up of the magnetic hysteresis loop is also expected below the blocking temperature. In magnetisation measurements, superparamagnetic particles show a typical behaviour as shown in the Fig. 21.8. The characteristics of the FC magnetisation curve depend on the nature of the interaction between the particles. If the particles are well separated in a non-magnetic matrix or by proper surface coatings, the different types of interactions between the particles, such as dipolar interactions or exchange interactions are suppressed. In this case, the FC magnetisation continuously increases below T_B as the temperature is decreased whereas the FC magnetisation remains constant or decrease slightly below T_B depending on the strength of the interactions between the particles. The dynamics of the nanoparticle systems are governed by the distribution of the relaxation times of the individual particles, arising from the particle-size distribution.

Saturation magnetisation has usually been thought of as being an intrinsic property of ferro- and ferrimagnetic materials. Therefore, the values of saturation magnetisation measured in bulk materials

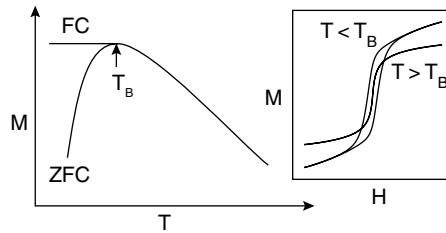


Fig. 21.8 Typical field cooled (FC) and zero field cooled (ZFC) magnetisation curves of magnetic nanoparticles showing the blocking temperature and the magnetisation behaviour below and above the blocking temperature as a function of field.

may be expected to apply for very small particles as well, irrespective of particle size or morphology. However, in nanostructured magnetic materials, a reduction in saturation magnetization is observed. For magnetic nanoparticles, there is no magnetic saturation even at moderately large fields. Extremely large magnetic fields are required for saturation of the magnetisation. The possible explanation for the reduced magnetisation of the nanoparticles is the core-shell morphology of the nanocrystallites. In this model, the magnetisation is originating only from the core of the particles, and non-collinear spin structure is present predominantly on the surface of each particles. The core-shell model assumes a magnetically-dead layer of thickness t , which is a constant, and the magnetisation varies with size by the relation

$$M_s(d) = M_s (1 - \beta/d)$$

where M_s is the saturation magnetization of the bulk, $M_s(d)$ is the saturation magnetisation of the nanoparticles of diameter d , and β is a constant related to the thickness of the dead layer, $\beta \approx 6t$, where t is the thickness. Thus the saturation magnetisation is inversely related to the particle size.

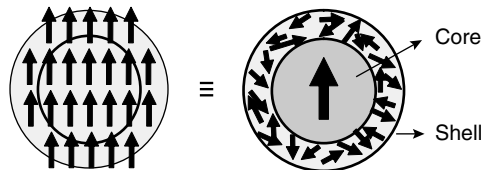


Fig. 21.9 The magnetic core-shell structure. The shell is assumed as a magnetically dead layer of thickness t . $t \approx 1$ unit cell dimension.

As the physical dimensions of the particles get smaller, the proportion of the magnetic centers at or near the surface of a particle increases. Thus, small particles offer the potential of exhibiting special effects that are not observed in bulk materials and a great deal of research effort is devoted to this field. Surface effects arise due to spin-canting anomaly. This is attributed to a random canting or noncollinearity of the spins at the surface of the particles due to a differing balance of exchange interactions at sites near the surface. Saturation magnetisation less than the bulk value may indicate some changes in the magnetic spin structure. Evidence for the magnetic spin structure of fine particles,

which differs from that of the bulk is obtained by using Mössbauer spectroscopic studies. Mössbauer spectroscopy technique provides a direct way of investigating the nanosized magnetic particles and their spin structures. For studying noncollinear spin structure, an external magnetic field is applied parallel to the direction of propagation of γ -rays. This orients the magnetisation in the direction of external fields.

Apart from the changes in the magnetic properties of ferro- or ferrimagnetic materials on reduction of their particle sizes to the nanometer regime, unusual changes in the properties are observed for anti-ferromagnetic nanomaterials also. Here again, it is the surface contribution of magnetism, which determines the resulting magnetic behaviour. It may be recalled that the net magnetic moment is zero below the Neel temperature in the case of antiferromagnetic materials due to the opposite alignment of the moments of adjacent magnetic ions/atoms in a lattice. However, when the size of the magnetic particles are reduced to nanometer dimensions, the moments on the surface need not cancel each other or aligned randomly and this can give rise to enhanced net magnetic moment for the particles. One of the best examples is nickel oxide. NiO is paramagnetic above 250 °C and anti-ferromagnetic below this Neel temperature. When the size of NiO particles is reduced below 10 nm, it exhibits huge increase in the magnetic susceptibility below the Neel temperature and show superparamagnetic behaviour at room temperature.¹² Similar effects are known for many other anti-ferromagnetic materials also. Even non-magnetic materials can be made magnetic when the particle sizes are reduced to nanodimensions.¹³

21.6 SYNTHESIS OF MAGNETIC NANOPARTICLES

The method of preparation of the nanomagnetic materials represents one of the most important challenges that will determine the particle size, size distribution, surface chemistry, and consequently, the magnetic properties.¹⁴ Again, depending upon the mechanism of formation, the particles obtained can be amorphous or crystalline if it results from a disordered or ordered aggregation of crystallites, respectively. In addition, the preparation method determines, to a great extent, the degree of structural defects or impurities in the particles. The distribution of such defects within the particles governs the magnetic behaviour. Recently, many attempts have been made to develop processes and techniques that would yield monodisperse colloids consisting of uniform nanoparticles both in size and shape.

The elements Fe, Co and Ni are ferromagnetic at room temperature. Fe is one of the commonly used elemental magnetic materials, with a Curie temperature of 770 °C and very high saturation magnetisation. Nanoparticles of Fe find numerous applications, including in catalysis. Fe nanoparticles are generally synthesised by the thermal decomposition of iron pentacarbonyl $\text{Fe}(\text{CO})_5$. The reaction can be carried out in the presence of a surfactant and the only byproduct is carbon monoxide. Depending on the characteristics of the surfactant, well-dispersed nanoparticles of iron can be obtained. Instead of thermal decomposition, sonochemical decomposition has been used effectively. This process produces local heating, giving rise to iron nanoparticles. However, in this case, control of the particle size and morphology are very difficult. Other soft chemical methods, such as reduction of iron salts in solution or from iron oxides also produce iron nanoparticles. The iron salts can be reduced in the presence

of a surfactant by micellar or microemulsion methods. Iron salts can be reduced easily by using the common reducing agents, such as hydrazine, sodium borohydride, etc. Co and Ni nanoparticles can be synthesised by the polyol reduction method, where the metal salts are refluxed in the presence of a weak reducing agent containing hydroxyl groups such as ethylene glycol.

The alloy FePt is highly magnetic and its nanoparticles are more stable than that of the elemental magnets as well as some other alloy based magnetic materials.¹⁵ High coercivity nanoparticles of FePt can be synthesised relatively easily, rendering them useful for many applications. The as-synthesised FePt powders are having the disordered face-centered cubic structure and very low coercivity. On annealing, the structure transforms to face-centered tetragonal with large coercivity. However, this leads to agglomeration and wide particle size distribution. Chemical syntheses methods offer narrow-size distribution. Monodisperse FePt nanoparticles can be obtained by the thermal decomposition of iron pentacarbonyl and reduction of platinum acetyl acetate in the presence of 1,2-alkanediol. The thermal decomposition of $\text{Fe}(\text{CO})_5$ produces Fe and the reduction yields Pt, which combine to form FePt clusters and then to nanoparticles. The first step is to reduce Pt and then decompose the carbonyl by heating to 300°C. Oleic acid and oleylamine are usually used as surfactants to passivate the surface of the particles. The particle size can be controlled by varying the surfactant to metal ratio. It is also possible to control the particle size by simultaneous decomposition and reduction processes without using the diol. The FePt nanoparticles can be stabilised by coating the surface by a suitable surfactant or by using excess Fe in the reaction mixture. The excess Fe will be deposited on the FePt surface forming a FePt/Fe interface and this on partial oxidation produces FePt/Fe₃O₄.

The most stable magnetic nanomaterials are based on iron oxides. Being oxides, they are chemically stable to oxidizing and thermal environments. Iron oxides such as $\gamma\text{-Fe}_2\text{O}_3$ (maghemite) and Fe₃O₄ (magnetite) are magnetic ($\alpha\text{-Fe}_2\text{O}_3$ is not magnetic) and superparamagnetic iron oxide nanoparticles, known as SPIONs, can be synthesised relatively easily with out much precaution. The iron oxides can be easily coated with surfactants or other inert oxides, such as silica, and these oxides are bio-compatible. Therefore, much importance is given to the synthesis and studies of magnetic iron oxide nanoparticles. Fe₃O₄ nanoparticles can be synthesised very easily using the coprecipitation technique involving ferrous and ferric salts taken in the 1:2 molar ratio. Direct addition of NH₄OH or NaOH precipitates the oxide. The particle size, distribution and morphology can be controlled by the concentration of the reactants, pH of the solution, temperature, and rate of precipitation. Suitable surfactants can be coated on the surface of the particles after filtration or during the precipitation itself in the presence of a surfactant. Silica coated Fe₃O₄ nanoparticles (core-shell structure) can be obtained by the controlled hydrolysis of tetraethylorthosilicate (TEOS) in presence of the nanoparticles. The silica shell thickness can be controlled by varying the concentration of TEOS. Other methods commonly being used are the micellar methods, sol-gel synthesis, etc. $\gamma\text{-Fe}_2\text{O}_3$ can be obtained from Fe₃O₄ by oxidation. The uncoated Fe₃O₄ will be air oxidized to Fe₂O₃.

The magnetic nanoparticles when coated with a surfactant—hydrophilic or hydrophobic—can be dispersed in a suitable medium, such as water or oil. The action of the surfactant is to prevent the agglomeration of the magnetic nanoparticles, even in the presence of a strong magnetic field. A colloidal suspension of the surfactant coated magnetic nanoparticles in a carrier liquid is known as a

ferrofluid.¹⁶ As a result of anisotropic dipolar attraction, pristine magnetic particles tend to aggregate into large clusters, and therefore, it loses the specific properties associated with single domain magnetic nanoparticles. Therefore, the colloidal stability of the fluid depends upon the size, charge and surface chemistry which give rise to both steric and coulombic repulsions.

21.7 APPLICATIONS OF NANOMAGNETIC MATERIALS

Magnetic nanoparticles find numerous applications in many modern technological and biomedical areas. Since the size, shape, orientation, distribution, etc., of the magnetic nanoparticles can be manipulated by controlling the processing conditions; it will be possible to tailor the particles for specific applications. Some of the major applications are in high density magnetic recording media or information storage where single nanoparticle can act as an individual bit of information providing high density data storage, magnetic refrigeration, magnetic sensors for different applications, and biomedical applications, such as targeted drug delivery, magnetic separation, magnetic resonance imaging, magnetic hyperthermia, etc.

Non-volatile magnetic data storage is still the major application of magnetic nanoparticles.¹⁷ Current research work on information storage is aiming to achieve higher storage density without affecting the quality and life of the stored data. There are many parameters needed to be considered when one thinks about increasing information storage density from the present stage. The ultimate goal in magnetic storage technology is the quantised or single particle per bit recording. It is possible to increase magnetic storage density by decreasing the magnetic particle size. However, there is a limitation imposed by the thermal flipping of the magnetic moments in superparamagnetic particles, because of the constraint $KV \approx 25kT$. Because of the fast flipping of the moments in superparamagnetic particles due to the available thermal energy, it is not possible to store information for a long time in such particles, and therefore, there is a “superparamagnetic limit” for magnetic information storage. For example, for 10-nm-sized spherical particles, the flip rate is approximately one per week, whereas when the size is increased to 20 nm, the flip rate can be increased to almost 10^{100} years. One way to control this size limit is to increase the anisotropy so that $KV \gg 25kT$ at room temperature. The coercivity, size, shape and orientation of the particles in the storage media need to be controlled to achieve these expectations. The coercivity is time dependent and can be different at reading, writing and storage times. Apart from these size limitations, there are factors, such as signal to noise ratio. Very large value of the anisotropy is required to attain higher signal to noise ratio when the particle size is reduced to very low values. Moreover, magnetic interactions between the particles are also of prime importance in determining the maximum possible storage density using the magnetic nanoparticles. Thus, the product KV is an important parameter in designing high density storage media. At present, the future of magnetic recording using nanoparticles is not clear because of several limitations.

Another issue concerning the storage density is the storing and retrieval processes. The magnetic read/write heads also need to be revolutionised for faster reading and writing to cop with the increased storage density. Here again, magnetic nanostructures come in to picture. Magnetic sensors based on giant magnetoresistance (GMR) are already employed in today’s hard disc drives. Magnetoelectronics

or spintronics is the catch word for most of the future technological advancements. This is based on various magnetoelectronic features, such as diluted magnetic semiconductors, tunneling magnetoresistance, spin valves, etc.

Hard magnetic materials, having high coercivity, high saturation magnetisation and remnance are required for permanent magnet applications in various devices. Thus, by controlling the particle size, composition of the material, anisotropy, morphology of the particles, etc., it would be possible to make permanent magnets with the required performance parameters. Similarly, soft magnetic materials, such as different ferrites are desirable for telecommunications, electromagnetic shielding, etc.¹⁸ The current trend is to enhance the working limit of the materials to higher and higher frequency limits for telecommunications, absorption of high frequency electromagnetic waves, high permeability applications, enhanced magnetoresistance, magnetoimpedance, magnetostriction, magnetocaloric effect, etc.

Ferrofluids were originally developed in the 1960s at NASA for space applications. The magnetic moments of the nanoparticles in the suspension are randomly aligned in all directions, and therefore, the net magnetisation is zero, as in the case of paramagnetic substances. When a magnetic field of suitable strength is applied, all the magnetic moments will rotate in the direction of the applied field. The fluid, as a whole, will try to move towards the region of high magnetic field. When this happens, the particles in the suspension are no longer in a position to move and the fluid as a whole become rigid-like as if the viscosity of the fluid is increased. Ferrofluids find numerous applications in different areas¹⁹. Ferrofluids are suitable to study the effect of interparticle magnetic interactions. The strength of the interactions can be tuned by varying the fluid concentration and a very dilute fluid is an experimental model system for the study of superparamagnetism. The fact that the properties of a ferrofluid can be controlled by a magnetic field offers numerous applications. One of the important features of a ferrofluid is that it becomes solid when a magnetic field is applied and reverts back to a fluid when the magnetic field is removed. This property is utilised in different applications. Some of the important applications of ferrofluids are their utilisation in sealing for rotating shafts and for the cooling and damping of loudspeakers. Apart from these, ferrofluids can be effectively used in level sensors, magnetic inks and there are various possibilities in biomedical applications as a carrier liquid. They are used in inclinometers, accelerometers and flow meters, tilt, vibration, pressure and level sensors, and various switches. Ferrofluids are being tested for their possible applications in electrical transformers. It can be used as the coolant, dielectric medium, as well as to increase the efficiency of the transformers. The stability and suitability of a ferrofluid for specific applications depend on various parameters, such as the surfactant, the suspension medium, viscosity of the fluid, characteristics of the magnetic particles, such as magnetisation, coercivity, size, shape, etc.

Furthermore, applications in biology, medical diagnosis and therapy require the magnetic particles to be stable in water at neutral pH and physiological salinity. For applications in biomedicine, there are various parameters that need to be considered during the synthesis of the nanoparticles.²⁰ Recently, great efforts have been made in the direction of developing aqueous ferrofluids for their biomedical applications. For *in-vivo* applications, the magnetic particles must be coated with a biological polymer so as to prevent the formation of large aggregates.²¹ The polymer will also allow bonding of drugs by

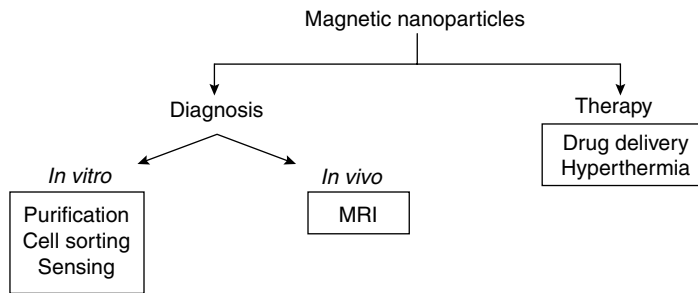


Fig. 21.10 Medical applications of magnetic nanoparticles.

covalent attachment, adsorption or entrapment on the particles. Important factors, which determine the biocompatibility and toxicity of these materials, are the nature of the magnetically responsive component. Nanoparticles of iron oxide, such as Fe_3O_4 and $\gamma\text{-Fe}_2\text{O}_3$, are the most commonly studied for biomedical applications. Highly magnetic materials such as cobalt and nickel, are toxic, susceptible to oxidation and hence are of little interest. The magnetic nanoparticles offer many exciting applications in biomedicine. The nanosized magnetic particles can get closer to the biological entity of interest. This is due to their controllable sizes to the dimensions that are smaller than or comparable to those of a cell, a virus, a protein or a gene. The fact that these nanoparticles are magnetic means that they obey Coulomb's Law, and therefore, can be manipulated by an external magnetic field gradient. This opens up an area of application, which involves transport and/or immobilisation of magnetic particles. In this way, they can be made to deliver a package, such as an anti-cancer drug to a targeted region of the body such as tumor cells. After the pioneering concept in 1960 that the fine magnetic particles could be transported through the vascular system with the aid of a magnetic field,²² the use of magnetic nanoparticles for delivery of drugs or antibodies to the organs or tissues altered by diseases has become an attractive field of research.

The major disadvantages of most chemotherapies lie in deleterious side effects as the drug attacks the normal healthy cells in addition to the target tumor cells. This has motivated the researchers to use the magnetic carriers to target specific sites within the body. Drug targeting can be passive, active or physical, depending on the properties of the drug and the carrier, specific targeting using specific recognition mechanisms and distribution through external mechanisms, such as magnetic field or heat. In magnetically targeted therapy, a drug is attached to the biocompatible magnetic nanoparticle carrier. These drug/carrier complexes, usually in the form of a biocompatible ferrofluid, are injected into the patient via the circulatory system. When the particles have entered the blood stream, external high gradient magnetic fields are used to concentrate the complex at specific target site within the body. Generally, in site-specific drug delivery, the magnetic components of the particles are coated with micelles, liposomes, and biocompatible polymers such as PVA, starch and dextran. However, they suffer from limitations including poor thermal and chemical stability and their rapid elimination by the immune system. In contrast, silica particles offer biocompatible, stable and stealthy alternatives. Also, the reactivity of the magnetic nanoparticles has been shown to be greatly increased when

their dimensions are reduced and the particles that are relatively smaller in size may undergo rapid biodegradation when they are directly exposed to biological environments. Formation of passive coating of silica on the surface of magnetic nanoparticles not only helps in preventing aggregation due to anisotropic dipolar attraction but also improves their chemical stability.

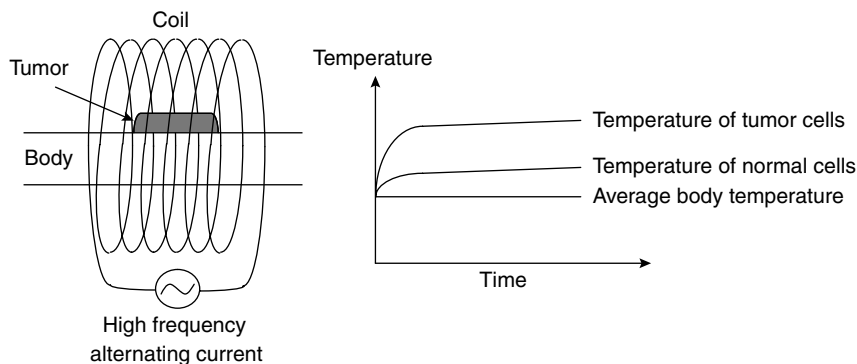


Fig. 21.11 Schematic illustration of magnetic hyperthermia treatment.

The magnetic nanoparticles can be made to resonantly respond to an ac magnetic field. The heat loss involved in the process of magnetisation has been explored for their use as hyperthermia agents, delivering sufficient thermal energy locally to a tumor cell, sparing the nearby healthy cells. Therefore, another exciting application of nanomagnetic particles in biology is as hyperthermia agent. Hyperthermia (means overheating in Greek) is a therapeutic procedure used to raise temperature of a region of a killing effect to temperatures above 41–42 °C. The majority of the hyperthermia devices are restricted in their utility because of unacceptable coincidental heating of healthy cells. Magnetic hyperthermia is, therefore, very exciting because it offers a way to ensure that only the target tissues are getting heated. Magnetic hyperthermia is expected to have fewer side effects when compared to radiotherapy and chemotherapy.²³

Magnetic hyperthermia can be achieved by using fine iron oxide particles. The physical principles by which a magnetic material can be heated by the action of an external alternating magnetic field are the heat loss process that occurs during the magnetisation. When a high-frequency alternating magnetic field is applied to the superparamagnetic nanoparticles, gradual alignment of the magnetisation takes place through the process of relaxation. The relaxation takes place by two mechanisms, the Brownian relaxation and the Neel relaxation. The Brownian relaxation relates to the rotation of the particle whereas the Neel relaxation is the rotation of the magnetic moment in each particle. The Brownian relaxation involves the rotation of the particle as a whole to align its magnetic moment along the direction of the magnetic field. Brownian relaxation dominates when the particles are of size less than 10-nm and the Neel relaxation dominates in larger particles. Higher heating rates can be achieved by the Brownian relaxation process. Magnetic hyperthermia can be used to destroy cancer cells, blood coagulation in small vessels, selective temperature increase in virus infected cells, and also for targeted drug delivery, where the drug molecules can be delivered at specific sites by a little heating. Magnetic materials with

a Curie temperature in the range 41–45 °C are preferred for use in magnetic hyperthermia, because it can take care of the effect of overheating. Once the temperature is increased, the material will be in the paramagnetic state so that the heating action will be automatically reduced.

Further, medical use of magnetic nanoparticles extends to modern diagnostic methods such as magnetic resonance imaging (MRI), taking advantage of the magnetic properties of hydrogen present in the body tissues.²⁴ MRI is based on the large number of protons present in the biological tissues having very small magnetic moments which release sufficient signal in the presence of large magnetic fields. The resonant absorption of radiofrequency waves in a large magnetic field (same as the principle of proton NMR) and the associated relaxation processes give rise to measurable signals. In many clinical situations, a contrast agent can greatly improve the diagnostic value of MRI. This is done by altering the relaxation of water by introducing colloidal superparamagnetic iron oxide particles, which play an important role as MRI contrast agent. The spin-lattice and spin-spin relaxation times (T_1 and T_2) are reduced by the use of a contrast agent. The superparamagnetic iron oxide nanoparticles largely affect T_2 , enhancing the quality of the image in the vicinity of the particles.

The MRI applications have steadily widened over the past decades. Currently, it is the preferred cross-sectional imaging modality in most diseases of brains, spine and musculo-skeleton system. The quality of the images can be enhanced by a contrast agent, which sharpens the contrast by affecting the behaviour of protons in their proximity. Magnetic nanoparticles with a size less than 10 nm have been developed as contrast agents for MRI. The superparamagnetic behaviour of these magnetic particles is similar to that of paramagnetic substances, in that they lose their magnetisation when the magnetic field is removed, but differ by value of the magnetic moments, which is significantly higher. Therefore, their relaxivities are much higher than those of paramagnetic contrast agents. Basically, the phenomenon may be described from the large magnetic-field heterogeneity around the nanoparticle, through which water molecules diffuse. Diffusion induces de-phasing of the proton magnetic moments resulting in T_2 (spin-lattice relaxation) shortening. Such contrast agents are also called susceptibility agents because of their effect on the magnetic field. Commercial iron oxide nanoparticles have been used as contrast agents in MRI.

Separation by adsorption is widely used in the chemical, biological, analytical, and environmental applications. Nanoparticles having high surface area are extremely useful for such applications. Nanoparticles have the advantage that the separation process is less resistive to diffusion because of the absence of pore structures. One of the most widespread uses of magnetic nanoparticles in biological systems is in magnetic cell separation. The magnetic nanoparticles are used in the form of “magnetic beads” where the magnetic nanoparticles are encapsulated in polymers. The cells are attached to the beads because of the hydrophilic or hydrophobic nature of the bead surfaces. Magnetic separation is a convenient method for the isolation or concentration of specific biological entities. In this case, the magnetic nanoparticles are first coated with a suitable biocompatible molecule, such as dextran or phospholipids. The free end of the attached molecules act as a link to the specific cells and are then targeted to the specific sites. The entities attached to the nanoparticles can be separated easily using a small magnetic field. Directly using magnetic nanoparticles or incorporating magnetism with the nonmagnetic nanoparticles is a promising method to facilitate the recovery and manipulation of the

used materials. Thus, magnetic nanoparticles offer wide applications in water purification, separation of components from a mixture, removal of radioactive wastes and as ion exchangers with the advantage that the used material can be easily recovered using an external magnet. It has been shown that the decontamination of low-level radioactive wastes can be achieved effectively and selectively by the use of magnetic nanoparticles coated with suitable molecules.²⁵ Magnetite nanoparticles coated with polyacrylic acid are found to be very effective as nanoadsorbents. It has been effectively demonstrated that arsenic can be removed from solution by sorption on Fe_3O_4 nanoparticles.²⁶ As particle size of Fe_3O_4 is decreased from 300 to 12 nm, the adsorption capacities for both As(III) and As(V) are increased nearly 200 times. Recently, it has been shown that Ni nanowires are superior to the magnetic beads both in purity and yield of the separated cell populations.²⁷ Hollow tubular structure of a magnetic nanotube is one of the most promising candidates for various applications. Magnetic nanotubes can be more effective than nanoparticles, because magnetic nanoparticles have the structural limitation when multi-functionality is required on the surface whereas nanotubes can be effectively used for different applications. The magnetic nanotubes can be from a magnetic material, or any other nanotubes coated with a magnetic material on the inner and/or outer surfaces. For example, drug-friendly interior and target-specific exterior of a nanotube can open a new field for the multifunctional targeted drug delivery and selective bioseparation.²⁸

Thus, in the recent years, nanotechnology places a vital role in providing a stage, where it is possible to produce, characterise and specifically tailor the magnetic nanostructures for many exciting applications. However, for certain applications, such as magnetic recording, there are limitations, and therefore, the future is unclear. Despite the numerous reports on the synthesis of magnetic nanoparticles and their use in biomedical applications, their large-scale use is still very limited. However, the exceptions to certain extent are magnetic separation which is found in most biomedical and biochemistry laboratories and MRI contrast enhancement using commercially available encapsulated superparamagnetic iron oxide particles. Investigations on targeted-drug delivery via coating of nanoparticles are still in the preliminary stage, though it has shown some promising results from trials on animals. Hyperthermia treatment of tumors is not yet accessible in humans, despite having been proven to be effective in animals. Therefore, one of the biggest challenges in biomedical applications of magnetic nanoparticles lies in dealing with the issue of technology transfer.

REFERENCES

1. C. Kittel, 'Domain theory and the dependence of the coercive force of fine ferromagnetic powders on particle size', *Phys. Rev.*, 73, (1948), 810–11.
2. J.F. Bobo, L. Gabillet and M. Bibes, 'Recent advances in nanomagnetism and spin electronics', *J. Phys.: Condens. Matter.*, 16, (2004), S471–96.
3. J.F. Gregg, I. Petej, E. Jouguelet and C. Dennis, 'Spin electronics—A review', *J. Phys. D: Appl. Phys.*, 35, (2002), R121–55.
4. B.D. Cullity, 'Introduction to Magnetic Materials', Addison Wesley, Reading MA, (1972).

5. D.J. Craik, R.S. Tebble and E.P. Wohlfarth, *Ferromagnetism and Ferromagnetic Domains*, North-Holland, Amsterdam, (1965).
6. F.J. Himpsel, J.E. Ortega, G.J. Mankey and R.F. Willis, 'Magnetic nanostructures', *Adv. Phys.*, 47, (1998), 511–97.
7. R.H. Kodama, 'Magnetic nanoparticles', *J. Magn. Mater.*, 200, (1999), 359–72.
8. C.P. Bean and J.D. Livingston, 'Superparamagnetism', *J. Appl. Phys.*, 30, (1959), S120–29.
9. Z.X. Tang, C.M. Sorensen, K.J. Klabunde and G.C. Hadjipanayis, 'Size-dependent Curie temperature in nanoscale MnFe_2O_4 particles', *Phys. Rev. Lett.*, 67, (1991), 3602–05.
10. S. Verma and P.A. Joy, 'Magnetic properties of superparamagnetic lithium ferrite nanoparticles', *J. Appl. Phys.*, 98, (2005), 1243121–29.
11. J.L. Dormann, D. Fiorani and E. Tronc, 'Magnetic relaxation in fine particle systems', *Adv. Chem. Phys.*, 98, (1997), 283–494.
12. J.T. Richardson and W.O. Milligan, 'Magnetic properties of colloidal nickelous oxide', *Phys. Rev.*, 102, (1956), 1289–94.
13. A. Sundaresan, R. Bhargavi, N. Rangarajan, U. Siddesh and C.N.R. Rao, 'Ferromagnetism as a universal feature of nanoparticles of the otherwise nonmagnetic oxides', *Phys. Rev. B.*, 74, (2006), 161306.1–161306.4.
14. O. Masala and R. Seshadri, 'Synthesis routes for large volumes of nanoparticles', *Annu. Rev. Mater. Res.*, 34, (2004), 41–81.
15. S. Sun, 'Recent Advances in Chemical Synthesis, Self-Assembly, and Applications of FePt Nanoparticles', *Adv. Mater.*, 18, (2006), 393–403.
16. N. Buske, H. Sonntag and T. Ggtze, 'Magnetic fluids—their preparation, stabilisation and applications in colloid science', *Colloids and Surfaces*, 12, (1984), 195–202.
17. D.A. Thompson and J.S. Best, 'The future of magnetic data storage technology', *IBM J. Res. Develop.*, 44, (2000), 311–22.
18. M.E. McHenry, M.A. Willard and D.E. Laughlin, 'Amorphous and nanocrystalline materials for applications as soft magnets', *Prog. Mater. Sci.*, 44, (1999), 291–433.
19. K. Raj and R. Moskowitz, 'Commercial applications of ferrofluids', *J. Magn. Mater.*, 85, (1990), 233–45.
20. P. Tartaj, M.P. Morales, S.V. Verdaguer, T. Gonzalez-Carreno and C.J. Serna, 'The preparation of magnetic nanoparticles for applications in biomedicine', *J. Phys. D: Appl. Phys.*, 36, (2003), R182–97.
21. E. Duguet, S. Vasseur, S. Mornet, G. Goglio, A. Demourgues, J. Portier, F. Grasset, P. Veverka and E. Pollert, 'Towards a versatile platform based on magnetic nanoparticles for *in-vivo* applications', *Bull. Mater. Sci.*, 29, (2006), 581–86.
22. M.W. Freeman, A. Arrot and H.H.L. Watson, 'Magnetism in Medicine', *J. Appl. Phys.*, 31, (1960), S404–05.
23. X. Wang, H. Gu and Z. Yang, 'The heating effect of magnetic fluids in an alternating magnetic field', *J. Magn. Mater.*, 293, (2005), 334–40.
24. R. Lawaczeck, M. Menze and H. Pietsch, 'Superparamagnetic iron oxide particles: Contrast media for magnetic resonance imaging', *Appl. Organometal. Chem.*, 18, (2004), 506–13.

25. R.D. Ambashta, P.K. Wattal, S. Singh and D. Bahadur, 'Nano-aggregates of hexacyanoferrate (II)-loaded magnetite for removal of cesium from radioactive wastes', *J. Magn. Mater.*, 267, (2003), 335–40.
26. C.T. Yavuz, J.T. Mayo, W.W. Yu, A. Prakash, J.C. Falkner, S. Yean, L. Cong, H.J. Shipley, A. Kan, M. Tomson, D. Natelson and V.L. Colvin, 'Low-Field Magnetic Separation of Monodisperse Fe₃O₄ Nanocrystals', *Science*, 314, (2006), 964–67.
27. A. Hultgren, M. Tanase, C.S. Chen, G.J. Meyer and D.H. Reicha, 'Cell manipulation using magnetic nanowires', *J. Appl. Phys.*, 93, (2003), 7554.
28. S.J. Son, J. Reichel, B. He, M. Schuchman and S.B. Lee, 'Magnetic Nanotubes for Magnetic-Field-Assisted Bioseparation, Biointeraction, and Drug Delivery', *J. Amer. Chem. Soc.*, 127, (2005), 7316–17.

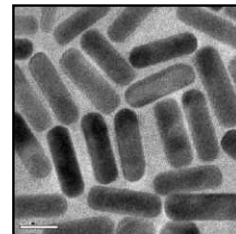
ADDITIONAL READING

1. A. Earnshaw, *Introduction to Magnetochemistry*.
2. D. Jiles, *Introduction to Magnetism and Magnetic Materials*.
3. K.H.J. Buschow and F.R. De Boer, *Physics of Magnetism and Magnetic Materials*.
4. J.P. Jakubovics, *Magnetism and Magnetic Materials*.
5. H. Martin, *Magnetism in Solids*.
6. J.L. Dormann and D. Fiorani (Ed.), *Magnetic Properties of Fine Particles*.
7. B. Berkovski (Ed.), *Magnetic Fluids and Applications Handbook*.
8. B. Aktas, L. Tagirov and F. Mikailov (Ed.), *Nanostructured Magnetic Materials and Their Applications*.
9. H.S. Nalwa (Ed.), *Magnetic Nanostructures*.
10. R. Hashemi and W.G. Bradley, *MRI: the Basics*.

REVIEW QUESTIONS

1. What are the different forms of magnetism?
2. What is superparamagnetism?
3. What is the difference between paramagnetism and superparamagnetism?
4. What is superparamagnetic limit for magnetic recording?
5. Define superparamagnetic blocking temperature and its relation to particle size.
6. What are magnetic domains? Distinguish between single domain and multidomain materials.
7. What is a magnetic hysteresis loop? What happens to coercivity when the particle size is reduced?
8. What is a magnetic core-shell structure?
8. What are the possible applications of magnetic nanoparticles?
10. Explain the principle of magnetic hyperthermia.
11. Explain the application of magnetic nanoparticles in MRI.

NANOBIOLOGY



“Almost all aspects of life are engineered at the molecular level, and without understanding molecules we can only have a very sketchy understanding of life itself.”

Francis Crick

What Mad Pursuit: A Personal View of Scientific Discovery (1988), 61

Nanobiology deals with fundamental understanding of interaction of nanomaterials with biological matter ranging from mRNA to DNA, proteins, organelles, cells, organs, system as a whole such as human body and other animal species which are all part of the eco-system. This understanding is critical in seeking answers for two basic questions: (i) How do the altered physico-chemical interactions of nanomaterials with biological systems adversely affect the normal functioning of biological systems at the molecular and macroscopic levels? (ii) How can the unique properties of nanomaterials be utilized to improve the fundamental understanding of biological systems and to develop new methods to identify and treat deadly diseases like cancer, AIDS, malaria, tuberculosis, etc. In this chapter, we present both fundamental and applied aspects of nanobiology. We specially emphasize on enquiry as to how different nanomaterials could find great applications in biology and medicine. In essence, this chapter highlights the merging of chemistry, biology, physics, materials science and engineering to give a new interdisciplinary subject, nano biology.

Learning Objectives

- What is nanomedicine?
 - What is the interaction between biomolecules and nanoparticles?
 - What are the nanosystems used for therapeutic applications?
 - What are the nanosystems used for diagnostic applications?
 - What are theragnostics and the role of nanomedicine in theragnostics?
-
-

22.1 INTRODUCTION

Medicine is a constantly evolving field. New concepts, diagnostic and therapeutic strategies are incorporated into daily practice on a regular basis. The factors deciding the introduction of new

technologies into medicine are: improved safety and efficiency, reduced cost and compliance of the current generation of medical practitioners toward the change. The marriage of nanotechnology and medicine has yielded an offspring that is set to bring momentous advances in the fight against a range of diseases.^{1,2} Realization of the usefulness of biotechnology has enabled a rapid progress in the concept of personalized medicine, which again is not a branch of medicine but simply indicates a trend in health-care and simply means the prescription of specific treatments and therapeutics best suited for an individual.³ Similarly, the introduction of nanobiotechnologies into medicine is not to create a new specialty, but simply aims at the improvement in the efficiency of current diagnosis and therapy, and this can be referred to as nanomedicine.

‘Nanomedicine’ is already a recognized term. The field is based on three mutually overlapping and progressively more powerful technologies:⁴

- (a) Nanoscale-structured materials and devices, which hold great promise for biosensors for advanced diagnostics, targeted drug delivery and smart drugs.
- (b) Benefits of molecular medicine via genomics, proteomics and artificially engineered micro-organisms.
- (c) Molecular machine systems such as nanorobots that will allow instant diagnosis with destruction of cause of pathology, chromosome replacement and individual cell surgery *in vivo* and the efficient augmentation and improvement in natural physiological function.

Since the last edition of this book, nanotechnology and its applications in medicine have grown by leaps and bounds. Development of novel diagnostic tools has allowed imaging of molecular pathways at the sub-cellular level, thus early detection of pathological conditions even before the symptomatic manifestations of the disease. Starting from ‘effective drug delivery’, it has evolved to ‘targeted drug therapies’ or “smart drugs” which, apart from being more effective, have lesser side effects. Also, novel strategies like hyperthermia therapy using nanoparticles are being extensively studied. We will be discussing the chapter under the following sub-titles:

1. Interaction between biomolecules and nanoparticle surfaces
2. Applications of various nanomaterials in biology
 - (i) Therapeutics
 - (ii) Diagnostics
 - (iii) Theragnostics
3. Challenges
4. Conclusion and future perspectives

22.2 INTERACTION BETWEEN BIOMOLECULES AND NANOPARTICLE SURFACES

One of the objectives in nanotechnology is to pack the nanoparticles in ordered arrays with the ability to tailor the size and the inter particle distance. While assembly of nanoparticles from solution into

hexagonally close-packed monolayers and super lattice structures on solid surfaces has met with a fair degree of success, the progress on controlled assembly of nanoparticles in solution has been relatively slower. The construction of three-dimensional arrays of nanoparticles in aqueous phases can be achieved by bioconjugation, the phenomenon in which intermolecular interactions lead to assembly. The interaction of nanoparticles functionalized with conjugate biomolecules can lead to the formation of desired superstructures in aqueous phases. The first step in this direction, leading to the construction of hybrid bio-nano assemblies, were taken by the groups of Mirkin⁵ and Alivisatos,⁶ who demonstrated that DNA-modified nanoparticles could be assembled into superstructures by hybridization of complementary base sequences of the surface-bound DNA molecules. From a fundamental point of view, Mirkin *et al.* have used this strategy to critically study the role of inter particle separation⁵ and aggregate size on the optical properties of DNA-modified colloidal gold solution. Other interactions such as the biotin-avidin molecular recognition process, hydrogen bonding between suitable terminal functional groups bound to the nanoparticle surface, electrostatic assembly on DNA templates, and control over electrostatic interactions stabilizing nanoparticles in aqueous phase, have been used to construct the nanoparticle assembly in solutions.⁷ Capping of the silver particles with cysteine was accomplished by a thiolate bond between the amino acid and the nanoparticle surface. The silver colloidal particles were stabilized electrostatically by ionizing the carboxylic acid groups of cysteine. The amino acid, cysteine ($\text{H}_2\text{N}-\text{CH}(\text{CH}_2\text{SH})-\text{CO}_2\text{H}$) plays an important role in defining the tertiary structure of proteins through disulfide (cystine) bridges.⁸

Main biophysicochemical influences on the interface between nanomaterials and biological systems are described below:⁹

Nanoparticle properties:

- (i) Size, shape and surface area
- (ii) Electronic states
- (iii) Surface charge, surface energy
- (iv) Roughness and porosity
- (v) Functional groups
- (vi) Ligands
- (vii) Crystallinity and defects
- (viii) Hydrophobicity
- (ix) Hydrophilicity

Solid-liquid interface properties:

- (i) Surface hydration and dehydration
- (ii) Surface reconstruction
- (iii) Ion adsorption and charge neutralization
- (iv) Electrical double-layer formation
- (v) Zeta potential and isoelectric point

- (vi) Sorption of steric molecules and toxins
- (vii) Electrostatic and electrosteric interactions
- (viii) Aggregation, dispersion and dissolution
- (ix) Hydrophilic and hydrophobic interactions

Suspending media:

- (i) Water
- (ii) Acids and bases
- (iii) Salts and multivalent ions
- (iv) Natural organic matter (proteins, lipids)
- (v) Surfactants
- (vi) Polymers
- (vii) Polyelectrolytes

Nano-bio interface:

- (i) Particle-membrane interactions
- (ii) Receptor-ligand interactions
- (iii) Membrane wrapping
- (iv) Biomolecule interactions
- (v) Free energy transfer to biomolecules
- (vi) Conformational change in biomolecules
- (vii) Oxidant injury to biomolecules
- (viii) Mitochondrial and lysosomal damages

22.3 INFLUENCE OF ELECTROSTATIC INTERACTIONS IN BINDING OF PROTEINS TO NANOPARTICLES

In the case of gold nanocomposites, it is suggested that each particle has an Au (0) core and an Au (I) surface, as a result of preferential adsorption of Au (I) ions on the surface at the time of its formation. Citrate ions coordinate to the Au (I) atoms on the surface, giving an overall negative charge for each particle. Nanoparticles are capable of binding to oppositely charged species in aqueous solutions through electrostatic interactions based on the ionic characteristics of their surfaces¹⁰. Amphiprotic species, such as peptides and proteins, have unique isoelectric points (pI). When the pH of a protein solution is below the value of the pI of the protein, the protein molecules attain a net positive charge. That means, by increasing the pH from 0 to 14, the molecules become more and more negatively charged due to increased extent of removal protons. At certain intermediate pH, molecules will have a net zero charge. This point is called the isoelectric point (pI) of the protein under consideration. Below the pI value, the molecule is positively charged. Under such a condition, negatively charged gold nanoparticles tend to attract positively charged protein molecules. On the other hand, if the pH

of a protein solution is above the pI , the protein molecules are negatively charged and hence, would repel any negatively charged gold nanoparticles in the vicinity. Thus, while considering the nature of interaction of the biomolecule and nanoparticle, it is very clear that the interaction is electrostatic in nature. The electrostatic force of attraction between two opposite point charges is given by,

$$\text{Electrostatic force, } F = (1/4\pi\epsilon) (q_+q_-/r^2)$$

Here, ϵ is the permittivity, r is the distance between the point charges, q_+ and q_- are the quantities of positive and negative charges, respectively. For simplicity, we can consider r and q_- (the charge on the nanoparticle surface) to be constants.

Thus, the electrostatic force between the biomolecule and nanoparticle,

$$F \propto q_+, \text{ the net charge on the biomolecule.}$$

From the above equation, it is clear that the pI is the key factor in the binding of the biomolecule on the nanoparticle. Above the pI value, there is no attraction between the biomolecule and the nanoparticle, because, the biomolecule becomes negatively charged. The binding of proteins on nanoparticle surfaces as a function of pH is illustrated by matrix assisted laser desorption ionization mass spectrometry (MALDI TOF MS). The pI values of cytochrome c and myoglobin are 10.6 and 7, respectively.¹¹

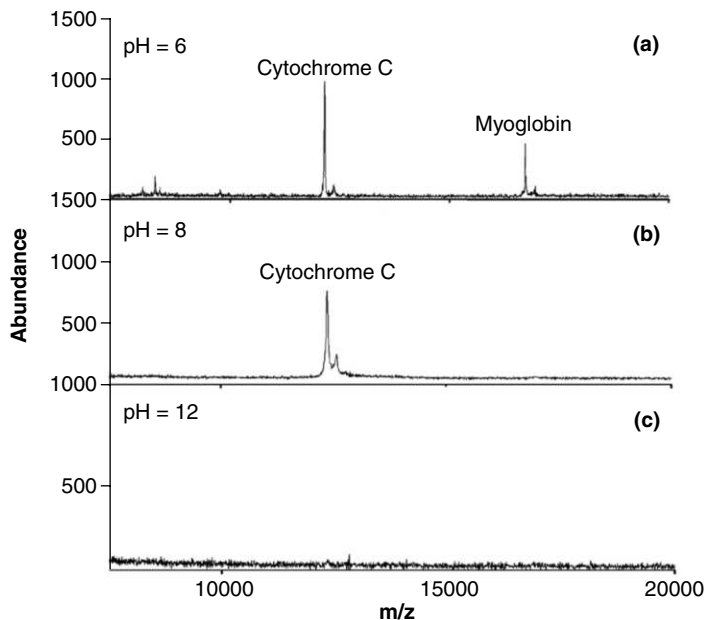


Fig. 22.1 MALDI TOF mass spectra obtained from a mixture of cytochrome c and myoglobin at (a) pH 6, (b) pH 8 and (c) pH 12.¹²

The absence of adsorption of cytochrome c and myoglobin on gold nanoparticles, in solutions with pH higher than their pI values, is reported by Teng *et al.*⁸ Aqueous solutions containing both

cytochrome c and myoglobin have been employed to demonstrate this fact (Fig. 22.1): At pH 6, both cytochrome c and myoglobin were detected (Fig. 22.1a), at pH 8, only cytochrome c was detected (Fig. 22.1b), and neither is observed at pH 12 (Fig. 22.1c).¹³ These results demonstrate that isoelectric point of a protein plays an important role in bonding between a nanoparticle and the protein. Thus, gold nanoparticles can be used to bind to one or more proteins in a solution containing a mixture of proteins by adjusting the pH.

22.4 THE ELECTRONIC EFFECTS OF BIOMOLECULE-NANOPARTICLE INTERACTION

When a biomolecule interacts with a noble metal nanoparticle, surface charge density of both the nanoparticle and the biomolecule get perturbed. This perturbation of surface electron density is manifested in the change in the electronic spectrum of both the nanoparticle and the biomolecule. The functional groups of the molecules which are close to the nanoparticle surface get more perturbed. The binding of biomolecule can affect the surface plasmon resonance of the nanoparticle. Sometimes, this interaction can be manifested in the assemblies of nanoparticles and biomolecules. The surface electron density of the spherical nanoparticle is spherically symmetric. The perturbation to charge density of nanoparticle induced by the interaction with biomolecule is isotropic. But, in the case of noble metal nanorods, their charge density is anisotropic. Hence, the interaction with biomolecule can lead to anisotropic perturbation of electron density of the nanorod. The difference in the interactions of biomolecule with nanorod and with nanoparticle is manifested in UV/Visible spectrum. Surface plasmon resonance (SPR) of noble metal nanoparticles is due to the polarized oscillations of electron cloud, induced by the oscillating electric field of the incident electromagnetic wave, according to Mie's theory. This phenomenon is highly sensitive to the dielectric constant of the micro environment around the nanoparticle. Thus, such an interaction with a biomolecule can be manifested as alterations in the SPR band. Molecular diameter of a biomolecule is a key factor which decides the biomolecule—nanoparticle interaction. Bigger molecules form stable nano-bio conjugates. They form thicker shells around the nanoparticles. Such shell-formations can prevent the aggregation of nanoparticles. As an example, we can consider the interaction between an antibiotic vancomycin and gold nanoparticle.¹⁴

The changes in the SPR band of the nanoparticle and the dimensions of the interacting molecule are directly related. In Fig. 22.2, the dashed line corresponds to the free nanoparticle. After the capping of vancomycin, the SPR band is broadened and slightly shifted from 520 to 528 nm. This indicates the change in the dielectric constant of the micro environment around the gold nano core. The formation of aggregated structures is well observable from the SPR features of the Au@cysteine, including the shifting of SPR band to 631 nm as well as the increase in background intensity. Similar kind of an aggregation is reported for cysteine-capped silver nanoparticles (Ag@cysteine). In contrast, the effect of vancomycin-capping is different: The bare nanoparticles (AuNP) stabilized with tetra N-octylammonium bromide show a SPR band at 520 nm. After capping with vancomycin, the SPR feature has no significant shift. This indicates that, due to bigger molecular diameter of vancomycin, the nanoparticle aggregation is absent.

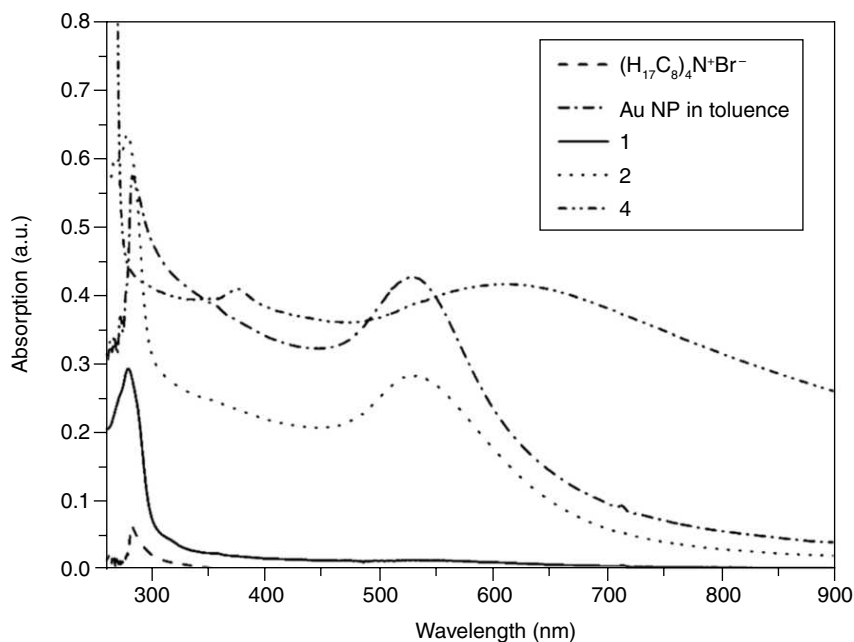


Fig. 22.2 UV/Visible spectrum of (1) vancomycin, (2) Au@vancomycin and (4) Au@cysteine.¹⁴

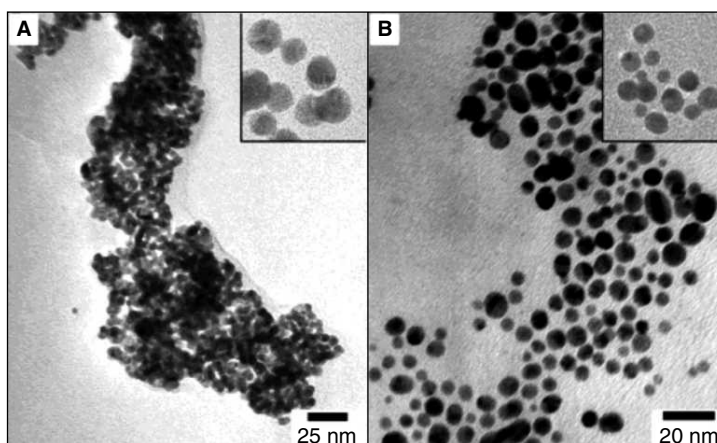


Fig. 22.3 TEM images of (A) cysteine- and (B) vancomycin-capped gold nanoparticles in the aggregated state after cryodrying at concentrations of 6.7 and 50 $\mu\text{g/mL}$.¹⁴

The TEM image (Fig. 22.3 A, B) clearly illustrates the difference between the interactions of bigger biomolecules and of smaller biomolecules with the nanoparticle. In the TEM image, Au@cysteine shows an aggregated structure, while the Au@vancomycin shows well-separated particles. The latter indicates a thicker shell of vancomycin around the gold core which prevents the aggregation of nanoparticles. Similar observations are reported in the case of cytochrome c-capped nanoparticles.¹⁵

Absence of nanoparticle aggregation is due to electrostatic repulsion between thicker cytochrome c shells of neighboring nanoparticles. Also, due to the formation of aggregates or scaffolds in bio-nano hybrid system, two nano particles may come close to each other. As a result, their electron clouds influence each other. This kind of perturbation can be manifested as coupling between the SPR bands. In the case gold nanoparticle—biomolecule hybrid systems, this inter plasmon coupling is isotropic. But, in the case of gold nanorod-biomolecule hybrid systems, the inter plasmon coupling is anisotropic. This kind of electronic interactions are manifested in color changes of both gold nanoparticles and nanorods after binding with biomolecules. This observation can be used for developing cheaper and efficient technologies for medical diagnosis, proteomics, genomics and biotechnology. In 2005, Thomas *et al.*¹⁶ reported the inter plasmon coupling of cysteine-capped and glutathione-capped Au nanorods. Gold nanorods possess two plasmon absorption bands. In the case of both cysteine and glutathione, a dramatic decrease in the intensity of the longitudinal surface plasmon absorption band, with a concomitant formation of a new band, was observed (Fig. 22.4). The appearance of a new band at 850 nm in the presence of cysteine/glutathione results from the coupling of the plasmon oscillations of Au nanorods. The longitudinal alignment of nanorods, after the binding of cysteine and of glutathione, has resulted in the anisotropic coupling of SPR band.

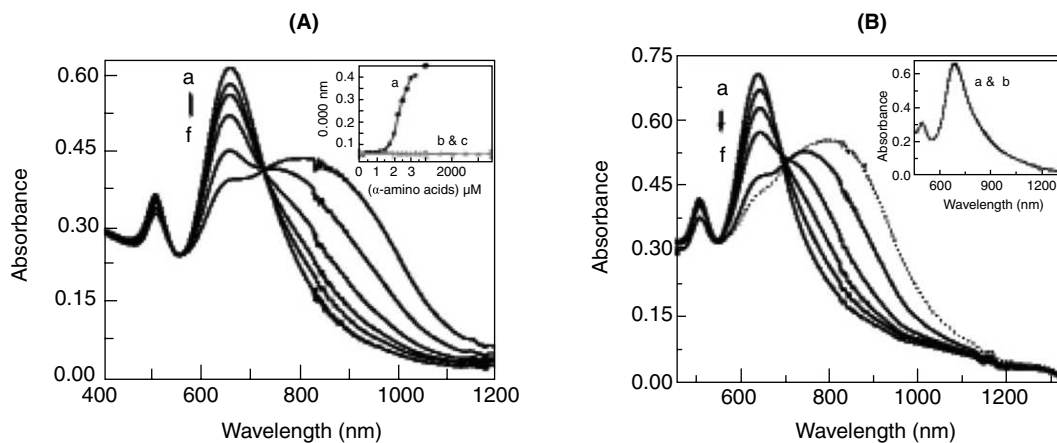


Fig. 22.4 (A, B) Absorption spectral changes of Au nanorods (0.12 nM) in acetonitrile/water (4:1) on addition of (A) cysteine at (a) 0 (b) 1.75 (c) 2.0 (d) 2.25 (e) 2.5 and (f) 3 μM or (B) glutathione at (a) 0, (b) 7, (c) 9, (d) 11, (e) 13, and (f) 14 μM . Figure 22.3A (inset): changes in optical density at different concentrations of (a) cysteine, (b) tyrosine, and (c) leucine. Figure 22.3B (inset): effect of addition of 1-hexylmercaptan at (a) 0 and (b) 10 μM ¹⁶.

22.5 APPLICATIONS OF NANOMATERIALS IN BIOLOGY

22.5.1 Therapeutic Applications

Although, conventional chemotherapeutic agents are relatively specific, they also kill normal cells which are dividing very rapidly such as cells in gastrointestinal tract, bone marrow cells, and hair

follicles. This causes some of the side effects of chemotherapy, including gastrointestinal distress, low white blood cell count and hair loss. Moreover, many of the clinically used chemotherapeutics require high tissue concentrations which are associated with systemic toxicity. Hydrophobic drugs, which are administered intravenously with solubilizing adjuvant like ethanol or Cremophor EL, often cause toxic side effects. Drug resistance has emerged as a major obstacle limiting the therapeutic efficacy of chemotherapeutic agents. These mechanisms allow tumors to evade chemotherapy. For example, multidrug resistance (MDR), a term to describe the broad spectrum resistance to chemotherapy in human cancer, is one of the most important problems in chemotherapy. MDR is the phenomenon in which exposure of tumor cells to a single cytotoxic agent accounts for cross-resistance to other, structurally unrelated, classes of cytotoxic agents.

Therefore, improving the therapeutic index by increasing the therapeutic effects to tumor cells with decreasing toxicity to normal cells is a central issue in improving cancer therapy. Delivering therapeutically active molecule to a target site is a challenging task. Poor aqueous solubility and non specific targeting are limitations of current treatment methods. Nanostructures have the potential to overcome these limitations by acting as carriers for therapeutic agents, such as drugs, genes etc., targeted to specific cancer cells and used as imaging agents.¹⁷ Recent developments in nanomedicine for cancer treatment surmount various challenges in this field.

Rationale for developing nanomaterials for cancer treatment includes: (i) multifunctionality (ii) increased potency and multivalency (iii) increased selectivity for targets (iv) theragnostic potential (v) altered pharmacokinetics (vi) controlled synthesis (vii) controlled agent release and kinetics (viii) novel properties and interactions (ix) lack of immunogenicity and (x) enhanced physical stability.¹⁸

Box 22.1 Definition of Nanomaterial Cancer Drugs¹⁸

- Size: 1–100 nm in dimension
- Agents are composed of synthetic materials, at least in part
- The size and shape confer unique properties
- The agent is multi functional
- The agent is multimeric

Nanoparticle-mediated delivery of cancer therapeutic agents can be done either by passive targeting or by active targeting (Fig. 22.5). In the case of passive targeting, a drug loaded nanoparticle enters into the tumor tissue owing to the enhanced permeability and retention effect (EPR) provided by the anatomical and pathophysiological abnormality of tumor vasculature. EPR effect is considered as a gold standard in the design and development of anticancer nanomedicines. Important hallmarks of EPR effect includes, extensive angiogenesis, imperfect vascular architecture and impairs lymphatic drainage system of the tumor. It is reported that this enhanced permeability of tumor tissue is due to the elevated levels of bradykinin, nitric oxide, peroxynitrite, vascular endothelial growth factors etc. Hence, the drug-loaded nanomaterials can extravasate through the leaky architecture of tumor

vasculature. The absence of lymphatic drainage from the tumors causes retention of the nanodrugs at the site of the lesion. Active targeting utilizes specific biomarkers, such as cell surface receptors, for specifically targeting tumor tissues. Active targeting improves relative tumor localization. At the target site, the cells will internalize the nanoparticle and accumulate the therapeutic agents and thus, enhancing the efficiency. Monoclonal antibodies specific to the antigens over expressed in cancer cells are the major targeting ligands. Other targeting moieties for cancer therapy are listed in Table 22.1. Examples for cancer associated targets are listed in Box 22.2. In addition, therapy can be achieved by means of externally applied stimuli to the nanoparticles as well as localized sustained delivery of drug during surgical intervention of tumors.

Table 22.1 *Ligands for active cancer targeting*

Type	MW (KDa)	Dimension (nm)	Features
Monoclonal antibodies			
Whole antibodies	15	15–20	High affinity, divalent, may clinically approved examples, contains biologically active constant (Fc) region long circulation
Engineered fragments (Monovalent)			
ScFv	25	3–5	Lowered affinity, rapid clearance from circulation, renal retention. Reduced stability, reduced immunogenicity
Fab'	50	5–10	Can be produced genetically or enzymatically by cleavage of monoclonal antibodies
Nanobody	15	2–3	Smallest antigen-binding fragment, single domain, can bind cryptic epitopes
Engineered fragments (Divalent)			
F(ab') ₂	100	10–15	Improved affinity, can be engineered to a variety of sizes and arrangements of protein domains
Diabodies	50–80	5–10	Monospecific or bi-specific dimer or ScFv
Minibodies	80	10	Can be produced genetically
Aptamers			
RNA	10–30	2–3	Rapid clearance, automated chemical synthesis, susceptible to nucleases without chemical modification
DNA	10–30	2–3	Rapid clearance, automated chemical synthesis, susceptible to nucleases without chemical modification
Receptor ligands			
Peptides	0.5–10	Variable	Facile synthesis and modification, diverse libraries and screening technologies, susceptible to peptidase, renal retention
Whole protein	30–150	Variable	Produced using recombinant DNA technologies, can be biologically active, susceptible to protease
Small molecules	0.1–	0.5–2	Chemical synthesis, simple modification and coupling chemistries, can be biologically active, highly variable affinities

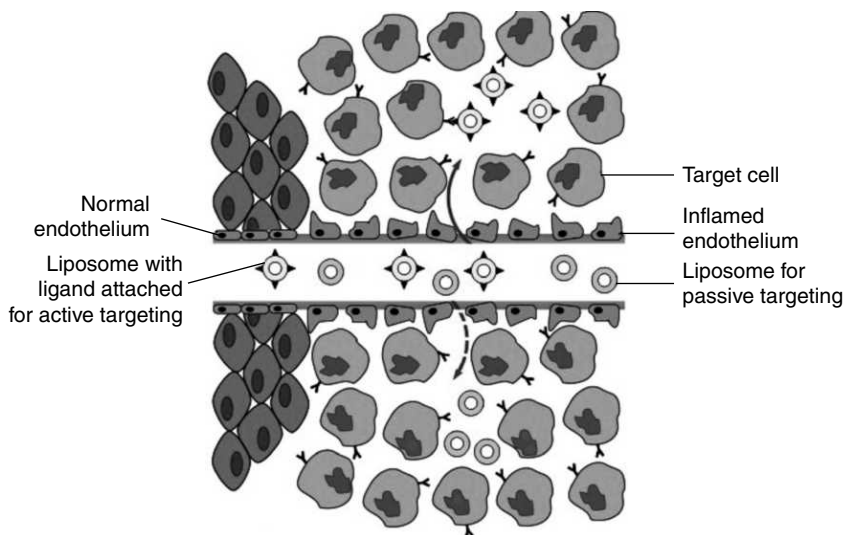


Fig. 22.5 *Passive (liposome) and active (liposome with targeting ligand) drug targeting to tumor site. Passive accumulation of liposomes is essentially due to non specific EPR effect. Active targeting is by specific interactions of the ligands with tumor cells¹⁹.*

Development of nanomedicine is a complex procedure. Since these new agents are similar to the devices exposed to blood stream, they should have similar effects as that of medical devices such as grafts, catheters, valves etc. Hence, their effect on hemolysis, thrombosis and platelet aggregation etc. should be studied prior to clinical application. Steps involved in the development of nanomedicine are described in Fig. 22.6.

Box 22.2 Cancer Associated Targets

Hematologic antigens

- B cells: CD19, CD 20, CD 21, CD22, CD 23
- T cells: CD4, CD 25, CD 30
- Myeloid precursors: CD 33, CD 66

Solid tumor antigens

- Colon: Integrin, A33 glycoprotein, Tag 72, epithelial cell adhesion molecule (EpCAM)
- Breast: Her2/neu, Lewis-Y, carcino embryonic antigen (CEA)
- Prostrate: Prostrate-specific membrane antigen (PSMA), Prostrate stem cell antigen (PSCA)
- Other: GD2 ganglioside (glioblastoma), MUC1 mucin like glycoprotein (Pancreatic cancer), folate receptor (FR), epidermal growth factor receptor (EGFR), transferrin receptor (TfR)

Vascular antigens

- Vascular endothelial cadherin (VE-cadherin), vascular endothelial growth factor receptor (VEGFR), integrins (such as alpha V-beta -3)

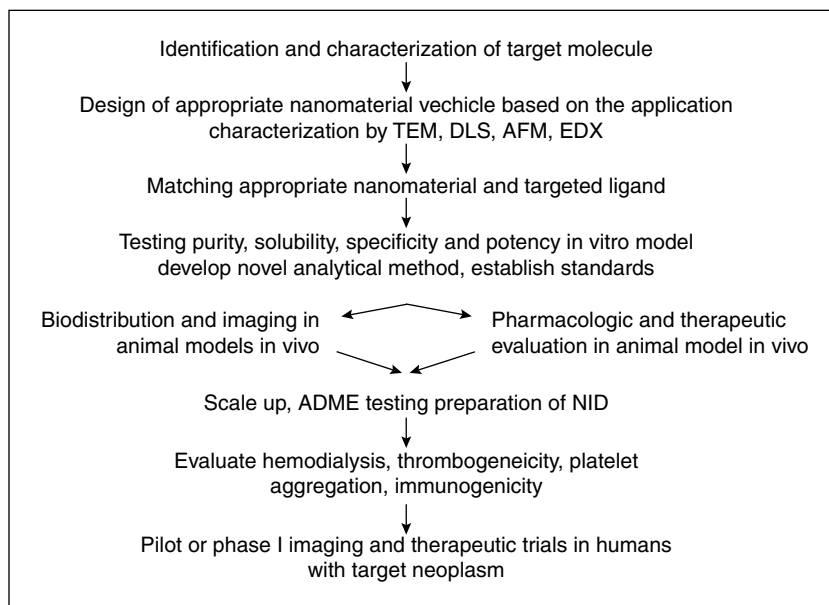


Fig. 22.6 *Some proposed steps in the development of a nanomaterial anti-cancer agent.*

First generation nanomedicines were centered on the concept of improving the bio-availability and reducing the toxicity of some of the clinically used, highly hydrophobic drugs such as paclitaxel, doxorubicin etc. The best examples are AbraxaneTM, which is albumin bound paclitaxel, and Doxil, which is a liposomal formulation of Doxorubicin. Both of these nanomedicines are approved for clinical use and found to be highly successful in improving the specificity with minimal toxic side effects. Abraxane uses albumin to deliver chemotherapeutic agent without chemical solvents such as CremophorTM. Moreover, premedication with steroids reduces the risk of hypersensitivity reactions. Side effects of this formulation were less and the overall response rate was superior to that of Taxol (Paclitaxel). DOXIL is a pegylated liposome-encapsulated form of doxorubicin, used mainly for treating Kaposi's sarcoma, ovarian cancer and multiple myeloma. Other formulations that are in clinical trials include DaunoXome, Myoset and Oncaspar.

22.5.1.1 Polymers

Nanoparticles used for anticancer drug delivery can be made from a variety of materials such as polymers, dendrimers, liposomes, viruses, carbon nanotubes and inorganic materials. Several polymers are suitable for nanoparticle synthesis. They have excellent drug- and protein-loading/releasing properties with enhanced shelf life. The essential characteristics of polymeric nanoparticles are biocompatibility, biodegradability, ease of surface modification through chemical transformations, high entrapment efficiency, excellent pharmacokinetic control and ability for controlled drug release. Commonly used polymeric materials include poly-lactic acid (PLA), polyglycolic acid (PGA), polylactic glycolic acid (PLGA), poly caprolactone (PCL), polyglutamic acid, polymalic acid (PMA) and their copolymers.²⁰ Figure 22.7 shows a schematic representation of drug loaded PLGA nanoparticle. Polyethylene glycol

(PEG) is another extensively studied polymer used for drug delivery application. It is hydrophilic in nature and hence used to coat the surfaces of other nanoparticles. PEG coating improves the stability and bioavailability of nanoparticles considerably.²¹ Polymeric nanoconjugates constitute another effective carrier system for nanomedicine. They have several functional groups on their surfaces and are useful in conjugating with biochemically active groups so as to direct them towards tumor tissue¹⁷. Since a single nanoconjugate can accommodate several targeting ligands, nanoconjugates can be efficiently used to kill cancer cells by inhibiting several signaling pathways. Polymeric nanocarriers, currently in the clinical trials, include N-(2-hydroxypropyl) methacrylamide copolymer, camptothecin [MAG-CPT],²² Paclitaxel poliglumex [Xyotax],²³ HPMA-DOX [PKI].²⁴ HPMA Dox exhibited a 5-fold reduction in anthracycline-related toxicity and enhanced antitumor activity. Xyotax was reported to be effective for patients with non-small-cell lung cancer in phase III clinical trials.

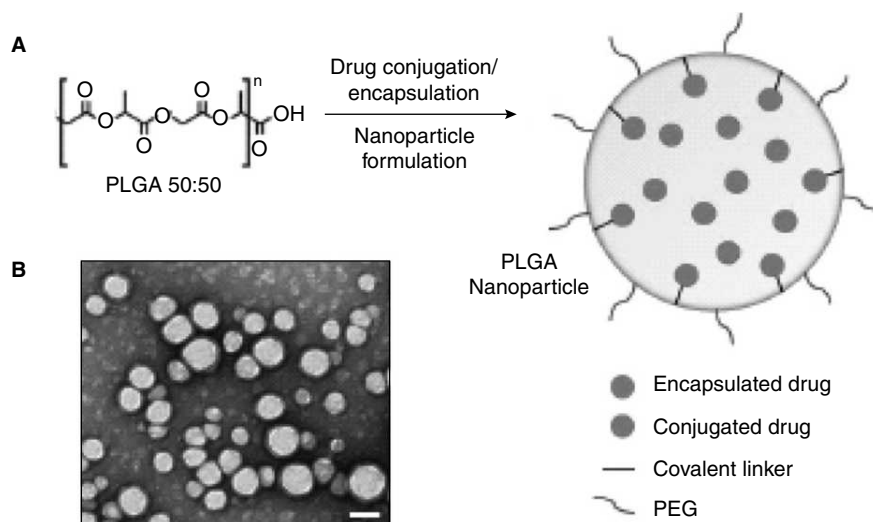


Fig. 22.7 (A) PLGA as a nanoparticle formulation with chemical conjugation or simple encapsulation of chemotherapeutic agents, with PEG modification. (B) Transmission electron microscopy image of PLGA nanoparticle.²⁵

22.5.1.2 Micelles

Micelles are small spherical, colloidal particles with size 1–100 nm, formed by self assembling molecules such as amphiphilic diblock or triblock—opolymers. Sizes of micelles depend on the chemical nature of the drug and the micelle core. Micelles have core shell architecture which consists of two distinct regions: a hydrophilic head and a hydrophobic tail in aqueous media. Figure 22.8 showing schematics of NK012, a nanomicellar assembly, made up of self assembled amphiphilic block copolymer of polyethylene glycol-polyglutamic acid incorporated SN-38 which is an active metabolite of topoisomerase I inhibitor. At low concentrations in an aqueous medium, the components exist as separate monomers. However as concentration increases, they agglomerate to form typical micelles.

The concentration of monomers at which this agglomeration takes place is known as critical micelle concentration (CMC). The CMC of a micelle depends on the composition and type of block copolymer²⁶, and is usually in the order of 10^{-6} to 10^{-7} M for polymers and is very low compared to CMC of low molecular weight surfactants. Moreover, polymeric micelles remain stable at very low polymer concentrations, resulting in enhanced circulation time compared to surfactants.²⁷ Figure 22.9 demonstrates the biodistribution and tumor accumulation of targeted and non targeted block copolymer micelles.

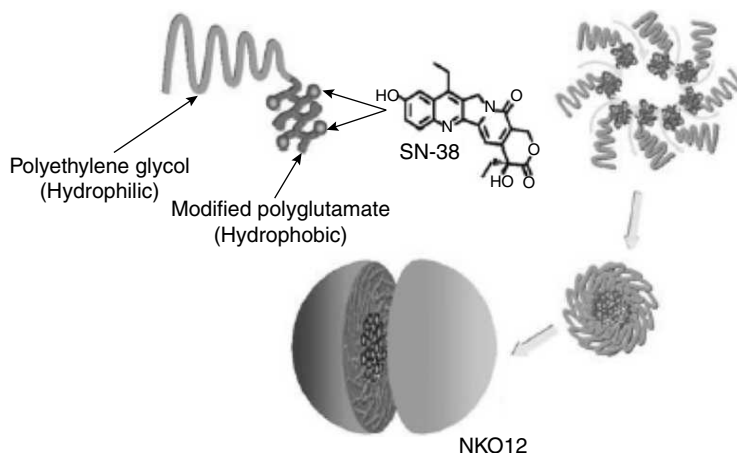


Fig. 22.8 Schematic structure of NK012, consisting of PEG and partially modified polyglutamate. PEG is used to form the hydrophilic segment, and SN-38 was incorporated into the hydrophobic core of the micelle.²⁸

22.5.1.3 Liposomes

Liposomes are self-assembled, colloidal nanostructures with globular shape, composed of a lipid bilayer which encapsulates a central aqueous liquid. The lipid bilayer of liposome can fuse with cell membrane at the site of interest and deliver its contents in to the cytoplasm (Fig. 22.10). Liposomal formulations of therapeutic agents show enhanced pharmacokinetics and pharmacodynamics. Liposome-based formulations of anticancer agents, such as a *stealth* liposomal doxorubicin (Doxil), liposomal daunorubicin (DaunoXome) and liposomal doxorubicin (Myocet), have been approved for the treatment of metastatic breast cancer. Liposome conjugated with an antibody specific to CD44 has shown improved therapeutic efficacy.³⁰ Cisplatin, an anti cancer agent with poor efficacy, exhibited enhanced results when loaded in antibody-conjugated liposomes.³¹ Several studies have been reported on the influence of pegylated liposomes in treatment of metastatic stomach cancer. Small interfering RNA (siRNA)-mediated therapy is potential for the treatment of pediatric bone and soft tissue sarcomas such as Ewing sarcoma, rhabdomyosarcoma and synovial sarcoma.³² Moreover, exciting applications to pediatric cancer therapeutics using liposome-mediated siRNA involve neuroblastoma, chronic myeloid leukemia and hepato blastoma. In addition, liposome-mediated siRNA delivery has

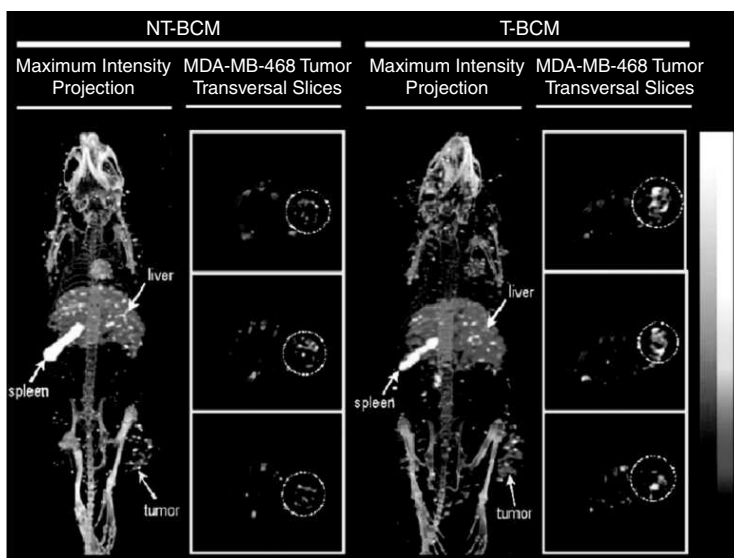


Fig. 22.9 *MicroSPECT/CT images illustrating the whole body biodistribution of the non-targeted block copolymer micelles (NT-BCM) and targeted block copolymer micelles (T-BCM) labeled with ^{111}In in MDA-MB-468 tumor-bearing mice. The images were acquired at 48 h post injection.²⁹ (For clarity see colour figure.)*

been successful in case of several adult malignancies such as melanoma, lung cancer, breast cancer and ovarian cancer. Liposomal formulations that are available and currently in pediatric clinical trials include Depocyte “Cytarabine”, 1-Annamycin “Annamycin”, Marquibo “Vincristine sulfate”, ThermoDox “Doxorubicin” and CPX-351 “Daunorubicin + Cytarabine”³².

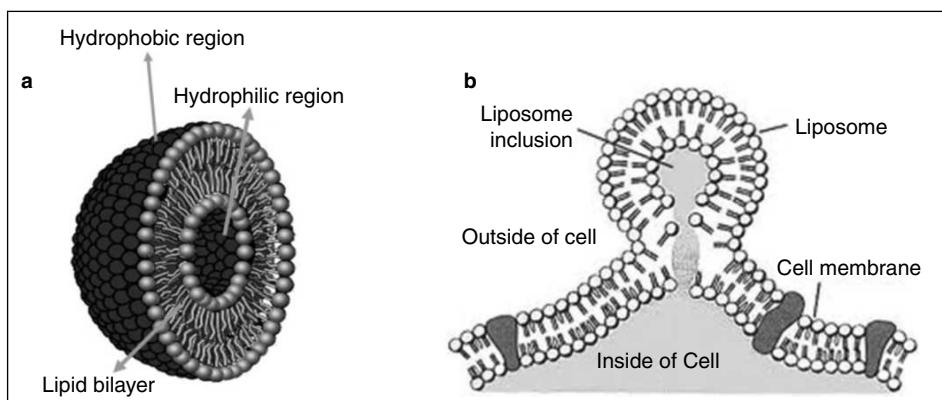


Fig. 22.10 *(a) 3D structure of liposome demonstrating the lipid bilayer encapsulating a central aqueous core. (b) Fusion of lipid bilayer of liposomes to the cell membrane with internalization of its contents (adapted from <http://www.nanoconductor.org/gallery/>, thehormoneshop.net).*

22.5.1.4 Protein Nanoparticle

Protein-based nanomedicine platforms for drug delivery comprise of naturally self-assembled protein subunits of the same protein or a combination of proteins making up a complete system. They are ideal for drug-delivery platforms due to their biocompatibility and biodegradability coupled with low toxicity. A variety of proteins have been used and characterized for drug-delivery systems including the ferritin/apoferritin protein cage, plant-derived viral capsids, the small Heat shock protein (sHsp) cage, albumin, soy and whey protein, collagen and gelatin.^{33, 34, 35} Protein-based templates used in the development of nanoparticles for drug delivery include elastin-like polypeptide, cationic bovine serum albumin, human serum albumin and gliadin. Albumin-based drug delivery system is made by combining albumin and paclitaxel to form Abraxane. It is now a FDA-approved nanomedicine for treatment of metastatic breast cancer.^{36, 37}

22.5.1.5 Inorganic Nanomaterials

22.5.1.5.1 Gold Nanoparticles

Gold nanoparticles are the most efficient inorganic platform for drug delivery application. Synthesis techniques for gold nanoparticles having size scale of 1–150 nm with limited dispersity have been well established.³⁸ They are non-toxic, biocompatible and inert. Furthermore, using ligand place-exchange reactions, multifunctional monolayers can be fabricated, thereby leading to the development of multiple targeting agents.³⁹ Several studies on the use of gold nanoparticle for drug delivery application have been reported. Visaria *et al.* described the delivery of TNF- α using PEG-coated gold nanoparticle and thereby maximizing the tumor damage with reduced systemic toxicity.⁴⁰ In addition, a combinational therapy, which uses heating as well as delivery of TNF- α , showed enhanced therapeutic effect than that of gold nanoparticle alone. Phase 1 clinical trial of gold nanoconjugate, called CYT-6091, has been going on in order to study the pharmacokinetics and pharmacodynamics of this formulation⁴⁰. Another nanomedicine, MTX-Gold nanoparticle conjugate, where gold particles are conjugated with methotrexate, an inhibitor of dihydrofolate reductase, is reported to have enhanced anti tumor effect *in vitro* and *in vivo*.⁴¹ Controlled release of doxorubicin was achieved by a tumor mRNA-dependent nanogold drug carrier in breast cancer cells.⁴² Development of photothermally modulated drug delivery system using nanoshell is also established, wherein, irradiation of nanoshells with 1024 nm electromagnetic waves leads to enhanced drug delivery.⁴³ Physical dimensions of gold nanoparticles have crucial role in intracellular uptake⁴⁴. Targeted drug delivery using gold nanoparticles *in vivo* has not yet been established because of large size of nanoparticles after conjugating with various ligands for targeting.⁴⁵ Recently, Khan *et al.* made an attempt to target pancreatic cancer cells *in vivo* and *in vitro* by conjugating with EGFR antibody specific to EGFR receptors expressed on tumor cells.⁴⁶ Gene silencing of HDFG by siRNA in ovarian cancer cells by modulation of protein corona around surface-functionalized gold nanoparticles have been reported by Arvizo *et al.*⁴⁷ PEG-modified lipid gold porphyrin is another system which leads to the efficient cellular uptake and tumor destruction.⁴⁸ Recently Ratnakumari *et al.* have reported on internalization of protein-protected CD 33 antibody-conjugated gold nanoparticles by leukemia cells. This report demonstrates potential application of

gold nanoparticles in targeted nanomedicines⁴⁹. Characterization of gold nanoclusters described in detail in Fig. 22.11.

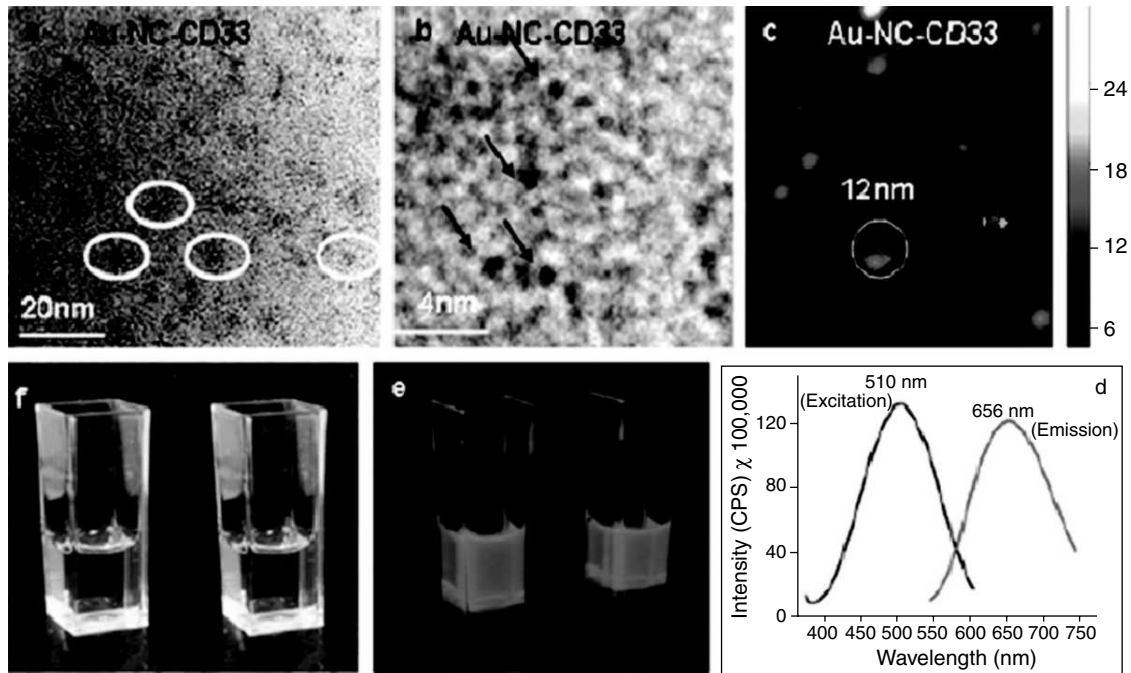


Fig. 22.11 (a) TEM image of Au-NC-CD33 showing nanoclusters of 10–12 nm size, (b) a higher magnification TEM image showing <1 nm sized spherical nanoclusters, (c) AFM image of Au-NC-CD33 showing spherical aggregates of size 12 nm, (d) fluorescence spectra of Au-NC-CD33 showing a peak maximum at 510 nm and the emission peaking at 656 nm and extending up to 800 nm, (e) red fluorescence emitted by Au-NCs and Au-NC-CD33 excited with 365 nm hand-held UV, (f) Au-NCs and Au-NC-CD33 under visible light⁴⁹. (For clarity see colour figure.)

22.5.1.5.2 Calcium Phosphate

The potential of calcium phosphate nanoparticles (nCP) is being widely investigated for the delivery of nucleic acids and drugs. One of the main advantages of using calcium phosphate-based delivery system is its high biocompatibility, which is due to the fact that it forms the mineral component of human bone and teeth, and also due to the presence of calcium (Ca^{2+}) and phosphate ions (PO_4^{3-}) in millimolar concentration within the blood stream. Calcium phosphate is an excellent delivery vehicle for nucleic acids due to the high interaction between positively charged Ca^{2+} in nCP and the negatively charged phosphate group in the nucleotides. But, the poor stability of the calcium phosphate suspension and the large size of the particles were obstacles for successful intracellular delivery applications. Capping of nCP with various polymers and adjustment of synthesis parameters such as pH of the

reaction medium has helped to improve colloidal stability and to reduce the particle size. Recently, a number of studies have been reported on the development of nCP-based nucleic acid delivery systems for DNA⁵⁰ as well as siRNA molecules⁵¹. The development of multi-shell nanoparticles, consisting of alternate layers of calcium phosphate and nucleic acid, has helped to improve the stability of the nucleotides as well as their transfection (introduction of nucleic acids into host nucleus) efficiency.⁵² In addition to nucleic acid delivery, nCPs were also tested for the *in vivo* delivery of drugs such as ceramide,⁵³ cisplatin,⁵⁴ docetaxel,⁵⁵ and methotrexate.⁵⁶ The major advantage of using nCP-based drug delivery agent is the specific solubility of the material in acidic pH of ~ 4 which enable the release of the incorporated drug within lysosomes of cells or within the tumor tissue which has a relatively more acidic microenvironment. The possibility of combined imaging and therapy of cancer cells using nCP was also demonstrated by Morgan *et al.*⁵³ The cytotoxic drug, ceramide, was incorporated into nCPs along with fluorescent dyes such as fluorescein. The study proved that the Ceramide-fluorescein-incorporated nCP was almost 25 times more effective towards human vascular smooth muscle cells than the free ceramide drug dissolved in DMSO⁵³. Preclinical evaluation of nCP-based drug delivery systems needs to be validated *in vivo*.

22.5.1.5.3 Silica Nanoparticles

Another inorganic material, which is being extensively studied for drug delivery applications, is silica nanoparticles (Fig. 22.12). Recent advancements in improved control of particle size, morphology and porosity have made the material more attractive for drug delivery applications. The large surface area and porous interior structure of mesoporous silica nanoparticles (MSN) helps in effective encapsulation of drugs and prevents degradation before reaching the target site. The size and shape of MSN can also be tuned to increase the particle uptake by cells. Hydrophobicity of certain chemo drugs limits their clinical applications which may be overcome by the effective incorporation of drugs within MSN. This was demonstrated by Lu *et al.* using the chemo drug camptothecin.⁵⁷ Also, there are

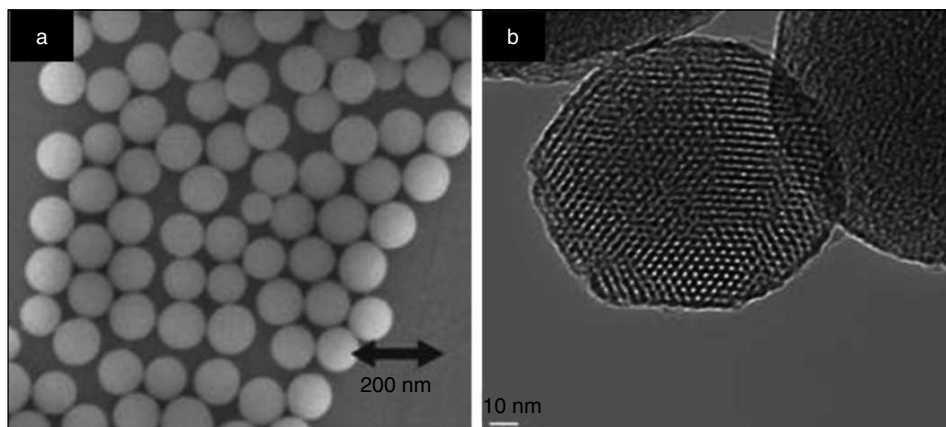


Fig. 22.12 (a) Scanning Electron Microscopy (SEM) and (b) Transmission Electron Microscopy (TEM) images of silica nanoparticles. <http://www.furukawa.co.jp>

reports on effective encapsulation and controlled delivery of drugs such as ibuprofen, erythromycin, and alendronate through MSN. Drug-loaded MSN showed stability for over 2 months when stored at 4°C, without its cytotoxic property being lost. The safe delivery of MSN up to a concentration of 40 mg/kg has been demonstrated *in vivo*, but the material is lethal at a concentration of 1.2 g/kg.⁵⁸ More studies are required to study the treatment efficiency of MSN-based drug delivery systems under *in vivo* conditions.

22.5.1.5.4 ZnO Nanoparticle

Zinc oxide (ZnO) is an important II–VI group semiconductor material with a direct band-gap of 3.37 eV and large exciton binding energy of ~ 60 meV, making it a promising candidate for many technological applications (Fig. 22.13). For over a decade, ZnO has been extensively studied as a potential antimicrobial agent.⁵⁹ Owing to their fascinating physicochemical properties, recently, ZnO NPs have attracted the scientific community for their applications as nanomedicine in cancer treatment. Recently, Shen *et al.*⁶⁰ have reported the low level cancer biomarker detection capability of polymethyl methacrylate-capped ZnO nanoparticles using mass spectrometry. In another study, Dorfman *et al.*⁶¹ have reported on the high-throughput detection of ultra-low levels of telomerase activity using zinc oxide nanorods for cancer diagnosis and screening. More recently, tetrapod-like ZnO nanostructures have been synthesized for gene delivery applications. This type of structures, surface modified with silica and amine groups, are able to bind plasmid DNA and show enhanced transfection efficiency in A375 cells. In addition, polycation-capped luminescent ZnO quantum dots showed excellent DNA transfer capability and have been further explored for real time imaging of gene transfer.⁶²

Recently, a number of reports have appeared on the interesting anti-cancer property of ZnO NPs. Several studies have demonstrated the preferential *in vivo* toxicity exerted by ZnO nanoparticles, towards different types of cancer cells such as glioma, breast, bone, colon, leukemia and lymphomas.⁶³ These studies showed that cancer cells were 30–40 times more susceptible to ZnO NPs-induced toxicity compared to their corresponding normal healthy counter parts. ZnO NPs, conjugated to a porphyrin photo drug, which were tested in *in vivo* on ovarian cancer models, showed higher activity of the system under UV irradiation in contrast to negligible cell death observed in the dark.⁶² Guo *et al.*⁶⁴ have proposed to augment cancer therapy by synergistic administration of ZnO NPs with chemo drug, daunorubicin, which also showed enhanced cancer cell killing ability under UV irradiation. Yuan *et al.*⁶⁵ have attempted to develop a new generation of cancer therapeutics. They used chitosan to encapsulate blue emitting luminescent ZnO QDs loaded with anticancer drugs for tumor targeted drug delivery. Lately, Abhilash *et al.*⁶⁶ have carried out an extensive study to elucidate the preferential toxicity mechanism of ZnO NCs towards cancer cells. These authors have reported that, irrespective of the size-scale and surface chemistry differences, ZnO NCs exhibited multiple stress mechanisms against cancer cells. The mechanism behind the preferential toxicity was found to be the acidic cancer microenvironment mediated rapid dissolution of ZnO NCs and associated oxidative stress mediated toxicity. These studies showed the promising potential of ZnO NPs in targeted gene delivery, gene silencing and selective destruction of cancer cells.

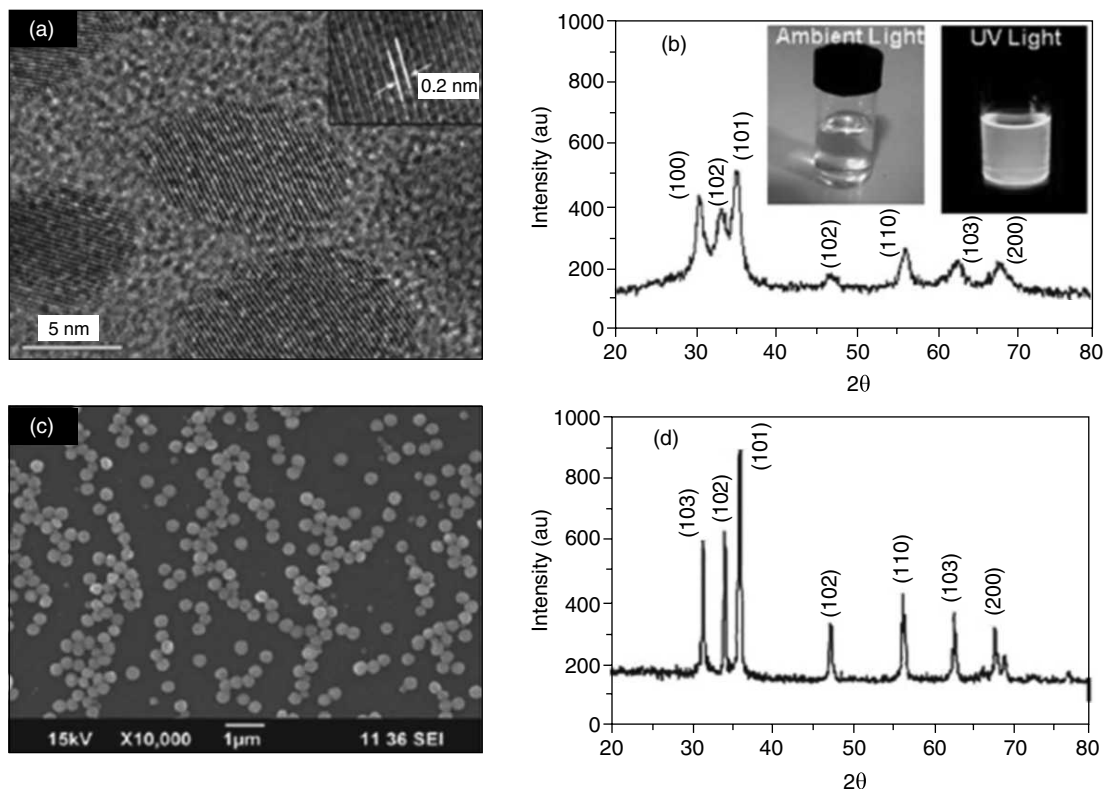


Fig. 22.13 (a) High Resolution (HR) TEM and (b) X ray Diffraction (XRD) pattern of 5 nm sized ZnO NCs, (b, inset) Optical photograph of 5 nm sized ZnO colloidal NCs emitting bright yellow fluorescence under UV excitation, (c) SEM image and (d) XRD pattern of 200 nm sized ZnO⁶⁶.

22.5.1.5.5 TiO₂ Nanoparticles

TiO₂ nanoparticles have also emerged as a drug carrier system for cancer treatment apart from their efficient photocatalytic activity. Their application in cancer therapy through drug delivery is studied by various researchers. Li *et al.* incorporated anti cancer drug, daunorubicin, on titanium dioxide nano whiskers for drug delivery application. In this study, they found that TiO₂ particles efficiently enhance the concentration of daunorubicin drug in human hepato carcinoma cells, indicating their efficiency as anti cancer nanocarrier system. Further, daunorubicin-incorporated TiO₂ nanoparticles have great potential in inhibition of multi drug resistance in leukemia cells.⁶⁷ Here, Song *et al.* have observed that nano-TiO₂ enhances the drug accumulation in target cancer cells and causes considerable membrane damage in leukemia cells⁶⁸.

22.5.1.6 Magnetic Nanoparticles

With the advancements in nanotechnology, new nanoparticle-based probes are being developed for localized/targeted hyperthermia. Hyperthermia, in the clinical setting today, refers to localized heating of tumors to a temperature of 41–43 °C or whole-body heating to 40–42 °C⁶⁹. The term is often used synonymously with thermo ablation. But, technically the latter term refers to application of temperatures in excess of 50 °C. Several techniques have been developed to deliver thermal energy in various forms, such as radiofrequency, microwaves, electrocautery, magneto/photo thermal, focused ultrasound etc., to tumors. Nanoparticles (NPs) exhibit unique energy absorption properties and their biodistribution can be controlled by simple manipulation of their structure, thus producing the concept of “silver-bullets” that specifically kill only diseased cells. NPs also exploit the tumor’s rapidly formed vasculature, and enhanced permeability to aid in the targeting—PR effect. As biomaterials, NPs are composed of elements generally understood to be biocompatible. To improve the biocompatibility further, ‘stealth’ polymers, such as polyethylene glycol (PEG), can be grafted to their surfaces.

Here, we explain three techniques of hyperthermia which employ nanoparticles: (i) magnetic hyperthermia with super paramagnetic iron oxide, (ii) radiofrequency-induced hyperthermia with gold and carbon based nano structures and (iii) photothermal therapy using gold nanoshells. The basic principle, advantages, current progress and associated limitations in each method will be discussed.

22.5.1.6.1 Magnetic Hyperthermia

Magnetic hyperthermia or magnetic fluid hyperthermia (MFH) refers to a hyperthermic treatment technique based on the observation that magnetic nanoparticles (MNPs), when subjected to an alternating magnetic field, exhibit significant heating. Incorporation of the MNPs within a tumor and exposing the region/whole patient to an alternating magnetic field of appropriate frequency, results in heating of the malignant cells, which subsequently, are either destroyed or made susceptible to other treatments like chemotherapy and radiation. Apart from achieving localization of heat, MNPs offer the possibility of self-limitation of temperature increase when magnetic materials with suitable Curie temperatures are used.⁶⁹

The power dissipated by a magnetic material subjected to an alternating magnetic field is referred to as ‘Specific Loss Power’ (SLP). It is measured in watts per gram (W/g) and its value must be high enough to make the material to be useful therapeutically. For magnetic hyperthermia applications, following groups of nanoparticles have been described:

- (i) (a) Superparamagnetic iron oxide nano particles (SPIONs), (b) magnetite (Fe_3O_4) nanoparticles stabilized by a variety of ligands such as dextran, cationic liposomes, polyvinyl alcohol, hydrogel, lauric acid and (c) maghemite ($\gamma\text{-Fe}_2\text{O}_3$) nanoparticles stabilized by ligands such as dextran.
- (ii) Ferrites such as cobalt ferrite (CoFe_2O_4), manganese ferrite (MnFe_2O_4), nickel ferrite (NiFe_2O_4), lithium ferrite ($\text{Li}_{0.5}\text{Fe}_{2.5}\text{O}_4$), mixed ferrites of nickel-zinc-copper (e.g. $\text{Ni}_{0.65}\text{Zn}_{0.35}\text{Cu}_{0.1}\text{Fe}_{1.9}\text{O}_4$) and cobalt-nickel ferrites ($\text{Co}_x\text{Ni}_{1-x}\text{Fe}_2\text{O}_4$).

- (iii) Ferromagnetic nanoparticles such as Fe-doped Au nanoparticles, Zn-Mn-doped iron oxides ($\text{Zn}_x\text{Mn}_{(1-x)}\text{Fe}_3\text{O}_4$) and Mn-Zn-Gd-doped iron oxides ($\text{Mn}_x\text{Zn}_x\text{Gd}_x\text{Fe}_{(2-x)}\text{O}_4$) composites.
- (iv) Metallic nanoparticles of iron, cobalt or alloys of the two. (This system has recently gained attention due to its high heating performance.)

22.5.1.6.1a Magnetic Loss Processes

The heating in magnetic hyperthermia arises due primarily to three processes involving repeated reversal of magnetization in the particle system: (i) hysteresis losses, (ii) relaxation losses and (iii) frictional losses in viscous suspensions. Though, magnetic losses by generation of eddy currents do contribute for heating, their contribution is negligibly small.⁷⁰

Hysteresis losses: The energy dissipated as heat per cycle of magnetization reversal can be determined by integrating the area of the hysteresis loop (Fig. 22.14). This process is the dominant contributor to the thermal energy for $>1\mu\text{m}$ diameter (or multidomain) particles. Nano scale magnetic particles behave as single domain particles and their magnetization reversal can be explained using the uniform mode described by Stoner and Wohlfarth.⁷¹ The factors that affect hysteresis loss in magnetite particles for field amplitudes below 10kA/m are particle size, shape and microstructure. A maximum hysteresis loss in SPIONs is expected near a mean diameter of 30 nm.

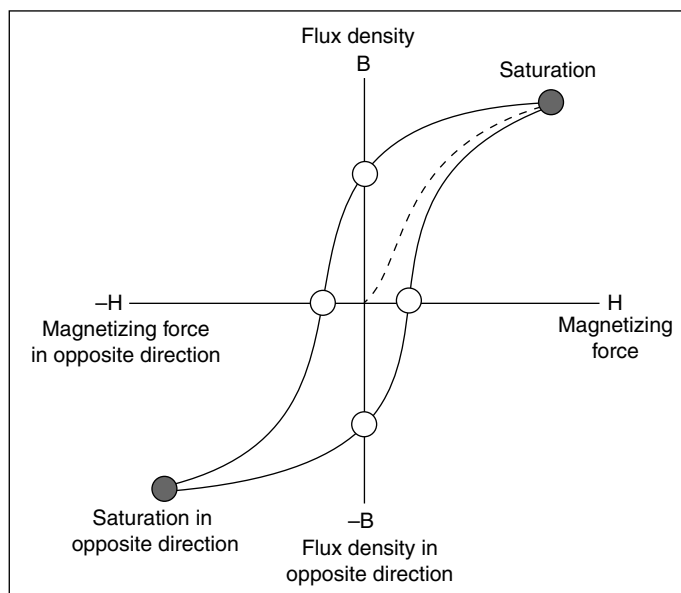


Fig. 22.14 A typical Hysteresis loop—closed curve showing the variation of the magnetic flux density of a ferromagnetic material with the external magnetic field producing it, when this field is changed through a complete cycle of magnetization and demagnetization. Area within the loop represents the energy lost (as heat).

Relaxation losses: As the particle size decreases, so does the energy barrier for magnetization reversal. Consequently, the hysteresis loops become narrower⁷⁰. Therefore, the SLP calculated from the loop is less than the value measured directly by calorimetry. The relaxation loss in single domain MNPs is explained by two modes: rotational (Brownian) mode and Néel mode [Fig. 22.15(a) and (b), respectively]. The Néel mechanism is analogous to the hysteresis loss in multi-domain magnetic particles, whereby there is an ‘internal friction’ due to the movement of the magnetic moment in an external field that results in heat generation. In the Brownian mode, the whole particle oscillates towards the field with the moment locked along the crystal axis under the effect of a thermal force against a viscous drag in a suspending medium.⁷²

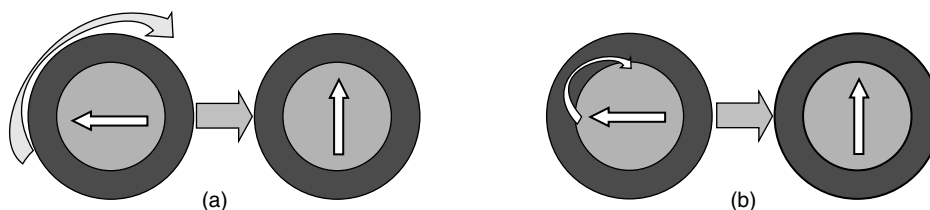


Fig. 22.15 Relaxation mechanisms of MNP: (a) Brownian relaxation: the entire particle rotates in fluid. (b) Néel relaxation: the direction of magnetization rotates in the core. The structure of MNP: core (yellow, magnetic), shell (blue, nonmagnetic). The arrow inside the core represents the direction of magnetization.

Viscous losses: The Brownian mechanism (mentioned above) essentially represents the mechanical friction between the rotating particles and the surrounding medium. The energy loss per cycle of rotation, where the viscous drag of the fluid is countered by a magnetic torque T , equals the value $2\Delta T$ ⁷².

22.5.1.6.1b Factors Determining Hyperthermia of MNPs

On evaluating the different principles explaining the loss mechanisms, it can be realised that, in principle, specific loss power is an increasing function of the frequency and the amplitude of the magnetic field. The enhancement of SLP by increasing either of these factors is limited for medical reasons and the technical difficulty in realization of large field amplitudes at high frequencies in a volume appropriate for hyperthermia. The most important factor however, is considered to be the particle size. A steep decline of SLP with decreasing particle size has been demonstrated⁷⁰.

22.5.1.6.1c Superparamagnetic Iron Oxide Nanoparticles (SPIONs)

Super paramagnetic iron oxide nanoparticles (Fig. 22.16), sometimes referred to as ‘ultrashall superparamagnetic iron oxide particles’ (USIOP), are considered as an important class of MNPs and have been tested by several authors. Despite having many advantages in using them, development of SPIONs is also left with challenges such as (i) need for high frequency of oscillating magnetic fields, (ii) the need to be injected directly into tumors as tumor targeting is still being studied, (iii) low SLP which directly correlates with the hyperthermic effect and (iv) bio-incompatibility of those with higher SLP like cobalt and manganese ferrite nanoparticles.⁷³ Recently, incorporation of optically active

components onto MNPs has attracted considerable attention. Dumbbell-like gold coated SPIONs⁷⁴ are very attractive composite systems owing to their interesting optical and magnetic properties. However, the decrease in the magnetic moment in such composite materials needs to be addressed. Mohammad *et al.* have demonstrated a 4- to 5-fold increase in the amount of heat released with gold coated SPIONs in comparison with regular SPIONs, on application of low frequency oscillating magnetic fields (44–430 Hz).⁷⁵

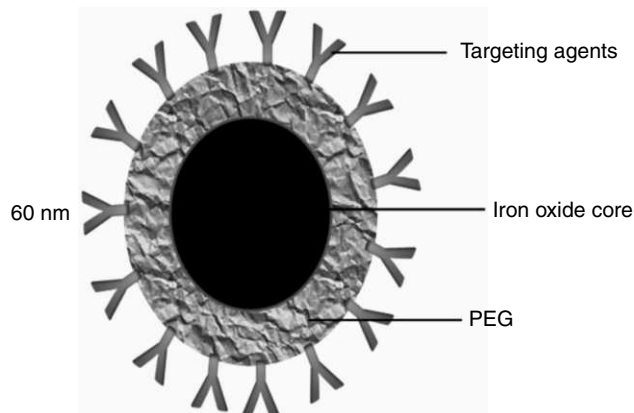


Fig. 22.16 Diagrammatic representation of a SPION which has an iron oxide core and is pegylated to allow better solubility *in-vivo*. Also shown is an outer layer of targeting ligands attached for tissue specific localization.

Clinical studies have been published.⁷⁶ The first is a study in which a 67 year-old patient with prostate cancer received an intratumoral injection of aminosilan-coated SPIONs followed by exposure to an alternating magnetic field (100 kHz) once weekly for 6 weeks. The results showed that the particles were retained at the tumor for the entire period and adequate temperatures for ablation of the tumor cells were achieved. The second report is a feasibility and tolerability study on 14 patients with glioblastoma multiforme.⁷⁷ Again, intratumoral administration of aminosilan-coated SPIONs was made followed by the exposure to the magnetic field. The overall findings were that the technique does not cause any adverse effects on the patients. Further studies are under way to determine the efficacy of this technique.

22.5.1.7 Nanoparticle-Mediated Targeted Therapy

Targeted therapeutic nanomedicines are second generation nanomedicines. This research field primarily focuses on the development of new nanocarriers, which specifically target the cancer cells, without affecting the normal functions of healthy cells. Properly designed nanoparticles can specifically target tumor tissues and can get accumulated in tumors. This new generation nanomedicines comprises of nanocarriers loaded with one or more cancer therapeutics, chemosensitizer, imaging components and an active targeting element such as folate receptor.⁷⁸ Pinhassi *et al.* demonstrated the selective targeting and cytotoxicity of a FA (Folic acid) and methotrexate conjugate arabinogalactan to FR (Folate

Receptor) over-expressing cells.⁷⁹ Albumin-based nanoparticle carriers have been extensively studied by various groups.^{80, 81} Pegylated liposome-encapsulated Doxorubicin, carbon nanotubes, micellar NPs etc., are also the extensively studied nanoformulations for targeted delivery. A combination of cancer diagnostic aid and therapeutic agent loaded onto same NP system, called theragnostic NPs, is also studied.⁸² Different strategies for targeted cancer therapy are discussed in detail in the following section.

22.5.1.8 Targeting Aberrant Cancer Kinome

Kinome, the full complement of protein kinases in a genome, drives signal transduction in eukaryotic cells to orchestrate virtually all cellular processes, including metabolism, transcription, cell cycle progression, cytoskeletal rearrangement, cell movement, apoptosis, and differentiation. However, deregulation of kinase activity has emerged as a major mechanism by which cancer cells evade normal physiological constraints on growth and survival. This scenario have propelled kinases to the upfront as a new class of drug targets and led to the development of small molecule kinase inhibitors (SMI) for the treatment of cancer. SMI modulates kinase activity by competing with the ATP binding site of the catalytic domain of oncogenic tyrosine kinases. The approval of the first kinase inhibitor, imatinib, for the treatment of chronic myelogenous leukemia (CML) and the success of antibody-based drugs that targeted the epidermal growth factor receptor (erbB2) in breast cancer (trastuzumab) and colon cancer (cetuximab) heralded the current period of intensive kinase drug development efforts. They have come up as well tolerated anti-cancer agents with high molecular specificity and a favorable safety profile. Conventional cytotoxic chemotherapy although directed toward certain macromolecules or enzymes, typically does not discriminate effectively between rapidly dividing normal cells and tumor cells leading to severe toxic side effects and partial, brief, or unpredictable tumor response. In contrast, targeted therapies interfere with molecular targets that have a role in tumor growth or progression and thus have a high specificity towards tumor cells, providing a broader therapeutic window with less toxicity. Moreover, they can work in combination with cytotoxic chemotherapy or radiation to produce additive or synergistic anticancer activity, because, their toxicity profiles often do not overlap with traditional cytotoxic chemotherapy. Thus, targeted therapies represent a new and promising approach to cancer therapy, one that is already leading to beneficial clinical effects. The small molecule kinase inhibitors which have been approved for the treatment of cancer includes imatinib, dasatinib, nilotinib, gefitinib, lapatinib, sunitinib, sorafenib and everolimus, to name a few, which have been developed to specifically target the kinases, c-Abl (and Bcr-Abl), PDGFR, cKit, EGFR, VEGFR2 and mTOR.⁸³

22.5.1.9 Nanoparticle-Mediated Gene Silencing

RNA interference (RNAi) is a potent gene-silencing phenomenon induced by double-stranded RNAs.⁸⁴ The phenomenon was first described by Andrew Fire and Craig Melo in 1998 during their studies in *C.elegans*⁸⁵. The high efficiency as well as its remarkable specificity combined with the ease of application makes RNAi an attractive novel therapeutic approach as well as a major reverse genetic tool. Although other gene silencing approaches using ribozymes, DNazymes and antisense

oligonucleotides have evolved over the past few years, RNAi being endogenous machinery conserved in almost all eukaryotes generated considerable interest among the researchers.⁸⁵ The advantages of siRNAs over small molecule drugs are that (i) sequences can be rapidly designed for highly specific inhibition of the target of interest, (ii) even picomolar concentrations of siRNA can induce silencing and (iii) synthesis does not require a cellular expression system, complex protein purification, or refolding schemes.⁸⁶ Hence, RNAi holds promise as a therapeutic tool to reduce the expression of disease-causing genes through the sequence specific degradation of mRNA at the post-transcriptional level before translation in to oncoproteins. The major limitation is the highly anionic charge offered by the phosphate backbone of siRNA and consequent electrostatic repulsion from the anionic cell membrane surface, which prevents its passive diffusion in to cytoplasm and also the rapid enzymatic degradation by serum nucleases.⁸⁷ Moreover, the presence of double stranded RNAs may switch on the immune response machinery. Hence, siRNAs can be delivered to the cells only by carrier mediated delivery. The carrier mediated delivery can be either viral mediated or non-viral delivery of siRNAs using polymers, lipids, proteins, peptides or electroporation. Because of the invasiveness of the electricity of electroporation and cytotoxicity of some lipid reagents, non-viral transfection methods have become less efficient for *in vivo* delivery. Moreover, conventional non-viral siRNA delivery systems are limited by packaging efficiency and colloidal stability and non-specificity.⁸⁸ In the case of viral delivery systems, there is possibility of immune and toxic reactions in addition to the potential for viral recombination.⁸⁹ In this scenario, nanoparticles hold great promise for the intracellular delivery of siRNAs. Nanoparticle-based delivery systems have already shown great promise in *in vitro* as well as *in vivo* systems.⁹⁰ Schematics of steps involved in the targeted degradation of mRNA is showed in Figure 22.17. Recently, phase I clinical trial had been conducted using siRNAs targeted against RRM2 gene over-expressed in melanoma. The cyclodextrin nanoparticles were modified using transferrin-targeting ligand, to engage the transferrin receptors over-expressed in melanoma cells. The study holds great promise in terms of targeted delivery of siRNAs using nanoparticles.⁹¹

22.5.1.10 Targeting Tumor Angiogenesis, Metastasis

Angiogenesis is the formation of new blood capillaries from existing blood vessels. It is important for normal embryonic vascular development as well as various physiological processes in adults. A tumor cannot grow more than 2mm diameter without proper angiogenesis (Fig. 22.18). Unlike normal angiogenesis, tumor angiogenesis results in leaky and convoluted blood vessels which are often inflamed. Such a deregulated angiogenesis in tumor is mainly associated with over expression of some growth factors and cytokines such as vascular endothelial cell growth factor (VEGF), angiopoietin etc., as well as $\alpha_v\beta_3$ integrin. Anti-angiogenic therapy is basically blocking or disrupting the newly formed blood vessels with the help of therapeutic agents. Examples for such molecules include TNP 470, endostatin, angiostatin, combretastatin etc. The first anti-angiogenic therapy used avastin monoclonal antibody that specifically targets VEGF over-expressed colorectal cancer cells.⁹³ Though these anti-angiogenic therapies are superior to conventional chemotherapy, limitations pertaining to conventional therapy are still associated with this.

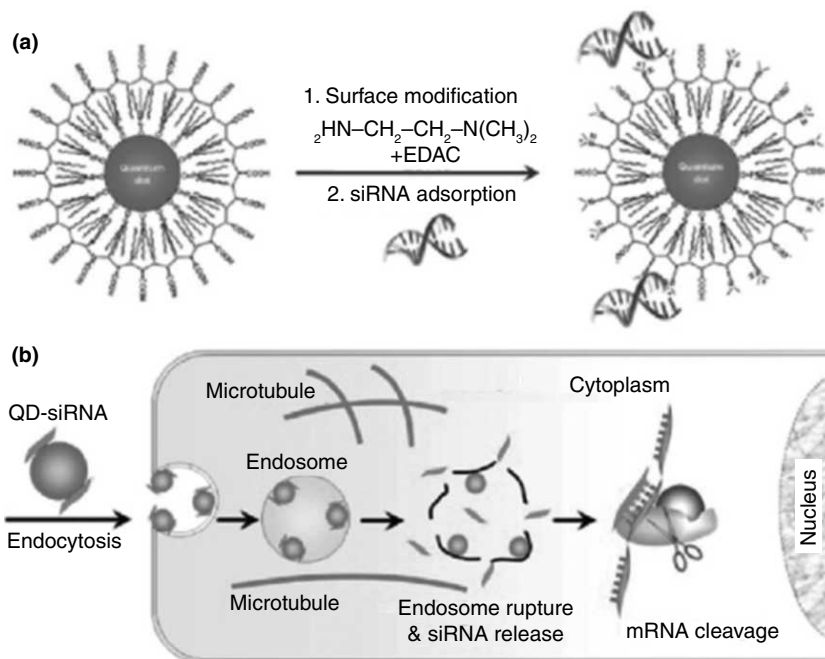


Fig. 22.17

(a) Chemical modification of polymer-encapsulated QDs to introduce tertiary amine groups, and adsorption of siRNA on the particle surface by electrostatic interactions. (b) Schematic diagram showing the steps of siRNA-QD in membrane binding, cellular entry, endosomal escape, capturing by RNA binding proteins, loading to RNA-induced silencing complexes (RISC), and target degradation⁹².

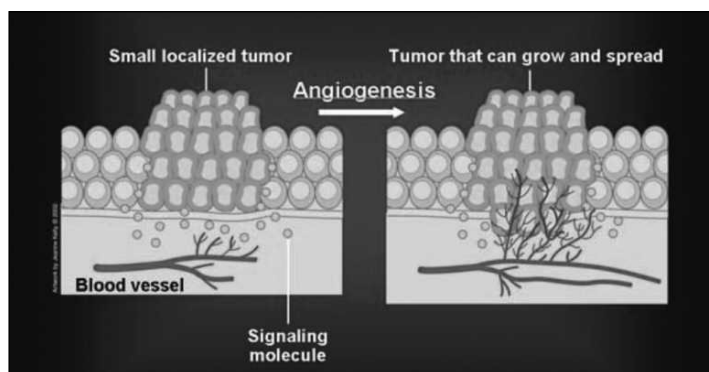


Fig. 22.18

Tumor angiogenesis actually starts with cancerous tumor cells releasing molecules that send signals to surrounding normal host tissue. This signaling activates certain genes in the host tissue that, in turn, makes proteins to encourage growth of new blood vessels.

Metastasis is the spread of cancer cells from a primary tumor site to a distantly placed secondary site (Fig. 22.19). Nanoparticle-mediated targeting of metastasis can be either primary targeting or secondary targeting. Primary targeting refers to targeting diagnostic and therapeutic agents to the organ in which metastases are located. It was reported that brain, lungs, liver, lymph and bones are most challenging organs to be targeted by nanomedicines.⁹⁴ Targeting specific cell type in a target organ is another challenge in treatment of metastatic cancer. Secondary targeting mainly focuses on this aspect. Conventional approaches include use of magnetic field to accumulate iron oxide nanoparticles in cancer cells or use of acoustic waves to trigger micro bubble localization. Metastatic cancer cells always express certain cell surface markers as well as secreted factors, which usually over-expressed during embryonic development. In addition, metastatic cells also express surface markers from its site of origin. This understanding favors active targeting of metastatic cells using nanotechnology. Conjugating antibodies specific to these surface markers as well as peptide for integrin binding domain were reported for enhanced targeting of specific cell types within a tissue.⁹⁵ Nanoparticles coated with folic acid demonstrated their affinity to folate receptors over-expressed in oral carcinoma, metastatic breast, colorectal cancer as well as other cancers.⁹⁶

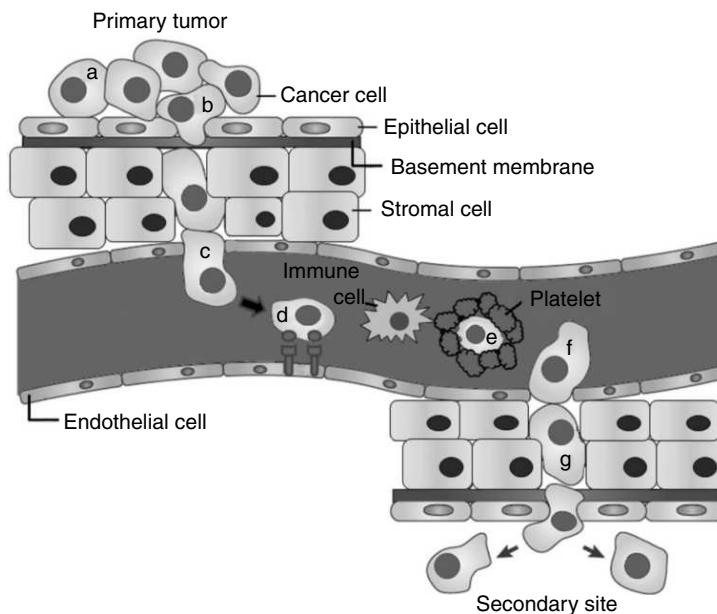


Fig. 22.19 Steps of metastasis: The metastatic cells (a) reduce adhesion to neighboring cells and (b) migrate into the vasculature. In the vasculature, cells can move freely through the blood. If the vasculature is continuous, the cells (c) intravasate by endothelial cell retraction or endothelial cell death. Cancer cells trapped in the narrow capillaries (d) can express receptors that bind to metastasis supporting sites or to platelets (e). Platelets protect the cancer cells from immune system. At the secondary site, the cell can cause endothelial retraction or death, or, the cell can proliferate with the help of growth factors released by the neighboring cells.

22.5.2 Diagnostic Applications: *Imaging*

Early diagnoses of cancer and other diseases are another potent application of nanomaterials. More efficient nanoparticle systems, with better body compartment distribution and tissue targeting capability than conventional contrast agents, have been established recently. Semiconductor nanocrystals (quantum dot, quantum rods, and quantum beacons), immunofluorescence biomarkers and immunogold labeling are important systems for nanoparticle-mediated imaging.

22.5.2.1 *Quantum Dots, Quantum Rods, Quantum Beacons*

Quantum dots are small (<10 nm) inorganic nanocrystals which possess unique luminescent properties (Fig. 22.20). Their fluorescence emission is stable and could be tuned by varying the particle size or composition. They are generally composed of two types of atoms from groups IIB and VI or from III and V of the periodic table. They are defined as particles with physical dimensions smaller than the exciton Bohr radius. The small size leads to a quantum confinement effect, which endows nanocrystals with unique optical and electronic properties. Semiconductor nanocrystals can be capped with inert oxides or sulphides, and can be attached to a biomolecule that has a specific function. The salient features of semiconductor nanocrystals are given below:

1. Quantum dots have size-tunable emission (from the UV to the IR)
2. Narrow spectral line widths
3. Efficient luminescence
4. Continuous absorption profiles
5. Stability against photo bleaching
6. Ideal immuno labels for *in vitro* and *in vivo* fluorescent imaging



Fig. 22.20 Bioconjugated quantum dots as contrast agent for tumor imaging.⁹⁷ (For clarity see colour figure.)

Quantum dots have been developed as tumor-targeting contrast agents. Dual functioning beads made up of QDs and iron oxide nanocrystals embedded in silica nanocrystals could efficiently target specific cells and are shown to have excellent imaging qualities. In order to improve the biofunctionality, quantum dots were conjugated to different biological molecules using different approaches such as non-specific adsorption, electrostatic interaction, thiol exchange and covalent linkage (Fig. 22.21).

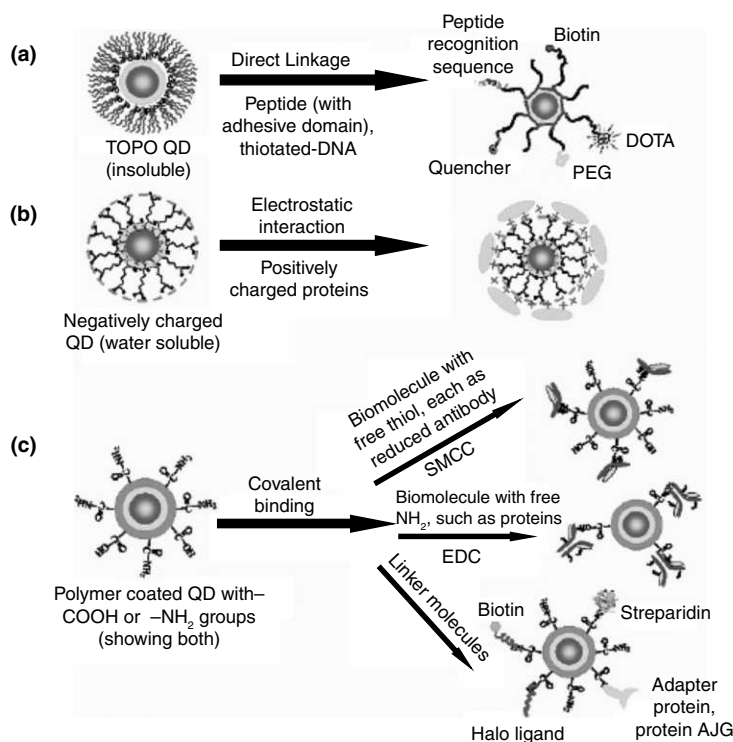


Fig. 22.21 Different methods used for quantum dot biofunctionalization (a) direct linkage to TOPO coated QDs, (b) Electrostatic interaction (c) covalent binding⁹⁷.

Owing to the high surface-to-volume ratio of nanomaterials, it is possible to link multiple functionalities on single QDs while keeping the overall size within the optimal range. For example, the QD core can serve as the structural scaffold, and the imaging contrast agent and small molecule hydrophobic drugs can be embedded between the inorganic core and the amphiphilic polymer coating layer. Hydrophilic therapeutic agents (including small interfering RNA [siRNA] and antisense oligodeoxynucleotide [ODN]) and targeting biomolecules (such as antibodies, peptides and aptamers), in turn, can be immobilized on the hydrophilic side of the amphiphilic polymer via either covalent or non-covalent bonds.

This fully integrated nanostructure may behave like magic bullets that will not only identify, bind to and treat diseased cells, but also emit detectable signals for real-time monitoring of its trajectory. However, in the case of *in vivo* imaging, a major challenge is to generate high contrast due to the molecular differences in different tissues and organs and this can be achieved by conjugating with specific antibodies (Figure 22.22). The understanding of cancer specific biomarkers further improved efficiency of cancer imaging. The concept of individualized therapy can be achieved by designing multifunctional nanoparticles with appropriate combination of therapeutic agents based on the molecular biomarker profiling of the patient along with imaging materials.

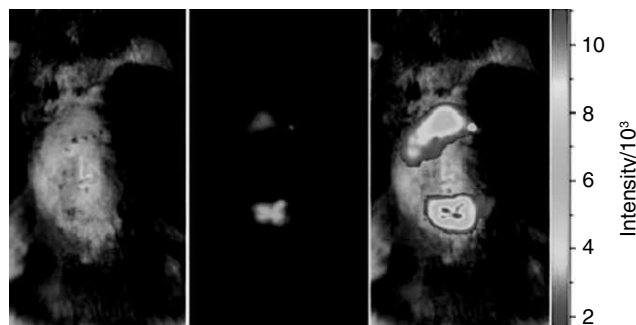


Fig. 22.22 Subcutaneously injected carbon dots (upper spot) and CZnS-Dots (lower spot) of similar optical densities in mice (470 nm and 525 nm band-pass filters were used for excitation and emission, respectively)⁹⁸ (For clarity see colour figure.)

Quantum rods are rod shaped semiconductor nanocrystals which are more luminescent than QDs. Their role in *in vitro* and *in vivo* imaging was recently demonstrated by Yong *et al.*,⁹⁹ who demonstrated the uptake of transferring conjugated QRs by cells over-expressing Tf receptors. Quantum beacons are another variation of QDs. It uses the technique of molecular beacons, where the oligonucleotide-based probes hybridized with complementary sequences which cause change in probe configuration that separate quencher from reporter and emit fluorescence. Since appropriate quencher and the linkage is very crucial in the functioning of QD molecular beacon, detailed investigation is underway.¹⁰⁰

22.5.2.2 Gold Nanoparticles for Imaging

Gold nanoparticles constitute another important nanosystem for *in vitro* and *in vivo* imaging in which versatile optical properties are made use of. Several research groups have reported the use of gold nanoparticles in generating photothermal interference contrast,¹⁰¹ dark field imaging,¹⁰² reflectance imaging,¹⁰³ as well as fluorescence imaging¹⁰⁴. Recently gold nanoshells were reported as good contrast agents in *in vivo* imaging of blood vessels, which suggested their use in MR angiography as blood pool agents.

Gold nanoparticles conjugated with specific antibodies can be made to target cancer cells for imaging. For example, gold nanoparticles labeled with EGFR antibodies via non specific adsorption are recognized and specifically bind to EGFR over expressing cervical carcinoma cells and tissues. Highly fluorescent Au25 clusters, stabilized in bovine serum albumin (BSA) using a green-chemical reducing agent, ascorbic acid (vitamin-C), were developed by Ratnakumari *et al.*¹⁰⁵ For targeted-imaging-based detection of cancer cells, the clusters were conjugated with folic acid (FA) through amide linkage with the BSA shell. Receptor-targeted cancer detection using Au clusters is demonstrated on FR⁺ oral squamous cell carcinoma (KB) and breast adenocarcinoma cell MCF-7, where the FA-conjugated Au25 clusters were found internalized in significantly higher concentrations compared to the negative control cell lines (Figure 22.23).

Raman spectroscopy is another imaging technique which can make use of gold nanoparticle-based contrast agents. Recently, Qian *et al.* and Keren *et al.* have reported *in vivo* targeted imaging of

cancer using Raman spectroscopy.^{106, 107} Studies are going on for improvement of Raman imaging so that Raman technique will become a clinical reality.

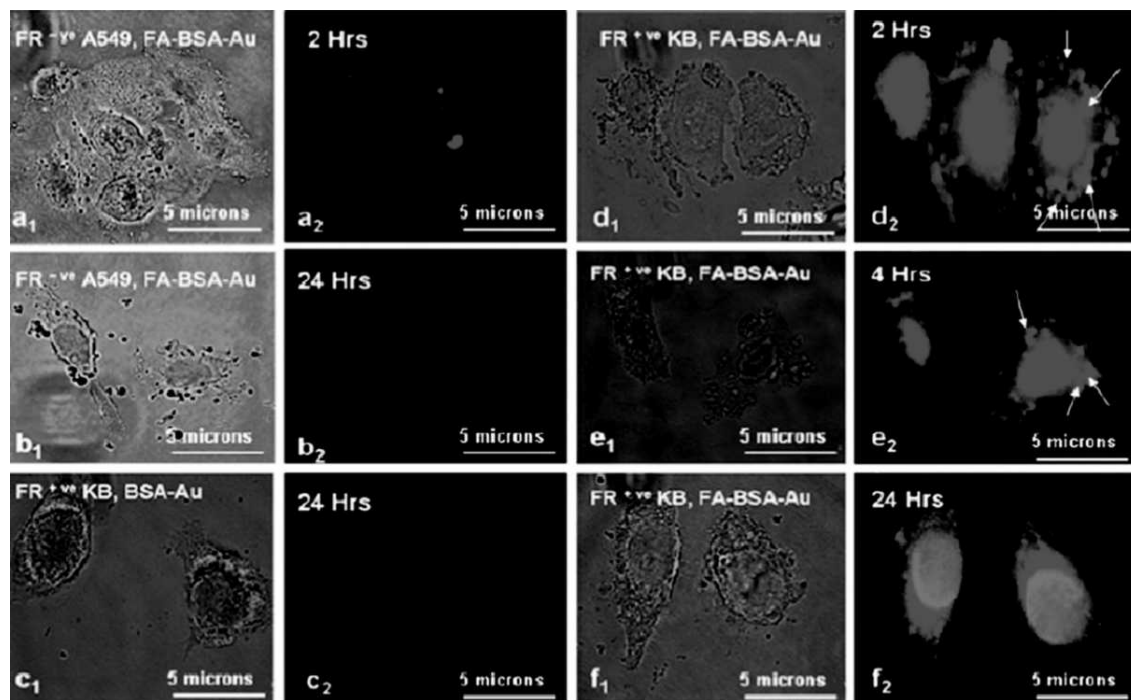


Fig. 22.23 Fluorescent microscopic images showing interaction of Au-BSA-FA NCs with different types of cell lines: (a1)–(a2) FR-ve lung carcinoma A549, (b1)–(b2) FR-depressed oral cell carcinoma, KB, (c1)–(c2) FR+ve KB cells with unconjugated Au clusters, (d1)–(d2) FR+ve KB cells with FA-conjugated Au clusters at 2 h, (e1)–(e2) 4 h and (f1)–(f2) 24 h of incubation. (For clarity see colour Fig. 11.13.)

22.5.2.3 Nano Hydroxy Apatite

Hydroxy apatite, HAp ($\text{Ca}_{10}(\text{PO}_4)_6(\text{OH})_2$), is the bio-mineral component of human bone and teeth and hence highly biocompatible. Recently, synthetically prepared $\text{Ca}_3(\text{PO}_4)_2$ nanoparticles were successfully used for the delivery of genes,¹ siRNA¹⁰⁸ and chemodrugs.¹⁰⁹ as the were also modified for imaging applications by suitable doping with rare-earth impurities (Eu^{3+} and Gd^{3+}). Synthetic nanoparticles of phase pure HAP can be engineered to provide multifunctional contrast properties. For *in vivo* fluorescence imaging applications, the contrast agent should have NIR excitation and emission properties within the range of 700–900 nm, where the tissue penetration of light is maximum. Recently, a novel hydroxyapatite nanoparticle (nHAP)-based multimodal contrast agent for combined near-infrared (NIR), MR and X-ray imaging was developed by Ashokan *et al.*¹¹⁰ Figure 22.24 showing the characterization of 50 nm sized indocyanin green (ICG) doped nanohydroxyapatite (nHAP) which was developed as MRI contrast agent.

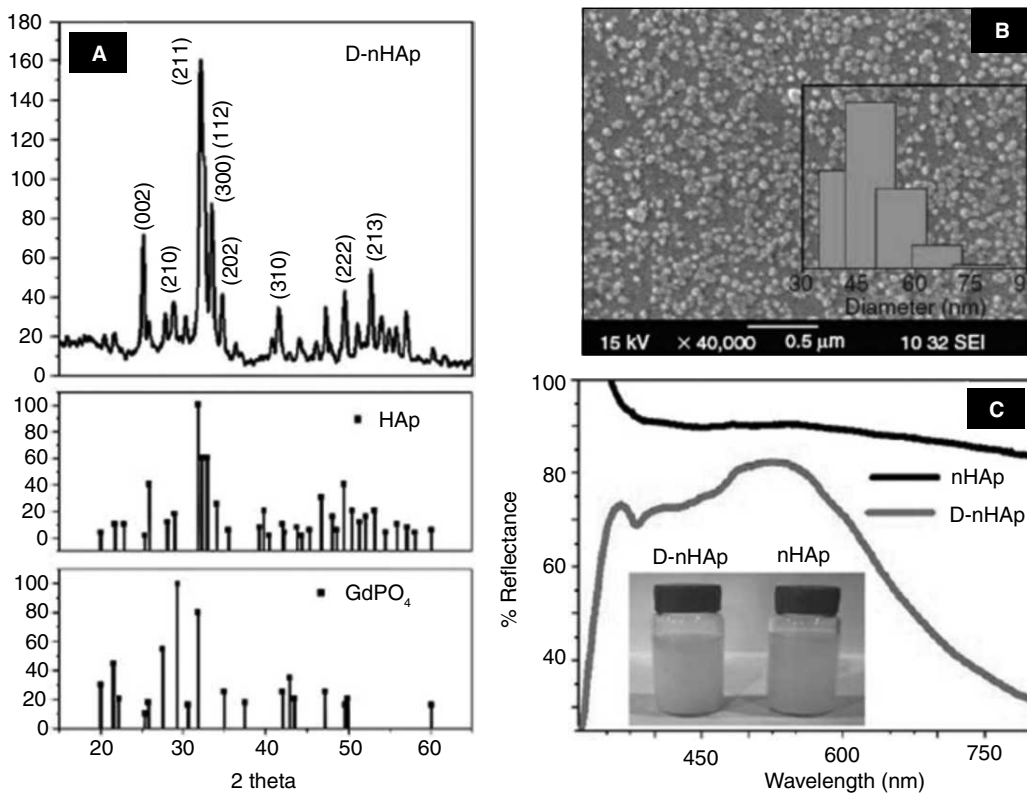


Fig. 22.24 (A) XRD of D-nHAp showing hexagonal HAp crystal structure along with the reference patterns of HAp and GdPO₄ (Gadolinium PO₄). (B) SEM image of D-nHAp showing particle size ~ 50 nm. Inset: DLS data of D-nHAp showing an average size ~ 50 nm. (C) Diffuse reflectance spectra showing characteristic features of ICG in D-nHAp samples compared to undoped nHAp. Inset: Digital photograph of D-nHAp and nHAp solutions (~ 20 mg/mL) indicating the greenish body colour due to ICG doping. nHAp, hydroxyapatite nanoparticle; D-nHAp, doped nHAp; ICG, indocyanine green¹¹⁰.

22.5.2.4 Metal Oxides

Recently Chandran *et al.*¹¹¹ reported MR contrast agent using gadolinium doped TiO₂. TiO₂ was found to be biocompatible compared to other metal oxides like ZnO. Doping with Gd³⁺ ions conferred TiO₂ with paramagnetic functionality suitable for T1 weighted MR imaging. Phantom MR images taken with 1.5 Tesla clinical MR system proved the potential of the material as MR contrast agent. Nanotoxicity studies including cell-viability, plasma membrane integrity, reactive oxygen stress analysis and expression of pro-inflammatory cytokines, performed on human primary endothelial cells (HUVEC), human peripheral blood mononuclear cells (PBMC) and nasopharyngeal epidermoid carcinoma (KB) cells and showed no apparent toxicity. Gadolinium doped TiO₂ with molecular imaging functionality in accord with biocompatibility and molecular receptor specific targeting capability presents a promising MR contrast agent. Figure 22.25 shows the characterization of Gadolinium-doped nano TiO₂¹¹¹.

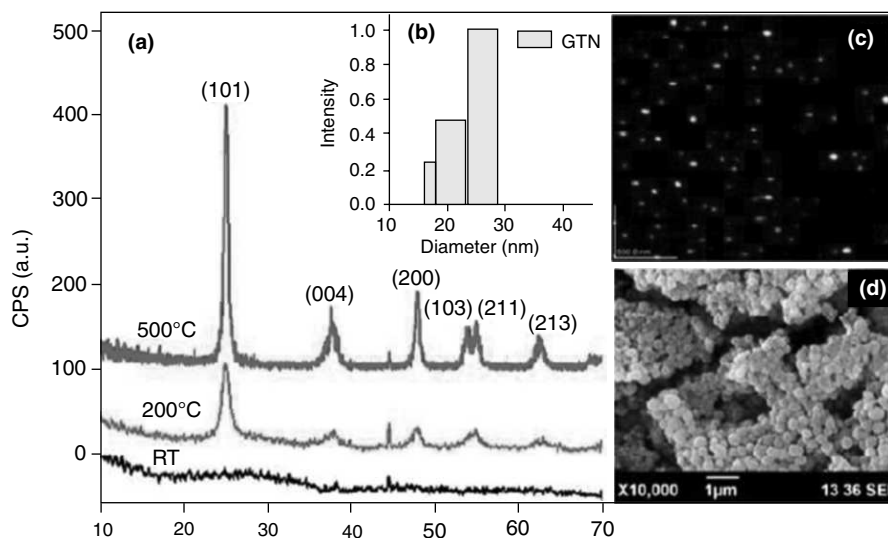


Fig. 22.25 (a) XRD spectra of gadolinium doped TiO_2 (GTN) samples; as prepared (RT), annealed at 250°C and 500°C (b) Dynamic light scattering data of as prepared GTN sample showing major (90%) size distribution $\sim 20\text{--}25$ nm (c) AFM image of as prepared GTN sample (scale 500 nm) (d) SEM image of GTN sample annealed at 500°C showing spherical nanoparticles of increased size ~ 200 nm.

22.6 THERAGNOSTICS

The term ‘theragnostics’ or ‘theranostics’ was originally coined to describe a treatment platform that combines a diagnostic test with targeted therapy based on the test results. However, in the field of nanomedicine, it is often used to refer to a paradigm that allows an ultra-sensitive imaging function as well as targeted therapy within a single nanoparticle system. This has been primarily developed to address the challenges of tumor heterogeneity and adaptation. Figure 22.26 shows a schematic representation of a theragnostic nanoparticle. The figure shows a silica core which is tagged with both magnetic NPs and gold NPs. Gold increases the optical visibility via surface plasmon resonance scattering. The primary therapeutic agent carried is curcumin.

In theragnostics, the molecular imaging allows precise identification of the tumor site and characterizes the cell type, in addition to the target specific delivery of the therapeutic agent. Cancer, being a heterogenous and constantly evolving disease, requires regular monitoring of the molecular changes associated with the disease so that the treatment can be precisely tailored. A theranostic approach provides pre-validation of appropriate targeting, tracks the expression pattern of surface markers for adaptive targeting and provides real-time information on tumor response. The chart shown in Fig. 22.27 depicts current development stages and theragnostic nanomedicines, and further hurdles in the pipeline development.

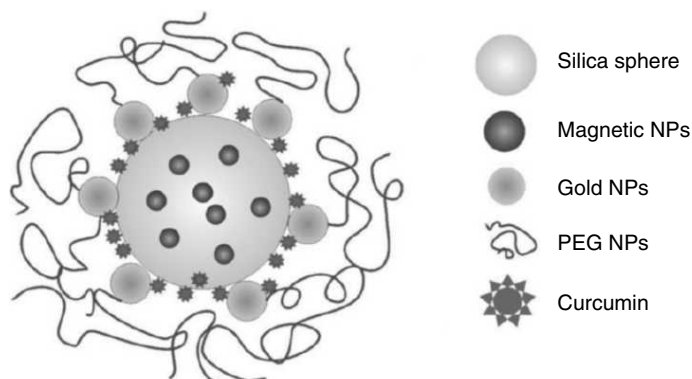


Fig. 22.26 Schematic of drug-loaded magneto plasmonic assembly with PEG "camouflage" coating.

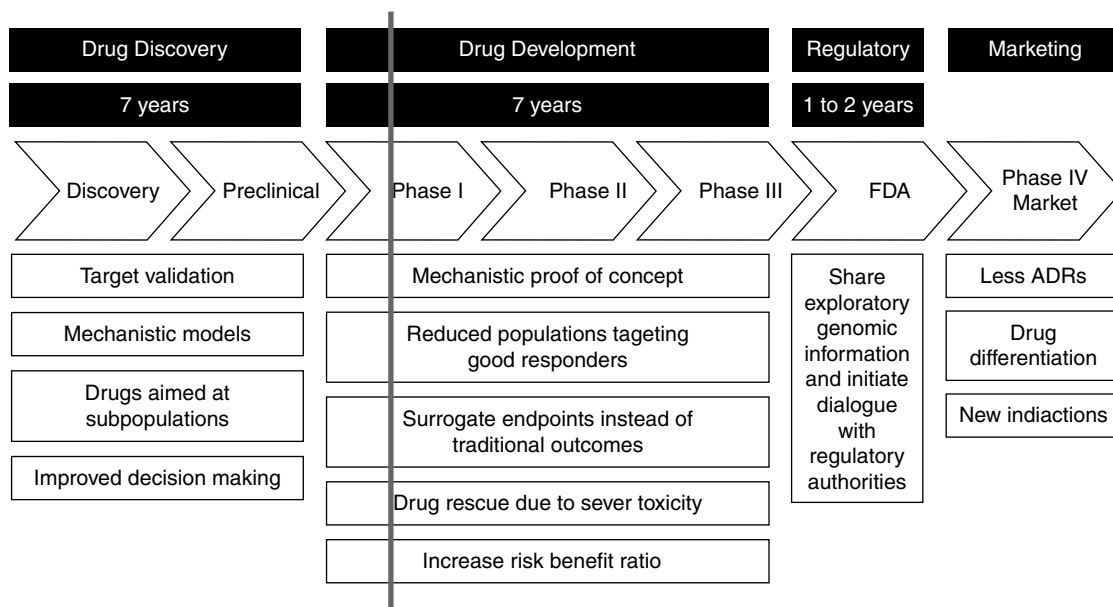


Fig. 22.27 Currently theranostic nanomedicines are here (Gray line) in the established drug development pipe line¹¹².

22.7 CHALLENGES IN THE TRANSLATION OF NANOMEDICINE

Though nanomedicine promises a transfigured portrait of better healthcare, health economics and personalised medicine, major challenges need to be overcome to achieve these goals. The FDA (Food and Drug Administration) and the Alliance for NanoHealth (ANH) have identified the top scientific hurdles in bringing nanoengineered products to patients, specifically in the pre-clinical, clinical and manufacturing phases of product development.¹¹³

The top priority is the identification of biodistribution of the nanomedicines within the body following systemic administration. The second concern is the development of appropriate imaging modalities for the identification of the biodistribution over time. It is concluded that, though the pictorial evidence of *in vivo* accumulation can be obtained by anatomical imaging techniques like X-ray, Ultrasonography, Computed Tomography and Magnetic Resonance Imaging, the only technique that can give quantitative mass-balance information is radionuclide imaging.

The mass transport of the agents across compartmental boundaries within the body also needs to be understood because this directly affects the biodistribution (Fig. 22.28). The behavior of the nanoparticles must be identified to understand their basic biology, have better control over adverse effects and ultimately develop an improved class of nanomedicines. Two other priorities are the development of new mathematical and computer models that will contribute to a 'periodic table' of nanoparticles for predicting the risk-benefit parameters. The standard or reference materials and consensus testing protocols need to be standardized. The final objective is the realization of an analytical toolkit for nanopharmaceuticals manufacturing, accompanied by specification sheet of toxicological, safety, and biodistribution properties obtained through standardized, validated methods. Apart from these, the other commonly encountered issues and their possible solutions are listed in Table 22.2.

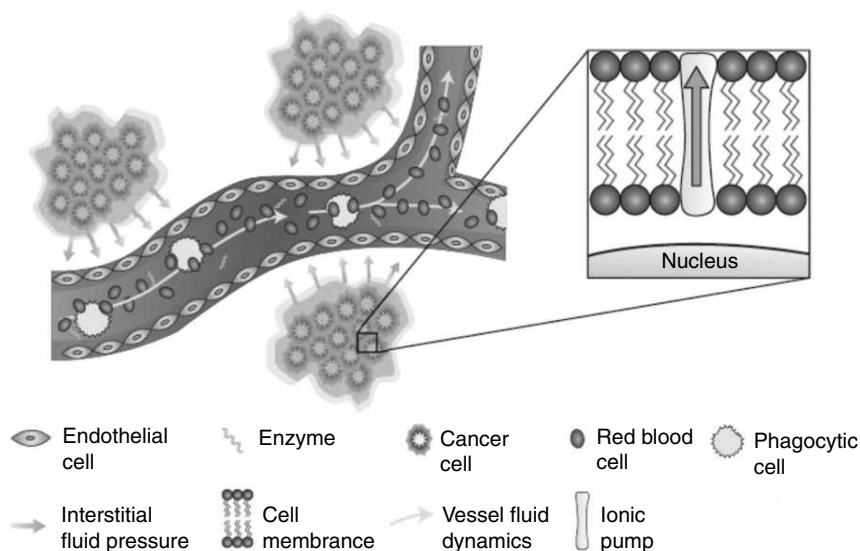


Fig. 22.28 *Negotiating with the body's defence systems. Several extremely effective obstacles, called biological barriers, largely prevent injected chemicals, biomolecules, nanoparticles and any other foreign agents of therapeutic action from reaching their intended destinations. The barriers include: the reticulo-endothelial system, endothelial/epithelial membranes, complex networks of blood vessels, abnormal flow of blood, and interstitial pressure gradients. Inset: A magnified region of a tumor cell offers additional biological challenges: cellular/nuclear membranes and ionic/molecular pumps that can expel drugs from the cancerous cells creating drug resistance.*

Table 22.2 *Desired features and solutions for nanomedicines for cancer*

Specification or Hurdle	Possible Solutions
Not detected by human immune system	Use of human-derived antibodies, proteins, receptors, ligands or enzymes for functionalization of platforms. Study of the antigen presentation characteristics of the new materials to understand how to reduce recognition of haptens.
Resistance to proteases, nucleases and esterases	Use of aptamers with altered DNA backbone chemistry, peptide ligands with unnatural amino acids, pegylation. Take advantage of the process to engineer desired clearance and delivery of cargo.
Biocompatibility, catabolism and clearance issues	Engineered sizes, charge, and shape compatible with desired clearance; biofunctionalization to make soluble and biocompatible; use of structures that degrade or release cargo within cells. Preference for degradable components or linkers with small renally cleared agents; controlled degradation after use of agent by enzymatic cleavage.
Specificity for or retention near tumors and cancer cells	Platforms contain peptide or small molecule ligands, aptamers or antibodies/ fragments; agent takes advantage of enhanced permeability and retention effect to increase selectivity of delivery; multistep pre-targeting approaches are used to increase therapeutic index.
Potency	Surface multivalency to increase affinity and cargo delivery; contained spaces for multiple copies of cargo; use of enzymes to multiply effects, such as prodrug conversion at tumor site.
Reporting and accountability	Use of theranostics: radiotraced; MRI active agents, optical or infra-red tracers; caged reporters that signal upon binding, activation or delivery to or into the cell; use of genetic reporters.
Controllability	Control by infused second ligands, by focused radio-frequency of magnetic fields; use of intrinsic sensors or tumor activatable agents; use of artificial cells or viruses; suicide genes; controlled design of degradation pathways.
Intrinsic dynamics and information content	Use of addressable DNA sequences, proteins or sugar polymers; design multivalent ligands to encode avidity for the target. Use built-in mechanical or enzymatic machinery or pirating such activities from the target cell.
Safety and environmental concerns	Science should be built on known agents and components already in use <i>in vivo</i> , then developed individually after pharmacologic study.
Political and social issues	Enhanced efforts to educate the public; careful toxicologic analyses. Avoid overstating the promise.

22.8 CONCLUSIONS AND FUTURE PERSPECTIVES

Nanomedicine has now reached a level of an efficient and mature technology platform to meet the requirements of advanced molecular diagnosis and therapy. This novel technology is now a powerful tool capable of even replacing some of the conventional diagnostic and therapeutic techniques that are practiced today. The unique pharmacological, biochemical and physiochemical properties of nanoformulations allow their easy modulation to address an array of clinical situations commonly encountered in disease diagnosis and treatment. For example, the emerging concepts of theranostics

may hold the key to the future of disease care. It will pave the way for the ultimate goal of individual patient specific disease management protocols. Though the potential of nanomedicines are immense, the path is not going to be easy because of toxicity concerns pertaining to most of the nanoparticles known today. Considerable standardization is needed in terms of testing and evaluation protocols, fool-proof methods for evaluation of the toxicity, biodistribution and *in vivo* behavior of the formulations. The responsibility of nanochemistry community lies with the development of better bio-compatible nanomaterials systems for applications in biology and medicine.

REFERENCES

1. Ferrari, M., *Nature Reviews Cancer* 5, 161–171, 2005.
2. La Van, D.A, McGuire, T. and Langer, R., *Nature Biotechnology*, 21, 1184–91, 2003.
3. Jain, R.K., Tong, R.T., and Munn, L.L., *Cancer Res*, 67, 2729–2735, 2007.
4. Robert A. Freitas Jr., *Inform.* 80; 45–59, 2002.
5. Mirkin, C.A.; Letsinger, R.L.; Mucic, R.C.; Storhoff, J.J., *Nature* 1996, 382, 607–608.
6. Iivissatos, A.P.; Johnsson, K.P.; Peng, X.G.; Wilson, T.E.; Loweth, C.G.; Bruchez, M.P.; Schultz, P.G., *Nature* 1996, 382, 609–611.
7. Rosi, N.L.; Mirkin, C.A., *Chem. Rev.* 2005, 105, 1547–1562.
8. Brennan, L.; Turner, D.L.; Fareleira, P.; Santos, H., *J. Mol. Biol.* 2001, 308, 353–365.
9. Andre E. Nel, *Nature materials* Vol. 8, July 2009, 543.
10. Storhoff, J.J.; Lazarides, A.A.; Mucic, R.C.; Mirkin, C.A.; Letsinger, R.L.; Schatz, G.C., *J. Am. Chem. Soc.* 2000, 122, 4640–4650.
11. Pan, P.; Gunawardena, H.P.; Xia, Y.; McLuckey, S.A., *Anal. Chem.*, 2004, 76, 1165–1174.
12. Teng, C.-H.; Ho, K.-C.; Lin, Y.-S.; Chen, Y.-C., *Anal. Chem.*, 2004, 76, 4337–4342.
13. Teng, C.-H.; Ho, K.-C.; Lin, Y.-S.; Chen, Y.-C., *Anal. Chem.*, 2004, 76, 4337–4342.
14. Gu, H.; Ho, P.L.; Tong, E.; Wang, L.; Xu, B., *Nano Lett.*, 2003, 3, 1261–1263.
15. Jiang, X.; Jiang, J.; Jin, Y.; Wang, E.; Dong, S., *Biomacromolecules*, 2005, 6, 46–53.
16. Sudeep, P.K.; Joseph, S.T.S.; Thomas, K.G., *J. Am. Chem. Soc.*, 2005, 127, 6516–6517.
17. Kateb, B., Chiu, K., Black, K.L., Yamamoto, V., Khalsa, B., Ljubimova, J.Y., Ding, H., Patil, R., Portilla-Arias, J.A., Modo, M., Moore, D.F., Farahani, K., Okun, M.S., Prakash, N., Neman, J., Ahdoot, D., Grundfest, W., Nikzad, S., Heiss, J.D., “Nanoplatfoms for constructing new approaches to cancer treatment, imaging and drug delivery: what should be the policy?”, *Neuroimage*, 54, pp. S106–S124, 2011.
18. Scheinberg, D.A., Villa, C.H., Escorcia, F.E., McDevitt, M.R., “Conscript of the infinite armada: systemic cancer therapy using nanomaterials”, *Nature Reviews*, 7, pp. 266–276, 2010.
19. Malam, Y., Loizidou, M., Seifalian, A.M., *Liposomes and nanoparticles: nanosized vehicles for drug delivery in cancer*, 2009, 30(11), 592–599.
20. Gilding, D.K., Reed, A.M., “Biodegradable polymers for use in surgery—polyglycolic/poly (lactic acid) homo- and copolymers: 1”, *Polymer*, 20(12), pp. 1459–1464, 1979.
21. Lockman, P.R., Mumper, R.J., Khan, M.A., Allen, D.D., “Nanoparticle technology for drug delivery across the blood–brain barrier”, *Drug Dev. Ind. Pharm.*, 28(1), pp. 1–13, 2002.

22. D. Bissett, D., Cassidy, de Bono, J.S., Muirhead, F., Main, M., Robson, L., Fraier, D., Magne, M.L., Pellizzoni, C., Porro, M.G., Spinelli, R., Speed, W., Twelves, C., "Phase I and pharmacokinetic (PK) study of MAG-CPT (PNU 166148): a polymeric derivative of camptothecin (CPT)", *Br. J. Cancer*, 91(1), 2004, 50–55.
23. Boddy, A.V., Plummer, E.R., Todd, R., Sludden, J., Griffin, M., Robson, L., Cassidy, J., Bissett, D., Bernareggi, A., Verrill, M.W., Calvert, A.H., "A phase I and pharmacokinetic study of paclitaxel poliglumex (XYOTAX), investigating both 3-weekly and 2-weekly Schedules", *Clin. Cancer Res.*, 11(21), 2005, 7834–7840.
24. Vasey, P.A., Kaye, S.B., Morrison, R., Twelves, C., Wilson, P., Duncan, R., Thomson, A.H., Murray, L.S., Hilditch, T.E., Murray, T., Burtles, S., Fraier, D., Frigerio, E., Cassidy, J., "Phase I clinical and pharmacokinetic study of PK1 [N-(2-hydroxypropyl) methacrylamide copolymer doxorubicin]: first member of a new class of chemotherapeutic agents-drug-polymer conjugates", Cancer Research Campaign Phase I/II Committee, *Clin. Cancer Res.*, 5, 1999, 83–94.
25. Banerjee, D., Harfouche, R., Sengupta, S., Nanotechnology mediated targeting of tumor angiogenesis. *Vascular cell*, 2011, 3:3.
26. Kwon, G.S., Naito, S., Kataoka, K., Yokoyama, M., Sakurai, Y., Okano, T., "Block copolymer micelles as vehicles for hydrophobic Drugs", *Colloids Surf B Biointerfaces*, 1994, 16, 429–434.
27. Adams, M.L., Lavasanifar, A., Kwon, G.S. "Amphiphilic block copolymers for drug delivery", *J Pharm Sci.*, 92(7), 2003, 1343–55.
28. Koizumi, F., Kitagawa, M., Negishi, T., Onda, T., Matsumoto, S., Hamaguchi, T., *et al.* Novel SN-38-incorporating polymeric micelles, NK012, eradicate vascular endothelial growth factor secreting bulky tumors. *Cancer Res.*, 2006; 66: 10048–56.
29. Lee, H., Hoang, B., Fonge, H., Reilly, R.M., Allen, C., *In vivo* distribution of polymeric nanoparticles at the whole-body, tumor, and cellular levels, *Pharm Res*, (2010).
30. Eliaz, R.E., Nir, S., Marty, C., Szoka, F.C., Jr., "Determination and modeling of kinetics of cancer cell killing by doxorubicin and doxorubicin encapsulated in targeted liposomes", *Cancer Res*, 64, 2004, 711–8.
31. Wagner, V., Dullaart, A., Bock, A.K., Zweck, A., "The emerging nanomedicine landscape", *Nat Biotechnol*, 24, 2006, 1211–7.
32. Federman, N., and Denny, C.T. "Targeting liposomes toward novel pediatric anticancer therapeutics", *Pediatr Res*, 67, (5), 2010, 514–519.
33. W. Lu, J. Wan, Z. She, X. Jiang, J. Controlled Release, 2007, 118, 38. D.Y. Furgeson, M.R. Dreher, A. Chilkoti, J. Controlled Release, 2006, 110, 362.
34. C. Duclairoir, A.M. Orecchioni, P. Depraetere, E. Nakache, J. Microencapsul, 2002, 19, 53.
35. C. Duclairoir, A.M. Orecchioni, P. Depraetere, F. Osterstock, E. Nakache, *Int. J. Pharm.*, 2003, 253, 133.
36. N.K. Ibrahim, N. Desai, S. Legha, P. Soon-Shiong, R.L. Theriault, E. Rivera, B. Esmali, S.E. Ring, A. Bedikian, G.N. Hortobagyi, J.A. Ellerhorst, *Clin. Cancer Res.*, 2002, 8, 1038.
37. N.K. Ibrahim, B. Samuels, R. Page, D. Doval, K.M. Patel, S.C. Rao, M.K. Nair, P. Bhar, N. Desai, G.N. Hortobagyi, *J. Clin. Onco. L* 2005, 23, 6019.
38. Templeton, A.C., Wuelfing, W.P., Murray, R.W., "Monolayer-protected cluster molecules", *Accounts of Chemical Research*, 33(1), 1999, 27–36.
39. Bhattacharya, R., Mukherjee, P., "Biological properties of "naked" metal nanoparticles", *Advanced Drug Delivery Reviews*, 60(11), 2008, 1289–1306.

40. Visaria, R.K., Griffin R.J., Williams, B.W., Ebbini, E.S., Pacciotti, G.F., Song, C.W., Bischof, J.C., "Enhancement of tumor thermal therapy using gold nanoparticle-assisted tumor necrosis factor alpha delivery", *Mol Cancer Ther*, 5(4), 2006, 1014–20.
41. Chen, Y.H., Tsai, C.Y., Huang, P.Y., Chang, M.Y., Cheng, P.C., Chou, C.S., Chen, D.H., Wang, C.R., Shiau, A.L., Wu, C.L., "Methotrexate conjugated to gold nanoparticles inhibits tumor growth in a syngeneic lung tumor model", *Mol Pharm*, 4(5), 2007b, 713–22.
42. Qioa, G., Zhuo, L., Gao, Y., Yu, L., Li, N., Tang, B., "A tumor mRNA-dependent gold nanoparticle-molecular beacon carrier for controlled drug release and intracellular imaging", *Chem Commun*, 47(26), pp. 7458–60, 2011.
43. Bikram, M., Gobin, A.M., Whitmire, R.E., West, J.L., "Temperature-sensitive hydrogels with SiO₂-Au nanoshells for controlled drug delivery", *J Control Release*, 123(3), 2007, 219–27.
44. Chithrani, B.D., Ghazani, A.A., Chan, W.C., "Determining the size and shape dependence of gold nanoparticle uptake into mammalian cells", *Nano Lett*, 6(4), 2006, 662–8.
45. Cai, W., Gao T., Hong H., Sun Jiangtao., "Application of gold nanoparticles in cancer nanotechnology", *Nanotechnology: Science and applications*, 2008(1), 17–32.
46. Khan, J.A., Kudgus, R.A., Szabolcs, A., Dutta, S., Wand, E., Cao, S., Curran, G.L., Shah, V., Curley, S., Mukhopadhyay, D., Robertson, J.D., Bhattacharya, R., Mukherjee, P., "Designing nanoconjugates to effectively target pancreatic cancer cells *in vivo* and *in vivo*", *PLoS One*, 2011, 6(6), e20347.
47. Arvizo, R.R., Girik, Miranda A.R., Madden, B., McCormick, D.J., Bhattacharya, R., Rotello, V.M., Kocher, J.P., Mukherjee, P., "Identifying new therapeutic targets via modulation of protein corona formation by engineered nanoparticles", *PLoS One*, 7(3), 2012, e33650.
48. Lee, P., Zhang, R., Li, V., Liu, X., Sun, R.W., Che, C.M., "Wong KK. Enhancement of anticancer efficacy using modified lipophilic nanoparticle drug encapsulation", *Int J Nanomedicine*, 2012(7), 731–7.
49. Archana Retnakumari, Jasusri Jayasimhan, Parwathy Chandran, Deepthy Menon, Shantikumar Nair, Ullas Mony1 and Manzoor Koyakutty1. CD33 monoclonal antibody conjugated Au cluster nano-bioprobe for targeted flow-cytometric detection of acute myeloid leukaemia. *Nanotechnology*, 22 (2011), 285102 (11pp).
50. Sokolova, V.V., Radtke, I., Heumann, R., Eppler, M., Effective transfection of cells with multi-shell calcium phosphate-DNA nanoparticles, *Biomaterials*, 27(16), pp. 3147–3153, 2006.
51. Zhang, X., Kovtun, A., Mendoza-Palomares, C., Oulad-Abdelghani, M., Fioretti, F., Rinckenbach, S., Mainard, D., Eppler, M., Benkirane-Jessel, N., SiRNA-loaded multi-shell nanoparticles incorporated into a multilayered film as a reservoir for gene silencing, *Biomaterials*, 31(23), pp 6013–6018, 2010.
52. Sokolova, V., Kovtun, A., Prymak, O., Meyer-Zaika, W., Kubareva, E., A Romanova, E., A, Oretskaya, T.S., Heumann, R., Eppler, M., Functionalisation of calcium phosphate nanoparticles by oligonucleotides and their application for gene silencing, *J. Mater. Chem.*, 17(8), pp. 721–727, 2007.
53. Morgan, T.T., Muddana, H.S., Altinoglu, E.I., Rouse, S.M., Tabaković, A., Tabouillot, T., Russin, T.J., Shanmugavelandy, S.S., Butler, P.J., Eklund, P.C., Yun, J.K., Kester, M., Adair, J.H., Encapsulation of organic molecules in calcium phosphate nanocomposite particles for intracellular imaging and drug delivery, *Nano Lett.*, 8(12), pp 4108–4115, 2008.
54. Barroug, A., Kuhn, L.T., Gerstenfeld, L.C., Glimcher, M.J., Interactions of cisplatin with calcium phosphate nanoparticles: *in vivo* controlled adsorption and release, *J Orthop Res.*, 22(4), pp. 703–708, 2004.

55. Luo, Y., Ling, Y., Guo, W., Pang, J., Liu, W., Fang, Y., Wen, X., Wei, K., Gao, X., Docetaxel loaded oleic acid-coated hydroxyapatite nanoparticles enhance the docetaxel-induced apoptosis through activation of caspase-2 in androgen independent prostate cancer cells, *J Control Release*, 147(2), pp. 278–288, 2010.
56. Mukesh, U., Kulkarni, V., Tushar, R., Murthy, R.S., Methotrexate loaded self stabilized calcium phosphate nanoparticles: a novel inorganic carrier for intracellular drug delivery, *J Biomed Nanotechnol.*, 5(1), pp. 99–105, 2009.
57. Lu, J., Liong, M., Zink, J.I., Tamanoi, F. Mesoporous silica nanoparticles as a delivery system for hydrophobic anticancer drugs, *Small*, 3(8), pp. 1341–1346, 2007.
58. Doadrio, J.C., Sousa, E.M.B., Izquierdo-Barba, I., Doadrio, A.L., Perez-Pariente, J., Vallet-Regí, M., Functionalization of mesoporous materials with long alkyl chains as a strategy for controlling drug delivery pattern, *J. Mater. Chem.* 16(5), pp. 462–466, 2006.
59. Liong, M., Lu, J., Kovoichich, M., Xia, T., Ruehm, S.G., Nel, A.E., Tamanoi, F., Zink, J.I., Multifunctional inorganic nanoparticles for imaging, targeting, and drug delivery, *ACS Nano*, 2(5), pp. 889–896, 2008.
60. Hudson, S.P., Padera, R.F., Langer, R., Kohane, D.S., The biocompatibility of mesoporous silicates, *Biomaterials*, 29(30), pp. 4045–4055, 2008.
61. Lu, J., Liong, M., Li, Z., Zink, J.I., Tamanoi, F., Biocompatibility, biodistribution, and drug-delivery efficiency of mesoporous silica nanoparticles for cancer therapy in animals, *Small*, 6(16), pp. 1794–1805, 2010.
62. Shen, W., Xiong, H., Cai, S., Lu, H., Yang, P., ZnO-poly(methyl methacrylate) nanobeads for enriching and desalting low-abundant proteins followed by directly MALDI-TOF MS analysis. *Analytical chemistry*, 80(17), pp. 6758–63, 2008.
63. Dorfman, A., Parajuli, O., Kumar, N., Hahm, J.I., Novel telomeric repeat elongation assay performed on zinc oxide nanorod array supports, *Journal of nanoscience and nanotechnology*, 8(1), pp. 410–5, 2008.
64. Nie, L., Gao, L., Feng, P., Jhang, J., Fu, X., Liu, Y., Yan, X., Wang, T., “Three-dimensional functionalized tetrapod-like ZnO nanostructures for plasmid DNA delivery”. *Small* (Weinheim an der Bergstrasse, Germany), 2(5), pp. 621–5, 2006.
65. Zhang, P. and Liu, W., “ZnO QD@PMAA-co-PDMAEMA nonviral vector for plasmid DNA delivery and bioimaging.” *Biomaterials*, 31(11), pp. 3087–94, 2010.
66. Nair, S., Sasidharan, A., Rani, V.V.D., Menon, D., Manzoor, K. and Raina, S., “Role of size scale of ZnO nanoparticles and microparticles on toxicity toward bacteria and osteoblast cancer cells”, *J.Mater. Sci: Mater. Med.*, 20, pp. S235–241, 2009.
67. Li, Q., Wang, X., Lu, X., Tian, H., Jiang, H., Lv, G., Guo, D., Wu, C., Chen, B., The incorporation of daunorubicin in cancer cells through the use of titanium dioxide whiskers, *Biomaterials*, 30, 4708–4715, 2009.
68. Song, M., Pan, C., Li, J., Wang, X., Gu, Z., Electrochemical study on synergistic effect of the blending of nano TiO₂ and PLA polymer on the interaction of antitumor drug with DNA. *Electroanalysis*, 18(19–20), 1995–2000, 2006.
69. Manthe, R.L., Foy, S.P., Krishnamurthy, N., Sharma, B., Labhassetwar, V., “Tumor ablation and nanotechnology”, *Molecular Pharmaceutics*, 7(6), pp. 1880–1898, 2010.
70. McTaggart, R.A., Dupuy, D.E., “Thermal ablation of lung tumors”, *Tech. Vasc. Interv. Radiol.*, 10, pp. 102–113, 2007.

71. Aharoni, A., "Introduction to the theory of Ferromagnetism", *Oxford: Clarendon*.
72. Hergt, R., Dutz, S., Muller, R., Zeisberger, M., "Magnetic particle hyperthermia: nanoparticle magnetism and materials development for cancer therapy"; *J. Phys: Condens. Matter*, 18, pp. S2919–S2934, 2006.
73. Johannsen, M., Gneveckow, U., Eckelt, L., Feussner, A., Waldofner, N., Scholz, R., Deger, S., Wust, P., Loening, S.A., Jordan, A., "Clinical Hyperthermia of prostate cancer using magnetic nanoparticles: presentation of a new interstitial technique"; *Int. J. Hyperthermia*, 21(7), pp. 637–647, 2005.
74. Maier-Hauff, K., Rothe, R., Scholz, R., Gneveckow, U., Wust, P., Thiesen, B., Feussner, A., Von Deimling, A., Waldofner, N., Felix, R., Jordan, A., "Intracranial thermo therapy using magnetic nanoparticles combined with external beam radiotherapy: results of a feasibility study on patients with glioblastoma multiforme", *J. Neuro-Oncol.*, 81(1), pp. 53–60, 2007.
75. Yu, H., Chen, M., Rice, P.M., Wang, S.X., White, R.L., Sun, S., "Dumbbell-like bifunctional Au-Fe₃O₄ nanoparticles", *Nano Lett.*, 5, pp. 379, 2005.
76. Frey, N.A., Srinath, S., Srikanth, H., Chao, T., Sun, S., "Static and Dynamic Magnetic Properties of Composite Au-Fe₃O₄ Nanoparticles". *IEEE Trans Magn.*, 43, pp. 3094, 2007.
77. Morales, M.P., Veintemillas-Verdaguer, S., Montero, M.I., Serna, C.J., Roig, A., Martinez, B., Casas, L., Sandiumenge, F. "Surface and Internal Spin Canting in γ -Fe₂O₃ Nanoparticles", *Chem. Mater.*, 11, p. 3058, 1999.
78. Visaria, R.K., Griffin, R.J., Williams, B.W., Ebbini, E.S., Pacciotti, G.F., Song, C.W., Bischof, J.C., "Enhancement of tumor thermal therapy using gold nanoparticle-assisted tumor necrosis factoralpha delivery", *Mol Cancer Ther*, 5(4), pp. 1014–20, 2006.
79. Pinhassi, R.I., Assaraf, Y.G., Farber, S., Stark, M., Ickowicz, D., Drori, S., Domb, A.J., Livney, Y.D., Arabiunogalactan-folic acid-frug conjugate for targeted delivery and target activated release of anticancer drugs to folate receptor overexpressing cells. *Biomacromolecules*, 11(1), 294–303, 2010.
80. Shapira, A., Livney, Y.D., Broxterman, H.J., Assaraf, Y.G., "Nanomedicine for targeted cancer therapy: Towards the overcoming drug resistance", *Drug resistance updates*, 14, pp. 150–163, 2011.
81. Basu, S., Harfouche, R., Soni, S., Chimote, G., Mashelkar, R.A., Sengupta, S., "Nanoparticle-mediated targeting of MAPK signaling predisposes tumor to chemotherapy", *Proc Natl Acad Sci USA*, 106, pp. 7957–7961, 2009.
82. Chien, A.J., Illi, J.A., Ko, A.H., Korn, W.M., Fong, L., Chen, L.M., "A Phase I study of a 2-day lapatinib chemosensitization pulse preceding nanoparticle albumin-bound paclitaxel for advanced solid malignancies", *Clin. Cancer Res.*, 15(17), pp. 5569–5575, 2009.
83. Arora, A., Scholar, E.M., Role of Tyrosine Kinase Inhibitors in Cancer Therapy, *J Pharmacol Exp Ther*, 315(3), pp. 971–9, 2005.
84. Natalie, P.P., Mamdal, P.K. *et al.*, Engineered Nanoparticles in Cancer Therapy. *Recent Patents on Drug Delivery & Formulation*, 1(1), pp. 37–51, 2007.
85. Fire, A., Xu, S., Montgomery, M.K., Kostas, S.A., Driver, S.E., Mello, C.C., "Potent and specific genetic interference by double-stranded RNA in *Caenorhabditis elegans*", *Nature*, 391, pp. 806–811, 1998.
86. Plasterk, R.H., "RNA silencing: the genome's immune system", *Science*, 296 (5571), 1263–1265, 2002.
87. Myers, J.W., Jones, J.T., Meyer, T., Ferrell, J.E. Jr, "Recombinant Dicer efficiently converts large dsRNAs into siRNAs suitable for gene silencing", *Nat Biotechnol*, 21(3), pp. 324–328, 2003.

88. Bumcrot, D., Manoharan, M., Koteliansky, V. and Sah, D.W.Y., "RNAi therapeutics: a potential new class of pharmaceutical drugs", *Nature Chem. Biol.*, 2, 711–719, 2006.
89. Juliano, R., Bauman, J., Kang, H., and Ming, X., "Biological Barriers to Therapy with Antisense and siRNA Oligonucleotides", *Molecular Pharmaceutics*, 6 (3), 686–695, 2009.
90. Reischl, D., Zimmer, A., "Drug delivery of siRNA therapeutics: potentials and limits of nanosystems", *Nanomedicine: Nanotechnology, Biology, and Medicine*, 5, pp. 8–20, 2009.
91. Howard, K.A., Rahbek, U.L., Liu, X., Damgaard, C.K., Hovgaard, M.B., Schmitz, A., Nyengaard, J.R., Besenbacher, F. and Kjems, J., "RNA Interference *in vivo* and *in vivo* Using a Chitosan/siRNA Nanoparticle System", *Molecular Therapy*, 14, 2006.
92. Yezhelyev, M.V., Qi, L., O'Regan, R.M., Nie, S., Gao, X., Proton-sponge coated quantum dots for siRNA delivery and intracellular imaging, 130(28), 9006–12, 2008.
93. Katas, H., Alpar, H.O., "Development and characterisation of chitosan nanoparticles for siRNA delivery", *J Control Release*, 115(2), pp. 216–25, 2006.
94. Murugesan, S., Mousa, S.A., O'connor, L.J., Lincoln, D.W., Linhardt, R.J., "Carbon inhibits vascular endothelial growth factor-and fibroblast growth factor promoted angiogenesis", *FEBS Lett*, 581(6), pp. 1157–1160, 2007.
95. Cervantes, A., Alsina, J., Taberero, J.R., Infante, J.R., LoRusso, P., Shapiro, G., Paz-Ares, L.G., Falzone, R., Hill, J., Cehelsky, J., White, A., Toudjarska, I., Bumcrot, R., Meyers, R., Hinkle, G., Svrzikapa, N., Sah, D.W., Vaishnav, A., Gollob, J., Burris, H.A., "Phase I dose-escalation study of ALN-VSP02, a novel RNAi therapeutic for solid tumors with liver involvement", *J. Clin. Oncol. Abstr.*, 29, 3025, 2011.
96. Jain, R.K., Lee, J.J., Hong D., Markaman, M., Gong, J., Naing, A., Wheeler, J., Kurzrock, R., "Phase I oncology studies: evidence that in the era of targeted therapies patients on lower doses do not fare worse", *Clin. Cancer Res.*, 16(4), pp. 1289–1297, 2010.
97. S. Nie, Y. Xing, G.J. Kim and J.W. Simons, Nanotechnology Applications in Cancer, *Ann Rev Biomed Eng*, 9 (2007), 257–288.
98. Cao, L., Yang, S.-T., Wang, X., Luo, P.G., Liu, J.-H., Sahu, S., Liu, Y., Sun, Y.-P., Competitive performance of carbon quantum dots in optical bioimaging, *Theranostics*, 2012, 2(3), 295–301.
99. Yong, K.T., Qian, J., Roy, I., Lee, H.H., Bergey, E.J., Tramposch, K.M., He, S., Swihart, M.T., Maitra, A., Prasad, P.N., 2007. Quantum rod bioconjugates as targeted probes for confocal and two-photon fluorescence imaging of cancer cells, *Nano Lett.*, 7(3), 761–765.
100. Cady, N.C., Strickland, A.D., Batt, C.A., 2007, Optimized linkage and quenching strategies for quantum dot molecular beacons, *Mol. Cell. Probes*, 21(2), 116–124.
101. Cognet, L., Tardin, C., Boyer, D., *et al.* 2003. Single metallic nanoparticle imaging for protein detection in cells, *Proc Natl Acad Sci USA*, 100: 11350–5.
102. Dunn, A.R., Spudich, J.A., 2007, Dynamics of the unbound head during myosin V processive translocation, *Nat Struct Mol Biol*, 14: 246–8.
103. Nitin, N., Javier, D.J., Roblyer, D.M., *et al.* 2007b. Widefield and high-resolution reflectance imaging of gold and silver nanospheres. *J Biomed Opt*, 12: 051505.
104. Shi, X., Wang, S., Meshinchi, S., *et al.* 2007a. Dendrimer-entrapped gold nanoparticles as a platform for cancer-cell targeting and imaging, *Small*, 3: 1245–52.

105. Archana Retnakumari, Sonali Setua, Deepthy Menon, Prasanth Ravindran, Habeeb Muhammed, Thalappil Pradeep, Shantikumar Nair and Manzoor Koyakutty, Molecular-receptor-specific, non-toxic, near-infrared-emitting Au cluster-protein nanoconjugates for targeted cancer imaging, *Nanotechnology*, 21 (2010) 055103 (12pp).
106. Qian, X., Peng, X.H., Ansari, D.O., *et al.* 2008, *In vivo* tumor targeting and spectroscopic detection with surface-enhanced Raman nanoparticle tags, *Nat Biotechnol*, 26: 83–90.
107. Keren, S., Zavaleta, C., Cheng, Z., *et al.* 2008. Noninvasive molecular imaging of small living subjects using Raman spectroscopy, *Proc Natl Acad Sci USA*, 105: 5844–9.
108. Sokolova, V., Kovtun, A., Prymak, O., Meyer-Zaika, W., Kubareva, E.A., Romanova, E.A., *et al.* 2007. Functionalisation of calcium phosphate nanoparticles by oligonucleotides and their application for gene silencing, *J Mater Chem.*, 17: 721–727.
109. Kester, M., Heakal, Y., Fox, T., Sharma, A., Robertson, G.P., Morgan, T.T., *et al.* 2008. Calcium phosphate nanocomposite particles for *in vitro* imaging and encapsulated chemotherapeutic drug delivery to cancer cells, *Nano Lett.*, 8: 4116–4121.
110. Anusha Ashokan, Parwathy Chandran, Aparna R. Sadanandan, Chaitanya K. Koduri, Archana P. Retnakumari, Deepthy Menon, Shantikumar Nair and Manzoor Koyakutty. Development and haematotoxicological evaluation of doped hydroxyapatite based multimodal nanocontrast agent for near-infrared, magnetic resonance and X-ray contrast imaging. *Nanotoxicology*, DOI: 10.3109/17435390.2011.600839.
111. Chandran, P., Sansidharan, A., Ashokan, A., Menon, D., Nair, S., Koyakutty, M., Highly biocompatible TiO₂:Gd³⁺ nano-contrast agent with enhanced longitudinal relaxivity for targeted cancer imaging.
112. Amir-Aslani and Manggematin. *Technological Forecasting & Social change*. 77, 203–217, 2010.
113. Wendy, R., Sanhaai, Jason, H., Sakamoto, Richard Canady and Mauro Ferrari. Seven challenges in nanomedicine, *Nature Nanotechnology*, 3, 242–244, 2008.

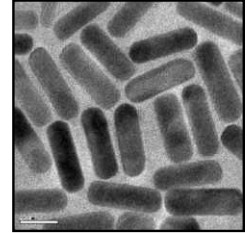
ADDITIONAL READING

1. Mansoor, M. Amiji, *Nanotechnology for cancer therapy*. CRC Press, 2006, USA.
2. Patrick Boisseau and Marcel Lahmani, *Nanoscience: Nanobiotechnology and Nanobiology*. Springer, 2009, USA.
3. Stergios Logothetidis, *Nanomedicine and Nanobiotechnology (Nano Science and Technology)*. Springer, 2012, USA.
4. Pavel Broz, Harry Kroto and Paul O'Brien, *Polymer-based Nanostructures: Medical Applications (RSC Nanoscience & Nanotechnology)*. RSC Publishing, 2010, UK.
5. Guozhong Cao. *Nanostructures and nanomaterials—synthesis, properties and applications*, Imperial College Press, 2004, UK.
6. Kewal, K. Jain, *The Handbook of Nanomedicine*. Humana Press, 2007, USA.
7. Sandra J. Rosenthal and David W. Wright, *Nanobiotechnology protocols*, Humana Press, 2005, USA.

REVIEW QUESTIONS

1. What are the biophysiochemical influences on the interface between nanomaterials and biological systems?
2. What is the influence of isoelectric point of a protein on the behaviour of in a solution containing nanoparticles and a protein?
3. What are the properties of nanomaterials relevant for biological applications?
4. What are the different modes of cancer targeting in nanomedicine? List the major ligands used for active targeting.
5. What are the applications of nanomaterials in medicine?
6. Compare and contrast the different nanosystems used for therapeutic applications?
7. What is hyperthermia cancer therapy? What is the role of magnetic nanoparticles in it?
8. Describe different types of nanoparticles-mediated targeted cancer therapy?
9. What are quantum dots? Describe their role in nanomedicine.
10. What are the challenges faced in the development of nanomedicine? Suggest methods to overcome these challenges.

OPTICAL NONLINEARITY IN NANOSCALE MATERIALS



“In the right light, at the right time, everything is extraordinary.”

Aaron Rose,
quoted in The Reader’s Digest Vol. 152 (1998) 185

In Non-linear Optics (NLO), one investigates the physical consequences of the interaction of intense light fields with matter. Interest in NLO grew substantially after its advent in 1961, when second harmonic generation in a quartz crystal was demonstrated experimentally for the first time. Now, the field has evolved into an independent research area. NLO has thrown new light into the nature of fundamental light-matter interactions and has provided practical solutions for several optical engineering problems. Processes like light frequency addition and subtraction, which occur only in the non-linear domain of electromagnetism are fascinating, and have several applications. Recently it has been found that nanomaterials are promising media for non-linear optical applications. Often they excel their bulk counterparts in the NLO efficiency. An introduction to this interesting area of research is given in this chapter with an emphasis on the optical nonlinearities exhibited by metal nanoparticles and semiconductor nanocrystallites.

Learning Objectives

- What is non-linear optics?
 - What are the physical origins of optical non-linearity in a medium?
 - What is the general relationship between induced polarization and applied optical field in a dielectric medium?
 - What are the different classifications of non-linear optical effects?
 - How do surface Plasmon resonances affect optical non-linearity in metal nanoparticles?
 - What are quantum-size effects?
 - What are the common experimental techniques used for measuring optical nonlinearities?
 - What are pump-probe experiments?
 - What are the applications of non-linear optical materials?
-
-

23.1 INTRODUCTION

Non-linear Optics (NLO) is the study of the interaction of strong light fields with matter. Light intensities required for observing non-linear optical effects are usually available only from laser sources. Experimental NLO began in 1961, when Franken and colleagues¹ observed second harmonic generation of ruby laser light in a quartz crystal at the University of Michigan. A general theoretical framework for three- and four-wave mixing at optical frequencies was then formulated by Bloembergen and colleagues at the Harvard University.² The quantum mechanical calculation of complex non-linear susceptibilities, based on the evolution of the density matrix, was soon applied to optical problems.³

Interest in NLO grew continuously since its inception, and the field has advanced over the years. NLO has enhanced our understanding of fundamental light-matter interactions and it provides solutions for several modern optical engineering tasks. After the advent of nanotechnology a large number of nanomaterials have been investigated for their non-linear optical properties. Often the nanostructures are found to exhibit better non-linear optical properties compared to their bulk counterparts.

In this chapter, we will discuss the origins of optical nonlinearity in material media and some of its real-life manifestations. The non-linear optical properties of metal nanoparticles and semiconductor nanocrystallites are discussed in particular. Some of the major experimental techniques employed for measuring optical nonlinearities and the typical results obtained are discussed towards the end of the chapter.

23.1.1 Optical Field-induced Electric Polarization in Media

In the presence of an applied optical field, the atoms or molecules of a medium may respond in the following two ways: (i) a real transition from one quantum state to another, and (ii) a perturbation of the spatial distribution, or motion, of the internal electric charges. For resonant excitation (absorbing medium) the former type of response is dominant, while for non-resonant excitation (transparent medium) the latter type will predominate. In either case, a field-induced electric dipole moment will result, which will act as a new source to emit a secondary electromagnetic wave.

For example, consider an electromagnetic radiation field applied to a simple atom having an electron. This will result in the oscillation of the electron, so that an oscillating electrical polarization (charge distortion) will be induced in the atom. The positively charged, but heavier nucleus, can also move to a smaller degree. The electron and nucleus, which oscillate about their equilibrium positions constitute an oscillating dipole, which will radiate energy. In addition to electronic polarization, there are also other physical mechanisms, which cause polarisation responses in a material medium. Some of these are intramolecular motion, molecular reorientation, electrostriction, and population redistribution, which are discussed in more detail later in this chapter.

Since light is electromagnetic radiation, when a light beam traverses matter, a fundamental interaction that takes place is this induced dipole oscillation (Macroscopically, a propagating electromagnetic wave will sense the response of the medium, which is made of numerous atoms, in the form of its dielectric constant or refractive index). If the electric-field amplitude of the exciting

radiation is weak or moderate, the dipole oscillation is nearly simple harmonic, and the induced polarization (dipole moment per unit volume) \mathbf{P} of the material has a linear dependence on the field amplitude, given by (in S.I. units)

$$\mathbf{P} = \varepsilon_0 \chi^{(1)} \mathbf{E}, \quad (1)$$

where ε_0 is the vacuum dielectric constant, $\chi^{(1)}$ is the linear susceptibility, and \mathbf{E} is the electric field vector. $\chi^{(1)}$, which is incidentally a second rank tensor, since it relates two vectors \mathbf{P} and \mathbf{E} , is responsible for the linear optical properties, namely, the refractive index (n_0) and absorption coefficient (α_0) of the medium. $\chi^{(1)}$ is a function of the frequency of the electromagnetic radiation. The refractive index, dielectric constant (ε) and linear susceptibility of the medium are related through the equation

$$\varepsilon = n_0^2 = 1 + \chi^{(1)}. \quad (2)$$

If the exciting radiation is sufficiently strong (as in the case of a laser), the dipole oscillations will become anharmonic and the i^{th} component (where i stands for x, y or z) of polarization vector \mathbf{P} can be written in terms of the tensor components of the susceptibility as

$$P_i = \varepsilon_0 \{ \chi_{ij}^{(1)} E_j + \chi_{ijk}^{(2)} E_j E_k + \chi_{ijkl}^{(3)} E_j E_k E_l + \dots \}, \quad (3)$$

where $\chi^{(2)}$ and $\chi^{(3)}$ are the second-order and third-order non-linear optical susceptibilities, respectively.⁴ Susceptibilities above the fifth-order are usually not very significant. $\chi^{(2)}$ is a third-rank tensor and $\chi^{(3)}$ is a fourth-rank tensor. The susceptibility of n^{th} order, $\chi^{(n)}$, is a tensor of rank $(n+1)$ with $[3^{(n+1)}]$ components in general. Equation 3 is the generalised equation for the polarization response of a medium to electromagnetic radiation, and Equation 1 is only a special case of the same, applicable to low light levels. Hence, in general, the polarization response of a medium is anharmonic to the applied light field. The magnitude of the nonlinearity will depend on the applied light intensity and the non-linear susceptibility coefficients. While $\chi^{(1)}$ leads to linear optical effects, $\chi^{(2)}$ leads to second-order nonlinearities and $\chi^{(3)}$ leads to third-order nonlinearities. In general, the non-linear susceptibilities cause modifications in the refractive index and/or absorption coefficient of the material system.

Nonlinear optical effects due to non-linear electronic polarization are normally measurable from an applied optical intensity of about 10^{15} W/m^2 onwards. Higher-order polarizations will be much weaker than the linear polarization at such intensities. On the other hand, the second- and third-order polarizations will become comparable to the linear polarization, when E is as high as the electric field between the electron and proton of a hydrogen atom (approximately 10^{11} V/m). The corresponding optical intensity is about 10^{20} W/m^2 , and this can be obtained only from very powerful laser systems. However, at such intense fields, the power series expansion given by Eq. 3 need not necessarily converge, and the relationship between material response and applied electric field has to be expressed in other forms (this regime of non-linear optics which is referred to as “intense-field non-linear optics” will not be covered in the present discussion).

It is possible to show from symmetry considerations that media with inversion symmetry lack nonlinearities of even order, while those lacking a symmetry axis can display both even and odd order nonlinearities. For this reason, anisotropic crystals are used as media for producing $\chi^{(2)}$ effects, while

$\chi^{(3)}$ effects are generally realised in isotropic media, like liquids, gases and amorphous solids (e.g., glass). It may be noted that molecules, which are anisotropic (i.e., molecules displaying an anisotropic—direction dependent—linear polarisability) will tend to show an optically isotropic behaviour in the bulk when their orientations are randomly distributed. This is true for several liquids (e.g., CS₂) as well as for liquid crystals above the transition to a mesoscopic phase.

In the regime of linear optics, optical properties are independent of light intensity, the principle of superposition holds, and the light frequency is independent of the material medium. On the other hand, in the regime of non-linear optics, refractive index and absorption coefficient change with light intensity, principle of superposition is violated, and light frequencies can change in a medium. An example for light changing its frequency while passing through a non-linear medium is second harmonic generation (SHG), possible in crystals like KDP. A well known application of SHG is the conversion of the 1064-nm infrared radiation from an Nd:YAG laser to the second harmonic wavelength of 532-nm in the green region of the visible spectrum. Such phenomena are possible in non-linear media, because the non-linear terms in Eq. 3 cause mixing of frequencies and wave vectors whereby electric fields multiply, and light frequencies get added or subtracted. To visualize this, let $E_1 = E_{01} \cos \omega_1 t$ and $E_2 = E_{02} \cos \omega_2 t$ be the magnitudes of the field amplitudes of two laser beams of frequencies ω_1 and ω_2 respectively, passing through a second order non-linear medium. Eq. 3 tells us that a resultant field of magnitude of the form

$$\mathbf{E}_1 \mathbf{E}_2 = \mathbf{E}_{01} \mathbf{E}_{02} \cos(\omega_1 t) \cos(\omega_2 t) = (1/2) \mathbf{E}_{01} \mathbf{E}_{02} \{ \cos(\omega_1 + \omega_2)t + \cos(\omega_1 - \omega_2)t \} \quad (4)$$

will be generated, which contains the new frequencies $\omega_1 + \omega_2$ and $\omega_1 - \omega_2$. These frequencies will travel in directions determined by the corresponding wave vectors $\mathbf{k}_1 + \mathbf{k}_2$ and $\mathbf{k}_1 - \mathbf{k}_2$. This effect is known as parametric mixing. In general, depending on the order of the nonlinearity, effects like second harmonic generation (a $\chi^{(2)}$ process, whereby two photons of the same frequency ω interact together to form a single photon of frequency 2ω), Pockels effect (a $\chi^{(2)}$ process, where the refractive index of a material varies linearly with an applied electric field), Optical Kerr effect (a $\chi^{(3)}$ process, whereby the refractive index of a medium varies quadratically with an applied electromagnetic radiation field) etc., can take place.

For example, consider a third-order non-linear medium exhibiting an electronic nonlinearity. The real and imaginary parts of the degenerate non-linear susceptibility $\chi^{(3)}(\omega; \omega, -\omega, \omega)$ are related to optical Kerr effect and two-photon absorption, respectively. These are given through the expressions

$$\text{Re}\chi^{(3)} = (4/3)n_0^2 n_2 \epsilon_0 c, \quad (5)$$

and

$$\text{Im}\chi^{(3)} = \beta \epsilon_0 n_0^2 c \lambda / 3\pi \quad (6)$$

where c is the light velocity in ms^{-1} , λ is the light wavelength in meters, β is the two-photon absorption coefficient in mW^{-1} , and n_2 is the non-linear refractive index coefficient in m^2W^{-1} . The refractive index of the medium is given by

$$n = n_0 + n_2 I \quad (7)$$

and the absorption coefficient is given by

$$\alpha = \alpha_0 + \beta I \quad (8)$$

where I is the light intensity. I is related to the optical field \mathbf{E} through the relation

$$I = 2n_0(\epsilon_0/\mu_0)^{1/2} |E|^2 = (2n_0/Z_0) |E|^2; \quad (9)$$

where $\mu_0 = 4\pi \times 10^{-7}$ H/m is the permeability, and $Z_0 = 377$ Ohms is the characteristic impedance of free space. The propagation equation for light traveling in the z direction through a third-order non-linear medium can then be written as

$$dI/dz = -(\alpha_0 + \beta I) I. \quad (10)$$

The modification in the refractive index can give rise to self-focusing effects if the laser beam has a non-uniform cross-section (e.g., the Gaussian beam). As for the absorption coefficient, the modification will lead to an increase in the net absorption.

23.1.2 Classifications of Optical Nonlinearities

Depending on their physical origin optical nonlinearities can be classified into different categories like resonant and nonresonant, parametric and nonparametric, instantaneous and cumulative, etc.^{5,6} When a medium is transparent to the applied light frequency, the resultant nonlinearity is nonresonant, but when the medium is absorbing the nonlinearity is resonant. Similarly in a parametric process, the initial and final quantum states of the system are identical, whereas in a nonparametric process, the population is transferred from one real level to another. An instantaneous nonlinearity takes place with electronic response times while cumulative nonlinearities need relatively more time to manifest. For example, SHG is a nonresonant, parametric and instantaneous nonlinearity, while saturable absorption is a resonant, nonparametric nonlinearity. Thermal nonlinearities are cumulative in nature (e.g. thermal lensing). Since most nanomaterials of interest have some absorption in the visible spectral region (400–700 nm), they often exhibit resonant, nonparametric and cumulative nonlinearities when excited in this spectral region.

23.1.3 Non-linear Refraction

Nonlinear refraction can be defined as a change in the refractive index or the spatial distribution of refractive index of a medium in the presence of optical fields. A few areas where non-linear refraction has been used or has potential applications are non-linear spectroscopy, optical switching, optical communications, optical limiting, passive laser mode-locking and waveguide switches and modulators. Several physical effects can contribute to the non-linear index of refraction in a medium. A few of these are discussed below.

23.1.3.1 Electronic Polarization

Electronic polarization involves a distortion of the electron cloud about an atom or molecule in the presence of an external optical field. For a third-order non-linear medium, this results in a refractive index change. The timescale of this nonlinearity is typically in the order of femtoseconds or less (10^{-15} to 10^{-16} seconds).

23.1.3.2 Intramolecular Motion

Intramolecular motion is the polarization contribution from a light field-induced relative motion between the nuclei (or ions) within a molecule. The response time of this mechanism is in the order of 10^{-12} to 10^{-14} seconds.

23.1.3.3 Molecular Orientation

Molecular orientation is the field-induced reorientation of anisotropic molecules, which are randomly oriented in the usual state. Here the induced dipole moments of the molecules experience a torque, which tries to align the most polarizable axis with the applied field, working against thermal fluctuation forces (molecular collisions). When the applied field is DC, the effect is called the Kerr effect. If the applied field is AC as in the case of electromagnetic radiation then the system responds not to the instantaneous field, but to the time-averaged square of the field. The effect is then termed the AC or Optical Kerr effect. The alignment of the molecules in the field direction will present a modified refractive index to a propagating light beam polarized in the same direction. Typical response times depend on the rotational viscosity of the molecules, and are usually in the range of 10^{-12} to 10^{-13} sec. Systems with long-range order like liquid crystals in their isotropic phase will exhibit relatively larger orientational nonlinearities, but their response times are larger as well.

23.1.3.4 Electrostriction

Electrostriction is a phenomenon that happens in the presence of an inhomogeneous field, two examples of which are a spatially Gaussian laser beam, and the interference pattern formed by the superposition of coherent beams. In such non-uniform fields, the induced dipoles will experience a translational force that is proportional to the gradient of the field. This force will move the dipoles into regions of higher intensity, resulting in an increased local density and hence an enhanced local refractive index. The response time of electrostriction is approximately 10^{-9} ~ 10^{-10} sec, depending on the phase state of the medium (solid, liquid or gas). Systems of isotropic molecules also will be electrostrictive.

23.1.3.5 Population Redistribution

When the frequency of incident radiation is resonant with an electron transition in an atom or molecule, transitions between real energy states will occur, i.e., electrons can occupy real excited states for finite periods of time, causing a population redistribution. The optical polarization is dependent on the relative distribution of atoms and molecules in the permissible eigen states, and hence, a population redistribution can produce a change in the net polarization. Refractive index changes due to population redistribution can be seen in semiconductors, solutions of organic molecules, etc.

23.1.3.6 Changes in Physical Properties

A strong optical wave can sometimes induce changes in the physical properties of a medium. For example, absorption of photons can raise the temperature. A temperature rise ΔT can result in a refractive index change given by

$$\Delta n_0 = (dn/dT) \Delta T, \quad (11)$$

where dn/dt is called the thermo-optic coefficient. The index change can be proportional to the light intensity, but may also depend on the time-integrated intensity (fluence).

A few areas, where non-linear refraction has been used or has potential applications, are non-linear spectroscopy, optical switching, optical communications, optical limiting, passive laser mode-locking and waveguide switches and modulators.

23.1.4 Non-linear Absorption

Normally, the absorption coefficient of a medium, which depends on the concentration of the absorbing species, will be independent of the input light intensity. However at sufficiently high intensities, this need not be the case. As a result, the transmittance of the medium will be either enhanced or reduced at the excitation wavelength. Non-linear absorption refers to this change in transmittance of a material which happens at high input light intensities. Broadly, the underlying mechanisms of non-linear absorption can be divided into those, which reduce the absorption and those which enhance the absorption.

23.1.4.1 Reduction of Absorption

Processes that reduce the absorption of a medium are generally known as saturable absorption phenomena. In a two-level system, as photons from a high-intensity incident beam pump electrons to the higher energy level, the ground state will get depleted. Moreover, stimulated emission and spontaneous emission will occur from the excited state. As a result, the system cannot absorb as many photons as it would at low-input intensity conditions, thereby saturating the absorption. The absorption coefficient α becomes a function of the incident intensity, and for a homogeneously broadened system, it is given by the expression,

$$\alpha = \alpha_0 / [1 + I/I_s]; \quad (12)$$

and for an inhomogeneously broadened system, it is given by

$$\alpha = \alpha_0 / [1 + I/I_s]^{1/2} \quad (13)$$

where I_s is the saturation intensity (intensity at which the absorption coefficient drops to half of its original value). The attenuation of the incident light is given by

$$dI/dz = -\alpha(I)I. \quad (14)$$

In polyatomic molecules with a large number of excited states (which are typically modeled as a five-level system), saturable absorption can occur if the absorption coefficient of the excited states is smaller than that of the ground state. In this case, the attenuation of the incident light is given by

$$dI/dz = -\sigma_0 S_0 NI - \sigma_1 S_1 NI - \sigma_2 T_1 NI; \quad (15)$$

where σ_0 , σ_1 and σ_2 are the absorption cross-sections for the ground, first excited singlet, and first excited triplet states, respectively. N is the number density of molecules in the system and S_0 , S_1 and T_1 are the fractional number densities of the corresponding states such that $S_0 + S_1 + T_1 = 1$.

Saturable absorbers have several applications. For instance, saturable absorbers can be used in Q-switching and mode-locking of lasers, to generate short and ultrashort laser pulses, respectively.

Another application is to make an optically bistable element, by placing a saturable absorber between two mirrors of a Fabry-Perot interferometer.

23.1.4.2 Enhancement of Absorption

In general, materials exhibiting an enhanced absorption at higher input light fields are known as Optical Limiters. An optical limiting device is very useful for protecting sensitive optical detectors and human eyes from accidental exposure to dangerous levels of light. Many materials including metal and semiconductor nanoparticles can function as potential optical limiters. A few processes, which result in the enhancement of optical absorption in a medium irradiated by strong optical fields, are discussed below:

Multi-photon absorption: In a multi-photon absorption process, either two or more photons will be absorbed by the atom or molecule in a single event. As the name implies, two-photon absorption (2PA) involves the simultaneous absorption of two photons from an incident field of radiation, resulting in a transition from the ground state to an excited state. Since the selection rules applicable for TPA are different from those of single-photon absorption, 2PA spectroscopy is a valuable complement to linear absorption spectroscopy in studying the excited states of atomic and molecular systems.

The mechanism of 2PA is illustrated in Fig. 23.1. Two photons from the incident field at frequency ω are absorbed simultaneously to make a transition, which is resonant at 2ω . The intermediate level is referred to as a virtual state, since it is not a real stationary state of the system. Since the system absorbs both photons simultaneously, the process is sensitive to the instantaneous intensity. 2PA is proportional to the square of the instantaneous intensity (I), and the optical loss in a medium with 2PA is given by

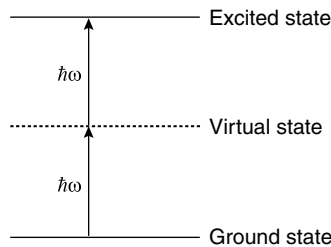


Fig. 23.1 The two-photon absorption process.

$$dI/dz = -\alpha_0 I - \beta I^2. \quad (16)$$

The 2PA cross-section β is a macroscopic parameter characterising the material, whereas the individual molecular 2PA property is given by the 2PA cross-section σ . The relation between σ and β is given by

$$\sigma = \hbar\omega\beta/N; \quad (17)$$

and β is related to the imaginary part of the third-order susceptibility, $\chi^{(3)}$, as given by Eq. 6.

Similarly, the beam attenuation in a sample having Three-Photon Absorption (3PA) in addition to linear absorption is given by:

$$dI/dz = -\alpha_0 I - \gamma I^3; \quad (18)$$

where γ is the 3PA coefficient. γ is related to the fifth-order non-linear susceptibility $\chi^{(5)}$, and hence, 3PA is a fifth-order non-linear process. In general, an n-photon absorption process can be described by the equation:

$$\frac{dI}{dz} = -(\alpha + \gamma^{(n)} I^{n-1})I; \quad (19)$$

where $\gamma^{(n)}$ is the n-photon absorption coefficient.

Excited-state absorption: Polyatomic molecules are characterized by a number of allowed excited states (e.g., the excited singlet and triplet manifolds of organic molecules). If the incident intensity is well above the saturation intensity I_S , then the excited state can become significantly populated. The excited electron normally relaxes to one of the intermediate levels in the excited state, before eventually returning to the ground state. However, there is another possibility that the excited molecule absorbs one more photon and undergoes a transition to a higher level, before relaxing to the ground state. This process is known as excited-state absorption (ESA), and it is observed when the absorption cross-section of the excited state is larger than that of the ground state. When only a single excited state is taking part in the ESA process, the propagation equation can be written as

$$dI/dz = -\sigma_0 N_0 I - \sigma_1 N_1 I; \quad (20)$$

where σ_0 and σ_1 are the absorption cross-sections, and N_0 and N_1 are the population densities of the ground and excited states, respectively.

Free-carrier absorption: The free-carriers generated by linear absorption in semiconductors may experience subsequent phonon-assisted absorption to higher lying (lower-lying) states in the conduction (valence) band. This process is called free-carrier absorption (FCA). This can happen in metal nanoparticles too, which are sufficiently small in size. In the weak absorption regime, the attenuation may be described by

$$dI/dz = -\alpha_0 I - \sigma_c N_c(I)I; \quad (21)$$

where $N_c(I)$ is the intensity dependent carrier density, and σ_c is the free-carrier absorption cross-section.

Phenomenologically, ESA and FCA are known as reverse saturable absorption (RSA) processes.

23.2 OPTICAL NON-LINEARITIES IN METAL NANOSTRUCTURES

About two-thirds of the chemical elements are metals, and these include all main group heavy elements and transition elements. An important characteristic of metals is that the outer-valence electrons can be easily removed from the atom, making them electropositive in nature. A metal consists of a regular lattice of positively charged metal ions embedded in a gas of quasi-delocalised electrons. In simple

terms, the generation of a metal can be understood as the formation of a large number of infinitely extended molecular orbitals (MO). Since these orbitals are very close in energy, together they form energy bands. The connection between the MO description of a finite molecular system and the “infinite” situation in a bulk metal is that the highest occupied molecular orbital (HOMO) is now called the Fermi energy (E_F). Since E_F depends only on the density of the electrons, it is independent of the particle size.

The most important property of a metal is electrical conductivity, which arises from its ability to transport electrons. Electrons can be mobile only when either the energy band that contains them is not fully occupied, or when a nearby band is empty. For example, in bulk Lithium it is the half-occupied s-band that renders mobility to its electrons, while in Beryllium, it is the proximity to the empty p-band that makes the electrons from the fully occupied s-band mobile. Similarly, most of the d-type transition metals have partially filled d-orbitals facilitating electron mobility.

Delocalisation of electrons in the conduction band of a metal is possible as long as the dimension of the metal particle is a multiple of the de Broglie wavelength, given by

$$\lambda = h/(mv); \quad (22)$$

where h is the planck's constant (6.626×10^{-34} J.sec.), m is the mass of the electron (9.109×10^{-31} kg), and v is the velocity of the electron. However, if a particle is smaller than this dimension, then the electrons are localised between the atomic nuclei, so that they behave as typical molecules. The quantum mechanical model of “electron in a box,” which is normally used for describing atoms is useful to describe the situation in small metal nanoparticles also, where size restrictions begin to influence electronic energy levels.

The study of metallic nanostructures has been a subject of considerable interest in recent years. A nanoscale metal-dielectric boundary produces significant changes in the optical properties, making them size- and shape-dependent. Since metal clusters are normally embedded or dispersed in some kind of a surrounding medium, the metal-dielectric boundary is often realized in practice. The major consequence of optical excitations is the collective oscillation of conduction band electrons, which are localised along the interface between the metal and the surrounding dielectric. This oscillation happens when the nanoparticle size is sufficiently small so that the mean free path of the electrons exceeds the particle radius. It is known as a “surface plasmon wave” (Fig. 23.2), and the corresponding absorption band is called the surface plasmon resonance (SPR). For noble metal nanoparticles, the SPR appears in the visible region of the spectrum, and it can be measured using a UV/Vis spectrophotometer.

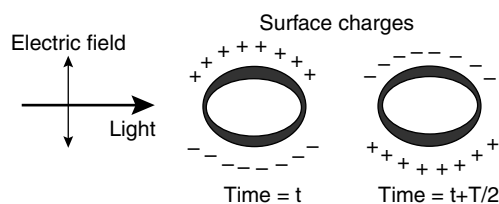


Fig. 23.2 The surface plasmon resonance. T is the time period of electromagnetic oscillation.

23.2.1 The Surface Plasmon Resonance

Though metal nanostructures can exhibit distinct dipole, quadrupole, and higher order multipole plasmon resonances depending on their size and shape, often a dipole approximation is used, where the conduction electrons are considered to produce oscillating dipoles along the field direction. The original classical dipolar model proposed by Mie⁷ can be used to describe the optical properties of metal nanospheres successfully. This dipolar-type displacement is particularly applicable to smaller size particles, and gives rise to an extinction coefficient k_{ex} (collective measure of absorption and scattering losses) by the following equation

$$k_{ex} = \frac{18\pi NV\epsilon_d^{3/2}}{\lambda} \frac{\epsilon_2}{[\epsilon_1 + 2\epsilon_d]^2 + \epsilon_2^2}; \quad (23)$$

where N is the particle number density, V is the volume, ϵ_d is the dielectric constant of the surrounding medium, and λ is the excitation wavelength. ϵ_1 and ϵ_2 represent the real and imaginary parts of the complex dielectric constant ϵ_m of the metal ($\epsilon_m = \epsilon_1 + i\epsilon_2$), which are dependent on the light frequency ω . If ϵ_2 is small or weakly dependent on ω , the absorption maximum will occur when $\epsilon_1 = -2\epsilon_d$, leading to a vanishing denominator. Thus, a surface plasmon resonance (SPR) is produced at the optical frequency ω at which the condition $\epsilon_1 = -2\epsilon_d$ is fulfilled. The plasmon resonance peak is dependent on the nanoparticle size, because the dielectric constant ϵ of the metal is size-dependent.

While metal nanospheres show only a single plasmon band, metal nanorods exhibit a plasmon band with two peaks corresponding to the oscillation of the free electrons along the parallel (longitudinal) and perpendicular (transverse) directions with respect to the long axis of the rod. Even though the transverse mode resonance is close to that observed for spherical particles, the longitudinal mode is considerably red-shifted. The magnitude of this red-shift depends on the aspect ratio, which is the length of the rod divided by the width. Similarly, in core-shell nanostructures, where either the core or shell material is metallic, the optical properties are again governed by plasmon resonances. Dramatic changes in the resonance can be seen with metallic shells of varying thickness, because here the plasmon resonance frequencies and the spectra are described by dielectric functions, that incorporate changes due to enhanced-electron scattering derived from the ultra-thin metallic layer structure.

It is interesting to note that while major modifications to the optical spectra of metal nanoparticles are derived from effects that can be explained, within a classical dielectric framework, in semiconductor nanoparticles these are caused from quantum confinement effects that lead to the quantization of the electron and hole energy states. Though quantum confinement will modify the spacing of the energy in the conduction band of metal nanoparticles, it affects only the conductive properties of the metal, and is often used to describe the metal-to-insulator transition that happens as the particle is reduced from microscopic to nanoscopic sizes. The energy-level separations are essentially too small to affect the optical properties of the metals in the UV to the IR range.

23.2.1.1 Local Field Enhancement

When metal nanoparticles are optically excited at or near the SPR wavelength, the local electric field gets enhanced close to the metal-dielectric boundary. When an ensemble of metal nanoparticles of

dielectric constant ϵ_m distributed uniformly and randomly in a dielectric host of dielectric constant ϵ_d is optically excited, the local electric field near the particle surface is given by

$$E_l = \frac{3\epsilon_d}{\epsilon_m + 2\epsilon_d} E_o; \quad (24)$$

where E_o is the applied optical field amplitude. Since $\epsilon_m + 2\epsilon_d$ is a minimum near the SPR, E_l will be a maximum if the excitation is close to the surface plasmon resonance. The existence of local field enhancement has been known for a long time, and it is used in surface-enhanced Raman spectroscopy (SERS), and more recently, for apertureless near-field microscopy. Recently, Schatz and coworkers⁸ have studied local field enhancement in metallic nanoparticles using the discrete dipole approximation. According to their calculation, for spherical Ag particles of radius less than 20 nm, the maximum field enhancement is close to 200 near the plasmon resonance at the wavelength of 410 nm. For an Ag sphere of 90 nm radius, the plasmon resonance is shifted to 700 nm and the field enhancement is only 25. On the other hand, for a dimer composed of 36 nm Ag particles separated by 2 nm, there is a dipolar plasmon resonance at 520 nm, and a maximum electric-field enhancement of 11,000 is found to occur at the midpoint between the two spheres.

23.2.1.2 Enhanced Optical Non-linearity

Local field enhancement results in the enhancement of non-linear optical effects in the vicinity of a metallic nanoparticle. Optical properties of noble metal nanoparticles are primarily determined by the electrons occupying the 'd' and conduction bands. From studies in gold nanoparticles, Hache *et al.*⁹ have shown that there are three major electronic contributions to the third-order nonlinearity. These originate from the intraband, interband and hot-electron transitions. The first of these, $\chi^{(3)}_{\text{intra}}$, is derived from the excitation of intraband conduction electrons. It is electric dipole in nature, originates totally due to the confinement of the free electrons, and is strongly size-dependent. The second term, $\chi^{(3)}_{\text{inter}}$, originates from interband transitions between the d-bands and the conduction band, which is size and shape independent down to very small sizes of about 2.5 nm. The third and most important contribution $\chi^{(3)}_{\text{hot}}$ arises from hot electrons, which are conduction electrons that are easily elevated to temperatures of several hundred degrees by photoexcitation as their specific heats are very small. Calculations⁹ and experiments¹⁰ show that the hot electron and interband contributions are mainly imaginary in nature and are much stronger than the intraband contribution. They have opposite signs though: while interband transitions result in an induced transmission behaviour (saturable absorption), hot electron excitations lead to an induced absorption (reverse saturable absorption) behaviour.

An interesting phenomenon associated with hot electron excitation is the transient modification of the surface plasmon absorption band. The excited hot electrons will take a few picoseconds to thermalise with the lattice, during which time the Fermi–Dirac electron distribution will be modified, since part of the one-electron levels below the Fermi level is emptied and part of those above is occupied. This leads to a momentary modification of the dielectric constant ϵ_m , which results in a transient re-distribution of the equilibrium plasmon band. As a result, the absorption around the SPR peak is reduced and that at the wings is increased. This “plasmon band bleach” takes place immediately

after laser excitation, and its dynamics can be measured from pump-probe experiments.^{11, 12} The SPR bleach lasts only for the duration of the hot electron relaxation which is typically a few picoseconds.

Experiments reveal that metal nanoparticles generally show saturable absorption at moderate input intensities, and reverse saturable absorption at higher intensities.^{13, 14} Interestingly, in metal nanoclusters, which are too small to sustain an SPR, the absorption saturation effect is nearly absent.¹⁵ The optical limiting effect at higher intensities arises from the enhanced role of hot-electron excitations and free carrier absorption in this intensity regime.

23.2.1.3 Induced Thermal Scattering of Light

Due to the metal-dielectric interface, an inherent refractive index mismatch exists between the nanoparticles and the surrounding medium, which results in a weak scattering of an incident beam of light. In addition, absorbing nanoparticles excited by a strong laser pulse will undergo transient heating, resulting in a transient refractive index change given by $\Delta n_0 = (dn/dT) \Delta T$, where dn/dT is the thermo-optic coefficient (see Eq. 11). ΔT is given by

$$\Delta T = F_0 \alpha_0 / 2\rho C_V; \quad (25)$$

where F_0 is the laser fluence, ρ is the density and C_V is the specific heat at constant volume. Thus at high input energies, the laser pulse will be strongly scattered in a large-solid angle from the transient inhomogeneity in the refractive index, so that the transmitted energy along the incident beam direction becomes less. This phenomenon can be used for optical limiting applications.

Since temperature build-up in the medium is a relatively slow process, this nonlinearity will be more prominently observed if longer laser pulses are used for excitation. For example, Francois *et al.*¹⁶ reported that when gold clusters of 5 nm and 30 nm average diameters were excited by picosecond and nanosecond laser pulses respectively, the observed reduction in transmission was more pronounced in the latter case. Similarly, for thiol-capped Ag, Au and Ag-Au alloy nanoclusters in solution, the non-linear transmission of nanosecond laser pulses was less than that of picosecond pulses.¹⁷ Both these results indicate that the use of relatively longer nanosecond pulses leads to a larger amount of thermal scattering. Induced thermal scattering is believed to contribute to the optical limiting effect in a number of materials, like carbon black, carbon nanotube suspensions and metal – dendrimer nanocomposites.

Substantial optical nonlinearities are found in nanoparticles of the noble metals Cu, Ag and Au, which can be employed for non-linear optical applications, such as optical limiting, switching, and saturable absorption. For instance, it should be possible to use metal nanocomposite glasses as ultrafast optical switches.

23.3 OPTICAL NON-LINEARITIES IN SEMICONDUCTOR NANOCRYSTALLITES

Semiconductor quantum dots (SQD) exhibit several features that render them as attractive candidate materials for non-linear optical applications. The main limitation in the efficient exploitation of

non-linear optical processes in device applications appears to be the simultaneous requirement of materials with large non-linear coefficient as well as fast response. Several materials with large values of non-linear optical susceptibilities exhibit large values of the response time τ also, making the figure of merit for switching applications (the ratio of the non-linear susceptibility to the response time) rather low. This is known to be the case with most of the bulk semiconductor materials.¹⁸ For example, the typical value of $\chi^{(3)}$ arising from non-parabolicity mechanism is of the order of $10^{-10}\text{m}^2\text{V}^{-2}$ with a corresponding response time of 10^{-7}s . On the other hand, bound electron anharmonicity provides fast response ($\tau \approx 10^{-15}\text{s}$), but with poor strengths of non-linearity ($\chi^{(3)} \approx 10^{-19}\text{m}^2\text{V}^{-2}$).

It seems that the limitation on the figure of merit values is not so decisive in the case of low-dimensional semiconductors. Several mechanisms of refractive as well as absorptive non-linearity are possible in SQDs, owing to their origin to specific features of quantum confinement. Further, several new and modified mechanisms of non-linearity are found to contribute to an enhancement in the optical non-linearity in confined structures, making the study of their non-linear response challenging as well as rewarding. This has motivated several studies over the past two decades in the second- and third-order non-linearities of SQD media.

23.3.1 Enhancement of Second-order Non-linearity

Non-linearity arises from two contributions in quantum confined systems: a contribution from the bulk and another from the surface or interface. The enhanced ratio of the number of atoms or molecules on the surface to that within the bulk in the case of SQDs is a factor of considerable significance in this regard. This effect is particularly important in the case of quantum dots of extremely small sizes. Though SHG is symmetry-forbidden in centrosymmetric media within the dipole approximation, this limitation is no longer valid at the interfaces. Thus the study of second harmonic processes becomes an important tool in probing surfaces and interfaces.

Second harmonic generation (SHG) with SQDs as media was investigated by several groups and it has been shown that the non-linearity is enhanced considerably from that of the bulk.¹⁹⁻²² Sauvage *et al.* have reported²¹ on the observation of SHG in self-assembled quantum dots of InAs/GaAs. The efficiency of SHG is enhanced by the double resonance between the pump beam (of wavelength $20\mu\text{m}$) and the inter-sub level transitions. The second-order susceptibility has been found experimentally to be enhanced by four orders of magnitude in comparison with bulk GaAs. The size dependence of SHG efficiency in CdSe nanocrystals has been studied using the technique of Hyper-Rayleigh scattering method and the normalised per-unit cell value of the first hyper polarisability has been found to exhibit a substantial enhancement in nanocrystals of very small dimensions.²²

23.3.2 Mechanisms of Third-order Non-linearity

Resonant as well as non-resonant mechanisms contribute to non-linearity in SQDs. While resonant mechanisms tend to possess high efficiencies, their response is slower in comparison to that of non-resonant mechanisms. Resonance transitions include interband transitions, free-carrier absorption, and transitions involving excitons, excitonic complexes and impurity levels. Since excitons tend to

be long-lived in SQDs in comparison to the bulk, exciton-related mechanisms play a major role in determining their non-linear optical response. The other major modification in the case of SQDs is the enhancement of the local field and the influence of the increased surface area. The main non-resonant mechanisms are anharmonic response of bound electrons and non-linear motion of carriers. Thermal mechanism plays a major role in the case of continuous wave and even nanosecond-pulsed excitation. Orientational mechanism and band gap distortions also contribute to optical non-linearity in SQDs. The increased surface area implies a large scope for defect-related processes to influence the optical properties. Excitons can get trapped at defect sites and their response can get modified. The local field experienced by an electron in SQDs can be very different from that in the bulk, leading to an enhancement in optical non-linearity.

The Initial results on enhancement of non-linearity in SQDs were not without some controversy,²³ presumably arising out of the difference in the conditions of preparation of the samples and the limited understanding of the role of the surrounding matrix. Uncertainties on the shape, size, surface, stoichiometry and the nature of defects present make a comparison of the results rather difficult. Systematic experimental analysis of the effect of size variation on the non-linearity of semiconductor nanoclusters has been few and far between, and further concentrated efforts in this direction would be rewarding. It has been shown²⁴ that the third-order susceptibility $\chi^{(3)}$ gets enhanced considerably in the case of strong quantum confinement.

Excitation of a semiconductor nanocluster by a short-laser pulse results in the generation of an exciton bound by the cluster surface. The lifetime of the exciton is short and it is rapidly trapped by surface defects, leading to the formation of a trapped electron-hole pair. The non-linear response of SQDs often results from a combination of a fast free carrier component due to untrapped electron-hole pairs and a slow component due to trapped carriers, as explained by Ghanassi *et al.*²³ The contribution from free carriers is important in short-time domains, such as picoseconds and arises from the saturation of the lowest exciton band. In the case of nanosecond excitation, contribution from trapped carriers dominates, provided the pulse width and repetition rate are such that thermal mechanisms are not operative in the material under study. Trapped carriers modify the optical properties of the materials through phase space filling or through the static electric fields they create. However, deeply-trapped electrons and holes are ineffective for phase space filling and the nonlinearity may arise from bleaching of the exciton absorption because of the reduced overlap of the electron and hole wave functions in the presence of a trapped electron-hole pair.²⁴ Theoretical and experimental work done over the years has resulted in a considerable amount of information on the physical processes underlying the mechanisms of optical nonlinearity in SQDs.²⁵⁻²⁹

The nature of intraband transitions (between the confined sublevels within the conduction or the valence bands) in SQDs are different from those in the bulk as the 3-D confinement modifies the density of states as described in an earlier chapter. The dipole lengths corresponding to these transitions extend over the quantum dot size. Two- or three-photon transitions among excited states involved in the intraband transitions can be achieved by monitoring the dot size and geometry of the quantum dots. Further, the narrow homogeneous line width of the intraband transitions of individual quantum dots is also expected to enhance the non-linear susceptibility. In view of these

factors, the optical non-linearities associated with intraband transitions are expected to be enhanced considerably.

SQDs also exhibit phenomena, such as multiphoton absorption, saturable absorption and free carrier absorption, which are processes described in earlier sections of this chapter. The actual mechanism depends on parameters such as the wavelength, pulse duration and intensity of the exciting radiation. Factors such as the nature of the surface of the nanocluster, the particle size and the distribution also influence the response. In fact, it is a combination of several of these factors that determines the ultimate nature of non-linear absorption in SQDs.^{30, 31} An example is the non-linear optical response of the semiconducting nanocrystal CdSe, which has been studied under excitation by laser pulses of duration from hundred femtoseconds to ten picoseconds. It was found that mechanisms of two-photon absorption and related processes tend to dominate in the spectral regime, where the single-photon energy ($\hbar\omega$) is less than the band gap (E_g). On the other hand, saturable absorption due to band filling mechanism plays an important role when $\hbar\omega > E_g$.

23.4 EXPERIMENTAL TECHNIQUES

A number of experimental methods are available for measuring the optical non-linearity in material systems.⁵ However, Z-scan and degenerate four wave mixing (DFWM) are the techniques usually adopted for measuring the third-order non-linear optical parameters of isotropic media. Pump-probe type experiments, using ultrafast-laser pulses, are employed for observing the temporal evolution of the non-linearity. These are discussed in the following sections.

23.4.1 Z-scan

The z-scan is a single-beam experiment using which the non-linear refractive index and non-linear absorption coefficient of a material can be measured. Originally, the z-scan was used to characterise the non-linear susceptibility of materials, which are transparent at the excitation wavelength. However, now its use has been extended to the study of absorbing media as well. In the z-scan scheme, a laser beam having a Gaussian spatial distribution is initially focused by a lens. The beam direction is taken as the z-axis, and the beam focus is taken as $z = 0$. The sample to be measured is then translated in short steps from a negative z to a positive z , and the sample transmission corresponding to each z is measured using a detector (Fig. 23.3). In practice, the sample can be mounted on a motorised translation stage. There are two variations of the z-scan arrangement: in the closed aperture z-scan an aperture is placed in front of the detector, whereas in the open aperture z-scan no aperture is used. The closed aperture z-scan utilises the self-focusing property of a Gaussian beam in a non-linear medium, and a plot of the normalised transmittance versus sample position in this configuration will provide information regarding the real part of the non-linearity (non-linear refractive index). A similar plot for the open-aperture configuration will give information on the imaginary part of the non-linearity (non-linear absorption coefficient).

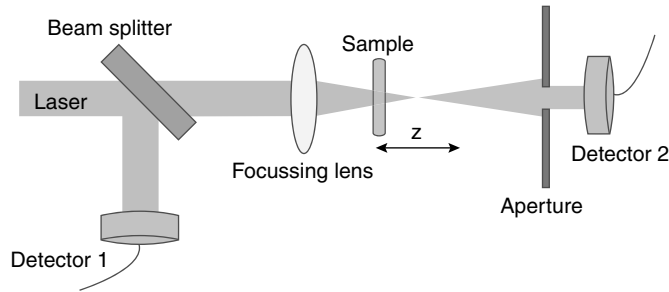


Fig. 23.3 The schematic arrangement of a closed aperture z-scan experiment. The aperture will be removed in the open aperture z-scan experiment.

Closed-aperture z-scan: The closed-aperture z-scan is based on the self-focusing or self-defocusing of a spatially Gaussian optical beam by a thin non-linear medium. For a medium with a Kerr non-linearity, the refractive index can be written as $n = n_0 + n_2 I$, where n_0 is the linear refractive index, n_2 is the non-linear refractive index coefficient, and I is the time averaged intensity of the optical field. When the laser beam cross-section is Gaussian given by $I = I_0 \exp(-2r^2/\omega^2)$, the intensity will be a maximum at the beam centre, which will drop exponentially along the radial direction. Therefore, a Gaussian laser beam passing through a non-linear medium will see maximum refractive index at the beam centre, which will decrease radially. This results in a phase modulation of the wavefront, and hence, the beam will get focused by itself. If n_2 is negative, then the beam will be defocused. If the non-linear medium is thin (i.e., $l \ll z_R$, where l is the sample length and $z_R = \pi\omega_0^2/\lambda$ is the Rayleigh range of the focused beam in air, where ω_0 is the $1/e^2$ beam radius at focus and λ is the excitation wavelength), the non-linear phase $\Delta\phi(z, t)$, which is impressed on the wave can be written as (ignoring the radial component of phase variation)

$$\Delta\phi(z, t) = \Delta\phi_0(t) / [1 + (z/z_R)^2], \quad (26)$$

and the phase distortion will be a maximum when the sample is at the beam focus. A typical closed aperture z-scan will look like the curve as shown in Fig. 23.4, which was measured in CS_2 using 300 ps laser pulses, at an excitation wavelength of 800 nm. Here the normalized transmittance (measured transmission divided by the linear transmission) is plotted against the z position. The symmetric valley-peak structure shown in the figure is typical for a sample, which shows self-focusing, while a peak-valley structure will appear for a self-defocusing sample.

If the on-axis phase shift is small (i.e., when $|\Delta\phi_0| < \pi$), the non-linearity can be calculated using the following expression (which is an approximation valid to within 3% error) given for the difference between the peak and valley transmittance values, ΔT_{p-v} :

$$\Delta T_{p-v} = 0.405 (1-S)^{0.25} \langle \Delta\phi_0 \rangle, \quad (27)$$

where S is the linear aperture transmittance given by $1 - \exp(-2r_a^2/\omega_a^2)$, where r_a is the aperture radius and ω_a is the beam radius at the aperture. Thus, a simplified analysis of the closed aperture z-scan

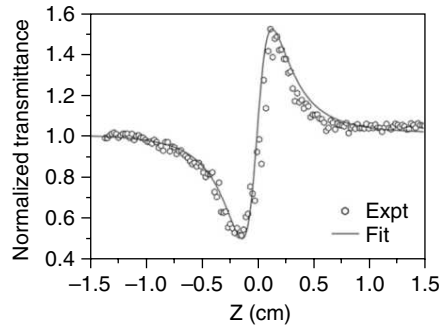


Fig. 23.4 A closed aperture z-scan measured in CS_2 . The circles show data points while the solid curve is a theoretical fit using equations given in ref. 32.

measurement involves finding ΔT_{p-v} from the curve and estimating $\langle \Delta \phi_0 \rangle$ using the above equation. The non-linear refractive index coefficient can then be determined from the relation

$$n_2 = 0.38 (\lambda \omega_0^2 / I_{\text{eff}}) (t_{\text{FWHM}} / E_i) \langle \Delta \phi_0 \rangle, \quad (28)$$

where E_i is the input energy, t_{FWHM} is the pulse width (full width at half maximum), and $I_{\text{eff}} = [1 - \exp(-\alpha_0 l)] / \alpha_0$, where l is the sample length. If the on-axis phase shift is larger than π , then the above approximations have to be replaced by more precise expressions, and n_2 can then be obtained from numerical calculations³².

Open-aperture Z-scan: In this case, no aperture will be kept before the detector so that the detected output becomes insensitive to the non-linear refraction effects. Therefore, only the change in transmission due to various non-linear absorption phenomena will be measured by the detector. The open-aperture z-scan trace will be symmetric with respect to the focus ($z = 0$), where it will show a minimum transmittance or maximum transmittance, depending on the sign of the dominant non-linear absorption process. In the case of reverse saturable absorption, the transmittance will be a minimum at the focus, and for saturable absorption, the transmittance will be a maximum at the focus. The normalised transmittance of the medium for a third-order optical nonlinearity is given by³²

$$T = \frac{1}{\sqrt{\pi} q_0(z, 0)} \int_{-\infty}^{+\infty} \ln [1 + q_0(z, 0) \exp(-t^2)] dt; \quad (29)$$

with $q_0(z, 0) = \beta I_0 I_{\text{eff}} / [1 + (z/z_0)^2]$, where I_0 is the on-axis peak intensity at the focal point. I_{eff} is given by $[1 - \exp(-\alpha_0 l)] / \alpha_0$, with l being the sample thickness. β denotes the non-linear absorption coefficient, the magnitude and sign of which can be determined from numerical evaluation.

A typical open-aperture Z-scan curve, measured in 29kDa Au nanoclusters containing about 140 atoms each, is shown in Fig. 23.5. The surface plasmon resonance is nearly absent in these clusters due to their very small size (approximately 1 nm). The clusters behave like reverse saturable absorbers. Figure 23.6 shows results from bigger nanoparticles, in which both saturable and reverse saturable absorption are seen. In Fig. 23.7, results from a PbS nanocomposite film are shown.

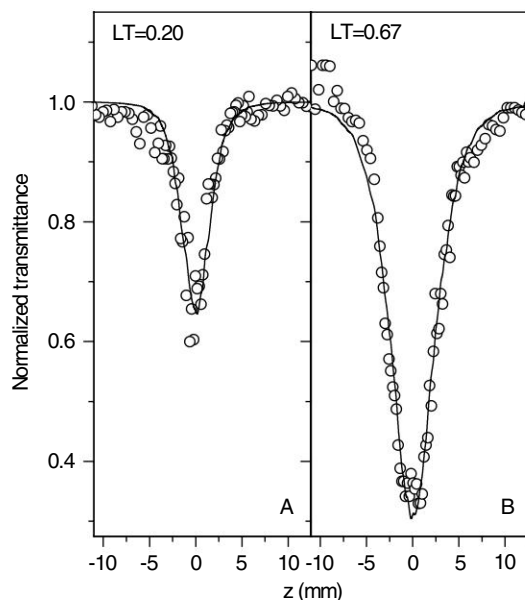


Fig. 23.5 Open-aperture z-scan curves measured in suspensions of 29kDa Au@alkanethiol nanoclusters at two different concentrations (LT is linear transmission). 7 ns laser pulses at 532 nm have been used for excitation. Each cluster contains approximately 140 Au atoms. The SPR is very weak in these clusters. An optical limiting behaviour is seen (from ref. 15: J. Thomas, M. Anija, J. Cyriac, T. Pradeep, R. Philip, *Chem. Phys. Lett.*, 403, (2005) 308).

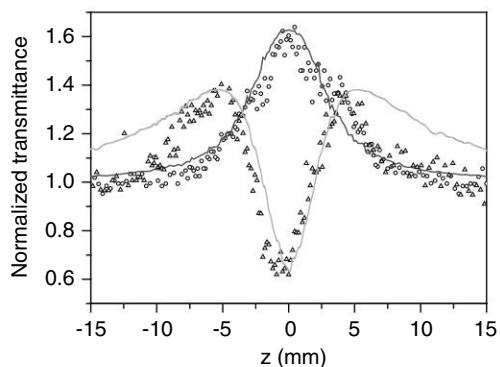


Fig. 23.6 Open-aperture z-scan curves obtained in Au-PVA and Au:Ag-PVA nanocomposite polymer films, when excited by 532 nm, 7 ns pulses. Humps indicate absorption saturation while the valley indicates reverse saturable absorption (from ref. 33: B. Karthikeyan, M. Anija and Reji Philip, *Appl. Phys. Lett.*, 88, (2006), 053104).

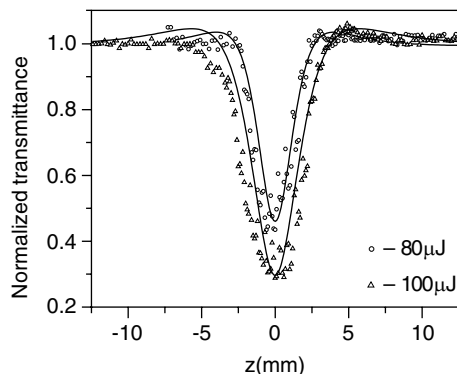


Fig. 23.7 Open-aperture z-scans obtained in a PbS nanocomposite film, at two input pulse energies (80 microjoules, 100 microjoules), when excited by 532 nm, 7 ns laser pulses. Efficient optical limiting is seen (from ref. 30: P.A. Kurian, C.Vijayan, C.S. Suchand Sandeep, R.Philip and K. Sathiyamoorthy, *Nanotechnology*, 18, (2007), 075708).

23.4.2 Degenerate Four Wave Mixing (DFWM)

DFWM is one of the most commonly employed techniques for the measurement of $\chi^{(3)}$ in isotropic media. In a z-scan measurement, the non-linear absorption and non-linear refraction can be separately measured, from which $\chi^{(3)}$ can be calculated. However, being a single-beam technique, the z-scan cannot provide information on the temporal evolution of the optical non-linearity. On the other hand, DFWM can be configured as a pump-probe technique that offers this capability. It requires slightly more complex experimental apparatus, but provides several advantages. Since the setup involves temporal and spatial overlapping of three separate beams, it permits increased flexibility, such as the possibility of measuring different tensor components of $\chi^{(3)}$, and a measurement of the temporal evolution of the non-linearity.

Four-wave mixing refers to the interaction of three electromagnetic fields in a non-linear medium to produce a fourth field, through the third-order non-linear polarisation. In DFWM, three waves (two pump beams and one probe, all at the same frequency) are spatially and temporally overlapped in the sample, and the fourth beam is generated at the same frequency. Several configurations of DFWM are possible, including phase-conjugate or backward geometry, folded boxcars, and two beam DFWM or forward geometry. The principle underlying all these geometries is the same: two beams interfere to form some type of a grating (e.g., intensity grating) and a third-beam scatters off this grating, generating the fourth beam which is known as the signal beam.

The most frequently used DFWM configuration is the phase-conjugate geometry, shown in Fig. 23.8. Here, two counter-propagating pump beams and a probe beam are incident on the non-linear material. The pump beams will be strong and approximately equal in intensity, while the probe is weaker, with an intensity of only about 20 per cent of the pumps. The angle between the forward pump and probe will be small, usually less than 10 degrees. Since the pump beams are collinear and

counter-propagating the propagation vectors are opposite to each other: $\mathbf{k}_1 = -\mathbf{k}_2$. The fourth beam generated by third order non-linear polarization is exactly counter-propagating to the probe beam, and is referred to as the conjugate beam. Therefore $\mathbf{k}_4 = -\mathbf{k}_3$. The physical mechanism of grating formation can be understood in two different ways: in one, the forward and the probe beams interfere to form a grating and the backward beam scatters from it, generating the conjugate beam. In the other, the backward and probe beams create a grating from which the forward beam scatters and generates the conjugate beam.

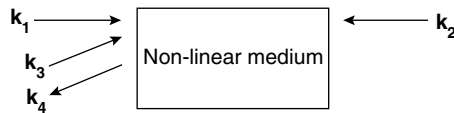


Fig. 23.8 The phase-conjugate geometry of the DFWM experiment.

A typical experimental setup for DFWM is shown in Fig. 23.9. The three beams are derived from the same laser by the appropriate use of beam splitters. The path difference between the beams should be less than the coherence length of the laser, since the beams must coherently interact in the sample to generate the signal beam. The laser wavelength and pulse width are selected appropriately for the particular phenomenon under study in the sample. The DFWM signal $I(\omega)$ is proportional to the cubic power of the input intensity $I_0(\omega)$, given by the equation

$$I(\omega) \propto (\omega/2\epsilon_0 c n_0^2)^2 |\chi^{(3)}|^2 I_0^3(\omega); \quad (30)$$

where, l is the interaction length of the three beams.

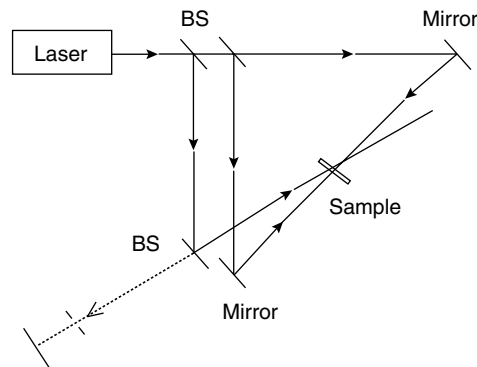


Fig. 23.9 A typical experimental setup for DFWM in the phase-conjugate geometry. The signal beam, which is phase-conjugate to the probe beam, is shown in dotted lines.

In the experiment, initially a standard sample like CS_2 , the $\chi^{(3)}$ of which is known at the excitation wavelength, is used. The intensity of the pump beam is gradually increased, and the corresponding values of the signal beam intensity are measured. A graph is then plotted between the pump intensity and the signal intensity, which gives a curve like that shown in Fig. 23.10. The value of I/I_0^3 is then

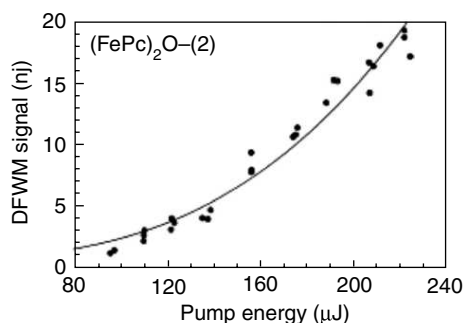


Fig. 23.10 DFWM signal vs input energy for an iron phthalocyanine sample (from ref. 34: R. Philip, M. Ravikanth, G. Ravindrakumar, *Opt. Commun.*, 165 (1999) 91). The sample was irradiated with 35 ps laser pulses at 532 nm.

calculated from the graph. The experiment is now repeated for the sample to be studied. The third-order susceptibility $\chi^{(3)}$ is then calculated from the equation

$$\chi^{(3)} = \chi^{(3)}_{\text{ref}} [(I/I_0)^3 / (I/I_0)_{\text{ref}}^3]^{1/2} [n_0/n_{0\text{ref}}]^2 [I_{\text{ref}}/I] [\alpha_0 l / (1 - \exp(-\alpha_0 l) \exp(-\alpha_0 l/2))]; \quad (31)$$

where the subscript “ref” refers to the corresponding quantities measured for the standard reference CS_2 under identical conditions.

23.4.3 Pump-probe Experiments

The pump-probe technique can be used to study the kinetic behavior of a system, like energy relaxation and energy transfer processes and orientation dynamics. A pump-probe experiment requires two short intense light pulses, namely a pump pulse, which excites the system to be investigated and a delayed probe pulse, which explores the relaxation of the excited system. The dynamics being studied will be impressed on the optical properties of the probe pulse, like its transmittance or spectral profile. A large number of pump-probe pairs for which the delay is progressively varied from zero to a maximum value, are typically required to map out the transient dynamics in a given system.

A typical pump-probe experimental setup is shown in Fig. 23.11. In most situations, both the pump and probe pulses can be derived from the same laser pulse, by using a beam splitter as shown. Consider a system, in which a transient state (eg: a short-lived excited state) is generated by a light pulse. The pulse duration is kept shorter than the lifetime of the transient state. For example, if the lifetime is of the order of nanoseconds, then the pump duration can be a few picoseconds. The system is then allowed to evolve freely during which time the transient state decays. During this evolution, the system is probed with the probe pulse. The delay between the pump and probe pulses can be varied by means of a translation stage. Initially, the delay can be zero, which is increased in steps for the successive laser pulses. For example, if the transient state decays within 10 nanoseconds, and the time resolution of the delay stage is 100 picoseconds, then a hundred successive laser pulses will be sufficient to record the temporal decay of the transient state with sufficient resolution. The pump and probe pulses should have good spatial overlap inside the sample, i.e., the diameter of the probe beam

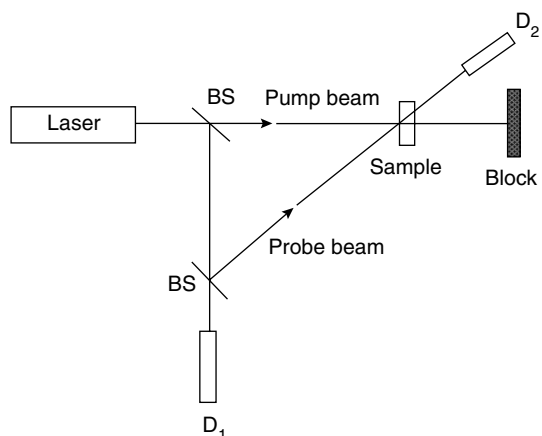


Fig. 23.11 Schematic diagram of a pump-probe experimental setup.

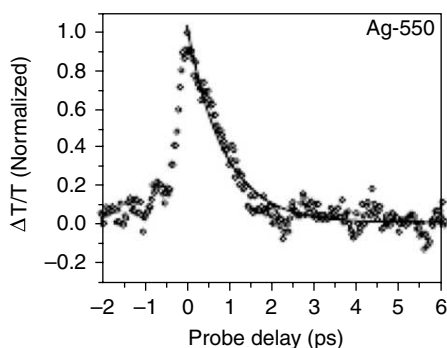


Fig. 23.12 Electron-phonon relaxation in ion-exchanged Ag nanoclusters of approximately 6 nm size. 100 fs laser pulses at a wavelength of 404 nm have been used for excitation (from ref. 35: B.Karthikeyan, J. Thomas, R. Philip, *Chem.Phys.Lett.* 414 (2005) 346).

should be less than that of the pump beam. Similarly, the length of the sample should be less than the pump-probe interaction distance, so that the probe sees uniform optical properties in the medium.

Using the pump-probe experiment, many ultrafast processes can be studied. For example, femtosecond pump-probe techniques can be applied successfully to the study of the photophysics of organic molecules and primary biological processes. Similarly, many fundamental processes in matter like electron-phonon scattering, which occur on a time scale ranging from hundreds of femtoseconds to several picoseconds, can be investigated. Some other areas of interest are imaging using femtosecond time resolved gating, electron dynamics of nanometer-sized metallic clusters, monitoring of biological processes by laser-induced fluorescence, etc.

Figure 23.12 shows the results obtained from femtosecond pump-probe measurements of electron-phonon relaxation in ion-exchanged Ag nanoparticles of size approximately 6 nm.³⁵ The pump energy

is kept low enough so that the excitation is limited to the low-perturbation regime, where the decay rate is independent of the pump fluence. The experimental points fit well to a single exponential decay, which is consistent with the two-temperature model of electron relaxation in the low-perturbation regime.³⁶ From the numerical fit, the relaxation lifetime is calculated to be 860 femtoseconds. There are other reported values of 700 fs³⁷ and 530 fs³⁸ for Ag clusters of similar size embedded in various media. Obviously, in optical switching applications, such short lifetimes can turn out to be important.

23.5 TECHNOLOGY PERSPECTIVES

The large non-linearities exhibited by metal and semiconductor nanostructures make them suitable materials for non-linear optical applications, such as optical power limiting, optical switching and pulse shaping. For instance, chalcogenide semiconductor nanocrystals are found to exhibit an ultrafast optical response, high non-linear figures of merit and a large dynamic range of excitation wavelengths. The large dynamic range is a result of a strong blue shift of the band gap, and the non-linearity enhancement mainly results from the effect of surface trapped states of nanoscale materials. Large optical non-linearities have been observed in SQDs embedded in transparent solid matrices which make them device-friendly.^{24, 30, 31} Noble metal nanoclusters and nanoparticles are found to behave as saturable absorbers and optical limiters at different size regimes, depending on the excitation wavelength and intensity.¹³ These can be used in solution¹⁵, film³⁹ or matrix-embedded⁴⁰ forms, and have ultrafast response times⁴¹. The design of a passive all-optical diode has been reported by using a saturable absorber in conjunction with a reverse saturable absorber.⁴²

Optical non-linearity can be utilised in many key-devices for the telecom industry, such as switches, routers, wavelength converters, etc. For example, optical logic gates realised with non-linear Mach-Zehnder interferometers (MZI) offer attractive features for mass manufacturing, such as scalability and flexibility.⁴³ Silicon nanocrystals (Si-nc) have been already shown to be excellent non-linear materials which can be exploited in Si photonics.^{44, 45} The full process-compatibility of Si-nc with SiO₂ mainstream CMOS technology renders this technology very attractive.⁴⁶ The non-linear refractive index and non-linear absorption coefficient of Si nanocrystals grown by PECVD have been measured in the third telecom window (1552 nm)⁴⁷ and the results appear to hold promise for device applications.

REFERENCES

1. P.A. Franken, A.E. Hill, C. W. Peters and G. Weinreich, *Phys. Rev. Lett.*, 7, (1961), 118.
2. J.A. Armstrong, N. Bloembergen, J. Ducuing and P.S. Pershan, *Phys. Rev.*, 128, (1962), 606.
3. N. Bloembergen and Y.R. Shen, *Phys. Rev.*, 133, (1963), 37A.
4. R.W. Boyd, *Non-linear Optics*, (2nd edn), Academic Press, (2003).
5. R.L. Sutherland, *Handbook of Non-linear Optics*, Marcel Dekker, NY, (1996).
6. L.W. Tutt and T.F. Boggess, *Prog. Quant. Electron.*, 17, (1993), 299.
7. M. Born and E. Wolf, *Principles of Optics*, (7th edn), Pergamon Press, Oxford, (1998).

8. E. Hao and G. C. Schatz, 'Electromagnetic fields around silver nanoparticles and dimers', *J. Chem. Phys.*, 120, (2004), 357.
9. F. Hache, D. Ricard, C. Flytzanis and U. Kreibig, *Appl. Phys. A.*, 47, (1988), 347.
10. G.L. Eesley, *Phys. Rev. B.*, 33, (1986), 2144.
11. S.L. Logunov, T.S. Ahmadi, M.A. El-Sayed, J.T. Khoury and R.L. Whetten, *J. Phys. Chem. B.*, 101, (1997), 3713.
12. P.V. Kamat, M. Flumiani and G.V. Hartland, *J. Phys. Chem. B.*, 102, (1998), 3123.
13. R. Philip, G. Ravindra Kumar, N. Sandhyarani and T. Pradeep, *Phys. Rev. B.*, 62, (2000), 13160.
14. A.S. Nair, V. Suryanarayanan, T. Pradeep, J. Thomas, M. Anija and R. Philip, *Materials Science and Engineering B.*, 117, (2005), 173.
15. J. Thomas, M. Anija, J. Cyriac, T. Pradeep and R. Philip, *Chem. Phys. Lett.*, 403, (2005), 308.
16. L. Francois, M. Mostafavi, J. Belloni, J.-F. Delouis, J. Delaire and P. Feneyrou, *J. Phys. Chem. B.*, 104, (2000), 6133.
17. R. Philip, S. Mujumdar, H. Ramachandran, G. Ravindra Kumar, N. Sandhyarani and T. Pradeep, *Non-linear Optics*, 27, (2001), 357.
18. R.K. Jain and R.C. Lind, 'Degenerate four-wave mixing in semiconductor doped glasses', *J. Opt. Soc. Am.*, 73, (198), 647–53.
19. T. Brunhes, P. Boucaud, S. Sauvage, A. Lemaitre, J.-M. Gérard, V. Thierry-Mieg, F. Glotin, R. Prazeres and J.-M. Ortega, 'Second-harmonic generation in InAs/GaAs self-assembled quantum dots', *Physica E: Low-dimensional Systems and Nanostructures*, 7, (2000), 155–58.
20. A. Guerrero and Bernardo S. Mendoza, 'Model for great enhancement of second-harmonic generation in quantum dots', *J. Opt. Soc. Am B: Optical Physics*, 12, (1995), 559–69.
21. S. Sauvage, T. Brunhes, P. Boucaud, A. Lemaitre, J.-M. Gérard, F. Glotin, R. Prazeres and J.-M. Ortega, 'Mid-Infrared Second-Order Non-linear Susceptibility in InAs/GaAs Quantum Dots', *Physica Status Solidi (b)*, 224, (2001), 595–98.
22. M. Jacobsohn and U. Banin, 'Size Dependence of Second Harmonic Generation in CdSe Nanocrystal Quantum Dots', *J. Phys. Chem. B.*, 104(1), (2000), 1–5.
23. M. Ghanassi, L. Piveteau, L. Saviot, M. C. Schanne-Klein, D. Recard and C. Flytzanis, 'Origin of the resonant optical Kerr nonlinearity in Cd(S, Se) doped glasses and related Optics', *Appl. Phys. B.*, 61, (1995), 7–26.
24. P. Nandakumar, C. Vijayan and Y.V.G.S. Murti, 'Quantum size effects on the third order optical nonlinearity of CdS quantum dots in Nafion', *Opt. Commun.*, 185, (2000), 457–65.
25. R.A. Fisher (Ed.), 'Optical phase conjugation', *Acad. Press*, NY, (1983).
26. B. Ya Zel'dovich, N.F. Pilipetsky and V.V. Shkunov, *Principles of Phase Conjugation*, Springer-Verlag, Berlin, (2004).
27. U. Woggon, *Optical Properties of Semiconductor Quantum Dots*, Springer, Berlin, (1997).
28. G.P. Banfi, V. Degiorgio and D. Ricard, 'Nonlinear optical properties of semiconductor nanocrystals', *Adv. hys.*, 47, (1998), 447–510.
29. K.C. Rustagi and D.D. Bhawalkar, 'Optical nonlinearities in semiconductor doped glasses', *Opt. Lett.*, 9, (1984), 344–46.

30. P.A. Kurian, C. Vijayan, C. S. Suchand Sandeep, R. Philip and K. Sathiyamoorthy, 'Two-photon-assisted excited state absorption in nanocomposite films of PbS stabilised in a synthetic glue matrix', *Nanotechnology*, 18, (2007), 075708_01–075708_08.
31. P.A. Kurian, K. Sathiyamoorthy, C. Vijayan, C.S. Suchand Sandeep and R. Philip, 'Excitonic transitions and off-resonant optical limiting in CdS quantum dots stabilised in a synthetic glue matrix', *Nanoscale Research Letters*, 2, (2007), 561–68.
32. M. Sheik Bahae, A.A. Said, T.M. Wei, D.J. Hagan and E.W. Van Stryland, *IEEE J. Quant. Electron.*, 26, (1990), 760.
33. B. Karthikeyan, M. Anija and Reji Philip, *Appl. Phys. Lett.*, 88, (2006), 053104.
34. R. Philip, M. Ravikanth and G. Ravindrakumar, *Opt. Commun.*, 165, (1999), 91.
35. B. Karthikeyan, J. Thomas and R. Philip, *Chem. Phys. Lett.*, 414, (2005), 346.
36. C.K. Sun, F. Vallee, L.H. Acioli, E.P. Ippen and J.G. Fujimoto, *Phys. Rev. B.*, 50, (1994), 15337.
37. N. Del Fatti, F. Vallee, C. Flytzanis, Y. Hamanaka and A. Nakamura, *Chem. Phys.*, 251, (2000), 215.
38. A. Arbouet, C. Viosin, D. Christofilos, P. Langot, N. Del Fatti, F. Vallee, J. Lerme, G. Celep, E. Cottancin, M. Gaudry, M. Pellarin, M. Broyer, M. Maillard, M.P. Pileni and M. Treguer, *Phys. Rev. Lett.*, 90, (2003), 177401.
39. B. Karthikeyan, M. Anija and R. Philip, *Appl. Phys. Lett.*, 88, (2006), 053104.
40. B. Karthikeyan, M. Anija, C.S. Suchand sandeep, T.M. Muhammad Nadeer and R. Philip, *Opt. Commun.*, 281, (2008), 2933.
41. B. Karthikeyan, M. Anija, P. Venkatesan, C.S. Suchand Sandeep and R. Philip, *Opt. Commun.*, 280, (2007), 482.
42. R. Philip, M. Anija, C.S. Yelleswarapu and D.V.G.L.N. Rao, *Appl. Phys. Lett.*, 91, (2007), 141118.
43. H. Sun, Q. Wang, H. Dong and N. K. Dutta, XOR performance of a quantum dot semiconductor optical amplifier based Mach-Zehnder interferometer, *Optics Express*, 13, (2005), 1892–99.
44. M.C. Beard, K.P. Knutsen, P. Yu, J.M. Luther, Q. Song, W.K. Metzger, R.J. Ellingson and A.J. Nozik, Multiple Exciton Generation in Colloidal Silicon Nanocrystals, *Nano Lett.*, 7, (2007), 2506–12.
45. S. Vijayalakshmi, M.A. George and H. Grebel, 'Nonlinear optical properties of silicon nanoclusters', *Appl. Phys. Lett.*, 70, (1997), 708–10.
46. C. Koos, L. Jacome, C. Poulton, J. Leuthold and W. Freude, 'Nonlinear silicon-on-insulator waveguides for all-optical signal processing', *Optics Express*, 15, (2007), 5976–90.
47. M. Cazzanelli, D. Kovalev, L. D. Negro, Z. Gaburro and L. Pavesi, 'Polarised Optical Gain and Polarisation-Narrowing of Heavily Oxidized Porous Silicon', *Phys. Rev. Lett.*, 93, (2004), 207402_01–207402_04.

ADDITIONAL READING

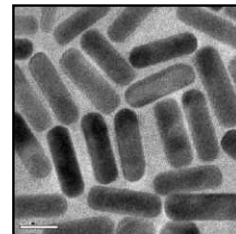
1. R.W. Boyd, *Non-linear Optics* (2nd edn), Academic Press, (2003).
2. N. Bloembergen, 'Nonlinear Optics and Spectroscopy', in *Reviews of Modern Physics*, Vol. 54, 685–95, (1982).
3. R.L. Sutherland, *Handbook of Non-linear Optics*, Marcel Dekker, (1996).

4. G.S. He and S.H. Liu, *Physics of Non-linear Optics*, World Scientific, (1999).
5. C. Kittel, *Introduction to Solid State Physics* (5th edn), Wiley Eastern Limited, (1976).
6. K.J. Klabunde (Ed.), *Nanoscale Materials in Chemistry*, Wiley Interscience, (2001).
7. U. Kreibig and M. Vollmer, *Optical Properties of Metal Clusters*, Springer, Berlin, (1995).
8. T. Pradeep, *Nano: the Essentials*.

REVIEW QUESTIONS

1. The non-linear optical susceptibilities are tensor quantities in general. Why?
2. Distinguish between Pockels effect and Kerr effect.
3. Second order optical non-linearity is normally not seen in isotropic media. Why?
4. Distinguish between saturable and reverse saturable absorbers.
5. How are resonant and non-resonant non-linearities distinguished from each other?
6. Explain the three major electronic contributions to the third order non-linearity in metal nanoparticles.
7. What is meant by induced thermal scattering of light?
8. What are the origins of optical non-linearity in semiconductor quantum dots?
9. Distinguish between the closed aperture and open aperture z-scan techniques.
10. What is Four Wave Mixing? Explain the technique of Degenerate Four Wave Mixing (DFWM) to measure $\chi^{(3)}$ of a sample.
11. What is the typical relaxation time of hot electrons in metal nanoparticle systems?
12. What are the relative merits and demerits of z-scan and four wave mixing techniques for measuring $\chi^{(3)}$?
13. Explain Optical Limiting and its potential applications.

NANOMATERIALS FOR ENVIRONMENTAL REMEDIATION



“The struggle to save the global environment is in one way much more difficult than the struggle to vanquish Hitler, for this time the war is with ourselves. We are the enemy, just as we have only ourselves as allies.”

Al Gore, “Earth in the Balance; Ecology and the Human Spirit”
(Houghton Mifflin, 1992, Page No. 275)

Environmental remediation is a global issue, which has caught the urgent attention of scientists, technologists, and governments. Environmental contamination aggravates on a day-to-day basis and the challenge involved in keeping the environment clean and safe has become formidable. Nanomaterials, because of their unique physical and chemical characteristics, have a decisive role to play in this situation. This chapter details in some length on the role of various nanomaterials in remedying the contaminants. Metal and semiconductor nanoparticles, carbon nanomaterials, dendrimers, and nanoscale biopolymers degrade/remove the contaminants by green methodologies, which give tremendous expectations for a cleaner environment. The deployment of these materials for the applications must be such that they do not cause additional environmental effects.

Learning Objectives

- What makes nanomaterials ideal candidates for futuristic environmental remediation technologies?
 - How do metal and semiconducting nanoparticles remedy halocarbons/pesticides?
 - Are carbon-rich materials superior to their bulk counterparts in environmental remediation?
 - How nanomaterials can help in providing affordable drinking water?
-
-

Environmental remediation has become a subject of global importance with immediate priority because of massive pollution witnessed by water bodies, air and soil due to heavy industrialisation, urbanisation and unprecedented changes in the lifestyles of people. The need to provide safe and clean drinking water to people is of paramount importance and in most developing nations; the responsibility is bestowed on federal and locally-elected governments. Adequate and sustainable drinking water sources and clean environment for people are of vital importance and these are taken

as the indices of a nation's growth and prosperity. Due to extended drought, population growth and urbanisation, there is enormous pollution of water bodies, air and soil and the challenge involved in keeping the environment clean and safe is formidable. The financial burden involved in the cleanup of these polluted environments is massive, and hence, scientists have been exploring cheap but efficient methodologies for environmental remediation. Nanotechnology has become the natural choice for environmental remediation because of the unusual properties and diversity in applications associated with nanomaterials.¹ Nanomaterials have huge surface area and chemical reactivity compared to their corresponding bulk analogues and they can be fabricated in a variety of shapes and present various lattice planes for reactions. This is the most important and unique aspect about the nanomaterials for their end use in environmental remediation. Also, the nanomaterials are highly dispersible and can be anchored onto solid supports for desired applications and deployed in different environments.¹ Nanotechnology-based environmental remediation offers immense scope and potential for a clean and sustainable environment. This chapter looks at an overview of the use of nanomaterials for environmental remediation in some detail.

A variety of nanostructured materials find extensive uses in environmental remediation. Reactive metal and semiconductor nanoparticles, Dendrimers, carbon nanotubes, and nanoscale biopolymers are the most commonly-used nanomaterials for environmental remediation. These either transform the contaminants to harmless products chemically or adsorb/absorb onto the surfaces/cavities and hence removing/scavenging them. Let us look at the contributions of each of these classes of nanomaterials separately in some detail.

24.1 NANOPARTICLES: ENVIRONMENTAL REMEDIATION BY CHEMICAL DEGRADATION/REMOVAL OF CONTAMINANTS

Nanocatalysts and redox-active catalysts have major stakes in remedying the environment through cleaner and greener methodologies. Metal and semiconductor nanoparticles are the major players in the field and particularly promising is the role of iron (Fe), its oxides, gold (Au), silver (Ag), TiO₂, and MgO nanoparticles in remediation. One of the early reports on the same was about the remediation of heavy metals, Cr(VI) and Pb(II), from aqueous solutions using Fe (0) nanoparticles supported on silica gel or polymeric resins.² Schrick *et al.*³ found the hydrodechlorination of trichloroethylene (TCE) using Ni-Fe bimetallic nanoparticles. In the case of the bimetallic nanoparticles, Fe acts as the reductant for water and Ni as catalyst to prevent the formation of harmful products during the degradation. Transmission electron micrograph (TEM) of the bimetallic nanoparticles and the mechanism of degradation of the TCE are shown in Fig. 24.1. The electrons released by the oxidation of Fe nanoparticles were transferred to the Ni-rich catalytic regions of the nanoparticles, where C-Cl bond rupture and transfer of hydride ions take place. The degraded products are hydrocarbons and H₂. The remediation of TCE by Fe and palladised Fe nanoparticles supported on hydrophilic carbon and poly(acrylic acid) and their application as delivery vehicles was reported by Schrick *et al.*⁴ Figure 24.2 shows a schematic of the degradation of trichloroethylene mediated by palladised Fe nanoparticles in water. The electrons released by the corrosion of nano Fe are directed to the catalytic

Pd regions, where the halocarbons are degraded to hydrocarbons. Metalloporphyrinogens, which are nanosized molecules, are known to dechlorinate a variety of halocarbons, such as tetrachloroethylene, trichloroethylene, carbon tetrachloride, chloroform and dichloromethane. Metalloporphyrinogens were found to be one of the best catalysts for the near-complete dechlorination of halocarbons under ambient conditions.⁵

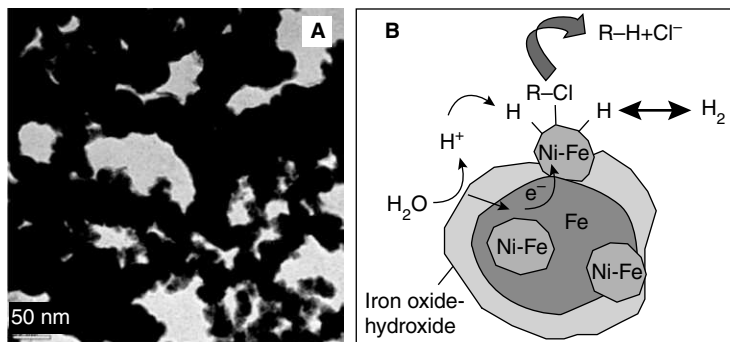


Fig. 24.1 Figure A is the transmission electron micrograph of Fe-Ni bimetallic nanoparticles. Figure B shows the mechanism of degradation of TCE by the nanoparticles. Electrons were transferred to the Ni-rich catalytic regions by the corrosion of Fe, which in turn brings about the C-Cl bond rupture and transfer of hydride ions (reprinted with permission from Schrick *et al.*, *Chem. Mater.*, 2002, 14, 5140–47. Copyright (2002) American Chemical Society).

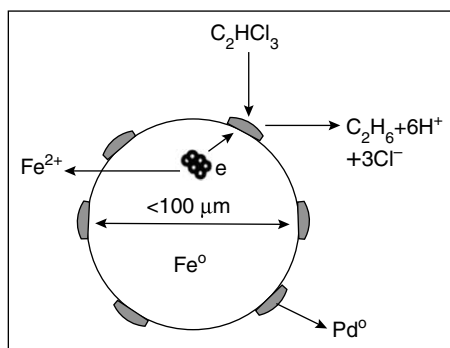


Fig. 24.2 A schematic of the palladised-Fe nanoparticles-mediated remediation of trichloroethylene in water (from Zhang *et al.*, *J. Nanopart. Res.*, 2003, 5, 323–32).

Nanoscale Fe particles were found to be excellent materials for the removal of humic acids. Giasuddin *et al.*⁶ demonstrated the efficacy of nano Fe on humic acid removal and the effect of the adsorbed humic acids on arsenic (As) removal capacity of Fe. A review on the use of Fe nanomaterials in the transformation and detoxification of a variety of organic solvents, organochlorine pesticides, and PCBs was undertaken by Zhang *et al.*⁷ A list of the common environmental contaminants that can

Table 24.1 List of common environmental contaminants that can be remediated by nanoscale Fe and palladised Fe particles (from Zhang *et al.*, *J. Nanopart. Res.*, 2003, 5, 323–32).

Chlorinated methanes	Trihalomethanes
Carbon tetrachloride (CCl ₄)	Bromoform (CHBr ₃)
Chloroform (CHCl ₃)	Dibromochloromethane (CHBr ₂ Cl)
Dichloromethane (CH ₂ Cl ₂)	Dichlorobromomethane (CHBrCl ₂)
Chloromethane (CH ₃ Cl)	Chlorinated ethenes
Chlorinated benzenes	Tetrachloroethene (C ₂ Cl ₄)
Hexachlorobenzene (C ₆ Cl ₆)	Trichloroethene (C ₂ HCl ₃)
Pentachlorobenzene (C ₆ HCl ₅)	<i>cis</i> -Dichloroethene (C ₂ H ₂ Cl ₂)
Tetrachlorobenzenes (C ₆ H ₂ Cl ₄)	<i>trans</i> -Dichloroethene (C ₂ H ₂ Cl ₂)
Trichlorobenzenes (C ₆ H ₃ Cl ₃)	1,1-Dichloroethene (C ₂ H ₂ Cl ₂)
Dichlorobenzenes (C ₆ H ₄ Cl ₂)	Vinyl chloride (C ₂ H ₃ Cl)
Chlorobenzenes (C ₆ H ₅ Cl)	Other polychlorinated hydrocarbons
Pesticides	PCBs
DDT (C ₁₄ H ₉ Cl ₅)	Dioxins
Lindane (C ₆ H ₆ Cl ₆)	Pentachlorophenol (C ₆ HCl ₅ O)
Organic dyes	Other organic contaminants
Orange II (C ₁₆ H ₁₁ N ₂ NaO ₄ S)	N-nitrosodimethylamine (NDMA) (C ₄ H ₁₀ N ₂ O)
Chrysoidine (C ₁₂ H ₁₃ ClN ₄)	TNT (C ₇ H ₅ N ₃ O ₆)
Tropaeolin O (C ₁₂ H ₉ N ₂ NaO ₅ S)	Inorganic anions
Acid Orange	Dichromate (Cr ₂ O ₇ ²⁻)
Acid Red	Arsenic (AsO ₄ ³⁻)
Heavy metal ions	Perchlorate (ClO ₄ ⁻)
Mercury (Hg ²⁺)	Nitrate (NO ₃ ⁻)
Nickel (Ni ²⁺)	
Silver (Ag ⁺)	
Cadmium (Cd ²⁺)	

be transformed by nanoscale Fe particles is given in Table 24.1. Paknikar *et al.*⁸ reported the degradation of lindane (γ -hexachlorocyclohexane) using FeS nanoparticles supported by a biopolymer. This involved catalytic dechlorination using FeS nanoparticles followed by microbial degradation. The main advantage of the degradation process is the precipitation of the nanoparticles after the degradation, thereby enabling their efficient removal. Chitose *et al.*⁹ studied the degradation of phenol by irradiation in presence of TiO₂ nanoparticles. Phenol is oxidised to CO₂ and H₂O by the process. Song *et al.*¹⁰

found that WO_x modified emission response of TiO_2 nanoparticles could degrade organic dyes, such as methylene blue and other contaminants, such as CHCl_3 under visible light irradiation. It was found that the optimum amount of WO_x in TiO_2 matrix for best photocatalysis performance was 1 wt%. Mertens *et al.*¹¹ reported the dechlorination of lindane by Pd nanoparticles precipitated on the biomass, *Shewanella oneidensis* in the presence of formate as electron donor. Investigations showed that bio-Pd was more effective for the dechlorination of lindane than commercially available Pd. Sobana *et al.*¹² studied the photo degradation of azo dyes by Ag nanoparticles-doped TiO_2 particles. The presence of Ag was found to enhance the degradation of dyes by TiO_2 due to the enhancement of electron-hole separation by electron trapping of Ag. Priya and Madras¹³ investigated the effectiveness of combustion-synthesised nano- TiO_2 for the degradation organic contaminants, such as nitrobenzenes, nitrophenols and chloronitrobenzenes under irradiation. Feitz *et al.*¹⁴ studied the degradation of a herbicide, molinate by nano Fe under oxygen presence. Hariharan¹⁵ explored sensing and catalytic degradation of aliphatic and aromatic chloro contaminants in water by ZnO nanoparticles. Aarathi and Madras¹⁶ reported photocatalytic degradation of a variety of Rhodamine dyes by nano- TiO_2 and investigated the effects of organic solvents and metal ions on the degradation by TiO_2 nanoparticles. The potential of nanomaterials, especially TiO_2 and ZnO in environmental remediation has been reviewed by Kamat and Meisel¹⁷. Figure 24.3 shows the promise of nano ZnO in simultaneous sensing and degradation of organic contaminants (halogen containing compounds). The emission quenching of ZnO is sensitive (quantitative) to the presence of organic compounds as the extent of quenching is determined by adsorption equilibrium. Figure 24.4A shows a general mechanism of charge separation in semiconductor nanoparticles as a result of band-gap excitation.¹⁷ The photogenerated electrons and holes oxidize/reduce the contaminants on the surfaces. An alternative mechanism involves charge transfer between two adsorbed molecules mediated by the nanoparticles. Here, the semiconductor nanoparticles

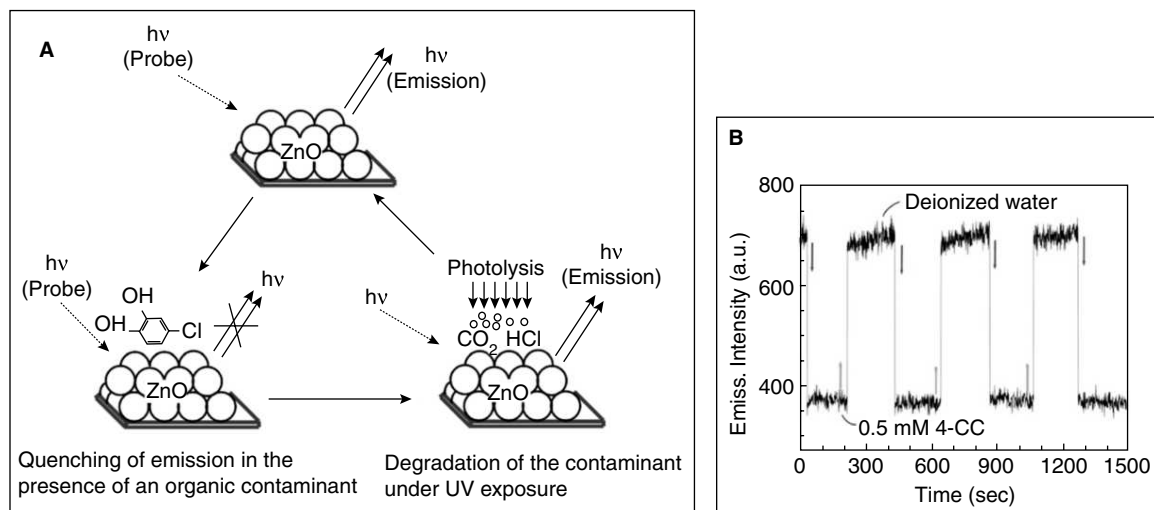


Fig. 24.3 Simultaneous degradation (Fig. A) and sensing (Fig. B) methodology of contaminants by ZnO nanoparticles in photocatalysis (with permission from C.R. Chimie, 2003, 6, 999–1007).

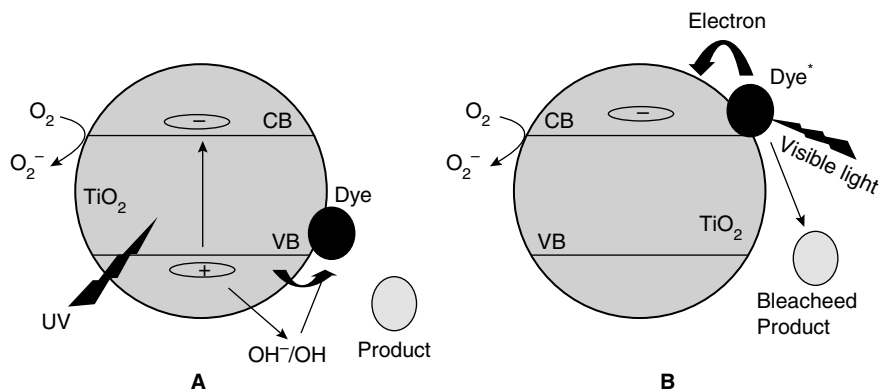


Fig. 24.4 Mechanism of photo-induced charge transfer in TiO_2 nanoparticles by band-gap excitation (a) and excited-state charge injection by the contaminant dye molecules (b). VB and CB in the figures refer to valence band and conduction bands respectively, of the nanoparticles (from Kamat and Meisel, *C.R. Chemie*, 2003, 6, 999–1007).

quench the excited state dye by accepting electron and transfer the charge to another substrate (Fig. 24.4B). Varanasi *et al.*¹⁸ studied the remediation of soils contaminated with polychlorinated biphenyls (PCBs) using Fe nanoparticles and a comparison of the efficiency of dechlorination by the same vs $\text{V}_2\text{O}_5/\text{TiO}_2$. A comprehensive review on the use of nanomaterials for water purification was undertaken by Savagel and Diallo.¹⁹ Ngomsik *et al.*²⁰ reviewed the applications of magnetic nano- and microparticles for heavy metal removal and environmental remediation by magnetically assisted chemical separation. Badr and Mahmoud²¹ investigated the photocatalytic degradation of methyl orange (MO) by Au-Ag core/ SiO_2 shell nanoparticles. The photocatalytic degradation property of the SiO_2 towards MO is enhanced by the Au ($\text{SiO}_2@Au$) and Ag ($\text{SiO}_2@Ag$) cores. SiO_2 nanoparticles under UV irradiation produce positively charged hole in the valence band and negative charge in the conduction band. The valence band holes interact with the chemisorbed H_2O molecules producing OH radicals, and the conduction band electrons react with the dissolved O_2 producing O_2^- . The OH and O_2^- species attack the MO molecules in bringing about the complete degradation. Figure 24.5 shows the absorption spectra of MO (the peak at 510 nm is due to MO) in the presence of the supported nanoparticles (Figure A in presence of $\text{SiO}_2@Ag$ and B, in presence of $\text{SiO}_2@Au$, respectively) under irradiation showing its complete degradation. Nanoparticles of silver (Ag) and gold (Au) degrade a variety of halocarbons at room temperature. Halocarbons, such as CCl_4 , CHBr_3 , CCl_3F , and benzylchloride, could be degraded to metal halides and amorphous carbon by the nanoparticles.²² Investigations by spectroscopy and microscopy, as also time-dependent pH and conductivity measurements revealed mechanistic aspects of the degradation. While, the halocarbons directly react and degrade at the Ag nanoparticles' surfaces to metal halides and carbon, they adsorb onto the surfaces of Au and react and degrade over a period of time resulting in interesting changes to the surface plasmon characteristics. Figure 24.6(A and B) shows the degradation of CCl_4 by the Ag and Au nanoparticles. The progressive reduction in the surface plasmon characteristic of the nanoparticles is due to their conversion to metal halides by the reaction. Figure 24.6C is the UV-visible spectra in a time-dependent

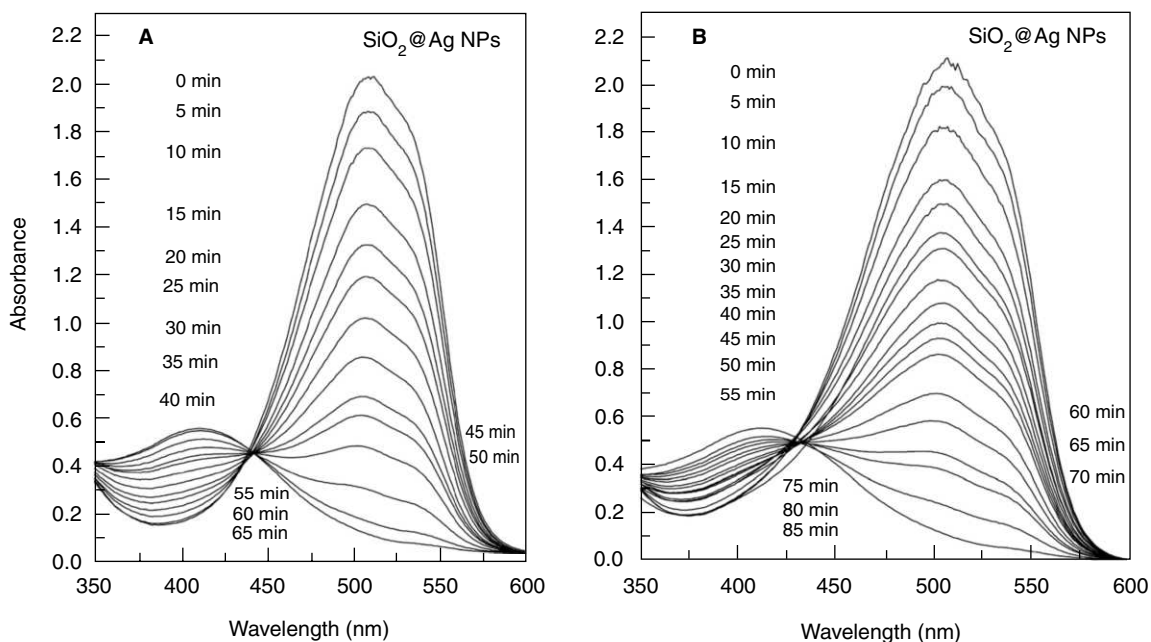


Fig. 24.5 Absorption spectra of the methyl orange after irradiation in a time-dependent manner in the presence of $\text{SiO}_2\text{@Ag}$ (A) and $\text{SiO}_2\text{@Au}$ (with permission from Badr and Mahmoud, *J. Physics and Chemistry of Solids*, 2007, 68, 413–19).

manner (taken in every 3 min intervals) of the interaction of CHBr_3 with Ag nanoparticles. The formation of metal halides and amorphous carbon was confirmed by X-ray diffraction and spectroscopy.²² Figure 24.6D shows a schematic of the degradation of the halocarbons by the metal nanoparticles. The drastic reduction in the pH during the course of the reaction is attributed to the formation of H^+ by the conversion of 2-propanol to acetone via ketyl radicals.²² Bare and supported (on activated alumina) nanoparticles of silver and gold were found to be extremely useful in detecting (sensing) and extracting pesticides, such as endosulfan, chlorpyrifos and malathion, from water.^{23, 24} These are illustrated in Fig. 24.7. Figure 24.7A shows the changes to the absorption spectrum of Au nanoparticles (trace a) when they are exposed to endosulfan of different concentrations (traces b, c, d and e correspond to absorption spectra at 2, 10, 100 and 250 ppm endosulfan, respectively). The decrease in the intensity of the original plasmon feature and the concomitant emergence of another broad plasmon feature at longer wavelengths is characteristic of adsorbate-bound aggregation of the nanoparticles. Inset shows the colour changes to the original Au nanoparticles (picture A) when exposed to endosulfan of different concentrations (pictures B, C and D, respectively). Figure 24.7B shows time-dependent absorption spectra of the interaction of endosulfan with Au nanoparticles, showing a sequence of changes to the surface plasmon band of Au. In order to exploit the pesticide sensing/removal properties of the nanoparticles and make filters for remediation, it is necessary to incorporate them on to supports. Several support materials, such as clays, activated alumina, and nanofibers are currently in use. The authors have chosen activated alumina, because it is a known player

in water purification process and the Au and Ag nanoparticles loaded onto activated alumina were employed for making filters for the contaminant removal from water. Figure 24.7C shows the removal of chlorpyrifos from water using the supported nanoparticles of Ag. The absorption feature of the chlorpyrifos decreases in a time-dependent manner upon interaction with the supported nanoparticles, implying their removal from water by adsorption onto the Ag surfaces. Figure 24.7D shows a pesticide filter cartridge made of the supported nanoparticles. A pesticide filter using the nanotechnology-based cartridge has now hit the domestic market in India.

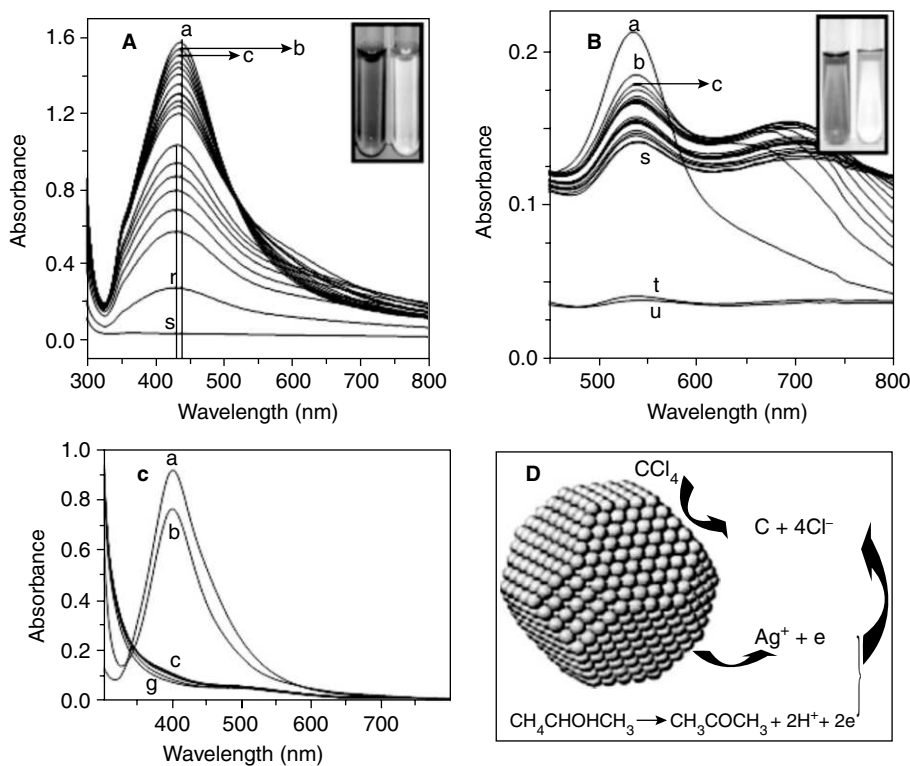


Fig. 24.6 Figure A, B and C show changes to the surface plasmon characteristics of Ag and Au nanoparticles (mixed with 2-propanol to increase the miscibility of halocarbons) upon exposure to the halocarbons. Figure A shows the interaction of Ag nanoparticles with CCl_4 and the time-dependent reduction in the surface plasmon band of Ag is due to its conversion to metal halide. The traces (a-r) were recorded at 30 min intervals and the trace s was recorded after 12 hr. Figure B shows the changes to the absorption profile of Au nanoparticles upon exposure to CCl_4 . Trace b was taken immediately after the exposure to CCl_4 and the subsequent traces were taken in 20 min intervals. The trace u is taken after 48 hr showing the complete degradation. Insets of Figure A and B show the colour changes to the nano reaction mixture before (left) and after (right) the degradation reaction. A similar kind of interaction takes place in the case of CHBr_3 with Ag (Fig. C). The traces recorded in 3 min intervals show the rapid affinity of Ag towards the halocarbon. Figure D shows a schematic of the degradation of halocarbons by the nanoparticles (from author's work). (For clarity see colour figure.)

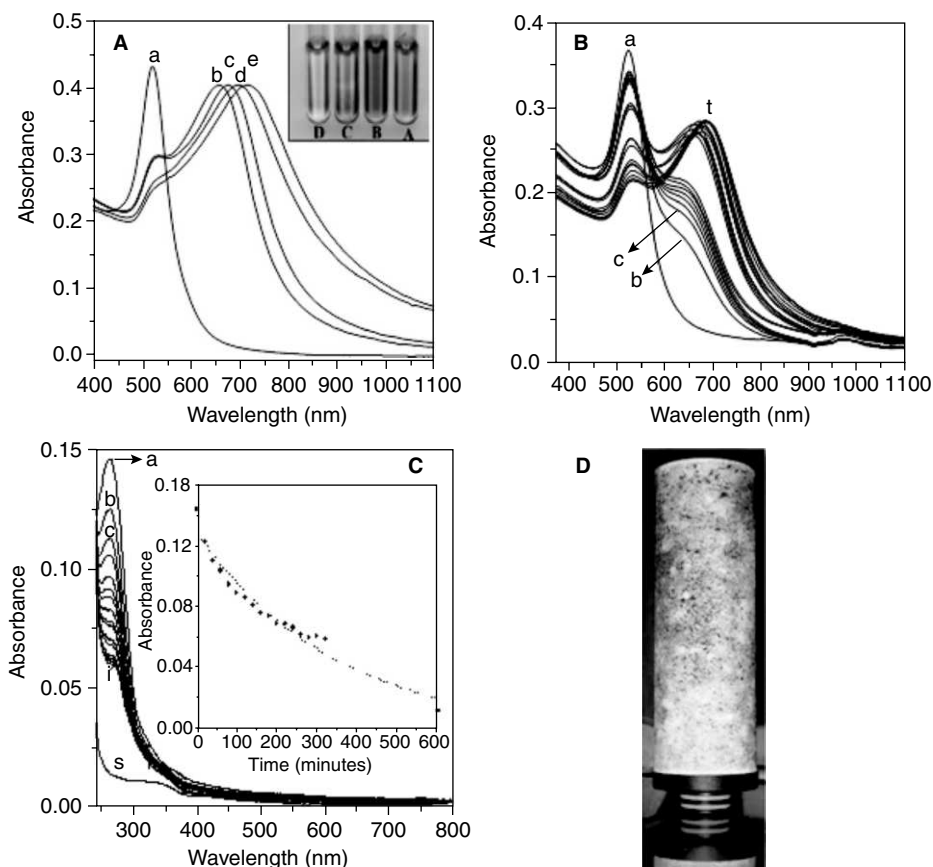
**Fig. 24.7**

Figure A shows the changes to the absorption spectrum of citrate-stabilised gold nanoparticles (trace a) when exposed to endosulfan of different concentrations (trace b) 2 ppm, (trace c) 10 ppm, (trace d) 100 ppm, and (trace e) 250 ppm. The solutions have the same composition, except for endosulfan. Photographs showing colour changes to the gold nanoparticles upon exposure to endosulfan are shown in the inset. Photograph (A) shows citrate-stabilised nanoparticles and (B), (C) and (D) correspond to the nanoparticles having 2, 10 and 100 ppm endosulfan, respectively. Figure B shows a time-dependence of the absorption spectrum of citrate-stabilised gold nanoparticles upon exposure to 10 ppm endosulfan. (a) original nanoparticle solution, (b) 3 hr after adding endosulfan solution, (c) to (t), at 20-min intervals thereafter. Figure C shows the time-dependent UV-visible spectra showing the adsorption of chlorpyrifos (1 ppm) on supported nanoparticles of Ag ($\text{Al}_2\text{O}_3@Ag$). Trace a is the absorption spectrum of chlorpyrifos (1 ppm) and traces (b-r) were taken at 20-min intervals after interaction with the nanoparticles. Trace s was taken after 10 hr showing the complete disappearance of chlorpyrifos from water. The inset shows decrease in absorbance vs time from the absorption spectroscopy data for the traces (a-s). The dotted line in the inset shows a fit of the exponential decrease in absorbance with time. Figure D is a pesticide filter devised by the methodology (from author's work). (For clarity see colour figure.)

We would like to point out another promising catalytic activity of nano Au in converting the most poisonous carbon monoxide (CO) to carbon dioxide (CO₂). Nano Au has traditionally been in use in catalysis and medicine and its catalytic activity was unravelled by Haruta *et al.*²⁵ Chen and Goodman²⁶ have proposed the existence of quantum size effects to explain the CO oxidation activity claiming that the presence of two atomic layers of Au could be the key parameter for the unusual catalytic activity. There are also claims on the presence of uncoordinated and cationic Au atoms as the reason for its catalytic activity. Though the exact mechanistic aspects of the oxidation are still unresolved, it is established that the presence of oxide support is essential to obtain highly active Au catalysts for CO oxidation.²⁷ Guzman and Gates²⁸ investigated the correlation between the oxidation states of Au and its catalytic activity for CO oxidation. Au(I) sites in the catalyst are supposed to be the catalytically active and CO plays the dual role as reactant and reducing agent that converts Au(I) to Au(0).

In summary, metal nanoparticles find widespread use in sensing and removing/degrading contaminants from environment. Advantages, such as cost-effectiveness, ease of surface modification and dispersibility, and the ease with which the nanoparticles could be anchored onto solid supports for *in-situ* and *ex-situ* applications envisage a greater role for nanomaterials in environmental remediation.

24.2 NANOMATERIALS AS SORBENTS

Pollutants could be removed from water by sorption and the efficiency of the sorption process could be enhanced by many orders of magnitude using nanomaterials as sorbents. Fe oxides were traditionally employed to remove contaminants from water by ion exchange, adsorption to surface bound groups or co-precipitation. The removal of As (V) by akaganeite (β -FeO (OH)) nanoparticles by adsorption, and the effect of temperature, contact time, pH, and ionic strength on sorption were investigated by Deliyanni *et al.*²⁹

Nanocrystallites of akaganeite were also used as sorbents to sequester Cr(VI) from water by Lazaridis *et al.*³⁰ Zhao and Nagy³¹ devised dodecyl sulfate-hydrocalcite nanocomposites (which act as catalysts and ion-exchangers) using sodium dodecyl sulfate and Mg-Al layered double hydroxide capable of sorbing chlorinated organic pollutants (mainly trichloroethylene and tetrachloroethylene) from water. Fryxell *et al.*³² developed an innovative way for sequestering actinides by creating a powerful new class of sorbent materials by self-assembling monolayers (SAMs) on mesoporous supports (MSs), abbreviated as SAMMS. In SAMMS, all the interfacial binding sites is accessible to contaminant species thanks to its porous, rigid, and open structure and which is the reason for their superior sorbing activity. A general synthetic scheme to devise SAMMS is shown in Fig. 24.8. Contaminants, such as oxalometalate anions, heavy metals and radionuclides, could be selectively removed by fine tuning the interfacial chemistry of the SAMMS for the specific ions. Lin *et al.*³³ modified the methodology by attaching hydroxyl pyridinones on self-assembled monolayers on mesoporous supports (HOPO-SAMMS) to get superior nanoporous materials, making it feasible multiple ligand-metal interactions for rapid sequestration of actinides from water. Tungittiplakorn *et al.*³⁴ have explored the use of nonionic amphiphilic polyurethane nanoparticles in the solubilisation of polyaromatic hydrocarbons (PAHs)

from contaminated soil. Also, the polyethylene glycol modified urethane acrylate nanoparticles (PMUA), which have hydrophilic polyethylene glycol chains extending out from their surfaces and a hydrophobic polyurethane acrylate, enhance the remediation of PAHs and phenanthrene. Tunability of the interfacial chemistry of SAMMS for sorbing specific metal ions makes these nanomaterials excellent candidates as sorbents in environmental remediation.

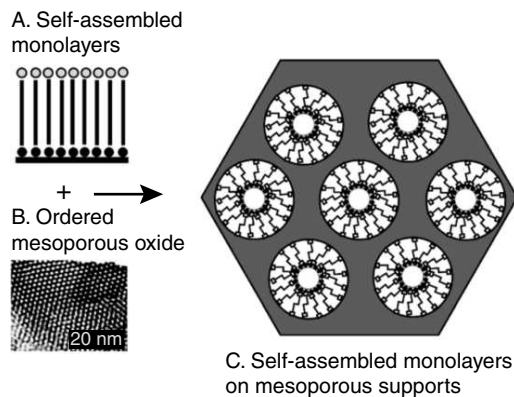


Fig. 24.8 Schematic for making self-assembled monolayers (SAMs) on mesoporous supports (MSs), that is (SAMMS) (reprinted with permission from Fryxell *et al.*, *Environ. Sci. Technol.*, 2005, 39, 1324–31. Copyright (2005) American Chemical Society).

24.3 NANOFILTRATION—A NEW TECHNIQUE FOR CLEAN WATER

Membrane filtration and nanofiltration techniques were used in water purification for water softening and wastewater remediation. Nanofiltration plays a significant role in water purification—thanks to the fabrication of novel nanoporous membranes. An early lead in the area was by Stoimenov *et al.*³⁵ who reported the antibacterial activity of MgO nanoparticles (fabricated by aerogel procedures) and their halogenated derivatives. The small size of the nanoparticles allows them to cover the surfaces of the bacteria cells to a large extent, thereby bringing the active halogen in high concentration to the cell walls resulting in cell rupture and collapse. These are evident from the set of TEM images in Fig. 24.9; wherein the close proximity of the MgO nanoparticles to the cell wall results in its rupture and destruction. Fabrication of Fe, Mn and La doped-alumina ultrafiltration membranes, dependence of pore size, pore-size distribution and molecular weight cut off on membrane efficiency were reported by DeFriend *et al.*³⁶ Treatment of brackish water by nanofiltration was reported by Mohsen *et al.*³⁷ Fabrication of nanofiltration membranes by deposition of polyelectrolytes, namely, polystyrene sulfonate/poly (allylamine hydrochloride), on porous alumina and their ability to reject ionic species, such as CaSO_4 and MgCl_2 were studied by Stanton *et al.*³⁸

Electrostatic exclusion (called Donnan exclusion) being the major mechanism in removing the ionic impurities from water, the selectivity and exclusion parameters could be tailored by changing the outer-layer charges in polystyrene-sulfonate/poly (allylamine hydrochloride) membranes. A review

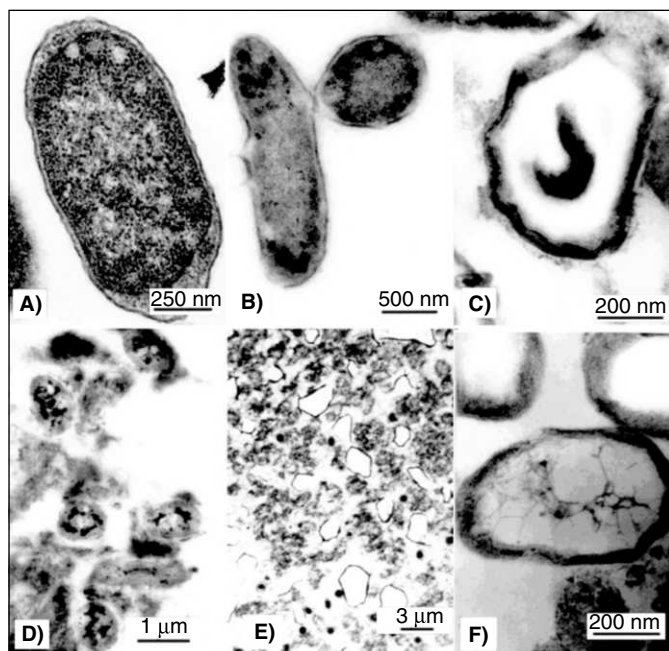


Fig. 24.9 Figure A, B and C are the transmission electron micrographs of *E. coli*, *B. megaterium* and *B. subtilis* bacteria cells. D, E and F are the TEM images of the corresponding cells after treatment with MgO/Cl_2 for 1 hr. From the TEM images, it is clear that the nanoparticles could penetrate the cells and thus rupture and damage the membranes (reprinted with permission from Stoimenov et al., *Langmuir*, 2002, 18, 6679–86. Copyright (2002) American Chemical Society).

on the removal of pollutants from water by ultrafiltration was attempted by Van der Bruggen and Vandecasteele.³⁹ Ag nanoparticles could be used as potential antibacterial agents as was revealed by Sondi and Salopek-Sondi.⁴⁰ The Ag nanoparticles, upon treatment with the *E. coli* cells, introduced pits in the cell walls, which imply a strong bactericidal action of the nanoparticles. The antibacterial tests of Ag nanoparticles performed on ‘*E. coli* strain B’ showed excellent antibacterial activity, as is evident from Fig. 24.10. The nanoparticles at a concentration of $10 \mu\text{g}/\text{cm}^3$ applied on 10^5 colony forming units (CFU) inhibited the bacterial growth by 70 per cent. Complete suppression (100%) of the bacterial growth was achieved with Ag nanoparticles concentration of $50\text{--}60 \mu\text{g}/\text{cm}^3$. Silver nanoparticles coated uniformly on polyurethane membrane demonstrated excellent antibacterial activity as was demonstrated by Jain and Pradeep.⁴¹ The antibacterial action of the Ag nanoparticles-coated polyurethane film is shown in Fig. 24.11. In Fig. A, photographs ‘a and b’, respectively are the polyurethane foam before and after coating the Ag nanoparticles. Due to saturation coverage of the nanoparticles in the foam, it becomes golden yellow in colour. Figure B shows the antibacterial effects of the coated-polyurethane. The characteristic metallic sheen of the *E. coli* bacteria (picture a in Fig. B) is seen in polyurethane exposed to *E. coli* (picture b in Fig. B), but after exposure to the Ag

nanoparticles-coated polyurethane film (picture c in Fig. B), there was no metallic sheen implying that the bacterial count in it is zero. Such polymer-nanoparticle composites provide feasible platforms for making devices for water and air purification.⁴¹

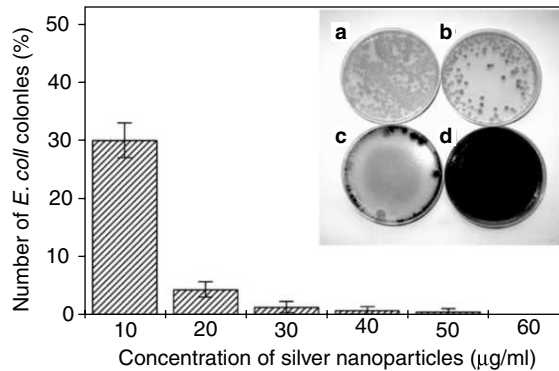


Fig. 24.10 Number of *E. coli* colonies present as a function of the concentration of the Ag nanoparticles in LB agar plates expressed as a percentage of the number of colonies grown on silver-free control plates. The inset shows the photographs of the plates with different concentrations of Ag nanoparticles a) 0, b) 10, c) 20 and d) 50 $\mu\text{g cm}^{-3}$ (adapted with permission from Ref. Sondi and Salopek-Sondi, *J. Colloid and Interface Sci.*, 2004, 275, 177–82).

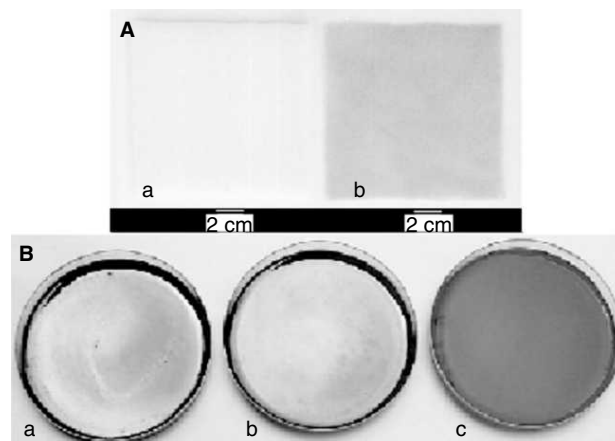


Fig. 24.11 Figure A shows photographs of (a) polyurethane film before Ag coating, and (b), after Ag coating. Golden yellow colour in photograph 'b' is due to the saturation coverage of silver nanoparticles. Figure B shows test tube results for *E. coli* MTCC 1302 for 10^{-2} dilution for 5-min exposure. a) initial count b) after exposure to pure polyurethane and c) after exposure to nanoparticle-coated polyurethane. Characteristic metallic sheen shown by *E. coli* is clearly visible in a, and b, while the bacterium count was zero in c (from Jain and Pradeep, *Biotechnology and Bioengineering*, 2005, 90, 59–63). (For clarity see colour figure.)

24.4 DENDRIMERS—THE NANOREACTORS FOR REMEDIATION

The application of dendrimers in environmental remediation is well explored. Dendrimers are considered as nanoreactors having suitable ligand sites to trap metal ions on their surfaces or interiors by sorption/complexation. Different dendrimers have been in place to immobilise and extract various contaminants from water. Polyamidoamine (PAMAM) dendrimers are a class of dendrimers, which solubilise many organic materials, metals and metal ions by complexation or encapsulation because of the presence of high density of nitrogen ligands. The use of polyamidoamine starburst dendrimers in the extraction of uranyl ions was reported by Ottaviani *et al.*⁴² The dendrimers serve as some kind of ‘uranyl ion sponges’ in removing the uranyl ions by sorption. The dendrimers are very stable and hence act as robust protective shell for the uranyl ions to prevent their diffusion into the environment. Dendrimers open up possibilities in remedying the risks associated with nuclear energy production, storing uranium derivatives, and nuclear wastes. Ag complexes of PAMAM and Ag-PAMAM nanocomposite solutions show excellent antimicrobial properties, as reported by Balogh *et al.*⁴³ Dendrimer biocides formed by functionalising end groups of dendrimers with quaternary ammonium salts were found to be much more active in bactericidal applications than the small molecule counterparts, namely, quaternary ammonium salts, because of their local high density on dendritic species.⁴⁴ The dendrimer biocides are believed to alter the surface charge and denature the bacterial membrane proteins and eventually cause complete disintegration of the bacterial membrane. Water insoluble nanosponges, prepared by functionalising poly (propylene imine) dendrimers with long aliphatic chains via treatment with long-chain N-alkylisocyanates render water insoluble dendrimeric species, were found to be useful in removing polycyclic aromatic hydrocarbons (PAHs) from water to a few ppb levels by inclusion process.⁴⁵ The removal of Cu(II) ions from water by treatment with ethylene diamine core-poly (amidoamine) shell dendrimers was investigated by Diallo *et al.*^{46,47} A general scheme of dendrimer-enhanced ultrafiltration is shown in Fig. 24.12. The methodology provides a means for the recovery of the contaminant metal ions and reuse of the dendrimers. Their structural versatility provides unprecedented options for developing cost-effective and environmentally-benign nano catalysts/reactors for remediation.

24.5 CARBON NANOMATERIALS—VERSATILE NEW ADSORBENTS FOR REMEDIATION

Traditionally, activated granulated carbon has been used as a means for remedying water from certain contaminants, though the carbon-based methodology lacks 100 per cent working efficiency, compounded by poor selectivity and slow adsorption kinetics. Many innovations have taken place in the area of carbon science for environmental remediation and the latest entry into this field is the carbon nanotubes (CNTs) and carbon nanofibers (CNFs). Carbon nanostructures have attracted the attention of scientists as new adsorbents because of their large surface area and the ease with which their surface could be functionalised for desired applications. The efficacy of CNTs in removing dioxins was reported by Long and Yang.⁴⁸ Peng *et al.*⁴⁹ had shown that as-grown and graphitised CNTs are good adsorbents for 1,2 dichlorobenzenes from water in a wide pH range of 3–10. Mangun *et al.*⁵⁰ reported

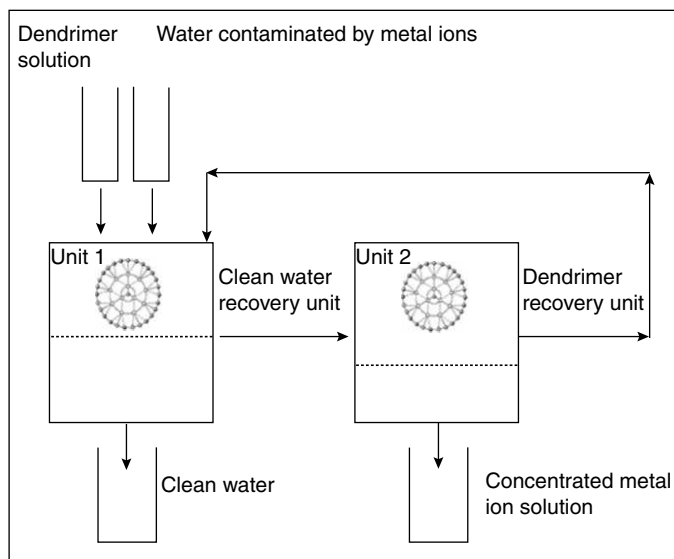


Fig. 24.12 Schematic of the recovery of metal ions from water solutions by dendrimer-enhanced filtration techniques (reprinted with permission from Diallo *et al.*, *Environ. Sci. Technol.*, 2005, 39, 1366–77. Copyright (2005) American Chemical Society).

the removal of trace amounts organic contaminants namely, benzene, toluene, ethylbenzene, p-xylene and chemical warfare agents, such as diisopropylmethyl phosphonate and half mustard from water using coated-glass activated carbon fibers. Li *et al.*⁵¹ found that the acid treated multi-walled CNTs (MWCNTs) show high adsorption capacities for the heavy metal ions, such as Pb^{2+} , Cu^{2+} and Cd^{2+} , with the affinity for the metal ions following the order, $\text{Pb}^{2+} > \text{Cu}^{2+} > \text{Cd}^{2+}$. The acid treated MWCNTs have negative charges because of oxidised surfaces, which favour electrostatic attractions with the metal ions and hence their removal by adsorption. The adsorption isotherms for the metal ions are shown in Fig. 24.13. Ceria supported CNTs are effective for the removal of arsenate from water. Srivastava *et al.*⁵² fabricated uniform macroscopic cylinders with radially aligned CNTs walls for the effective removal of heavy hydrocarbons from petroleum by adsorption. The filters also removed bacterial contaminants such as *E. coli* and the nanometer-sized poliovirus from water. These are shown in Figs 24.14 and 24.15. Figure 24.14 shows the gas chromatograms (GCs) of the petroleum before (A) and after (B) injection through the CNTs filter. Note the absence of heavier hydrocarbons (indicated by asterisks in Fig. A) in the filtered petroleum (Fig. B). Inset of Fig. A depicts the CNTs filter. The ability of the CNTs filter to remove bacteria from water is shown in Fig. 24.15. Figure A shows unfiltered water containing *E. coli* bacteria. The turbidity and pink colour (due to Phenol red indicator) is indicative of the *E. coli* bacteria in the unfiltered water. Figure B shows the colonies of *E. coli* grown by the culture of the polluted water. Figures C and D show the water filtered through the CNTs filter showing the absence of bacterial colonies. The CNTs filter also works satisfactorily with other microorganisms, namely, *S. aureus* bacterium and polio-1 virus.⁵² The nanotube filter has the advantage of repeated use with little or no efficiency loss in performance after ultrasonication and autoclaving. The scope of

the CNTs filter could be tuned by proper surface functionalisation. Fugetsu *et al.*⁵³ found that carbon nanotubes encapsulated in cross-linked alginate microvesicles are excellent substrates for the removal of ionic dyes namely, acridine orange, ethidium bromide, eosin bluish, and orange G, from water by affinity-based adsorption. The cross-linked alginate vesicles constitute polymer cage having physically trapped CNTs. When filtered through the CNTs-alginate polymer cage, the ionic dyes partition into the vesicles and are then adsorbed onto the CNTs. Adsorptive removal is facilitated by Van der Waals interactions between the aromatic backbone of the dyes and the hexagonal carbon sheets of the CNTs. A schematic of the cross-linked microvesicles-encapsulated CNTs is shown in Fig. 24.16. In summary, the carbon nanostructures are gaining popularity for adsorption-based remediation of heavy metal ions, organic dyes and microorganisms in water. The ease with which CNTs could be incorporated/granted onto polymers, membranes, and the feasibility of surface modification for targeted metals/ions, proteins and germs present a robust picture for carbon nanostructures in the remediation scenario.

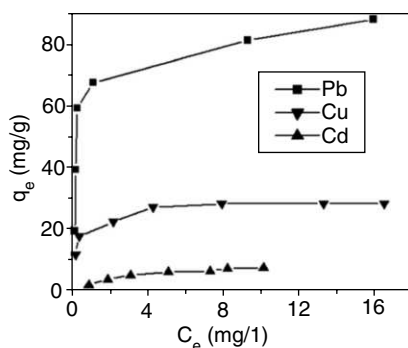


Fig. 24.13 Adsorption isotherms for Pb^{2+} , Cu^{2+} and Cd^{2+} on HNO_3 -treated CNTs at room temperature and at pH 5. The surfaces of MWCNTs become negatively charged because of the acid treatment and which cause electrostatic attractions of the metal ions toward the CNTs. ' C_e ' is the equilibrium metal ion concentration and q_e is the amount adsorbed at equilibrium (reprinted with permission from Li *et al.*, *Carbon*, 2003, 41, 2787–92).

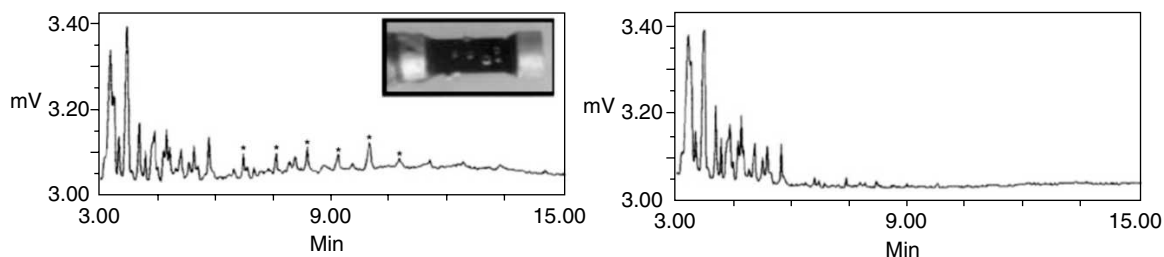


Fig. 24.14 Removal of heavier hydrocarbons by a CNTs filter. Figure A shows the gas chromatogram (GC) of unfiltered petroleum and B is that after filtering through the CNTs filter (the filter is shown in the inset of Fig. A). Note the absence of heavier hydrocarbon peaks (indicated by asterisks in Fig. A) in the GC of the filtered petroleum (reprinted with permission from Srivastava *et al.*, *Nat. Mater.*, 2004, 3, 610–14).

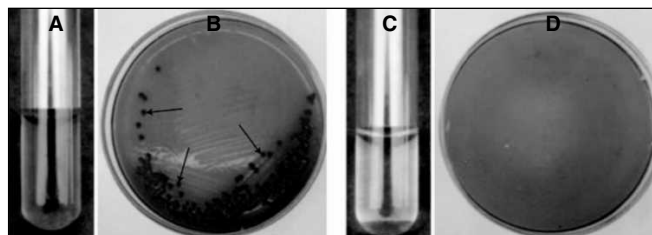


Fig. 24.15 Removal of *E. coli* bacteria by CNTs filter. The turbidity and pink colour in Fig. A is indicative of *E. coli* bacteria in the unfiltered water. Figure B shows the *E. coli* bacterial colonies (indicated by arrows) cultured from the unfiltered water. Note the absence of *E. coli* colonies when the water is filtered through the CNTs filter (Figs C and D). This shows that bundles of CNTs could effectively filter water (from Srivastava et al., *Nat. Mater.*, 2004, 3, 610–14.) (reprinted with permission). (For clarity see colour figure.)

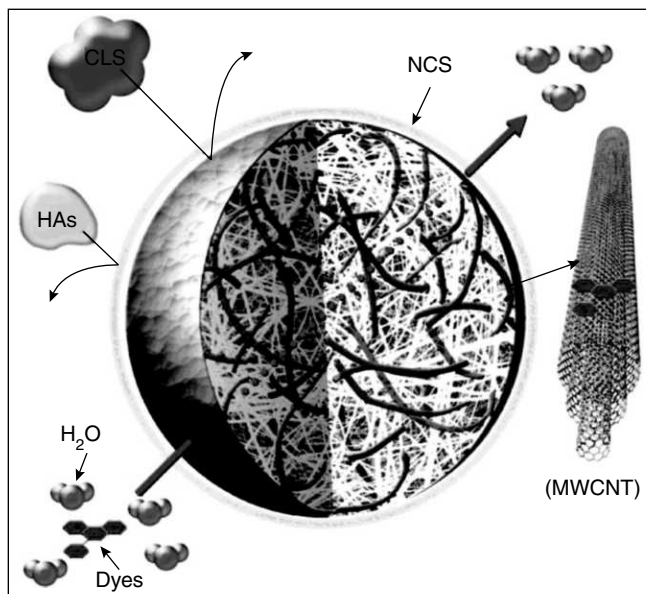


Fig. 24.16 Schematic of the cross-linked microvesicles-CNTs cage structure. The cage restricts the access of negatively charged ions (the surface of the cage is negatively charged and hence by repulsion) and colloids of large size (by size exclusion). The dyes are captured by CNTs by way of Van der Waals interactions between hexagonal carbon sheets of the CNTs and the aromatic backbone of the dyes (reprinted with permission from Fugetsu et al., *Environ. Sci. Technol.* 2004, 38, 6890–96. Copyright (2004) American Chemical Society). (For clarity see colour figure.)

24.6 NANOSCALE BIOPOLYMERS— BENIGN MATERILS FOR REMEDIATION

The use of stimuli responsive nanoscale polymers, such as PNIPAM (poly-(N-isopropylacrylamide)), is gaining importance in heavy metal remediation of soil and water. Customizable biopolymers could be synthesised with high specificity and tunable phase transition. Selective metal binding proteins could be easily fused to these nanoscale biopolymers for higher specificity and affinity towards heavy metals.⁵⁴ A typical example is the attachment of polyhistidine units to the biopolymers for scavenging Cd^{2+} . Similar examples are the use of MeR and Ars R proteins (two regulatory proteins used for controlling the expression of enzymes responsible for mercury (Hg) and arsenic (As) detoxification, respectively) in biopolymers for detoxifying Hg and As.^{55, 56} The nanoscale biopolymers have the advantage of zero toxicity and the ease of mass production from environmentally benign materials. By using the materials, a lower detection limit of the order of 10^{-10} M could be attained.⁵⁴ Figure 24.17 shows a schematic of the methodology for heavy metal removal by the nanoscale biopolymers and how the methodology could be adapted for groundwater treatment. The nanoscale biopolymers offer an environmentally benign route for the remediation of heavy metals in water and soil.

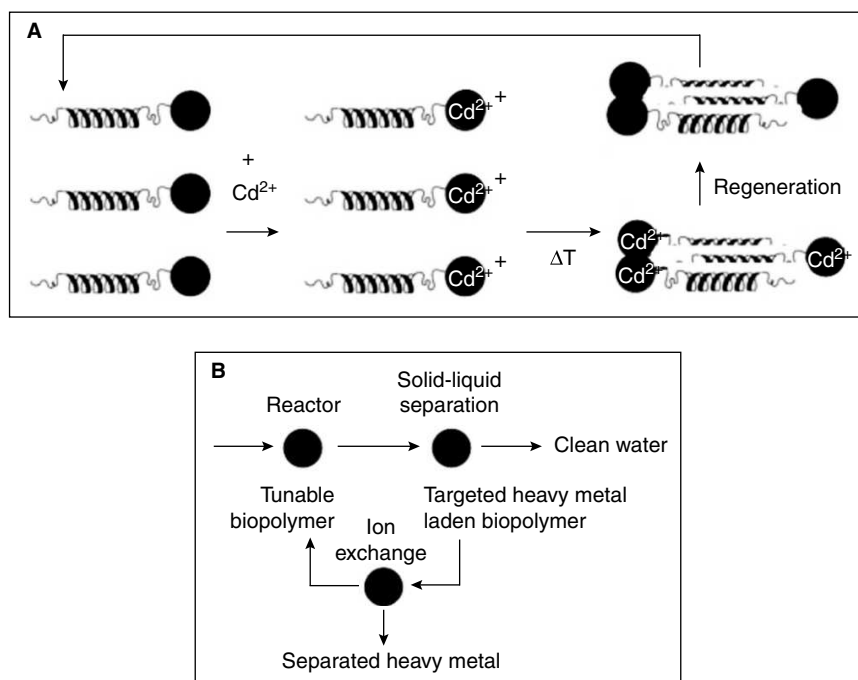


Fig. 24.17

Figure A shows a schematic of the methodology for the removal of heavy metals by nanoscale biopolymers. Schematic B shows heavy metal removal methodology for groundwater treatment by nanoscale biopolymers (reprinted with permission from Kostal et al., *J. Nanopart. Res.*, 2005, 7, 517–23).

24.7 CONCLUSIONS AND FUTURE PROSPECTS

The chapter presented an overview on the use of nanomaterials for environmental remediation. Reactive metal and semiconductor nanoparticles, dendrimers, carbon nanomaterials and nanoscale biopolymers have found extensive uses in the remediation of contaminants and offer great promises and expectations for a clean and sustainable environment. The unique characteristics of the nanomaterials, such as unusual crystal shapes and lattice orders, high surface to volume ratio, high chemical reactivity of the surface atoms and the ease with which they could be mounted on solid supports for *in-situ* and *ex-situ* applications, make them versatile agents for environmental remediation. Reactive metal and semiconductor nanoparticles degrade/remove the contaminants to harmless products by chemical means/adsorption. While dendrimers remedy the environmental contaminants via sorption and encapsulation, carbon nanomaterials do so via adsorption. Nanoscale biopolymers present an environmentally benign route for heavy metal remediation. However, there is a word of caution. Like any other technology, nanotechnology is also a double-edged sword. The exact implications associated with the fate, transport, transformation and exposure of these anthropogenic nanoparticles are not yet fully assessed. Though nanotechnology is revolutionary in nature and immense scope is in the offing, it is essential to assess the toxicological impacts of the nanomaterials in human body and the environment. We believe, this is absolutely essential for the public acceptability of the technology.

REFERENCES

1. T. Masciangioli and W. Zhang, 'Environmental nanotechnology: Potential and Pitfalls', *Environ. Sci. Technol.*, 37, (2003), 102A–108A.
2. S.M. Ponder, J.G. Darab, J. Bucher, D. Caulder, I. Craig, L. Davis, N. Edelstein, W. Lukens, H. Nitsche, L. Rao, D.K. Shuh and T.E. Mallouk, 'Surface Chemistry and Electrochemistry of Supported Zerovalent Iron Nanoparticles in the Remediation of Aqueous Metal Contaminants', *Chem. Mater.*, 13, (2001), 479–86.
3. B. Schrick, J.L. Blough, A.D. Jones and T.E. Mallouk, 'Hydrodechlorination of Trichloroethylene to Hydrocarbons Using Bimetallic Nickel-Iron Nanoparticles', *Chem. Mater.*, 14, (2002), 5140–47.
4. B. Schrick, B.W. Hydutsky, J.L. Blough and T.E. Mallouk, 'Delivery Vehicles for Zerovalent Metal Nanoparticles in Soil and Groundwater', *Chem. Mater.*, 16, (2004), 2187–93.
5. I. Dror, D. Baram and B. Berkowitz, 'Use of Nanosized Catalysts for Transformation of Chloro-Organic Pollutants', *Environ. Sci. Technol.*, 39, (2005), 1283–90.
6. A.B.M. Giasuddin, S.R. Kanel and H. Choi, 'Adsorption of Humic Acid onto Nanoscale Zerovalent Iron and Its Effect on Arsenic Removal', *Environ. Sci. Technol.*, 41, (2007), 2022–27.
7. W. Zhang, 'Nanoscale Iron Particles for Environmental Remediation: An Overview', *J. Nanopart. Res.*, 5, (2003), 323–32.
8. K.M. Paknikar, V. Nagpal, A.V. Pethkar and J.M. Rajwade, 'Degradation of Lindane from Aqueous Solutions using Iron Sulfide Nanoparticles Stabilized by Biopolymers', *Sci. Technol. Adv. Mater.*, 6, (2005), 370–74.

9. N. Chitose, S. Ueta, S. Seino and T.A. Yamamoto, 'Radiolysis of Aqueous Phenol Solutions with Nanoparticles. Phenol Degradation and TOC Removal in Solutions Containing TiO₂ Induced by UV, c-ray and Electron Beams', *Chemosphere*, 50, (2003), 1007–13.
10. H. Song, H. Jiang, X. Liu and G. Meng, 'Efficient Degradation of Organic Pollutant with WO_x Modified Nano TiO₂ under Visible Irradiation', *Journal of Photochemistry and Photobiology A: Chemistry*, 181, (2006), 421–28.
11. J.B. Mertens, C. Blothe, K. Windey, W.D. Windt and W. Verstraete, 'Biocatalytic Dechlorination of Lindane by Nano-scale Particles of Pd(0) Deposited on *Shewanella Oneidensis*', *Chemosphere*, 66, (2007), 99–105.
12. N. Sobana, M. Muruganadham and M. Swaminathan, 'Nano-Ag Particles Doped TiO₂ for Efficient Photodegradation of Direct Azo Dyes', *J. Mole. Catal. A: Chemical*, 258, (2006), 124–32.
13. M.H. Priya and G. Madras, 'Photocatalytic Degradation of Nitrobenzenes with Combustion Synthesized Nano-TiO₂', *J. Photochem. Photobiol. A: Chemistry*, 178, (2006), 1–7.
14. A.J. Feitz, S.H. Joo, J. Guana, Q. Sun, D.L. Sedlak and T.D. Waite, 'Oxidative Transformation of Contaminants using Colloidal Zero-valent Iron', *Colloids and Surfaces A: Physicochem. Eng. Aspects*, 265, (2005), 88–94.
15. C. Hariharan, 'Photocatalytic Degradation of Organic Contaminants in Water by ZnO Nanoparticles: Revisited', *App. Catal. A: General*, 304, (2006), 55–61.
16. T. Aarthi and G. Madras, 'Photocatalytic Degradation of Rhodamine Dyes with Nano-TiO₂', *Ind. Eng. Chem. Res.*, 46, (2007), 7–14.
17. P.V. Kamat and D. Meisel, 'Nanoscience Opportunities in Environmental Remediation', *C.R. Chimie*, 6, (2003), 999–1007.
18. P. Varanasi, A. Fullana and S. Sidhu, 'Remediation of PCB Contaminated Soils Using Iron Nanoparticles', *Chemosphere*, 66, (2007), 1031–38.
19. N. Savage and M.S. Diallo, 'Nanomaterials and Water Purification: Opportunities and Challenges', *J. Nanopart. Res.*, 7, (2005), 331–42.
20. A-F. Ngomsik, A. Bee, M. Draye, G. Cote and V. Cabuil, 'Magnetic Nano- and Microparticles for Metal Removal and Environmental Applications: A Review', *C.R. Chimie*, 8, (2005), 963–70.
21. Y. Badr and M.A. Mahmoud, 'Photocatalytic Degradation of Methyl Orange by Gold Silver Nano-core/silica Nano-shell', *Journal of Physics and Chemistry of Solids*, 68, (2007), 413–19.
22. A.S. Nair and T. Pradeep, 'Halocarbon Mineralisation and Catalytic Destruction by Metal Nanoparticles', *Curr. Sci.*, 84, (2003), 1560–64.
23. A.S. Nair, R.T. Tom and T. Pradeep, 'Detection and Extraction of Endosulfan by Metal Nanoparticles', *J. Environ. Monitor.*, 5, (2003), 363–65.
24. A.S. Nair and T. Pradeep, 'Quantitative Extraction of Chlorpyrifos and Malathion from Water by Metal Nanoparticles', *J. Nanosci. Nanotechnol.*, 7, (2007), 1811–17.
25. M. Haruta, Y. Yamada, T. Kobayashi and S. Lijita, 'Gold Catalysis Prepared by Coprecipitation for Low-temperature Oxidation of Hydrogen and of Carbonmonoxide', *J. Catal.*, 115, (1989), 301–09.
26. M.S. Chen and D.W. Goodman, 'The Structure of Catalytically Active Gold on Titania', *Science*, 306, (2004), 252–55.

27. Z.-P. Liu, X.-Q. Gong, J. Kohanoff, C. Sanchez and P. Hu, 'Catalytic Role of Metal Oxides in Gold-Based Catalysts: A First Principles Study of CO Oxidation on TiO₂ Supported Au', *Phys. Rev. Lett.*, (2003), 91, 266102.1–266102.4.
28. J. Guzman and B.C. Gates, 'Catalysis by Supported Gold: Correlation between Catalytic Activity for CO Oxidation and Oxidation States of Gold', *J. Am. Chem. Soc.*, 126, (2004), 2672–73.
29. E.A. Deliyanni, D.N. Bakoyannakis, A.I. Zouboulis and K.A. Matis, 'Sorption of As(V) ions by Akaganeite-type Nanocrystals', *Chemosphere*, 50, (2003), 155–63.
30. N.K. Lazaridis, D.N. Bakoyannakis and E.A. Deliyanni, 'Chromium(VI) Sorptive Removal from Aqueous Solutions by Nanocrystalline Akaganeite', *Chemosphere*, 58, (2005), 65–73.
31. H. Zhao and K.L. Nagy, Dodecyl, 'Sulfate–Hydrotalcite Nanocomposites for Trapping Chlorinated Organic Pollutants in Water', *Journal of Colloid and Interface Science*, 274, (2004), 613–24.
32. G.E. Fryxell, Y. Lin, S. Fiskum, J.C. Birnbaum, H. Wu, K. Kemner and S. Kelley, 'Actinide Sequestration Using Self-Assembled Monolayers on Mesoporous Supports', *Environ. Sci. Technol.*, 39, (2005), 1324–31.
33. Y. Lin, S.K. Fiskum, W. Yantasee, H. Wu, S.V. Mattigod, E. Vorpapel, G.E. Fryxell, K.N. Raymond and J. Xu, 'Incorporation of Hydroxypyridinone Ligands into Self-Assembled Monolayers on Mesoporous Supports for Selective Actinide Sequestration', *Environ. Sci. Technol.*, 39, (2005), 1332–37.
34. W. Tungittiplakorn, C. Cohen, and L.W. Lion, 'Engineered Polymeric Nanoparticles for Bioremediation of Hydrophobic Contaminants', *Environ. Sci. Technol.*, 39, (2005), 1354–58.
35. P.K. Stoimenov, R.L. Klinger, G.L. Marchin and K.J. Klabunde, 'Metal Oxide Nanoparticles as Bactericidal Agents', *Langmuir*, 18, (2002), 6679–86.
36. K.A. DeFriend, M.R. Wiesner and A.R. Barron, 'Alumina and Aluminate Ultrafiltration Membranes Derived from Alumina Nanoparticles', *J. Memb. Sci.*, 224, (2003), 11–28.
37. M.S. Mohsen, J.O. Jaber and M.D. Afonso, 'Desalination of Brackish Water by Nanofiltration and Reverse Osmosis', *Desalination*, 157, (2003), 166–68.
38. B.W. Stanton, J.J. Harris, M.D. Miller and M.L. Bruening, 'Ultrathin, Multilayered Polyelectrolyte Films as Nanofiltration Membranes', *Langmuir*, 19, (2003), 7038–42.
39. B. Van der Bruggen and C. Vandecasteele, 'Removal of Pollutants from Surface Water and Groundwater by Nanofiltration: Overview of Possible Applications in the Drinking Water Industry', *Environmental Pollution*, 122, (2003), 435–45.
40. I. Sondi and B. Salopek-Sondi, 'Silver Nanoparticles as Antimicrobial Agent: a Case Study on *E. coli* as a Model for Gram-negative Bacteria', *Journal of Colloid and Interface Science*, (2004), 275, 177–82.
41. P. Jain and T. Pradeep, 'Potential of Silver Nanoparticle-Coated Polyurethane Foam As an Antibacterial Water Filter', *Biotechnology and Bioengineering*, 90, (2005), 59–63.
42. M.F. Ottaviani, P. Fayuzza, M. Bigazzi, N.J. Turro, S. Jockusch and D.A. Tomalia, 'A TEM and EPR Investigation of the Competitive Binding of Uranyl ions to Starburst Dendrimers and Liposomes: Potential Use of Dendrimers as Uranyl ion Sponges', *Langmuir*, 16, (2000), 7368–72.
43. L. Balogh, D.R. Swanson, D.A. Tomalia, G.R. Hagnauer and A.T. McManus, 'Dendrimer-Silver Complexes and Nanocomposites as Antimicrobial Agents', *Nanolett.*, 1, (2001), 18–21.

44. C.Z. Chen and S.L. Cooper, 'Interactions between Dendrimer Biocides and Bacterial Membranes', *Biomaterials*, 23, (2002), 3359–68.
45. M. Arkas, D. Tsiourvas and C.M. Paleos, 'Functional Dendrimeric "Nanosponges" for the Removal of Polycyclic Aromatic Hydrocarbons from Water', *Chem. Mater.*, 15, (2003), 2844–47.
46. M.S. Diallo, S. Christie, P. Swaminathan, L. Balogh, X. Shi, W. Um, C. Papelis, W.A. Goddard and J.H. Johnson, Jr., 'Dendritic Chelating Agents. 1. Cu(II) Binding to Ethylene Diamine Core Poly(amidoamine) Dendrimers in Aqueous Solutions', *Langmuir*, 20, 2, (2004), 640–51.
47. M.S. Diallo, S. Christie, P. Swaminathan, J.H. Johnson and W.A. Goddard III, 'Dendrimer Enhanced Ultrafiltration. 1. Recovery of Cu(II) from Aqueous Solutions Using PAMAM Dendrimers with Ethylene Diamine Core and Terminal NH₂ Groups', *Environ. Sci. Technol.*, 39, (2005), 1366–77.
48. R.Q. Long and R.T. Yang, 'Carbon Nanotubes as Superior Sorbent for Dioxin Removal', *Journal of American Ceramic Society*, 123, (2001), 2058–59.
49. X. Peng, Y. Li, Z. Luan, Z. Di, H. Wang, B. Tian and Z. Jia, 'Adsorption of 1,2-Dichlorobenzene from Water to Carbon Nanotubes', *Chem. Phys. Lett.*, 376, (2003), 154–58.
50. C.L. Mangun, Z. Yue, J. Economy, S. Maloney, P. Kemme and D. Cropek, 'Adsorption of Organic Contaminants from Water Using Tailored ACFs', *Chem. Mater.*, 13, (2001), 2356–60.
51. Y-H Li, J. Ding, Z. Luan, Z. Di, Y. Zhua, C. Xu, D. Wu and B. Wei, 'Competitive Adsorption of Pb²⁺, Cu²⁺ and Cd²⁺ Ions from Aqueous Solutions by Multi-walled Carbon Nanotubes', *Carbon*, 41, (2003), 2787–92.
52. A. Srivastava, O.N. Srivastava, S. Talapatra, R. Vajtai and P.M. Ajayan, 'Carbon Nanotube Filters', *Nat. Mater.*, 3, (2004), 610–14.
53. B. Fugetsu, S. Satoh, T. Shiba, T. Mizutani, Y-B. Lin, N. Terui, Y. Nodosaka, K. Sasa, K. Shimizu, T. Akasaka, M. Shindoh, K-I. Shibata, A. Yokoyama, M. Mori, K. Tanaka, Y. Sato, K. Tohji, S. Tanaka, N. Nishi and F. Watari, 'Caged Multi-walled Carbon Nanotubes as the Adsorbents for Affinity-Based Elimination of Ionic Dyes', *Environ. Sci. Technol.*, 38, (2004), 6890–96.
54. Kostal, G. Prabhukumar, U.L. Lao, A. Chen, M. Matsumoto, A. Mulchandani and W. Chen, 'Customisable Biopolymers for Heavy Metal Remediation', *J. Nanopart. Res.*, 7, (2005), 517–23.
55. J. Kostal, A. Mulchandani and W. Chen, 'Tunable Biopolymers for Heavy Metal Removal', *Macromolecules*, 34, (2001), 2257–61.
56. J. Kostal, A. Mulchandani, K.E. Gropp and W. Chen, 'A Temperature Responsive Biopolymer for Mercury Remediation', *Environ. Sci. Technol.*, 37, (2003), 4457–62.

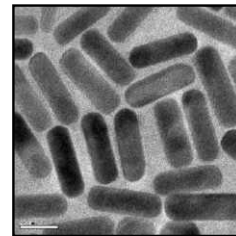
ADDITIONAL READING

1. *Environmental Applications of Nanomaterials-Synthesis, Sorbents and Sensors*, 2007, Imperial College Press, Edited by G.E. Fryxell and G. Cao.
2. *Environmental Nanotechnology-Applications and Impacts of Nanomaterials*, 2007, C.H.I.P.S, Edited by M.R. Wienser.

REVIEW QUESTIONS

1. What is unique about nanomaterials for their use in environmental remediation?
2. What structural characteristics of dendrimers are useful for remedying the contaminants?
3. Describe the mechanism of degradation of TCE by bimetallic nanoparticles. What are the advantages of using bimetallic nanoparticles over metallic nanoparticles?
4. Describe with a diagram, how semiconductor nanoparticles degrade organic contaminants by photosensitization.
5. Why Ag and MgO nanoparticles bactericidal?
6. Read on the environmental impacts of nanomaterials and comment on the hazards associated with the use of nanomaterials for environmental remediation.
7. What are the other ways by which how nanotechnology could transform our environment (other than those described here)?

CATALYSIS USING TRANSITION METAL NANOCCLUSERS



“This new force, which was unknown until now, is common to organic and inorganic nature. I do not believe that this is a force entirely independent of the electrochemical affinities of matter; I believe, on the contrary, that it is only a new manifestation, but since we cannot see their connection and mutual dependence, it will be easier to designate it by a separate name. I will call this force catalytic force. Similarly, I will call the decomposition of bodies by this force catalysis, as one designates the decomposition of bodies by chemical affinity analysis.”

Jöns Jacob Berzelius

‘Some Ideas on a New Force which Acts in Organic Compounds’,
Annales chimie physiques, 1836, 61, 146. Translated in Henry M. Leicester
and Herbert S. Klickstein, A Source Book in Chemistry 1400-1900 (1952), 267

Catalysis of nanomaterials, in general, and metal nanoparticles, in particular, is an emerging and important field. Here, we show that the change in the electronic energy levels of a growing cluster is the principal reason for its catalytic activity. This is illustrated with selected examples, which show increased activity and selectivity. Several aspects of relevance to catalysis at the nanoscale are mentioned.

Learning Objectives

- Size and shape dependent surface energy variation for metallic nanoparticles.
 - Shift of Fermi potential with and without nucleophile for metallic clusters at their nanoregion.
 - Variation of reduction potential for metal nanoparticles with agglomeration number.
 - Thermodynamic effect of noble metal core and less noble metal shell structure for bimetallics.
-
-

25.1 INTRODUCTION

The word ‘catalysis’ first came into being in the year 1835 to describe the action of ‘catalysts’ on the rate of the certain chemical reactions. A catalyst is regarded as a species that accelerates a chemical reaction

without itself being altered. Initially, its role was restricted to providing the reactant molecules with energy needed to overcome the activation energy barrier for the reaction. But later, the definition of catalyst was modified as a substance that changes a chemical reaction kinetically, but not thermodynamically.¹ The catalyst reduces the activation energy of the reaction. According to Boudart, catalysts undergo only transient change during the course of the process, but at the end, returns to its initial status.² Catalyst operates in a versatile way, like it controls the reaction, improves the yield, minimises the amount of unwanted byproducts (improve the selectivity), provides milder reaction conditions, reduces waste and its environmental impact. Transition metals, especially metals of group 8, are active catalysts being used on a large scale for refining of petroleum, conversion of automobile exhausts, hydrogenation of carbon monoxide (CO), hydrogenation of fats and many other processes.³⁻⁷ Recently, nanomaterials attracted special interest in catalysis as they provide access to more number of catalytically active sites due to large surface to volume ratio than the corresponding bulk components. The catalytic activity of finely-dispersed metal catalysts is known to be a strong function of the metal particle size. This is due to a number of factors including the increase of the specific surface area with diminishing particle size, size variation of the surface morphology (in particular, contribution of different crystallographic planes), modification of the type of surface defects, etc. These effects are particularly noticeable when the metal particle size diminishes down to nanometer range. However, being small in size, it is expected that the surface tension in the nano regime is increased, which makes their surface atoms very active.

Purnell *et al.* investigated the catalytic behaviour of clusters of four and six iridium atoms on solid support. They find different catalytic activity both from each other and from metallic Ir.⁸ The effect of the size of metal particles upon their electronic structure is of fundamental importance for the variety of their properties including adsorption and catalysis. It is observed that the electronic property changes with the size and that affect the catalytic property.⁹ For some redox reactions, the rate of catalysis by growing particles is distinctly faster, compared to that of stable and larger silver particles, which are the final products of growing particles.^{10, 11, 12} The metal clusters are formed as transient intermediates during the formation of metal colloids by the reduction of metal ions in solutions. At the initial stage of colloid formation, the metal atoms are formed, which subsequently agglomerate.¹³⁻¹⁷ Henglein *et al.* considered these particles as growing microelectrodes (GME). The progressive decrease in size of metal particles having a diameter in the nanometer regime is accompanied by an increase in Fermi potential.^{13, 15-17} Thus a step-wise lowering in the redox potential takes place. The redox potential of the particle for a particular metal depends on the value of agglomeration number, n , and the nature of associated ligand. The redox potential is as negative as -2.7 , -1.8 , and -1.5 V (vs. NHE) for $n=1$ for copper, silver and gold respectively.^{13, 16, 18} Figure 25.1 shows how the redox potential changes with the agglomeration number.¹⁷ During the growth of such small-scale particles, their redox potentials vary continuously. The redox potential of the ultradivided metal particles could be increased further to a considerable extent in the presence of nucleophiles.^{16, 17} The art of making small metal particles and incorporation of nucleophiles thus help in attaining a very low redox potential for a metal aqueous $\text{metal}_{\text{aqueous}}^{n+}/\text{metal}_{\text{atom}}$ system. As a matter of fact, these growing particles can take part in reactions, where electrons are transferred across the particle-solution interface similar to electrode reactions in electrochemistry.

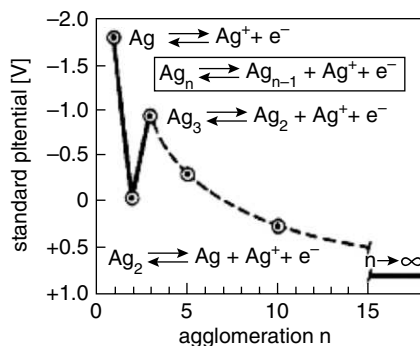


Fig. 25.1 Electrochemical standard potential of the silver microelectrode as a function of the agglomeration number.

It has been well recognised that the reaction rate per unit catalyst surface area can vary with particle size and decreasing particle size will not always result in an increased reaction rate per unit mass of transition metal.¹⁹ Catalytic reactions that proceed at rates (per unit surface area of metal) that vary substantially from one metal crystallite size to another are called structure sensitive. Structure-sensitive reactions also proceed at substantially different rates on different crystal planes of single crystals of a metal. Structure-sensitive catalytic reactions include those that involve breaking or making of C-C, N-N, or C-O bonds.²⁰ El-Sayed suggested the general trend of increased catalytic activity with decrease in particle size, which intimate that the low-coordination number vertex and edge atoms on the particle surface are active sites for the Suzuki reaction.²¹ Recently, it has been shown that the activities of dissimilar shapes are different for the same electron transfer reaction in colloidal solution. This potential shape-dependent catalysis adds advantage of using nanoparticles as catalysts. For any size and shape, the catalytic activity of the nanoparticles is found to correlate with the fraction of surface atoms located on corners and edges. However, this high reactivity leads to surface reconstruction and shape changes in colloidal systems.²²

Multimetallic systems, or better called bimetallic catalysts is one of the most important breakthroughs in catalysis research. “Bimetallics” is a term introduced by J.H. Sinfelt, and it holds a preference over the classical term of alloys. The addition of promoters has a profound effect on the performance of the catalysts. The promoting effect can be achieved not only by adding another catalytically active metal, but also by adding an inert one. Besenbacher *et al.* found that gold forms a random surface alloy on nickel. Gold itself is not catalytically active, but it alters the surface in such a way that it prevents formation of large clusters of Ni. This inhibits carbon deposition, increasing the stability of steam reforming. It was found that bimetallic catalysts were able to selectively increase the reaction rate to the desired products, even though the reactions to the undesired products were thermodynamically and kinetically favourable.²³ Bimetallic catalysts are widely used in relevant processes like naphtha reforming, selective hydrogenation and dehydrogenation of light products. Especially, in selective hydrogenations, bimetallic catalysts have proven to exhibit superior performance as compared to their monometallic counterparts. Two effects of major importance are: electronic effects and ensemble

effects.^{24, 25} The latter were believed to be explained by the Rigid Band Theory (RBT). When going from left to right in the periodic table, the RBT explained that the “rigid” band of energy levels of the valence electrons was being filled successively.²⁶ By alloying, it was believed that the d-band was filled by electrons of the second metal; therefore, electronic charge transfer between the metals was expected as well as the creation of a new band.²⁷ As the individuality of the metals is lost, the alloys formed were considered as a new metals. The basis of ensemble effects is that the surface of the catalyst requires a specific arrangement of atoms to be able to catalyse a reaction. For example, it was found that the activity of the transition metals for hydrogenolysis reactions of hydrocarbons was drastically decreased by the presence of a group 11 metal. Normally, hydrogenolysis is an undesired reaction. The inhibition of hydrogenolysis leads to improved selectivity for alkane isomerisation reactions and for reactions in which saturated hydrocarbons are converted to aromatic hydrocarbons.²⁵ Another important structure in bimetallic nanoparticle is core-shell. Schmid *et al.* reported the preparation and catalytic properties of Au/Pd core-shell nanoclusters for the hydrogenation of hex-2-ene. The Au/Pd bimetallic nanoclusters are much more catalytically active than monometallic palladium, although gold itself is inert for this reaction.²⁸ Toshima *et al.* reported the construction of Pd/Pt and their inverted structures in setting up a novel method using sacrificial hydrogen to control the core-shell structure. The Pt/Pd structure shows much higher catalytic activity than Pd monometallic nanoclusters, but the inverted structure has catalytic activity between two monometallic nanoclusters due to low activity of Pt nanoparticles.²⁹

25.2 GROWING AND FULL GROWN PARTICLES AS REDOX CATALYSTS

The precise size and shape controlled synthesis, stabilisation and fascinating designing of metal nanoparticles are now the upcoming field of nanoscience and nanotechnology. Exploitation of metal nanoparticles in catalysis has already brought a revolution in chemistry. Spiro and Miller *et al.* suggested catalysis proceeds through an electrochemical mechanism, where electron transfer occurs via the particle.^{30, 31} The catalytic efficiency of such particles for electron transfer processes is generally explained by their size-dependent redox properties, which control their role as an electron relay. The required potential of the particle is intermediate between that of the electron donor and the acceptor. The reactions catalysed by growing particles were also studied by Henglein^{13, 32} and Belloni *et al.*^{16, 33} They have employed growing silver particles to catalyse the reduction of excess Ag^+ ions by a weak reductant present in the system. In these systems, during the course of growth, when the size of silver particle reaches a certain critical level, the electrochemical standard potential of the (silver particle/silver ion) system becomes less negative compared to that of the weak reductant. Then, the latter gives up electrons, reducing excess Ag^+ ion present in the system. Keeping this idea in mind, the activity of growing metal nanoparticles (GME) and full-grown metal nanoparticles (FGME) for the dye reduction reactions have been studied.^{10–12, 34}

Growing silver has been observed to be more efficient catalyst than the stable colloidal particles for specific reactions. These growing particles catalyse borohydride reduction of several organic dyes, like methylene blue (MB), phenosafranin (PS), fluorescein (F), 2,7-dichlorofluorescein (DCF), eosin (E) and rose bengal (RB). To demonstrate the effect of GME, Ag^+ ion is reduced *in-situ* in the reaction medium. On the other hand, FGME, the preformed particles are added to the mixture of a

dye and NaBH_4 and the reduction process is monitored spectrophotometrically. All these chosen dyes have a widely different absorption peak in comparison to the plasmon peak of silver nanoparticles. The reduction of the dye by borohydride occurs very fast in the presence of AgNO_3 . The colour of the dye gradually vanishes, which is indicated by the gradual decrease in absorbance value at the λ_{max} and concomitantly the plasmon peak of silver appears at ~ 400 nm. The time required to initiate the process, i.e., induction period is observed for both the growing and full-grown particles in a solution with stabiliser, but for growing particles, greater induction period is observed. This is due to the encapsulation of stable particles by a temporary barrier of the stabiliser that controls the adsorption of BH_4^- ions to the particle surface. For stabiliser-free particles, no induction period was observed. Figure 25.2 show the reduction of a cationic dye, PS in CTAB solution.

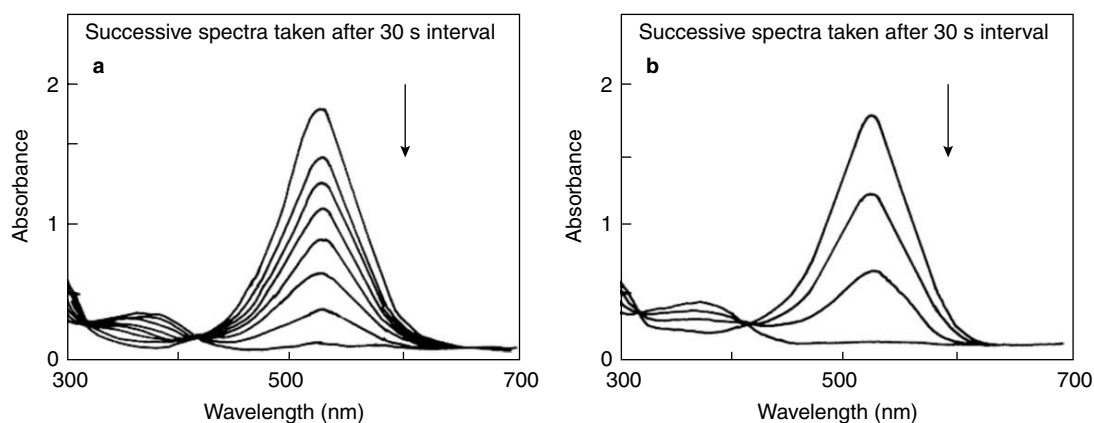


Fig. 25.2 Successive UV-visible spectra of cationic dye phenosafranin (PS) during its catalytic reduction by (a) growing and (b) stable silver particles in aqueous CTAB solutions containing $[\text{AgNO}_3] = 10^{-5} \text{ mol dm}^{-3}$, $[\text{CTAB}] = 0.01 \text{ mol dm}^{-3}$, $[\text{NaBH}_4] = 5 \times 10^{-3} \text{ mol dm}^{-3}$, and $[\text{PS}] = 10^{-4} \text{ mol dm}^{-3}$.

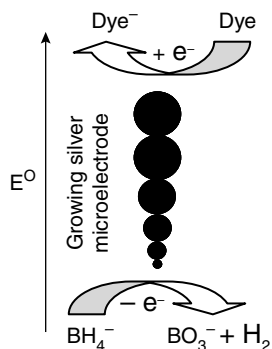
The redox catalytic property of still-growing and final particles of palladium has also been investigated using methylene blue (MB) and fluorescein (F) as redox probes. Reductions of MB by N_2H_4 and of F by NaBH_4 are observed to be catalysed by both the still-growing and the final Pd particles. Here, the still-growing particle catalysed dye reduction has been observed without any induction time as reported earlier. This is due to faster reduction of Pd^{II} to Pd^0 .

Although the reduction potentials of MB, PS, F, and DCF are almost comparable, borohydride reduction rates become faster for MB and PS with Pd particles. Probably, the nature of the dyes (i.e., charge, hydrophobicity, presence of S/N donor atom, etc.) is also an important feature. The nature of the dye determines its adsorption equilibrium with the catalyst surface and thus controls the effective concentration of the dye at the catalyst surface. Of the four anionic dyes, F and DCF have a higher reduction potential than E and RB. Still, borohydride reduction rates are higher for E and RB. Here, increased hydrophobicity of E and RB, due to the presence of Br and I in their skeleton, may be responsible for the facile reaction. The rates of reduction of dyes catalysed by the still-growing particles

are either fast or slow compared to those for reduction catalysed by the final particles and that they depend on the nature of the dye.

In many cases, the catalysed dye reduction stops after some time in the absence of a surfactant. This is due to the deactivation or poisoning of the catalyst surface through adsorption of the dye. In the presence of surfactant, the static adsorption of dye onto the catalyst surface is inhibited due to the predominant and dynamic adsorption of surfactant.³⁵ Above the cmc, surfactants form micelles, which can interact with dye molecules preventing static adsorption of the dye on the catalyst surface. Thus deactivation of catalyst becomes inhibited in the presence of a surfactant. Below the cmc, surfactants form a monolayer, bilayer, etc., on the surface of the Pd particles depending upon the concentration of surfactant. Organised assemblies of surfactants act as a catalyst in a way that is distinctly different from micellar catalysis. In this case, the surfactant layer acts as a binding site for the dye/reducing agent. As a result, reactants are concentrated onto the catalyst surface, leading to rate enhancement. The monolayer of the surfactant formed on the particle surface attracts dyes and reducing agent from the bulk by both hydrophobic and electrostatic interactions. The observed oscillation of rates with increased surfactant concentration is probably due to the formation of surfactant multilayer. When the surfactants have a similar charge to that of the dye and the reducing agent, the electrostatic repulsion may predominate over the hydrophobic interaction and this causes a decrease in rate.

To explain the rate of catalysis, we propose that electron transfer occurs via the growing particles, similar to (stable) colloid particle catalysed redox reactions. Earlier work shows that the reduction potential of a silver wire decreases with the increase in BH_4^- concentration in water due to the adsorption of BH_4^- ion onto the electrode surface.³⁶ A similar effect is also expected with silver particles. However, the potential of growing particles containing BH_4^- adsorbed on their surface, unlike that for stable particles, will gradually increase with the increasing size of the particle, because the inherent particle potential gradually increases with increasing nuclearity (size). The resultant potential of the particles with adsorbed BH_4^- will obviously be anodic to the reductant (BH_4^- ion) and cathodic to the oxidant (dye). Thus, an electron relay via particle to dye is possible. Scheme 25.1 shows the schematic representation of this electron transfer, where the growing particle in its intermediate stage accepts electrons from BH_4^- ions and conveys them to the dye.



Scheme 25.1 Scheme for growing silver catalysed redox reaction.

The higher catalytic behaviour of growing particles may be attributed to the following two properties: first, its continuously renewable surface and, second, its large negative electrochemical potential, which arises owing to the very small size. The catalytic reduction rate should be surface and/or diffusion controlled. For surface controlled reactions, the rate of catalytic reduction should be determined by the difference in potential of the BH_4^- adsorbed particle and the potential of the oxidant system. The smaller the size of the particle, the more is the potential difference leading to a higher rate of reduction.³⁷ Interestingly, for two dyes MB and F, the catalytic rates for still-growing and final particles are different for silver. For MB, it was found that the rate is faster with final particles than still growing one. But, it is opposite with F. This is explained by the poisoning action of the dye. At the initial stage of particle growth the $[\text{Pdparticle}]/[\text{dye}]$ is low so the dye will provide more poisoning action to the catalyst particles. As a result, the poisoning action is more prominent in still-growing particles. This fact is more prominent in MB than F due to presence of sulfur in methylene blue skeleton. As time passes, the $[\text{Pdparticle}]/[\text{dye}]$ ratio increases and rate increases as well. Exceptions were noted in the case of cationic dyes (PS and MB). For MB, stable-particle catalysed reduction was faster in aqueous as well as in surfactant media, irrespective of the nature of surfactant. But interestingly, the performance of growing particles can be again improved over stable particles for PS in SDS.

Interestingly, it is observed that some dyes are reduced at a faster rate with GME and some with FGME. In the former case, the plasmon band is not observed so long as the dye remains in solution in the unreduced form. In the latter case, the plasmon band is observed before the dye reduction starts, i.e., prior to the formation of particles. From this observation, the size effect in catalysis is demonstrated for dye reduction. So one can think about the usefulness of size dependence, i.e., alternation of agglomeration number of a metal catalyst for very many reactions.

As an eventful application, the reduction of 4-nitrophenol has been examined in our laboratory for the first-time employing metallic hydrosols as catalysts. Esumi *et al*³⁸ extended the reduction reaction in dendrimer-encapsulated gold nanoparticles as catalysts. Ballauff reported the better catalytic activity of 2 nm particles over 20 nm particles for the reduction of 4-nitrophenol.³⁹ We studied the detail kinetics for both the GME- and FGME-catalysed reactions for the reduction of 4-nitrophenol (4NP) shown in Fig. 25.3. In NaBH_4 medium ($\text{pH} > 12.0$) the peak of 4NP ($\lambda_{\text{max}} \sim 377 \text{ nm}$) is red shifted due to the formation of 4-nitrophenolate ion ($\lambda_{\text{max}} \sim 400 \text{ nm}$).⁴⁰ As the reaction was over involving GME, the peak at 400 nm vanished and a new peak in the blue region appeared due to the corresponding amino compound ($\lambda_{\text{max}} \sim 290 \text{ nm}$). The reduction of 4-nitrophenol with silver FGME and GME was taken as representative of the coinage metal catalysed reactions. The rate of the reaction decreases slowly and followed first-order kinetics (Fig. 25.3a) without any IT for FGME. But, in the case of a GME-catalysed reaction, the reaction follows zero-order kinetics (Fig. 25.3b).

The rate of catalysis was compared for all coinage metals. In the case of GMEs, the rate follows zero-order kinetics with IT for all. The observed IT for the Cu-catalysed reaction was maximum but its rate of reduction was found to be minimum. Just the reverse was the case for Au. And an intermediate value was obtained for the Ag-catalysed reaction. Figure 25.4 shows the reduction of 4-NP by Cu, Ag and Au nanoparticles.

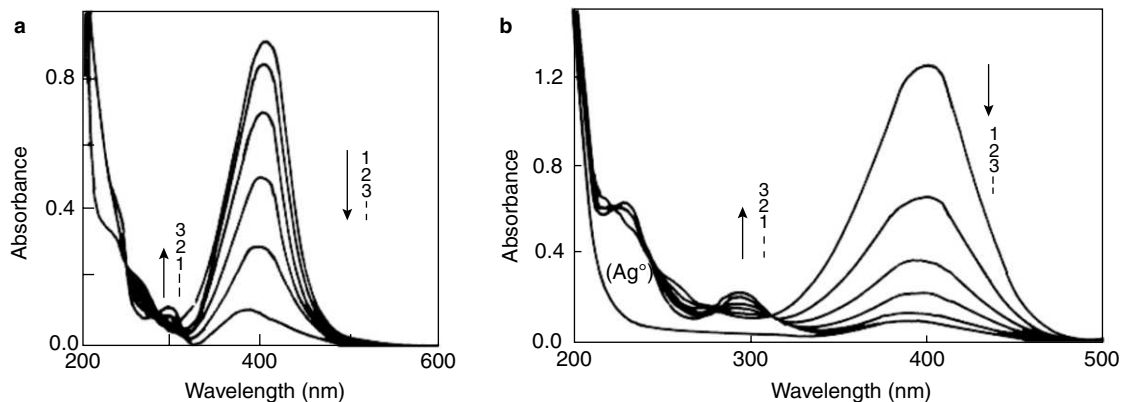


Fig. 25.3 Successive UV-visible spectra (1-min time interval) of 4-nitrophenol using (a) GME and (b) FGME of silver colloids.

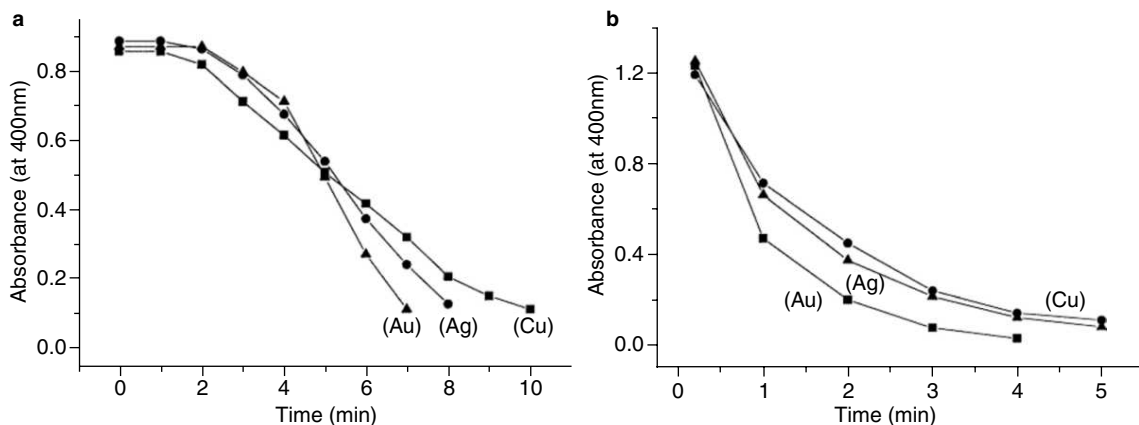


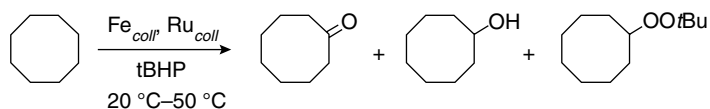
Fig. 25.4 Absorbance vs time plot of reduction of 4-nitrophenol (4NP) using Cu, Ag, and Au colloids: (a) GMEs and (b) FGMEs. Conditions: (a) $[Cu] = [Ag] = [Au] = 1.0 \times 10^{-6} \text{ mol dm}^{-3}$, $[4NP] = 4.0 \times 10^{-5} \text{ mol dm}^{-3}$, $[NaBH_4] = 1.0 \times 10^{-2} \text{ mol dm}^{-3}$; (b) $[Cu] = [Ag] = [Au] = 5.0 \times 10^{-6} \text{ mol dm}^{-3}$, $[4NP] = 6.0 \times 10^{-5} \text{ mol dm}^{-3}$, $[NaBH_4] = 3.0 \times 10^{-2} \text{ mol dm}^{-3}$.

25.3 REACTIONS CATALYSED BY MONO AND BIMETALLIC NANOPARTICLES

25.3.1 Oxidation Catalysed by Metallic Nanoparticles

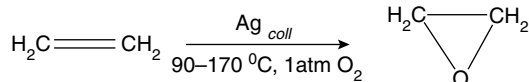
The oxidation of cycloalkane by *t*-butylhydroperoxide (*t*BHP) catalysed by transition metal colloids has been studied.^{41,42} This reaction was performed with Fe nanoparticles in reverse microemulsions or with Ru colloids in biphasic water/organic media (Scheme 25.2).

Efficient and highly-selective conversion of cyclooctane into cyclooctanone is obtained under pure biphasic conditions through t-butylhydroperoxide activation by the *in situ* formation of colloidal ruthenium species arising from $\text{RuCl}_3 \cdot 3\text{H}_2\text{O}$. The substrate cyclooctane was used as the organic phase, whereas the Ru nanoparticles were dispersed in the aqueous phase. This biphasic system allows the recycling of the aqueous phase containing the Ru particles without any loss of activity. After optimising the reaction conditions, cyclooctanol and cyclooctanone were the main reaction products. The standard oxidation of cycloheptane, cyclohexane, cyclopentane was carried out at room temperature. The results show that cycloheptane and cyclooctane yield similar results and appear to be three times more reactive than cyclohexane.



Scheme 25.2 Catalytic oxidation of cyclooctane with tBHP and colloidal metals.

Toshima *et al.* used Au colloids stabilised by PVP or by sodium polyacrylate to oxidise ethane.^{43,44} The oxidation reaction of ethane was catalysed by silver colloids stabilised by sodium polyacrylate at 170 °C and under oxygen/ethene atmosphere produced best results (Scheme 25.3).



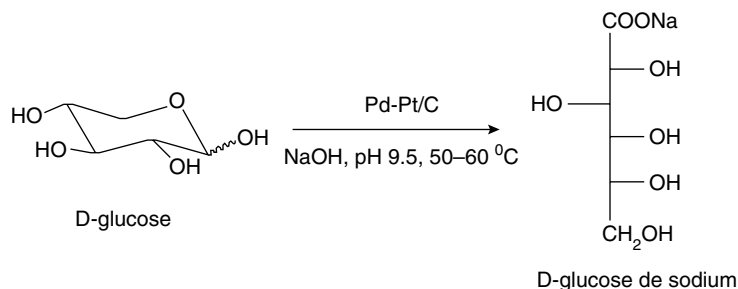
Scheme 25.3 Catalytic oxidation of Ethane.

Oxidation of *p*-Phenylenediamine Derivatives

The oxidation by $\text{Co}(\text{NH}_3)_5\text{Cl}_2^+$ of *N,N,N',N'*-tetramethyl-*p*-phenylenediamine (TMPPD) catalysed by nanoparticles of palladium in an aqueous buffer/AOT/*n*-heptane microemulsion has been studied by Spiro and coworkers.^{45,46} The kinetic and mechanistic aspects of formations of *p*-semiquinonediimine derivatives have been described. The initial rates of the catalysed reaction at 25 °C were found to be first order in palladium, and the authors conclude that the rate determining step of the catalysis is probably diffusion of $\text{Co}(\text{NH}_3)_5\text{Cl}_2^+$ ions through a layer of adsorbed DMPPD to reach the metal. Finally, electrons are transferred via the metal from the adsorbed DMPPD molecules to $\text{Co}(\text{NH}_3)_5\text{Cl}_2^+$ ions.

Glucose Oxidation

Presently oxidation of D-glucose to obtain D-sodium gluconate is performed by enzymatic oxidation. Recently, a bimetallic Pd/Pt catalyst supported on charcoal was developed by Degussa to perform this reaction under oxygen atmosphere and in a basic media (Scheme 25.4).



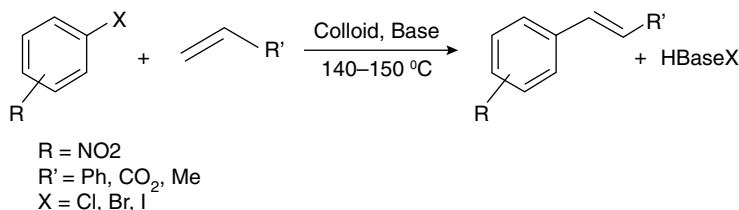
Scheme 25.4 Catalytic oxidation of D-Glucose.

Bönnemann conducted this reaction with bimetallic Pt-Pd colloids stabilised by tetraalkylammonium salts.^{47, 48a} These nanoparticles were obtained *in situ* by co-reduction of Pt and Pd salts and then immobilised on charcoal. The activity and lifetime of this new catalyst was investigated and showed a better activity than the Degussas's catalyst. Here, the quaternary ammonium salt present at the surface of the bimetallic particles protects them from poisoning. It is also observed that Pt–Pb alloy nanoparticle/multi-walled carbon nanotube exhibited much stronger electrocatalytic activity toward glucose oxidation than Pt–Pb on glassy carbon.^{48b}

25.3.2 C-C Coupling Reaction Catalysed by Metallic Nanoparticles

Heck Reactions

During the past decade, several groups have tried to use colloidal suspensions to catalyse Heck coupling reaction (Scheme 25.5). Herrmann was the first to describe the use of Pd nanoparticles to catalyse this coupling reaction.⁴⁹ Reetz has also used Pd to prepare via their electrochemical process a colloidal suspension in propylene carbonate.⁵⁰ These nanoclusters were efficient to catalyse Heck coupling reactions at high temperature. Crooks^{51a} *et al.* considered block copolymers perfluorinated polyether-poly (propylene imine) (PPPI) dendrimers to stabilise Pd nanoparticles used in Heck coupling reactions. In all cases, the catalytic activity observed during the Heck coupling depended on the substrate studied. Generally, a higher activity was observed when arenes are substituted with an electron-withdrawing group, such as nitro or carbonyl. These observations are similar to those observed in the case of Pd molecular complexes. Bradley and co-workers studied a series of well-defined homopolymer-stabilised Pd colloids with varying metal particle for Heck coupling reaction

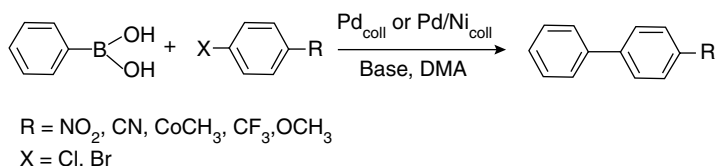


Scheme 25.5 Colloidal metal as catalyst for Heck coupling reaction.

between aryl halides and olefins. They observed high total turnover numbers and turnover frequencies are easily attainable with poly(vinylpyrrolidone)-stabilised colloidal palladium in the coupling of *p*-bromobenzaldehyde with butyl acrylate.^{51b}

Suzuki Reactions

Reetz and co-workers have described the use of Pd or Pd/Ni nanoparticles as catalysts for the Suzuki coupling reaction (Scheme 25.6).⁵² As for the classical Suzuki reaction, bromide derivatives showed a better activity than chloride derivatives. Moreover, the use of substrates with electron-withdrawing substituents increases the activity. Finally, bimetallic Pd/Ni colloids lead to a better conversion rate. Recently, El-Sayed describes the synthesis of palladium nanoparticles prepared in the presence of different stabilisers, such as poly(amido-amine) dendrimers (PAMAM), block copolymer polystyrene-*b*-poly(sodium acrylate), poly(*N*-vinyl-2-pyrrolidone) and PVP. In presence of these stabilisers, the reaction rate has been found to increase.⁵³ More detailed study was conducted with Pd nanoparticles catalysing the Suzuki reaction between phenylboronic acid and iodobenzene.

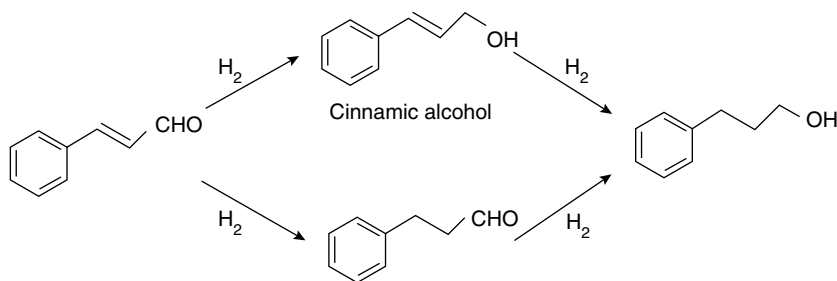


Scheme 25.6 Colloidal metal as Catalyst for Suzuki coupling reaction.

25.3.3 Hydrogenation Catalysed by Metal Nanoparticles

Selective Hydrogenation of Unsaturated Aldehydes

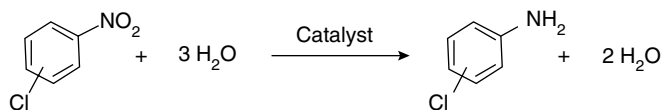
Selective hydrogenation of α,β -unsaturated aldehydes to α,β -unsaturated alcohols is difficult reaction, because the C=C bond is more reactive than the C=O bond for hydrogenation over typical noble metal catalysts. Crotonaldehyde was used for a target molecule of the selective hydrogenation over supported metal catalysts. Some useful catalysts have been proposed for the selective hydrogenation of crotonaldehyde to crotyl alcohol. Recently, Liu and co-workers achieved the reduction of cinnamaldehyde into cinnamic alcohol with Pt nanoparticles stabilised by PVP as catalyst (Scheme 25.7).^{54,55} The reaction was performed under 40 atm of hydrogen and a selectivity of 12 per cent in cinnamic alcohol was obtained after 38 per cent conversion. The selectivity increases by addition of various cations, such as Fe^{3+} or Co^{2+} . The authors proposed that an interaction between the cation and the oxygen of the carbonyl could facilitate the adsorption of the double bond on the metallic surface, thus justifying the activity and selectivity obtained with their Pt colloids. Liu used Pt/Co bimetallic colloids stabilised by PVP to perform this reaction with a cinnamic alcohol selectivity of almost 100 per cent. Similar results were obtained using Pt colloids immobilised onto various supports, such as polystyrene, alumina, Ti(IV) oxide, or Mg(II) oxide.⁵⁶ Ru or Pt nanoparticles stabilised by PVP were employed as catalyst to achieve the hydrogenation of citronellal into citronellol with a selectivity of 95 per cent.⁵⁷



Scheme 25.7 Metal nanoparticles for hydrogenation of cinnamaldehyde.

Hydrogenation of Chloronitrobenzene

Catalytic hydrogenation has attracted much attention for its atomic economy and lower impact on the environment. However, it has been found that it is difficult to apply the process of catalytic hydrogenation to the production of chloroanilines because of extensive dehalogenation. Liu studied the atmospheric pressure hydrogenation of *o*-chloronitrobenzene into *o*-chloroaniline catalysed by various colloidal suspensions, such as Pt⁵⁸ and Ru nanoparticles⁵⁹ or Ru/Pt,⁶⁰ Ru/Pd⁶⁰ or Pd/Pt bimetallic colloids (Scheme 25.8). The best results in terms of selectivity and activity were obtained with the Ru and the Ru/Pt colloids, which showed a good stability. Here, the authors observed that addition of metallic ions (Co²⁺) during the reaction increased the catalytic activity. All these reactions were conducted with supported colloids. The same procedure was used by Liao to obtain *p*-chloroaniline by hydrogenation of *p*-chloronitrobenzene.⁶¹ The catalysts were bimetallic suspensions of Pd/Ru or Pd/Pt stabilised by PVP. Bönemann and co-workers were able to hydrogenate 3,4-dichlorobenzene with Pt nanoparticles immobilised on charcoal and stabilised by several betains.⁶² These catalysts showed a good activity and stability under the drastic reaction conditions (150 °C, 100 atm of hydrogen).



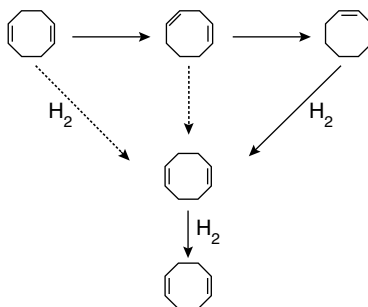
Scheme 25.8 Hydrogenation of chloronitrobenzene.

Pal *et al.* reported for the catalytic reduction of several aromatic nitro compounds to generate the corresponding amino derivatives using NaBH₄ by Ni-Pt bimetallic nanoparticles. Pt–Ni bimetallic nanoparticles, displays higher catalytic activity and corrosion resistance in comparison to the monometallic platinum particles. The increased amount of Ni in the bi-metallic nanoparticles leads to the electron enrichment onto the surface Pt atoms, which in turn facilitates the relaying of electrons to the substrate from borohydride ions.⁶³ The different rates of nitrophenol reduction using alloy catalysts of variable compositions could be ascribed to the modified electronic structure and the influence of surface segregation of the material on the alloy surface. Mukherjee and Moran-Lopez⁶⁴ has shown that,

in the Pt–Ni alloy, Pt is enriched on the surface. Therefore, the catalytic effects were due to the active sites on Pt and Ni acting as catalytically enhancing agents.

Hydrogenation of Conjugated Dienes into Monoolefins

Hirai studied extensively the use of colloidal catalysts for the selective hydrogenation of dienes to form monoenes. Hydrogenation of cyclopentadiene to cyclopentene was performed with a colloidal suspension of Pd particles stabilised by PVP.⁶⁵ Cyclooctene was also obtained by selective hydrogenation of cycloocta-1,5-diene with Pd colloids.⁶⁶ Hydrogenation of the 1,3-isomer occurs faster than hydrogenation of 1,5- and 1,4-isomers. In fact, these two compounds isomerise first to form conjugated dienes and which are partially hydrogenated. The selectivity of the olefin increases with the diminution of the size of the Pd nanoparticles. The use of a ratio Pd/Pt = 4 led to a 3-fold increase in catalytic activity over the use of Pd monometallic colloids. Pd/Pt,⁶⁷ Au/Pd,⁶⁸ or Cu/Pt⁶⁹ bimetallic colloids stabilised by PVP were also used by Toshima to perform this reaction.



Scheme 25.9 Hydrogenation of 1,5-cyclooctadiene.

PVP-stabilised Pd–Pt and Au–Pd bimetallic nanoparticles with various metal compositions were used as catalysts for the selective hydrogenation of 1,3-cyclooctadiene to cyclooctene. In both cases, the bimetallic nanoparticles with Pd content of 80 per cent showed the highest activity, which is greater than Pd nanoparticles themselves (Fig. 25.5).

25.3.4 Hydration of Acrylonitrile

The selective hydration of acrylonitrile to acrylamide, and the hydrogenation of carbon-carbon double bonds under mild conditions are interesting properties of this light transition metal-precious metal bimetallic nanoparticle. The rate of this reaction catalysed by PVP-stabilised Cu–Pd (2 : 1) bimetallic nanoparticles is about seven times higher than that of the PVP-stabilised Cu nanoparticles, and the activity depends on the Cu : Pd ratio.^{70,71} The higher the Cu : Pd ratio is, the higher the catalytic activity is within a range of Cu : Pd ratio from 1 to 3. With this catalyst, the reaction product is the amide with nearly 100 per cent selectivity. The coordination of the C=C double bond of acrylonitrile to the Pd site brings the C≡N triple bond close to the Cu active site, which makes the hydration easy. This is ensemble effect of two metals in Pd and Cu in bimetallic particles.

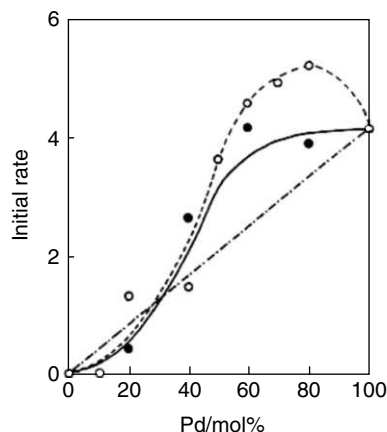


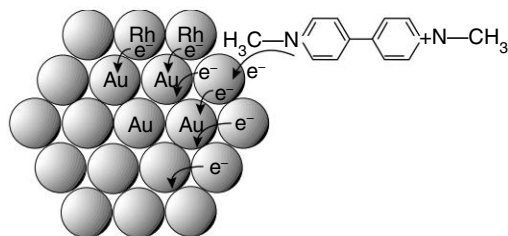
Fig. 25.5 Relationship between catalytic activity and metal composition of (o) colloidal dispersions of PVP-stabilised Au-Pd bimetallic nanoparticles prepared by co-reduction under ambient air conditions and (●) a mixture of Au and Pd monometallic nanoparticles, for the hydrogenation of 1,3-cyclooctadiene. $[1,3\text{-COD}] = 2.5 \times 10^{-2} \text{ mol dm}^{-3}$, $[\text{catalyst}] = 1.0 \times 10^{-5} \text{ mol dm}^{-3}$, ethanol solvent at 30°C , $p(\text{H}_2) = 1 \text{ atm}$.

25.3.5 Photo-induced Hydrogen Generation from Water

Many studies on artificial photosynthesis have been published and photochemical hydrogen generation from water has received much attention for its potential to convert solar energy into chemical energy. The bimetallic nanoclusters, thus analysed to have core-shell structures, as well as monometallic nanoclusters, work as catalysts for visible-light-induced hydrogen generation from water. The rate of electron transfer from the methyl viologene cation radical to the metal nanoclusters is proportional to the hydrogen generation rate at the steady state. All the electrons accepted by the metal nanoclusters are used for the hydrogen generation. Pt nanoparticles have also been frequently used as catalysts to mediate H_2 production from H_2O and reduced methyl viologen (MV^+). The electron transfer from the methyl viologen cation radical to monometallic Pt or Au nanoparticles has been studied. It was observed that both electron transfer and hydrogen generation rates increase when the Pt/Au bimetallic nanoclusters are used in place of the corresponding monometallic nanoclusters. The most active catalysts were Au/Rh and Pt/Ru bimetallic nanoclusters. The hydrogen generation rate coefficients are in proportion to the electron transfer rate coefficient from methyl viologen cation radical to metal nanoclusters at a steady state.⁷² The higher catalytic activity of the bimetallic nanoclusters having the core-shell structure can also be understood by the electronic effect of the core upon the surface atoms (Scheme 25.10).

25.4 SIZE-DEPENDENT CATALYSIS

Spiro *et al.* reported the gold particle catalysed reaction between ferricyanide and thiosulfate ions. It has been documented that the catalytic rate increases linearly with the concentration of catalyst. The



Scheme 25.10 Schematic illustration of electronic effect of central metal on electron transfer rate from methyl viologen cation radical to surface metal of core-shell-structured bimetallic nanoclusters.

reaction has been shown to be surface controlled while the magnitude of the catalytic rate constant and the particle dimensions were related.⁷³ Again monodisperse gold nanocrystals were exploited as catalyst to study the aerobic oxidation of benzylic alcohols with a focus on the cluster-size effect in catalysis. The higher catalytic activity of smaller particles are explained by O_2 adsorption onto the low coordination site.⁷⁴

We recently described size-regime dependence catalysis with gold nanoparticles for dye reduction.⁷⁵ It has been explained that the rate first decreases in a particular size domain and after that rate increases (Fig. 25.6). In this reaction, the total number of particles decreased with the increase in particle size since the concentration of gold is constant. If concentration is a factor, then there should be fall of rate as the particle size increases, i.e., the total surface area decreases. But, the deviation in catalytic rate is accounted per unit area of a particle rather than comparing the them per particle. The inverse relationship for small particles can be explained through the diffusion controlled reaction at the catalyst surface. For smaller particles, the higher driving force for particle-mediated electron transfer caused by their larger Fermi level shift in presence of highly electron injecting BH_4^- ions. But, for larger particles Fermi level shift is negligible. Moreover, if mass effect is taken into account, that is, catalytic rate is determined in terms of per unit mass per unit surface area, then resulting catalytic rate falls with the rise in particle size over the whole range of the size studied.

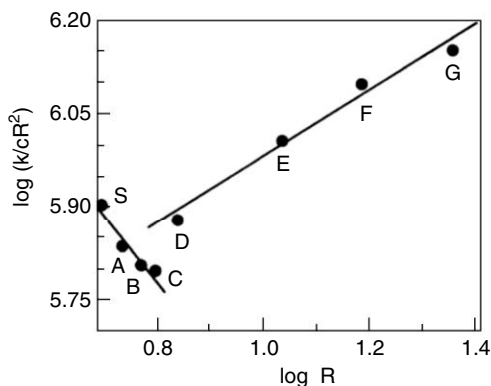


Fig. 25.6 Variation of specific reaction rate per unit area of catalyst particle with its size.

Recent electron microscopy studies reveal that small nanoparticles are highly ordered and bound by crystal faces of low Miller index.⁷⁶ This observation explains great similarity of catalytic behaviour of metal single-crystal surfaces and nanoparticles. The synthesis of metallic nanoparticles with well-defined crystal faces opens the door to the utilisation of a greater body of data on catalysis on metal single crystal surfaces.⁷⁷ The reactivity of specific surfaces of single crystals can be used to guide the propagation of reaction with optimal crystal faces. The particle size effect on the NO-CO reaction over Pd/MgO (100) model catalysts has been studied by Piccolo and Henry. The rate-limiting step of the reaction at low temperature is NO dissociation.⁷⁸ The smaller clusters exhibiting mainly (111) facets, which are much more active in contrary to the larger particles with (100) facets. Among the small particles, the smallest are found to be less active because of the increased proportion of strongly adsorbed nitrogen species when cluster size decreases due to the proportion of low coordinated sites is increased. Similar conclusion was drawn from Suzuki reaction involving Pd nanoparticles of different dimension by El-Sayed *et al.* The general trend is that the catalytic activity of Pd nanoparticles increases as the particle size decreases. However, for the smallest particle, relative proportion of edge and vertex sites to face sites increases as the particle size decreases. Thus strongly adsorbed substrates tend to cover the particle surface that catalyzes product formation thereby decreasing the rate of the reaction.

25.5 SHAPE-DEPENDENT CATALYSIS

Nanoparticles of different shapes have also different facets. Furthermore, they have different fractions of atoms located at different corners, edges, and at different defects (resulting from the loss of atoms at these locations). It is reported that the activation energy is different for the electron-transfer reaction between hexacyanoferrate (III) ions and thiosulfate ions in colloidal solution containing dominantly tetrahedral, cubic, or “near spherical” platinum nanoparticles as catalysts during the early stages of the reaction before any shape changes occur.⁷⁹ Tetrahedral nanoparticles are small (4.8 nm), composed entirely of (111) facets with sharp edges and corners, which comprise ~28 per cent of the total atoms and ~35 per cent of the surface atoms. Cubic nanoparticles are larger (7.1 nm) and composed entirely of (100) facets with a smaller fraction of atoms on their edges and corners, which comprises ~0.5 per cent of total atoms and ~4 per cent of surface atoms. The “near spherical” nanoparticles are formed with (100) and (111) facets with numerous edges and corners. The activation energy is least for tetrahedral particles. It is concluded that the 4.8 nm tetrahedral nanoparticles are the most active and the 7.1 nm cubic nanoparticles are the least active, while the 4.9 nm “near spherical” nanoparticles are in between. Taking this idea into consideration we performed the oxidative phenol coupling (OPC) of 2-naphthol moieties using copper nanoparticles.⁸⁰ The copper rods and spheres were individually exploited as viable catalyst for C–C bond formation via oxidative phenol coupling. It was found that the rod-shaped particles selectively catalyse the coupling to produce 1, 10 coupled product with a good yield. It has been reported that the reactivity and stability of nanoparticles depend on the aspect ratio and spheroids are more reactive than spheres. During the reaction, the spheroids transform into spheres, whereas the spheres do not react. So in our case, the OPC might be due the preferential adsorption of 2-naphthol onto the copper nanorod surfaces and higher catalytic activity of the rod shaped particles are observed in comparison to spheres.

25.6 CONCLUSIONS

As a fundamental aspect, we have underlined here the shift of Fermi potential of metal nanoparticles in relation to their size and electron injection capacity of nucleophiles present. Thus exploitation of metal nanoparticles in catalysis for many important reactions has been possible using GME & FGME metal particles. However, the real size-dependent properties are still to be penned down in the literature. It might so happen one day that only one metal, bearing variable size and shape, would be thought of to perform innumerable redox reactions because of its size and shape-dependent redox potentials. The mono and bimetallic colloids are known to be active species in reactions presumed some years ago to be catalysed by molecular complexes and are successfully used in an increasing number of reactions. The better catalytic properties of bimetallic nanoparticles were explained by the electronic and ensemble effect of two metals.

REFERENCES

1. E.K. Riedel and H.S. Taylor, *Catalytic in Theory and Practice*, (1919), MacMillan: London.
2. M. Boudart, *Perspectives in Catalysis*; J.M. Thomas and K.I. Zamaraev, (eds), (1992), Blackwell: Oxford, 183.
3. J.R. Anderson, *Structure of Metallic Catalysts*, (1975), Academic Press: New York.
4. M.J. Boudart, *Mol. Catal.*, 30, (1985), 27.
5. J.H. Sinfelt and Bimetallic, *Catalysts: Discoveries, Concepts, and Applications*, (1983) Exxon Monograph; Wiley: New York.
6. M. Boudart, *Adv. Catal.*, 20, (1969), 153.
7. M. Boudart, and G. DjBga-Mariadassou, *Kinetics of Heterogeneous Catalytic Reactions*, (1984), Princeton University Press: Princeton, N.J.
8. Z. Xu, F.S. Xiao, S.K. Purnell, O. Alexeev, S. Kawi, S.E. Deutsch and B.C. Gates, *Nature*, 372, (1994), 346.
9. R.A. Van Santen and H.P.C.E. Kuipers, *Adv. Catal.*, 35, (1987), 265.
10. N.R. Jana, T.K. Sau and T.J. Pal, *Phys Chem B.*, 103, (1999), 115.
11. N.R. Jana, Z.L. Wang and T. Pal, *Langmuir*, 16, (2000), 2457.
12. N.R. Jana and T. Pal, *Curr. Sci.*, 75, (1998), 145.
13. A. Henglein, *Chem. Rev.*, 89, (1989), 1861.
14. G. Schmid, *Chem. Rev.*, 92, (1992), 1709.
15. M. Mostafavi, J.L. Marignier, J. Amblard and J. Belloni, *Radiat. Phys. Chem.*, 34, (1989), 605.
16. J. Belloni, *Curr. Opin. Colloid Interface Sci.*, 1, (1996), 184.
17. A. Henglein, *J. Phys. Chem.*, 97, (1993), 5457.
18. S. Mosseri, A. Henglein and E. Janata, *J. Phys. Chem.*, 93, (1989), 6791.
19. (a) A. Benedetti, G. Fagherazzi, F. Pinna, G. Rampazzo, M. Selva and G. Strukul, *Catal. Lett.*, 10, (1991), 215. (b) R.L. Augustine and S.T. O'Leary, *J. Mol. Catal. A: Chem.*, 95, (1995), 277. (c) S. Mukerjee and J. McBreen, *J. Electroanal. Chem.*, 448, (1998), 163. (d) J. Le Bars, U. Specht, J.S. Bradley and D.G. Blackmond, *Langmuir*, 15, (1999), 7621.

20. L.M. Falicov and G.A. Somorjai, *Proc. Natl. Acad. Sci.*, 82, (1985), 2207.
21. Y. Li, E. Boone and M.A. El-Sayed, *Langmuir*, 18, (2002), 4921.
22. R. Narayanan and M.A. El-Sayed, *J. Phys. Chem. B.*, 108, (2004), 8572.
23. J.H. Sinfelt, *Bimetallic Catalysis: Discoveries, Concepts, Applications*, (1983), John Wiley, New York.
24. G.M. Schwab, *Discuss. Faraday Soc.*, 8, (1950), 166.
25. R.J. Best and W.W. Russell, *J. Am. Chem. Soc.*, 76, (1954), 838.
26. V. Ponc, *Appl. Ca. A.*, 222, (2001), 31.
27. N.F. Mott and H. Jones, *Theories of the Properties of Metals and Alloys*, (1936), Oxford University Press, London.
28. A.V. Ruban, H.L. Skriver and J.K. Norskov, *Phys. Rev. B.*, 59, (1999), 15990.
29. N. Toshima, Y. Shiraishi, A. Shiotsuki, D. Ikenaga and Y. Wang, *Eur. Phys. J.D.*, 16, (2001), 209.
30. (a) M. Spiro, *J. Chem. Soc., Faraday Trans.*, 1, (1979), 75, 1507. (b) M. Spiro and P.L. Freund, *J. Chem. Soc., Faraday Trans.*, 1, (1983), 79, 1649. (c) P.L. Freund and M. Spiro, *J. Phys. Chem.*, 89, (1985), 1074. (d) P.L. Freund and M. Spiro, *J. Chem. Soc., Faraday Trans.*, 1, (1986), 82, 2277.
31. D.S. Miller, A.J. Bard, G. McLendon and J. Ferguson, *J. Am. Chem. Soc.*, 103, (1981), 5336.
32. A. Henglein and R. Tausch-Treml, *J. Colloid Interface Sci.*, 80, (1981), 84.
33. M. Mostafavi, J.L. Marignier, J. Amblard and Belloni, *J. Radiat. Phys. Chem.*, 34, (1989), 605.
34. N.R. Jana and T. Pal, *Langmuir*, 15, (1999), 3458.
35. R.L. Whetten, J.T. Khoury, M. Alvarez, S. Murthy, I. Vezmar, Z.I. Wang, P.W. Stevens, C.L. Cleveland, W.D. Luedtke and U. Landman, *Adv. Mater.*, 8, (1996), 428.
36. C.G. Blatchford, O. Siimon and M. Kerker, *J. Phys. Chem.*, 87, (1983), 2503.
37. R. Elghanian, J.J. Storhoff, R.C. Mucic, R.L. Letsinger and Mirkin, *C.A. Science*, 277, (1997), 1078.
38. K. Hayakawa, T. Yoshimura and K. Esumi, *Langmuir*, 19, (2003), 5517.
39. Y. Lu, Y. Mei and Ballauf, *M. Angew. Chem.*, 45, (2006), 813.
40. N. Pradhan, A. Pal and T. Pal, *Langmuir*, 17, (2001), 1800.
41. F. Launay and H. Patin, *New J. Chem.*, 21, (1997), 247.
42. F. Launay, A. Roucoux and H. Patin, *Tetrahedron Lett.*, 39, (1998), 1353.
43. Y. Shiraishi and N. Toshima, *J. Mol. Catal. A: Chem.*, 141, (1999), 187.
44. Y. Shiraishi and N. Toshima, *Colloids Surf. A.*, 169, (2000), 59.
45. M. Spiro and D.M. De Jesus, *Langmuir*, 16, (2000), 2464.
46. D.M. De Jesus and M. Spiro, *Langmuir*, 16, (2000), 4896.
47. H. Bönemann, W. Brijoux, A. Schulze Tilling and K. Siepen, *Top. Catal.*, 4, (1997), 217.
48. (a) H. Bönemann, W. Brijoux, R. Brinkmann, A. Schulze Tilling, T. Schilling, B. Tesche, K. Seevogel, R. Franke, J. Hormes, G. Köhl, J. Pollmann, J. Rothe and W. Vogel, *Inorg. Chim. Acta*, 270, (1998), 95. (b) H.F. Chi, J.-S. Ye, X. Liu, W.D. Zhang and F.S. Sheu, *Nanotechnology*, 17, (2006), 2334.
49. M. Beller, H. Fischer, K. Kühlein, C.-P. Reisinger; W.A. Herrmann, *J. Organomet. Chem.*, 520, (1996), 257.
50. M.T. Reetz and G. Lohmer, *Chem. Commun.*, (1996), 1921.

51. (a) L.K. Yeung and R.M. Crooks, *Nano Lett.*, 1, (2001), 14. (b) J.L. Bars, U. Specht, J.S. Bradley and D.G. Blackmond, *Langmuir*, 15, (1999), 7621.
52. M.T. Reetz, R. Breinbauer and K. Wanninger, *Tetrahedron Lett.*, 37, (1996), 4499.
53. Y. Li, X.M. Hong, D.M. Collard and M.A. El-Sayed, *Org. Lett.*, 2, (2000), 2385.
54. W. Yu, H. Liu and Q. Tao, *Chem. Commun.*, (1996), 1773.
55. W. Yu, H. Liu, M. Liu and Q. Tao, *J. Mol. Catal. A: Chem.*, 138, (1999), 273.
56. W. Yu, H. Liu and X. An, *J. Mol. Catal. A: Chem.*, 129, (1998), 9.
57. W. Yu, M. Liu, H. Liu, X. Ma and Z. Liu, *Journal of Colloid Interface Science*, 208, (1998), 439.
58. X. Yang, Z. Deng and H. Liu, *J. Mol. Catal. A: Chem.*, 144, (1999), 123.
59. M. Liu, W. Yu and H. Liu, *J. Mol. Catal. A: Chem.*, 138, (1999), 295.
60. M. Liu, W. Yu, H. Liu and J. Zheng, *Journal of Colloid Interface Science*, 214, (1999), 213.
61. Z. Yu, S. Liao, Y. Xu, B. Yang and D. Yu, *J. Chem. Soc., Chem. Commun.*, (1995), 1155.
62. S.K. Ghosh, M. Mandal, S. Kundu, S. Nath and T. Pal, *Appl. Catal. A.*, 268, (2004), 61.
63. S. Mukherjee and J.L. Moran-Lopez, *Surf. Sci.*, 189, (1987), 1135.
64. H. Hirai, H. Chawanya and H. Toshima, *React. Polym.*, 3, (1985), 127.
65. H. Hirai, H. Chawanya and N. Toshima, *Bull. Chem. Soc. Jpn.*, 58, (1985), 682.
66. N. Toshima, T. Yonezawa and K. Kushihashi, *J. Chem. Soc., Faraday Trans.*, 89, (1993), 2537.
67. N. Toshima, M. Harada, Y. Yamazaki and K. Asakura, *J. Phys. Chem.*, 96, (1992), 9927.
68. N. Toshima and Y. Wang, *Langmuir*, 10, (1994), 4574.
69. N. Toshima and Y. Wang, *Chem. Lett.*, (1993), 1611.
70. N. Toshima and Y. Wang, *Adv. Mater.*, 6, (1994), 245.
71. N. Toshima, *Pure Appl. Chem.*, 72, (2000), 317.
72. D.M. Lde Jesus and M. Spiro, *Langmuir*, 16, (2000), 4896.
73. H. Tsunoyama, H. Sakurai, Y. Negishi and T. Tsukuda, *J. Am. Chem. Soc.*, 127, (2005), 9374.
74. T.K. Sau, A. Pal and T. Pal, *J. Phys. Chem.*, 105, (2001), 9266.
75. T.S. Ahmadi, Z.L. Wang, T.C. Green, A. Henglein and M.A. El-Sayed, *Science*, 272, (1996), 1924.
76. G.A. Somorjai and Y.G. Borodko, *Catalysis Letters*, 76, (2001), 1.
77. L. Piccolo and C.R. Henry, *J. Mol. Catal. A: Chem.*, 167, (2001), 181.
78. R. Narayanan and M.A. El-Sayed, *Nano Lett.*, 4, (2004), 1343–48.
79. S. Panigrahi, S. Kundu, S.K. Ghosh, S. Nath, S. Praharaj, S. Basu and T. Pal, *Polyhedron*, 25, (2006), 1263.

ADDITIONAL READING

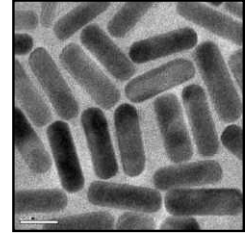
1. M.R. Crooks, M. Zhao, L. Sun, V. Chechik and K.L. Yeung, *Acc. Chem. Res.*, 34(3), (2001), 181.
2. H. Lee, S.E. Habas, S. KweSkin, D. Butcher, G.A. Somorjai and P. Yang, *Angew. Chem. Int. Ed.*, 45(46), (2006), 7824.
3. C.J. Zhong and M.M. Maye, *Adv. Mater.*, 13(19), (2001), 1507.

4. M-C. Daniel and D. Astruc, *Chem. Rev.*, 104(1), (2004), 293.
5. J. Dupont, G.S. Fonseca, A.P. Umpierre, P.F.P. Fichtner and S.R. Teixeira, *J. Am. Chem. Soc.*, 124(16), (2002), 4228.

REVIEW QUESTIONS

1. State the nobility of silver and gold considering their standard reduction potential values.
2. Between silver and sodium, which metal is easily oxidized?
3. Compare the size dependent reduction potential value of a metal.
4. How the standard reduction potential value for a metal changes in presence of a solution with strong nucleophile?
5. How a metal nanoparticle is oxidized in NaBH_4 containing solution?
6. What will happen if HAuCl_4 is added to a solution containing silver nanoparticle?
7. Why co-reduction of Ag(I) and Au(III) easily brings alloying?

NANOFLUIDS FOR COOLING TECHNOLOGY



“An Experiment, like every other event which takes place, is a natural phenomenon; but in a Scientific Experiment, the circumstances are so arranged that the relations between a particular set of phenomena may be studied to the best advantage.”

James Clerk Maxwell in ‘General Considerations Concerning Scientific Apparatus’, 1876. In W.D. Niven (ed.), [The Scientific Papers of James Clerk Maxwell] (1890), Vol. 2, 505

The electronic revolution of the 20th century is facing an unprecedented bottleneck at the beginning of 21st century in the form of thermal dissipation strategy needing a paradigm shift in thermal management and cooling technologies. The conventional fluids and the associated cooling technologies suffer from the poor thermal conduction in fluid. Along with that, the laminar flow in small channels, lowers the heat transfer capability. In recent times, nanoparticle suspensions, known as nanofluids, have made an effort to address the above shortcomings. It has been found that the increase in thermal conductivity of the fluid by suspending nanoparticle is higher than what the conventional microsuspensions predict. Although there is a fair amount of controversy in the whole proposition, a large number of experimental observations and their theorisation have come out during the last decade. The present chapter aims to present a glimpse of developments in this area. Subsequently, an effort has been made to present a convective experiment to demonstrate how nanofluids can enhance cooling. The entire chapter is aimed at understanding the challenges and future potentials for nanofluids in cooling technology.

Learning Objectives

- What are nanofluids?
 - How are they different from microsuspensions in terms of thermal conductivity enhancement?
 - Whether the enhancement in cooling capability of nanofluids are limited to their thermophysical property enhancement?
 - What are the additional mechanisms for convective cooling with nanofluids?
-
-

26.1 CHALLENGES IN COOLING TECHNOLOGY

In modern day electronic, automobile and industrial equipment, improving the system performance often throws up greater thermal challenges. Large-scale miniaturisation of electronic components in recent times is resulting in increasing volumetric heat generation rates and surface heat fluxes. As per the Moore's Law proposed for semi-conductor technology, the logic density of silicon-integrated circuits closely follows the equation, $\text{bits}/\text{inch}^2 = 2^{(n-1962)}$, where n is the present year. This implies that as information storable per square inch approximately doubles each year, the thermal management of devices must also match up with the power densities to maintain an acceptable operational temperature. Recently, the International Technology Roadmap for Semiconductors (ITRS) projected that high-performance integrated circuits will contain more than 9.8 bn transistors on a chip area of 280 mm^2 by 2018, which is more than 40 times as many as today's chips of 90-nm node size. Future processors for high-performance computers and servers have been projected to dissipate higher power, in the range of $100\text{--}300 \text{ W}/\text{cm}^2$. In fact, hardware manufacturers have determined that dual and quadra-core processor technologies are the path to profitability. The demand for increased processing speed has resulted in increased packaging densities, because the signal-delay times are directly proportional to the physical distance between components. Additionally, faster clock rates call for faster logic, which necessitates more power, while an increase in the functional density of processors also results in a larger power requirement. At the chip level, maximum performance can be obtained if the junction temperature can be maintained at a tolerable level. Ideally, a reduced temperature and a closely-controlled thermal environment are needed. The best way to ensure this is an effective cooling methodology. The higher the temperature of a typical semiconductor, the lower is its performance reliability and life expectancy. Since high temperature is recognised as the most severe and important stress condition, electronic package cooling is an active branch of hardware design. At a constant ambient air temperature, dissipating the ever-increasing heat flux without significantly altering the junction-to-ambient temperature variation will only be possible through the introduction of advanced cooling systems. Examples include active heat sinks, air jet impingement, micro-channel cooling, heat pipes, immersion cooling, and spray cooling. These systems, though far superior in heat removal rates, pose more challenges to designers and require novel tools for their design and analysis. Miniaturised devices are not the only ones demanding improved cooling techniques; most systems with higher power consumption levels will also require them, in general. LASERs, high power X-rays, optical fibres, fuel cells, automotive engines and food storage systems are some of the typical examples in this category.

Most electronic systems make use of all the basic modes of heat transfer to some extent. For small thermal loads, heat loss by conduction through the substrate of the printed circuit board, radiation heat loss to the ambient and heat loss by natural convection to the surrounding air medium may meet the cooling requirements. However, for higher heat loads, active cooling methods are required. Bergles¹ dwelt on the effectiveness of many possible active methods of heat transfer enhancement such as twisted tape inserts, swirl flow devices, surface vibration, usage of extended surfaces, boundary-layer injection/suction, etc. Moreover, heat pipes, microchannel cooling and liquid convective cooling are the newly adopted cooling techniques in electronic industry. While these active methods may be efficient in cooling, the associated large pressure drops in the coolant flow circuit may consume

large pumping powers. In order to achieve higher cooling rates at moderate pumping cost, some novel solutions are necessary. Increasing the thermal conductivity of the coolant fluid is one such option. A survey of the thermal properties of liquid coolants used today shows that most of these fluids have poor thermal conductivity values. For example, water is roughly three orders of magnitude poorer in heat conduction as compared to copper. Similar is the case with engine coolants, lubricants and organic coolants. Thus, it is natural that efforts will be made to increase the thermal conduction behaviour of cooling fluids by suspending solid particles in these fluids.

26.2 EVOLUTION OF NANOFLUIDS FROM MICRO-SUSPENSIONS

The idea of improving the conductivity by suspending particles in a fluid was known to the scientific world more than a century back. Maxwell² was the pioneer in this area, who presented a theoretical basis for calculating effective thermal conductivity of suspensions. After Maxwell's theoretical treatment on the enhancement of thermal conductivity of particle suspensions, researchers across the world have been trying to bring the concept to reality. Mixing of solid particles (oxide and metallic) into heat carrying fluids has been attempted, mainly using water and oil, which are the coolants widely used in many applications. Maxwell's model predicted that thermal conductivity of suspensions containing particles (having higher thermal conductivity than the carrying fluid) increases with the volume fraction of the solid particles. But, the use of micron-sized particles in a heat transfer fluid gives rise to following disadvantages: All of these studies were limited to suspensions of micro to micrometer-sized particles and such suspensions bear the following major disadvantages.

1. The particles settle rapidly, forming a layer on the surface and reducing the heat transfer capacity of the fluid.
2. If the circulation rate of the fluid is increased, sedimentation is reduced, but erosion of the heat transfer devices, pipelines, etc., increases rapidly.
3. The large size of the particles tends to clog the flow channels, particularly if the cooling channels are narrow.
4. The pressure drop in the fluid increases considerably.
5. Finally, we achieve conductivity enhancement based on particle concentration, i.e., the more the particle volume fraction is, more the enhancement and more the problems, as indicated in 1–4 above.

It was also evident from the Maxwell's model that the thermal conductivity of suspensions increases with the surface area to volume ratio of the particles used. This triggered the concept of using nano-sized particles in suspensions, since the production of nano-sized particles with controlled material properties has been feasible in recent times. Pioneering work of dispersing nano-sized particles in a fluid has been carried out by Choi³ at the Argonne National Laboratory (ANL), Chicago. Thus, a new class of heat-transfer fluids has evolved, which has been subsequently named as 'nanofluid'.

The terminology of 'nanofluid' is a misnomer, and from a puritan's point of view, this may not be acceptable, because any fluid contains molecular chains of nanometer size; but, the term has been

accepted and has become popular in the scientific community (Das *et al.*⁴). A disperse system, by definition, consists of fine insoluble particles distributed throughout a continuous medium. The particles constitute the dispersed phase, while the continuous phase (basefluid) is termed as the dispersion medium. The distinction between the terms dispersion and suspension is vague and is not universally accepted. According to the definition of International Union of Pure and Applied Chemistry (IUPAC), a dispersion is colloidal, if at least, one dimension of the dispersed phase is between 1 μm and 1 nm. If the particles are larger than 1 μm , the system is called a 'suspension' and a concentrated solid-in-liquid system of non-buoyant coarse particles is called a 'slurry'. Since the particle sizes used in nanofluids are of the order of 100 nm, nanofluids may be rightly called as dilute colloidal dispersions.

The nano-materials *per se* are not new. We have been using them for centuries to impart improved properties into other materials and nature has made use of nano-materials long before mankind learnt how to leverage them. The Chinese are known to have used gold nano particles in inorganic dyes to introduce red colour into their ceramic porcelains more than thousand years ago. Colloidal gold (known by name *swarna-bhasma* (meaning gold powder)) was used for treatment of arthritis in *Ayurveda* (ancient Indian medical practice). Similarly, systems, such as human blood, sea or river water, pharmaceuticals, dispersion paints and many modern chemicals can, in fact, be considered as nanofluids. Nano-materials, even though known to mankind in general, have not been explored fully due to the fact that their sizes lie far below the 200 nm resolution of an optical microscope, and were not visible until the invention of electron microscopy in the 20th century. Thus, the development of nanotechnology has been spurred by the refinement of tools to see the nano-world, such as more sophisticated electron microscopy and scanning tunnelling microscopy along with the modern capabilities of synthesising nanomaterials with good control over their properties.

26.3 FEATURES AND CHARACTERISTICS OF NANOFUIDS

Modern technology has enabled the production of metallic or nonmetallic nanoparticles with average crystallite sizes below 100 nm. The mechanical, optical, electrical, magnetic and thermal properties of nanoparticles are different from those of conventional bulk materials with coarse grain structures. Nano (word meaning 'dwarf' in Greek, which is now adopted as a unit of length= 10^{-9}m) has become a buzz-word in current research and a material is called nanomaterial, if its characteristic size is below 100 nm. It is seen that many physical and chemical properties of a material change significantly below 100 nm size. The reasoning for the above observation is shown in Fig. 26.1(a). Here, dependence of the percentage of surface molecules (N_s), relative to total number of molecules (N) on the diameter of a spherical nanoparticle is depicted. It may be noted from the figure that the particle size is below 100 nm, N_s/N ratio increases steeply (Oberdoerster *et al.*⁵). It is known that the atoms on the material surface are highly unstable and are very active in chemical reactions. As a result, an increase in the surface area to volume ratio will greatly enhance the rates of chemical reactions, surface absorption, and the catalytic ability of the material. In order to visualise the increase in surface area with reduction in particle size, an in-scale distribution of spherical particles in a confined volume is made as shown in Figs. 26.1(b) and (c). The dimension of the cube is taken to be 700 nm in length and a particle volume fraction of 0.5

per cent is considered. Figure 26.1(b) shows the surface distribution, when 50 nm particles are used and Fig. 26.1(c) depicts the distribution, when 10 nm particles are used. It is seen that there is a huge increase in surface area to volume ratio, when smaller particles are used at a given volume concentration. Figure 26.1(b) could also be viewed as an agglomerate of smaller particles used in Fig. 26.1(c). The high surface area of nanoparticles enhances the heat conduction of nanofluids since heat transfer occurs at the surface of the particle. In addition to the ability to conduct heat, mechanical strength as well as the optical properties of nanomaterials are also very different from those of bulk systems. For example, the melting point of metallic gold is about 1000 °C, whereas for the nano-sized gold grains with a typical size of 2 nm, the melting point is down to 330 °C. The absorption of ultraviolet of some nanomaterials can be enhanced significantly. The ductility of PMMA polymer filled with 2 wt per cent nanoscale alumina particles is reported to be one order of magnitude larger than the ductility of the unfilled polymer (Putnam *et al.*⁶). Hence, a class of new materials emerges at nano-scale.

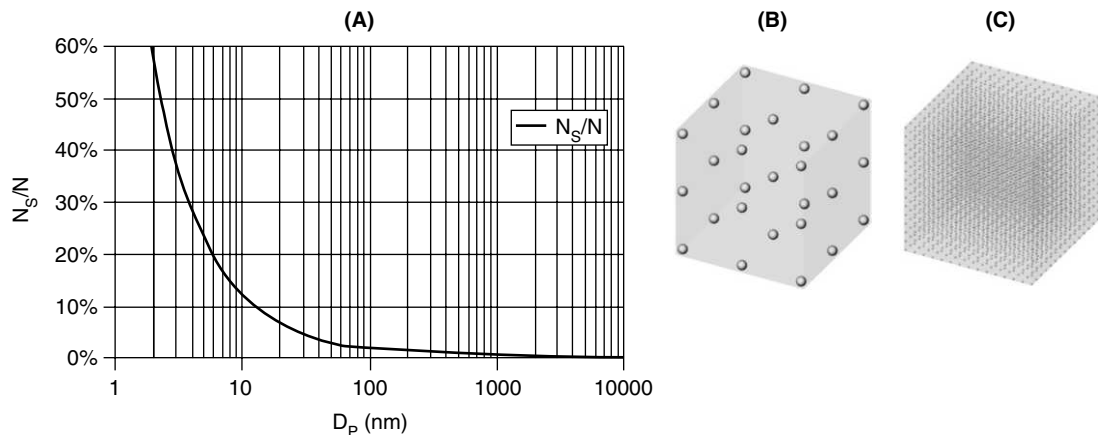


Fig. 26.1 (a) Dependence of the percentage of surface molecules, relative to total number of molecules of spherical nano-particles on the diameter of particles (Oberdoerster *et al.*⁵). (b) 50 nm particle with 0.5 vol%. (c) 10 nm particle with 0.5 vol%.

The attractive features, which project nanoparticles as promising entities for suspension in fluids, are the large surface area, less particle momentum, and high mobility. At the very first sight, these are expected to give higher effective conductivity, less sedimentation, less abrasion, and less clogging. This is the motivation behind using nanofluids in heat transfer applications.

26.4 ADVANTAGES OF NANOFLUIDS

When properly dispersed, the above features of nanofluids are expected to give the following benefits.

(a) Stability: As nanoparticles are small in size and weight, the chances for their sedimentation are also less. A balance of buoyancy and viscous forces will give the settling velocity through the expression

$$\frac{\pi}{6} d_p^3 (\rho_p - \rho) g = 3\pi d_p \mu V. \quad (1)$$

The settling velocity, V , calculated from Eq. 1 for 100 nm size alumina particles in water is of the order 10^{-8} m/s (Das *et al.*⁷). These velocities are very much less when compared to the characteristic velocities in flow conditions. Thus, the major drawback of micro-particle suspensions, viz., settlement of particles, can be avoided.

(b) More heat transfer: It is a known fact that the metals in solid form have thermal conductivities that are several orders higher than those of fluids. Thus, by suspending metallic particles in these fluids can increase their heat transfer capabilities. Also as shown in Figs. 26.1 (b) and (c), the surface area to volume ratio increases as particle size reduces. The large surface area of nanoparticles raises the scope for more heat transfer, making them potential candidates for use in heat transfer applications. Particles finer than 10-nm have 10 per cent of their atoms on their surface making them instantaneously available for thermal interactions.

(c) Less pumping power: Increasing the Figure of Merit of a heat transfer system is one of the primary motives for any heat transfer specialist. Figure of Merit may be defined as the increase in heat transfer for a system at a given pumping power. Usually, to increase the heat transfer of conventional fluids by a factor of two, pumping power has to be increased by a factor of about ten. It can be shown that if we can multiply the conductivity by a factor of three, the heat transfer usually becomes double in the same apparatus. The increase in the pumping power for this will be very moderate unless there is a sharp increase in the fluid viscosity. Thus, a very large saving in pumping power can be achieved if large thermal conductivity increase can be brought about with small volume fraction of particles.

(d) Less erosion: The nanoparticles have very small size, and hence, the momentum they can impart to the solid wall is much smaller. This reduces the chance of erosion of the component such as heat exchangers, pipelines, and pumps.

(e) Less clogging: Due to small particle sizes, the chances of clogging in the pumping circuit are minimal, while using nanofluids. Nanofluids will not only be better media for heat transfer in general, but ideal for microchannel applications, where high heat loads are encountered. The combination of microchannels and nanofluids will give rise to both highly conducting fluids as well as large heat transfer areas. Nanoparticles are actually of the size of a few hundreds or thousands of atoms, which are orders of magnitude lower in dimension compared to microchannels. In addition, nanofluids are likely to reduce the size of heat transport and transfer systems, giving smaller fluid inventory as well as less material of construction resulting in substantial energy and cost savings.

With the above potential advantages, it is expected that the nanofluids can evolve as major contenders for use in future generation cooling technologies. As the area of research of nanofluid is interdisciplinary, it requires knowledge and technological collaboration from many fields of studies such as chemistry, mechanical engineering, physics, material science, etc. This collaborative research can result in the development of a highly conducting and stable nanofluid, which can have promising future applications. Apart from the above said advantages, there exist some practical problems while using them as heat transfer fluids. One major concern is about the issue of agglomeration as the particle sizes go down to nano-scale. Das *et al.*⁸ have seen considerable amount of agglomeration of Al_2O_3 and CuO particles under atmospheric conditions. How well these agglomerates can be dispersed depends

on the method of dispersion used. So, in order to achieve the proper merit of nanofluids and to apply them as real-time coolants, care on preparation and dispersion is to be taken.

26.5 APPLICATION OF NANOFULIDS

Nanofluid research could lead to a major breakthrough in developing next-generation coolants for numerous engineering applications and some of the possible areas of application are listed below. A more detailed review on application of nanofluids has been presented by Yu *et al.*⁹.

(a) Coolant: Potential application of nanofluids lies mainly in the thermal management scenario. Some of the possible cooling applications are:

Electronic cooling: Nanofluids can be effectively used in microchannels as the particle sizes are much smaller than the channel dimensions. Thus, conventional coolants used in Micro Electro Mechanical Systems (MEMS) may be replaced with nanofluids.

Engine cooling: The addition of nanoparticles to the standard engine coolant has the potential to improve automotive and heavy-duty engine cooling rates. Because engine coolants (ethylene glycol-water mixture), engine oils and automatic transmission fluids have inherently poor heat transfer capabilities, transportation industry could benefit from the higher thermal conductivity offered by nanofluids. A smaller nanofluid coolant system can be used to transfer the dissipated engine heat, resulting in smaller and lighter radiators.

Transformer cooling: A potential alternative in many cases is the replacement of the conventional transformer oil with a nanofluid, which can result in considerable cost-reduction. Recent study of nanoparticle-laden transformer oil showed improved dielectric characteristics. The breakdown voltage was observed to be increased along with increase in heat transfer characteristics (Chiesa and Das¹⁰).

(b) Lubricant: In automotive lubrication applications, surface-modified nanoparticles stably dispersed in mineral oils are reported to be effective in reducing wear and enhancing load-carrying capacity (Zhang and Que¹¹).

(c) Bio-medical applications: Nanofluids and nanoparticles have many applications in the biomedical industry. Hyperthermia is currently under consideration as a non-invasive approach to cancer therapy, in which biological tissues are exposed to higher than normal temperatures to promote the selective destruction of abnormal cells. Tumours are selectively destroyed in the temperature range of 40 °C–47 °C because of their reduced heat tolerance due to poor blood supply as compared to normal tissue. However, the heating sources used in hyperthermia, damage the surrounding healthy tissues also. Tremendous improvement has occurred with the introduction of LASER as it can penetrate tissues with sufficient intensity and provide higher spatial precision for localised hyperthermia. The use of gold nanoparticles as photo-thermal agents with higher absorptivity improves the efficiency of the process. Gold is well suited for these biological applications as it is non-toxic. Typical therapeutic laser irradiations cause increase in temperature and continued irradiation causes ablation of tissue. Apart from laser therapy, the nanoparticles may be used for drug delivery also. Magnetic nanoparticles

may be directed and remotely controlled to release the drug load at localised body tissues. Nanofluids could also be used for safer surgery by producing effective cooling around the surgical region, thereby enhancing the patient's chance of survival and reducing the risk of organ damage.

26.6 PREPARATION OF NANOFLUIDS

The first step in the preparation of nanofluids is the production and characterisation of nanoparticles, which is dealt elsewhere in this book. The next most critical step is to properly disperse the particles, because the nanoeffect can only be observed only if the particles are well dispersed in the fluid. What differentiates the nano-particles from the traditional micro particles is their ability to remain suspended while the micro particles easily settle down under gravity due to their weight. However, with decreasing size particles may have a tendency to form agglomerates that can be of micrometer size and will eventually settle down in a way similar to micro particles. Thus, in order to have a stable nanofluid the particles should be dispersed with no or very little agglomeration giving 'true nano' behaviour. This can be done by a variety of methods including electrical, physical or chemical methods. However, the best way may be to produce them by single step method, where instead of nanoparticles, the nanofluids are directly produced reducing the chance of agglomeration.

To understand the dependence of sedimentation ratio on different parameters one can look at the explanation given by Choi *et al.*¹² Let us consider a particle of spherical shape with radius r_p and density ρ_p . From Stokes-Einstein theory,¹³ the sedimentation rate of particles can be given by (ρ_f and μ_f are fluid density and fluid viscosity, respectively),

$$v = \frac{2r_p^2 |\rho_p - \rho_f| g}{9\mu_f}. \quad (2)$$

The equation indicates that sedimentation will decrease if the density difference is low, viscosity is high and particles are small. Density difference can be reduced by the proper choice of material but most of the metals, which are attractive from conductivity point of view, have large density compared to water or oils. Increase of viscosity is obviously ruled out because of its adverse effect on heat transfer. Thus, the key to the issue of stability (smaller rate of sedimentation) is reduction of particle size. This essentially means breaking the agglomerates and dispersing the particles well into the liquid. The other factors, which may play role are electrical charge, pressure of surfactants, mechanical agitation, etc. A small amount of laurate salt was used by Xuan and Li¹⁴ as stabilising agent that improved the stability of pure copper particles drastically. Thus, nanofluids can be prepared by the physical or chemical dispersion techniques used for colloidal solutions.^{13,15}

26.6.1 Physical Dispersion Technique

The physical methods used so far are mechanical and ultrasonic dispersion. Mechanical method means breaking the agglomerates by high shear mixing. These are usually known as rotor-stator methods. Homogenizer, Kady Mill and Colloid Mill are some of the methods in their category. High impact grinding by small grinding material can also be used—attritor and ball-and-pebble mill are examples.

Compared to mechanical dispersion techniques ultrasonic vibration is found to be better option for nanofluids. Das *et al.*¹⁶ used ultrasonic vibration for four hours to get excellent dispersion of nanoparticles. The ultrasonic vibration was created in water in a bath, where the container containing primary solution of nanoparticles (agglomerates) was suspended. The ultrasonic sends an elastic wave giving mechanical and thermal interaction. The thermal interaction was evident from the elevated temperature after the dispersion process. It was found that the type of ultrasonic source (immersed type or bath type) did not make much of a difference, but the time under vibration was found to be important. The time was reduced from 12 hr to 4 hr by trial and error. However, no systematic study of the effect of ultrasonic frequency on dispersion was made. The other work, in which multiple physical dispersion technique was used, came from Xie *et al.*,¹⁷ who dispersed SiC particles in ethylene glycol by ultrasonic and magnetic stirring.

26.6.2 Chemical Dispersion Method

Chemical methods are primarily aimed at disrupting long-range attractive Van der Waals force that is of the order of $k_b T$ (k_b = Boltzmann constant, T = absolute temperature). This can be done in a number of ways. Chemical dispersions can be done by electrostatic, steric dispersion or functional group coating technique. Electrostatic method basically is to charge the particles with similar charges, create the repulsive electrostatic forces, which are just sufficient to oppose the long range Van der Waals forces. These charges can be brought about by ionic species, such as detergents or adding electrolytes.¹⁸⁻²⁰ This is same as stabilisation of suspensions by pH control. However, these forces are quite sensitive to the pH value and at certain concentration, electrolyte may even promote agglomeration and sedimentation. They may also change the thermo-physical as well as chemical properties of the base fluid that may be undesirable.

Compared to this steric stabilisation prevents agglomeration by surfactants. Mostly polymeric surfactants are used. The long chain of the organic molecules creates steric repulsion. A number of chemicals are used as surfactants. They usually use an anchor molecule and a stabilising molecule. Anchor molecules can be a variety of polymers, such as polyarylonitrile, PVC, polydimethylsiloxane along with stabilising molecules, such as poly lauryl methacrylate or polyvinyl methyl ether. For aqueous systems, a separate group of chemicals are suggested with anchors, such as polystyrene, polyvinyl acetate and stabiliser such as polyvinyl alcohol or polymethacrylic acid. Xuan and Li¹⁴ used a combined physical and chemical dispersion method, where addition of oleic acid of fairly large amount (up to 22% by wt) was followed by 10 hr of ultrasonic vibration for oil-based Cu nano fluids and smaller amount (7% by wt) of laurate salt addition followed by similar duration of ultrasonic vibration for water-based nanofluids. Of course, one must appreciate that the particle used by them were much larger (~100 nm) and keeping that in mind the stabilisation was quite satisfactory.

26.6.3 One-step Methods

The other stabilising technique of surface coating has got the advantage that they can give the single-step method of producing nanofluids as suspensions itself without the need of separate particle production. Surface coating is a method that is much simpler from chemical point of view, but it also acts as a thermal barrier between the particle surface and fluid that may impede heat transfer. Usually

for chemical dispersion, surface coating or surface modification is widely accepted.²¹ This can be done by adding various functional groups to the surface. While making gold and silver based nanofluids, Patel *et al.*²² used octadecanethiol for forming a monolayer around gold or silver nanoparticles. This was done by the well known Brust²³ method. Similarly, as described earlier, the single-step citrate reduction method²⁴ was used for production of nanofluids with bare gold and silver particle, which can be termed as electrolytic stabilisation through the chemical synthesis process itself. The direct evaporation-condensation (DEC) method used by the ANL group also produced highly-stable nanofluids²² with and without thioglycolic acid. In recent times, one of maximum thermal conductivity enhancement was reported in nanofluids with carbon nanotubes,²⁵ which were also dispersed in poly (α - olefin) oil using usual dispersion technique. The possibility of producing MWNT (multi-walled nanotubes) based nanofluids by a single-step method is under investigation.

Chen *et al.*²⁶ suggested using electro hydrodynamic spraying system,²⁷ for production of nanofluids. Even though it will be a two-step method in the strict sense, the steps can be so coupled that it gives a continuous production of nanofluid. This is because of the fact that rate of particle production by this method is quite high (10 bn particles per second). The particles are charged, and hence, do not coagulate and the particles can directly be injected into a flowing fluid, which can be called a pseudo-single-step method. The novel one-step method by Zhu *et al.*²⁸ is also notable.

26.7 THERMAL CONDUCTIVITY ENHANCEMENT IN NANOFLUIDS

The fact that generated primary interest in nanofluids is that thermal conductivity of nanofluids is much improved compared to usual suspensions. The observed enhancement of effective thermal conductivity over that of the base-fluid is often few times for nanofluid compared to what would have been given by usual micrometer-sized suspensions. The base fluids used so far are water, ethylene glycol, transformer oil, toluene, etc., keeping in mind the applications of these fluids for cooling. The nanoparticles used can be broadly divided into ceramic particles and pure metallic particles.

Nanofluids containing ceramic particles were the first type of nanofluids investigated by the ANL group. The first major publication in this area by Lee *et al.*²⁹ presented measurement with fluids of Al_2O_3 and CuO in water and ethylene glycol. The measurement was made by the traditional transient hot-wire method (THWM). The same technique was also used by the Patel *et al.*²² to measure thermal conductivity for metallic nanofluids. The result of Lee *et al.*²⁹ clearly indicated that the thermal conductivity enhancement of the Al_2O_3 and CuO nanofluids were high. They used volume fractions of only 1 per cent–5 per cent. The enhancement was higher with ethylene glycol as base fluid. An enhancement of 20 per cent was observed at 4 per cent volume fraction of CuO. The enhancement with water as base fluid was lower, but still substantial with 12 per cent enhancement at 3.5 per cent CuO and 10 per cent enhancement with 4 per cent Al_2O_3 . The higher enhancement for CuO nanofluids could be their smaller size (23 nm) compared to Al_2O_3 particles (38 nm). Figure 26.2 shows the measurements of Lee *et al.*²⁹ These results were high compared to the model for suspensions proposed by Maxwell² as early as in 1882. The theory of Maxwell² was later improved by Hamilton and Crosser³⁰ in 1962 to include the effect of particle shape. These models are essentially some kind of weighted average of solid and liquid conductivity.

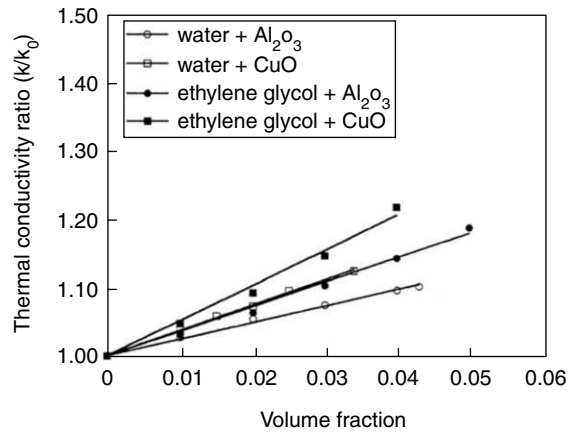


Fig. 26.2 Thermal conductivity ratio vs volume fraction for different nanofluids.

The original Maxwell model reads as

$$\frac{k_{eff}}{k_f} = 1 + \frac{3(k_p/k_f - 1)\phi}{(k_p/k_f + 2) - (k_p/k_f - 1)\phi}; \quad (3)$$

Maxwell–Garnett³¹ as

$$\frac{k_{eff}}{k_f} = \frac{(1 - \phi)(k_p + 2k_f) + 3\phi k_p}{(1 - \phi)(k_p + 2k_f) + 3\phi k_f}; \text{ and} \quad (4)$$

The Hamilton–Crosser³⁰ model reads

$$\frac{k_{eff}}{k_f} = \frac{k_p + (n - 1)k_f - (n - 1)\phi(k_f - k_p)}{k_p + (n - 1)k_f + \phi(k_f - k_p)}; \quad (5)$$

where, k_{eff} = Effective thermal conductivity of slurry

k_f = Thermal conductivity of liquid

k_p = Thermal conductivity of solid particles

ϕ = Volume fraction of nano particles

n = Shape factor (for sphere = 3, for cylinder = 6).

It should be noted that both these correlations do not include particle size as a parameter. Figures 26.3(a) and 26.3(b) shows the comparison of Lee *et al.*'s²⁹ measurement with the Hamilton–Crosser³⁰ model. It is interesting to note that Lee *et al.*²⁹ found that the Hamilton–Crosser³⁰ model was approximately able to predict the enhancement of Al₂O₃–water nanofluids, but not the CuO–water nanofluid (Fig. 26.3(b)). However, it will be seen later that this match for prediction of Al₂O₃–water nanofluid was purely accidental due to temperature effect (Das *et al.*¹⁶).

Wang *et al.*^{32, 33} also measured the thermal conductivity of CuO and Al₂O₃–water nanofluids, but their particle size was smaller (23 nm for CuO and 28 nm for Al₂O₃). They also measured the

nanofluids with ethylene glycol and engine oil (Pennzoil 10W-30) as the base fluids. The measurement showed a clear effect of particle size and the method of dispersion. These parameters will assume greater significance later on as we will see subsequently. Xie *et al.*³⁴ measured aqueous Al_2O_3 nanofluid, but for even reduced particle size. Their range of particle size was 1.2 to 302 nm. They also observed effect of particle size and in addition effect of pH value of the solution base. Thus, it has been generally found that oxide ceramic particles, which themselves do not have very high thermal conductivity can enhance the thermal conductivity of fluids in nano suspensions. The main reason for many studies on oxide particle-based nanofluids is the availability of oxide nanoparticles and the relative ease with which stable suspension can be made with them. A number of companies today have started producing nano-particles of oxide ceramics commercially. However, it has to be kept in mind that the investigators need to characterise them. Das *et al.*¹⁶ found that the particle-size distribution of Al_2O_3 nanoparticles is quite different from that suggested by the manufacturer. This affects the thermal conductivity values severely. Measurement for non-oxide ceramic (SiC particles with ethylene glycol) nanofluid was made by Xie *et al.*¹⁷ For particle sizes between 26 nm and 600 nm, they observed that at lower particle size, the Hamilton–Crosser³⁰ model underpredicts the thermal conductivity, while at higher size it predicts well.

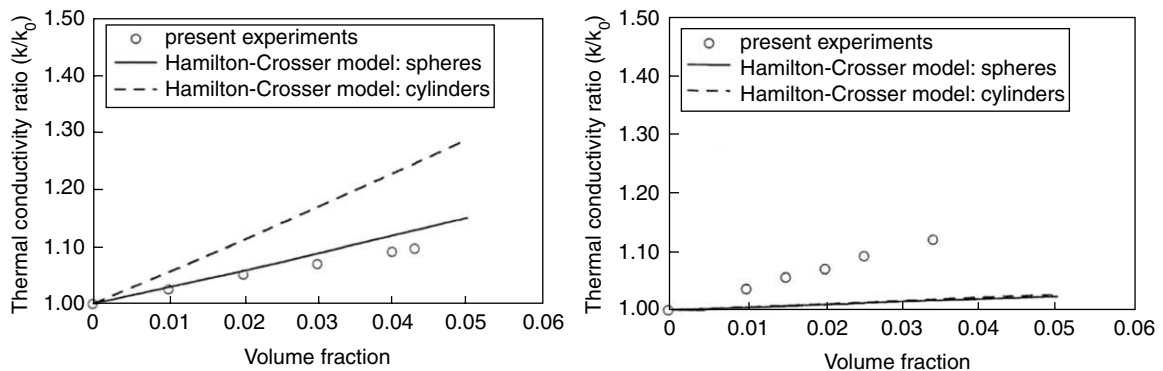


Fig. 26.3 (a) Thermal conductivity ratio vs volume fraction for different models. (b) Thermal conductivity ratio vs volume fraction for different models.

Although the ceramic nanofluids demonstrated the potential of nanofluid a big step forward was the emergence of metallic particles-based nanofluids. Xuan and Li¹⁴ were the first to try copper particle-based nanofluids of transformer oil. Their enhancement was comparable with oxide nanofluids mainly due to the fact that they used a much larger (~ 100 nm) particle size due to limitation of their method of synthesis, they reported 55 per cent enhancement with 5 per cent volume fraction. It should also be kept in mind that due to the ball milling technique used by them, they had a wide size distribution of particles.

However, the real breakthrough was from the ANL group reporting a 40 per cent enhancement of conductivity with only 0.3 per cent copper particles of 10 nm size.³⁵ This clearly shows the particle-size effect and the potential of nanofluids with smaller particle sizes. They were stabilised with thioglycolic

acid. They also observed significant difference between freshly prepared and old samples of nanofluids, which can be attributed to oxidation of the particles. The figure also contains the values for ceramic nanofluids to indicate the leap that occurs in the metal-based nanofluids. This was probably the first one to indicate that nano fluids can give significant progress in cooling technology. The study also indicated a mild 'aging effect' with freshly prepared nanofluids showing higher conductivity.

Liu *et al.*³⁶ confirmed the tremendous potential of metallic nanofluids by showing an enhancement of about 23 per cent at as low concentration as 0.1 per cent volume of copper nanoparticles of 75–100 nm size suspended in water without any surfactant. They also showed that the thermal conductivity enhancement decreases with time, due to sedimentation. Xie *et al.*³⁷ made a study the dependence of effective thermal conductivity of nanoparticles-fluid mixture on the nature of the base fluid. Nano-sized α - Al_2O_3 was dispersed in deionised water, glycerol, ethylene glycol, pump oil, ethylene glycol-water mixture, glycerol-water mixture and study was conducted. It was found that thermal conductivity ratios decrease with an increase in thermal conductivity of base fluid.

Hong *et al.*³⁸ achieved enormous magnitude of increase in the thermal conductivity of nanofluids of Fe nanoparticles of 10 nm size suspended in ethylene glycol. They got an enhancement of 18 per cent with just 0.55 per cent volume fraction. They also showed that the sonication of the nanofluid has an important effect on the thermal conductivity of nanofluid, indirectly proving the particle size effect on the thermal conductivity of nanofluids. Chopkar *et al.*³⁹ have obtained very promising features of metallic nanofluids. They observed 120 per cent enhancement for just 2 per cent volume of Al70Cu30 particles in ethylene glycol. They also observed a strong non-linear dependence of thermal conductivity enhancement on particle volume fraction. In addition, they have shown a strong effect of crystalline size on the enhancement.

26.7.1 Temperature Effect

Nanofluids are unique in many respects, such as their sensitivity to change. One important contribution on nanofluid in this direction was from Das *et al.*¹⁶, who discovered a very strong temperature dependence of nanofluids with the same Al_2O_3 and CuO particles as used by Lee *et al.*²⁹ The results were astonishing. It was found almost three times increase in enhancement (10% became about 30%) for copper oxide and alumina nanofluids as shown in Fig. 26.4, and Fig. 26.5, respectively. One important observation here is that in contrary to what was observed at room temperature²⁹ both Al_2O_3 and CuO do not agree with Hamilton–Crosser³⁰ model, because the model is not sensitive to temperature at all over this small temperature range. Thus, it can be said that for each nanoparticle fluid combination there is a threshold temperature, below which it behaves like normal suspensions, but above this, it behaves as a nanofluid. It was concluded that the agreement of Al_2O_3 —water nanofluid with Hamilton–Crosser model at room temperature was purely accidental because of its larger particle size. These results have revolutionised the concept about nanofluids from application point of view, because much larger thermal conductivity in the heated state makes them 'smart fluid' at elevated temperature. This also indicates that some kind of particle movement (probably that of Brownian type) dramatically changes with temperature must be taking place inside the fluid.

Chon *et al.*⁴⁰ also confirmed the temperature effect got by Das *et al.*¹⁶ with similar nanofluid. They also showed the inverse dependence of thermal conductivity enhancement on the particle size. These findings were also confirmed by Li *et al.*,⁴¹ who showed a little stronger effect of temperature for the same nanofluids as that used by Das *et al.*¹⁶ They observed an increase in the enhancement from 8 per cent to 20 per cent for a temperature rise from 28 °C to 36 °C for 2 per cent volume of alumina nanoparticles suspended in water and 30 per cent to 40 per cent for 2 per cent volume of CuO nanoparticles suspended in water in the same temperature range. Murshed *et al.*⁴² have also observed the temperature effect for aluminium–engine oil nanofluids (80 nm particle size). They found an enhancement of 20 per cent to 36 per cent for a temperature rise of 20 °C to 60 °C for 3 per cent volume fraction.

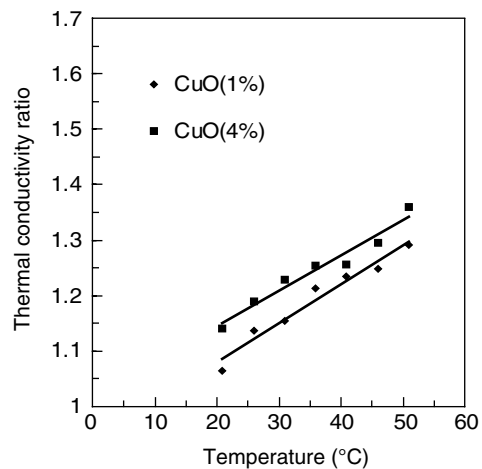


Fig. 26.4 Thermal conductivity ratio vs temperature for copper oxide nanofluids.

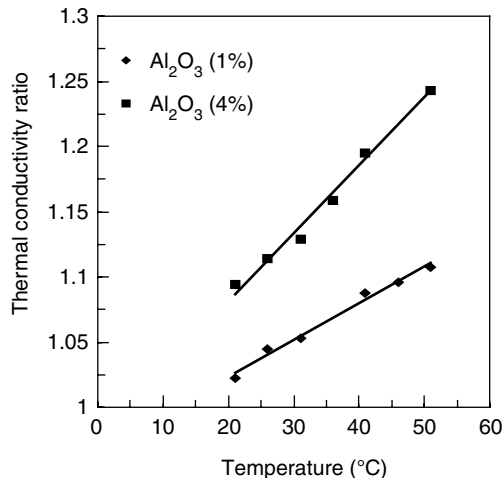


Fig. 26.5 Thermal conductivity ratio vs temperature for Alumina nanofluids.

However, recently, Zhang *et al.*⁴³ observed no enhancement in the thermal conductivity as well as thermal diffusivity of nanofluids above that of predictions of the Hamilton–Crosser model neither did they observed any temperature effect as observed by Das *et al.*¹⁶ They speculated that the enhancement observed in literature might be due to the possible leakage of electricity in the measurement cell (while using THW instrument for thermal conductivity measurement), thereby inducing error in the thermal conductivity measurement. Zhang *et al.*⁴³ have also reached the same conclusions from the measurement of thermal conductivity and thermal diffusivity of Al_2O_3 , ZrO_2 , TiO_2 and CuO nanofluids. Putnam *et al.*⁴⁴ have also measured thermal conductivity of C60–C70 fullerenes in toluene and suspensions of alkanethiolate protected Au nanoparticles to maximum volume fractions of 0.6 per cent and 0.35 per cent using optical beam deflection technique and observed no significant enhancement in thermal conductivity of these nanofluids above that predicted by effective medium theory.

These studies bring out some scepticism in the measurement method used in literature as well as the basic phenomenon itself. However, an overwhelming majority of investigation, including the studies in convection and boiling (discussed later) indicate that the nano-effect in nanofluids is not measurement inconsistency alone.

26.8 THEORIES ON THERMAL CONDUCTIVITY OF NANOFUIDS

Right from the time when Choi¹⁶ invented nanofluids, there has been a continuous effort to look for the causes of the ‘anomalous’ increase in thermal conductivity of nanofluids. Starting from simple Brownian motion to complicated fractals, by revisiting Maxwell and assuming formation of liquid layer around particle many propositions have been tried. During the last three to four years this effort of theorising nanofluid behaviour has intensified. However, it appears that the truth is still at least half revealed.

The traditional theories of Maxwell,² Hamilton–Crosser,³⁰ Wasp,⁴⁵ Bruggeman,⁴⁶ Bonnacaze^{47, 48}, etc. explained the thermal conductivity enhancement of usual slurries and suspensions quite extensively. The basic model of Maxwell² was extended by the following investigators by including the effect of shape,³⁰ particle interactions^{49–53} and particle distribution.⁵⁴

Generally Maxwell’s method works well for low-thermal conductivity ratio between the solid and the fluid (~ 10). Also, all these effective medium theories consider the particle as point mass sources without accounting for their sizes. As far as the enhancement of the conductivity with concentration is concerned, nanofluid shows qualitatively similar trends as predicted by the classical models. This is evident from the near linear variation of conductivity enhancement reported by Lee *et al.*²⁹, Das *et al.*¹⁶ and Patel *et al.*²² However of enhancement is much higher compared to what is predicted by these models.

As has been already pointed out the temperature effect makes this deviation more even for the oxide nanoparticles that appears to be close to the Maxwell model. Lee *et al.*²⁹ and Wang *et al.*³² have also shown that even at room temperature, the results for oxide nanoparticles start deviating from the Maxwell’s theory at lower concentration. This gives an impression that particle movement (and hence the mean free path) is important for effective thermal conductivity enhancement.

The failure of the classical theories to predict nanofluid behaviour gave rise to hypothesis regarding the mechanism of heat transfer in nanofluids. Wang *et al.*³² attributed the enhancement due

to particle motion, surface action and electro kinetic effects. Electro kinetic forces may be Van der Waals, electrostatic or microstochastic forces. They indicated that electric double layer⁵⁵ can play a significant role in it. The hydrodynamic force in the form of microconvection can also be a cause of the enhancement. Their TEM studies showed some chain structures and they suggested that these structures can also be the cause of conductivity enhancement.

A serious look at the various possibilities of enhancement mechanism was focused by Keblinski *et al.*⁵⁶ The mechanism considered by them were Brownian motion, ballistic conduction, liquid layering, particle clustering.

At the very first sight, even though the Brownian motion appears to be a probable mechanism, it was rejected to be the major responsible mechanism by them from a time-scale study. It must also be mentioned here that the studies of Wang *et al.*,³² also showed that Brownian motion does not contribute significantly. Keblinski *et al.*⁵⁶ showed that liquid layering around the particle 'could give' the path for rapid conduction. This has given rise a number of studies on this theory later, but the existence and the real nature of such layers still an open question.

A novel approach in the modeling of nanofluids was done by Xue.⁵⁷ He considered the particles to be ellipsoids interacting with spherical fluid particles. The model utilises as field-factor approach with depolarisation factor and effective dielectric constant. The main assumption of this model is the existence of a conducting shell that is equivalent to liquid layering theory. The surface activity is taken to be the responsible factor and he showed that for specified value of the shell thickness ($\delta \sim 3$ nm) and shell conductivity ($k_1 = 5$ W/mK for carbon nanotube-oil nanofluid and $k_1 = 2.1$ W/mK for Al_2O_3 -water nanofluid) the theory matches with the measured value. However, it must be said that it uses these two adjustable parameters to match the experimental value and no evidence of such layer and the values of either the thickness or the conductivity of such shell has yet been found, hence the model requires approximation for these two fitting parameters, the nature of variation of which is unknown. Thus, the model is insufficient to predict the enhancement of any unknown combination of particles and fluid.

The interfacial layer model was also used by Yu and Choi.⁵³ They decided to use the classical Maxwell model as the base model, into which the liquid layer around the particle that has a "solid-like" behaviour, is introduced. This increases in the effective concentration. Here also, they used a liquid layer thickness and a layer conductivity that have been adjusted for matching. However, they used equivalent particle conductivity as given by Schwartz⁵⁸ for calculation. The ranges of the liquid layer thickness which could predict the results were ~ 2 nm. They claimed that the model was not very sensitive to the conductivity of the layer and a value of layer conductivity 10 times the fluid conductivity provides a good match. The results for copper oxide (CO) with ethylene glycol and copper particles (3 nm) in ethylene glycol were quite close to experimental values but for copper particles with surfactant, where maximum enhancement was observed (40 per cent with 0.3 per cent volume fraction) the model failed miserably. Like Xue⁵⁷, this model also uses adjustable parameters and predicts well under certain conditions.

Taking effective medium theory approach, Prasher *et al.*⁵⁹ have shown the importance of the fractal clusters in the increased thermal conductivity of nanofluids. Feng *et al.*⁶⁰ have also shown the effect

of aggregation on thermal conductivity of nanofluids by coupling it with liquid layering and effective medium theory. By approximating the actual particle volume fraction to effective volume fraction, they have matched their model predictions with some of the experimental data to validate the volume fraction effect.

Another approach has gained momentum in explaining the thermal conductivity enhancement and that is the incorporation of particle motion mainly due to the need to explain temperature effect. Even though it has been started earlier that Brownian motion alone cannot account for this enhancement a new look at the Brownian motion^{61,62} has been given. Based on a drift velocity model, Yu, *et al.*⁵³ have first shown that the collision of particles and the drift velocity can account for a very small part of the enhancement. With a specific example of copper particles in ethylene glycol they showed that at least the order of the enhancement could be guessed if a nano convection in the space between the particles is assumed. This is quite logical, because in usual Brownian motion in gases between the particles (molecules), there is only void while in nanofluids these fluids, which will be participating in a nano convection, which may even be set by electrical dipole. They⁵³ even pointed out the possibility of a Soret effect.⁶³ This work although does not present a complete accurate model, but throws light at a very much possible mechanism and more importantly tries to model the phenomenon from the fundamental physics without any adjustable parameters. It will be interesting to see the efforts of modeling in this direction.

The true nature of enhancement as well as temperature effect was modelled recently by two groups using essentially the Brownian motion concept. However, the approach and explanations were different in the models. Jang and Choi⁶⁴ have modelled nanofluids based on conduction, Kapitza resistance at particle surface and convection. In deriving their model, they considered four modes of energy transport: 1) collisions between base fluid molecules, i.e., thermal conductance of fluid; 2) thermal diffusion in nanoparticles; 3) collision between nanoparticles due to Brownian motion, which by order of magnitude analysis was neglected; and 4) thermal interaction of dynamic nanoparticles with base fluid. Brownian motion produced convection like effects at nanoscale.

The effective thermal conductivity was given as,

$$k_{eff} = k_{BF}(1 - f) + k_{nano}f + 3C_1 \frac{d_{BF}}{d_{nano}} k_{BF} Re_{d_{nano}}^2 Pr f \quad (6)$$

where, k_{BF} = thermal conductivity of base fluid
 f = volume fraction of nanoparticles
 k_{nano} = thermal conductivity of nanoparticles
 C_1 = proportional constant
 d_{BF} = diameter of base fluid molecules
 d_{nano} = diameter of nanoparticle
 $Re_{d_{nano}}$ = Particle Reynolds number
 Pr = Prandtl no. of nanofluid.

This model was able to predict a particle size and temperature-dependent conductivity accurately. In the similar lines of the above model, Xu *et al.*⁶⁵ presented a model, which added the convection

effects coupled with fractal analysis to the effective conductivity of nanofluid, as derived from the classical model of Hamilton and Crosser.³⁰ The model was validated against thermal conductivity of some of the oxide nanofluids using an empirical constant.

In an effort to include all observed effects, Hemanth *et al.*⁶⁶ have presented a model, which accounts for the dependence of thermal conductivity on particle size, concentration and temperature. The proposed model has two aspects. The stationary particle model accounts for the geometrical effect of increase in surface area per unit volume with decreasing particle size. It assumes two parallel paths of heat flow through the suspension, one through the liquid particles and other through the nanoparticles.

Here, direct dependence of thermal conductivity enhancement on volume fraction and inverse dependence of thermal conductivity enhancement on particle diameter has been suggested, which is as follow,

$$k_{eff} = k_m \left[1 + \frac{k_p \phi r_m}{k_m (1 - \phi) r_p} \right]; \tag{7}$$

where, k_m = thermal conductivity of base fluid medium

k_p = thermal conductivity of particles phase

ϕ = volume fraction of nanoparticles

r_m = liquid particle radius

r_p = nanoparticle radius.

The moving particle model developed from the Stokes-Einstein formula¹³ explains the temperature effect on thermal conductivity enhancement.

$$\frac{k_{eff}}{k_m} - 1 = c \cdot \bar{u}_p \frac{\phi r_m}{k_m (1 - \phi) r_p} \tag{8}$$

where, c = proportionality constant, and

\bar{u}_p = Brownian motion velocity of nanoparticles.

Here the effective particle conductivity is taken as $k_p = c \cdot \bar{u}_p$, where \bar{u}_p is the average particle velocity and c is a constant. This model originates from the observation that temperature effect is proportional to Brownian velocity.

The Brownian velocity was calculated from the Stokes-Einstein equation given by¹³

$$\bar{u}_p = \frac{2k_b T}{(\pi \mu d^2)}. \tag{9}$$

Predictions from the combined model agree with the experimentally-observed values of conductivity enhancement of nanofluids with vanishingly small particle concentration.

They also showed, by order of magnitude analysis, that the value of the constant “ c ” is consistent with that predicted by kinetic theory. However, in the above two models, the constant used is empirical one and varies over several orders of magnitude for different combinations of the particle—

fluid mixture. Recently, it has been tried to model the thermal conductivity of nanofluid empirically. Patel *et al.*⁶⁷ used a new, semi-empirical approach to model the thermal conductivity of nanofluids. The high enhancements are attributed to the increase in the specific surface area as well as Brownian motion based microconvection. The Brownian motion based microconvection is modeled with an empiricism in Nusselt number definition. With that, the model is found to be working excellently over a wide range of combination of nanofluids and over a wide range of parameters. Xuan *et al.*⁶⁸ have also given a model in similar vein using superposition principle and the Green-Kubo theorem. They have analysed the stochastic motion of nanoparticles to obtain the stochastic temperature variation in the nanoparticles. The semi-empirical model, which accounts for the Brownian motion, induced microconvection around the nanoparticles as well as for interfacial resistance, matches well with some of the experimental data from literature. Recently, Patel *et al.*⁶⁹ have proposed a cell model which is also based on the Brownian motion driven microconvection around nanoparticles considering the liquid conduction in parallel with the series combination of conduction and microconvection. The model is semi-empirical in nature and found to be addressing all the major issues, like non-linear dependence of thermal conductivity on volume fraction at low concentrations, particle size effect and temperature effect and is validated against lot of experimental data from literature (Fig. 26.6).

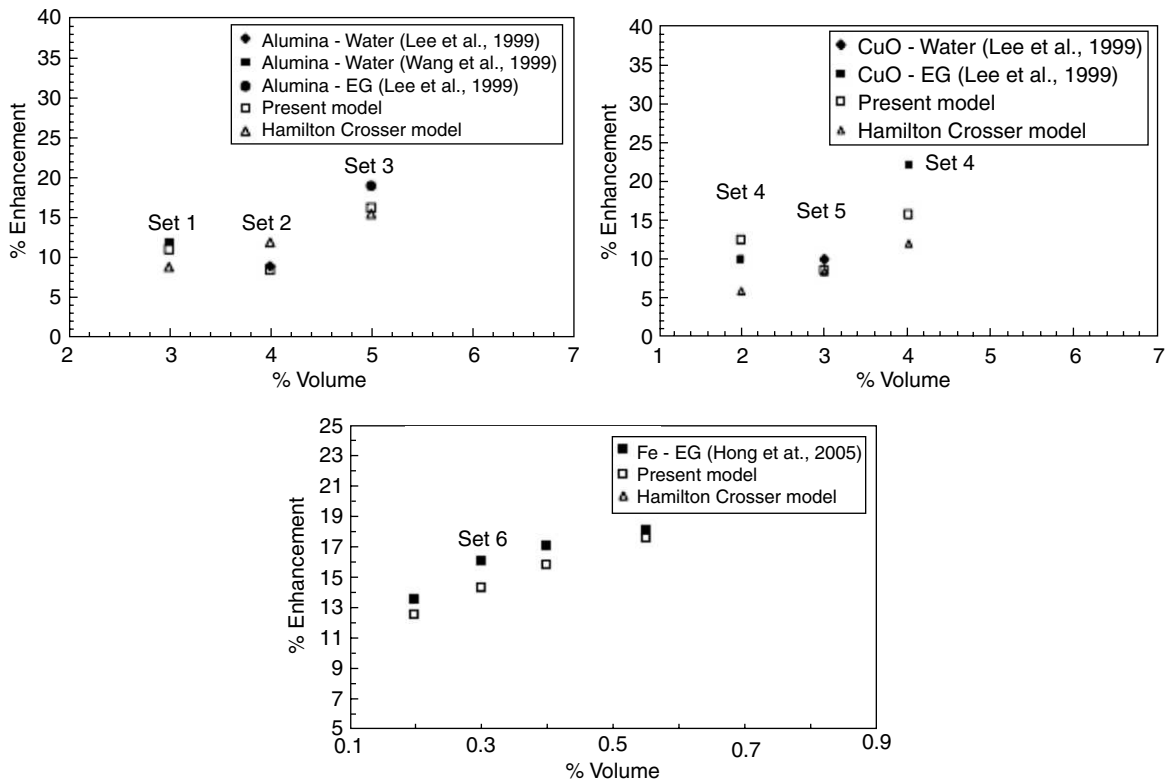


Fig. 26.6 Variation of thermal conductivity enhancement with volume concentration.

In the similar way, a completely empirical model is given by Chon *et al.*,⁷⁰ in which, they have given an empirical correlation for alumina nanofluids by fitting a curve through regression analysis to the existing experimental data. In this modeling, the microconvection around particles is modeled considering diffusive velocities of the particles with mean free path of the liquid molecules as characteristic length. This is a new approach in modeling the thermal conductivities of nanofluids.

A more logical formulation in modeling has been proposed by Patel *et al.*⁷¹ recently, in which the microconvection and particle conduction are put in series, which is parallel with fluid.

Nan *et al.*⁷² presented a simple formula for the thermal conductivity enhancement in carbon nanotube composites, which is derived from Maxwell–Garnett model³¹ by effective medium approach. Thus, it can be said that a variety of models and mechanisms depending extension of classical theory, liquid layering, particle aggregation and particle movement has been tried to explain the nanofluid behaviour. However, the success of these models has been very limited and no clear picture has emerged till recent times. Quite often, these models require adjustable fitting parameters, which are difficult to justify. However, these works have definitely shed light on the various mechanisms of thermal transport in nanofluids.

26.9 CONVECTIVE HEAT TRANSFER STUDIES IN A LAMINAR THERMALLY DEVELOPING FLOW

Given the fact that an increase in thermal conductivity would result in an increase in convective heat transfer coefficient (with effects solely due to the enhancement in thermo-physical properties), more heat transfer enhancement can be expected in the developing flow region. Available literatures also show that higher enhancements in heat transfer coefficients were observed for nanofluids in the entrance region (Wen and Ding⁷³). We present here, experimental investigations on the convective heat transfer behaviour of water-based alumina nanofluids, in the laminar thermally developing flow region. Fig. 26.7 shows the schematic diagram of the convective loop used by the present author for the investigation. The experimental loop is designed for conducting heat transfer experiments in the laminar flow regime.

Figure 26.8 shows the variation in Nusselt number (Ratio of convective to conductive heat transfer = hD/k) along the non-dimensional length of the tube for pure water flow. A comparison of the experimental data with the existing correlation for developing flow⁷⁴ shows reasonable agreement. The correlation plotted in the figure is for a simultaneously developing flow for a constant heat flux condition and it is given as

$$\begin{aligned} Nu_{x,H} &= 3.302 x_+^{-1/3} - 1 && \text{for } x_+ \leq 0.00005 \\ &= 1.302 x_+^{-1/3} - 0.5 && 0.00005 \leq x_+ \leq 0.0015 \\ &= 4.364 + 8.68 (10^3 x_+)^{-0.506} e^{-41x_+} && x_+ \geq 0.0015; \end{aligned} \quad (10)$$

where, $x_+ = \frac{x}{D \cdot \text{Re} \cdot \text{Pr}}$ and subscript H stands for a constant heat flux case.

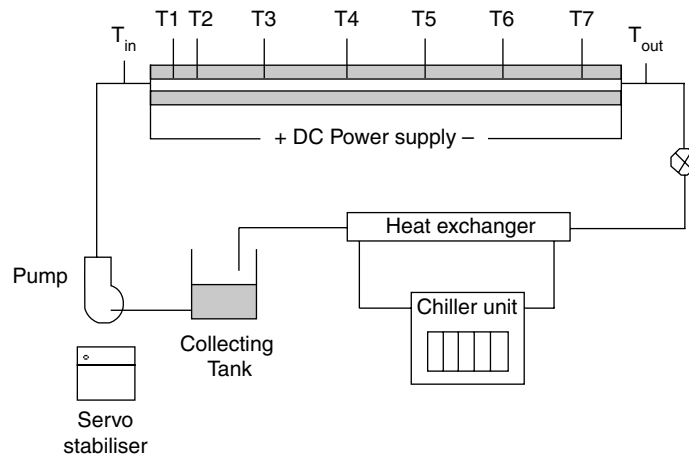


Fig. 26.7 Schematic of the convective loop for laminar thermally developing flow.

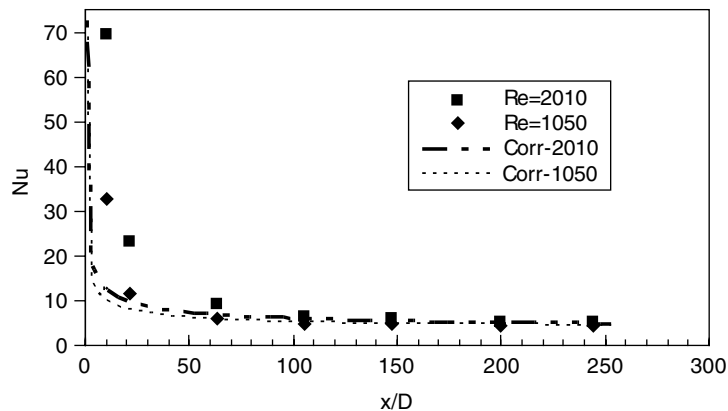


Fig. 26.8 Validation results for the laminar convective flow loop using water.

Thus, it can be inferred that beyond $x/D=50$, the deviation from the correlation is within the acceptable limit and the results may be accepted with confidence. The edge heat losses may be the reason for inaccuracy in the region $x/D < 50$. For the nanofluids, only experimental data for $x/D > 50$ is considered for this reason. Figure 26.9 shows dimensional and non-dimensional heat transfer characteristics for nanofluid with 150 nm particle size at various particle concentrations at an axial location of $x/D=147$. In order to conclude whether the increase in heat transfer coefficient is brought about by increase in thermal conductivity or other thermo-physical properties, dimensional as well as non-dimensional plots of heat transfer coefficient are made and compared. As can be observed from Fig. 26.9(a), at this axial position ($x/D=147$), there is increase in heat transfer for both nanofluids as well as basefluid with respect to increase in velocity. Figure 26.9(b) shows the same results as shown in Fig. 26.9(a) in a non-dimensional form. Comparing both the figures, it is evident that nanofluids give

higher heat transfer coefficients compared to those of the basefluid. In addition, both the figures show the effect of particle concentration. With increase in the concentration, the heat transfer coefficient is increased. A similar plot for 50 nm particle-based nanofluid is shown in Fig. 26.10. It is observed that although the trend is similar to that for larger particle size, the magnitude of enhancement is greater with smaller particles. On closer observation, it can be seen that the data points in non-dimensional form (Fig. 26.10(b)) have slightly shifted towards left. This effect is mainly brought about by the increase in viscosity while using nanofluids.

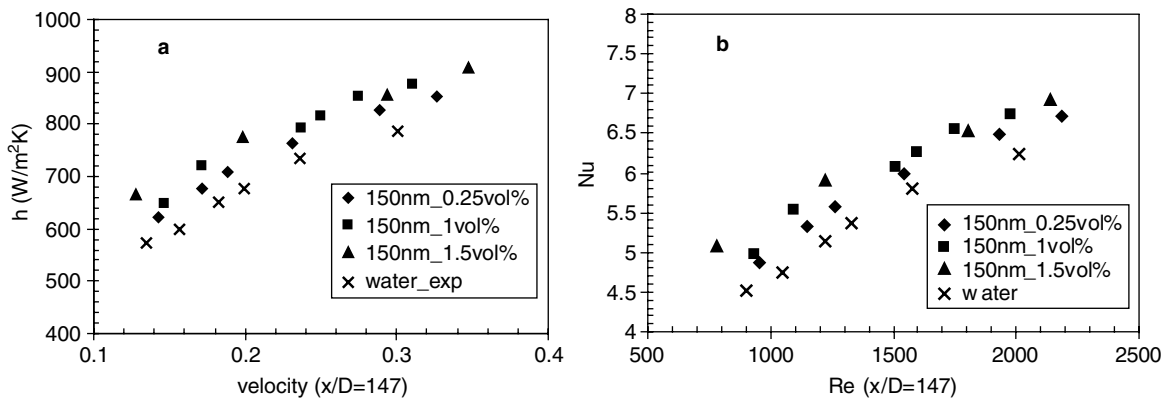


Fig. 26.9 (a) Heat transfer variation with flow velocity at $x/D=147$ for 150 nm alumina nanofluids. (b) Nusselt number variation with Re at $x/D=147$ for 150 nm alumina nanofluids.

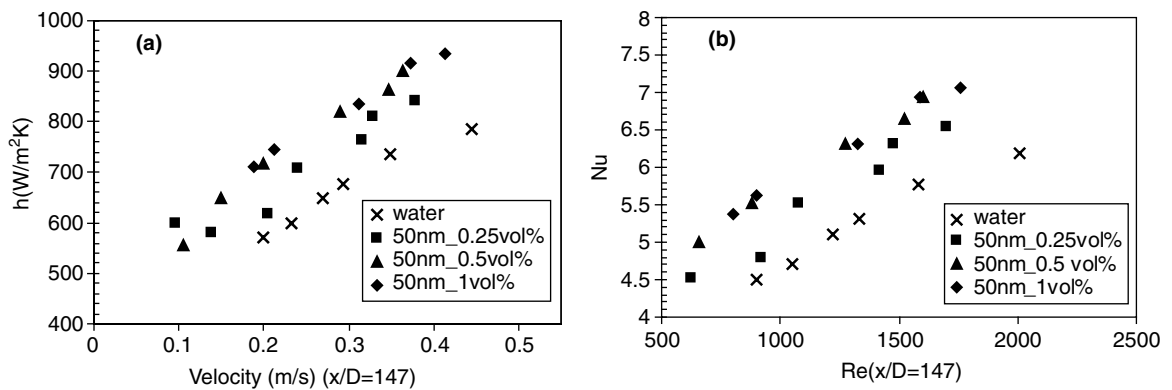


Fig. 26.10 (a) Heat transfer variation with flow velocity at $x/D=147$ for 50 nm alumina nanofluids. (b) Nusselt number variation with Re at $x/D=147$ for 50 nm alumina nanofluids.

Figure 26.11(a) shows the dimensional heat transfer variation for 150 nm and 50 nm alumina-based nanofluids at 1 vol per cent with varying flow velocity, whereas Fig. 26.11(b) shows the non-dimensional heat transfer variation for the same case. Here, the estimations are carried out at a larger axial distance than the previous cases at $x/D=244$.

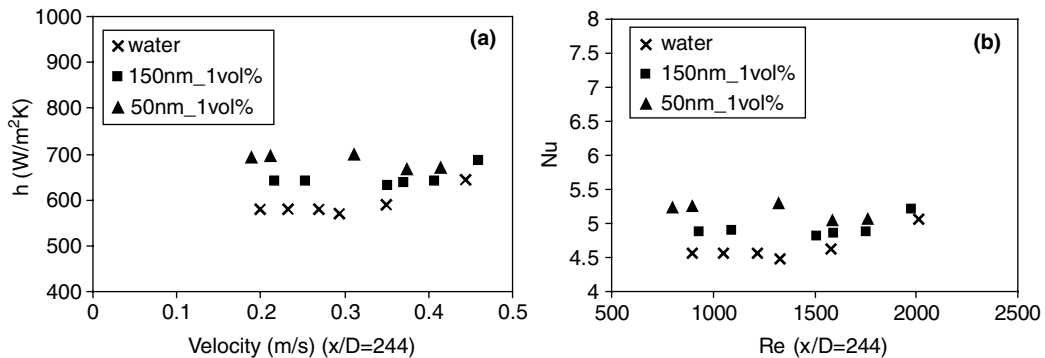


Fig. 26.11 (a) Heat transfer coefficient variation with flow velocity at $x/D=244$ for 50 nm and 150 nm alumina-water nanofluids at 1 vol per cent. (b) Nusselt number variation with Re at $x/D=244$ for 50 nm and 150 nm alumina-water nanofluids at 1 vol%.

It is observed that at a given particle concentration, 50 nm alumina-water nanofluids exhibit higher heat transfer enhancement compared to 150 nm nanofluids. Another observation that can be made is that the increase in heat transfer coefficient with respect to flow velocity is not prominent at the present axial location ($x/D=244$), as compared to that at the axial position of $x/D=147$. Thus, it can be inferred that the increase in heat transfer due to velocity for both basefluid and nanofluid is predominant in the thermally developing flow region than in the nearly developed region.

Figure 26.12(a) shows the variation of heat transfer coefficient along the length of the tube for 1 vol per cent concentration for the two particle sizes. Here, Re is of the order of 1550 and the axial locations beyond $x/D=50$ are only considered. It may be observed here that as particle size reduces, the heat transfer coefficient increases. Nanofluids with 50 nm particle size gave more enhancements in heat transfer coefficient than those of 150 nm particle size nanofluids as well as water. From this plot, it may also be inferred that the increase in the heat transfer coefficient is much higher compared to the increase in thermal conductivity enhancement. For example, at $x/D=147$, for 50 nm alumina nanofluid at $Re=1550$, the enhancement in heat transfer coefficient is around 19 per cent whereas the thermal conductivity for the same has increased only by 5 per cent. Similarly for 150 nm alumina nanofluid, the heat transfer coefficient enhancement is around 11 per cent, whereas the thermal conductivity increase is around 4 per cent only. Thus, it may be observed that the convective heat transfer enhancement with nanofluids is contributed by some effects other than the increase in thermal conductivity. Also, the increase is more predominant in the entrance region, i.e., at lower x/D . The above fact can be better visualised in Fig. 26.12(b), where the Nusselt number variation with Re (Ratio of inertia force to viscous force) is plotted at different x/D for nanofluids with 50 nm particle size and for water. It is observed that at lower x/D , the heat transfer coefficient varies with Re and at $x/D>200$, it becomes independent of Re . It may also be observed that the enhancement is also more at the entrance region than at a higher x/D . For instance, at $Re\sim 1550$, the enhancement in heat transfer coefficient is 28 per cent at $x/D=63$, whereas it is 19 per cent and 10 per cent at $x/D=147$ and 244, respectively. These trends could be attributed to larger property variation in the developing region

due to stronger temperature gradient, along with the possibility of larger particle migration at lower particle sizes. Thus, it can be inferred that applications of nanofluids as heat transfer media is more appropriate for the laminar developing region.

After conducting sufficient number of experiments with nanofluids, a correlation for Nusselt number has been derived using a non-linear regression analysis. For alumina nanofluids in the developing region ($50 < x/D < 200$) of laminar flow ($500 < Re < 2000$), the correlation can be expressed as

$$Nu_x = 4.36 + \left[a \cdot x_+^{-b} (1 + \phi^c) \cdot \exp(-d \cdot x_+) \right] \left[1 + e \cdot \left(\frac{d_p}{d_{ref}} \right)^{-f} \right]; \tag{11}$$

where $a = 6.219 \times 10^{-3}$, $b = 1.1522$, $c = 0.1533$, $d = 2.5228$, $e = 0.57825$, $f = 0.2183$, $d_{ref} = 100$ nm.

Theoretical analysis of laminar thermally developing region, as seen from the experimental observations, the pressure drop occurring in nanofluids could be predicted using conventional correlations once the thermo-physical properties are known accurately, whereas enhancements in convective heat transfer coefficients are observed to be beyond the increase brought in by thermal conductivity enhancement. One major reason for the above observation could be that heat transfer in convective flow occurs at a dynamic flow condition, where mechanisms, such as shear driven particle migration can be active, while thermal conductivity measurement was performed at static conditions. On the other hand, viscosities of nanofluids are measured under dynamic shearing conditions, and hence, the shear-induced particle migration effects get included in the effective viscosity values. Thus, the pressure drop does not show any deviation from the well-known correlations since the effective viscosity is used for these correlations.

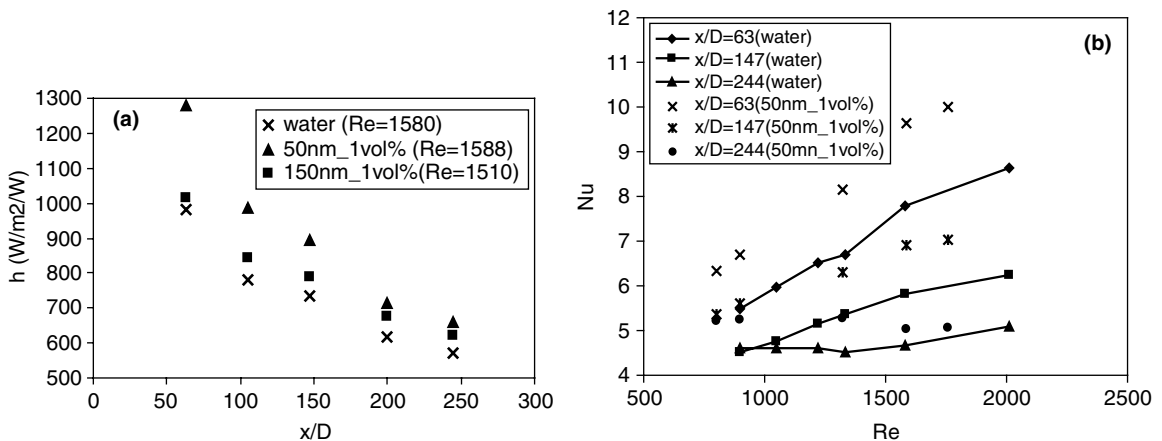


Fig. 26.12 (a) Heat transfer coefficient variation with axial distance at a given Re . (b) Nusselt number variation with Re at different x/D positions for 50 nm alumina nanofluids.

Heat transfer coefficient is not a fluid property and it describes the heat transfer occurring, when a fluid flows over a solid at a different temperature. Theoretically, it is directly proportional to the thermal

conductivity of the fluid and inversely proportional to the thermal boundary-layer thickness (Ding *et al.*⁷⁵). Thus, an increase in convective heat-transfer coefficient can be either due to increase in thermal conductivity or due to decrease in thermal boundary layer thickness or both. The effect of nanofluids in decreasing the thermal boundary-layer thickness is already seen in Fig. 26.12(a). The exact reasons for heat transfer enhancements under dynamic flow conditions are not yet known. Some speculations based on observations in literature, together with a thermal dispersion model to predict the heat transfer characteristics of nanofluids in a laminar thermally developing flow is presented next.

In a theoretical study by Buongiorno⁷⁷, it was shown that in a laminar flow (in the absence of eddies), two slip motions can be significant. They were suggested to be thermophoresis and Brownian diffusion based on scaling analysis. Thermophoresis is the phenomenon of motion of suspended particles induced by temperature gradient in the fluid. Apart from these effects, particle migration can occur under dynamic flow conditions under shear (Ding and Wen⁷⁶). In a tube flow, the highest shear occurs near the wall and the lowest near the tube centre. Thus, a non-uniform shear field exists in a tube flow, which further induces a non-uniform viscosity and temperature profile. Thus, three mechanisms were proposed to be responsible for particle migration in a non-uniform shear flow. They are: (a) Shear induced migration, where the particles move from a region of high shear rate to region of lower shear rate; (b) viscosity gradient induced migration, where the particles move from a region of higher viscosity to that of lower viscosity and (c) by self-diffusion due to Brownian motion, through which particles move from region of higher concentration to that of lower concentration. It was theoretically proved that the non-uniform thermal conductivity profile caused by particle migration could result in higher Nusselt number. Thus, the particle migration occurring under shear can increase the heat transfer coefficient. This means that the slip velocity between the fluid and the particles may not be zero, although the particles are ultrafine. Irregular and random movement of the particles increases the energy exchange rates in the fluid, i.e., thermal dispersion takes place in the flow of the nanofluid. The thermal dispersion could flatten the temperature distribution and make the temperature gradient between the fluid and wall steeper, which could augment heat transfer rate between the fluid and the wall. Therefore, the enhancement mechanism of heat transfer by the nanofluid can be explained from the following two aspects: one is that the suspended particles increase the thermal conductivity of the two-phase mixture and the other is that the chaotic movement of the ultrafine particles, the thermal dispersion, accelerates the energy exchange process in the fluid.

The idea of applying thermal dispersion effects to nanofluids was initially proposed by Xuan and Roetzel⁷⁸. A similar approach to that of Xuan and Roetzel⁷⁸ is made, with the exception that instead of using dispersion in thermal conductivity, a dispersion in heat transfer coefficient is used. In a thermal dispersion model (Xuan and Roetzel⁷⁸), it is assumed that the irregular movement of particles induce small perturbations in both velocity and temperature, which can be given as, T' and u' . The intrinsic phase averages will then take the form

$$T = \langle T \rangle^{bf} + T'; \quad (12)$$

$$u = \langle u \rangle^{bf} + u'; \quad (13)$$

where $\langle T \rangle^{bf}$ and $\langle u \rangle^{bf}$ are the volume averaged fluid temperatures and velocities. Substituting Eq. (12) and (13) in the basic energy equation give

$$(\rho C_p)_{nf} \left[\frac{\partial \langle T \rangle^{bf}}{\partial t} + \langle u \rangle^{bf} \cdot \nabla \langle T \rangle^{bf} \right] = \nabla \cdot (k_{nf} \nabla \langle T \rangle^{bf}) - (\rho C_p)_{nf} \nabla \langle u' T' \rangle^{bf}. \quad (14)$$

The thermal dispersion caused by the irregular movement of particles is indicated in the second term on right-hand side of Eq. 14. Taking an analogy to turbulence and comparing the thermal dispersion in nanofluid to that in a porous media, Xuan and Roetzel⁷⁸ proposed the dispersion in thermal conductivity can take the form as given below:

$$q_d = (\rho C_p)_{nf} \langle u' T' \rangle = -k_d \cdot \nabla \langle T \rangle^{bf}. \quad (15a)$$

By comparing the thermal dispersion to that in porous medium, they proposed the thermal dispersion in nanofluids to take the form

$$k_d = C(\rho C_p)_{nf} u d_p R \phi \quad \text{or} \quad k_d = C^*(\rho C_p)_{nf} u R; \quad (15b)$$

where C and C* are constants, which are to be determined by matching with experimental data.

In order to explain the thermal dispersion phenomenon in the present case, the heat transfer coefficient for 150 nm alumina nanofluid at 1.5 vol per cent is re-plotted again as shown in Fig. 26.13. Here, the solid line shows the theoretical predictions using water properties. Now changing the properties (thermal conductivity, viscosity, density and specific heat) with those of 150 nm alumina-water nanofluids at 1.5 vol per cent, the heat transfer prediction will be higher than that of water, and this is shown as dotted line in Fig. 26.13.

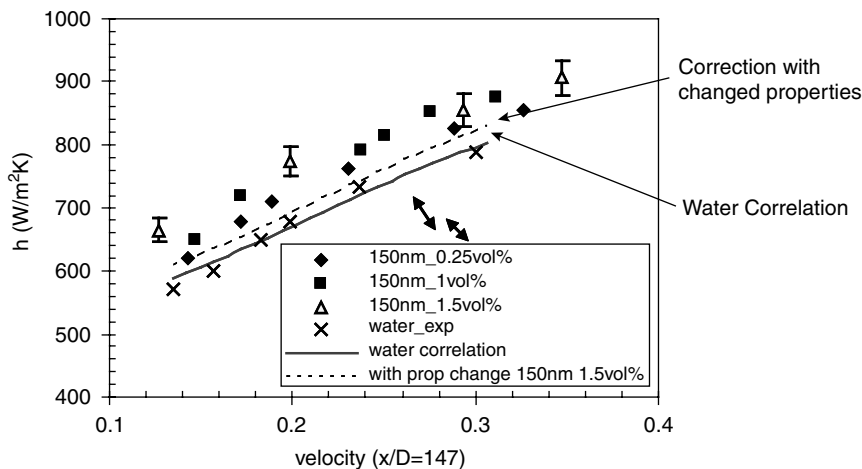


Fig. 26.13 Heat transfer coefficient variation with flow velocity at $x/D=147$ for 150 nm alumina-water nanofluids at 1.5 vol%.

Thus, it is seen that the theoretical predictions by property change alone could not predict the experimental observations. The enhancement in heat-transfer coefficient observed experimentally is beyond the enhancement brought in by property changes. This difference is presently modeled in terms of the thermal dispersion occurring at dynamic flow conditions. The effective thermal conductivity is obtained under static conditions, whereas effective viscosities are measured under dynamic shearing conditions. This can be one reason why the theoretical comparison of predicted pressure drop and measured pressure drop matched as viscosity is the major thermo-physical property that influences pressure drop. Thus, the effective heat transfer can be modeled by incorporating property changes together with the heat transfer increase due to dynamic flow conditions

$$h_{eff} = h_{static} + h_{dynamic}; \quad (16)$$

$$h_{eff} = h_{with\ property\ changes} + h_{thermal\ dispersion}; \text{ and} \quad (17)$$

$$\frac{h_{eff}}{h_{with\ property\ changes}} = 1 + \frac{h_{thermal\ dispersion}}{h_{with\ property\ changes}}. \quad (18)$$

This normalised thermal dispersion coefficient can be modeled similar to the one proposed for thermal conductivity dispersion by Xuan and Roetzel⁷⁸. Thus,

$$\frac{h_{thermal\ dispersion}}{h_{with\ property\ changes}} = C^* x_+^a \phi^b \left(\frac{d_p}{d_{ref}} \right)^c. \quad (19)$$

The above equation attempts to account for the thermal dispersion effects in a thermally developing flow regime. The value of C^* in this equation is to be obtained by matching with the experimental results. Data fitting is carried out with the experimental results using non-linear regression methods to evaluate the values of C^* , a , b , and c . Thus, after estimation of the constants, the Eq. 18 turns out to be

$$\frac{h_{eff}}{h_{with\ property\ changes}} = 1 + 1.802E - 03 x_+^{-1.1397} \phi^{0.113533} \left(\frac{d_p}{d_{ref}} \right)^{-0.1263}. \quad (20)$$

The above equation gives an idea of the increase in heat transfer due to thermal dispersion beyond the property effects. As seen, it increases with particle concentration, but has inverse dependency with respect to particle size and x_+ . After having evaluated the heat-transfer characteristics in a laminar thermally developing regime, experiments are now conducted in a fully turbulent flow regime. Details of the modified experimental setup and the discussion of results observed are described next.

26.10 CONVECTIVE HEAT TRANSFER STUDIES IN A TURBULENT FLOW REGIME

Convective heat-transfer measurements using alumina-water nanofluids are carried out. It is believed here that the real nature of heat-transfer enhancement may be revealed by plotting dimensional results rather than non-dimensional ones. This is mainly due to the reason that non-dimensionalisation

sometimes does not provide a complete picture of the variations in all the individual factors. Both dimensional and non-dimensional plots have been made in order to highlight the effects of individual parameters and their net effect as a non-dimensional group. Figure 26.14(a) shows the heat-transfer coefficient variation plotted against the flow velocity, whereas a non-dimensionalised plot of the same is given in Fig. 26.14(b). Non-dimensionalisation for heat-transfer coefficient and flow velocity is carried out using the scaling factors depicted in Eq. 19. It is seen that the basefluid (water), follows the theoretical trend as given by Gnielinski correlation.⁷⁹ Data lie scattered within the uncertainty limits of experimentation. Exact reasons for this cannot be ascertained at this stage, but given below are some plausible explanations. The heat-transfer characteristics of nanofluids in turbulent regime may be explained based on two types of analyses. One is based on the flow scales and the other is based on thermo-physical properties. Transport in a turbulent flow occurs primarily by eddy mixing and by energy dissipation of eddies. From an analysis in line with Buongiorno,⁷⁷ it can be shown that particles in a nanofluid do not exhibit individual effects as they move along with the eddies. It may be seen that the smallest eddy would be very much larger than the particle sizes involved and there would not be any major slip motion between particles and eddies giving an extra heat transfer effect. The size of the largest eddy would be of the order of the tube diameter.

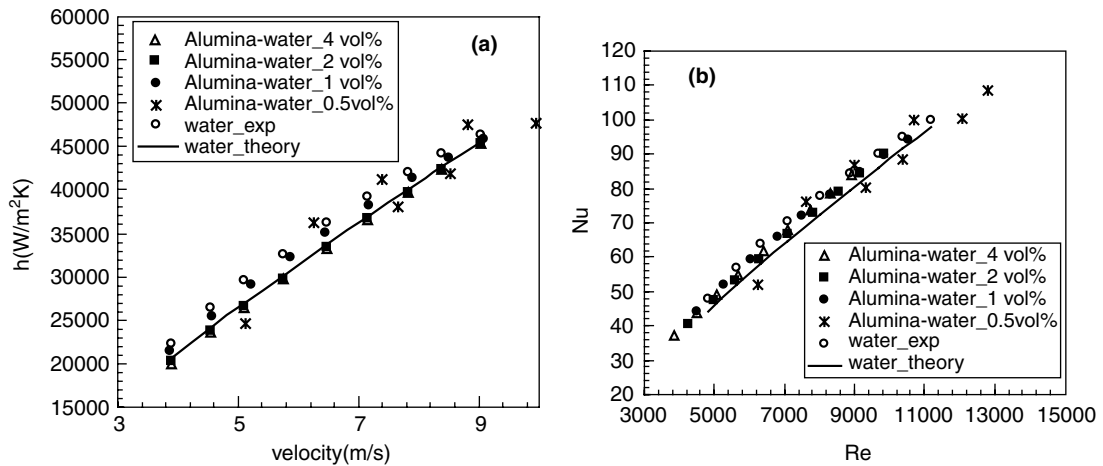


Fig. 26.14 (a) Heat transfer coefficient variation with velocity for different nanofluids. (b) Nusselt number variation with Re for different nanofluids.

26.11 SCALING ANALYSIS

An analysis of length and time scale related to the movement of nanoparticles inside the liquid in a nanofluid system can be extremely important in understanding the mechanisms of thermal transport in a nanofluid as well as the relative importance of various forces at the nanoscale. In the following section, a scaling analysis is presented to demonstrate that.

$$l_0 \sim \text{Diameter of tube} \sim 1.3\text{mm} \quad (21)$$

and the smallest eddy size according to Kolmogorov's scale, would be

$$l_s \sim l_0 \text{Re}^{-3/4} \quad (22)$$

For the largest Re considered in the present case, the smallest eddy would be of the order of 1 micron size. Thus, the particles would be easily carried along with eddies.

On a similar ground, an analysis based on the particle-laden flow, Stanton number would also reveal similar results. Usually Stanton number is evaluated in the numerical modeling of a multi-phase flow to determine which scheme of particle modelling (mixture method, discrete phase method, etc.) would be appropriate for the particular flow situation. Stanton number gives the relation between the particle response time and the fluid system response time in the form

$$\text{Stanton Number} = \text{St} = \frac{\text{Particle response time}}{\text{System response time}} = \frac{\tau_d}{\tau_s}. \quad (23)$$

Considering particle slip from the balance of particle inertial forces to drag forces, the particle response time can be derived as (Buongiorno⁷⁷)

$$\tau_d = \frac{\rho d_p^2}{18\mu}. \quad (24)$$

For alumina nanofluids, with density of the order 4000kg/m³ and 100 nm particle size having viscosities of approximately 1mPas, the particle response time would be of the order of 2 ns.

The system response time is basically the time scale of the smallest eddy. The time scale of the largest eddy could be evaluated from the tube dimension and mean velocity of flow as approximately 0.1 ms. Again from scaling law, the time scale of the smallest eddy would be,

$$t_s \sim t_0 \text{Re}^{-1/2} \sim 0.001 \text{ ms}. \quad (25)$$

Evaluation of Stanton number from Eq. 24 and Eq. 25 shows a low value (order of 10⁻³), which suggests that particles would be carried along with the flow. From these two observations, it may be reasoned that nanofluids at low particle concentrations under turbulent flow conditions may not exhibit an enhanced heat-transfer coefficient beyond the property enhancement/deterioration.

Next, an evaluation of particle stopping distance is made. Particle stopping distance, is the distance a particle can move by inertia, once the eddies come to rest. If these particles could penetrate into the laminar sub-layer, it could influence in changing the sub-layer characteristics and there, by increase the heat transfer. The particle stopping distance (d_s) is defined as (Buongiorno⁷⁷),

$$d_s = \tau_d V_s, \quad (26)$$

where V_s is the eddy velocity, which is approximately equal to the shear velocity of flow and τ_d the particle response time Eq. 24. The shear velocity may be evaluated for the present flow condition as

$$V_s \sim \sqrt{\frac{\tau_w}{\rho}} = V_{mean} \sqrt{\frac{f}{8}} \sim 0.6 \text{ m/s}. \quad (27)$$

The particle stopping distance as evaluated from Equations 24 and 27 is of order 1 nm for the present flow situation. The laminar sub-layer thickness near the wall (from definition) would be

$$\delta \sim 5 \frac{\mu/\rho}{\sqrt{\tau_w/\rho}} \sim 3 \text{ microns.} \quad (28)$$

Thus, it can be seen that the particle stopping distance is far less than the laminar sub-layer thickness, and hence, the particles cannot penetrate into the sub-layer to alter the rate of heat transfer.

From the above scaling analysis, it is observed that the nanoparticles individually cannot have an effect in the flow and the heat transfer characteristics would be overridden by the eddy mixing characteristics. Thus, the overall effect on heat transfer is brought about by thermo-physical property changes alone, in the turbulent regime.

REFERENCES

1. A.E. Bergles, 'Heat transfer enhancement—The encouragement and accommodation of high heat fluxes', *Journal of Heat Transfer*, 119, (1997), 8–19.
2. J.C. Maxwell, *A Treatise on Electricity and Magnetism* (2nd Ed.), Clarendon Press, Oxford, UK, (1881).
3. S.U.S. Choi, 'Enhancing thermal conductivity of fluids with nanoparticles', in D.A. Singer and H.P. Wang (eds), *Developments and Applications of Non-Newtonian Flows*, FED 231 ASME, New York, (1995), 99–105.
4. S.K. Das, S.U.S. Choi, W. Yu and T. Pradeep, *Nanofluids: Science and Technology*; John Wiley & Sons Inc., NJ, (2008).
5. G. Oberdoerster, E. Oberdoerster and J. Oberdoerster, 'Nanotoxicology: An emerging discipline evolving from studies of ultrafine particles', *Environment Health Perspective*, 113, (2005), 823–39.
6. S.A. Putnam, D.G. Cahill, B. Ash and L. Schadler, 'High-precision thermal conductivity measurements as a probe of polymer/nanoparticle interfaces', *Journal of Applied Physics*, 94, (2003), 6785–88.
7. S.K. Das, S.U.S. Choi and H.E. Patel, 'Heat transfer in nanofluids—a review', *Heat Transfer Engineering*, 27, (2006), 3–19.
8. S.K. Das, N. Putra and W. Roetzel, 'Pool boiling characteristics of nano-fluids'. *Int. J. Heat and Mass Trans.*, 46, (2003), 851–62.
9. W. Yu, D.M. France, J.L. Routbort and S.U.S. Choi, 'Review and comparison of nanofluid thermal conductivity and heat transfer enhancements', *Heat Transfer Engineering*, 29, (2008), 432–60.
10. M. Chiesa and S.K. Das, 'Experimental investigation of the dielectric and cooling performance of colloidal suspensions in insulating media', *Colloids and Surfaces A: Physicochemical and Engineering Aspects*, 335, (2008), 88–97.
11. Z. Zhang and Q. Que, 'Synthesis, structure and lubricating properties of Dialkyldithiophosphate—Modified Mo-S compound nanoclusters', *Wear*, 209, (1997), 8–12.
12. *Handbook of Nanotechnology: Nanometer Structure Theory, Modeling, and Simulation* (<http://members.asme.org/catalog/ItemView.cfm?ItemNumber=802159>).
13. P.C. Hiemenz and R. Rajagopalan, *Principles of Colloid and Surface Chemistry* (3rd ed.), Marcel Dekker, New York, (1997).

14. Y. Xuan and Q. Li, 'Heat Transfer Enhancement of Nano-Fluids', *Int. J. Heat Fluid Flow*, 21, (2000), 58–64.
15. S. Ross and I.D. Morrison, *Colloidal Systems and Interfaces*, Wiley, New York, (1988).
16. S.K. Das, N. Putra, P. Thiesen and W. Roetzel, 'Temperature Dependence of Thermal Conductivity Enhancement for Nanofluids, ASME', *Journal Heat Transfer*, 125, (2003), 567–574.
17. H. Xie, J. Wang, T. Xi and Y. Liu, 'Study on the Thermal Conductivity of SiC Nanofluids', *Journal of the Chinese Ceramic Society*, 29(4), (2001), 361–64.
18. B.V. DeJaguin and L.D. Landau, 'Theory of Stability of Highly Charged Lyophobic Sols and Adhesion of Highly Charged Particles in Solutions of Electrolytes', *Acta Physiochim. USSR*, 14, (1941), 633–52.
19. E.J.W. Verwey and J.T.G. Overbeek, *Theory of Stability of Lyophobic Colloids*, Elsevier, Amsterdam, (1948).
20. H. Reerink and J.T.G. Overbeek, 'The Rate of Coagulation as a Measure of the Stability of Silver Iodide Solutions', *Discuss. Faraday Soc.*, 18, (1954), 74–84.
21. T. Sugimoto (ed.), 'Fine Particles: Synthesis, Characterisation, and Mechanism of Growth', *Surfactant Science*, 92, Marcel Dekker, New York, (2000), 290–99.
22. H.E. Patel, S.K. Das, T. Sundararajan, N.A. Sreekumaran, B. George and T. Pradeep, 'Thermal Conductivities of Naked and Monolayer Protected Metal Nanoparticle Based Nanofluids: Manifestation of Anomalous Enhancement and Chemical Effects', *Appl. Phys. Lett.*, 83(14), (2003), 2931–33.
23. M. Brust, M. Walker, D. Bethell, D.J. Schiffrin and R. Whyman, 'Synthesis of Thiol Derivatized Gold Nanoparticles in a Two-Phase Liquid/Liquid System', *J. Chem. Soc., Chem. Commun.*, (1994), 801–02.
24. B.V. Enustun and J. Turkevich, 'Coagulation of Colloidal Gold', *J. Am. Chem. Soc.*, 85, (1963), 3317–28.
25. R. Andrews, D. Jacques, A.M. Rao, F. Derbyshire, D. Qian, X. Fan, E.C. Dickey and J. Chen, 'Continuous Production of Aligned Carbon Nanotubes: A Step Closer to Commercial Realisation', *Chem. Phys. Lett.*, 303, (1999), 467–74.
26. D.R. Chen and S.L. Kaufman, 'Electrospraying of Conducting Liquids for Monodisperse Aerosol Generation in the 4 nm to 1.8 μm Diameter Range', *J. Aerosol Sci.*, 26, (1995), 983–77.
27. D.R. Chen and D.Y.H. Pui, 'Experimental Investigation of Scaling Laws for Electro-spraying: Dielectric Constant Effect', *Aerosol Sci. Technol.*, 27, (1997), 367–80.
28. H.T. Zhu, Y.S. Lin and Y.S. Yin, 'A Novel One-Step Chemical Method for Preparation of Copper Nanofluids', *Journal of Colloid and Interface Science*, 277, (2004), 100–03.
29. S. Lee, S.U.S. Choi, S. Li and J.A. Eastman, 'Measuring Thermal Conductivity of Fluids Containing Oxide Nanoparticles', *Journal of Heat Transfer*, 121, (1999), 280–89.
30. R.L. Hamilton and O.K. Crosser, 'Thermal Conductivity of Heterogeneous Two Component Systems', *I & EC Fundam*, 1(3), (1962), 187–91.
31. J.C. Maxwell-Garnett, 'Colours in Metal Glasses and in Metallic Films', *Philos. Trans. Roy. Soc. A.*, 203, (1904), 385–420.
32. X. Wang, X. Xu and S.U.S. Choi, 'Thermal Conductivity of Nanoparticle-Fluid Mixture', *Journal of Thermophysics and Heat Transfer*, 13, (1999), 474–80.
33. X.Q. Wang and A.S. Mujumdar, 'Heat transfer characteristics of nanofluids: a review', *International Journal of Thermal Sciences*, 46, (2007), 1–19.

34. H.Q. Xie, J.C. Wang, T.G. Xi, Y. Liu, F. Ai and Q.R. Wu, 'Thermal Conductivity Enhancement of Suspensions Containing Nanosized Alumina Particles', *Journal of Applied Physics*, 91(7), (2002), 4568–72.
35. J.A. Eastman, S.U.S. Choi, S. Li, W. Yu and L.J. Thomson, 'Anomalous Increased Effective Thermal Conductivities of Ethylene Glycol Based Nanofluids Containing Copper Nanoparticles', *Appl. Phys. Lett.*, 78(6), (2001), 718–20.
36. M.S. Liu, Mark Ching-Cheng Lin, C.Y. Tsai and Chi-Chuan Wang, 'Enhancement of thermal conductivity with Cu for nanofluids using chemical reduction method', *International Journal of Heat and Mass Transfer*, 49, (2006), 3028–33.
37. H.Q. Xie, J.C. Wang, T.G. Xi, Y. Liu, F. Ai, 'Dependence of Thermal Conductivity of Nanoparticles-fluid Mixture on the Base Fluid', *Journal of Material Science Letters*, 21, (2002), 1469–71.
38. T.K. Hong, H.S. Yang and C.J. Choi, 'Study of the enhanced thermal conductivity of Fe nanofluids', *Journal of Applied Physics*, 97, (2005), 064311.
39. M. Chopkar, Prasanta K. Dasb and Indranil Manna, 'Synthesis and characterisation of nanofluid for advanced heat transfer applications', *Scripta Materialia*, 55, (2006), 549–52.
40. C.H. Chon and K.D. Kihm, 'Thermal Conductivity Enhancement of Nanofluids by Brownian Motion, Tans. of ASME', *Journal of Heat Transfer*, 127, (2005), 810.
41. C.H. Li and G.P. Peterson, 'Experimental investigation of temperature and volume fraction variations on the effective thermal conductivity of nanoparticle suspensions (nanofluids)', *Journal of Applied Physics*, 99, (2006), 084314.
42. S.M.S. Murshed, K.C. Leong, C. Yang, 'Investigations of thermal conductivity and viscosity of nanofluids', *International Journal of Thermal Sciences*, vol. 47, Issue 5, (2008), 560–68.
43. X. Zhang, H. Gu and Motoo Fujii, 'Effective thermal conductivity and thermal diffusivity of nanofluids containing spherical and cylindrical nanoparticles', *Experimental Thermal and Fluid Science*, 31, (2007), 593–99.
44. S.A. Putnam, David G. Cahill, Paul V. Braun, Zhenbin Ge and Robert G. Shimmin, 'Thermal conductivity of nanoparticle suspensions', *Journal of Applied Physics*, 99, (2006), 084308.
45. F.J. Wasp, *Solid-Liquid Slurry Pipeline Transportation*, *Trans. Tech.*, Berlin, (1977).
46. D.A.G. Bruggeman, 'Berechnung Verschiedener Physikalischer Konstanten von Heterogenen Substanzen, I. Dielektrizitätskonstanten und Leitfähigkeiten der Mischkörper aus Isotropen Substanzen', *Annalen der Physik. Leipzig*, 24, (1935), 636–79.
47. R.T. Bonnecaze and J.F. Brady, 'A Method For Determining the Effective Conductivity of Dispersions of Particles', *Proc. R. Soc. Lond. A.*, 430, (1990), 285–313.
48. R.T. Bonnecaze, and J.F. Brady, 'The Effective Conductivity of Random Suspensions of Spherical Particles', *Proc. R. Soc. Lond. A.*, 432, (1991), 445–65.
49. D.J. Jeffrey, 'Conduction Through a Random Suspension of Spheres', *Proc. R. Soc. London, Series A*, 335–1602, (1973), 355–67.
50. R.H. Davis, 'Effective Thermal Conductivity of a Composite Material with Spherical Inclusions', *International Journal of Thermophysics*, 7(3), (1986), 609–20.
51. S. Lu and H. Lin, 'Effective Conductivity of Composites Containing Aligned Spheroidal Inclusions of Finite Conductivity', *Journal of Applied Physics*, 79, (1996), 6761–69.

52. S.C. Cheng and R.I. Vachon, 'The Prediction of the Thermal Conductivity of Two and Three Phase Solid Heterogeneous Mixtures', *International Journal of Heat and Mass Transfer*, 12, (1969), 249.
53. W. Yu and S.U.S. Choi, 'The Role of Interfacial Layers in the Enhanced Thermal Conductivity of Nanofluids: A Renovated Maxwell Model', *Journal of Nanoparticles Research*, 5(1–2), (2003), 167–71.
54. C.S. Hirtzel and R. Rajagopalan, *Colloidal Phenomena*, Noyes Publications, Park Ridge, NJ, (1985).
55. W. Czarnetzki and W. Roetzel, 'Temperature Oscillation Techniques for Simultaneous Measurement of Thermal Diffusivity and Conductivity', *International Journal of Thermophys*, 16(2), (1995), 413–22.
56. P. Keblinski, S.R. Phillpot, S.U.S. Choi and J.A. Eastman, 'Mechanisms of Heat Flow in Suspensions of Nano-Sized Particles (Nanofluids)', *International Journal of Heat and Mass Transfer*, 45, (2002), 855–63.
57. Q.Z. Xue, 'Model for Effective Thermal Conductivity of Nanofluids', *Phys. Lett. A*, 307, (2003), 313–17.
58. L.M. Schwartz, E.J. Garboczi and D.P. Bentz, 'Interfacial Transport in Porous Media: Application to DC Electrical Conductivity of Mortars', *Journal of Applied Physics*, 78(10), (1995), 5898–908.
59. R. Prasher, William Evans, Paul Meakin, Jacob Fish, Patrick Phelan and Pawel Keblinski, 'Effect of aggregation on thermal conduction in colloidal nanofluids', *Applied Physics Letters*, 89, (2006), 143119.
60. Y. Feng, Boming Yu, Peng Xu and Mingqing Zou, 'The effective thermal conductivity of nanofluids based on the nanolayer and the aggregation of nanoparticles', *J. Phys. D: Appl. Phys.*, 40, (2007), 3164–71.
61. R. Wojnar, 'The Brownian Motion in a Thermal Field', *Acta Physica Polonica B*, 32(2), (2001), 333–49.
62. M. Gitterman, 'Brownian Motion in Fluctuating Media', *Physical Review E*, 52(1), (1995), 303–06.
63. A.S. Gupta, 'Soret Effect on Propagation of Thermo Convective Waves in a Binary Mixture', *Journal of Heat and Mass Transfer*, 35(4), (1999), 315–20.
64. S.P. Jang and S.U.S. Choi, 'Role of Brownian Motion in the Enhanced Thermal Conductivity of Nanofluids', *Applied Physics Letters*, 84(21), (2004), 4316–18.
65. J. Xu, Boming Yu, Mingqing Zou and Peng Xu, 'A new model for heat conduction of nanofluids based on fractal distributions of nanoparticles', *J. Phys. D: Appl. Phys.*, 39, (2006), 4486–90.
66. K.D. Hemanth, H.E. Patel, K.V.R. Rajeev, T. Sundararajan, T. Pradeep and S.K. Das, 'Model for Heat Conduction in Nanofluids', *Physical Review Letters*, 93(14), (2004), 144301–1–4.
67. H.E. Patel, T. Sundararajan, T. Pradeep, A. Dasgupta, N. Dasgupta and S.K. Das, 'A micro-convection model for thermal conductivity of nanofluids', *Pramana—Journal of Physics*, 65, (2005), 863–69.
68. Y. Xuan, Li Qiang, Xing Zhang and Motoo Fujii, 'Stochastic thermal transport of nanoparticle suspensions', *Journal of Applied Physics*, 100, (2006), 043507.
69. H.E. Patel, T. Sundararajan and Sarit Kumar Das, 'A cell model approach for thermal conductivity of nanofluids', *Journal of Nanoparticles Research*, vol. 10, Number 1, (2007), 87–97.
70. C.H. Chon, K.D. Kihm, S.P. Lee and S.U.S. Choi, 'Empirical correlation finding the role of temperature and particle size for nanofluid (Al₂O₃) thermal conductivity enhancement', *Applied Physics Letters*, 87, (2005), 153107.
71. H.E. Patel, T. Sundararajan and S.K. Das, 'A Micro-convective Cell Model for the Prediction of Thermal Conductivity of Nanofluids', *Journal of Nanoparticle Research*, vol. 10, 1, (2008), 87–97.
72. *Chinese Engineering Thermophysics*, Shanghai, (2002), 889–92.
73. C.W. Nan, Z. Shi and Y. Lin, 'A Simple Model for Thermal Conductivity of Carbon Nanotube-Based Composites', *Chem. Phys. Lett.*, 375, (2003), 666–69.

74. D. Wen and Y. Ding, 'Experimental investigation into convective heat transfer of nanofluids at the entrance region under laminar flow conditions', *International Journal of Heat and Mass Transfer*, 47, (2004), 5181–88.
75. Bejan, *Heat Transfer Hand Book*, vol. 1, (2003).
76. Y. Ding, H. Alias, D. Wen and A.R. Williams, 'Heat transfer of aqueous suspensions of carbon nanotubes (CNT nanofluids)', *International Journal of Heat and Mass Transfer*, 49, (2006), 240–50.
77. J. Buongiorno, 'Convective transport in nanofluids', *Journal of Heat Transfer*, 128, (2006), 240–50.
78. Y. Ding and D. Wen, 'Particle migration in a flow of nanoparticle suspensions', *Powder Technology*, 149, (2005), 84–92.
79. Y. Xuan and W. Roetzel, 'Conceptions for heat transfer correlation of nanofluids', *International Journal of Heat and Mass Transfer*, 43, (2000), 3701–07.

ADDITIONAL READING

1. Sarit K. Das, Stephen U.S. Choi, Wehua Yu and T. Pradeep, *Nanofluids Science and Technology*, John Wiley & Sons, (2008).
2. Liqiu Wang, *Advances in Transport Phenomena*, Springer, (2009).
3. Sebastian Volz, *Thermal Nanosystems and Nanomaterials*, Springer, (2010).
4. S.N. Sahu, R.K. Choudhury and P. Jena, *Nano-Scale Materials From Science to Technology*, Nova Publishers, (2006).
5. Zhuomin M. Zhang, *Nano/Microscale Heat Transfer*, McGraw-Hill Professional, (2007).

REVIEW QUESTIONS

1. What is nanofluid and why is it important in device cooling ?
2. What are the advantages and disadvantages of nanofluids?
3. What are the different methods of preparing nanofluids?
4. What are the major shortcomings of different theories on nanofluid thermal conductivity?
5. How does the thermal conductivity of nanofluids vary with temperature?
6. How does the particle concentration affect the thermophysical properties of nanofluids?
7. How convection in nanofluid is different from clear fluid flow?
8. What are the additional mechanisms in thermal convection which enhances heat transfer beyond that affected by property change?
9. Describe nanofluid convection in laminar and turbulent region, from scaling consideration.

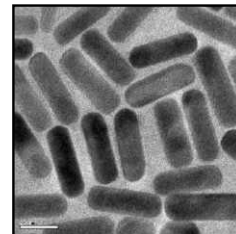
**PART
SEVEN**

Nano and Society: A Dialogue

- **Nano and World Societies**
Societal Aspects of Nanoscale Science, Engineering and Technology
- **Nano-Generated Wealth and World Societies**
Nano-Economics: A New Socioeconomic Divide?
- **Nanomaterials: World Societies and the Natural Environment**
The Rise of Nanotoxicology
- **Nano-Politics: Governance and Regulation of Nanotechnoscience**
Policy Debates and Public Engagement

NANO AND WORLD SOCIETIES

Societal Aspects of Nanoscale Science, Engineering and Technology



“What the future will bring us, we do not know. But the achievements of the past and of our own time show us what is humanly possible.”

Karl R. Popper (1963)

Popper, K.R., *Conjectures and refutations: the growth of scientific knowledge*, Routledge, London, (1989) 376, first published in 1963

Why does knowledge and understanding of the societal aspects of nanoscale materials-based science, engineering and technology matter? This section addresses and tries to explain the relevance of this and other key questions that have surfaced in contemporary debates on the opportunities and challenges of nanoscience and nanotechnologies and awoken scholarly interest. Is there any reason to believe that nanotechnology is harmful to society? Are societal concerns a problem only of the economically-advanced countries, or are they affecting poorer nations likewise? What has civil society movements prompted to stand up against nanotech? Are their worries and those of the lay publics justified? Who will enjoy the benefits of nano, and who will lose out? This kind of questions are presented and discussed against the backdrop of their actual and perceived repercussions for world citizens, communities, societies and the natural environment. Cross-perspectives I-III is a themed series of imagined conversations among members of the wider international nanotechnoscientific community. The purpose of presenting multiple perspectives on the pros and cons of nanoscale technoscience is to introduce the reader to the social and political environment, in which key-debates on nano-focused topics are held. Illustrative examples drawn from public discourses of Nano and Society are used as an entry point to provide first insights into what, why, and how, social scientists have begun to investigate, examine, and evaluate societal issues that have been associated with the advance of nanotechnoscience at national, regional, and global, scales. Excerpts taken from written and publically available sources help convey a sense of what is at stake and how the members of the many different stakeholder groups of the nano-enterprise have formulated the potential benefits and risks of nanotechnoscientific activities to secure sustained public approval and support for this young, but rapidly growing and bustling, field of research and innovation. By no means do these discursive fragments intend to produce an all-encompassing picture of the societal implications of nanotech nor does the coursework provide any conclusive answers to the questions raised. That is beyond its scope. A critical engagement with the ensuing discussions however, is not only desired, but required for an understanding of the problematised issues within their respective contexts.

Learning Objectives

- Get a general idea of what key-debates on the societal issues of nanoscale science, engineering and technology are about.
 - Begin to understand the scholarly interest and analytical focus of social scientists investigating nano-related phenomena and the practical importance of their research findings.
 - Be able to respond to why interpretative perspectives of various experts of the wider nanotech community have been deployed in this introduction, rather than a theoretical approach.
 - Become aware of the multiple and intertwined dimensions that give the social sphere of nanotech its paradigmatic complexity.
 - Understand the scope of this introduction as a preparation for the following chapters.
-
-

27.1 INITIAL REFLECTIONS ON A SCIENCE WITH A MISSION TO PROMOTE SOCIOECONOMIC AND HUMAN DEVELOPMENT

27.1.1 Nano: a Car, “Science of the Small”, or 0.00000...?

“Most Americans have not yet heard of nanotechnology, and many of those who have cannot offer a working definition of the term”,² reads the first sentence of the preface to *Nanoscale: Issues and Perspectives for the Nano Century*.³ Can the same be said of other world societies?

The rolling out of the smallest and cheapest car of the Indian automobile maker Tata Motors⁴ has helped popularise “*vāvoç*”—the Greek word for “dwarf”— throughout the Indian Subcontinent, and probably beyond. Even though Indians, akin to their fellow American citizens, may not provide a working definition for the term if asked, or get the number of zeroes after the decimal point right, they are likely to associate nano with smallness and unprecedented opportunities. “Now you can.” reads the marketing slogan of the “nano”, and its corollary sentences strike the same optimistic note: “Stop crossing your fingers. And biting your nails. Because your wait is over.”⁵ Even though this promotional motto has been created for giving a distinct identity to a car, so different from others in terms of size and affordability, it lends itself well to introduce some of the core issues other unprecedented technoscientific innovations have raised, such as nano-engineered solutions. The marketing slogan of Tata’s promotional campaign, in fact, leaves little doubt that it has been fabricated with expert knowledge, skill and care. In a nutshell, it gives the general public, including those having hardly any experience with cars, a broad idea about its distinct profile. And, the message evokes, or at least attempts to evoke, emotions.

Opportunities and challenges of nano-engineered products, devices and services that have been discussed in relation to their potential impact on the every-day life of world citizens, communities and societies because of their distinct characteristics, will be scattered through the prism of “*Now you can.*” This step-by-step approach is one possible way of beginning to question and examine the multiple and entrenched dimensions that give the social sphere of nanomaterials-based science and technology

its paradigmatic complexity. The transposition of the marketing slogan to contemporary, and yet unresolved questions pertaining to the societal realm of nanotechnoscientific development is meant to stimulate both interest and curiosity, as well as critical thinking about a science with a mission to promote socioeconomic and human development. For didactic reasons, this analytical approach will be made explicit in Cross-perspective I, and it is assumed that by the end of the first chapter, the reader will be sufficiently familiar with this method to make further guidance redundant.

27.1.2 Why “Cross-perspectives”?

The interpretative perspectives on the opportunities and challenges of nanotechnoscientific development in this section are unfolding in a flow of imagined conversations. This approach attempts to impart in the reader a sense of the pluralism in ideas and opinions that have contributed to influence and shape key-debates on the present and future benefits and risks of the commercial applications of nanoscientific research findings for humans and their habitat. The rationale of introducing the topic by means of “Cross-perspectives” is to foreground the coexistence and confluence of various kinds of thought, knowledge and expertise in contemporary discourses of Nano and Society. The confrontation of different views tries to shed light on how individuals, research teams and expert groups of the wider science and technology policy community (including, besides academic and industrial nanoscientists and nanotechnologists, business representatives and professional policy makers) consider and try to resolve conflicting situations that have emerged with the advance of nanoscale research and development (R&D). There can be no conclusive or exhaustive answers to the questions raised herein, for there are as many possible responses as there are ways of looking at the problems that have been associated with nanoscience. Even though the identified issues could be treated in an abstract, or say a theoretical way, their practical importance is emphasised in the discussions of core issues that have emerged from the interface between the social and the nanotechnoscientific life worlds.

An ever more internationalised and interdisciplinary research setting makes it nearly compulsory to consider the forms and ways, in which nano-related hopes and concerns have been brought to the public in countries of the developed and the developing world. Besides commonalities across institutional sectors and geographical regions, there are also differences in how individuals, expert groups and policy makers view and think about the opportunities and challenges of applying nano-based knowledge to promote socioeconomic and human development.

Discussions in scientific publications, policy reports, the media, and other interactive platforms, do not take place in a vacuum. They are situated in a specific tempo-spatial context. In the light of this, the issues discussed here are not treated as fictive or theoretical, but as actual and existing problems in concrete institutional settings. It goes without saying that the positions presented in *Cross-perspectives I-III* reflect individual and perhaps, vested, interests. People have views and opinions, and they hold positions in the communities and society in which they work and live. These initial reflections, in fact, are premised on the assumptions that there is nothing such as a “neutral” stance and secondly, that generalisations can not be made. Thus, the analytic focus is on the particular, the specifics of singled-out

and identifiable moments or situations that have received scholarly attention of both natural and social scientists, and policy makers.

It should be made clear at the outset that the presented discussions, which are no more than a collection of discursive fragments, do not intend to entice the reader to side with the supporters or the opponents of nanotech. Instead of acerbating existing ideological divides or attempting to streamline or “harmonise” conflicting positions, attention is paid to what constitutes yet unresolved controversies and how differently positioned experts have tried to find and negotiate viable solutions to those challenges. The premise upon which *Cross-perspectives I-III* rests, is the idea and belief that divergence in opinion can be instructive and, at the same time, be constructive too, if discussions are held in a spirit of mutual respect for diversity and pluralism of ideas and interests.

27.1.3 A Note on the Coursework

This coursework understands itself as an intellectual training and testing ground, on which to get acquainted with the *essentials*, so as to be prepared for taking part in informed discussions about the societal implications of nanoscience and nanotechnologies. In the course of this introduction into nano-centred key-debates, the reader will familiarise with what is at stake when questions of societal import are debated in the public domain. It is hoped that the study of these chapters will further a greater and deeper understanding of the multiple and diverse dimensions and aspects intrinsic to the multi-faceted and dynamic relationship between nano and society.

This introduction does not endeavour to give a comprehensive overview on nano in society. That is not the scope. Secondly, it would be rather difficult, if not all together impossible, to establish an all inclusive framework of the societal aspects of nanoscience and nanotechnologies. The open-ended questions intend to sensitise students and professionals, who have embarked on nanomaterials-based studies, research, development and innovation to reflect on the raised issues and the possible orientation and directions their scientific and engineering disciplines are taking. They also invite the readers to reflect on the eventual positive and negative effects of their present and previous work activities. Overall, it is hope that the study of the following chapters will support, encourage, and stimulate, critical thinking on the introduced topical issues, foremost because they leave little to no room for indifference. Because of their practical import and relevance, they deserve more than a mere afterthought.

27.2 STUDYING THE NANO-REALM

In *Anthropos Today: Reflections on Modern Equipment*, anthropologist Paul Rabinow⁶ writes that “even the smallest detail of daily life presents an ‘infinite multiplicity’ of possible things to know”.⁷ It seems, that in the exploration of the nano-realm, “there is plenty of room at the bottom”⁸ not only for natural, but social scientists, too. It looks like comparable opportunities existed for social scientists to generate a greater knowledge and understanding of nano-related phenomena, although in different ways. Social scientists also are confronted with similar challenges as nanomaterials scientists and

nanotechnologists are, in that they operate under conditions of partial knowledge in their exploratory, investigational, and interpretative research enterprises. Established scientific paradigms, analytical methods and approaches may not be applicable or suited for the study of nano-focused science and societal problems arising from nanotechnoscientific theory and practice.

Past attempts to frame societal issues of nanotechnologies in a comprehensive and all-encompassing way revealed problematic on numerous counts. A major problem with holism is its purview. That is its inadequacy for approaching highly complex phenomena in detail. Nevertheless, there have been social scientists and policy advisors who have attempted to provide a whole picture, albeit openly acknowledging the shortcomings of their holistic perspective. The limitations of the conceptual framework Ronald Sandler,⁹ for instance, has put forward in *'Nanotechnology: the Social and Ethical Issues'*¹⁰ to study real social and ethical issues are self-explaining. Sandler's analytical tool for studying the social and ethical implications of nanotechnoscientific development excludes the workplace, and professional ethics in the classified categories he proposes, in spite of endorsing by now diffused demands for a responsible development of nanomaterials-based science and technology.¹¹ Supposing these technoscientific advancements were to progress in socially responsible ways, one could probably ask if the workspace of nanoscientists, engineers and technologists should not be at the centre, rather than at the periphery, of empirical inquiries into Nano and Society. It might be worth recalling that by definition, the generation, dissemination, and the use of technoscientific knowledge, regardless of where it falls on the metric scale, are intrinsically social processes.

Bibliometric data on Nano and Society publications indicate a growing scholarly interest in the social issues and concerns associated with the growth and expansion of nanoscience-related disciplines. Although the number of published work is on the rise, it should not get unnoticed that there have been considerably fewer publications in science and technology studies (STS) devoted to nanotech in low- and middle-income countries. In an attempt to counterweight this noticeable imbalance, the ensuing discussions include views and positions of South-based scholars and research scientists, policy advisory committees and policy-makers, to illustrate, with concrete examples, how economically and scientifically weaker countries have taken up controversially discussed questions related to Nano and Society.

27.3 CROSS-PERSPECTIVES I-III

The question of who will benefit from nano-based innovations and who may lose out is so central to the Nano and Society debate that it will be discussed on various occasions throughout this coursework. The propositions and arguments put forward reveal that the socioeconomic development status of a country can be, but not necessarily is, a decisive factor of how questions of equality and equity in respect to nanoscale technoscientific advancement are presented and conceptualised in contemporary discourses. Scholars, researchers and policy-makers of developed, and advanced developing, countries that have opted for promoting nanoscience seem to struggle with similar issues. Commonalities can be found in negotiations on research priority-setting in national science, technology, and innovation agendas, the allocation of public resources for nanotechnoscientific research and development (R&D), governance and regulatory settlements, such as the opening or restriction of emerging nano-centred

markets and businesses, and even in deliberations that are not directly linked with public science and technology investment policies.

Discussions in *Cross-perspective I* focus on controversies that have emerged in public debates on the potential socioeconomic benefits of nanoscientific research and innovation to alleviate world poverty. Whilst some commentators of the developed, as well as the developing, world are outspokenly optimistic about the socioeconomic potential of nano-engineered solutions, others keep a rather sceptical stance on overcoming developmental inhibitors with the application of commodified nanotechnoscientific knowledge. Yet another aspect that will be problematised in the context of nanotechnoscience-powered world economies relates to the difficulties of forecasting possible impacts of nanoscale research and innovation on life-systems since technoscientific developments do not necessarily follow a predictable path or trend. Groundbreaking work achieved in the nano-realm is difficult to be compared with earlier technoscientific phenomena chiefly because of nano-engineered matter's distinctiveness. This is significant in at least two respects. The drawing of analogies, albeit its methodological appeal, can be misleading, as the comparison of the intensely and controversially discussed digital divide with a potential nano-divide brings to light. It also would be untenably reductionist and simplistic to assume the trajectory of bionanotechnological engineering were similar to that of genetic engineering. Even though some commentators have considered nanobiotechnology as a natural continuation of biotechnology, there are significant differences that deserve analytical attention and reorientation. Problems that are specific to nanoscale science, engineering and technology, and which may, or may not have materialised in the course of previous "technological revolutions" therefore, receive particular consideration.

Concerns about possible health, and environmental, risks that have been associated with nanomaterials are introduced in *Cross-perspectives II* and discussed in the context of the rise of a novel nanoscale science and engineering discipline. If nanotoxicology can keep up with the developments of its fellow disciplines is among the questions that will be discussed in greater detail. The scientifically disputed role of size of matter will be discussed against the backdrop of research findings on nanomaterials toxicity suggesting that size is just one dimension, but not necessarily the decisive factor to determine the potential hazardous nature of nano-engineered compounds. In light of existing fears of the down-sides of nanotechnologies among the wider public, particular attention is given to health and safety issues in the laboratory. The laboratory is the immediate environment of the academic and industrial scientist and technologist and also, it is one of the primary locations where potential opportunities, but also risks of nanotechnoscientific research, development and innovation can materialise.

Governance and regulatory issues, and the ethical aspects of nanoscience and related technologies are addressed in the last chapter of this introductory coursework. *Cross-perspective III* includes discussions of how persisting knowledge gaps affect the work of scientists and policy-makers in decision-making. This concluding section provides an excellent opportunity for the reader to recapitulate how the scientific, political, legal and regulatory, financial and economic, social and ethical dimensions, of nanotechnoscience translate into each other and affect one another. For instance, a particular concern about a publicly disputed innovation framed and understood as an ethical issue, because scientific

evidence proves its harm outweighs its benefit, is likely to translate into a regulatory issue that later may become a law, having repercussions for the scientific development of nanoscale materials-based research and innovation, and with a potential backlash on the nano-economy.

Before getting started, it might be apt reiterating that students, researchers, scientists and technologists, studying and working in nano-centred disciplines, and their respective workplaces, can not be taken out of the equation of a responsible development of nanotechnologies.

REFERENCES

1. K.R. Popper, *Conjectures and refutations: the growth of scientific knowledge*, Routledge, London, 1989 (1963), 376.
2. All referenced quotes in speech marks [...] are as in the original text, with exception of spellings that differ from British Standard English (BSE). All views expressed in this section reflect those of the author and any misunderstanding or misinterpretation of referenced passages is the author's sole responsibility.
3. N.M. de S. Cameron and M.E. Mitchell, (Eds.), *Nanoscale: Issues and Perspectives for the Nano Century*, John Wiley & Sons, Hoboken, New Jersey (2007), xvii.
4. The brand name of the car in question is "nano".
5. The marketing slogan can be accessed at [http://tatanano.inservices.tatamotors.com/tatamotors/\(05.07.09\)](http://tatanano.inservices.tatamotors.com/tatamotors/(05.07.09)).
6. P. Rabinow is Professor of Anthropology at the University of California (Berkeley), Director of the Anthropology of the Contemporary Research Collaboratory (ARC), and Director of Human Practices for the Synthetic Biology Engineering Research Center (SynBERC), USA.
7. P. Rabinow, *Anthropos Today: Reflections on Modern Equipment*, Princeton University Press, New Jersey (2003), 35.
8. 'There is plenty of room at the bottom' is the title of the infamous talk Richard P. Feynman presented to the Annual Meeting of the American Physical Society in 1959.
9. Ronald Sandler is Assistant Professor of Philosophy and a Member of the Nanotechnology and Society Research Group at Northeastern University, USA.
10. R. Sandler, *Nanotechnology: the Ethical and Social Issues*, Woodrow Wilson International Centre for International Scholars, Washington D.C., 2009, p. 21, available at http://www.nanotechproject.org/process/assets/files/7060/nano_pen16_final.pdf (05.07.09).
11. *Ibid.*

ADDITIONAL READING

1. W.S. Bainbridge and M.C. Roco (Eds.), *Managing nano-bio-cogno innovation*, Springer, Dordrecht, (2006).
2. J.S. Hall, *Nanofuture: What's next for nanotechnology?* Prometheus Books, Amherst, New York, (2005).
3. N. Invernizzi, G. Foladori and D. Maclurcan, 'The role of nanotechnologies in development and poverty alleviation: A matter of controversy', *Journal of Nanotechnology Online* (AZojono) (2007) available at <http://www.azonano.com/details.asp?articleid=2041> (12.09.09).

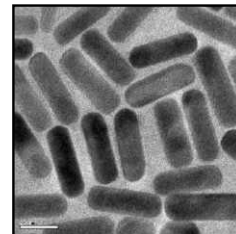
4. M. Leslie, 'Gauging nanotech risks', *Science* 309 1467 (2005).
5. P. McCray, 'Will small be beautiful? Making policies for our nanotech future', *History of Technology* 21(2) (2005), 177–203.
6. A. Gelfert, 'Nanotechnology as ideology: towards a critical theory of converging technologies', *Science, Technology & Society* 171 (March 2012), 143–164.

REVIEW QUESTIONS

1. Why and how has the marketing slogan of India's smallest car been used in the opening of the introduction into key-debates on Nano and Society?
2. What is the purpose of exploring and examining the societal aspects of nanoscale science, engineering and technology by the means of "Cross-perspectives"?
3. Discuss who constitutes of the wider nanoscale science and technology policy community?
4. Why is there "plenty of room at the bottom" not only in the natural, but the *social sciences*, too?

NANO-GENERATED WEALTH AND WORLD SOCIETIES

Nano-Economics: A New Socioeconomic Divide?



“Though, our generation might not see the fruits of nanotechnology, I have been pursuing this. I want India to be in the forefront of nanosciences. Young scientists should venture [into nanosciences] and not be afraid, and the country should liberally fund.”

C.N.R. Rao (2006)

Quoted from Somasekhar, R., ‘CNR Rao—the evergreen researcher’,
The Hindu Business Line, 03.01.2006, available at <http://www.thehindubusinessline.com/2006/01/04/stories/2006010403480900.htm> (21.06.09)

The supporters of nanoscience and nanotechnologies trust the generation, dissemination and use of nanotechnoscientific knowledge will contribute to socioeconomic development, growth and greater well-being. But, will “nano-generated wealth” benefit world societies at large? Will public and private investments into nano-focused education, and research and development (R&D) pay off? And if so, when is it to happen? The critics of nanoscale science and technologies question the opportunities and benefits of nano-engineered solutions as their focus is on their potential risks. The first signs of emerging forms of exclusion along socioeconomic fault lines have alimanted fears of a new global innovation divide. No matter how divisive the presented views are, the stakeholders of the international nano-enterprise are aware of the possible negative externalities scientific breakthroughs in the nano-realm engender. Even if these challenges are still difficult to establish and validate because of the nano-economy’s infancy stage, members of the wider science and technology policy community have become susceptible to fears of an imbalanced distribution of scientific, and economic nano-wealth. Three key issues that have been intensively debated in the context of growing and expanding nanomaterials-based commodity markets will be introduced by scattering them through the three corollary sentences of Tata Motors’ nano marketing campaign “Now you can”. These are the “nano-hype”; the “nano-divide”; and the “nano-business”.

Learning Objectives

- Acquire a basic understanding of the controversies surrounding the three presented key issues.
- Be in a position to explain the origins and the underlying relationship between the controversially discussed concepts that have emerged with the “Nano century”.

- Ability to set into context problematic issues related to public and private investment in nano-focused education, teaching and training, and research and development (R&D) in institutional settings of a) developed and b) advanced developing countries.
-
-

27.1 DISENCHANTING NOW YOU CAN I: THE “NANO-HYPE”

27.1.1 “Stop Crossing your Fingers.”

According to the Indian car manufacturer Tata Motors, the company has delivered a technological solution that meets people’s apparent need for unlimited mobility, in India and beyond. Can the same be said of nano-engineered solutions? Are they, or will they be made available through local and global market systems and mechanisms to the end-users as promptly and timely as the marketing slogan—‘Now you can’—promoting the car named ‘nano’ promises? Will they, or could they, correspond to the needs and desires of people aspiring for an ever-more “modern” lifestyle? Or, are we witnessing the culturing of needs in laboratories, where future nanotechnological solutions are being researched and developed for a better, healthier and more comfortable life? Disputed, and yet unresolved questions of availability and affordability of nanotechnology-based consumer products and services are likely to entice those who have a stake in the nano-enterprise to keep their fingers crossed.

Scientific claims raise hopes and expectations, especially if they revolve around something unprecedented: a novelty. News reports about the potential and future applications of groundbreaking discoveries and developments made at the scale of the nanometre abound in the mass media. But, will these scientifically informed claims really meet what they promise? M. Ellen Mitchell² analysed the promises of nanoscientific research findings in the media and concluded “the recent decades have been fertile with findings and seeming facts that eventuate to be wrong, incomplete or even dangerous.”³ In her study of the effect of inflated hopes and expectations scientific claims and propositions can produce in the mind of the lay publics, Mitchell argued that it would be of less relevance whether these claims were true or false. What they represented would matter more, than what they actually were because “in the absence of sound and reliable information, conjecture and speculation have as much meaning and values as anything else.”⁴

A greater knowledge of how the nano-hype influences the way people view and think about the actual and potential applications of nanoscientific research findings to every-day life is important to understand the wider public’s attitudes to nanoscale materials-based innovations, since “the attitudes of the public are influenced by tendencies and biases in estimations about the potential impact of future events.”⁵ For nanoscale materials-based disciplines and businesses, public acceptance is critical on a number of grounds. Supposing a state authority were to evaluate a public quest for a general nanotechnology moratorium positively, then the prospects of these still young scientific and engineering disciplines would look rather daunting in that country.

With psychological insight, Mitchell described the underlying working mechanisms of the nano-hype, how it impacts the human mind and in what ways it shapes people's attitudes towards the advance of nanotechnologies. "The magnitude of the gap between the over-inflated promise and the severely contrasting reality contributes to greater amplitude in the emotional circle. The alternating high hope and steep disillusionment cycles have an impact on internal states like mood, as well as on views of, and beliefs about, external events like scientific advances gone awry."⁶ Whilst disentangling nano-related claims, Mitchell uncovered the "elusive truth" which is at their core. The popular and diffused belief about the potential application of nanoscience and nanotechnology to virtually everything is one of them. Nanoscientists and nanotechnologists know well that this can not be the case. But, does the general public have knowledge about the technical and practical limitations of building novel materials from scratch?

Another critical question the nano-hype raises relates to who has interest in exploiting the gap between what is being promised and what can actually be delivered. Is it just the mass media? In a book entirely devoted to the nano-hype,⁷ David Berube⁸ argued that this was not necessarily so. It would be too simplistic to blame the mass media for the presence of "*nano-hyperboles*" in public domains. The empirical research findings of Berube's cultural study of nanoscience and nanotechnology communication leave little doubt that scientific claims can be used, and rendered functional, for the attainment of strategic goals and objectives by members of the nano-business community, which includes industrial leaders, bankers, investors, researchers, reporters, visionaries, bureaucrats, and others.⁹ In his understanding, they all are players in the emerging nanotech enterprise, whose global market value is reported to reach USD 2.5 tr by 2015, regardless of global recession trends.¹⁰

In her comment on Berube's interpretation of the nano-hype as "a cycle of hope, hype, inflated expectations, disillusionment, and then a shake out period of enlightenment,"¹¹ Mitchell observed: "The question that remains unanswered, however, pertains to the cost of such cycles in terms of actions not taken, cultural mood, and individual responsibility. The manufacture of desire has an attendant corollary of dissatisfaction with the present. Chronic cycles of hope and disillusionments make for moods filled with dissatisfaction and longing. Thus, hype about the future also foments discontent with the present and gives rise to cycles of seeking that can never really be gratified."¹² What she has tried to highlight, besides people's cultural disposition to accept and embrace technoscientific innovations and the responsibility of those making scientific propositions, are the cost implications of the nano-hype phenomenon. These are relevant in policy-focussed debates on nano and society insofar they have potential to influence and direct financial decisions, such as public investment in technoscientific research and innovation, and whose fruits might not be harnessed and enjoyed by the present generation, as C.N.R. Rao foreshadowed.

Inflated hopes and expectations the nano-hype generates furthermore risk diverting the focus not only from alternative and more economical solutions to environmental and developmental problems and challenges, but risk to sideline the possible social inequalities and inequities resulting from the advance of nano-centred innovation. Projections of the potential contribution of nano-generated wealth to lift the economic status of nations and the well-being of populations globally may look promising, but if they can keep, what they tell, is difficult to establish.

27.1.2 Mixed Feelings about Nano-powered World Economies

Opinions about the potential of nanomaterial-based health and environmental technologies to contribute to poverty alleviation, better health, and higher levels of well-being differ remarkably. If nano-engineered solutions can promote global economic growth, prosperity and peace have been intensively discussed on national and international interactive platforms. A prominent question in debates on nano-powered world economies relates to the direct and indirect costs of opting in or opting out of nanotechnoscience. Because of the controversies about “actions not taken” it is felt opportune to explore how representatives of the various interest and stakeholder groups constituting the global nano-enterprise have discussed present and future economic opportunities and benefits of nano-focused research and development (R&D).

Nanoscale materials-based science and innovation requires large up-front investments. Even though the private sector plays a central role in the nano-business, the private sector alone can not shoulder the large R&D costs. Leaders in politics, and academics, with trust in the socioeconomic potential of nano-engineered goods and services have urged their governments to liberally fund nanoscale materials-based education and training. It is noteworthy that public funded nanoscience programmes and public-private R&D partnerships have been established not only in the world’s most advanced economies. Advanced developing countries also have begun to allocate government funds to national nanoscience and nanotechnology initiatives so as to create and promote opportunities for local scientists and engineers, and to build and develop national capacity and strength in research areas of advanced science and technology with the aim to enhance their level of international competitiveness and global positioning in niche markets.

Public investments have opened up not only prospects for South-based innovation driven institutions to participate in international academic and industrial nanoscale research, they also have triggered controversies about their appropriateness in scientifically weaker countries. A UK-based policy advisory committee¹³ extensively discussed the problem of “actions not taken” in respect to knowledge-based socioeconomic development. This expert working group cautioned about the risk of excessive hopes about the developmental potential of nanomaterial-based health and environmental technologies. “A parallel danger that could arise if the more radical ‘visions’ of the promise of nanotechnologies were realised, is that enthusiasm for developing a ‘technical fix’ to a range of global and societal ills might obscure or divert investment from cheaper, more sustainable, or low-technology solutions to health and environmental problems.”¹⁴ Dough Parr,¹⁵ a consultant to the RS working group, also expressed mixed feelings about the socioeconomic benefits of nanomaterial-based solutions for people living in developing countries. Parr approved of their potentially beneficial applications for poverty alleviation, but he also voiced concern about nanotechnologies becoming yet another “opportunity lost” for low- and middle-income countries.¹⁶

27.1.3 North-South Perspectives on Nano as an Economic and Developmental Power-engine

The concentration of nanoscale science and engineering activities is undisputedly higher in some parts of the world than in others. This implies that the accumulation of economic value, generated

by nano-based assets, is more pronounced in geographical areas where intense nanoscale materials-based R&D activity is high. The uneven distribution of capital gains from investments in nano-focused research and innovation has been brought in connection with a new *innovation divide*. The general recognition that the contingency costs of “actions not taken” are linked with “opportunity lost” is relevant insofar projected socioeconomic opportunities and benefits inform, influence and shape high-level policy making.

Nanotech sceptics expressed fears that excessive hopes and expectations of nano-generated wealth and prosperity—nano-wealth, in short—could easily be exploited and rendered instrumental in the assignments of research priorities on national, regional, and even international science, technology and innovation agendas. Their assumptions provide sufficient reason to question portrayals of nano as a global “economic and developmental power-engine”.

In her analysis of state-commerce interactions and public investment of developing countries in large-scale science projects, Carin Holroyd¹⁷ contested the assumption that the higher research concentration in the North implicated that low- and middle-income countries were disadvantaged. “It emphasises the continuing discussion about the competitiveness of nations, the global restructuring of manufacturing and the challenges facing industrial nations, as countries the world over struggle to respond to the rise of industrial China and India and seek to maintain current levels of prosperity. The theme emphasises the growing challenges of raising the economic prospects for emerging nations; those who wondered how the poorest countries would respond to the challenges of freer global trade in manufacturing have difficulty imagining these same states competing in the fields of synchrotron science and nanotechnology.”¹⁸

One session of the 2007 World Science Forum ‘Investing in Knowledge: Investing in the Future’¹⁹ interrogated the economic and developmental opportunities of advanced science and technology, including nanotechnology, for poverty alleviation. The meeting concluded: “Science and Technology are keys to Millennium Development Goals (MDGs) achievements. Governments have to focus on investment in education (technological developments in education and in teaching), in cutting-edge technologies (biotechnology, space sciences and technologies, nanotechnology) and in infrastructure [...] The role of government is to involve the private sector in the financing of R+D+I (Research, development and innovation) activities. These policies should be integrated with policies of other fields.”²⁰

Statistical data of global public R&D expenditure²¹ over the past decades reflect the strife of developing countries to compete at international levels, as Holroyd pointed out. These figures indicate a trend suggesting that government funding for higher education and state-of-the-art research infrastructure has been progressively increasing in low- and middle-income countries with a growing science capacity.²² These trends invite a closer examination of claims projecting a new innovation divide along the classic socioeconomic fault line of North and South. Unsurprisingly then, what we may call the “*nano-devise*”, like the nano-hype, is a conceptual notion that has originated in the West.

27.2 DISENCHANTING NOW YOU CAN II: THE “NANO-DIVIDE”

27.2.1 “Stop Biting your Nails”

Despite the comparably low cost of Tata’s nano, it is obvious that not everyone will benefit in the same way of this technological innovation. Not all people have the means and entitlements, in terms of knowledge, skills, economic and social freedom required to drive even one of the cheapest cars on the international automobile market. Similar observations could be made regarding nanoscale materials-centred innovations. Should these turn out to be as revolutionising as they have been presented to the publics, who would benefit from those nano-engineered solutions? For whom would they be designed and whose needs would they meet?

Questions of this kind have surfaced in public debates on the socioeconomic implications of nanotechnologies. These uncomfortable, yet important, questions are closely linked with the socioeconomic opportunities and benefits that nanomaterial-based health and environmental technologies impart for some people, while excluding others.

With the market entrance of nano-engineered commodities (i.e., products, processes, methods and systems), issues of access and affordability have become more prominent in contemporary discourses of Nano and Society. Concerns about a new societal divide growing out of global disparities because of unequal access to, and distribution of, nanotechnoscientific knowledge, goods and services have flared up and given rise to much controversy even within the nano-community.

27.2.2 The Origins of the “Nano-divide”

The notion of “nano-divide” first appeared in a publication on the societal implications of nanotechnologies. Mihail C. Roco²³ used this concept to describe the hypothesis of a new social fault line between countries with significant differentials in nanoscience research and innovation capacity that has begun to unfold with the advance of nanotechnologies. “Another potential consequence that would need to be addressed is the potential increase of inequality in the distribution of wealth that we may call the ‘nano-divide’. Those who participate in the ‘nano-revolution’ stand to become very wealthy. Those who do not may find increasingly difficult to afford the technological wonders that it engenders.”²⁴

Roco’s phrasing at that time was vague, even visionary. In the early years of the 21st century, there were insufficient signs to make a strong case for what he called “second-order consequences”. A few years later, the RS working group debated Roco’s idea of a possible nano-divide. “Concerns have been raised over the potential for nanotechnologies to intensify the gap between rich and poor countries because of their different capacities to develop and exploit nanotechnologies, leading to a so-called ‘nanodivide’. If global economic progress in producing high-value products and services depends upon exploiting scientific knowledge, the high entry price for new procedures and skills (for example, in the medical domain) is very likely to exacerbate existing divisions between rich and poor.”²⁵

Even though the commodification and commercialisation of nanoscientific knowledge may widen socioeconomic disparities between the developed and developing world, the critical question here

is not just about opting in or opting out of nanoscale materials science, but the appropriateness of comparing technoscientific innovation divides to gain knowledge and predict future trends. In short, it is a methodological question with epistemological implications. Roco, the RS working group and other scholars have adopted comparative research methods in their social science analyses. Some have compared and contrasted the potential risk of a nanotech innovation divide between societies of the developed and developing world with the “digital-divide”.²⁶

27.2.3 The Non-recursivity of Technoscientific Innovation Processes

Why the nano-divide is *not* a natural continuation of earlier innovation divides is an intriguing question. All too often analogies have been drawn in discussions of the societal impacts of nanotechnologies. A major problem with deploying analogies to forecast future trends partly resides in the difficulty to identify and establish the truly matching elements that constitute the investigated phenomenon. Innovation divides are not mere replicas of previous factual events and trends in technoscientific development.

Holroyd compared a number of different innovation divides by positing them into relation with one another and observed that “the concerns raised by the earlier debate over the digital divide could pale in comparison to those generated by the innovation revolution.”²⁷ And, she regretted that neither the “nano-divides” nor the “biotech-gaps” received comparable attention in public science and technology debates. So tempting the search for analogies might be, it can be argued that the nano-divide is quite different from its precursors, not the least because of the often-stated wide ramification of nanotechnologies. Therefore, it is unlikely to witness a repetition of previous technological divides held accountable for having driven societies of the developed and the developing world further apart. Events and processes related to scientific discovery and invention are not recursive occurrences. They do not necessarily share common patterns even if, at the outset, that seems to be the case.

The non-recursivity of innovation processes renders the use of analogies as proxies to explain possible consequences of the application of nanoscientific knowledge to every-day needs and wants problematic. This helps explain why it is so challenging a task to specify and make predictions of how, and whether, commercially available nanomaterials-based products will unleash societal changes comparable to those of the semi-conductor revolution. To recall, the latter has paved the way for the information age and significantly contributed to the growth and worldwide expansion of knowledge-based economies and information societies. Social sciences research into the ways in which societies across the globe embrace and adapt to nano-induced transformal changes may contribute to establish the chances of a global “nano-society” emerging from a nanotechnological revolution.

27.3 DISENCHANTING NOW YOU CAN III: THE “NANO-BUSINESS”

27.3.1 “Your Wait is Over”

Tata’s nano has been designed and developed for both, domestic and global markets even though the car’s intellectual creator reportedly had in mind an Indian family, sitting in four or five on a motor-scooter,

when he designed what eventually became not only India's, but one of the world's most economic four-wheel cars. Will nano-engineered solutions be designed, developed, and marketed in comparable ways? Will nano-focused R&D create new employment and business opportunities, incentivise national economies and create socioeconomic prosperity as countless news articles predicted?

Questions of this kind are pertinent to projections of the global nano-business volume and the distribution of nano-based economic and scientific wealth. They speak to the socioeconomic as well as the socio-cultural disparities reflected in the visible imbalance of the global distribution of wealth-generating resources. Does this disequilibrium signify that without nanoscience there will be no nano-wealth? However reductionist such a statement may seem it brings into perspective the cost implications of Mitchell's remarks on "actions not taken" and Parr's on "opportunity lost".

As it has been mentioned earlier, nanoscale research and innovation are a resource-intensive undertaking. Whether to invest in nanoscientific R&D, or to wait and see, is not an easy to take decision. Both options entail actual direct costs, and opportunity, costs. Nano-economic studies revealed that the public financing of nanotechnology can be a rather thorny topic for policy-makers because of the contentious interplay and power-play between and among scientific, political, and business interests. It need hardly be said that science and innovation financing policy negotiations have potential to create tension among the numerous stakeholders and interest groups of the nano research and business enterprise. At stake are not only state-funded education, teaching and research in nanoscale materials-based disciplines, but also the commercial exploitation of nanoscientific research findings, emanating from government-sponsored nanoscale science, engineering and technology innovation programmes.

27.3.2 Preparing the Terrain for Domestic and International Nano-businesses

Laying the grounds for the nano-business, a knowledge-based business, is cost-intensive. Without substantial and sustained public and private-sector investment in science-driven institutions, infrastructure, and human resources, competitive participation in global nano-centred research and innovation is unattainable.

C.N.R. Rao²⁸ proposed that ideally two to three percent of a country's gross domestic product (GDP) should be allocated for higher education, and at least one percent to science and technology.²⁹ Similar investment propositions were advanced during the 2007 World Science Forum, signally that other developing nations have also begun to consider the channelling public funds to domestic nanoscience and nanotechnology initiatives. In her analysis of the socioeconomic potential of nano-based innovations, Holroyd called to mind that economic prosperity correlates with the capability of national economies to switch to state-of-the-art manufacturing systems and processes to become, and stay, internationally competitive.³⁰ From her observations emerges that public and private investment in advanced science and technology programmes is critical for a country's technoscientific capacity and international competitiveness.

Government funding requires sustained political and financial commitment not only of the science and technology policy groups and networks, but the wider society. India and China have both opted for nanoscale sciences and technologies to invigorate their domestic economies through the creation of nano-based employment and business opportunities. Compared to their counterparts in the developed world, the political and intellectual leaderships of countries with emerging economies, wanting their nation to be competitive in advanced fields of research, face additional challenges. It hardly needs mentioning that the financing of nanoscience is a politically sensitive subject, especially for policy-makers and scientists of developing countries, foremost because of the difficulties to assess the actual potential of nano-engineered solutions to boost socioeconomic growth, prosperity and overall wellbeing. An additional constraint represents the fact that the direct costs for developing countries to participate in the global nanotech enterprise are multiplied because the cost implications of “actions not taken” and “opportunity lost” are working both ways.

To internationally competitive, countries with developing and emerging economies need to prioritize public investment in science and technology over other, and eventually, more basic needs.³¹ Holroyd considered the controversially discussed pros and cons of science and technology investment policies in different parts of the world and remarked: “The innovation conundrum draws attention to the impact of the new economy on the global economic order and adds a major agenda item to the debate about appropriate strategies for addressing the social, environmental, and economic needs of the world. Moreover, the changing pace of innovation and the increasing difficulty in determining the likely commercial outcome of innovation investments clearly present national and regional governments with perplexing choices as they endeavour to support and create competitive economies.”³²

27.3.3 Catching up with the Global Leaders

Questions of how close, and how advanced national nanoscience programmes are in different parts of the world have been controversially discussed. Expert views on how low “nano-fruits” hang, or how long they take to ripen in different geophysical and political climates can oscillate between outspoken optimism and scepticism. Their underlying arguments may be no less conflicting than what the disputed nano-divide has brought to light.

V. Srivastava³³ commented on the development status of India’s nano-business, saying “India is not too far behind the world in nanoscience. In nanotechnology activities, especially in private sector, the differential between India and the developed nations is closer to five to seven years.”³⁴ But, is India truly catching up with the global leaders of nanoscience and technology? And if so, what are the indicators for measuring nanoscientific productivity, aside from the numbers of scientific publications, citations and patents?

Of comparable importance in this context are questions related to the adopted measures and interventions, in other words “actions taken”, that have catapulted countries with emerging economies in an advantageous position to engage with nano-focused research and innovation internationally. In position statement about India’s participation and competitiveness in the global nano-enterprise,

Srivastava reportedly identified the following factors as critical: strength in a particular nanoscale materials-based research area (e.g., nano-fluid sensors); private-sector involvement (e.g., start-ups); and a dedicated venture capital fund for nanotechnology initiatives.³⁵ In his reply to the question of what fuels nanotech research and innovation in China, Chunli Bai³⁶ adopted a similar position. “In China, government priorities, public needs and rising demand for new materials at home and abroad are among the factors contributing to advances in the field [...] Developing countries, such as China and India have also begun to look to the growing private sector for financial support for nanoscience and technology R&D. This trend should help to add new sources of capital, and improve the prospects for public/private partnerships that combine the research skills of universities and research institutes with the entrepreneurial skills of private firms.”³⁷

Considering the optimism of scientists and policy-makers of developing countries about the potential social and economic benefit of nanotechnologies, why then have economists and social, and political, analysts of the world’s most advanced economies cautioned about a widening gap between the highly industrialised countries and the developing world? A critical reflection on this question helps elucidate the visible differentials in how actual and perceived imbalances in the global distribution of economic and scientific nano-assets are conceived, conceptualized, and understood.

27.3.4 The Role of Nano-politics in Directing the Advance of Nanotechnologies

The pros and cons of developing world countries’ engagement with the global nano-enterprise have been discussed in terms of opportunities and challenges. Nanoeconomics experts have commented on the risk of developing countries’ losing out as early as the RS working group warned of significant risks that “some short-term developments in nanotechnologies will be exclusive to those who already own wealth and power, to the detriment of wider society.” But, in the same report these experts also mentioned the potential benefits these investments encompass for low-and middle income countries. They maintained that “equally, opportunity to apply nanotechnologies in ways that will benefit developing countries should not be overlooked.”³⁸

In spite of Bai’s outspoken optimism regarding “big payoffs” of government-funded nanoscience programmes, he voiced similar concerns. “A critical question is whether research in this field will focus on providing products or services that will serve the needs of poor people in developing countries, for example super-sensitive water filters to improve access to safe drinking water, or whether it will instead focus on upscale markets in developed countries to produce, for example, stain resistant trousers.”

These observations open up a wider range of questions about how, and if, future trajectories of nanotechnologies could be directed towards the resolution of developmental and environmental problems rather than commercially attractive user-oriented innovations. Should government authorities intervene to prevent and mitigate the possible negative consequences of a potential nano-divide? And if so, what regulatory actions could a State adopt and implement to redirect the course of nanoscale science development?

If developing countries do not feel excluded, but on the contrary, conceive themselves as international competitors on the forefront of global nanoscale science and technology, it becomes difficult to discuss how the consequences of inequalities and inequities in the global distribution of nano-wealth could be addressed and redressed. Such incongruences shed light on why even well-intended government-funded international development interventions have potential to constrain bilateral, and multi-lateral, relations between countries of different economic strength that have decided to invest public funds in nanoscale materials science.

To the foregoing question of how to rectify an eventual nano-divide, Bai replied, “the involvement of scientists from developing countries could help to ensure that the global R&D agenda achieves a balance between the marketplace for upscale products and services and the United Nations (UN) Millennium Development Goals.” In contrast to the sceptical voices of some Western commentators about public investment in nanotechnologies, Bai maintained that “nanoscience and technology are among the few fields where cutting-edge research can translate into immediate benefits to society. That is good news for science and societies everywhere. It provides just one of many reasons why the world needs the full and active participation of scientists in the developing countries.”³⁹ Despite their scepticism, the RS working group expressed a similar position for it acknowledged that “nanotechnologies could offer new opportunities for some developing countries to participate more directly in global technology through their own initiatives.”⁴⁰

From the other end of this polarized spectrum, Holroyd voiced doubts about the actual benefits of public investments plans for national high-tech research in developing countries. “Governments around the world speak enthusiastically, but without context and understanding, of reproducing the Silicon Valley model in their countries.”⁴¹ Her reservations relate to the difficulties with predicting the social benefit of nanotechnological innovations. “Even as governments are pressed to increase their commitment to the area, it is too early to determine the benefits of the investment in the science and technology, let alone the commercialisation of research results.”⁴²

Some may agree, others disagree, with the statements portrayed, but what is essential here is to discuss and evaluate the cost implications of “actions not taken” and “opportunity lost” within their respective social, and institutional contexts. The comparison and juxtaposition of these views and positions has served to elucidate why it is that joint investment in the nano-business can, but need not be a zero-sum game.

27.4 AN ETHICS PERSPECTIVE ON THE GLOBAL TRADE WITH NANOMATERIAL-BASED TECHNOLOGIES

The internationalisation of academic and industrial nanoscale research and innovation, together with an intensified competition in nano-focused R&D worldwide, have contributed to reduce the time required for translating scientific research findings into a marketable commodities. As the number of commercially available nano-based commodities is on the increase, questions about their eventual application to reduce the global burden of development-related problems, such as food insecurity, inappropriate health and sanitation, environmental degradation and other priority issues on the

international development agenda, have become more prominent in the Nano-Society discourse. Questions about the availability and affordability of nano-engineered solutions brings into focus critical aspects of nanotechnological innovation, such as sustainability and equity.⁴³

At a high-level Global Health conference, Margaret Chan⁴⁴ drew attention to a widening of the world's socioeconomic divide. "The gaps and inequalities that we are all trying so hard to address are likely to grow even greater. The price of failure will keep getting higher."⁴⁵ Parr and Mitchell's observations resonate in Chan's speech. Access to high-tech solutions inevitably bring up questions of their affordability.

Given the high up-front investment nano-centred R&D requires, it is legitimate to ask whether low-cost manufacture of nano-engineered products, which heavily depend upon industrial bulk production, will be attainable in the foreseeable future. Ashok Raichur⁴⁶ discussed the practical constraints impinging upon the commodification and commercialisation of nanoscientific research findings that are of interest and relevance to low- and middle-income countries. "With demand rising in developing countries, using nanotechnology to produce clean and safe drinking water seems a viable option. But making the leap to commercial applications is complicated and still is a distant goal for most developing countries. Just producing nanomaterials in quantities large enough for industrial applications is challenging and can be expensive."⁴⁷ No matter if it is a commercially viable, or a not-for-profit commodity, it is the principle of economies of scale, which is critical in determining the cost structure of nano-engineered solutions, and hence, their affordability.

Nigel M. de S. Cameron⁴⁸ investigated concerns of equality and equity in the context of using nanotechnology to improve people's life expectancy and quality of life.⁴⁹ His research focused on the medical application of nanotechnology, in particular nano-engineered health diagnostics and therapeutics. Cameron observed that people's assumptions of everyone benefitting in similar ways from technological advance are considerably high and could be linked with common beliefs about their ability to help defeat virulent diseases. Similar to Mitchell, who remarked that "medical science has bestowed incredible advances upon us that have improved the quality of life of many, but there have also been failures and unwanted effects,"⁵⁰ Cameron voiced concern about excessive expectations for nano-engineered health solutions. "Despite the hopes of some that technology at the nanoscale will prove ultimately very cheap, it is a reasonable assumption that its industrial application to medicine will result in very costly treatments. Thus, the suggestion that 'all cancer' will be curable by 2015 is unlikely to include the cancer of all persons afflicted with the disease, but rather the cancers of the wealthy and those with access to medical insurance, private or social."⁵¹

This final observation of a bioethicist, which comes very close to that of the aforementioned nanoscientist, brings the discussion of the three disenchanting concepts related to nano-powered world economies to a full circle. It takes Berube's *nano-hyperboles* and Mitchell's *elusive truth* to its logical conclusion for it reveals the underlying mechanism of the perpetual cycle of hope and disillusionment, which is symptomatic of the nano-hype, the nano-divide, and the nano-business.

REFERENCES

1. Quoted from R. Somasekhar, 'CNR Rao—the evergreen researcher', *The Hindu Business Line*, 03.01.2006, available at <http://www.thehindubusinessline.com/2006/01/04/stories/2006010403480900.htm> (21.06.09).
2. M.E. Mitchell is Director of the Institute of Psychology at the Illinois Institute of Technology, USA.
3. M.E. Mitchell, 'Scientific promise: reflections on nano-hype', in N.M. de S. Cameron and M.E. Mitchell (Eds.) *Nanoscale: Issues and Perspectives for the Nano Century*, John Wiley & Sons, Hoboken, New Jersey, (2007), 52.
4. *Ibid.*, 53.
5. *Ibid.*
6. *Ibid.*, 52.
7. D.M. Berube, *Nano-hype: The Truth behind the Nanotechnology Buzz*, Prometheus Books, New York, (2006).
8. D.M. Berube is Professor of Communication Studies at North Carolina State University, and Communications Director of the International Council for Nanotechnology (ICON) hosted at Rice University, USA.
9. In her reflection on the elusive truth, Mitchell refers to the stakeholder list of D.M. Berube. See Mitchell, M.E., *Op. cit.*, 47.
10. Lux Research, 'Economy blunts nanotech's growth', Press Release, 24.06.2009, available at <http://www.marketwire.com/press-release/Lux-Research-1008498.html> (10.07.09).
11. M.E. Mitchell, *Op. cit.*, 47.
12. *Ibid.*
13. The Royal Academy of Engineering and the Royal Society have been commissioned to investigate the actual and potential societal benefits and risks accruing to nanotechnologies. The expert working group (hereafter referred to as the 'RS working group') prepared evidence and recommendations to support policy-makers in their deliberations on nano-governance and regulation. *Nanoscience and nanotechnologies: Opportunities and uncertainties (in the text abbreviated to 'RS report')*, is available at <http://www.nanotec.org.uk/report/Nano%20report%202004%20fin.pdf> (28.06.09).
14. *Ibid.*, 52–3.
15. D. Parr is Chief Scientist at Greenpeace, UK.
16. The Royal Academy of Engineering and the Royal Society, *Op. cit.*, 53.
17. C. Holroyd is Senior Fellow at the Canada-based think-tank Centre for International Governance Innovation (CIGI), and a Senior Research Analyst with the Asia-Pacific Foundation of Canada.
18. C. Holroyd, Science and technology policies, national competitiveness, and the innovation divide, CIGI Working Paper: Economic Policy, Centre for International Governance Innovation (CIGI), Ontario, 2007, 33, available at http://www.cigionline.org/sites/default/files/Paper_32-web.pdf (29.06.2009).
19. The biennial World Science Forum, co-organised by the United Nations Educational, Scientific and Cultural Organisation (UNESCO) and the Third World Academy of Science (TWAS), is an international platform that promotes cross-sector dialogues on the role and standing of science, technology, innovation and higher education in a global society.

20. The summary report of the 2007 World Science Forum is available at http://www.sciforum.hu/index_2007.php?content=news_20071110b (01.07.09).
21. UNESCO Institute of Statistics, A global perspective on research and development, Fact sheet, No. 05, October 2007, UNESCO-UIS, Montreal, available at www.unesco.org/science/psd/wsd07/global_perspective.pdf (10.07.09).
22. UNESCO Institute of Statistics, Global education digest 2009: comparing education statistics across the world, UNESCO-UIS, Montreal, 2009, available at http://www.uis.unesco.org/template/pdf/ged/2009/GED_2009_EN.pdf (10.07.09).
23. M.C. Roco is the Founding Chair of the US National Science and Technology Council's Subcommittee on Nanoscale Science, Engineering and Technology (NSET), and Senior Advisor for Nanotechnology at the National Science Foundation.
24. M.C. Roco and W.S. Bainbridge, *Societal Implications of Nanoscience and Nanotechnology*, Kluwer Academic Publisher, Dordrecht, 2001, 13.
25. *Ibid.*
26. The digital divide relates to the "semiconductor revolution" and connotes with the capacity and capability of world societies to adopt, absorb and adapt to the information age that resulted from the rapid growth and expansion of electronic interconnectivity by means of information and communication technologies (ICTs).
27. C. Holroyd, *Op. cit.*, 13.
28. C.N.R. Rao is Professor and Chairman of India's 'Nano Mission'.
29. C.N.R. Rao, 'Basics matter', in *A world of Science in the Developing World, TWAS Supplement to Nature*, 45 (30 October 2009), 45, available at <http://www.nature.com/nature/journal/v456/n1s/pdf/twas08.45a.pdf> (28.06.09).
30. C. Holroyd, *Op. cit.*, 10–1.
31. For instance primary education, general and medical health care, social welfare, etc.
32. *Ibid. Op. cit.*, 33.
33. V. Srivastava is the Co-founder of Q_Tech Nanosystems, India.
34. *EE Times Asia*, 'India drafts nanotech policy to keep up with rivals' by K.C. Krishnadas, 03.01.08, available at http://www.eetasia.com/ART_8800496140_480200_NT_5fe78664.HTM (14.07.09).
35. *Ibid.*
36. C. Bai is Executive Vice President of the Chinese Academy of Sciences and Director of the National Center for Nanoscience and Technology (NCNST), China.
37. C. Bai., 'Nano rising', in *A World of Science in the Developing World, TWAS Supplement to Nature*, 45 (30 October 2009), 36–7, available at <http://www.nature.com/nature/journal/v456/n1s/full/twas08.36a.html> (28.06.09).
38. *The Royal Academy of Engineering and the Royal Society, Op. cit.*, 53.
39. C. Bai., *Op. cit.*, 36–7.
40. *The Royal Academy of Engineering and the Royal Society, Op. cit.*, 53.
41. C. Holroyd, *Op. cit.*, 13.
42. *Ibid.*, 33.

43. Equity is not to be confused with equality.
44. M. Chan is Director-General of the World Health Organization (WHO), Geneva, Switzerland.
45. The speech of M. Chan 'Why the world needs global health initiatives', 22.06.09, is available at http://www.who.int/dg/speeches/2009/global_health_initiatives_20090622/en/index.html (24.06.09).
46. A. Raichur is Assistant Professor at the Indian Institute of Science, Bangalore, India.
47. A. Raichur, 'Nanoscale water treatment needs innovative engineering', *Science and Development Network*, London, 06.05.09, available at <http://www.scidev.net/en/new-technologies/opinions/nanoscale-water-treatment-needs-innovative-engineer.html> (5.07.09).
48. N.M. de S. Cameron is President of the Center for Policy on Emerging Technologies, Washington DC, and a Research Professor at the Illinois Institute of Technology, USA.
49. N.M. de S. Cameron, 'Towards Nanoethics?', in N.M. de S. Cameron and M.E. Mitchell (Eds.) *Nanoscale: Issues and Perspectives for the Nano Century*, John Wiley & Sons, Hoboken, New Jersey, 2007, pp. 281–94.
50. M.E. Mitchell, *Op. cit.*, 44.
51. N.M. de S. Cameron, *Op. cit.*, 288–90.

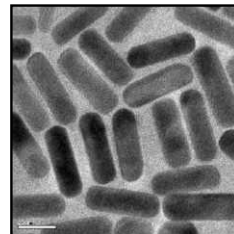
ADDITIONAL READING

1. F. Allhoff, *et al.* (Eds.), *Nanoethics: the Ethical and Social Implications of Nanotechnology*. New Jersey: John Wiley & Sons, Inc. (2007).
2. D. Bennett-Woods, P. Boucher, T. Frye, S. Priest and J. Shatkin, 'Societal implications of Nano'. In G.L. Hornyak, H.F. Tibbals, and J. Dutta, *Introduction to Nanoscience and Nanotechnology*, Florida: CRC Press (2008).
3. M.D. Cobb and J. Macoubrie, 'Public perceptions about nanotechnology: Risks, benefits and trust'. *Journal of Nanoparticle Research: An interdisciplinary Forum for Nanoscale Science and Technology*, 6(4) 395–405 (2004).
4. R. Gordon, 'Future hopes, future fears: predicting public attitudes toward nanotechnology', *Nanologues*, 2(4). 2006.
5. N. Invernizzi, G. Foladori and D. Maclurcan, 'Nanotechnology's controversial role for the South', *Science Technology & Society*, 13(1), 123–148 (2008).
6. L. Mazzola, 'Commercialising nanotechnology'. *Nature Biotechnology*, 21(10), 1137–43 (2003).

REVIEW QUESTIONS

1. Why have the three "disenchanted" core concepts given rise to controversies? Explain how they relate to each other.
2. For what reasons is the nano-divide different from previous innovation divides?
3. Try to establish those controversies that have emerged due to increased public investment in national nanoscience programmes in low- and middle-income countries. Present and discuss your position.
4. What are the cost-implications of "actions not taken" and "opportunity lost"? Give examples of why views diverge in matters of public investment in national advanced science and technology programmes.

NANOMATERIALS: WORLD SOCIETIES AND THE NATURAL ENVIRONMENT



The Rise of Nanotoxicology

“Some readers will think that it is about time I talked of Nature and the real objects behind the texts and behind the labs. But it is not I who am late in finally talking about reality. Rather, it is Nature who always arrives late, too late to explain the rhetoric of scientific texts and the building of laboratories.”

Bruno Latour (1987)

Latour, B., *Science in Action: How to Follow Scientists and Engineers through Society*, Harvard University Press, Cambridge Massachusetts, (1987), 94

The heated debates between opponents and supporters of nanoscience and nanotechnologies at the beginning of the 21st Century have given rise to the question if a “rational” dialogue among the various stakeholders and interest groups at all is possible. A number of civil society organizations, including environmental advocacy groups and social movements, felt pressured to react to the ways in which the commodification and commercialisation of nano-centred knowledge pressed ahead. Alarmed by the first signs of an impending new technological era—the “Nano-century”—a number of interest groups found a yet unexploited niche. The growing number of nano-based consumer products not only opened up new business opportunities, but also it has fuelled public fears of the negative consequences of nano-engineered matter on human health and other organic life systems. Higher and intensified levels of research and development (R&D) in the nano-realm, and finally the commercial production of these novel materials inevitably have led to their appearance outside of the laboratory. Even though incorrect, assumptions about the potentially unlimited physical presence of nanoparticles in organic and inorganic systems have begun to undermine the rather positive attitudes people nurtured for nanoscience and nanotechnologies when these were at an embryonic stage. In response to claims of civil society groups telling nanomaterials are dangerous, members of the nanotech enterprise and the wider nanoscience and technology community have become active on several fronts. Research into the potential downsides of nanoscientific development has led to the establishment of a new discipline. Pre-emptive measures to prevent and mitigate potential harm have been adopted and implemented regardless the difficulties with establishing their health and environmental threat. The emphasis on the smallness of nanoparticles has fomented fears among the lay publics. Scientific evidence however, proved that the size, which in itself is subject to intense scientific discussion, is just one among other dimensions to determine and define the potential toxicity of nanomaterials.

Learning objectives

- Have a general understanding of why an informed and constructive dialogue about the benefits and risks of nanoscientific development seemed impossible at the turn of the millennium.
 - Describe and explain with concrete examples why it is too simplistic to associate nanotoxicity with the smallness of nanoparticles.
 - Have a basic understanding of problems related to efforts to standardise measures at the atomic and molecular levels.
 - Be able to explain why this is relevant, who the parties involved in these deliberations are, and what is at stake from the perspectives of (a) scientists, (b) policy-makers and (c) environmental activists.
-
-

27.1 PUBLIC DEBATES ON THE DOWNSIDES OF NANOTECH

27.1.1 World Societies and Human Habitats at Risk?

The scientific fact, that atoms and molecules are omnipresent in artificial and natural life-worlds, has given rise to fears about the spatial ubiquity of nano-engineered matter. The emphasis on the smallness of nanoparticles in public debates on Nano and Society has rendered it quite difficult to explain to the lay publics that nano is not just about size. It hardly needs mentioning that small is easily associated with something that can infiltrate anything. That has given rise to questions if these novel materials are really ubiquitous or not, and if so, how they “behave” outside of the laboratory. If nanoparticles are truly able to penetrate everything in a presumably uncontrollable way has revealed difficult to establish empirically. As the following discussions will elucidate, nanotoxicity is not a mere question of *Science Fiction* or *Science Facts*.

Members of the science and innovation policy community and the nano-business have begun to openly discuss how difficult it is to address and deal in an all-encompassing, comprehensive way with the complex challenges nanomaterials pose. Especially their potential toxicity is still little understood. Growing interest in the toxicological aspects of nanomaterials has brought alive a new nano-based discipline. Nanotoxicology is a fast developing research area within nanoscale science, engineering and technology. As the volume of empirical studies on human toxicity and ecotoxicity increases, so are concerns of the public about the negative aspects of nanoscale research and innovation activities. The ever-increasing number of scientific publications on the potential risks, linked to the distinct morphological characteristics of nanomaterials, reflects the scholarly interest in the downsides of nanotech.

Nanotoxicology has appeal for natural researchers, as well as social scientists. It is a scientific field, in which transdisciplinary research activities can flourish. Although the bibliometric patterns are significantly different, it can be argued that in the natural science literature the uneven geographical distribution of scientific publications is less pronounced compared to the social sciences literature on

nano-focused topics. Considerably fewer social sciences studies have been conducted in the developing world compared to natural sciences research. Publications concentrating on Nano and Society in the developing world are still rare despite global trends indicating an expansion and intensification of international nanoscale materials-based research and development (R&D), including industrial nanotechnology-centred manufacture. The visible imbalance in the body of social science literature may well change as low- and middle-income countries with nanoscience initiatives have begun to draft institutional and legal frameworks to regulate nanoscience and nanotechnologies.

Ongoing public debates on the benefits and the risks of nano-engineered solutions between experts of different scientific disciplines and institutional sectors show that a considerate and constructive dialogue is possible, indeed. Even though the fierce debates between nanotech supporters and opponents at the beginning of the 21st Century suggested otherwise, this dialogical relationship has never come to a complete halt.

27.1.2 Public Debates on the Potential Risks of Nanotech

“What are the dangers to ourselves and the environment?”² This question was posed to an expert panel in 2002. If the organisers of the public science debate “Technology: Taking the Good without the Bad”,—a round-table discussion on the possible risks of novel technologies including nanotechnology—expected the magnetic effect of their question, is hard to determine. In any event, it yielded a report within one year of the broadcasted debate.³

The controversies about the potential danger of nanomatters for human and other organic life systems have not diminished since they first appeared in the public domain. On the contrary, with the commodification and commercialisation of nanoscientific research findings, arguments and counter-arguments have gained visibility. Nananotoxicology, as a distinct nanoscale materials-based discipline, partly has crystallised, from the interest of the scientific, and policy communities in claims about the actual and potential threat of nanotechnologies. Whether or not these are true or false is of lesser relevance because, Mitchell remarked in her analysis of the nano-hype, “in the absence of sound and reliable information, conjecture and speculation have as much meaning and values as anything else.”⁴

Such disputed claims have noticeably contributed to a hardening of the polarised positions between the various interest and stakeholder groups in countries with national nanoscience and nanotechnology initiatives. In the early years of the new millennium, clashes between the opponents and supporters of nanotech have escalated in the West. These were fierce enough to legitimise the question if a “rational dialogue” with the public at all were possible. In neither defence, the UK government felt the need to intervene. In 2003, the Royal Academy of Engineering and the Royal Society⁵ were commissioned to investigate the opportunities and challenges the advance of nanotechnologies possibly imparted. They set up an expert working group who, in the course of their deliberations, consulted with nanotechnology opponents and nanotechnology supporters to establish, if amendments of existing regulatory science and technology frameworks were required. The ‘Nanoscience and Nanotechnologies: Opportunities and Uncertainties’⁶ report exposed, the potential health and environmental risks the study group had addressed and debated during the proceedings.

This report has been the first in a series of UK government-commissioned reports on the societal implications of nanoscale science, engineering and innovation.

A further UK-government sponsored study was published in 2008. Conversely to the earlier investigations, this one focused on the toxicological aspects of nanomaterials. The study team of the Royal Commission on Environment Pollution (RCEP), who authored the report 'Novel Materials in the Environment: the Case of Nanotechnology,⁷ has taken up the previous observations and recommendations of the RS working group. These developments prove continuity of public science and policy debates that have begun to prosper in Britain and other techno-scientifically advanced countries at the turn of the millennium. Public debates on the possible negative implications of nanotech development in low- and middle-income countries, such as China and India, have become more acute in recent years, and thus, deserve particular attention.

27.1.3 Nanotoxicology: A Technoscientific Field of Research and Innovation with Economic Prospects?

With the translation of scientific findings into commercial applications, public pressures on scientists and technologists to provide evidence on the potential risks of nanomaterials have grown stronger. Regulatory requirements that apply to the manufacture of nano-engineered commodities may, or may not yet, include provisions to evaluate their possible health and environmental risks at all stages of the product life-cycle. In order to comply with requests of that kind, presumed these have been put in place, their producers need test instruments to ascertain their harmlessness. What at the outset might look like a routine exercise, in actual fact, is not because of the lack of adequate tools for establishing the toxicity profile of nanomaterials.

In view of the course, the nano-business has taken, nanotoxicology's future looks bright. Associated with this relatively new academic and industrial field of research and innovation is an emergent, and eventually prosperous niche market within the nano-based businesses. Investments have been, and continue being made to build research capacity in nanotoxicology. Universities are, by no means, the only science-based institutions active in the development of innovative scientific methods, approaches and instruments to empirically establish the possible adverse effects of nanomaterials. A number of contract research organisations (CROs) have already sensed the looming opportunities and stepped into the nanotoxicological research enterprise. Public-private R&D ventures and other forms of inter-sectoral science and innovation collaboration have also opened up fresh prospects. In spite of this positive outlook on the business potential of nanotoxicological research and innovation, there are persisting challenges, which need mentioning.

27.1.4 Can Nanotoxicology Keep the Pace with Advances in Nanoscience and Nanotechnology?

If the young, but fast-growing and expanding discipline of nanotoxicology will keep up with the developments in other nano-centred disciplines is difficult to predict. First of all, it needs to be made clear what "keeping the pace means," What could be the appropriate parameters for such kinds of cross-comparison? Who keeps up with whom, and what with what?

These are tricky questions and they have contributed to controversies even within the ranks of the same nano-community. Participants at the first International Conference on Nanomaterial Toxicology (ICONTOX)⁸ in India agreed that: “Historically, toxicology has lagged behind technology, but nanotechnology is an exception where toxicology concerns can keep in step with emerging technology. However, nanotechnology is also expected to progress faster than previous technological initiatives. Thus, there is a need for greater vigilance, scientific rigour, curiosity-driven research and mechanisms-based explications of nanotoxicological observations.”⁹ A more sceptical stance took Alok Dhavan and team¹⁰ for they expressed concerns about the implications of yet unresolved epistemological and methodological problems in this emerging field of research. “Nanotoxicology” they write, “has lagged far behind nanotechnology due to a number of experimental challenges and issues faced in designing studies involving toxicological assessment of nanomaterials.”¹¹

If nanotoxicology can develop as fast as other disciplines is likely to depend on a number of factors, including socioeconomic factors since these influence the trajectory of this young discipline. The 2008 ICONTOX declaration hints at the need for political, financial, and also public support to warrant that nanotoxicology can keep up with the developments of its fellow disciplines. If India’s public authorities will follow suit, and allocate the recommended three percent of the annual government budget, designated for the country’s ‘Nano Mission’, to nanotoxicology research remains to be seen. It is also hard to predict if this projected financial commitment will materialise, because there are other prioritised research areas within India’s nanoscience policy framework. Negotiations for a national regulatory framework on nanoscience and nanotechnology, for instance, are underway and the drafting of a nano-focused science and technology policy may require additional funds.

As to why public and private investment in nanotoxicological research was critical, Michael Kovoichich¹² and his collaborators responded: “As nanotechnology develops, it is essential that the toxicological approach also evolves and stays up to date. This will provide an important safeguard for the continued expansion of the nanotechnology industry.”¹³ This statement reads similar to the recommendations the ICONTOX meeting adopted, and furthermore, it mentions the commercial aspects of nanotoxicological R&D.

Even if opinions about the likeliness of nanotoxicology keeping the pace with the development in related disciplines vary visibly, nanoscience and technology policy communities in different parts of the world have begun to consider and evaluate the cost-implications of “actions not taken” and “opportunity lost” in regard to this evolving sub-discipline.

27.2 HANDLING ISSUES REVOLVING AROUND NANOMATERIALS WITH RESPONSIBILITY AND CARE

27.2.1 Responsibilities Arising from Dealing with Nanomaterials Physically

Empirical evidence proving that nano-engineered materials can be harmful for living systems and the wider ecosystem disconcert scientists and technologists, but also students in nano-based disciplines

because such research findings may affect them individually, in terms of personal health, as well as their career. Studies in biomedical occupational health research suggested that the main source of inhalation exposure to potentially hazardous manufactured nanoparticles and nanotubes occurs in laboratories. Earmarked locations, besides laboratories of universities, government, science-based corporate and non-profit organisations, include incubator facilities, such as start-ups, where novel products are tested and piloted prior to enter the marketplace.

Albeit the future of any discipline depends on factors that are beyond an individual's influence and control, students, researchers, scientists and technologists can not be taken out of the equation of a responsible development of nanoscale materials-based science. In the light of the central role the laboratory plays in the nano-enterprise, attention should be paid to what happens within these spatially confined work places, and more precisely, to how laboratory workers handle nano-engineered matter. "Nanomaterials can also pose problems when they are handled and used. Put simply, their very small size makes them easily airborne and hard to contain. [...] And while the ill effects remain far from understood, we must be careful when using nanoparticles. [...]"¹⁴ These personal insights of a nanoscientist speak to the question of how possible health and environmental risks, emanating from nanoscientific research, can be limited and contained. At the heart of such health and safety related issues are best laboratory practices specifically referring to the handling of nano-engineered substance. The following two examples draw on two sets of recommendations, adopted in two countries at different times. They convey an idea of how experts have framed interventions that aim to minimise the negative impacts on human health and the natural environment.

"The nanoscale materials, which do not exist in nature, should be handled with care. [...] With regard to evaluating the safety and toxicity of nanomaterials, the first step would definitely involve tracing the pattern of distribution of the material once it is released into the environment or within an organism."¹⁵ Whereas the "handling with care" mentioned in the 2008 ICONTOX declaration is a *preventive* measure to avoid negative consequences of nano-focused activities, the "first step" is a possible measure to *mitigate* possible negative consequences of hazardous materials outside of the laboratory.

In disregard of the few nanomaterial toxicity studies available at the time when the RS working group made recommendations in 2004, these experts proposed *precautionary* measures. "Until more is known about environmental impacts of nanoparticles and nanotubes, we recommend that the release of manufactured nanoparticles and nanotubes into the environment be avoided as far as possible. Specifically, in relation to two main sources of current and potential release of free nanoparticles and nanotubes to the environment, we recommend: (i) that factories and research laboratories treat manufactured nanoparticles and nanotubes as if they were hazardous, and seek to reduce or remove them from waste streams; and (ii) that the use of free (that is, not fixed in a matrix) manufactured nanoparticles in environmental application such as remediation be prohibited until appropriate research has been undertaken and it can be demonstrated that the potential benefits outweigh the potential risk."¹⁶

The rationale of precautionary measures imparts besides ethical, commercial aspects. Kovoichich and colleagues considered *ex-ante* approaches to help prevent human-induced hazards, whereas

retroactive approaches would compromise the public perception of nanoscience applications and inflict harm to the nanotechnology industry. Concluding on a pragmatic note, they remarked that “it makes much more sense to instigate preventive measures to avert such a disaster.”¹⁷ Yet, large-scale disastrous events associated with nanotechnology have not occurred. The consternation the recall of a cleansing product containing nanoparticles from the German market caused because of suspected health risks, however, revealed how threatening such allegations can be, even if the suspected toxicity of this product was not confirmed.

Apart from the aforementioned risk factors, there is yet another problem that deserves mention, even though strictly speaking, it is not about the physical handling of nanomaterials. The ways in which nanotechnoscientific data, information and knowledge are dealt with in the rhetoric of scientific text can also have repercussions on people’s attitudes toward nanotech. Albeit from a different perspective, the discussion on the nano-hype addressed the problem with overstated hopes and expectations, caused by inflated scientific claims and propositions. It is, therefore, critical to include the immaterial aspects of knowledge transactions in discussions on the professional obligations and responsibilities of nanotech research practitioners vis-à-vis society.

27.2.2 Responsibilities Arising from Dealing with Nanomaterials in Scientific Text

Production of technoscientific knowledge, its dissemination and use can not be disassociated from the laboratory. In addition to the recommendations for the proper treatment of nanomaterials in their physical form, the 2008 ICONTOX declaration advised on how to deal with nanoscientific data, information and knowledge in a considerate way. “The terms ‘nanotechnology’ and ‘nanomaterials’ should be used responsibly, particularly by marketing professionals and those in the communication media. Science, technology and biomedicine researchers should rigorously self-regulate their own claims and those of their peers in presenting and communicating their research results pertaining to the use of nanomaterial and nanotechnology.”¹⁸ The RCEP report, published in the same year, also regarded laboratory practices and publishing ethics norms and principles an important tool to prevent, limit, and mitigate the extent of potential harm emanating from the laboratory.

Research councils, policy advisory boards and other regulatory authorities drafting deontological codes for nano-centred education, training and R&D, showed a preference for anticipatory approaches. The ‘Code of conduct for responsible nanosciences and nanotechnology research’ of the European Commission (EC), and the ‘Responsible nanocode for nano-businesses’ the UK Royal Society and affiliated partners had drafted, opted for precautionary measures.

The RCEP study group, however, pronounced reservations about non-compulsory regulatory schemes, such as self-policing measures precisely because “voluntary codes of conduct are likely to be most effective when they are backed up at appropriate points by ‘harder’ legal and regulatory measures.”¹⁹ If other countries with nanoscience and nanotechnology initiatives will join Canada and replace legally non-binding guidelines with enforceable legal provisions, is likely to depend on their effective implementation within the country.²⁰

27.3 EPISTEMOLOGICAL, METHODOLOGICAL, AND PRACTICAL CHALLENGES IN THE EXPLORATION OF TECHNOSCIENTIFIC NEWLANDS

27.3.1 Core Aspects of Yet Little Investigated Technoscientific Terrains

The starting phase for any discipline is hard. There is an array of hurdles, especially if, as it is the case with nanotoxicology, the application of previously established scientific theories, methods, tools, and approaches reveals inappropriate. Nanoscience, and in particular, nanotoxicology and nanometrology are confronted with novel epistemological, methodological and practical issues. These challenges not only affect professionals working in a relatively young research area, but also those doing research about these recently institutionalised disciplines in the social studies of science and technology (STS).

One issue that has already been introduced, but needs further discussion, relates to the standing of nanotoxicology vis-à-vis its fellow disciplines. Nanotoxicology has fundamental links with nanometrology, the discipline dealing with problems of measurements related to the physical dimensions of atomic and molecular matter. Nanometrologists produce and deliver the kind of scientific evidence regulators rely on national and international standard measurements policy deliberations.

The general recognition that the current state of knowledge on how to measure toxicity at the scale of the nanometre is inadequate has emerged as a major problem in policy debates on standardising toxicity measurements at the atomic and molecular levels. In light of the global expansion of nanoscientific research and innovation activities, the fact that there are no universally applicable standards for dose measurement at these scales, such as internationally recognised toxicity grades, is problematic. The fact that there is little to no agreement on the size of the nanometer, let alone dose specifications of nanotoxicity, aggravates this situation further.

How do nanotoxicologists respond to questions arising from inadequate dose measurement instruments, methods and approaches to assess and establish the potential toxicity of nanomatter? In the absence of recognised dose standards and measurements for establishing the potential threat of nanomaterials, they obviously need to be inventive. At the core of this problem is the question of how to generate scientific knowledge about the potential health, and environmental, risks without appropriate devices. A number of nanotoxicologists commented with surprising openness on the scientific and technological challenges they associated directly with nanomaterials toxicity assessments.

An array of analytical tools and methods to establish the toxicological aspects of nano-engineered compounds, such as nanoparticles, would dispose of some of the concerns inadequate test facilities for product safety assurance pose to scientists and consumer protection organizations. However, without adequate scientific methods and tools to characterise and measure these properties and establish their potential toxicity profile, the demands of control bodies are difficult to meet. This is situation likely to have repercussions for the commercial release of nano-engineered consumer goods, devices and services.

27.3.2 Nanomaterial Toxicity: A Matter of Size?

How small is “small”, and does small equals dangerous? If in the absence of appropriate test methods, size comparison can be used as an alternative analytical tool, is a scientifically disputed argument. Nanoscientists have interrogated assumptions about a direct correlation between size and toxicity, precisely because they rely on nominal size measurement, which in itself is a disputed subject matter. Even though nanoscientists have drawn attention to this epistemological problem, policy advisers repeatedly referred to size in reference to why nanomatter might be dangerous.

“Few studies have been published on the effects of inhaling free manufactured nanoparticles and we have had to rely mainly on analogies with results from studies about exposure to other small particles—such as the pollutant nanoparticles known to be present in large numbers in urban air, and the mineral dusts in some workplaces.”²¹ Similar to the RCEP study team, the 2008 ICONTOX recommendations invited scientists to conduct safety/toxicity investigations concurrently on materials in the nanometre as well as the micrometer or millimetre size range.²²

Policy advisory bodies have recurred to foregrounding the size, chiefly because of the status of knowledge and progress achieved in this field at the time they formulated their recommendations. Already in 2004, the RS working group referred to the problems of accurately determining the dimensions or shape in all axes.²³ Though the nanometre has been nominally defined in the International System of Units (SI), it remains subject to scientific discussions. Thus, it is no surprise that as yet, there are no clearly-defined, standardised units for nanotoxicity.

The need to resolve a seemingly irresolvable problem has become more prominent in recent years with key-findings demonstrating that size is not the only factor to distinguish an innocuous from a noxious nanoparticle. Composition, shape, surface properties, solubility and aggregations are all factors that give nanomaterials their distinct physiochemical and morphological identity. In short, these are as relevant as the size. One of the major reasons why the characterisation of nanomaterials has become so central relates to mounting demands for nano-centred toxicity classification systems. Toxicity profiles of nano-engineered matter need to be established before novel compounds can be assigned to a particular category, or class.

The work of Katrina Waters²⁴ and colleagues on the correlation between nanoparticle size and toxicity is just one example to show that apart from the size, there are other factors to determine the toxicity level of nano-engineered compounds. Their investigational study was motivated by “concerns about the potential adverse health effects of engineered nanoparticles stems in part from the possibility that some materials display unique chemical and physical properties at the nanoscales which could exacerbate their biological activity.”²⁵ They concluded that the effect of particle size across a comprehensive set of biological responses could not be confirmed, and therefore, toxicity could not simply be attributed to size, but the surface area. “Whole genome microarray analysis of the early gene expression changes induced by 10- and 500-nm particles showed that the magnitude of change for the majority of genes affected correlated more tightly with particle surface area than either particle mass or number [...] However, the overall biological processes represented by all gene expression changes were nearly identical, irrespective of particle diameter.”²⁶ Nanotoxicologist Brian

Thrall, who commented on those findings, told Nanowerk News “If you consider surface area as the dose metric, then you get similar types of responses independent of the size of the particle [...] That suggests the chemistry that drives the biological responses doesn’t change when you get down to the smallest nanoparticle.”²⁷

27.3.3 Need-based Approaches to Ascertain Nanomaterials’ Toxicity

The need for adequate methods and tools to establish toxicity profiles of nanomaterials has become more visible with ground-breaking research findings demonstrating that the size is just one of many aspects to give nanoparticles their distinct identity profile. Pressures of science governance bodies to standardise dose measurement at atomic and molecular levels have brought into focus the regulatory aspects of scientific disputes about definitions of size at the nanometre scale. These should not be underestimated because of their possible implications for ongoing, and likely future, research and innovation processes.

Set into *text*, pre-emptive measures resulting from the uncertainties of the potential risks of nanomaterials, could read as follows: “Until further toxicological studies have been undertaken, human exposure to airborne nanotubes in laboratories and workplaces should be restricted.”²⁸ Set into the laboratory *context*, this could signify that unless dose measurements for nano-engineered matter have been established, a restrictive use will be the rule.

From the position of state authorities, it looks as if it were in the very interest of academic and industrial nanoscientists and nanotechnologists to cooperate with public and international science governance agencies. This could mean to expose the identity profiles of nanomaterials and their potential health and environmental risks, and if requested, disclose them to the public. The scientific nano-community is aware that regulatory authorities rely on expert knowledge for taking informed, and evidence-based, decisions; two recognised principles of good governance and decision-making practice in science and innovation policy making.

These observations shed light on the potential tensions that can arise at the injunctions of science and policy. Who could better predict the consequences of stricter legal and regulatory frameworks than those, whose research work would directly be affected by policy reforms? To prevent pre-emptive approaches of policy-makers, Kovoich and colleagues advanced a position statement. In anticipation of tighter rules and regulations, “it should be our goal to develop appropriate methods to assess the safety of nanomaterials and, by so doing, help to safeguard the future of nanotechnology without the fear of negative public perception, government overregulation, and potentially costly litigation.”²⁹

27.3.4 Possible Limits and Limitations of Pre-emptive Interventions

Since existing technoscientific paradigms, used for the characterisation, profiling and toxicity modelling of materials, revealed inadequate for the testing of nanoscale materials, nanotoxicologists have begun to develop innovative scientific tools, methods, and approaches for measuring nanomaterials toxicity. Be it the macrophage cell model in the study of Waters and colleagues, the test model of Kovoich and team, or the ‘QSTR (GQSTR)’ approach of Ajmani demonstrated at the 2008 ICONTOX

conference,³⁰ these scientists emphasised the newness, the uniqueness and distinctiveness of their analytic models and experimental study approaches. Repeatedly they mentioned the need for fresh thinking to overcome the persisting challenges inhibiting nanotech innovation. But, can these, and other model approaches actually be used as prognostic tools?

Despite the acknowledged limits and limitations of their scientific approaches, the response of Kovochich and colleagues was affirmative. They were confident that the oxidative paradigm—an established science-based approach that has been developed into a comprehensive disease model—could be upgraded and become a predictive paradigm for toxicity testing of nanomaterials.³¹ Ajmani also mentioned that his method could generate an understanding of the toxicity aspects of groups in the molecular size range.³²

The advantages of these model approaches seem evident, but, will these help detect the underlying structures and mechanisms of toxicity? Are these approaches just theoretical, or can they be applied in the open environment? This last question is discomfiting for it gives rise to questions about preventive measures in general. If identified problems are contextualised in real-world settings, the situation can look quite different compared to the confined and controlled laboratory space, where hypothetical and abstract models and simulations are developed and tested. Kovochich's answer to the foregoing question is considerably less assuring. "It is important to mention the potential significant difficulties that may be encountered in conducting *in-vitro* and *in-vivo* studies with engineered nanomaterials. This has largely to do with lack of real-world exposure to nanomaterials, including dosage, complexity of working/living environment, aggregation status, and so on."³³

The scientific and technological limits and limitations of novel methods and techniques represent a concrete problem. It has surfaced not only in published research findings, but also in policy briefings. The recognition of the shortcomings of precautionary approaches clearly reiterates what the RCEP study team and the RS reports discussed extensively. Already in 2004, these expert working groups acknowledged the problems with measuring nanomaterial toxicity outside of controllable and confined spaces, and described it as "particularly problematic when measurement is required in 'real-world' situations, as opposed to carefully controllable laboratory conditions."³⁴ Fluctuating environmental conditions, as well as background particles already present in the environment, were identified among other potential factors to taint readings of investigational nanomaterial compounds. Because consumer commodities are used predominantly outside of laboratory settings, it is essential to find test methods that also work in the open environment.

27.3.5 Steering towards Cross-sector Involvement and Public Engagement

The limitations of toxicological working concepts for assessing the potential danger of nanomaterials have received national and international attention. To overcome these multi-faceted and multi-layered challenges, it is critical to elucidate the inter-relationship between policy-focused debates and the development of adequate science-based systems, methods and approaches, such as benchmark toxicity standards and accessible nanotoxicological online databanks.

Methods, like those earlier discussed characterisation profiles, in theory, could help narrow the persistent knowledge gap insofar they provide the much sought for evidence for standardising measurement used in nano-based dosimetry, toxicokinetics, and toxicodynamics. In principle, these could be useful for establishing user-friendly data repositories storing information about the toxicological characteristics of identified nano-engineered compounds.

In recognition of the actual need to expand the body of evidence-based knowledge on material properties at the atomic and molecular levels, national science and innovation funding bodies have committed political and financial support to build and strengthen nanotoxicological research. It is hoped that intensified research activities would contribute to generate the necessary knowledge so as to overcome persisting bottlenecks in international, and national policy deliberations on the standardisation of metric and toxicological grading systems. Further, these financing policy interventions enable and foster a potentially constructive and favourable climate, in which scientific inquiry into the downsides of novel materials can be catalysed, and engagement with the wider society be enacted.

In addition to the recommended financing policy strategies for nanotoxicological research and innovation, the ICONTOX delegates decided that the development of a “priority list” of nanomaterials to be studied for potential toxicity, should receive immediate attention. They also proposed the setting up of ‘libraries’ of well-characterised nanomaterials used in different applications for use as standards.³⁵ But, what might happen, should a classified nanoparticle fall outside an particular classification scheme? Would it undermine “nano-banking altogether”?

The initiators of the self-policing ‘UK Voluntary Reporting Scheme for Engineered Nanoscale Materials’,³⁶ a pilot project conducted in Britain between 2006 and 2008, addressed exactly this question. They made explicit that data on engineered nanoscale materials falling outside the limit of the indicated size range were welcome if relevant and providing valuable information on their potential risks.³⁷ This arguably atypical flexibility of a government regulatory authority underpins the immediacy of the need for innovative conceptual and analytical methods, and instruments to ascertain the potential hazardous nature of nano-engineered matter.

27.4 AFTERTHOUGHTS ON “GROUNDED” NANOTOXICOLOGY

Public expectations towards experimental test methods and approaches are considerably high, especially in respect to the delivery of reliable and valid predictions of hazardous risks for humans and the natural environment. Since the toxicological aspects of nanomaterials have potential to compromise the future development of nanoscientific research, development and innovation, problematic issues have been explored through multiple perspectives to show how potential risks are perceived, explored, investigated, conceptualised, and framed in contemporary discourses of Nano and Society. Although pre-emptive approaches to divert potential harm have become *praxis courante* in a number of countries with national nanoscience and nanotechnology programmes, they have their limits and limitations.

The implications of such approaches have been discussed in the contexts of science, as well as policy-focused debates to draw attention to the interrelatedness of these two institutional spheres.

Apprehension about the possible health and environmental risks of nano-engineered solutions has proved relevant to understand the pressure from some government regulatory authorities, research councils, international science agencies, civil society organisations and other interest groups to develop and extend the evidence base of nanomaterials' toxicity. Persisting knowledge gaps are problematic insofar they risk obstructing informed and evidence-based decision-making but also, because of their potential to compromise future investments in nanoscience and its deriving technologies. Both scientists and policy makers have interest in limiting potential negative externalities, such as trade-offs. And that can help explain why they have become active on various fronts in political, and public life.

Since scientific and regulatory debates on the risks and benefits of nanotechnologies and their present and future applications are ongoing, the closing remarks of Mitchell may stimulate further reflection: "Grounding nanotechnology in the present and in reality is a daunting, but important, task if nanoscience is to be directed to inventing and developing materials, devices and methods that can make a difference in the quality of life for people."³⁸

REFERENCES

1. B. Latour, *Science in Action: How to Follow Scientists and Engineers through Society*, Harvard University Press, Cambridge Massachusetts, (1987), 94.
2. Information on the New Scientist-Greenpeace UK 2002 science debate 'Technology: Taking the Good without the Bad' is available at <http://uk.greenpeace.org.uk/about/new-scientist-and-greenpeace-science-and-technology-debates> (04.07.09).
3. K. Kulinowski mentioned this event in the context of the historical developments of cross-sector dialogues on nanotechnology. See K.M. Kulinowski, 'The International Council on Nanotechnology: a new model of engagement', in N.M. de S. Cameron and M.E. Mitchell (Eds.), *Nanoscale: Issues and Perspectives for the Nano Century*, John Wiley & Sons, Hoboken, New Jersey, (2007), 397.
4. M.E. Mitchell, 'Scientific promise: reflections on nano-hype', in N.M. de S. Cameron and M.E. Mitchell (Eds.) *Nanoscale: Issues and Perspectives for the Nano Century*, John Wiley & Sons, Hoboken, New Jersey (2007), 53.
5. The members of this study team, hereafter referred to as the 'RS working group', were tasked to explore and evaluate the actual and potential risks and the benefits of nanotechnologies, including eventual toxicological effects of nanomaterials on human health and the natural environment.
6. The Royal Academy of Engineering and the Royal Society, 'Nanoscience and nanotechnologies: opportunities and uncertainties', The Royal Academy, 2004. The report, hereafter referred to as the 'RS report', is available at <http://www.nanotec.org.uk/report/Nano%20report%202004%20fin.pdf> (28.06.09).
7. Royal Commission on Environment Pollution (RCEP), 'Novel materials in the environment: the case of nanotechnology', The Stationary Office (TSO), Norwich, 2008. The report, hereafter referred to as the 'RCEP report', is available at <http://www.rcep.org.uk/reports/27-novel%20materials/documents/Novel-Materials-report.pdf> (5.07.09).
8. The 'International Conference on Nanomaterial Toxicology', at which the recommendations, hereafter referred to as the '2008 ICONTOX declaration', were adopted, was jointly organised by the Indian

Institute of Toxicology Research and the Indian Nanoscience Society and held in Lucknow, India from 5–7 February (2008).

9. The report with the recommendations and declaration of the International Conference on Nanomaterial Toxicology (ICONTOX-2008) was published in The Council of Scientific & Industrial Research (CSIR). See: CSIR News, 58 (10), 2008 and is available at http://niscair.res.in/ScienceCommunication/RnDNewsLetters/csirnews2k8/csirnews_30May08.pdf (05.07.09). The abstracts of the conference papers were published in *Nanotoxicology*, 2(s1): S2-S88, (2008).
10. A. Dhawan is a Scientist at the Indian Institute of Toxicology Research (IITR), India.
11. A. Dhawan, V. Sharma and D. Parmar, 'Nanomaterials: a challenge for toxicologists', *nanotoxicology* 3(1), (2009), 1–9.
12. M. Kovichich is based at the Department of Medicine, University of California Los Angeles (UCLA), USA.
13. M. Kovichich, *et al.*, 'Principles and procedures to assess nanomaterial toxicity', in M.R. Wiesner and J-Y. Bottero, *Environmental Nanotechnology: Applications and Impacts of Nanomaterials*, The McGraw-Hill Companies, New York, (2007), 225.
14. A. Raichur, 'Nanoscale water treatment needs innovative engineering', Science and Development Network, London, 06.05.09, available at <http://www.scidev.net/en/new-technologies/opinions/nanoscale-water-treatment-needs-innovative-engineer.html> (5.07.09).
15. Council of Scientific and Industrial Research (CSIR), *Op. cit.*, 171.
16. The Royal Academy of Engineering and the Royal Society, *Op. cit.*, 85.
17. *Ibid.*
18. Council of Scientific and Industrial Research (CSIR), *Op. cit.*, 169.
19. Royal Commission on Environment Pollution (RCEP), *Op. cit.*, 68.
20. This issue will be discussed in greater detail in the next chapter.
21. The Royal Academy of Engineering and the Royal Society, *Op. cit.*, 4.
22. See point 3 of the 2008 ICONTOX declaration.
23. The Royal Academy of Engineering and the Royal Society, *Op. cit.*, 14.
24. K. Waters is based at the Pacific Northwest National Laboratory, US Department of Energy, USA.
25. K. Waters, *et al.*, Macrophage responses to silica nanoparticles are highly conserved across particle sizes, *Toxicological Sciences*, (2009), 107(2), 553–69.
26. *Ibid.*
27. Nanowerk, Nanotoxicology: big and small nanoparticles affect most genes similarly, Nanowerk News, 14.02.09, available at <http://www.nanowerk.com/news/newsid=9275.php> (05.07.09).
28. The Royal Academy of Engineering and the Royal Society, *Op. cit.*, ix.
29. M. Kovichich, *et al.*, *Op. cit.*, 206.
30. Council of Scientific and Industrial Research (CSIR), *Op. cit.*, 168.
31. M. Kovichich, *et al.*, *Op. cit.*, 206.
32. Council of Scientific and Industrial Research (CSIR), *Op. cit.*, 168.
33. M. Kovichich, *et al.*, *Op. cit.*, 225.

34. The Royal Academy of Engineering and the Royal Society, *Op. cit.*, 76.
35. Council of Scientific and Industrial Research (CSIR), *Op. cit.*, 171.
36. Department for Environment, Food and Rural Affairs (DEFRA), UK voluntary reporting scheme for engineered nanoscale materials, 2008, available at <http://www.defra.gov.uk/environment/quality/nanotech/documents/vrs-nanoscale.pdf> (07.07.09).
37. *Ibid.*, 4.
38. M.E. Mitchell, 'Scientific promise: reflections on nano-hype', in N.M. de S. Cameron and M.E. Mitchell (Eds.) *Nanoscale: Issues and Perspectives for the Nano Century*, John Wiley & Sons, Hoboken, New Jersey (2007) 60.

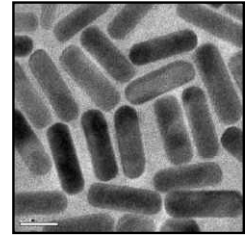
ADDITIONAL READING

1. V.L. Colvin, 'The potential environmental impact of engineered nanomaterials', *Nature Biotechnology* (21), (2003), 1166–70.
2. International Council on Nanotechnology, 'Current practices for working with nanomaterials', Rice University Center for Biological and Environmental Nanotechnology, 2006.
3. F. Jotterand, (ed.), *Emerging Conceptual, Ethical and Policy Issues in Bionanotechnology*, Springer Science + Business Media B.V., (2008).

REVIEW QUESTIONS

1. Explain why at the beginning of the 21st century a rational dialogue seemed impossible. Present and discuss your view.
2. What does it mean to handle nanomaterials in responsible ways? Give a few examples of the relatedness of professional, and publishing, ethics to laboratory work. If you have experienced a situation in which you were confronted with an ethical problem, how did you address it?
3. What do pre-emptive approaches, adopted by scientists and policy makers, have in common, and what are they trying to prevent?
4. Describe at least two situations, in which the inappropriateness of existing tools, methods and approaches has materialised.
5. Present and explain why the size has been extensively discussed in the context of public debates on nanomaterials' toxicity.

NANO-POLITICS: GOVERNANCE AND REGULATION OF NANOTECHNOSCIENCE



Policy Debates and Public Engagement

“What we cannot speak about we must pass over in silence.”

Ludwig Wittgenstein (1921)

Wittgenstein, L., *Tractatus logico-philosophicus*, translated by D.F. Piers and B.F. McGuinness, Routledge & Kegan Paul, Oxon, 2002 [1961] (first published in *Annalen der Naturphilosophie*, 1921), 89

There is general acknowledgement that policy frameworks for investment, governance and regulation of nanotechnoscience influence and shape the developmental trajectory of nanoscience, engineering and technology. At the centre of contemporary science and technology policy debates are questions about the need of public interventions to direct the advance of nanotechnologies. The desirability of such interference has given rise to controversies. A number of countries administrating national nanoscience and nanotechnology initiatives have opted for policy reforms and introduced regulations, including trade regulations, to control nanotechnoscientific research and innovation. Persisting knowledge gaps on the downsides of nano-engineered commodities are a major constraint in the formulation of nano-specific governance and regulatory frameworks. Government authorities struggle with what has been conceptualised as the “control dilemma”. Finding consensus among the many stakeholder and interest groups can be a costly, and time-consuming, process. Deliberations on controversially debated policy-focused nano-issues, asking for clear and firm positions and precise formulations, have revealed particularly challenging. Public debates on issues of standardisation, such as quality control in nano-centred manufacture or the definition and determination of a nominal unit for dose measurement, have brought to light that such deliberation processes are besides a scientific, a political, act. Political, because scientific arguments can be used to critical effect in policy proceedings, not to say rendered instrumental in the pursuit of particular interests and goals, as the earlier discussions about the nano-hype and the nano-divide have shown.

Learning objectives

- Understand the potential repercussions of nano-governance and regulation on scientific research and innovation practices.
- Become aware of the problems that may arise from initiated science and technology policy reforms.

- Understand the relevance of the principle of inclusiveness in nano-related policy, and regulatory, deliberations.
 - Ability to lead an informed and constructive discussion on the earmarked aspects of nano-politics.
-
-

27.1 ACTUAL AND PERCEIVED NEEDS OF GOVERNING AND REGULATING NANOTECHNOSCIENCE

27.1.1 International and State Control of Nanoscale Science, Engineering and Technology

Central to contemporary science and technology policy debates are questions about the desirability of public interventions to control the advance of nanotechnologies. Views and ideas about public interference into nano-related matters vary across countries and scientific communities. Some countries administrating national nanoscience and nanotechnology programmes have decided to tighten existing science and technology policy and regulatory frameworks.²

Calls for policing nanoscale materials-based science and technologies are not necessarily well received by professionals who have a stake in the nano research and development (R&D) enterprise, and the affiliated nano-businesses. Reactions to proposals for nano-specific policy frameworks or plans to reform existing science and technology policies to steer the trajectory of nanotechnologies in a particular direction are mixed. Nevertheless, a number of countries have opted for policy reforms and introduced stricter regulatory norms.

Given the fears of an emerging nano-divide, is it not legitimate to ask if there is any international science agency assigned to authoritatively intervene in nano-related affairs that are deemed of global importance and relevance? Although a number of international organisations have initiated regional and cross-regional negotiations on policy issues related to the governance and regulation of nanotechnologies, yet there is not a world umbrella organisation acting as an international regulator and governing body of nanotechnoscience.³

27.1.2 Need for Nano-centred Policy Frameworks

Views on the need and desirability of the interference of public authorities in the development of nanotechnologies vary within the nanoscience community, and the wider science and technology policy communities. Diana Bowman and Graeme Hodge⁴ examined possible rationales for subjecting nanoscale science, engineering and innovation to a specific state-controlled regulatory agency. “Technically, there is little doubt that nanotechnology itself provides a new and unique combination of characteristics, and as such could attract a unique and comprehensive regulatory regime covering only this technology.”⁵

The 2009 policy-level meeting ‘National Conference on Nanotechnology and Regulatory Issues (NCNRI)’⁶ addressed the practicalities and technicalities of governing and regulating nanotechnology

development in India. The conference delegates agreed that several of the challenges nanotechnology poses were not new and had been confronted and addressed at the time of biotechnology. But, they also conceded that certain challenges required an “entirely new paradigm of regulatory approach and the charting of new regulatory pathways.”⁷ Contrary to the two Australian analysts, the NCNRI delegates felt, in the Indian context, new comprehensive laws on nanotechnology were not needed but some amendments in the relevant legislation were necessary. In addition, they proposed the establishment of an expert committee to make “short-term recommendations in the light of growing applications and commercialization of the technology.”⁸ This attitude reflects the observations of Bowman and Hodge for they remarked that some countries preferred to control nanotechnology through their existing legislative science and technology frameworks.⁹

Why have some countries opted for nano-specific legal arrangements, whilst others have decided to delay policy reforms? Bowman and Hodge highlighted the commercial implications of such political choices. Government authorities might not want to “unduly stifle economic development and research through the introduction of overly prescriptive regulatory hurdles aiming towards broader issues of public interest or harm minimization.”¹⁰ In view of this potential bias, Suranjan Das¹¹ emphasized the need to strike a balance between concerns about present risks and the potential commercial opportunities nanotechnologies harbour.¹² A few years earlier, a UK government-commissioned policy advisory team concluded: “Our very limited set of case studies has demonstrated that it will be necessary to modify individual regulations within existing frameworks or their supporting standards, to reflect the fact that materials have new and enhanced properties at the nanoscale that in some cases may be associated with a greater toxicity that is seen in the same materials in the larger size ranges.”¹³

At the time these recommendations were published, little empirical evidence about the correlation between the level of toxicity and particle size existed. Bowman and Hodge recognised that poor scientific evidence presented a serious problem for policy-makers. “An important issue here is that regulatory responses cannot sensibly be made based on vague concerns that dire consequences may occur if a technology develops sufficiently at some time in the future. What is clear here is that as science advances towards second- and third-generation nanotechnology applications, the potential of nanotechnology to challenge conventional national regulatory frameworks will increase commensurately.”¹⁴ But, do technoscientific developments in the nano-realm precede regulatory regimes, with the latter acting in response to the former?

27.1.3 The Temporal Trajectory of Nano-centred Governance and Regulatory Policy Development

If policy development keeps the pace or lags behind the advance of nanotechnologies is a disputed topic. Even within the ranks of the same science policy communities positions diverge. The idea of a phased policy development process in itself is difficult to conceive and so is the idea of a gradual nanotechnology development process. This mainly relates to the genealogy of policy documents and nanotechnoscientific developments, both not necessarily following a progressive, linear trajectory. Assumptions that technoscientific developments precede regulatory regimes, with the latter acting in response to the former, could be explained with existing theories. But, instead of framing the underlying

question theoretically, it is preferred to look at the ways in which nano-related policy issues have been discussed in contemporary Nano and Society discourses.

Similar to Bowman and Hodge, the NCNRI delegates established a direct relationship between the development of nano-specific laws and regulations, and nanotechnoscientific development. “Regulatory frameworks should take into account the phase of Nanotechnology development and the regulatory intervention should be as per the stage of development and knowledge of risk.”¹⁵

As the organisers of the 2008 International Conference of Nanomaterial Toxicology (ICONTOX) asserted, it is indeed difficult to establish when “the time has come to pay due attention to the demands of ensuring and documenting that nanomaterials prepared by new and existing processes are safe for human use and benign towards the environment.”¹⁶ Contrary to the delegates of the 2009 NCNRI meeting, the ICONTOX delegates agreed that there was an urgent need for the “adoption of informed regulatory guidelines to govern the use of nanotechnology and nanomaterials in different areas of application.”¹⁷ They based their conclusions on the shared concerns about the possibility of unforeseen hazards accompanying the use of nanometre-size material in consumer products. They therefore commended risks be “investigated, contained, monitored and ameliorated by joint and responsible action by all sections of the society.”¹⁸

The ‘2007 Bangalore Nano Convention’, historically could be taken as the starting point of the Indian Subcontinent’s “regulatory pathways”¹⁹ in matters of nanoscience and nanotechnology governance and regulation. It marked the moment of the establishment of the ‘Vision Group on Nanotechnology’, a policy advisory body bestowed with a state order.²⁰ This expert group is likely to face problems comparable to those other policy advisory committees have encountered in their respective countries, especially in drafting recommendations based on empirical evidence.

The 2008 Royal Commission on Environment Pollution (RCEP) framed the predicament of partial knowledge as a “control dilemma”.²¹ The persisting knowledge gaps about the societal impact of nanotechnoscientific knowledge applications are likely to affect decision-makers in similar ways, even though they may not acknowledge it as eloquently as the RCEP working group did in 2008: “We are operating under conditions of partial knowledge and significant ignorance.”²²

Some critics have argued in favour of anticipated actions to prevent unwanted effects of nanotechnologies, while others opposed such moves. Contested scientific arguments are never politically neutral. They are politically biased insofar scientific claims can be used to critical effect in policy proceedings, and hence, rendered instrumental in the pursuit of particular interests and goals.

27.1.4 The “Control Dilemma”

The conditions and circumstances under which the study team of Ann Dowling had formulated nano-focused policy recommendations have not improved considerably. It is no mystery then that the wider policy community of the nanotechnoscience enterprise continues to rely on poor evidence in their deliberations on nano-related governance and regulatory issues. “Few studies have been published on the effects of inhaling free manufactured nanoparticles and we have had to rely mainly on analogies

with results from studies on exposure to other small particles, such as the pollutant nanoparticles known to be present in large numbers in urban air, and the mineral dusts in some workplaces,”²³ the RS working group admitted in 2004.

Four years later, in 2008, Sir John Lawton²⁴ hinted at the inappropriateness of existing measurement instruments for nanomaterial toxicity. “In the Royal Commission study, we looked hard for evidence of nanomaterials causing harm to human health or to the environment, and found no such evidence. However, it is very early in the development of this technology, and the amount of testing has been relatively limited.”²⁵

The “control dilemma” paradigm foregrounds the indissoluble connection between knowledge gaps and regulatory gaps. In the understanding of the 2008 RCEP working group, the control dilemma is a product of two conditions; the condition of “ubiquity”, and that of “ignorance”. Both factors risk to undermine an environment that endeavours informed, and evidence-based decision-making. “In the early stages of development of a technology, we do not know enough about its future implications to establish the most appropriate management regime. But, by the time problems emerge, the technology is likely to have become too embedded to change without significant social and economic disruption.”²⁶

An additional challenge of controlling nano-engineering materials relates to the fact that nanomaterials are generally contained within products and not “encountered as discrete entities”.²⁷ In light of this general recognition, the generation, collection, and storage of data and information about the potentially hazardous characteristics of nanomaterials, has become a policy priority for a number of countries with nanoscience initiatives. Perhaps, it is premature to discuss “nano-banking”, however, certain policy moves, such as proposals for nano data and information repositories, are pointing in that direction.

27.1.5 Impact of Legal and Regulatory Arrangements on Nanoscale Materials-based Research and Innovation

In 2002, C.N.R. Rao commented on the interdependent relation between the lack of incentives for Indian scientists to publish in vernacular journals and their low impact factor. “The number of good papers coming out of India is not large. So a good journal in India cannot be maintained. Suppose you want to have a journal like *Physical Review Letters*, *Journal of the American Chemical Society*, etc., there are not enough papers from India to maintain such a journal. Even for the small number of papers that are published, people would like to get the maximum notice or attention. So they go for higher impact factor journals.”²⁸ A possible solution, Rao suggested, would be to produce a thousand good papers in every subject so as to have good journals in India. The policy advisory team developing guidelines for the design of research projects under the government-funded ‘Nano Mission’ considered this problem. It decided that investigators to publish the work of government-funded projects in Indian journals.²⁹ The ‘*Nano Digest*’³⁰ for example, is a result of the sustained political and financial commitments of scientists and policy-makers to strengthen the national science capacity whereof science publications are a critical indicator.

Another concrete example that lends itself well to illustrate the vivid interplay between policy decisions and research are self-policing schemes. The UK Department for Environment Food and Rural Affairs (DEFRA) invited private, and public-sector nanoscientists and nanotechnologists, and any other developers of nanomaterials, to participate in the piloting of the 'UK Voluntary Reporting Scheme for Engineered Nanoscale Materials'.³¹ Its aim and rationale were "to provide an indication of those nanomaterials, which are currently in development or production. Even basic details, such as the identity of an engineered nanomaterial, are helpful in building up this picture, which will inform high-level policy decisions and enable our effort and resources to be focused in areas, which are relevant to the UK's current nano manufacturing and research base."³²

No doubt, an extensive data repository on health, and environmental hazards of nano-engineered materials would definitely put policy-makers in a much better position to make a strong case for narrowing regulatory gaps. The formulators of the aforesaid voluntary scheme listed yet another critical factor. Strictly speaking, it is, social, rather than less technical. "Building an evidence base in this way will allow for a more informed debate about the nature of appropriate controls. It will also lead to appropriate controls in the shortest time frame giving a predictable regulatory environment for all."³³

The NCNRI delegates valued such pioneering reporting schemes, as in their recommendations they clearly stated that "all evidence based data should be admissible irrespective of the country of study, while designing the regulatory framework for Nanotechnology."³⁴

27.1.6 Domestic and International Calls for "Closing" Nanotechnoscience Development

The DEFRA scheme, however, has delivered only a partial response to requests on tighter regulation of nanotechnoscience activities in spite of the well-intended intentions, to prevent possible harm to human health and the natural environment. It is partial in that the scheme is not compulsory. Although legal, and other regulatory arrangements can affect the research work of nanoscientists and nanotechnologists directly and immediately, the response of UK-based research practitioners to the DEFRA scheme was daunting.

Katharine Sanderson³⁵ examined the willingness of nanoscientific communities to cooperate with government authorities in matter of voluntary data reporting in the USA and across countries of the European Union (EU). Sanderson also informed about the Canadian government's decision to introduce a mandatory programme, which requests companies to present any details about the physical, chemical, and toxicological properties of nanomaterials they develop or import in quantities greater than one kilogram.³⁶ Her investigational study concluded that reservations, like those expressed in the 2008 RCEP report on voluntary codes, related to views holding that reporting schemes were likely to be most effective when backed up "by 'harder' legal and regulatory measures."³⁷

But, how successful Canada's mandatory reporting scheme could probably become, given the poor results the UK voluntary reporting scheme yielded, is difficult to assess. Pekka Sinervo³⁸ was quoted as saying that its success depended on how well it fitted the regulatory approaches of Canada's

international trade partners.³⁹ In view of global market economies and international trading of nano-based commodities, this is a critical point. Sinvervo's observation, in fact, supports the argument that the reluctance of some governments to reform their science and technology governance and regulatory frameworks resided in fears of their negative economic impact.

When the delegates of the 2008 ICONTOX decided that "new recommendations, however, need to be drawn up with due thought to the special properties of nanomaterials, to enable a rational regulatory environment as well as to harmonise experimental procedures across different laboratories worldwide,"⁴⁰ they took into account the internationalisation of nanoscale materials-based research, development and innovation, and the global trade with nano-engineered commodities.

Besides their ubiquity, which theoretically can not be excluded because of the circulation of nanomaterials in international technoscientific networks and commodity markets, the lack of absolute measurement norms is yet another unresolved regulatory problem. It ongoing international and national negotiations on the standardisation of nanoparticle size and toxicological measurement systems epitomise the technoscientific, economic, political, legal, and the social and cultural, aspects of nano governance and regulation.

In spite of the wider science and technology policy community taking distance from viewing particle size as the most critical dimension in the toxicity profiling of nanomaterials, it still is the nanoparticles' "smallness" the lay public fears in respect to unregulated nanoscience and nanotechnology.

27.2 PUBLIC ENGAGEMENT ALONG FAULT LINES: SEARCHING FOR "CROSS-PERSPECTIVES"

27.2.1 Engaging with Civil Society and Social Activist Groups in Nano-policy and Regulation Proceedings

"We believe that a constructive and proactive debate about the future of nanotechnologies should be undertaken now—at a stage when it can inform key decisions about their development and before deeply entrenched or polarised positions appear."⁴¹ In the midst of the heated debates between fierce supporters and opponents of nanotechnoscience, policy-makers of countries with large government-funded nanoscience programmes opted for inclusionary approaches in their science and technology policy deliberations. UK policy advisory groups on nanotechnology have engaged in dialogues with civil society groups and social activists as early as 2003.

Working toward the creation of a climate in which a "rational" dialogue with nanotechnology critics could take place emerged as a need at a time when controversies about nanotechnology's potential harm to society and the natural environment shook the hitherto largely positive perceptions of nanoscale science, engineering and technology. Kristen Kulinowski⁴² traced the historical origins of fears about the development of nanotechnologies going awry among lay public. "Inspired in part by Bill Joy's *Wired* convergence nightmare and Drexler's grey-goo scenario, Michael Crichton penned the ultimate fictional nanothriller, *Prey*. For many in the lay public, this was the first time they had heard the term nanotechnology."⁴³

A polarisation of intractable views and positions has emerged not only from science fiction films, but from public debates on the downsides of nanotechnologies. Even though numerous of the hitherto advanced hypothetical assumptions lacked empirical evidence, they have influenced and shaped people's perceptions and therefore, their attitudes towards nanoscale materials-based science and technology. Public discontent about nanoscientists' venturing into realms they ought not enter, have caused much heated debate. Cognitive and physical enhancement of the human body⁴⁴ is one such controversially discussed topic, but there are more examples.

Why, and when, was it that policy-makers decided to adopt the principle of inclusiveness when spearheading science and technology policy reforms? Kulinowski referred to the worst case scenario for any scientists engaging with frontier sciences and technologies: the open, and explicit call for a moratorium. Pat Roy Mooney⁴⁵ substantiated the request of the Erosion, Technology and Concentration (ETC) Group for a nanotechnology moratorium with the argument that "science will always seek to control the basic building blocks of nature and, as atoms are more basic than genes, science would soon seek control over these through the emerging field of nanotechnology."⁴⁶

Pressure from civil society groups and environmental activist movements supporting the ETC Group's demand for an end of nanotechnology forced the nanotech community to take a position. The NanoBusiness Alliance⁴⁷ can be regarded as one such response to the moratorium threat. The interest group grew into one of the fiercest opponents of the moratorium supporters.⁴⁸ Their reasons were economic, and they called upon the wider have forced the nanoscience and technology community to act. Nigel M. de S. Cameron⁴⁹ suggested that economic loss was due to an inappropriate and untimely consideration of public discontent. "The fundamental lesson of the costly European GMO fiasco lies in the need to build public confidence in new technology in order to ensure a market for the resulting products. [...] After disaster struck, Monsanto's chairman took the unprecedented step of apologising to the conference of the environmentalists group Greenpeace with 'We forgot to listen.'⁵⁰

27.2.2 Creating a Climate for a "Reasoned Dialogue" along Fault Lines and Amidst Misconceptions

Opposing views and positions on display in the public sphere have contributed to undermine public acceptance of nanotechnoscience, not to mention consumer goods containing nanomaterials. Proactive and inclusive approaches have been recommended to policy-makers so as to overcome the entrenched positions between the various stakeholders and interest groups and society at large. "We have reviewed, and are in broad agreement with a number of submissions and papers that have argued for a wider public dialogue and debate about the social and ethical impact of nanotechnologies. However, the evidence presented to us also suggests that specifying the precise forms of such dialogue will be no simple matter."⁵¹

To identify and embark on avenues leading to informed and constructive debates between opposing groups is decisively a demanding task, even more so if misconceptions among the lay publics are widespread. Jerry Collins⁵² examined if a "rational" dialogue with the public, at all, was possible. "Public news media are certainly culpable in public disinformation. [...] Media and politics are

particularly culpable of disinformation. [...] Powerful economic forces that serve good purposes, but are also driven by problematic goals, also deserve mention. [...] As is the case with medium content in general, the problem is not that advertising is innately wrong, but that it can be used excessively, and to mislead.”⁵³

Pre-conceived judgments, and misunderstandings about nanotechnologies are problematic in that they inevitably weaken joint and concerted efforts for reasoned multi-party dialogues. Diffused, but mistaken ideas about nanotechnoscience being “the science of the small”, “applicable to everyone and everything”, or “comparable to genetic engineering”, are unquestionably disturbing. This becomes evident when they are set into their respective contexts. “The emphasis on size alone in defining nanomaterials is misplaced, and tends to trivialise the challenges and opportunities of nanotechnology,”⁵⁴ the 2008 ICONTOX declaration asserted. The RS report correspondingly concluded: “In any revision to existing regulations, the relevant authorities should focus specifically on the properties and functionalities of nanomaterials, rather than size.”⁵⁵ The scientific evidence of size not being the sole critical factor in determining the potential risk of nanomatter seems not to have reached the public. The corollary assumption that nanoscience “can be applied to virtually anything ranging from materials to circuitry, computing to engineering, cosmetics to biomedicine, the environment, and more,”⁵⁶ as Mitchell pointed out, is therefore another of those preconception, that not only are utterly imprecise, but incorrect and moreover awaking excessive hopes and expectations. The technoscientific challenges associated with the scaling up nanomaterial productivity⁵⁷ proves that such conceptions of nanotechnologies are overtly simplistic and reductionist.

Size is likely to be what worries people most about nanotechnology. Small relates to ubiquity and pervasiveness; something small can be everywhere and penetrate everything without limitation or control. Public acceptance of novel technologies largely depends on how people view and think about their actual and potential benefits and risks for individuals, groups and communities, societies and the natural environment.

Opposition to nanotechnology emanated from various groups, and has been undertaken within the broader frames of, but not exclusively, social justice and environmental movements, anti-neoliberalism and anti-globalisation groups, on the basis of professional and moral commitments, as Alexandra Plows and Michael Reinsborough argued in their work on the ethical aspects of bionanotechnology in civil society discourses.⁵⁸ Kulinowski also mentioned that the call for a moratorium by the ETC Group had originated from ethical concern namely from “seeds that were planted a decade earlier”⁵⁹ she wrote with reference to a personal communication with the group’s executive director. Cameron argued likewise, for he also raised the Monsanto debacle.

Learning lessons from past events has appeal. Collins for instance, noticed that “Interestingly, technologies that offer real threats in the present tend not to be newer.”⁶⁰ It would however, be misleading to establish a direct link between bionanotechnology⁶¹ and conventional biotechnology. Putting them on the same order of scale for an analytical comparison neglects the distinctiveness of their respective disciplinary tenets. A possible way out of this conundrum would be to recognise that “rethinking a scientific model is always painful, particularly to those who have their work and reputations tied to a model being brought into question.”⁶²

27.3 CLOSING REMARKS ON “CROSS-PERSPECTIVES”

Thinking through the more prominent, as well as the hidden, aspects of nano-related concerns and issues that have surfaced in contemporary debates on Nano and Society through “Cross-perspectives” has shown the coexistence of different and sometimes conflicting and competing world-views resulting from distinct ontological and epistemological positions and premises. They might not stand harmoniously side-by-side, or be coherent in their argumentative structure. Notwithstanding, the selected discursive fragments, taken from a wide range of literary sources, have “opened the floor” to further critical discussions and reflections.

Public engagement along fault lines, and in the midst of diffused misconceptions about nanoscale science and engineering, certainly is anything but easy, but necessary for creating an environment in which multiple viewpoints can be expressed and heard in dialogue with one another. Collin, in his closing remarks, asserted that he remained hopeful that the development of nanotechnology could occur in a climate of reasoned public discussion. He advised his students to learn to be able to “perceive an ethical situation as it may arise, to become knowledgeable about details of the situation as it emerges, and perhaps most importantly, to be able to be conditional in one’s approach, to see a situation from many different perspectives. Perhaps the science and technology of nanotechnology can proceed similarly.”⁶³

REFERENCES

1. L. Wittgenstein, *Tractatus logico-philosophicus*, translated by D.F. Piers and B.F. McGuinness, Routledge & Kegan Paul, Oxon, 2002 [1961] (first published in *Annalen der Naturphilosophie*, 1921), 89.
2. Regulatory control instruments can include trade regulations of nano-engineered consumer products, funding policies for national nanoscience programmes, limits of exposure to hazardous materials in health and safety guidelines, the institutionalisation of a governmental nanoscience and technology surveillance committee, and others for the spectrum is wide.
3. The International Organization for Standardization (ISO), for example, is a multilateral organisation dealing with nano-related subject matters of international import.
4. D. Bowman and G. Hodge are based at the Faculty of Law, Monash University, Australia.
5. D.M. Bowman, and G.A. Hodge, ‘Nanotechnology: mapping the wild regulatory frontier’, *Futures*, 38 (9), 1060–73 (2006) 1064.
6. Department of Law, Calcutta University and The Energy Research Institute (TERI), Recommendations adopted during the ‘National Conference on Nanotechnology and Regulatory Issues (NCNRI)’ organised by Calcutta University and TERI, 9–10 January 2009, Centre for Research on Nanoscience and Nanotechnology, Kolkata, India. The recommendations are available at http://www.teriin.org/events/nano_pressnote.pdf (11.07.09).
7. See point 2 of the NCNRI recommendations.
8. Department of Law, Calcutta University and The Energy Research Institute, *Op. cit.*
9. D.M. Bowman and G.A. Hodge, *Op. cit.*, 1065.

10. *Ibid.*
11. S. Das is Vice Chancellor of Calcutta University, Kolkata, India.
12. Department of Law, Calcutta University and The Energy Research Institute, *Op. cit.*
13. The Royal Academy of Engineering and the Royal Society, Nanoscience and Nanotechnologies: Opportunities and Uncertainties, The Royal Academy, July 2004, 76. The report, hereafter referred to as the 'RS report' is available at <http://www.nanotec.org.uk/report/Nano%20report%202004%20fin.pdf> (28.06.09). Ann Dowling, Professor of Mechanical Engineering and Fellow of the Royal Society and the Royal Academy of Engineering, UK, chaired this expert working group (2003–04), hereafter referred to as the 'RS working group'.
14. D.M. Bowman and G.A. Hodge, *Op. cit.*, 1065.
15. Department of Law, Calcutta University and The Energy Research Institute, *Op. cit.*
16. The report with the recommendations and declaration of the International Conference on Nanomaterial Toxicology (ICONTOX-2008) was published in The Council of Scientific & Industrial Research (CSIR). See: CSIR News, 58(10), 2008. Available at http://niscair.res.in/ScienceCommunication/RnDNewsLetters/csirnews2k8/csirnews_30May08.pdf (05.07.09). The abstracts of the conference papers were published in *Nanotoxicology*, 2(s1): S2–S88, 2008.
17. See point 12. v., Council of Scientific and Industrial Research (CSIR), *Op. cit.*, 171.
18. Council of Scientific and Industrial Research (CSIR), *Op. cit.*, 169.
19. A 14-member expert group, led by C.N.R. Rao, Professor and Chairman of the Scientific Advisory Council to the Prime Minister, and Chair of India's 'Nano Mission', committed to draft a 'Roadmap for development of nanotechnology in Karnataka'.
20. See Government Order No. DST 156 STS 2007, Bangalore, dated: 29-10-2007, available at http://www.bangaloreitbt.in/worddocument/pdf/Gos/VGB_nano.pdf (12.07.09).
21. Royal Commission on Environment Pollution, 'Novel Materials in the Environment: the case of nanotechnology', *The Stationary Office* (TSO), Norwich, 2008, 7. The report, hereafter referred to as the 'RCEP report' is available at <http://www.rcep.org.uk/reports/27-novel%20materials/documents/Novel-Materials-report.pdf> (05.07.09).
22. *Ibid.*, 56.
23. The Royal Academy of Engineering and the Royal Society, *Op. cit.*, ix.
24. Sir John Lawton chaired the RCEP working group.
25. Royal Commission on Environmental Pollution, 'Urgent action needed on testing and regulation of nanomaterials', *News Release*, 28.11.2008 available at <http://www.rcep.org.uk/reports/27-novel%20materials/documents/Novel%20materials%20press%20release.pdf> (05.07.09).
26. Royal Commission on Environment Pollution, *Op. cit.*, 56.
27. *Ibid.*
28. N. Sen, 'In conversation: interview with C.R.N. Rao', *Current Science*, 82 (7), 10 April 2002, 791, available online at <http://www.ias.ac.in/currsci/apr102002/788.pdf> (28.06.09).
29. The directives of the respective funding agency are available at http://www.nanomission.gov.in/formats/formats_Guidelines_nano.htm (30.06.09).

30. The *Nano Digest* is an Indian monthly nanotechnoscience magazine. In recognition of Rao's personal commitment, the first edition featured the future plans of the 'Nano Mission' in a lead article. See: *Nano Digest* 1(1), June 2009.
31. Department for Environment, Food and Rural Affairs (DEFRA), UK voluntary reporting scheme for engineered nanoscale materials, 2008, available at <http://www.defra.gov.uk/environment/quality/nanotech/documents/vrs-nanoscale.pdf> (07.07.09).
32. *Ibid.*, 2.
33. *Ibid.*
34. Department of Law, Calcutta University and The Energy Research Institute, *Op. cit.*
35. K. Sanderson is a Physical Science Reporter with the scientific journal *Nature*.
36. K. Sanderson, 'Tighter nanotech regulations touted', *Nature* 457, 05.02.09, 647.
37. Royal Commission on Environment Pollution (RCEP), *Op. cit.*, 68.
38. P. Sinvervo, Physicist at University of Toronto, Ontario, Canada chaired the expert panel who drafted Canada's first mandatory scheme for nanomaterials.
39. K. Sanderson, *Op. cit.*, 647.
40. Council of Scientific and Industrial Research (CSIR), *Op. cit.*, 170.
41. The Royal Academy of Engineering and the Royal Society, *Op. cit.*, xi.
42. K. Kulinowski is Faculty Fellow in the Department of Chemistry, Rice University, and Director for External Affairs, Center for Biological and Environmental Nanotechnology, USA.
43. K.M. Kulinowski, 'The International Council on Nanotechnology: a new model of engagement', in N.M. de S. Cameron and M.E. Mitchell (Eds.) *Nanoscale: Issues and Perspectives for the Nano Century*, John Wiley & Sons, Hoboken, New Jersey, (2007), 396.
44. Scholarly work on human performance enhancement technologies (HPETs) in relation with nanotechnoscience has been done by a number of researchers of social studies of science and technology (STS). See the examples stated in Cameron, N.M. de S., 'Towards Nanoethics', in N.M. de S. Cameron and M.E. Mitchell (Eds.), *Nanoscale: Issues and Perspectives for the Nano Century*, John Wiley & Sons, Hoboken, New Jersey (2007), 281–94.
45. P.R. Mooney is the Executive Director of Erosion, Technology and Concentration (ETC) Group, a Canada-based non-governmental organisation (NGO).
46. K.M. Kulinowski, *Op. cit.*, 396.
47. This has been the first nanotechnology industry trade association, and was established by nanotechnology industrialist Mark Modzelewski.
48. *Ibid.*, 398–99.
49. N.M. de S. Cameron is President of the Center for Policy on Emerging Technologies, Washington DC, and a Research Professor at the Illinois Institute of Technology, USA.
50. N.M. de S. Cameron, 'Nanotechnology and the global future: points to consider for policymakers', in N.M. de S. Cameron and M.E. Mitchell (Eds.), *Nanoscale: Issues and Perspectives for the Nano Century*, John Wiley & Sons, Hoboken, New Jersey, (2007), 427.

51. The Royal Academy of Engineering and the Royal Society, 'Nanoscience and nanotechnologies: opportunities and uncertainties', The Royal Academy, London, (2004), 64.
52. J. Collins is a Research Associate Professor at Vanderbilt University, Nashville, USA.
53. J.C. Collins, 'Nanotechnology and society: a call for rational dialogue', in N.M. de S. Cameron and M.E. Mitchell (Eds.), *Nanoscale: Issues and Perspectives for the Nano Century*, John Wiley & Sons, Hoboken, New Jersey, (2007), 124–25.
54. See 'Point 1' of the 2008 ICONTOX declaration.
55. The set of recommendations of the 2008 RCEP Commission are available at <http://www.nanotechia.org/news/global/uk-royal-commission-on-environmental-pollution-fin> (05.07.09).
56. In her analysis, Mitchell clarified that even though nanoscientists manipulate matter at the scale of atoms and molecules, it does not mean their discoveries and inventions can be applied to anyone and anything. See Mitchell, M.E., 'Scientific promise: reflections on nano-hype', in Cameron, Nigel M. de S. and Mitchell, M. Ellen (Eds.), *Nanoscale: Issues and Perspectives for the Nano Century*, John Wiley & Sons, Hoboken, New Jersey, (2007), 46.
57. The problem with higher productivity has been discussed in the context of bulk production of nano-engineered commodities.
58. A. Plows and M. Reinsborough, 'Nanobiotechnology and ethics: converging civil society discourses', in F. Jotterand (Ed.), 'Emerging conceptual, ethical and policy issues in bionanotechnology', *Springer Science + Business media B.V.*, (2008), 133–56.
59. K.M. Kulinowski, *Op. cit.*, 396.
60. J.C. Collins, *Op. cit.*, 123.
61. The difference between bionanotechnology and nanobiotechnology will not be discussed here.
62. J.C. Collins, *Op. cit.*, 120.
63. *Ibid.*, 127.

ADDITIONAL READING

1. K.W. Abbott, G.E. Marchant and J.S. Douglas, 'A framework convention for nanotechnology? Policy review', *Environmental Law Reporter*, Vol. 38, No. 8, (2008), 10507–514.
2. D. Bennett-Woods, *Nanotechnology: Ethics and Society*, (2008), CRC Press.
3. R. Berne, *Nanotalk: Conversations with scientists and engineers about ethics, meaning, and belief in the development of nanotechnology*, (2005), Mahwah, New Jersey: Lawrence Erlbaum Associates Publisher.
4. R. Lee and E. Stokes, 'Twenty First Century Novel: Regulating Nanotechnologies', *Journal of Environmental Law*, 21(3), (2009), 469–82.
5. J.H. Matsuura, *Nanotechnology regulation and policy worldwide*, (2009), Artech House Publisher.

REVIEW QUESTIONS

1. Discuss the direct, and the indirect, implications of the “control dilemma” on nano-policy deliberations.
2. How can nanoscientists and nanotechnologists contribute to efforts of public authorities to overcome the challenges resulting from quests of civil society organizations for tighter nanotechnology rules and regulations?
3. Give a few examples as to why it is problematic to compare the temporal trajectories of nanotechnoscience with those of nano governance and regulation frameworks.
4. What has prompted policy-makers to opt for inclusionary approaches in their normative deliberations on nanotechnoscience regulation policy?

PART EIGHT

Appendices: A Practical Course on Nanoscience and Nanotechnology

Part I

1. Verification of the Beer-Lambert Law using Gold Nanoparticles
2. Adsorption of Biomolecules on Gold Nanoparticles
3. Determination of the Band Gap of Semiconductor Nanoparticles
4. Nanochemistry of Silver Nanoparticles in Converting *p*-Nitrophenol to *p*-Aminophenol
5. Surface Enhanced Raman Scattering Activity of Silver Nanoparticles
6. Conversion of Gold Nanorods into Gold Nanoparticles
7. Removal of Mercury by Supported Nanoparticles
8. Demonstration of Liquid Magnets
9. Bimetallic Nanoparticles
10. Gold Nanoparticles for Enhanced Visual Detection of Pesticides
11. Reactivity of Gold Clusters Towards Metal Ions
12. Study of Silver Nanoparticles
13. Synthesis of ZnO Nanoparticles
14. Preparation of Tellurium Nanowires
15. Synthesis of Luminescent Gold Nanoparticles by Core Etching

Note: This is an attempt to collect a set of experiments with which essential aspects of nanoscience could be demonstrated in classroom experiments, with minimum infrastructure. These experiments use minimum consumables and simple instruments. We use only the most common wet laboratory instruments such as weighing balance, UV/Vis spectrometer and Raman spectrometer for these experiments. It is possible to limit the experiments only to UV/Vis spectrometer also. The investment envisaged to build these facilities to conduct such experiments would be less than about \$20,000.

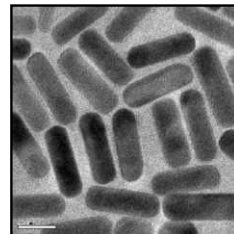
The first six experiments may be used to run a one semester experimental course to introduce the topic. Depending on the number of laboratory hours available, one can run 10 or 12 experiments per semester. Some of the other experiments collected here may also be chosen. Several of the experiments may be adapted to the requirements of the classroom by the teacher concerned.

Most of these experiments are from published research work of the authors. Here, with certain modifications, the presentation is kept as in the original papers. As a result, the style of presentation may differ from one Appendix to the other. Authors recommend that teachers adapt these experiments with changes they think appropriate to suit their classroom and lab environment.

All of these experiments have been tried several times in the laboratory with undergraduate and graduate students. All of them are highly reproducible. All the data presented here are from these experiments.

Most of the systems used here are large nanoparticles of 15 nm size or larger. Only a few experiments are there on sub-nanometer particles or quantum clusters. In the case of large particles, measured optical transmittance will include the contribution from scattering by particles. Thus, it is important to mention that what we measure is extinction and not absorbance. However, we have retained the word 'Absorbance' as it is still the common term used. Similarly, the nanoparticle suspensions are often referred to as 'solutions' and use of this word is not correct for such systems. The reader is expected to keep these differences in mind.

VERIFICATION OF THE BEER-LAMBERT LAW USING GOLD NANOPARTICLES



1.1 OBJECTIVES

- Preparation of gold nanoparticles using the citrate method
- Verification of the Beer-Lambert law

1.2 BACKGROUND

The Beer-Lambert law predicts a linear relation between the absorbance and molar concentration of an absorbing species. It relates to the absorption of light to the properties of the material through which the light is traveling [1]. It is a simple solution to the more general description of Maxwell's far-field equations describing the interaction of light with matter. In practice, the Law is accurate enough for a range of species, solvents and concentrations, and is a widely used equation in quantitative spectroscopy. Most often, it is used in quantitative determination of an absorbing species in a solution. Absorbance is measured using a spectrophotometer by passing a collimated beam of light at wavelength λ through a plane parallel slab of material that is normal to the beam. For liquids, the sample is held in an optically transparent, flat container called cuvette. Absorbance (A) is calculated knowing the intensity of light energy transmitted through the sample (I) and the intensity of light energy that is incident on the sample (I_0) [2].

$$A = \log_{10} \left(\frac{I_0}{I} \right)$$

According to Beer-Lambert law, absorbance is given by [1–3],

$$A = \alpha l$$

$$A = (\epsilon c) l \quad \alpha = \epsilon c$$

$$A = \epsilon c l$$

where ϵ is constant, for a given wavelength of light, and can be obtained from the absorbance values of solutions with different concentrations. The quantity, absorbance, has no units, while the units of ϵ , c , and l are $\text{L}\cdot\text{mol}^{-1}\cdot\text{cm}^{-1}$, $\text{mol}\cdot\text{L}^{-1}$ and cm , respectively. The same law was independently discovered

(in various forms) by Pierre Bouguer before 1729, Johann Heinrich Lambert in 1760 and August Beer in 1852 [3]. Beer extended the exponential absorption law to include the concentration of solutions in the absorption coefficient [1].

1.3 EXPERIMENT

1.3.1 Materials

- Tetrachloroauric acid trihydrate ($\text{HAuCl}_4 \cdot 3\text{H}_2\text{O}$)
- Trisodium citrate ($\text{Na}_3\text{C}_6\text{H}_5\text{O}_7$)

1.3.2 Apparatus

- 50 mL flat bottomed flask
- 5 mL standard flask
- 1 mL pipette-2 Nos.
- 25 mL measuring jar
- Heating mantle
- Wash bottle
- 100 mL beaker

1.3.3 Procedure

1. Prepare 10 mM HAuCl_4 solution in a 5 mL standard flask by dissolving 19.7 mg of $\text{HAuCl}_4 \cdot 3\text{H}_2\text{O}$ in water.
2. Prepare ~0.5% solution of trisodium citrate in a 10 mL sample bottle by dissolving 25 mg of $\text{Na}_3\text{C}_6\text{H}_5\text{O}_7$ in 5 mL of water.
3. Take 0.5 mL of 10 mM HAuCl_4 solution in a 50 mL flat bottomed flask using a 1 mL pipette and add 13 mL of distilled water to it using a 25 mL measuring jar.
4. Heat the solution over a heating mantle and bring the solution just to a boil.
5. To the boiling solution, add 1 mL of the trisodium citrate solution using a 1 mL pipette.
6. Continue heating (with boiling) till the colour turns to wine-red. This may take about 1–2 minutes.
7. Remove the flask from the mantle and keep it for cooling in air, for about 15–20 minutes.
8. To account for loss of water during boiling, make the solution to 14.5 mL (i.e. to the original volume) in a 25 mL measuring jar.
9. Calculate the concentration of gold nanoparticles in the solution in terms of Au. We shall call this solution AuNP solution.
10. Prepare the following solutions of different concentrations.

- 4.5 mL AuNP
 - 4 mL AuNP + 1 mL DW
 - 3 mL AuNP + 2 mL DW
 - 2 mL AuNP + 3 mL DW
 - 1 mL AuNP + 4 mL DW
11. Record UV/Vis spectra of all the solutions, using distilled water as reference.
 12. Note the values of absorbance at 520 nm.
 13. Plot a graph of absorbance (at 520 nm) vs. concentration.

1.4 RESULTS AND DISCUSSION

Appearance of wine-red colour in step 6 indicates the formation of colloidal gold or gold nanoparticles. Figure 1.1 shows UV/Vis absorption spectra of AuNPs with various dilutions. The peak appearing at a wavelength (λ_{\max}) of ~ 520 nm in all the spectra is attributed to the plasmon resonance of gold nanoparticles.

Figure 1.2 shows the plot of absorbance vs. concentration for the gold nanoparticles of different dilutions. It can be observed that all the data points fit into a straight line, thus conforming to the Beer-Lambert law. Slope of the above plot gives the absorption coefficient of the gold nanoparticles. For the calculation of the absorption coefficient, path length is being taken as equal to the width of the cuvette used for recording the spectrum (in the present experiment, it is 1 cm). From the above data, the value of absorption coefficient is calculated as $\sim 3.36 \text{ L}\cdot\text{mol}^{-1}\cdot\text{cm}^{-1}$. By making use of the above plot (Fig. 1.2), we can calculate the concentration of gold nanoparticles solution of an unknown concentration.

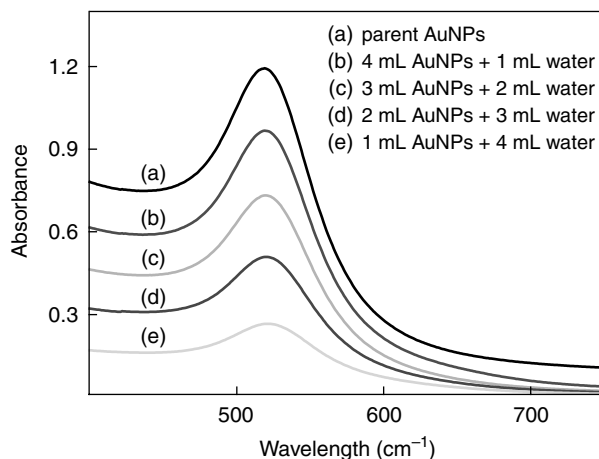


Fig. 1.1 UV/Vis absorption spectra of gold nanoparticles of different dilutions.

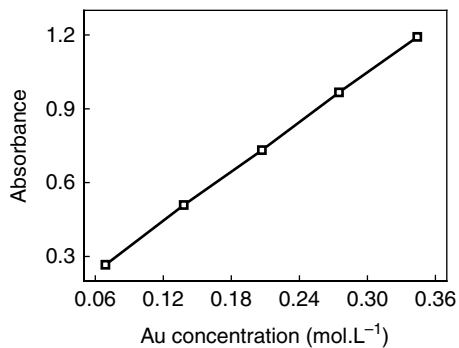


Fig. 1.2 Graph of absorbance vs. concentration of Au.

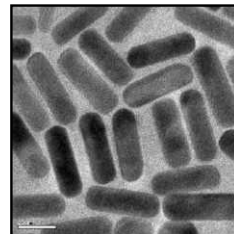
QUESTIONS

1. What is Beer-Lambert law?
2. What is surface plasmon resonance?
3. How can Beer-Lambert law be used in analytical spectroscopy?

REFERENCES

1. http://en.wikipedia.org/wiki/Beer-Lambert_law accessed on 24-10-2010.
2. <http://www.oceanoptics.com/technical/beerslaw.asp> accessed on 24-10-2010.
3. http://www.wordiq.com/definition/Beer-Lambert_law accessed on 24-10-2010.
4. Modified substantially from the original reference of J. Turkevich, P.C. Stevenson and J. Hillier, *Discuss. Faraday Soc.*, 11, (1951), 55-75.

ADSORPTION OF BIOMOLECULES ON GOLD NANOPARTICLES



2.1 OBJECTIVE

- Investigating the adsorption of bio-molecules (hemoglobin) on gold nanoparticles.

2.2 BACKGROUND

2.2.1 Gold Nanoparticles

Modern history of gold nanoparticles (AuNPs) is said to be started with the synthesis of gold colloid by Michael Faraday in 1857. The brilliant colours of stained glass windows of European cathedrals, which date back to many centuries, are attributed to the presence of noble metal NPs [1–2]. Surface Plasmon Resonance explains why AuNPs are wine-red, while bulk gold has a yellowish hue [3]. Modern science is fascinated by the usefulness of AuNPs in drug delivery, cancer treatment, catalysis, etc. While ancient people believed in the healing power of gold, which is evident from their use of gold preparations for the treatment of disfiguring skin lesions and ulcers, gold-leaf is used for the treatment of chronic skin ulcers in modern times. Over 5,000 years ago, Egyptians used gold in dentistry and ingested it for mental, bodily, and spiritual purification. Ancients believed in the existence of the ‘Elixir of life’ (liquid gold) which can bestow its drinker with eternal life or youth. Alchemists believed that gold represented the perfection of matter, and that its presence in the body would enliven, rejuvenate, and cure a multitude of disturbances in the life force balance of the body by stimulating the *chi* (life force) and raising the level of vibration at all levels. It was used to improve mental attitude and treat unstable mental and emotional states such as depression, melancholy, sorrow, fear, despair, anguish, frustration, suicidal tendencies, seasonal affective disorder, poor memory, poor concentration, and many other imbalances in mind, body, and spirit [1]. Several references to gold based medical preparations exist in Ayurveda, the Indian medical system, for conditions such as those mentioned above.

Gold coated pills and colloids (gold water) were extremely popular in medieval Europe. Powdered gold was used to ‘comfort sore limbs’, while today it is used in the treatment of rheumatoid arthritis. By the end of 16th century, people were aware of gold ruby glass. Highly successful treatments were developed by Paracelsus using gold, added to his claim of being created a potion called *Aurum Potabile*

(in Latin, meaning potable gold) in 16th century. John Herschel invented a photographic process called Chrysotype (from Greek, word for gold), in 1842, to record images on paper using colloidal gold. Paracelsus' work inspired Michael Faraday to prepare the first pure sample of colloidal gold, 'activated gold', in 1857. In 1890, German bacteriologist Robert Koch discovered that gold compounds inhibited the growth of bacteria. Even today, people in China cook rice with a gold coin in order to help replenish gold in their bodies, and fancy Chinese restaurants put 24-karat gold-leaf in their food preparations [1,4].

2.2.2 Hemoglobin

Hemoglobin is the iron-containing oxygen-transport metalloprotein in the red blood. Besides transporting oxygen from lungs to the rest of the body, it performs other roles such as gas transport and effect-modulation which vary from species to species. In humans, hemoglobin is an assembly of four globular protein subunits. Each subunit is composed of a protein chain tightly associated with a non-protein heme group in a globin fold arrangement. A heme group consists of an iron ion (Fe^{2+} or Fe^{3+}) held in a heterocyclic ring, known as a porphyrin. The iron ion, which is the site of oxygen binding, bonds with four nitrogens of the porphyrin ring, all of which lie in one plane [1]. It has been found that the binding of heme on gold is a slow process which takes about three days to complete. However, in the present experiment, we shall analyse the products after allowing the reactants to react for about 10 minutes.

2.3 EXPERIMENT

2.3.1 Materials

- Tetrachloroauric acid trihydrate ($\text{HAuCl}_4 \cdot 3\text{H}_2\text{O}$)
- Trisodium citrate ($\text{Na}_3\text{C}_6\text{H}_5\text{O}_7$)
- Sodium dihydrogen phosphate (NaH_2PO_4) (anhydrous)
- Disodium hydrogen phosphate (Na_2HPO_4) (anhydrous)
- Sodium chloride (NaCl)
- Hemoglobin (bovine)

2.3.2 Apparatus

- Round bottom flask (50 mL)
- Measuring jar
- Sample bottles
- Micro-pipette
- Heating mantle
- pH meter

2.3.3 Procedure

2.3.3.1 Preparation of AuNPs

1. Prepare 5 mM HAuCl₄ solution in a 10 mL standard flask by dissolving 19.7 mg of HAuCl₄·3H₂O in water and make up to the mark. HAuCl₄·3H₂O is hygroscopic and it is best to make a stock solution of appropriate concentration first and then give a known fixed volume to each of the students to make up to 10 mL.
2. Prepare ~ 0.5% citrate solution in a flask by dissolving 25 mg of Na₃C₆H₅O₇ in 5 mL of water.
3. Take 1 mL of 5 mM HAuCl₄ solution in a 50 mL RB flask and add 18 mL of water to it.
4. Heat the solution over a mantle and bring the solution just to a boil, marked by the appearance of bubbles.
5. Add 1 mL of 0.5 % citrate solution to the boiling solution.
6. Continue to heat the solution, till its colour changes to wine red. (It takes about ~10 min.)
7. AuNPs thus produced are of 15–20 nm in diameter.

Note: To study the growth of AuNPs with time, collect samples of around 4 mL (depending on the cuvette capacity of the available spectrophotometer) with a pipette.

2.3.3.2 Preparation of gold nanoparticle + hemoglobin solution

1. Prepare a phosphate-buffered saline (PBS) solution of ~7.2 pH in a 250 mL beaker, by adding 3.2 g of NaH₂PO₄, 1.09 g of Na₂HPO₄ and 9 g of NaCl to 100 mL of water. Thoroughly stir the solution using a magnetic pellet.
2. Prepare 10 mL of hemoglobin (Hb) solution of 0.02 mg/mL concentration in 20% aqueous ethanol by dissolving 0.2 mg of hemoglobin in 10 mL of the solvent.
3. Prepare 5 samples (each with a final volume of 5 mL) with the following amounts:
 - i. 1 mL AuNP + 4 mL PBS
 - ii. 1 mL AuNP + 1 mL Hb + 3 mL PBS
 - iii. 1 mL AuNP + 2 mL Hb + 2 mL PBS
 - iv. 1 mL AuNP + 3 mL Hb + 1 mL PBS
 - v. 1 mL AuNP + 4 mL Hb
4. Record the absorption spectra of the above samples after 10 minutes.

Note: PBS buffer is taken as the reference solution. The purpose of PBS is to maintain the pH around 7.2 so that Hb will be active.

2.4 RESULTS AND DISCUSSION

2.4.1 Gold Nanoparticles

Figure 2.1 shows the colour changes observed during the synthesis of AuNPs. Colour of the solution changes from colourless to wine red. Similarly, Fig. 2.2 shows the absorption spectra collected

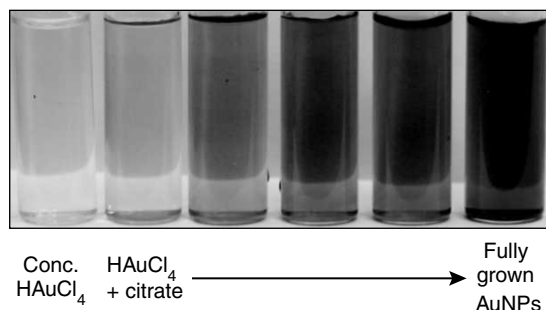


Fig. 2.1 Evolution of AuNPs over time; from concentrated HAuCl_4 to fully grown AuNPs.

during the synthesis of nanoparticles. The bottom curve (black trace) in Fig. 2.2 is collected from the chloroauric acid solution just before the addition of sodium citrate. Subsequent curves of Fig. 2.2 are collected for the same solution at different intervals after the addition of sodium citrate. The top curve corresponds to fully grown particles. Initially, there are no nuclei present, but as the synthesis proceeds, nuclei get generated. This is reflected as the increased absorbance of AuNPs. The presence of AuNPs is recognized by the surface plasmon band of the absorption spectrum (absorption maximum around 520 nm), which is characteristic of the AuNPs. We also observe a decrease in the absorption intensity with a decrease in AuNPs, core size along with a slight blue shift and broadening of the plasmon band. Analysis of absorption spectrum reveals that the deep-red colour of AuNP sols in water and in gold-dispersed glasses is due to the surface plasmon band (SPB), a broad absorption band in the visible region around 520 nm. SPB is due to the collective oscillations of the electron gas at the surface of nanoparticles (6s electrons of the conduction band for AuNPs) that is correlated with the electromagnetic field of the incident light, i.e., the excitation of the coherent oscillation of the

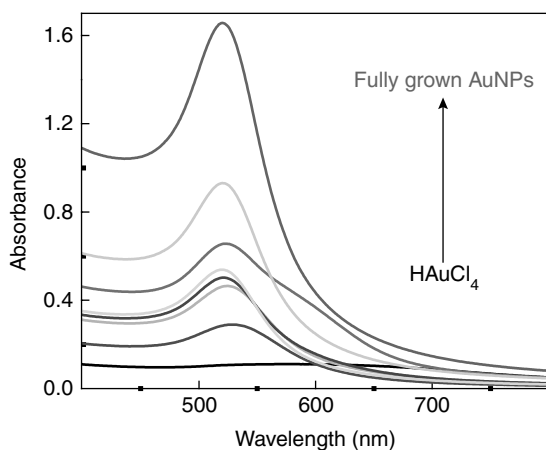


Fig. 2.2 Evolution of AuNPs seen by absorption spectra.

conduction band. SPR position is dependent on the particle size. It's maximum position and bandwidth are also influenced by the particle shape, core charge, medium dielectric constant, temperature and refractive index of the solvent.

2.4.2 Adsorption of Hemoglobin Molecules on Gold Nanoparticles

Figure 2.3 shows colour change due to hemoglobin addition. UV/Vis spectra (Fig. 2.4) illustrate the effect of binding of hemoglobin on gold nanoparticles. It is clear that the traces of absorption due to SPR of Au particles are retained even after bonding. The number of hemoglobin molecules per nanoparticle is calculated from the relative change in Soret band intensity of hemoglobin.

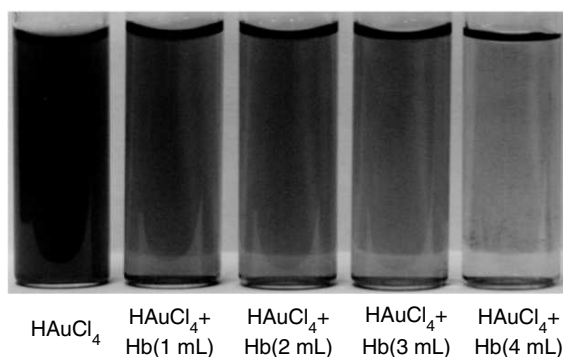


Fig. 2.3 Colour change of gold colloid with the addition of hemoglobin and PBS solutions.

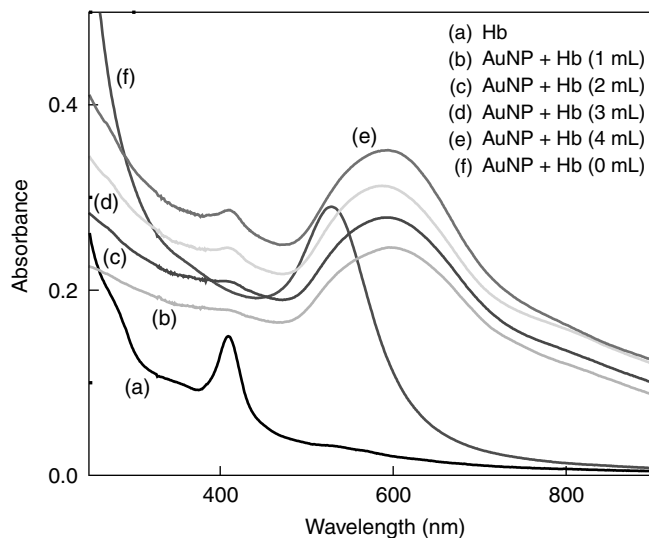


Fig. 2.4 UV/Vis spectra showing the effect of adsorption of hemoglobin on AuNPs.

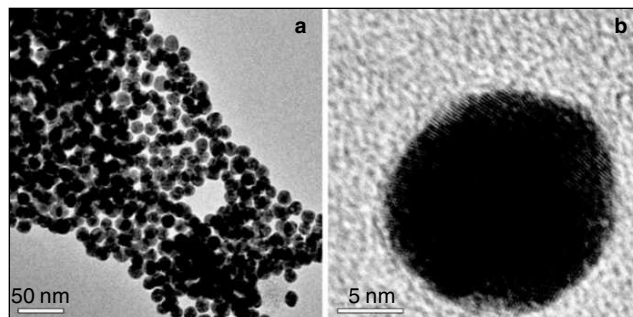


Fig. 2.5 (a) TEM image of citrate-capped gold nanoparticles, as prepared and (b) an expanded image of a single gold nanoparticle.

TEM images (Fig. 2.5) show that the diameters were in the range of 15–20 nm, with a predominance of spherical structures. It is also seen that the particles are uniform in size and shape, and well-dispersed, well-defined in shape and spherical in nature. No deviations or distortions in the structure were encountered.

QUESTIONS

1. What are AuNPs? Write a short note on various uses to which they have been put into in history.
2. What are the various methods by which AuNPs can be synthesised? How are they synthesised in Turkevich reaction?
3. Write a note on various applications of AuNPs.
4. Elucidate the characterization techniques of AuNPs.
5. What is hemoglobin? Explain the adsorption of bio molecules on AuNPs.
6. What do the absorption spectra that are obtained indicate about the formation of AuNps and hemoglobin –AuNP interaction?
7. In the present experiment, we know the initial amount of hemoglobin taken, i.e. 0.02 mg of Hb per mL. Let us assume that we are analysing the second mixture. With the help of the absorption spectra you have taken, calculate the total number of hemoglobin molecules per gold nanoparticle.

Answer to Question No. 7

This problem can be solved in following steps:

1. Calculation of no. of gold atoms present in a single AuNP
2. Calculation of no. of AuNPs formed in a preparation
3. Calculation of no. of Hb molecules present in 1 mL of initial solution
4. Calculation of fraction of Hb molecules adsorbed
5. Calculation of no. of Hb molecules adsorbed per AuNp

1. Calculation of no. of gold atoms present in a single AuNP

Given: Density of solid gold = 19.3 g cm^{-3} = density of AuNPs.

Given: Atomic mass of Au = 197

Thus, we know that 197 g of gold (i.e. 1 mol of gold) consists of Avogadro no. of Au atoms.

$$\therefore \text{No. of Au atoms present in } 1 \text{ cm}^3 \text{ of solid gold} = \frac{6.022 \times 10^{23} \text{ mol}^{-1}}{197 \text{ g mol}^{-1}} \times 19.3 \text{ g} = 5.9 \times 10^{22}$$

\therefore Average volume required for one single Au atom (including void space) in solid gold

$$= \frac{1 \text{ cm}^3}{5.9 \times 10^{22}} = 1.7 \times 10^{-23} \text{ cm}^3 = 1.7 \times 10^{-23} \times 10^{-6} \text{ m}^3 = 1.7 \times 10^{-29} \text{ m}^3$$

Given: The size of gold nanoparticles = 15 nm.

\therefore Radius, $r = 7.5 \text{ nm} = 7.5 \times 10^{-9} \text{ m}$

$$\text{Volume of a single AuNP} = \frac{4}{3} \pi r^3 = \frac{4}{3} \pi (7.5 \times 10^{-9} \text{ m})^3 = 1.77 \times 10^{-24} \text{ m}^3.$$

$$\begin{aligned} \text{So, no. of Au atoms in a single NP} &= \frac{\text{Volume occupied by all atoms in a single NP}}{\text{Volume required in the solid for one Au atom}} \\ &= \frac{1.77 \times 10^{-24} \text{ m}^3}{1.7 \times 10^{-29} \text{ m}^3} \approx 1 \times 10^5 \text{ (i.e. about one lakh gold atoms)} \end{aligned}$$

2. Calculation of no. of AuNPs formed in a preparation

Final volume of AuNP solution $\approx 1 + 18 + 1 = 20 \text{ mL}$

All gold present in 1 mL of 5 mM HAuCl₄ solution was transformed into AuNPs with a final volume of $\sim 20 \text{ mL}$.

No. of gold atoms that can be formed in this solution after reduction = $6.023 \times 10^{23} \text{ mol}^{-1} \times 5 \times 10^{-3} \text{ mol L}^{-1} / 1000 \text{ mL} \times 1 \text{ mL} = 3 \times 10^{18}$.

No. of NPs that can be formed in this solution

$$= \frac{\text{Total no. of gold atoms in } 20 \text{ mL}}{\text{No. of gold atoms in one single NP}} = \frac{3 \times 10^{18}}{1 \times 10^5} = 3 \times 10^{13}$$

$$\therefore \text{No. of NPs per mL of this solution} = \frac{3 \times 10^{13}}{20} = 1.5 \times 10^{12}.$$

3. Calculation of no. of Hb molecules present in 1 mL of initial solution

Given: Molecular mass of Hb = 16125

Concentration of Hb solution prepared = 20 ppm.

Mass of Hb that would be present in 1 L of 20 ppm Hb solution = 20 mg = 20×10^{-3} g

$$\begin{aligned} \text{No. of moles of Hb present in 1 L of same solution} &= \frac{\text{Mass of Hb present in 1L}}{\text{Gram molecular mass of Hb}} \\ &= \frac{20 \times 10^{-3} \text{ g}}{16125 \text{ g mol}^{-1}} = 1.24 \times 10^{-6} \text{ mol} \end{aligned}$$

No. of Hb molecules in 1 L of above solution = No. of moles of Hb in 1L \times Avogadro no.

$$= 1.24 \times 10^{-6} \text{ mol} \times 1.622 \times 10^{23} \text{ mol}^{-1} = 2 \times 10^{17} \text{ molecules}$$

\therefore No. of Hb molecules in 1 mL of above solution,

$$N_{\text{total}} = \frac{\text{No. of molecules in one L}}{1000} = \frac{2 \times 10^{17}}{1000} = 2 \times 10^{14} \text{ molecules.}$$

4. Calculation of fraction of Hb molecules adsorbed

From the experimental spectra, determine A_{total} and A_{unads} . Here, A_{total} is the absorbance of the mixture (i) with 1 mL AuNP + 4 mL PBS; A_{unads} is the absorbance of mixture (ii) with 1 mL AuNP + 1 mL Hb + 3 mL PBS.

We know, by Beer-Lamberts Law, that absorbance is directly proportional to the concentration.

i.e. $A_{\text{unads}} \propto C_{\text{unads}}$ and $A_{\text{total}} \propto C_{\text{total}}$.

$$\therefore \text{Fraction of unadsorbed Hb} = \frac{C_{\text{unads}}}{C_{\text{total}}} = \frac{A_{\text{unads}}}{A_{\text{total}}}.$$

We know that, sum of the fractions of adsorbed Hb and unadsorbed Hb = 1

$$\therefore \text{Fraction of adsorbed Hb} = 1 - \frac{A_{\text{unads}}}{A_{\text{total}}} = \frac{A_{\text{total}} - A_{\text{unads}}}{A_{\text{total}}}.$$

$$\text{Let } \frac{A_{\text{total}} - A_{\text{unads}}}{A_{\text{total}}} = y.$$

5. Calculation of no. of Hb molecules adsorbed per AuNP

As calculated above, total no. of Hb molecules in the mixture = $N_{\text{total}} = 2 \times 10^{14}$

Let total number of Hb adsorbed = N_{ads} .

We have $N_{\text{ads}} = N_{\text{total}} \times \text{fraction of adsorbed Hb} = (N_{\text{total}}) \times y = 2 \times 10^{14} \times y$.

$$\therefore \text{No. Hb adsorbed per AuNP} = \frac{\text{No. of adsorbed Hb molecules}}{\text{No. of nanoparticles}} = \frac{2 \times 10^{14} \times y}{1.5 \times 10^{12}} = 133 \times y.$$

Note: If the mixture no. (iv), with 1 mL AuNP + 3 mL Hb + 1 mL PBS, is considered, then (1) N_{total} will be 3 times and (2) A_{unads} value would be higher and hence, y would be lower.

Note: Some of the solution required for the experiment may be prepared by the teachers themselves. Calculations for two of the solutions are given below:

Formula mass of $\text{HAuCl}_4 \cdot 3\text{H}_2\text{O} = 393.8$

Formula mass of trisodium citrate dehydrate, $\text{Na}_3\text{C}_6\text{H}_5\text{O}_7 \cdot 2\text{H}_2\text{O} = 294.10$

A batch of 20 students, say.

Total volume of 5 mM solution needed: 10 mL per student \times 20 students = 200 mL

Teacher makes 100 mL of more concentrated solution using 500 mg of $\text{HAuCl}_4 \cdot 3\text{H}_2\text{O}$

Conc. of this solution = $(0.5 \text{ g}/393.8 \text{ g per mole}/100 \text{ mL}) = 12.7 \times 10^{-6} \text{ mol}/10^{-3} \text{ L} = 12.7 \times 10^{-3} \text{ mol/L}$
 $= 12.7 \text{ mmol/L} = 12.7 \text{ mM}$

3.9 mL of this, when made to 10 mL with water gives a solution of 5 mM conc.

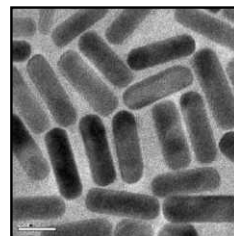
Out of 100 mL stock solution, $3.9 \times 20 = 78 \text{ mL}$ is taken by the students.

Similarly, teacher makes ~5% citrate solution by dissolving 125 mg of trisodium citrate dihydrate in 25 mL of water. Each student would take 1 mL of this to be used as such.

REFERENCES

1. http://en.wikipedia.org/wiki/Colloidal_gold accessed on 21/09/2010.
2. J. Turkevich, *Gold. Bull.*, 18, (1985), 3 and 4.
3. S. Eustis, M.A. El-Sayed, *Chem. Soc. Rev.*, 35, (2006), 209–17.
4. T. Pradeep, *Nano: The Essentials*, Tata McGraw Hill, New Delhi, 4th reprint, 2010.
5. <http://legacy.owensboro.kctcs.edu/gcaplan/anat2/notes/Image332.gif> accessed on 17/08/2010.
6. Renjis T. Tom and T. Pradeep, *Langmuir*, 21, (2005), 11896–902.

DETERMINATION OF THE BAND GAP OF SEMICONDUCTOR NANOPARTICLES*



3.1 OBJECTIVE

- Determination of the band gap of lead sulfide (PbS) nanoparticles using optical absorption spectroscopy.

3.2 BACKGROUND

Low-dimensional semiconductors or semiconductor nanostructures are novel materials with fascinating physical properties which can be engineered to suite device applications. The concept of band gap is not so well defined in the nano regime. The 'band gap' energy can be altered by changing the size of the nano particle, though, chemically the compound remains the same. For example, bulk PbS crystals are black in color as the optical absorption cut off is near 3000 nm (0.40 eV) whereas nano-PbS can be obtained in various shades of red, brown yellow, etc. This is a practical example of the quantum mechanics of particle in a box, where the 'particle' is the electron in the 'box' of the particle. Such 'band gap engineering' can alter the optical and electrical properties of the semiconductor considerably. Exciton levels become prominent even at room temperature which show up in optical spectra in the case of nanoparticles, thus providing new features in the optical absorption spectra [1]. Energy levels of a quantum dot can be estimated with the help of particle-in-a-box model. So, the lowest allowed energy level for a particle in a one-dimensional well (or box) is given by [2],

$$E_{\text{well}(1D)} = \frac{h^2}{8md^2}$$

where d is the width of the quantum well. Charge carriers in a quantum dot, namely the electrons and holes, are confined in all three dimensions. So we are effectively looking at particles trapped in an infinite 3-dimensional potential well. The potential energy is zero everywhere inside the well but at and after the walls, it is infinite. The simplest shapes of a three-dimensional box can be, for instance, a sphere or a cube. Extending the concept of energy in a one-dimensional potential well to the case of a sphere, which is of our interest, the lowest allowed energy level is [2, 3]

* A modified form of this experiment was developed by Prof. C. Vijayan, Department of Physics, IIT Madras, Chennai in his laboratory course.

$$E_{Well, Sphere(3D)} = \frac{h^2}{2md^2} = \frac{h^2}{8mR^2}$$

where $d (= 2R)$ is the diameter of the quantum dot. While the above equation is for one particle in a quantum sphere, extending the same concept to the electron-hole pair in a quantum dot we have [2, 3]

$$E_{Well} = \frac{h^2}{8R^2} \left(\frac{1}{m_e} + \frac{1}{m_h} \right)$$

where R is the radius of the quantum dot, m_e and m_h are the masses of the electrons and holes, respectively.

Quantum confinement is a result of size of nanocrystal being smaller than that of the Bohr exciton radius of the bulk semiconductor. By forcing electrons and holes to occupy a space smaller than the normal equilibrium distance in the bulk material, more energy is required to promote the electron from the valance band to the conduction band. Hence, smaller the nanocrystal, larger is the band gap and more blue-shifted is the absorption/emission in the nanocrystals. What we really mean by band gap energy in the case of quantum dot is the minimum energy required for the creation of an electron-hole pair. Band gap energy of the bulk semiconductor and the quantum dot can be related by the following equation [2, 3].

$$E_g(dot) = E_g(bulk) + E_{ex}$$

$$E_{ex} = E_{Well} + E_{Coul}$$

$$\text{where } E_{Coul} = -\frac{1.8e^2}{4\pi\epsilon_{sc}\epsilon_0 R} \text{ and hence } E_g(dot) = E_g(bulk) + \frac{h^2}{8R^2} \left(\frac{1}{m_e} + \frac{1}{m_h} \right) - \frac{1.8e^2}{4\pi\epsilon_{sc}\epsilon_0 R}$$

This equation can be simplified further by neglecting the third term

$$E_g(dot) = E_g(bulk) + \frac{h^2}{8R^2} \left(\frac{1}{m_e} + \frac{1}{m_h} \right)$$

3.2.1 Calculation of Band Gap using the Absorption Spectrum

By absorbing the incident radiant energy, electrons in the valance band can get excited to the conduction band. This absorption of light occurs when energy of a quantum ($h\nu$) is equal to the band gap energy (E_g) of the material [4].

$$E_g = h\nu_g = \frac{hc}{\lambda_g} \cong \left(\frac{1240}{\lambda_g} \right) eV$$

Here, λ_g is the wavelength corresponding to the band gap energy at room temperature, that present inside the bracket is its value when expressed in nm. E_g can be obtained once we know the value of λ_g , which in turn can be obtained by calculating the point of abrupt change in the corresponding absorption spectrum of the sample.

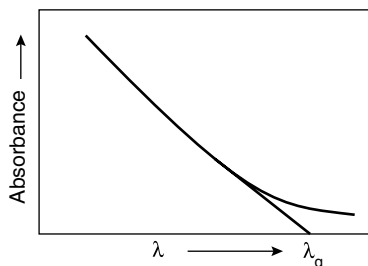


Fig. 3.1 Plot of absorbance vs. wavelength of the semiconductor quantum dot.

Figure 3.1 illustrates how to calculate λ_g from the absorption spectrum of a sample. The same can be used to calculate the band gap energy and hence the size (R) of the quantum dots.

3.3 EXPERIMENT

3.3.1 Materials

- Lead acetate (AR)
- Sodium sulphide (AR)
- Transparent, water soluble PVAc glue

3.3.2 Procedure

3.3.2.1 Synthesis of PbS Nanocrystals in Synthetic Glue Medium

1. Lead acetate and sodium sulphide are used as reactants, while the commercially available, transparent, water soluble PVAc glue is used as the host matrix.
2. A composite is prepared by continuously stirring, equimolar quantities of lead acetate and sodium sulphide in the glue medium.
3. The mixture is then poured into a petri-dish and dried in air. A stable optical quality film is obtained.

3.3.2.2 Determining the Band Gap

1. Place glass slides in both the sample holder and the reference sample holder of the UV/Vis/NIR spectrophotometer.

2. Select 800 nm as scanning wavelength maximum and 200 nm as minimum in the window for scan settings and carry out baseline correction.
3. Place the film containing lead sulfide quantum dots in the sample holder of spectrophotometer and record the absorption spectrum.
4. Plot the data as absorbance vs. wavelength and draw a tangent to the curve at the point of curvature change, as shown in Fig. 3.1 (This point indicates the energy above which the quantum dot absorbs the incident light).
5. Calculate the band gap of the quantum dot using the following relation:

$$E_g \text{ in eV} = \frac{1240}{\lambda_g}, \quad (\lambda_g \text{ is given in nm units}) \quad (1)$$

6. Calculate the size of quantum dots using the following relation:

$$\text{Exciton } (\Delta E) = E_g(\text{QD}) - E_g(\text{bulk}) = \frac{h^2}{8R^2} \left\{ \frac{1}{m_e} + \frac{1}{m_h} \right\} \quad (2)$$

Here, $h = 6.63 \times 10^{-34}$ Js, $m_e = 1.1$ (electron mass), $m_h = 0.7$ (electron mass), electron mass = 9.1×10^{-31} kg, R is the size of the quantum dot in m and E's are energies expressed in J.

3.4 RESULTS AND DISCUSSION

When radiation with continuously increasing energy is incident on quantum dots, absorption begins at the point when photon energy is equal to the band gap. Figure 3.2 shows the optical absorption spectrum of the PbS quantum dots. As illustrated in Fig. 3.1, the value of λ_g is calculated as 588 nm.

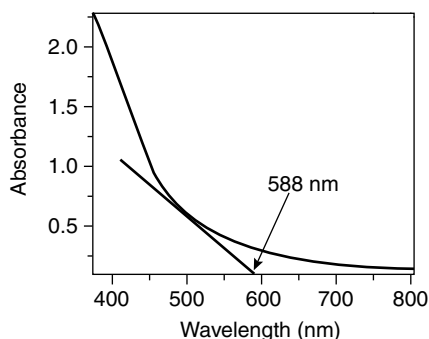


Fig. 3.2 Optical absorption spectrum of the PbS quantum dots.

From equation (1), the band gap of PbS quantum dot is:

$$E_g = \frac{1240}{588} \text{ eV} \approx 2.11 \text{ eV}$$

After substituting this value in equation (2), we get,

$$2.72 \times 10^{-19} \text{ J} = (2.11 - 0.41) \text{ eV} \times 1.602 \times 10^{-19} \frac{\text{J}}{\text{eV}}$$

$$= \frac{(6.626 \times 10^{-34} \text{ Js})^2}{8R^2} \left\{ \frac{1}{1.1(9.1 \times 10^{-31} \text{ kg})} + \frac{1}{0.7(9.1 \times 10^{-31} \text{ kg})} \right\}$$

$$\Rightarrow R = 7.2 \times 10^{-10} \text{ m} = 0.72 \text{ nm}$$

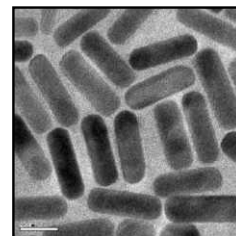
QUESTIONS

1. What are the ways to measure band gap of semiconductors?
2. Why is absorption spectroscopy used here to measure band gap?
3. What are the other ways to determine radii of small particles?

REFERENCES

1. C. Vijayan, Experimental Manual for M.Sc. Students, IIT Madras.
2. G. Schmid, Nanoparticles: From theory to application, Wiley-VCH, 2004, 21–24.
3. T. Kippeny, L.A. Swafford and S.J. Rosenthal. *J. Chem. Edu.*, 79 (9), (2002), 1094–1100.
4. (a) J.G. Ibanez, O. Solorza and E.G. Campo. *J. Chem. Edu.*, 68 (10), (1991), 872–875, (b) J.G. Ibanez, F. Gomez, I. Konik, D.E. Lozano, A. Mugica, C.G. Mesa, M.M. Singh, Z. Szafran and R.M. Pike. *J. Chem. Edu.*, 74 (10), (1997), 1205–1207.

NANOCHEMISTRY OF SILVER NANOPARTICLES IN CONVERTING *p*-NITROPHENOL TO *p*-AMINOPHENOL



4.1 OBJECTIVE

- Investigation of the nanochemistry of silver nanoparticles, particularly towards the conversion of phenolic groups.

4.2 BACKGROUND

p-Aminophenol (or 4-Aminophenol, 4-AP) is a highly useful chemical in industry. It is an aromatic amine as well as an aromatic alcohol having the chemical formula, $C_6H_4(NH_2)(OH)$ [1]. It is an isomer of Aminophenol, the other two isomers being *o*-Aminophenol (2-Aminophenol) and *m*-Aminophenol (3-Aminophenol). It is a white powder at room temperature. It is used as an intermediate in the production of pharmaceuticals such as paracetamol or acetaminophen (a widely used analgesic and antipyretic) and in the production of dyestuffs such as sulfur dyes. *p*-Aminophenol is well known for its use in the black-and-white film developer, Rodinal. It is a potent allergen that causes dermatitis, asthma, and methemoglobinemia. Although there are several routes for the production of *p*-Aminophenol, widely employed methods involve reduction of synthesis using *p*-Nitrophenol or the reduction of Nitrobenzene in dilute sulfuric acid over platinum catalyst. Here, we will restrict our discussion to synthesis using *p*-Nitrophenol. Reduction of nitro compounds can be facilitated by many different reagents and reaction conditions. Historically, the nitro group is one of the first functional groups to be reduced, due to the ease of nitro group reduction. Presence of neighboring hydrogen makes nitro groups behave differently [2].

Similar to *p*-Aminophenol, *p*-Nitrophenol (4-Nitrophenol, 4-NP) belongs to a family of isomers (*o*-, *p*- and *m*-) with chemical formula, $HOC_6H_4NO_2$. Nitrophenols are highly poisonous. In earlier days, the soil near an explosives' factory, fabric factory and military plants occasionally used to get contaminated with nitrophenols. *p*-Nitrophenol exhibits two crystalline structures, α and β , in the solid state. The α -form occurs as colourless rods, unstable at room temperature and stable towards sunlight, while β -form occurs as yellow rods, stable at room temperature and turns, gradually, to red form upon exposure to sunlight. A sample of normal *p*-nitrophenol exists as a mixture of both the

forms. It is useful as a pH indicator due to its colour-changing property. It is used as a fungicide raw material and is used in the preparation of phenetidine and acetophenetidine. In environment, aerobic decomposition of *p*-Nitrophenol is rather slow [2].

Sodium borohydride is an important reducing agent which is used in the manufacture of pharmaceuticals and other compounds. It is one of the most useful reagents for reducing aldehydes, ketones, acid halogenides, acyl chlorides and some esters. However, NaBH_4 has no ability, on its own, to reduce esters, carboxylic acids, nitriles, amides and nitro compounds to corresponding primary amines. To increase its reduction ability, some mixed systems as well as catalytic reactions were considered. Conversion (or reduction) of *p*-Nitrophenol to *p*-Aminophenol is an important step from the point of view of industrial applications. NaBH_4 is not effective in this regard unless provided with some catalysts to decrease the kinetic barrier of the reaction. Various catalysts have been used in the past. Recently silver nanoparticles were used for the same purpose [1–3]. Conversion of 4-NP into 4-AP is an industrially important reduction reaction. Catalytic reduction method can be used in place of conventional reduction methods in the industries.

In the present experiment, we study the catalytic activity of the silver nanoparticles in conversion of nitrophenol to aminophenol with sodium borohydride as reducing agent. Nanoparticles offer convenience in the analysis of elementary steps in the catalyzed reaction through simple and basic instruments like a spectrophotometer, due to their optical transparency. Another added advantage is that the huge surface area of these particles makes them ideal as catalysts. Rich plasmon resonance of silver nanoparticles in the visible region makes the whole study an interesting one [4]. The overall chemical reaction can be summarized as follows,

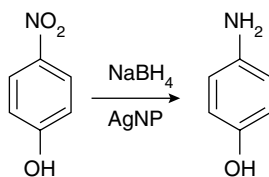


Fig. 4.1 Schematic representation of the reaction.

4.3 EXPERIMENT

4.3.1 Materials

- *p*-Nitrophenol
- NaBH_4
- Silver nanoparticles

4.3.2 Apparatus

- Perkin–Elmer Lambda 25 spectrometer was used for UV/Vis absorption measurements.

4.3.3 Procedure

4.3.3.1 Preparation of Silver Nanoparticles

1. Prepare about 15 mL of 1 mM silver nitrate solution and take it in a burette.
2. Take 30 mL of 2 mM NaBH_4 solution, prepared using ice-cold distilled water, in a conical flask and keep it under ice cold condition.
3. Add dropwise 10 mL of the AgNO_3 solution from the burette into the conical flask with vigorous stirring.
4. A wine-red coloured solution of silver nanoparticles is observed, which shows an absorption around 390–420 nm.

4.3.3.2 Catalytic Reduction of 4-Nitrophenol to 4-Aminophenol

1. Take two 50 mL conical flasks. To each, add 10 mL of 1.2 mM 4-Nitrophenol and 10 mL of 12 mM sodium borohydride solutions and record the absorption spectrum of one of the mixtures.
2. Record the absorption spectra of Ag nanoparticles and of 4-Nitrophenol.
3. During UV/Vis absorption measurements, in each case, use a mixture of 0.5 mL sample and 2.5 mL distilled water.
4. Add 0.4 mL of silver nanoparticles to the other conical flasks containing the mixture of 4-Nitrophenol and sodium borohydride. Record the absorption spectra of this mixture at different intervals of time. The results are discussed below.

4.4 RESULTS AND DISCUSSION

Absorption spectra of silver nanoparticles and 4-Nitrophenol show peaks at 391 and 317 nm, respectively. When sodium borohydride is added to 4-Nitrophenol, the pale yellow colour of 4-Nitrophenol turns

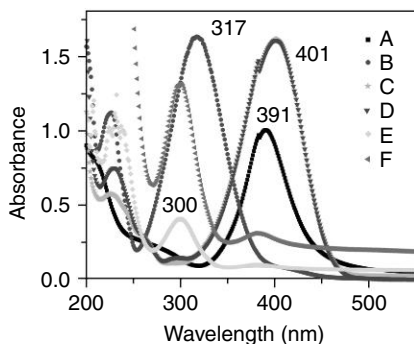
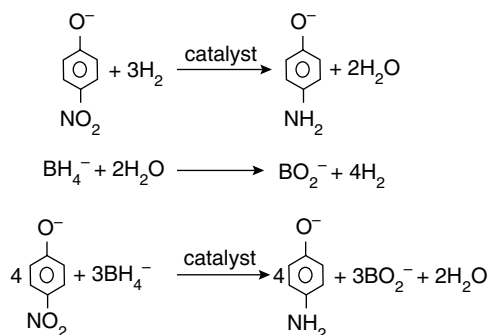


Fig. 4.2 UV/Vis absorption spectra of (A) silver nanoparticles, (B) 4-Nitrophenol, (C) 4-Nitrophenol + NaBH_4 , (D) 4-Nitrophenol + NaBH_4 + silver nanoparticles after 5 minutes, (E) same as D, but after 15 minutes and (F) same as D but after 60 minutes.

to intense yellow colour, which is also reflected in the peak position of 4-Nitrophenol at 317 nm being shifted to 401 nm. This is due to the formation of phenoxide ions by the abstraction of phenolic protons by BH_4^- ions (base). The phenoxide ion formed would be stabilized by resonance which leads to a quinonoid structure having absorption around 400 nm. When Ag nanoparticles are added, a time evolution of peak at 300 nm is observed, which is due to the formation of increased amounts of 4-Aminophenol. This is accompanied by a decrease in intensity of the 401 nm peak. These observations indicate the conversion of nitro groups to amino groups. Following equations show the steps in a possible reaction path [5].



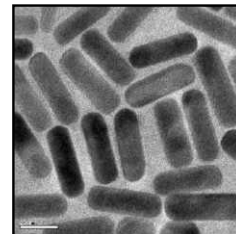
QUESTIONS

1. When sodium borohydride solution is added to 4-Nitrophenol, the absorption peak shifts from 320 nm to 400 nm. What is the reason for this shift?
2. Write a note on the physical and chemical characteristics of *p*-aminophenol.
3. Why does the adsorption of nucleophiles on to metal nanoparticles result in decrease of reduction potential values?

REFERENCES

1. Lain-tze Lee, M.H. Chen and C.N. Yao. *U.S. Patent number 4885389*, (1989).
2. <http://en.wikipedia.org/wiki/4-Nitrophenol>; <http://en.wikipedia.org/wiki/4-Aminophenol> accessed on 24/09/2010.
3. T. Satoh, S. Suzuki, Y. Suzuki, Y. Miyaji and Z. Imai. *Tetrahedron Lett.*, 52, (1969), 4555–58.
4. N. Pradhan, A. Pal and T. Pal. *Colloids Surf. A*, 196, (2002), 247–57.
5. J. Huang, S. Vongehr, S. Tang, H. Lu and X.J. Meng. *J. Phys. Chem. C*, 114, (2010), 15005–010.

SURFACE ENHANCED RAMAN SCATTERING ACTIVITY OF SILVER NANOPARTICLES



5.1 OBJECTIVES

- Study of surface-enhanced Raman scattering of silver nanoparticles.
- Calculation of enhancement factor.

5.2 BACKGROUND

5.2.1 Spectroscopy

Original definition of the term spectroscopy refers to the study of the interaction between radiation and matter as a function of wavelength (λ). Modern definition of the term, however, is modified to include any measurement of a quantity as a function of either wavelength or frequency. Plot of the response as a function of wavelength (or more commonly frequency) is referred to as a spectrum. Spectroscopy is often used in analytical and physical chemistry to identify the substances through the spectrum emitted from or absorbed by the substance. It is also used heavily in astronomy and remote sensing. There are various spectroscopic techniques based on the type of interaction that is used and the physical quantity being measured [1].

5.2.2 Raman Scattering and Spectroscopy

5.2.2.1 Raman Scattering

Raman scattering or more popularly known as Raman effect is nothing but the inelastic scattering of light, occurring when light is illuminated upon a molecule when it interacts with the electron cloud and the bonds of that molecule. It was first reported for liquids in 1928 by Sir C.V. Raman and hence the name. The principle behind Raman effect can be explained as follows: When light is scattered from an atom or a molecule, most of the photons (remember, photon is a basic unit of light!) undergo elastic scattering, with the energy of scattered photons being the same as that of the incident photons. However, a small fraction of the scattered light (~ 1 in 10^7 photons) undergoes inelastic scattering, resulting in the energy (frequency) of the scattered photons being different from that of the incident photons. In other words, a photon excites an electron in the atom or the molecule from the ground

state to a virtual energy state and when the electron relaxes, it emits a photon, returning to a different rotational or vibrational state. The energy difference between the original ground state and the new state leads to a shift in the emitted photon frequency compared to that of the incident photon. This shift is known as the 'Raman shift'. If the final electronic state of the molecule is higher in energy compared to the initial state, then the emitted photon will have a lower frequency in order for the total energy of the system to remain balanced. This type of shift in frequency is designated as 'Stokes shift'. Similarly, if the final electronic state has lower energy than the energy of initial state, then the emitted photon will have a higher frequency, and this is designated as 'anti-Stokes shift'. It should be noted that Raman scattering is highly sensitive to vibrational modes of a system, which is the reason why it is known as the fingerprint of a molecule [1–2].

5.2.2.2 Raman Spectroscopy

Raman spectroscopy is unique among various spectroscopic techniques available. It is widely used for studying vibrational, rotational and other low-frequency modes in a system. Raman spectroscopy is based on the Raman scattering of monochromatic light, common source of which is a laser in the visible, near infrared or near ultraviolet region. Interaction of the laser photons with molecular vibrations, phonons or other excitations in the system, results in a shift in the energy of the scattered photons. Such a shift in energy gives information about the phonon modes in the system and is used to analyse the composition and nature of bonding in the given material. Phonons are quantized vibrational modes in a rigid crystal lattice. Vibrational modes in a system are specific to the type of chemical bond as well as the symmetry of the molecules. This makes Raman spectroscopy a common tool for chemists. It provides a fingerprint by which a molecule can be identified. For example, organic molecules have a fingerprint in the range of 500–2000 cm^{-1} . Also, this technique can be used to study the changes in the chemical bonding. It should be mentioned, however, that strength of Raman signal is very low. This is the main disadvantage of Raman spectroscopy that prevented its active use for a long time, until the discovery of surface enhanced Raman spectroscopy (SERS). There exist several variations of Raman spectroscopy, apart from SERS, to address other limitations of conventional Raman spectroscopy [1–2].

5.2.2.3 Surface Enhanced Raman Spectroscopy

Surface enhanced Raman spectroscopy (SERS) is a surface sensitive technique in which Raman signal from molecules is enhanced as a result of adsorption of the molecules on rough metal surfaces. The enhancement factor can be as high as 10^{14} – 10^{15} , which makes the technique to be sensitive enough to detect even single molecules. SERS was first reported in 1974 by Fleischman et. al., who reported 10^5 – 10^6 times enhancement in Raman signals from pyridine adsorbed on electrochemically roughened silver. Such enhancement in Raman signal, however, was wrongly interpreted to be due to the additional surface area provided by the roughening of the surface. Later, in 1977, it was shown that even minimally roughened surfaces show enhancement in Raman signal, and these enhancements could not be explained by the increased surface area. Currently, SERS is a universally accepted surface sensitive technique, quite useful for analytical applications [1–2].

5.3 Experiment

5.3.1 Materials

- Silver nitrate
- Trisodium citrate
- Sodium chloride
- Crystal violet (CV)

5.3.2 Apparatus

- RB flask, 50 mL
- Glass bottle, 5 mL
- Heating mantle
- Raman spectrometer

5.3.3 Procedure

5.3.3.1 Preparation of Silver Nanoparticles

For making Ag@citrate nanoparticles, 4.5 mg of AgNO₃ was dissolved in 25 mL of water in a 50 mL RB flask and the solution was heated to boil. To this solution, 1 mL of 1 % (10 mg in 1 ml H₂O) trisodium citrate solution was added and kept boiling until the color of the solution changed to pale yellow.

5.3.3.2 SERS Experiment Details

For the SERS experiments, glass slides were thoroughly cleaned with chromic acid solution and washed with distilled water several times. 30 μ L of Ag@citrate colloidal suspension was mixed with 30 μ L of 10⁻⁵ M crystal violet (CV) solution and 10 μ L of distilled water. Resultant solution was spotted onto a glass slide. The objective lens was brought into direct contact with this sample solution. After collecting the spectrum, 10 μ L of 50 mM NaCl solution was added to the above solution (to induce particle aggregation) and the Raman spectrum was collected after 10 min. Experiment was repeated with CV solution of varying concentrations such as 10⁻⁶ and 10⁻⁷ M. In each case, spectra were also collected after adding 10 μ L of 50 mM NaCl solution.

5.3.3.3 Instrumentation

Raman spectra were measured using a CRM 200 confocal Raman spectrometer (WiTec GmbH). The substrate was mounted on the sample stage of the spectrometer. The SERS spectra were collected by exciting the sample with a 532 nm laser. Back-scattered light was collected by the 60 x objective and sent to the spectrometer through a multimode fiber. It was then dispersed using a 600 grooves/mm grating and the dispersed light was collected by a Peltier-cooled charge coupled device (CCD).

5.4 RESULTS AND DISCUSSION

Aggregation of nanoparticles is found to increase the SERS activity. Even single molecule detection can be achieved by using such aggregated systems. Increasing the ionic strength of the medium is one

method to induce the aggregation of the nanoparticles. NaCl is a good salt which can be used for this purpose.

The enhancement in the SERS activity of Ag@citrate nanoparticle upon aggregation has been demonstrated in Fig. 5.1. Here, the SERS property was investigated using crystal violet as the analyte. For that, the SERS spectra at three different concentrations of CV adsorbed on Ag@citrate nanoparticles were collected (Figure 5.1). Spectra were also collected after adding 10 μL of 50 mM NaCl solution. In each case, the intensity of the Raman spectral features of CV was found to be enhanced after the addition of NaCl solution. At a concentration of 10^{-7} M of CV, distinct Raman features of CV was observed only after the addition of NaCl, which was not seen in the absence of NaCl. Here, the addition of NaCl causes aggregation of nanoparticles, which generates large number of hot spots. Hot spots are regions from which higher intensity is observed due to nanoparticle aggregates and the presence of analyte in-between the particles. The crystal violet molecules sitting in close proximity with these hot spots experience extremely high oscillating electromagnetic fields which results in the increase in number of Raman transitions per unit time and hence an enhancement of the scattering signals.

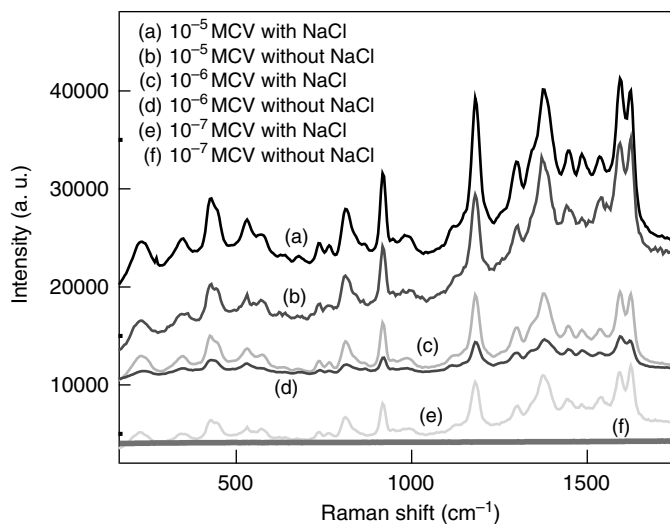


Fig. 5.1 SERS activity of Ag@citrate for various CV concentrations with and without NaCl.

5.4.1 Enhancement Factor

The enhancement factor 'G' can be calculated using the standard formula [3]:

$$G = \frac{I_{\text{SERS}} * C_{\text{NR}}}{I_{\text{NR}} * C_{\text{SERS}}}$$

where, I_{SERS} = Integral intensity of SERS signal of a selected band,

I_{NR} = Integral intensity of normal Raman signal of the same band,

C_{SERS} = Nominal concentration of molecules used for SERS measurements,

C_{NR} = Nominal concentration of molecules used for normal Raman measurements.

As shown in Fig. 5.2, the Raman band at 1593 cm^{-1} is selected for the enhancement factor calculation. Values of various quantities are: $I_{\text{SERS}} = 11627$, $I_{\text{NR}} = 8095.5$, $C_{\text{SERS}} = 10^{-5}\text{ M}$, $C_{\text{NR}} = 10^{-5}\text{ M}$.

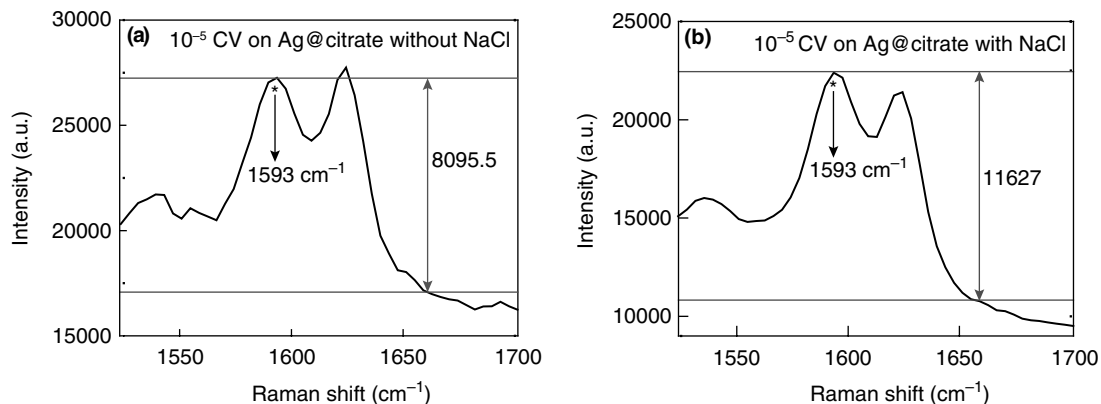


Fig. 5.2 Raman spectrum of CV on Ag@citrate nanoparticles.

Thus, value of enhancement factor is calculated as,

$$G = \frac{11627 * 10^{-5}}{8095.5 * 10^{-5}} \approx 1.44$$

Here the calculation is for additional enhancement due to NaCl. If we take in the calculation the I_{NR} for crystal violet without enhancement by silver, G would be 10^{+5} or more.

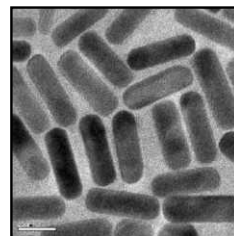
QUESTIONS

1. What is SERS?
2. Why is SERS intensity high in particle aggregates compared to that in nonaggregates?
3. Where can the SERS be applied?
4. Give a brief description of your plan on an alternate experiment with SERS.

REFERENCES

1. (a) <http://en.wikipedia.org/wiki/Spectroscopy>; (b) http://en.wikipedia.org/wiki/Raman_spectroscopy; (c) http://en.wikipedia.org/wiki/Surface_enhanced_Raman_spectroscopy; accessed on 24/09/2010.
2. U.K. Sur. *Resonance*, 2, (2010), 154–64.
3. G.V. Pavan Kumar, S. Shruthi, B. Vibha, B.A.A. Reddy, T.K. Kundu and C. Narayana. *J. Phys. Chem. C*, 111, (2007), 4388–92.

CONVERSION OF GOLD NANORODS INTO GOLD NANOPARTICLES



6.1 OBJECTIVES

- Preparation of gold nanorods of different aspect ratios.
- Conversion of gold nanorods into particles.

6.2 BACKGROUND

Nanorods belong to the class of non-spherical nanoparticles. Most of the synthesized nanorods are cylindrical in shape. They are characterized, structurally, by their length and diameter, and are differentiated by their aspect ratio (ratio of length to diameter). Nanorods are often classified as 1-D nanostructures and have lower aspect-ratios compared to other class of 1-D nanostructures (e.g., nanowires). Length of nanorods fall in the 10–100 nm range with an aspect ratio below 20, with a typical value of 4. Historically, Gans is the first to visualize (in 1912) non-spherical nanoparticles. He predicted that the single surface plasmon mode of spherical nanoparticles would split into two distinct modes for an ellipsoid. Initial reports on the production of non-spherical particles involve formation of glasses containing colloidal silver. Lengths of silver particles so produced were a few nanometers with an aspect-ratio of 1.5–3. Emergence of various methods to chemically synthesize gold nanorods is quite recent [1–3].

Gold nanorods are excellent anisotropic structures. Optical absorption spectrum of gold nanorods in the UV/Vis range is characterized by two peaks: one due to transverse surface plasmon (TSP) resonance and the other due to longitudinal surface plasmon (LSP) resonance. TSP is located around 520 nm and a blue shift in TSP resonance wavelength is observed with an increase in nanorod aspect-ratio. On the other hand, LSP resonance occurs at much longer wavelengths, is very sensitive to nanorod aspect-ratio and exhibits a red shift with increase in length. Chemistry of gold nanorods is considerably different from that of colloidal gold particles. This is due to their surface structure and the presence of the {110} facet on the nanorod surface (this feature is absent in the spherical nanoparticles) owing to the use of cetyltrimethylammonium bromide (CTAB) as the capping agent. Atoms in {110} facet are easily accessible compared to the atoms on other facets, due to larger interatomic distance between atoms in the {110} facet. Hence CTAB has better chance of forming strong bonds with

the atoms of $\{110\}$ facet and to stabilize it. This is the reason for the existence of $\{110\}$ facets on most of the nanorods. In a nanocrystal, different planes have different surface energies, which can be related to the stability (hence reactivity) of these surfaces. This fact enables us in selective synthesis/modification of the nanocrystals. The $\{110\}$ facet is susceptible to reconstruction due to its higher surface energy. Reconstructions do take place with CTAB capping layer disruption, by the addition of external stimuli, etc. Properties of nanorods are highly dependent on their aspect ratios as well. In the present study, we are interested only in preparing monodisperse nanorods from the applications point of view [2–6].

6.3 EXPERIMENT

6.3.1 Materials

- Tetrachloroauric acid trihydrate ($\text{HAuCl}_4 \cdot 3\text{H}_2\text{O}$)
- Cetyltrimethylammonium bromide (CTAB)
- Sodium borohydride (NaBH_4)
- Silver nitrate (AgNO_3)
- Ascorbic acid (AA)

6.3.2 Apparatus

- Standard laboratory glasswares

6.3.3 Procedure

1. Prepare the ‘growth solution’ containing 5 mL of 100 mM CTAB, 250 μL of 10 mM of $\text{HAuCl}_4 \cdot 3\text{H}_2\text{O}$, 32.5 μL of 10 mM AgNO_3 , and 35 μL of 100 mM of ascorbic acid.
2. Prepare 5 mL of 1.67 mM solution of NaBH_4 in ice-cold water.
3. Take six 10 mL test tubes and take, respectively, 50, 100, 200, 300, 400 and 500 μL of freshly prepared ice-cold solution of NaBH_4 . To each, add 5 mL of growth solution.
4. Mix well and record the absorption spectrum of each mixture.

6.4 RESULTS AND DISCUSSION

Information about the aspect ratio of gold nanorods (GNRs) can be obtained by knowing the position of plasmon resonance. Once the nanorods are formed, further chemical reaction of the nanorods with NaBH_4 results in complete conversion of nanorods to nanoparticles. Figure 6.1 shows the absorption spectrum of the gold nanorod solution. It can be observed that spectrum has two peaks: at 796 and 511 nm. These peaks correspond to the longitudinal and transverse surface plasmons, respectively.

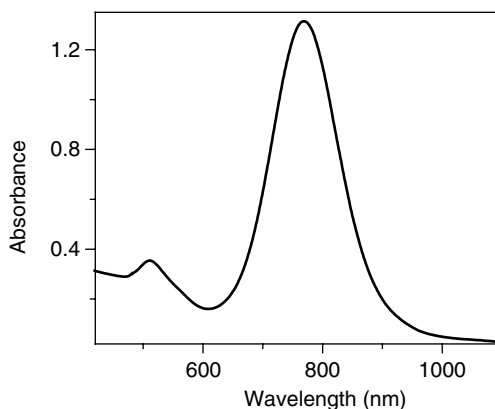


Fig. 6.1 *UV/Vis absorption spectrum of gold nanorods showing LSP and TSP resonances at 511 nm and 796 nm, respectively.*

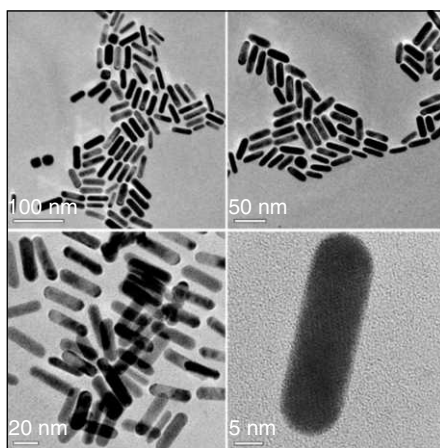


Fig. 6.2 *TEM images of gold nanorods at different magnifications.*

These positions suggest an aspect ratio of 3.4 [7]. Figure 6.2 shows the TEM images of gold nanorods. The aspect ratio can be tuned by varying the volume of NaBH_4 solution added to the growth solution, as shown in Fig. 6.3. It is observed that the aspect ratio decreases with increase in the volume of NaBH_4 used, finally resulting in the formation of spherical nanoparticles (aspect ratio, 1), at 0.5 mL NaBH_4 (trace e in Fig. 6.3) (keeping all other parameters the same). Under optimum conditions, GNRs formed have the highest aspect ratio of 3.4.

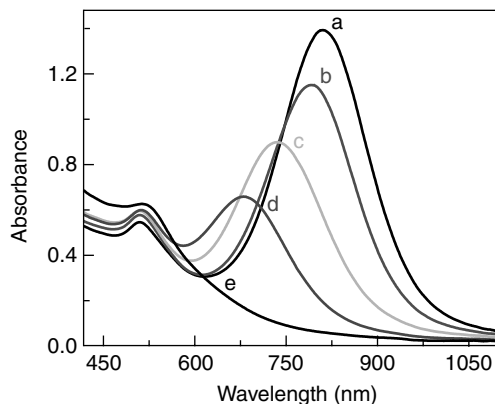


Fig. 6.3 UV/Vis absorption spectra of GNRs formed with addition of different amounts of NaBH₄: (a) 50 μ L, (b) 100 μ L, (c) 200 μ L, (d) 300 μ L and (e) 500 μ L.

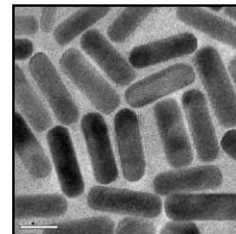
QUESTIONS

1. What is meant by aspect ratio of a nanorod?
2. Among various facets, what is unique about the {110} facets?
3. What are the features of gold nanorods that make them widely applicable?
4. Explain the methods used to prepare gold nanorods, and their limitations, if any.
5. Why are nanorods not formed on addition of higher amounts of NaBH₄?

REFERENCES

1. <http://en.wikipedia.org/wiki/Nanorod> accessed 24/09/2010.
2. J.P. Juste, I.P. Santos, L.M. Liz-Marz'an and P. Mulvaney. *Coord. Chem. Rev.*, 249, (2005), 1870–01.
3. C.J. Murphy, T.K. Sau, A.M. Gole, C.J. Orendorff, J. Gao, L. Gou, S.E. Hunyadi and T. Li. *J. Phys. Chem. B*, 109, (2005), 13857–70.
4. T.S. Sreeprasad, A.K. Samal and T. Pradeep. *Bull. Mater. Sci.*, 31 (3), (2008), 219–24.
5. T.S. Sreeprasad, A.K. Samal and T. Pradeep. *Langmuir*, 23, (2007), 9463–71.
6. T.S. Sreeprasad, A.K. Samal and T. Pradeep. *Langmuir*, 24, (2008), 4589–99.
7. A.K. Samal, T.S. Sreeprasad and T. Pradeep. *J. Nanopart. Res.*, 12, (2010), 1777–86.

REMOVAL OF MERCURY BY SUPPORTED NANOPARTICLES



7.1 OBJECTIVES

- Removal of inorganic mercury (metal ions) from drinking water using gold nanoparticles as adsorbent.
- Studying the efficiency of nanoparticles in removing impurities.

7.2 BACKGROUND

Mercury is a highly volatile and highly toxic heavy metal present in the environment, in various forms, i.e., elemental, inorganic and organic forms. Elemental mercury is the predominant form and can exist in the vapour and liquid forms. Inorganic mercury in water is seen mainly in the +2 oxidation state. Methyl mercury is one of the most toxic pollutants present in the environment. Mercury is released into the atmosphere through a variety of natural and anthropogenic sources. Natural sources include volcanic eruptions, mercury rich soils and forest fires. Mobilization of mercury from fossil fuels, incinerators, chlor-alkali industries, gold mining, processing and refining of mercury ores are a few of the major anthropogenic sources. Once released into the environment, mercury undergoes complex physical and chemical transformations. Released vapour gets converted into soluble form and enters soil and water through rain. Due to microbial action, inorganic mercury gets converted into methyl mercury and enters the food chain of predatory species. In low doses, mercury exposure can affect various organ systems of adults and children. In adults, it can lead to memory loss, Alzheimer's like dementia, impairment of hearing and vision, sensory disturbances, decreased muscular strength, decreased overall immunity of the body, decreased rate of fertility, birth of abnormal offspring, etc. In children, the effects include autism, late walking and deficit in memory and language. The first mercury pollution was reported in Minamata City located on the Yatsushiro sea coast in Kumamoto Prefecture of Japan in 1956. In 1968, it was verified that Minamata disease, the poisoning of the central nervous system, is caused by methyl mercury that entered through food chain and accumulated in fish and shellfish, which was released into Minamata Bay. In 2001, 2,265 victims have been found to be infected with this disease, officially certified, out of which 1,784 have died. Due to the severe effects of mercury on mankind, World Health Organization (WHO) has set the limit for mercury in drinking water to be 0.001 mg/L.

Due to its diverse properties, mercury is still used in different areas like electrical industry, dentistry, mining, catalysis etc. Studies show that mercury pollution is a threat to human beings in the developing countries even now. Reports show that the concentrations of mercury in ground water in a few industrial areas of India are higher than the standards set by WHO and the Bureau of Indian Standards. In a few industrial areas of Gujarat, West Bengal, Orissa, Haryana and Andhra Pradesh, the concentration of mercury is ten or twenty times higher than the maximum permissible limit. These alarming levels are mainly due to the discharge of mercury-bearing effluents having concentrations ranging from 0.058 to 0.268 mg/L. It is against the permissible limit of mercury (0.01 mg/L) set by Indian standards for effluent discharge. Although technologies like adsorption, ion exchange, amalgamation and chemical precipitation are used to remove mercury from contaminated water, nanomaterials are highly promising in this process due to their unique properties like higher surface area per unit volume, ease with which they can be anchored onto solid matrices and the ability to get functionalized with different functional groups to enhance their affinity towards target molecules.

Gold nanoparticles have been used for the detection and removal of various organochlorine compounds (e.g. pesticides such as chlorpyrifos and halocarbons such as carbon tetrachloride) from drinking water. Gold nanoparticle supported on silica has been investigated for catalytic hydrogenation of various aromatic nitro compounds to corresponding amines. Bimetallic Au-Pd has been investigated for the degradation of p-nitroaniline, hydrogenation of 4-pentanoic acid and hydrodechlorination of Trichloroethene. Photocatalytic decomposition of 4-Chlorophenol and hydrogenation of substituted nitroaromatics by Au supported on alumina have been investigated. Alumina nanoparticles prepared by sol gel method have been investigated for mercury removal. An alumina refinery aqueous stream was treated with nanoparticle systems like gold-impregnated silica and silver-impregnated silica for the removal of mercury. Studies have been carried out with conductive sulfophenylenediamine copolymer nanoparticles to remove mercury from aqueous solutions. Dimercaptosuccinic acid-functionalized superparamagnetic Fe_3O_4 nanoparticles were also tried. Complete removal of mercury from water using gold nanoparticles supported on alumina is described in the present experiment. Affinity of mercury towards gold is well-known and nanomaterials are well-known for their large surface area. We amalgamated these two aspects for effective removal of mercury from water. Batch and column experiments were conducted to assess the mercury removal capacity of supported gold nanoparticles. Various spectroscopic and microscopic examinations were also carried out to understand the interaction between gold and mercury.

7.3 EXPERIMENT

7.3.1 Materials

- Tetrachloroauric acid trihydrate ($\text{HAuCl}_4 \cdot 3\text{H}_2\text{O}$)
- Neutral activated alumina (140 mesh, $150 \text{ m}^2/\text{g}$)
- Sodium borohydride (NaBH_4)
- Mercuric chloride (HgCl_2)

- Trisodium citrate
- Aquaregia

7.3.2 Apparatus

- Standard laboratory glasswares

7.3.3 Procedure

7.3.3.1 Synthesis of Gold Nanoparticles

Thoroughly clean all the glassware with aquaregia before starting the experiment. Gold nanoparticles with an average diameter of 10–20 nm are synthesized by the reduction of $\text{HAuCl}_4 \cdot 3\text{H}_2\text{O}$ with trisodium citrate. In this method, 10 mL of 5 mM $\text{HAuCl}_4 \cdot 3\text{H}_2\text{O}$ is diluted with 180 mL distilled water and heated until it begins to boil. 10 mL of 0.5% trisodium citrate solution was added and continued heating till the solution turns wine red. It is then cooled under ambient conditions. We have discussed this method in Appendix 1.

7.3.3.2 Synthesis of Supported Gold Nanoparticles

1. Neutral activated alumina (10g) was mixed with 25 mL of gold nanoparticle suspension, stirred for 10 minutes and allowed to stand for 30 minutes.
2. Once the supernatant became colourless, 25 mL of AuNP suspension was newly added.
3. This procedure of addition and stirring was repeated till there was no colour change of the supernatant.
4. The supernatant was decanted. The slurry containing AuNP-coated alumina was washed thoroughly with distilled water. It is then dried under ambient conditions.
5. Intake of gold nanoparticle by alumina should be about 738 mg per kg of alumina.

7.3.3.3 Preparation of Stock Solution

A stock solution of 500 mg/L of $\text{Hg}(\text{II})$ in water is prepared using HgCl_2 . Solutions with desired dilutions are prepared using this stock solution.

7.3.3.4 Uptake of Mercury

1. A column of alumina-supported AuNPs (2g) is packed in a burette.
2. A solution of Hg^{+2} (1.0 mg/L) is passed through the column at a flow rate of 5 mL/minute.
3. After every 100 mL of treated water passing out of the burette, 5 mL is collected separately and analysed for Hg. Rhodamine 6G forms a complex with divalent mercury having an absorption peak at 575 nm [Ref. 2].
4. This is continued till detectable amounts of mercury begin to appear in the treated sample.
5. A solution containing Hg^0 is prepared by reducing Hg^{+2} (1.0 mg/L) with dilute aqueous NaBH_4 (taken 10 times excess). The reaction mixture was allowed to stand for 1 h.
6. It is then passed through a fresh column containing 2 g of alumina supported AuNPs.

7. As above, 5 mL of treated water was collected at 100 mL intervals.
8. In every 5 mL collections, the Hg is oxidized by treatment with conc. HCl.
9. The experiment is continued till mercury begins to appear at detectable levels in the treated water.
10. Divalent mercury is reduced to elemental Hg and analysed as follows: 1 mL of the sample is treated with 9 mL of HNO_3 and 2 mL of stannous chloride. The concentration of mercury could be determined by monitoring the intensity of absorption at 253.7 nm using a Mercury analyzer.

7.3.3.5 Reaction of Unsupported AuNPs with Mercury

1. A suspension of gold nanoparticles (2.5 mL) is added to a solution containing Hg^{+2} (2.5 mL of 2.0 mg/L) and NaBH_4 (0.1 mL 0.5 M).
2. After 1 hour, UV/Vis absorption spectrum is recorded.
3. TEM and SEM analysis of the sample before and after the addition of mercury can be useful in understanding the mercury-induced changes in morphology.

7.3.4 Characterization

UV/Vis absorption spectroscopy, transmission electron microscopy (TEM) and scanning electron microscopy (SEM) were used for characterization of AuNPs.

7.4 RESULTS AND DISCUSSION

Figure 7.1 shows the UV/Vis absorption spectra of gold nanoparticles before and after mercury treatment. Trace 'a' is the absorption spectrum of the as prepared gold nanoparticles. It exhibits a characteristic absorption peak at 520 nm which is characteristic of surface plasmon resonance. Trace 'b' is that of gold colloid after treatment with Hg_2^+ and NaBH_4 . We observe a small shift in peak position. This is due to a change in morphology of Au nanoparticles with the introduction of Hg. Inset shows the photographs of the as prepared gold nanoparticles (A) and mercury-treated gold nanoparticles (B). We see that the wine red colour of the gold nanoparticle solution changes into brownish orange after the addition of mercury solution.

Figure 7.2A shows a large area TEM image of the as prepared gold nanoparticles. The nanoparticles are spherical in shape and are uniformly distributed as typical of citrate synthesis. Their size distribution is remarkably narrow (16 ± 2 nm). Lattice resolved image of an individual gold nanoparticle is given in Fig. 7.2B. A lattice spacing of 2.35 \AA is seen, which corresponds to the distance between adjacent (111) planes in solid gold. Figure 7.2C shows a large area image of mercury-treated gold nanoparticles. Now, the nanoparticles are of varying sizes with wide distribution. The image shows several larger particles being surrounded by smaller ones. It may be a snap shot when the larger particles are undergoing Ostwald ripening. Figure 7.2D shows the lattice resolved image of an individual, mercury-treated gold nanoparticle. The nanoparticle is oriented showing a lattice spacing of 2.24 \AA , which corresponds to the distance between adjacent (101) planes of Au_3Hg alloy. No core-shell morphology is seen and it

appears that the product formed is a continuous phase. It is clear that the ionic shell formed by the protecting group is disturbed due to Hg uptake, which results in the fusion of particles.

SEM images of mercury-treated gold nanoparticles are taken for understanding the morphology (Fig. 7.3). The images show that some particles are very large in size and are distributed randomly. Compared to that before treatment, the morphology of the particles is different: they possess a thin surface layer which may be due to the presence of mercury. Elemental maps of Au and Hg, overlaid on Si (from glass substrate), are shown in Figures 7.3C and 7.3D, respectively. From the elemental analysis, it is clear that gold and mercury are uniformly distributed in the particles which may be due to the amalgam formation. This is supported by the TEM measurements as well.

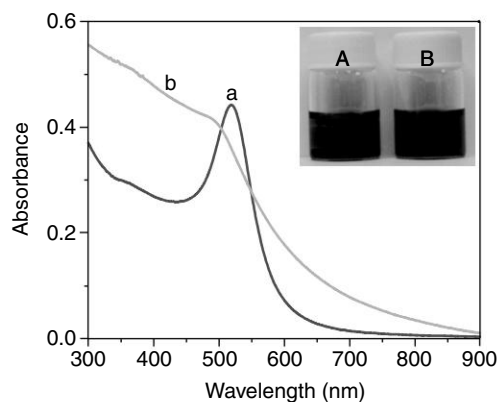


Fig. 7.1 UV/Vis absorption spectra of gold nanoparticles (a) before and (b) after mercury treatment. Inset shows photographs of corresponding solutions.

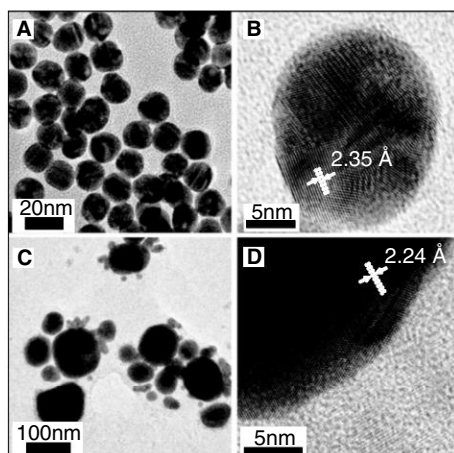


Fig. 7.2 TEM images of gold nanoparticles before and after mercury treatment. (A) Large area image of gold nanoparticles before the reaction. (B) The corresponding lattice resolved image of a single nanoparticle. (C) Large area image of mercury-treated gold nanoparticles. (D) The corresponding lattice resolved image of a single nanoparticle.

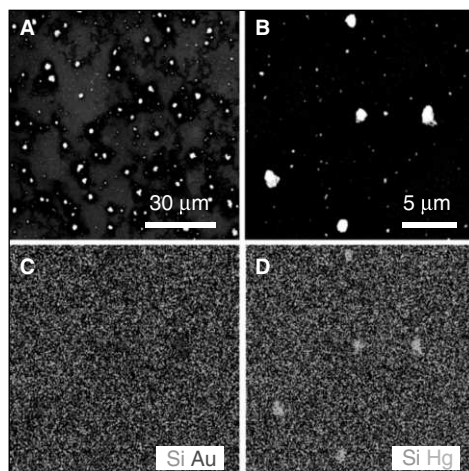


Fig. 7.3 SEM images of mercury-treated gold nanoparticles. (A) Large area image, (B) magnified image of few particles, (C) elemental map of Au and (D) elemental map of Hg.

Note: It is possible to estimate the efficiency of Hg^{2+} uptake of gold nanoparticles by quantitative determination using rhodamine 6G-based colorimetric method also. In this case, only a UV/Vis spectrometer is needed for this experiment.

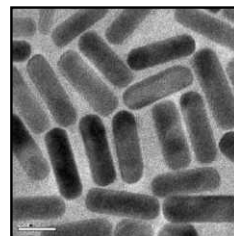
QUESTIONS

1. What are the consequences of mercury pollution?
2. Why was gold chosen to remove mercury from water?
3. How do we conclude, neglecting the cost factor, that gold nanoparticles supported on alumina form an excellent system for the removal of Hg^0 from water?
4. Is this an efficient method for the removal of mercury? Analyse the results.

REFERENCES

1. Method modified from K.P. Lisha, Anshup and T. Pradeep. Towards a practical solution for removing inorganic mercury from drinking water using gold nanoparticles. *Gold Bulletin*, 42, (2009), 144–52.
2. T.V. Ramakrishna, G. Aravamudan and M. Vijayakumar, Spectrophotometric determination of mercury(II) as the ternary complex with rhodamine 6g and iodide, *Analytic Chimica Acta*, 84, (1976), 369–75.

DEMONSTRATION OF LIQUID MAGNETS



8.1 OBJECTIVES

- Synthesis of ferrofluids, otherwise known as ‘liquid magnets’.
- Exploring some of their interesting properties and analysing their absorption spectra.

8.2 BACKGROUND

Ferrofluid, first developed and classified in the 1960s by Stephen Pappell at NASA [1], is a colloidal mixture comprising of extremely small magnetic particles (of magnetite, hematite or some other compound, usually containing iron, with $\text{dia} \leq 10 \text{ nm}$) suspended in a carrier fluid (usually an organic solvent or water). They become strongly polarized in the presence of a magnetic field. A surfactant (a soap or a detergent) is also added to prevent particle agglomeration due to van der Waals and magnetic interactions. A typical ferrofluid contains about 5% magnetic solids, 10% surfactant and 85% carrier, by volume. Since the particles are extremely small, a slight thermal agitation is enough for their even dispersion within the carrier fluid; uniform distribution is important for the overall magnetic response of the fluid. Ferrofluids do not exhibit ferromagnetism, as against their name may suggest, because they do not retain magnetism in the absence of an external magnetic field. But they do exhibit paramagnetism and are often referred to as ‘super paramagnetic’ on account of their large magnetic susceptibility. Ferrofluids are often confused with magneto-rheological (MR) fluids. One major difference between these two classes of materials is that nanoparticles of ferrofluids, which are suspended by Brownian motion, will not settle under normal conditions, where as, micron-scale particles of MR fluid are too heavy for the Brownian motion to keep them suspended, and hence, settle over a period of time due to gravity. These two fluids differ in their applications too.

Properties of ferrofluids are combinations of properties of two states of matter (solid and liquid). In the absence of an external magnetic field, a ferrofluid is non-magnetic because the magnetic moments of individual magnetite particles would be randomly oriented at any instant of time. But, on application of an external magnetic field, individual magnetic moments align in the direction of applied magnetic field. This property can be exploited to make a liquid that changes its density with the strength of the applied magnetic field. This ability makes them useful in sealing, lubrication, centrifuges, computer hard disk drives and future nano-electromechanical systems. Most of the surfactants are very effective

in stabilizing the colloids. However, the surfactant molecules too tend to break down over a period of time (a few years), and eventually the nanoparticles will agglomerate, and they will separate out and no longer contribute to the magnetic response of the overall fluid. Ferrofluids lose their magnetic properties at sufficiently high temperatures, known as the Curie temperature, which varies depending on the composition of the ferrofluid (compounds used for the nanoparticles, surfactant, and carrier fluid) [2]. Three factors that influence the viscosity of ferrofluids are:

- The interaction of the magnetic nanoparticles with the solvent
- The interaction among nanoparticles, and
- Relative strengths of gravity and Brownian motion.

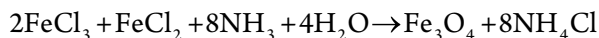
Application of a shear stress on a ferrofluid causes the surfactant chains and magnetic nanoparticles to move along the shear direction. There are two kinds of viscosity variations for ferrofluids when the shear rate increases: Newtonian and shear-thinning behaviours. Increasing the shear rate may result in decrease of viscosity, showing a shear-thinning behaviour. The opposite can be said with lower shear rates: At lower shear rates, disordered arrangement of nanoparticles would increase the resistance to flow, and hence a reduction, in fluidity.

8.2.1 Synthesis

Two major steps in ferrofluid synthesis are [1]:

1. Preparation of chemically stable (in liquid carrier) magnetic nanoparticles dispersed in the form of a colloidal suspension.
2. Redispersion of the magnetic particles in a carrier liquid by utilizing a surfactant to create a stabilized colloidal suspension.

Our synthesis of ferrofluid involves the use of FeCl_2 , FeCl_3 as salts, NaOH as base and TMAH as surfactant, to prepare Fe_3O_4 nanoparticles-based ferrofluid [1,4]. Underlying reaction behind the experimental procedure is,



Common magnetic particles used in ferrofluids are generally magnetite, Fe_3O_4 , although other magnetic particles have been used. The liquid (or fluid) property of a ferrofluid is mostly derived from carrier fluid (base), enabling free movement of particles as a liquid. Magnetic particles in an ideal ferrofluid do not settle out, even when exposed to a strong magnetic or gravitational field. However, most of the ferrofluids are non-ideal. In such cases, addition of suitable surfactants helps in retarding the settling rate of particles. Surfactant has a polar head and non-polar tail (or vice versa), one of which gets attached to the surface of a nanoparticle, while the other group is projected out into the carrier medium. Thus, surfactant-protected particles are prevented from agglomeration. Surface-adsorption is the reason why very small quantities of surfactants are effective in stabilizing the colloids. Some of the common surfactants used include oleic acid, tetramethylammonium hydroxide (TMAH), citric acid, and soy lecithin.

8.3 EXPERIMENT

8.3.1 Materials

- Ferrous chloride (FeCl_2)
- Ferric chloride (FeCl_3)
- Ammonia (NH_3)
- Tetramethylammonium hydroxide (TMAH)
- Conc. HCl
- Commercial conc. HCl and commercial conc. HNO_3 (for preparing aqua regia)
- Distilled water

8.3.2 Apparatus

- A bar magnet, for testing magnetic particles.
- Measuring jars: 10 mL capacity, 2 nos (one for measuring the volume of HCl and another for NH_3), 50 mL capacity, 1 no. (for measuring the volume of water).
- Magnetic stirrer with a teflon-coated magnetic stirring bar of 8 mm \times 12 mm size.
- Burette, 50 mL, for dropwise addition of ammonia solution.
- Glass beakers: 50 mL capacity, 3 no. (one for preparing dilute HCl, one for FeCl_2 solution and one for FeCl_3 solution), 100 mL capacity, 2 nos (one for preparing ammonia solution and another for mixing FeCl_2 and FeCl_3 solutions), 5 mL capacity, 1 no. (a 10 mL sample bottle can also be used) (to prepare TMAH solution).
- Micro pipette of 1 mL capacity and micro tips of 1 mL capacity, for measuring volumes of TMAH and water during preparation of 25% TMAH solution.
- Wash bottle

8.3.3 Procedure

1. Thoroughly clean all the glassware with aquaregia before starting the experiment. Prepare 25 mL of 2M HCl (~ 4.3 mL conc. HCl in 25 mL water). Prepare 50 mL of 1M NH_3 (~ 4 mL of conc. NH_3 in 60 mL of water).
2. Prepare solutions of 2M FeCl_2 and 1M FeCl_3 in 2M HCl (To prepare 10 mL of 2M FeCl_2 solution, dissolve ~ 4 g of $\text{FeCl}_2 \cdot 4\text{H}_2\text{O}$ in 10 mL of 2M HCl. To prepare 10 mL of 1M FeCl_3 solution, dissolve ~ 2.7 g of $\text{FeCl}_3 \cdot 6\text{H}_2\text{O}$ or ~ 1.63 g of FeCl_3 in 10 mL of 2M HCl).
3. Mix 1.0 mL of 2M FeCl_2 and 4.0 mL of 1M FeCl_3 solutions in a 100 mL beaker, using a magnetic stirrer.
4. Slowly add, using a burette, 50 mL of 1M NH_3 solution to the above mixture over a period of five minutes with continued stirring. Avoid addition that is faster than the stirrer can

cope with. Also, avoid addition that is so slow that enables particles to grow large. A black precipitate of magnetite will be formed.

5. Turn off the stirrer, remove the magnetic pellet and allow the precipitate to settle for about 10 min. A strong magnet can be placed below the beaker to speed up the settling process.
6. Remove the supernatant liquid by decantation. Wash the slurry 2–3 times with water, to ensure complete removal of NH_3 .
7. Add 2 mL of 25% TMAH and mix well.
8. Move the north or the south pole of a bar magnet around the beaker to see the region closer to magnet becoming dense with magnetic particles. Alignment of particles along the field lines may give an spike-like appearance, which again ensures the formation of magnetic particles.

Note: A bar magnet is preferred over a circular magnet (field for a circular magnet is uniformly distributed and the effect will not be felt strongly). Water removal (transparent top layer) must be as efficient as possible. Ensure that water is added to rinse three to four times. Fe^{2+} salts get easily oxidised; so, close the containers tightly when not in use. Ideally they should be of light green colour.

8.4 RESULTS AND DISCUSSION

Physical observations play important role in this experiment. Formation of ferrofluid is confirmed by bringing a magnet near to the ferrofluid which brings about observable changes in the orientations of particles in solution. One simple method to recognize the formation of ferrofluid is to take some amount of ferrofluid in a test tube and bring a magnet near to the wall of test tube which instantaneously causes ferrofluid to spike. Another method is to take ferrofluid in a glass plate and bring a magnet to the bottom of plate. Similar methods are available to recognize and demonstrate properties of ferrofluids [1]. Various methods and instruments like Transmission Electron Microscopy, X Ray Diffraction, X-ray Photoelectron Spectroscopy, etc. have been used to characterize ferrofluids. However,

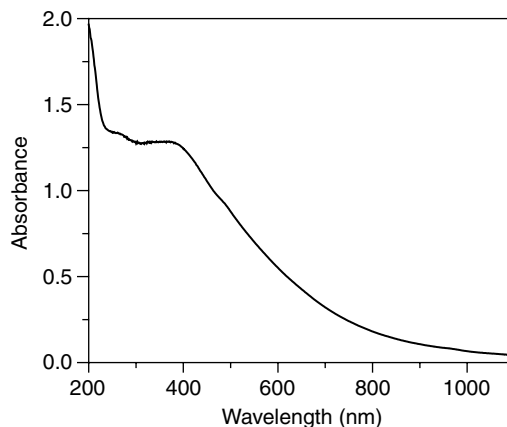


Fig. 8.1 UV/Vis absorption spectrum of the ferrofluid.

the easiest method to detect the formation of a ferrofluid is to bring a magnet close to the fluid. We have used TEM and UV/Vis spectroscopy to characterize the iron oxide nanostructures synthesized via above method. TEM measurements give good indication of the size, shape and crystallography of the ferrofluid particles (Fig. 8.2). The UV/Vis spectrum obtained (Fig. 8.1) is very similar to that of semiconductor nanoparticles. It should be kept in mind that, while we call the end product a ferrofluid, in reality, we have synthesized only iron oxide nanoparticles.

If there appears a large amount of scattering in the absorption spectrum, dilute the sample until the desired spectral pattern is obtained and scattering is eliminated.

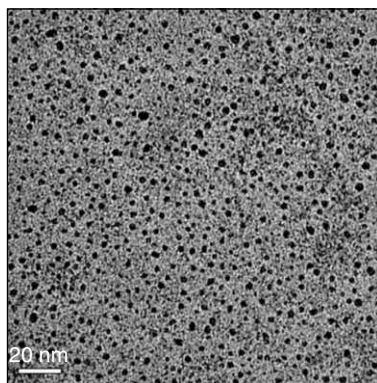


Fig. 8.2 HRTEM image of oleic-acid capped Fe_3O_4 nanoparticles (prepared following a similar procedure as described in the text, but with a different surfactant, oleic acid).

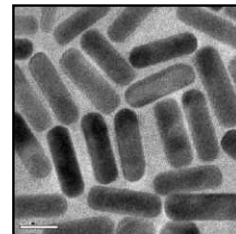
QUESTIONS

1. What are ferrofluids? In what way are they novel?
2. What are the main constituents for a simple ferrofluid?
3. What are the applications of ferrofluids?
4. What is the underlying reaction on which the present method is based?
5. What is the role of tetramethylammonium hydroxide in this experiment?
6. Why is it necessary to remove the transparent supernatant once the black solution is formed?
7. What is the easiest way to characterize a ferrofluid?

REFERENCES

1. P. Berger, N.B. Adelman, K.J. Beckman, D.J. Campbell, A.B. Ellis and G.C. Lisensky, *J. Chem. Edu.*, 76, 7, (1999), 943–48.
2. <http://en.wikipedia.org/wiki/Ferrofluid> accessed on 24/09/2010.
3. R.Y. Hong, Z.Q. Ren, Y.P. Han, H.Z. Li, Y. Zheng and J. Ding, *Chem. Engg. Sci.*, 62, (2007), 5912–24.
4. R.A. May, K.J. Stevenson and D.A. Vanden Bout, *IGERT Summer Teacher Academy Manual*, (2007).

BIMETALLIC NANOPARTICLES



9.1 OBJECTIVES

- Synthesis of two types of core-shell bimetallic nanoparticles: (1) Gold core-silver shell (Au@Ag) and (2) silver core-gold shell (Ag@Au).
- Exploring the role and unfolding the reaction mechanism of β -cyclodextrin, a useful compound in biology, used as a reducing agent here.
- Calculating the number of nanoparticles synthesized and percentage conversion of Ag used in the experiment.

9.2 BACKGROUND

Bimetallic nanoparticles (NPs) are novel substances that have come to light because of their novel electronic, optical, catalytic and magnetic properties which are not observed in single-metal nanoparticles. Depending on the type of spacial distribution of metal atoms in the particles, bimetallic NPs may be categorized as: (1) random alloy, (2) alloy with an intermetallic compound, (3) cluster-in-cluster and (4) core-shell structures [1]. Two types of metal-metal bonds could exist in bimetallic compounds:

1. Homoatomic bond (A-A and B-B bonds)
2. Heteroatomic bond (A-B bond)

Depending on the relative binding energies of these bonds, different types of structures could be formed under equilibrium conditions. For example, if the average binding energy A-A and B-B bonds is less than or equal to that of the B-B bond, then the random alloy structure will be thermodynamically the most stable one. On the other hand, if the A-B bond is much weaker, atomic level mixing will not arise, and bimetallic nanoparticles would be thermodynamically unstable. In the case of a pair of metals, for which energies of A-A and B-B bonds are almost equal, two types of cluster-in-cluster structures can be obtained depending on the preferential bonds in the structure. When homobond is preferred over the heterobond, the cluster-in-cluster structure is known as homobond-philic structure and *vice versa*. Hence a homobond-philic core-shell structure is thermodynamically stable structure while an

1. A@B terminology implies particles with A as the core and B as the shell.

inverted core-shell (heterobond-philic) structure is thermodynamically metastable (assuming that homobond is stronger than heterobond) [2]. Fig. 9.1 shows pictorial representation of different types bimetallic particles.

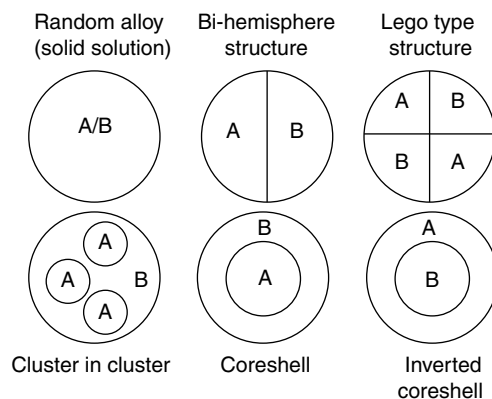


Fig. 9.1 Different types of bimetallic nanoparticles

Structure and properties of bimetallic nanoparticles depend on the nature of elements used. When a nanoparticle has more than one type of metal atoms in it, spacial distribution of different kinds of atoms within the particle is of prime importance in interpreting the optical properties. For a bimetallic system, free energy-driven distribution of atoms of one element to form a distinct core and formation of a shell of atoms of the other element would be ideal in realizing a stable core-shell structure. In the case of gold-silver system, arrangement of atoms is particularly difficult to control, since these elements are perfectly miscible with each other (FCC lattice parameters being 407.8 pm for Au and 408.6 pm for Ag) and form alloys over the whole composition range. There still is a debate as to whether or not pure core-shell geometries could be obtained. Here, in our experiment, we demonstrate that successive reduction of Au and Ag salts can lead to the formation of multilayered Au@Ag nanoparticles. During particle growth, geometry of the particles changes progressively as new layers are deposited, maintaining approximately a concentric geometry throughout the formation. It must also be noted that with the exception of Au@Ag nanoparticles, dispersions of Ag-containing bimetallic nanoparticles have not been studied extensively. Possible reasons for this might be that Ag (I) ion readily reacts with halide ions to produce water-insoluble silver halides [1].

Besides metal-metal type core-shell structures, other variations are possible, all of which are called core-shell structures [3]. Different types of such systems, with known examples (including examples for bimetallic systems) are:

- Metal-'Metal oxide' core-shell nanoparticles (e.g. Au@SiO₂)
- Bimetallic core-shell nanoparticles (e.g. Au@Ag, Ag@Au, Pt@Pd, Cu@Pd, etc.)
- Semiconductor core-shell nanoparticles (e.g. CdSe@ZnS)
- Polymer coated core-shell nanoparticles (e.g. polystyrene@polybutylmethacrylate)

9.2.1 Role of the Shell

Apart from acting as a protective coating or covering, preventing the core from any physical or chemical damage, the shell imparts some functional properties to the bimetallic structure. Some such properties are:

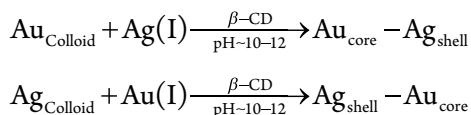
- Monodispersity in size
- Processibility of core and shell species
- Solubility and stability
- Ease of self assembly
- Enabling varied applications (from optics to nanoelectronics)

These additional properties stress the importance of shell in a bimetallic structure in retaining its unique position in a particular technology. Apart from these functionalities, shells can alter the surface charge, reactivity and functionality of the metal core, thereby enhancing the stability and dispersibility of the particles. They may also contribute, largely, to the magnetic, optical and catalytic properties of the nanoparticle. In case of bimetallic systems, shells are known to enhance the physical and chemical properties of the bimetallic system as compared to those of monometallic nanoparticle [3].

9.2.2 Role of β -Cyclodextrin (β -CD)

β -CD was used as an organic receptor in the present experiment. CDs are non-reducing cyclic glucose oligosaccharides resulting from cyclomaltodextrin glucanotransferase-catalyzed degradation of starch. There are three common CDs with 6, 7 or 8 D-glucopyranosyl residues (named α -, β -, and γ -CDs, respectively) linked by α -1, 4 glycosidic bonds. All CDs have cyclic structures. They present a bottomless bowl-shaped (truncated cone) molecule stiffened by hydrogen bonding between 3-OH and 2-OH groups around the outer rim. Order of hydrogen bond strength of these CDs is, α -CD < β -CD < γ -CD. The main reason for using β -CD is the diameter of its internal cavity (600-650 pm) which is suitable for nanoparticle capping.

Use of β -CD as complexing agent represents a useful strategy for minimizing the photo-induced biological damage associated with many non-steroidal anti-inflammatory drugs (NSAIDs). Moreover, the weak binding forces responsible for the association of a nanoparticle with the β -CD cavity provide a useful model for mimicking the interactions of drugs with hydrophobic pockets of the biological substrates. As the size of metal particles involved in a chemical reaction decrease to enter the nanorange, electrostatic or steric stabilization of the particles must occur to overcome the instability associated with the very high surface energies. β -CD is quite useful in this regard. Deprotonation of alcohol functionalities of β -CD molecules is facilitated by alkaline conditions (promotes the kinetic evolution and stabilization of the nanoparticles). In the present experiment, β -CD is used as a reducing agent and a stabilizing agent in an alkaline medium and as a capping agent [5–6]. Reaction mechanism of the experiment can be summarised as follows:



9.3 EXPERIMENT

9.3.1 Materials

- HAuCl₄
- β -cyclodextrin
- AgNO₃
- NaOH
- Aqua regia

9.3.2 Apparatus

- Round bottom flask
- Standard measuring flask
- Magnetic stirrer and pellet
- Electronic weighing balance
- Conical flask
- Glass beaker
- Centrifuge
- Glass syringe
- Micro pipette
- Rotavapor

9.3.3 Procedure

9.3.3.1 Synthesis of Au and Ag Colloids

Monometallic colloids of respective metals need to be prepared before we can take up the task of synthesizing bimetallic nanoparticles. As we wish to synthesize Au@Ag and Ag@Au bimetallic nanoparticles in this experiment, first let us prepare colloidal solutions of Au and Ag in two separate preparations. You can refer to the previous experimental procedures for the preparation of gold and silver colloids. In addition, following procedure can also be used for the synthesis.

1. Thoroughly clean all the glassware with aquaregia and then with distilled water before starting the experiment. Add HAuCl₄ solution (0.02 mL, 10 mM to prepare Au colloid) or AgNO₃ solution (0.02 mL, 10 mM to prepare Ag colloid) to a β -CD solution (4 mg in 5 mL of water).

2. Add NaOH solution (0.05 mL, 1.0 M) to the mixture after, say, 2 min, so that the pH of the solution is around 10–12.
3. Stir the solution well and transfer the container to a water bath for heating.
4. After about 20 min, a change in the colour (to pink, for gold and to yellow, for silver) of the solution is observed, indicating the formation of the metal colloid or metal nanoparticles. These are used as such without further purification.
5. UV/Vis spectrometer can be employed to confirm the formation of metal colloid: A peak around 520 nm is observed for gold and around 400 nm for silver.

9.3.3.2 Synthesis of Au@Ag Core-shell Nanoparticles

1. Add AgNO₃ (0.04 mL, 10 mM) solution slowly to the preformed gold colloidal solution (5 mL) with continuous stirring.
2. Incubate the solution for 5 min; then heat on a water bath.
3. Gradual colour change (pink to yellow) of the solution is observed, during a period of about 30 min, indicating the formation of Au@Ag particles.
4. Gold to silver concentration is adjusted to get finally a molar ratio of 2:1.
5. Alkalinity of the gold colloidal solution itself is sufficient to induce the chemical reduction of Ag ions during shell formation and hence no extra β -CD or NaOH was added.

Note 1: If, for tracking the progress of reaction, absorption spectra are to be recorded after every 2–5 minutes, then, initial mixing could be started with large quantities of the reactant solutions. While heating would be continued on a water bath, aliquots could be withdrawn at fixed intervals which are used for absorbance measurement after cooling, and then discarded.

Note 2: A peak at 400 nm in the absorption spectrum confirms the presence of Ag shell around the gold core.

9.3.3.3 Synthesis of Ag@Au Core-shell Nanoparticles

The procedure is similar, except for the reactant solutions.

1. Add HAuCl₄ (0.04 mL, 10 mM) solution dropwise to the preformed silver colloidal solution (5 mL) and stir the contents vigorously.
2. Follow the same steps as described above for Ag shell formation on Au core.

Note 1: In this case, an absorption peak at 520 nm is characteristic of Au shell.

9.3.4 Precautions

1. Cleanliness and dryness of the instruments, especially glassware, must be ensured, otherwise it increases the possibility of aggregation.
2. A slight excess of the shell-forming reagents may not alter the reaction significantly, but its deficiency might not take the reaction to its conclusion i.e. it may lead to incomplete formation of shell over the core particle. For example, if the amount of AgNO₃ added is a little less than

what is needed to coat all the particles in the gold colloid, then, not every gold nanoparticles would be coated with silver shells. This will be reflected in the UV/Vis spectrum in which a peak at 520 nm characteristic of gold nanoparticles would be still present in addition to the peak at 400 nm.

9.4 RESULTS AND DISCUSSION

9.4.1 Color Change

Formation of core-shell particles can be recognized visibly by observing colour change: In Au@Ag synthesis, AuNP solution is pink in colour; a solution containing Au@Ag is yellowish (Fig. 9.2). In Ag@Au preparation, a solution containing AgNP is yellow in colour while that having Ag@Au is pink (Fig. 9.3).

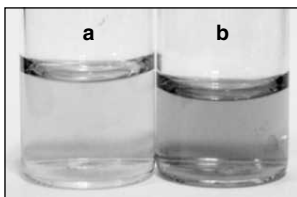


Fig. 9.2 Colours of (a) AuNP solutions and (b) solution containing Au@Ag bimetallic nanoparticles.

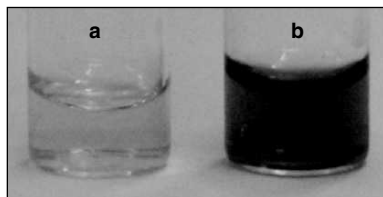


Fig. 9.3 Colours of solutions containing (a) AgNP and (b) Ag@Au particles.

9.4.2 UV/Vis Spectra

9.4.2.1 Au@Ag Core-shell Nanoparticle

It should be noted that curve 'a' of the Fig. 9.4 actually corresponds to the gold nanoparticle solution (peak is observed at 520 nm, characteristic of AuNPs). Curves a-e depict the growth of Ag shell on Au core as inferred by absorbance at 400 nm that increases with time. This indicates that as the reaction proceeds, concentration of naked gold nanoparticles (not covered by silver shell) decreases while amount of silver (in the form of Au@Ag core-shell nanoparticles) increases. Once the colour change (pink to yellow) is complete, the spectrum (trace after 24 minutes, Fig. 9.4) shows a peak at 400 nm.

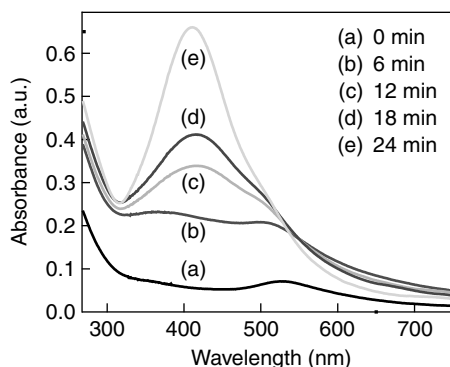


Fig. 9.4 Absorption spectra of the reaction mixture during formation of Au@Ag bimetallic nanoparticles.

9.4.2.2 Ag@Au Core-shell Nanoparticle

In this case, initially, a peak is observed at 400 nm, which is characteristic of Ag nanoparticles (Fig. 9.5, trace a). After addition of Au(III), a peak at 520 nm evolves with time indicating the formation of Au shell.

When all the silver particles are consumed for core-shell formation, absorption spectra settle with a peak at 520 nm. At this point, the colour of the solution had changed from yellow to pink, indicating the formation of Ag@Au bimetallic nanoparticles.

Note that absorption spectra taken for both the Au@Ag and Ag@Au bimetallic nanoparticles clearly rule out the presence of Au Ag alloy nanoparticles. Otherwise, there would have been a single peak in the absorption spectra of the final product, in between 400 and 520 nm, expected for alloy particles.

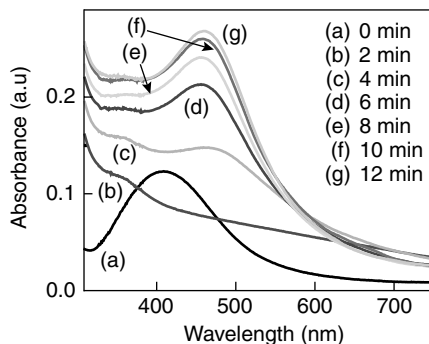


Fig. 9.5 Absorption spectra of the reaction mixture during formation of Ag@Au bimetallic nanoparticles.

Note: To further confirm the formation of bimetallics, cyanide dissolution reaction may be performed, which involves the addition of KCN to the bimetallic solution. A gradual change in surface plasmon absorption upon gradual dissolution of the shell, and then of the core, due to reaction with cyanide, supports the formation of bimetallic core-shell structures. But, due to poisonous nature of KCN, we do not perform this confirmation test.

QUESTIONS

1. What are bimetallic nanoparticles?
2. What are the various methods by which bimetallics can be synthesised? How are they synthesised in the present experiment?
3. Write a note on core-shell nanoparticles.
4. Describe various techniques available for the characterization of bimetallic nanoparticles, an interesting sub-division being core-shell nanoparticles.
5. How is β -cyclodextrin important to this reaction?
6. Analyse and comment on the absorption spectra of the reaction mixture during the formation of Au@Ag and Ag@Au bimetallics.
7. Write a note on the applications of bimetallics.
8. In an experiment of Au@Ag synthesis, assume that the same concentrations and volumes of AgNO_3 and HAuCl_4 were used as in the experiment described above. All the HAuCl_4 was consumed in the formation of Au NPs, but only a part of added Ag (in the form of AgNO_3) was used in shell-formation. Assuming the size of the gold nanoparticles to be 10 nm, and the thickness of the silver shell to be 1.5 nm, calculate the number of gold nanoparticles formed initially, and the fraction of Ag that was consumed for formation of shells.

Note: Densities and atomic masses of Au and Ag, and Avogadro no. are provide by the teacher.

Answer to Question No. 8

The Au@Ag system is considered here. Similar calculations can be performed for the Ag@Au system also.

Given:

1. Concentration of HAuCl_4 : 10 mM
2. Volume of HAuCl_4 taken: 0.02 mL
3. Density of solid gold: 19.3 g cm^{-3}
4. Atomic mass of Au: 197
5. Concentration of AgNO_3 : 10 mM
6. Volume of AgNO_3 taken: 0.04 mL
7. Density of solid Ag: 10.49 g cm^{-3}
8. Atomic mass of Ag: 108

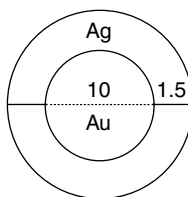


Fig. 9.6 Line diagram of Au-Ag core-shell nanoparticle (all dimensions in nm).

9. Diameter of AuNPs: 10 nm
10. Diameter of Au@Ag NPs: 13 nm

The problem can be solved using following steps:

1. Calculation of no. of Au atoms in the HAuCl_4 solution taken for preparation of particles.
2. Calculation of volume needed for a single gold atom in solid gold.
3. Calculation of no. of Au atoms in a single AuNP.
4. Calculation of total no. of AuNPs formed.
5. Calculation of volume needed for a single silver atom in solid silver.
6. Calculation of total volume occupied by Ag atoms present in shells of all Ag@Au NPs.
7. Calculation of no. Ag atoms present in the shell of a single Ag@Au NP. Calculation of total no. of Ag atoms present in all shells.
8. Calculation of no. of Ag ions in the AgNO_3 solution taken for the preparation of particles.
9. Calculation of percentage of Ag ions consumed for shell formation.

1. Calculation of no. of Au atoms that would be formed on reduction of all Au^{3+} in 0.02 mL of 10 mM HAuCl_4 solution

$$\begin{aligned} \text{No. of Au atoms} &= \frac{\text{Concentration} \times 0.02 \text{ mL}}{1000 \text{ mL dm}^{-3}} \times N_A \\ &= \frac{10 \times 10^{-3} \text{ mol dm}^{-3}}{1000 \text{ mL dm}^{-3}} \times 0.02 \text{ mL} \times 6.022 \times 10^{23} \text{ mol}^{-1} \\ &= 1.204 \times 10^{17} \end{aligned}$$

2. Calculation of volume needed for a single gold atom in solid gold

Given: density of Au = 19.3 cm^{-3}

Given: Atomic mass of Au = 197

\therefore 197 g of Au contains N_A atoms of Au

No. of Au atoms in 19.3 g of Au

$$= \frac{N_A}{197 \text{ g mol}^{-1}} \times 19.3 \text{ g}$$

$$= \frac{6.022 \times 10^{23} \text{ mol}^{-1}}{197 \text{ g mol}^{-1}} \times 19.3 \text{ g}$$

$$= 5.9 \times 10^{22}$$

Thus, 5.9×10^{22} Au atoms occupy a volume of 1 cm^3 .

∴ Volume needed (including void space) for a single Au atom in solid gold

$$= \frac{1 \text{ cm}^3}{5.9 \times 10^{22}} = 1.69 \times 10^{-23} \text{ cm}^3$$

$$= 1.69 \times 10^{-29} \text{ m}^3$$

3. Calculation of no. of Au atoms present in a single AuNP

Given: diameter of a AuNP = 10 nm

$$\therefore \text{Radius} = \frac{10 \text{ nm}}{2} = 5 \text{ nm} = 5 \times 10^{-9} \text{ m}$$

∴ Volume of a single AuNP

$$= \frac{4}{3} \pi r^3$$

$$= \frac{4}{3} \pi (5 \times 10^{-9} \text{ m})^3 = 5.24 \times 10^{-25} \text{ m}^3$$

Now, a single Au atom needs a volume of $1.69 \times 10^{-29} \text{ m}^3$.

∴ No. of Au atoms that can be accommodated in a volume of $5.24 \times 10^{-25} \text{ m}^3$

$$= \frac{\text{Volume of all Au atoms in a NP}}{\text{Volume needed for a single Au atom}}$$

$$= \frac{5.24 \times 10^{-25} \text{ m}^3}{1.69 \times 10^{-29} \text{ m}^3} = 3.1 \times 10^4$$

4. Calculation of total no. of AuNPs formed

No. of AuNPs formed

$$= \frac{\text{Total no. of Au atoms formed by reduction}}{\text{No. of Au atoms in a single AuNP}}$$

$$= \frac{1.204 \times 10^{17}}{3.1 \times 10^4} = 3.9 \times 10^{12}$$

5. Calculation of volume needed for a single silver atom in solid silver

Given: density of solid Ag = 10.49 g cm^{-3} .

Given: atomic mass of Ag = 107.9

Now 1 mol of Ag (=107.9 of Ag) contains N_A atoms of Ag.

∴ No. of atoms of Ag in 10.49 g of Ag

$$\begin{aligned} &= \frac{N_A}{107.9 \text{ g mol}^{-1}} \times 10.49 \text{ g} \\ &= \frac{6.022 \times 10^{23} \text{ mol}^{-1}}{107.9 \text{ g mol}^{-1}} \times 10.49 \text{ g} \\ &= 5.85 \times 10^{22}. \end{aligned}$$

Thus, 5.85×10^{22} Ag atoms occupy a volume of 1 cm^3 .

∴ Volume needed for a single Ag atom (including void space) in solid Ag

$$= \frac{1 \text{ cm}^3}{5.85 \times 10^{22}} = 1.71 \times 10^{-23} \text{ cm}^3 = 1.71 \times 10^{-29} \text{ m}^3$$

6. Calculation of total volume occupied by Ag atoms present in shells of all Ag@Au NPs

Given: diameter of AuNP = 10 nm; that of Au@Ag NP = 13 nm.

∴ Radii = 5 nm and 6.5 nm respectively

Now volume of only shell in a single Au@Ag NP

$$\begin{aligned} &= \text{Volume of Au@Ag NP} - \text{Volume of AuNP} \\ &= \frac{4}{3} \pi R^3 - \frac{4}{3} \pi r^3 \\ &= \frac{4}{3} \pi (R^3 - r^3) \\ &= \frac{4}{3} \pi \{ (6.5 \times 10^{-9} \text{ m})^3 - (5 \times 10^{-9} \text{ m})^3 \} \\ &= 6.27 \times 10^{-25} \text{ m}^3 \end{aligned}$$

∴ Total volume of shells of all Au@Ag NPs

$$\begin{aligned} &= \text{Volume of shell in a single Au@Ag NP} \times \text{total no. of particles} \\ &= 6.27 \times 10^{-25} \text{ m}^3 \times 3.9 \times 10^{12} \\ &= 2.45 \times 10^{-12} \text{ m}^3 \end{aligned}$$

7. Calculation of total no. of Ag atoms present in shells of all Ag@Au NPs

Total no. of Ag atoms in all shells

$$\begin{aligned} &= \frac{\text{total volume of all shells}}{\text{volume needed for a single Ag atom}} \\ &= \frac{2.45 \times 10^{-12} \text{ m}^3}{1.71 \times 10^{-29} \text{ m}^3} = 1.43 \times 10^{17} \end{aligned}$$

8. Calculation of no. of Ag ions in the AgNO₃ solution taken for the preparation of particles

Given: concentration of AgNO₃ = 10 mM

Given: volume of AgNO₃ = 0.04 mL

No. of Ag ions

$$\begin{aligned} &= \frac{\text{Concentration}}{1000 \text{ mL dm}^{-3}} \times 0.04 \text{ mL} \times N_A \\ &= \frac{10 \times 10^{-3} \text{ mol dm}^{-3}}{1000 \text{ mL dm}^{-3}} \times 0.04 \text{ mL} \times 6.022 \times 10^{23} \text{ mol} \\ &= 2.41 \times 10^{17} \end{aligned}$$

9. Calculation of percentage of Ag ions consumed for shell formation

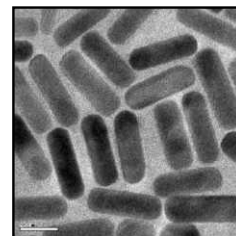
Per cent of Ag⁺ consumed

$$\begin{aligned} &= \frac{\text{Total no. of Ag atoms in shells of all Au@Ag NPs}}{\text{Total no. of Ag}^+ \text{ ions taken}} \\ &= \frac{1.43 \times 10^{17}}{2.41 \times 10^{17}} \times 100\% = 59.3\% \end{aligned}$$

REFERENCES

1. N. Toshima and T. Yonezawa. *New J. Chem.*, 22, (1998), 1179–01.
2. J.A. Schwarz, C.I. Contescu and K. Putyera, *Dekker Encyclopedia of Nanoscience and Nanotechnology*, 3, (2004), 1874.
3. T. Pradeep, *Nano: The Essentials*, Tata McGraw Hill, New Delhi, 4th reprint, (2010), 236–64.
4. M. Adachi, D.J. Lockwood, *Self-organized Nanoscale Materials*, (2006), 251.
5. S. Pande, S.K. Ghosh, S. Praharaj, S. Panigrahi, S. Basu, S. Jana, A. Pal, T. Tsukuda and T. Pal. *J. Phys. Chem. C*, 111, (2007), 10806–13.
6. <http://www.lsbu.ac.uk/water/cyclodextrin.html> accessed on 24/09/2010.

GOLD NANOPARTICLES FOR ENHANCED VISUAL DETECTION OF PESTICIDES



10.1 OBJECTIVE

- Exploit the properties of gold nanoparticles to remove certain pesticides (e.g. chlorpyrifos, Malathion) from drinking water.

10.2 BACKGROUND

Water pollution due to pesticides is an alarming problem in developing countries. Several methods exist to monitor the concentration levels of pesticides in water samples. Established techniques, such as liquid and gas chromatography and mass spectrometry, provide information with the detection limit of ppb level. These techniques are highly sensitive but time consuming and expensive. In the present experiment, however, a very simple and inexpensive method is demonstrated for the detection of two common pesticides, chlorpyrifos and malathion, in ppb levels. For this, we make use of the color change of gold nanoparticles (AuNPs) from red to blue by aggregation by pesticides enhanced by salt. The key to this detection strategy is to make the nanoparticle system sensitive by the addition of a suitable salt. The response is very fast and observable to the naked eye.

Chlorpyrifos is a broad-spectrum organophosphorus insecticide, widely used for crop protection and mosquito control. It can act as an inhibitor for cholinesterase enzyme, an enzyme that catalyzes the hydrolysis of neurotransmitter acetyl choline into choline and acetic acid. Once cholinesterase enzyme is inactivated, acetyl choline will accumulate in the nervous system which results in over stimulation of acetyl choline receptors. This will result in disorders in the central nervous system, cardiovascular system and respiratory system. Malathion is a degradable pesticide which breaks down in the environment by hydrolysis, biodegradation and photolysis. It is suspected to cause kidney problems, human birth defects and child leukemia.

AuNPs are highly attractive materials for optical applications due to the localized surface plasmon resonance (LSPR) exhibited by them. It is the collective oscillation of surface electrons induced by visible light which results in an extinction band in the visible region of the optical spectrum. The extinction band can be tuned by varying the particle size, shape and structure as well as the distance between the particles, refractive index of the surrounding medium and by adsorbed molecules on the

particle surface. The intense red color of aqueous AuNP solution is an expression of LSPR. AuNPs have been effectively utilized for the recognition of pesticide molecules in the environment, for example, endosulfan, at parts per million (ppm) levels. A biosensor was fabricated by covalently linking AuNPs with acetylcholinesterase (AChE) and was used for the detection of paraoxon. Combination of AChE with AuNPs has been used in different biosensor configurations to detect entities such as carbofuran, monocrotophos, methyl parathion, malathion and organophosphorus agents.

10.3 EXPERIMENT

10.3.1 Materials

- Tetrachloroauric acid trihydrate ($\text{HAuCl}_4 \cdot 3\text{H}_2\text{O}$)
- Trisodium citrate
- Chlorpyrifos (Technical grade)
- Malathion (Technical grade)
- Silver nitrate (AgNO_3)
- Activated alumina
- Salts such as Na_2SO_4 , NaCl , K_2SO_4 , MgSO_4 , $(\text{NH}_4)_2\text{SO}_4$, etc.

10.3.2 Apparatus

- Glass vials
- Round bottom flask
- Standard measuring flask
- Magnetic stirrer and pellet
- Electronic weighing device
- Conical flask
- Glass beakers
- Glass syringe
- Micro pipette of 1 mL capacity and micro tips of 1 mL capacity, for measuring volumes of TMAH and water during preparation of 25% TMAH solution.
- Rotavapor
- Sonicator
- Goggles and mask
- Spatula, tissue papers

10.3.3 Procedure

10.3.3.1 Synthesis of Gold Nanoparticles

Gold nanoparticles with an average diameter of 10–20 nm could be synthesized by the reduction of $\text{HAuCl}_4 \cdot 3\text{H}_2\text{O}$ with trisodium citrate. In this method, 10 mL of 5 mM $\text{HAuCl}_4 \cdot 3\text{H}_2\text{O}$ is diluted with 180 mL distilled water and heated till boiling just begins. 10 mL of 0.5% trisodium citrate solution is added to the hot solution and heating is continued till the solution turns wine red. It is then cooled to room temperature under ambient conditions.

10.3.3.2 Synthesis of Silver Nanoparticles Supported on Alumina

Silver nanoparticles with an average diameter of 40–60 nm could be synthesized by the citrate reduction method. In this method, 500 mL of 1 mM AgNO_3 solution is allowed to boil. 20 mL of 1% trisodium citrate solution is added into this and heating is continued till the solution turns pale yellow. It is cooled in a water bath. Procedure for the preparation of silver nanoparticles supported on alumina is as follows:

1. Soak neutral activated alumina (10 g) in silver nanoparticle suspension (25 mL) with stirring for 10 minutes and allow it to stand for half an hour.
2. Replace the supernatant with another 25 mL of AgNP suspension after it becomes colorless.
3. Repeat this replacement procedure till there is no further disappearance of color.
4. Decant the supernatant, wash the slurry with distilled water and dry under ambient conditions.

10.3.3.3 Synthesis of Pesticide Stock Solution

Prepare a 100 ppm stock solution of pesticide in 2-propanol. Dilute the solution to appropriate concentrations with water for further experiments.

10.3.3.4 UV/Vis Spectroscopic Analysis and Colorimetric Detection

1. Mix Na_2SO_4 solution (2 mL, 5000 ppm) with 1 mL of Au@citrate solution in each of 4 test tubes.
2. Add 1 mL of chlorpyrifos solution (of concentrations: 12, 25, 125 and 250 ppb respectively) to this mixture and note the colour change.
3. A control experiment is done with water in place of the pesticide solution.
4. Record the absorption spectra of the samples before and after the pesticide addition.
5. For finding the effect of Na_2SO_4 on the colour change, add pesticide solution to the Au@citrate without the addition of salt solution, and measure the absorption spectrum.
6. Use salts such as NaCl , K_2SO_4 , $(\text{NH}_4)_2\text{SO}_4$ and MgSO_4 instead of Na_2SO_4 and see their effect in enhancing the detection ability.

10.4 RESULTS AND DISCUSSION

Figure 10.1 shows the UV/Vis spectra of various mixtures. As-prepared Au@citrate solution exhibits an absorption peak at 520 nm (trace a) which is characteristic of surface plasmon resonance of AuNPs. Addition of Na_2SO_4 results in slight decrease in peak intensity (trace b). Addition of 12 ppb of chlorpyrifos to Au@citrate/ Na_2SO_4 mixture seems to have no effect on the spectrum (trace c). This is due to the pesticide concentration being too low to show any effect. When the concentration of pesticide is 25 ppb and above, we observe the following: (i) A peak around 680 nm appears. On increasing the pesticide concentration, (ii) peak's intensity increases (iii) peak gets red-shifted and (iv) the intensity of peak at 520 nm decreases. The emergence of longer wavelength plasmon and the decrease in intensity of the 520 nm plasmon may be due to the adsorption of chlorpyrifos on the Au@citrate surface.

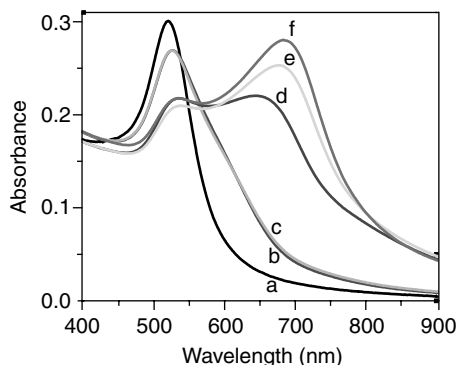


Fig. 10.1 UV/Vis spectra of (a) As-prepared Au@citrate (b) Au@citrate + Na_2SO_4 mixture without pesticide (c) to (f) after addition of 12, 25, 125 and 250 ppb respectively, of chlorpyrifos.

Figure 10.2 shows photographs of different solutions. The wine red colour of the Au@citrate turns to purple by the addition of Na_2SO_4 solution. Then, on addition of 12 ppb chlorpyrifos, the colour remains almost the same, consistent with unchanged absorption peak shown in previous Fig. When the pesticide solution added is 25 ppb or above, the colour changes to blue immediately after addition, giving a visual confirmation of pesticide's presence.

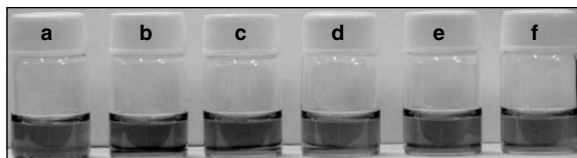


Fig. 10.2 Photographs of Au@citrate before and after the addition of Na_2SO_4 and chlorpyrifos: (a) As prepared Au@citrate, (b) Au@citrate/ Na_2SO_4 mixture and (c-f) 12, 25, 125 and 250 ppb chlorpyrifos in Au@citrate/ Na_2SO_4 mixture, respectively.

Changes in absorption spectra and visual colours in the case of the insecticide, malathion, are analogous to the changes observed for chloropyrifos (Figs 10.3 and 10.4).

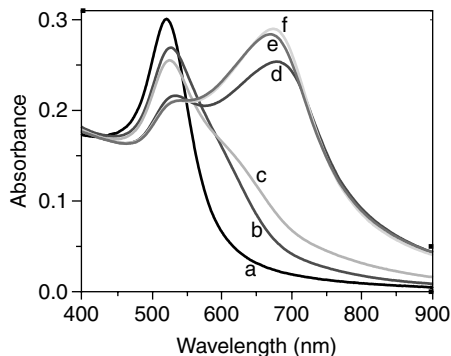


Fig. 10.3 UV/Vis absorption spectra of (a) Au@citrate solution, (b) Au@citrate after the addition of Na_2SO_4 , (c) to (f) after addition of, respectively, 25, 125, 250 and 500 ppb of malathion.

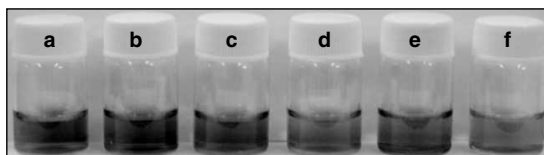


Fig. 10.4 Photographs of (a) as prepared Au@citrate, (b) Au@citrate + Na_2SO_4 mixture, and (c) to (f) 25, 125, 250 and 500 ppb malathion, respectively, in Au@citrate + Na_2SO_4 mixture.

When a 125 ppb chlorpyrifos solution is mixed with silver nanoparticles supported on alumina, most of the pesticide gets adsorbed on the nanoparticle surface and hence its concentration in the solution goes below the detection limit. Therefore, this solution (or the supernatant) will not change the colour of Au@citrate. This aspect may also be brought into the experiment.

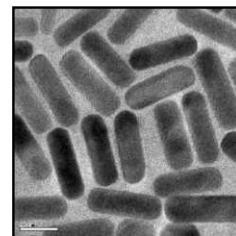
QUESTIONS

1. Why does aggregation lead to colour change of solutions of gold nano particles?
2. Propose methods to enhance the limit of detection?
3. What are the other methods available for detecting pesticides?
4. What are the other experiments which are useful for pesticide detection?

REFERENCES

1. Experiment adopted from K.P. Lisha, Anshup and T. Pradeep. Enhanced visual detection of pesticides using gold nanoparticles, *J. Envi. Sci. Health B, Pesticides, Food Contaminants and Agricultural Wastes*, 44, (2009), 697–05.

REACTIVITY OF GOLD CLUSTERS TOWARDS METAL IONS



11.1 OBJECTIVES

- Preparation of gold clusters (glutathione-capped gold nanoparticles).
- Study of reactivity of these clusters towards chosen metal ions.

11.2 BACKGROUND

Nano world has attracted attention from every field of research because materials at the nanoscale exhibit unusual behaviour, which is manifested neither in the bulk state nor in the molecular (atomic) state of the material. Continuous reduction in the size of bulk material leads us to a point where the bulk properties are either completely or partially lost while gaining new properties. The nano regime exists between micro and molecular (atomic) regimes. Nano regime can be further divided into two: clusters and colloids. If a metal is reduced in size of a few thousand atoms, we enter the world of metal colloids. The term, colloid, implies a dispersion of one phase, either solid or liquid, in a second phase, and the term was used for those suspensions which would not phase separate or sediment spontaneously unless centrifuged. Usual size range of colloidal particles is 10^{-6} - 10^{-9} m. The particles with a few hundreds or dozens of atoms are usually called clusters. Alternately, any molecular species containing only a few atoms (not necessarily of same element) or any compound containing two or more atoms bonded to one another can be called a cluster [1]. Clusters contain inter-atomic bonding. The bonding may be between metal atoms or between metal and non-metal atoms. Effectively, the structural hierarchy of any material is as follows: atoms, molecules, nanoparticles (clusters or colloids), microparticles (as in suspensions) and bulk materials. Major classes of cluster compounds that have been discovered can be summarized in four groups [2]:

- Clusters in gas phase and in matrices (e.g. Ag_3 and Ag_4 , matrix isolated)
- Clusters on oxide supports (e.g. Au on Al_2O_3)
- 'Naked' metal clusters (eg. Bi_5^{3-} , Sn_5^{2-} , Sb_7^{3-})
- Molecular clusters (e.g. metal carbonyls and related clusters)
- Ligand-protected clusters (e.g. $\text{Au}_{25}\text{SG}_{18}$, where SG is glutathione ligand with the H lost from its -S-H group)

We have discussed, in the previous experiments, about the properties and synthesis of gold colloids and gold nanorods. Here, we shall limit our discussion to gold clusters consisting of only a few tens of atoms. Gold clusters are compounds with a core of multiple gold atoms, the core being surrounded with organic groups (ligands) attached covalently to the exterior (surface) gold atoms. Examples of the well-known gold molecular clusters are $[\text{Au}_6(\text{P}(\text{C}_6\text{H}_5)_3)_6]^{2+}$ and $[\text{Au}_9(\text{P}(\text{C}_6\text{H}_5)_3)_8]^{3+}$. Mc Partlin was the first to describe one such structure, undecagold, $\text{Au}_{11}(\text{P}(\text{C}_6\text{H}_5)_7)$, with the help of X-ray diffraction. The structure was found to contain a core, of diameter 0.82 nm, containing 11 gold atoms. By altering the organic ligands, undecagold can be made water soluble. Subsequently, larger gold clusters containing ~67 gold atoms in the core, and having a diameter of 1.4 nm, have been prepared. Gold clusters differ in many respects from colloidal gold: (1) Colloidal gold is a dispersion of metal particles, where as, gold clusters are compounds with definite formulae. There exists a whole family of stable gold cluster compounds, such as Au_6 , Au_{11} , Au_{13} , Au_{55} , Au_{67} , etc. Commonly known preparations for gold clusters generally yield mixtures of these. (2) Gold clusters are more stable than colloidal gold. The higher stability is due to the covalent bonding with organic molecules. (3) The tissue penetration capacity is higher for Au clusters. (4) Gold clusters of given formula have uniform and specific sizes where as particles in colloidal gold are highly irregular. (5) Gold clusters do not aggregate, where as, gold colloids tend to aggregate unless protected (capped) by external reagents [2–4]. (6) Of late, another important aspect of gold clusters has come to the attention. This relates to their use as labeling agents in biology in view of their red/near-infrared emission, a radiation which has a large tissue penetration.

In the present experiment, we are going to prepare $\text{Au}_{25}\text{SG}_{18}$ and investigate its reactivity in the presence of metal ions with different reduction potentials. The list of metal/complex ions used in this investigation are: AuCl_4^- , Ag^+ , Fe^{3+} , Cu^{2+} , Ni^{2+} , Cd^{2+} , Zn^{2+} and Sr^{2+} . The order of their standard reduction potentials is Ag^+ (+0.80 V) > Fe^{3+} (+0.77 V) > Cu^{2+} (+0.34 V) > Ni^{2+} (–0.23 V) > Cd^{2+} (–0.40 V) > Zn^{2+} (–0.76 V) > Sr^{2+} (–2.89 V). [Though we have chosen various ions to study the reactivity, teachers, when they adapt this experiment to suit their class-room and lab environment, could select metals ions which they think would be appropriate.]

11.3 EXPERIMENT

11.3.1 Materials

- Glutathione (GSH) (reduced)
- Chloroauric acid ($\text{HAuCl}_4 \cdot 3\text{H}_2\text{O}$)
- Methanol
- Sodium borohydride
- Metal ion sources: $\text{HAuCl}_4 \cdot 3\text{H}_2\text{O}$ or any available hydrate, AgNO_3 , anhydrous FeCl_3 , $\text{CuCl}_2 \cdot 2\text{H}_2\text{O}$, NiCl_2 , $\text{CdCl}_2 \cdot \text{H}_2\text{O}$, ZnBr_2 and $\text{SrCl}_2 \cdot 6\text{H}_2\text{O}$.

11.3.2 Apparatus

- Beaker
- Measuring jar
- Standard flask
- Vacuum dryer
- Magnetic stirrer with pellets
- Centrifuge
- Sample bottles

11.3.3 Methods

11.3.3.1 Synthesis of Au@SG Clusters

1. Add solid GSH (2.0 mmol, 612 mg) to a methanolic solution of $\text{HAuCl}_4 \cdot 3\text{H}_2\text{O}$ (5 mM, 100 mL).
2. Cool the mixture in an ice bath to $\sim 0^\circ\text{C}$.
3. Add rapidly, with vigorous stirring, an ice-cold, aqueous solution of NaBH_4 (25 mL, 0.2 M).
4. Allow the contents to react for about an hour.
5. Separate the resulting precipitate by centrifugation and wash several times with methanol.
6. On vacuum-drying the precipitate, a dark brown powder is obtained. It consists of different Au@SG clusters along with some gold nanoparticles.

11.3.3.2 Synthesis of $\text{Au}_{25}\text{SG}_{18}$

1. Pure $\text{Au}_{25}\text{SG}_{18}$ can be prepared from the above Au@SG clusters through ligand etching:
2. Dissolve the powder containing Au@SG clusters and Au nanoparticles in water (25 mL).
3. Add solid GSH (2.0 m mol, 612 mg) to the mixture and stir the contents at 55°C .
4. Monitor the reaction with optical absorption spectroscopy.
5. Stop heating when the absorption features of $\text{Au}_{25}\text{SG}_{18}$ (a peak around 670 nm) appear in the UV/Vis absorption spectrum.
6. Centrifuge the solution and discard any residue. Add methanol to the supernatant to precipitate $\text{Au}_{25}\text{SG}_{18}$ clusters.
7. On vacuum-drying the slurry, $\text{Au}_{25}\text{SG}_{18}$ clusters are obtained in powder form.
8. The etching may also be carried out at room temperature instead of at 55°C .

11.3.3.3 Reactions between $\text{Au}_{25}\text{SG}_{18}$ and Metal Ions

1. Add, separately, different metal ions (AuCl^+ , Ag^+ , Fe^{3+} , Cu^{2+} , Ni^{2+} , Cd^{2+} , Zn^{2+} and Sr^{2+} [50 μM]) to samples of cluster powder (250 $\mu\text{g}/\text{mL}$, pH 3.3).
2. Stir the solutions and monitor the reactions using optical absorption spectroscopy.

11.4 RESULTS AND DISCUSSION

Formation of $\text{Au}_{25}\text{SG}_{18}$ clusters can be confirmed by TEM and by various spectroscopic techniques such as infrared, NMR and optical absorption (simplest of all). Figure 11.1 is the UV/Vis absorption spectrum of the Au_{25} . The absorption features are explained in the next paragraph. Figure 11.2 shows the HRTEM image of the clusters. Faint spots (marked with circles) of average diameter 0.7 nm are due to isolated Au_{25} clusters. These clusters are extremely sensitive to the electron beam; long time exposure results in aggregation.

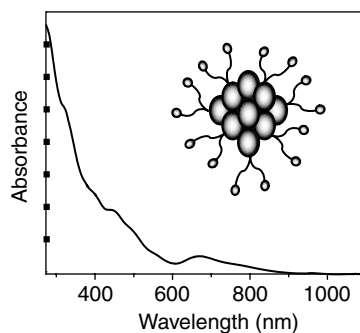


Fig. 11.1 UV/Vis absorption spectrum of aqueous solution of $\text{Au}_{25}\text{SG}_{18}$. Inset shows the schematic of a cluster.

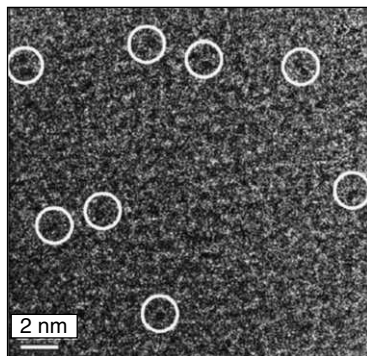


Fig. 11.2 HRTEM image of $\text{Au}_{25}\text{SG}_{18}$ clusters. The clusters are marked with circles.

Instantaneous decomposition of cluster solution was observed with the addition of AuCl_4^- ions to the cluster solution (Fig. 11.3). The process of decomposition was rather slow in the case of other ions. The product of this decomposition is thought to be an insoluble gold-glutathione coordination polymer, Au_nSG_m , consisting of gold in the form of Au^+ ions. So, in effect, the polymer formed is a $\text{Au}(\text{I})$ -glutathione complex. The characteristic absorption features of the $\text{Au}_{25}\text{SG}_{18}$ cluster, originating from intraband transitions in the visible region and interband transitions in the ultraviolet region, vanish

immediately after the addition of AuCl_4^- ions. The supernatant was colourless and the precipitate, formed in about 10 minutes, was white in colour. There was no characteristic peak in the UV/Vis spectrum of the supernatant liquid, indicating the absence of nanoparticles or clusters.

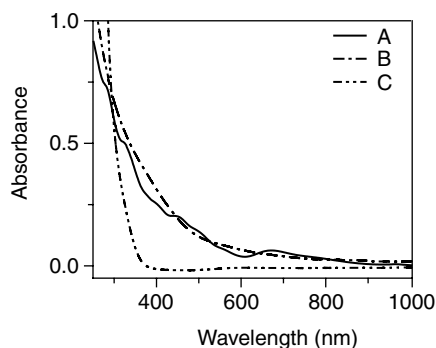


Fig. 11.3 Optical absorption spectra of (A) a solution of parent $\text{Au}_{25}\text{SG}_{18}$ clusters, (B) immediately after adding $50 \mu\text{M}$ AuCl_4^- ions to the clusters and (C) the synthesized Au(I)SG polymer.

Consumption of Au^{3+} (AuCl_4^-) can also be monitored with the help of spectrophotometry. For this, record the absorption spectrum of the diluted AuCl_4^- before adding it to the cluster solution. (In water, AuCl_4^- is characterized by a peak at 330 nm). Then add the $\text{Au}_{25}\text{SG}_{18}$ cluster powder in increasing quantities and record the absorption spectra after each addition. As the reaction progresses, the intensity of 330 nm peak keep decreasing, and finally goes to zero. The disappearance of the peak indicates that the added AuCl_4^- was consumed completely.

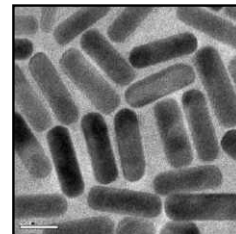
QUESTIONS

1. What are clusters and why are they different from nanoparticles?
2. Why do gold clusters react with gold ions?
3. How can one identify the products of the reaction?
4. Why are clusters more reactive than nanoparticles?

REFERENCES

1. G. Schmid. *Clusters and colloids: From theory to application*, VCH, (1994).
2. D.M.P. Mingos. *Gold Bull.*, 17(1), (1984), 5–12.
3. J.F. Hainfeld and R.D. Powell. *J. Histochem. Cytochem.*, 48(4), (2000), 471–80.
4. J.F. Hainfeld, R.D. Powell, F.R. Furuya and J.S. Wall. *Gold cluster crystals* accessed from web (<http://www.nanoprob.com/MSAXTALS00.html>).
5. M.A.H. Muhammed and T. Pradeep. *Chem. Phy. Lett.*, 449, (2007), 186–90.

STUDY OF SILVER NANOPARTICLES



12.1 OBJECTIVES

- Synthesis of silver nanoparticles using NaBH_4 as reducing agent.
- Determination of minimum quantity of PVP required to stabilize AgNPs.

12.2 BACKGROUND

Compounds of silver have a long history in medicine. Silver nitrate solutions were introduced by Credé in 1880 to protect newborn infants' eyes from infection. Colloidal silver was widely used by physicians as a mainstream antibiotic. Silver is being produced by pharmaceutical companies under various names, including *Protargol* and *Argyrol*. Silver nanoparticles neither dissolve nor get metabolized in the human body. In the body, they remain always as nanoparticles, performing their catalytic action. However, more recently, concerns about the after-effects due to accumulation of silver nanoparticles in the body have been raised. At the domestic level, they are used in washing machines, air conditioners, refrigerators, HVAC (heating, ventilating and air conditioning) filters and brooms. Even certain food containers are incorporated with silver nanoparticles to kill bacteria and to limit mould growth. They can also be used to break down halocarbons such as CCl_4 , and thus have a potential to be used in waste water treatment [1].

Silver nanoparticles had drawn much of their attention from medicine and other related fields because of their attractive physicochemical properties. SPR (surface plasmon resonance) and large effective scattering cross-section make them ideal candidates for molecular labeling with the help of surface enhance Raman scattering (SERS). In addition, the strong toxicity that silver exhibits in various chemical forms to a wide range of micro organisms is well-known, and hence, silver in the form of nanoparticles is a promising antimicrobial material.

12.2.1 Effect of Surfactants on the Stability of Nanoparticles

Silver nanoparticles have a tendency to aggregate and form bulk particles, owing to van der Waals attraction between them. In order to prevent aggregation, synthesized nanoparticles are stabilized by protective layers (e.g., a layer of adsorbed borohydride ions). Salts (NaCl or KI) can neutralize the surface charges and create conducive environment for particle aggregation. Polyvinyl pyrrolidone

(PVP), a polymer of N-vinyl pyrrolidone, is used to stabilize the colloidal silver. PVP is soluble in water and other polar solvents. In solution, it has excellent wetting properties and readily forms films. This property makes it to be used as a coating material for protecting nanoparticles. PVP is safe to human body, if consumed orally. Hence it is used as a binder in pharmaceutical tablets. Also, it has been used as a blood plasma expander for trauma victims in the later half of 20th century.

12.2.2 Characteristics of Absorption Spectra

Solutions of silver nanoparticles absorb in the visible region with a peak at 400 nm, when the particle sizes are in the range of 10–13 nm. For larger particles, as in the case of aggregated AgNPs, the absorption maximum shifts to longer wavelengths and the peak width increases. Peak position and FWHM values (see Fig. 12.1 for a definition of FWHM) for silver particles of different sizes are given in Table 1. [2].

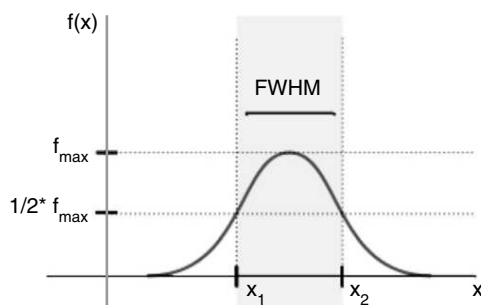


Fig. 12.1 Illustration showing calculation of full width at half maximum (FWHM) of a peak.

Table 1 Peak position and FWHM values of peaks in the UV/Vis absorption spectrum of AgNPs of different sizes.

Particle Size (nm)	Peak Position (nm)	FWMH (nm)
10–14	~ 400	50–70
35–50	420	100–110
60–80	438	140–150

12.2.3 Role of NaBH₄ and PVP

NaBH₄ has dual role in the present synthesis: (1) It reduces Ag⁺ to Ag and (2) it stabilizes silver nanoparticles by being adsorbed (Fig. 12.2). It is suggested that concentration of NaBH₄ should be twice as that of AgNO₃. A higher concentration may result in aggregation of silver nanoparticles due to an increased ionic strength [1]. Neutralization of surface charges may lead to particle aggregation. Hence, aggregation may be enhanced by the addition of an electrolyte. Interestingly, when PVP is used to stabilize the nanoparticles, the stability is retained even in the presence of ionic salts [2].

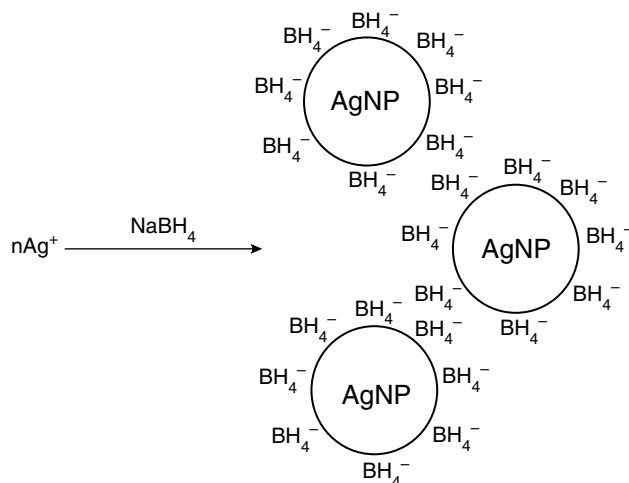
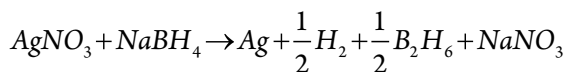


Fig. 12.2 Formation of silver nanoparticles by borohydride-reduction followed by adsorption of negative ions, and prevention of aggregation due to repulsive electrostatic forces between them. (For simplicity, sodium ions and other products are not shown on the right hand side).

12.2.4 Synthesis

The chemical reaction behind our experiment is reduction of Ag^+ in silver nitrate to Ag by sodium borohydride. This method is very convenient and often employed to produce silver nanoparticles over a short span of time; the synthesized particles are usually of dia 12–14 nm [2].



12.3 EXPERIMENT

12.3.1 Materials

- Silver Nitrate
- NaBH_4 (99% purity, an ice-cold solution must be freshly prepared just before its use)
- Poly vinyl-pyrrolidone
- Sodium chloride

12.3.2 Apparatus

- Glass vials
- Round bottom flask

- Standard measuring flask
- Magnetic stirrer
- Electronic weighing device
- Conical flask
- Glass beakers
- Spatula, tissue papers

12.3.3 Procedure

12.3.3.1 Preparation of Silver Nanoparticles

1. Thoroughly clean all the glassware with aquaregia before starting the experiment.
2. Take 30 mL of 0.002 M NaBH_4 in a 250 mL flask and cool it, with stirring, in an ice bath for about 20 minutes.
3. Using a burette, add dropwise 10 mL of 0.001 M AgNO_3 solution.
4. The solution turns light yellow (by the time about 2 mL of AgNO_3 is added) before acquiring a darker yellow shade.
5. Record the absorption spectrum, after dilution, if needed, using distilled water as reference.

12.3.3.2 Aggregation and Preventions of Aggregation

1. Take 2 mL of the silver nanoparticle solution (the yellow product) in a clean test tube; add a drop of 1.5 M NaCl to it. Particle aggregation is seen.
2. Upon aggregation, the solution turns dark yellow, then violet and finally grey. This change may be followed by recording absorption spectrum.
3. Repeat the experiment of addition of NaCl in another test tube except that, before adding salt solution, add a drop of 0.3% PVP solution to AgNP . Now, no change in the colour is observed indicating that PVP acts as a protective agent and hence prevents aggregation.
4. Repeat the above process with more and more dilute PVP solutions. At certain stage, when the concentration of PVP reaches to about 0.1%, the colour changes as outlined in step 1 are observed. This indicates that, at this concentration of PVP, the amount of PVP is insufficient to fully cover the surfaces of AgNPs .

12.3.4 Precautions

1. Silver nitrate causes burns in contact with skin and eyes.
2. Sodium borohydride is flammable and toxic.
3. While preparing silver nanoparticles, once the addition of AgNO_3 is complete, stirring should be stopped. Otherwise, particles may aggregate (as seen by colour change of solution from yellow to grey).

4. Use of sodium borohydride solutions with purity less than 99% had resulted in the formation of aggregated silver nanoparticles.
5. All the equipment that comes in contact with nanoparticle solution must be cleaned thoroughly in order to reduce the possibility of aggregation.
6. It is preferable to carry out all the reactions in a fume cupboard.

12.4 RESULTS AND DISCUSSION

Formation of silver nanoparticles is revealed by the colour changes (Fig. 12.3). Colour changes associated with (a) coagulation of AgNPs by added electrolyte and (b) prevention of coagulation due to PVP coating are shown in Fig. 12.4, a and b, respectively. Fig. 12.5 is a typical absorption spectrum of a solution of AgNPs. The peak position at 400 nm indicates that the particles fall in the size range of 12–14 nm.



Fig. 12.3 Colour changes observed on adding NaBH_4 to AgNO_3 solution.

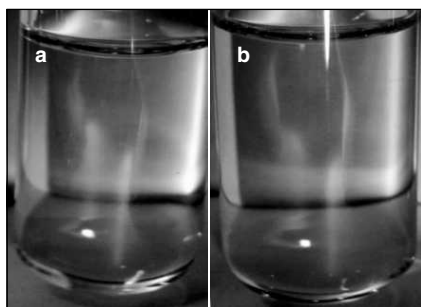


Fig. 12.4 Contrasting hues AgNP solutions, (a) after the addition of NaCl and (b) when PVP is added before the addition of NaCl .

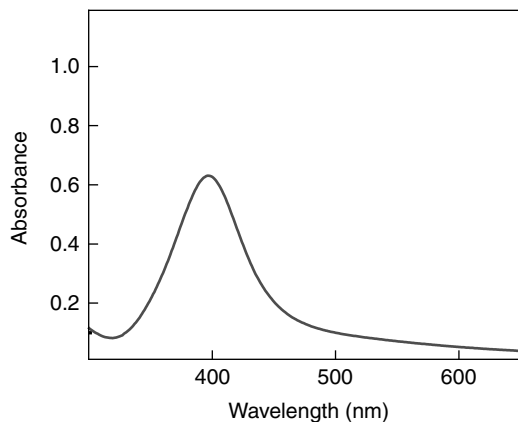


Fig. 12.5 *UV/Vis absorption spectrum of a diluted solution containing silver nanoparticles.*

QUESTIONS

1. Assume that the size of the silver nanoparticles formed is 13 nm. In these particles, assume that each silver atom effectively occupies a volume equivalent to the volume of a cube of edge length 0.3 nm. Calculate the number of silver atoms present in a single nanoparticle.
2. Explain the role of borohydride in the present method. Why is it added in excess?
3. In the experiment, nanoparticles, agglomeration is accompanied by a colour change. What is the reason for this change in occur?
4. What does NaCl do in agglomeration process? What does PVP do?

Answers to Question No. 1

Volume of each spherical nanoparticle with diameter of 13 nm $= \frac{4}{3}\pi r^3$

$$= \frac{4}{3}\pi \left(\frac{13 \times 10^{-9} \text{ m}}{2} \right)^3$$

$$= 1.15 \times 10^{-24} \text{ m}^3$$

Volume of the given cube of edge length 0.3 nm = (edge length)³

$$= (0.3 \times 10^{-9} \text{ m})^3$$

$$= 2.7 \times 10^{-29} \text{ m}^3$$

= effective volume occupied by a single Ag atom.

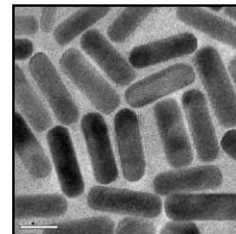
$$\begin{aligned} \therefore \text{No. of Ag atoms in a single AGNP} & \\ &= \frac{\text{Volume of a single AgNP}}{\text{Volume needed for a single Ag atom}} \\ &= \frac{1.15 \times 10^{-24} \text{ m}^3}{2.7 \times 10^{-29} \text{ m}^3} \\ &= 42605 \end{aligned}$$

i.e. around 40 thousand Ag atoms.

REFERENCES

1. http://en.wikipedia.org/wiki/Silver_nanoparticles accessed on 24/09/2010.
2. S.D. Solomon, M. Bahadory, A.V. Jeyarajasingam, S.A. Rutkowsky, C. Boritz and L. Mulfinger, *J. Chem. Edu.*, 84, (2007), 322–25.

SYNTHESIS OF ZnO NANOPARTICLES



13.1 OBJECTIVES

- Synthesis of ZnO nanoparticles using reaction of Zn acetate with propanol in the presence of NaOH.
- Characterization of the nanoparticles using UV/Vis absorption spectroscopy.

13.2 BACKGROUND

ZnO nanoparticles are very important in the category of semiconductor nanoparticles (SCNPs). ZnO is one of the few ceramic oxides that shows quantum confinement effects in experimentally accessible size. Other reasons for its importance are its wide band gap of 3.4 eV and large excitation binding energy of 60 meV. In addition, its specific chemical, surface and nanostructural properties make it widely useful in gas sensing applications where exposing a large surface area of the material to the gas is very important. As the particle size decreases, sensitivity of the gas sensor increases. Here, we shall discuss about semiconductor nanocrystals in general and ZnO nanoparticles in particular [1–3].

13.2.1 Semiconductor Nanoparticles

An electronic excitation in a bulk semiconductor leads to the formation of a pair of an electron and a hole, usually separated by long distances. This large separation, along with the high dielectric constant of the material, makes their binding energy relatively small. The characteristic distance is known as the Bohr radius and is of the order of a few nanometers. Band gap energy of a semiconductor can be defined as the minimum amount of energy required for the formation of a pair of these charge carriers; it is the energy difference between the top of the valence band and the bottom of the conduction band. Its value increases when the size of the semiconductor particles becomes smaller than the Bohr radius. Thus, the band gap absorption (and hence the colour of the nanoparticle) and the emission energies are sensitive to the size and shape of the particles. Similarly, other physical and chemical (e.g., oxidation-reduction) properties of the material become sensitive to the size and shape. It is possible to control size and shape by manipulating the region of space in which the nanoparticles grow. In bottom-up approach of synthesis, control is achieved by adjusting the concentration ratio of the chemicals used [3–7].

Semiconductor nanoparticles can also be called quantum dots (QDs) as their electrons are confined to points in space. Electrons have no freedom in any dimension and are said to be localized at points, implying that, a change in any direction changes the properties. An ideal quantum dot is realizable only when the electronic states within the dot encounter a discontinuity at the edges of the material. Due to this, the electron within the dot feels an insurmountable barrier at the edge. It is found that, spacial confinement of electrons and holes in a semiconductor leads to increased efficiency in light emission.

13.2.2 Relationship Between Band Gap and Particles Size

For a QD, the band gap is related to its size, though, the particle size, shape, solvent or adsorbate refractive index, and the interparticle distance also influence the position of its exciton transition. For a ZnO particle of 3 nm diameter, the absorbance maximum, λ_{max} is at ~365 nm. For smaller particles, a slight blue-shift, of the order of a few nm, is expected, whereas, for larger particles, a red-shift is expected. Peak widths of spectra give information about the width of size distribution of particles in the colloidal solution. A broader peak indicates a larger width. For a spherical nanoparticle of given radius, the band gap is related to its size by the equation:

$$E_g^* \cong E_g^{\text{bulk}} + \frac{\hbar\pi^2}{2r^2} \left(\frac{1}{m_e^* m_e} + \frac{1}{m_h^* m_e} \right) - \frac{1.8e^2}{4\pi\epsilon\epsilon_0 r} + \frac{0.124e^4}{\hbar^2 (4\pi\epsilon\epsilon_0 r)^2} \left(\frac{1}{m_e^* m_e} + \frac{1}{m_h^* m_e} \right)^{-1}$$

Here, $E_g^{\text{bulk}} = 3.4$ eV is the band gap of bulk material, $\hbar = \frac{h}{2\pi}$, h = Plank's constant, r = particle radius, m_e^* = effective mass of electrons, m_h^* = effective mass of holes, m_e = rest mass of free electrons, e = standard unit charge, ϵ_0 = permittivity of free space, ϵ = relative permittivity of the solid and $E_g^* = \frac{hc}{\lambda}$.

When we consider synthesis of nanoparticles by a bottom-up process, in the initial stages of the experiment, small particles dominate in number. Also, rate of dissolution of smaller particles is much higher than that of larger particles. (The rates are governed by surface tension and surface-to-volume ratio). Smaller particles get dissolved and the dissolved material gets precipitated onto larger particles. Thus, smaller particles act as “nutrients” for bigger particles and the average particle size increases with progress of reaction. Rate of this growth process decreases as the particles grow bigger in size which is accompanied by the particle size distribution becoming narrower. While the formation of smaller particles is kinetically favored, that of larger particles is thermodynamically favored (because of their smaller surface area to volume ratio) [9].

13.3 EXPERIMENT

13.3.1 Materials

- Zinc acetate ($\text{Zn}(\text{CH}_3\text{CO}_2)_2 \cdot 2\text{H}_2\text{O}$)

- Propanol
- NaOH

13.3.2 Apparatus

- Glass vials
- Round bottom flask
- Standard measuring flask
- Magnetic stirrer with a teflon-coated magnetic stirring bar of 8 mm × 12 mm size.
- Electronic balance
- Conical flask
- Glass beakers
- Spatula, tissue papers, etc
- Containers for ice and water bath
- Thermometer
- Mantle heater
- Ice

13.3.3 Procedure

1. Thoroughly clean all the glassware with aquaregia before starting the experiment.
2. Prepare 0.2 mM zinc acetate solution in 2-propanol in a 50 mL flask under vigorous stirring at 65°C. Prepare 0.02 M NaOH solution in 2-propanol.
3. Take 16 mL of the zinc acetate solution in a 200 mL beaker and dilute it with 168 mL of 2-propanol (kept at 0°C) and cool the resulting solution to 0°C.
4. To this, add 16 mL of the NaOH solution in ~1 min under constant stirring.
5. A suspension is formed. Immerse the beaker containing the suspension in a water bath maintained at 65°C for about 2 h.
6. During this time, take out 5 mL quantities of sample after 0, 2, 4, 8, 15, 20 and 30 minutes, cool to room temperature and record the absorption spectra.

13.3.4 Precautions

1. Isopropanol, when used at high temperatures, emits hazardous vapours .
2. Experiment to be performed in a fume hood or in a well ventilated room.
3. Care should be taken in handling solid NaOH since solid NaOH is highly hygroscopic and is corrosive on skin. While preparing NaOH solution of desired concentration, weigh a beaker containing small amount of water, then add to this a few pellets of NaOH with minimum

exposure to atmosphere and weigh again the beaker together with water and NaOH. Knowing the amount of NaOH taken, decide the final volume of NaOH solution to be made.

13.4 RESULTS AND DISCUSSION

Figure 13.1 shows absorption spectra of ZnO nanoparticles recorded at various stages of growth up to 30 minutes.

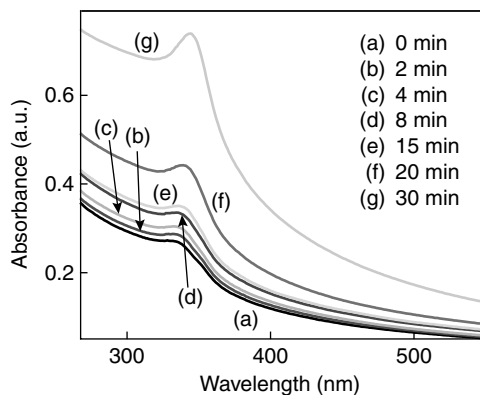


Fig. 13.1 *UV/Vis absorption spectra of reaction mixtures at various stages of formation of ZnO nanoparticles.*

Band gap can be calculated from the cut-off wavelength in the absorption spectra, as described in Appendix 2 for PbS nanoparticles.

QUESTIONS

1. What are quantum dots? Why are they known by that name?
2. Briefly describe some of the applications of semiconductor nanoparticles.
3. Write a note on various methods available in the literature for the preparation of semiconductor nanoparticles.
4. What are the different methods available for characterizing ZnO nanoparticles?
5. With the help of absorption spectrum recorded immediately after mixing the reactants (trace (a) in Fig. 13.1), calculate the band gap for ZnO nanoparticles.

Answers to Question No. 5

Consider the absorption spectra. Let us take the first spectrum. The cut-off wavelength estimated for this sample is 410 nm. The equation for the calculation has already been explained in the theory section. This equation can be written as,

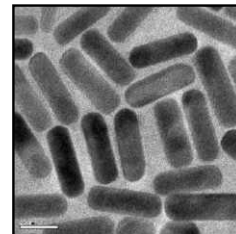
$$E_g^* \cong E_g^{\text{bulk}} + \frac{\hbar\pi}{2r^2} \left(\frac{1}{m_e^* m_e} + \frac{1}{m_h^* m_e} \right) - \frac{1.8e^2}{4\pi\epsilon\epsilon_0 r} + \frac{0.124e^4}{\hbar^2 (4\pi\epsilon\epsilon_0 r)^2} \left(\frac{1}{m_e^* m_e} + \frac{1}{m_h^* m_e} \right)^{-1}$$

Significance of every term has already been explained. In this section we are concerned only with the numerical aspect. Substitute all known terms and solve for r , and we get a value approximately equal to 1 nm.

REFERENCES

1. http://en.wikipedia.org/wiki/Zinc_oxide accessed on 24/09/2010.
2. E.A. Meulenkaamp, *J. Phys. Chem. B*, 102, (1998), 5566–72.
3. M. Bangal, S. Ashtaputer, S. Marathe, A. Ethirj, N. Hebalkar, S.W. Gosavi, J. Urban and S.K. Kulkarni, *Hyperfine Interactions*, 160, (2005), 81–94.
4. C. Wang, E. Wang, Y. Lan, Q. Li, B. Mao and C. Tian, *Thin Solid Films*, 516(18), (2008), 6058–62.
5. J. Xu, Q. Pan, Y. Shun and Z. Tian, *Sensors and Actuators B*, 66(1–3), (2000), 277–79.
6. M.S. Tokumoto, A. Smith, C.V. Santilli, S.H. Pulcinelli, E. Elkaim and V. Briois, *J. Non-Cryst. Solids*, 273, (2000), 302–06.
7. M.A. El-Sayed, *Acc. Chem. Res.*, 37(5), (2004), 325–33.
8. T. Pradeep, *Nano: The Essentials*, Tata McGraw Hill, New Delhi, 4th reprint, (2010).
9. P.S. Hale, L.M. Maddox, J.E. Shapter, N.H. Voelcker, M.J. Ford and E.R. Waclawik, *J. Chem. Edu.*, 82(5), (2005), 775–78.

PREPARATION OF TELLURIUM NANOWIRES



14.1 OBJECTIVE

- Synthesis of tellurium nanowires

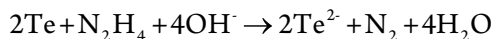
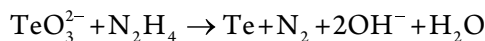
14.2 BACKGROUND

Nanowires belong to the class of 1-D nanostructures with very high aspect ratios of 1000 or more (typically not less than 20). Diameter of a typical nanowire is of the order of a few nanometers while their length may extend to micrometer range. Nanowires are also known as ‘quantum wires’, as, quantum mechanical effects play vital role in their properties because of their size scales. As the diameter of a nanowire becomes smaller quantum effects become more pronounced. Depending on the type of parent material a nanowire can be metallic, semiconducting or insulating in nature. Examples of nanowires include organic nanowires (DNAs), inorganic molecular nanowires (e.g. $\text{Mo}_6\text{S}_9\text{I}_x$, $\text{Li}_2\text{Mo}_6\text{Se}_6$), nanowires based on metals (Ni, Pt, Au), semiconductors (Si, InP, GaN) and insulators (SiO_2 , TiO_2). To bring about manifestation of contrasting properties along their length, nanowires, during their synthesis, can be doped in the growth stage itself. Nanowires, atomic structure can range from crystalline, to polycrystalline, to nearly amorphous. Functionalization and processing can help us in modifying the chemistry of nanowires. These methods are compatible with post-processing techniques, including harsh chemical treatments and plasma treatments.

VLS (vapour-liquid-solid) techniques are commonly employed in synthesizing nanowires, which involve the preparation of a catalytic liquid alloy phase (droplets) on a substrate. The substance to be grown is introduced as a vapour. The liquid alloy phase rapidly absorbs the vapours to supersaturation levels and an axial crystal growth subsequently occurs from nucleated seeds at the liquid-solid interface. Size and other physical properties of the liquid alloy determine the diameter of the nanowires grown. Final length can be controlled by cutting the source supply at appropriate stage. Techniques such as thermal chemical vapour deposition (thermal CVD), low pressure CVD (LPCVD), plasma enhanced CVD (PECVD), metalorganic CVD (MOCVD), etc. have been employed to synthesize various nanowires through the VLS mechanism. Nanowires are not the kind of materials that are readily available in nature. In laboratory, they can be synthesized from elements via suspension or deposition processes. Semiconducting nanowires have potential applications in future computing era, in transistors, and in optoelectronics.

Tellurium is a p-type semiconductor with a broad absorption band around 300 nm (bulk) and band gap energy of 0.35 eV. It can make a potential material in fabrication of nanodevices. Tellurium has high anisotropic growth tendency due to its unique helical chain conformation in its crystal structure. Van der Waals interactions between the atoms of tellurium are responsible for its crystal structure. Methods which have been employed for the preparation of nanowires include (1) layer-by-layer assembly technique to obtain photoactive Te nanowires, (2) self seeding approach for large yields of 1D t-Te nanowires at 197 °C, (3) biomolecules-assisted synthesis for the preparation of t-Te nanowires at 150–160 °C, (4) microwave-assisted method for the preparation of nanowires at 180 °C, (5) employing starch to synthesize t-Te nanowires at 160 °C (6) use of PVP as both reductant and template for the preparation of Te nanorods, nanowires, and nanotubes at 180–220 °C.

Here, we present a method for the synthesis of tellurium nanowires. It involves reduction of TeO_3^{2-} at room temperature by N_2H_4 in aqueous solutions. The reactions involved are:



14.3 EXPERIMENT

14.3.1 Materials

- Tellurium oxide
- Hydrazine hydrate
- Sodium dodecyl sulfate (SDS)

14.3.2 Apparatus

- Round bottom flask
- Standard measuring flask
- Magnetic stirrer with a teflon-coated magnetic stirring bar of 8 mm × 12 mm size.
- Electronic weighing device
- Glass beakers
- Centrifuge
- Spatula, tissue papers

14.3.3 Procedure

1. Thoroughly clean all the glassware with aquaregia before starting the experiment . Add TeO_2 (16 mg) powder, slowly to a beaker containing hydrazine hydrate (10 mL). Ensure constant mixing and leave the contents undisturbed.
2. At the end of one hour, colour of the solution changes from colourless to blue, indicating complete dissolution of the powder and formation of tellurium nanowires.

3. Dilute the solution to 10 fold by adding required volume of 10 mM SDS, in order to terminate the reaction.
4. Centrifuge the as prepared solution, twice, for 10 minutes at 8,000 rpm to remove excess hydrazine and SDS.

14.3.4 Precautions

Care must be taken while handling hydrazine hydrate. It is combustible and incompatible with a wide variety of materials. Its contact with materials can cause fire or explosive decomposition. Its vapours can explode if ignited. It is toxic, and may be fatal, if inhaled, swallowed or absorbed through the skin. Contact with eye may cause serious damage. It is corrosive and very irritating to respiratory tract even at lower concentrations.

14.4 RESULTS AND DISCUSSION

Results of characterization are presented in Figs 14.1, 14.2 and 14.3.

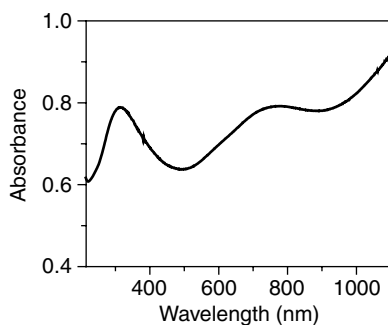


Fig. 14.1 Absorption spectrum of tellurium nanowires.

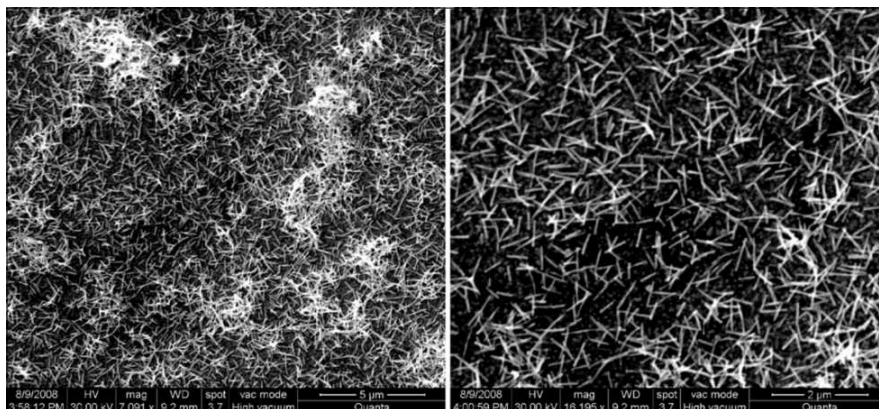


Fig. 14.2 SEM images of the tellurium nanowires at different magnifications.

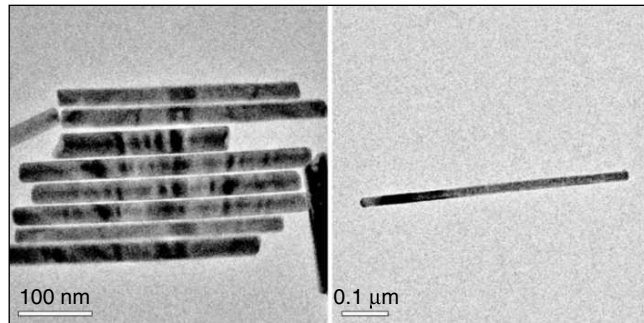


Fig. 14.3 TEM images of the tellurium nanowire(s).

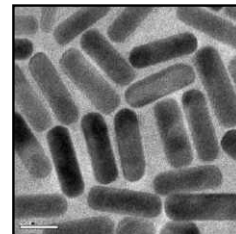
QUESTIONS

1. What are nanowires?
2. Why is tellurium better in forming nanowires?
3. What are the characteristic features of Te nanowires and what are they due to?

REFERENCES

1. (a) <http://en.wikipedia.org/wiki/Nanowire> (b) <http://www.etamota.com/technology/nanowires/> accessed on 24/09/2010
2. Z.H. Lin, Z. Yang and H.T. Chang. *Crystal Growth and Design*, 8(1), (2008), 351–57.
3. C.J. Murphy and N.R. Jana. *Adv. Mater.*, 14(1), (2002), 80–82.
4. A. Zhao, L. Zhang, Y. Pang and C. Ye. *Appl. Phys. A*, 80, (2005), 1725–28.

SYNTHESIS OF LUMINESCENT GOLD NANOPARTICLES BY CORE ETCHING



15.1 OBJECTIVES

- Synthesis of Au@GSH
- Etching of Au@GSH with BSA

15.2 BACKGROUND

Luminescence is a form of cold body radiation, light occurring usually at normal or low temperatures. This distinguishes it from incandescence, which is light generated at high temperatures. Luminescence can also be thought of as light from non-thermal sources. In luminescence, emission of light cannot be attributed merely and solely to the temperature or rise in the temperature of the emitting material. In other words, luminescence is the emission of light from a material due to radiative decay of excited electrons in that material. There exist various kinds of luminescence, each resulting from a different kind of excitation. For example, chemoluminescence is due to chemical reaction, crystalloluminescence occurs during crystallization, electroluminescence occurs when an electric current is passed through the material and photoluminescence occurs when photons cause electronic excitation. We shall be focusing on photoluminescence in the present experiment.

Among various nanostructures synthesized in the recent past, quantum clusters (QCs) or sub-nanoclusters are attracting enormous attention due to their novel optical and electronic properties. They are composed of very few atoms, with a core size in the sub-nanometer regime, which is the reason for the name sub-nanocluster. Owing to the sub-nanometer core size, they do not possess continuous bands of energy states but have discrete electronic energy levels. Consequently they show “molecule-like” optical transitions in absorption and emission and can be termed also as molecular clusters. One of the most promising properties of QCs is their photoluminescence with appreciable quantum yield (QY), as high as 70 per cent in certain cases. It is also possible to tune their emission wavelength from the ultraviolet (UV) to the near-infrared (NIR) range by changing the number of core atoms. Unlike organic dyes, they are photostable, a quality that widens their area of potential applications. These QCs can be readily conjugated with several biological molecules, which further enhances their application potential.

In the core-etching method, a nanoparticle is treated with excess amount of molecules such as thiols, dendrimers, and Au³⁺ [1] ions, which can etch the core of the metallic nanoparticle leading to

the formation of QCs. A blue-emitting Au₈ QC was synthesized by the core etching of dodecylamine-capped gold nanoparticles (AuNPs) by polyethylenimine (PEI). Two different QCs with Au₂₅ and Au₈ cores have been synthesized from mercaptosuccinic acid (MSA)-capped AuNPs by etching with glutathione at two different pH values. A red-emitting gold QC was synthesized by etching organic-soluble didodecyldimethylammonium bromide-capped AuNPs with gold ions and subsequently transferring it to the aqueous phase by dihydrolipoic acid.

15.3 EXPERIMENT

15.3.1 Materials

- Tetrachloroauric acid trihydrate (HAuCl₄·3H₂O)
- Mercaptosuccinic acid (MSA)
- Sodium borohydride (NaBH₄)
- Bovine serum albumin (BSA)

15.3.2 Procedure

15.3.2.1 Synthesis of MSA-Capped AuNPs (AuNP@MSA)

1. Add MSA (20 mM) to HAuCl₄·3H₂O in methanol (100 mL, 5 mM).
2. Cool the mixture to 0 °C in an ice bath for 2 h.
3. Rapidly inject an aqueous solution of NaBH₄ (25 mL, 0.2 mM), cooled at 0 °C, into the mixture under vigorous stirring.
4. Allow the mixture to react for an hour.
5. Collect and wash the resulting precipitate repeatedly with methanol/water through centrifugal precipitation and dry it to obtain the AuNP@MSA as a dark brown powder.

15.3.2.2 Synthesis of Au_{QC}@BSA

1. Dissolve the as-synthesized AuNP@MSA (10 mg) in distilled water (5 mL).
2. Adjust the pH of the solution to 12 by adding NaOH solution.
3. Add BSA (100 mg) to the solution and stir the mixture well for 5 min.
4. If necessary, readjust the pH of the resulting solution to 12 and stir the solution for 6–8 h at 37 °C.
5. Centrifuge the solution at 20000 rpm for 30 min. to separate the QCs. Purify the product by extensive dialysis for 24 h using doubly distilled water, changing the water once for every 8 h.
6. Evaporate the solvent by freeze-drying and store the product as a powder.

Details of the experimental procedure may be found in Ref. 1.

15.4 RESULTS AND DISCUSSION

The UV/Vis absorption spectrum of $\text{Au}_{\text{QC}}@BSA$ is shown in Fig. 15.1, trace (a). The spectrum is almost featureless but has a different slope around 375 nm. We see a gradual rise in absorbance starting at 800 nm. The spectrum is different from that of the parent $\text{AuNP}@MSA$. In our preparation, we presume that gold QCs are encapsulated by BSA (as confirmed by the mass spectrum). Ligands, such as thiols and dendrimers, can perform core etching of nanoparticles with ligand exchange. When they are added in limited quantity, only ligand exchange would happen. However, when added in excess, core etching with complete ligand exchange occurs. For example, when MSA-protected nanoparticles are etched with glutathione, the MSA protection is completely removed. Therefore, in the present case also, we believe that the MSA molecules are removed completely, though, we do not have experimental evidence at present.

Photoluminescence spectra of pure BSA and $\text{Au}_{\text{QC}}@BSA$ are shown in Fig. 15.2 along with their excitation spectra. Pure BSA shows excitation and emission at 290 and 345 nm, respectively.

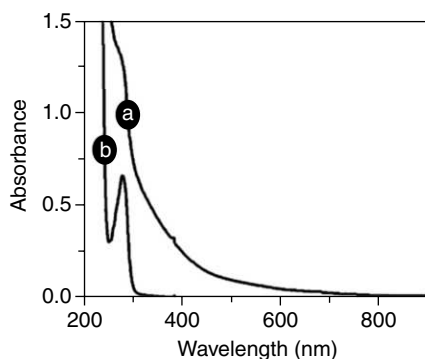


Fig. 15.1 Optical absorption spectra of (a) $\text{Au}_{\text{QC}}@BSA$ and (b) free BSA.

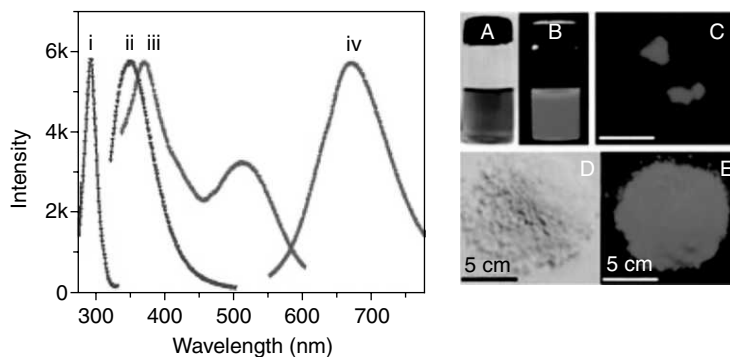


Fig. 15.2 Left: Photo excitation and luminescence profiles of BSA (traces i and ii) and $\text{Au}_{\text{QC}}@BSA$ (traces iii and iv). Right: photographs of $\text{Au}_{\text{QC}}@BSA$ solution under white light (A) and UV light (B), confocal luminescence image of the QC (C), and photographs of QC powder under irradiation by white light (D) and UV light (E).

BSA-protected QCs show two absorption maxima (at 370 and 510 nm) and a single emission maximum (at 660 nm). The luminescence of QCs may be due to interband transitions: to the $5d^{10}$ band from the $6(sp)^1$ band. The QY of the emission is ~4 per cent. On the right hand side of Fig. 15.2, other optical images of Au@BSA are shown.

QUESTIONS

1. Why are these nanoparticles luminescent?
2. What is core etching?
3. Why does BSA etch the core?
4. Justify the name 'quantum cluster'.

REFERENCE

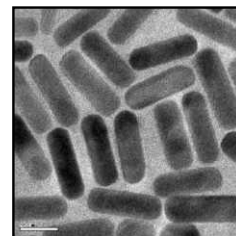
1. Method modified from M.A. Habeeb Muhammed, P.K. Verma, S.K. Pal, A. Retnakumari, M. Koyakutty, S. Nair and T. Pradeep. Luminescent quantum clusters of gold in bulk by BSA-induced core etching of nanoparticles: Metal ion sensing, metal enhanced luminescence and biolabeling. *Chem. Eur. J.*, 16(33), (2010), 10103–112.

Appendices:
A Practical Course on Nanoscience
and Nanotechnology

Part II

1. Diverse Nanoparticles Prepared by Various Routes

DIVERSE NANOPARTICLES PREPARED BY VARIOUS ROUTES



Section I: Metals (arranged in the order of atomic numbers)

Metal Particle Prepared	Starting Material	Reducing Agent	Medium	Stabiliser	Phase Transfer (Yes/No)	Condition	Re-dispersible	Mean Particle Dia. (nm)	Typical Application	Reference Number
Ti	Titanium tetrachloride	Ar-H ₂ plasma	Gas	No	No	Plasma	Not specified	2–10 nm	anti-microbial, anti-biotic and anti-fungal agent	1
V	Bulk metal	Annealing	Not specified	No	No	300 K	Not specified	2–9 nm	Multi-functional catalysis and photocatalytic applications	2
Cr	Chromium Fischer carbene complex	TOP/ Temperature	Biphase Water/ CHCl ₃	TOP	No	300°C	Yes	2.5 nm	Catalysis	3
Mn	Mn powder	Arc discharge	Ar gas	Not specified	No	Not specified	Yes	Upto 80 nm	Material Science and catalysis	4
Mn	...	Bioreduction with Hyacinth	1–4 nm	...	5
Fe	Fe(NO ₃) ₃ ·9H ₂ O	Hydrogen	Gas (fluidised bed reactor)	No	No	160–300°C	Not specified	300–500 nm	Electronics and catalysis	6
Fe	FeCl ₂	NaBH ₄	Triphase (Xylene/water/pyridine)	TOPO	No	RT	Not specified	3 nm	Electro catalysis	7
Fe	Fe(CO) ₅	High temperature	Oleic acid	Oleic acid	No	300 °C.	Yes	11–20 nm	Electronics and drug delivery	8

(Contd...)

Metal Particle Pre-prepared	Starting Material	Reducing Agent	Medium	Stabiliser	Phase Transfer (Yes/No)	Condition	Re-dispersible	Mean Particle Dia. (nm)	Typical Application	Reference Number
Co	Co(eta(3)-C ₈ H ₁₃)(eta(4)-C ₈ H ₁₂)	dihydrogen	THF	PVP	No	0°C, 20°C, 60°C	Not specified	1–1.5 nm	Catalysis	9
Co	Co(AOT) ₂ (cobalt bis(2-ethylhexyl)-sulpho-succinate)	NaBH ₄	Water/oil	TOP	No	RT	Yes	5.8 nm	Data storage device, sensors, catalysis	10
Co	Co ₂ (CO) ₈	Thermolysis in presence of Aluminum alkyls	Toluene	KorantinSH, oleic acid, LP-4, AOT	No	110°C	Yes	10±1.1 nm	Technical and biomedical applications	11
Co	CoCl ₂ vapor	H ₂	Ar gas	Nil	No	800–950°C	Not specified	50–78 nm	electronic, magnetic, optical, and chemical properties	12
Co	Co ⁺ ions	Ion implantation	SiO ₂ matrix	Nil	No	RT	No	1–10 nm	Magnetic storage devices	13
Co	CoCl ₂	lithium hydrotriethylborate (LiBH(C ₂ H ₅) ₃)	THF	3-(N,N-dimethyl)dodecylammonia)propanesulphonate (SB12)	No	RT	Yes	< 5 nm	Data storage device, biomedical engineering	14
Ni	Ni(COD) ₂	H ₂	CH ₂ Cl ₂	PVP	No	RT	Yes	20–30 nm	Catalysts, engineering	15
Ni	NiCl ₂	Hydrazine	water/CTAB /n-hexanol	water/CTAB /n-hexanol	No	73°C	Redispersible	4.6 nm	Catalysts, engineering materials, drug-delivery	16
Ni	Ni(COD) ₂	Hydrazine	CH ₂ Cl ₂	PVP	No	RT	Yes	30 nm	Magnetic and electronic applications	17
Ni (Rods)	NiCl ₂	HDA/TOPO	THF	HDA	No	RT	Yes	...	Catalysis, drug-delivery, electronics	18
Ni	NiCl ₂	Hydrazine	Aqueous	CTAB/TC ₁₂ AB	No	60°C	Yes	10–36 nm	Catalysis, drug-delivery, electronics	19
Ni	NiCl ₂	Hydrazine	ethylene glycol	Nil	No	60°C	Yes	9.2 nm	Catalysis, drug-delivery, electronics	20

(Contd...)

Metal Particle Pre-prepared	Starting Material	Reducing Agent	Medium	Stabiliser	Phase Transfer (Yes/No)	Condition	Re-dispersible	Mean Particle Dia. (nm)	Typical Application	Reference Number
Ni	NiCl ₂	H ₂	Ar gas	Oxide layer formed on the surface	No	800 to 950°C.	Not mentioned	31–106 nm	drug-delivery, electronics	21
Ni	Ni(NO ₃) ₂	CNT	N ₂ atmosphere	CNT	No	600°C	Yes	10–50 nm	catalyst and conducting or magnetic materials	22
Cu	Cu ²⁺	NaBH ₄ /hydrazine	Water/AOT	AOT revece micelles	No	RT	Not specified	2–10 nm	Catalysis	23
Cu	copper(II) acetate	hydrazine	water and 2-ethoxyethanol	PVP	No	Refluxing condition	Yes	6.6–30.2 nm	Catalysis	24
Cu	CuCl ₂	NaBH ₄	Water in oil micro-emulsions	w/o micelles	No	RT	Not specified	5–15 nm	Catalysis	25
Cu	copper(II) hydrazine carboxylate Cu(N ₂ H ₃ COO) ₂ ·2H ₂ O	Thermal/sonochemical	Water	Nil	No	~80°C	Not specified	200–250 nm	Catalysis	26
Cu	Cu salt	H ₂	Water	Carbon nanotube template	No	Below 773 K	Yes	100 nm to several micrometers	Catalysis	27
Cu	Cu(NO ₃) ₂	NaBH ₃ CN/TMPD	Water in supercritical fluid micro-emulsion	perfluoropolyether-phosphate	No	38°C	Not mentioned	5–15 nm	Catalysis	28
Cu	Cupric nitrate IPA (Cu(NO ₃) ₂ ·2SH ₂ O)	IPA	Water-IPA mixture	CTAB	No	Ambient conditions	Not mentioned	5–20 nm	Catalysis	29
Cu	CuSO ₄	Hydrazine	Ethylene glycol	Ethylene glycol	No	Microwave irradiation	Yes	~ 15 nm	Catalysis	30
Cu	CuSO ₄ ·SH ₂ O	NaH ₂ PO ₂ ·H ₂ O	Ethylene glycol	Ethylene glycol	Polyvinylpyrrolidone	Microwave irradiation	Yes	~20 nm	Thermal conductivity	31
Zn	[Zn(C ₆ H ₁₁) ₂]	Thermal reduction	Anisole/water	PVP	No	130°C	Not specified	6–17 nm	Sensors, transducers, photocells	32

(Contd...)

Metal Particle Pre-prepared	Starting Material	Reducing Agent	Medium	Stabiliser	Phase Transfer (Yes/No)	Condition	Re-dispersible	Mean Particle Dia. (nm)	Typical Application	Reference Number
Ga	Pure Ga metal	Evaporation-condensation	Sapphire	SiO _x	No	High temperature	No	10–18 nm	Electronic and photonic applications	33
Ga	Bulk Gallium	Evaporation-condensation	Al ₂ O ₃ /SiO _x	Al ₂ O ₃ /SiO _x	No	High temperature	No	10–60 nm	Electronic and photonic applications	34
Ga	Bulk Gallium	light-assisted self-assembly technique.	High vacuum	Not specified	No	100 K	Not specified	50 ± 14 nm	Electronic and photonic applications	35
Ga	GaCl ₃	Insitu reduction	Benzene	SBA-H	No	Not specified	No	Not mentioned	photonic applications	36
Ge (Nano-wires)	GeCl ₄ /phenyl-GeCl ₃	Na metal	pentane / hexane	Alkyl group	No	275°C	Yes	7–30 nm	optoelectronic applications	37
Ge	GeCl ₄	NaK alloy	heptane	R-GeCl ₃	No	270°C During crystallisation	Yes	6–20 nm	optoelectronic applications	38
Ge	Me ₃ GeS (CH ₂) ₃ Si (OMe) ₃	H ₂	Air/H ₂	SiO ₂ xero gel	No	900°C	Not specified	2.5–14.5 nm	optoelectronic applications	39
Ge	GeCl ₄	H ₂	H ₂ in Argon	Zeolite Y	No	470°C	Not specified	3 nm	optoelectronic and photonic applications	40
Ge	Sodium germanide (NaGe)/GeCl ₄	Metathesis reaction	Diglyme/glyme/triglyme	methylithium, butyllithium, or octylmagnesium bromide	No	Refluxing conditions	Yes	6.2–6.5 nm.	optoelectronic and photonic applications	41
Ge	GeI ₄	LiAlH ₄	CTAB/toluene	n-alkene	No	Refluxing conditions	Yes	2–7 nm	optoelectronic and photonic applications	42
Ge (Nano-cubes)	GeCl ₄ /phenyl-GeCl ₃	Na	Hexane	heptaethylene glycol monododecyl ether (C ₁₂ E ₇)	No	280°C	No	100 ± 20 nm	optoelectronic and photonic applications	43
Ge	Ge[N(SiMe ₃) ₂] ₂	Thermal Reduction	octadecene	oleylamine	No	285°C	Yes	7 ± 4 nm	optoelectronics	44
Ge	GeCl ₄	sodium naphthalide	glyme	Butyl (-C ₄ H ₉)	No	0°C	Yes	6.1 ± 2 nm	photonic applications	45

(Contd...)

Metal Particle Pre-prepared	Starting Material	Reducing Agent	Medium	Stabiliser	Phase Transfer (Yes/No)	Condition	Re-dispersible	Mean Particle Dia. (nm)	Typical Application	Reference Number
Se	Selenious acid (H ₂ SeO ₃)	Hydrazine	Heptane/water	AOT	No	RT	Not specified	4–300 nm	rectifiers, solar cells, photographic exposure meters, and xerography	46
Se (Nano-wires)	Sodium selenite (Na ₂ SeO ₃)	Glutathione (GSH).	Water	Nil	No	RT	No	60 ± 5 nm	photographic exposure meters	47
Y	Bulk Y	Pulsed laser deposition	Not mentioned	Nil	No	Not mentioned	No	32 nm	Television and laser systems	48
Mo	Mo(CO) ₆	Thermal decomposition	Octyl ether solution/N ₂ atmosphere	octanoic acid/ bis-2-ethylhexylamine	No	Not mentioned	Yes	3–14 nm	catalysis, magnetism, electronics	49
Ru	RuCl ₃	Ethylene glycol	Ethylene glycol	PVP	No	150°C	Yes	2 nm	Catalysis	50
Ru	Ru(COD) (COT) COD - 1,5-cyclooctadiene COT - 1,3,5-cyclooctatriene	H ₂	THF	PVP and cellulose acetate.	No	RT	Yes	2–3 nm	Catalysis	51
Ru	RuCl ₃	Ethylene glycol	Ethylene glycol	Ethylene glycol	No	453 K	No	5 nm	Catalysis	52
Ru	RuCl ₃	NaBH ₄	Water	Ethylene diamine	No	RT	Yes	~2.1 nm	Catalysis	53
Ru	Ru(cod)(cot)	dihydrogen	THF-methanol solution	Chiral N-donor ligands	No	RT	Yes	1.6–2.5 nm.	Catalysis	54
Rh	RhCl ₃ ·3H ₂ O	High temperature, high pressure	PVP	Water-ethanol mixture	No	473 K	No	2.7 nm–4.6 nm	Environmental, chemical and sensing	55
Rh	RhCl ₃	lithium triethylborohydride [LiB(C ₂ H ₅) ₃ H]	1-Dodecane-thiol [CH ₃ (CH ₂) ₁₁ -SH]	THF	No	60°C	Yes	1–3 nm	catalysis, chemical sensing, nanoscale capacitors, and semiconductor devices	56

(Contd...)

Metal Particle Pre-prepared	Starting Material	Reducing Agent	Medium	Stabiliser	Phase Transfer (Yes/No)	Condition	Re-dispersible	Mean Particle Dia. (nm)	Typical Application	Reference Number
Pd	[PdCl ₄] ²⁻	Photosensitised reduction	PVP	Alcohols	No	RT	Yes	1.7–3 nm	Catalysis	57
Pd	PdCl ₂	NaBH ₄	Tetra <i>n</i> -octyl ammonium bromide (TOABr)	Toluene-aqueous	Yes	RT	Yes	1–5 nm	Catalysis	58
Pd	Pd(NH ₃) ₄ Cl ₂	Hydrazine	Water-in-oil micro-emulsions	CTAB	No	RT	Yes	4 ± 0.9 nm	Catalysis	59
Pd	Pd surfactant complex	Thermal decomposition	...	Surfactant	Yes	3–7 nm	...	60
Pd	K ₂ PdCl ₄	NaBH ₄	Water	Dendrimers	No	Not specified	Yes	1.4, 1.7 ± 0.4 nm	Catalysis	61
Pd	TPP and TOP	No	...	Yes	...	Catalysis	62
Pd	Pd(fod) ₂	Thermally induced reduction	<i>o</i> -xylene/DMF/1-octanol	CTAB/DTAB/MTAB/andOTAB	No	Refluxing condition	Yes	6.2–18.5 nm	Catalysis	63
Pd	Pd(NO ₃) ₂	Photoexcited Keggin ions	Water	Keggin ions	Yes	RT	Yes	4 ± 2 nm	Catalysis	64
Pd	Pd(NO ₃) ₂	Sonochemical reduction	Water	PVP	No	Not specified	Yes	3–6 nm	Catalysis	65
Ag	Silver bis(2-ethylhexyl) sulpho-succinate, Ag(AOT)	Hydrazine	Water/AOT	Dodecane thiol	No	RT	Yes	3.4 nm	Catalysis, optical and electronics	66
Ag	AgNO ₃	Trisodium citrate	Water	Trisodium citrate	No	Boiling condition	No	40–60 nm	Electronics	67
Ag	AgNO ₃	NaBH ₄	Biphase (toluene/water)	1-dodecane thiol	Yes	RT	Yes	5–8 nm	Catalysis, optical and electronics	68
Ag	AgNO ₃	Ultrasound	Water	NTA	No	20°C	Yes	20 nm	Catalysis, optical and electronics	69
Ag	AgNO ₃	Amine (APS, AES)	ethanol	Amine.	No	60°C	Yes	1–2 nm	Catalysis	70
Ag (Nano-wires)	AgNO ₃	NaBH ₄ /Ascorbic acid	Water	cetyltrimethyl ammonium bromide (CTAB)	No	RT	Yes	42 ± 3 nm	Catalysis, optical and electronics	71

(Contd...)

Metal Particle Prepared	Starting Material	Reducing Agent	Medium	Stabiliser	Phase Transfer (Yes/No)	Condition	Re-dispersible	Mean Particle Dia. (nm)	Typical Application	Reference Number
In	[In(eta(5)-C ₅ H ₅)]	72
In	[In(eta(5)-C ₅ H ₅)]	...	Toluene	15±2 nm	...	73
In	Bulk Indium	Ultrasound irradiation	paraffin oil	Nil	No	473 K	Not specified	50–2000 nm	Photonic devices	74
In	Anhydrous indium trichloride	Sodium metal	DMF or TOP	TOP	No	120–150°C	Yes	15–50 nm	bio-nano-technology, nano-xerography	75
Sn	SnCl ₂ ·2H ₂ O	Mg	Water		No	RT	No	Not specified	rechargeable batteries, gas sensors	76
Sn	SnCl ₄ /Mg ₂ Sn	Metathesis reaction	Ethylene glycol dimethyl ether (glyme)	n-butyl group	No	Refluxing conditions	No	6.5±1.7 nm	rechargeable batteries, gas sensors.	77
Sn	Bulk Tin.	Dispersion method	paraffin oil	Oxide formed on the surface	No	240°C	Not specified	30–40 nm,	gas sensors	78
Sn	SnCl ₄	KBH ₄	Water	Cellulose fibres	No	RT	Yes	20–30 nm	Lithium-ion batteries	79
Sn	SnCl ₄	NaBH ₄	1,2-Dimethoxyethane/deoxygenated water (Argon atmosphere)	hydrobenzamide, No citrate, and polyvinyl pyrrolidone (PVP)	No	RT	No	~50 nm/ ~100–300 nm	Batteries	80
Sb	Bulk metal	Thermal evaporation	Ultra high vacuum	HOPG surface	No	830 K	Not specified	120 nm	flame retardants	81
Sb (nano-wire)	SbCl ₃	NaBH ₄	DMF	PVP	No	RT	Not specified	~20 nm	Catalysis	82
Te	orthotelluric acid (H ₆ TeO ₆) or tellurium dioxide (TeO ₂)	hydrazine	water, EG, and water-EG	Nil	No	20–200°C.	No	50–100 nm	Opto-electronic devices	83
Te (Rods)	(NH ₄) ₂ TeS ₄	Na ₂ SO ₃	Water	NaDDBS	No	RT	No	14 nm	Opto-electronic devices	84
Te (Rods)	(NH ₄) ₂ TeS ₄	sodium sulphite Na ₂ SO ₃	Water	SDBS/SDS/PVP	No	RT	No	10–40 nm	Opto-electronic devices	85

(Contd...)

Metal Particle Prepared	Starting Material	Reducing Agent	Medium	Stabiliser	Phase Transfer (Yes/No)	Condition	Re-dispersible	Mean Particle Dia. (nm)	Typical Application	Reference Number
Te (nanotubes)	sodium tellurate ($\text{Na}_2\text{TeO}_4 \cdot 2\text{H}_2\text{O}$)	formamide (HCONH_2)	200–600 nm	Photo-conducting devices	86
Sm	$\text{Sm}(\text{NO}_3)_3 \cdot 5\text{H}_2\text{O}$	Bioreduction alfalfa (Medicago sativa)	Water	Nil	No	25°C	Not specified	10 nm	Drug delivery, medicines	87
Eu	$\text{EuCl}_3 \cdot 6\text{H}_2\text{O}$...	Water-in-oil	(3-aminopropyl) triethoxysilane	No	RT	No	36 ± 4 nm	Biological detection and biotechnology	88
Gd	GdCl_3	Alkalide reduction	THF	Nil	No	RT	Yes	12 nm	Drug-delivery	89
Gd	Gadolinium hexanedione (GdH)	Polyoxyl 20-stearyl ether	Oil in water micro emulsions	Emulsifying wax	No	55°C,	No	85±9 nm	Drug-delivery (cancer therapy)	90
Tb	Bulk metal	Sputtering	Cr or W matrix	Cr or W matrix	No	Not specified	Not specified	8 nm	Biological detections	91
Tb	Tb^{3+} chelate	$\text{NH}_3/\text{H}_2\text{O}/$ Trixon-X-100,	Oil in water micro emulsions	Water-in-oil micro emulsion	No	RT	No	45 ± 3 nm	Biological detections	92
Dy	Bulk metal	Vapour deposition/sputtering	Gas	Nil	No	Not mentioned	No	4–12 nm	Magnetic applications	93
Dy	DyCl_3	Alkalide reduction	THF	Crown ether (15-crown-5)	No	Not mentioned	No	8–16 nm	Magnetic applications	94
Yb	Yb salt	Bioreduction	Water	Nil	No	RT	No	2–10 nm	Fiber amplifier and fiber optic technologies	95
Ta	Bulk tantalum	Hydrogen arc plasma method		Nil	No	10,000 °C	No	Less than 10 nm	Super-conductor, as a dopant in photo-electrode materials	96
W	WO_3 powder	Electron beam irradiation	Nil	Nil	No	RT	No	2–6 nm	Semi-conductor devices	97
W	tungsten hexacarbonyl	Thermal decomposition						15–60 nm	Semi-conductor devices	98

(Contd...)

Metal Particle Pre-prepared	Starting Material	Reducing Agent	Medium	Stabiliser	Phase Transfer (Yes/No)	Condition	Re-dispersible	Mean Particle Dia. (nm)	Typical Application	Reference Number
Re	Re-2(CO) (10)	Thermal decomposition	6–12.8 nm	...	99
Ir	hexa-chloroiridic acid (ABCR)	Ethylene glycol	Ethylene glycol	Nil	No	100°C	Yes	3 nm	catalysts, electro-catalysts, chemical synthesis	100
Pt	RT	101
Pt	Pt(dba) ₂	CO	toluene	CO/Phosphine ligands/ solvent	No	RT	Yes	1–2 nm	Catalysis	102
Pt	H ₂ PtCl ₆ . 6H ₂ O	ethanol reduction	ethanol/water	PNIPAAm/PVP	No	Refluxing conditions	Yes	0.5–4.5 nm	Catalysis	103
Pt	H ₂ PtCl ₆ . 6H ₂ O/ K ₂ PtCl ₄	lithium triethylborohydride	THF	Octadecane thiol	No	RT/35°C	Yes	~3 nm,	Hydrogen storage and electronics	104
Pt	H ₂ PtCl ₆ . 6H ₂ O	H ₂	Acetone	Nanostructured carbon	No	300°C	Yes	~3 nm,	Fuel cell systems	105
Pt	disodium hexahydroxyplatinate (Na ₂ Pt(OH) ₆)	NaBH ₄	Water	Thiol-functionalised ionic liquids (TFILs)	No	RT	Yes	2–4.2 nm	Electronics and catalysis	106
Au	HAuCl ₄	Na3Cit	Water	Cit3-	No	RT	No	12–60 nm	Sols	107, 108, 109
Au	HAuCl ₄	Ascorbic acid	Water	?	No	RT	No	12 nm	Biology	110
Au ₁₁	Au-Aryl-phosphine complexes	NaBH ₄	Water	Aryl phosphine	No	Inert	yes	0.82 nm	Biology, TEM labeling	111
Au	HAuCl ₄	Ethyl alcohol	Water	?	No	Ultrasonication	No	10 nm	Biology	112
Au	HAuCl ₄	P (white) in ether	Water	?	No	Boiling	No	3–5 nm	Biology	113, 114
Au	HAuCl ₄	NaSCN	Water	SCN-	No	RT	No	2.6 nm	Biology	115
Au	HAuCl ₄	Na3Cit/tannic acid	water	Cit3-, tannic acid	No	Heating	No	3–17 nm	Biology	116, 117
Au	HAuCl ₄	NaBH ₄	Water	Cit3-	No	4°C	No	4 nm	Sols	118
Au	HAuCl ₄	NaBH ₄	Biphase (toluene/water)	Thiol	Yes	RT	Yes	3 nm	Powder, Solution, chemistry	119

(Contd...)

Metal Particle Pre-prepared	Starting Material	Reducing Agent	Medium	Stabiliser	Phase Transfer (Yes/No)	Condition	Re-dispersible	Mean Particle Dia. (nm)	Typical Application	Reference Number
Au	HAuCl ₄	Na ₃ Cit/ NaBH ₄	Water	Cit ³⁻	No	0°C	No	4 nm	Sols	120
Au ₅₅	HAuCl ₄	(Ph ₃ P)AuCl	Benzene	B ₂ H ₆	Yes	Not specified	Yes	1.4 nm	catalysis, sensors, and molecular electronics	121
Hg	Hg(ClO ₄) ₂	γ-irradiation	water	γ-radiolytic reduction	No	γ-irradiation	Not mentioned	~100 nm	Optical devices	122
Pb	...	melt-spinning and ball-milling techniques	5–30 nm	Biological and chemical sensors	123
Pb	[Pb{N(SiMe ₃) ₂ } ₂]	[H ₂ Al(OtBu)] ₂	THF/ acetonitrile	Not specified	No	–100°C	Yes	10–200 nms	Biological and chemical sensors	124
Bi	Bismuth (III) citrate	NaBH ₄	poly (oxyethylene) ₉ , nonyl phenol ether, poly (oxyethylene) ₅ , nonyl phenol ether/ water emulsion	PVP	No	RT	Yes	18–105 nm	electronics	125
Bi	Bismuth 2-ethyl-hexanoate	LiBEt ₃ H	dioctyl ether	TOP/oleic acid	No	175 °C	Yes	15 ± 2 nm.	thermo-electronics	126
Bi	Bulk metal	High energy electron beam	Ar and He gas	Nil	No	High temperature	No	4.5–10 nm	thermo-electronics	127
Bi	Bulk Bismuth	Solution dispersion method	paraffin oil	Nil	No	280°C	Yes	40–50 nm	“green” lubricant materials and electronics	128

Section II: Oxide Nanoparticles

I. Aqueous media

Nanomaterial	Starting Material	Precipitating	Stabilising Agent	Conditions	Size (nm)	Reference
VO ₂ (B)	NH ₄ VO ₃	N ₂ H ₄ /H ₂ O	none	calcined 300 °C	35	129
Cr ₂ O ₃	K ₂ Cr ₂ O ₇	N ₂ H ₄ /H ₂ O	none	calcined 500 °C	30	129
γ-Mn ₂ O ₃	KMnO ₄	N ₂ H ₄ /H ₂ O	none		8	129
Ni _{0.5} Zn _{0.5} Fe ₂ O ₄	Ni, Zn, Fe nitrates	NaOH		Anneal 300°C	9–90	130
MgFe ₂ O ₄	Nitrates	NaOH				131
Sm _{1-x} Sr _x FeO _{3-δ}						132
Ce _{1.8} Y _{0.2} O _{1.9}	Nitrates	Oxalic acid		Anneal 500, 1000°C	10–100	133
CeO ₂	Nitrate	(NH ₄) ₂ CO ₃		Anneal 300°C	6	134
NiO	Ni ²⁺ salts	(NH ₄) ₂ CO ₃		Anneal 400°C	10–15	135
Bi ₄ Ti ₃ O ₁₂	Basic TiO ₂ , Bi(NO ₃) ₃	H ⁺		500–800°C	16–48	136
TiO ₂	TiCl ₃	NH ₄ OH	PMMA	RT	50–60	137
Fe ₃ O ₄	Fe ²⁺ , Fe ³⁺	NaOH		70°C		138
MnFe ₂ O ₄	Mn ²⁺ , Fe ²⁺	NaOH		<100°C	5–25	139
Pr doped CeO ₂	Ce(NO ₃) ₃ , PrCl ₃		HMT	100°C	13	140
CoFe ₂ O ₄	Fe ³⁺ , Co ²⁺	NaOH		<100°C	14–18	141
CoFe ₂ O ₄			H ⁺			142
Fe ₃ O ₄						143, 144
MnFe ₂ O ₄	MnCl ₂	NaOH	none	100 °C	5–25	145
FeCl ₃						
Fe ₃ O ₄	FeCl ₃	NH ₄ OH	H+	N ₂ atm	8–50	146
FeCl ₃						
NiO	NiCl ₂	NH ₄ OH	CTAB	annealed 500 °C	22–28	147
ZnO	ZnCl ₂	NH ₄ OH	CTAB	annealed 500 °C	40–60	147
SnO ₂	SnCl ₄	NH ₄ OH	CTAB	annealed 500 °C	11–18	147
Sb ₂ O ₃	SbCl ₃	NaOH	PVA	annealed 350 °C	10–80	148

II. Non-Aqueous media

Nanomaterial	Starting Material	Medium	Precipitating Agent	Stabilising Agent	Conditions	Size (nm)	Reference
LiCoO ₂	LiNO ₃ , Co(NO ₃) ₂	Ethanol	KOH		400–700°C anneal	12–41	149
RuO ₂	RuNO(NO ₃) ₂	Ethanol	TMAH	–	90°C for precipitation 500°C anneal		150
γ-Fe ₂ O ₃	Fe(NO ₃) ₃	Steric acid	Steric acid	–	125°C ppt, 200°C Cal	5–20	151, 152
BaTiO ₃	BaTi(O ₂ C(CH ₃) ₆ CH ₃)[OCH(CH ₃) ₂] ₅	DPE	H ₂ O ₂	Oelic acid	100°C	6–12	153
MFe ₂ O ₄ M=Mn, Fe, Co, Ni, Zn	Chlorides	DEG	-	DEG	Heat	3–7	154
Fe ₃ O ₄	Fe(acac)	diethyl ether	ethanol	various	HDD, OA, OAc	4	155
γ-Fe ₂ O ₃ MnO Cu	FeCup ₃ MnCup ₂ CuCup	OA	TOA	OA	300°C	4–10	156

Section III: Nanoparticles using Microemulsion-based Methods

Metals

Metal	Starting Material	Surfactant	Reductant	Reaction Conditions	Product Size (nm)	Reference
Co	CoCl ₂	AOT	NaBH ₄		<1	157
Ni	NiCl ₂	CTAB	N ₂ H ₄ ·H ₂ O	pH ~13	4	16
Cu	Cu(AOT) ₂	AOT	N ₂ H ₄		2–10	158, 159
	Cu(AOT) ₂	AOT	NaBH ₄		20–28	158, 159
Se	H ₂ SeO ₃	AOT	N ₂ H ₄ ·HCl		4–300	45
Rh	RhCl ₃	PEGDE	H ₂		3	160
Pd	PdCl ₂	PEGDE	N ₂ H ₄ ·H ₂ O	pH~7	4	160
Ag	AgNO ₃	PEGDE	NaBH ₄		3–9	161
Ir	IrCl ₃	PEGDE	H ₂	70 °C	3	160
Pt	H ₂ PtCl ₆	PEGDE	N ₂ H ₄ ·H ₂ O		3	160
Bi	BiOClO ₄	AOT	NaBH ₄	Ar atm	2–10	161
FePt	Fe ²⁺ , Pt ²⁺		NaBH ₄			162, 163
Fe ₂ Pt						
FePt ₃						

Oxides

Oxide	Starting Material	Surfactant	Precipitating Agent	Reaction Conditions	Size (nm)	Reference
LiNi _{0.8} Co _{0.2} O ₂	LiNO ₃	NP-10	kerosene	calcined 400–800 °C	19–100	164
	Ni(NO ₃) ₂					
	Co(NO ₃) ₂					
Al ₂ O ₃	AlCl ₃	Triton X-114	NH ₄ OH	calcined 600–900 °C	50–60	165
TiO ₂	Ti(OiPr) ₄	AOT	H ₂ O		20–200	166
Mn _{1-x} Zn _x Fe ₂ O ₄	Mn(NO ₃) ₂	AOT	NH ₄ OH	calcined 300–600 °C	5–37	167
	Zn(NO ₃) ₂					
	Fe(NO ₃) ₃					
Fe ₃ O ₄	FeCl ₂	AOT	NH ₄ OH		~2	168
	FeCl ₃					
Fe ₃ O ₄	FeSO ₄	AOT	NH ₄ OH		10	169

(Contd...)

Oxide	Starting Material	Surfactant	Precipitating Agent	Reaction Conditions	Size (nm)	Reference
CoCrFeO ₄	CoCl ₂ CrCl ₃ Fe(NO ₃) ₃	SDS	CH ₃ NH ₂	calcined 600 °C	6–16	170
CoFe ₂ O ₄	CoCl ₂ FeCl ₃	SDS	CH ₃ NH ₂	dried 100 °C	6–9	171
Ni _{1-x} Zn _x Fe ₂ O ₄	Ni(NO ₃) ₂ Zn(NO ₃) ₂ Fe(NO ₃) ₃	AOT	NH ₄ OH	calcined 300–600 °C	5–30	172
CuM ₂ O ₅ (M = Ho, Er)	Cu(NO ₃) ₂ Ho(NO ₃) ₃ Er(NO ₃) ₃	CTAB	(NH ₄) ₂ CO ₃	calcined 900 °C	25–30	173
Y ₃ Fe ₅ O ₁₂	Y(NO ₃) ₃	Igepal	NH ₄ OH +	calcined 600–1000 °C	3	174
Fe(NO ₃) ₃	CA-520	(NH ₄) ₂ CO ₃				
YBa ₂ Cu ₃ O _{7-δ} BaCO ₃	Y(OAc) ₃ CA-430 Cu(OAc) ₂	Igepal	oxalic acid		3–12 430	175
SnO ₂	SnCl ₄	AOT	NH ₄ OH	calcined 600 °C	30–70	176
BaFe ₁₂ O ₁₉	Ba(NO ₃) ₂ Fe(NO ₃) ₃	CTAB	(NH ₄) ₂ CO ₃	calcined 950 °C	5–25	177, 178
CeO ₂	Ce(NO ₃) ₃	CTAB	NH ₄ OH	calcined 500–700 °C	6–10	179
Chalcogenides						
PbS, PbSe	Pb(NO ₃) ₂		Na ₂ S		2–4	180
ZnS (Mn doped)	ZnCl ₂ , MnCl ₂		Na ₂ S		~5	181

Section IV: Anisotropic Nanoparticles

1D Nanoparticle-Rods

Material	Starting Material	Seed	Reducing Agent	Stabiliser	Medium/ Condition	Redis-persibility	Particle Dimensions	Typical Applications	Reference
Au	HAuCl ₄	Au 4 nm	NaBH ₄ / Ascorbic Acid	CTAB	Aqueous RT	Yes	d: 15 l: variable	Nano Laser optics, therapeutics, and sensor devices	182
Au	Au		Au-Anode and Pt- Cathode	CTAB	Aqueous 42°C	Yes	d: 10 l: variable	biological labels and sensor devices	183, 184
Au	HAuCl ₄		NaBH ₄ / Na ₃ Citrate	CTAB	Aqueous Laser irradiation	Yes	d: 15 l: variable		185
Ag	AgNO ₃	Ag 4 nm	NaBH ₄ / Ascorbic Acid	CTAB	Aqueous RT	Yes	d: 30 l: variable	SERS	71, 186
CdS	CdCl ₂ , Na ₂ S			CTAB	Aqueous 40°C	Yes	d: 10 l: variable	Semi- conductor	187
CdS	Cd, S		Ethylene Diamine	Ethylene Diamine	Organic 120– 190°C	Yes	d: 10 l: variable	Light emitting devices	188
CdSe	CdCl ₂ , Na ₂ Se			CTAB	Aqueous 40°C	No	d: 10 l: variable	Semi- conductor, Light emit- ting device	187
CdSe	CdCl ₂ , Se, Na		Ethylene Diamine	Ethylene Diamine	Organic 80–100°C	No	d: 20 l: variable	Semi- conductor	189
CdSe	Cd(CH ₃) ₂ , Se		Hexylphos- phonic acid	TOPO	Organic 290°C	No	d: 5 l: variable	Light emitting diode, Photovoltaic devices	190
ZnO	ZnAc ₂		Hydrazine Monohydrate	DBS	Organic Heated up to boiling point of xylene	Not mentioned	d: 150 l: 2170	potential applications (solar cells), nanolasers	191
ZnO	ZnAc ₂		Hydrazine Hydrate	SDS	Organic 90°C	Not mentioned	d: 80 l: variable	Semi- conductor	192
ZnO	Zn(NO ₃) ₂		NaOH	Ethylene Diamine	Aqueous 180°C	Not mentioned	d: 45 l: 1540	Photonic and Electronic material	193

3D Nanoparticle-Triangles

Material	Starting Material	Seed	Reducing Agent	Stabiliser	Medium/ Condition	Redis-persibility	Particle Dimensions	Typical Applications	Reference
Au	HAuCl ₄	Au 4–6 nm	NaBH ₄ / Ascorbic Acid	CTAB	Aqueous RT	No	35	Sensors	194
Au	Au		Lemon grass extract		Aqueous RT	No	440 thickness: 8–14	Therapeutics	195
Ag	AgNO ₃	Ag 2–15 nm	NaBH ₄ / Na ₃ Citrate	Na ₃ Citrate	Aqueous Laser irradiation	No	40–110	SERS	196

Other anisotropic shapes:

Material	Starting Material	Seed	Reducing Agent	Stabiliser	Medium/ Condition	Redis-persibility	Particle Dimensions	Typical Applications	Reference
Au (Prisms)	HAuCl ₄	Au 4–6 nm	NaBH ₄ / Ascorbic Acid	CTAB	Aqueous RT	Not mentioned	144	Atomic probes, SERS	197
Ag (Prisms)	AgNO ₃	Ag 8 nm	NaBH ₄ / Na ₃ Citrate	BSPP	Aqueous Laser Irradiation	Not mentioned	variable edge length	SERS	198
Au (Plates)	HAuCl ₄		Na ₃ Citrate	PVP	Aqueous Heat	Not mentioned	width: 310 thickness: 28	SERS	199
Ag (Plates)	AgNO ₃	Ag 15 nm	NaBH ₄ / Na ₃ Citrate	CTAB	Aqueous RT	Not mentioned	width: 200 thickness: 20	SERS	200
Pd (Triangular and Hexagonal plates)	Na ₂ PdCl ₄		Ethylene Glycol	PVP	Organic 85°C	Not mentioned	edge length: 28 thickness: 5	Colorimetric sensing	201
PbSe (Cubes)	Pb-(Ac) ₂ , 3H ₂ O, (TOP)-Se		Oleic Acid	TOP	Organic 230°C	No	Smallest cube: 3–5 and variable	Semi- conductor	202
Au (Star Shape)	HAuCl ₄	Au 4–6 nm	NaBH ₄ / Ascorbic Acid	CTAB	Aqueous RT	No	edge length: 66	SERS	194

(Contd...)

Material	Starting Material	Seed	Reducing Agent	Stabiliser	Medium/ Condition	Redis- persibility	Particle Dimensions	Typical Applications	Reference
Au (Star Shape)	HAuCl ₄		Ascorbic Acid	PVP	Aqueous RT	No	edge length: 83 thickness: 25	SERS	203
Au (bipod, tripod, tetrapod)	HAuCl ₄		Ascorbic Acid	CYAB	Aqueous RT	No	Variable	Inter-connectors in nanodevices	204
Co (Nano-cubes)	Co ₂ (CO) ₈		O, O'- (bis2-amino-propyl)- polypropy- leneglycol	Hexane	Organic 187°C	Not mentioned	edge length: 50–60	Magnetic nano-particles	205

Notes:

(TOP)-Se: Trioctylphosphine selenide

acac: acetylacetonate

BSPP: Bis(p-sulphonatophenyl) phenylphosphine dihydrate dipotassium salt solution

Cit: citrate

CTAB: Cetyl trimethyl ammonium bromide

CTAC: Cetyl trimethyl ammonium chloride

Cup: Cupferron, C₆H₃N(NO)O-

DBS: Dodecyl Benzene Sulphonic Acid

Glyme: Ethylene glycol dimethyl ether

GSH: Glutathione

HAD: Hexadecylamine

HDD: 1,2-hexadecanediol

HMT: Hexamethylenetetramine

NaDDBS: Sodium dodecyl benzenesulfonate

NTA: Nitrotriacetate

OA: Oleylamine

OAc: Oleic acid

PNIPAAm: Poly(N-isopropylacrylamide)

PMMA: Polymethylmethacrylate

PVP: Poly vinyl pyrrolidone

RT: Room temperature

SDBS: sodium dodecyl benzenesulfonate

SDS: sodium dodecyl sulfonate

THF: Tetrahydrofuran

TMAH: Tetramethyl ammonium hydroxide

TMPD: Tetramethyl p-phenylenediamine

TOA: Trioctylamine

TOAB: Tetractyl ammonium bromide

TOABr: Tetra n-octylammonium bromide

TOP: Trioctyl phosphine

TOPO: Tri-n-octylphosphine oxide (C₈H₁₇)₃PO

REFERENCES

1. A.B. Murphy, 'Formation of titanium nanoparticles from a titanium tetrachloride plasma', *J. Phys. D. Appl. Phys.*, 37, (2004), 2841–47.
2. W.Y. Hu, S.G. Xiao, J.Y. Yang and Z. Zhang, 'Melting evolution and diffusion behaviour of vanadium nanoparticles', *Eur. Phys. J.B.*, 45, (2005), 547–54.
3. S.U. Son, Y.J. Jang, K.Y. Yoon, C.H. An, Y. Hwang, J.G. Park, H.J. Noh, J.Y. Kim, J.H. Park and T. Hyeon, 'Synthesis of monodisperse chromium nanoparticles from the thermolysis of a Fischer carbene complex', *Chem. Commun.*, (2005), 86–88.
4. P.Z. Si, E. Bruck, Z.D. Zhang, O. Tegus, W.S. Zhang, K.H.J. Buschow and J.C.P. Klaasse, 'Structural and magnetic properties of Mn nanoparticles prepared by arc-discharge', *Mater. Res. Bull.*, 40, (2005), 29–37.
5. G.R. Ortega, P.S. Retchkiman, C. Zorrilla, H.B. Liu, G. Canizal, P.A. Perez and J.A. Ascencio, 'Synthesis and characterisation of Mn quantum dots by bioreduction with water hyacinth', *J. Nanosci. Nanotechnol.*, 6, (2006), 151–56.
6. E. Bermejo, T. Becue, C. Lacour and M. Quarton, 'Synthesis of nanoscaled iron particles from freeze-dried precursors', *Powder Technol.*, 94, (1997), 29–34.
7. L. Guo, Q. J. Huang, X. Y. Li and S. H. Yang, 'Iron nanoparticles: Synthesis and applications in surface enhanced Raman scattering and electrocatalysis', *Phys. Chem. Chem. Phys.*, 3, (2001), 1661–65.
8. T. Hyeon, S.S. Lee, J. Park, Y. Chung, and H.B. Na, 'Synthesis of Highly Crystalline and Monodisperse Maghemite Nanocrystallites without a Size-Selection Process', *J. Am. Chem. Soc.*, 123, (2001), 12798–801.
9. J. Osuna, D. DeCaro, C. Amiens, B. Chaudret, E. Snoeck, M. Respaud, J.M. Broto and A. Fert, 'Synthesis, characterisation, and magnetic properties of cobalt nanoparticles from an organometallic precursor', *J. Phys. Chem.*, 100, (1996), 14571–74.
10. C. Petit, A. Taleb and M.P. Pileni, 'Cobalt Nanosized Particles Organised in a 2D Superlattice: Synthesis, Characterisation, and Magnetic Properties', *J. Phys. Chem. B.*, 103, (1999), 1805–10.
11. H. Bonnemann, W. Brijoux, R. Brinkmann, N. Matoussevitch, N. Waldofner, N. Palina and H. Modrow, 'A size-selective synthesis of air stable colloidal magnetic cobalt nanoparticles', *Inorg. Chim. Acta.*, 350, (2003), 617–24.
12. H.D. Jang, D.W. Hwang, D.P. Kim, H.C. Kim, B.Y. Lee and I.B. Jeong, 'Preparation of cobalt nanoparticles by hydrogen reduction of cobalt chloride in the gas phase', *Mater. Res. Bull.*, 39, (2004), 63–70.
13. L.G. Jacobsohn, M.E. Hawley, D.W. Cooke, M.F. Hundley, J.D. Thompson, R.K. Schulze and M. Nastasi, 'Synthesis of cobalt nanoparticles by ion implantation and effects of postimplantation annealing', *J. Appl. Phys.*, 96, (2004), 4444–50.
14. Y.J. Song, H. Modrow, L.L. Henry, C.K. Saw, E.E. Doomes, V. Palshin, J. Hormes and C.S.S.R. Kumar, 'Microfluidic synthesis of cobalt nanoparticles', *Chem. Mater.*, 18, (2006), 2817–27.
15. T.O. Ely, C. Amiens, B. Chaudret, E. Snoeck, M. Verelst, M. Respaud and J.M. Broto, 'Synthesis of nickel nanoparticles. Influence of aggregation induced by modification of poly(vinylpyrrolidone) chain length on their magnetic properties', *Chem. Mater.*, 11, (1999), 526–29.
16. D.H. Chen and S.H. Wu, 'Synthesis of nickel nanoparticles in water-in-oil microemulsions', *Chem. Mater.*, 12, (2000), 1354–60.

17. M.P. Zach and R.M. Penner, 'Nanocrystalline nickel nanoparticles', *Adv. Mater.*, 12, (2000), 878–83.
18. N. Cordente, M. Respaud, F. Senocq, M.J. Casanove, C. Amiens and B. Chaudret, 'Synthesis and magnetic properties of nickel nanorods', *Nano Lett.*, 1, (2001), 565–68.
19. D.H. Chen and C.H. Hsieh, 'Synthesis of nickel nanoparticles in aqueous cationic surfactant solutions', *J. Mater. Chem.*, 12, (2002), 2412–15.
20. S.H. Wu and D.H. Chen, 'Synthesis and characterisation of nickel nanoparticles by hydrazine reduction in ethylene glycol', *J. Colloid Interface Sci.*, 259, (2003), 282–86.
21. Y.J. Suh, H.D. Jang, H.K. Chang, D.W. Hwang and H.C. Kim, 'Kinetics of gas phase reduction of nickel chloride in preparation for nickel nanoparticles', *Mater. Res. Bull.*, 40, (2005), 2100–09.
22. J.P. Cheng, X.B. Zhang and Y. Ye, 'Synthesis of nickel nanoparticles and carbon encapsulated nickel nanoparticles supported on carbon nanotubes', *J. Solid State Chem.*, 176, (2006), 91–95.
23. M.P. Pileni and I. Lisiecki, 'Nanometer metallic copper particles synthesis in reverse micelles', *Colloids Surfaces A: Physicochem. Eng. Aspects*, 80, (1993), 63–68.
24. H.H. Huang, F.Q. Yan, Y.M. Kek, C.H. Chew, G.Q. Xu, W. Ji, P.S. Oh, and S.H. Tang, 'Synthesis, characterisation, and nonlinear optical properties of copper nanoparticles', *Langmuir*, 13, (1997), 172–75.
25. L.M. Qi, J.M. Ma and J.L. Shen, 'Synthesis of copper nanoparticles in nonionic water-in-oil microemulsions', *J. Colloid Interface Sci.*, 186, (1997), 498–500.
26. N.A. Dhas, C.P. Raj and A. Gedanken, 'Synthesis, characterisation, and properties of metallic copper nanoparticles', *Chem. Mater.*, 10, (1998), 1446–52.
27. P. Chen, X. Wu, J. Lin and K.L. Tan, 'Synthesis of Cu nanoparticles and microsized fibers by using carbon nanotubes as a template', *J. Phys. Chem. B.*, 103, (1999), 4559–61.
28. H. Ohde, F. Hunt and C.M. Wai, 'Synthesis of silver and copper nanoparticles in a water-in-supercritical-carbon dioxide microemulsion', *Chem. Mater.*, 13, (2001), 4130–35.
29. A.A. Athawale, P.P. Katre, M. Kumar and M.B. Majumdar, 'Synthesis of CTAB-IPA reduced copper nanoparticles', *Mater. Chem. Phys.*, 91, (2005), 507–12.
30. H.T. Zhu, C.Y. Zhang and Y.S. Yin, 'Novel synthesis of copper nanoparticles: influence of the synthesis conditions on the particle size', *Nanotechnology*, 16, (2005), 3079–83.
31. Hai-tao Zhu, Yu-sheng Lin, Yan-sheng Yin, 'A novel one-step chemical method for preparation of copper nanofluids', *Journal of Colloid and Interface Science*, 277, (2004), 100–03.
32. F. Rataboul, C. Nayral, M.J. Casanove, A. Maisonnat and B. Chaudret, 'Synthesis and characterisation of monodisperse zinc and zinc oxide nanoparticles from the organometallic precursor $[\text{Zn}(\text{C}_6\text{H}_{11})_2]$ ', *J. Organometallic Chem.*, 643, (2002), 307–12.
33. P. Tognini, A. Stella, P. Cheyssac and R. Kofman, 'Surface plasma resonance in solid and liquid Ga nanoparticles', *J. Non-Cryst. Solids*, 249, (1999), 117–22.
34. M. Nisoli, S. Stagira, S. DeSilvestri, A. Stella, P. Tognini, P. Cheyssac and R. Kofman, 'Ultrafast electronic dynamics in solid and liquid gallium nanoparticles', *Phys. Rev. Lett.*, 78, (1997), 3575–78.
35. K.F. MacDonald, V.A. Fedotov and N.I. Zheludev, 'Optical nonlinearity resulting from a light-induced structural transition in gallium nanoparticles', *Appl. Phys. Lett.*, 82, (2003), 1087–89.

36. L. Li and J.L. Shi, 'In situ reduction and nitrification method for the synthesis of Ga and GaN quantum dots in the channels of mesoporous silicon materials', *Nanotechnology*, 17, (2006), 344–48.
37. J.R. Heath and F.K. LeGoues, 'A liquid solution synthesis of single crystal germanium quantum wires', *Chem. Phys. Lett.*, 208, (1993), 263–68.
38. J.R. Heath, J.J. Shiang and A.P. Alivisatos, 'Germanium quantum dots: Optical properties and synthesis', *J. Chem. Phys.*, 101, (1994), 1607–15.
39. J.P. Carpenter, C.M. Lukehart, D.O. Henderson, R. Mu, B.D. Jones, R. Glosser, S.R. Stock, J.E. Wittig, and J.G. Zhu, 'Formation of Crystalline Germanium Nanoclusters in a Silica Xerogel Matrix from an Organogermanium Precursor', *Chem. Mater.*, 8, (1996), 1268–74.
40. H. Miguez, V. Fornes, F. Meseguer, F. Marquez and C. Lopez, 'Low-temperature synthesis of Ge nanocrystals in zeolite Y', *Appl. Phys. Lett.*, 69, (1996), 2347–49.
41. B.R. Taylor, S.M. Kauzlarich, G.R. Delgado and H.W.H. Lee, 'Solution synthesis and characterisation of quantum confined Ge nanoparticles', *Chem. Mater.*, 11, (1999), 2493–2500.
42. E. Fok, M.L. Shih, A. Meldrum and J.G.C. Veinot, 'Preparation of alkyl-surface functionalised germanium quantum dots via thermally initiated hydrogermylation', *Chem. Commun.*, (2004), 386–87.
43. W.Z. Wang, J.Y. Huang and Z.F. Ren, 'Synthesis of germanium nanocubes by a low-temperature inverse micelle solvothermal technique', *Langmuir*, 21, (2005), 751–54.
44. H. Gerung, S.D. Bunge, T.J. Boyle, C.J. Brinker and S.M. Han, 'Anhydrous solution synthesis of germanium nanocrystals from the germanium(II) precursor $\text{Ge}[\text{N}(\text{SiMe}_3)_2]_2$ ', *Chem. Commun.*, (2005), 1914–16.
45. H.W. Chiu and S.M. Kauzlarich, 'Investigation of reaction conditions for optimal germanium nanoparticle production by a simple reduction route', *Chem. Mater.*, 18, (2006), 1023–28.
46. J.A. Johnson, M.L. Saboungi, P. Thiyagarajan, R. Csencsits and D. Meisel, 'Selenium nanoparticles: A small-angle neutron scattering study', *J. Phys. Chem. B.*, 103, (1999), 59–63.
47. X.Y. Gao, T. Gao and L.D. Zhang, 'Solution-solid growth of alpha-monoclinic selenium nanowires at room temperature', *J. Mater. Chem.*, 13, (2003), 6–8.
48. G. Bour, A. Reinholdt, A. Stepanov, C. Keutgen and U. Kreibig, 'Optical and electrical properties of hydrogenated yttrium nanoparticles', *Eur. Phys. J. D.*, 16, (2001), 219–23.
49. Y. Li, J. Liu, Y.Q. Wang and Z.L. Wang, 'Preparation of monodispersed Fe-Mo nanoparticles as the catalyst for CVD synthesis of carbon nanotubes', *Chem. Mater.*, 13, (2001), 1008–14.
50. Y. Motoyama, M. Takasaki, K. Higashi, S.H. Yoon, I. Mochida and H. Nagashima, 'Highly-dispersed and size-controlled ruthenium nanoparticles on carbon nanofibers: Preparation, characterisation, and catalysis', *Chem. Lett.*, 35, (2006), 876–77.
51. C. Pan, K. Pelzer, K. Philippot, B. Chaudret, F. Dassenoy, P. Lecante and M.J. Casanove, 'Ligand-Stabilized Ruthenium Nanoparticles: Synthesis, Organisation, and Dynamics', *J. Am. Chem. Soc.*, 123, (2001), 7584–93.
52. A. Miyazaki, I. Balint, K. Aika and Y. Nakano, 'Preparation of Ru Nanoparticles Supported on $\gamma\text{-Al}_2\text{O}_3$ and Its Novel Catalytic Activity for Ammonia Synthesis', *J. Catal.*, 204, (2001), 364–71.
53. J.Y. Lee, J. Yang, T.C. Deivaraj and H.P. Too, 'A novel synthesis route for ethylenediamine-protected ruthenium nanoparticles', *J. Colloid Interface Sci.*, 268, (2003), 77–80.

54. S. Jansat, D. Picurelli, K. Pelzer, K. Philippot, M. Gomez, G. Muller, P. Lecante and B. Chaudret, 'Synthesis, characterisation and catalytic reactivity of ruthenium nanoparticles stabilised by chiral N-donor ligands', *New J. Chem.*, 30, (2006), 115–22.
55. M. Harada, D. Abe and Y. Kimura, 'Synthesis of colloidal dispersions of rhodium nanoparticles under high temperatures and high pressures', *J. Colloid Interface Sci.*, 292, (2005), 113–21.
56. M. Marin-Almazo, J.A. Ascencio, M. Perez-Alvarez, C. Gutierrez-Wing and M. Jose-Yacamán, 'Synthesis and characterisation of rhodium nanoparticles using HREM techniques', *Microchem. J.*, 81, (2005), 133–38.
57. T. Teranishi and M. Miyake, 'Size control of palladium nanoparticles and their crystal structures', *Chem. Mater.*, 10, (1998), 594–600.
58. S.W. Chen, K. Huang and J.A. Stearns, 'Alkanethiolate-protected palladium nanoparticles', *Chem. Mater.*, 12, (2000), 540–47.
59. C.C. Wang, D.H. Chen and T.C. Huang, 'Synthesis of palladium nanoparticles in water-in-oil microemulsions', *Colloids Surf, A- Physicochemical and Engineering aspects*, 189, (2001), 145–54.
60. S.W. Kim, J. Park, Y. Jang, Y. Chung, S. Hwang, T. Hyeon and Y.W. Kim, 'Synthesis of monodisperse palladium nanoparticles', *Nano Lett.*, 3, (2003), 1289–91.
61. R.W.J. Scott, H.C. Ye, R.R. Henriquez and R.M. Crooks, 'Synthesis, characterisation, and stability of dendrimer-encapsulated palladium nanoparticles', *Chem. Mater.*, 15, (2003), 3873–78.
62. S.U. Son, Y. Jang, K.Y. Yoon, E. Kang and T. Hyeon, 'Facile synthesis of various phosphine-stabilised monodisperse palladium nanoparticles through the understanding of coordination chemistry of the nanoparticles', *Nano Lett.*, 4, (2006), 1147–51.
63. P.F. Ho and K.M. Chi, 'Size-controlled synthesis of Pd nanoparticles from beta-diketonato complexes of palladium', *Nanotechnology*, 15, (2004), 1059–64.
64. S. Mandal, A. Das, R. Srivastava and M. Sastry, 'Keggin ion mediated synthesis of hydrophobised Pd nanoparticles for multifunctional catalysis', *Langmuir*, 21, (2005), 2408–13.
65. A. Nemamcha, J.L. Rehspringer and D. Khatmi, 'Synthesis of palladium nanoparticles by sonochemical reduction of palladium(II) nitrate in aqueous solution', *J. Phys. Chem. B.*, 110, (2006), 383–87.
66. A. Taleb, C. Petit and M.P. Pileni, 'Synthesis of highly monodisperse silver nanoparticles from AOT reverse micelles: A way to 2D and 3D self-organisation', *Chem. Mater.*, 9, (1997), 950–59.
67. P.V. Kamat, M. Flumiani and G.V. Hartland, 'Picosecond Dynamics of Silver Nanoclusters. Photoejection of Electrons and Fragmentation', *J. Phys. Chem. B.*, 102, (1998), 3123–28.
68. B.A. Korgel, S. Fullam, S. Connolly and D. Fitzmaurice, 'Assembly and self-organisation of silver nanocrystal superlattices: Ordered soft spheres', *J. Phys. Chem. B.*, 102, (1998), 8379–88.
69. J.J. Zhu, S.W. Liu, O. Palchik, Y. Koltypin and A. Gedanken, 'Shape-controlled synthesis of silver nanoparticles by pulse sonoelectrochemical methods', *Langmuir*, 16, (2000), 6396–99.
70. A. Frattini, N. Pellegri, D. Nicastro and O. de Sanctis, 'Effect of amine groups in the synthesis of Ag nanoparticles using aminosilanes', *Mater. Chem. Phys.*, 94, (2005), 148–52.
71. N.R. Jana, L. Gearheart and C.J. Murphy, 'Wet chemical synthesis of silver nanorods and nanowires of controllable aspect ratio', *Chem. Commun.*, (2001), 617–18.

72. K. Soulantica, A. Maisonnat, M.C. Fromen, M.J. Casanove, P. Lecante and B. Chaudret, 'Synthesis and self-assembly of monodisperse indium nanoparticles prepared from the organometallic precursor $[\text{In}(\eta(5)\text{-C}_5\text{H}_5)]$ ', *Angew. Chem., Int. Ed.*, 40, (2001), 448–51.
73. K. Soulantica, L. Erades, M. Sauvan, F. Senocq, A. Maisonnat and B. Chaudret, 'Synthesis of indium and indium oxide nanoparticles from indium cyclopentadienyl precursor and their application for gas sensing', *Adv. Funct. Mater.*, 13, (2003), 553–57.
74. Z.W. Li, X.J. Tao, Y.M. Cheng, Z.S. Wu, Z.J. Zhang and H.X. Dang, 'A simple and rapid method for preparing indium nanoparticles from bulk indium via ultrasound irradiation', *Mater. Sci. Eng., A.*, 407, (2005), 7–10.
75. P.K. Khanna, K.W. Jun, K.B. Hong, J.O. Baeg, R.C. Chikate and B.K. Das, 'Colloidal synthesis of indium nanoparticles by sodium reduction method', *Mater. Lett.*, 59, (2005), 1032–36.
76. N. Avramova, N.S. Neykov and S.K. Peneva, 'A calorimetric study of tin grown by reduction of SnCl_2 with Mg', *J. Phys. D: Appl. Phys.*, 29, (1996), 1300–05.
77. C.S. Yang, Q. Liu, S.M. Kauzlarich and B. Phillips, 'Synthesis and Characterisation of Sn/R, Sn/Si-R, and Sn/SiO₂ Core-Shell Nanoparticles', *Chem. Mater.*, 12, (2000), 983–88.
78. Y.B. Zhao, Z.J. Zhang and H.X. Dang, 'Preparation of tin nanoparticles by solution dispersion', *Mater. Sci. Eng. A*, 359, (2003), 405–07.
79. A. Caballero, J. Morales and L. Sanchez, 'Tin nanoparticles formed in the presence of cellulose fibers exhibit excellent electrochemical performance as anode materials in lithium-ion batteries', *Electrochem. Solid-State Lett.*, 8, (2005), A464–A466.
80. Y. Kwon, M.G. Kim, Y. Kim, Y. Lee and J.P. Cho, 'Effect of capping agents in tin nanoparticles on electrochemical cycling', *Electrochem. Solid-State Lett.*, 9, (2006), A34–A38.
81. B. Stegemann, C. Ritter, B. Kaiser and K. Rademann, 'Crystallisation of antimony nanoparticles: Pattern formation and fractal growth', *J. Phys. Chem. B.*, 108, (2004), 14292–97.
82. Y.W. Wang, B.H. Hong, J.Y. Lee, J.S. Kim, G.H. Kim and K.S. Kim., 'Antimony nanowires self-assembled from Sb nanoparticles', *J. Phys. Chem. B.*, 108, (2004), 16723–26.
83. B. Mayers and Y.N. Xia, 'One-dimensional nanostructures of trigonal tellurium with various morphologies can be synthesised using a solution-phase approach', *J. Mater. Chem.*, 12, (2002), 1875–81.
84. Z.P. Liu, Z.K. Hu, Q. Xie, B.J. Yang, J. Wu and Y.T. Qian, 'Surfactant-assisted growth of uniform nanorods of crystalline tellurium', *J. Mater. Chem.*, 13, (2003), 159–62.
85. Z.P. Liu, Z.K. Hu, J.B. Liang, S. Li, Y. Yang, S. Peng and Y.T. Qian, 'Size-controlled Synthesis and Growth Mechanism of Monodisperse Tellurium Nanorods by a Surfactant-Assisted Method', *Langmuir*, 20, (2004), 214–18.
86. G.C. Xi, Y.Y. Peng, W.C. Yu and Y.T. Qian, 'Synthesis, characterisation, and growth mechanism of tellurium nanotubes', *Cryst. Growth Des.*, 5, (2005), 325–28.
87. J.A. Ascencio, A.C. Rincon and G. Canizal, 'Synthesis and theoretical analysis of samarium nanoparticles: Perspectives in nuclear medicine', *J. Phys. Chem. B.*, 109, (2005), 8806–12.
88. M.Q. Tan, G.L. Wang, X.D. Hai, Z.Q. Ye and J.L. Yuan, 'Development of functionalised fluorescent europium nanoparticles for biolabeling and time-resolved fluorometric applications', *J. Mater. Chem.*, 14, (2004), 2896–2901.

89. J.A. Nelson, L.H. Bennett and M.J. Wagner, 'Solution synthesis of gadolinium nanoparticles', *J. Am. Chem. Soc.*, 124, (2002), 2979–83.
90. M.O. Oyewumi, R.A. Yokel, M. Jay, T. Coakley and R.J. Mumper, 'Comparison of cell uptake, biodistribution and tumor retention of folate-coated and PEG-coated gadolinium nanoparticles in tumor-bearing mice', *J. Controlled Release*, 95, (2004), 613–26.
91. Z.C. Yan, Y.H. Huang, Y. Zhang, H. Okumura, J.Q. Xiao, S. Stoyanov, V. Skumryev, G.C. Hadjipanayis and C. Nelson, 'Magnetic properties of gadolinium and terbium nanoparticles produced via multilayer precursors', *Phys. Lett. B.*, 67, (2003), 054403.
92. Z.Q. Ye, M.Q. Tan, G.L. Wang and J.L. Yuan, 'Development of functionalised terbium fluorescent nanoparticles for antibody labeling and time-resolved fluoroimmunoassay application', *Talanta*, 65, (2005), 206–10.
93. N.B. Shevchenko, J.A. Christodoulides and G.C. Hadjipanayis, 'Preparation and characterisation of Dy nanoparticles', *Appl. Phys. Lett.*, 74, (1999), 1478–80.
94. J.A. Nelson, L.H. Bennett and M.J. Wagner, 'Dysprosium nanoparticles synthesised by alkalide reduction', *J. Mater. Chem.*, 13, (2003), 857–60.
95. J.A. Ascencio, A.C. Rodriguez-Monroy, H.B. Liu and G. Canizal, 'Synthesis and structure determination of ytterbium nanoparticles', *Chem. Lett.*, 33, (2004), 1056–57.
96. Y. Wang, Z. L. Cui and Z.K. Zhang, 'Synthesis and phase structure of tantalum nanoparticles', *Mater. Lett.*, 58, (2004), 3017–20.
97. Y. Tamou and S. Tanaka, 'Formation and coalescence of tungsten nanoparticles under electron beam irradiation', *Nanostruct. Mater.*, 12, (1999), 123–26.
98. M.H. Magnusson, K. Deppert and J.O. Malm, 'Single-crystalline tungsten nanoparticles produced by thermal decomposition of tungsten hexacarbonyl', *J. Mater. Res.*, 15, (2000), 1564–69.
99. G.H. Lee, S.H. Huh, S.H. Kim, B.J. Choi, B.S. Kim and J.H. Park, 'Structure and size distribution of Os, Re, and Ru nanoparticles produced by thermal decomposition of $\text{Os}_3(\text{CO})_{12}$, $\text{Re}_2(\text{CO})_{10}$ and $\text{Ru}_3(\text{CO})_{12}$ ', *J. Korean Chem. Soc.*, 42, (2003), 835–37.
100. F. Bonet, V. Delmas, S. Grugeon, R.H. Urbina, P.Y. Silvert and K.T. Elhsissen, 'Synthesis of monodisperse Au, Pt, Pd, Ru and Ir nanoparticles in ethylene glycol', *Nanostruct. Mater.*, 11, (1999), 1277–84.
101. T.S. Ahmadi, Z.L. Wang, T.C. Green, A. Henglein and M.A. ElSayed, 'Shape-controlled synthesis of colloidal platinum nanoparticles', *Science*, 272, (1996), 1924–26.
102. A. Rodriguez, C. Amiens, B. Chaudret, M.J. Casanove, P. Lecante and J.S. Bradley, 'Synthesis and isolation of cuboctahedral and icosahedral platinum nanoparticles. Ligand-dependent structures', *Chem. Mater.*, 8, (1996), 1978–86.
103. C.W. Chen and M. Akashi, 'Synthesis, characterisation, and catalytic properties of colloidal platinum nanoparticles protected by poly(N-isopropylacrylamide)', *Langmuir*, 13, (1997), 6465–72.
104. C. Yee, M. Scotti, A. Ulman, H. White, M. Rafailovich and J. Sokolov, 'One-phase synthesis of thiol-functionalised platinum nanoparticles', *Langmuir*, 15, (1999), 4314–16.
105. S.H. Joo, S.J. Choi, I. Oh, J. Kwak, Z. Liu, O. Terasaki and R. Ryoo, 'Ordered nanoporous arrays of carbon supporting high dispersions of platinum nanoparticles', *Nature*, 412, (2001), 169–72.
106. K.S. Kim, D. Demberelnyamba and H. Lee, 'Size-selective synthesis of gold and platinum nanoparticles using novel thiol-functionalised ionic liquids', *Langmuir*, 20, (2004), 556–60.

107. J. Turkevich, P. Stevenson and J. Hillier, 'A study of the nucleation and growth processes in the synthesis of colloidal gold', *Discussions Faraday Soc.*, 11, (1951), 55–75.
108. G. Frens, 'Controlled nucleation for the regulation of the particle size in monodisperse gold suspensions', *Nature*, 241, (1973), 20–22.
109. J. De Mey, 'The preparation and use of gold probes', In Polak JM, Van Norden S (eds), *Immunocytochemistry: Modern methods and applications*, 2nd edn., J. Wright, Bristol, (1986), pp. 115–45.
110. E.C. Stathis and A. Fabrikanos, 'Preparation of colloidal gold', *Chem. Ind. (London)*, 27, (1958), 860.
111. P.A. Bartlett, B. Bauer and S. Singer, 'Synthesis of water-soluble undecagold cluster compounds of potential importance in electron microscopic and other studies in biological systems', *J. Am. Chem. Soc.*, 100, (1978), 5085–89.
112. C.L. Baigent and G. Muller, 'A colloidal gold prepared with ultrasonics', *Experientia*, 36, (1980), 472.
113. J. Roth, 'The preparation of protein A-gold complexes with 3 nm and 15 nm gold particles and their use in labeling multiple antigens on ultra-thin sections', *Histochem. J.*, 14, (1982), 791.
114. W.P. Faulk and G.M. Taylor, 'An immunocolloid method for the electron microscope', *Immunochemistry*, 8, (1971), 1081–83.
115. W. Baschong, J.M. Lucocq and J. Roth, 'Thiocyanate gold: Small (2–3 nm) colloidal gold for affinity cytochemical labeling in electron microscopy', *Histochemistry*, 83, (1985), 409.
116. H. Mühlpfordt, 'The preparation of colloidal gold particles using tannic acid as an additional reducing agent', *Experientia*, 38, (1982), 1127.
117. J.W. Slot and H.J. Geuze, 'A new method for preparing gold probes for multiple labeling cytochemistry', *Eur. J. Cell Biol.*, 38, (1985), 87.
118. G.B. Birrell, K.K. Hedberg and O.H. Griffith, 'Pitfalls of immunogold labeling: Analysis by light microscopy, transmission electron microscopy and photoelectron microscopy', *J. Histochem. Cytochem.*, 35, (1987), 843–853.
119. M. Brust, M. Walker, D. Bethell, D.J. Schiffrin and R. Whyman, 'Synthesis of thiol derivatised gold nanoparticles in a two-phase liquid-liquid system', *Chem. Commun.*, (1994), 801–02.
120. S.O. Obare, R.E. Hollowell and C.J. Murphy, 'Sensing strategy for lithium ion based on gold nanoparticles', *Langmuir*, 18, (2002), 10407–10.
121. G. Schmid, R. Boese, R. Pfeil, F. Bandermann, S. Meyer, G.H.M. Calis and J.W.A. van der Velden, 'Au₅₅[P(C₆H₅)₃]₁₂C₁₆—ein Goldcluster ungewöhnlicher Größe (Au₅₅[P(C₆H₅)₃]₁₂C₁₆—a Gold Cluster of an Exceptional size)', *Chem. Ber.*, 114, (1981), 3634–42.
122. A. Henglein and M. Giersig, 'Optical and chemical observations on gold-mercury nanoparticles in aqueous solution', *J. Phys. Chem. B.*, 104, (2000), 5056–506.
123. H.W. Sheng, G. Ren, L.M. Peng, Z.Q. Hu and K. Lu, 'Superheating and melting-point depression of Pb nanoparticles embedded in Al matrices', *Philos. Mag. Lett.*, 73, (1996), 179–86.
124. M. Veith, S. Mathur, P. Konig, C. Cavellius, J. Biegler, A. Rammo, V. Huch, S. A. Hao and G. Schmid, 'Template-assisted ordering of Pb nanoparticles prepared from molecular-level colloidal processing', *Comptes Rendus Chimie*, 7, (2005), 509–19.
125. J.Y. Fang, K.L. Stokes, J.A. Wiemann, W.L. Zhou, J.B. Dai, F. Chen and C.J. O'Connor, 'Microemulsion-processed bismuth nanoparticles', *Mater. Sci. Eng. B*, 83, (2001), 254–57.

126. J.Y. Fang, K.L. Stokes, W.L.L. Zhou, W.D. Wang and J. Lin, 'Self-assembled bismuth nanocrystallites', *Chem. Commun.*, (2001), 1872–73.
127. A. Wurl, M. Hyslop, S.A. Brown, B.D. Hall, and R. Monot, 'Structure of unsupported bismuth nanoparticles', *Eur. Phys. J. D.*, 16, (2001), 205–08.
128. Y.B. Zhao, Z.J. Zhang and H.X. Dang, 'A simple way to prepare bismuth nanoparticles', *Mater. Lett.*, 58, (2004), 790–93.
129. Z. Gui, R. Fan, W. Mo, X. Chen, L. Yang and Y. Hu, 'Synthesis and characterisation of reduced transition metal oxides and nanophase metals with hydrazine in aqueous solution', *Mater. Res. Bull.*, 38, (2003), 169–76.
130. A.S. Albuquerque, J.D. Ardisson and W.A. Macedo, 'Nanosized powders of NiZn ferrite: Synthesis, structure, and magnetism', *J. Appl. Phys.*, 87, (2000), 4352–57.
131. Q. Chen, A.J. Rondinone, B.C. Chakoumakos and Z.J. Zhang, 'Synthesis of superparamagnetic $MgFe_2O_4$ nanoparticles by coprecipitation', *J. Magn. Mater.*, 194, (1999), 1–7.
132. J.F. Wang, C.B. Ponton and I.R. Harris, 'Ultrafine SrM particles with high coercivity by chemical coprecipitation', *J. Magn. Mater.*, 242–245, (2002), 1464–67.
133. Y. Gu, G.Z. Li, G. Meng and D. Peng, 'Sintering and electrical properties of coprecipitation prepared $Ce_{0.8}Y_{0.2}O_{1.9}$ Ceramics', *Mater. Res. Bull.*, 35, (2000), 297–304.
134. J.-G. Li, T. Ikegami, Y. Wang and T. Mori, 'Reactive Ceria Nanopowders via Carbonate Precipitation', *J. Am. Ceram. Soc.*, 85, (2002), 2376–79.
135. L. Xiang, X.Y. Deng and Y. Jin, 'Experimental study on synthesis of NiO nano-particles', *Scr. Mater.*, 47, (2002), 219–24.
136. Y. Du, J. Fang, M. Zhang, J. Hong, Z. Yin and Q. Zhang, 'Phase character and structural anomaly of $Bi_4Ti_3O_{12}$ nanoparticles prepared by chemical coprecipitation', *Mater. Lett.*, 57, (2002), 802–06.
137. P.H. Borse, L.S. Kankate, F. Dassenoy, W. Vogel, J. Urban and S.K. Kulkarni, 'Synthesis and investigations of rutile phase nanoparticles of TiO_2 ', *J. Mater. Sci. -Mater. Electron*, 13, (2002), 553–59.
138. P.C. Kuo and T.S. Tsai, 'New approaches to the synthesis of acicular alpha- $FeOOH$ and cobalt modified iron-oxide nanoparticles', *J. Appl. Phys.*, 65, (1989), 4349–56.
139. Z. X. Tang, C. M. Sorensen, K. J. Klabunde and G.C. Hadjipanayis, 'Preparation of manganese ferrite fine particles from aqueous solution', *J. Colloid Interface Sci.*, 146, (1991), 38–54.
140. T.C. Rojas and M. Ocana, 'Uniform nanoparticles of Pr(III)/Ceria solid solutions prepared by homogeneous precipitation', *Scr. Mater.*, 46, (2002), 655–60.
141. C.N. Chinnasamy, B. Jeyadevan, O. Perales-Perez, K. Shinoda, K. Tohji and A. Kasuya, 'Growth Dominant Co-Precipitation Process to Achieve High Coercivity at Room Temperature in $CoFe_2O_4$ Nanoparticles', *IEEE Trans. Magn.*, 38, (2002), 2640–42.
142. J. Li, D. Dai, B. Zhao, Y. Lin and C. Liu, 'Properties of ferrofluid nanoparticles prepared by coprecipitation and acid treatment', *J. Nanopart. Res.*, 4, (2002), 261–64.
143. K.T. Wu, P.C. Kuo, Y.D. Yao and E.H. Tsai, 'Magnetic and optical properties of Fe_3O_4 nanoparticle ferrofluids prepared by coprecipitation technique', *IEEE Trans. Magn.*, 37, (2001), 2651–53.
144. W. Voit, D.K. Kim, W. Zapka, M. Muhammed and K.V. Rao, 2001; Y 7.8.1.

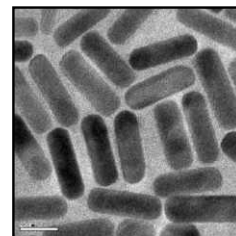
145. Z.X. Tang, C.M. Sorensen, K.J. Klabunde and G.C. Hadjipanayis, 'Size-dependent Curie temperature in nanoscale MnFe₂O₄ particles', *Phys. Rev. Lett.*, 67, (1991), 3602–05.
146. Z.L. Liu, Y.J. Liu, K.L. Yao, Z.H. Ding, J. Tao and X. Wang, 'Synthesis and Magnetic Properties of Fe₃O₄ Nanoparticles', *J. Mater. Synth. Process.*, 10, (2002), 83–87.
147. Y. Wang, C. Ma, X. Sun and H. Li, 'Preparation of nanocrystalline metal oxide powders with the surfactant-mediated method', *Inorg. Chem. Commun.*, 5, (2002), 751–55.
148. Z. Zhang, L. Guo and W. Wang, 'Synthesis and characterisation of antimony oxide nanoparticles', *J. Mater. Res.*, 16, (2001), 803–05.
149. H. Chen, X. Qiu, W. Zhu and P. Hagenmuller, 'Synthesis and high rate properties of nanoparticled lithium cobalt oxides as the cathode material for lithium-ion battery', *Electrochem. Commun.*, 4, (2002), 488–91.
150. S. Music, S. Popovic, M. Maljkovic, K. Furic and A. Gajovic, 'Influence of synthesis procedure on the formation of RuO₂', *Mater. Lett.*, 56, (2002), 806–11.
151. P. Deb, T. Biswas, D. Sen, A. Basumallick and S. Mazumder, 'Characteristics of Fe₂O₃ Nanoparticles Prepared by Heat Treatment of a Nonaqueous Powder Precipitate', *J. Nanopart. Res.*, 4, (2002), 91–97.
152. G. Ennas, G. Marongiu, A. Musinu, A. Falqui, P. Ballirano and R. Caminiti, 'Characterisation of nanocrystalline γ -Fe₂O₃ prepared by wet chemical method', *J. Mater. Res.*, 14, (1999), 1570–75.
153. S. O'Brien, L. Brus, and C.B. Murray, 'Synthesis of Monodisperse Nanoparticles of Barium Titanate: Toward a Generalised Strategy of Oxide Nanoparticle Synthesis', *J. Am. Chem. Soc.*, 123, (2001), 12085–86.
154. D. Caruntu, Y. Remond, N.H. Chou, M.-J. Jun, G. Caruntu, J. He, G. Goloverda, C. O'Connor and V. Kolesnichenko, 'Reactivity of 3d Transition Metal Cations in Diethylene Glycol Solutions. Synthesis of Transition Metal Ferrites with the Structure of Discrete Nanoparticles Complexed with Long-Chain Carboxylate Anions', *Inorg. Chem.*, 41, (2002), 6137–46.
155. S. Sun and H. Zeng, 'Size-controlled synthesis of magnetite nanoparticles', *J. Am. Chem. Soc.*, 124, (2002), 8204–05.
156. J. Rockenberger, E.C. Scher and A.P. Alivisatos, 'A new nonhydrolytic single-precursor approach to surfactant-capped nanocrystals of transition metal oxides', *J. Am. Chem. Soc.*, 121, (1999), 11595–96.
157. J.P. Chen, K.M. Lee, C.M. Sorensen, K.J. Klabunde and G.C. Hadjipanayis, 'Magnetic properties of microemulsion synthesised cobalt fine particles', *J. Appl. Phys.*, 75, (1994), 5876–78.
158. I. Lisiecki and M.P. Pileni, 'Synthesis of copper metallic clusters using reverse micelles as microreactors', *J. Am. Chem. Soc.*, 115, (1993), 3887–96.
159. M. Boutonnet, J. Kizling, P. Stenius and G. Maire, 'The preparation of monodisperse colloidal metal particles from microemulsions', *Colloids Surf.*, 5, (1982), 209–25.
160. P. Barnickel, A. Wokaun, W. Sager and H.-F. Eicke, 'Size tailoring of silver colloids by reduction in W/O microemulsions', *J. Colloid Interface Sci.*, 148, (1992), 80–90.
161. E.E. Foos, R.M. Stroud, A.D. Berry, A.W. Snow and J.P. Armistead, 'Synthesis of Nanocrystalline Bismuth in Reverse Micelles', *J. Am. Chem. Soc.*, 122, (2000), 7114–15.
162. E.E. Carpenter, J.A. Sims, J.A. Wienmann, W.L. Zhou and C.J. O'Connor, 'Magnetic properties of iron and iron platinum alloys synthesised via microemulsion techniques', *J. Appl. Phys.*, 87, (2000), 5615–17.

163. E.E. Carpenter, A. Kumbhar, J.A. Wiemann, H. Srikanth, J. Wiggins, W. Zhou and C.J. O'Connor, 'Synthesis and magnetic properties of gold-iron-gold nanocomposites', *Mater. Sci. Eng. A*, 286, (2000), 81–86.
164. C.-H. Lu and H.-C. Wang, 'Synthesis of nano-sized $\text{LiNi}_{0.8}\text{Co}_{0.2}\text{O}_2$ via a reverse-microemulsion route', *J. Mater. Chem.*, 13, (2003), 428–31.
165. Y.-X. Pang and X. Bao, 'Aluminium oxide nanoparticles prepared by water-in-oil microemulsions', *J. Mater. Chem.*, 12, (2002), 3699–3704.
166. P.D. Moran, J.R. Bartlett, G.A. Bowmaker, J.L. Woolfrey and R.P. Cooney, 'Formation of TiO_2 Sols, Gels and Nanopowders from Hydrolysis of $\text{Ti}(\text{OiPr})_4$ in AOT Reverse Micelles', *J. Sol-Gel Sci. Technol.*, 15, (1999), 251–62.
167. D.O. Yener and H. Giesche, 'Processing of Pure and Mn, Ni, and Zn Doped Ferrite Particles in Microemulsions', *Ceram. Trans.*, 94, (1999), 407–18.
168. H.S. Lee, W.C. Lee and T. Furubayashi, 'A comparison of coprecipitation with microemulsion methods in the preparation of magnetite', *J. Appl. Phys.*, 85, (1999), 5231–33.
169. C.J. O'Connor, C.T. Seip, E.E. Carpenter, S. Li and V.T. John, 'Synthesis and reactivity of nanophase ferrites in reverse micellar solutions', *Nanostruct Mater.*, 12, (1999), 65–70.
170. C.R. Vestal and Z.J. Zhang, 'Synthesis of CoCrFeO_4 Nanoparticles Using Microemulsion Methods and Size-Dependent Studies of Their Magnetic Properties', *Chem. Mater.*, 14, (2002), 3817–22.
171. C. Liu, A.J. Rondinone and Z.J. Zhang, 'Synthesis of magnetic spinel ferrite CoFe_2O_4 nanoparticles from ferric salt and characterisation of the size-dependent superparamagnetic properties', *Pure Appl. Chem.*, 72, (2000), 37–45.
172. D.O. Yener and H. Giesche, 'Processing of Pure and Mn, Ni, and Zn Doped Ferrite Particles in Microemulsions', *Ceram. Trans.*, 94, (1999), 407–18.
173. F. Porta, C. Bifulco, P. Fermo, C.L. Bianchi, M. Fadoni and L. Prati, 'Synthesis of spherical nanoparticles of $\text{Cu}_2\text{L}_2\text{O}_5$ (L=Ho, Er) from W/O microemulsions', *Colloids Surf. A*, 160, (1999), 281–90.
174. P. Vaqueiro, M.A. Lopez-Quintela and J. Rivas, 'Synthesis of yttrium iron garnet nanoparticles via coprecipitation in microemulsion', *J. Mater. Chem.*, 7, (1997), 501–04.
175. P. Kumar, V. Pillai, S.R. Bates and D.O. Shah, 'Preparation of $\text{YBa}_2\text{Cu}_3\text{O}_{7-x}$ superconductor by coprecipitation of nanosize oxalate precursor powder in microemulsions', *Mater. Lett.*, 16, (1993), 68–74.
176. K.C. Song and J.H. Kim, 'Synthesis of high surface area tin oxide powders via water-in-oil microemulsions', *Powder Technol.*, 107, (2000), 268–72.
177. V. Pillai, P. Kumar, M.S. Multani and D.O. Shah, 'Structure and magnetic properties of nanoparticles of barium ferrite synthesised using microemulsion processing', *Colloids Surf. A*, 80, (1993), 69–75.
178. B.J. Palla, D.O. Shah, P. Garcia-Casillas and J. Matutes-Aquino, 'Preparation of Nanoparticles of Barium Ferrite from Precipitation in Microemulsions', *J. Nanopart. Res.*, 1, (1999), 215–21.
179. Z. Wu, J. Zhang, R. E. Benfield, Y. Ding, D. Grandjean, Z. Zhang and J. Xin, 'Structure and Chemical Transformation in Cerium Oxide Nanoparticles Coated by Surfactant Cetyltrimethylammonium Bromide (CTAB): An X-ray Absorption Spectroscopic Study', *J. Phys. Chem. B*, 106, (2002), 4569–77.

180. T. Hirai, Y. Tsubaki, H. Sato and I. Komasaawa, 'Mechanism of Formation of Lead Sulfide Ultrafine Particles in Reverse Micellar Systems', *J. Chem. Eng. Jpn.*, 28, (1995), 468–73.
181. L.M. Gan, B. Liu, C.H. Chew, S.J. Xu, S.J. Chua, G.L. Loy and G.Q. Xu, 'Enhanced Photoluminescence and Characterisation of Mn-Doped ZnS Nanocrystallites Synthesised in Microemulsion', *Langmuir*, 13, (1997), 6427–31.
182. N.R. Jana, L. Gearheart and C.J. Murphy, 'Wet Chemical Synthesis of High Aspect Ratio Cylindrical Gold Nanorods', *J. Phys. Chem. B.*, 105, (2001), 4065–67.
183. Y.Y. Yu, S.S. Chang, C.L. Lee and C.R.C. Wang, 'Gold Nanorods: Electrochemical Synthesis and Optical Properties', *J. Phys. Chem. B.*, 101, (1997), 6661–64.
184. S. Link, M.B. Mohamed and M.A. El-Sayed, 'Simulation of the Optical Absorption Spectra of Gold Nanorods as a Function of Their Aspect Ratio and the Effect of the Medium Dielectric Constant', *J. Phys. Chem. B.*, 103, (1999), 3073–77.
185. F. Kim, J.H. Song and P. Yang, 'Photochemical Synthesis of Gold Nanorods', *J. Am. Chem. Soc.*, 124, (2002), 14316–17.
186. K. Aslan, Z. Leonenko, J.R. Lakowicz and C.D. Geddes, 'Fast and Slow Deposition of Silver Nanorods on Planar Surfaces: Application to Metal-Enhanced Fluorescence', *J. Phys. Chem. B.*, 109, (2005) 3157–62.
187. C.C. Chen, C.Y. Chao and Z.H. Lang, 'Simple Solution-Phase Synthesis of Soluble CdS and CdSe Nanorods', *Chem. Mater.*, 12, (2000), 1516–18.
188. Y.D. Li, H.W. Liao, Y. Ding, Y.T. Qian, L. Yang and G.E. Zhou, 'Nonaqueous Synthesis of CdS Nanorod Semiconductor', *Chem. Mater.*, 10, (1998), 2301–03.
189. W. Wang, Y. Geng, P. Yan, F. Liu, Y. Xie and Y. Qian, 'Synthesis and characterisation of MSe (M = Zn, Cd) nanorods by a new solvothermal method', *Inorganic Chemistry Communication*, 2, (1999), 83–85.
190. L. Manna, E.C. Scher and A.P. Alivisatos, 'Synthesis of Soluble and Processable Rod-, Arrow-, Teardrop-, and Tetrapod-Shaped CdSe Nanocrystals', *J. Am. Chem. Soc.*, 122, (2000), 12700–06.
191. L. Guo, Y.L. Ji and H. Xu, 'Regularly Shaped, Single-Crystalline ZnO Nanorods with Wurtzite Structure', *J. Am. Chem. Soc.*, 124, (2002), 14864–65.
192. A. Dev, S.K. Panda, S. Kar, S. Chakrabarti and S. Chaudhuri, 'Surfactant-Assisted Route to Synthesise Well-Aligned ZnO Nanorod Arrays on Sol-Gel-Derived ZnO Thin Films', *J. Phys. Chem. B.*, 110, (2006) 14266–72.
193. B. Liu and H. Chun Zeng, 'Hydrothermal Synthesis of ZnO Nanorods in the Diameter Regime of 50 nm', *J. Am. Chem. Soc.*, 125, (2003), 4430–31.
194. T.K. Sau and C.J. Murphy, 'Room Temperature, High-Yield Synthesis of Multiple Shapes of Gold Nanoparticles in Aqueous Solution', *J. Am. Chem. Soc.*, 126, (2004), 8648–49.
195. S.S. Sankar, A. Rai, B. Ankamwar, A. Singh, A. Ahmad and M. Sastry, 'Biological synthesis of triangular gold nanoprisms', *Nature Materials*, 3, (2004), 482–88.
196. H. Jia, W. Xu, J. An, D. Li and B. Zhao, 'A simple method to synthesize triangular silver nanoparticles by light irradiation', *Spectrochimica Acta, Part A*, 64, (2006), 956–60.
197. J.E. Millstone, S. Park, K.L. Shuford, L. Qin, G.C. Schatz and C.A. Mirkin, 'Observation of a Quadrupole Plasmon Mode for a Colloidal Solution of Gold Nanoprisms', *J. Am. Chem. Soc.*, 127, (2005), 5312–13.

198. R. Jin, Y.W. Cao, C.A. Mirkin, K.L. Kelly, G.C. Schatz and J.G. Zheng, 'Photoinduced Conversion of Silver Nanospheres to Nanoprisms', *Science*, 294, (2001), 1901–03.
199. C.S. Ah, Y.J. Yun, H.J. Park, W.J. Kim, D.H. Ha and W.S. Yun, 'Size-Controlled Synthesis of Machinable Single Crystalline Gold Nanoplates', *Chem. Mater.*, 17, (2005), 5558–61.
200. S. Chen and D.L. Carroll, 'Silver Nanoplates: Size Control in Two Dimensions and Formation Mechanisms', *J. Phys. Chem. B.*, 108, (2004), 5500–06.
201. Y. Xiong, J.M. McLellan, J. Chen, Y. Yin, Z.Y. Li and Y. Xia, 'Kinetically Controlled Synthesis of Triangular and Hexagonal Nanoplates of Palladium and Their SPR/SERS Properties', *J. Am. Chem. Soc.*, 127, (2005), 17118–27.
202. Y. Ding, Z.L. Wang, W. Lu and J. Fang, 'Spontaneous Fractal Aggregation of Gold Nanoparticles and Controlled Generation of Aggregate-Based Fractal Networks at Air/Water Interface', *J. Phys. Chem. B.*, 109, (2005), 19213–18.
203. M. Yamamoto, Y. Kashiwagi, T. Sakata, H. Mori and M. Nakamoto, 'Synthesis and Morphology of Star-Shaped Gold Nanoplates Protected by Poly(N-vinyl-2-pyrrolidone)', *Chem. Mater.*, 17, (2005), 5391–93.
204. S. Chen, Z.L. Wang, J. Ballato, S.H. Foulger and D.L. Carroll, 'Monopod, Bipod, Tripod, and Tetrapod Gold Nanocrystals', *J. Am. Chem. Soc.*, 125, (2003), 16186–87.
205. C.P. Graf, R. Birringer and A. Michels, 'Synthesis and magnetic properties of cobalt nanocubes', *Physical Review B.*, 73, (2006), 212401–404.

INDEX



- ¹H NMR 406, 407
- Abalone shell, nacre in, bionanocomposite 514
- Abbe criterion* 32
- Abraxane™ 628, 632
- Absorption coefficient 253
- Activity factor 539, 571
- Addenda atom in heteropolyanion 506
- Agrarian era 8
- Alumina 382, 407
- Amphiprotic species 620
- Angle-resolved photoelectron spectroscopy (ARPES) 95
- Anisotropic molecules 665
- Anisotropic nanoparticles 228, 345
- Antibacterial activity 700
- Antibody 391, 394
- Anti-Stokes shift 158
- Arsenic detection from drinking water 462
- Artificial solids 311
- Ascorbic acid 287
- Assembly of Ag nanostructures 447
- Assembly of CdS/CdSe 452
- Assembly of GNRs by biological interactions 420
- Assembly of long GNRs and nanowires 442
- Astigmatism 37, 38
- Atom transfer radical polymerization 503
- Atomic Force Microscopy (AFM) 71
- Atomic Layer Deposition (ALD) 546, 551
- Atomic manipulations 67
- Attenuation length 44
- Auger effect 89
- Ayurveda* 13
- Back folding in dendritic structures 479
- Ball-and-pebble mill 739
- Ballistic or Coherent resonant tunneling regime 562–570
- Band dispersion 95
- Band gap 252, 325, 395, 404, 406
- Bardeen-Cooper-Schrieffer (BCS) theory 92
- Bargg's law 56, 118
- Barrier height 543
- Bathochromic shift 336
- Berkovich indenter 523
- Bilayer 385, 386
- Binding constant 484, 494
- Binding energy 85
- Bio-conjugation 308, 368, 619
- Biological synthesis 227, 356
- Biomolecule-nanoparticle interaction 622
- Biomolecules 381, 394
- Biotin-avidin 619, 646
- Blocking temperature 605
- Bottom-up self-assembly 312
- Bovine serum albumin 287, 336
- Bavarian limestone 573
- Break-junction technique 586
- Bremsstrahlung isochromat spectroscopy (BIS) 97

- Bright field image 45
Brillouin scattering 170
Brownian diffusion 756
Brownian motion 261
Brust reduction, synthesis 215, 286
- Calcium phosphate nanoparticles, nCP 633, 634
Cancer associated targets, list of 627
Canonical partition function 264
Carbon nanomaterials 702
Carbon nanotubes (CNT) 552, 702
Cassie equation 183
Catalyst 307, 713
Cavitation 401
Central difference algorithm 266
Ceramic particles 741, 743
Chain transfer agent 509
Chalcogenides 220
Charge-density-wave (CDW) 95
Chemical degradation 690
Chemical vapour deposition (CVD) 543, 551
Chemomechanical polishing (CMP) 551, 552
Chimie douce 491
Chromatic aberration 36
Chromophore 297
Circular nanocrystal assembly 329
Citrate route 214
Civil society 769, 792, 804, 813, 814, 815
Classical or incoherent transfer 562
Classification 666
Clean room 578
Clogging 737
CMOS 538–548
Cobalt chains 111
Cold field emitter 33
Colloids 383, 388, 399, 401, 405
Colloid mill 739
Commercialisation of nanoscientific knowledge 782, 788, 809
- Computer simulation 262
Conductivity measurements 185
Confinement 255
Confocal microscopy 76
Contact angle 182
Contrast factor 132
Contrast transfer function 46
Control dilemma 807, 810, 811
Copper interconnects 447, 551
Core etching 286
Core level 85
Core-shell 223, 509–513
Coulomb band 339
Critical micellar concentration 481
Critical size 101
Cross section 670
Crystallization 312
Cuboctahedral 330
Curie temperature 595
CVD 181
Cyclic voltammetry 138
Cysteine 394, 619, 622–624
Cytochrome 180
Cytotoxicity 303
- Dark field 45
Dawson anion 506
Debye-Scherrer formula 127
Debye-Scherrer method 125
Dendrimer 285, 487, 702
Dendritic structure 479
Dendron 482, 483, 488
DENs 485
Density functional theory 303
Density of states (DOS) 91, 255
Detection of ions 461
Device electrostatics, in molecular electronics 561
Dielectric constant 542–544
Differential pulse voltammetry 147

- Diffraction 37, 118
Diffusive or coherent non-resonant tunneling regime 562
Digestive ripening 313
Digital imaging 49
Dip coating 497
Dipole moment 157, 528, 663
Dipole moment orientation 328
Dip-pen lithography 586–587
Divergent method 479
DNA hybridisation detection 465, 466
Double gate SOI MOSFET 548
Double layer 386
Downscaling 537–541
Doxil 628, 630
Drain induced barrier lowering (DIBL) 539
Drexler, Eric 7
Drug delivery 738
Dry nanotechnology 3
DSC 197
d-spacing 120
Ductility 736
DWFM 681
Dye reduction 716
Dye-sensitised 106
Dynamic light scattering 129, 481
Dynamic thermo mechanical analysis 519
Dynes function 92
- EBL 583
EELS 193
Eigler 67
Einstein, Albert 85
Elastic modulus 521
Electrochemical 381, 382, 383, 384
Electrochemical synthesis 364
Electroluminescence 296
Electromagnetic lenses 31
Electromagnetic wave 663
- Electron detector 39
Electron diffraction 53, 316
Electron doping 84
Electron energy analyser 87
Electron energy loss spectroscopy (EELS) 46
 EELS at the nanometer scale 50, 51
Electron gun 33
Electron hole pair 256
Electron lenses 35
Electron microscopic imaging 312
Electron microscopies 25
Electron spectroscopy for chemical analysis (ESCA) 85
Electron transfer 300
Electron hole recombination 298
Electronic cooling 738
Electronic effects 311
Electrostatic assembly 619
Electrostatic self-assembly 312
Electrostriction 667
Elemental analysis 195
EMS model 258
Energy dispersive spectrometry (EDS) 42
Energy eigen values 254
Energy levels 252
Energy transfer 299
Environmental remediation 689
Environmental risks 774, 792, 794, 797, 799, 801, 802, 803, 804, 812, 813, 815
Environmental sensitive fluorophores 335
Environmental transmission electron microscopy (ETEM) 50
Epitaxial growth 349
EPR effect 625, 627
Ergodicity 265
Erosion 734, 737
ESI 176
Ethics 773, 774, 787, 788, 797, 798, 810, 814, 815, 816

- Evaporation-induced self-assembly 495
Everhart-Thornley (E-T) detector 39
Exchange coupling 91
Excited state absorption 670
Exciton 256, 675
Exciton Bohr radius 257
Experiment on
 adsorption of biomolecules on AuNPs 828
 AgNPs 887
 band gap of semiconductor NPs 836
 Beer-Lambert Law, AuNPs 823
 bimetallic NPs 865
 catalysis using AgNPs 842
 conversion of gold NRs into NPs 850
 liquid magnets 860
 pesticide detection using AuNPs 877
 preparation of Te nanowires 899
 reactivity of Au clusters towards metal ions 882
 removal of Hg using supported NPs 854
 SERS activity of AgNPs 845
 synthesis AuNPs by core etching 903
 synthesis of ZnO NPs 894
Extinction 188

FAB 179
Faraday 12
Fermi energy 671
Fermi energy, in HOMO-LUMO gap 561
Fermi level 92
Fermi wavelength 284
Fermi wavelength, Momentum relaxation length,
 Phase relaxation length 560
Fermi-Dirac function 92
Ferro, ferri and antiferromagnetism 597
Ferrofluids 610
Feynman, Richard 14
FIB 181
Field emission 33
Florescence imaging 325

Fluorescence 258
Fluorescence resonance energy transfer (FRET) 27,
 80
Folic acid 303
Force-extension curve 514
Fourier transform 119
Frechet type dendrimer 478
Free carrier absorption 670
Free energy 263, 385, 404
Fullerenes 230
Fully-depleted SOI MOSFET 548

GAE 181
Galvanic replacement reaction 360
Gas proportional counter 46
Gate all around (GAA) SOI MOSFET 548
Gel glass dispersed liquid crystalline device 524
Glass transition temperature 521
Glucose biosensor 464
Glutathione 284, 394
GMR 609
GNR assembly
 by covalent bonding 425
 by electrostatic forces 426
 by hydrogen bonding 426
 by magnetic field 442
 by polymer tethering 440
 by surface anchored crown ethers 441
 involving van der Waals and dipole interaction
 428
 layer-by-layer assembly 441
 on substrates 434
 on templates 431
Gold nanorod assembly 415
Growing catalyst 715
Growth process 385, 391, 400

Hamilton–Crosser model 744, 746
Henry's equation 187

- Hertz, Heinrich 84
Heteropoly anion 506
Heterostructure 549
HfO₂ 540–545
Hierarchical self-assembly 312
High pressure Raman 167
Highest occupied molecular orbital 294
High-k dielectric 541–546, 551
Hole doping 84
Hollow nanostructures 362
Homogenizer 739
Host-guest 480
HREELS 194
Hybrid 491
Hydrogen bonding 312
Hydrogenation 307
Hydrophilic 428, 430, 435–450
Hydrophobic 430
Hydrothermal 313, 401, 402, 403, 407
Hydrothermal synthesis 358
Hydroxy apatite (HAp) 518, 648, 649
Hyper-branched 476, 477
Hyperthermia, Magnetic 637
- Imaging 285
Immersion technology 550, 551
Impedance analysis 142
Indenter 521
Indium chains 111
Industrial age 8
Inelastic mean free path 86
Inert gas condensation 228
Information age 8
Infra-red absorbing material 373
In-situ nano measurements 51
Insulator 91
Interactions 619, 620, 643, 645
Interband transitions 675
Intercalation 519
Inter-plasmon coupling 311
Inverse photoelectron spectroscopy (IPES) 96
Inversion symmetry 664
Ion sensor 300
Isoelectric point 619, 620, 622
Isopoly anion 506
Isostructural 329
Isotropic nanoparticles 344
- Kady mill 739
Keggin anion 506
Kikuchi patterns 45
Kinetic energy 85
Kinome 641
Kolmogorov's scale 760
- LaB₆ 33
Laboratories 774, 778, 792, 798, 801, 802, 813
Lactobacillus 14
Lamellar 495
Langevin equation 273
Layered double hydroxides 516
Leeuwenhoek, Antony van 30
Ligand exchange 288
Ligands 284
Ligands for active cancer targeting 626
Light matter interaction 155
Lindqvist ion 506
Line shape 90
Liposomes 627, 630, 631, 637
Lithium-drifted silicon 42
Lithium-ion batteries 465
Local field enhancement 672
Localised surface plasmon resonance 367
Long-range periodic order 314
Lorentz factor 120
Loss modulus 520
Loss tangent 521
Low dimensional 252, 253

- Low voltage SEM 40
Lowest unoccupied molecular orbital 294
Low-k dielectric 547–548
Lycurgus cup 12
- Macromolecule 475
Magic number 103
Magnetic anisotropy 600
Magnetic circular dichroism (MCD) 111
Magnetic moment 597
Magnetic nanomaterials 227
Magnetic nanoparticles 738
Magnetic nanostructures 601
Magnetic properties 312
Magnetisation 597
Magnetism 303
Magnetosperillum magentotactium 14
MALDI 176, 179
Malignant cells 391, 392, 393, 394
Mass spectrometry 176, 289
Maxwell Garnett model 742, 751
Maxwell's model 742
Melting of alkyl chains 193
Membrane- and nano-filtration 699
Mesoflowers 351
Mesoporous 494
Mesoporous silica nanoparticles (MSN) 634, 635
Metal and semiconductor nanoparticles 690
Metal clusters 100
Metal nanostructures 670
Metal to insulator transition 311
Metal-based nanofluids 743, 744
Metal-metal 313
Metalloporphyrinogens 691
Metal-semiconductor 313
Metastasis 642, 644
Metropolis Algorithm 266
M-H curves 600
Micelles 629–631
Micremulsion 222
Microanalysis 42
Microcontact printing 497
Microconvection 747
Microfluidic device 497
Micromolar detection of amino acids 461
Micro-Raman 160
Molecular dynamics 265
Molecular motors 7
Molecular nanotechnology 7
Molecular orbital 671
Molecular sensing from SERS 462
Molecule-electrode coupling, in molecular electronics 561
Monodisperse particles 218, 307, 447, 607
Monolayer 284
Monte Carlo 265
Montmorillonite 518
Moore, Gordon 15
Moore's Law 15, 538
Multidrug resistance (MDR) 625
Multi-photon absorption 669
Multiple quantum well 253
- Nacre in abalone shell, bionanocomposite 514
Nano convection 748
Nano MOS 538, 539, 540, 546, 548
Nano-banking 803
Nanobuilding block 490, 492, 502
Nano-businesses 774, 777, 778, 780, 783, 784, 785, 787, 788, 793, 795, 798, 808
Nanocages 362
Nanocomposite 491
Nanocubes 353, 368
Nano-divide 777, 782, 783, 785, 786, 787, 788, 807, 808
Nano-economy 775, 777
Nano-enterprise 769, 777, 778, 779, 780, 784, 785, 786

- Nanofluid 734–744
Nano-focused policy development 809, 810, 811
Nano-hype 777, 778, 779, 781
Nanoindentation 521
Nanoinkshuks 362
Nanolaminate 499
Nanolithography 572
Nanomanipulation 590
Nanomaterials 689
Nanomaterials as sorbents 698
Nanometrology 799
Nanoparticle 283
Nanoparticle crystals 311
Nanoparticle mediated gene silencing 641
Nanoparticles 735–761
Nanoparticles, SPIONs 637, 639
Nanopore 559
Nanoprism 347, 364
Nanoprobe station 99
Nanorod heterostructures as biomarkers 463
Nanoscale biopolymers 706
Nanoshell 632, 637, 647
Nanotechnology 690
Nanotechnology moratorium 778, 814, 815
Nanotoxicology 774, 792, 793, 794, 795, 796, 797, 798, 799, 800, 801, 802, 803, 804
Nanotubes 232
Nano-wealth 777, 781, 784, 787
Natural convection 733
Navier-Stokes equation 277
Neel temperature 599
Negative bias temperature instability (NBTI) 541
Negative differential resistance (NDR) 564, 566
NIPAm 509
Nitrophenol 718
NMR 195
Noble metals 311
NOESY 481
Nomenclature 88
Nonlinear absorption 668
Non-linear optical material 528
Non-linear Raman 168
Nonlinear refraction 666
Normalised thermal dispersion coefficient 758
Nucleic acid 368, 414, 422, 466, 633, 634
Nusselt number 750, 751
Nyquist plot 145
Octasilicate anion 503
Ohm's law 143
Olfactory receptors 6
One-step method 740, 741
Optical absorption 258
Optical coherence tomography 370
Optical contrast agents 369
Optical imaging 325
Optical Kerr effect 665
Optical limiting 668
Optical lithography 550, 581
Optical nonlinearity 663
Optical properties 312
Optical spectroscopy 188
Optoelectronic 254
Orthotelluric acid 399, 400
Oxidation 720, 721
Oxides 106
Oxygen vacancy 106
Pair correlation function 271
PAMAM dendrimer 478
PAMAM 702
Parametric mixing 665
PEG 486
Peptide 515, 516
Periodic boundary conditions 267
Phase transfer 286
Phenylethane thiol 288
Phonon modes 162, 163

- Photocatalysis 693
Photochemical 381, 383, 384, 394
Photochemical synthesis 364
Photoelectric effect 84
Photoelectron spectroscopy (PES) 84
Photogenerated electrons and holes 693
Photographic films 49
Photo-induced charge transfer 694
Photolithography 581
Photoluminescence 284, 329
Photon antibunching 298
Photoreactivity 300
Photostable 296
Photosynthesis 6
Photothermal therapy 370
Photovoltaic devices 6, 465
Piezoelectric drives 65
Plasmon resonance 388, 390
Plasmonic waveguides 460
Pockels effect 665
polarisability 157
Polarization 663
Polarization factor 120, 126
Policy debates 771, 774, 779, 781, 784, 786, 793, 794, 795, 796, 798, 799, 802, 803, 807, 808
Poly(amido amine) 722
Poly(aryl ether) 478
Polyacrylamide gel electrophoresis 285
Polyaromatic hydrocarbons 698
Polymers 628, 630, 633, 637, 642, 653
Polyol synthesis 352
Polyoxometalate 506
Polyoxotungstate 507
Poly(propyleneamine), PPI 479, 481, 484
Polystyrene sulfonate 391
Positive and negative resists 575
Powder diffraction 121
Power dissipation 539, 540, 541, 542, 557
Precautionary measures 797, 798, 802
Pre-emptive measures 792, 801, 803
Principle of superposition 665
Pseudo-single-step method 741
p-type semiconductor 325
Public engagement 802, 803, 813, 816
Pump-probe experiments 683
Pure metallic particles 741
Quantised electronic structure 308
Quantum cluster 283
Quantum confinement 312
Quantum corral 68
Quantum dots (QDs) 190, 252, 297, 635, 637, 645–647
Quantum well states 108
Quantum wells 253
Quantum wires 255
Quantum yield 283
Raman 380, 389
Raman, C.V. 155
Raman scattering 155
Raman spectra of nanotube 161
Rayleigh 156
Rayleigh criterion 32
Rayleigh scattering 675
Reactive oxygen 303
Reactivity 101
Redox active catalysts 690
Reflectometry 133
Refractive index 664
Relaxation time 604
Repulsion 624, 642
Resolution 30
Resolving power 30, 32
Resonant photoelectron spectroscopy (RESPES) 97
Reversible addition fragmentation chain transfer method 509
Rietveld profile refinement 125, 126

- Rotor-stator methods 739
Rubbery plateau 521
- Saturable absorption 668
Saw-tooth 514
Scan coils 37
Scanning electrochemical microscopy 148
Scanning electron microscope (SEM) 30
Scanning near field optical microscopy (SNOM) 28
Scanning probe lithography (SPL) 73
Scanning probe microscopies (SPM) 63
Scanning thermal microscopy (S_{Th}M) 72
Scanning tunneling microscopy (STM) 64
Scanning tunneling spectroscopy (STS) 64
Scattering
 elastic 156
 inelastic 156
Scattering factor 119
Scattering vector 118
Schottky field emission 33
Science and technology policy reforms 801, 807, 808, 809, 813
Science and technology studies (STS) 773, 799
Second harmonic generation 665
Sedimentation 312, 734, 736, 739, 740, 744
Seebeck coefficient 406
Seed nanoparticles 346
Seedless 386
Seed-mediated synthesis 346
Selenides 107
Self-assembled monolayers on mesoporous support 698
Self-assembly 311, 492, 587
Self-assembly of gold nanorod 417
Self-cleaning surfaces 372
Self-organization 312
Semiconductor 91
Semiconductor-semiconductor 313
Sensor 394
SERS 164, 673
SERS enhancement factor 164
Shape and size 726
Shear driven particle migration 755
Short channel effects (SCE) 539
Siegbahn, Kai 85
Silafins 515
Silicon nanowire 110
Silicon-on-insulator (SOI) 539, 547, 548
Silsesquioxane 503
Silver microelectrode 714
SIMS 177
Single level programme 567
Single-cluster 300
Single-photon emitter 296
Size focusing 286
Size tuning 306
SMAD 313
Small angle neutron scattering 129
Small angle X-ray 129
Small angle XRD 319
Small interfering RNA, siRNA 630, 632, 634, 642, 646, 648
Smart drugs 618
Smart fluid 744
Smoluchowski's formula 187
SNMS 177
Social scientists 769, 772, 773, 793
Societal aspects of nanotechnoscience 769, 770, 772
Soft lithography 301, 587
Solvated metal atom dispersion 313
Solvothermal 313
Solvothermal synthesis 224
Sonochemical 401
Spherical aberration 36
Spherical Bessel functions 258
Scanning probe lithography (SPL) 585
Stamp 574
Standard deviation 210

- Stanton number 760
Static light scattering 128
STEM 47
Stokes shift 158
Stokes-Einstein equation 197
Stokes-Einstein theory 739
Storage modulus 520
Strain broadening 127
Strained channel MOSFET 549
Stress-induced leakage current (SILC) 545
Strong-coupling 93
Structure factor 119, 130
Sulphides 107
Superconductivity 92
Superhydrophobic surfaces 372
Superhydrophobicity 184
Superlattices 311
Superparamagnetic iron oxide 608, 639
Superparamagnetism 603
Supramolecular interaction 312
Surface enhanced Raman scattering 336, 371
Surface plasmon 671
Surface plasmon resonance 284, 316
Surfactants 620, 630, 739, 740
Susceptibility 597, 598, 664
Suzuki reaction 714, 722, 727
Synchrotron radiation 98
Synthesis, general issues of concern 205
Synthesis of nanomaterials (table) 909
- Tantalum nitride (TaN) 547
Tantalum silicon nitride 547
Telechelic di-anion 505, 506
Telluride 395, 405, 406
Template mediated 381, 382
Tensile strained 549
Tensor components 664
TERS 166
Theragnostics 618, 650
- Therapeutic applications 624
Thermal analysis 197
Thermal broadening 92
Thermal conductivity 732–758
Thermal dispersion 756–758
Thermal scattering 674
Thermophoresis 756
Thermo-sensitive 509, 511
Thomson, J.J. 85, 176
Three photon absorption 670
Threshold frequency 85
Threshold temperature 744
Tight binding approximation 259
Time correlation function 271
Titanium nitride (TiN) 547
Titanium silicon nitride 547
Top down vs bottom up 556
Toxicity 482–484
Transient absorption 294
Transient hot-wire method 741
Transition dipole moment 192
Translation of nanomedicine 651
Transmission electron microscopy (TEM) 44, 293
Trapped carriers 676
Triple-gate SOI MOSFET 548
Tsallis statistics 278
Tungsten nitride 547
Tungsten silicon nitride 547
Two-photon absorption 294, 665, 669
- Ultra high vacuum 67, 86, 87, 194, 231, 915
Undulator 98
UV irradiation 487
- Valence band 85
Valence state 90
van der Waals force 395, 398, 740
van Hove correlation function 272

- Vapor phase 396
Vascular endothelial growth factor (VEGF) 627
Vibrational spectroscopy 191
Volume concentration 736
Volume fraction 744, 748
Voluntary reporting scheme 803
- Warburg impedance 145
Water-gas shift reaction 106
Water-oil interface 326
Wavelength dispersive spectrometry (WDS) 42
Weak-coupling 93
Wehnelt cap 33
Wenzel equation 183
Wet deposition 312
- Wet nanotechnology 7
Wiggler 98
Work function 85
- X-ray & neutron diffraction 121, 122
X-ray absorption spectroscopy (XAS) 97
- Young's modulus of a nanotube 51
Young-Dupre equation 183
- Zeta potential 187, 619
Zinc oxide, ZnO 635
Zisman plot 183, 184
ZrO₂ 542–544
Z-scan 677



Fig. 1.2 Faraday's gold preserved in Royal Institution (Source: <http://www.rigb.org/rimain/heritage/faradaypage.jsp>).



Fig. 1.3 The Lycurgus Cup made of glass appears red in transmitted light and green in reflected light. The glass contains 70 nm particles as seen in the transmission electron micrograph. The cup itself is dated to 4th century AD, but the metallic holder is a later addition. (Source: <http://www.thebritishmuseum.ac.uk>).

Plate 2

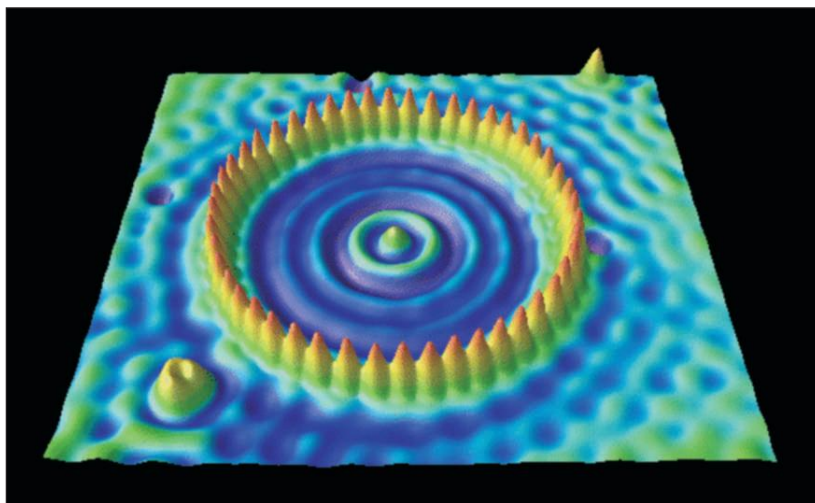


Fig. 3.6 Quantum corral made of 48 Fe atoms on a Cu(111) surface. Colour image taken from the website, <http://www.almaden.ibm.com/vis/stm/stm.html>. Original image was published in, M.F. Crommie, C.P. Lutz and E. Eigler, *Science*, 262 (1993) 218. (Copyright AAAS, Used with permission.).

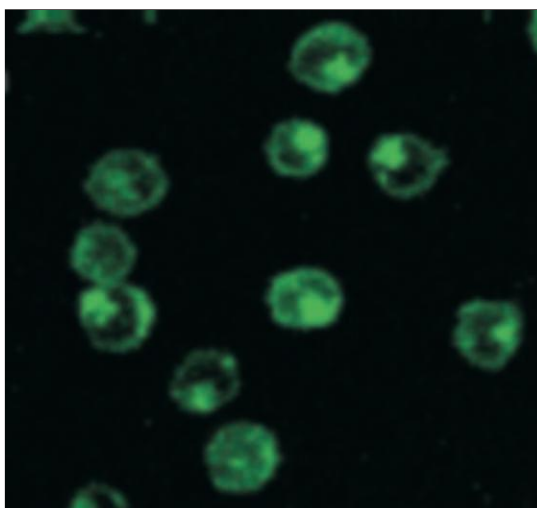


Fig. 3.11 Confocal fluorescence image of human promyelocytic leukemia (HL 60) cells after incubation with fluorescein isothiocyanate labeled single wall carbon nanotube solution for 1 h. The image shows that nanotubes have been delivered into the cells (Source: Nadine Wong Shi Kam, Theodore C. Jessop, Paul A. Wender, and Hongjie Dai, *J. Am. Chem. Soc.*, 2004; 126(22); 6850–51.).

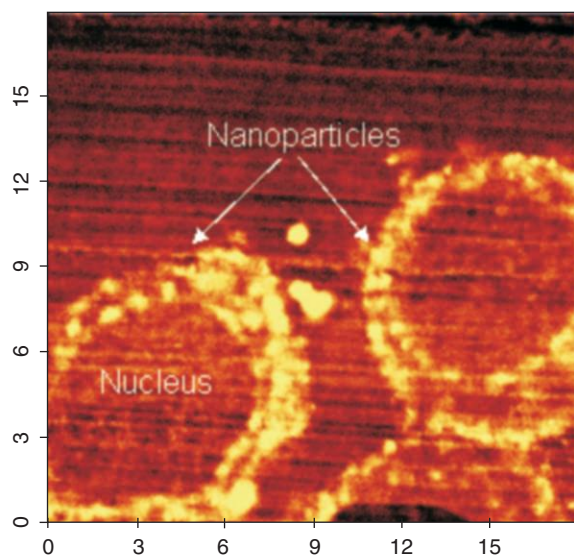


Fig. 3.13 SNOM image of SiHa cells incubated with gold ions showing the formation of nanoparticles in the cytoplasm (from the author's work).

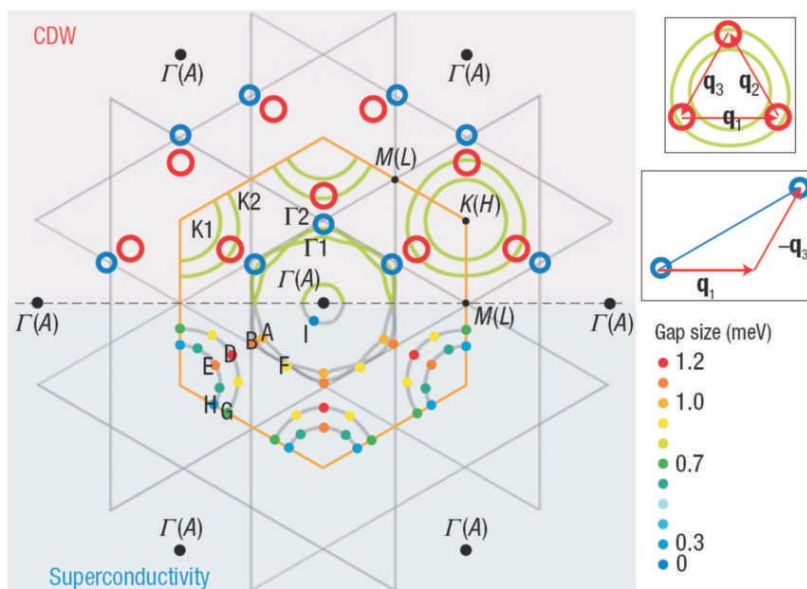


Fig. 4.8 Mapping of special k -points corresponding to CDW (upper half) and k -dependent superconducting gap (lower half). The experimentally determined Fermi Surfaces (green curves) show primary CDW vectors (q_1, q_2, q_3) connect red circles, while blue circles are connected by secondary CDW vectors ($q_i \pm q_j$) with $i, j = 1, 2, 3$. Superconducting gap values are mapped with a colour scale in the lower half of the figure (from Ref. 23).

Plate 4

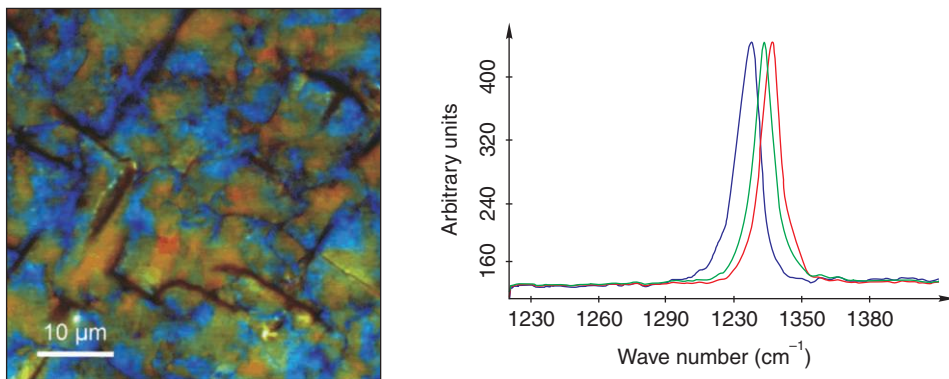


Fig. 8.11 Raman micrograph of a CVD grown diamond film. The spectra from various regions are shown on the right. Spectra of different colours are used to construct the images of the same colours (data and image are with the courtesy of, www.witec.de.).

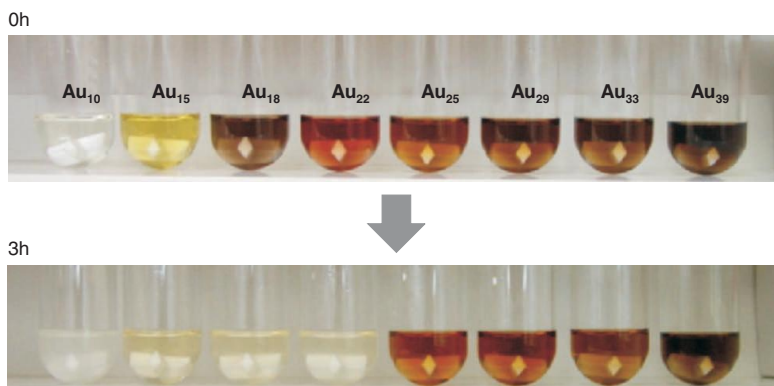


Fig. 11.3 Colour changes of aqueous solutions of $Au_n(SG)_m$ QCs with $(n, m) = (10,10), (15,13), (18,14), (22,16), (25,18), (29,20), (33,22)$ and $(39,24)$ before (0 h) and after (3 h) reaction with GSH (reprinted with permission from Small, 3 (2007) 835. Copyright (2009) John Wiley & Sons).

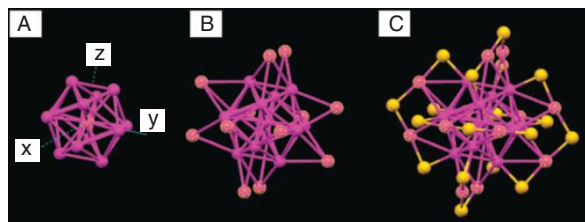


Fig. 11.6 Crystal structure of a $Au_{25}(SR)_{18}$ (R is phenylethyl group): (A) the icosahedral Au_{13} core; (B) the Au_{13} core covered by additional 12 Au atoms; (C) the whole Au_{25} is protected by 18 thiolate ligands (for clarity, only S atoms are shown, magenta, Au; yellow, S) (reprinted with permission from J. Am. Chem. Soc., 130 (2008), 5883. Copyright (2008) American Chemical Society).

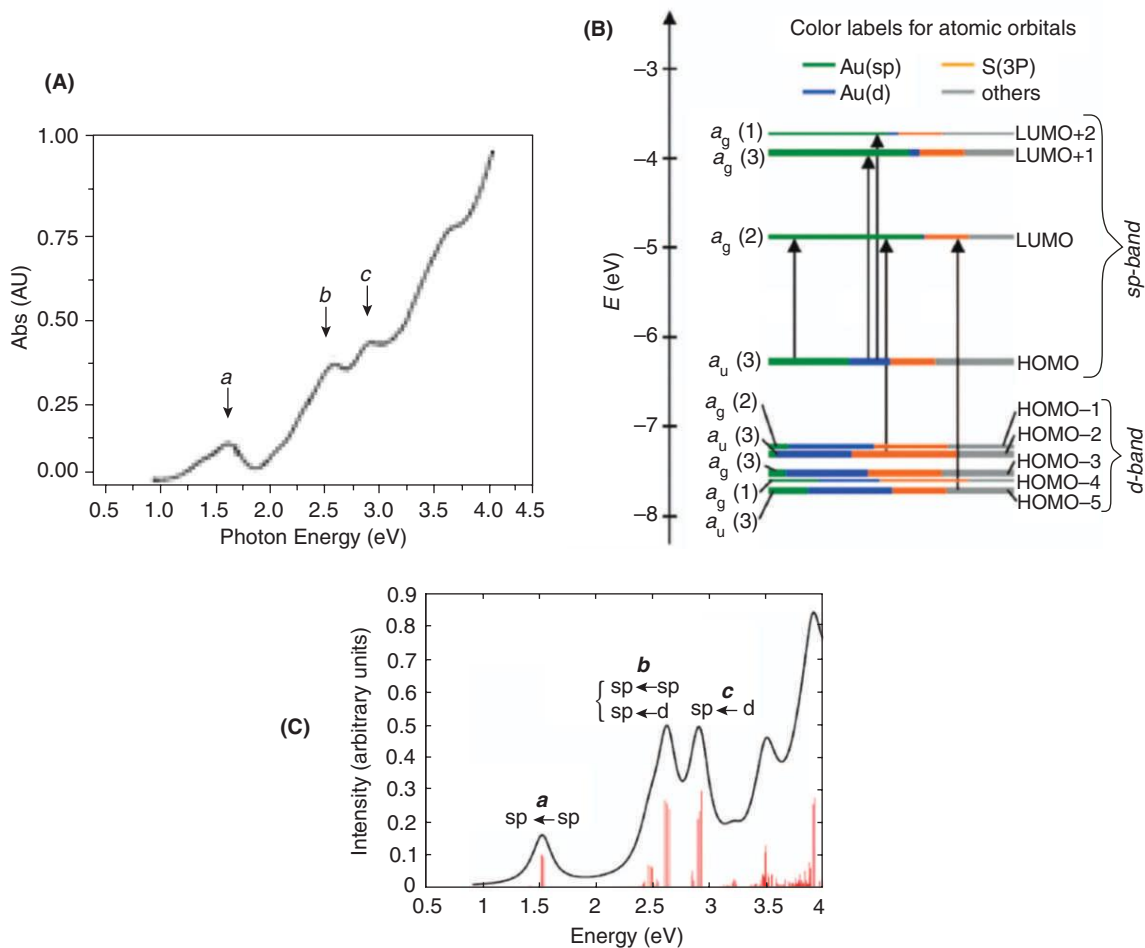


Fig. 11.7 (A) The absorption spectrum of $\text{Au}_{25}(\text{SH})_{18}^-$. (B) Kohn-Sham orbital energy level diagram for $\text{Au}_{25}(\text{SH})_{18}^-$. (C) The theoretical absorption spectrum of $\text{Au}_{25}(\text{SH})_{18}^-$. Peak assignments: peak a corresponds to 1.8 eV (observed), peak b corresponds to 2.75 eV (observed), and peak c corresponds to 3.1 eV (observed) (adapted from Ref. 25. Reprinted with permission from *J. Am. Chem. Soc.*, 130 (2008), 5883. Copyright (2008) American Chemical Society).

Plate 6

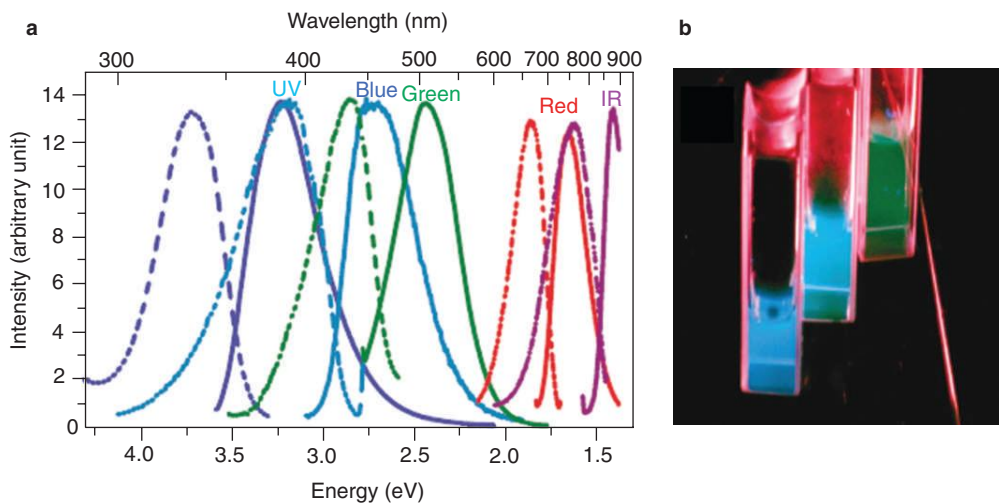


Fig. 11.8 (a) Excitation (dashed) and emission (solid) spectra of different Au QCs. Excitation and emission maxima shift to longer wavelength with increasing QC size. (b) Appearance of the three shortest wavelength-emitting Au QC solutions (from left to right) under UV irradiation (366 nm) (reprinted with permission from *Phys. Rev. Lett.*, 93 (2004), 077402. Copyright (2004) American Physical Society).

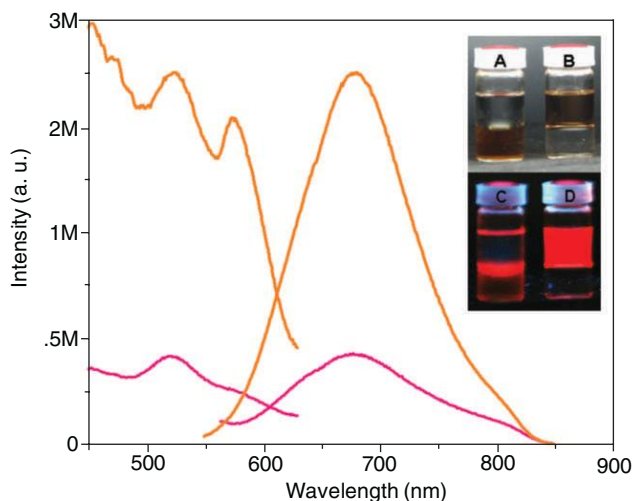


Fig. 11.10 Photoluminescence profile of Au₂₃ before (pink trace) and after (orange trace) phase transfer. Emission of the QC enhances considerably after phase transfer. Photographs of the aqueous-toluene mixture containing the QC before and after phase transfer under white light (A and B, respectively) and UV light (C and D, respectively). In C, only the interface is illuminated as the UV radiation is attenuated as the sample was irradiated from the top (reprinted with permission from *Chem. Eur. J.*, 15 (2009), 10110. Copyright (2009) John Wiley & Sons).

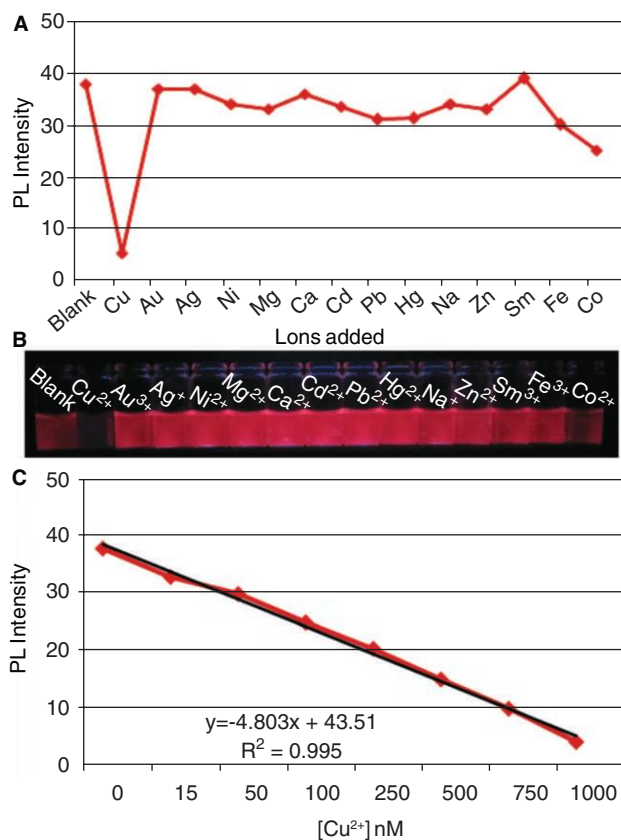


Fig. 11.11

(A) Plot of photoluminescence (PL) intensity of Au_{QC}@BSA in the presence of various metal ions. (B) Photographs of aqueous solutions of the QC in the presence of the corresponding ions under irradiation by UV light. (C) Plot of PL intensity of the QC as a function of [Cu²⁺] ($y = -4.803x + 43.51$ and $R^2 = 0.995$) (reprinted with permission from Chem. Eur. J. 16 (2010), 10103. Copyright (2010) John Wiley & Sons).

Plate 8

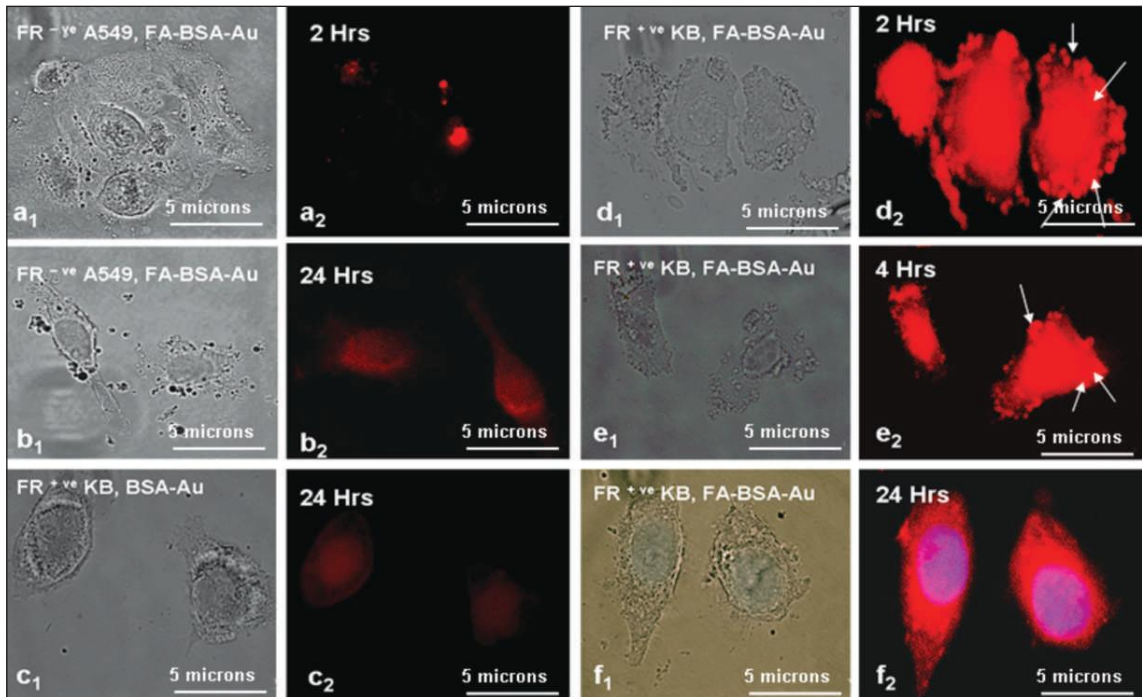


Fig. 11.13 Luminescent microscopic images showing interaction of Au-BSA-FA QCs with different types of cell lines: (a1 and a2) FR-ve lung carcinoma A549 after 2 h of incubation; (b1 and b2) FR-ve lung carcinoma A549 after 24 hours of incubation; (c1 and c2) FR+ve KB cells with unconjugated Au QCs, (d1 and d2) FR+ve KB cells with FA conjugated Au QCs at 2 h; (e1 and e2) 4 h and (f1 and f 2) 24 h of incubation (reproduced with permission from Archana, R., S. Sonali, M. Deepthy, R. Prasanth, Habeeb Muhammed, T. Pradeep, S. Nair, and K. Manzoor, *Nanotechnology*, 21 (2010), 055103. Copyright (2010) IOP publishing Ltd).

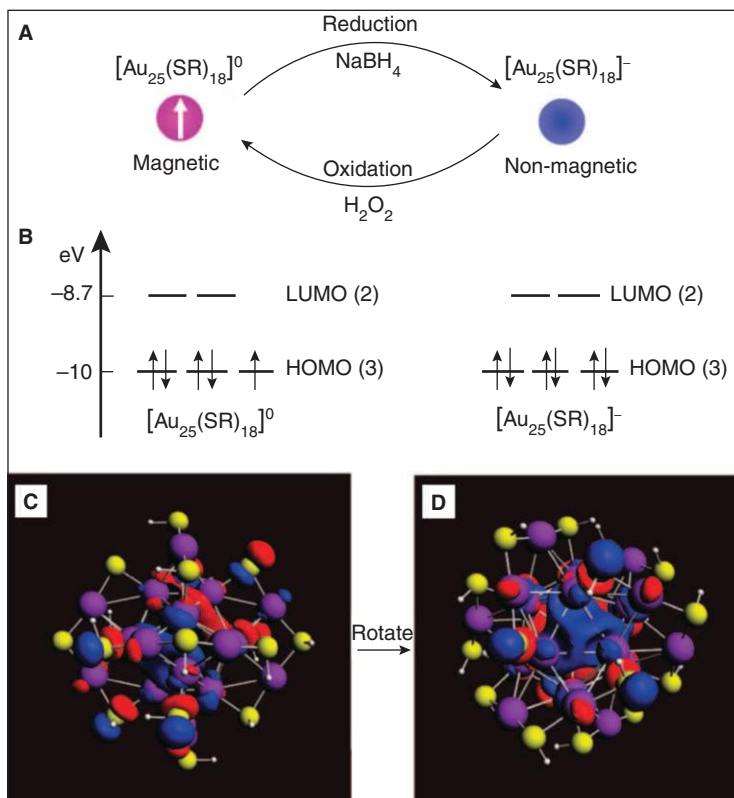


Fig. 11.14

(A) Reversible conversion between the neutral and anionic Au_{25} . (B) DFT-calculated Kohn-Sham orbital energy level diagrams for the neutral and anionic Au_{25} , respectively. (C and D) Views of the Kohn-Sham HOMO for $[\text{Au}_{25}]^0$. The HOMO possesses two lobes and exhibits distinct P-like character. (D) is rotated relative to (C) to show one of the lobes (contributed by three Au atoms in the icosahedral shell). Colour code: purple, Au; yellow, S; white, H (reprinted with permission from *J. Am. Chem. Soc.*, 131 (2009), 2490. Copyright (2009) American Chemical Society).

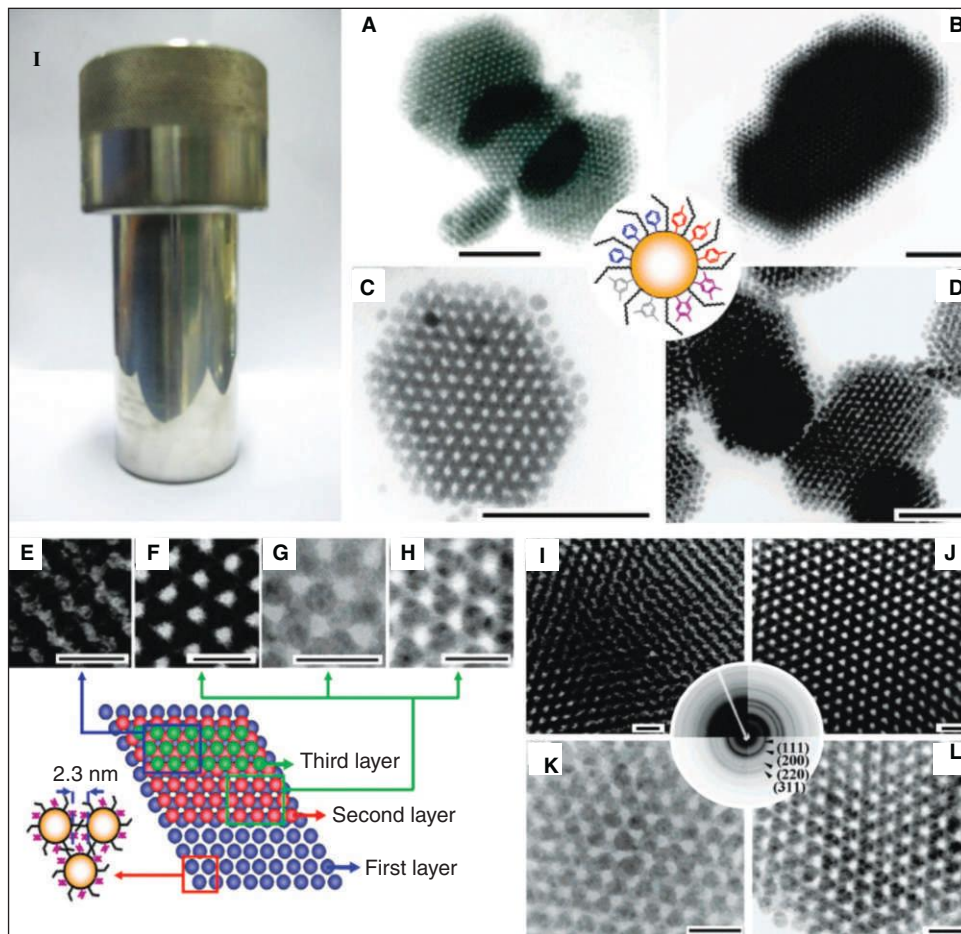


Fig. 12.2 (I) Photograph of a hydrothermal bomb. (A–D) TEM images and schematic drawing of Ag nanoparticles capped with a mixture of two capping molecules, sodium oleate and aromatic carboxylic acid; (A) benzoic acid (blue), (B) 1,4-benzenedicarboxylic acid (red), (C) 1,3,5-benzenetricarboxylic acid (grey), and (D) 1,2,4,5-benzenetetracarboxylic acid (violet). All scale bars represent 97 nm. (E–L) High-resolution TEM images and corresponding electron diffraction patterns of all the above four SLs, respectively. Schematic representation of Ag nanoparticles with two different capping molecules, view of the topology of one, two and three layers of Ag nanoparticles with mixture of capping molecules are also shown (adapted from Ref. 42).

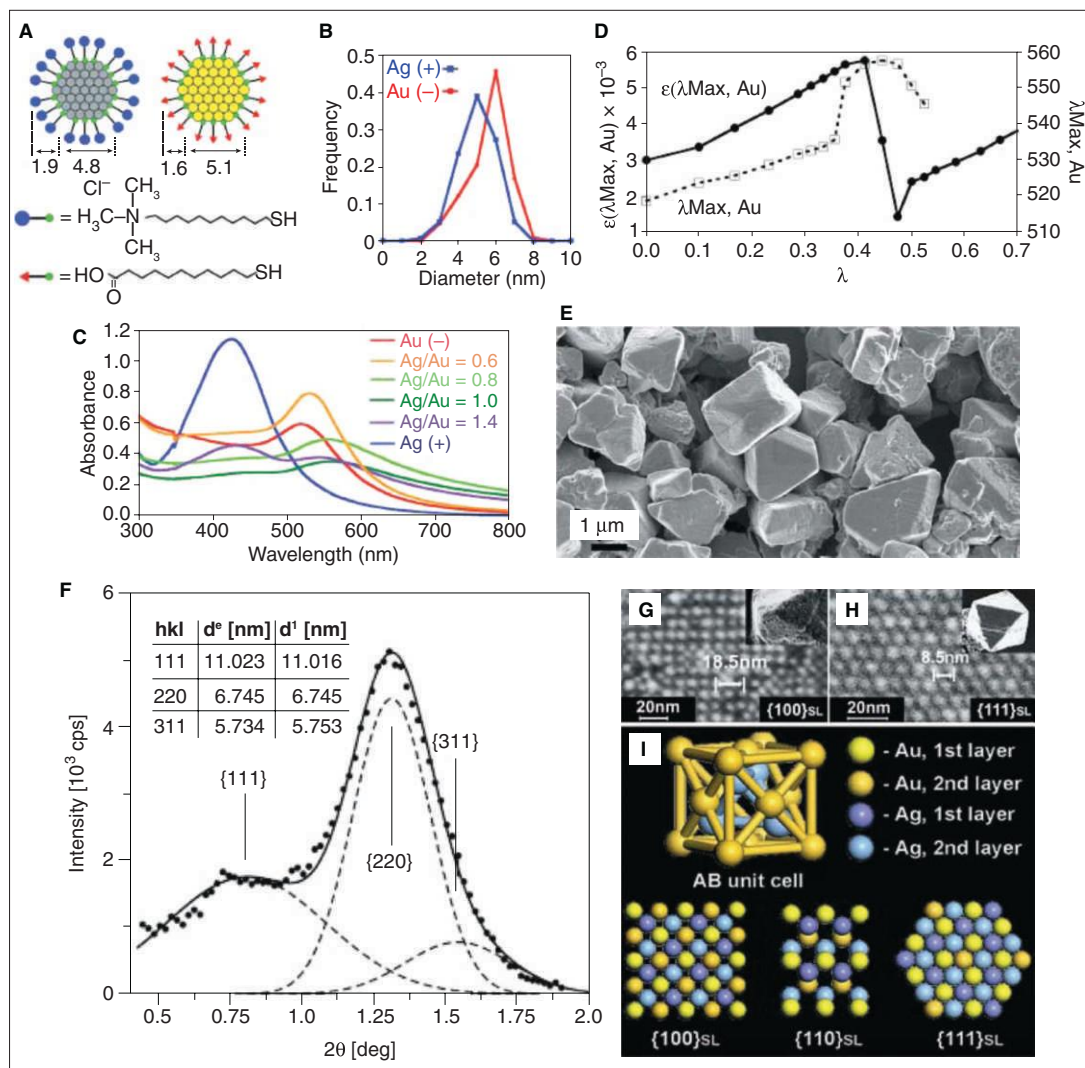


Fig. 12.5 (A) Scheme and average dimensions (in nm) of Au@MUA and Ag@TMA nanoparticles used as the model system. (B) Experimental, normalised size distributions of metallic cores of Ag and Au NPs (C) Typical UV-Vis spectra for the titration of Au@MUA solution with small aliquots of Ag@TMA solution. (D) (Solid curve) Progress of the titration represented by absorption coefficient $\epsilon(\lambda_{\text{Max}}, \text{Au})$. (E) Large-area SEM image of binary crystals obtained from Au@MUA/Ag@TMA precipitates. (F) Small-angle powder XRD spectrum of the crystals. Bragg's reflections specified by Miller indices shown are characteristic of a diamond-like structure. (Inset) Comparison between experimental (d^e) and theoretical (d^t) spacing between crystal planes with Miller indices $\{hkl\}$. (G) An SEM image of a $\{100\}_{\text{SL}}$ square face taken from a twinned octahedron crystal (inset). (H) An SEM image of a $\{111\}_{\text{SL}}$ plane of a triangular face of an octahedron (inset) with estimated interparticle distance of 8.5 nm. (I) Scheme of an AB unit cell and the projections of $\{100\}_{\text{SL}}$, $\{110\}_{\text{SL}}$, $\{111\}_{\text{SL}}$ planes (adapted from Ref. 12).

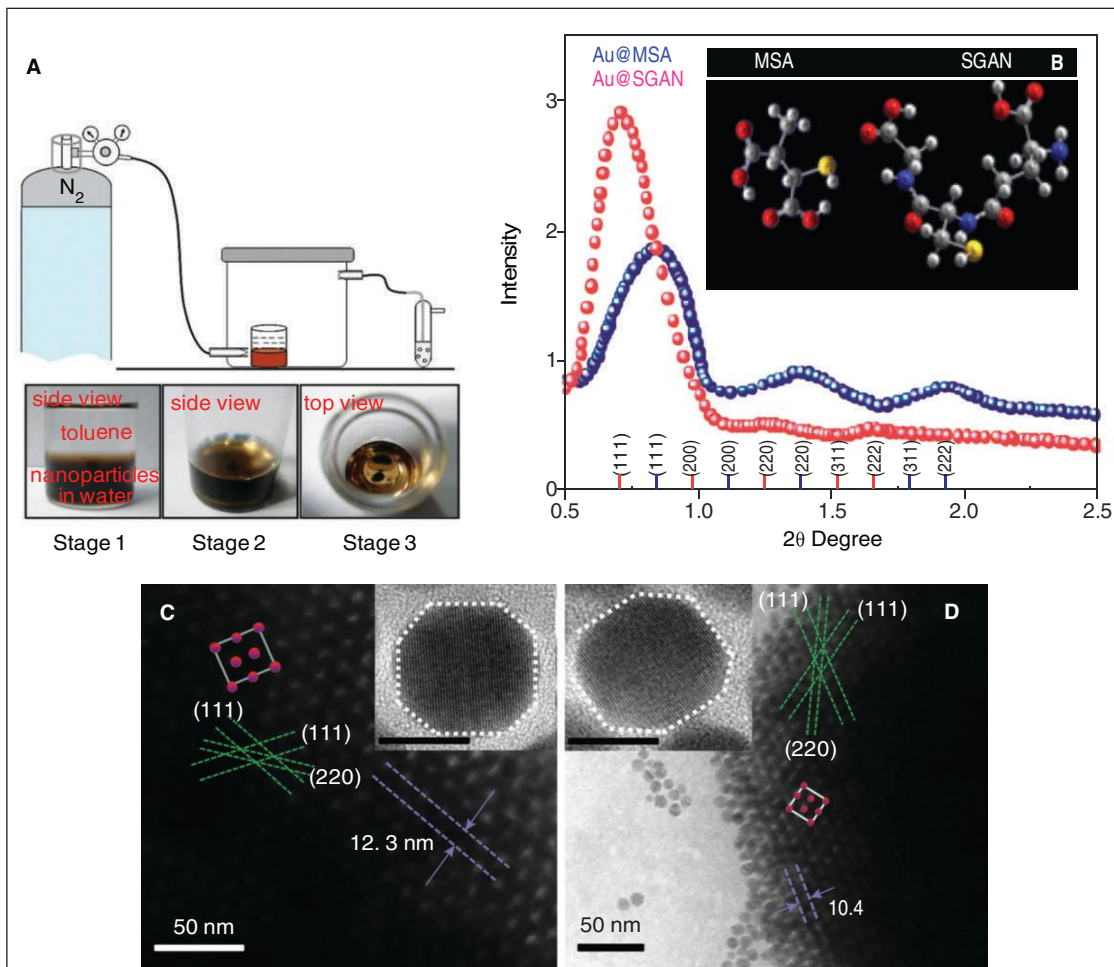


Fig. 12.8 (A) Cartoon representation of the setup used for the SL Formation. The photographs show different stages of crystal formation (stage 1 and 2). The top view of the SL crystals (stage 3) clearly shows a continuous film at the interface. (B) Background and baseline corrected intensity vs 2θ data of Au@SGAN and Au@MSA SLs, respectively. The indexing is done for a fcc unit cell in both cases. The inset shows the energy minimum structure of MSA and SGAN. (C and D) HRTEM images of Au@SGAN and Au@MSA SLs, respectively. The inset of each figure shows the truncated octahedral shape of the nanoparticles with $\{100\}$ and $\{111\}$ facets (adapted from Ref. 40).

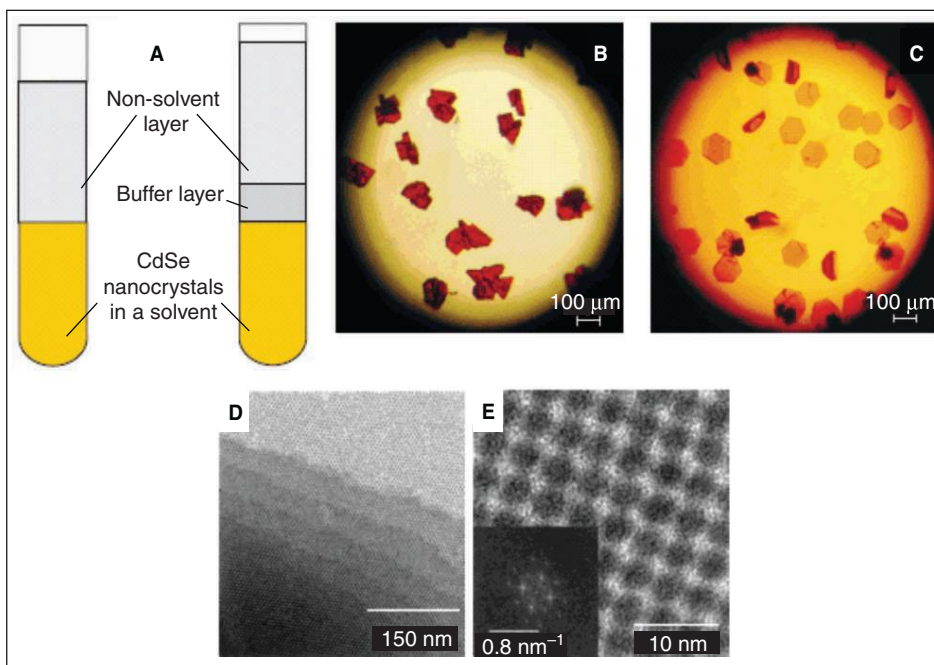


Fig. 12.10 (A) Cartoon representation of the concept of the nucleation procedure. Left tube: The non-solvent (methanol) diffuses directly into a dispersion of CdSe nanocrystals in toluene. Right tube: A buffer layer of propan-2-ol slows down the diffusion of methanol. (B and C) Optical micrographs of colloidal crystals of CdSe nanocrystals taken by a digital camera through the objective of an optical microscope. (B) Faster nucleation, irregular shaped crystals and (C) slower nucleation and perfectly faceted hexagonal platelets. Transmission electron microscopy images of a 3-D arrangement of the 3.5 nm CdSe nanocrystals. (E) Overview of a fcc-like superlattice (adapted from Ref. 29).

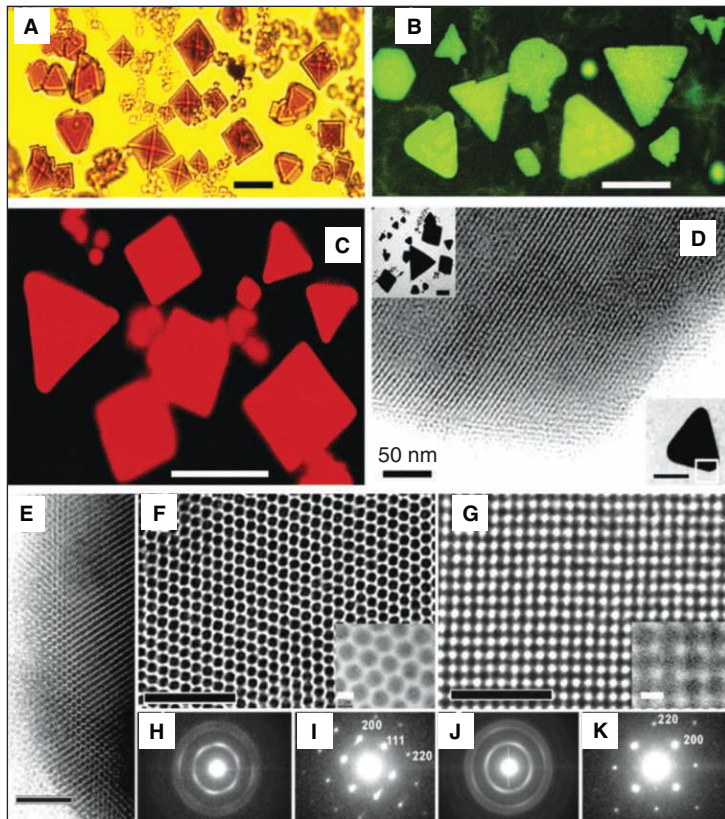


Fig. 12.11 (A) optical transmission micrograph of three-dimensional, faceted SLs formed from 5.3 nm NC solution; (B) and (C) fluorescence microscope images of crystals obtained, respectively, from 3.5 and 5.3 nm NCs; (D) TEM image taken from the edge of a colloidal crystal formed from 5.3 nm CdSe NCs. (E) typical image of a crystal edge; (F and G) $\langle 110 \rangle$ and $\langle 100 \rangle$ projections obtained in the thin areas close to the edges (H and I) show partial alignment of NCs within an fcc superlattice identified by small-angle electron diffraction (J and K) (adapted from Ref. 45).

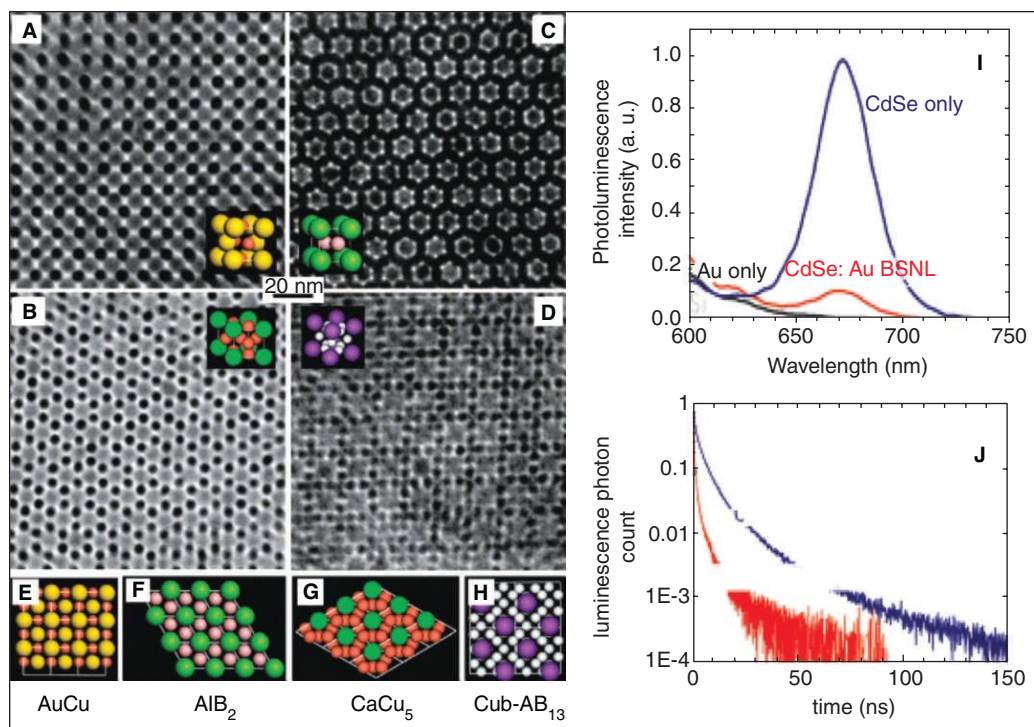


Fig. 12.13 TEM images of (001) projections of BSNLs self-assembled from 8.7 nm CdSe and 5.5 nm Au NCs and isostructural with (A) AuCu, (B) AlB₂, (C) CaCu₅ intermetallic compounds and (D) cub-AB₁₃. Insets in (A–D) depict the unit cells of subsequent structures. (E–H) Modeled (001) projections of AuCu, AlB₂, CaCu₅, and cub-AB₁₃ lattices, respectively. (I) Time-integrated fluorescence spectra and (J) time-resolved fluorescence transients of a close-packed CdSe NCs-only superlattice (blue curves) and of a BSNL of CdSe and Au NCs (red curves). Integrated fluorescence spectra of the Si substrate and of a superlattice of Au NCs are also shown in (I) (adapted from Ref. 47).

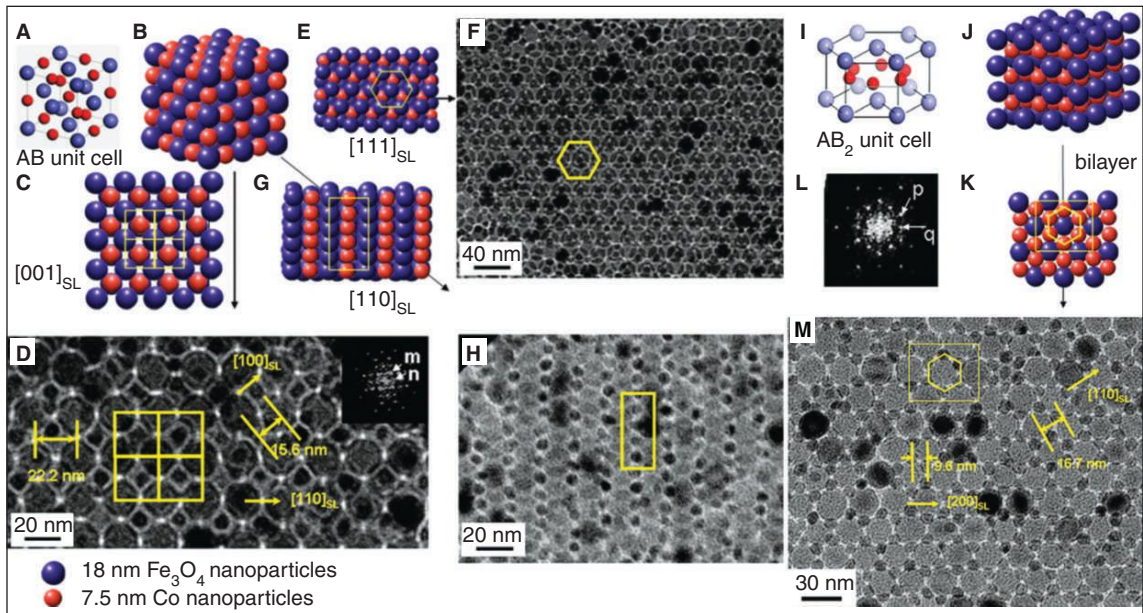


Fig. 12.17 (A and B): The unit cell (A) and the extended cell (B) of the NaCl type AB binary structure. (C–H): TEM images of our binary SLs (D, F and H) and the corresponding AB structure (C, E and G). (I–K): Figures of the unit cell (I), the extended cell (J) and bilayers along c axis (K) of the hexagonal AB_2 binary structure. (L) Small-angle electron diffraction (SAED) pattern of AB_2 bilayers. (M) TEM image of our AB_2 SLs (adapted from Ref. 51).

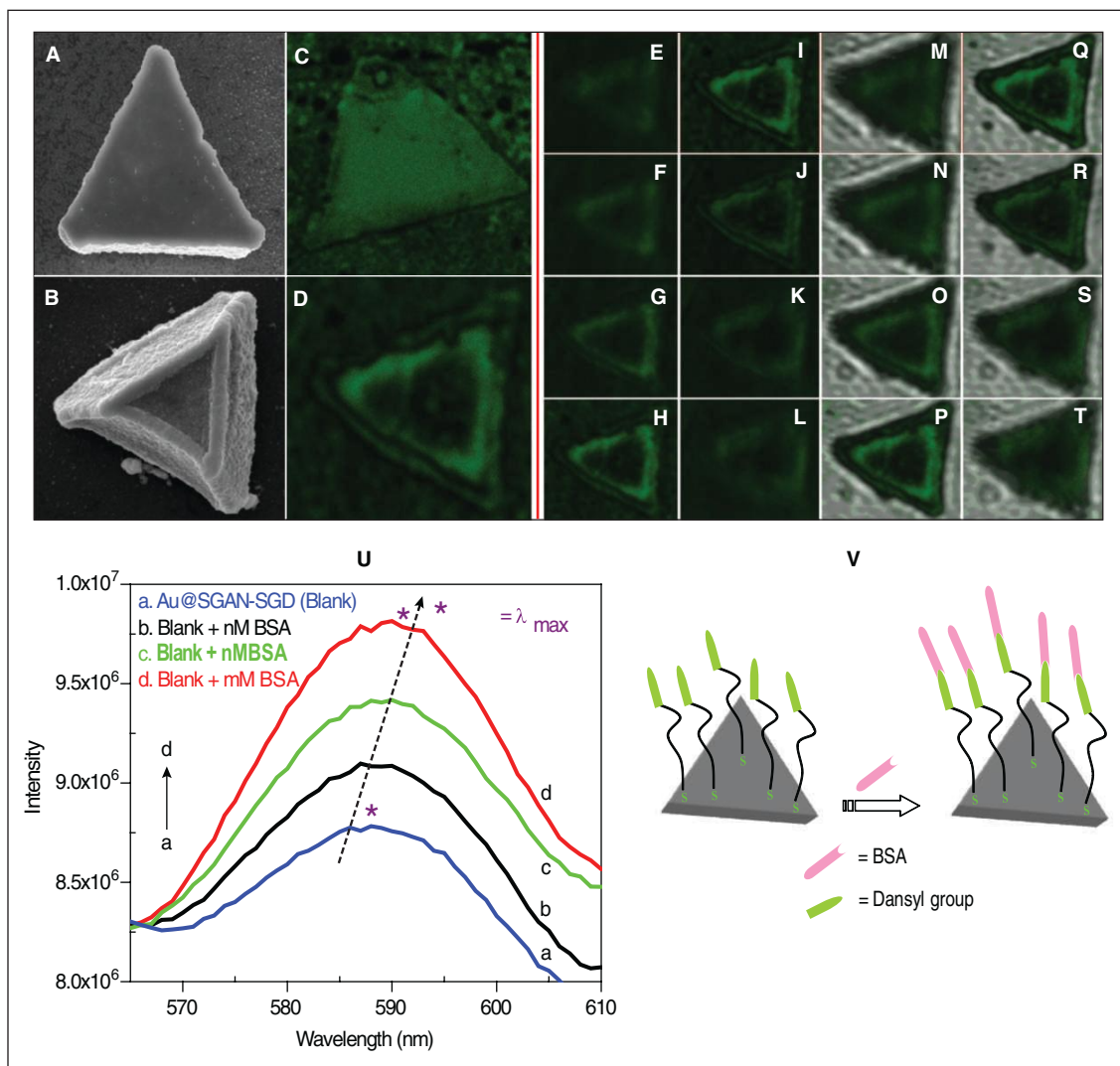


Fig. 12.19 (A–D): The two different morphological crystals of Au@SGAN/AGD and their corresponding fluorescence images. (E–T): The inverted confocal fluorescence images and corresponding overlay structure of triangle 2. (U) Fluorescence spectra of Au@SGAN/SGD superlattice film during the course of fluorimetric titration with different concentrations of BSA; a, blank; b, nM; c, μ M and d, mM. The excitation wavelength was 330 nm. The spectra show a bathochromic shift from 587 to 592 nm. (V) Schematic representation of the specific binding of the naphthalene ring with BSA (adapted from Ref. 39).

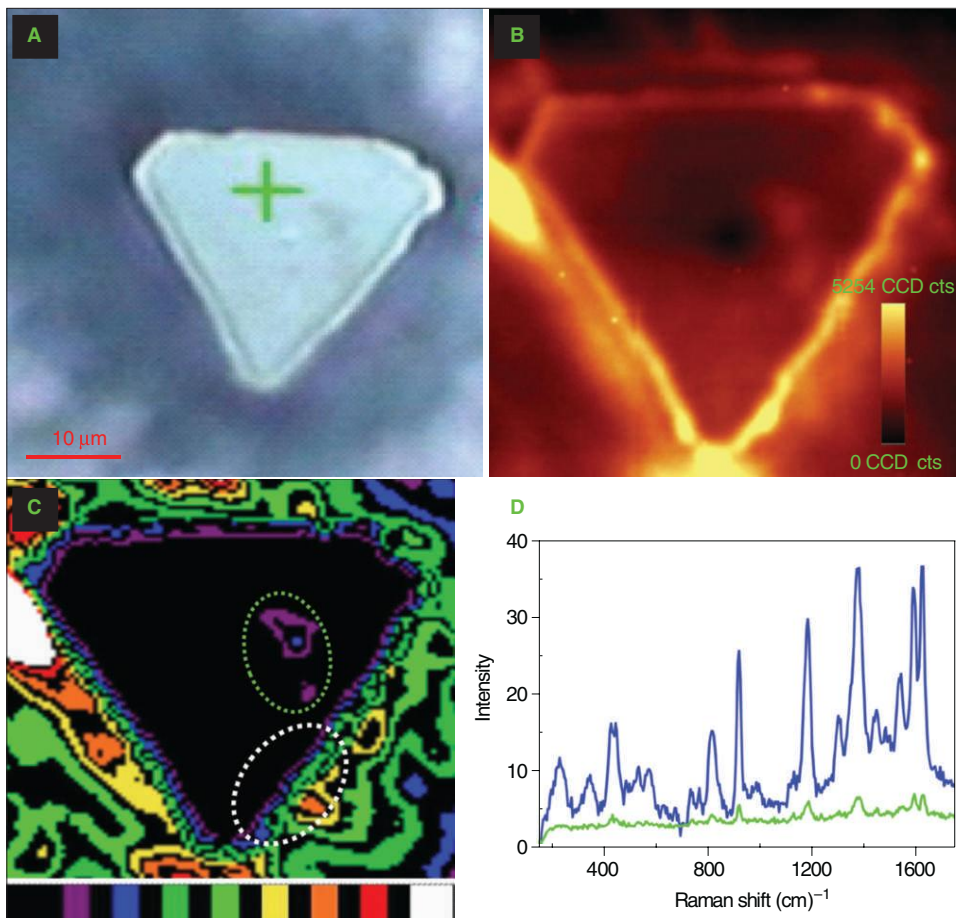


Fig. 12.20 (A) Optical image (under white light illumination) of the Au@MSA SL triangle. (B) Raman image of the same crystal (at 514.5 nm excitation) collected from an area of $12\ \mu\text{m} \times 12\ \mu\text{m}$ using the intensities of CV features in the $200\text{--}2000\ \text{cm}^{-1}$ window. The concentration of CV exposed was $10^{-5}\ \text{M}$. (C) Colour coded Raman image of Au@MSA SL triangle shown in part A. The intensity is in the order: green>blue>pink>black. (D) Raman spectra collected from the edge (blue) and surface (green) of the crystal shown in part B (adapted from Ref. 40).

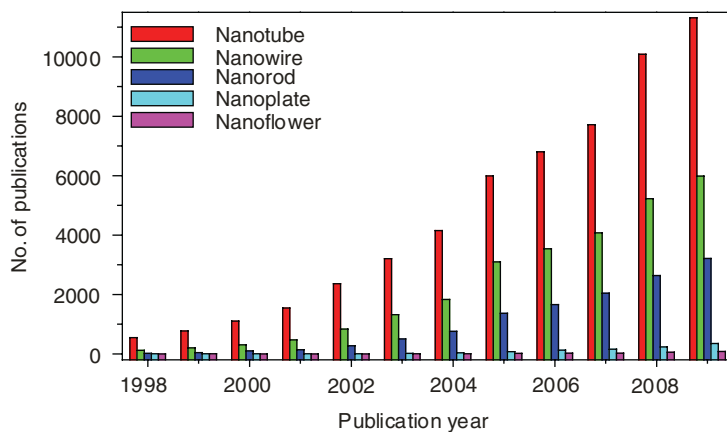


Fig. 13.3 Time evolution of the number of papers published during the last decade (1998–2009), including certain keywords (as indicated) in their title (source: ISI Web of Science).

Plate 20

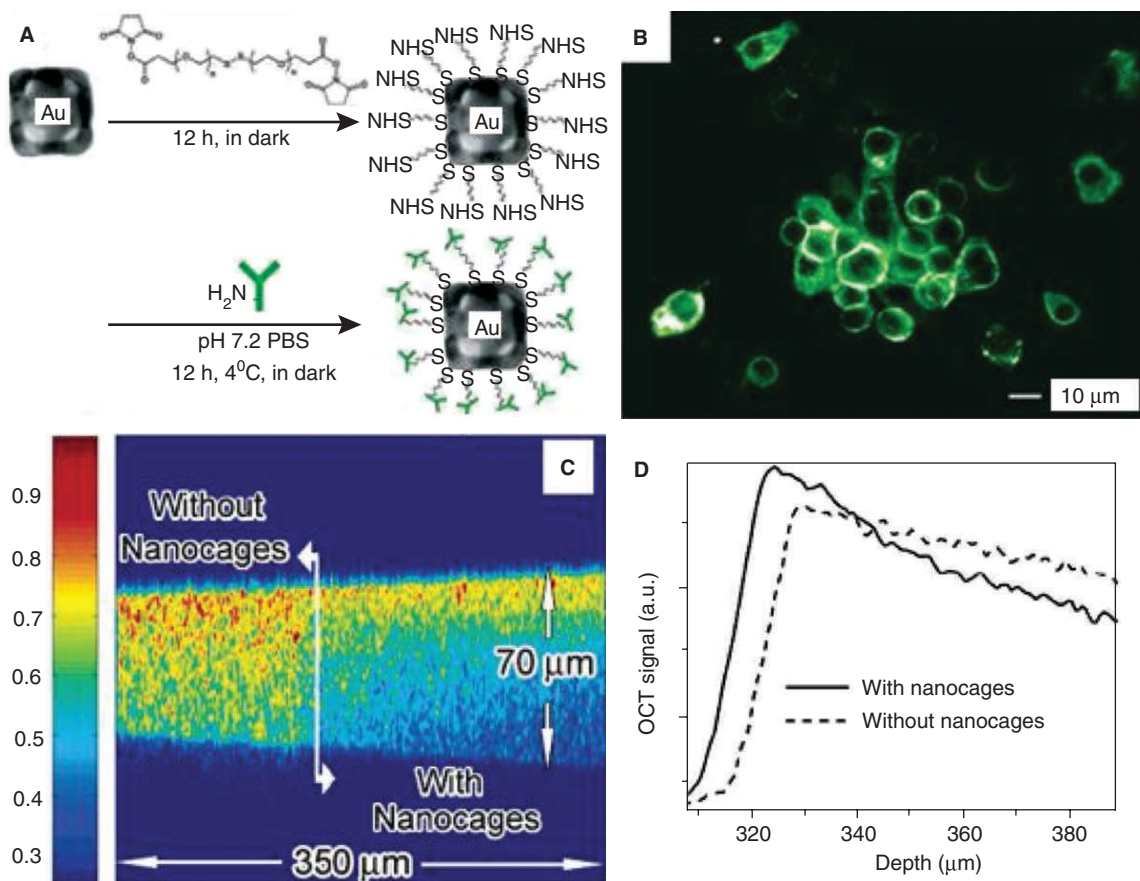


Fig. 13.21 (A) Schematic illustration of the protocol used to conjugate antibodies to the surface of Au nanocages. (B) A fluorescence image of SK-BR-3 cells whose surfaces were treated with the anti-HER2 antibodies, followed by incubation with fluorescence-labeled IgG (adapted from Ref. 71. Copyright (2007) Wiley). (C) OCT image of a gelatin phantom embedded with TiO₂, and the concentration of TiO₂ was controlled at 1 mg/mL to mimic the background scattering of soft tissues. (D) Plots of the OCT signals on a log scale as a function of depth (adapted from Ref. 70. Copyright (2005) American Chemical Society).

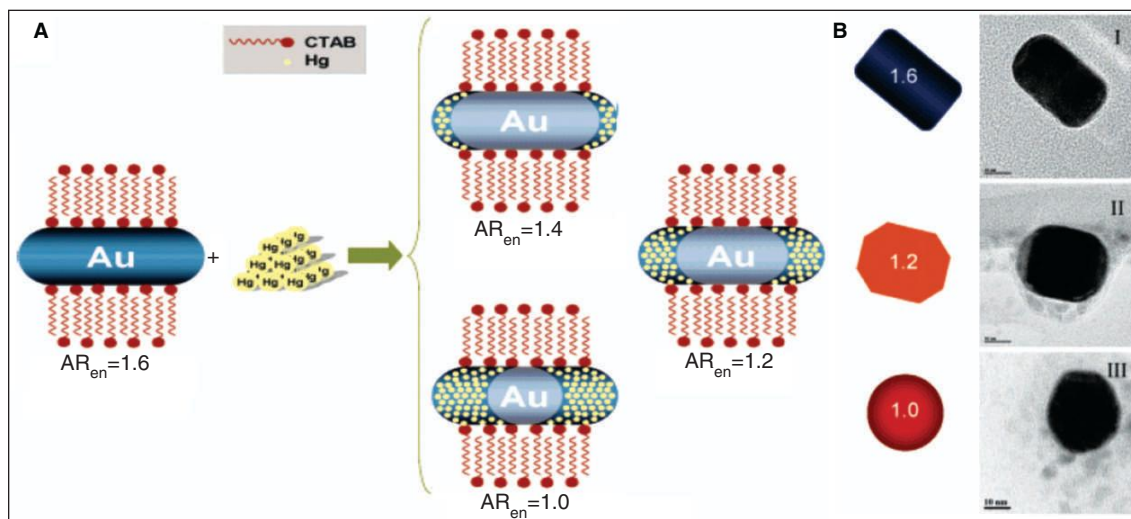


Fig. 14.10 (A) Schematic representation of the amalgamation of Hg with gold nanorods. (B) TEM images of gold nanorods in the absence and the presence of Hg. I) no Hg; II) $1.25 \times 10^{-5} M$ and III) $1.57 \times 10^{-4} M$ of Hg^{2+} (reprinted with permission from Rex, et al. (Ref. 39). Copyright (2006) American Chemical Society).

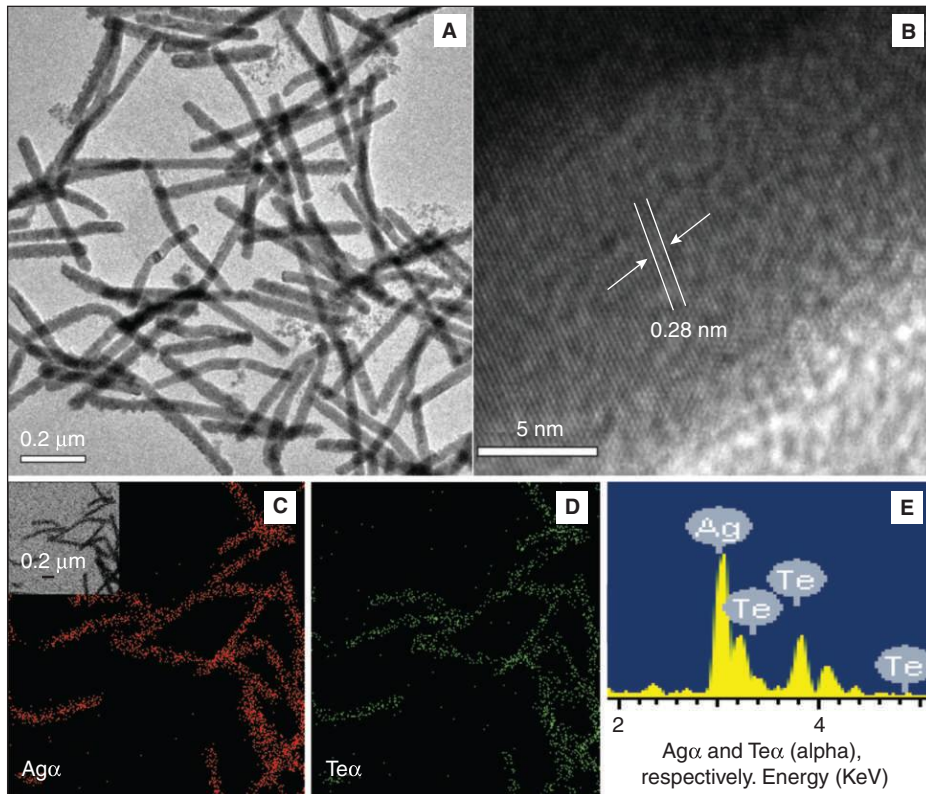


Fig. 14.21

(A) Large area TEM image of Ag_2Te nanowires, (B) lattice resolved HRTEM of a single Ag_2Te nanowire, (C) elemental mapping using Ag and (D) Te and (E) EDAX spectrum of Ag_2Te nanowires. The TEM image corresponding to the elemental maps of C and D is shown in the inset of C (reprinted with permission from Samal, et al. (Ref. 68). Copyright (2008) American Chemical Society).

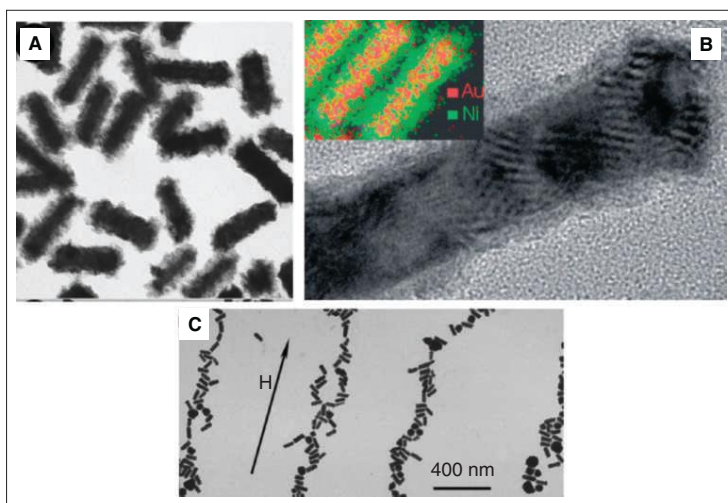


Fig. 15.24 (A) Large area TEM of nickel coated GNRS in the absence of magnetic field. (B) High magnification image of a single Au@Ni NR. Inset shows STEM-XEDS analysis of Au@Ni NRs, showing the relative distribution of the elements (Au = red; Ni = green). (C) Au@Ni NRs, dried on the TEM grid under an external magnetic field (0.2 T) (adapted from Liz-Marzán, et al. (Ref. 36). Copyright (2007) by the John Wiley & Sons, Inc.).

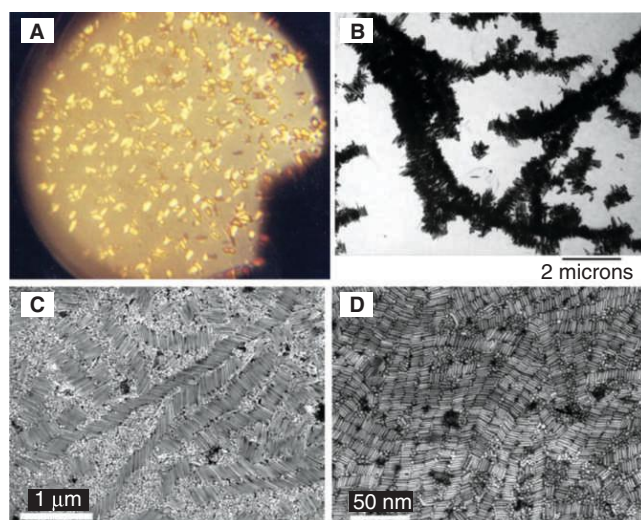


Fig. 15.25 (A) Polarising light microscope image of 5–10 wt% concentrated gold nanorods (B) TEM image of ~5–10 wt% dispersion, showing linear stacks of gold nanorods (adapted from Murphy, et al. (Ref. 37). Copyright (2002) by the Royal Society of Chemistry, London). (C) and (D) SEM images of gold nanorod self-assemblies with different aspect ratios through self-selective behaviour (adapted from Gao, et al. (Ref. 38). Copyright (2006) by Elsevier B.V.).

Plate 24

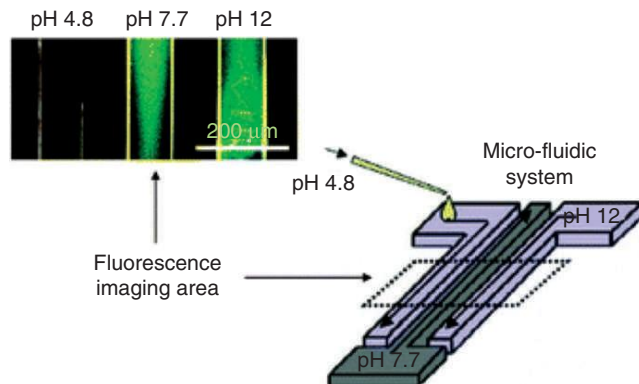


Fig. 17.9 The fluorescence image of the microfluidic device with region marked with dots shows pH dependence. The device was charged with solutions of pH 4.8, 7.7 and 12 (reprinted from Ref. 5. Copyright (2005) Royal Society of Chemistry).



Fig. 19.2 Break-junction setup: a very narrow contact is stretched by flexing the support until single atom makes the contact (adapted from a website (ref. 7)).



Fig. 20.5 A clean room for lithography usually hosts a self-contained infrastructure. Commonly seen facilities are spin-coater, mask aligner, photolithography stage, lamellar chemical hood, physical vapor deposition unit, microscopes, etc. (reproduced from ref. 7).

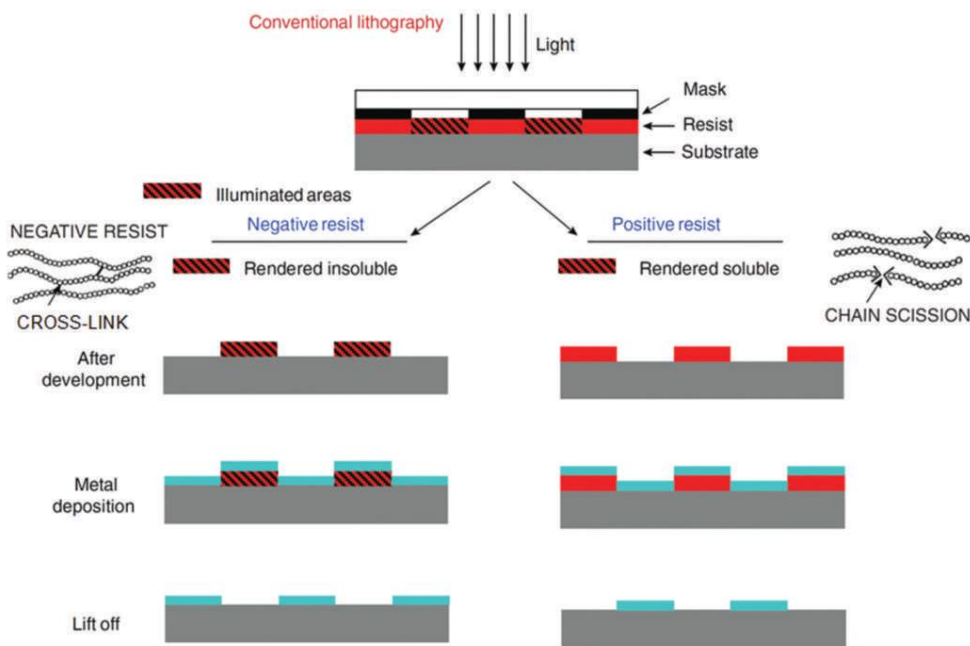


Fig. 20.6 A typical photolithographic procedure adopted to get metal patterns by lift off process.

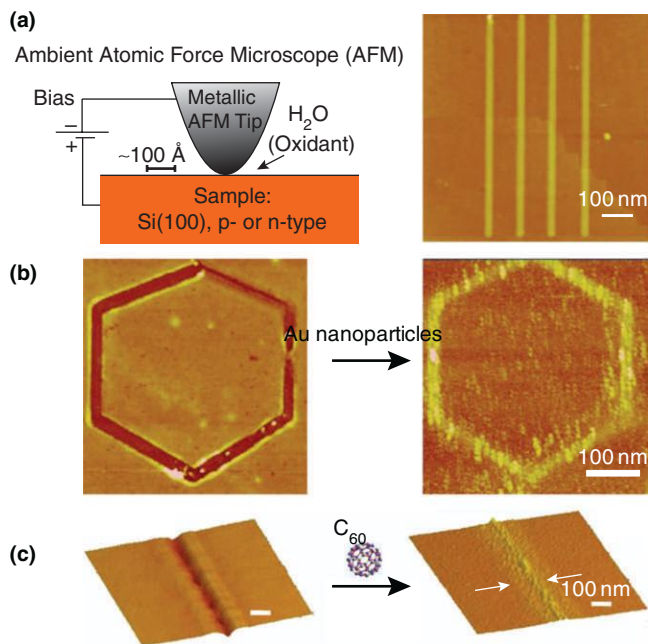


Fig. 20.12 (a) Local anodic oxidation (LAO) patterning using a conducting AFM setup. Electrostatic nanolithography to cut nanotrenches in a polymer film to selectively fill in (b) Au nanoparticles and (c) fullerene molecules. The arrows on the right image in (c) point to chemical adsorption of fullerene on extended regions of the trench (reproduced from refs. 21 and 22).

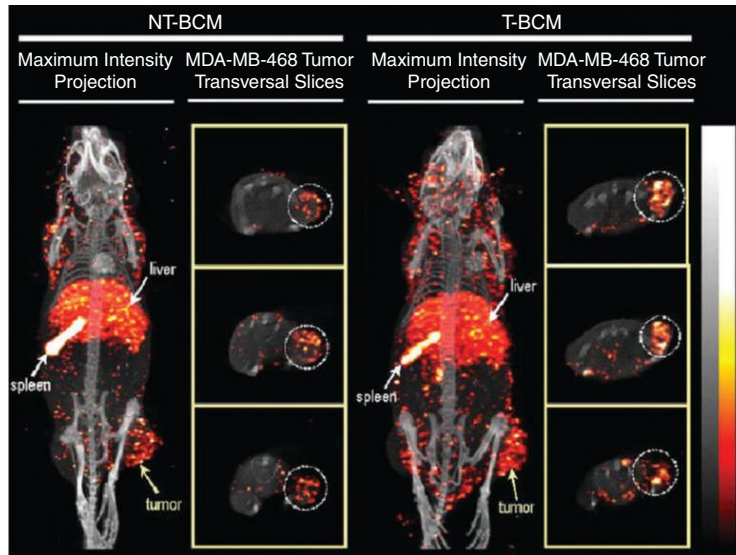


Fig. 22.9 *MicroSPECT/CT images illustrating the whole body biodistribution of the non-targeted block copolymer micelles (NT-BCM) and targeted block copolymer micelles (T-BCM) labeled with ¹¹¹Indium, in MDA-MB-468 tumor-bearing mice. The images were acquired at 48 h post injection.*

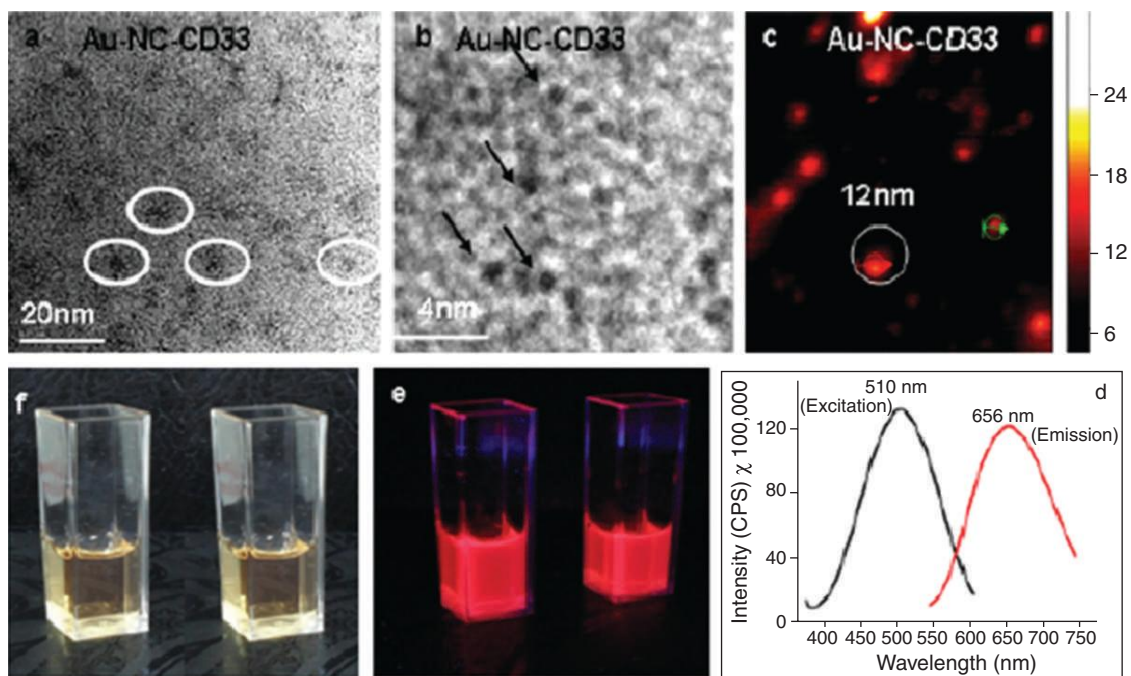


Fig. 22.11 (a) TEM image of Au-NC-CD33 showing nanoclusters of 10–12 nm size, (b) a higher magnification TEM image showing <1 nm sized spherical nanoclusters, (c) AFM image of Au-NC-CD33 showing spherical aggregates of size 12 nm, (d) fluorescence spectra of Au-NC-CD33 showing a peak maximum at 510 nm and the emission peaking at 656 nm and extending up to 800 nm, (e) red fluorescence emitted by Au-NCs and Au-NC-CD33 excited with 365 nm hand-held UV, (f) Au-NCs and Au-NC-CD33 under visible light.

Plate 28

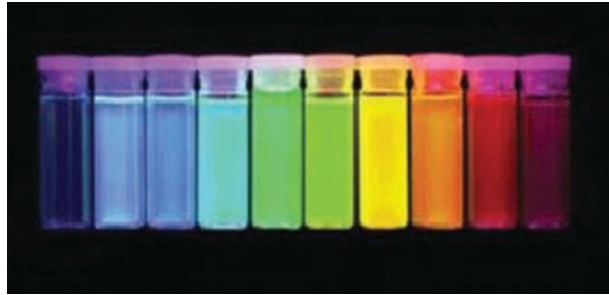


Fig. 22.20 *Bioconjugated quantum dots as contrast agent for tumor imaging.*

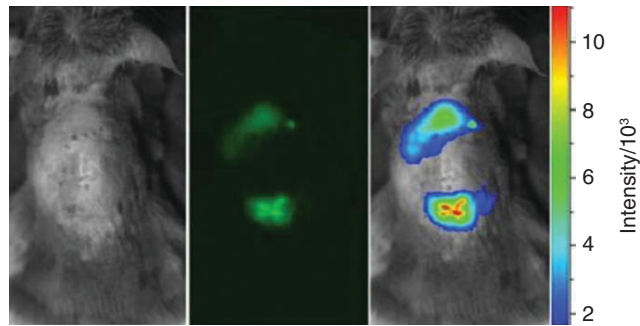


Fig. 22.22 *Subcutaneously injected carbon dots (upper spot) and CZnS-Dots (lower spot) of similar optical densities in mice (470 nm and 525 nm band-pass filters were used for excitation and emission, respectively)*

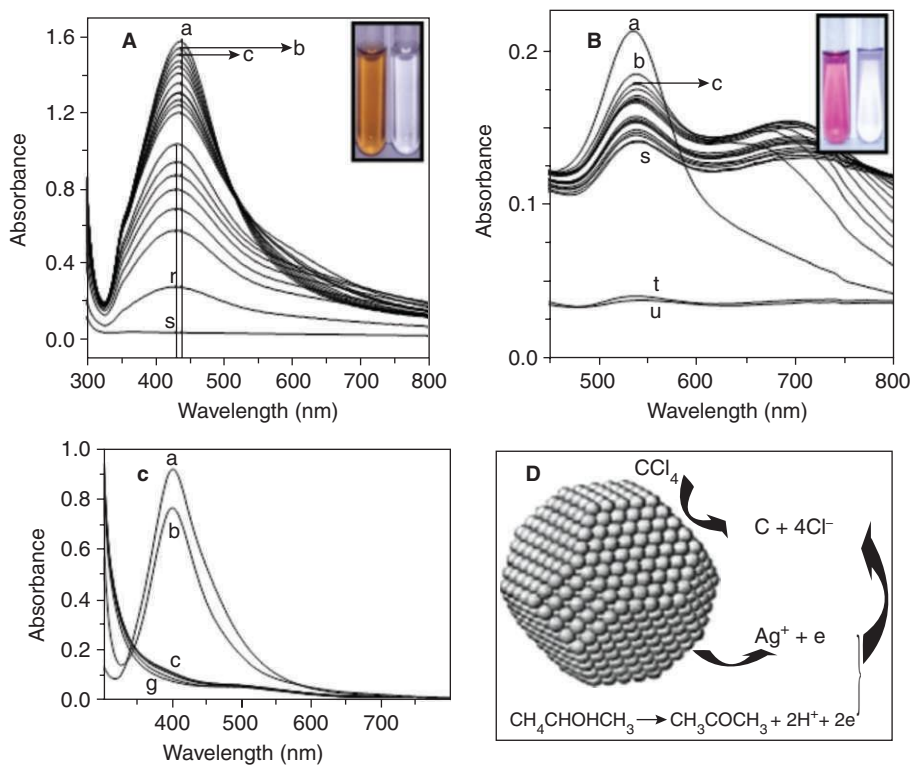


Fig. 24.6

Figure A, B and C show changes to the surface plasmon characteristics of Ag and Au nanoparticles (mixed with 2-propanol to increase the miscibility of halocarbons) upon exposure to the halocarbons. Figure A shows the interaction of Ag nanoparticles with CCl_4 and the time-dependent reduction in the surface plasmon band of Ag is due to its conversion to metal halide. The traces (a-r) were recorded at 30 min intervals and the trace s was recorded after 12 hr. Figure B shows the changes to the absorption profile of Au nanoparticles upon exposure to CCl_4 . Trace b was taken immediately after the exposure to CCl_4 and the subsequent traces were taken in 20 min intervals. The trace u is taken after 48 hr showing the complete degradation. Insets of Figure A and B show the colour changes to the nano reaction mixture before (left) and after (right) the degradation reaction. A similar kind of interaction takes place in the case of CHBr_3 with Ag (Fig. C). The traces recorded in 3 min intervals show the rapid affinity of Ag towards the halocarbon. Figure D shows a schematic of the degradation of halocarbons by the nanoparticles (from author's work).

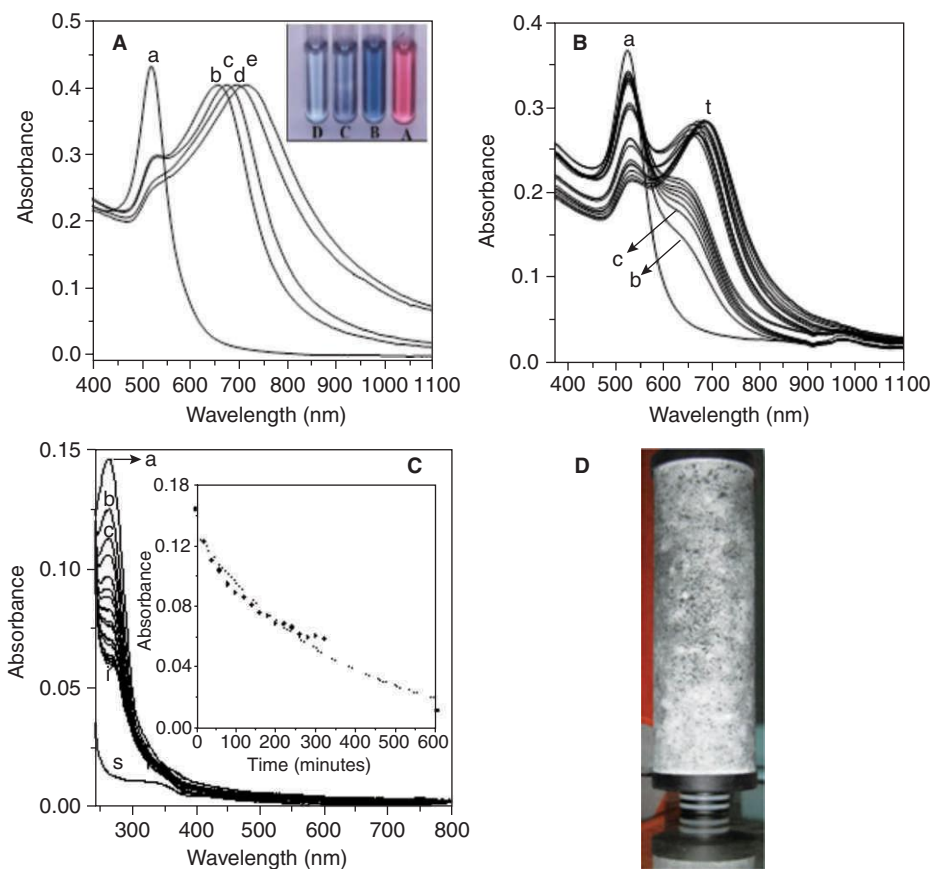


Fig. 24.7 Figure A shows the changes to the absorption spectrum of citrate-stabilised gold nanoparticles (trace a) when exposed to endosulfan of different concentrations (trace b) 2 ppm, (trace c) 10 ppm, (trace d) 100 ppm, and (trace e) 250 ppm. The solutions have the same composition, except for endosulfan. Photographs showing colour changes to the gold nanoparticles upon exposure to endosulfan are shown in the inset. Photograph (A) shows citrate-stabilised nanoparticles and (B), (C) and (D) correspond to the nanoparticles having 2, 10 and 100 ppm endosulfan, respectively. Figure B shows a time-dependence of the absorption spectrum of citrate-stabilised gold nanoparticles upon exposure to 10 ppm endosulfan. (a) original nanoparticle solution, (b) 3 hr after adding endosulfan solution, (c) to (t), at 20-min intervals thereafter. Figure C shows the time-dependent UV-visible spectra showing the adsorption of chlorpyrifos (1 ppm) on supported nanoparticles of Ag ($Al_2O_3@Ag$). Trace a is the absorption spectrum of chlorpyrifos (1 ppm) and traces (b-r) were taken at 20-min intervals after interaction with the nanoparticles. Trace s was taken after 10 hr showing the complete disappearance of chlorpyrifos from water. The inset shows decrease in absorbance vs time from the absorption spectroscopy data for the traces (a-s). The dotted line in the inset shows a fit of the exponential decrease in absorbance with time. Figure D is a pesticide filter devised by the methodology (from author's work).

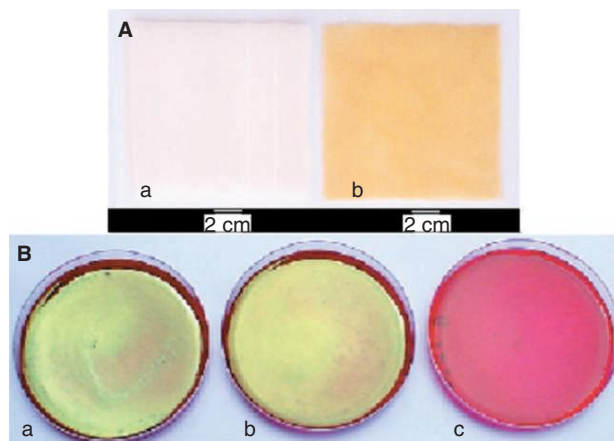


Fig. 24.11 Figure A shows photographs of (a) polyurethane film before Ag coating, and (b), after Ag coating. Golden yellow colour in photograph 'b' is due to the saturation coverage of silver nanoparticles. Figure B shows test tube results for *E. coli* MTCC 1302 for 10^{-2} dilution for 5-min exposure. a) initial count b) after exposure to pure polyurethane and c) after exposure to nanoparticle-coated polyurethane. Characteristic metallic sheen shown by *E. coli* is clearly visible in a, and b, while the bacterium count was zero in c (from Jain and Pradeep, *Biotechnology and Bioengineering*, 2005, 90, 59–63).

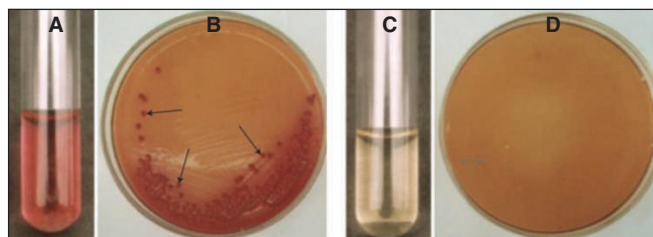


Fig. 24.15 Removal of *E. coli* bacteria by CNTs filter. The turbidity and pink colour in Fig. A is indicative of *E. coli* bacteria in the unfiltered water. Figure B shows the *E. coli* bacterial colonies (indicated by arrows) cultured from the unfiltered water. Note the absence of *E. coli* colonies when the water is filtered through the CNTs filter (Figs C and D). This shows that bundles of CNTs could effectively filter water (from Srivastava et al., *Nat. Mater.*, 2004, 3, 610–14.) (reprinted with permission).

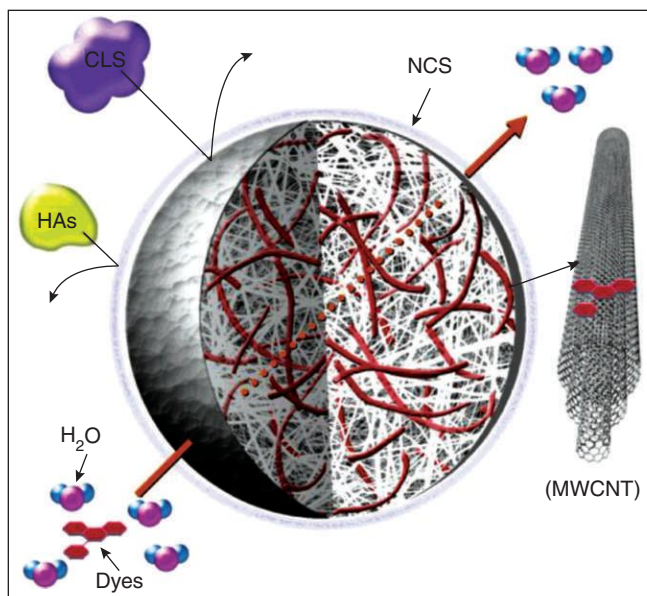


Fig. 24.16 Schematic of the cross-linked microvesicles-CNTs cage structure. The cage restricts the access of negatively charged ions (the surface of the cage is negatively charged and hence by repulsion) and colloids of large size (by size exclusion). The dyes are captured by CNTs by way of Van der Waals interactions between hexagonal carbon sheets of the CNTs and the aromatic backbone of the dyes (reprinted with permission from Fugetsu et al., *Environ. Sci. Technol.* 2004, 38, 6890–96. Copyright (2004) American Chemical Society).